Journal of the European Ceramic Society 16 (1996) 1001–1008

S0955-2219(96)00014-3
0955-2219/96/$15.00

Decomposition of Sm α-SiAlON Phases during Post-Sintering Heat Treatment

Rupeng Zhao & Yi-Bing Cheng*

Department of Materials Engineering, Monash University, Melbourne 3168, Australia

(Received 1 November 1995; revised version received 13 December 1995; accepted 5 January 1996)

Abstract

The microstructural characteristics and the phase assembly of Sm (α+β)-SiAlON ceramics before and after post-sintering heat treatment at 1450°C have been investigated by scanning electron microscopy (SEM), transmission electron microscopy (TEM) and X-ray diffraction (XRD). Grain boundary glass crystallization and the α-SiAlON to β-SiAlON (i.e. α' to β') phase transformation were observed as the major phase transformations occurring during the heat treatment. TEM studies indicated that the α' to β' transformation process itself could produce a nano-sized liquid phase inside the SiAlON grains, which could facilitate the transformation. Based on these observations, it is proposed that the α' to β' phase transformation in Sm SiAlONs is essentially a self-decomposition process of α' phases and may be described as:

$$\alpha' \rightarrow \beta' + M' + AlN\ polytypoid\ phase(s)$$

Therefore, for an unstable α' phase, it would decompose, i.e. proceed α' → β' transformation without having to involve large amounts of grain boundary liquid. However, the existence of the grain boundary liquid and β' grains as nuclei could reduce the activation energy barrier andaccelerate the α' decomposition. © 1996 Elsevier Science Limited.

1 Introduction

Liquid phase sintering, using metal oxides and/or rare earth oxides as sintering additives, is commonly employed for densification of silicon nitride based ceramics. The oxides react with the silica on the surface of silicon nitride powder, resulting in the formation of an oxynitride liquid at sintering temperatures. This liquid phase assists densification but usually remains at grain boundaries as a glassy phase upon cooling, which impairs the high-temperature mechanical properties of the material.[1,2] Post-sintering heat treatment of SiAlON ceramics is used to crystallize the grain boundary glassy phase and subsequently improve the high-temperature properties of the materials.[3,4] Recently, Mandal *et al.*[5]revealed that some rare earth α-SiAlON (α') phases could undergo transformation to β-SiAlON (β') in the heat treatment temperature range between 1100 and 1550°C. α- and β-SiAlONs have different mechanical properties;[6] therefore this discovery may open new routes for tailoring the microstructures and controlling the properties of (α+β)-SiAlON ceramic composites.

The α' and β' phases have distinct compositions and possess different crystal structures.[6] The transformation between α' and β' involves lattice reconstruction and requires a high degree of atomic diffusion. As a result of the strong covalent nature of the bonding associated with both the α' and β' structures, the atomic diffusivity of the species making up the lattices is inherently low. It is, therefore, generally assumed that the α' → β' phase transformation requires a liquid phase to assist the necessary atomic diffusion, but the actual role of the liquid phase has not been fully understood. Recent experiments showed that the amount of grain boundary liquid phase in the sample had marked effects on the transformation, and the introduction of an additional amount of glass into a previously stable α' composition could significantly destabilize the α' phase and promote the α' → β' transformation.[7] Comparing the results in different rare earth SiAlON systems, Mandal and Thompson[7] suggested that the residual grain boundary liquid phase was one of the most important factors influencing the transformation; the rate of the transformation depended mainly on the amount and viscosity of the intergranular liquid phase present during the heat treatment. Shen *et al.*,[8] on the other hand, proposed two possible transformation

*To whom correspondence should be addressed.

routes, one involving a liquid phase, i.e. α' + liquid $\rightarrow$ β' + M' and the other being a direct decomposition of the α' phase to form β' and the aluminium-containing melilite ($Sm_2Si_{3-x}Al_xO_{3+x}N_{4-x}$, M')[9] phases in the Sm ($\alpha+\beta$)-SiAlON system, without the involvement of a liquid phase.

In the present work, X-ray diffraction (XRD), scanning electron microscopy (SEM) and transmission electron microscopy (TEM) are used in the study of the $\alpha' \rightarrow \beta'$ transformation and the associated microstructural changes taking place in isothermal heat treatments at 1450°C. The involvement of liquid phase in the transformation at different stages of heat treatment is assessed through microstructural observations and analyses.

2 Experimental

Samples were pressureless sintered at 1820°C in a nitrogen atmosphere for 4 h, from Si_3N_4, AlN, Al_2O_3 and Sm_2O_3 powders with a starting composition (in wt%) of 72·50Si_3N_4, 14·27AlN, 2·00Al_2O_3 and 11·23Sm_2O_3. Full details of the sample preparation can be found in Ref. 9. XRD analyses revealed that the as-sintered materials contained mainly α' and β' phases and a trace of the 21R polytypoid phase. An amorphous grain boundary phase was also observed in the sample by electron microscope.

The sintered specimen was subsequently heat-treated at 1450°C for a total of 360 h in an alumina tube furnace in flowing high purity nitrogen, with both heating and cooling rates being 3°C min^{-1}. The heat treatment procedure was as follows: after the first 24 h of heat treatment at 1450°C, the sample was cooled down to room temperature and characterized using XRD, SEM and TEM; the same specimen was then reheated to 1450°C for another 36 h, making a total heat treatment time of 60 h. This procedure was repeated five times for the same sample with an interval of 60 h until the total heat treatment time reached 360 h. Three TEM specimens were prepared from the as-sintered sample, and from samples heat-treated for a total of 24 and 120 h. The purpose of this procedure was to ensure that all results were obtained from the same sample, so that any difference in crystalline phases observed can be mainly attributed to the heat treatment process. A thin oxidation layer appeared on the surface of the sample after each heat treatment, which was completely removed by grinding on SiC paper before XRD and SEM examinations.

Specimens for TEM study were carefully cut from the bulk of the sample and were mechanically ground, dimpled to a thickness of ~20 μm, and then ion-milled to electron transparency. All specimens were carbon-coated before TEM and SEM studies to avoid surface charging. XRD was performed using a Rigaku X-ray diffractometer. The relative amount of α' and β' phases, i.e. the β':(α'+β') weight ratio, was measured using the calibration curves developed by Liddell[10] with the intensities of both the α' and β' phases. Micro-structural observations were carried out on a Jeol 840A SEM and a Philips CM20 TEM equipped with an ultrathin-window EDS system.

3 Results

3.1 Rate of the α' to β' transformation

The α' phase was the predominant phase in the as-sintered sample with a β':(α' + β') weight ratio of 11%. Figure 1 shows the XRD patterns of the sample after the heat treatment at 1450°C for various durations. The intensities of the characteristic α' peaks decreased continuously with heat treatment time, whereas β' peak intensities increased. After 240 h, the proportion of the β' phase reached 85 wt% and α' eventually became a minor phase in the sample. This is clear evidence of $\alpha' \rightarrow \beta'$ transformation during the isothermal heat treatment. Accompanying this transformation was the formation of M' phase, which was a combined result of grain boundary glass devitrification[9] and the $\alpha' \rightarrow \beta'$ transformation.[8,11] Quantified β':(α'+β') ratios are presented in Fig. 2, in which the different rates of increase in β': (α'+β') have separated the heat treatment process into several stages. In the first 24 h, the amount of β' increased rapidly. Between 24 and 240 h, the rate of increase in β' was reduced but nearly maintained as a constant. After 240 h, the rate was further slowed down.

A total of 20 wt% increase in β' was found in the initial 24 h, giving an average rate of β' increase of around 0·8 wt% per hour. As pointed out in a previous paper,[11] the simultaneous grain boundary glass crystallization taking place at the same temperature in the initial few hours of the heat treatment could contribute to the increase in the β':(α'+β') ratio. About 7 vol% (i.e. ~11 wt%) of grain boundary glass was detected using an SEM image analyser in the as-sintered sample. Even if taking an overestimation that half of this glass (~5 wt%) crystallized to form β', the average rate increase in the β':(α'+β') ratio resulting from the α' to β' transformation in the initial 24 h would still be greater than 0·6 wt% per hour. This figure is notably higher than that of the subsequent stages, indicating the significance of the grain boundary glass (liquid at 1450°C) in facilitating the $\alpha' \rightarrow \beta'$ transformation. Between 24 and

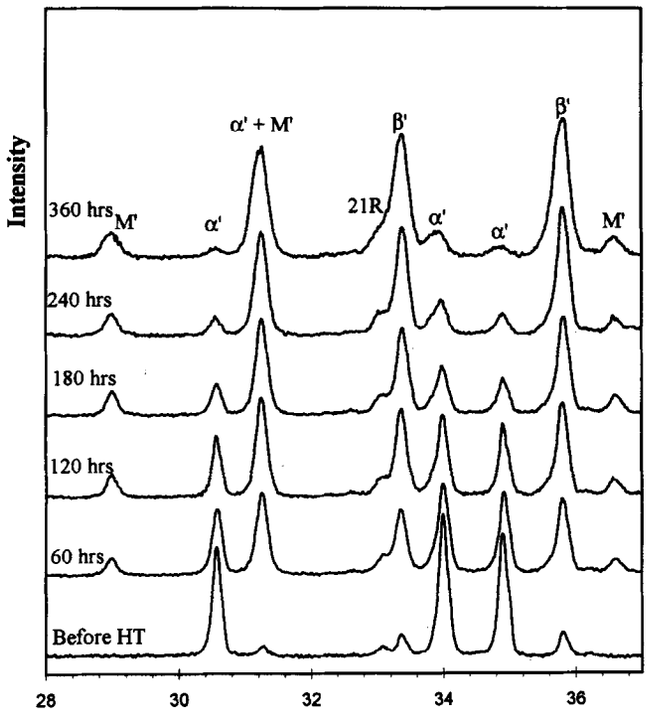

Fig. 1. XRD patterns for the Sm (α+β)-SiAlON specimen after heat treatment at 1450°C for a total of up to 360 h.

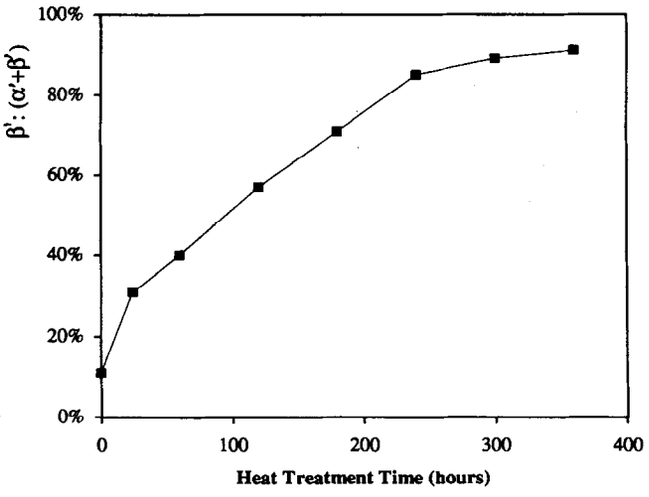

Fig. 2. The β':(α'+β') ratio of the samples heat-treated at 1450°C as a function of heat treatment time.

240 h, the β':(α'+β') ratio increased from 31 to 85 wt% with an almost constant rate of 0·2 wt% per hour. The marked reduction in the rate of β' increment at this stage corresponds to the fact that most of the glassy phase has crystallized after the early heat treatment. Further extension of the heat treatment time up to 360 h resulted in only a slight increase (~0·05 wt% per hour) in the β':(α'+β') ratio, indicating that the system was approaching an equilibrium state.

3.2 Devitrification of the grain boundary glass

The microstructure of the samples before and after the heat treatment was investigated by TEM. Figure 3 shows typical bright-field and dark-field

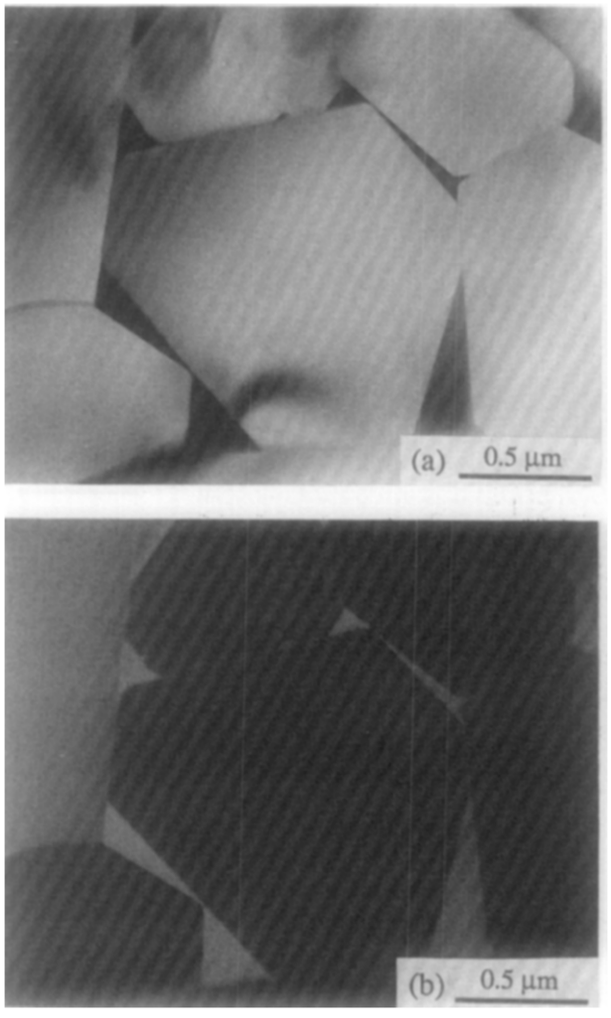

Fig. 3. TEM (a) bright-field and (b) diffused dark-field images from the as-sintered specimen.

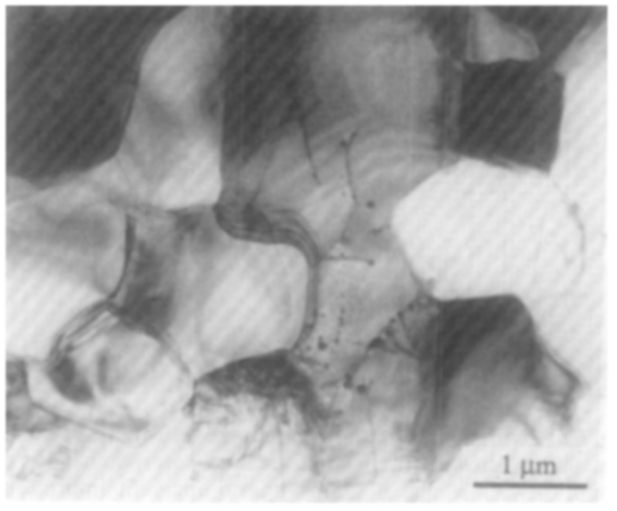

Fig. 4. Typical TEM bright-field image of the sample heat-treated at 1450°C for 24 h.

images of the as-sintered sample. In the bright-field image, the glassy phase appears darker because of its high Sm content, whereas in the diffused dark-field image, the glassy phase appears brighter.[12] It can be seen from Fig. 3 that in addition to the large glassy pockets at multiple grain junctions, every grain in the material is

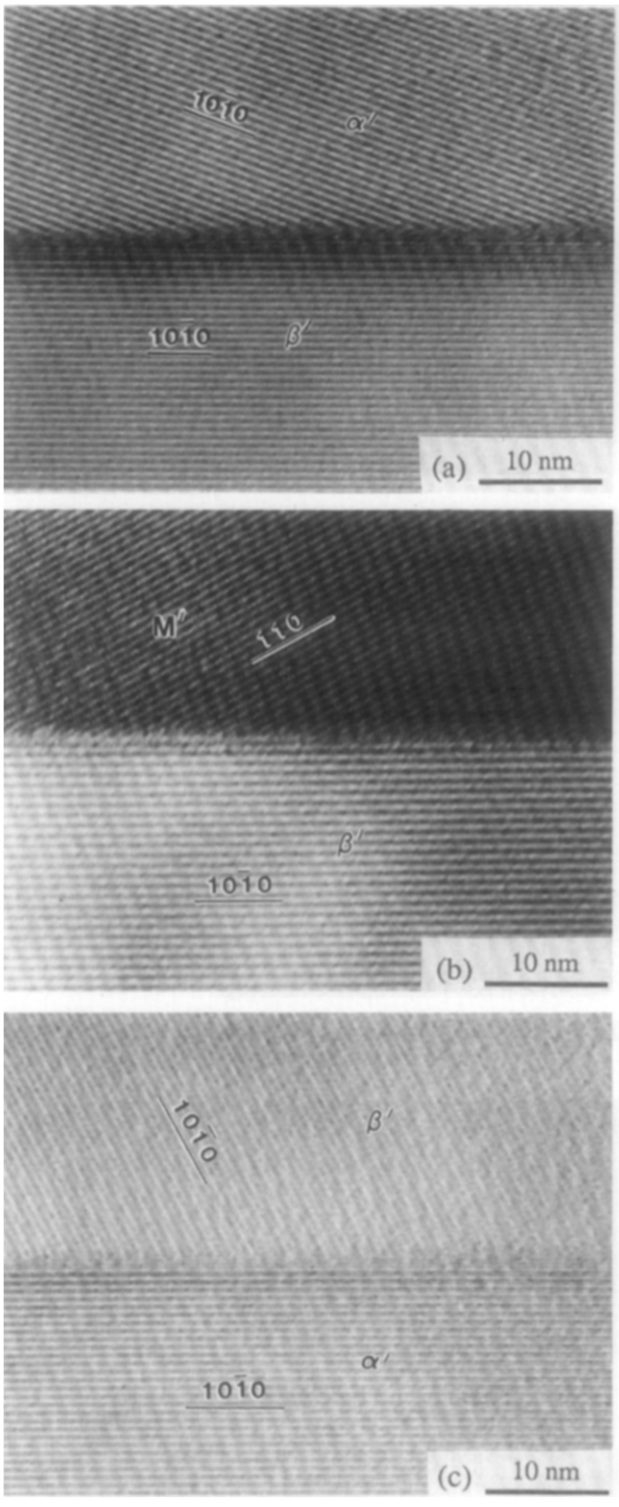

Fig. 5. TEM lattice images of the sample heat-treated for 120 h at 1450°C showing (a) in some areas an amorphous layer of ~1 nm between α' and β' grains; but no apparent amorphous layer is observed (b) between β' and M' grains, and (c) between α' and β' grains in other areas.

surrounded by an amorphous layer, suggesting that the liquid phase forms a three-dimensional interconnected network during sintering. Crystallization of the glassy phase was observed in the sample after heat treatment at 1450°C for 24 h. Extensive TEM observations indicated that all glassy multiple junctions in the samples were crystallized, giving M' as a stable grain boundary phase.[11] A

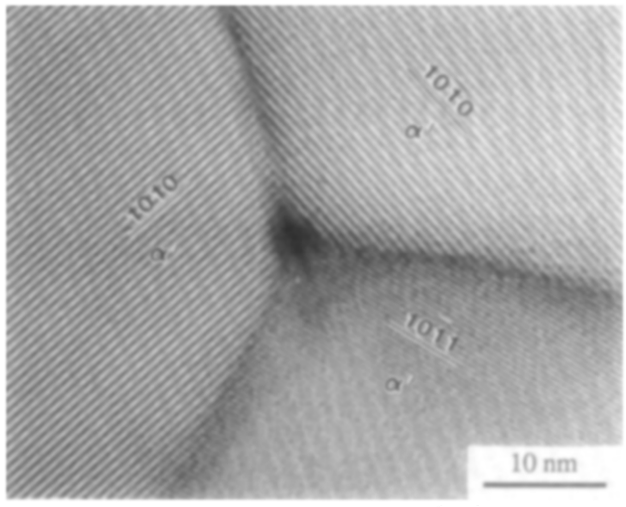

Fig. 6. TEM lattice image of a triple junction among three α' grains, showing a ~2 nm triple pocket in the sample heat-treated for 120 h at 1450°C.

typical bright-field image is shown in Fig. 4. Details of the grain boundaries were further studied by lattice imaging on the samples heat-treated for 24 and 120 h. The results from both samples revealed that, in some areas, an amorphous layer of ~10 Å was observed between SiAlON grains [as shown in Fig. 5(a)], consistent with other observations in silicon nitride ceramics.[13] In other areas, however, no apparent amorphous layer was found [Figs 5(b) and (c)]. The size of the multi-grain pockets was reduced to around 20 Å after the heat treatment (Fig. 6). These observations suggest that post-sintering heat treatment above the eutectic temperature of the system has the potential to fully remove the glassy interface in SiAlON materials.[9]

From the TEM study, the amount of remaining grain boundary glass is very limited after the heat treatment at 1450°C for 24 h. Even assuming that all grains in the heat-treated material are still surrounded by a residual amorphous film 10 Å thick, for a sample with an average grain size of ~1·5 μm it is estimated that the actual volume percentage of this residual glassy phase should not be greater than 0·3%. It is thought that such a small amount of grain boundary glass may only have a very limited role to play in the subsequent α' to β' transformation process.

3.3 Evidence of self-generated liquid in the transforming α' phase

Because of the strong covalent bonding in both α' and β' phases, the atomic diffusivity of the species in SiAlON structures would be extremely low without the assistance of a liquid phase. TEM microstructural study[14] revealed that the transformed β' grains in a sample heat-treated for 120 h have unique microstructural features consisting of a high density of dislocations and nano-sized spherical inclusions (Fig. 7). The inclusions are

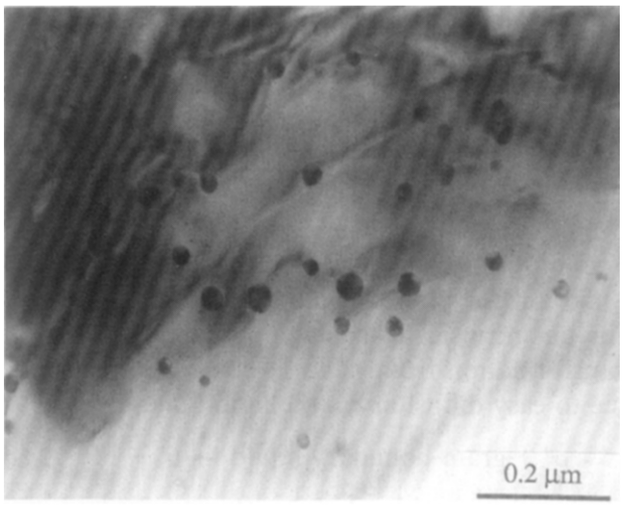

Fig. 7. TEM image of nano-sized spherical inclusions within a transformed β' grain. The area fraction of the inclusions in this area was 6%, corresponding to a volume fraction of 2·5%. The sample was heat-treated at 1450°C for 120 h.

often closely associated with dislocations and rich in Sm, coinciding with the expectation that the $\alpha' \rightarrow \beta'$ transformation requires the rejection of the stabilizing cation (Sm^{3+} in the present case) from the α' lattice. The perfect spherical shape of these inclusions implied that they were of a liquid nature at the heat treatment temperature. Similar microstructural features have also been observed in the sample heat-treated for 24 h. Figure 8 is an enlargement of a grain in Fig. 4 and shows bright-field and diffused dark-field images of a β' grain containing many spherical inclusions. It can be seen that most inclusions in a widely dispersed area appeared brighter in the diffused dark-field image [Fig. 8(b)], indicating the possible amorphous status of these inclusions. Because there is no mechanism for the β' phase to accommodate the Sm-rich inclusions inside its structure, it is postulated that the spheroid-containing β' grain is virtually the one that has transformed from an α' structure, and the nano-sized inclusions are liquid regions produced as a result of the rejection of Sm species from the original α' grain. The exact mechanism of this local liquid phase formation is unclear at this stage and deserves further investigation. In this paper, the dispersed liquid phase found inside the SiAlON grains is referred to as the *self-generated liquid* to distinguish it from the grain boundary liquid formed during sintering.

The volume percentage of these inclusions in the area shown in Fig. 7 is around 2·5%, estimated on the basis of the measured thickness of the specimen and the area fraction of the inclusions in the image. The quantity of this internal self-generated liquid in local areas is significantly higher than that of the residual glass at grain boundaries. Therefore it is expected that the self-generated liquid phase would play a more active role in

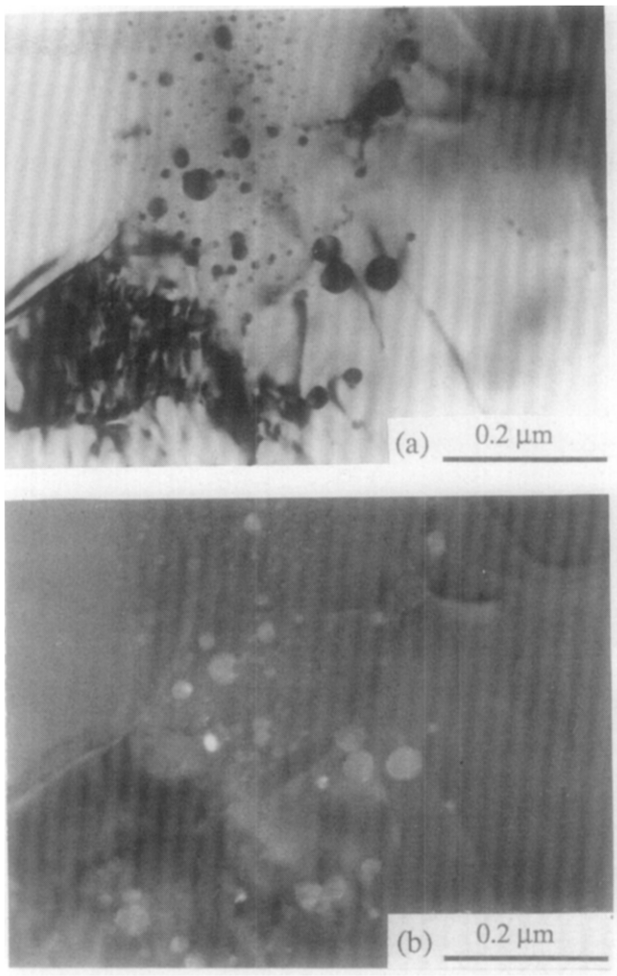

Fig. 8. TEM (a) bright-field and (b) diffused dark-field images of inclusions in the sample heat-treated for 24 h at 1450°C. The brighter contrast of the inclusions in the diffused dark-field image suggests that they are of an amorphous nature.

facilitating the $\alpha' \rightarrow \beta'$ transformation after the grain boundary crystallization. Although the inclusion-containing β' grains are commonly observable in these samples, it is generally true that they do not appear in a great quantity and tend to be isolated by less characteristic SiAlON grains of both α' and β' forms (Fig. 4), which corresponds to a very sluggish transformation process (<1 wt% per hour). It is not exactly clear how this type of microstructure has developed at the moment, but it may denote the importance of suitable nucleating sites to the transformation.

4 Discussion

4.1 Involvement of the grain boundary liquid in the transformation

The observation of $\alpha' \rightarrow \beta'$ transformations in rare earth SiAlON systems has indicated the unstable characteristic of some α' compositions in a certain temperature range. However, the strong covalent bonding in both the α' and β' lattices and the reconstructive nature of this phase transformation may prevent the process from occurring

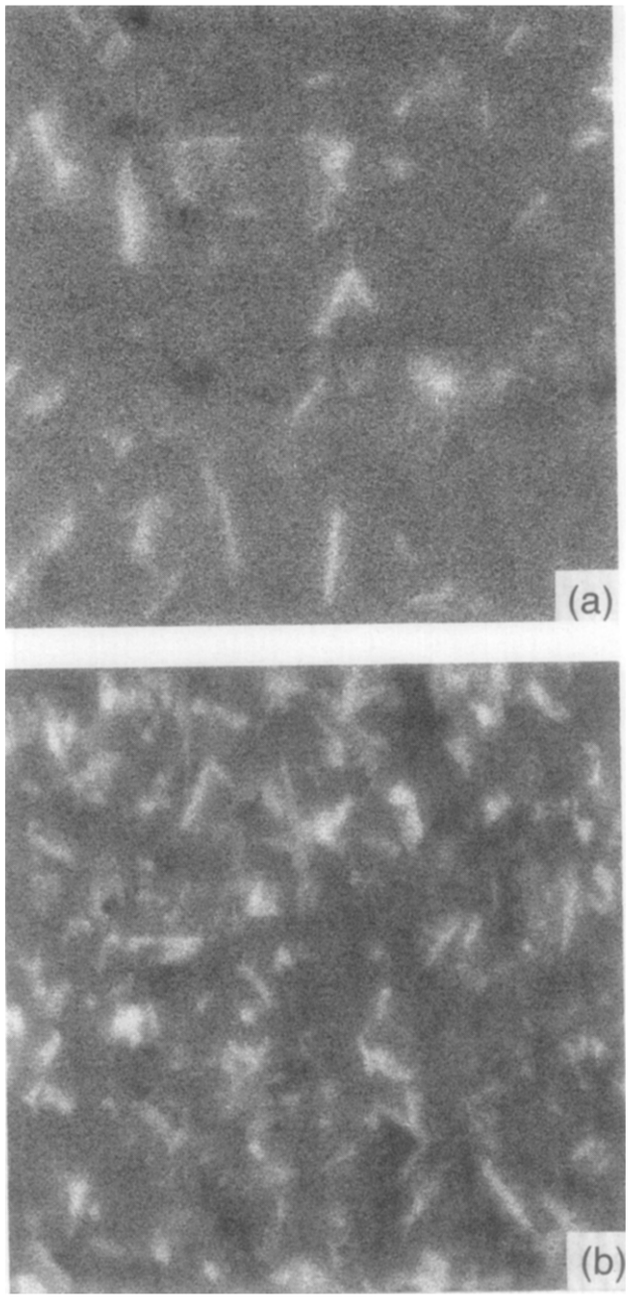

Fig. 9. EDS Al X-ray maps of (a) the as-sintered sample and (b) the sample heat-treated for a total of 360 h at 1450°C. The bright regions in the Al X-ray maps correspond to the 21R phase ($SiAl_6O_2N_6$), which has the highest Al concentration in the material.

if the material was fast cooled or if no liquid phase existed to assist the necessary atom diffusion. On the other hand, there is always a glassy phase remaining at SiAlON grain boundaries after liquid phase sintering. This glass is a supercooled oxynitride liquid and softens above the glass transition temperature (T_g), ranging between 900 and 1000°C.[5] The viscosity of a liquid phase drops exponentially with increasing temperature above the T_g,[15] and it is thought that the grain boundary liquid would become very reactive at 1450°C. Although melting of the grain boundary glass may not ensure an $\alpha' \rightarrow \beta'$ phase transformation, it would promote chemical reactions between molten glass and α' phases, modifying the α' compositions, and foster lattice diffusion.

The active involvement of the grain boundary liquid in the transformation process is marked by the highest $\alpha' \rightarrow \beta'$ transformation rate achieved in the initial 24 h of heat treatment (Fig. 2). Two types of reactions involving both the grain boundary liquid and α' phases could take place at 1450°C. For an intrinsically unstable α' composition, the transformation from α' to β' could be accelerated due to easy diffusion via the liquid phase:[8,16,17]

$$\alpha' + \text{grain boundary liquid} \rightarrow \beta' + \text{M}' \quad (1)$$

whereas for a stable α' phase, its composition may be altered through a chemical reaction:[8]

$$\alpha'_1 + \text{grain boundary liquid} \rightarrow \alpha'_2 + \text{M}'. \quad (2)$$

The stability of the α'_2 phase is dictated by the new composition as well as the continuing reaction with the liquid. Obviously, a larger volume of the grain boundary liquid phase in the materials would greatly extend change the α' composition and even destabilize α' structures. This is in agreement with the reported experimental results.[7]

The interaction between the grain boundary liquid and SiAlON phases at 1450°C is also imperative for M' to form as a grain boundary crystalline phase. The maximum nitrogen concentration in an Sm oxynitride glass is about 40 eq%.[18] Both reactions (1) and (2) could lead to an increase in the N content of the liquid from which the M' phase, containing 53 eq% nitrogen, could precipitate.[9] The M' phase has a high Sm content and it is more stable than some of the α' compositions at the heat treatment temperature. As a result, the formation of M' provides an additional driving force for the $\alpha' \rightarrow \beta'$ transformation. It becomes clear from the above discussion that the volume and the viscosity of the grain boundary liquid phase can markedly affect the $\alpha' \rightarrow \beta'$ transformation process at the initial stage of heat treatment when the grain boundary crystallization is not yet complete.

4.2 Role of the self-generated liquid in the transformation

After the initial period of heat treatment (e.g. $t >$ 24 h), the volume percentage of the residual grain boundary glass is reduced from ~7 vol% to <0·3 vol%, hence its role in the transformation would be severely restricted. Moreover, the M' phase is very stable at 1450°C; once it has formed, it would not remelt to become a grain boundary liquid phase and to be involved in the $\alpha' \rightarrow \beta'$ transformation at this temperature.[8,9] The rate of the $\alpha' \rightarrow \beta'$ transformation at the second stage ($24 < t$

< 240 h) is lower than that at the first stage (t < 24 h) but the process continues at a nearly constant rate, suggesting an additional mechanism(s) to be operative. The activation energy of a reconstructive phase transformation will be significantly reduced if the atomic diffusion is assisted by a liquid phase and/or if there exist nuclei to reduce the interfacial energy. The occurrence of the self-generated liquid in transformed β' grains leads to a logical assumption that this liquid phase may have played a major role in promoting atomic diffusion and facilitating α' → β' transformation after crystallization of the grain boundary liquid. Because it involves a liquid phase emerging from the transforming α' phase itself, the transformation from α' to β' can proceed without involving much grain boundary liquid and a steady rate of the transformation is expected. This is in agreement with the experimental observation. The appearance of the Sm-rich spheroids in the β' phase results in thermodynamic instability, hence these nano-sized inclusions would eventually diffuse out of the transformed β' grains through the easy path of dislocations. It is, therefore, suggested that the amount and viscosity of the self-generated liquid within the transforming α' grains is a determining factor in controlling the rate of the α' → β' transformation when most of the grain boundary glass has been crystallized.

4.3 Decomposition of α-SiAlON phases

Without much involvement of grain boundary glass, the α' → β' transformation at the second stage may be regarded as a decomposition process of α-SiAlON phases. This suggests that, below a certain temperature, some of the α' compositions have a higher free energy than β' phases, and the transformation from α' to β' would occur if it could be thermally activated. Because of the compositional difference between α' and β' phases, the decomposition of an α' phase must produce other phase(s) in addition to a β' composition. Shen *et al.*[8] suggested a possible route for this reaction:

$$\alpha' \rightarrow \beta' + \mathrm{M}' \qquad (3)$$

which seemed reasonable according to the XRD observations (Fig. 1). If the actual compositions of all the phases involved are considered, however, the proposed reaction (3) would yield excessive amounts of Al and N. To balance the compositions, therefore, one has to assume the formation of AlN polytypoid in addition to the β' and M' phases. AlN polytypoids are compatible with α', β' and M' phases in the Sm and Nd SiAlON systems,[19] and the 21R polytypoid phase was commonly observed in the present samples before and after heat treatments.

There are some experimental difficulties in quantifying the AlN polytypoid phase by using the XRD and SEM backscattered imaging techniques. Almost all the XRD peaks of the 21R polytypoid strongly overlap with those of α', β' or M' phases, and there are no detectable differences between the polytypoid and β' phases in SEM backscattered images because of the similar atomic weights of Si and Al elements. For these reasons, there have been few reports on the quantification of AlN polytypoid phases in the literature. Nevertheless, our recent study has showed that it is possible to analyse the amount of the 21R polytypoid phase by using the EDS X-ray mapping technique. Details of this work will be reported elsewhere.[20] Figure 9 shows the Al X-ray maps from the (a) as-sintered and (b) 360 h heat-treated samples. The bright regions in the Al maps correspond to the 21R phase ($SiAl_6O_2N_6$), which has the highest Al concentration among all phases in the samples. It can be seen that the amount of the 21R phase increases considerably after the heat treatment, which cannot be simply accounted for the grain boundary glass devitrification. The increase in the 21R phase appearing in the XRD profiles (Fig. 1) is not as clear as that showed in the X-ray maps and the difference is not fully understood at the present time. Considering the strong overlap in the XRD peaks and the excellent resolution of the characteristic X-ray maps, however, it is plausible to conclude that the AlN polytypoid phase is also a product of the α' → β' phase transformation. With this result and the observed self-generated liquid phase, a new reaction path is proposed for the decomposition of the Sm α-SiAlON phases:

$$\alpha' \xrightarrow{\text{internal liquid}} \beta' + \mathrm{M}' + 21\mathrm{R}. \qquad (4)$$

It is suggested that an unstable α' phase could decompose into a β' phase plus M' and 21R polytypoid, and the process is assisted by the self-generated liquid phase formed during the decomposition. It is thought that the α' decomposition is a dominant phenomenon proceeding during this phase transformation and the grain boundary glass is mainly involved in the initial stage of the process. From this point of view, the α' → β' transformation may be considered as a part of the story of the α' phase decomposition.

5 Conclusions

Some of the Sm α-SiAlON compositions are thermodynamically unstable and may decompose at

elevated temperatures (e.g. 1450°C). The result of this decomposition appears most prominently in the form of the $\alpha' \rightarrow \beta'$ transformation, although other phases have also been produced. At the initial stage, the decomposition process is assisted by the grain boundary liquid phase and progresses readily. When most of the grain boundary glass is crystallized, the rate of this decomposition becomes much slower but is maintained roughly constant until the system is close to equilibrium. The α' decomposition produces a self-generated liquid phase inside the SiAlON grains, which could in turn facilitate atom diffusion. The final products of the α' decomposition include β', M' and 21R polytypoid phases.

Acknowledgement

This work was supported by the Australian Research Council.

References

1. Jack, K. H., Review: SiAlONs and related nitrogen ceramics. *J. Mater. Sci.*, **11** (1976) 1135–58.
2. Ekström, T. & Nygren, M., SiAlON ceramics. *J. Am. Ceram. Soc.*, **75** (1992) 259–76.
3. Lewis, M. H., Crystallisation of grain boundary phases in silicon nitride and SiAlON ceramics.In *Silicon Nitride 93, Key Engineering Materials Vol. 89–91*, eds M. J. Hoffmann, P. F. Becher & G. Petzow. Trans Tech Publ. Switzerland, 1993, pp. 333–8.
4. Thompson, D. P., New grain boundary phases for nitrogen ceramics. In *MRS Symposium Proceedings Vol. 287, Silicon Nitride Ceramics — Science and Technological Advances*, eds I-Wei Chen *et al.* MRS, Pittsburgh, PA, 1993, pp. 79–92.
5. Mandal, H., Thompson, D. P. & Ekström, T., Reversible $\alpha \leftrightarrow \beta$ SiAlON transformation in heat-treated SiAlON ceramics. *J. Eur. Ceram. Soc.*, **12** (1993) 421—9.
6. Hampshire, S., Nitride Ceramics, In *Materials Science and Technology, Vol. 11 Structure and Properties of Ceramics*, ed. M. Swain. VCH, Weinheim, 1994, pp. 121–71.
7. Mandal, H. & Thompson, D. P., Mechanisms for α to β-SiAlON transformation. *Proc. 4th Conf. Eur. Ceram. Soc. Conf.*, Italy, 1995, pp. 327–34.
8. Shen, Z. J., Ekström, T. & Nygren, M., Temperature stability of samarium doped α-SiAlON ceramics. *J. Eur. Ceram. Soc.*, **16** (1996) 43–54.
9. Cheng, Y.-B. & Thompson, D. P., Preparation and grain boundary heat-treatment of samarium α-SiAlON ceramics. *J. Eur. Ceram. Soc.*, **14** (1994) 13–21.
10. Liddell, K., "X-ray analysis of nitrogen ceramic phases." M.Sc. Thesis, University of Newcastle upon Tyne, 1979.
11. Zhao, R. & Cheng, Y.-B., Phase transformation in Sm (α+β)-SiAlON ceramics during post-sintering heat treatments. *J. Eur. Ceram. Soc.*, **15** (1995) 1221–8.
12. Clark, D. R., On the detection of thin intergranular films by electron microscopy. *Ultramicroscopy*, **4** (1979) 33–44.
13. Kleebe, H. J., Cinibulk, M. K., Cannon, R. M. & Ruhle, M., Statistical analysis of intergranular film thickness in silicon nitride ceramics. *J. Am. Ceram. Soc.*, **76** (1993) 1969–77.
14. Zhao, R., Cheng, Y.-B. & Drennan, J., Microstructure features of the α to β-SiAlON phase transformation. *J. Eur. Ceram. Soc.*, **16** (1996) 529–34.
15. Paul, A., *Chemistry of Glasses*, Chapman and Hall, London, 1990.
16. Cheng, Y.-B., & Thompson, D. P., Aluminium-containing nitrogen melilite phases. *J. Am. Ceram. Soc.*, **77** (1994) 143–8.
17. Shen, Z. J., Ekström, T. & Nygren, M., Homogeneity region and thermal stability of neodymium doped α-SiAlON ceramics. *J. Eur. Ceram. Soc.*, in press.
18. Tu, H. Y., Sun, W. Y., Wang, P. L. & Yan, D. S., Glass-forming region in the Sm–Si–Al–O–N system. *J. Mater. Sci. Lett.*, **14** (1995) 1118–22.
19. Sun, W. Y., Yan, D. S., Gao, L., Mandal, H., Liddell, K. & Thompson, D. P., Subsolidus phase relationships in the systems Ln_2O_3–Si_3N_4–AlN–Al_2O_3 (Ln = Nd, Sm). *J. Eur. Ceram. Soc.*, **15** (1994) 349–55.
20. Zhao, R. & Cheng, Y.-B., The formation of AlN polytypoid phases during α-SiAlON decomposition. *J. Am. Ceram. Soc.*, submitted.

Journal of the European Ceramic Society 16 (1996) 1009–1020

S0955-2219(96)00020-9
0955-2219/96/$15.00

High-temperature Fatigue of a Gas-Pressure-Sintered Silicon Nitride

M. Wang, M. Li, A. J. Bushby, F. Guiu, M. J. Reece* & M. F. R. Sammur†

Department of Materials, Queen Mary & Westfield College, Mile End Road, London E1 4NS, UK

(Received 20 September 1995; revised version received 20 December 1995; accepted 3 January 1996)

Abstract

The fatigue behaviour of a gas-pressure-sintered silicon nitride has been investigated at 1000°C. The growth of long (>100 μm) subcritical fatigue cracks was observed directly and the time to failure of uniaxially loaded specimens caused by the growth small (<100 μm), machining flaws was measured. Oxidation in the crack-tip region reduced the fatigue resistance of the material. Cracks grew under the co-operative effect of stress, oxidation and flow of the viscous oxide phase formed. This mechanism would explain why crack growth rates were greater under static loading than cyclic loading because of the more damaging effect of sustained crack opening. Because of the relatively small size of the oxidized crack-tip region and its slow advancement, the high temperature fast fracture behaviour was similar to that at room temperature and a similar value of K_{IC} *was estimated.* © *1996 Elsevier Science Limited.*

1 Introduction

In recent years silicon nitride has emerged as an important ceramic for high-temperature structural applications mainly owing to its high strength, good oxidation resistance and excellent thermal shock resistance. Extensive research has been conducted on the room-temperature mechanical properties of this material and its associated composites.[1,2] It is generally recognized that the optimum microstructure of monolithic silicon nitride should consist of randomly oriented, acicular β-Si_3N_4 grains in order to achieve high strength together with high fracture toughness. Such a microstructure can provide the grain bridging and/or crack deflection mechanisms which are necessary for crack shielding and hence improve fracture toughness and flaw tolerance. However, the amount and composition of residual glass after sintering as a result of using oxide additives such as MgO, Al_2O_3 and/or Y_2O_3 to assist the α-Si_3N_4 to β-Si_3N_4 transformation and densification, affect the high temperature properties, particularly creep, of the ceramic.

If silicon nitride components are to be subjected to high-temperature exposure as well as sustained cyclic loading in service, the accumulation of damage in the material due to oxidation and stress loading needs to be understood and predictable before ceramic components can be used confidently.[3] However, only limited work has been done and we are still a long way from being able to predict accurately the long-term performance of silicon nitride components.

The mechanical fatigue behaviour of ceramic materials has attracted increasing attention ever since it was found that ceramics are, like metals, susceptible to a degradation of properties when subjected to fluctuating loading.[4] More recent experimental results show that subcritical crack growth can occur in various ceramics and ceramic matrix composites during static and cyclic loading at room temperature.[5–13] Generally, cyclic loading is more detrimental than static loading at room temperature, with higher crack growth rates under cyclic loading than under static loading at the same maximum stress intensity factor.[5–9,13] The high-temperature fatigue results of some selected ceramics and ceramic matrix composites[14–19] suggest that the viscous intergranular glassy phase, a product of either the sintering process due to the addition of sintering additives or oxidation at high temperature, significantly influences crack propagation behaviour and fatigue life. In most cases, cyclic loading leads to lower crack growth rates at elevated temperatures than static loading with the same maximum stress intensity factor.[15,19–21] This is the reverse of what has been reported from room-temperature studies. This difference is attributed to the rate-dependent nature of viscous deformation of the grain boundary glassy phases at high temperatures.[14,15,18,19]

*To whom correspondence should be addressed.
†Nuclear Electric, Technology Division, Canal Road, Gravesend DA12 2RS, UK.

Assuming that the mechanisms of crack growth under static and cyclic loads are the same, the relative crack growth rates under cyclic and static loading can be predicted by an integration of the crack growth velocity.[19,21–24] The crack velocity, v, has the following power-law dependence on the applied stress intensity factor, K

$$v = AK^n \tag{1}$$

where A and n are constants for the material under a particular set of conditions and K is equal to

$$K(t) = \sigma(t) Y \sqrt{\pi a} \tag{2}$$

where $\sigma(t)$ is the time-dependent applied stress, Y is a geometric factor (which is dependent on normalized crack length in finite specimen geometries, but is often assumed to be effectively independent of crack length) and a is the crack length.

The ratio of the cyclic and static velocities, and therefore inverse times to failure, is approximately

$$\frac{v_c}{v_s} = \frac{t_s}{t_c} = \frac{\int_0^{1/f} \sigma_c^n(t)dt}{\sigma_c^n} \tag{3}$$

where f is the cyclic test frequency. For a static load equal to the peak cyclic load, this predicts that cyclic growth rates will be smaller than static rates. At room temperature the measured cyclic crack growth rates are in fact higher than the static fatigue rates. This indicates that a true mechanical fatigue effect exists and that cyclic fatigue is not simply a manifestation of static fatigue effects.[24] At high temperature the cyclic crack growth rates are lower than the static rates, but their ratios are not necessarily consistent with the ratios predicted above.[21] It is therefore obvious that different fatigue mechanisms must operate for the same ceramic material at different temperatures. The adhesive effect of viscous grain boundary phases on crack surfaces was proposed to explain the deviations between the predictions and measurements for the high-temperature fatigue of ceramics.[14] Cyclic fatigue behaviour and lifetime predictions are consequently even more complicated at high temperatures than at room temperature. Factors such as test frequency, cyclic waveform and creep, which may have little relevance at room temperature, become important at high temperatures.

The high-temperature fatigue life of silicon nitride has been investigated by several workers,[14,17,25,26] but there are only a few publications concerning high-temperature fatigue crack growth in silicon nitride or other ceramics.[19,21,27] In most of the reported investigations, the fatigue specimens were enclosed in a large, fully closed furnace and the tests were periodically interrupted for the crack length measurements. This involved lengthy periods for furnace cool-down and heat-up together with careful preparation of specimen surface replicas. It was justified that such interruptions did not affect the measured crack growth rates.[21]

In this study, a furnace arrangement was used that eliminated the need to interrupt the fatigue test and enabled the subcritical growth of long cracks (>100 μm) to be monitored continuously *in situ*.[28,29] Also, the fatigue crack growth behaviour of small surface flaws (>50 μm) was investigated by push–pull fatigue testing of machined cylindrical specimens. The fatigue crack growth behaviour of a silicon nitride at 1000°C is reported, and a possible crack growth mechanism is proposed in light of the fatigue test results and microscopic observations.

2 Materials and Experimental Techniques

The material studied was a gas-pressure-sintered silicon nitride (GPSSN) with yittra and alumina additives supplied by NGK Spark Plug Co., Japan. The as-received material consisted principally of β-Si_3N_4, which had an elongated grain structure with the aspect ratio of the grains varying from between 1 to 5. The grain diameter (measured across the basal plane) was up to 1·0 μm (Fig. 1). The porosity of the material was low (<1%). The silicon nitride grains were separated by a very thin, glassy, intergranular phase, which was found through high-resolution lattice imaging to be 1·0–2·0 nm thick between adjacent Si_3N_4 grains. This amorphous glassy phase, which was located mainly at multi-grain junctions, contained Y, Al, Si and O [Fig. 2(a)]. Most of the glassy phase crystallized at some grain boundaries during the high-temperature fatigue testing [Fig. 2(b)]. Similar crystallization behaviour was found in a

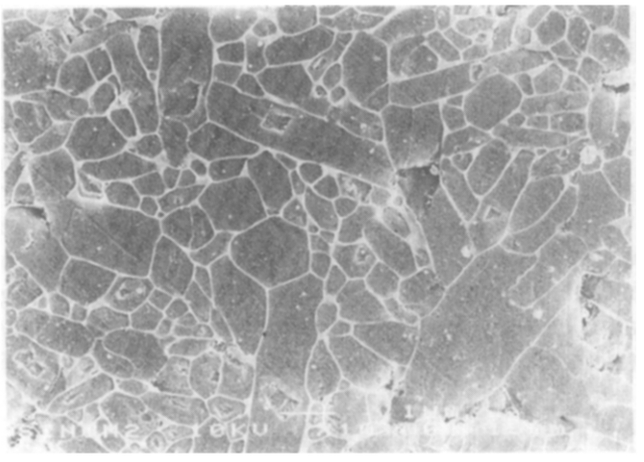

Fig. 1. Microstructure of as-received gas-pressure-sintered silicon nitride revealed by plasma etching.

similar silicon nitride after high-temperature annealing and creep testing.[30] The crystallization of the intergranular phase is likely to have a significant influence on high-temperature mechanical behaviour.

Double cantilever beam (DCB) specimens were used for the slow crack growth experiments [Fig. 3(a)]. These specimens were polished progressively using 14 μm, 6 μm, 3 μm and 1 μm diamond pastes on a lapping machine. They were subsequently cleaned ultrasonically in an acetone bath to reveal polished, shiny surfaces which were necessary for crack observation and length measurements during the high-temperature fatigue tests. A groove, 0·7 mm wide and 1 mm deep, was cut into the reverse side of the specimens in order to confine the growth of the fatigue crack through the centre of the specimen.

For the slow crack growth experiments a compact and accessible furnace was used in which the DCB specimens were heated directly by infra-red radiation.[28,29] This furnace allowed both cold gripping of the specimen and direct viewing of the growing crack. It was installed on a Mayes servo-hydraulic testing machine. The crack was monitored through air-cooled windows and its length measured with a travelling microscope which was mounted on a micrometer stage on the furnace casing. The furnace temperature was measured using a Pt/Pt–13Rh thermocouple placed at the base of the specimen notch.

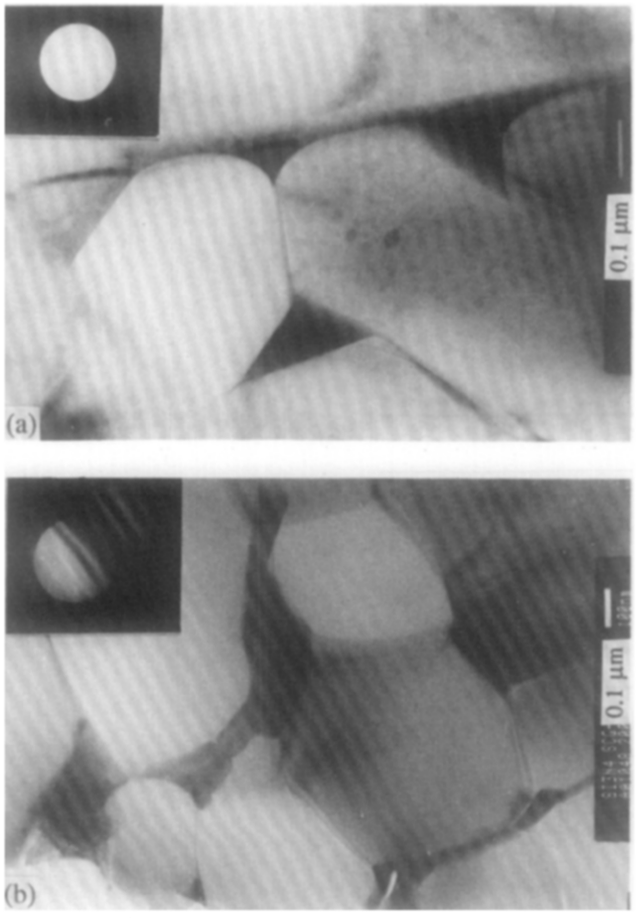

Fig. 2. Intergranular phases in silicon nitride and corresponding convergent beam electron diffraction patterns: (a) as-received material; and (b) material tested at 1000°C.

In the current investigation, the infra-red radiation from the heaters was de-focused to produce bands of heating near the specimen edges. A near constant temperature distribution (1010 ± 10°C) was obtained across the specimen in the area of interest [Fig. 4(a)]. The temperature gradient introduced thermal stresses in the specimen and these were calculated from the temperature distribution via a finite element method. The most important thermal stress components caused by the furnace set-up were the stresses normal to the direction of crack propagation. For a crack of 16·5 mm in length (a/w = 0·43), the normal stress was tensile within a distance of 3 mm ahead of the crack tip and was compressive over greater distances. This stress distribution translated with the tip of the crack as it propagated, so that the stress profile seen by the crack tip remained nearly constant. The magnitude of the stress intensity factor, K_t, produced by these normal thermal stresses was calculated and found to be of the order of 0·4 MPa $m^{1/2}$ for most crack lengths. In the calculations, it was assumed that the temperature distribution was not changed when the crack propagated. The value of K_t is taken into account in our calculation of the total stress intensity factor at the crack tip during the high-temperature fatigue test.

Because there are no published formula for the short DCB specimen geometry used in the current investigation, the compliance method was used to experimentally obtain the stress intensity factor K_I for a varying crack length. A steel specimen of the same geometry and size as the ceramic specimen was used and a capacitance displacement transducer was attached to the specimen to measure the notch opening displacement with a resolution of better than 0·1 μm. Figure 5 shows the experimentally determined calibration of the normalized stress intensity factor, $K_I B\sqrt{w}/P$, with crack length for the short DCB specimen (w/h = 3·0), together with published data for DCB specimens of different dimensions. B is the specimen thickness, w is the specimen length shown in Fig. 3(a) and P is the applied load.

The slow crack growth experiments were conducted using both static loading and cyclic sinusoidal loading at a frequency of 1 Hz. The specimen was pre-cracked at 1000°C prior to the beginning of the fatigue test by slowly applying a monotonic tensile load while the notch tip was being observed through the travelling microscope. As soon as a crack appeared at the notch tip, the

load was reduced to zero. The pre-crack length obtained was then approximately 4 mm. The testing was started with an initial static load of 50 N which was increased in steps of 10 N every 30 min until crack propagation was observed. Each time the loading condition (static or cyclic) was changed, the test was re-started with a low load and the procedure described above was repeated. In between the different loading conditions, the testing was stopped, the load reduced to zero before the specimen was cooled and the specimen removed from the testing machine for examination of the crack path under a field-emission scanning electron microscope (JEOL 6300F). The specimen fractured catastrophically at the end of the final static fatigue test when no attempt was made to reduce the crack growth rate. The heaters were switched off instantly and compressed air jets forced rapid cooling of the fractured specimen.

The push–pull specimens were machined by rotary grinding with a diamond-bonded wheel (grit size 240) into double-waisted cylindrical specimens [Fig. 3(b)]. The specimens were machined to strict tolerances of both size and straightness to minimize bending stresses on loading. Some of the specimens were tested in this as-machined state and others were annealed at 1000°C in air for 27 h prior to testing; to distinguish between them they are referred to 'as-machined' and 'annealed', respectively. In the push–pull tests the specimens were heated using two parabolic radiant heaters, of 750 W power each, focused into spots of 6 mm diameter on the central gauge length. The ends of the specimens were friction clamped with water-cooled hydraulic grips with facilities for alignment and adjustment in tilt and shift. The specimen temperature was controlled to ±2°C with a thermocouple (Pt.Pt–13%Rh) looped around the centre of the gauge length. The temperature profile along the specimens is shown in Fig. 4(b), where it can be seen that there was a temperature drop of less than 100°C between the centre and end of the specimen gauge length. Of the 21 specimens tested, only four

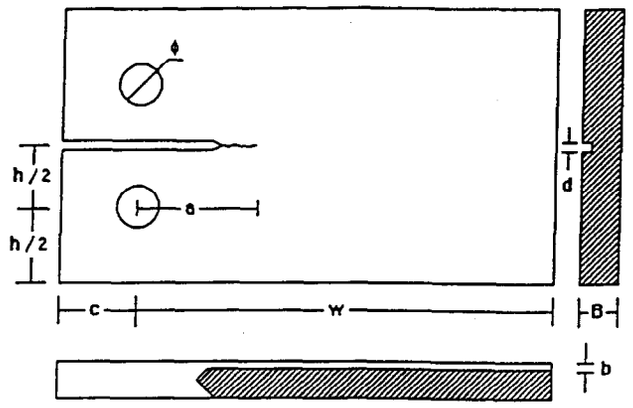

	h	ϕ	c	w	d	B	b
Dimension (mm)	12.50	4.50	7.56	38.00	0.70	4.00	1.00

(a)

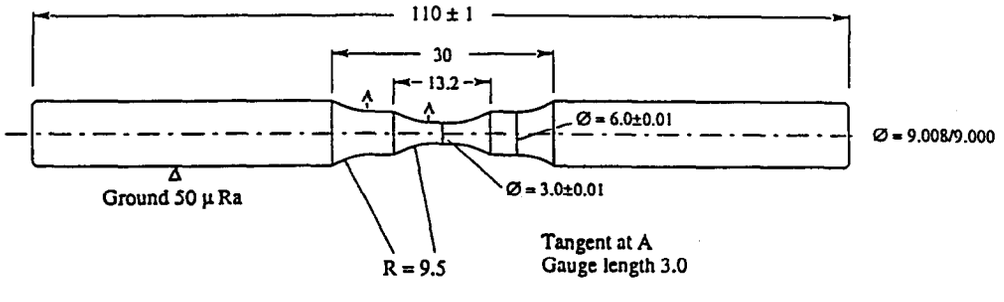

(b)

Fig. 3. Specimen geometries used for fatigue testing: (a) slow crack growth; and (b) push–pull.

did not fail at the very centre of the gauge length, and the results of these tests have not been used. For the other specimens, the regions where fatigue failure occurred corresponded therefore to the region with the maximum, nominal test temperature. The cyclic tests were performed at a frequency of 10 Hz, using fully reversed loading ($R = -1$, where the load ratio, R = minimum load/maximum load) and a sine waveform. The load amplitude was applied slowly by increasing from zero to the test amplitude at a rate of 10 MPa s^{-1}.

The scatter of push–pull fatigue data is strongly influenced by the inherent scatter of the strength of the ceramic. For this reason it is necessary to test many specimens in order to plot an S–N fatigue curve. The magnitude of this scatter is inversely related to the Weibull modulus, m, of the material. Additional scatter of the data is introduced by bending strain introduced by specimen misalignment. In fact, the most critical part of uniaxial push–pull testing is to achieve good alignment. This is difficult and time-consuming to achieve, and it is therefore necessary to determine some 'appropriate' level of alignment that needs to be achieved. If the scatter introduced by the inherent variability of the strength of the material is relatively large, small misalignments may have a negligible influence on the results. The Weibull cumulative probability of failure is defined as

$$P_f = 1 - \exp\left\{-\left[\frac{\sigma - \sigma_u}{\sigma_o}\right]^m \frac{V}{V_o}\right\} \tag{4}$$

$$Ln(1 - P_f) = -\left[\frac{\sigma - \sigma_u}{\sigma_o}\right]^m \frac{V}{V_o}. \tag{5}$$

The terms V_o and σ_o are normalizing volume and stress terms, respectively, and V is the specimen

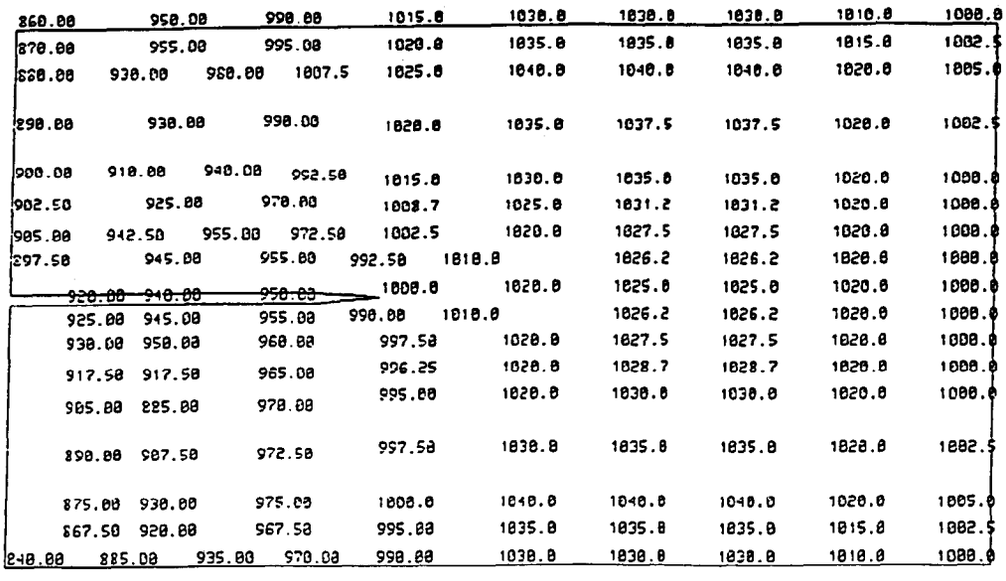

Fig. 4. Temperature distribution in fatigue specimens: (a) slow crack growth; and (b) push–pull.

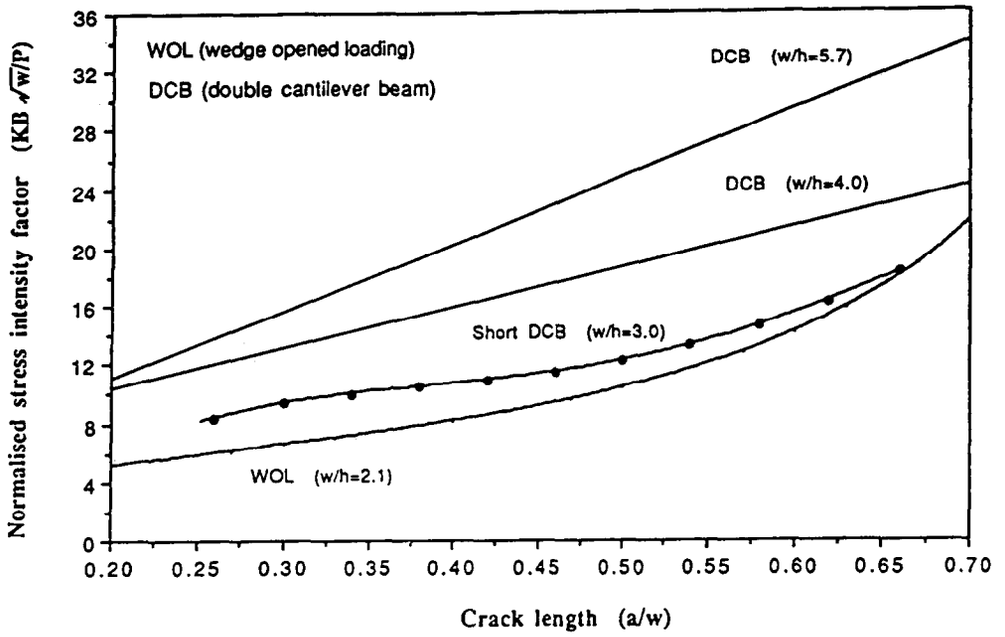

Fig. 5. Calibrated normalized stress intensity factor as function of crack length for slow crack growth specimen geometry.

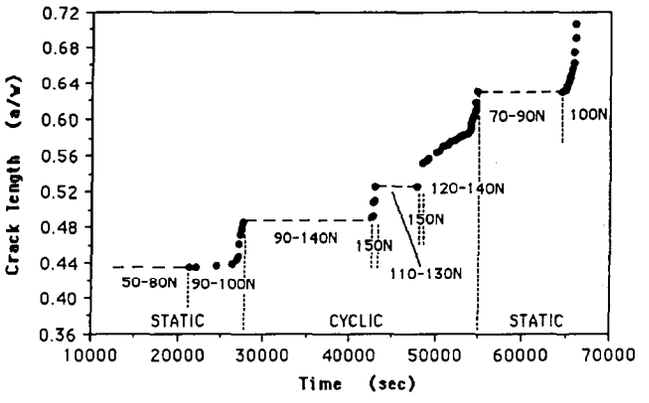

Fig. 6. Crack length as a function of time during static and cyclic slow crack growth experiments. Indicated are initial and final maximum applied loads for each loading sequence.

test volume, which is the same for identical specimens. The threshold stress, σ_u, is usually assumed to be zero, so that

$$Ln(1 - P_f) \propto -\sigma^m. \tag{6}$$

The ratio of the failure stresses corresponding to probabilities of failure of 0·95 and 0·05 is therefore

$$\frac{\sigma_{0.95}}{\sigma_{0.05}} = \left[\frac{Ln(1-0.95)}{Ln(1-0.05)}\right]^{1/m}. \tag{7}$$

If we arbitrarily say we will tolerate scatter produced by bending equivalent to 10% of this, the relative bending stress would be

$$\frac{\Delta\sigma}{\sigma} = 0.1\left(\frac{\sigma_{0.95}}{\sigma_{0.05}} - 1\right). \tag{8}$$

Assume $m = 10$ typically

$$\frac{\Delta\sigma}{\sigma} = 0.05 \tag{9}$$

and therefore the corresponding relative bending strain is

$$\frac{\Delta\varepsilon}{\varepsilon} = 0.05 = 5\%. \tag{10}$$

The alignment of the test machine was measured and corrected using a push–pull specimen with a triad arrangement of strain gauges. This enabled both the direction and magnitude of the relative bending strain to be determined. On initial loading the relative bending strain was usually >5%. With increasing stress the bending strain decreased exponentially, and extrapolated to the failure stresses, the relative bending strain at failure was always <5%.

3 Results

3.1 Mechanical experiments

The normalized crack length (a/w) as a function of test time for the different loading conditions for the slow crack growth experiments at 1000°C is shown in Fig. 6. Values in the figure indicate the applied constant tensile loads for static fatigue or the maximum applied loads for cyclic fatigue. When the maximum load was progressively increased the initial and final maximum loads are indicated. The crack started advancing at a static load of 90 N with a crack growth rate of approximately 2×10^{-8} m s^{-1} and accelerated at the constant load of 100 N. The static load was then reduced to 90 N to achieve stable crack propagation. The initial static fatigue test was stopped at the normalized crack length of $a/w = 0{\cdot}486$. Subsequently, the loading condition was changed to cyclic loading with $R = 0{\cdot}3$. The crack did not

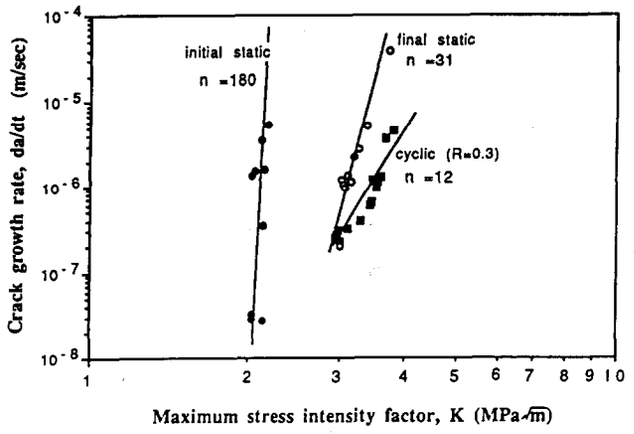

Fig. 7. Fatigue crack growth rates for static and cyclic fatigue at 1000°C and R = 0·3 (data corrected for thermal stress intensity factor).

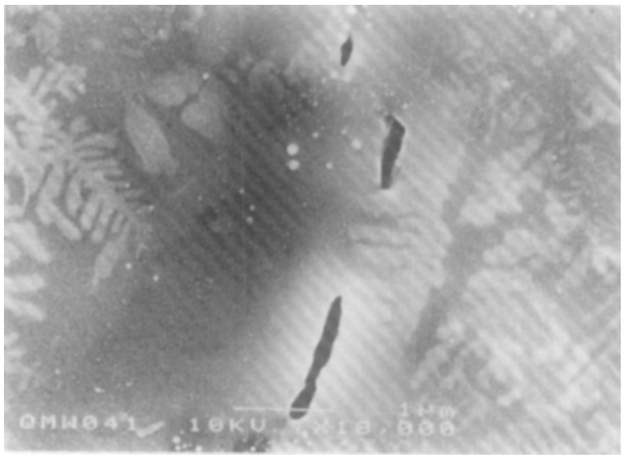

Fig. 8. Crack path profile. Note residual opening, rounded appearance of oxidized grain surfaces and mismatch of crack faces.

propagate until the maximum load was increased to 150 N. A series of static and cyclic tests was then performed (Fig. 6) until the specimen eventually fractured.

Using the data of Fig. 6, the crack growth rates were determined from the gradients of the curves. The corresponding stress intensity factors were determined using the data for the DCB specimen geometry (see w/h = 3·0 in Fig. 5). Figure 7 shows the logarithmic crack growth rate plotted as a function of the logarithmic maximum stress intensity factor. The data have been corrected to account for the stress intensity factor K_t produced by the thermal gradients in the specimen. The crack growth rate can be reasonably well fitted to a power-law relationship like eqn (1).

The exponent n is larger for static fatigue than for cyclic fatigue. Similar results have been reported for other ceramics where the stress intensity factor range, ΔK, was found to characterize the crack growth rates.[21] The crack propagated faster under static loading than under cyclic loading

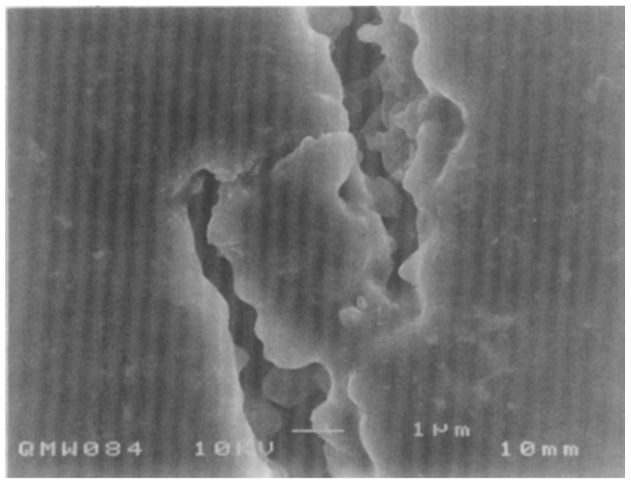

Fig. 9. SEM micrograph of fatigue fracture path at 1000°C in slow crack growth specimen, showing creep cavities ahead of statically grown crack.

with the same maximum stress intensity factor. This observation is consistent with the results reported for other ceramics,[15,19] and is also consistent with the longer lifetime obtained for silicon nitride under cyclic loading at high temperatures.[14,17,25,26] The fatigue behaviour at elevated temperatures is contrary to what is found at room temperature, where cyclic loading has a more deleterious effect on resistance to fatigue fracture than static loading.[11,13] These results are also in agreement with a previous observation by others that the GPSSN studied is highly fatigue-resistant up to 900°C but becomes susceptible to cyclic and static slow crack growth at 1000°C.[26] The large differences in the sets of data for the initial and final static fatigue tests may be attributed to increasing crack growth resistance with increasing crack length.

The crack paths and profiles were examined by scanning electron microscopy (SEM) on the surface of the specimen after the different loading conditions. The crack always had a large residual opening over its entire length and it was easy to look into its wake. The grain and fracture facets were rounded and their shape obliterated by a solidified amorphous layer (Fig. 8). Hence the fracture surfaces were heavily mismatched and this must have been largely responsible for the residual opening of the crack. Rounded large cavities could be seen ahead of the crack tip after the initial static fatigue test (Fig. 9). This cavitation may have been a surface effect not characteristic of the bulk behaviour since we believe it was associated with the presence of a viscous glass layer formed by the relatively heavy oxidation of the specimen surface. Evidence of this oxidized surface is provided by the dendritic growth of a crystalline phase in the oxide (Fig. 9) and by observations of the fracture surfaces, as discussed later. No large differences existed between the crack profiles of

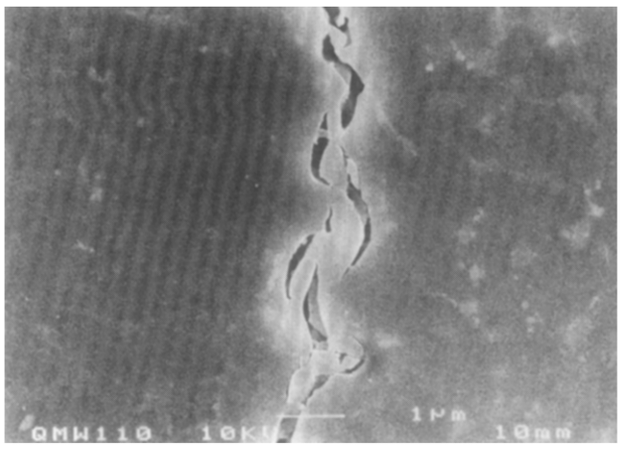

Fig. 10. Secondary cracking and the formation of crack wedges during cyclic loading.

cracks grown statically and cracks grown under cyclic loading, except that more secondary cracks appeared in the latter. With an increasing number of cycles some of the secondary cracks (which always appeared open) propagated and linked with the main crack, forming wedges between the crack faces (Fig. 10).

On the fracture surfaces of broken specimens the regions of slow crack growth and the regions of fast fracture were clearly distinguishable. The slow crack growth regions were covered with an amorphous layer of solidified glass that was produced by oxidation. Near the crack mouth (notch end), where the surfaces were exposed to air for a longer time, the grain texture was completely destroyed [Fig. 11(a)]. Nearer the tip of the crack, where the oxidation was less severe, some granular texture remained [Fig 11(b)]. All around the edges of the fracture surface a 10-μm-thick oxidized surface layer was apparent (Fig. 12). This process of oxidation must have played an important part in the slow growth of the crack.

The cyclic push–pull fatigue data are shown in Fig. 13(a). The strength of the as-machined and annealed specimens, extrapolated to a fracture time of 10 s, is ~500 MPa and 700 MPa, respectively. The annealed specimens are therefore approximately 40% stronger than the as-machined specimens. The difference was such that the annealed specimens did not fail after 10^6 cycles under cyclic loading, whereas these conditions caused fatigue fracture of the as-machined specimens. This increase in strength and fatigue resistance could have been a consequence of flaw healing during the annealing treatment and this possibility is examined later. The cyclic fatigue data for the annealed specimens are compared with static fatigue data for annealed specimens in Fig. 13(b). Consistent with the v–K data in Fig. 7(b), static loading is considerably more damaging than cyclic loading.

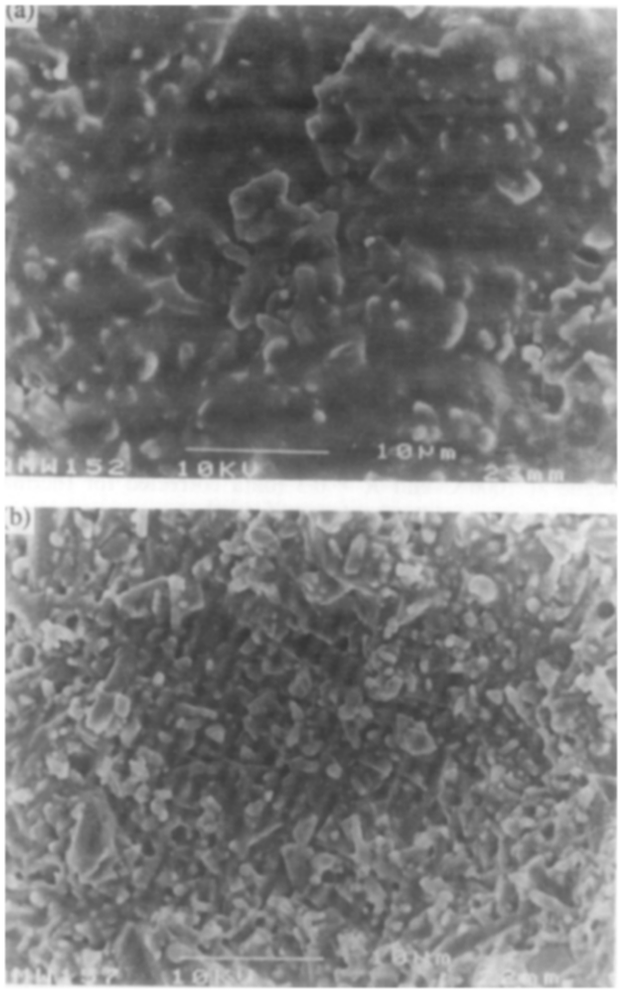

Fig. 11. Fracture surfaces: (a) near crack notch; (b) nearer crack tip just prior to fast fracture.

Assuming crack growth was controlled by static fatigue effects during cyclic loading, the relative times to failure under static and cyclic loading can be calculated using eqn (3). Using a value of n = 60, this gives the ratio of times to failure tc/t_S = 19·5. The broken line in Fig. 13(b) shows the position of the predicted static data based on the cyclic data, and there is clearly no correlation with the experimentally determined static data.

The stress exponents n, determined from the push–pull testing are 16 and 60 for static and cyclic fatigue, respectively. Accepting that the intrinsic scatter of the data is large, there is no correlation of these values and those generated by the v–K curves from the slow crack growth experiments (Fig. 7). The reason for this is not clear, and may be a consequence of the large differences in the crack length in the two types of test, implying that n has little meaning as a fatigue parameter.

Microscopical observation of the specimens fractured under both static tensile load and push–pull revealed a dark band with a thickness of between 10 and 70 μm, which corresponded to an oxidation layer [Figs 14(a) and (b)]. This surface

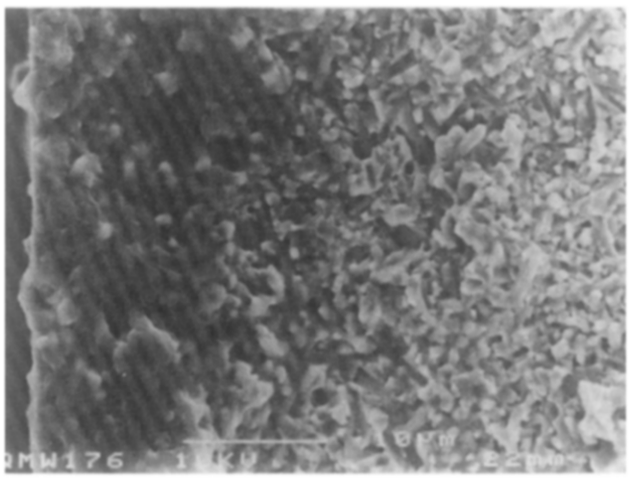

Fig. 12. Oxidized surface layer (~10-μm-thick) at the edge of a tested slow crack growth specimen.

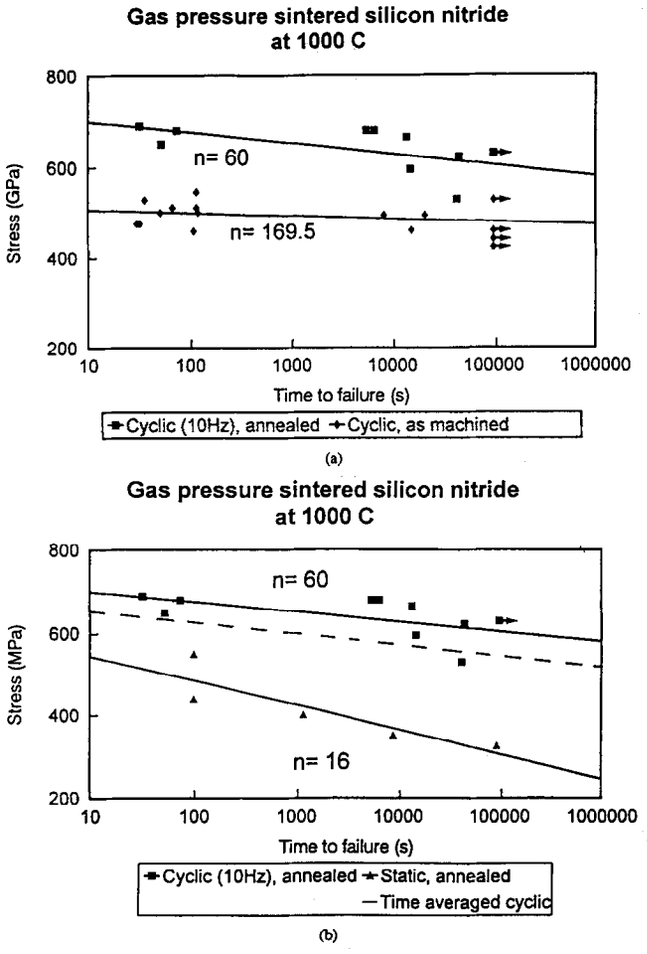

Fig. 13. Static and cyclic push–pull fatigue data at 1000°C and $R = -1$: (a) comparison of cyclic data for as-received and annealed specimens; and (b) comparison of cyclic and static data. Broken line represents time-averaged predicted static fatigue data based on the cyclic data.

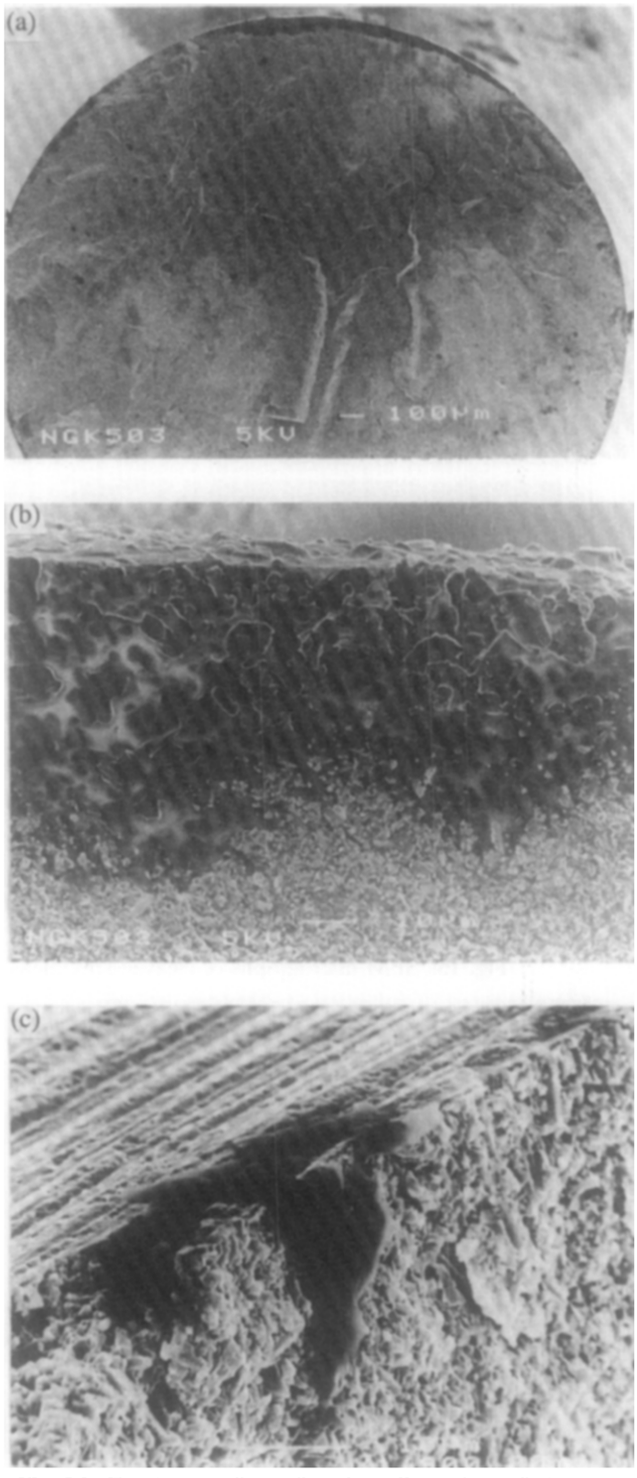

Fig. 14. Fracture surface of push–pull specimen fatigue tested at 1000°C: (a) dark band around the edge of specimen was produced by oxidation, and the widest region of the band (~70 μm) corresponds to fracture origin; (b) high magnification image of edge of fracture surface; and (c) extruded debris at edge of specimen.

oxide layer was, not surprisingly, similar to that observed on the surface of the slow crack growth specimens. The low-magnification fractography of these specimens clearly showed the regions of crack initiation, slow crack growth and fracture. The region where the oxidation layer was thickest corresponded to the crack initiation region. At places around the surfaces of the tested push–pull specimens, tongues of extruded material could be seen [Fig. 14(c)]. These gave the impression of being the oxide glass having been exuded from the cracks during the compressive loading.

3.2 Oxidation experiments

In order to study in a controlled manner the formation of the oxide glass phase on the exposed surfaces of the specimens at 1000°C, some small

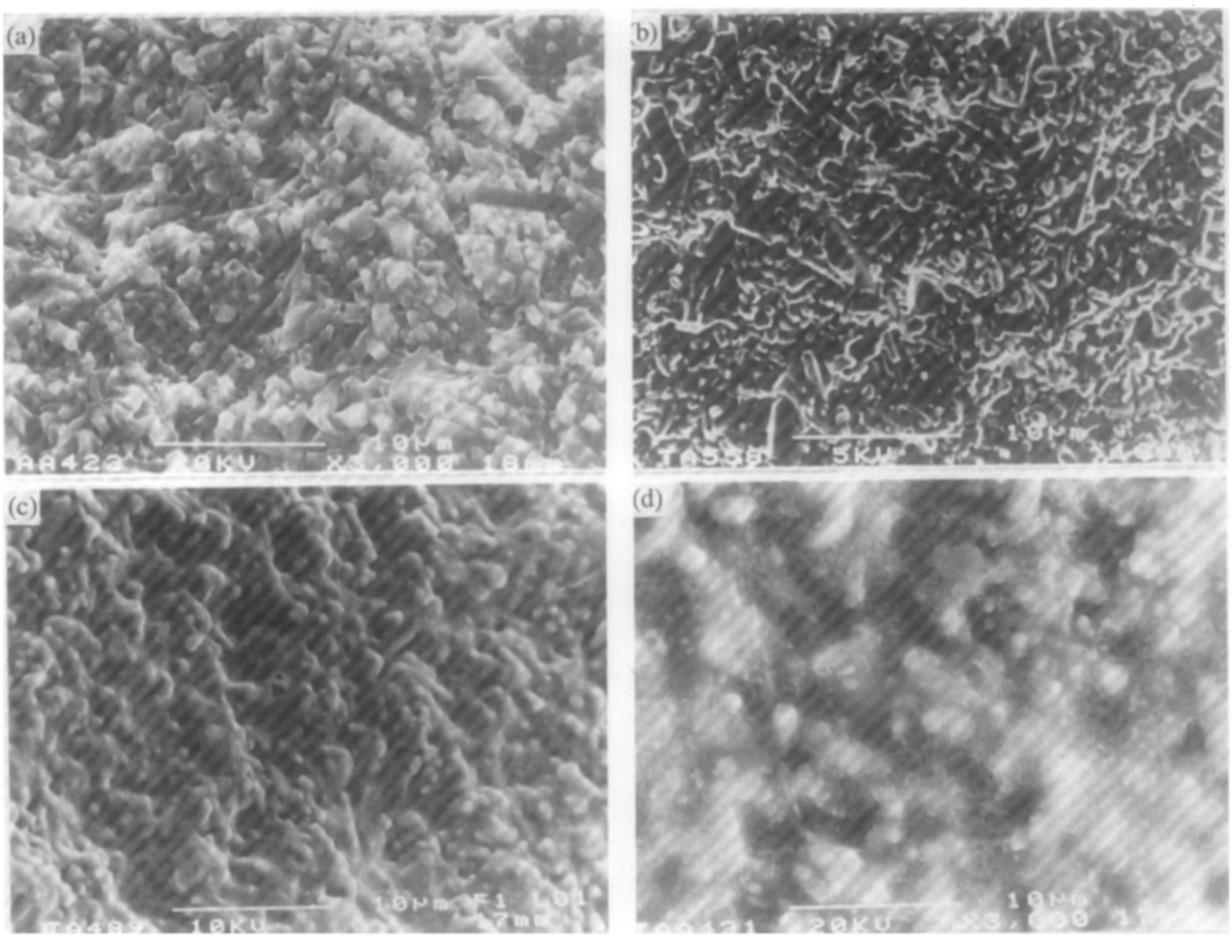

Fig. 15. SEM micrographs of cleaved specimens oxidized at: (a) 850; (b) 900 (c) 950; and (d) 1000°C.

samples with freshly cleaved surfaces and some with polished surfaces were anncaled in air for 27 h at temperatures of 850, 900, 950 and 1000°C. The oxidized cleaved surfaces had exactly the same appearance as those of the oxidized fractured specimens. Heat treatment above 950°C produced a thin layer of glassy phase within which a needle-like crystalline phase had precipitated (Fig. 15). Examination by transmission electron microscopy (TEM) and energy-dispersive spectroscopy analysis of the oxidized surfaces confirmed that the needle-like phase was an yttrium silicate containing Al and Ca. The glass layer was silica formed by the oxidation of the silicon nitride. This oxidation is very rapid on an uncontaminated, freshly cleaved surface and it was accompanied by the diffusion of the cation additives (Y^{3+} and Al^{3+} and impurities, Ca^{2+}) from the grain boundaries. Small concentrations of the low melting point elements dramatically reduce the viscosity of the glass which evidently could flow very easily at 1000°C and washed-out the granular texture of the fracture surfaces. No significant oxidation of the material was detected after heating for 27 h below 950°C (Fig. 15). TEM observations also revealed numerous voids in the intergranular regions close to the oxidized surface in specimens annealed at 1000°C (Fig. 16).

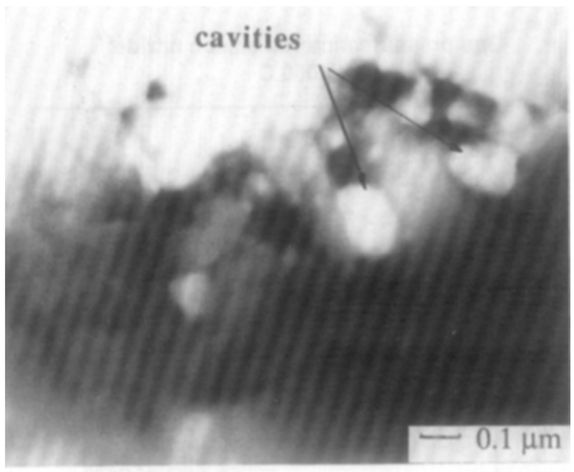

Fig. 16. TEM micrograph at interface between silicon nitride and surface oxide layer produced at 1000°C. Cavities are apparent at some grain boundaries.

The possibility of crack healing at high temperature was investigated by annealing experiments with indentation-produced flaws [Fig. 7(a)]. After annealing at 1000°C for 3 h the radial surface cracks were no longer clearly apparent and appeared to be welded together at some local regions by an amorphous phase [Fig. 17(b)]. This is confirmation that it is possible that surface machining flaws can be healed locally by what appears to be a glassy phase (produced by oxida-

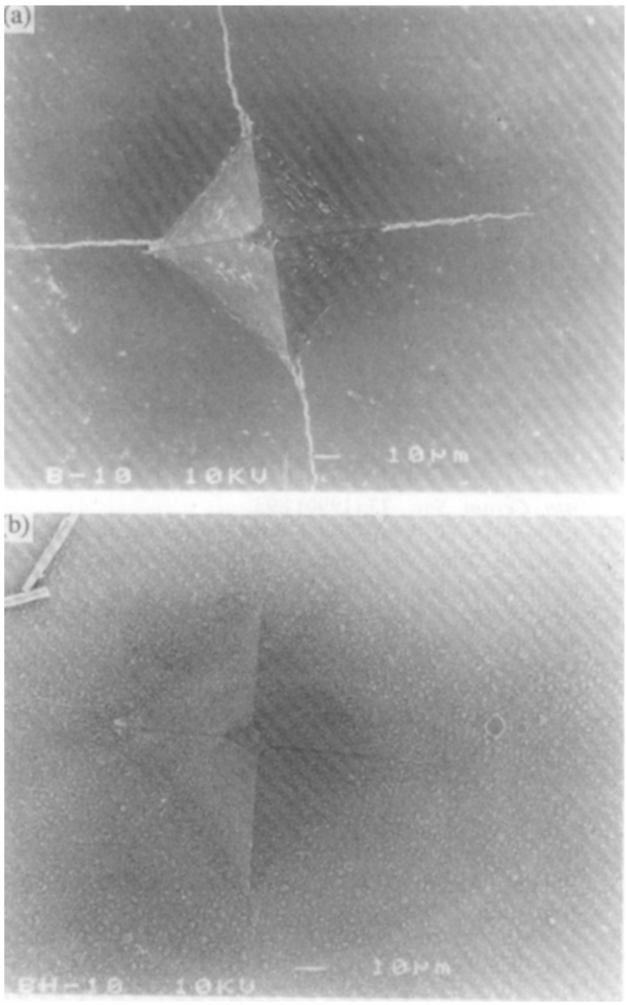

Fig. 17. Vickers indentation impression: (a) before; and (b) after annealing for 3 h at 1000°C.

tion) which can flow easily at the temperature of the tests. The closure of the crack also indicates that the plastic zone at the indentation impression, which produces the residual stress that opens the radial cracks, must have been relaxed by annealing.

4 Discussion

The results of the present investigation have revealed the importance of oxidation in the process of slow crack growth in Si_3N_4 at 1000°C in air. Our observations are consistent with the findings of others that isostatically pressed Si_3N_4 was not susceptible to subcritical crack growth in an inert environment at 1370°C, whereas the same material tested in air showed a strong fatigue susceptibility.[31] Other work[26] on the same material used in our study showed that, up to 900°C, the material has similar crack propagation properties and strength as at room temperature, while these properties are considerably degraded at 1000°C, coincident with the temperature at which oxidation becomes significant. All these observations suggest that the low-temperature crack growth mechanism changes at 1000°C when oxidation takes place and a relatively low viscosity phase is formed. In these oxidizing conditions, a crack, or pre-existing flaw, can grow by the co-operative effect of stress, oxidation and flow of the glass phase. The effect of stress, by forcing the crack open, is that of assisting the oxygen transport to the crack tip where an oxidized zone (not necessarily very deep) is formed and the crack can eventually advance by the flow of the low viscosity oxide phase. The rate of growth of the crack is determined in a complex manner by the applied stress, rate of oxidation, the rate at which Al^{3+} and Ca^{2+} can diffuse from the grain boundaries to the oxide layer and by the rate of flow of the glass. It is therefore not surprising to find that the relationship between crack velocity and applied stress intensity factor is different for different specimen geometries and different crack lengths, since geometrical factors can influence the rates of oxide formation at the tip of cracks and the rate of its viscous flow. It is noted, for example, that the average subcritical velocities in the tensile and push–pull specimens ($\sim 5 \times 10^{-9}$ m s^{-1}) were considerably slower than those measured in the slow crack growth experiments. The surface cracks in the former are very short (20–100 μm) and their faces are more effectively welded together by the glass phase. This could explain the flaw healing effect of the annealing heat treatment at 1000°C and the strength increase of the annealed specimens. Both the slower growth of cracks, and longer fatigue life of specimens under cyclic fatigue have also been observed by others in Si_3N_4 and Al_2O_3 at high temperatures.[14,15,17–20,26] This behaviour points to the absence of genuine cyclic fatigue effects at high temperature, and that periods of crack opening are more damaging than crack cycling.

The oxidized fracture surface regions, observed by other workers and described by them as degradation zones,[31] act as markers for the crack geometry. On the tensile and push–pull specimens these markers revealed that the fracture origins were associated with surface cracks with a maximum depth of $a \approx 70$ μm. This information can be used to estimate fracture toughness using the expression $K = Y\sigma\sqrt{\pi a}$, where for half-penny cracks on a cylindrical rod, $Y = 0{\cdot}7$, and σ is the maximum tensile stress.[32] The critical value of K thus obtained is about 5·7 MPa m$^{1/2}$. This is similar to the values typically quoted for the fracture toughness, K_{IC}, of Si_3N_4 at room temperature determined using the indentation fracture toughness method. It should be noted that K_{IC} is relatively insensitive to temperature up to 1200°C,[33] as it

should be if the toughness is determined by the onset of fast, unstable, crack propagation into the bulk material in the absence of oxidation effects. In the slow crack growth experiments, a well defined boundary between oxidation and fast fracture was not seen because the crack accelerates continually towards its critical length. Since crack length readings were taken at intervals, the true crack length at instability could not be determined from these tests.

5 Conclusions

(1) An experimental method has been developed that enables direct observation of the growth of subcritical fatigue cracks at high temperatures.

(2) The stress exponents, n, determined from high-temperature push–pull fatigue testing and slow crack growth experiments are inconsistent, indicating that n has little physical significance and is geometry-dependent.

(3) Annealing at 1000°C increases the strength of GPSSN by 40% as a consequence of oxidation-assisted crack healing and relaxation of surface-machining-induced residual stresses.

(4) The crack advancement mechanism at high temperature is influenced by oxidation at the crack-tip region and the formation of a viscous glassy phase. Oxidation ahead of the crack tip produces voids at the intergranular boundary. The stresses at the tip region of a tensile-loaded crack tend to increase the size and number of these voids by viscous flow. The coalescence of the voids produces a mechanism by which crack growth can occur. This mechanism explains the change in crack growth behaviour at high temperatures compared with room temperature.

Acknowledgements

We would like to thank NGK Spark Plug Co., Japan for supplying the GPSSN material. We also gratefully acknowledge the support of the SERC (now EPSRC), UK (GR/E 75844).

References

1. Ziegler, G., Heinrich, J. & Wotting, G., *J. Mater. Sci.*, **22** (1987) 3041.
2. Buljan, S. T. & Baldoni, J. G., in *Preparation and properties of Silicon Nitride Based Materials*, eds D. A. Bonnell & T. Y. Tien. Trans Tech Publications, Switzerland, 1989, p. 249.
3. Tressler, R. E., in *Ceramic Transactions, Vol. 10*, eds R. E. Tressler & M. McNallan. American Ceramic Society, Westerville, OH, 1990, p. 99.
4. Guiu, F., *Mater. Sci.*, **13** (1978) 1357.
5. Ewart, L. & Suresh, S., *J. Mater. Sci.*, **22** (1987) 1173.
6. Reece, M. J., Guiu, F., & Sammur M. F., *J. Am. Ceram. Soc.*, **72** (1989) 348.
7. Horibe, S., *J. Eur. Ceram. Soc.*, **6** (1990) 89.
8. Dauskardt, R., H., Marshall, D. B. & Ritchie, R. O., *J. Am. Ceram. Soc.*, **73** (1990) 893.
9. Kishimoto, H., Ueno, A. & Kawamoto, H., in *Fatigue of Advance Materials*, Proc. Engineering Foundation Int. Conf. CA, USA, 1991, p. 255.
10. Ritchie, R. O. & Dauskardt, R. H., *J. Ceram. Soc. Jpn*, **99** (1991) 1047.
11. Guiu, F., Li, M. & Reece, M. J., *J. Am. Ceram. Soc.*, **75** (1992) 2976.
12. Dauskardt, R. H., *Acta Metall. Mater.*, **41** (1993) 2765.
13. Li, M. & Guiu, F., *Acta Metall. Mater.*, **43** (1995) 1859.
14. Fett, T., Himsolt, G., & Munz, D., *Adv. Ceram. Mater.*, **1** (1986) 179.
15. Han, L. X. & Suresh, S., *J. Am. Ceram. Soc.*, **72** (1989) 1233.
16. Suresh, S., in *Fracture 90, Vol. 2*, eds H. Kitagawa & T. Tanaka. Materials and Component Engineering Publications Ltd, Birmingham, UK, 1990, p. 759.
17. Masuda, M., Soma, T. & Matsui, M., *J. Eur. Ceram. Soc.*, **6** (1990) 253.
18. Lin, C. K. J. & Socie, D. F., *J. Am. Ceram. Soc.*, **74** (1991) 1511.
19. Ewart, L. & Suresh, S., *J. Mater. Sci.*, **27** (1992) 5181.
20. Liu, S.-Y, Chen, I.-W. & Tien T.-Y., *J. Am. Ceram. Soc.*, **77** (1994) 137.
21. Ramamurty, U., Hansson, T. & Suresh, S., *J. Am. Ceram. Soc.*, **77** (1994) 2985.
22. Evans, A. G. & Fuller, E. R., *Metall. Trans.*, **5A** (1974) 27.
23. Evans, A. G., Russell, L. R. & Richerson, D. W., *Metall. Trans.*, **6A** (1975) 707.
24. Evans, A. G., *Int. J. Fract.*, **16** (1980) 485.
25. Lin, C. K., Jenkins, M. G. & Ferber, M. K., *J. Mater. Sci.*, **29** (1994) 3517.
26. Talima, Y., Urashima, K., Watanabe, M. & Matsuo, Y., *Ceram. Mater. Comp. Engines*, (1989) 719.
27. Evans, A. G. & Wiederhozn, *J. Mater. Sci.*, **9** (1974) 270.
28. *UK Patent Application No. 9219221.0.*
29. Bushby, A. J., Guiu, F. & Sammur, M. F. R., in *Ultra Temperature Mechanical Testing*, eds R. D. Lohr & M. Steen. Woodhead Publishing Ltd, Cambridge, UK, 1995, p. 214.
30. Chadwick, M. M. & Wilkinson, D. S., *J. Am. Ceram. Soc.*, **76** (1993) 376.
31. Wereszczak, A. A., Breder, K. & Ferber, M. K., *J. Am. Ceram. Soc.*, **76** (1993) 2919.
32. Astiz, M. A., *Int. J. Fract.*, **31** (1986) 105.
33. Mizuno, M. & Okuda, H., *J. Am. Ceram. Soc.*, **78** (1995) 1793.

Journal of the European Ceramic Society 16 (1996) 1021–1025

S0955-2219(96)00021-0
0955-2219/96/$15.00

Controlled Crack Growth in Ceramics: The DCB Specimen Loaded with Pure Moments

Bent F. Sørensen,[a] Philippe Brethe[b] & Peder Skov-Hansen[a]

[a]Materials Department, Risø National Laboratory, DK-4000 Roskilde, Denmark
[b]Ecole Nationale Supériere de Céramique Industrielle, Limoges, France

(Received 3 November 1995; revised version received 13 December 1995; accepted 3 January 1996)

Abstract

The energy release rate of a double cantilever beam (DCB) loaded with pure bending moments is independent of crack length, allowing stable crack growth in even truly brittle materials. The method is thus suitable for measuring fracture toughness and R*-curve behaviour of ceramics. This paper describes the development of a new test configuration and reports the testing results from two ceramics: one with constant fracture toughness and one possessing* R*-curve behaviour due to phase transformation. Stable crack growth was obtained for both materials. © 1996 Elsevier Science Limited.*

1 Introduction

Generally, the fracture toughness of technical ceramics is low. This limits the number of applications in which ceramics can be used. In order to enhance the fracture toughness, energy-absorbing mechanisms must be built into the microstructure. Typically, the effect of the toughening mechanism increases as the crack grows, leading to rising crack growth resistance (*R*-curve behaviour). In parallel with the development of tougher ceramics, it is equally important to develop experimental methods that allow controlled (stable) crack growth, such that the *R*-curve behaviour can be properly measured.

Many of the fracture mechanics tests methods that work well for metals are not suited for controlled crack growth in ceramics because the test configurations are unstable in nature; i.e. for a fixed external load, the energy release rate $\mathcal{G}$ increases with crack length. Then, controlled crack growth is only possible when the tests are performed on servo-hydraulic test machines controlled by the crack opening displacement (feedback from a clip-on extensometer), such that the specimen is rapidly unloaded as soon as crack growth takes place. It is difficult to perform such experiments in ceramic.[1] Typically, it is only possible to control the crack growth for a few millimetres before the crack extends unstably.[2]

Chevron-notched specimens give stable crack growth,[3] but cannot be used for characterizing *R*-curve behaviour since the crack extension varies along the crack front (in order to be able to measure *R*-curve behaviour properly, the crack front should be straight, such that the full crack width experiences the same state of toughening). It is possible to obtain controlled crack growth of straight through the thickness cracks in ceramics by controlling the crack opening displacement utilizing the Poisson's effect of a rod loaded in compression.[4] The calculation of $\mathcal{G}$, however, is sensitive to the accuracy with which the Poisson's ratio of the rod is known, and $\mathcal{G}$ depends on the crack length. Stable crack growth can also be obtained by compressing a square specimen with a circular hole in the centre.[5] However, machining a pre-crack from the circular hole is quite difficult. Also, the energy release rate depends on the stiffness of the support areas and varies with crack length. Another method utilizes torsion moments on a double cantilever beam (DCB) specimen.[6] For this method the energy release rate is independent of crack length. However, the crack front is not straight through the width. Therefore the measured resistance may, at least in the initial stages of crack extension, represent an averaged value. After completion of this work we discovered an older paper by Freiman *et al.*,[7] which describes a loading arrangement for loading a DCB specimen with pure bending moments. This method also gives an energy release rate that is independent of crack length. The moments were applied by forces acting through wires at external beams bonded perpendicular to the DCB arms. However, if rigid supports are used[8] instead of the wire arrangement,[7] then the external beams slide over the support points as the DCB specimen opens, so that the test becomes sensitive to friction.

In this paper a novel arrangement is proposed for loading a DCB specimen with pure bending

moments. Using a special fixture which moves with the beams of the DCB, the problems of bonding are avoided. The bending moments are created by loading the DCB specimen by compressive forces. The potential of the method is demonstrated by the characterization of two ceramics: one with and one without R-curve behaviour.

2 Analysis of Test Configuration

2.1 Conditions for stable crack growth

A material's resistance to crack growth $\mathcal{R}$ may increase during crack extension, i.e. $\mathcal{R} = \mathcal{R}(\Delta a)$, where Δa is the crack extension. Denoting the decrease in the potential energy (per unit width of the specimen) of the system by $\mathcal{G}$ (the energy release rate), the Griffith criterion for crack growth can be formulated as follows. Crack growth takes place when the decrease in the potential energy during an incremental crack growth equals or exceeds the energy consumed in the fracture process: $\mathcal{G} \geq \mathcal{R}$. Crack growth is stable if $d\mathcal{G}/da < d\mathcal{R}/da$ and unstable if $d\mathcal{G}/da > d\mathcal{R}/da$.

2.2 Fracture mechanics analysis of the DCB loaded with pure moments

The DCB specimen consists of two slender beams each with the thickness H and width B. The crack growth takes place in the mid-plane between the beams, such that the crack growth is in pure mode I. Each beam end is loaded with a bending moment M [Fig. 1(a)]. The plane strain energy release rate can be found by taking the J-integral[9] along the boundaries of the specimen, giving

$$\mathcal{G} = 12(1 - \nu^2)\frac{M^2}{EB^2H^3} \tag{1}$$

where E and ν denote Young's modulus and Poisson's ratio. Since $\mathcal{G}$ is independent of the crack length a, it follows that $\partial\mathcal{G}/\partial a = 0$ (constant moment). If

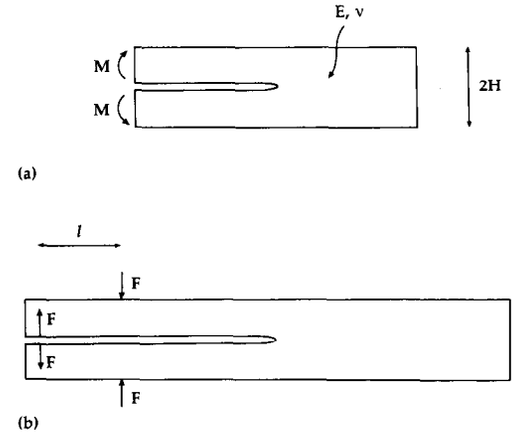

Fig. 1. The geometry and loading of the DCB: (a) loaded by pure bending moments; (b) loaded with compressive forces creating pure moments in the inner parts of the beams.

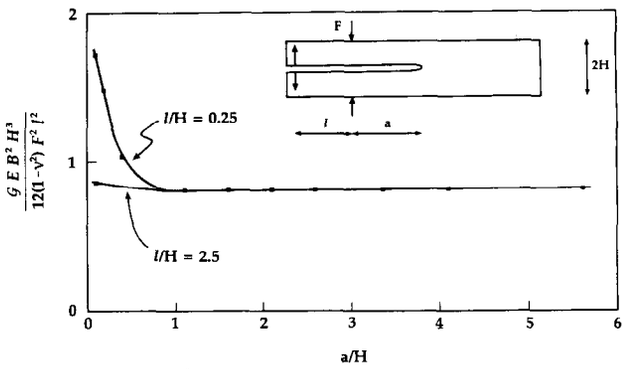

Fig. 2. The computed value of the energy release rate (normalized by the value calculated by simple beam theory) as a function of the distance a from loading point B to the crack tip. $\mathcal{G}$ approaches a constant value for $a/H \geq 1$.

the test is performed in displacement control then $d\mathcal{G}/da = \partial\mathcal{G}/\partial a$ (constant rotation) < 0, such that crack growth is stable even in materials with constant fracture toughness $d\mathcal{R}/da = 0$. This is the prime advantage of the DCB loaded with pure moments.

In our design the bending moments are created by applying two compressive forces, separated by a distance l, to each beam [Fig. 1(b)] such that the moment is

$$M = Fl \tag{2}$$

where F is the magnitude of the force. In order to assess how far away the forces should be from the crack tip, the stress distribution of the specimen was analysed using the finite element method (FEM).[10] A typical mesh consisted of 1698 eight-noded, isoparametric, plane strain elements and 5321 nodes. Singular elements were used at the crack tip. The energy release rate, calculated by a virtual crack extension technique, is shown in Fig. 2 as a function of the distance a from the crack tip to the nearest loading point for two different moment arms ($l/H = 0{\cdot}25$ and $l/H = 2{\cdot}5$). It is seen that $\mathcal{G}$ is essentially independent of a for $l/H = 2{\cdot}5$. For $l/H = 0{\cdot}25$, the steady-state value of $\mathcal{G}$ is attained when $a/H \geq 1$. For small values of a/H and l/H the stress field from the forces acting at the crack face is directly affecting the stress field near the crack tip. Therefore, $l/H = 2{\cdot}5$ was chosen in the current design.

3 Experimental Method

3.1 Practical design of test specimen

For practical reasons, modifications are required to the idealized specimen geometry. A slot must be introduced at the inner part of the beam ends to give room for the brads. Also, a side groove must be introduced in order to guide the direction of the crack. Grooves can be made to both sides of the specimen to ensure symmetrical deformation.

3.2 Description of fixture

In order to apply the moments to the beams without inducing wedging forces or friction, a fixture utilizing a wire and rollers was developed (Fig. 3). The wire runs via two transverse rollers, mounted at the top and bottom grips of a standard tensile machine such that the forces in the wire at the front and rear sides of the fixture are identical. If the friction from the rollers is neglected and the gravity forces on the fixture are small (the weight of each fixture part is 570 g), then the force in the wire has the same magnitude everywhere, and it follows that each beam is loaded with a pure moment

$$M = P(2R + d) \tag{3}$$

where P is the applied force, R is the radius of the rollers and d is the horizontal distance between the centre of the rollers (Fig. 3). The moment is transferred to the specimen by two brads (separated by the distance l), welded to the fixture. Note that the specimen and fixture parts are free to move up and down without inducing any forces in the wires; only a rotation does. The uncracked end is supported from the sides and the bottom (snug fit only), in order to ensure that the specimen does not rotate (e.g. due to gravity forces).

3.3 Test procedure

The experiment should be performed under displacement control (i.e. under a constant crosshead speed) to obtain stable crack growth. An extensometer can be mounted at the end of the specimen (point A, Fig. 3) to detect crack growth. Acoustic emission can also be used for detecting crack growth. The crack length is recorded prior to loading. The load P is increased until crack growth is detected, whereafter the specimen is unloaded, and the new crack length is measured. Then the load can be increased again until further crack growth has taken place, etc. The load at the onset of crack growth can be converted into a moment M [eqn (3)] and the critical energy release rate $\mathcal{G}_{Ic}$ can be calculated from eqn (1). The crack growth resistance can then be calculated from

$$\mathcal{R}(\Delta a) = \mathcal{G}_{Ic}(\Delta a)\frac{B}{b} \tag{4}$$

where b is the remaining ligament of side-grooved specimens (i.e. the beam width B minus the side groove depth), since the changes in strain energy occur over the full width B, while fracture energy is only consumed over the width b.

The crack extension Δa can be measured by several means. A face of the specimen can be polished, allowing the crack length to be measured by optical microscopy. The crack is easy to see, if it is coloured by a penetrating ink. Alternatively, a surface replica can be taken and the crack extension can be determined later. This is a precise and efficient method. These two methods rely on the crack extension at the surface. A third method is to determine the crack length by means of the changes in specimen compliance: the end-opening of the specimen (two times the deflection of a single beam) can be found from simple beam theory to be (plane strain)

$$\delta_A = 4(1 - \nu^2)\frac{2R + d}{B}\frac{P}{EH^3}(3a^2 + 2l^2 + 6la) \tag{5}$$

where l is the horizontal distance between the loading points A and B (see Fig. 3), and a is the crack length (the horizontal distance from B to the crack tip).

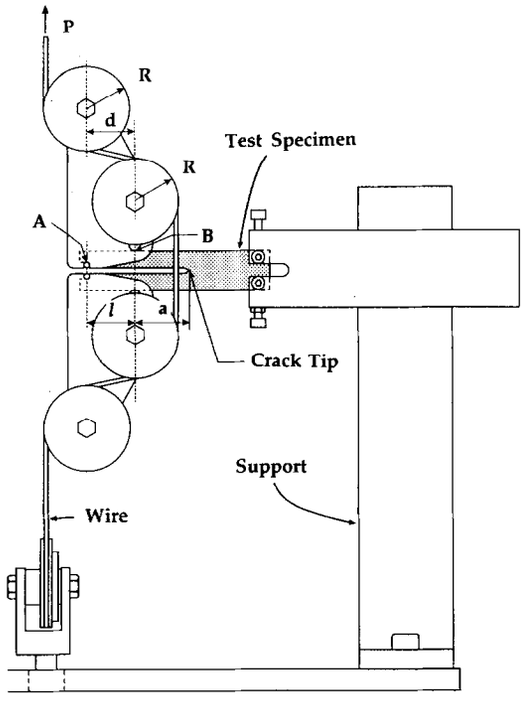

Fig. 3. Schematic illustration of the loading fixture.

4 Example of Stable Crack Growth in Ceramics

4.1 Processing of ceramics

CeO_2-stabilized ZrO_2 ceramics that may experience R-curve behaviour due to phase transformation (tetragonal to monoclinic crystal phase) were studied. Powders from two different companies (TZ-12CE from Tosoh Co., Japan and Z-65 from Ceramatec, USA) were used. The test specimens were made by slip casting. After pre-sintering (1 h at 1000°C), the slots for the brads, the side groove and a 1 mm thick notch were cut. A 0·1 mm thin slit (approximately 3 mm in length) was made at the end of the crack by a new razor blade. The specimens were sintered at 1500°C for 2 h. The linear shrinkage was nearly 20%. The specimens were nominally 100 mm long, with B = 5 mm, b = 2·5 mm and

H = 10 mm. The average grain size of both materials was approximately 2 μm.

4.2 Testing and results

Prior to the fracture mechanics testing, the elastic properties were determined by strain-gauge measurements on four beams loaded in four-point bending. This gave E = 187 GPa and ν = 0·30.

The fracture mechanics experiments were conducted using an Instron 1115 spindle-driven test machine at a constant crosshead speed of 0·2 mm min^{-1}. Acoustic emission (Spartan AT, Physical Acoustic Corporation) was used to monitor crack growth. Replicas (Struers Transcopy) were used to document crack extension. To start the measurements from a truly sharp crack, each specimen was pre-cracked in the following manner. The specimen was inserted in the fixture, and loaded until crack growth was detected. Then the specimen was unloaded and annealed at 1000°C for 30 min to reverse the transformation that might have occurred in connection with the crack initiation.[2] The specimens were tested in the procedure described above.

The measured crack growth resistance for typical specimens is shown in Fig. 4. For the Tosoh ceramic the R-curve is essentially flat (constant fracture toughness). The R-curve behaviour of the Ceramatec ceramic is much more pronounced. The full R-curve of this material has, as far as we are aware, not been measured before. The initial part of the R-curve has been measured by single-edge-notch-bend specimens by Yu and Shetty[2] (up to 1·5 mm crack extension, where unstable crack growth took place; i.e. before the steady-state level was attained). Their results are superimposed in Fig. 4. The agreement between their and our measurements is very good. One of our specimens of Ceramatec ceramic was annealed after 6 mm crack growth in order to reverse the transformation. This specimen was then used to measure the R-curve behaviour again. The measured R-curves coincide completely, suggesting a complete reverse transformation during the heat treatment. Such behaviour has also been demonstrated by Yu and Shetty.[2]

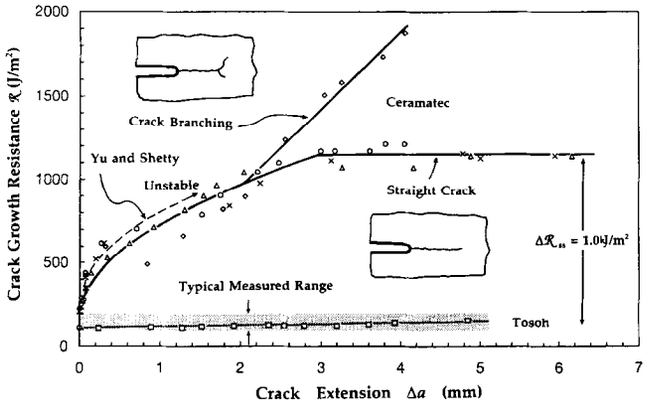

Fig. 4. The measured crack growth resistance $\mathcal{R}$ as a function of crack extension Δa for two ceramic materials. The Ceramatec material experienced a pronounced R-curve behaviour. Note that crack branching leads to erroneous measurements. The Tosoh ceramic showed no R-curve effect; it appears to have a constant fracture toughness.

As indicated in Fig. 4, for one of the specimens the crack branched and kinked away from the intended mode I crack direction after a growth of 2 mm. The crack branching was identified from the replicas and resulted in a higher apparent crack growth resistance (only growth of a single straight crack is valid for measurements of mode I R-curve behaviour).

4.3 Discussion

Under steady-state conditions, the J-integral taken along the external boundaries [Eqn (1)] can be split into parts associated with the unloading in the wake of the crack and the energy release rate at the crack tip.[11] Assuming that the critical energy release rate at the crack tip remains the same during crack growth, the increase in the global energy release rate [Eqn (1)] is predicted to be[12]

$$\Delta\mathcal{R}_{ss} = 2 f h \sigma_c \epsilon^T \qquad (6)$$

where f is the volume fraction of transforming particles within the transformation zone, h is the transformation zone height, σ_c is the critical transformation stress and ϵ^T is the transformation strain.

The transformation zone height h of the Ceramatec material was measured to be approximately 100 μm, similar to the measurements of Yu and Shetty.[2] The critical transformation stress σ_c is assumed to be approximately the yield stress, which is 200 MPa.[2] Assuming an average transformation fraction of 0·4 (Yu and Shetty[2] report f = 0·8 at the fracture surface and ϵ^T = 0·05) gives a prediction of $\Delta\mathcal{R}_{ss}$ = 0·8 kJ m^{-2}. From the experimental data (Fig. 4) $\Delta\mathcal{R}_{ss}$ is found to be 1·0 kJ m^{-2}. Thus, the agreement between experimental results and the prediction is satisfying.

5 Conclusions

A fracture mechanics testing technique, the DCB specimen loaded with pure bending moments, was developed and used to characterize the crack growth resistance of two ceramics. One of the materials experiences R-curve behaviour due to phase transformation. For this material the full R-curve was measured. The other material had a constant fracture toughness. Stable crack growth was obtained in both materials.

Acknowledgements

This work was supported by the Risø Engineering Science Centre for Structural Characterization and

modelling of Materials. The work of P.B. was performed when he was staying at Risø, during which time he was supported by the European Commett organization. The Ceramatec powder was kindly provided by Professor D. K. Shetty.

References

1. Nielsen, B. N., Thomsen, N. B. & Karihaloo, B. L., in *Proceedings of the 4th International Conference on Experimental Mechanics*, 20–24 August 1990, Lyngby, Denmark, p. 674.
2. Yu, C. S. & Shetty, D. K., *J. Mater. Sci.*, **25** (1990) 2025.
3. Blum, J. I., *Eng. Fract. Mech.*, **7** (1975) 593.
4. Calomino, A. M. & Brewer, D. N., *J. Am. Ceram. Soc.*, **75** (1992) 206.
5. Tirosh, J., Altus, E. & Yifrach, T., *Int. J. Fract.*, **58** (1992) 211.
6. Vekinis, G., Ashby, M. F. & Beaumont, P. W. R., *Acta Metall. Mater.*, **38** (1990) 1151.
7. Freiman, S. W., Mulville, D. R. & Mast, P. W., *J. Mater. Sci.*, **8** (1973) 1527.
8. Sohn, K.-S., Lee, S. & Baik, S., *J. Am. Ceram. Soc.*, **78** (1995) 1401.
9. Rice, J. R., *J. Appl. Mech.*, **35** (1968) 379.
10. SOLVIA 90, Solvia Engineering AB, Västerås, S-72214, Sweden.
11. Budiansky, B., Hutchinson, J. W. & Lambropoulos, J. C., *Int. J. Solids Struct.*, **19** (1983) 337.
12. Evans, A. G. & Cannon, R. M., *Acta Metall.*, **34** (1986) 761.

Journal of the European Ceramic Society **16** (1996) 1027–1034

S0955-2219(96)00011-8
0955-2219/96/$15.00

On the Contribution of Notches to the Failure Probability of Ceramic Components

Angelika Brückner-Foit, Armin Heger & Dietrich Munz

Institute of Reliability and Failure Analysis, Karlsruhe University, D-76021 Karlsruhe, Germany

(Received 21 July 1994; revised version received 18 December 1995; accepted 5 January 1996)

Abstract

The failure probability of tensile bars containing circular notches is calculated using the multiaxial Weibull theory. The influence exerted by the stress concentration factor, the stress gradient in the notch root, and the Weibull exponent are analysed. A local risk of rupture is defined, and it is shown how characteristic sub-volumes of the notched tensile bar contribute to the failure probability. An analytical expression is derived which is based on a linear approximation of the stress field in the vicinity of the notch root, and which yields the dependence of the leading term of the failure probability on characteristic quantities such as the stress concentration factor and the Weibull modulus. © 1996 Elsevier Science Limited.

1 Introduction

The design of ceramic components aims at meeting a specific level of reliability instead of specifying a minimum allowable strength due to the inherent scatter of strength. As failure is triggered by the most dangerous flaw, which may be located in a region of comparatively low stress, any stressed volume in the component contributes to the risk of rupture. Hence, the stress distribution of the entire component has to be calculated for design purposes.

This is obviously different from common design practice for metallic components, for which the maximum stress at the most critical point is compared to the strength. Frequently this maximum stress can be determined even if a full stress analysis of the component under consideration has not been made. A well-known example is provided by notches for which analytical and approximate values of the stress concentration factor in the notch root have been determined for a large number of notch geometries.[1,2]

The aim of this study is to investigate the influence of notches on the reliability of ceramic components in order to provide a database from which appropriate design rules can be derived. A well-established theory,[3–6] the so-called multiaxial Weibull theory, is now available, by which the reliability of a ceramic component subjected to an arbitrary stress state can be evaluated. Within the framework of this theory, the reliability is determined via an integral over the stress field. In general, a finite-element analysis of the component under consideration has to be performed prior to the reliability analysis in order to determine the complete stress field with sufficient accuracy. This implies that comparing alternative designs is an arduous task, since a comprehensive finite element analysis is required even for minor modifications of the original design.

It is desirable to assess the contribution of characteristic details such as notches on the basis of tabulated values or preferably on the basis of approximate analytical solutions. For this purpose, simple tensile bars containing notches of various geometries are analysed in this paper using the finite-element method to determine the stress field and using the multiaxial Weibull theory. The dependence of the reliability on the stress concentration factor, on the stress gradient in the notch root and on the material parameters of the ceramic material is determined. An approximate formula for the stress field of a certain class of notches is given from which the contribution of circular notch in a tensile stress field to the risk of rupture can be derived.

2 Weibull Theory for Multiaxial Loading

The failure behaviour of ceramic components subjected to a multiaxial stress state can be assessed using the multiaxial Weibull theory as developed by Batdorf *et al.*[3,4] Evans,[5] and Matsuo.[6] It is assumed that failure is caused by unstable extension of natural flaws of random size, of random location and of random orientation with respect to the principal stress axes. The worst flaw, i.e. the flaw for which the most unfavourable combination

of size, location and orientation is obtained, will propagate unstably and will cause catastrophic failure.

The probability that the size a of a given flaw exceeds the critical crack size a_c is given by:

$$Q_1 = \int_V f_{\mathbf{x}}(\mathbf{x}) \int_\Omega f_{\phi,\theta}(\phi, \theta) \int_{a_c(\mathbf{x},\phi,\theta)}^{\infty} f_a(a)\, da\, d\Omega\, d\mathbf{x} \quad (1)$$

where V denotes the volume of the component considered, Ω the surface of a unit sphere with the polar angles ϕ and θ and surface element $d\Omega = \sin\theta\, d\theta\, d\phi$, $\mathbf{x}$ the coordinate vector, and $f_{\mathbf{x}}(\mathbf{x})$, $f_{\phi,\theta}(\phi,\theta)$, $f_c(a)$ are the probability density functions of the corresponding random variables.

The critical crack size can be determined using fracture mechanics, if the natural flaws can be approximated by planar cracks. Within the framework of this model, a multiaxial stress state gives rise to mixed mode loading of a crack, and the critical crack size is a function of the mode I–III stress intensity factors K_I, K_{II}, K_{III}:

$$a_c = a_c(K_I, K_{II}, K_{III}) \quad (2)$$

with

$$\begin{aligned} K_I &= \sigma_n \sqrt{a}\cdot Y_I \\ K_{II} &= \tau \sqrt{a}\cdot Y_{II} \\ K_{III} &= \tau \sqrt{a}\cdot Y_{III}. \end{aligned} \quad (3)$$

The correction factors Y_I, Y_{II} and Y_{III} represent the influence of the crack geometry. The stress σ_n normal to the crack plane is given by the following relation:

$$\sigma_n = (\sigma_1 \cos^2\phi + \sigma_2 \sin^2\phi)\cdot\sin^2\theta + \sigma_3\cos^2\theta \quad (4)$$

where σ_1, σ_2, and σ_3 are the principal stresses and ϕ and θ are the polar angles determining the orientation of the crack plane relative to the principal axes. The shear stress τ in the crack plane is given by

$$\tau = \sqrt{\tau_{r\phi}^2 + \tau_{r\theta}^2} \quad (5)$$

with

$$\tau_{r\phi} = (\sigma_2 - \sigma_1)\cdot\sin\phi\, \cos\phi\, \sin\theta. \quad (6)$$

and

$$\tau_{r\theta} = (\sigma_1 \cos^2\phi + \sigma_2 \sin^2\phi - \sigma_3)\cdot\sin\theta\, \cos\theta. \quad (7)$$

An equivalent mode I stress intensity factor K_{leq} can be introduced with

$$K_{leq} = \sigma_{eq}\cdot\sqrt{a}\cdot Y_I \quad (8)$$

where the equivalent stress σ_{eq} depends on σ_n, τ and on Y_I, Y_{II}, and Y_{III}. The critical crack size is then given by:

$$a_c = \left(\frac{K_{Ic}}{\sigma_{eq}\cdot Y_I}\right)^2 \quad (9)$$

where K_{Ic} denotes the fracture toughness.

A variety of multiaxiality criteria are given in the literature leading to different expressions for σ_{eq}. A summary can be found in ref 7. An example of one of these criteria is:[8]

$$\sigma_{eq} = \sqrt{\sigma_n^2 + \left(\frac{2}{2-\nu}\right)^2\cdot\tau^2} \quad (10)$$

which is derived using the assumption that the value of the energy release rate in the crack plane determines the onset of unstable crack propagation, and a penny-shaped crack is a suitable model for the natural flaws.

In Weibull theory the following expression is used for the integral over the crack size in eqn (1):[7]

$$\int_{a_c(\mathbf{x},\phi,\theta)}^{\infty} f_a(a)\, da = \left(\frac{\sigma_{eq}(\mathbf{x},\phi,\theta)}{\tau_0}\right)^m \quad (11)$$

where eqn (9) was used for the critical crack size. The parameters m, τ_0 in eqn (11) depend on the toughness of the matrix material and on the statistical properties of the flaw size distribution.

If all locations of flaws and all orientations occur with equal probability, the material is homogeneous and isotropic, and $f_{\mathbf{x}}(\mathbf{x})$ and $f_{\phi,\theta}(\phi,\theta)$ can be replaced by uniform distributions. Hence, Q_1 in eqn (1) is equal to:

$$Q_1 = \frac{1}{V}\int_V \frac{1}{4\pi}\int_\Omega \left(\frac{\sigma_{eq}}{\tau_0}\right)^m d\Omega\, d\mathbf{x}. \quad (12)$$

The number n of cracks in the volume V is also a random variable and can be described by Poisson's distribution. The probability of having exactly n cracks in V is given by:

$$p_n = \frac{M^n\cdot e^{-M}}{n!}, \quad (13)$$

where M is the average number of cracks in V. The following relation for the failure probability P_f is obtained from eqns (12) and (13):[7]

$$P_f = 1 - \exp(-M\cdot Q_1). \quad (14)$$

With the definition of a new material parameter σ_0:

$$\sigma_0 = \tau_0\cdot\left(\frac{V}{V_0\cdot M}\right)^{\frac{1}{m}} \quad (15)$$

where V_0 is a reference or unit volume, the following relation is finally obtained for the failure probability:

$$P_f = 1 - \exp\left(-\frac{1}{V_0}\int_V \frac{1}{4\pi}\int_\Omega \left(\frac{\sigma_{eq}}{\sigma_0}\right)^m d\Omega\, d\mathbf{x}\right). \quad (16)$$

Equation (16) can be rewritten as:

$$P_f = 1 - \exp\left(\left(\frac{\sigma^*}{b}\right)^m\right) \quad (17)$$

where σ^* is a reference stress characterising the loading of the component, and

$$b = \frac{\sigma_0}{H} \tag{18}$$

with the normalised stress integral

$$H = \left(\frac{1}{V_0}\int_V \frac{1}{4\pi}\int_\Omega \left(\frac{\sigma_{eq}}{\sigma^*}\right)^m d\Omega\, dx\right)^{\frac{1}{m}}. \tag{19}$$

Equation (17) implies that the stress at fracture is a Weibull distributed random variable.

The normalised stress integral H is independent of the applied load level and is hence a convenient tool to characterise the effect of the spatial stress distribution on the failure probability, particularly if two components with different geometries are compared. In this case the corresponding Weibull parameters $b^{(1)}$, $b^{(2)}$ (eqn (17)) are related by:

$$\frac{b^{(1)}}{b^{(2)}} = \frac{H^{(2)}}{H^{(1)}}. \tag{20}$$

The allowable stress levels $\sigma^{*(1)}$, $\sigma^{*(2)}$ for two different designs of a component are related by:

$$\frac{\sigma^{(1)*}}{\sigma^{(2)*}} = \frac{H^{(2)}}{H^{(1)}} \tag{21}$$

at a given level of reliability which is characterised by a specific value of P_f. From eqns (17)–(21) it is clear that the information needed for the design of ceramic components is contained in the normalised stress integral, which will be used in the subsequent investigations. However, it should be kept in mind that the numerical value of H depends on the choice of the normalisation volume V_0. The same applies to the ratio of H-values, if the Weibull exponent m is not kept constant.

3 Numerical Evaluation of the Failure Probability

The five-dimensional integral eqn (19) has to be evaluated in order to determine the failure probability or the normalized stress integral H. Conventional numerical integration procedures such as the Gauss integration can be used to integrate over the orientation angles, whereas the integration over the volume is more difficult.

The stress tensor for real structures is generally determined by a finite element analysis, which yields the values of σ_{ij} at a limited number of points within each element, the so-called Gauss points. Because of the high value of m which is obtained for advanced ceramic materials, the gradients of the integrand within each element are very steep, and a large number of evaluation points are needed in order to achieve convergence of the numerical integration. A very fine finite-element mesh could be used to solve this problem, but then the computational costs of the stress analysis may become prohibitive.

An arbitrary number of evaluation points can be generated, if the shape functions of the finite-elements is used to interpolate the stress field between the Gauss points of the finite-element mesh. Using these additional points conventional numerical integration methods can again be applied to calculate the volume integral eqn (12) or eqn (19). This procedure is implemented in the STAU computer code and its extensions (STAULE for lifetime evaluation and STAUB for proof testing)

4 Notches in Ceramic Components

4.1 Normalised stress integral H

The stress field of a notched tensile bar for various notch geometries was calculated using a linear eleastic finite-element analysis. Figure 1 shows the geometry of the bar with a typical finite-element mesh. The stress field in the notched cross-section is given in Fig. 2, which also illustrates the characteristics of the stress field, namely the stress-concentration factor:

$$\alpha_k = \frac{\sigma_{1,\,max}}{\sigma_{nom}} \tag{22}$$

and the normalised stress gradient

$$\chi^* = \frac{1}{\sigma_{1,\,max}} \cdot \left.\frac{d\sigma_1}{dx}\right|_{x=0} \tag{23}$$

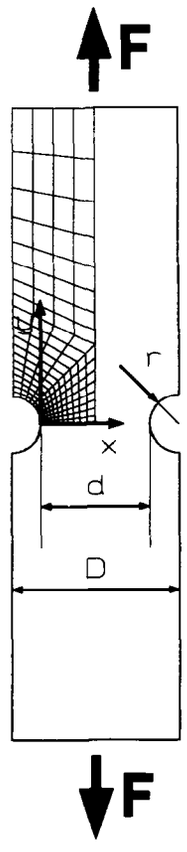

Fig. 1. Geometry of notched tensile bar with typical finite-element mesh.

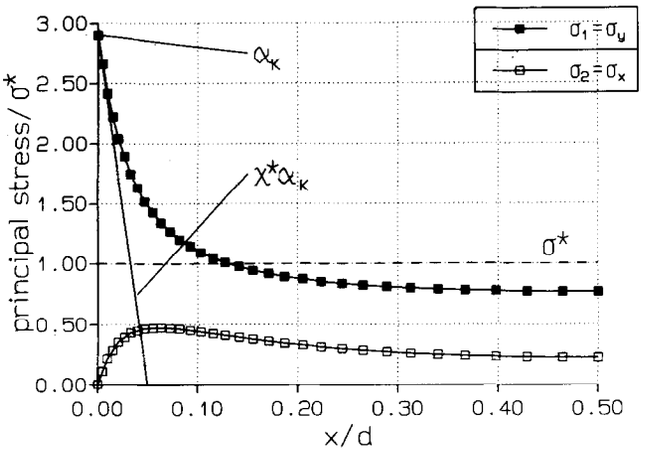

Fig. 2. Stress distribution in the notched cross-section.

where $\sigma_{1,max}$ is the maximum stress in the notch root ($x = 0$) and σ_{nom} is the nominal stress.

The geometries of the notches considered are shown in Fig. 3. The width of the notched cross-section d was kept constant in all cases. With these geometries a wide range of α_k–χ^*-values has been covered (see Table 1, $1{\cdot}9 < \alpha_k < 5$ and $0{\cdot}3 < \chi^* < 2$). The normalised stress gradient χ^* could be evaluated with sufficient accuracy only for those notches for which the notch roots were situated on the $y = 0$ symmetry line of the structure because of the limitations imposed by the finite-element mesh.

The normalised stress integral H, eqn (19), was calculated for these notched tensile bars using the finite-element code ABAQUS and the post-processor STAU.[10] The reference stress σ^* in eqn (19) was set equal to the nominal stress. The equivalent stress was determined using eqn (10).

All dimensions including the unit volume V_0 were given in mm. The thickness of the bars was assumed to be equal to 1, the nominal width d was 40, and the length L was 90.

Figure 4 shows the variation of the normalised stress integral H with the stress concentration factor α_k. For low values of the Weibull exponent m, the value of H depends only weakly on the stress concentration factor whereas H approaches α_k for

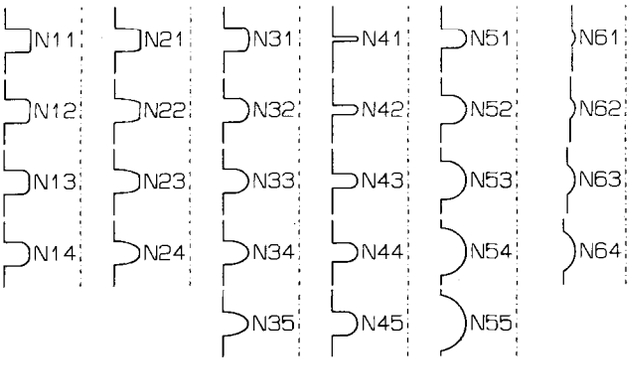

Fig. 3. Notch geometries.

Table 1. Dimension of notches defined in Fig. 3 in notched tensile bars with length L = 90 mm and nominal thickness d = 40 mm

Notch number	α_k, *eqn (22)*	χ^*, mm^{-1}, *eqn (23)*	$\frac{D}{d}$, *see Fig. 1*
N11	3·65	—	1·250
N12	2·99	—	1·250
N13	2·71	—	1·250
N14	2·55	—	1·250
N21	5·03	—	1·250
N22	4·05	—	1·250
N23	3·60	—	1·250
N24	3·32	—	1·250
N31	2·15	—	1·250
N32	2·48	—	1·250
N33	2·85	—	1·250
N34	3·17	—	1·250
N35	3·46	0·63	1·250
N41	4·97	1·21	1·250
N42	3·84	0·75	1·250
N43	3·27	0·50	1·250
N44	2·92	0·47	1·250
N45	2·67	0·38	1·250
N51	2·90	1·00	1·250
N52	2·47	0·70	1·250
N53	2·21	0·52	1·250
N54	2·04	0·42	1·250
N55	1·91	0·35	1·250
N61	1·95	1·19	1·030
N62	1·90	0·82	1·045
N63	1·92	0·57	1·075
N64	1·89	0·49	1·115

high values of m, i.e. low scatter of the materials' strength. In the deterministic limit ($m \to \infty$), only the maximum stress $\sigma_{1,max}$ contributes to the failure probability and H is equal to α_k. The influence of the shape of the notch is small compared to the influence of the stress-concentration factor for realistic values of m, as notches of very difficult shapes such as N21 and N41 yield H-values $H_{21} = 3{\cdot}53$ and $H_{41} = 3{\cdot}40$, respectively, for $m = 15$ which are

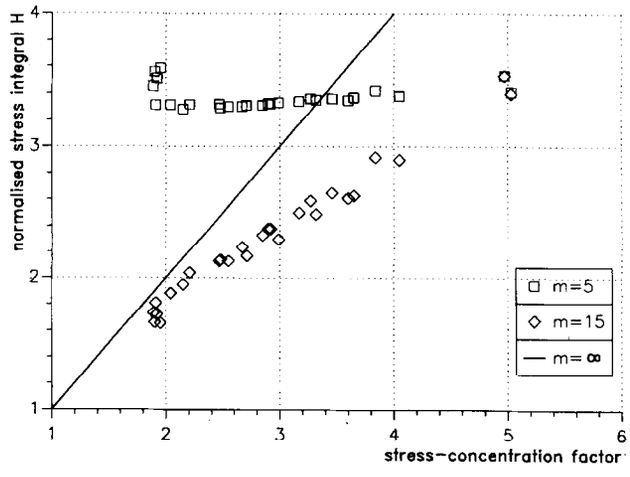

Fig. 4. Dependence of the normalised stress integral H on the stress concentration factor α_k; $m = \infty$ deterministic limit with $H = \alpha_k$.

much closer to each other than the values obtained from notches of similar shapes and different values of α_k (e.g. N11 and N21: $H_{11} = 2{\cdot}63$ and $H_{21} = 3{\cdot}40$).

Because of the strong correlation between α_k and χ^* for most of the examples studied here a special class of notches was selected with almost constant $\alpha_k = 1{\cdot}9$ and $0{\cdot}35 < \chi^* < 1{\cdot}2$ (N55, N61–64 in Fig. 3). These notches are compared to notches with $\alpha_k \propto \chi^*$ and χ^* in the same order of magnitude (N51–55 in Fig. 3). Figure 5(a, b) show the normalised stress integral H as a function of χ^* in both cases.

A reduced nominal thickness of $d = 20$ was used in this case in order to obtain more accurate values for the stress gradients. The effect of the nominal width on the normalised stress integral H is quite important, especially for low values of m, as can be seen by comparing Fig. 4 with Fig. 5(a).

The relationship between H and χ^* (Fig. 5(a)) looks very similar to that between H and α_k for N51–55 (Fig. 4), i.e. the effect of the stress gradient

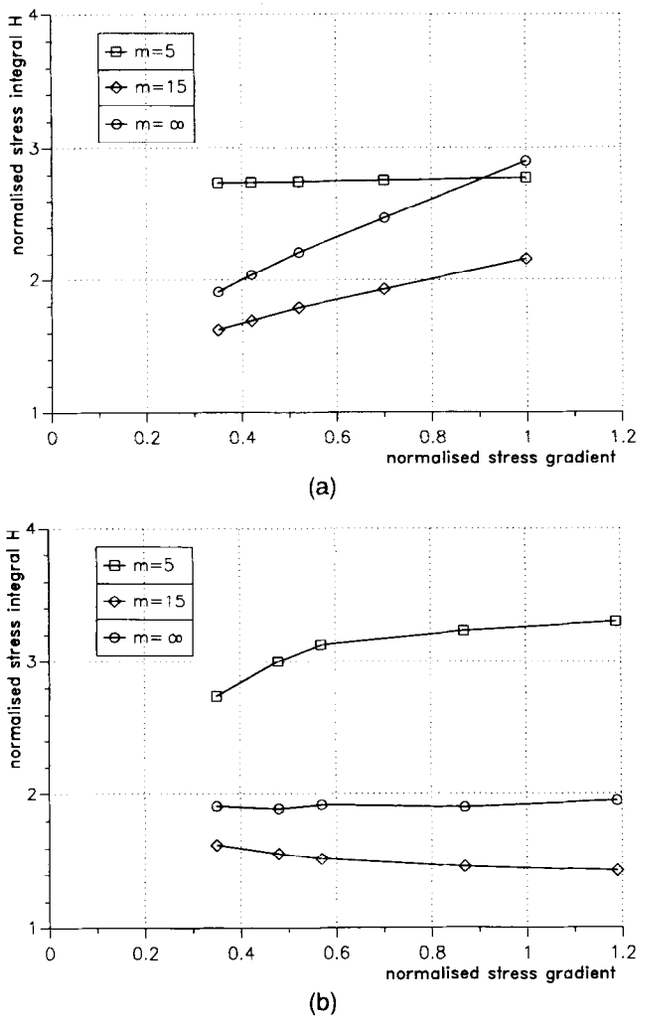

Fig. 5. (a) Dependence of the normalised stress integral H on the normalised stress gradient χ^*; notches with $\alpha_k \propto \chi^*$ (N51–55). (b) Dependence of the normalised stress integral H on the normalised stress gradient χ^*; notches with $\alpha_k \approx 1{\cdot}9$ (N55 and N61–64).

cannot be separated from the effect of the peak stress in the notch root. The increase in H with χ^* (i.e. a steeper gradient of the stress in the notch root) observed for $m = 5$ in the case of N55 and N61–64 (see Fig. 5(b)) is due to the fact that the stress gradient χ^* increases with increasing total width D (see Table 1). The nominal width and the nominal stress were kept constant, and hence a larger value of D implies that the stress in the remainder of the bar outside the notched cross-section decreases. H decreases with increasing χ^* for $m = 15$, because the width effect is suppressed and the change of the stressed volume in the notched cross-section becomes dominant.

4.2 Local risk of rupture for notches

The influences on the value or the normalised stress integral H can be clarified using the local risk of rupture as introduced in ref. 11. The following sub-volumes of the notched tensile bar are defined (see Fig. 6):

- V1 depending on the peak stress and on χ^* with

$$0 \le \rho \le r_\omega(\omega) = r_c \cdot (1 + \frac{4}{\pi}\omega), \qquad 0 \le \omega \le \frac{\pi}{2}$$

- V2 characterizing the distribution of the stress field in the centre of the notched cross-section with

$$r_\omega = r_c \cdot (1 + \frac{4}{\pi}\omega) < \rho \le \frac{d}{2} \qquad 0 \le \omega \le \frac{\pi}{2}$$

- V3 depending on the gradient of the stress field along the notch contour with

$$0 \le \rho \le 3r_c, \frac{\pi}{2} < \omega \le \frac{5\pi}{8}$$

- V4 linking V3 to the unnotched bar with

$$3r_c < \rho \le \frac{d}{2}, \quad \frac{\pi}{2} < \omega \le \frac{5\pi}{8}$$

- V5 taking care of the contribution from the remainder of the bar:

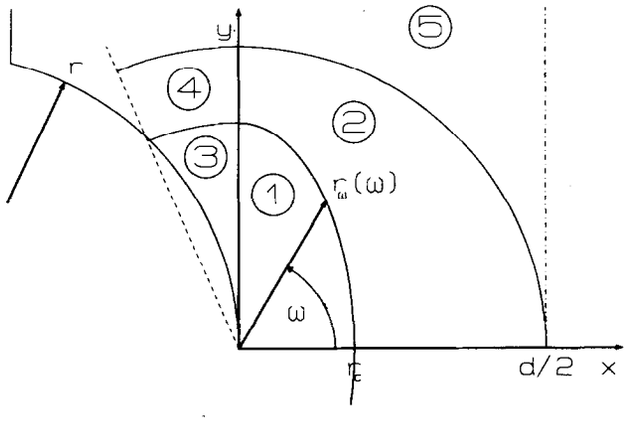

Fig. 6. Definition of the sub-volumes V1–5.

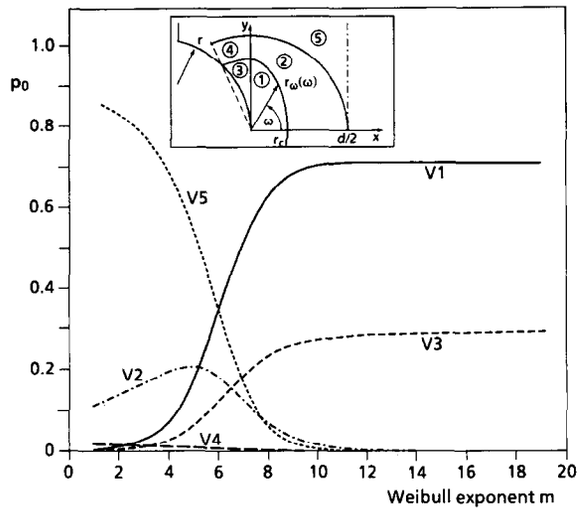

Fig. 7. Local risk of rupture p_0 for the sub-volumes V1–5; notch N51.

$$0 \le x \le \frac{d}{2} \text{ and } \frac{d}{2} < y \le \frac{L}{2};$$

$$0 \le x \le \frac{d}{2} \text{ and } \sqrt{x^2 + y^2} > \frac{d}{2}.$$

Here ρ denotes the distance from the notch root, ω the polar angle as shown in Fig. 6, and r_c is defined as

$$r_c = \frac{d}{2} \cdot \left(1 - \sqrt{1 - \frac{4(\alpha_k - 1)}{\alpha_k \cdot \chi^* \cdot d}}\right) \tag{24}$$

The local risk of rupture of sub-volume Vi is equal to:[9,11]

$$p_0(Vi) = \frac{\int_{Vi}\int_{\Omega} \sigma_{eq}{}^m \, d\Omega \, dV}{\int_{V}\int_{\Omega} \sigma_{eq}{}^m \, d\Omega \, dV} \tag{25}$$

$p_0(Vi)$ is equal to the probability that the worst flaw triggering fracture is contained in Vi. The local risk of rupture is depicted in Fig. 7 for notch N51. Similar pictures are obtained for other notch geometries. Figure 7 shows that the highest risk of rupture is associated with sub-volume V5 for low values of m. This implies that the stress field in the remainder of the notched tensile bar outside the notched cross-section dominates the failure probability. The notch geometry, on the other hand, influences the stress field in sub-volumes V1 and V3 which determine the failure probability for $m \ge 8$.

4.3 Approximation formula for H

The stress field of the notched tensile bars depends on the stress concentration factor α_k, the normalised stress gradient χ^*, and the relative notch depth d/D. Although the detailed stress distribution may be quite complicated (see e.g. ref. 1), a comparatively coarse approximation of the stress field may be sufficient in order to determine the normalised stress integral H, which depends mainly on α_k (m large) or on the stressed volume (m small).

The following relation is used for the maximum principal stress of a notched tensile bar:

$$\frac{\sigma_1}{\sigma^*} = \begin{cases} \alpha_k \cdot (1 - \chi^* \cdot r_c \cdot \dfrac{\rho}{r_\omega(\omega)}) \text{ in V1} \\ \alpha_k \cdot (1 - \chi^* \cdot r_c) \text{ in V2 and V4} \\ \alpha_k \cdot (1 - \chi^* \cdot \dfrac{\rho}{3}) \text{ in V3} \\ \dfrac{d}{D} \text{ in V5} \end{cases} \tag{26}$$

where V1–5 and $r_\omega(\omega)$ were defined in Section (2) and r_c follows from eqn (24). The approximate stress field, eqn (26), decreases linearly in the notched cross-section with the gradient—$\alpha_k \cdot \chi^*$ until it attains a constant value. It fulfils the equilibrium condition in the notched cross-section. The second principal stress is small compared to σ_1 in the vicinity of the notch root (see Fig. 2) and is set equal to zero.

The normalised stress integral H, eqn (19) can be split up into a volume integral and an integral over the orientation angles:

$$\begin{aligned} H &= H_v \cdot H_\Omega \\ H_v &= \frac{1}{V_0} \int_V \left(\frac{\sigma_1}{\sigma^*}\right)^m dV \\ H_\Omega &= \frac{1}{4\pi} \int_\Omega \left(\frac{\sigma_{eq}}{\sigma_1}\right)^m d\Omega. \end{aligned} \tag{27}$$

The following relations are obtained from eqn (26) for the contributions of the sub-volumes V1–5:

$$H^m_{V1} = \frac{13\pi}{6} \cdot \alpha_k{}^m \cdot \frac{1 - (1 - \chi^* r_c)^{m+1} \cdot (\chi^* r_c(m+1) + 1)}{(\chi^*)^2 \cdot (m+1) \cdot (m+2)} \tag{28}$$

$$H^m_{V2} = \frac{\pi}{12} \cdot \alpha_k{}^m \cdot (1 - \chi^* r_c)^m \cdot \left(\frac{3}{4}d^2 - 13r_c^2\right) \tag{29}$$

$$H^m_{V3} = \frac{9\pi}{8} \cdot \alpha_k{}^m \cdot \frac{1 - (1 - \chi^* r_c)^{m+1} \cdot (\chi^* r_c(m+1) + 1)}{(\chi^*)^2 \cdot (m+1) \cdot (m+2)} \tag{30}$$

$$H^m_{V4} = \frac{\pi}{16} \cdot \alpha_k{}^m \cdot (1 - \chi^* r_c)^m \cdot \left(\frac{1}{4}d^2 - 9r_c^2\right) \tag{31}$$

and

$$H^m_{V5} = \left(\frac{d}{D}\right)^m \cdot \frac{d^2}{4} \cdot \left(\left(\frac{L}{d} - 1\right) \cdot \frac{D}{d} + 1 - \frac{\pi}{4}\right). \tag{32}$$

The value of H_Ω eqn (27); can be determined by straightforward numerical integration, as the

equivalent stress σ_{eq} depends only on one polar angle for uniaxial stress states, (see eqns (4)–(8)). A closed-form analytical solution can be obtained in special cases (see Appendix). Combining eqns (28)–(32), the normalised stress integral follows from:

$$H = (4 \cdot (H'^{m}_{V1} + H'^{m}_{V2} + H'^{m}_{V3} + H'^{m}_{V4} + H'^{m}_{V5})^{\frac{1}{m}} \cdot H_{\Omega}. \quad (33)$$

Figure 8 shows the H-values obtained from eqns (8)–(33) and the H-values obtained by numerical integration of the stress field which had been determined by a finite-element analysis. The agreement obtained for notches N51 and N55 is very good.

It should be kept in mind, however, that eqns (27)–(33) are applicable only in cases where the notch root lies on the symmetry line. There are greater deviations for non-central notches as can be concluded from Fig. 4 which shows the variation of H for a given value of α_k. It may also be difficult in these cases to obtain reliable values of χ^*. In all cases considered in this paper the following relationships hold for $m > 10$

$$H \propto \frac{\alpha_k^m}{\chi^{*2} \cdot m^2} \quad (34)$$

and, according to eqn (A12):

$$H'^{m}_{\Omega} \propto \frac{1}{m} \quad (35)$$

with an accuracy of about 10%. Combining eqns (34) and (35) leads to the following expression for the stress integral H:

$$H \propto \frac{\alpha_k}{(\chi^{*2} \cdot m^3)^{\frac{1}{m}}}. \quad (36)$$

In using this relation it should be kept in mind that it was derived on the basis of a limited number of examples and is strictly speaking only applicable to cases with very similar notch contours in a uniaxial stress field. However, additional examples not included in this paper showed a very similar behaviour. Hence it is felt that the relation (36) can be used in a somewhat more general sense, and that it yields the dependence of the leading term of the failure probability on characteristic quantities such as the stress concentration factor, the normalised stress gradient, and the Weibull modulus.

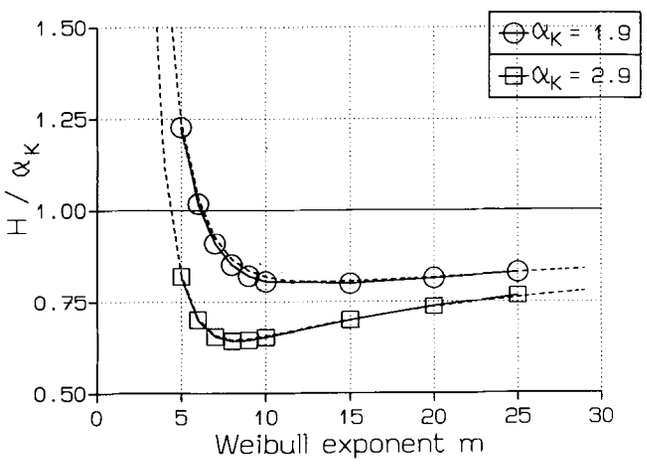

Fig. 8. Comparison of the analytical approximation for H, eqns (28)–(33), with the results of the finite-element analysis; - - - analytical solution; — numerical analysis.

5 Conclusion

The influence of notches on the reliability of ceramic components can be assessed using a normalised stress integral. The stress-concentration factor α_k in the notch root is the most important influencing factor which implies that notches of different shapes but similar values of α_k yield similar values of the stress integral. This conclusion was drawn from results obtained with tensile bars containing circular notches. The local risk of rupture in the vicinity of the notch root approaches unity for $m > 8$, i.e. failure is almost always caused by flaw located near the notch root. This is why a linear approximation of the stress field in the vicinity of the notch root, from which a closed-form solution of the stress integral can be derived, agrees very well with the values of the stress integral obtained by numerical integration of the exact stress field.

References

1. Neuber, H., *Kerbspannungslehre*, Springer Publ., Berlin, 1989.
2. Peterson, R. E., *Stress Concentration Factors*, J. Wiley Publ., New York, 1974.
3. Batdorf, S. B. & Crose, J. G., A statistical theory for the fracture of brittle structures subjected to nonuniform stress. *J. Appl. Mechanics*, **41** (1974) 459–61.
4. Batdorf S. B. & Heinisch, H. L., Weakest link theory reformulated for arbitrary fracture criterion. *J. Am. Ceram. Soc.*, **61** (1978) 355–8.
5. Evans A. G., A general approach for the statistical analysis of multiaxial fracture. *J. Am. Ceram. Soc.*, **61** (1978) 302–8.
6. Matsuo Y., A probabilistic analysis of fracture loci under bi-axial stress state. *Bull. JSME*, **24** (1981) 290–4.
7. Thiemeier, T., Brückner-Foit, A. & Kölker, H., Influence of the fracture criterion on the failure probability of ceramic components. *J. Am. Ceram. Soc.*, **74** (1991) 48–52.
8. Paris P. C. & Sih, G. C., Stress Analysis of Cracks. In *Fracture Toughness Testing and its Applications*, ASTM STP 381, American Society of Testing of Materials, Philadephia, PA, 1965, pp. 30–83.
9. Matsuo, Y. & Kitakami, K., On the statistical theory of fracture location combined with competing risk theory. In *Fracture Mechanics of Ceramics*, Vol. 7, eds, R. C. Bradt *et al.*, Plenum Press, New York, 1986, pp. 223–35.

10. Heger, A., Brückner-Foit, A. & Munz D., STAU — ein Programm zur Berechnung der Ausfallwahrscheinlichkeit mehrachsig beanspruchter keramischer Komponenten als Post-Prozessor für Finite-Elemente-Programme. Internal Report, Institute for Reliability and Failure Analysis, University of Karlsruhe, Germany, 1991.
11. Brückner-Foit A., Heger, A. & Munz D., Effect of proof testing on the failure probability of multiaxially loaded ceramic components. *ASTM STP 1202*, American Society for Testing and Materials Philadelphia, PA, 1993, pp. 346–59.

Appendix

A uniaxial stress state leads to the following relations for the normal stress σ_n (mode I loading) and the shear stress τ (mode II loading):

$$\sigma_n = \sigma_1^2 \cdot \cos^2\theta \tag{A1}$$

$$\tau = \sigma_1 \cdot |\sin\theta \cos\theta| \tag{A2}$$

where eqns (4)–(7) have been used. Equation (10) yields for the equivalent stress:

$$\sigma_{eq} = \sigma_1 \cdot |\cos\theta| \cdot \sqrt{\cos^2\theta + \left(\frac{2}{2-\nu}\right)^2 \sin^2\theta}\,. \tag{A3}$$

Hence the integral H_Ω, eqn (27), has the following form:

$$H\Omega^m = \int_0^{\frac{\pi}{2}} \left(\cos^2\theta + \left(\frac{2}{2-\nu}\right)^2 \sin^2\theta\right)^{\frac{m}{2}} \cdot \cos^m\theta \cdot \sin\theta \, d\theta \tag{A4}$$

which can be integrated in closed form for even values of m.

With the binomial relation

$$\left(\cos^2\theta + \left(\frac{2}{2-\nu}\right)^2 \sin^2\theta\right)^{\frac{m}{2}} = \sum_{k=0}^{m/2} \binom{m/2}{k} \cdot \left(\frac{2}{2-\nu}\right)^{2k} \cdot \sin^{2k}\theta \cdot \cos^{m-2k}\theta \tag{A5}$$

and the substitution $x = \cos\theta$, the integral eqn (A4) can be written as:

$$H\Omega^m = \sum_{k=0}^{m/2} \int_0^1 \binom{m/2}{k} \cdot \left(\frac{2}{2-\nu}\right)^{2k} x^{2m-2k} \cdot (1-x^2)^k \, dx \tag{A6}$$

The following relation can be derived by successive integration by parts:

$$\int_0^1 x^{2m-2k} \cdot (1-x^2)^k \, dx = \frac{k! \cdot 2^k}{(2m+1) \cdot (2m-1) \cdot \ldots \cdot (2m-2k+1)} \tag{A7}$$

which leads to the following expression for Hω:

$$H\Omega^m = \frac{1}{2m+1} \sum_{k=0}^{m/2} \left(\frac{2}{2-\nu}\right)^{2k} \cdot \frac{m \cdot (m-2) \cdot \ldots \cdot (m-2k+2)}{(2m-1) \cdot (2m-3) \cdot \ldots \cdot (2m-2k+1)} \tag{A8}$$

Equation (A8) is valid only for even values of m. The orientation integral Hω for general values of m can be obtained by interpolation.

Equation (A8) can be simplified using

$$\frac{m-2l}{2m-2l-1} \le \frac{m-2l}{2m-4l} = \frac{1}{2} \text{ for } l = 1, \ldots, \frac{m}{2} - 1 \tag{A9}$$

and

$$\frac{m-2l}{2m-2l-1} \ge \frac{m-2l}{2m-1} \ge \frac{2}{2m-1} \text{ for } l = 0, \ldots, \frac{m}{2} - 1. \tag{A10}$$

The following bounds are obtained for $H\Omega$ after some re-arrangement of the sums:

$$\frac{1}{2m+1} \cdot \frac{1 - \left(\left(\frac{2}{2-\nu}\right)^2 \cdot \frac{2}{2m-1}\right)^{\frac{m}{2}+1}}{1 - \left(\frac{2}{2-\nu}\right)^2 \cdot \frac{2}{2m-1}} \le H\Omega^m \tag{A11}$$

$$\le \frac{1}{2m+1} \cdot \frac{1 - \left(\left(\frac{2}{2-\nu}\right)^2 \cdot \frac{1}{2}\right)^{\frac{m}{2}+1}}{1 - \left(\frac{2}{2-\nu}\right)^2 \cdot \frac{1}{2}} - \frac{1}{(2m+1)(2m-1)}$$

These bounds can be used to obtain an estimate of $H\Omega$ for general values of m, since $H\Omega$ is a smooth function of m. Equation (A11) implies that

$$H\Omega^m \propto \frac{1}{m} \tag{A12}$$

for $m \ge 10$. The same relationship can be obtained for other criteria with the proportionality factor depending on the multiaxiality criterion.

Journal of the European Ceramic Society **16** (1996) 1035–1039

PII: S0955-2219(96)00029-5
0955-2219/96/$15.00

β-Conductivity Contrast at Barium Titanate Thermistor Grain Boundaries

J. D. Russell & C. Leach

Manchester Materials Science Centre, University of Manchester and UMIST, Grosvenor Street, Manchester, M1 7HS, UK

(Received 15 August 1995; revised version received 11 January 1996; accepted 12 January 1996)

Abstract

Barium titanate based PTC thermistor materials have been examined using the conductive mode of a scanning electron microscope. Under an applied voltage bias, at temperatures above the Curie temperature, bright and dark lines which are due to β-conductivity appear coincident with grain boundaries. The mechanisms of contrast formation are discussed. Such contrast can be used to evaluate the distribution of this type of active grain boundary.
© 1996 Elsevier Science Limited.

1 Introduction

The positive temperature coefficient (PTC) of resistance properties of barium titanate ceramics and similar materials has long been used for applications such as thermal protection and current-limiting devices.[1,2] Early models of the PTC effect invoked double Schottky barriers at grain boundaries due to a build-up of negatively charged acceptor states at the interface.[3] This gives rise to a potential barrier whose height at a given temperature depends on the dielectric constant, which changes rapidly around the Curie temperature (T_c). Extensions to this model by Jonker included the spontaneous polarization which occurs below T_c and reduces the expected potential barrier height.[4] Daniels and Wernicke[5] modelled the behaviour by considering an extended grain boundary layer in which the donor dopants are heavily compensated by barium vacancies, frozen-in during cooling from the sintering temperature. In practice, these models are still the subject of some debate,[6] and probably only represent special cases of the overall situation, with microstructural heterogeneity also being an issue in considering the overall electrical properties of electronic ceramics.[7]

Remote electron beam induced current (REBIC) is a specialized form of conductive mode microscopy, which essentially involves making two connections to the sample: one to earth, and one through a current amplifier to earth. The images and line-scans formed with the amplified output may show contrast due to three main mechanisms:

(I) *charge collection* due to separation of generated electron-hole pairs at built-in fields and their subsequent collection at the electrodes,[8]
(II) *β-conductivity*, a direct analogue of photoconductivity, due to the localized injection of charge carriers by the electron beam and increased local conductivity observed under voltage bias,[9,10] and
(III) *resistive contrast* due to the specimen acting as a current divider for the absorbed beam current to travel to earth[11] and non-linear resistance variations, giving a signal step at resistive barriers.

Resistive contrast is observed to some extent at most grain boundaries, and is rather weak, as the signal containing this effect is necessarily smaller than the beam current. The other two contrast types are caused by the electron-hole pairs generated by the electron beam, and as the electron beam energy is orders of magnitude greater than the electron-hole pair formation energy, each beam electron generates thousands of electron-hole pairs in the sample. The resulting signals are therefore much stronger than those due to resistive contrast. According to Heywang's model,[3] the grain boundary is characterized by interface charge which gives rise to a back-to-back Schottky diode structure. It is the electric field due to band bending associated with these barrier structures which can give rise to electron-hole pair separation and subsequent collection, resulting in contrast due to the first mechanism described above. The n–i–n grain boundary structure of Daniels' model has two regions of band-bending, which are separated by a boundary layer.

The REBIC technique has recently been applied to the study of electronic ceramic materials such as zinc oxide[12,13] and barium titanate.[14] REBIC offers one of the few means of visualizing such electrical properties

at individual grain boundaries. In this contribution, we describe β-conductivity contrast in PTC thermistors, an effect that has not previously been reported in these materials.

2 Method

Commercial barium titanate PTC thermistor material was cut into 1 mm thick sections and polished on nylon cloth using a water-based slurry of 0·3 μm α-alumina powder. Electrical contacts were formed by evaporating aluminium through a fine transmission electron microscope grid to form an array of closely spaced contacts. After mounting the samples on insulating stubs they were observed in a scanning electron microscope (SEM) fitted with an Oxford Instruments H1001 heating stage. Micromanipulator probes, attached through the side port of the SEM, were then placed directly in contact with the electrodes, and the collected REBIC signal amplified with a high-sensitivity current amplifier for both imaging and quantitative linescans.

3 Results

At room temperature the specimen resistance is very small and REBIC images are very noisy due to instrumentation considerations.[14] However, on

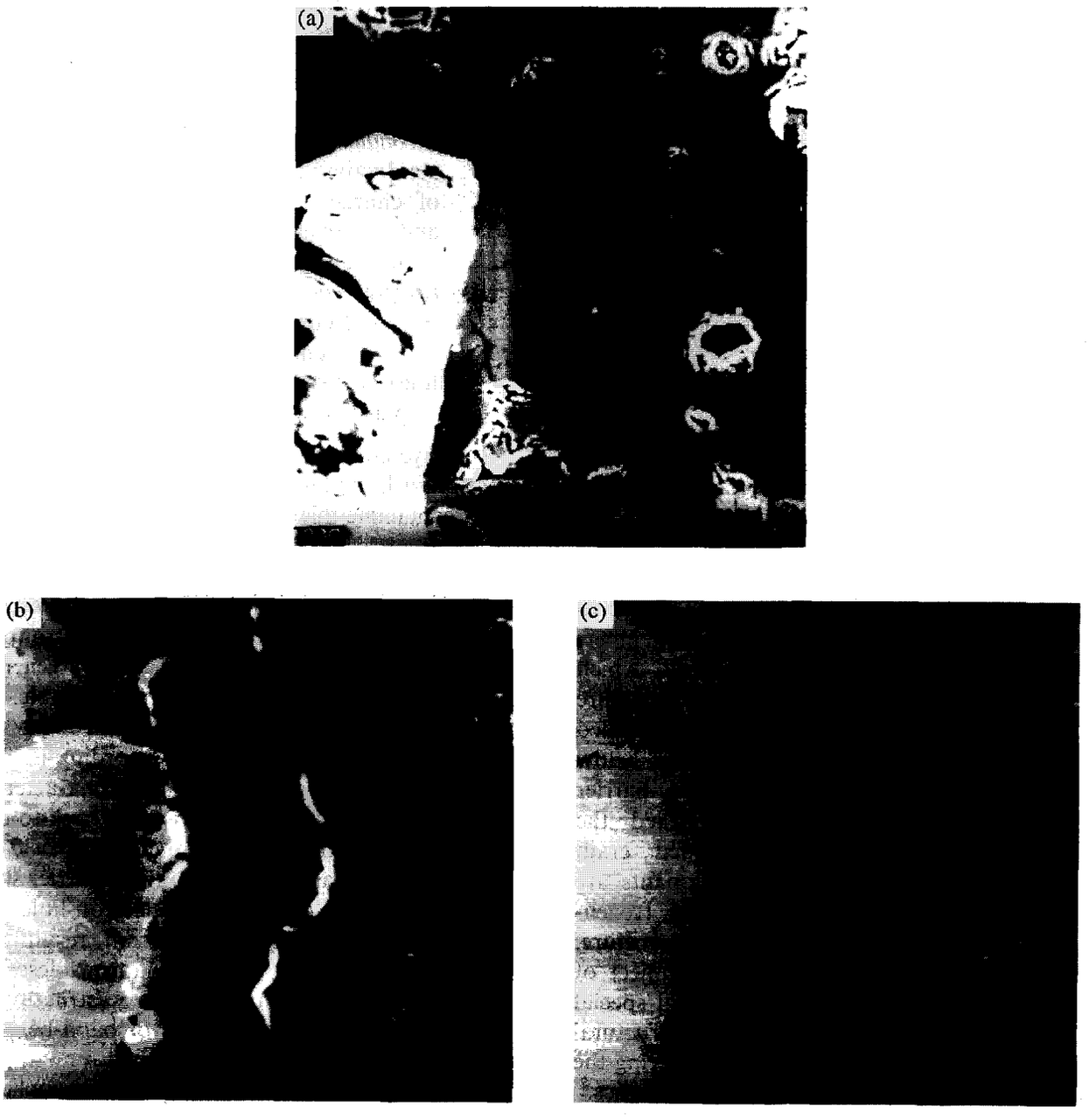

Fig. 1. SE (a) and REBIC images (b,c) taken at 180°C with biases of +0·161 V and –0·054 V respectively, showing a reversal in the β-conductivity contrast. The two aluminium contact pads can be seen on the left and right of the images, while one of the probes can be seen on the visible area of the left contact. The scale bar indicates 20 μm.

heating samples *in situ* above the Curie transition temperature, the specimen resistance becomes large enough to facilitate high-quality imaging of the electrical activity at the grain boundaries.

Previous studies have shown principally resistive contrast in this system, giving rise to a step in the signal level as the grain boundary is traversed by the electron beam scanning between the contacts,[14] and this effect is also observed in the samples described here. However, under an applied bias bright or dark lines also appear, coincident with some, but not all, grain boundaries [Figs 1(a) and (c)]. These lines are not due to any feature in the secondary or backscattered image of the SEM [Fig. 1(b)]. Often, the grain boundaries which show this contrast are those which are aligned transversely in the gap between the electrodes [on the left and right in Figs 1(b) and (c)], an orientation which corresponds geometrically to the maximum electric field gradient. It is also apparent that reversing the bias reverses the contrast at all active grain boundaries. For a given bias, only dark *or* bright contrast is observed. Notwithstanding the difficulties of imaging low-resistance samples, on decreasing the temperature towards the Curie temperature it is found that the contrast is steadily reduced until at the Curie temperature it has disappeared.

Quantitative linescans taken across an active grain boundary with positive and negative biases are shown in Fig. 2. The axes are offset to compensate for the large standing currents which flow between the contacts through the sample due to the applied bias. In these cases, the excess current which flows when the beam is incident at the grain boundary, I_{gb}, is about 15 nA, compared with the beam current of 1·6 nA.

4 Discussion

Polycrystalline materials often show bright or dark contrast caused by built-in fields at the

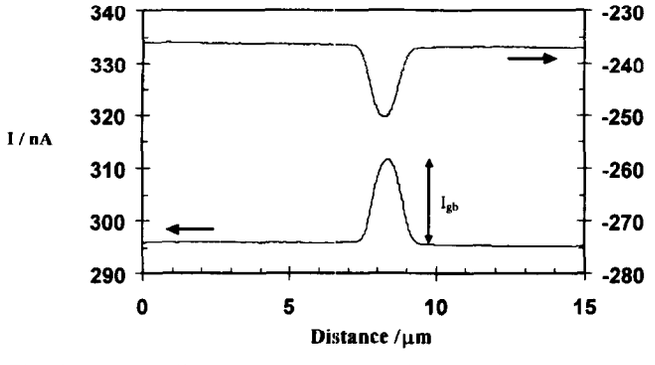

Fig. 2. REBIC linescans across a grain boundary like those shown in Fig. 1, with applied biases of +0·2 V and −0·2 V, and a beam current of 1·6 nA. The vertical scales of the two curves are offset to allow for the relatively large standing currents which flow.

Schottky barriers, due to charged grain boundary interface states. This contrast has been well characterized in silicon,[15] and several other semiconductors,[16,17] and has also been observed recently in electronic ceramics such as zinc oxide.[12] Such contrast consists of characteristic parallel bright and dark lines at a single grain boundary, although recently single line contrast which might also be due to built-in fields has been observed in such systems[13]

It would appear that the contrast observed here is due to β-conductivity rather than charge collection (of electron-hole pairs separated by built-in fields) for a number of reasons. Firstly, with no applied bias, it is very weak, and the contrast which does occur can be nulled completely to give a flat linescan profile by applying a very small bias (~mV) to compensate for the amplifier input offset voltage. Secondly, the contrast reversal with change in sign of the applied bias (which occurs for Schottky barrier contrast) would be accompanied by a lateral shift equal to the width of the electron beam excitation volume,[12] but no such shift is observed in these PTC thermistors. It is therefore concluded that the observed contrast is due to some form of enhanced conductivity induced by the electron beam. Since no type I contrast was observed here even though band bending is expected at both back-to-back Schottky barrier and n–i–n structures, we must conclude that either the band bending is too small to permit adequate charge separation or, more likely, that the generated electron-hole pairs recombine in and near the depletion region before becoming completely separated. This would make the charge collection currents too weak to be observed.

β-Conductivity depends on variations in the local resistivity under irradiation by the electron beam, and is a direct analogue of photoconductivity.[18] In the semiconducting grains of barium titanate, the conductivity σ is given by:

$$\sigma = e(n\mu_e + p\mu_h) \quad (1)$$

where e is the electronic charge, n and p are the carrier concentrations and μ_e and μ_h are the mobilities of electrons and holes, respectively. The generation of electron-hole pairs by the impinging electron beam increases the local carrier concentration, leading to a localized conductivity increase. When the beam is incident within the grains this effect is relatively small, because the carrier concentration is already large due to oxygen vacancies and aliovalent impurities which give strong n-type doping. At the grain boundaries, however, the conductivity is much smaller due to the barriers caused by charged grain boundary acceptor states,

and perhaps also by the presence of an intrinsic layer. In addition, lattice disorder, the presence of impurities and possibly also thin intergranular phases will reduce the carrier mobility. The local injection of excess electron-hole pairs can increase this grain boundary conductivity drastically either by simply increasing the number of carriers available for transport [eqn (1)] or by lowering the barrier itself when holes drift in the grain boundary electric fields to cause a transient, local neutralization of the grain boundary acceptor states.[19] Hence, although well above the Curie temperature grain boundary resistance is very large, it can be drastically reduced by electron-beam generated carriers, and give rise to a local increase in the current which flows under applied bias.

To describe how I_{gb} depends on the beam current and the applied bias, we assumed a simple, linear model of grains with low resistivity and grain boundaries with very high resistivity. Assuming that the excess carrier concentration (hence conductivity increment) at the grain boundary is proportional to the beam current I_b, it can be shown (Appendix A) that the expected variation of I_{gb} with beam current for the β-conductivity effect is of the form:

$$I_{gb} \propto \frac{V}{K + \frac{1}{I_b}} \qquad (2)$$

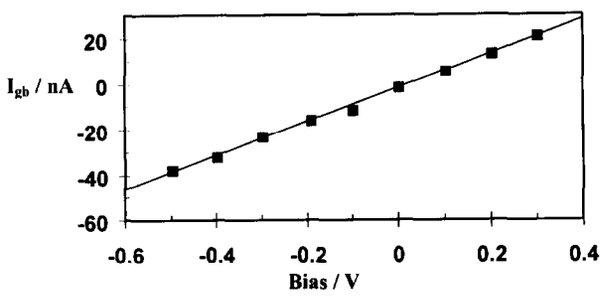

Fig. 3. Variation of the excess current which flows when the electron beam is incident at an active grain boundary, I_{gb} (see Fig. 2), as a function of applied bias.

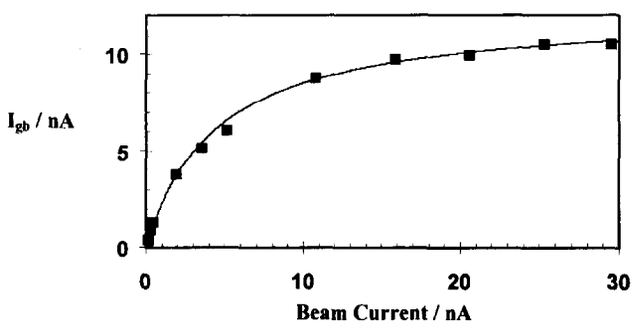

Fig. 4. Variation of I_{gb} with the beam current. The solid line is fitted to the expected form given by eqn (2).

where K is a constant and V is the applied bias. The experimental variation of I_{gb} with bias at constant beam current is shown in Fig. 3 and is linear, and hence consistent with eqn (2). The variation of I_{gb} with the beam current at constant bias was also measured (Fig. 4), and a best-fit line calculated using eqn (2). It can be seen that the predicted relationship is followed closely by the experimental measurements. At high beam currents I_{gb} saturates, since in this regime the resistivity of the thin insulating layer is sufficiently decreased by the electron beam that the overall sample resistance is dominated by grain resistances alone.

5 Conclusions

We have reported β-conductivity contrast in barium titanate PTC thermistor material for the first time, and discussed mechanisms by which it might arise. It provides a means of observing directly individual grain boundaries which are electrically active in this way.

The REBIC technique provides a very sensitive means by which many electrical properties of individual electronic ceramic grain boundaries can be characterized and compared, and is expected to become an important technique for studies of material behaviour and heterogeneity in the future.

References

1. Saburi, O. & Wakino, K., Processing techniques and applications of positive temperature coefficient thermistors. *IEEE Trans. Compon. Parts*, **CP-10** (1963) 53–67.
2. Kulwicki, B. M., Trends in PTC resistor technology. *SAMPE J.*, **23**[6] (1987) 34–38.
3. Heywang, W., Resistivity anomaly in doped barium titanate. *J. Am. Ceram. Soc.*, **47** (1964) 484–490.
4. Jonker, G. H., Some aspects of semiconducting barium titanate. *Sol. St. Electron.*, **7** (1964) 895–903.
5. Daniels, J. & Wernicke, R., New aspects of an improved PTC model. *Philips Res. Repts*, **31** (1976) 544–559.
6. Chiang, Y.-M. & Takagi, T., Grain-boundary chemistry of barium titanate and strontium titanate II, Origin of electrical barriers in positive-temperature coefficient thermistors. *J. Am. Ceram. Soc.*, **73**[11] (1990) 3286–3291.
7. Abelard, P., Present understanding of the grain boundary electrical characteristics of semiconducting $BaTiO_3$ and $SrTiO_3$ ceramics. In *Electroceramics IV*, eds R. Waser, S. Hoffmann, D. Bonnenberg & Ch. Hoffmann. Augustinus Buchhandlung, Aachen, Germany, 1994, pp. 541–548.
8. Holt, D. B., The conductive mode. In Microcharacterisation of Semiconductors, eds D. B. Holt & D. C. Joy. Academic Press, London, 1989, Ch. 6.
9. Munakata, C., An application of beta conductivity to measurement of resistivity distribution. *J. Sci. Instr. (J. Phys. E) Series 2*: **1** (1968) 639–642.
10. Gopinath, A., On scanning electron microscope conduction-mode signals in bulk semiconductor devices: linear geometry. *J. Phys. D. Appl. Phys.*, **3** (1970) 467–472.

11. Smith, C. A., Bagnell, C. R., Cole, E. I., Dibianca, F. A., Johnson, D. G., Oxford, W. V. & Propst, R. H., Resistive contrast imaging: a new SEM mode for failure analysis. *IEEE Trans. El. Dev.*, **ED-33** (1986) 282–284.
12. Russell J. D., Halls, D. C. & Leach, C., Direct observation of grain boundary Schottky barrier behaviour in zinc oxide varistor material. *J. Mater. Sci. Lett.*, **14** (1995) 676–678.
13. Russell, J. D. & Leach, C., Direct observation of grain boundary electrical activity in PTCR thermistor material using the REBIC mode of the SEM. In *Proc. IVth Eur. Ceram. Soc. Conf., Vol. 5 — Electroceramics*, pp. 45–66.
14. Russell, J. D. & Leach, C., Problems associated with imaging resistive barriers in $BaTiO_3$ PTC ceramics using the SEM conductive mode. *J. Eur. Ceram. Soc.*, **15** (1995) 617–622.
15. Palm, J., Local investigation of recombination at grain boundaries in silicon by grain boundary-electron beam induced current. *J. Appl. Phys.*, **74** (1993) 1169–1178.
16. Mataré, H. F. & Laakso, C. W., Space-charge domains at dislocation sites. *J. Appl. Phys.*, **40** (1969) 476–482.
17. Bubulak, L O. & Tennent, W. E., Observation of charge separating defects in HgCdTe using remote contact electron beam induced current. *Appl. Phys. Lett.*, **52** (1988) 1255–1257.
18. Sze, S. M., *Physics of Semiconductor Devices*, 2nd edn. J. Wiley, New York, 1981, p. 744.
19. Palm, J., Steinbach, D. & Alexander, H., Local investigation of the electrical properties of grain boundaries. *Mater. Sci. Eng.*, **B24** (1994) 56–60.

Appendix A: Derivation of Eqn (2)

We assume that the current path between the contacts can be treated one-dimensionally, and that there are two types of material:

(i) grain interiors consisting of extrinsic semiconductor with a high electron concentration; and
(ii) grain boundaries which have very low electron concentration.

The configuration we shall consider is shown in Fig. A1, from which we can write the total resistance between the contacts for the current path which traverses the grain boundary as:

$R = R_g + R_{gb}$ without the beam
$R' = R_g + R'_{gb}$ with the beam incident at the grain boundary

where R_g is the resistance which is unchanged by the beam and R_{gb} is the resistance at the grain boundary of interest. Throughout, priming indicates the new value of a variable when the electron beam is incident at the grain boundary. The excess current which flows due to the beam is given by:

$$I_{gb} = I' - I = \frac{V}{R_g + R'_{gb}} - \frac{V}{R_g + R_{gb}}$$

$$= V\left(\frac{R_{gb} - R'_{gb}}{(R_g + R_{gb})\,(R_g + R'_{gb})}\right) \qquad (A.1)$$

where I and V are the current through and potential difference across the structure under consideration (Fig. A1). In a real material, additional current will flow by other parallel current paths, but as such currents do not change when the beam is incident at the grain of interest, I_{gb} is unaffected.

Under low injection conditions, the effect of the electron beam is to increase the equilibrium free electron concentration n_0 by an amount $\hat{n}$ which is proportional to I_b:

$$\hat{n} = \left(\frac{k}{e\mu}\right) I_b \quad (k \text{ is a constant})$$

Thus, eqn (1) becomes

$$\sigma' = (n_0 + \hat{n})e\mu = n_0 e\mu = kI_b$$

and

$$R'_{gb} = \frac{d}{A(n_o e\mu + kI_b)} = \frac{R_{gb}}{1 + kI_b} \qquad (A.2)$$

where d is the thickness of the grain boundary layer, and A is the area of the grain boundary which is affected by the beam. In addition, it should be noted that when the beam is incident in a grain n_0 is already high, so that the change in carrier concentration has a negligible effect on σ, hence such regions show no change of I_{gb}.
Substituting eqn (A.2) into eqn (A.1) gives:

$$I_{gb} = V\left(\frac{R_{gb} - \dfrac{R_{gb}}{1 + kI_b}}{(R_g + R_{gb})\left(R_{gb} + \dfrac{R_{gb}}{1 - kI_b}\right)}\right)$$

$$= V\left(\frac{R_{gb} kI_b}{(R_g + R_{gb})\,(R_g + R_g\, kI_b + R_{gb}}\right)$$

$$= V\left(\frac{\dfrac{kR_{gb}}{(R_g + R_{gb})^2}}{\dfrac{[kR_g]}{(R_g + R_{gb})} + \dfrac{1}{I_b}}\right)$$

which is of the same form as eqn (2), with all terms apart from V and I_b constants.

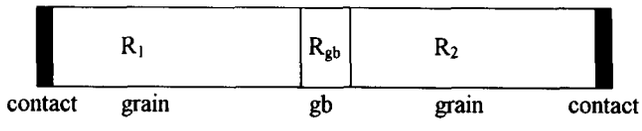

$R_g = R_1 + R_2$

Fig. A1 Geometry used to obtain eqn (2), with $R_g = R_1 + R_2$.

Journal of the European Ceramic Society **16** (1996) 1041–1050

PII: S0955-2219(96)00037-4
0955-2219/96/$15.00

Fabrication and Crystal Chemistry of $Bi_{3/2}ZnSb_{3/2}O_7$ Pyrochlore

A. Mergen & W. E. Lee*

University of Sheffield, Department of Engineering Materials, Sheffield S1 3JD, UK

(Received 20 July 1995; revised version received 18 January 1996; accepted 23 January 1996)

Abstract

$Bi_{3/2}ZnSb_{3/2}O_7$ pyrochlore was prepared both by conventional solid-state reaction of mixed oxides and by a coprecipitation method, and the reaction sequence to pyrochlore via both methods was investigated. In the mixed oxide powder pyrochlore is formed above 700°C with the appearance of $24Bi_2O_3.ZnO$ ($Bi_{48}ZnO_{73}$) compound at about 550°C due to the heterogeneity of the powder compact. Coprecipitated powder reacts directly to give pyrochlore at around 550°C without formation of any additional compound due to the atomic-scale mixing In the $Bi_{3/2-x/2}Zn_{1+x}Sb_{3/2-x/2}O_{7-x}$ pyrochlore system with zinc concentration between x = 0·1 and x = 1·2, Zn incorporation to replace Bi and Sb led to formation of spinel and Bi-rich liquid along with pyrochlore of undefined composition.

1 Introduction

The crystal structure of the mineral pyrochlore, $(Ca,Na)_2(Nb,Ta)_2(OH,F)_7$, was first determined by von Gaertner[1] to belong to the space group *Fd3m* (No. 227 in Volume 1 of the International Tables of X-ray Crystallography). Since then a large number of compounds have been discovered with this type of crystal structure, including many with potentially useful electrical properties. Interest in electrical pyrochlores has been high since Cook and Jaffe[2] discovered that $Cd_2Nb_2O_7$ was ferroelectric with a peak dielectric constant of about 1200.

The crystal structure of pyrochlore may be regarded as an anion-deficient fluorite structure in which the cations form a face-centred cubic array and the anions assume an ordered arrangement in the tetrahedral interstices of the cation array.[2] As well as being a fluorite derivative, the crystal structure of pyrochlore has been described as two interpenetrating cristobalite-like networks[3] and as a network of BX_6 octahedra (where B is a sixfold coordinated cation and X is an anion) linked corner to corner with the A cations filling the interstices.[4] These different descriptions arise because the cation coordination polyhedra change shape with the value of the anion positional parameter, x. The general formula for pyrochlore compounds is $A_2B_2X_7$ (whereas fluorite would be $A_2B_2X_8$) with large A-type cations in eightfold coordination, smaller B-type cations in sixfold coordination and X-type anions. Two different anion positions occur so that the general formula can be written $A_2B_2X_6Z$, with the X anions having two A and two B near neighbours and the Z anion having only A near neighbours. As the mineral formula indicates, multiple cation/anion replacements are possible.

Pyrochlores can be classified according to the ion sites and valency as *normal* $A_2^{3+}B_2^{4+}X_7$, $A_2^{2+}B_2^{5+}X_7$, types or, by removing combinations of A and Z ions, a variety of *defect* pyrochlores occur with non-stoichiometry on cation or anion sites. Defect pyrochlores have the general formula $A_{2-x}B_2X_6Z_y$ ($0 \leq x \leq 1$ and $0 \leq y \leq 1$) giving, for example, AB_2X_6, $A_2B_2X_6Z_{1-y}$. However, an enormous range of ions of various valencies can be substituted into the pyrochlore structure so that it is difficult to fully classify them. For example, the pyrochlore of interest in the present work is believed to be $Bi_{1.5}^{3+}Zn^{2+}Sb_{1.5}^{5+}O_7$.[5]

Normal $A_2^{3+}B_2^{4+}X_7$-type pyrochlores are the most common due to the many suitable A and B cations. An excellent review of the pyrochlore structure is given by Subramanian *et al.*[6]

Pyrochlore compounds have many potential applications due to their electrical, dielectric, magnetic, optical and catalytic properties. For example, $R_2Zr_2O_7$ (R = rare earth) pyrochlores have possible applications as fluorescence centre hosts, high-temperature heating elements and oxidation catalysts. $Bi_2Ru_2O_7$ pyrochlore, suitably modified by solid solution with $Cd_2Nb_2O_7$, has been suggested as a thermistor material and $Gd_2(Zr_xTi_{1-x})O_7$ is a prospective solid oxide fuel cell electrolyte. While these applications are for ceramics where the pyrochlore is the major phase, they may also occur in the microstructure as a second

* To whom correspondence should be addressed.

phase, where frequently they degrade the desired electrical behaviour. For example, many $Pb(A_xB_{1-x})O_3$ perovskite relaxor ferroelectrics such as $PbMg_{1/3}Nb_{2/3}O_3$ (PMN) contain pyrochlore as an unwanted intermediate polymorph. The transformation to the desired perovskite crystal structure is slow and the two polymorphs coexist with the non-ferroelectric pyrochlore dramatically reducing the dielectric constant.

ZnO varistors are composed of ZnO grains, Bi_2O_3-containing grain boundaries responsible for the non-linear response, and intergranular phases such as $Bi_{3/2}ZnSb_{3/2}O_7$ (BZS) pyrochlore and $Zn_7Sb_2O_{12}$ spinel.[7] In the pure $ZnO–Bi_2O_3–Sb_2O_3$ system pyrochlore forms above 650°C and melts at 1280°C. Inada[8] found that pyrochlore forms and disappears on heating [reaction(1)] but may be reproduced on slow cooling [reaction (2)]:

$$4Bi_{3/2}ZnSb_{3/2}O_7 + 17ZnO \xrightarrow{950–1050°C} 3Zn_7Sb_2O_{12} + 3Bi_2O_3 \quad (1)$$

$$3Zn_7Sb_2O_{12} + 3Bi_2O_3 \xrightarrow{950–850°C} 4Bi_{3/2}ZnSb_{3/2}O_7 + 17ZnO \quad (2)$$

The pyrochlore is undesirable in ZnO varistor systems since it ties up some of the Bi_2O_3 that would otherwise migrate to grain boundaries and provide the non-linear response and also because the ZnO–pyrochlore interphase boundaries do not show a non-linear response.[9]

If the α-spinel polymorph is stabilized by adding e.g. Co, Mn and Cr, which dissolve in the bismuth oxide liquid and appear in the spinel crystal structure,[7] reaction (2) will not occur. The amount of pyrochlore formed on slow cooling, therefore, depends on the additives present and can be reduced to low levels in commercial systems.

$Bi_{3/2}ZnSb_{3/2}O_7$ has been fabricated from solid-state reaction of mixed oxide powders and via powder produced by a coprecipitation method. Thermal analysis and X-ray diffraction have been used to investigate the reaction sequence and the microstructural evolution has been determined using electron microscopy. Moreover, the effect of Zn replacing Bi and Sb in the $Bi_{3/2}ZnSb_{3/2}O_7$ pyrochlore phase has been examined.

2 Experimental

$Bi_{3/2}ZnSb_{3/2}O_7$ pyrochlore powder was prepared both by solid-state reaction of bismuth oxide (Bi_2O_3, >99·9%), zinc oxide (ZnO, >99·9%) and antimony oxide (Sb_2O_3, >99%) powders,* which were wet-mixed and milled in ethanol for 4 h using zirconia balls before drying, and by a coprecipitation route involving preparation of cation solutions from antimony chloride ($SbCl_3$, >99·5%), zinc chloride ($ZnCl_2$, >98%) and bismuth oxide (Bi_2O_3, >99·9%). Figure 1 shows block diagrams of the main steps in the processing routes via mixed oxide [Fig. 1(a)] and coprecipitation [Fig. 1(b)]. In the coprecipitation route the starting materials were dissolved in HCl/H_2O by using excess acid and poured into KOH solution to give a pH of >12, which is neces-

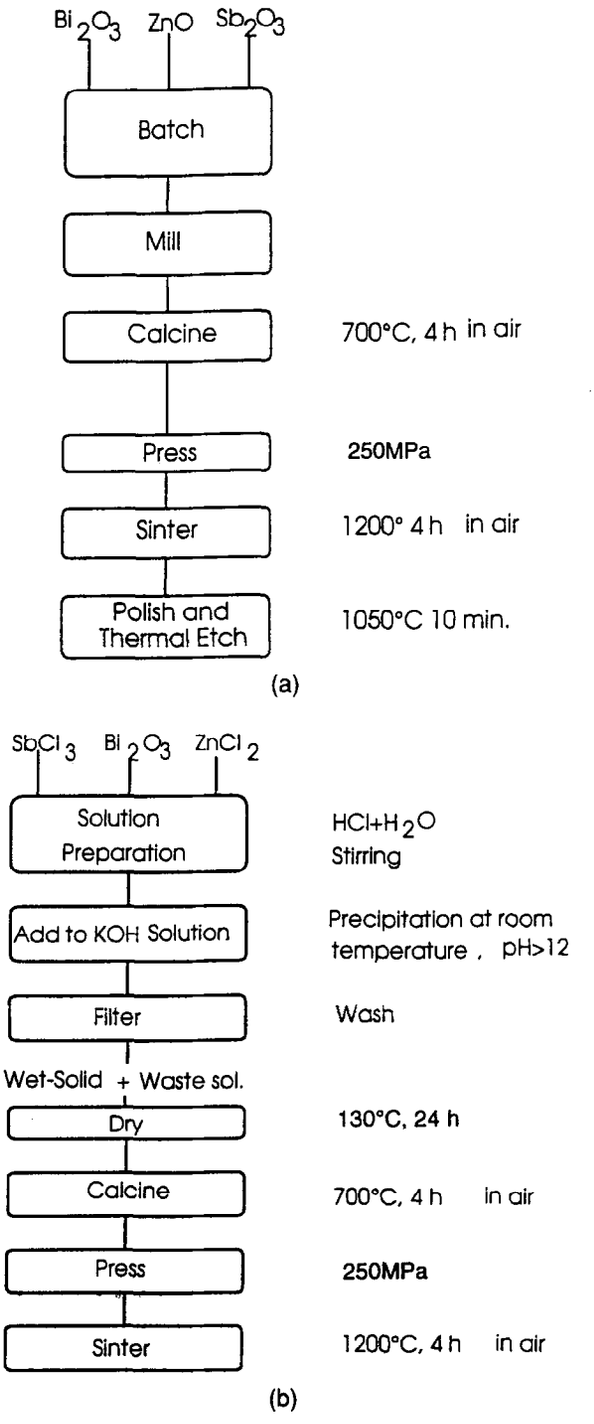

Fig. 1. The processing route for (a) mixed oxide powder and (b) coprecipitated powder.

* All chemicals were supplied by Aldrich Chemical Company Ltd, Dorset, UK.

sary to precipitate the pyrochlore powder. Bismuth and antimony metal salts could be precipitated at low pH values of between 1 and 2 with KOH.[7,10,11] Both of these hydroxides are weak bases and the salts of these metals are hydrolysed by water, yielding insoluble salts such as BiOCl and SbOCl.[12] Consequently, on preparing pyrochlore solution, excess acid is used to stabilize the solution of Bi and Sb.[12,13] However, zinc chloride could be precipitated with KOH at high pH values of around 10, giving zinc hydroxide.[7,11] Precipitates were removed from the solution by centrifuge and washed several times with distilled water. Wet-mixed oxide and coprecipitated powders were dried at 130°C for 24 h. Both dried mixed oxide and coprecipitated powders were calcined for 4 h at 700°C. After calcination the coprecipitated powder was ball-milled for 4 h in ethanol to break up the agglomerates. Chemical analysis of the natant solution remaining after precipitation was performed by inductively coupled plasma atomic emission spectrometry (ICP-AES).

The phase development in dried but uncalcined powders was examined using differential thermal analysis (DTA) and thermogravimetric analysis (TGA) at a heating rate of 10 K min^{-1} in air. In addition, pellets 10 mm diameter × ~1 mm thick were uniaxially pressed at 250 MPa from uncalcined powder, heated at a rate of 300 K h^{-1} and air-quenched at 50°C intervals between 350 and 800°C to determine the possible reaction sequence. The resultant powders and heat-treated pellets were then analysed by X-ray diffraction (XRD) with a Philips diffractometer using CuK_α radiation from 2θ = 10 to 85° at a speed of 1° min^{-1}. The lattice parameter of the pure pyrochlore phase based on XRD was determined using a least-squares method and an internal gold standard over a high-angle region and at a low speed of 0·25° min^{-1}.

An extensive study of the $Bi_{3/2-x/2}Zn_{1+x}Sb_{3/2-x/2}O_{7-x}$ pyrochlore system was made by changing the zinc concentration from x = 0·1 to x = 1·2. As indicated by the formula, as the Zn concentration increases, Bi and Sb decrease to accommodate the Zn cations into the Bi and Sb sites to make a substitutional solid solution. These compounds were sintered at between 1035 and 1200°C for 4 h after calcining at 700°C for 4 h. Changes in the XRD pattern and the lattice constant were determined to indicate the range of Zn content in the pyrochlore structure and the lattice distortion associated with its incorporation.

Dense, polycrystalline ceramic pellets were fabricated from the calcined powders by uniaxial pressing at 250 MPa and firing for 4 h in air at 700–1200°C. The resulting microstructures in polished samples were examined using scanning electron microscopy (SEM, Camscan series 2) and transmission electron microscopy (TEM; Jeol 200CX operated at 200 kV). SEM samples were thermally etched at ~1050°C in air for around 10 min. Energy-dispersive spectroscopy (EDS) was performed using a LINK AN 10000 system with a Be-window detector. Pellet density was determined with a mercury densitometer.

3 Results and Discussion

3.1 Powder characterization

Chemical analysis of the natant solution (Table 1) after precipitation and filtering the wet solid showed that 99·2% of the starting materials was precipitated at a pH value of about 12. After drying the coprecipitated powder at 130°C, the white precipitate became yellowish probably due to the decomposition of $Bi(OH)_3$ at around 100°C.[10] Although the decomposition temperature of bismuth hydroxide is around 415°C,[14] it starts to lose water to form BiO(OH), and subsequently Bi_2O_3 when heated to 100°C.[10]

Figure 2(a) shows the TG–DTA curves of the mixed oxides of $3Bi_2O_3$–$3Sb_2O_3$*–4ZnO prepared via the solid-state reaction. The exothermic peak at approximately 550°C is thought to be due to oxidation of antimony oxide as the TG shows a weight gain around this temperature. Carnelley and Walker[15] showed that pure Sb_2O_3 undergoes a weight gain between 400 and 600°C due to oxidation. In addition, Kim *et al.*,[16] report that pure Sb_2O_3 shows a sharp exothermic peak due to oxidation of Sb_2O_3 at about 530°C and also that in ZnO doped with 2·0 mol% Sb_2O_3, this exothermic peak occurs at a lower temperature. In addition to this peak, two smaller exothermic peaks were observed at temperatures of between 500–600°C and 700–800°C. The cause of these two peaks was determined by XRD on samples heated to temperatures either side of each peak using identical conditions as for the thermal analyses. The former peak was due to the formation of $24Bi_2O_3$.ZnO ($Bi_{48}ZnO_{73}$, JCPDS card no. 26-230) and the latter was because of formation of pyrochlore. The DTA curve fell in an endothermic direction indicating that melting occurred above 850°C, probably due to unreacted Bi_2O_3 (m.p. 825°C).

Table 1. ICP-AES chemical analysis of solutions after precipitation at pH 12.

Element	*Amount ($\mu g\ ml^{-1}$)*	*Accuracy ($\mu g\ ml^{-1}$)*
Zn	9	±2
Bi	<1	–
Sb	57	±3

*Antimony III oxide oxidizes to antimony V oxide and enables formation of the $Bi_{3/2}ZnSb_{3/2}O_7$ pyrochlore formula.

Figure 2(b) shows the TG–DTA curves of the coprecipitated mixture. No weight loss was observed since any possible hydroxides present were removed upon drying at 130°C for 24 h. The exothermic peak at about 400°C was considered to be due to the formation of antimony IV oxide (Sb_2O_4). Another exotherm at 570°C is due to the crystallization of pyrochlore directly from the coprecipitated powders.

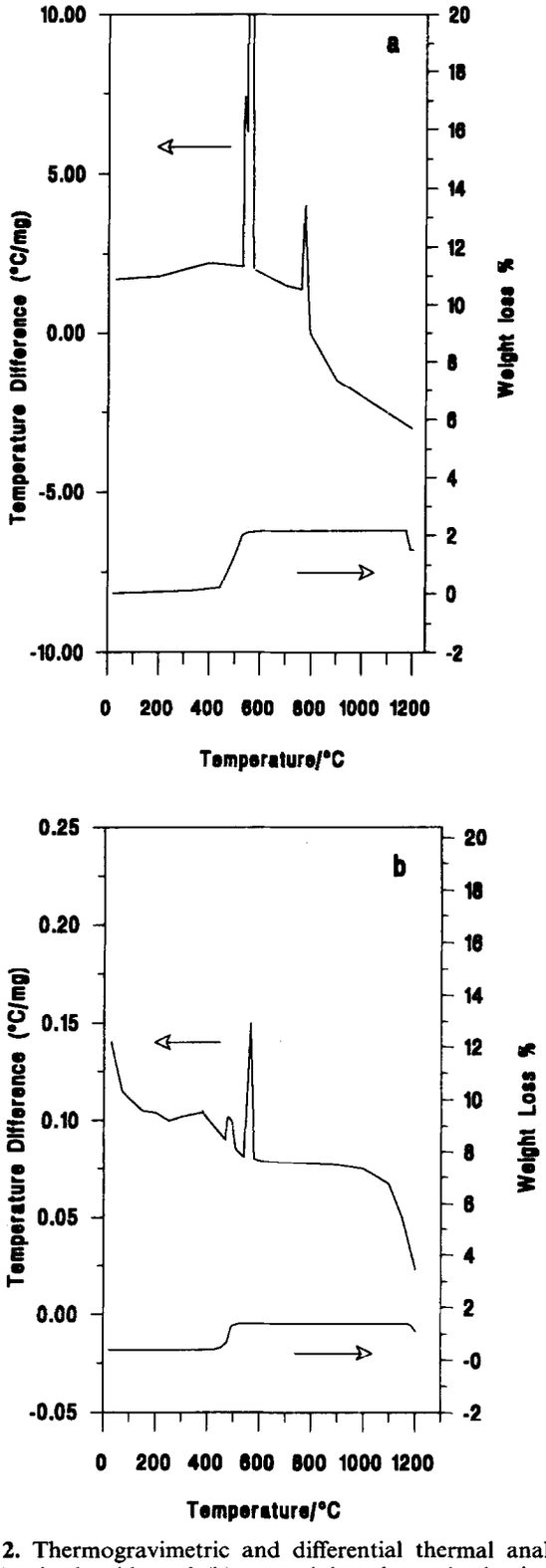

Fig. 2. Thermogravimetric and differential thermal analysis of (a) mixed oxide and (b) coprecipitated powder having an atomic ratio of Bi:Zn:Sb = 3:2:3. Note that DTA figures in (a) and (b) have different scales.

Subsequently, the DTA curve fell in an endothermic direction, after approximately 1000°C.

XRD analysis of the calcined mixed oxide powder [Fig. 3(a)] not only revealed pyrochlore but also β-Bi_2O_3, Sb_2O_4, ZnO and $Bi_{48}ZnO_{73}$ (BZ). However, XRD of the calcined coprecipitated powder [Fig. 3(b)] showed only single phase pyrochlore due to the higher reactivity of the coprecipitated powder. SEM images of these powders (Fig. 4) reveal that after calcination they consist of fine (sub micrometre) ultimate particles although in both cases the powders are highly agglomerated due to the calcination process. In addition, coprecipitated powders [Fig. 4(b)] have spherical and uniform particle shape.

3.2 Reaction sequence

XRD of crushed pellets of uncalcined powder [Fig. 5(a)] revealed no reaction of the mixed oxides up to ~550°C, with the appearance of $24Bi_2O_3.ZnO$ (BZ) being detected [reaction (3)] above 550°C. The formation of this compound produced the exothermic peak in the DTA [Fig. 2(a)]. At higher temperature, 700°C, the amount of BZ increased. This phase must arise because of poor mixing (heterogeneity) of the mixed oxide powders so that locally regions rich in Bi_2O_3 can react with ZnO to give BZ. Subsequently, at temperatures between 700 and 750°C, the BZS pyrochlore compound started to form from the reaction of BZ with the antimony oxide and unreacted ZnO and Bi_2O_3 [reaction (4)] or BZS compound may simply occur as in reaction (5) by reaction of the oxides after decomposition of BZ. Finally, nearly pure pyrochlore phase was observed at around 800°C, consistent with the DTA exotherm at 700–800°C [Fig. 2(a)].

$$24Bi_2O_3 + ZnO \xrightarrow{>550°C} Bi_{48}ZnO_{73} \quad (3)$$

$$Bi_{48}ZnO_{73} + 6Bi_2O_3 + 30Sb_2O_4 + 39ZnO + 15O_2 \xrightarrow{700–750°C} 40Bi_{3/2}ZnSb_{3/2}O_7 \quad (4)$$

$$3Bi_2O_3 + 3Sb_2O_4 + 4ZnO + 3/2O_2 \xrightarrow{500–550°C} 4Bi_{3/2}ZnSb_{3/2}O_7 \quad (5)$$

While intermediate reactions lead to pyrochlore formation in the mixed oxide powder, coprecipitated powder reacts directly to form pyrochlore at around 550°C without forming any intermediate compounds [reaction (5)] [Fig. 5(b)]. The formation of pyrochlore from coprecipitated powder gave an exothermic DTA peak at about 570°C [Fig. 2(b)]. The low formation temperature of pyrochlore in the coprecipitated powder can be attributed to the homogeneity of the coprecipitated powder [Fig. 4(b)]. Atomic-scale mixing of the components is considered to be attained in

coprecipitation. Consequently, the improved homogeneity and enhanced reactivity will decrease the diffusion path and encourage the reaction of BZS pyrochlore at lower temperatures.

3.3 Characterization of BZS pyrochlore

$Bi_{3/2}ZnSb_{3/2}O_7$ is isostructural with the pyrochlore type having general formula $A_2B_2O_7$. Its XRD peak data are listed in Table 2. Based on these results, $Bi_{3/2}ZnSb_{3/2}O_7$ was determined to have a cubic pyrochlore structure with the lattice parameter a_0 = 10·442 ± 0·001 Å. Inada[17] found a_0 for BZS pyrochlore to be 10·45 Å. Since XRD of BZS pyrochlore did not show any superlattice reflections, the cations are randomly distributed over the A and/or B sites in the $A_2B_2X_7$ pyrochlore structure.

Pellet densities after holding for 4 h at 700–1200°C are shown in Fig. 6. Densities of the coprecipitated

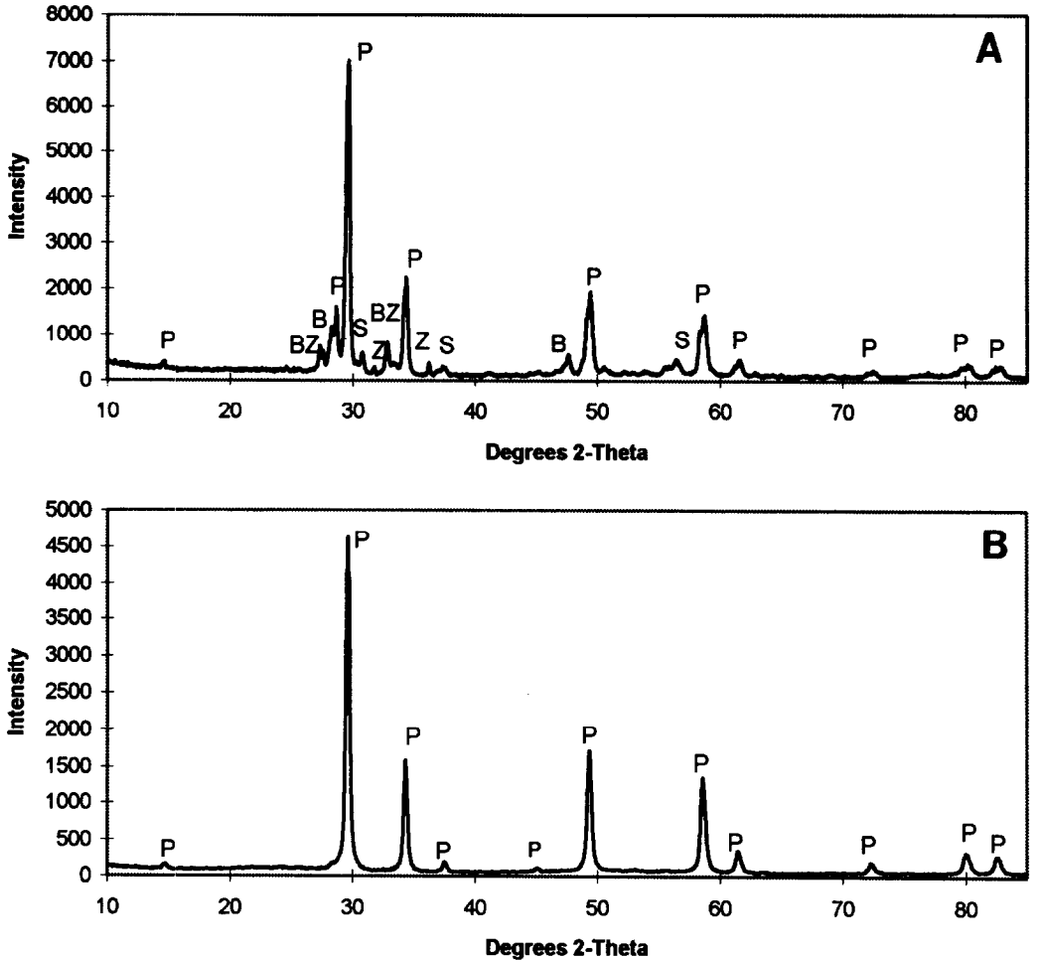

Fig. 3. XRD of calcined (a) mixed oxide and (b) coprecipitated powder. Calcination was for 4 h at 700°C. P = Pyrochlore, BZ = $Bi_{48}ZnO_{73}$, S = Sb_2O_4, B = β-Bi_2O_3 and Z = ZnO.

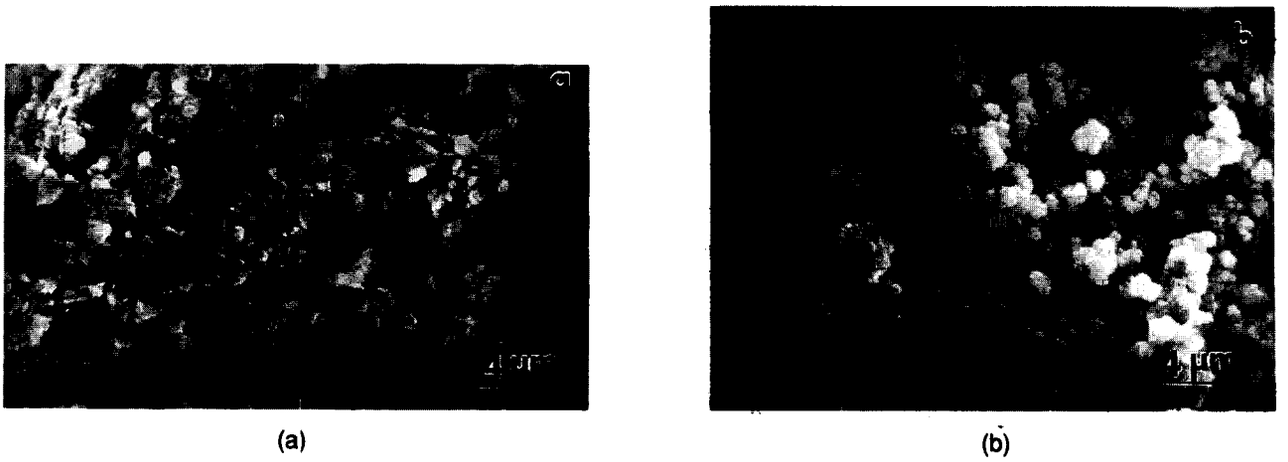

Fig. 4. SEM micrographs of (a) mixed oxide powder calcined at 700°C for 4 h and (b) coprecipitated powder calcined at 700°C for 4 h showing aggregated submicrometre primary particles.

powder pellets are generally higher since the starting powder has a lower ultimate particle size and more spherical particles, giving better packing. However, at the highest sintering temperature (1200°C) pellets from both powder types gave more than 90% of theoretical density, which is calculated as 7·86 g cm^{-3} from the X-ray results for a composition of $Bi_{3/2}ZnSb_{3/2}O_7$. At 1200°C the incomplete density of the pellets may be caused by the powder agglomerates (Fig. 4) and/or Bi_2O_3 and/or Sb_2O_3 volatilization since some weight loss was observed around this temperature in both powders (Fig. 2). Liquid-phase sintering is probable (Fig. 2), with melting occurring above 850°C for mixed oxide and 1000°C for coprecipitated powders. In addition, the sharp increase in density (Fig. 6) after approximately 1000°C suggests the occurrence of a liquid.

While SEM images of the dense pellets indicated only single pyrochlore phase [Figs 7(a) and 7(b)], TEM revealed occasional second phases at triple junctions consistent with liquid formation. Pellets made from coprecipitated powders have finer grains than those from mixed oxide. The second phases observed in the mixed oxide were generally crystalline and analysed as Bi_2O_3 by EDS [Fig. 8(a)], while in coprecipitated pellets these second phases were amorphous [Fig. 8(b)]. EDS analysis of the amorphous phase revealed Bi and a trace of K, a contaminant from the KOH used for precipitation which could flux the Bi_2O_3 and cause it to remain amorphous. No significant glassy phase was observed at the grain boundaries in both pellets, suggesting that any liquid is transient.[18]

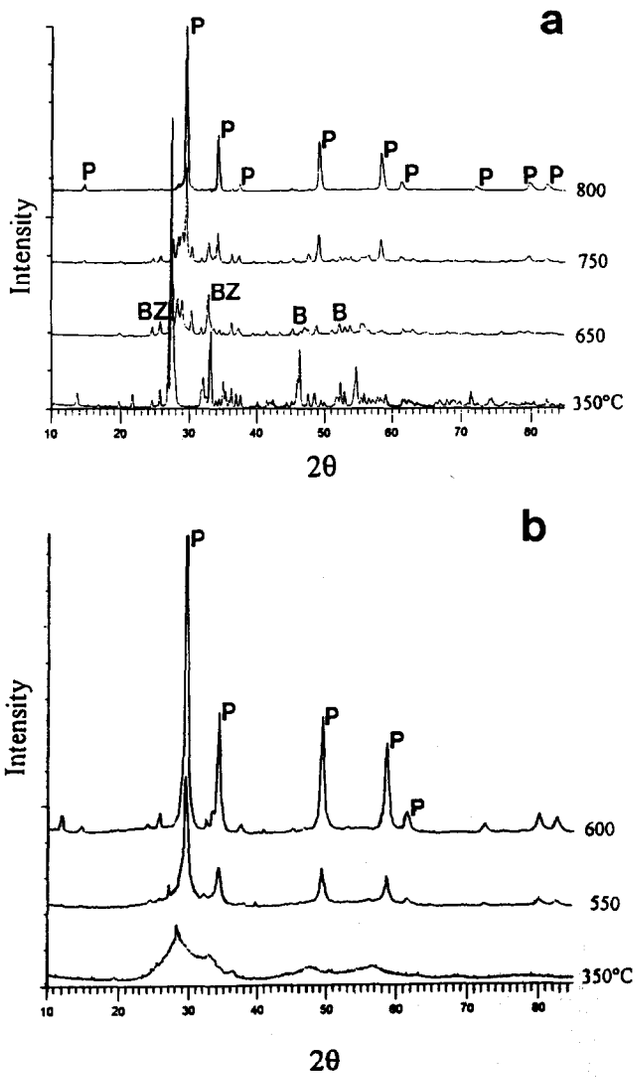

Fig. 5. XRD analysis of powders made from crushed pellets derived from (a) mixed oxide and (b) coprecipitation after air-quenching from different temperatures to determine the possible reaction sequence in both methods. P = Pyrochlore, BZ = $Bi_{48}ZnO_{73}$, B = Bi_2O_3.

Table 2. Powder XRD of $Bi_{3/2}ZnSb_{3/2}O_7$ pyrochlore

d (Å)	I/I_O	*hkl*
6·042	5	111
3·699	1	220
3·154	2	311
3·02	100	222
2·616	24	400
2·401	4	331
2·134	1	422
2·015	2	511
1·851	26	440
1·769	1	531
1·744	1	600
1·655	1	620
1·578	22	622
1·511	8	444
1·466	1	551
1·363	1	731
1·309	2	800
1·234	1	822
1·201	6	662
1·17	5	840

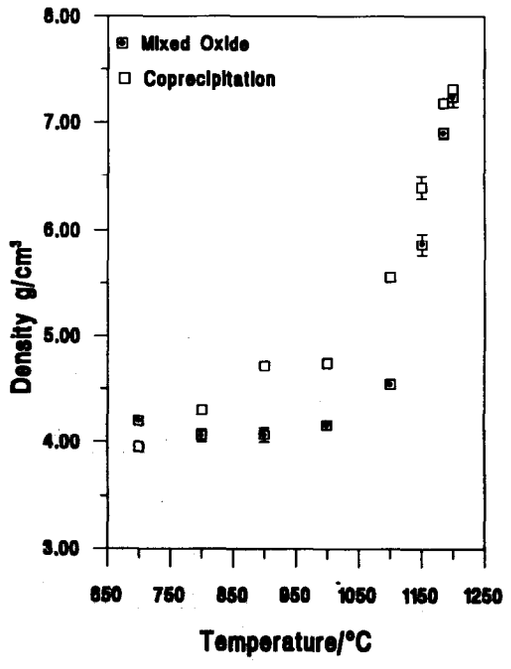

Fig. 6. Density of mixed oxide and coprecipitated pellets held for 4 h at temperature.

3.4 Zn cation incorporation into the BZS pyrochlore

XRD of Zn-doped samples is shown in Fig. 9 for $Bi_{3/2-x/2}Zn_{1+x}Sb_{3/2-x/2}O_{7-x}$ pyrochlore for x from 0·1 to 1·2. During incorporation of the Zn cation into the pyrochlore structure the spinel phase with the formula $Zn_7Sb_2O_{12}$ (beta spinel, JCPDS card no. 36-1445) forms and increases with greater Zn concentration. Figure 10 shows the relative peak intensities of the spinel (311) reflection, corresponding to a 3·577 Å d-spacing, and the BZS pyrochlore (400) reflection, which corresponds to a d-spacing of approximately 2·60 Å, as a function of excess Zn concentration, x. This gives a semi-quantitative measure of the spinel-to-pyrochlore ratio[19] and reveals that as the amount of Zn doping increases, the spinel percentage also increases. Consequently, it appears that increasing Zn concentration to replace Bi and Sb in the BZS pyrochlore was unsuccessful. Instead, spinel and Bi_2O_3 liquid formed along with pyrochlore of undefined composition.

The microstructure of the Zn-doped compound, after quenching from the sintering temperature, where $x = 1·2$ (Fig. 11), revealed not only pyrochlore and spinel phases, but also some Bi-rich phase present. This is consistent with reaction (1) where BZS pyrochlore in ZnO varistors takes the ZnO from the bulk matrix and transforms to spinel and liquid

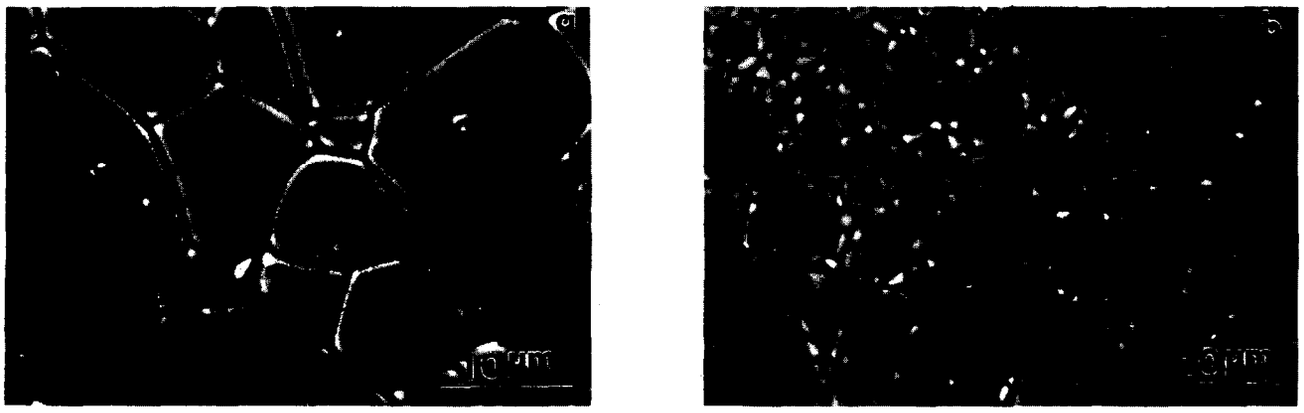

(a) (b)

Fig. 7. (a) Sintered mixed oxide pellet after 4 h at 1200°C showing only large (5–20 μm) single-phase grains. (b) Coprecipitated pellet after 4 h at 1200°C showing pyrochlore phase and finer (3–10 μm) grain structure.

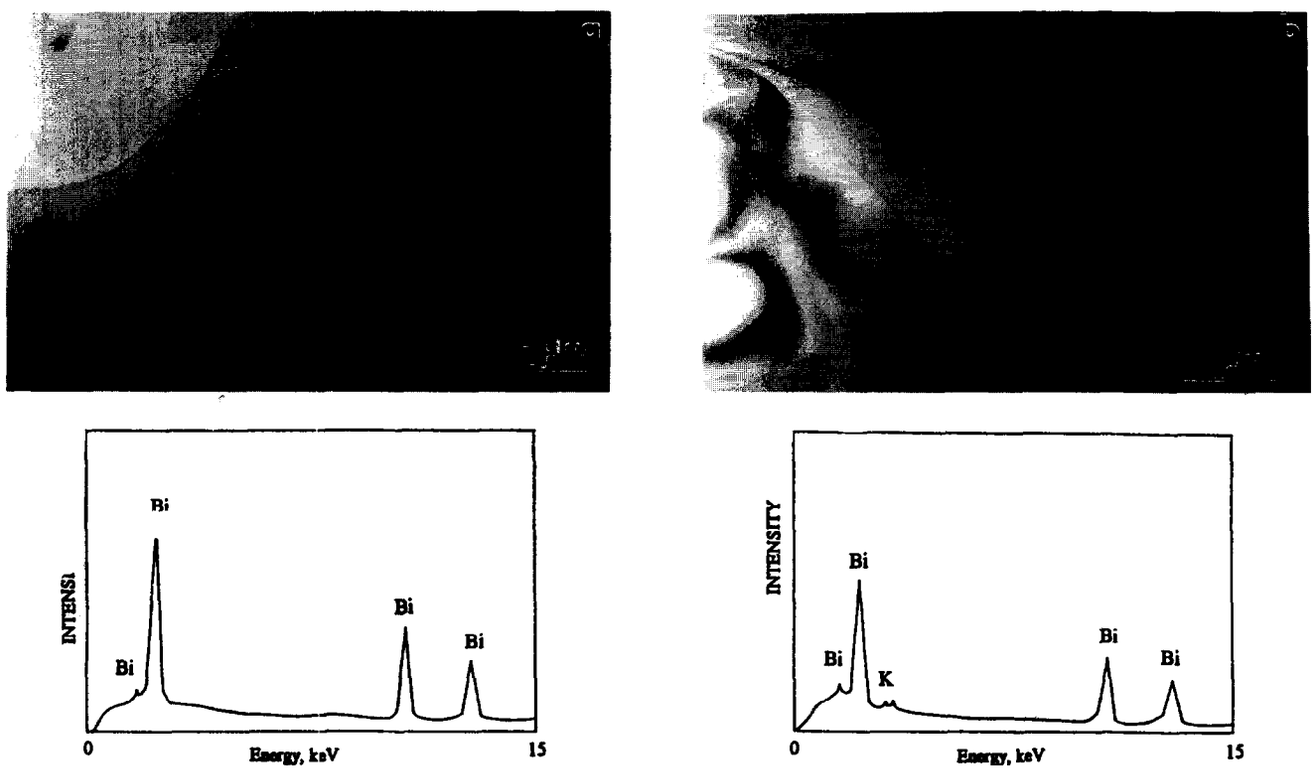

Fig. 8. (a) Bright-field (BF) TEM image of sintered mixed oxide pellet after 4 h at 1200°C showing crystalline second phase at grain junction. EDS analysis suggests the second phase is Bi_2O_3 (O is not detected). (b) TEM micrograph of coprecipitated pellet after 4 h at 1200°C showing glassy phase at triple junctions. EDS analysis reveals K as well as Bi.

Bi_2O_3.[8] Inada[8] showed that BZS pyrochlore reacts easily with ZnO to produce spinel and Bi_2O_3 liquid. SEM of this compound revealed large black (10–50 μm) spinel grains in the grey/white pyrochlore/Bi-rich phase matrix. Well developed faceted spinel grains indicative of crystallization from a liquid phase can be seen in the pyrochlore matrix [Fig. 11(a)]. In addition, spinel grains were frequently observed containing pyrochlore and Bi-rich phases [Fig. 11(b)].

TEM examination of Zn-doped samples sintered for 4 h at 1035°C reveals a range of grain sizes and additional intergranular phases (Figs 12 and 13). The TEM reveals the small pyrochlore grains (1–2 μm), large spinel grains (15–35 μm from SEM, Fig. 11) and impure Zn/Sb containing δ-Bi_2O_3 crystals (indicated by electron diffraction). Inada[8] found that Bi-rich liquid phase dissolves a large amount of Zn but much less Sb. δ-Bi_2O_3 is a high-temperature polymorph having a cubic structure and it completely surrounds the pyrochlore grains, suggesting that when liquid it was fully wetting.

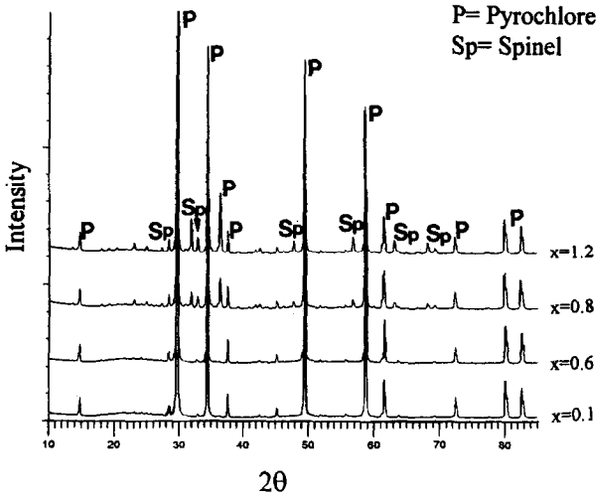

Fig. 9. XRD of $Bi_{3/2-x/2}Zn_{1+x}Sb_{3/2-x/2}O_{7-x}$ compositions sintered at 1200°C for x = 0·1 and 0·6, and sintered at 1035°C for x = 0·8 and 1·2. Sp = spinel, P = pyrochlore.

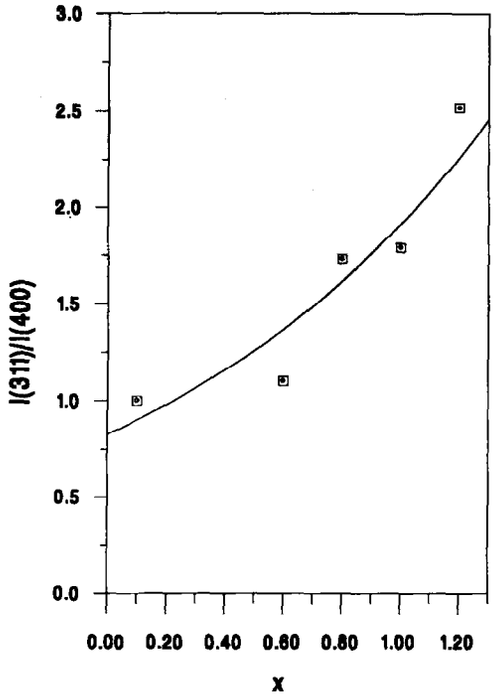

Fig. 10. Relative peak intensity ratio of spinel (311) to pyrochlore (400) as a function of excess Zn concentration, x, in $Bi_{3/2-x/2}Zn_{1+x}Sb_{3/2-x/2}O_{7-x}$.

In summary, addition of Zn to $Bi_{3/2}ZnSb_{3/2}O_7$ pyrochlore (and lower Bi and Sb) is observed to encourage it to transform to spinel with associated formation of Bi_2O_3-rich liquid which crystallizes to δ-Bi_2O_3 on cooling, rather than causing single-phase pyrochlore formation.

The lattice parameter of BZS pyrochlore increased with increasing Zn cation content (Fig. 14). Similar behaviour was reported by Inada,[17] who measured the lattice constant of BZS pyrochlore as a function of ZnO in the ZnO varistor system, and by Karanovic *et al.*,[20] who examined phase transformations in the system containing a mixture of varistor additives. The increased pyrochlore lattice parameter could be due to incorporation of Zn ions into the pyrochlore structure. The lattice parameter of BZS pyrochlore increased linearly up to x = 0·6 but then a sharp increase was observed. The last three samples were sintered at lower temperatures (1035°C) than the initial ones (1200°C) since these compounds

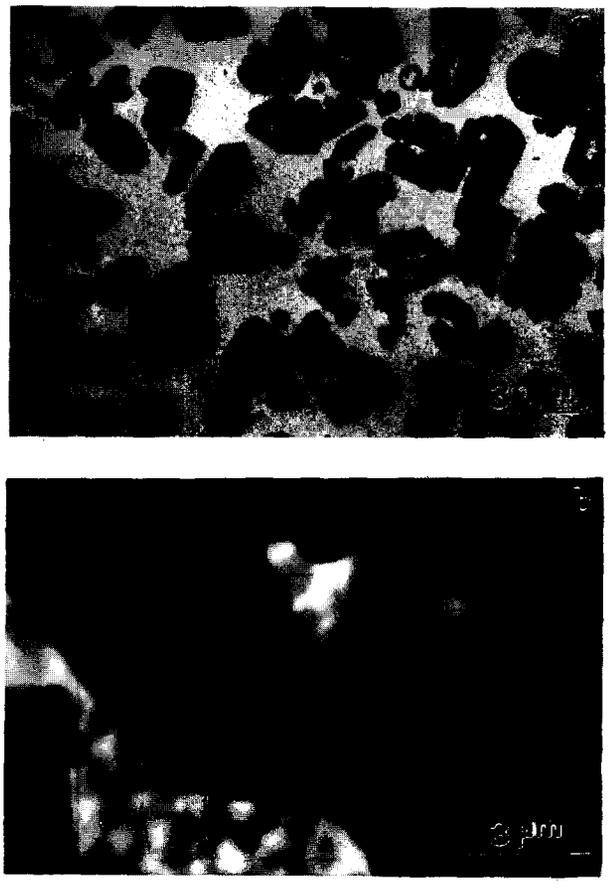

Fig. 11. Backscattered electron SEM images of a pellet of the $Bi_{3/2-x/2}Zn_{1+x}Sb_{3/2-x/2}O_{7-x}$ composition sintered at 1035°C for 4 h where x = 1·2: (a) large faceted spinel grains, (b) grey and white pyrochlore and Bi-rich phases.

partially or mostly melt at the higher sintering temperature. This may have caused the sharp increase because at high temperatures more Bi_2O_3 evaporates and a higher proportion of the large Bi atom (radius 1·17 Å) at the lower sintering temperature would increase the lattice parameter.

4 Conclusions

(1) $Bi_{3/2}ZnSb_{3/2}O_7$ pyrochlore was prepared both by conventional solid-state reaction of mixed oxides and by a coprecipitation method.

(2) Investigation of the reaction sequence to pyrochlore via both methods showed that, in the mixed oxide method, pyrochlore is formed with the appearance of $24Bi_2O_3.ZnO$ compound above 550°C due to powder inhomogeneity. However, coprecipitated powder reacts directly to form pyrochlore at around 550°C due to atomic-scale mixing.

(3) Incorporation of Zn to replace Bi and Sb causes pyrochlore–spinel transformation rather than forming a single pyrochlore phase This is thought to be due to the reaction of pyrochlore with ZnO forming spinel and Bi_2O_3-rich liquid, as observed in ZnO varistors. In addition, Zn incorporation leads to an increased lattice parameter of BZS pyrochlore.

Acknowledgements

This work was sponsored by the Turkish Ministry of Education in the form of a scholarship (A.M.).

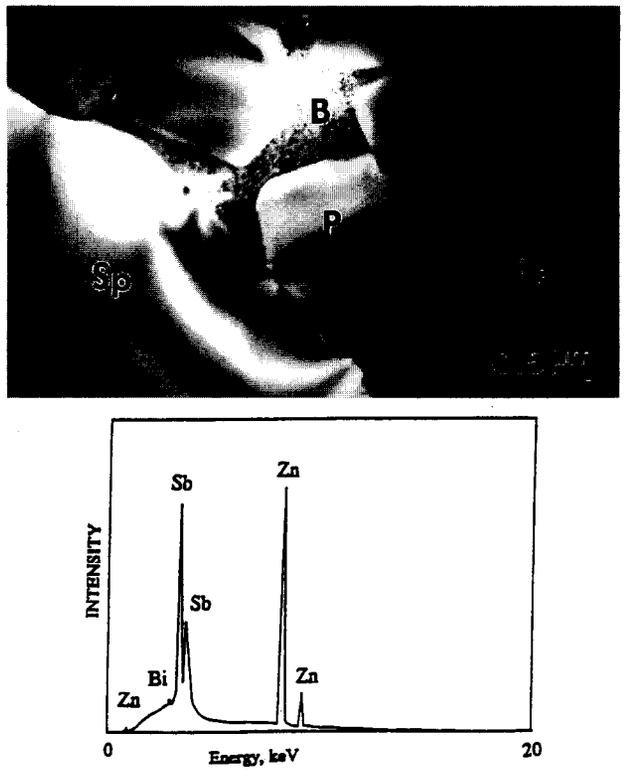

Fig. 13. BF TEM image of Zn-doped BZS pyrochlore ($Bi_{3/2-x/2}Zn_{1+x}Sb_{3/2-x/2}O_{7-x}$, x = 1·2) sintered for 4 h at 1035°C showing large spinel grains (Sp) with pyrochlore (P) and Bi-rich phase (B) with EDS analysis from spinel.

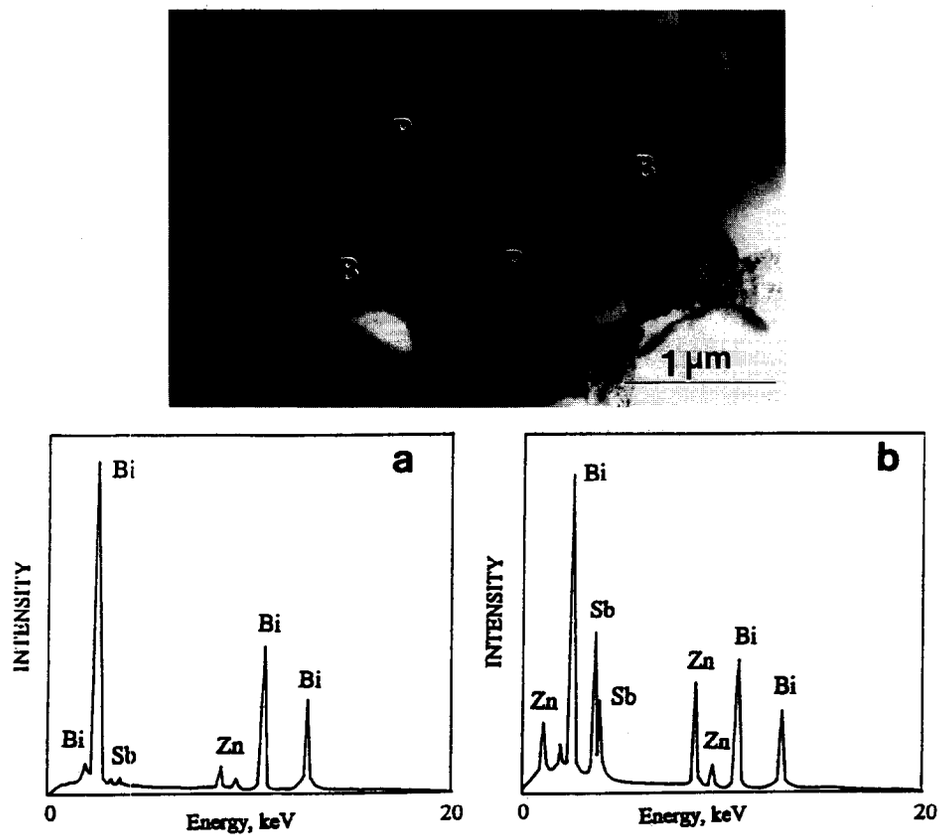

Fig. 12. BF TEM image of $Bi_{3/2-x/2}Zn_{1+x}Sb_{3/2-x/2}O_{7-x}$ composition where x = 1·2 sintered at 1035°C for 4 h with EDS analysis from (a) Bi-rich phase (B) and (b) pyrochlore (P).

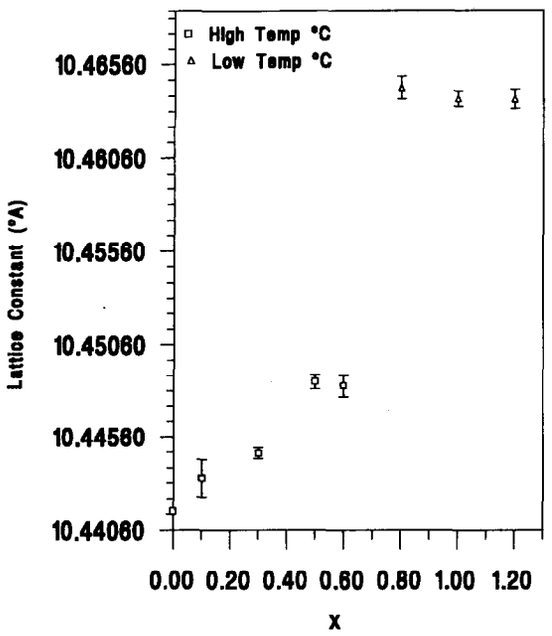

Fig. 14. Variation of the lattice constant with excess Zn concentration, x, in the $Bi_{3/2-x/2}Zn_{1+x}Sb_{3/2-x/2}O_{7-x}$ compositions sintered at 1200°C (first five samples) and at 1035°C (the last three samples) for 4 h.

References

1. von Gaertner, H., Die Kristallstrukten von Loparit und Pyrochlor. *Neues. Jahrb. Mineral Geol. Palaeontol.*, **61** (1930) 1–30.
2. Cook W. R. & Jaffe, H., Ferroelectricity in oxides of face-centered cubic structure. *Phys. Rev.*, **89** (1953) 1297–1298.
3. Sleight, A. W., New ternary oxides of mercury with the pyrochlore structure. *Inorg. Chem.*, **7**[9] (1968) 1704–1708.
4. Bystrom, A., X-ray analysis of $Ca_2Sb_2O_7$ and compounds of similar composition. *Ark. Kemi. Mineral Geol.*, **18A**[21] (1944) 1–8.
5. Kim, J, Kimura, T. & Yamaguchi, T., Sintering of zinc oxide doped with antimony oxide and bismuth oxide. *J. Am. Ceram. Soc.*, **72**[8] (1989) 1390–1395.
6. Subramanian, M. A., Aravamudan, G. & Subba Rao G. V., Oxide pyrochlores — a Review. *Prog. Sol. State Chem.*, **15** (1983) 55–143.
7. Karakas, Y. & Lee, W. E., Processing and phase evolution in a ZnO varistor prepared by oxide precipitation. *J. Brit. Ceram. Soc.*, **93**[2] (1994) 65–70.
8. Inada, M., Formation of nonohmic zinc oxide ceramics. *Jpn J. Appl. Phys.*, **19**[3] (1980) 409–419.
9. Olsson, E. & Dunlop, G. L., Characterization of individual interfacial barriers in a ZnO varistor material. *J. Appl. Phys.*, **66**[8] (1989) 3666–3675.
10. Durrant, P. J. & Durrant B., *Introduction to Advanced Inorganic Chemistry.* Longmans, Harlow, UK, 1962, pp. 771–772.
11. Durrant, P. J., *General & Inorganic Chemistry,* 3rd Edition. Longmans, Harlow, UK, 1952, pp. 548 and 684–685.
12. Vogel, A. I., *A Text Book of Macro & Semimicro Qualitative Inorganic Analysis,* 4th Edition. Longmans, Harlow, UK, 1955, p. 221
13. Hishita, S., Yao, & Shirasaki, S., Zinc oxide varistors made from powders prepared by amine processing. *J. Am. Ceram. Soc.*, **72**[2] (1989) 338–340.
14. Lide, D. R., *Handbook of Chemistry and Physics,* 73rd Edition. CRC Press, Boca Raton, FL, 1992–1993.
15. Carnelley, T. & Walker, J., The dehydration of metallic hydroxides by heat, with special reference to the polymerisation of the oxides, and to the Periodic Law. *J. Chem. Soc.*, **53** (1888) 59–101.
16. Kim, J., Kimura, T. & Yamaguchi, T., Sintering of Sb_2O_3-doped ZnO. *J. Mater. Sci.*, **24** (1989) 213–219.
17. Inada, M., Crystal phases of nonohmic zinc oxide ceramics. *Jpn J. Appl. Phys.*, **17**[1] (1978) 1–10.
18. Lee, W. E. & Rainforth, W. M., *Ceramic Microstructures, Property Control by Processing.* Chapman and Hall, London, 1994, pp. 46–47.
19. Wong, J., Microstructure and phase transformation in a highly non-ohmic metal oxide varistor ceramic. *J. Appl. Phys.*, **46**[4] (1975) 1653–1659.
20. Karanovic, L., Poleti, D. & Vasovic, D., On the possibility of pyrochlore phase formation in zinc oxide varistor ceramic. *Mater. Lett.*, **8** (1994) 191–196.

Journal of the European Ceramic Society **16** (1996) 1051–1056

PII: S0955-2219(96)00026-X
0955-2219/96/$15.00

Synthesis and Characterization of Dielectric Compositions in the BaO-rich Corner of the $BaO–Y_2O_3–TiO_2$ Ternary System

Ang Chen,[a] Yu Zhi,[b] V. M. Ferreira,[b] P. M. Vilarinho[b] & J. L. Baptista[b]*

[a]Department of Physics, Zhejiang University, Hangzhou 310027, People's Republic of China
[b]Department of Ceramic and Glass Engineering, University of Aveiro, 3800 Aveiro, Portugal

(Received 22 November 1995; accepted 8 January 1996)

Abstract

A single-phase $YBa_3Ti_2O_{8.5}$ ceramic located in the BaO-rich corner of the $BaO–Y_2O_3–TiO_2$ ternary system was synthesized. The dielectric properties of this material (permittivity $\epsilon = 29$, quality factor $Q = 1000$) are reported here for the first time. Compositions with the $BaO:Y_2O_3:TiO_2$ ratio equal to 6:1:5 and 5:1:4 were also synthesized. The Y615 ceramic consists of two phases ($YBa_3Ti_2O_{8.5}$ and $BaTiO_3$), and the Y514 ceramic consists of three phases ($YBa_3Ti_2O_{8.5}$, $BaTiO_3$, and Y_2TiO_5). They are dense ceramic composites. © *1996 Elsevier Science Limited.*

1 Introduction

Dielectric compositions with high-performance dielectric properties at high frequency or/and microwave frequency were discovered in the TiO_2-rich corner of the $BaO–Re_2O_3–TiO_2$ system (Re = rare earth).[1] Figure 1 shows their positions in the ternary system. Compositions with the proportion of $BaO:Re_2O_3:TiO_2$ equal to 1:1:2, 1:1:3, 1:1:4, 1:1:5, and even 1:1:7 have been synthesized.[2] In the case of compositions around the proportion 1:1:4 ($BaRe_2Ti_4O_{12}$) or 1:1:5 ($BaRe_2Ti_5O_{14}$), excellent microwave ceramics have been obtained for a variety of microwave devices such as filters and oscillators.[2]

The new compound $YBa_3Ti_2O_{8.5}$ was reported to occur when the high transition temperature superconductor $YBa_2Cu_3O_{7-\delta}$ film was deposited in a $SrTiO_3$ single crystal matrix[3] or when $YBa_2Cu_3O_{7-\delta}$ was composed with a $BaTiO_3$ ceramic.[4] Although this compound has been reported, its electrical characteristics, e.g. the dielectric properties, have not yet been studied. Compared with $BaRe_2Ti_4O_{12}$ (Re = La, Nd, Sm, ...), which is located in the TiO_2-rich corner of the $BaO–Re_2O_3–TiO_2$ ternary system, the $YBa_3Ti_2O_{8.5}$ is located in the BaO-rich corner. In recent work, the authors synthesized a new series of dielectric ceramics having general composition $ReBa_3Ti_2O_{8+\delta}$ (Re = rare earth, such as, Y, Nd, Sm, ...); they are in the BaO-rich corner of the $BaO–Re_2O_3–TiO_2$ system (see Fig. 1). The primary experimental results indicated that this group of materials has permittivity $\epsilon > 25$, and quality factor $Q > 1000$ at 1 MHz.[5]

It is important to study the chemical reactions among the starting materials, the phase-forming process, the crystal structure and the ceramic microstructure of this new series of materials. The present paper is concerned with the synthesis and characterization of these compounds in the BaO-rich corner of the $BaO–Y_2O_3–TiO_2$ ternary system.

2 Experimental Procedure

The ceramics were prepared by the mixed oxide method. High purity starting materials, $BaCO_3$ (May & Baker Co.), TiO_2 (Johnson Matthey Co.) and Y_2O_3 (Fluka Chemie AG Co.), were weighed according to the $BaO:Y_2O_3:TiO_2$ ratios of 6:1:4, 6:1:5 and 5:1:4 (where the ratios 6:1:4, 6:1:5 and 5:1:4 are denoted as Y614, Y615 and Y514, respectively). The weighed batches were wet-mixed in agate pots by a planetary-type ball mill for 5 h. Then the powders were dried and calcined at 1200°C for 2 h. The calcined powders were milled again, dried, and isostatically pressed into discs at 300 MPa. Finally, the samples were sintered in air at 1515°C for 6 h.

Moreover, the powder mixture for each composition from the starting materials $BaCO_3$, Y_2O_3 and TiO_2 was calcined at 900, 1000, 1100, 1200, 1300 and 1400°C for 2 h, in order to study the phase-forming process.

Thermogravimetric analysis (TGA) and differential thermal analysis (DTA) (Netzsch STA 409C) were

* To whom correspondence should be addressed.

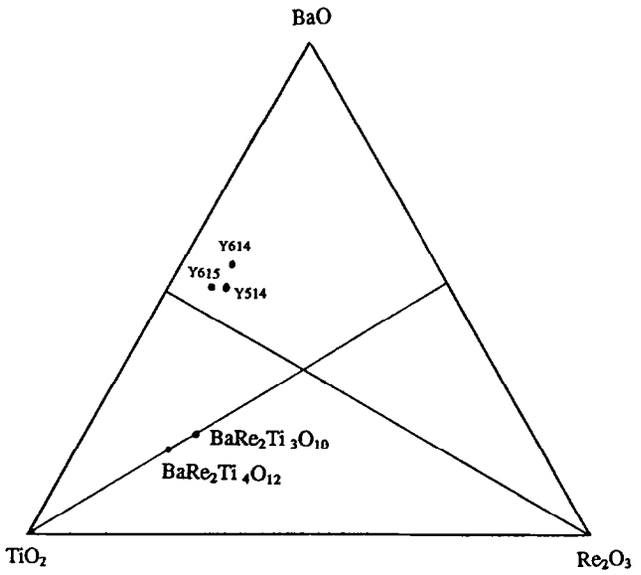

Fig. 1. Phase diagram of the $BaO–Re_2O_3–TiO_2$ ternary system (Re = Y, Nd, and Sm).

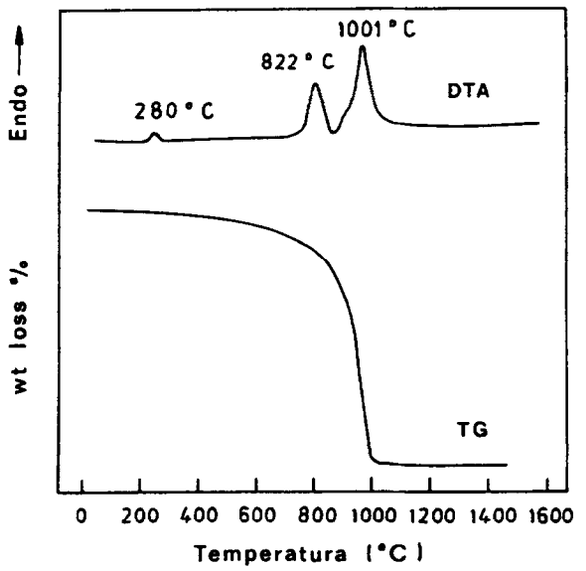

Fig. 2. Thermogravimetric and differential thermal analysis curves of the $6BaO–Y_2O_3–4TiO_2$ sample.

performed for the Y614 system with the heating rate of 10°C min^{-1}.

The calcinations at each calcining temperature and the final sintered samples were examined by X-ray powder diffraction (XRD) (Rigaku, Cu radiation) at room temperature to determine the phase assemblage. The microstructure of the sintered samples was observed by scanning electron microscopy (SEM) and electron probe microanalysis (EPMA) (Hitachi S4100 scanning electron microscope). The dielectric permittivity and dissipation factor of the samples were measured in the temperature range from 100 to 300 K at 1 kHz, 10 kHz, 100 kHz and 1 MHz (APD Cryogenics, Keithley 3330 LCZ, and HP4277A).

3 Results and Discussion

3.1 The phase-forming process in the BaO-rich corner of the $BaO–Y_2O_3–TiO_2$ system

3.1.1 $6BaO–Y_2O_3–4TiO_2$ ($YBa_3Ti_2O_{8.5}$) system

Figure 2 shows the TGA and DTA results for Y614. In the thermogravimetric curve, the small weight loss around 300°C is due to the evaporation of residual organic materials, caused by the manufacturing process, and absorbed water. A large weight loss occurring in the temperature range 850–1021°C corresponds to the release of CO_2. The DTA curve reveals two endothermic peaks in the range 801–850°C and 949–1045°C, which correspond to the phase transformation of $BaCO_3$. The first peak arose from the γ-$BaCO_3$ to β-$BaCO_3$ phase transformation,[6] while the second peak (949–1045°C) was attributed to the β-$BaCO_3$ to α-$BaCO_3$ phase transformation.[6] No peak in the DTA curve was observed above 1100°C.

The phases of powders calcined at various temperatures and of samples sintered at 1515°C were identified by XRD. The results are shown in Fig. 3.

It is assumed that the following chemical reactions occurred:

$$BaCO_3 + TiO_2 \rightarrow BaTiO_3 \quad (1)$$

$$BaCO_3 + TiO_2 \rightarrow Ba_2TiO_4 \quad (2)$$

$$BaTiO_3 + BaCO_3 \rightarrow Ba_2TiO_4 \quad (3)$$

$$BaTiO_3 + Ba_2TiO_4 + Y_2O_3 \rightarrow YBa_3Ti_2O_{8.5} \quad (4)$$

(1) The powder calcined at 900°C contains five phases: $BaCO_3$, Y_2O_3, $BaTiO_3$, Ba_2TiO_4 and $YBa_3Ti_2O_{8.5}$. The main phase is $BaTiO_3$, and only a small amount of the $YBa_3Ti_2O_{8.5}$ phase was formed. Some of the raw materials, $BaCO_3$ and Y_2O_3, remain. The TiO_2 phase has not been detected; this implies that TiO_2 has reacted completely. Reactions (1), (2) and (3) predominate at 900°C.

(2) The phases are $YBa_3Ti_2O_{8.5}$, Ba_2TiO_4, $BaTiO_3$, and Y_2O_3 for the powders calcined at 1000 and 1100°C.

(3) An increase in the $YBa_3Ti_2O_{8.5}$ takes place at 1200°C, with small amounts of the Ba_2TiO_4, $BaTiO_3$ and Y_2O_3 phases remaining. At 1300°C, the process is the same as that at 1200°C.

(4) Above 1400°C, only the single-phase $YBa_3Ti_2O_{8.5}$ is observed. The reaction predominating is illustrated by eqn (4).

Figure 4 shows the relative intensity of specific XRD peaks for each phase as a function of heating temperatures. It is clear that the relative intensity of the $YBa_3Ti_2O_{8.5}$ phase increases continuously

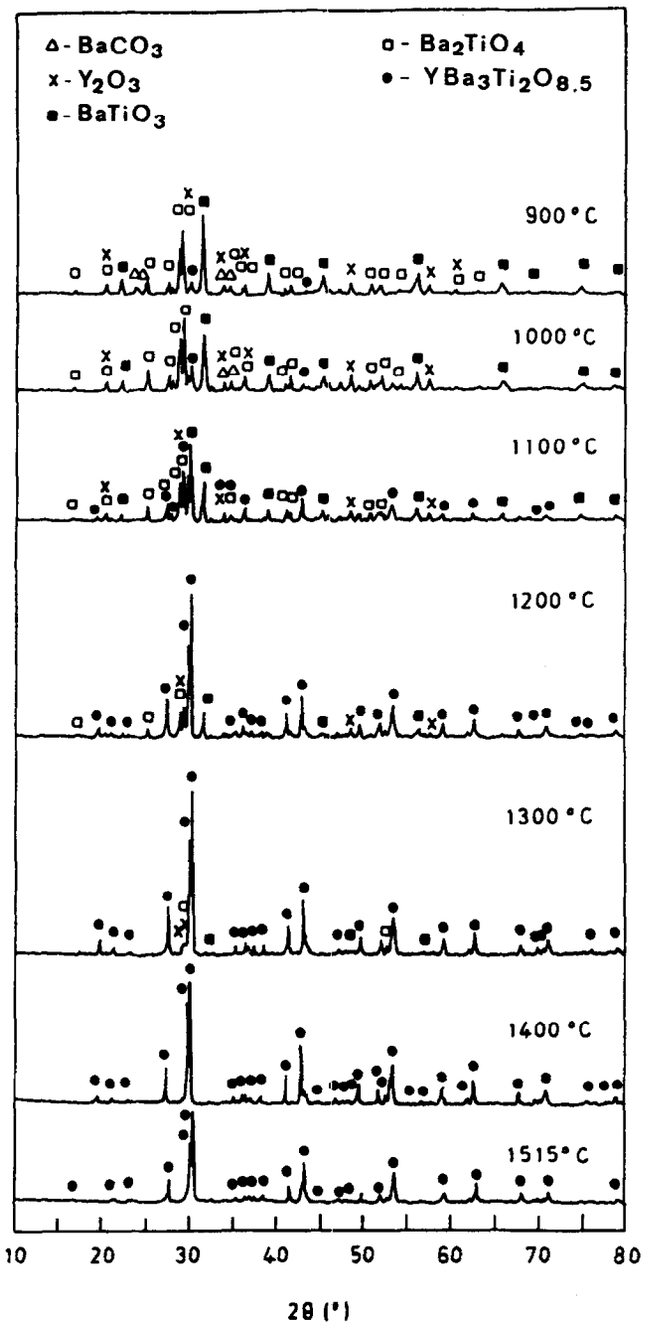

Fig. 3. X-ray powder diffraction patterns of $6BaO–Y_2O_3–4TiO_2$ powders calcined and sintered at various temperatures.

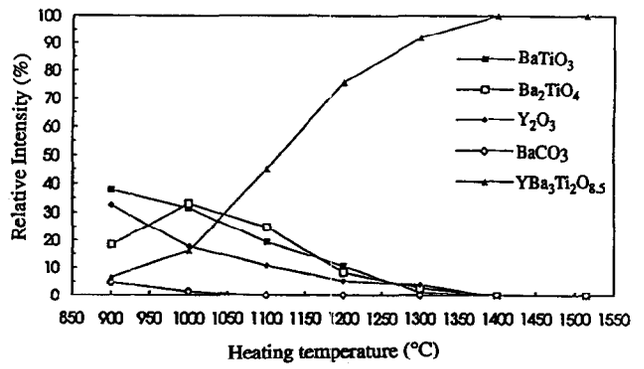

Fig. 4. Relative intensity of specific XRD peaks for each detected phase as a function of heating temperature for the Y614 sample.

and reaches nearly 100% in the high-temperature range (1400–1515°C), the relative intensities of the other phases decreasing with increasing temperature and becoming zero at 1400°C.

3.1.2 $6BaO–Y_2O_3–5TiO_2$ system

The typical composition of the TiO_2-rich phases of the $BaO–Re_2O_3–TiO_2$ ternary system is that with the $BaO:Re_2O_3:TiO_2$ ratio = 1:1:4 (written as $BaRe_2Ti_4O_{12}$). However, it is reported that the material with higher TiO_2 content, in which the ratio $BaO:Re_2O_3:TiO_2$ is 1:1:5, also exhibits excellent dielectric properties at microwave frequencies.[2] Correspondingly, it might be interesting to study the BaO-rich corner in the $BaO–Re_2O_3–TiO_2$ ternary system with high proportion of TiO_2. The

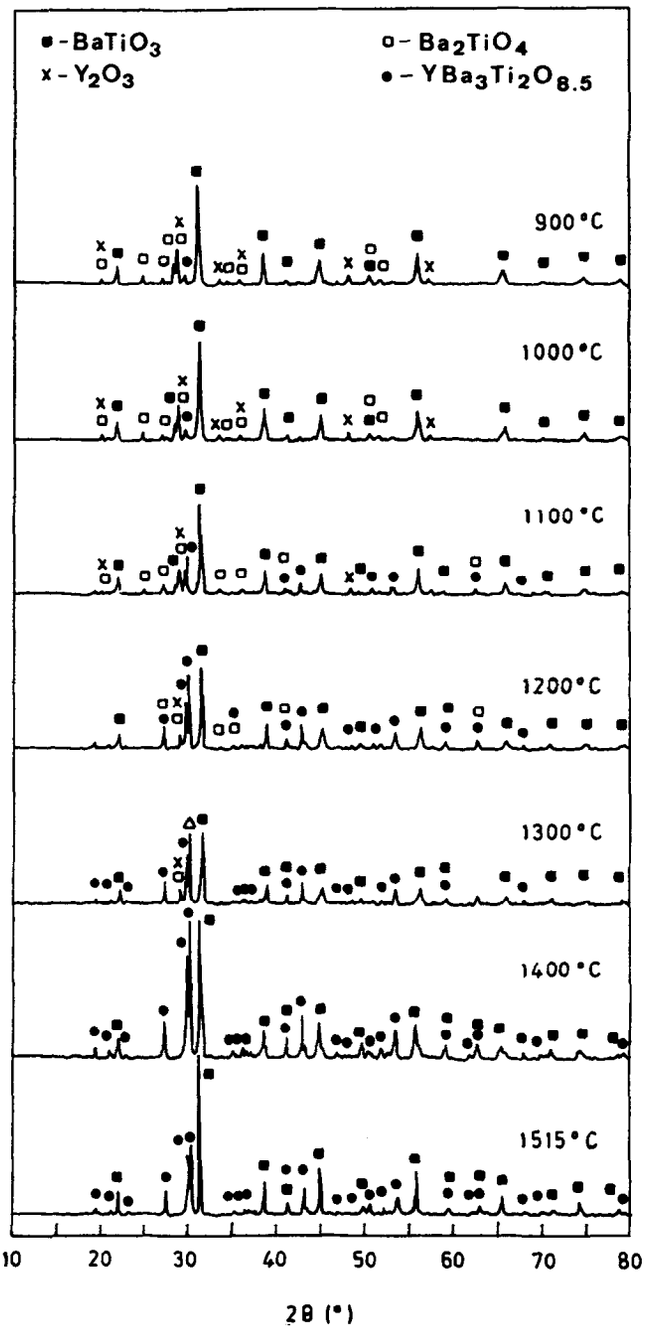

Fig. 5. X-ray powder diffraction patterns of $6BaO–Y_2O_3–5TiO_2$ powders calcined and sintered at various temperatures.

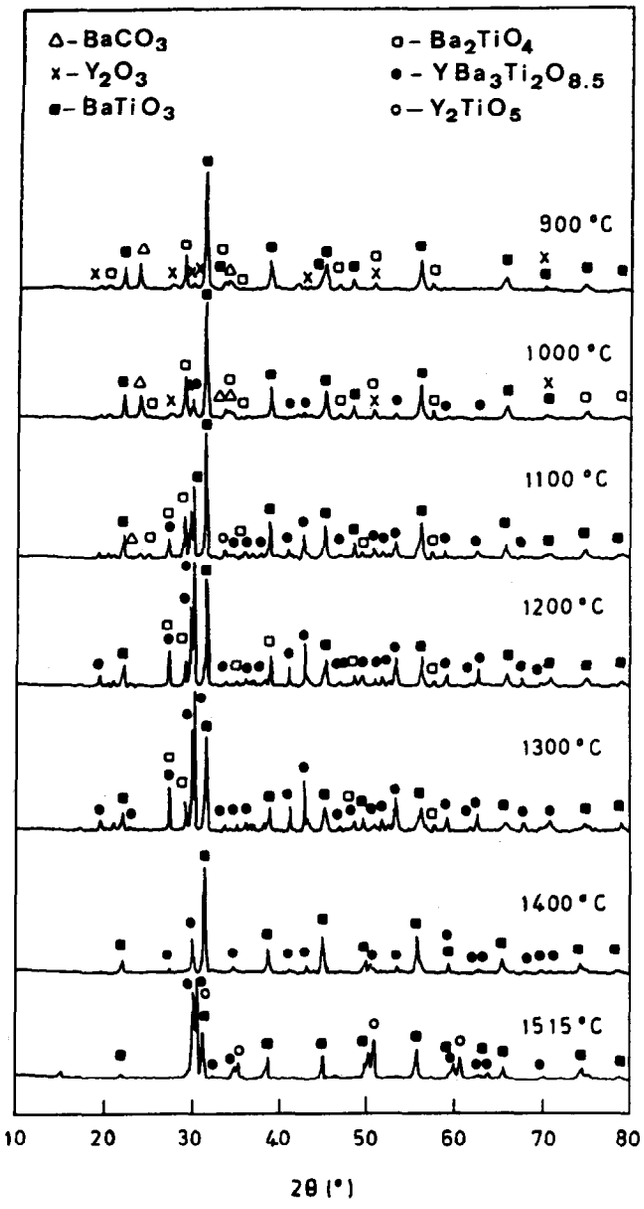

Fig. 6. X-ray powder diffraction patterns of $5BaO–Y_2O_3–4TiO_2$ powders calcined and sintered at various temperatures.

powder mixture with the $BaO:Y_2O_3:TiO_2$ ratio equal to 6:1:5 was calcined at 900, 1000, 1100, 1200, 1300 and 1400°C for 2 h and sintered at 1515°C for 6 h respectively. The X-ray powder diffraction results are shown in Fig. 5. The reactions can be also described by the eqns (1)–(4).

After calcining at 900°C for 2 h the powder contains four phases: $BaTiO_3$, Ba_2TiO_4, Y_2O_3 and a small amount of $YBa_3Ti_2O_{8.5}$. TiO_2 and $BaCO_3$ have not been observed; this implies that TiO_2 and $BaCO_3$ have reacted completely with each other and with Y_2O_3. After calcining at 1000°C for 2 h, and at 1100°C for 2 h, the results are the same as those at 900°C, and the amount of $YBa_3Ti_2O_{8.5}$ has increased. Three phases are observed: $BaTiO_3$, $YBa_3Ti_2O_{8.5}$ and a small amount of Y_2O_3, after calcining at 1200 and 1300°C for 2 h. Above 1400°C only two phases: $YBa_3Ti_2O_{8.5}$ and $BaTiO_3$, are observed by XRD. The sample sintered at 1515°C for 6 h also shows a two-phase structure consisting of $YBa_3Ti_2O_{8.5}$ and $BaTiO_3$ identified from the XRD results.

3.1.3 $5BaO–Y_2O_3–4TiO_2$ system

The phase-forming process of the ternary system $5BaO–Y_2O_3–4TiO_2$ was studied by the same method as used for the $6BaO–Y_2O_3–4TiO_2$ and $6BaO–Y_2O_3–5TiO_2$ systems. The XRD patterns of the $5BaO–Y_2O_3–4TiO_2$ powder calcined and sintered at various temperatures are shown in Fig. 6. The phase formation and chemical reactions for the Y514

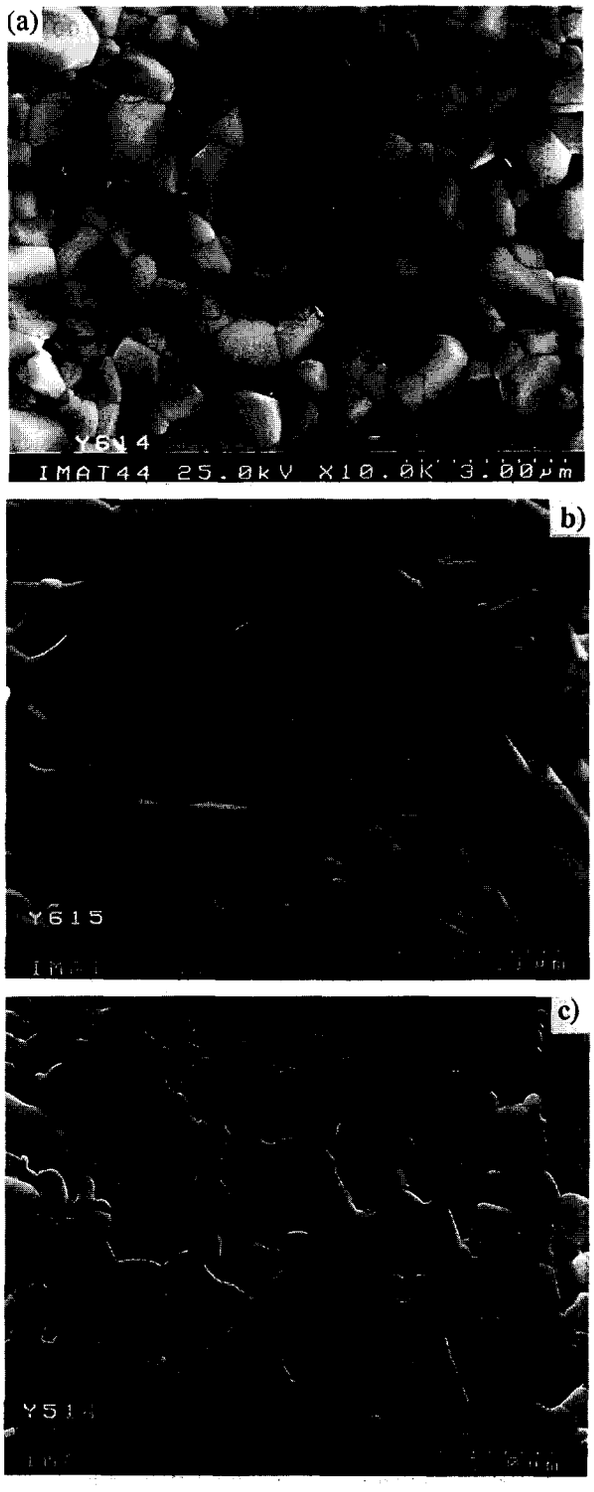

Fig. 7. SEM photomicrographs: (a) $YBa_3Ti_2O_{8.5}$, (b) Y615 and (c) Y514 sintered ceramics.

during calcining and sintering are similar to those of the Y615. However, besides the two main phases (Y614 and $BaTiO_3$), another phase was observed in the sintered samples which was identified as Y_2TiO_5. Here, another solid state reaction occurred:

$$TiO_2 + Y_2O_3 \rightarrow Y_2TiO_5 \quad (5)$$

3.2 Microstructure

Figure 7 shows photomicrographs of polished and thermally etched sections of Y614 ($YBa_3Ti_2O_{8.5}$), Y615 and Y514 samples sintered at 1515°C for 6 h. It can be seen that the $YBa_3Ti_2O_{8.5}$ ceramic sample shows a dense, single-phase microstructure with equiaxed grains. The Y615 ceramic sample shows a dense, but two-phase microstructure: one is the matrix phase with equiaxed grains, the other is the secondary phase with elongated grains. In the case of the Y514 ceramic, a small amount of a third (black) phase was observed besides the main two phases.

The phases were also microanalysed by EPMA. The results show that the composition of the matrix phase is near $YBa_3Ti_2O_{8.5}$; the elongated grains contain Ba and Ti in the case of the Y615 and Y514 ceramics; and the black grains contain Y and Ti in the case of the Y514 ceramics. By comparison with the XRD results, it is concluded that the matrix phase is $YBa_3Ti_2O_{8.5}$, the elongated phase is $BaTiO_3$ and the black grains, in the case of Y514 sample, are $Y_2Ti_2O_7$. In addition, it can also be seen that the grain size of the $YBa_3Ti_2O_{8.5}$ ceramic is small. The average grain size of the $YBa_3Ti_2O_{8.5}$ phase is less than 1 μm for single-phase Y614; and the grain size of the $YBa_3Ti_2O_{8.5}$ phase in the Y615 and Y514 compositions is about 2–3 μm.

3.3 Dielectric properties

The dielectric properties of this series of ceramics were measured and the results are shown in Table 1. It can be seen that all the samples are frequency-stable in the range 10 to 10^6 Hz. For the single-phase $YBa_3Ti_2O_{8.5}$, its relative permittivity is about 29 at 1 MHz, and dielectric dissipation factor is about 0·001; i.e. the quality factor is about 1000. For the Y615 and Y514 ceramics, the permittivity is about 100–120 and the dielectric dissipation factor is 0·0046–0·0066.

The temperature dependence of the permittivity of the $YBa_3Ti_2O_{8.5}$, Y615 and Y514 ceramics is shown in Fig. 8. The results indicate that no abnormal phenomenon occurred in the temperature interval from −173 to 127°C. The temperature coefficient in the temperature range −173 to 127°C is about +818 ppm $°C^{-1}$ for Y614, +132 ppm $°C^{-1}$ for Y615, and +222 ppm $°C^{-1}$ for Y514.

4 Conclusions

$YBa_3Ti_2O_{8.5}$ (Y614), a compound located in the BaO-rich corner of the BaO-Y_2O_3–TiO_2 ternary

Table 1. Dielectric properties of BaO–Y_2O_3–TiO_2 ceramics

	1 kHz		*10 kHz*		*100 kHz*		*1 MHz*	
Sample	ϵ	*tg*δ	ϵ	*tg*δ	ϵ	*tg*δ	ϵ	*tg*δ
Y614	30	0·005	29·5	0·0025	29·5	0·007	29	0·001
Y615	120	0·105	118	0·007	117	0·0074	115	0·0066
Y514	122	0·133	121	0·0085	117	0·008	115	0·0046

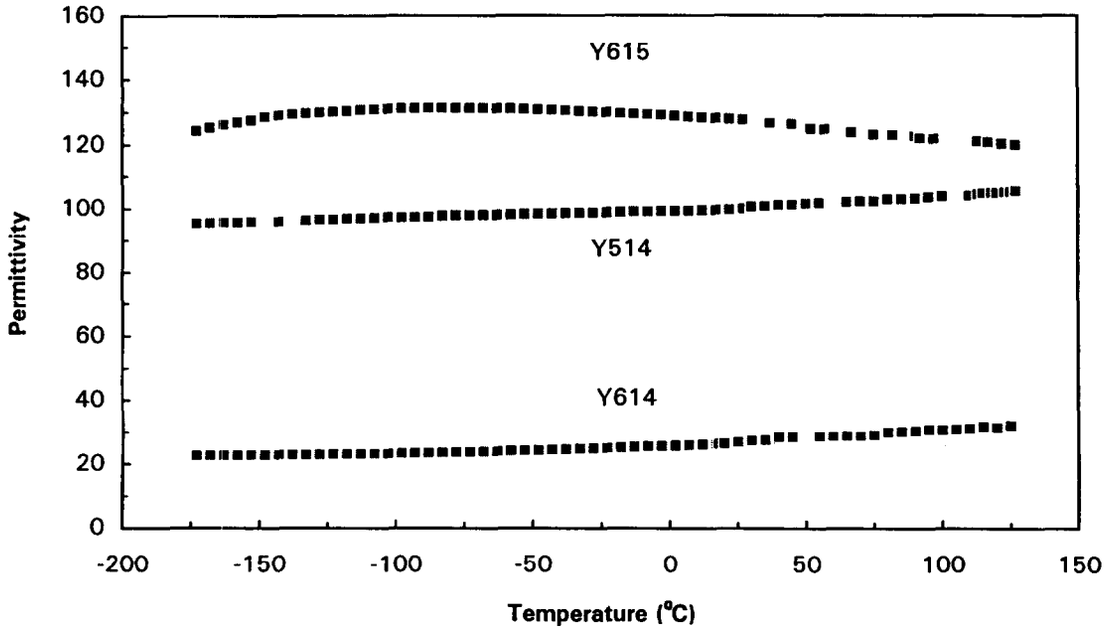

Fig. 8. Temperature dependence of permittivity of the Y614, Y615 and Y514 ceramics.

system, was synthesized and sintered as a single-phase ceramic. The dielectric properties of this material (permittivity $\epsilon = 29$, quality factor $Q = 1000$) are reported here for the first time.

Compositions with the ratio of $BaO:Y_2O_3:TiO_2$ equal to 6:1:5 and 5:1:4, were also synthesized. The Y615 ceramic consists of two phases ($YBa_3Ti_2O_{8.5}$ and $BaTiO_3$), and the Y514 ceramic consists of three phases ($YBa_3Ti_2O_{8.5}$, $BaTiO_3$ and Y_2TiO_5). They are dense ceramic composites.

This series of BaO-rich compositions in the BaO–Y_2O_3–TiO_2 ternary system with high-performance dielectric properties, are new kinds of ceramics. Their dielectric properties have not been reported before, to the authors' knowledge. The preliminary dielectric properties measurements indicate that this series of ceramic materials might be good candidate materials for high-voltage capacitors or electronic devices to be used at high frequency or even at microwave frequencies. Further work will be conducted to study the effect of doping with other elements (e.g. Pb, Bi) to promote their dielectric properties, and to understand the physical dielectric mechanisms responsible for the dielectric properties of the $YBa_3Ti_2O_{8.5}$ single-phase compound.

Acknowledgements

One of the authors (Ang Chen) would like to thank the partial support of the Oriental Foundation in Portugal, and to thank the University of Aveiro for its hospitality.

References

1. Kolar, D., Chemistry and properties of perovskite-type rare earth titanates for microwave applications. In *Proceedings of Electroceramics IV*, eds R. Waser, S. H. Hoffmann, O. Bonnerberg & Ch. Hoffmann, Aachen, Germany, September 1994, Vol. 1, pp. 3–10.
2. Tak, J., Ikegami, T. & Kageyama, K., Occurrence of dielectric 1:1:4 compound in the ternary system BaO–Ln_2O_3–TiO_2 (Ln = La, Nd, and Sm): I and II. *J. Am. Ceram. Soc.*, **74** (1991) 1868–72; 1873–1879.
3. Derks, W., Van Hal, H. & Langereis, C., *Physica B + C* (Amsterdam), **156** (1988) 62–68.
4. Chen, A., Zhi, Y., Bao, Y., Dai, X. & Jiang, Q., A study of the $BaTiO_3$–YBaCuO ceramic composite system. *J. Phys. CM*, **6** (1994) 3553–3558.
5. Chen, A., Zhi, Y., Ferreira, V. M., Vilarinho, P. M. & Baptista, J. L., Single phase dielectric compounds in the BaO-rich corner of the BaO–Re_2O_3–TiO_2 ternary system (Re = Y, Nd, and Sm). *J. Mater. Sci. Lett.*, (in press).
6. Pascal P., *Nouveau Traité de Chimie Minérale*. Masson Et Cie, Paris, 1958, pp. 904–907.

Journal of the European Ceramic Society **16** (1996) 1057–1061

PII: S0955-2219(96)00035-0
0955-2219/96/$15.00

Wet Chemical Synthesis of ZrO_2–SiO_2 Composite Powders

Shi-Wei Wang, Xiao-Xian Huang & Jing-Kun Guo

Shanghai Institute of Ceramics, Chinese Academy of Sciences, 1295 Ding-Xi Road, Shanghai 200050, People's Republic of China

(Received 10 March 1995; revised version received 16 January 1996; accepted 23 January 1996)

Abstract

Gels of composition $xZrO_2(1-x)SiO_2$, with x = 10, 20, 30 and 40 vol%, have been prepared by a wet chemical method using fumed silica and zirconyl chloride as precursors. Thermogravimetric analysis (TG) and differential thermal analysis (DTA) show that weight loss is caused by release of the absorbed water and decomposition of the $Zr(OH)_4$ gels. Gels were heat-treated for 2 h at 500, 700, 900, 1100 and 1350°C, and the products examined using infra-red (IR) spectroscopy. The increasing intensity of the peak at 800 cm^{-1} in the IR spectra with increasing temperature is attributed to the formation of Si–O–Si bonds among different SiO_2 particles, which means that the SiO_2 particles grow bigger with increasing temperature. The DTA exothermic peak as well as the IR results reveal that the crystallization of tetragonal zirconia (t-ZrO_2) begins at about 900°C, which is confirmed by X-ray diffraction (XRD). XRD curves also suggest that the silica matrix contributes to the thermal stability of t-ZrO_2. The stability of t-ZrO_2 is interpreted by the particle-size effect. © *1996 Elsevier Science Limited.*

1 Introduction

The discovery of the strength and toughness of CaO-TZP by Garvie *et al.*[1] and the role of tetragonal zirconia (t-ZrO_2) have stimulated world-wide interest in these ceramics. Tetragonal ZrO_2 is incorporated into ceramics both as precipitates and as dispersed particles. On the other hand, in the field of glass technology, zirconia has been used extensively as a nucleating agent and/or as an alkali-resistant agent in glass-ceramics. More recently, the preparation of ZrO_2-transformation-toughened glass-ceramics containing up to 20 to 30 wt% ZrO_2 was reported.[2] Generally, it is difficult to melt glasses containing high amounts of ZrO_2 because it requires a high temperature. The sol–gel method enables glass-ceramics with high ZrO_2 content to be fabricated at a lower temperature.

To date ZrO_2–SiO_2 monolithic glasses[3] and powders[4] have been prepared by means of the sol–gel process. However, the sol–gel method is time-consuming and the alkoxide precursors are expensive; moreover, supercritical conditions are needed to deal with the gels, otherwise monolithic glass cannot be obtained. The present work concerns the preparation of ZrO_2–SiO_2 composite powder by a co-precipitation approach using fumed silica and zirconium oxychloride octahydrate as raw materials. We have successfully obtained homogeneously dispersed ZrO_2–SiO_2 powders. The powders obtained were characterized by differential thermal analysis (DTA), thermogravimetric analysis (TG), X-ray diffraction (XRD), infra-red (IR) spectroscopy and transmission electron microscopy (TEM).

2 Experimental Procedure

Gels in the composition range $x$$ZrO_2$–(100–$x$)$SiO_2$, x = 10, 20, 30 and 40 vol%, were prepared from fumed silica and zirconyl chloride solution as starting materials. The fumed silica was first dispersed in distilled water, then $ZrOCl_2$ solution was added under stirring. Next, concentrated ammonia was added dropwise to the homogeneous slurry obtained above, under vigorous stirring. To ensure complete reaction, an excess of ammonia was used and the pH value of the mixed solution was maintained above 10 during precipitation.

The resulting gels were filtered and thoroughly washed with distilled water several times. Finally the gels were washed with ethyl alcohol and dried at 120°C for 24 h. The as-dried gels were then calcined in air for 2 h at 500, 700, 900, 1100 and 1350°C. A Netzsch STA429 thermal analyser was employed to detect the thermal evolution of the as-dried gels, at heating rate of 10°C min^{-1}. The calcined powders

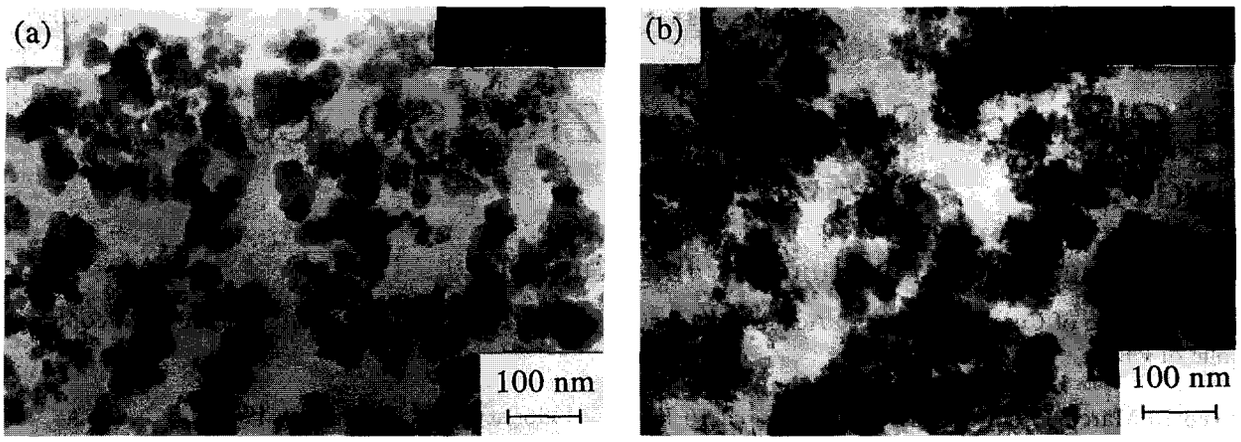

Fig. 1. TEM micrographs of (a) fumed silica after being dispersed in water and then dried, and (b) ZrO_2–SiO_2 composite powder (20ZR) heat-treated at 700°C for 2 h.

were characterized by XRD (RAX-10 diffractometer) using CuK_α radiation. Transmittance spectra were acquired with an IR spectrophotometer in the range 400–2000 cm^{-1}. The morphology, particle size and distribution of the powders calcined were observed by TEM using a JEM-200cx instrument.

3 Results and Discussion

3.1 TEM observations

The particle size of the fumed silica was determined to be about 20 nm, and some agglomerates were also found by transmission electron microscopy [Fig 1(a)]. Figure 1(b) shows the morphology of the 20 vol% ZrO_2–80 vol% SiO_2 sample (abbreviated as 20ZR) after calcination at 700°C for 2 h. It can be seen that the ZrO_2 agglomerates take on a sponge-like form and that the ZrO_2 agglomerates and SiO_2 particles overlap. SiO_2 agglomerates without the cover of the ZrO_2 sponge-like body can be seen in the middle of Fig. 1(b).

3.2 DTA–TG analysis

All DTA curves (Fig. 2) show an endothermic band attributed to water desorption at 100°C and an exothermic band (at 300–500°C) attributed to decomposition of the $Zr(OH)_4$ gels. These assignments are based upon the observation that both features are associated with a weight loss in the TG curve [Fig. 2(a)]. According to the thermochemical calculation, the enthalpy change of the reaction $Zr(OH)_4(s) = ZrO_2(s) + H_2O(g)$, i.e. ΔH = –93·6 kcal mol^{-1}, suggests that the decomposition of $Zr(OH)_4$ is responsible for the exothermic peak in the range of 300–500°C. Another weak exothermic peak appears at 900°C that does not correspond to a weight change and becomes stronger with increasing content of ZrO_2 (from 20ZR to 40ZR), indicating the crystallization of t-ZrO_2 from the amorphous state. This was corroborated by the XRD results (Fig. 3). A similar phenomenon was reported by Palladino *et al.*[3] who observed that the crystallization peak of t-ZrO_2 appears at 910–980°C in the formation of ZrO_2–SiO_2 glass-ceramics by the sol–gel route. For the pure ZrO_2 gel, however, metastable tetragonal ZrO_2 began to crystallize at 500°C.[5] We assume that the temperature differences of the crystallization of t-ZrO_2 are related to the different preparing methods, and to the situation around the ZrO_2 particles. In the ZrO_2–SiO_2 system, the crystallization of t-ZrO_2 at higher temperatures may be ascribed to the constraint of the SiO_2 matrix.

3.3 XRD results

ZrO_2–SiO_2 composite powders obtained from the co-precipitated method were amorphous to XRD (taken on sample 20ZR as an example). After calcination at 500°C for 2 h, the powder remained

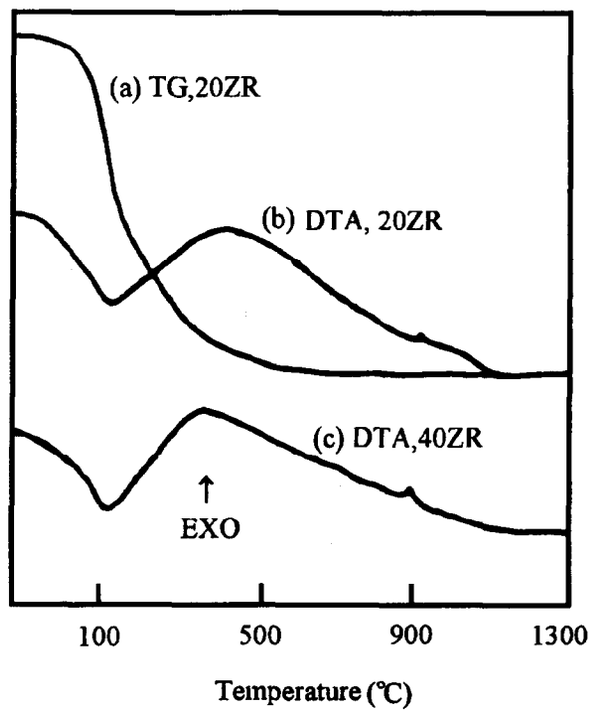

Fig. 2. DTA–TG curves of as-dried ZrO_2–SiO_2 gels.

amorphous [Fig. 3(a)]. The broad band at $2\theta = 30°$ suggests the ordering of small amounts of t-ZrO_2 for the sample calcined at 700°C for 2 h [Fig. 3(b)]. XRD on 20ZR powder heat-treated at 900°C identified the tetragonal phase, with four major peaks corresponding to the 1 1 1, 2 0 2, 1 3 1 and 2 2 0 planes in decreasing intensity [Fig. 3(c)]. This result is in consistent with that of Saha and Pramanik.[4] The increasing sharpness of the XRD peaks with increasing temperatures [Figs 3(d) and (e)] indicate the gradual ripening of the t-ZrO_2 phase and gradual growth of t-ZrO_2 particles. The formation of cristobalite or the trace of $ZrSiO_4$ was not observed in the XRD spectrum from the sample calcined at 1350°C [Fig. 3(e)]. The most striking feature of the XRD curves with increase of calcining temperature is that no evolution of monoclinic phase from t-ZrO_2 is detected in the present experiment. According to Ramamurthi *et al.*[5] the monoclinic phase gradually evolves with increasing temperature above 700°C for the pure ZrO_2 gel. For the Y-TZP powders co-precipitated by Xu,[6] the m-ZrO_2 phase emerged in the XRD spectra after the powders were calcined at 750°C for 2 h. Thus, the absence of m-ZrO_2 in the ZrO_2–SiO_2 system reveals that silica has the ability to stabilize the tetragonal zirconia phase.

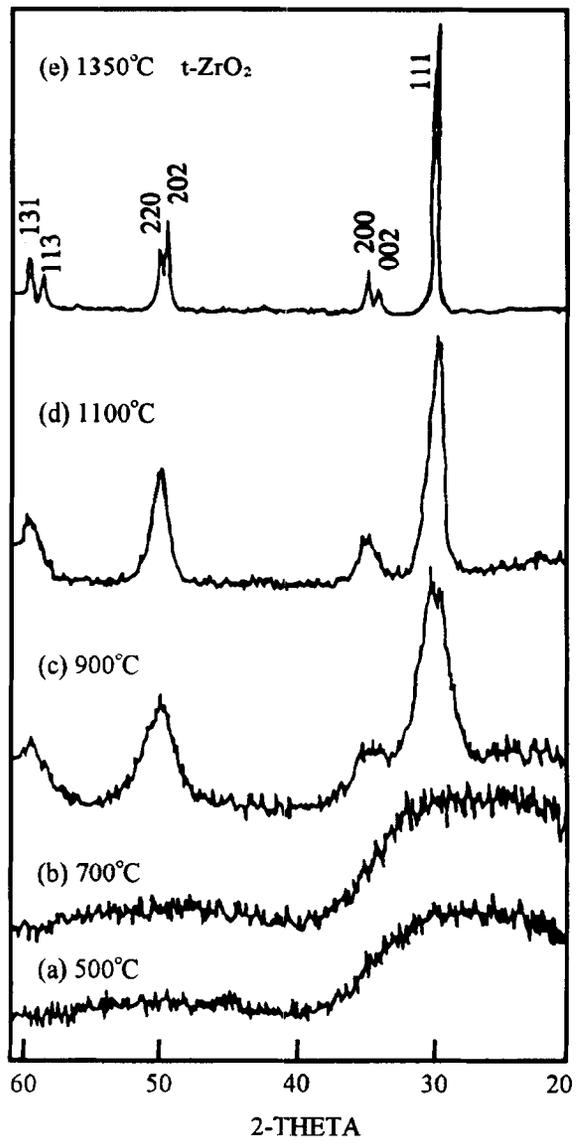

Fig. 3. XRD patterns of ZrO_2–SiO_2 gel (20ZR) calcined at different temperatures for 2 h.

According to the literature, the stabilization of the tetragonal phase in zirconia may be ascribed to the particle-size effect reported by Garvie:[7] i.e. the smaller the particle size of the t-ZrO_2 phase, the more stable it is at low temperature because of its larger specific area. The SiO_2 grains grow rapidly with increasing temperature, reaching 0·4–0·6 μm in size when the calcining temperature was raised to 1350°C (Fig. 4). At the same time ZrO_2 grains were encased in silica grains and, since the ZrO_2 particles were embedded in the silica matrix, grain growth of ZrO_2 was impeded. After calcining at 1350°C for 2 h, the average size of t-ZrO_2 particles was about 50 nm (Fig. 4, the dark round phase was zirconia particles). It has been reported that the critical size of free t-ZrO_2 particles is around 30 nm, while that of ZrO_2 particles in an Al_2O_3 matrix is larger, typically 600 nm.[7] It is suggested that the critical size of t-ZrO_2 grains has different values when the ZrO_2 grains are dispersed in different matrices. Therefore, the stability of 50 nm t-ZrO_2 grains is attributed to its smaller particle size than the critical size of t-ZrO_2 in the present system.

3.4 IR Spectra

From the IR spectra (Fig. 5) for the 20ZR sample calcined at different temperatures, it is easily seen that the observed frequencies of the vibration at 1200, 1100, 800 and 460 cm^{-1} for the Si–O–Si bond are in good agreement with the values reported by Phillippi and Mazdiyasni[8] and Nogami.[9] The bands at 1200 and 1100 cm^{-1} are assigned to the Si–O–Si asymmetric bond stretching vibration. The bands at 800 and 460 cm^{-1} are associated with the network

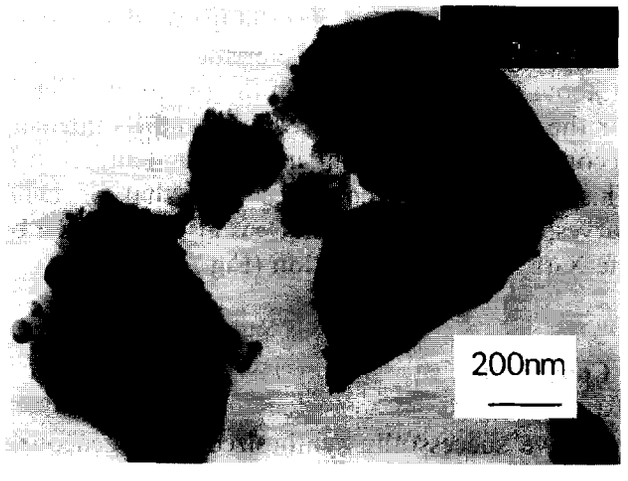

Fig. 4. TEM micrograph of ZrO_2–SiO_2 gel (20ZR) calcined at 1350°C for 2 h (the dark, round, embedded phase is zirconia particles).

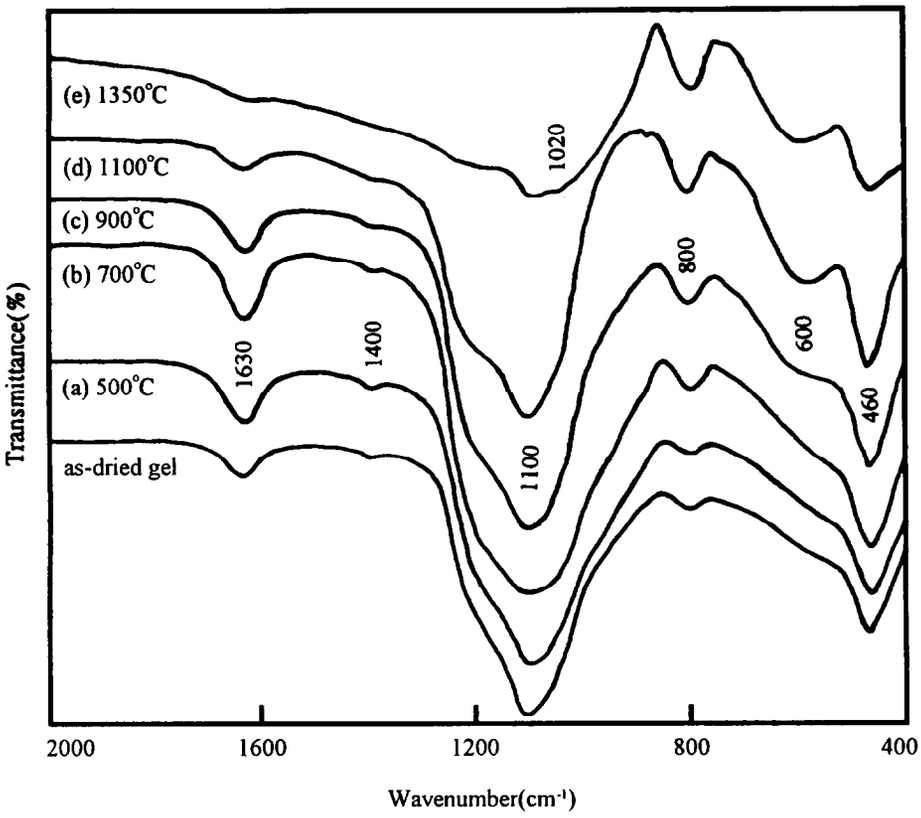

Fig. 5. IR spectra of ZrO_2–SiO_2 gel (20ZR) calcined at different temperatures for 2 h.

Si–O–Si symmetric bond stretching vibration and bond bending vibration, respectively. The increasing intensity of the 800 cm^{-1} peak with temperature indicates the formation of Si–O–Si bonds among the different SiO_2 particles. That is, the SiO_2 grains grow bigger with increasing temperature. The absorption peak at 1630 cm^{-1} is attributed to the coordinated and absorbed water and the peak at 1400 cm^{-1} is attributed to the bridging OH group in the $Zr(OH)_4$ gels, both of which decrease with increasing temperature. It is clear that the structurally coordinated water and the bridging OH group can survive higher temperatures. The weak absorption peak around 1020 cm^{-1} for the sample calcined at 1350°C suggests that a few Zr–O–Si bonds are formed,[10] but no trace of $ZrSiO_4$ was detected by XRD [Fig. 3(e)]. The characteristic band of t-ZrO_2 at about 600 cm^{-1} emerges on the IR profile (Fig. 5) for the sample calcined at 900°C, and its intensity becomes stronger with increasing temperature. This result is in accordance with that of DTA curves; the presence of t-ZrO_2 is also confirmed by the X-ray powder diffraction (Fig. 3).

4 Conclusion

We have successfully synthesized homogeneously dispersed ZrO_2–SiO_2 composite powders adopting fumed silica and zirconyl chloride as starting materials. The DTA–TG results show that the decomposition of $Zr(OH)_4$ gels is achieved below 500°C, accompanied by an exothermic phenomenon. The DTA exothermic peak at higher temperatures and the emergence of the band at about 600 cm^{-1}on the IR profiles reveal that the crystallization of t-ZrO_2 begins at about 900°C, which is confirmed by the X-ray diffraction. XRD curves also suggest that the silica matrix contributes to the thermal stability of the tetragonal zirconia. The t-ZrO_2 grains with smaller size, due to their encasement in the silica matrix, result in the survival of t-ZrO_2 in the ZrO_2–SiO_2 gels after calcination at elevated temperatures. The formation of Si–O–Si bonds among different SiO_2 particles means that the SiO_2 particle size grows bigger with increasing temperature.

References

1. Garvie, R. C., Hannink, R. H. & Pascoe, R. T., Ceramic steel? *Nature*, **258** (1975) 703–704.
2. Leatherman, G. L. & Tomozawa, M., Transformation toughened glass-ceramics. For abstract see *Am. Ceram. Soc. Bull.*, **63**[9] (1984) 1106.
3. Palladino, M., Pirini, F., Beghi, M., Chiulo, P., Cogliati, G. & Costa, L., Sol–gel formation of silica–zirconia glasses. *J. Non-cryst. Solids*, **147 & 148** (1992) 335–339.
4. Saha, S. K. & Pramanik, P., Aqueous sol–gel synthesis of powders in the ZrO_2–SiO_2 system using zirconium formate and tetraethoxysilane. *J. Non-cryst. Solids*, **159** (1993) 31–37.
5. Ramamurthi, S. D., Xu, Z. K. & Payne, D. A., Nanometer-size ZrO_2 particles by a sol-emulsion-gel method. *J. Am. Ceram. Soc.*, **73**[9] (1990) 2760–2763.

6. Xu, Y., Preparation, sintering kinetics and microstructure of Y-TZP superfine powders. PhD thesis, Shanghai Institute of Ceramics, China, 1991, pp. 71.
7. Garvie, R. C., The occurrence of metastable tetragonal zirconia as a crystallite size effect. *J. Phys. Chem.*, **69**[4] (1965) 1238–1243.
8. Phillippi, C. M. & Mazdiyasni, K. S., Infrared and Raman spectra of zirconia polymorphs. *J. Am. Ceram. Soc.*, **54** (1971) 254–258.
9. Nogami, M., Glass preparation of the ZrO_2–SiO_2 system by the sol–gel process from metal alkoxides. *J. Non-cryst. Solids*, **69** (1985) 415–423.
10. Abe, Y., Sugimoto, N., Nagao, Y. & Misono, T., Preparation of monolithic gels SiO_2–M_xO_y(M = Al,Zr) by the reaction of silicic acid with metal chelate compounds. *J. Non-cryst. Solids*, **108** (1989) 150–156.

Journal of the European Ceramic Society **16** (1996) 1063–1073

PII: S0955-2219(96)00036-2
0955-2219/96/$15.00

Nanometric Si-Based Oxide Powders: Synthesis by Laser Spray Pyrolysis and Characterization

Nathalie Herlin, Xavier Armand, Emmanuel Musset, Hervé Martinengo, Michel Luce & Michel Cauchetier

CEA/DSM/DRECAM, Service des Photons, Atomes et Molécules, CE Saclay, 91191 Gif-sur-Yvette Cedex, France

(Received 13 December 1995; revised version received 22 January 1996; accepted 23 January 1996)

Abstract

The versatility of the laser synthesis method has been improved during the last few years. In this paper we present the synthesis of amorphous, nanosized Si/C/O powders obtained via ultrasonic injection of aerosol droplets into the beam of a high-power tunable CO_2 laser, using $(CH_3)_xSi(OC_2H_5)_{4-x}$ ($0 \leq x \leq 3$) and hexamethyldisiloxane as alkoxysilane precursors. All these precursors strongly absorb the CO_2 laser emission between 9 and 11 μm. The addition of precursors containing Al or Ti in tetraethoxysilane ($x = 0$) leads to Si,Al or Si,Ti oxide composite powders. The evolution of the powders (chemical composition, crystallization, morphology) during heat treatment under air, argon or nitrogen is studied by infra-red absorption, thermogravimetric analysis, transmission electron microscopy and X-ray diffraction. Silica powders with specific surface area up to 500 $m^2\ g^{-1}$ are obtained when heating in air. © *1996 Elsevier Science Limited.*

1 Introduction

Since the first experiments by Haggerty *et al.*,[1] a wide variety of ultrafine powders has been obtained by the laser synthesis method. An important application of these powders is structural ceramic technology. The synthesis method is based on the resonance between the emission of a CO_2 laser (10·6 μm) and the absorption of a gaseous precursor. It offers several advantages: due to the coherent laser beam, the chemical reaction zone is very well defined and there is no interaction with the reactor walls. This ensures extreme purity and very fine sized particles. However, the process has not been scaled up due to several limitations: the resonance condition clearly limits the precursor choice. To obtain Si-based powders the most common precursor is silane, which is an expensive and hazardous gas.

Recently, taking advantage of new technical developments, the versatility of the method has been improved. The ultrasonic injection of liquid precursors into the beam of the laser greatly extends the choice for the reactants. Moreover, it allows the use of cheaper and safer products. An example is given by the synthesis of Si/C/N powders.[2–4] Also, high power CO_2 lasers tunable between 9 and 11 μm are now available.[5]

To our knowledge, only two oxide powders TiO_2[6,7] and Al_2O_3[8] have been obtained by laser driven reactions in gaseous phases. The possibility to synthesize SiO_2 from an aerosol of tetraethoxysilane has already been reported.[9] In this paper we present the synthesis results obtained with different organosilicon precursors. Some nanosized silicon-based oxide powders have been synthesized using tetraethoxysilane and/or appropriate organometallic liquid precursors. Such powders may find applications in various fields. The organosilicon precursors are inexpensive, compared with silane, and after annealing treatments it is possible to obtain nanosized SiC powder as shown by Li *et al.*[10] for dimethyldiethoxysilane. The incorporation of fine carbon particles in silicon oxycarbide glasses (black glasses) has improved mechanical properties and chemical stability compared with silica.[11] In the field of catalysis there is an interest in incorporating fine metallic particles with good dispersion in high specific surface area silica.

In this paper, we report some preliminary characterization results and the evolution of these powders to silica, oxycarbide glasses or oxide composites after firing in air, argon or nitrogen between 600 and 1600°C.

2 Experimental

2.1 Procedure

The experimental device with aerosol generator, reaction chamber and powder collector has already been described.[2,9] A PRC-Oerlikon 1500-W, fast axial flow CO_2 laser has been modified to accept a grating which makes it tunable between 9 and 11 μm.[5]

The liquid organosilicon precursors with a variable O/Si atomic ratio and general formula $R_xSi(OR')_{4-x}$ where $0 \leq x \leq 3$, $R = CH_3$, $R' = C_2H_5$ and hexamethyldisiloxane $[(CH_3)_3SiOSi(CH_3)_3]$ were supplied by Fluka Chemie A.G. or Sigma–Aldrich Chimie and used without further purification. Table 1 presents the different precursors with their chemical formulae: $x = 0$ corresponds to tetraethoxysilane $Si(OC_2H_5)_4$, $x = 1$ corresponds to triethoxymethylsilane $(CH_3)Si(OC_2H_5)_3$, $x = 2$ corresponds to diethoxydimethylsilane $(CH_3)_2Si(OC_2H_5)_2$ and $x = 3$ corresponds to ethoxytrimethylsilane $(CH_3)_2Si(OC_2H_5)_2$.

Some of these precursors have been used in the preparation of Si/C/O oxycarbide glasses, carbon–SiO_2 glass composites or SiC by the sol–gel process.[12–16] Recently, vaporized diethoxydimethylsilane has been irradiated with the focused beam of a high-power fixed-frequency CO_2 laser for SiC formation.[10] These precursors have been chosen because they absorb infra-red radiation in the 9–11 μm region corresponding to Si–O–C or Si–O–Si bonds. Weaker absorption bands appear near 10·6 μm for $0 \leq x \leq 3$ (see Table 1). Figure 1 presents the absorption lines of the different liquid precursors and the emission lines of the tunable CO_2 laser, showing that the resonance condition is easily achieved for this family of precursors.

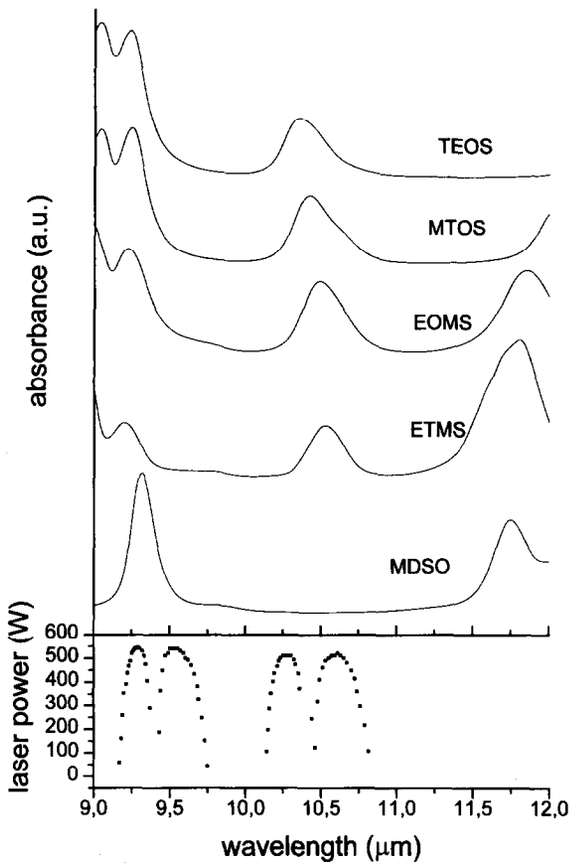

Fig. 1. Absorption spectra of the different precursors and emission lines of the laser at half discharge current (i = 30 mA).

Composite precursors were obtained by mixing liquid titanium propoxide — $Ti(OC_3H_7)_4$ — or solid aluminium isopropoxide — $Al(OCH(CH_3)_2)_3$ — with tetraethoxysilane. The Ti/Si and Al/Si atomic ratios are equal to 0·1 in the liquid phase.

The aerosols were produced by an ultrasonic spraying technique (Pyrosol process) which has been widely used in thin layer deposition.[17] The aerosol characteristics (such as droplet size and flow rate) depend on the liquid properties (viscosity, surface tension, volatility). The size of the aerosol droplets is given by:

$$d = \left(\frac{\pi \sigma}{4\rho f^2}\right)^{1/3}$$

where σ and ρ are the surface tension and density of the liquid respectively, and f is the frequency of the transducer (800 kHz). Using measured or calculated σ values,[18–20] the size of the droplets can be calculated for the different precursors: they are in the range 2·8–3·0 μm.

Table 1 summarizes some properties of the precursors used and laser irradiation conditions. The aerosol droplets are carried out in an argon flow through a 13 mm diameter nozzle into the reaction chamber. In order to keep the residence time in the laser beam (i.e. the reaction time) constant, the argon flow was fixed to 1280 cm^3 min^{-1}. The droplets intersect the laser beam (12 mm diameter) orthogonally with an incident power in the 350–400 W range (discharge current = 30 mA). Powders are collected in a glass chamber located between the reaction cell

Table 1. List of precursors and irradiation conditions

	Precursor	*Molecular weight (g)*	*Density of precursor (g cm^{-3})*	*Boiling point (°C)*	*Sample designation*	*Laser power (W)*	*Absorbed power (W)*	*Wavelength (μm)*
Tetraethoxysilane	$Si(OC_2H_5)_4$	208·3	0·934	165·8	TEOS	400	220–250	9·293
Triethoxymethylsilane	$(CH_3)Si(OC_2H_5)_3$	178·3	0·896	143	TEMS	430	220–250	9·293
Diethoxydimethylsilane	$(CH_3)_2Si(OC_2H_5)_2$	148·3	0·840	114–115	EOMS	420	280–290	9·260
Ethoxytrimethylsilane	$(CH_3)_3Si(OC_2H_5)$	118·3	0·757	75–76	ETMS	420	330–350	9·293
Hexamethyldisiloxane	$(CH_3)_3SiOSi(CH_3)_3$	162·4	0·759	99–101	MDSO	345	260–280	9·488
Tetraethoxysilane+ aluminium isopropoxide	0·9 $Si(OC_2H_5)_4$ + 0·1 $Al(OC_3H_7)_3$	204·25	1·035	solid	AlTEOS	440	290–310	9·293
Tetraethoxysilane + tetrapropylorthotitanate	0·9 $Si(OC_2H_5)_4$ + 0·1 $Ti(OC_3H_7)_4$	284·26	0·965	170/400 Pa	TiTEOS	430	280–300	9·293

and the vacuum pump. The typical duration of an experiment is 40 min.

2.2 Characterizations

Chemical analyses were achieved by conventional methods (CNRS analysis laboratory) as previously presented.[2] The relative uncertainty is equal to ± 2% for C and O, ± 3% for Si, Ti and Al. The heat treatments were carried out either dynamically by thermo- gravimetric analysis (TGA) in flowing air, argon or nitrogen, or statically in a Nabetherm HT08/1750 oven for oxidation in air or in a Pyrox GE80 graphite furnace for annealing in argon and nitrogen. The heating rate was 10°C min^{-1} and the dwell time 1 h.

X-ray diffraction (XRD) patterns of the crystalline phases were obtained with an automated powder diffractometer (Philips, APD 1700) using CuK_α radiation. Information on chemical bonding was obtained by infra-red (IR) spectrophotometry (Perkin–Elmer 580 spectrophotometer) in the 4000–400 cm^{-1} range using the KBr pellet technique. The specific surface areas were measured by the BET method using a Micromeretics Flowsorb 2300. The morphology was studied by transmission electron microscopy (TEM) (CM20 Philips).

3 Results and Discussion

3.1 Si/C/O powders

During laser pyrolysis a wide yellow flame is observed in the reaction zone. The production rate is rather low, from 8 to 27 g h^{-1}, but no effort has been made to optimize this. It is correlated with the weight of displaced precursor and is very close to our first results obtained in Si/C/N composite powder synthesis from laser pyrolysis of a hexamethyldisilazane aerosol.[2] As shown in Table 1, the absorbed laser power — in the range 50 to 80% of the incident power — is high compared with the absorption in gaseous laser-driven reactions, e.g. 10% for SiC synthesis.[21] A partial explanation is given by the power excess necessary to vaporize the liquid droplets. Table 1 also presents the abbreviations used in the following sections for the samples synthesized from the different precursors.

3.1.1 As-produced powders

In all cases the as-produced powders are black and amorphous as confirmed by XRD. Table 2 gives the chemical elemental analysis (wt%) of the produced powders together with the chemical composition of the reactive phase. An empirical chemical composition of the powders is also presented. The chemical composition of the powders is a function of the chemical composition of the reactive phase. The O and Si content is higher in the powder than in the precursor. The relative evolution is similar for all the chemical elements: for example, O content in the powders decreases when it decreases in the precursor. A more precise comment taking into account the nature of the chemical bond is presented in the following.

The TEM micrographs show that all the powders consist of round particles with low size dispersion. The particles stick together in a chain-like manner. Figure 2 presents micrographs of EOMS and TEOS samples, with a smaller grain size (≈ 20 nm) for the EOMS sample compared with all other samples (>30 nm). These observations are in agreement with BET measurements (Table 2). TEM micrographs at higher magnification show that most of the particles are slightly agglomerated and can be dispersed, but in some cases there is a strong connection between the particles. Also, some ribbons (similar to carbon ribbons) are present in all the samples. As an example, Fig. 2(a) presents the ribbons observed in a TEOS sample.

Table 2 shows no clear correlation between the BET surface of as-formed powders and the experimental synthesis conditions (such as size of the droplets, laser power and argon flow). One can see that for $R_xSiR'_{4-x}$, $x = 1$ to 3, the specific surface area decreases with increasing x.

Figure 3 presents the IR spectra of as-formed powders. The TEOS sample corresponds to pure amorphous silica (opaline type).[22,23] The peaks at 1100 and 810 cm^{-1} correspond to antisymmetric Si–O–Si stretching and the peak at 470 cm^{-1} corresponds to the Si–O–Si bending mode.[24] This

Table 2. Chemical analysis of precursors and as-formed produced powders

Precursor	*wt%*					*Samples*	*wt%*					*Equivalent chemical formula*	S_{BET} ($m^2 g^{-1}$)
	C	*O*	*Al*	*Ti*	*Si*		*C*	*O*	*Al*	*Ti*	*Si*		
$Si(OC_2H_5)_4$	46·1	30·7			13·4	TEOS	21·1	41·8			35·1	$SiO_{2.08}C_{1.40}$	133
$(CH_3)Si(OC_2H_5)_3$	47·1	26·9			15·7	MTOS	27·0	36·6			32·4	$SiO_{1.98}C_{1.94}$	228
$(CH_3)_2Si(OC_2H_5)_2$	48·5	21·6			18·9	EOMS	28·3	34·0			35·3	$SiO_{1.68}C_{1.87}$	210
$(CH_3)_3Si(OC_2H_5)$	50·7	13·5			23·7	ETMS	29·4	28·3			42·4	$SiO_{1.17}C_{1.62}$	133
$(CH_3)_3SiOSi(CH_3)_3$	44·3	9·8			34·5	MDSO	29·9	16·7			50·7	$SiO_{0.58}C_{1.38}$	70
$Si(OC_2H_5)_4$+ $Al(OCH(CH_3)_2)_3$	46·7	30·0	1·2		12·2	AlTEOS	19·2	43·8	3·6		33·8		84
$Si(OC_2H_5)_4$+ $Ti(OC_3H_7)_4$	46·6	29·7		2·0	11·8	TiTEOS	23·2	40·6		5·9	31·1		70

observation is in good agreement with the chemical composition of the powder: the O/Si atomic ratio is equal to 2·09, very close to the ratio of pure silica. The absorption lines of amorphous silica powders are observed in all spectra. In the MTOS sample, a new feature at 1260 cm^{-1} appears. This corresponds to a Si–CH_3 bond and is correlated with the presence of Si–CH_3 in the precursor. It is attributed to partially dissociated precursor remaining trapped in the powder. The peak is very weak, indicating that a very small part of the precursor remains in the powders. In TEOS and EOMS samples C atoms do not seem bonded to Si or O, suggesting the presence of an abundant phase composed of free carbon in good agreement with the presence of carbon ribbons observed by TEM. The samples MTOS, EOMS, ETMS and MDSO are produced from precursors containing an increasing number of Si–C bonds compared with Si–O bonds. The infra-red spectra show an increasing contribution of the feature located at 870 cm^{-1}, which is attributed to the Si–C bond.

From the TEM micrographs, the IR spectra and using the empirical chemical composition, it can be assumed that the samples are mainly composed of silica, silicon carbide and free carbon with different ratio (Table 3). These compositions are in good agreement with the relative intensities of SiC and SiO_2 observed in IR spectra. Also, this composition (SiC bonds) is related to the number of SiC bonds in the liquid precursor (Fig. 4). However, IR spectra alone do not enable any conclusions to be drawn about the local environment. As already observed for Si/C/O samples obtained by other methods (see, for example, Ref. 11), we think that in all our samples we have a distribution of SiO_xC_{4-x} tetrahedra. The local environment around Si and C atoms will be investigated more closely by nuclear magnetic resonance spectroscopy. The nature of the C excess, designated here as free carbon, should be clarified using (for example) Raman spectroscopy.

The powders obtained by irradiation of vaporized diethoxydimethylsilane with the focused beam of a

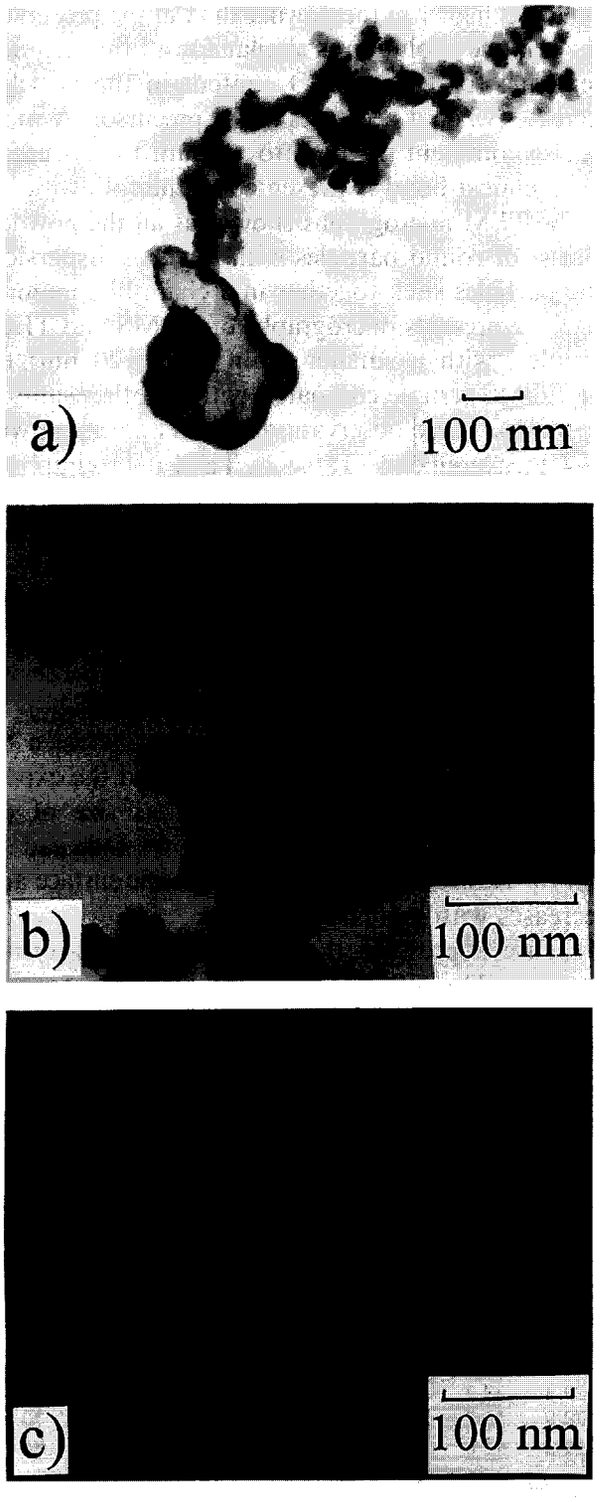

Fig. 2. TEM micrographs of as-formed TEOS (a,b) and EOMS (c) samples.

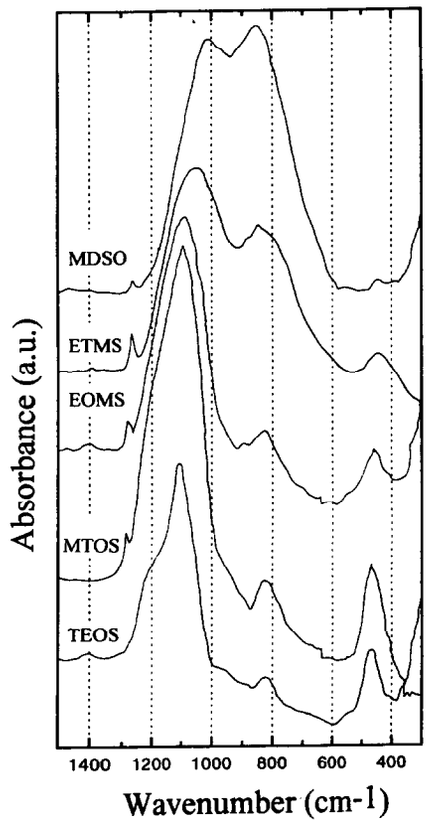

Fig. 3. IR spectra of as-formed Si/C/O powders.

Table 3. Assumed chemical composition of powders, calculated and measured weight evolution with oxidation

Sample	*Composition*	*Δm/m (%) [calculated]*	*Δm/m (%) [measured]*
TEOS	SiO_2 +1·4 C	−22	−21·8
MTOS	SiO_2 +1·94 C	−28	−28·4
EOMS	SiO_2 + 0·19 SiC + 2·03 C	−22	−21·8
ETMS	SiO_2 + 0·71 SiC + 2·05 C	−1	−7·8
MDSO	SiO_2 + 2·45 SiC + 2·30 C	+11	+12·2

high-power fixed-frequency CO_2 laser[10] can be compared with the EOMS sample. The grain size in each sample is of the same order of magnitude. The powders are amorphous. The chemical analysis shows that the EOMS sample is more oxidized (34/25 wt%). This result can be related to the different experimental conditions, in particular the laser power density is much lower in the present work: 100 W cm^{-2} compared with 5100 W cm^{-2} in Ref. 10.

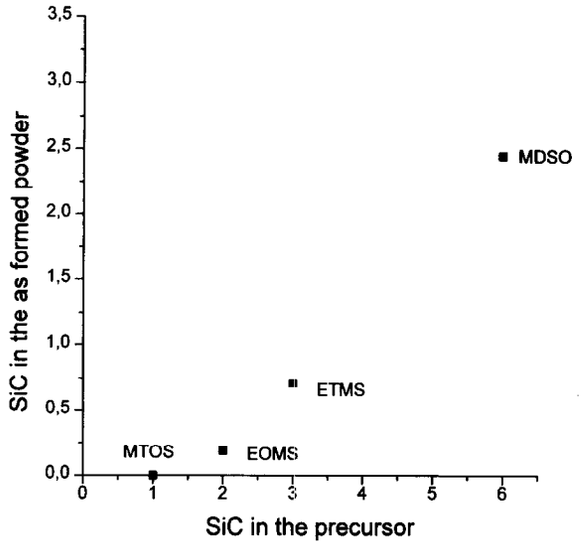

Fig. 4. Number of SiC bonds in the produced powders as a function of SiC bonds in the precursor.

3.1.2 Annealed powders

3.1.2.1 Annealing in air. Figure 5 presents TGA curves of Si/C/O samples after heating to 1600°C in air. The weight evolution shows a very different behaviour, correlated with the chemical composition of the sample. Assuming that annealing under air leads to complete oxidation of the different compounds of the powders and using the chemical composition of Table 3, two mechanisms are involved:

$$SiO_2 + \text{free C} + O_2 \rightarrow SiO_2 + CO_2 \quad (1)$$

$$SiO_2 + SiC + O_2 \rightarrow SiO_2 + CO_2 \quad (2)$$

It is easy to calculate the weight changes due to oxidation for the different samples. The result is presented in Table 3. The calculations are compared with the experimental results (Fig. 5). For TEOS and MTOS samples, the loss is attributed to oxidation of free carbon. The weight loss is of the same order of magnitude as the C content in the as-formed powders (Table 2). For other samples, there is a

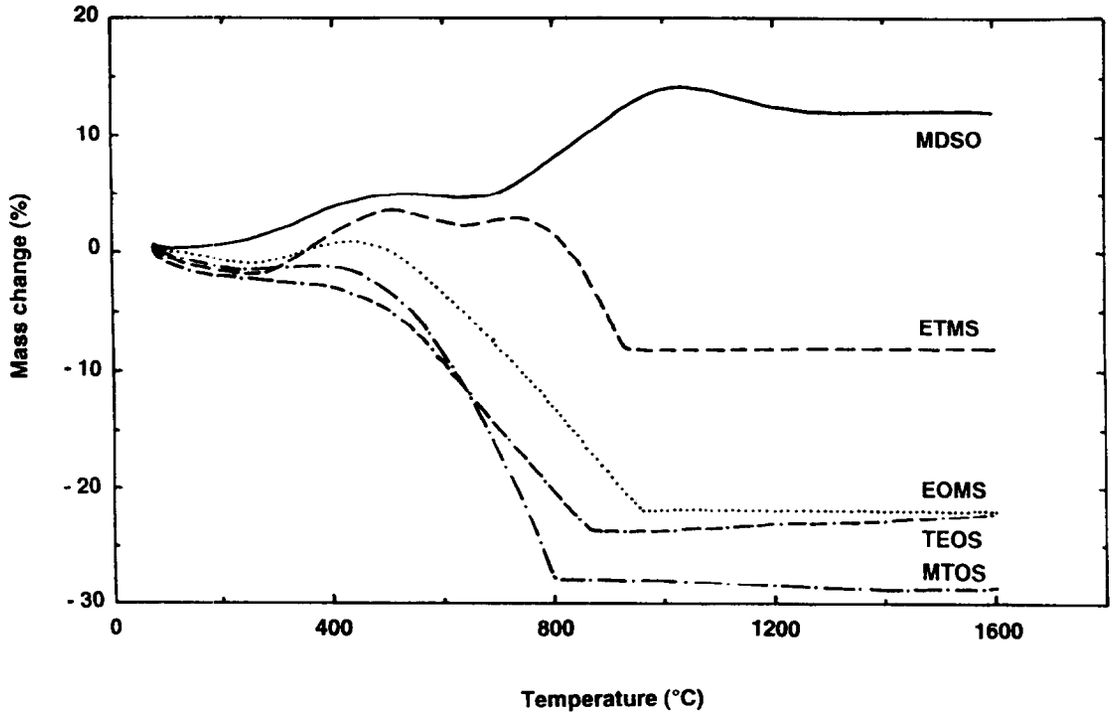

Fig. 5. TGA curves of Si/C/O powders fired under air up to 1600°C (heating rate 10°C min^{-1}, dwell time: 1 h).

competition between weight loss due to reaction (1) and gain due to reaction (2). For all samples the qualitative agreement is good between calculations and experimental measurements, which is a confirmation that the assumed mechanisms are dominant.

After heating for 3 h at 600°C under air, the chemical analysis shows that the C content is very weak (<0·5%) for all samples except MDSO, and the powders turn white. The chemical composition is already very similar to that of silica. For sample MDSO, after 3 h of heating at 600°C under air, the weight increases by 12% and the C content is still 14% because it is not so easy to oxidize C bonded to Si as compared with free C, as already shown in laser synthesized SiC powders.[25] IR spectra of annealed powder show the presence of SiC and SiO bonds, with a decreasing contribution of SiC compared with the as-formed powder. At higher temperature the 870 cm^{-1} absorption band of SiC disappears and the C content becomes negligible. All these observations are in good agreement with reactions (1) and (2).

Figure 6 shows that the specific surface area increases markedly after annealing at 600°C for samples with $x = 0$ to 3 and then decreases at higher temperatures. A value near 500 $m^2\ g^{-1}$ is measured for the MTOS sample. At 600°C TEM observations show no change in the morphology or size of the powders, grain growth begins around 900°C correlated with the decreasing specific surface area. The increase in specific surface area is thus attributed to an increased porosity due to the departure of C atoms. Porosity and density measurements are necessary to confirm this hypothesis. For the MDSO sample, the specific surface area is not as significantly modified at 600°C as it is in the other compounds. In this latter case, oxidation leads to a less porous material. MTOS sample is of special interest because the surface area is still very high at 900°C (273 $m^2\ g^{-1}$). At 1300°C, the specific surface area is below 1 $m^2\ g^{-1}$ for all samples, indicating high densification.

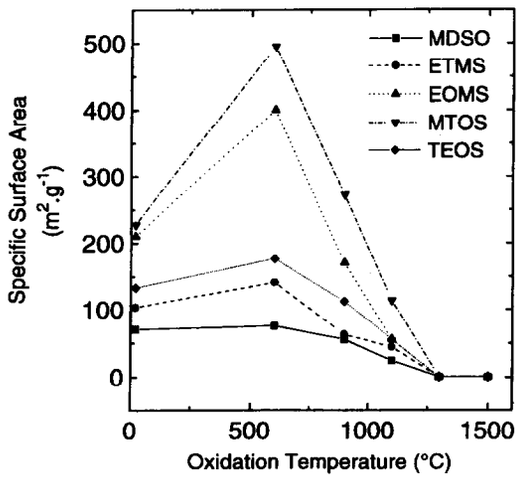

Fig. 6. Evolution of the specific surface area of Si/C/O powders with oxidation temperature.

Figure 7 presents the evolution of IR spectra of the TEOS sample after heat treatments under air at different temperatures, the general trend is identical for all the samples. After 1 h of heating at 600°C, the feature attributed to $Si–CH_3$ disappears from the IR spectra. The IR spectra still exhibit the characteristic features of opaline up to 1200°C. At this temperature, TEOS and EOMS samples are still amorphous as confirmed by XRD. The O/Si (wt) ratio is very close to 1·14 (pure silica) and the C content is about

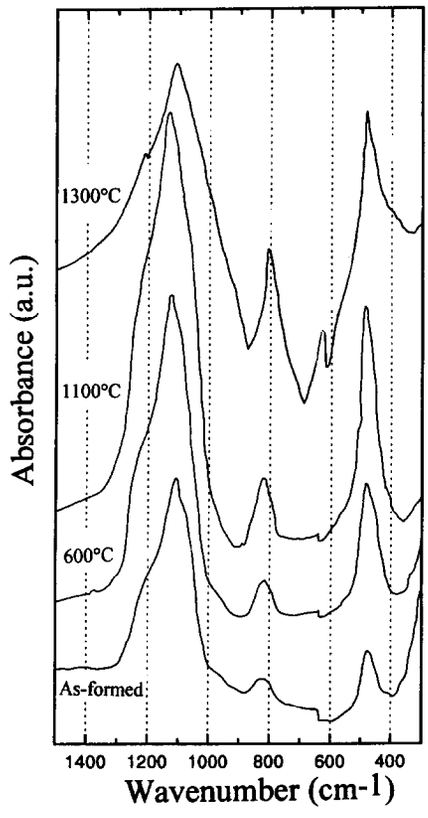

Fig. 7. Evolution of IR spectra of TEOS after annealing under air.

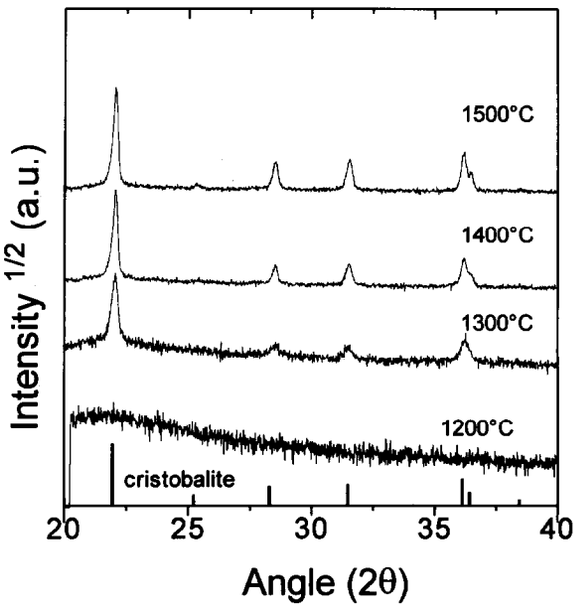

Fig. 8. Evolution of XRD patterns of TEOS.

≅ 100 ppm. After heat treatment in air at 1300°C, TEOS sample crystallizes as shown in Fig. 8. EOMS sample is also crystallized at this temperature. The cristobalite structure is identified through IR and XRD (JCPDS no. 39-1425) (Figs 7 and 8), which corresponds to the chemical analysis. A new peak at 620 cm^{-1} appears in the IR spectra (Fig. 7), characteristic of the cristobalite structure.[22,23] The broad structure between 1000 and 1300 cm^{-1} splits into two bands at 1100 and 1200 cm^{-1}, which correspond to the longitudinal and transverse mode of the SiO_2 lattice. This indicates a long-range crystalline order.[26]

Above 1300°C, the XRD patterns of TEOS sample show an increasing crystallite size with increasing temperature.

At 1300°C, MDSO sample is still amorphous under XRD. The cristobalite structure is identified after heat treatment at 1400°C, and the chemical analysis gives the composition of silica O/Si = 1·15 (wt).

3.1.2.2 Annealing under argon and nitrogen. Heat treatment in argon was performed at 1300°C, which is before the thermal reaction of silica (carboreduction), and at 1500°C after the carboreduction. Annealing under nitrogen was performed at 1500°C. At this temperature, nitrogen becomes active for nitridation. IR spectra of annealed powders are shown in Figs 9 and 10.

Under argon at 1300°C [Fig. 9(a)] the IR spectrum of the TEOS sample is very similar to that of silica. In the other spectra mixtures of silica and silicon carbide appear, the silicon carbide content increasing from MTOS to MDSO sample as shown by the change in relative intensities of IR bands at 1100 cm^{-1} for SiO_2 and at 870 cm^{-1} for SiC. At 1500°C [Fig. 9(b)] only IR bands of SiO_2 appear for the TEOS sample. In the other samples SiC is the dominant compound, with the IR band at 870 cm^{-1}. The pronounced dip near 1000 cm^{-1} was observed previously[2,27,28] and is generally related to the size increase obtained by the coalescence of particles following the carboreduction of silica.

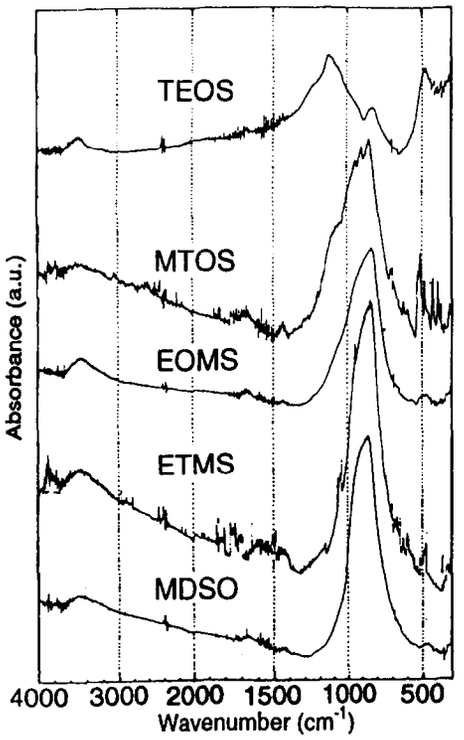

Fig. 10. IR spectra of Si/C/O powders after annealing under nitrogen at 1500°C.

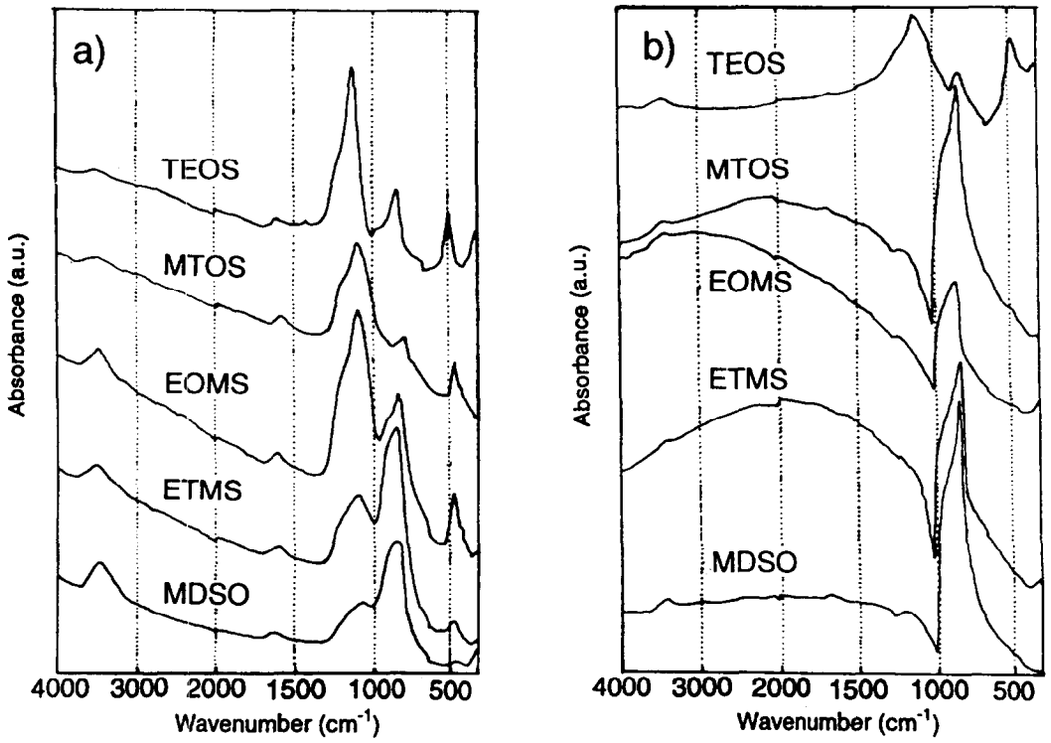

Fig. 9. IR spectra of Si/C/O powders after annealing under argon at 1300°C (left) and 1500°C (right).

IR spectra of the nitrided powders (Fig. 10) show differences relating to the initial sample. The IR spectrum of the TEOS sample is quite similar to the SiO_2 spectrum. In the other spectra, IR bands due to crystallized Si_3N_4 appear in the 500–400 cm^{-1} region.

Tables 4 and 5 present the characterizations and the chemical compositions of these powders. They show a good agreement with the IR results.

At 1500°C, under argon or nitrogen, coalescence of TEOS sample particles occurs promptly when the spe- cific surface area is decreased below 1 $m^2\ g^{-1}$ (Table 4). The remaining C content is low (about 2·5 wt%) and the nitridation under nitrogen is negligible (0·9 wt% N). The calculated chemical composi-tion (Table 5) shows silica as the predominant phase. The weight loss can be explained by $SiO_2 + C \rightarrow SiO\uparrow + CO\uparrow$ with SiO and CO volatilizations. The carbo-reduction reaction of the silica can be neglected for annealing under N_2. The non-nitridation of the TEOS sample appears to be different from result relating to the preparation of Si_3N_4 from alkoxide-derived oxides by carbothermal reduction and nitridation.[29]

In the other samples the C content after annealing at 1500°C under argon remains high (25–30 wt%) and the O content decreases below 10 wt%, relating to the carboreduction of the silica and the formation of silicon carbide. Similar high weight losses (Table 4) — up to 80 wt% — have been observed in the preparation of silicon carbide from organosilicon gels.[16,30,31] At 1300°C, XRD patterns show that the MDSO sample is slightly crystallized and the β-SiC structure is identified (JCPDS no. 29-1129). At higher temperature the crystallite size increases. The evolution of specific surface area shows that the nanometric structure is conserved up to 1300°C. As in the previous case, the specific surface area of the MTOS sample is quite high: 242 $m^2\ g^{-1}$.

Annealing under nitrogen at 1500°C leads to a very efficient nitridation for these samples. The N content seems related to the initial specific surface area of the samples and decreases from 24·1 to 11·0 wt% when the specific surface area decreases from 230 to 70 $m^2\ g^{-1}$ (Table 2). The corresponding Si_3N_4 content in the remaining powder is high, up to 60 wt% for MTOS sample (Table 5). The nitridation of the EOMS sample appears as different from results of Ref. 10, where the heat treatment under nitrogen at 1600°C leads to crystalline SiC containing 6 wt% of oxygen.

3.2 Titanium- and aluminium-doped silica powders

3.2.1 As-formed powders

Table 2 shows that the Al/Si and Ti/Si ratios are equal in the reactive phase and in the powders, which is interesting when it is intended to produce composites with controlled chemical composition. Figure 11 presents the IR spectra of as-formed powders compared with the spectrum of the pure TEOS sample. In TiTEOS, the absorption at 950 cm^{-1} is attributed to Si–O–Ti modes of vibration. No feature that could be attributed to a pure TiO_2 phase can be observed. In the AlTEOS sample, there is no specific feature that could be related to the presence of Al. In both cases, pure amorphous silica is identified.[22,23] It seems that the incorporation

Table 4. Characterizations of Si/C/O powders after annealing under argon and nitrogen

	Ar, 1300°C, 1 h				*Ar, 1500°C, 1 h*				*N_2, 1500°C, 1 h*				
	C *(wt%)*	O *(wt%)*	Δm *(%)*	S_{BET} *($m^2\ g^{-1}$)*	C *(wt%)*	O *(wt%)*	Δm *(%)*	S_{BET} *($m^2\ g^{-1}$)*	C *(wt%)*	O *(wt%)*	N *(wt%)*	Δm *(%)*	S_{BET} *($m^2\ g^{-1}$)*
TEOS	16·0	39·7	n.m.	85	2·5	53·6	−22·9	0·1	2·4	49·3	0·9	−19·5	0·2
MTOS	26·5	34·7	−24·1	242	26·6	8·6	−74·1	88	10·3	n.m.	24·1	−62·0	101
EOMS	25·5	32·7	−30·0	173	28·8	n.m.	−75·0	20	11·7	n.m.	23·5	−60·4	70
ETMS	26·9	21·5	−24·8	102	29·3	4·8	−49·3	25·5	20·1	6·7	13·4	−38·2	86
MDSO	28·8	15·5	−38·0	70	27·5	5·3	−33·7	36·5	20·4	5·9	11·0	−2·4	58

n.m.: not measured

Table 5. Chemical composition (in wt%) of Si/C/O powders after annealing under argon and nitrogen

	Ar, 1300°C, 1 h			*Ar, 1500°C, 1 h*			*N_2, 1500°C, 1 h*			
	SiO_2	*SiC*	*C*	*SiO_2*	*SiC*	*C*	*SiO_2*	*Si_3N_4*	*SiC*	*C*
TEOS	74·4	13·7	11·9	97·5	0	2·5	92·6	2·3	3·9	1·2
MTOS	65·2	11·9	22·9	16·2	69·4	5·8	n.c.	60·5	n.c.	n.c.
EOMS	61·5	18·7	19·9	n.c.	n.c.	n.c.	n.c.	58·9	n.c.	n.c.
ETMS	40·3	46·8	12·9	9·0	88·1	2·9	12·6	33·6	47·7	6·1
MDSO	29·1	59·0	11·1	10·0	89·1	0·8	11·1	27·4	58·7	2·8

n.c.: not calculated

of a second phase is related to a decrease of the specific surface: 133, 84 and 70 $m^2 g^{-1}$ for TEOS, AlTEOS and TiTEOS samples, respectively.

3.2.2 Annealed powders (under air)

3.2.2.1 Titania-silica composite. After heat treatment at 600°C the weight loss of the TiTEOS sample is 25%, which corresponds to the C content in the as-formed powder (Table 2). As in the case of TEOS, the weight loss is attributed to the oxidation of free C [reaction (1)]. The Si/Ti ratio is not modified by oxidation up to 1300°C. Figure 12 presents the XRD patterns of TiTEOS samples as a function of heat treatment. It shows that crystallization begins between 600 and 900°C. At 900°C, two different TiO_2 phases [anatase (JCPDS no. 21-1272) and rutile (JCPDS no. 21-1276)] are present simultaneously. At 1200°C, the dominant features are attributed to rutile. A beginning of silica crystallization into the cristobalite phase is observed, also seen on IR spectra (Fig. 13). At this temperature, pure silica obtained from TEOS is still amorphous. At 1400°C anatase has disappeared, cristobalite and rutile appear well crystallized.

In the IR spectra of TiTEOS (Fig. 13) only the peak at 950 cm^{-1}, already attributed to Si–O–Ti, is added to the pure silica spectra and there is no modification of this band with temperature. No band of pure TiO_2 can be observed.

The specific surface area evolution is similar to the specific surface area evolution of the TEOS sample, with a maximum value of 137 $m^2 g^{-1}$.

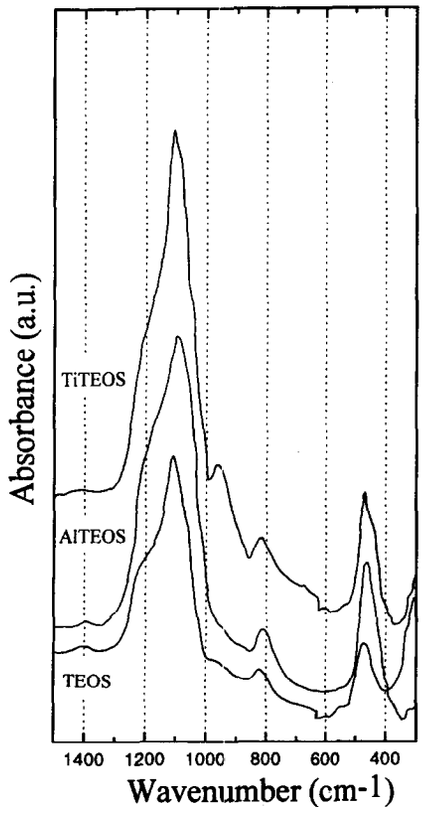

Fig. 11. IR spectra of as-formed Al and Ti (composite) powders.

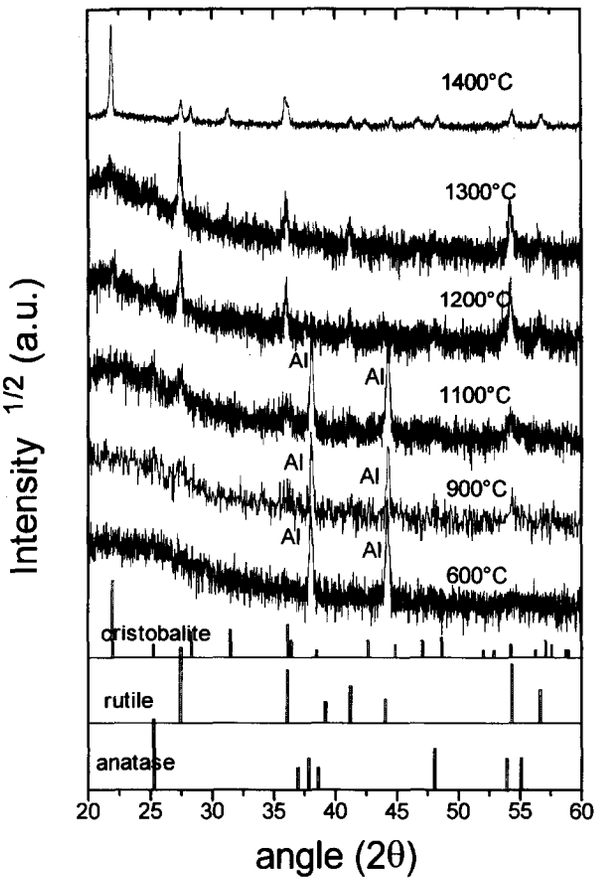

Fig. 12. Evolution of XRD patterns of TiTEOS sample as a function of oxidation temperature.

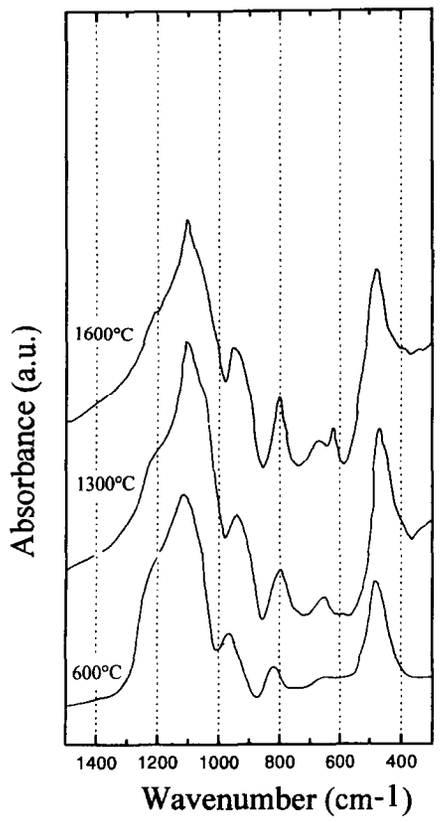

Fig. 13. Evolution of IR spectra of TiTEOS sample as a function of oxidation temperature.

3.2.2.2 Alumina–silica composite. After heat treatment at 600°C the weight loss of the AlTEOS sample is 17%, comparable with the C content in the as-formed powder (Table 2). As in the former case, weight loss is explained by reaction (1). Figure 14 presents the evolution of IR spectra as a function of annealing temperature. It is not possible to identify any line of pure alumina Al_2O_3 in these spectra. Only a line at 880 cm^{-1} is different from the silica spectra, it becomes a clear structure in the spectra at 1600°C and is usually attributed to Si–O–Al bonds.[35] XRD patterns presented in Fig. 15 show that the crystallization begins at 1200°C and cristobalite is identified, in good agreement with IR spectra. Another crystallized phase containing Al is present; it is not clear whether it is sillimanite or mullite, both of them being mixed phases composed of SiO_2 and Al_2O_3.[36]

4 Conclusion

In this paper we have shown that it is possible to produce amorphous, nano-sized, silicon-based oxide powders by laser–aerosol interaction. Silica powders with high specific surface area have been obtained. The incorporation of metallic elements (Al,Ti) in the powder is quite easy. In a first step, the evolution of the structure of the as-formed amorphous powders has been studied as a function of heat treatments using conventional characterization methods. The results concern long-range order and mainly the bulk.

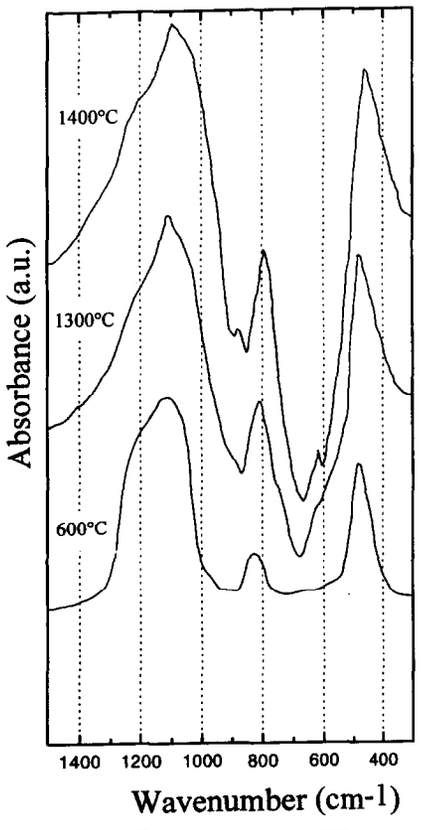

Fig. 14. Evolution of IR spectra of AlTEOS sample as a function of oxidation temperature.

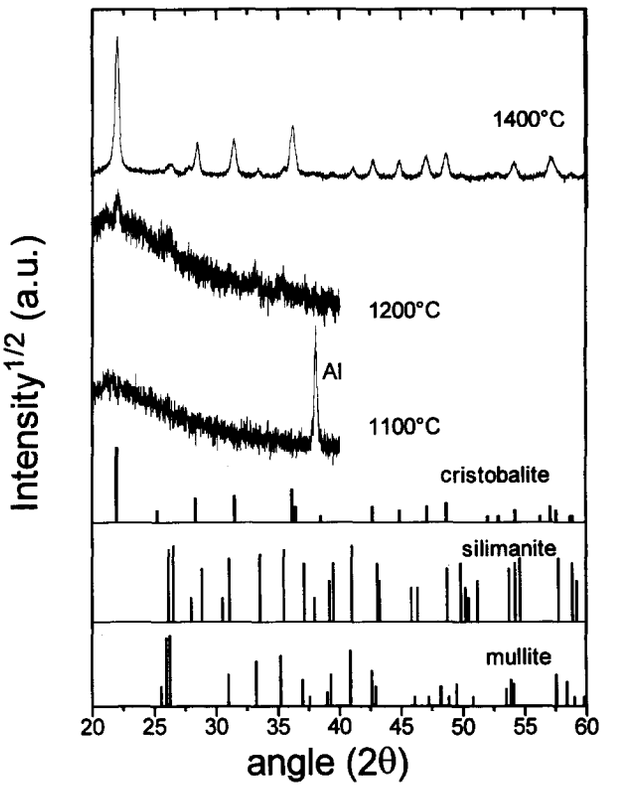

Fig. 15. Evolution of XRD patterns of AlTEOS sample as a function of oxidation temperature.

In the future, it seems important to characterize the microstructure and the short-range order to correlate these with the properties of the material (sintering behaviour). In particular, it would be interesting to clarify the C bonding and the role of free carbon in the evolution of specific surface area and reactivity.

New experiments are in progress to synthesize silica containing different amounts of C, Al, Ti or other metallic elements by adjusting the process parameters. The possibility of synthesizing a mixture of different phases with controlled chemical composition and good dispersion seems very promising, in particular for the production of heterogeneous catalysts. Work is in progress to compare the properties of such powders with properties of powders obtained by other methods.

Acknowledgements

The authors are very grateful to Mrs C. Robert and Mr H. Lathus from CEA-CEREM for performing the thermogravimetric analyses and high-temperature oxidation experiments, respectively.

References

1. Cannon, W. R., Danforth, S. C., Flint, J. H., Haggerty, J. S. & Marra, R. A., Sinterable ceramic powders from laser driven reactions. I. Process description and modeling. *J. Am. Ceram. Soc.*, **65**[7] (1982) 324–329.
2. Cauchetier, M., Croix, O., Herlin, N. & Luce, M., Nanocomposite Si/C/N powder production by laser–aerosol interaction. *J. Am. Ceram. Soc.*, **7**[4] (1994) 993–998.

3. Herlin, N., Musset, E., Luce. M. & Cauchetier, M., Synthesis of nanocomposite Si/C/N powders by laser spray pyrolysis of hexamethyldisilazane. *J. Eur. Ceram. Soc.*, **13**[2] (1994) 285–291.
4. Musset, E., Herlin, N., Cauchetier, M. & Luce, M., Nanometric Si/C/N composite powders elaboration by laser–aerosol interaction. *J. Aerosol Sci.*, **25**[7] (1994) 1364.
5. Whitehouse, D., Tullio, K. & Thomson, A., Industrial, kilowatt-class, tunable CO_2 laser. In *Laser Materials Processing*, Proceedings of ICALEO (Orlando, FL, 25–29 Oct. 1992). Laser Institute of America, Vol. 75, pp. 42–52.
6. Casey, J. D. & Haggerty, J. S., Laser-induced vapour phase synthesis of titanium dioxide. *J. Mater. Sci.*, **22**[12] (1987) 4307–4312.
7. Curcio, F., Musci, M., Notaro, M. & Quattroni, G., Laser induced synthesis of ultrafine TiO_2 powders. In *Ceramics Today — Tomorrow's Ceramics*, ed. P. Vincenzini. Materials Science Monographs 66D, Elsevier, Amsterdam, The Netherlands, 1991, pp. 2569–2578.
8. Borsella, E., Botti, S., Giorgi, R., Martelli, S., Turtu, S. & Zappa, G., Laser-driven synthesis of nanocrystalline alumina from gas phase precursors. *Appl. Phys. Lett.*, **63**[10] (1993) 1345–1347.
9. Luce, M., Herlin, N., Musset, E. & Cauchetier, M., Laser synthesis of nanometric silica powders. *NanoStruct. Mater.*, **4**[4] (1994) 403–408.
10. Li, Y., Liang, Y., Zheng, F. & Hu, Z., Carbon dioxide laser synthesis of ultrafine silicon carbide powders from diethoxydimethylsilane. *J. Am. Ceram. Soc.*, **77**[6] (1994) 1662–1664.
11. Soraru, G., Silicon oxycarbide from gels. *J. Sol–Gel Sci. Technol.*, **2** (1994) 843–848.
12. Babonneau, F., Thorne, K. & Mackenzie, J. D., Dimethyldiethoxysilane–tetraethoxysilane copolymers: precursors for the Si–C–O system. *Chem. Mater.*, **1**[5] (1989) 554–558.
13. Bois, L., Maquet, J., Babonneau, F., Mutin, H. & Bahloul, D., Structural characterization of sol–gel derived oxycarbide glasses. 1. Study of the pyrolysis process. *Chem. Mater.*, **6**[6] (1994) 796–802.
14. Babonneau, F., Hybrid siloxane–oxide materials via sol–gel processing: structural characterization. *Polyhedron*, **13**[8] (1994) 1123–1130.
15. Kamiya, K., Yoko, T., Sano, T. & Tanaka K., Distribution of carbon particles in carbon/SiO_2 glass composites made from $CH_3Si(OC_2H_5)_3$ by the sol–gel method. *J. Non-Cryst. Solids*, **119**[1] (1992) 14–20.
16. Hatakeyama, F. & Kanzaki, S., Synthesis of monodispersed spherical β-silicon carbide powder by a sol–gel process. *J. Am. Ceram. Soc.*, **73**[7] (1990) 2107–2110.
17. Langlet, M. & Joubert, J. C., The pyrosol process or the pyrolysis of an ultrasonically generated aerosol. In *Chemistry of Advanced Materials*, ed. C. N. R. Rao. Blackwell Scientific Publications, 1992, pp. 55–79.
18. Jasper, J., *J. Phys. Chem. Ref. Data*, **1**[4] (1972) 938.
19. Mills, A. & MacKenzie, C., The application of bond parachors to organosilicon chemistry. *J. Am. Soc.*, **76** (1954) 2672–2673.
20. Bretsznajder, S., Prediction of transport and other physical properties of fluids. *Int. Series of Monographs in Chemical Engineering Vol. 11*, ed. P. Danckwerts. Pergamon Press, 1971.
21. Croix, O., Gounot, M., Bergez, P., Luce, M. & Cauchetier, M., Sintering of laser formed silicon carbide powders. In *Ceramics Today—Tomorrow's Ceramics*, ed. P. Vincenzini. Materials Science Monographs 66B, Elsevier, Amsterdam, The Netherlands, 1991, pp. 1447–1455.
22. Moenke, H. H. W., in *The Infrared Spectra of Minerals*. Mineralogical Society, London, 1974, p. 42.
23. Ocana, M., Fornes, V. & Serna, C. J., The variability of the infrared powder spectrum of amorphous SiO_2. *J. Non-Cryst. Solids*, **107**[2–3] (1989) 1892.
24. Bertoluzza, A., Fagnano, C., Morelli, M. A., Gottardi, V. & Gugliemi, M., Raman and infrared spectra on silica gel evolving towards glass. *J. Non-Cryst. Solids*, **48**[1] (1982) 117–128.
25. Cauchetier, M., Croix, O. & Luce, M., Laser synthesis of silicon carbide powders from silane and hydrocarbon mixtures. *Adv. Ceram. Mater.*, **3**[6] (1988) 548–552.
26. Scott, J. F. & Porto, S. P. S., Longitudinal and transverse optical lattice vibrations in quartz. *Phys. Rev. A.*, **161**[3] (1967) 903–910.
27. Sazaki, Y., Nishita, Y., Sato, M. & Okamura, K., Optical phonon states of SiC small particles studied by Raman scattering and infrared absorption. *Phys. Rev. B: Condens. Mater.*, **40**[3] (1989) 1762–1772.
28. Boulanger, L., Herlin, N., Luce, M., Cauchetier, M., Tougne, P., Hommel, H. & Legrand, A. P., Evolution of the structure of nanometric SiC laser-formed powders. In *Third Euro-Ceramics, Vol. 1*, Proceedings of the European Ceramic Society Third Conference (Madrid, Spain, 12–17 Sept. 1993), eds P. Duran and J. F. Fernandez. Faenza Editrice Iberica S.L., Madrid, Spain, 1993, pp. 21–26.
29. Mitomo, M. & Yoshioka, Y., Preparation of Si_3N_4 and AlN powders from alkoxide-derived oxides by carbothermal reduction and nitridation. *Adv. Ceram. Mater.*, **2**[3A] (1987) 253–256.
30. Tanaka, O. & Kurachi, Y., Synthesis of β-SiC powder from organic precursors and its sinterability. *Ceram. Int.*, **14**[2] (1988) 109–115.
31. White, D. A., Oleff, S. M. & Fox, J. R., Preparation of silicon carbide from organosilicon gels: II, Gel pyrolysis and SiC characterization. *Adv. Ceram. Mater.*, **2**[1] (1987) 53–59.
32. Kusabiraki, K., Infrared spectra of vitreous silica and sodium silicates containing titanium. *J. Non-Cryst. Solids*, **79**[1–2] (1986) 208–212.
33. Aizawa, M., Nosaka, Y. & Fujii, N., Preparation of TiO_2–SiO_2 glass via sol–gel process containing a large amount of chlorine. *J. Non-Cryst. Solids*, **168**[1–2] (1994) 49–55.
34. Miranda Salvado, I. M. & Fernandez Navarro, J. M., TiO_2–SiO_2 glasses prepared by the alkoxide route. *J. Non-Cryst. Solids*, **147 & 148** (1992) 256–261.
35. Miranda Salvado, I. M. & Fernandez Navarro, J. M., Al_2O_3–SiO_2 glassy materials prepared by the alkoxide route. pp. 1115–1120 in Vol. 2 of Ref. 28.
36. Komarneni, S., Roy, R., Selvaraj, U., Malla, P. B. & Breual, E., Nanocomposite aerogels: the SiO_2–Al_2O_3 system. *J. Mater. Res.*, **8**[12] (1993) 2343–2358.

Journal of the European Ceramic Society **16** (1996) 1075–1081

PII: S0955-2219(96)00023-4
0955-2219/96/$15.00

Reaction and Sintering Mechanisms of Mullite in the Systems Cristobalite/α-Al_2O_3 and Amorphous SiO_2/α-Al_2O_3

B. Saruhan, W. Albers, H. Schneider & W. A. Kaysser

German Aerospace Research Establishment (DLR-Cologne),
Institute for Materials Research, D-51140 Köln, Germany

(Received 3 November 1995; revised version received 3 January 1996; accepted 8 January 1996)

Abstract

Powder mixtures of SiO_2 glass and cristobalite with fine α-Al_2O_3 were heat-treated at different temperatures up to 1700°C. Green samples consisting of SiO_2 glass plus α-Al_2O_3 (RSS) generally were sintered to higher densities than those consisting of cristobalite plus α-Al_2O_3 (RSC). In both powder compacts (RSS and RSC) two different sintering mechanisms were active before and after the onset of mullitization, respectively. Before mullite formation begins, densification occurs in the RSS sample through viscous flow sintering and in the RSC sample by solid-state sintering. After the formation of mullite crystals, transient liquid-phase sintering is assumed for both samples (RSS and RSC). The amount of SiO_2-rich liquid phase, which controls degree and rate of the second-stage sintering mechanism, depends on the amount of residual SiO_2 left unreacted after initial mullitization.

The temperature-dependent mullite formation process was complex. At 1700°C sample RSS formed ≈ 80% mullite, while the degree of mullitization of sample RSC at the same temperature was ≈ 90%. However, this tendency did not hold at higher temperatures, since both samples displayed near-total mullitization at 1750°C. Four different temperature-dependent steps of mullite formation could be distinguished: a temperature field where mullite nucleation was observed (<1500°C), a temperature range of high mullitization degree (1500–1550°C), followed by a low mullitization region (1550–1625°C). At higher temperatures (>1625°C) high mullitization rates were observed again. © 1996 Elsevier Science Limited.

Introduction

Reaction sintering of Al_2O_3 and SiO_2 powders is a low-cost processing route to achieve mullite ceramics with high quality.[1,2] The temperature and rates of mullite formation depend on different factors, the most important of which are the species used and their chemical purity and particle size distribution.[3–6] Most investigations on the reaction sintering of mullite were carried out by using diaspore (AlOOH), gibbsite ($Al(OH)_3$) or corundum (α-Al_2O_3) as Al-sources and silica glass powder, quartz or cristobalite as the Si-sources.[1–12] Mullitization mechanisms in mixtures of various polymorphs of Al_2O_3 and SiO_2 are greatly influenced by the properties of the reactants and less by the bulk chemical composition.[8] Therefore the processing parameters during reaction sintering have to be exactly tailored to produce complete mullitization and high densification of the mullite ceramics. It has been shown that, by using submicrometre-sized powders with high surface energies and choosing fast heating rates during sintering, almost the theoretical densities and very high mullite contents can be obtained at relatively low temperatures (>1600°C).[5–7]

Due to the wide variety of reaction parameters reported in previous studies, it is difficult to determine the sintering and mullitization mechanisms. The aim of this study was to clarify matters by a systematic investigation of the role of two SiO_2 reactants (amorphous glass and crystalline cristobalite) in mullitization and densification as well as the interactions between densification and mullitization during sintering, while the same α-Al_2O_3 powder was used in each case. Together with earlier studies on quartz/α-Al_2O_3,[9] it may develop a new understanding of the role of the SiO_2 source on the mullitization process.

Materials and Methods

Materials

The α-Al_2O_3 powder AKP-50 (corundum), provided by Sumitomo (Tokyo, Japan), is a highly

pure (>99·995 wt% Al_2O_3) and submicrometre-sized alumina powder was derived from aluminium alkoxide.

The SiO_2 glass powder, provided by Heraeus Quarzglas (Hanau, Germany), was achieved by melting quartz. The as-received powder has coarse particle sizes ranging from 63 to 125 μm and contains 99·9 wt% SiO_2 and a very low amount of Na_2O (119 ppm), K_2O (80 ppm) and CaO (80 ppm). In order to increase the sintering activity, the SiO_2 glass powder was previously ball-milled to a particle size of 2 to 3 μm. The particles after milling were irregularly shaped and had a smooth surface.

The cristobalite powder was achieved by heat-treating a quartz powder (Vp 795-10/1, Quarzwerke Frechen, Germany) at 1550°C for 10 h. The starting quartz powder has submicrometre size and consists of 98·5 wt% SiO_2, 1 wt% Al_2O_3, and 0·05 wt% Fe_2O_3, 0·1 wt% Na_2O + K_2O and 0·1 wt% CaO + MgO. After conversion of quartz to cristobalite, the concentrations of the impurities did not change. The cristobalite powder consists of spherical particles with smooth surfaces and particle sizes between 1 and 10 μm.

Powder processing and sintering

The starting oxide powders were mixed in the stoichiometric composition of 3/2 mullite (71·8 wt% α-Al_2O_3 and 28·2 wt% SiO_2). The mixed powders and 5 wt% of a combination of binders as pressing aids were dispersed in isopropanol and homogenized by ball-milling for 5 h in a polymer container with Si_3N_4 milling balls. After evaporation of isopropanol, the mixtures were dried, sieved in a sieving machine (500 μm) and finally granulated by a tumble-mixer. Granulation of the mixtures allowed homogeneous and reproducible filling of the die, thus minimizing density gradients in the uniaxially pressed bar samples which had dimensions of 5 × 6 × 55 mm. After uniaxially die-pressing, the waxes were carefully burned out at 600°C with a very slow heating rate. The samples were then pressureless sintered in air at temperatures ranging between 1100 and 1700°C.

Dilatometer measurements

Bar-shaped samples measuring 3·5 × 3·5 × 10 mm were heated up to 1700°C in air in a differential dilatometer (Bähr-Thermoanalyse GmbH, Hüllhorst, Germany). A constant heating rate of 400 K h^{-1} was applied. Dense α-Al_2O_3 was used as the reference material. The resulting data of length changes were differentiated using a computer program.

Microstructure and observation of the phase composition

Microstructural observations of fracture surfaces were carried out with a scanning electron microscope (Philips SEM 525 M). For further investigation, a transmission electron microscope (Philips EM 430) with an LaB_6 filament and an acceleration voltage of 300 kV was used. X-ray diffractometer studies were carried out with a computer-controlled powder diffractometer (Siemens D5000) using Ni-filtered Cu K_α radiation. Diffraction patterns were recorded in the 2θ range 10° to 80°, in step scan mode (3 s/0·02°, 2θ). Determination of the phase content was based on the comparison of X-ray diffraction intensities of samples with those of reference materials.

Results

Sintering behaviour

Dilatometer studies carried out on green samples display, for both Al_2O_3 plus SiO_2 combinations, similar sintering behaviours which can be divided into four stages, although the temperature limits of these stages and rates of densification are different for both samples [Fig. 1(a)].

During the first stage (up to 1100°C for RSS and 1200°C for RSC) no significant progress of the densification is observed, only a reversible low expansion effect at 270°C detected with the α-Al_2O_3 + cristobalite (RSC) sample by differenti-

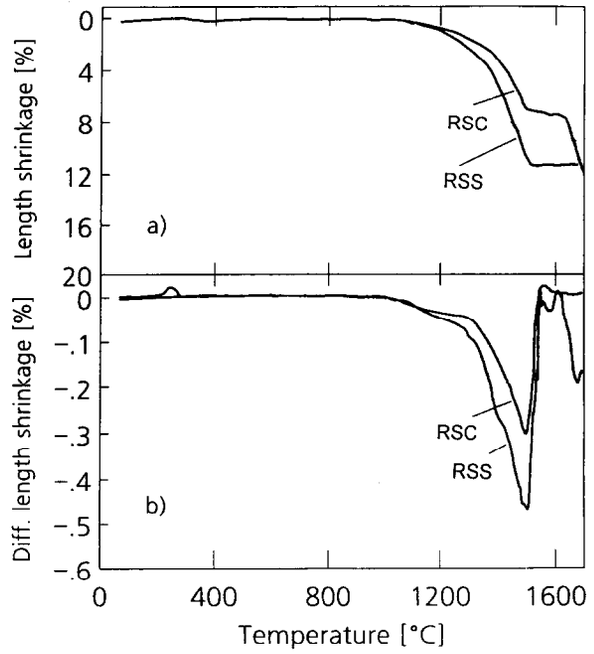

Fig. 1. Sintering behaviour of RSS and RSC samples during reaction sintering between room temperature and 1700°C, heated with a rate of 400 K h^{-1}, and illustrated as (a) length shrinkage (dl) and (b) differentiated length shrinkage (dl/dt) vs. temperature.

ating the shrinkage curves. This behaviour is related to the displacive low–high phase transition of cristobalite [Fig. 1(b)].

The second stage of densification starts with a relatively low rate above about 1200°C for the RSC sample and above about 1100°C for the RSS (α-Al_2O_3 plus SiO_2 glass) sample, and extends to the temperature at which mullitization starts (1500 and 1485°C, respectively). The rate and extent of densification depend on the SiO_2 reactant. Above 1200°C, the RSS and RSC samples densify with a higher rate. The extent of length shrinkage at the end of the second stage is 11·8% for RSS and 7·5% for RSC.

Due to the mullite formation, the third stage of the densification process starts at the temperature at which the densification decreases for both samples (RSS and RSC). For the RSS sample, this stage extends until the maximum temperature (1700°C, after 4 h) is reached.

For the RSC sample, after the third stage, a fourth stage above 1600°C has been observed. During this last stage, sample RSC exhibits a further length shrinkage of 4·7%. Counting the small amount of shrinkage which occurs during mullitization (0·6%), the total length shrinkage in the RSC sample amounts to 12·8% at about 1700°C. Sample RSS shows no length change during this stage.

Development of phase compositions

Before the beginning of the mullitization process by the reaction of Al_2O_3 and SiO_2, the amorphous SiO_2 particles of sample RSS transform partly to cristobalite. According to the literature data provided by Nurishi and Pask[3] on samples sintered using amorphous SiO_2 and α-Al_2O_3, amorphous SiO_2 transforms to cristobalite and the successive reaction of cristobalite with corundum results in the formation of a metastable eutectic liquid phase. In this study, it was also observed that amorphous SiO_2 transforms to cristobalite prior to mullitization. In the RSS sample, cristobalite appears in the temperature range extending from 1450 to 1650°C. Above about 1550°C, an amorphous SiO_2-rich liquid phase forms which is in agreement with the observations of Nurishi and Pask[3] (Fig. 2). Mullite formation in RSS sample occurs above about 1500°C and continues rapidly up to 1550°C. Between 1550 and 1600°C, the rate of mullitization slows down but takes up again above 1600°C with a relatively fast rate (Fig. 3). In agreement with previous observations,[7] it is determined that during reaction sintering of various Al_2O_3 and SiO_2 sources, mullitization is correlated to the presence of cristobalite.

Sample RSC begins to mullitize above about 1525°C. This temperature is somewhat higher than that of sample RSS, which starts at about 1500°C. Formation of amorphous SiO_2-rich liquid phase occurs in sample RSC above about 1500°C, being 50°C lower than that in sample RSS; the amount of this glass phase is significantly higher in sample RSC (Fig. 2).

Figure 3 shows that for both samples (RSS and RSC) mullite formation is a multiple-step process, extending over four temperature regions: nucleation (region I), a temperature range of high mullitization rates (region II), a temperature field of low mullitization rates (region III) and, finally, at high temperatures another high mullitization field (region IV).

Development of microstructure

By interrupting the heat treatment at definite temperatures in the range between 1000 and 1700°C and cooling the samples to room temperature, the development of grain morphology and the porosity have been observed for each sample by means of scanning electron microscopy (SEM). The first microstructural investigation was carried out on samples heat-treated at the temperature at which

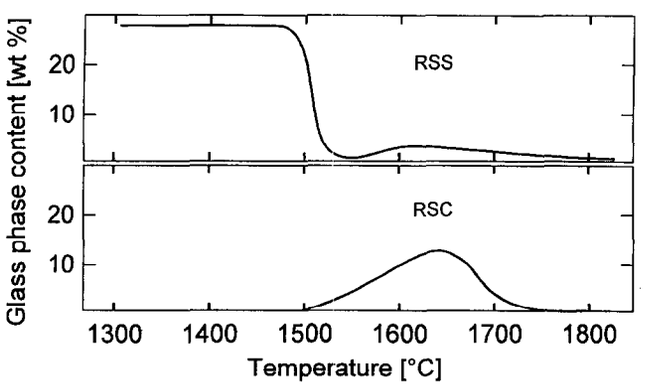

Fig. 2. Glass-phase formation in RSS and RSC samples during reaction sintering between room temperature and 1800°C with a constant heating rate of 400 K h^{-1}.

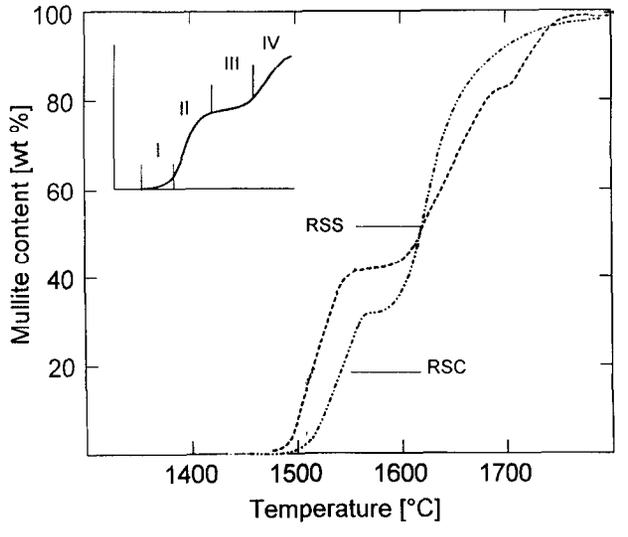

Fig. 3. Mullite formation in RSS and RSC samples during reaction sintering between room temperature and 1800°C with a constant heating rate of 400 K h^{-1}.

the initial shrinkage occurs (approximately 1200°C). The second check referred to the temperature of first appearance of mullite (approx. 1500°C). Finally, a third group of samples heat-treated at the temperature beyond the cristobalite stability field (>1600°C) were investigated microstructurally.

The RSS sample shows a particle rearrangement process during heating >1100°C [Fig. 4(a)]. Owing to the production route of the cristobalite powder, sample RSC contains a coexisting relatively alkali-rich glass phase which was formed during the transformation of mother quartz to cristobalite [Fig. 5(a)]. This coexisting glass phase is transient and disappears above about 1200°C [Fig. 5(b)].

Above the mullite formation at about 1500°C, both samples (RSC and RSS) generally show formation of contact points and strong adhesion of Al_2O_3 particles to the surfaces of SiO_2 particles. In the RSS sample, adhesion of the Al_2O_3 particles is so strong that the surfaces of the SiO_2 particles become round [Fig. 4(b)]. In the RSC sample, the Al_2O_3 particles attach themselves onto the cristobalite particle surfaces by neck formation [Fig.

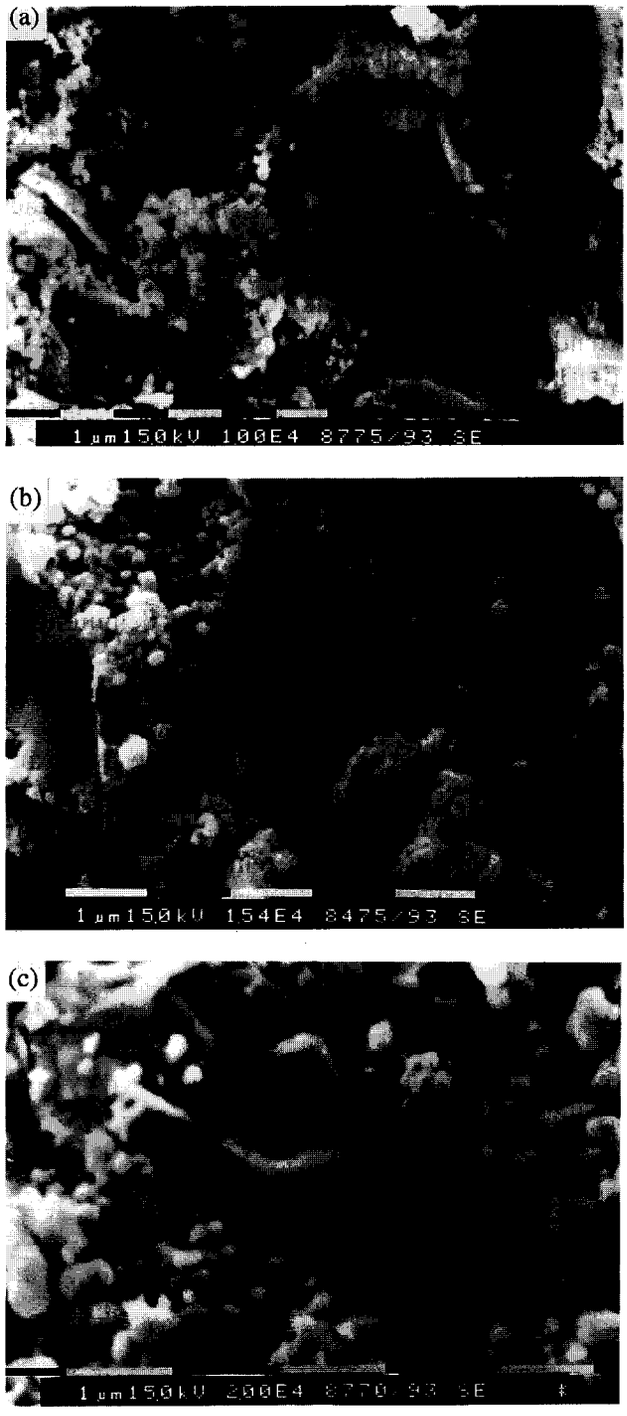

Fig. 4. SEM micrographs of RSS sample showing morphology changes during reaction sintering. Samples were heated to 1200°C (a), 1450°C (b) and 1600°C (c) with a rate of 400 K h^{-1}. No holding time was allowed at the temperature.

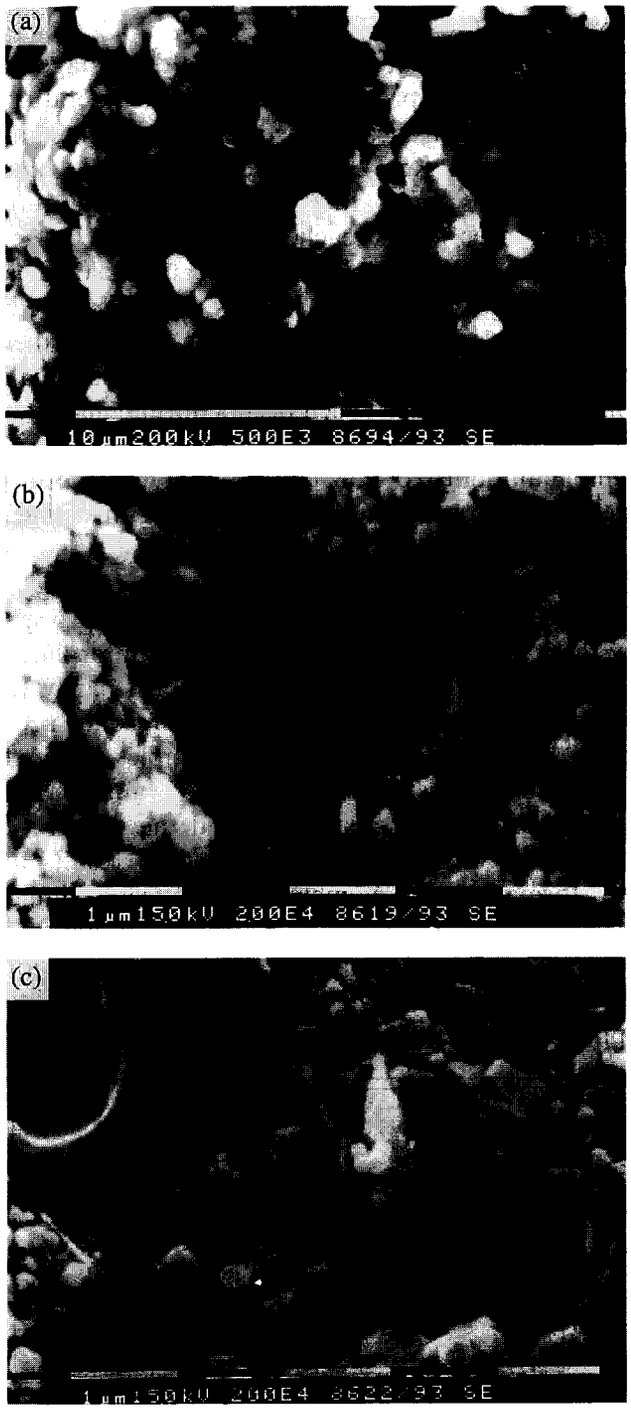

Fig. 5. SEM micrographs of RSC sample showing morphology changes during reaction sintering. Samples were heated to 1150°C (a), 1550°C (b) and 1625°C (c) with a rate of 400 K h^{-1}. No holding time was allowed at the temperature.

5(b)]. Therefore, the degree of shrinkage in sample RSC (7·5%) is not as high as in sample RSS (11·8%).

At temperatures higher than 1600°C cristobalite either melts or evaporates due to local reducing atmospheres, and, as a consequence, pores develop. These pores are surrounded by relatively coarse but well developed mullite grains and occur in previous contact areas of the Al_2O_3 and SiO_2 particles [Figs 4(c) and 5(c)].

Discussion

A schematic illustration of the microstructural development of reaction-sintered silica glass/α-Al_2O_3 phase assemblage (RSS) is given in Fig. 6. Impurity-free silica glass does not form a viscous liquid phase at temperatures lower than 1400°C but shows viscous softening only. Due to the superficial softening of the SiO_2 glass particles (>99·9 wt% SiO_2), the fine Al_2O_3 particles penetrate into the viscous particle surfaces, leading to a high degree of shrinkage. Especially above 1250°C, the densification rate becomes very high. We believe that sintering takes place by a semi-viscous flow mechanism of the solid Al_2O_3 particles in viscous SiO_2 (Fig. 6). At higher sintering temperatures up to 1450°C, the viscosity of the silica glass decreases, though the original grain shapes are preserved. Then, Al^{3+} ions may diffuse further within the SiO_2 particles until the stochiometrical mullite composition is achieved, although no mullite formation was observed [(Fig. 7(a)]. Above 1450°C, the SiO_2 glass starts to transform to crystalline cristobalite [Fig. 7(b)] and above 1500°C, mullite formation occurs by reaction of cristobalite and corundum (region I, Fig. 3). Due to the short diffusion distances achieved by viscous-flow-assisted sintering, the rate of mullitization is high [Figs 3 and 7(a)]. The newly formed mullite grains grow, successively replacing the SiO_2 particles (region II, Fig. 2). According to microstructural observations [Figs 4(c) and 7(c)] a ring-like formation of mullite grains develops around the former SiO_2 glass particles. Such mullite layers act as barriers for diffusing species and thus reduce the rate of mullitization (region III). Further increase in the sintering temperature above 1650°C causes melting of cristobalite and consequently promotion of mullitization (region IV, Fig. 2).

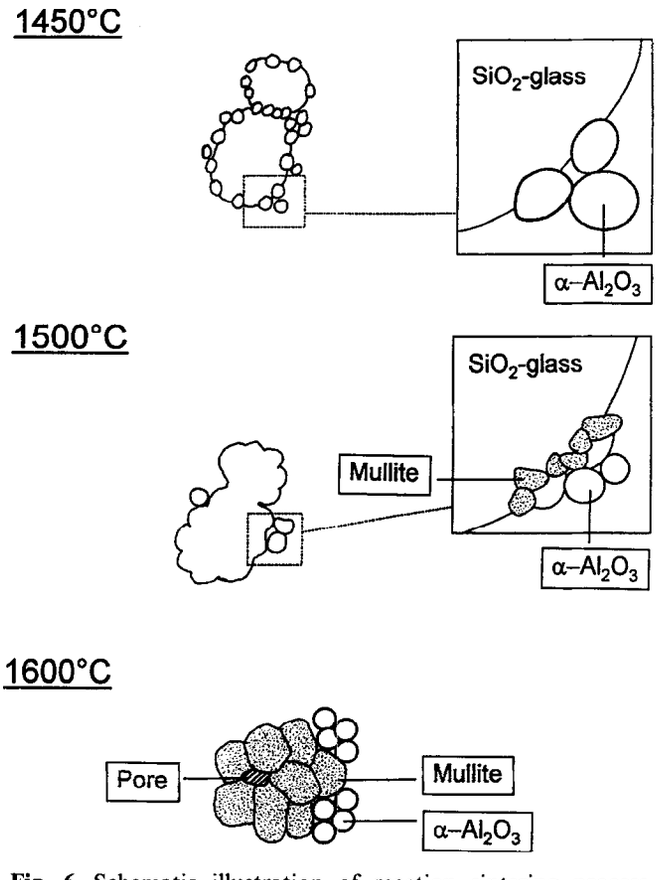

Fig. 6. Schematic illustration of reaction sintering process in RSS (amorphous SiO_2 + α-Al_2O_3) sample demonstrating sintering and mullitization mechanisms.

A schematic illustration of the microstructural development of reaction-sintered cristobalite/α-Al_2O_3 phase assemblage (RSC) is given in Fig. 8. The microstructural investigation carried out on the reaction couple cristobalite/α-Al_2O_3 (RSC) heat-treated at 1150°C indicates the formation of a metastable eutectic liquid phase [Fig. 5(a)]. This is in agreement with the observation of Rana *et al.*[4] and Risbud and Pask.[12] The occurrence of a metastable liquid phase, in our case, is attributed to the presence of some small amount of alkali and iron impurities, introduced into the system by the cristobalite raw material (see Materials section). Densification is promoted by the rearrangement of cristobalite and corundum particles at temperatures lower than 1300°C in the presence of coexisting viscous glass phase. The liquid phase is transient and disappears above 1300°C. As is shown in SEM micrographs [Fig. 5(b)], the particles of cristobalite and corundum form contact points allowing species transport and giving rise to the formation of neck areas, which is typical of a solid-state sintering.[13] The slow mullitization rate may be attributed to the low diffusion rates and to the large diffusion distances which have to be considered from the bulk to the neck areas. Formation of mullite at the neck areas leads to the build-up of a stiff skeleton which cannot shrink further. This may explain the formation of a porous structure which is associated with a low degree of densification for RSC. The increase of the surface area of cristobalite particles by a prolonged milling time does not increase the sinterability of the RSC sample but results in an increase in mullitization. This behaviour may be

attributed to the fact that the increase of particle contact areas promotes neck formation and mullitization but reduces the densification.

As the mullite grains around the former large cristobalite particles grow, diffusion barriers form between the reaction partners and therefore further reaction to mullite is hindered [Figs 5(c) and 8]. As a result, large residual SiO_2 regions are observed which are normally surrounded by layers of mullite. Above about 1620°C, cristobalite is converted to SiO_2-rich liquid which enhances densification by liquid-phase-assisted sintering but does not close all pores. This secondary densification, after mullitization, has been observed in cristobalite/α-Al_2O_3 (RSC) system but not in silica glass/α-Al_2O_3 (RSS) system (Fig. 1).

Conclusion

Silica glass/α-Al_2O_3 (RSS) and cristobalite/α-Al_2O_3 (RSC) samples display two different sintering mechanisms at low temperatures (<1500°C). RSS sample densifies through semi-viscous-flow sintering, whereas RSC sample is characterized by a solid-state sintering. Solid-state sintering in RSC

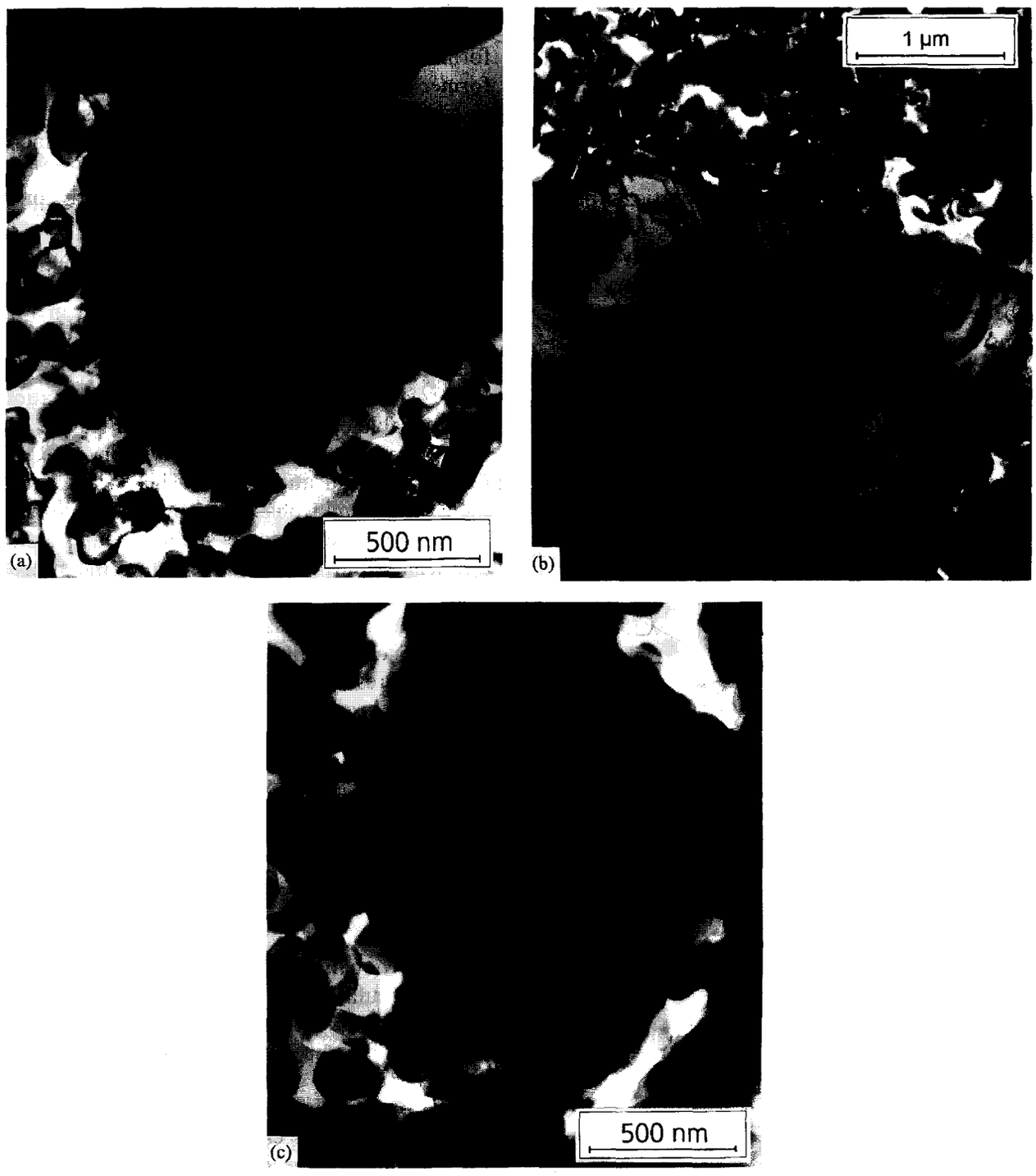

Fig. 7. TEM micrographs of reaction-sintered RSS sample at 1450°C (a), at 1625°C (b) and RSC sample at 1450°C (c). Samples were heated up with a rate of 400 K h^{-1} to the given temperature and no holding time was allowed.

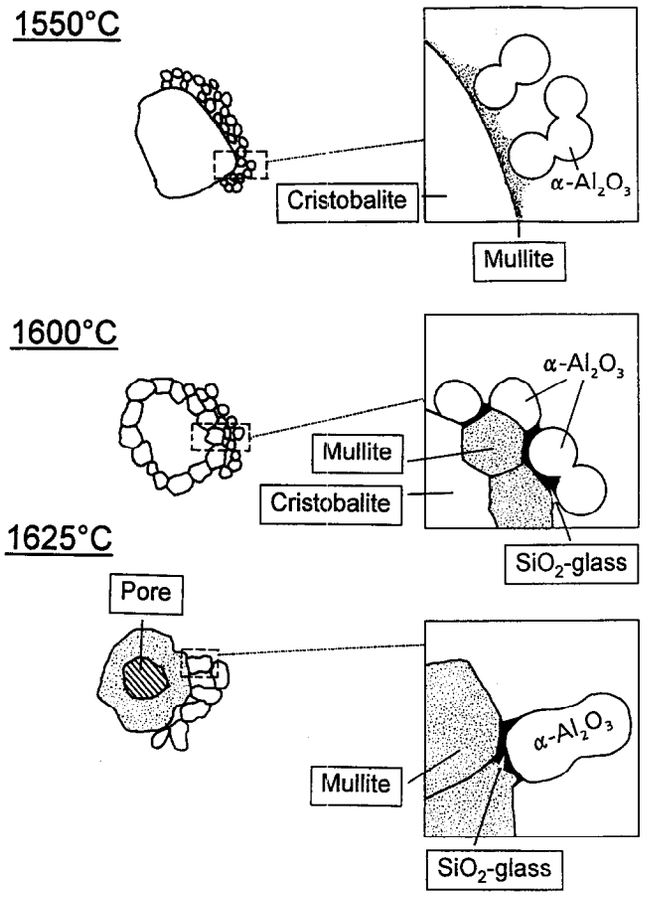

Fig. 8. Schematic illustration of reaction sintering process in RSC sample (cristobalite + α-Al_2O_3) demonstrating sintering and mullitization mechanisms.

samples causes a slower nucleation rate and a longer incubation period for mullite formation than does the viscous-flow sintering mechanism of RSS sample. This also can explain the higher mullitization temperatures in RSC sample than in RSS. At temperatures higher than 1600°C, further densification and mullitization are supported by a transient liquid-phase sintering in both RSS and RSC samples. Since a larger amount of unreacted SiO_2 remains in RSC sample during the solid-state sintering, due to the slower densification and mullitization rates at temperatures lower than 1500°C, formation of SiO_2 liquid phase at temperatures above 1600°C results in a higher mullitization rate and in an acceleration of densification compared with sample RSS [Fig. 1(a)]. The two-stage process leads to a bimodal grain morphology.

Acknowledgement

The TEM studies were performed by Dr M. Schmücker (DLR, Köln), who is gratefully acknowledged.

References

1. Aksay, I. A., Dabbs, D. M. & Sarikaya, M., Mullite for structural, electronic and optical applications. *J. Am. Ceram. Soc.*, **74** (1991) 2343–2358.
2. Hirata, Y., Matsushita, S., Ishihara, Y. & Katsuki H., Colloidal processing and mechanical properties of whisker-reinforced mullite matrix composites. *J. Am. Ceram. Soc.*, **74** (1991) 2438–2442.
3. Nurishi, Y. & Pask, J. A., Sintering of α-Al_2O_3/amorphous silica compacts. *Ceram. Int.*, **8** (1982) 57–59.
4. Rana, A. P. S., Aiko, O. & Pask, J. A., Sintering of α-Al_2O_3/quartz, and α-Al_2O_3/cristobalite related to mullite formation. *Ceram. Int.*, **8** (1982) 151–153.
5. Rodrigo. P. D. D. & Boch, P., High purity mullite ceramics by reaction sintering. *Int J. High Tech. Ceram.*, **1** (1985) 3–30.
6. Rodrigo, P. D. D., Reaction sintering of mullite base ceramics. PhD Thesis, University of Limoges, Limoges, 1986.
7. Boch, P., Chartier, T. & Rodrigo, P. D. D., High purity ceramics by reaction sintering. In *Ceramic Transactions 6: Mullite and Mullite Matrix Composites*, eds S. Somiya, R. F. Davis, & J. A. Pask. American Ceramic Society, Westerville, OH, 1990, pp. 353–374.
8. Wahl, F. M., Grim, R. E. & Graf, R. B., Phase transformations in silica–alumina mixtures as examined by continuous X-ray diffraction. *Am. Mineral*, **46** (1961) 1064–1076.
9. Schmücker, M., Albers, W. & Schneider, H., Mullite formation by reaction sintering of quartz and α-Al_2O_3 — A TEM study. *J. Eur. Ceram. Soc.*, **14** (1994) 511–515.
10. Pankratz, L. B., Weller, W. W. & Kelley, K. K., Low temperature heat content of mullite. US Bur. Mines Rep. Invest. No. 6287,7 (1963).
11. Johnson, S. M. & Pask, J. A., Role of impurities on formation of mullite from kaolinite and Al_2O_3–SiO_2 mixtures. *Am. Ceram. Soc. Bull.*, **61** (1982) 838–842.
12. Risbud, S. H. & Pask, J. A., Mullite, crystallization from SiO_2–Al_2O_3 melts. *J. Am. Ceram. Soc.*, **61** (1978) 63–67.
13. Kingery, W. D., Bowen, H. K. & Uhlmann D. R., *Introduction to Ceramics*, 2nd Edition. John Wiley, New York, 1976.

Journal of the European Ceramic Society **16** (1996) 1083–1088

PII: S0955-2219(96)00033-7
0955-2219/96/$15.00

Development of High-Strength Whiteware Bodies

Soumen Maity[a] & B. K. Sarkar[b]

[a]Central Glass & Ceramic Research Institute, P.O. Jadavpur, Calcutta–700 032, India
[b]Indian Association for Cultivation of Science, P.O. Jadavpur, Calcutta–700 032, India

(Received 15 November 1995; revised version received 16 January 1996; accepted 23 January 1996)

Abstract

The effect of sillimanite sand as a replacement for quartz and alumina/cordierite glass-ceramic for feldspar was studied. Compositional variations were due to the gradual incorporation of alumina in place of cordierite glass-ceramic. Increased replacement of cordierite glass-ceramic by alumina (20%) increased the flexural strength by 100%, giving a value of 195 MPa. Elastic modulus, microhardness and fracture toughness also showed sharp increases compared with values for conventional triaxial whiteware compositions. Improvement in mechanical properties was attributed to the presence of sillimanite and alumina particles present as fracture-resistant dispersoids in a viscous glassy matrix. Increased fracture behaviour is due to minimization of the glassy phase and limiting the size of Griffith's flaws. © 1996 Elsevier Science Limited.

1 Introduction

In recent years the electrical porcelain industry has been looking for higher mechanical strengths. The oldest bodies and those in most common use today are the felspathic porcelains made from clay, quartz and feldspar. Feldspar acts as a flux and quartz imparts rigidity to the wares. However, the unreacted residual quartz adversely affects the thermomechanical properties due to development of internal stresses in the glassy phase during phase transformation.

The function of quartz in the strength of a whiteware body is a subject of dispute. Some authors assume that quartz particles introduce a prestress in the overall body whereby the glass matrix is put into compression, thereby increasing strength.[1–4] Others oppose this theory.[5–7] Experimental evidence on both views is abundant but remains inconclusive.

Mullite content and its morphology have also been shown to affect the mechanical properties. It was reported[8,9] that the strength increased with increasing mullite content but that firing at high temperature coarsened the mullite and, as a consequence, the strength decreased.

Considerable improvement in the strength was also achieved by reducing the particle size of the quartz to the range 10–30 μm.[1,7] Attempts were also made to substitute quartz by non-conventional materials like alumina,[10,11] zircon,[12] alumino-silicates[13–15] and crystallizing glass,[16] resulting in fruitful compositions. It was also shown[17] that a dispersion-strengthened glass matrix with high-strength particles dispersed within the glass will limit the size of the Griffith flaw, thereby increasing the strength.

Fluxing of porcelain bodies with feldspar results in glass with brittle fracture character. In this study feldspar was substituted by cordierite-based crystallizing glass possessing low thermal expansion and high thermal shock resistance. Also, quartz was fully substituted by sillimanite sand in an attempt to reduce the microstress. The advantage of using sillimanite is twofold. Firstly, it is a waste material and is abundantly available. Secondly, being a volume-stable and highly fracture-resistant phase, it would result in improved mechanical properties. Alumina was substituted in place of cordierite glass-ceramic to further improve the mechanical properties.

2 Experimental Procedure

2.1 Raw materials

Raw materials used in the present investigation were china clay (Rajmahal, Bihar), talc (Jaipur, Rajasthan), feldspar (Rajmahal, Bihar), quartz (Ranchi, Bihar), calcined alumina (INDAL Co. Ltd), beach sand sillimanite (a by-product obtained after separation of zircon, rare earths and other minerals from beach sand in Kerala) and reagent-grade TiO_2. All the above materials were procured in ground form of at least –250 mesh (75 μm) size. X-ray powder diffraction (XRD) phase analysis and chemical analysis of the raw materials, given in Tables 1 and 2 respectively, confirmed that the impurities present were within the compositional range, and thus would not grossly affect the fired properties.

Table 1. XRD analysis of raw materials

Raw materials	*Major phase*	*Minor phase*
China clay	Kaolinite	Muscovite, rutile, quartz, illite
Quartz	Quartz	Rutile
Feldspar	Orthoclase	Illite, muscovite
Talc	Talc	Quartz, illite
Alumina	Corundum	
Sillimanite sand	Sillimanite	Quartz, zircon
Titanium dioxide	Anatase	

Table 2. Chemical analysis of raw materials

Constituents (wt%)	*China Clay*	*Feldspar*	*Talc*	*Quartz*	*Calcined alumina*	*Sillimanite sand*	*Titania*
SiO_2	47·63	65·63	63·29	99·06	0·09	37·50	0·38
Al_2O_3	37·89	19·19	0·76	0·30	99·93	59·78	Tr
Fe_2O_3	0·56	0·17	0·39	0·19	0·06	0·37	0·27
CaO	0·48	Tr	Tr	0·23	Tr	0·52	0·32
MgO	0·13	0·49	31·56	Tr	Tr	0·50	0·34
Na_2O	0·10	3·56	0·82	0·06	0·05	0·07	0·10
K_2O	0·18	10·42	0·06	0·09	–	0·04	0·26
TiO_2	0·61	Tr	Tr	Tr	Tr	0·76	98·01
L.O.I	12·42	0·65	1·80	0·28	–	0·30	0·32

The glass-ceramic used in the present investigation was essentially of cordierite composition. Raw materials used were 37% china clay, 32% talc, 12% feldspar, 9% calcined alumina and 10% TiO_2 as a nucleating agent. Raw mixes were melted in an electric furnace and cooled for nucleation and growth of crystalline constituents. XRD analysis confirmed the presence of α-cordierite as the principal constituent. The nucleated powder was ground and added as a replacement for feldspar.

2.2 Sample preparation

Respective batch compositions (Table 3) were mixed in the required proportions and wet-milled in porcelain pots for 20 h with porcelain grinding media. Resultant slurries were passed over a magnetic separator to remove iron contamination and sieved through –300 mesh (50 μm). They were further dried in Plaster of Paris moulds, just enough to make them amenable to extrusion. This was done to retain the plasticity of the clay. Previous experience with oven-dried powders did not give good results during extrusion as oven drying at 110°C for 24 h destroyed the plastic nature of clay mixes. Mould-dried compositions were further aged in a moist atmosphere for regaining additional plasticity.

Mixes were extruded in a vacuum extruder twice for thorough mixing. Resultant kneaded mixes were extruded in the form of cylindrical rods 6·0 cm in length and 0·8 cm diameter. After air drying at room temperature for 24 h they were further dried in an oven for 24 h at a temperature of 110°C.

Samples were biscuit fired at 1000°C and were again ground and milled to powder of –300 mesh. Resultant powders were uniaxially pressed in the form of rectangular bars of dimensions 9·0 × 1·0 × 1·0 cm. They were oven dried and machined to cylindrical rods of 5·0 cm length with a diameter of 0·7 cm prior to firing.

2.3 Measurements

Density and porosity of fired samples were determined by Archimedes' immersion technique, involving boiling in water for 2 h and a further soaking of 24 h at ambient temperature. Relative densities of the fired test bars were determined from the bulk densities divided by their respective true densities. True densities were calculated by the law of averages.

Bending strength was measured using an electromechanical universal tester (Instron 1195) in a four-point bending fixture. The crosshead speed was 2 mm min^{-1} with an inner and outer span of 20 and 40 mm, respectively.

Table 3. Raw material composition (wt%) used in the batches

Raw material	*Batch*				
	S_{15}	A_0	A_{10}	A_{15}	A_{20}
China clay	50	50	50	50	50
Sillimanite sand	25	25	25	25	25
Cordierite glass-ceramic	15	25	15	10	5
Alumina	–	–	10	15	20
Quartz	10	–	–	–	–

Modulus of elasticity was measured by the pulse–echo method by an ultrasonic tester (USIP 12).

Microhardness and fracture toughness were measured on mirror polished surface by the indentation technique in a Vickers microhardness tester (Shimadzu HMV 2000). For each case a mean of 10 measurements was taken. Fracture toughness was calculated from the formula given by Evans and Wilshaw.[18]

3 Results and Discussion

3.1 Vitrification behaviour

Five batch compositions (Table 3) of porcelain bodies were fired between 1250 and 1550°C and the fired linear shrinkage, apparent porosity and bulk density measured to determine the vitrification behaviour. Results are shown in Fig. 1. Upon firing, all the properties measured showed the trend typical of conventional porcelain compositions.

From Fig. 1 it is apparent that, in the present compositions, the porosity decreases with increasing firing temperature, with a corresponding rise in linear shrinkage and bulk density values. Optimum vitrification was achieved when the apparent porosity reached a minimum value tending to be nearly zero. Firing above the vitrified range resulted in a drastic fall of the physical properties due to forced expulsion of the entrapped gases, resulting in 'blisters' and 'bloating'. Samples with increased alumina content vitrified at higher temperatures, giving greater shrinkage values due to elimination of porosity. Increase in shrinkage values also ensured more complete wetting and densification of the individual grains during the vitrification process.

Differences in density of vitrified products is brought about primarily by the changes in porosity and the presence/formation of phases with varied densities. Correctly fired hard porcelain is non-porous in the sense that it is vacuum-tight and does not de-gas. On the other hand, it is porous as it has a number of closed unconnected pores, indicated by the difference between bulk and true powder densities. With increased replacement of cordierite glass-ceramic by alumina, bulk density increased with the rate decreasing comparatively at higher alumina (20%) content. Apparent porosity showed an inverse relation with bulk density, as expected.

Increase in bulk density resulted from the progressive addition of higher density alumina (3·98 g cm^{-3}) in place of nucleated cordierite (2·65 g cm^{-3}) and also due to less formation of closed pores. Addition of 15% quartz in place of alumina, however, increased the apparent porosity in vitrified samples. This was due to non-wettability of the crystalline phases by the lower amount of liquid phase formed. Simultaneously the bulk density also decreased.

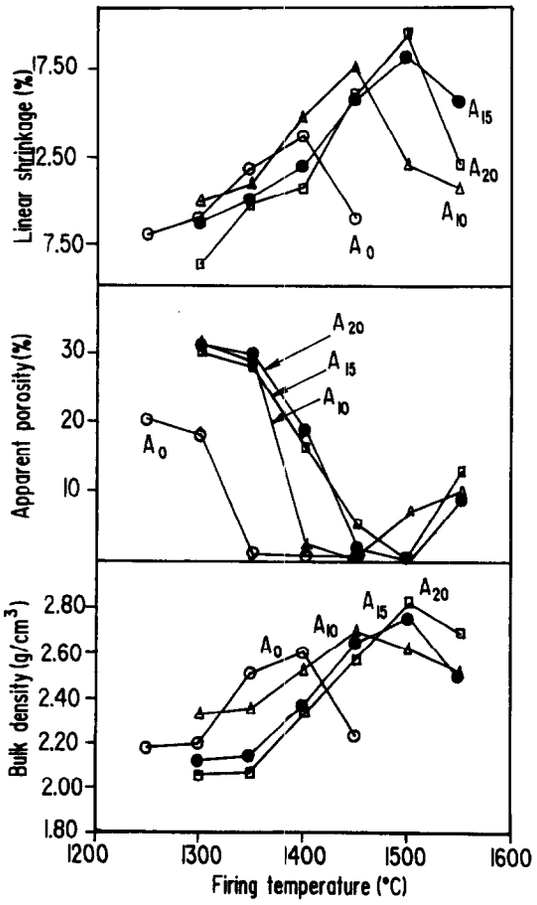

Fig. 1. Vitrification behaviour of porcelain compositions.

3.2 Densification and flexural strength

To discuss the degree of densification relative density rather than bulk density must be compared, because the contents of the crystalline phases differed in their compositions. Figure 2 shows the relative densities of the four batches. The relative

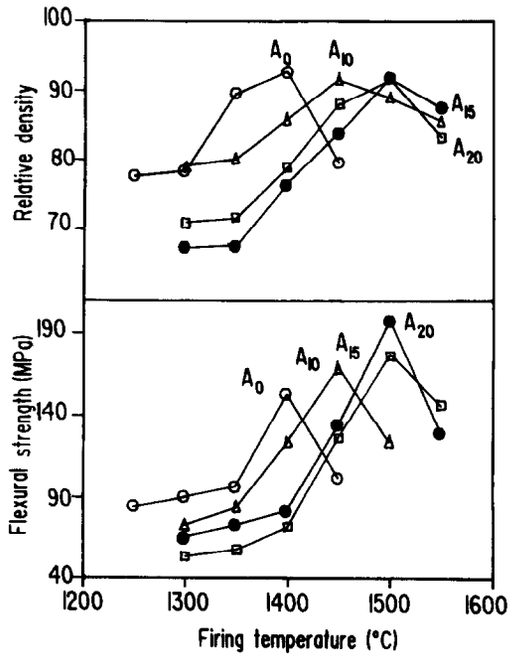

Fig. 2. Densification behaviour and flexural strength variation with firing temperature.

density did not vary between them; all the bodies achieved a relative density between 91 and 92%. Generally, after the apparent porosity reaches zero, the closed porosity on extended heating tends to increase because of so-called 'bloating' with an abrupt decrease in relative density. Although the closed porosity could not be measured, uniform relative density values ensured almost similar presence of closed porosity in the vitrified compositions.

In Fig. 2 the variation in flexural strength of the four compositions with increase in firing temperature is also shown. Flexural strength increased with increasing firing temperature reaching an optimum value at the respective relative density. Further heating decreased the flexural strength, similarly affecting the relative density. The temperature dependences of sintering and flexural strength were almost identical. Increased temperature of vitrification with higher alumina content was due to reduced glassy phase and increased presence of high refractory particles of alumina.

3.3 Effect of body composition and fired phase assemblages on mechanical properties

3.3.1 Flexural strength

Raw material compositions consisted of equal amounts of china clay and sillimanite sand, with a variation in the alumina and cordierite glass-ceramic contents. Fired compositions consisted almost wholly of mullite, undissolved sillimanite and an amorphous silica-rich phase.

With increasing alumina content replacing the cordierite glass-ceramic, the flexural strength of vitrified samples increased in a parabolic manner (Fig. 3). Increased strength was attributed to:

(i) the absence of quartz;
(ii) the formation of mullite; and
(iii) the presence of insoluble second phase.

The increase in strength with progressive substitution of cordierite glass-ceramic by alumina (Fig. 3) opposes the quartz prestressing theory.[1-4] To prove the present conclusions, alumina in A_{15} was substituted completely by quartz. The drastic fall in strength confirmed that quartz does have a deleterious effect on strength when present in a porcelain composition.

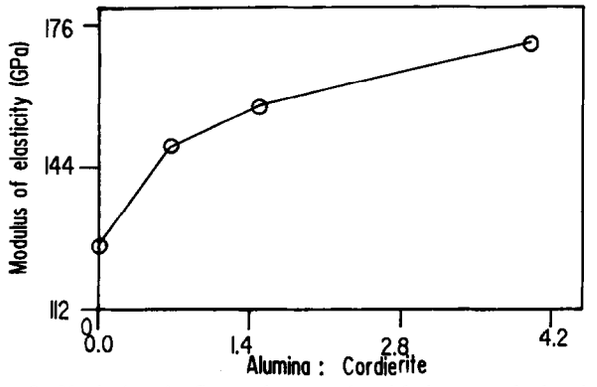

Fig. 3. Variation in flexural strength with increased alumina content.

Mullite in these compositions was formed from decomposition of the clay. With increased vitrification temperature, fine acicular needles of mullite dissolved and recrystallized as a stouter form. Thus the reported increase in strength was partly due to the stouter morphology of mullite needles. However, the observed variation in strength was also governed to a great extent by other factors, as the highest strength samples (A_{20}) showed no trace of mullite needles even when examined microscopically.

Increased strength in the present compositions was mainly due to a dispersion-strengthened glassy matrix reinforced by high-strength alumina and sillimanite particles dispersed within the glass. These particles acted as a barrier to crack propagation when a stress was applied and also limited the size of Griffith's flaws, thereby increasing strength.

An additional factor for increased strength was the incorporation of cordierite glass-ceramic in place of feldspar which, due to controlled crystallization during cooling, led to the formation of high-strength microcrystalline structures.

3.3.2 Modulus of elasticity (MOE)

Figure 4 shows the effect of increasing alumina content (in lieu of cordierite glass-ceramic) on the MOE of vitrified specimens. With increasing alumina content MOE increased in a parabolic manner. Since elasticity depends on the amount and nature of porosity, its dependence on porosity is also shown in Fig. 5. This plot showed an inverse linear dependence between elasticity and porosity, as expected. The widely held view that Young's modulus is directly proportional to the flexural strength[12] has also been confirmed here. Factors responsible for increased strength also governed the increase in MOE values.

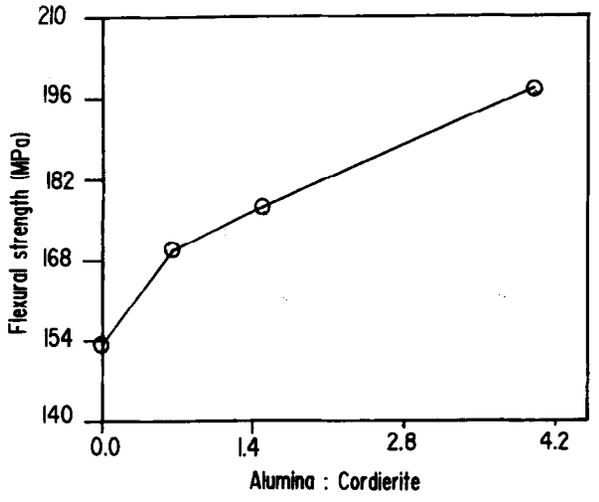

Fig. 4. Variation in MOE with increasing alumina content.

3.3.3 Microhardness and fracture toughness

Recently large toughness improvements were reported during the design of new microstructures consisting of refractory particles dispersed as a second phase in a ceramic matrix. According to Rice,[19] significant toughness improvements require (1) that the diameter of the particles should be smaller than the typical flaw size in the ceramic matrix (≅ 20–50 μm) and (2) that the second phase should be dense and uniform in order to reduce the interparticle distance to a dimension smaller than the typical flaw size of the matrix.[20]

With increased replacement of cordierite glass-ceramic by alumina, both the microhardness and fracture toughness increased considerably (Fig. 6) compared with those of conventional triaxial whiteware composition. Increase in microhardness values on gradual substitution of cordierite glass-ceramic by alumina was due to the presence of high-hardness and high-modulus sillimanite and alumina dispersoids embedded in a highly viscous glassy matrix.

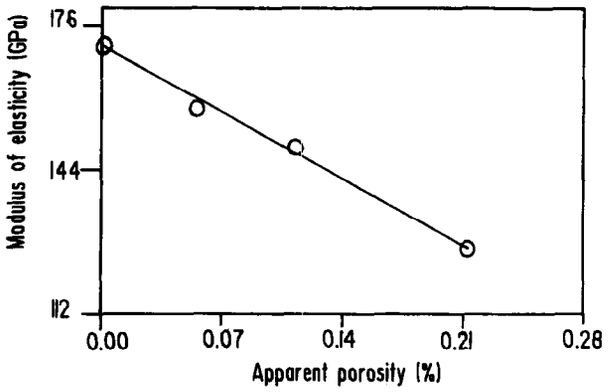

Fig. 5. Dependence of MOE on apparent porosity in vitrified samples.

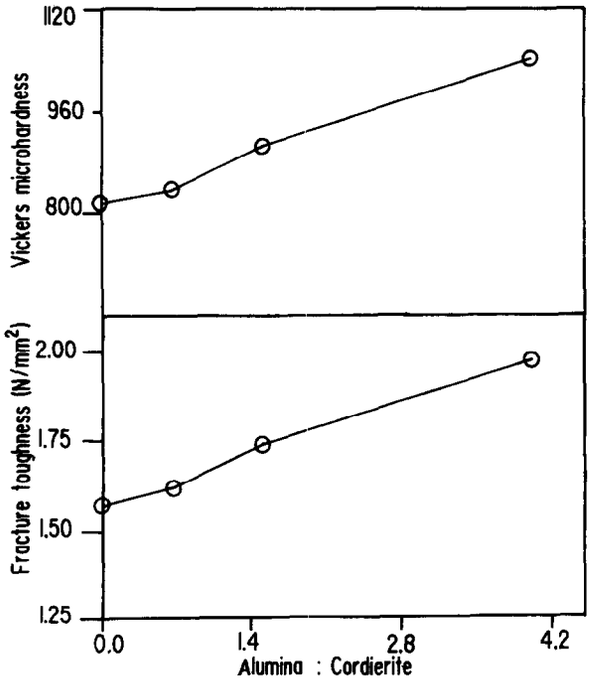

Fig. 6. Variation of Vicker's microhardness and fracture toughness with increasing replacement of cordierite glass-ceramic by alumina.

Increased toughness of vitrified specimens with increased alumina additions was due to crack impediment and deflection phenomena in a dispersion-strengthened high-viscous glassy matrix. This mechanism requires a fracture-resistant second phase, such as refractory particles (sillimanite and alumina particles in the present compositions) and is highly dependent on the dispersoid–matrix property mismatch.[21] The initial crack could be deflected by sufficiently weakened dispersoid–matrix interfaces which were preferred crack paths. The model of Faber and Evans[20] indicated that there was about a 100% increase in the toughness values for particulate composites reinforced with spherical particles like alumina, sillimanite or small rods of mullite with an aspect ratio lower than about 3. Disc-shaped particles also have a considerable effect on composite toughening.

4 Conclusion

Replacement of quartz and feldspar by sillimanite sand and alumina/cordierite glass-ceramic, respectively, in a conventional porcelain composition increased both the physical and mechanical properties of the fired bodies. Increased shrinkage values at higher alumina additions (replacing cordierite glass-ceramic) denoted a greater densification and lesser formation of porosity. At lower temperatures of firing, mullite formation aids in increasing strength. At higher firing temperatures (1500°C), although mullite dissolved in the glass, increased strength was due to a dispersion-strengthened glassy matrix. Rounded particles of sillimanite and alumina acted as dispersoids and helped in inhibiting crack propagation, thus increasing both the strength and fracture toughness values. Lowering of Griffith's flaws was also favourable in improving the mechanical properties.

Acknowledgements

The authors are deeply indebted to Shri. S. Mondal for sample extrusion and pressing, and Shri. D.K. Naskar for machining of green samples. Thanks are also due to the Council of Scientific & Industrial Research, Govt of India, for providing financial assistance in the form of a research fellowship grant during the course of the work.

References

1. Mattyasovsky-Zolsnay, L., Mechanical strength of porcelain. *J. Am. Ceram. Soc.*, **40** (1957) 299–306.

2. Winterling, A., Structure stress as the cause of increasing strength in porcelain. *Ber. Deut. Keram. Ges.*, **38** (1961) 9–22.
3. Dietzel, A., Significance of equilibrium diagrams for ceramics. *Sprechsaal*, **86** (1953) 251–252.
4. Marzhal, H., Influence of quartz on the strength of porcelain. *Ber. Deut. Keram. Ges.*, **32** (1955) 203–211.
5. Weidmann, T., Strength carriers in porcelain. *Sprechsaal*, **92** (1959) 2–5; 29–30; 52–55.
6. Weyl, D., Influence of internal strains on the texture and mechanical strength of porcelains. *Ber. Deut. Keram. Ges.*, **36** (1959) 319–324.
7. Warshaw, S. I. & Seider, R., Comparison of strength of triaxial porcelain containing alumina and silica. *J. Am. Ceram. Soc.*, **50** (1967) 337–343.
8. Schroeder, J. E., Inexpensive high strength electrical porcelain. *Am. Ceram. Soc. Bull.*, **57** (1978) 526.
9. Palatzky, A. & Werner, T., Increasing the mechanical strength of porcelain bodies. *Silikat. Tech.*, **9** (1958) 68–73.
10. Khandelwal, S. K. & Cook, R. L., Effect of alumina additions on crystalline constituents and fired properties of electrical porcelains. *Am. Ceram. Soc. Bull.*, **49** (1970) 522–526.
11. Kobayashi, Y., Ohira, O., Satoh, T. & Kato, E., Compositions for strengthening porcelain bodies in alumina–feldspar–kaolin system. *Trans. Brit. Ceram. Soc.*, **93** (1994) 49–52.
12. Frith, V., Heckroodt, R. O. & Schuller, K. H., The mechanical properties of zircon–feldspar porcelains. *Cfi/Ber. DKG.*, **64** (1987) 379–383.
13. Blodgett, W. E., High strength alumina porcelains. *Am. Ceram. Soc. Bull.*, **40** (1961) 74–77.
14. Maiti, K. N. & Kumar, S., Microstructure and properties of a new porcelain composition containing crystallizing glasses as replacement for feldspar. *Trans. Brit. Ceram. Soc.*, **91** (1992) 19–24.
15. Maiti, K. N. & Kumar, S., Effect of substitution of quartz by beach sand sillimanite on the properties of conventional porcelain. *Trans. Bri. Ceram. Soc.*, **89** (1990) 24–27.
16. Avgustinik, A. I. & Sintsova, I. T., Increasing the mechanical strength of porcelain by substituting crystallizing glass for quartz. *Glass & Ceramics*, **24** (1967) 322–326.
17. Hasselman, D. P. H. & Fulrath, R. M., Proposed fracture theory of dispersion-strengthened glass matrix. *J. Am. Ceram. Soc.*, **49** (1966) 68–72.
18. Evans, A. G. & Wilshaw, T. R., Quasi-static solid particle damage in brittle materials. *Acta. Metall.*, **24** (1976) 939–940.
19. Rice, R. W., Mechanisms of toughening in ceramic matrix composites. *Ceram. Eng. Sci. Proc.*, **6** (1985) 589.
20. Faber, K. T. & Evans, A. G., Crack deflection processes. *Acta Metall.*, **31** (1983) 565.
21. Lange, F. F., The interaction of a crack front with a second phase dispersion. *Phil. Mag.*, **22** (1970) 983.

Journal of the European Ceramic Society **16** (1996) 1089–1098

PII: S0955-2219(96)00024-6
0955-2219/96/$15.00

Phase Equilibrium Relationships in the System Al_2O_3–TiO_2–MnO, Relevant to the Low-Temperature Sintering of Alumina

M. C. Moreira & A. M. Segadães*

Departamento de Engenharia Cerâmica e do Vidro, Universidade de Aveiro, 3180 Aveiro, Portugal

(Received 20 September 1994; revised version received 4 January 1996; accepted 8 January 1996)

Abstract

A great deal of research work has been devoted to lowering the sintering temperature of ceramic powders of varied nature, to fulfil a variety of purposes. Both experimentation and theory show that the sintering temperature of alumina can be lowered to 1400°C and below by using small particle sizes and certain additives like TiO_2 and/or MnO. The general idea is that sintering is aided by the development of a liquid phase at this low temperature, due to the presence of the additives. However, there is no phase diagram available to throw light on this matter. For this reason, the present work was aimed at investigating the phase equilibrium relationships in the ternary, non-condensed system Al_2O_3–TiO_2–MnO, in air.

Selected compositions in this system were prepared from reagent-grade oxides, uniaxially pressed into 6 mm cylindrical pellets, fired at temperatures between 1000 and 1650°C for 2 to 22 h, water-quenched, and observed by X-ray diffraction and scanning electron microscopy, the composition of some of the phases identified being evaluated by energy-dispersive spectroscopy. These experiments led to the definition of the compatibility triangles and a tentative location of the boundary curves between primary phase fields is presented. © *1996 Elsevier Science Limited.*

1 Introduction

To aid the sintering process, i.e. to sinter faster or at lower temperatures, the reactivity of the particles to be sintered must be increased. In other words, finer grain sizes are needed. This effect is well documented in the literature, for a variety of systems. However, in those cases in which the properties of the sintered body are not unduly reduced by the use of sintering aids, this is still the easiest way of lowering the sintering temperature. These aids promote sintering either by causing the development of solid solutions and lattice defects, or the development of a liquid phase, both favouring the diffusion processes necessary to sintering.

A number of researchers have studied the effect of various additives on the densification of non-reactive alumina powders, based on the liquid-phase mechanism.[1–3] The general conclusion is that there is an optimum amount of each additive at a given temperature to reach maximum density and, the higher the temperature, the smaller the amount of additive needed. With a liquid phase present at high temperatures, the resulting sintered alumina bodies are not adequate for structural applications. But alumina is still the ideal material for cold abrasion/erosion applications (e.g. thread guides, spray nozzles), where it is important to be able to sinter at lower temperatures. In these cases, the high-temperature liquid phase can even enhance the cold mechanical strength, an indirect measure of the abrasion resistance of the ceramic body.

The work of Cutler *et al.*[1] on the effect of additions of manganese, copper and titanium oxides on the sintering behaviour of alumina, showed that combinations of manganese and titanium oxides were the most effective in lowering the sintering temperature, especially when present in equal amounts. The authors detected the presence of a liquid phase and found that minimum grain growth occurred for 3–4% mixed additive, sintered between 1300 and 1400°C, the resulting ceramic having reached densities of the order of 3·80 g cm.$^{-3}$ More recently, Filbri *et al.*[3] investigated this same system from a different perspective, since they were trying to sinter high alumina compositions without a significant reduction in porosity. The authors kept the total amount of additives very low (≤ 0·5%), to stay close to the solid solubility limits (although there is no consensus on this value) and avoid the development of a liquid phase.

*To whom correspondence should be addressed.

Research work such as this would be much easier if the phase diagram of the system Al_2O_3–TiO_2–MnO_2–MnO was available. This system is a non-condensed one, in which the phase stability is determined not only by the temperature and composition but also by the oxygen partial pressure in the gaseous phase. In air, it was observed[4] that the evolution of oxygen as the temperature rises is not easily reversed on cooling. In other words, the high-temperature reduced forms tend to be retained at lower temperatures. This will be more the case when other components are present, with which the reduced oxide can react. Therefore, the phase equilibrium relationships in the system Al_2O_3–TiO_2–MnO_2–MnO can be approximated by those for the Al_2O_3–TiO_2–MnO system at temperatures above 800°C.

In the literature, only the isobaric phase diagrams of the binary systems are available,[5] albeit old. Four binary compounds are reported, namely $Al_2O_3.TiO_2$ (AT), $MnO.Al_2O_3$ (MA), $MnO.TiO_2$ (MT) and $2MnO.TiO_2$ (M_2T). If no ternary compounds are formed within the system, its phase diagram should contain five solid-phase compatibility triangles and the corresponding five invariant points. The present work was aimed at investigating the phase equilibrium relationships in the ternary, non-condensed system Al_2O_3–TiO_2–MnO in air, and tentatively locating the position of the invariant points.

2 Experimental Procedure

In the present work, selected compositions were prepared from BDH alumina powder (chromatography), after dry grinding in a planetary mill for 30 min, TiO_2 (Merck) and MnO_2 (Merck) powders, all sieved through 43 μm (325 mesh).

Prior to any experiments, the mineralogy of the starting powders was confirmed by X-ray diffraction (XRD; using Cu K_α radiation). Moreover, the oxidation behaviour of the manganese oxide, kept dry in sealed containers, was investigated by thermogravimetric analysis (TGA) using a Stanton Redcroft thermobalance with a 2°C min^{-1} heating (and cooling) rate, up to 1200°C.

The appropriate amounts of the reactants were dry-mixed for 30 min in a Glen-Creston mixer–miller, and uniaxially dry-pressed into 6 mm cylindrical pellets using a hard-steel die under a pressure of ~50 MPa. Each pellet was then wrapped in platinum foil, lowered into the furnace held at the chosen soaking temperature (SiC vertical tube furnace for temperatures up to 1450°C or a molybdenum-wound vertical tube furnace for higher temperatures), kept at that temperature for 2 to 22 h, and water-quenched. Temperatures were measured with Pt/Pt–13% thermocouples.

To guarantee that equilibrium had been established, particularly in those samples fired at lower temperatures, the same composition was held for successively longer times at the particular temperature, until the phase assemblage observed did not change any further. The shortest time required to attain this was then considered to be enough to establish the equilibrium state. Naturally, samples fired at higher temperatures, most of which contained a liquid phase, needed shorter firing times.

The fired samples were then prepared for X-ray powder diffraction and/or scanning electron microscopy (SEM) analysis (Jeol JSM-35C) on epoxy-mounted polished surfaces. Different phases present different morphologies and colours, to each of which a typical composition could be indexed by semi-quantitative energy-dispersive spectrometer (EDS) analysis (Tracor TN 2000). Sample charging in SEM and EDS was prevented by carbon coating. EDS was carried out using elemental standards, the oxygen being calculated by difference.

Table 1 gathers the relevant data so obtained, after correcting the compositions for the corresponding oxygen loss. This table is constructed in the usual way for phase equilibrium studies in ceramic oxide systems,[6] i.e. only the major phases present are listed, those present in only trace amounts, or when they do not represent true equilibrium, being shown in parentheses. Sometimes, due to the poorly defined microstructure, some details could not be determined unambiguously during microscopic examination. In these cases the particular phase assemblage is listed as 'poor microstructure'.

3 Results and Discussion

3.1 Oxidation behaviour of manganese oxide

Although alumina and titania are stable oxides in air, even at high temperatures, in the Mn–O system the oxides MNO_2, Mn_2O_3, Mn_3O_4 and MnO exist as stable phases that can interconvert depending on the temperature and the oxygen partial pressure. The reactions between the condensed phases and the oxygen of the gaseous phase in such metal–oxygen systems can easily be investigated by TGA, where the oxygen evolution caused by the temperature rise translates into directly recordable weight loss. In the binary systems like Mn–O, it is particularly helpful to convert the weight loss curves into dissociation curves, plotting the remaining oxygen/initial metal molar ratio, O/Mn, against temperature.

Figure 1(A) shows the weight loss curve obtained in air from a sample of manganese oxide initially weighing 354·8 mg. As can be observed, there is an initial, small, slow weight loss corresponding to the change in oxygen stoichiometry as the isobar

Table 1. Selected compositions and phases identified in the system Al_2O_3–TiO_2–MnO (A = alumina; T = titania; M = manganesia)

Composition (wt%)			*Temp*	*Time*	*Phase identified*
Al_2O_3	*MnO*	*TiO_2*	*(°C)*	*(h)*	*(SEM)*
65·00	30·00	5·00	1457	4	MA+A+liquid
	(1)		1496	2	MA+A+liquid
			1600	4	MA+A+liquid
65·00	25·00	10·00	1300	18	MA+A+liquid
			1342	4	MA+A+liquid
			1386	4	MA+A+liquid
	(2)		1447	4	MA+A+liquid
			1496	2	MA+A+liquid
65·00	17·00	18·00	1250	16	A+MT+liquid
			1342	4	A(+MT)+liquid
			1396	19	A+liquid
	(3)		1447	4	A(+MT)+liquid
			1496	2	A+liquid
65·00	10·00	25·00	1335	4	Poor microstructure
			1378	4	Poor microstructure
	(4)		1447	4	A+AT+liquid
			1600	4	A+liquid
49·00	46·00	5·00	1100	22	MA+MT+liquid
	(5)		1200	12	MA(+MT)+liquid
			1300	19	MA+liquid
40·00	55·00	5·00	1290	10	MA(+T)+liquid
			1340	4	MA+liquid
			1381	4	MA+liquid
	(6)		1446	4	MA+liquid
			1535	2	MA(+T)+liquid
40·00	45·00	15·00	1100	22	MA+MT+liquid
			1340	4	MA(+MT)+liquid
	(7)		1381	4	MA(+MT)+liquid
			1457	4	MA+liquid
			1535	2	liquid(+MA)
40·00	35·00	25·00	1030	19	Poor microstructure
			1208	11	MT+MA+A(+liquid)
			1250	16	MT+MA(+A)+liquid
	(8)		1290	10	MT+MA(+A)+liquid
			1320	17	MT(+A)+liquid
			1400	4	Abundant liquid
40·00	20·00	40·00	1340	4	MT(+A)+AT+liquid
	(9)				
40·00	5·00	55·00	1342	4	AT+T(+A)+liquid
	(10)		1446	4	AT+T+liquid
			1650	6	AT+liquid
20·00	62·50	17·50	1100	22	MT+M_2T+liquid
	(11)				
20·00	54·00	26·00	1035	16	Poor microstructure
			1098	4	MT+MA+liquid
			1210	$7^{2/3}$	MT+MA+liquid
	(12)		1250	16	MT+MA+liquid
			1300	12	Abundant liquid
20·00	43·00	37·00	1035	16	Poor microstructure
			1098	19	Poor microstructure
			1210	$7^{2/3}$	Poor microstructure
	(13)		1250	19	MT+MA+liquid
			1300	18	MT+abundant liquid
			1380	16	Abundant liquid
20·00	20·00	60·00	1100	4	Poor microstructure
			1126	5	Poor microstructure
	(14)		1210	$7^{2/3}$	MT+AT+liquid
			1252	19	MT+AT+liquid
10·00	85·00	5·00	1200	12	M(+T)+MA+liquid
	(15)		1300	12	M(+T)+liquid
			1380	16	M(+T)+liquid
10·00	55·00	35·00	990	12	Poor microstructure
			1126	5	MT+MA(+A)+ab.liquid
	(16)		1252	19	MT+M_2T+liquid
			1290	11	MT+M_2T+liquid
10·00	5·00	85·00	1300	12	T+AT+liquid
	(17)				

traverses the dioxide single-phase field. At constant pressure, isothermal weight losses, corresponding to sharp changes in the O/Mn molar ratio, describe the isobaric invariant equilibrium between two condensed phases. Such a sharp change can be observed at ≈630°C, which corresponds to the invariant equilibrium between the original 'MnO_2' and non-stoichiometric Mn_2O_3. Up to ≈725°C a gradual conversion to Mn_3O_4 occurs, suggesting that there is a region of continuous mutual solid solubility between the sesquioxide and the spinel instead of invariant equilibrium between the two phases. This is followed by a second gradual conversion of the spinel to MnO, which is complete at ≈800°C. Above this temperature MNO is the stable oxide, showing clear oxygen deficiency above 960°C. Assuming that the O/Mn molar ratio at ≈800°C is unity, then, by working backwards, it is possible to calculate the oxygen stoichiometry in the starting manganese oxide and plot a corrected O/Mn molar ratio vs. temperature curve, as shown in Fig. 1(B). It is known that commercial 'MnO_2' varies from $MNO_{1.98}$ to $MnO_{1.75}$, and the starting oxide was found to be $MnO_{1.94}$.

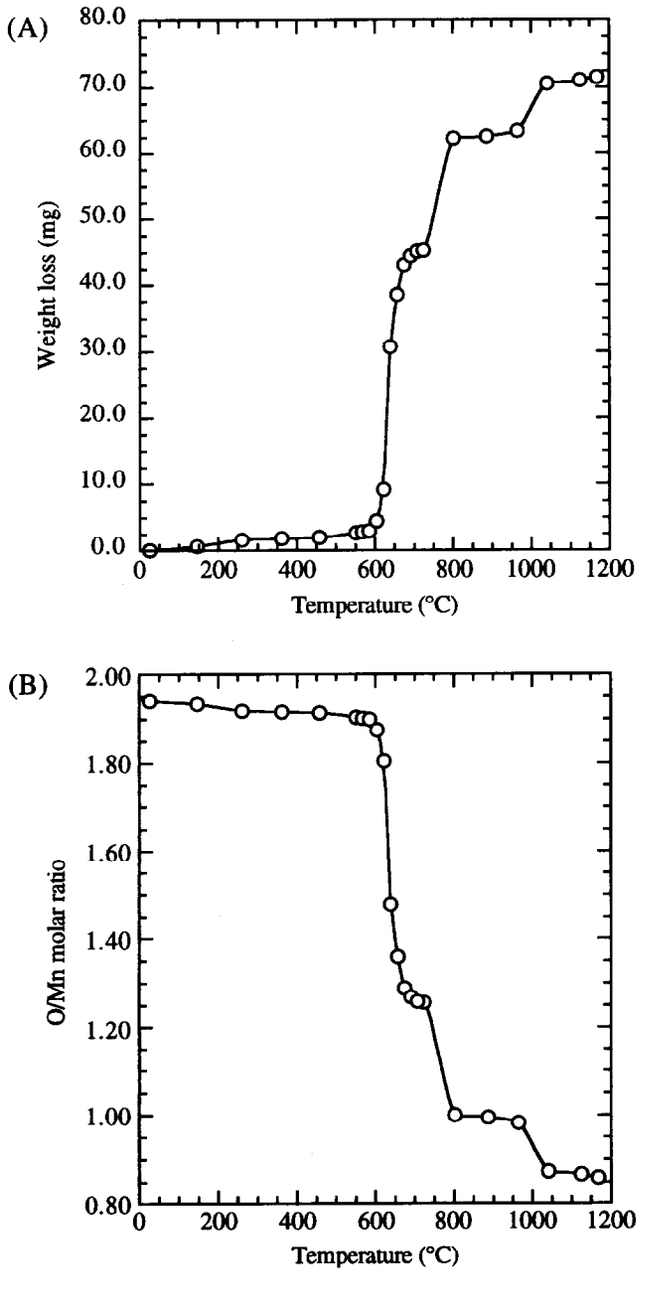

Fig. 1. TGA curves obtained for 354·8 mg of original MnO_2: (A) weight loss curve, and (B) corrected dissociation curve.

The difficulty in reversing the oxygen loss became apparent when no significant weight gain was recorded upon cooling. This was confirmed by X-ray diffraction of the powder after TGA, which showed only MnO and Mn_2O_3 (no MnO_2) peaks.

In the light of these findings, it is valid to approximate the phase equilibrium relationships in the system Al_2O_3–TiO_2–MnO_2–MnO to those for the Al_2O_3–TiO_2–MnO system at temperatures above 800°C.

3.2 Choice of the solid-phase compatibility triangles

Only the isobaric phase diagrams of the binary systems are available in the literature[5] and four binary compounds are reported: $Al_2O_3.TiO_2$ (AT), $MnO.Al_2O_3$ (MA), $MnO.TiO_2$ (MT) and $2MnO.TiO_2$ (M_2T). Of these, only MT shows incongruent melting behaviour. As for AT, there has been a recent resurgence of interest in this material due to radical improvements in microstructural control allied to its excellent thermal properties. Its successful application relies on the ability to control the microcracking phenomenon and understand the decomposition behaviour. Even though considerable work has been carried out to explain the mechanism of decomposition and the effect of additives on such behaviour, the important fact remains that AT is unstable below ≈1200°C.[7–9]

As described elsewhere,[10] preliminary work was carried out to investigate which were the compatibility triangles in the system. If no ternary compounds are formed within the system, its phase diagram should contain five solid-phase compatibility triangles (which can be arranged in seven alternative ways) and the corresponding five invariant points. A set of carefully chosen compositions was fired between 1100 and 1400°C for 4 to 7 h, to establish equilibrium, and slow-cooled to ambient temperature. Powder X-ray diffraction analysis carried out on these samples showed that no ternary compounds are indeed formed within the system and that the solid-phase compatibility triangles are set as shown in Fig. 2 (AT room-temperature instability is accounted for by showing the AT-MT tie-line as a dashed line).

3.3. Microstructure analysis of selected compositions

In all the samples, and when present, the titania grains appear as rounded white crystals [Fig. 3(A)]; alumina is always very dark grey (almost black) and

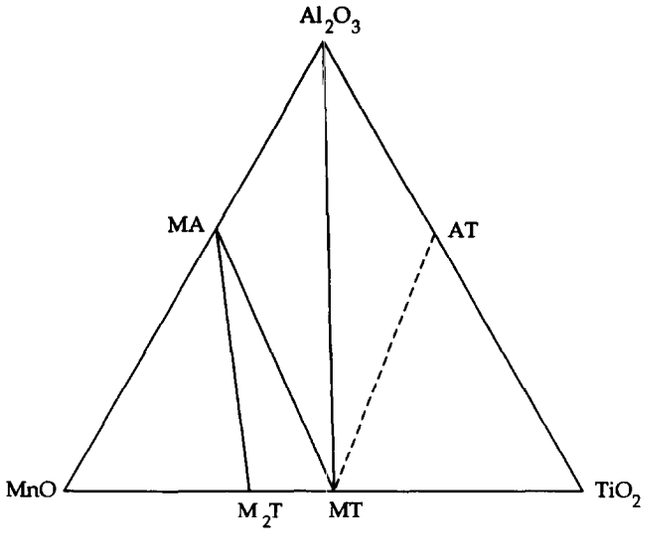

Fig. 2. Layout of solid-phase compatibility triangles[10] (AT room-temperature instability is accounted for by showing the AT–MT tie-line as a dashed line).

appears either as well developed long polygonal grains [Fig. 3(B)] or smaller round ones; AT crystals are also polygonal, but of a lighter grey [Figs 3(A), (B)]; MT grains show up with smooth contours and are very light grey [Figs 3(B), (C)] whereas MA grains are long, smooth and medium grey [Fig. 3(C)]. M crystals are polygonal and light grey. The M_2T phase is rather hard to pick up and usually appears as grey areas associated with T and/or MT grains. The intergranular phase of various greys (lighter in the alumina-rich compositions, darker in the manganesia-rich ones) is the liquid (glass) phase. Black spots are pores.

Samples frequently appear profusely cracked, particularly the glassy phase, due to the thermal shock during quenching. It was found that the liquid phase sometimes devitrifies during quenching, with crystallization of dendrites. Also, unreacted alumina and/or titania grains can sometimes be found. Such non-equilibrium phases, readily identified in the microstructure, are placed in parentheses in Table 1.

3.4 Tentative phase diagram for the system Al_2O_3–TiO_2–MnO

The first working hypothesis assumed during this investigation was that the MT phase would keep it perithetic behaviour inside the ternary system. That was never contradicted by the experimental data obtained. Then, the location and character of

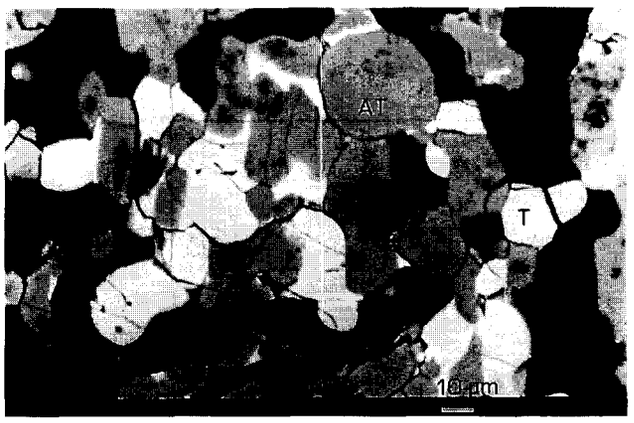

(A)

(B)

(C)

Fig. 3. Representative microstructures observed in the samples investigated: (A) 40 Al_2O_3 + 55 TiO_2 + 5 MnO, at 1342°C showing titania grains (white) and AT grains (grey), thermal shock cracks, liquid films and pores (black). (B) 40 Al_2O_3 + 40 TiO_2 + 20 MnO, at 1340°C, showing one unreacted alumina crystal (very dark grey), AT grains (grey), MT grains (light grey), a patch of devitrified liquid phase and extensive thermal shock cracks. (C) 20 Al_2O_3 + 26 TiO_2 + 54 MnO, at 1250°C, showing MA grains (medium grey), MT grains (light grey) and intergranular liquid films.

A1

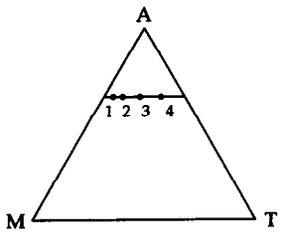

Key to symbols

- ○ Liquid (L)
- ▣ A+L
- × M+L
- \+ MA+L
- ◐ AT+L
- ▣ MT+L
- ⊕ M+MA+L
- ◇ A+MA+l
- □ A+AT+L
- ▲ A+MT+L
- ⌀ MA+MT+L
- △ AT+MT+L
- ◒ T+AT+L
- ▽ MT+M_2T+L
- ■ A+MA+MT
- ● poor microstructure

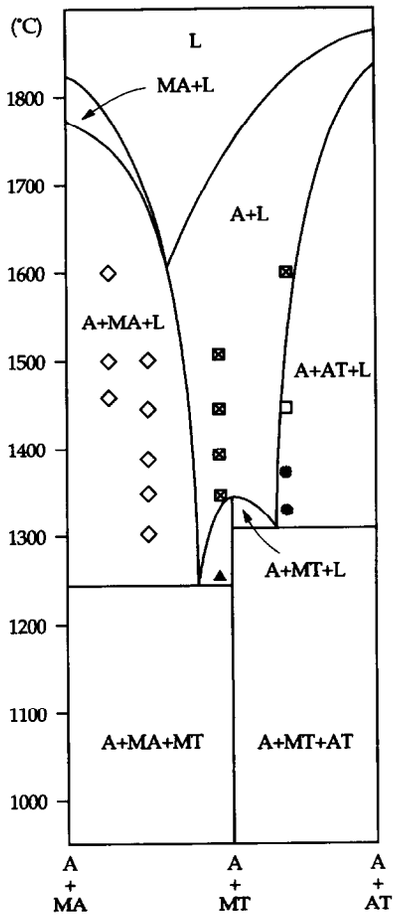

A2

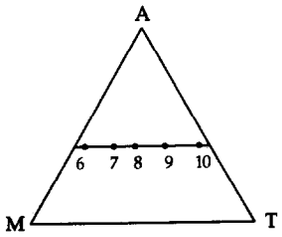

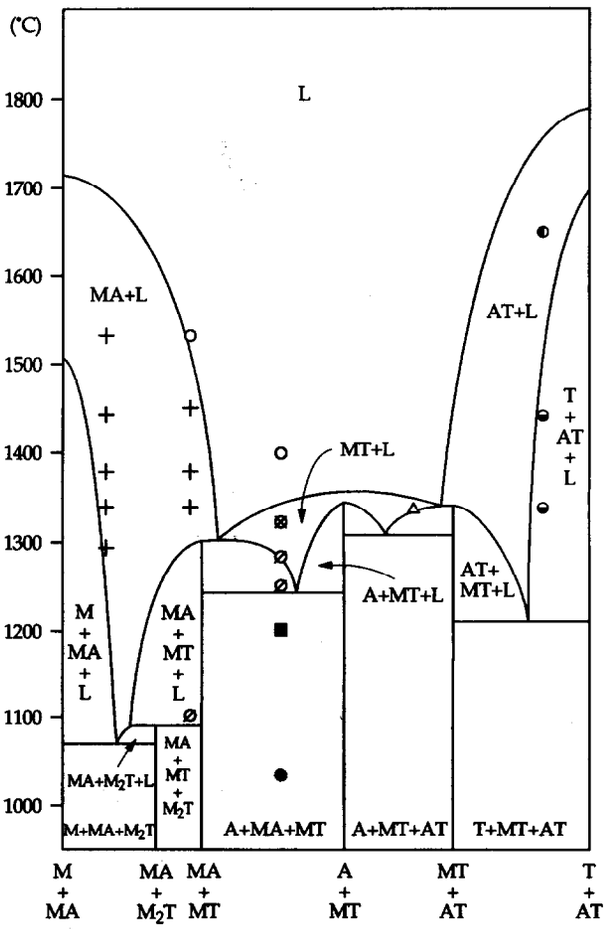

Fig. 4. Isoplethal sections: (A) at constant 65 and 40 wt% Al_2O_3 and key to symbols, (B) at constant 20 and 10 wt% Al_2O_3 and (C) at constant 5 wt% TiO_2 and 5 wt% MnO.

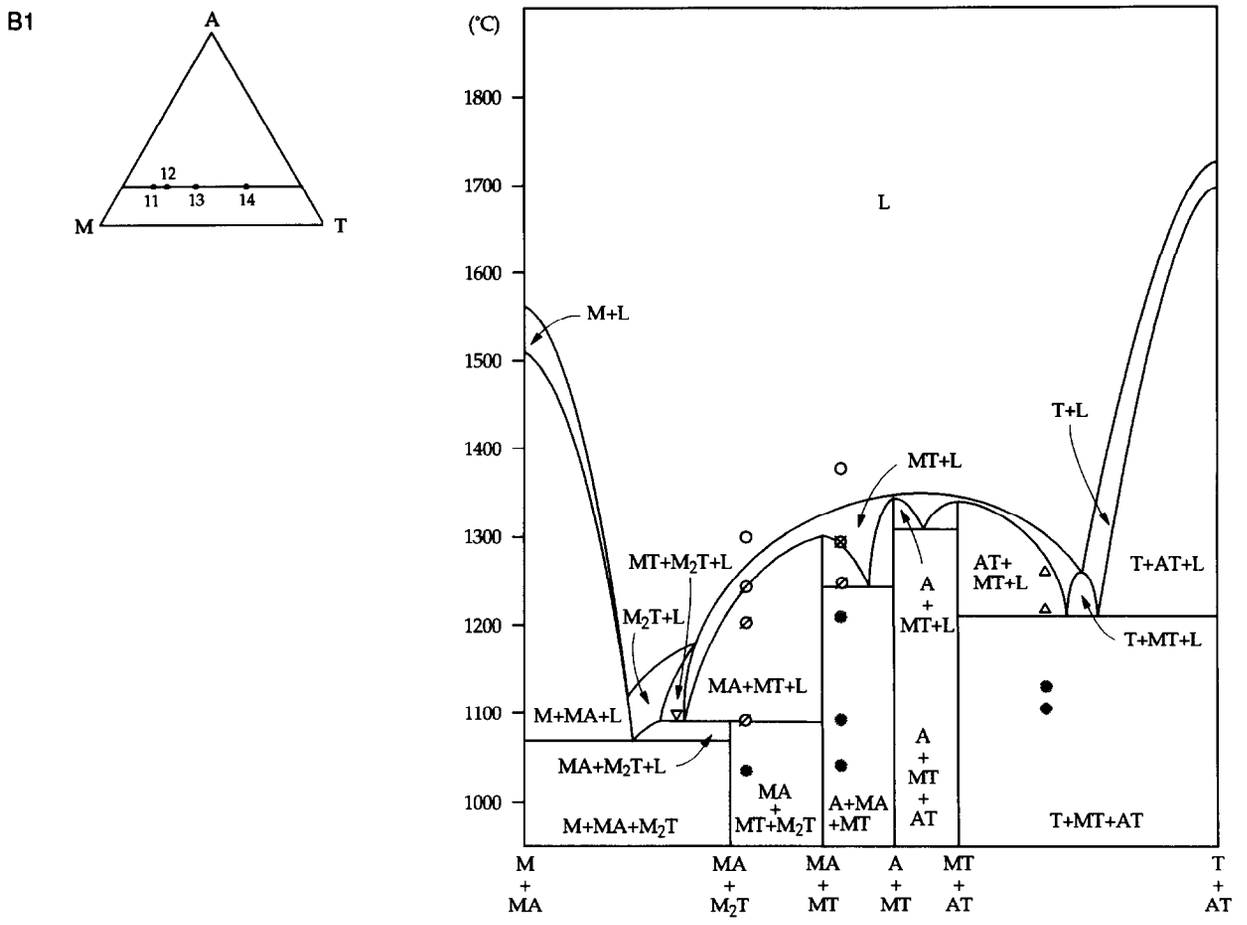

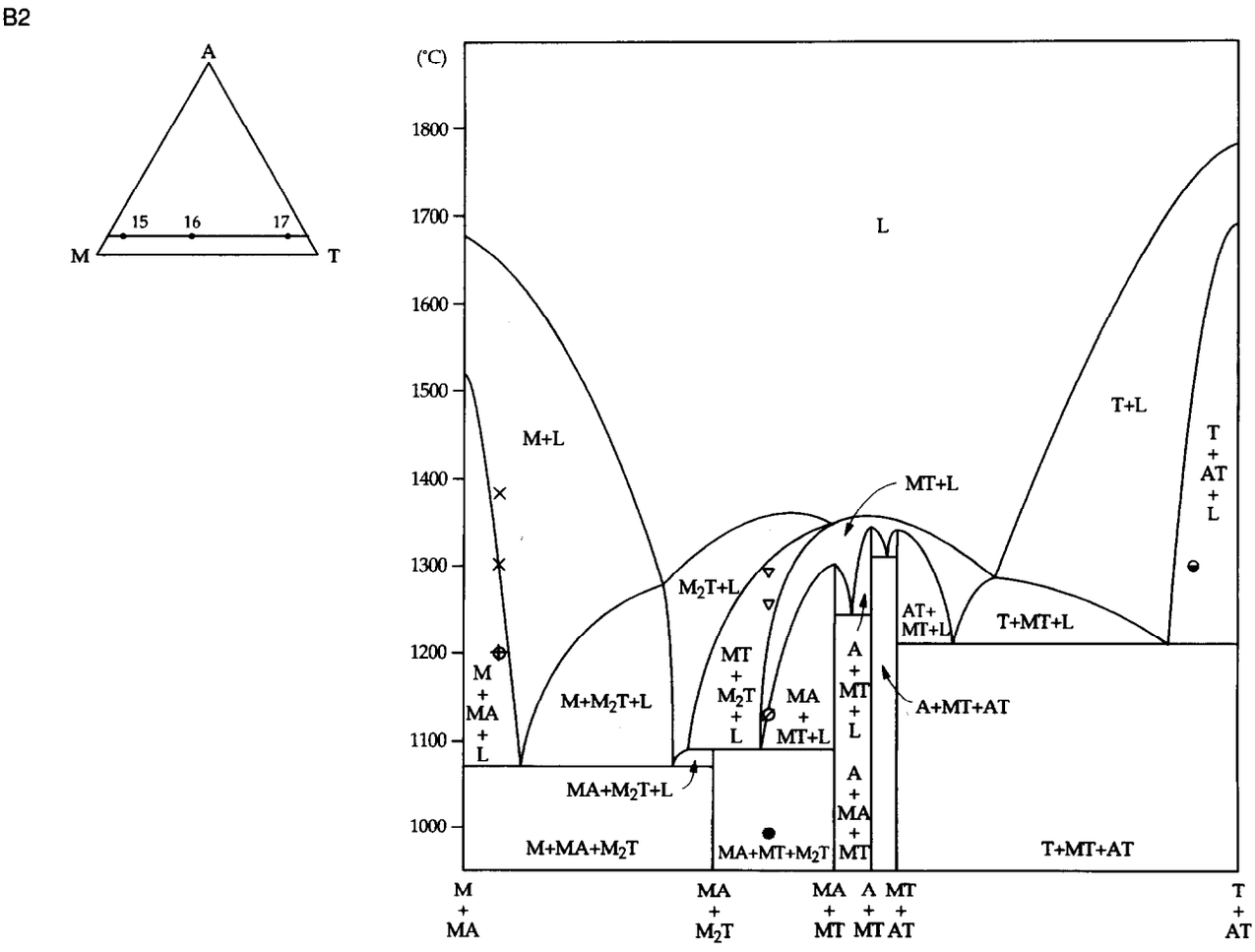

Fig. 4. Continued

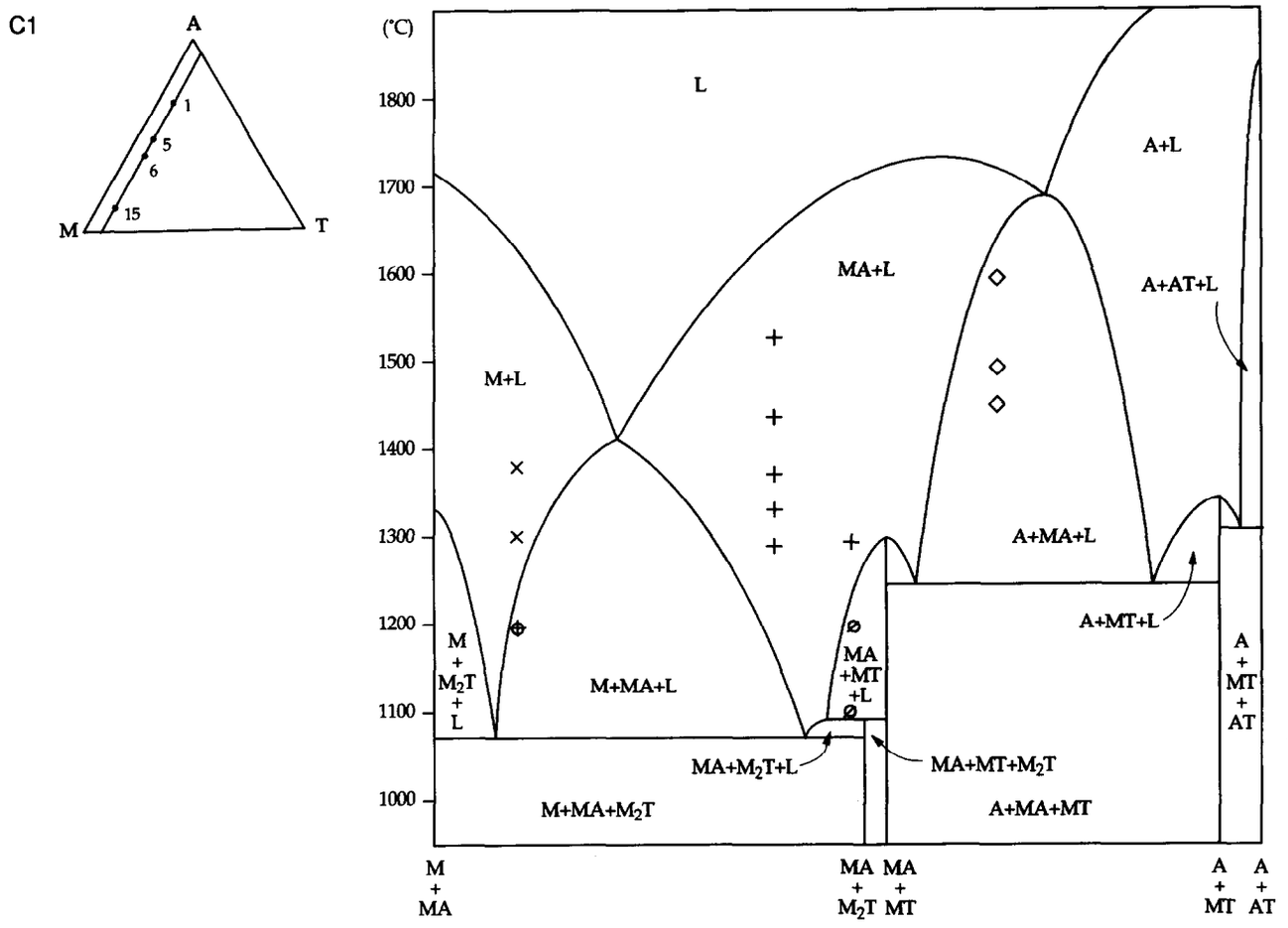

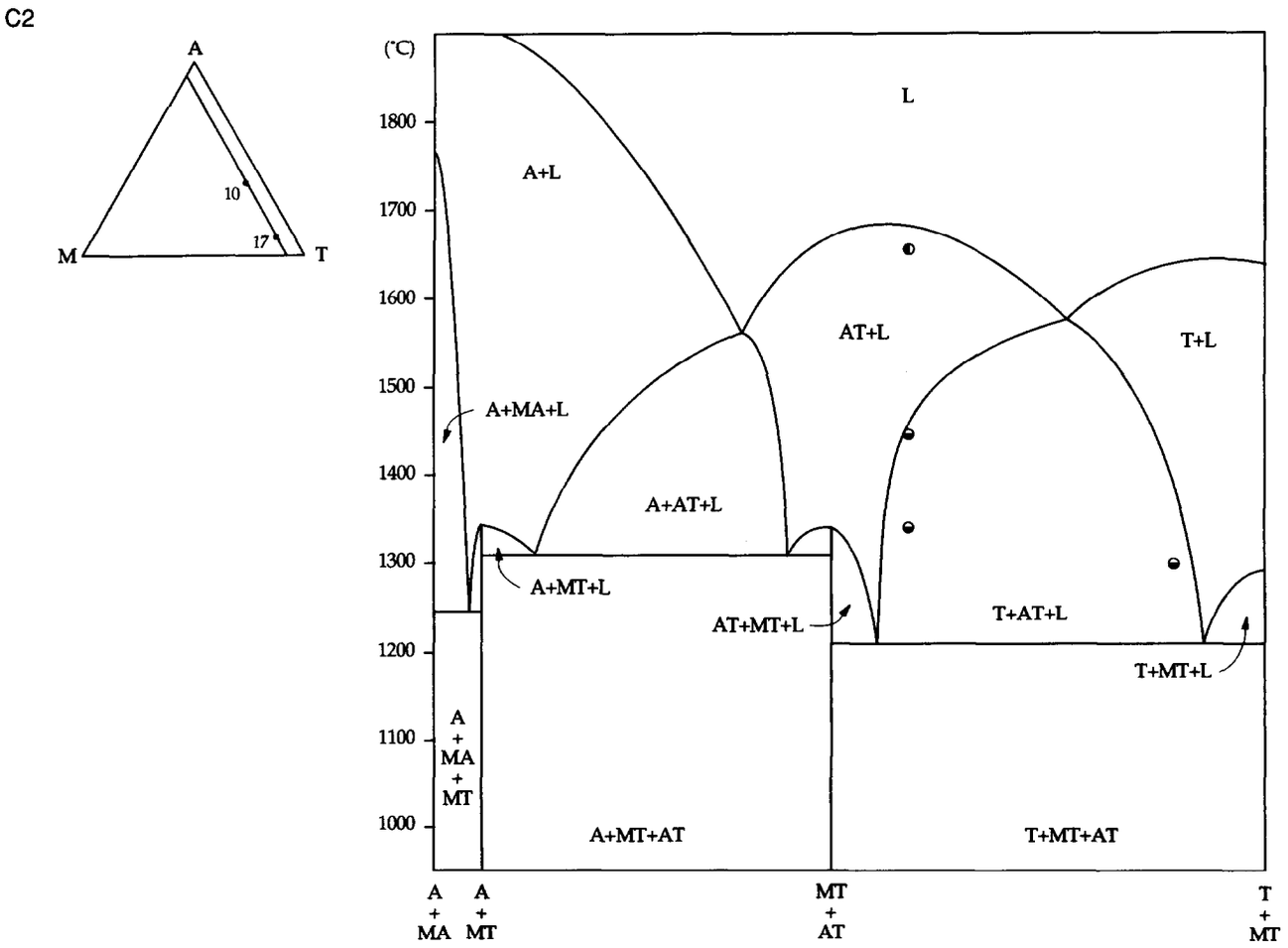

Fig. 4. Continued

the ternary invariant points had to be chosen and worked with. For each of these working hypotheses, isoplethal sections similar to those in Fig. 4 were constructed. When a conflict between the phase fields in the isoplethal sections and the experimental data was found, the location and/or character of the ternary invariant points (and the boundary lines connecting them) was changed in order to resolve the conflict. Several such iterations were needed until the final version of the isoplethal sections, presented in Fig. 4, was reached.

From them and the relevant information extracted from the binary systems,[5] Fig. 5 was constructed. Shown in the diagram are the composition points mentioned in Table 1 and the corresponding primary crystallization paths. In this diagram, the location of all the liquid isotherms and the invariant points are but educated guesses, to suit the experimental results obtained.

4 Implications for the Low-Temperature Sintering of Alumina

The ternary system Al_2O_3–TiO_2–MnO is a rather good example of how the combination of three refractory components can produce low-temperature liquid phases. From the three binary systems that compose the ternary Al_2O_3–TiO_2–MnO, only the liquid phases in the binary TiO_2–MnO can be considered as low-temperature ones. Thus, any low-temperature liquidus region within the ternary was expected to lie close to this binary. What could not have been guessed was the extension (and flatness) of the low-temperature liquidus plateau at about 1300°C, occupying most of the central region of the ternary, bordered by sharp rising liquidus surfaces towards the high-temperature binaries Al_2O_3–MnO and Al_2O_3–TiO_2. In fact, the results of the present work suggest that there might be a scant 100°C decrease in liquidus temperature over a composition range of roughly 40% in alumina.

Given the low solid solubility of TiO_2 and MnO in alumina reported by various authors, particularly at low temperatures,[3] the sintering-aid effect of these oxides would mostly be accomplished by a liquid-phase mechanism, noticeable at temperatures above 1300°C. Since the low-temperature liquidus plateau is roughly circular and located almost symmetrically in relation to the Al_2O_3–MnO and Al_2O_3–TiO_2 binaries, it is no surprise that equal amounts of manganese and titanium oxides are the most effective combination in lowering the sintering temperature of alumina. Also, the amount of liquid phase

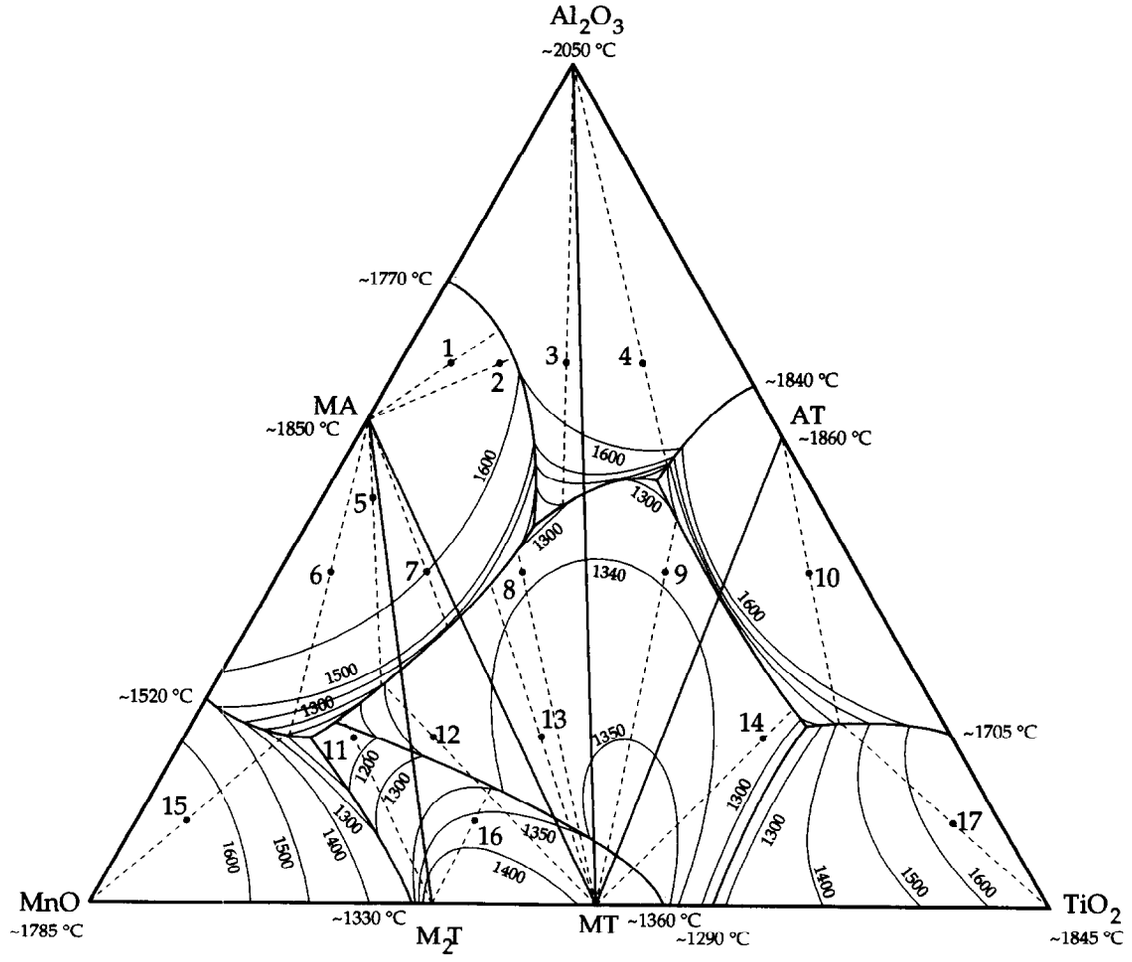

Fig. 5. Tentative phase diagram for the system Al_2O_3–TiO_2–MnO. The locations of all the liquid isotherms and the invariant points are but educated guesses, to suit the information extracted from the binary systems[5] and the experimental results obtained.

formed depends on the proximity of the eutectic valley to the alumina corner: the closer the valley, the larger the amount of liquid. This explains why that particular combination is an effective sintering aid even when present in such small amounts.

Another feature to note is the steepness of the liquidus surface towards the alumina corner and away from the central region. This implies that the quantity of liquid needed to aid sintering can be chosen carefully by selecting the correct composition; the quantity of liquid will then be relatively constant for a wide span of temperatures. This gives a highly convenient system from the point of view of manufacturing in precisely the same way that the liquid immiscibility plateau in the lime–silica system explains the special aptitude of lime as additive in the manufacture of silica bricks or that the silica viscosity makes the manufacturing of porcelains relatively forgiving. A quick calculation using the lever rule shows that 4% of the mixed oxides produce a quantity of liquid that varies very little with temperature, as shown below:

Temperature(°C)	1200	1250	1300	1400	1500
%Liquid phase	6·3	7·0	7·2	7·7	7·9

5 Conclusions

Earlier research work[1–3] showed that non-reactive alumina powders could be sintered at temperatures below 1400°C using combinations of titanium and manganese oxides as sintering aids. Phase equilibrium research work carried out with selected compositions in the system Al_2O_3–TiO_2–MnO, in air, led to the construction of a plausible version of its phase diagram. The tentative diagram shows that in the composition range for low-temperature sinterable aluminas (containing sintering aids), initial melting occurs below 1300°C and sintering is assisted by a liquid phase as proposed by the earlier authors. In this diagram, the location of the liquid isotherms and the invariant points are educated guesses and extensive experimental work would be needed to establish their exact location.

Acknowledgements

The authors wish to thank C. M. Sá from CEMUP, Portugal, for the SEM work carried out. The present work was partially funded by INIC, Portugal.

References

1. Cutler, I. B., Bradshaw, C., Christensen, C. J. & Hyatt, E. P., Sintering of alumina at temperatures of 1400°C and below. *J. Am. Ceram. Soc.*, **40**[4] (1957) 134–139.
2. Kostic, E., Kis, S. & Boskovic, S., Liquid phase sintering of alumina. *Powder Metall. Int.*, **19**[4] (1987) 41–43.
3. Filbri, J. W., Schram, H. L. & Sinnema, S., Sintering of porous alumina using MnO and TiO_2. In *Fourth EURO CERAMICS, Vol. 2*, ed. C. Galassi. Faenza Editrice SpA, 1995, pp., 257–264.
4. Oliveira, V. A. G. & Brett, N. H., Phase equilibria in the system MgO–Mn_2O_3–MnO–$CaSiO_3$ in air. *J. de Phys.*, **47**[2] (1986) Cl–453–459.
5. Levin, E. M., Robbins, C. R. & McMurdie, H. F., In *Phase Diagrams for Ceramists*, ed. M. K. Reser. The American Ceramic Soc., Columbus, OH, 1974, Figs 277, 316 and 4376.
6. Greca, M. C., Emiliano, J. V. & Segadães, A. M., Revised phase equilibrium relationships in the system Al_2O_3–ZrO_2–SiO_2. *J. Eur. Ceram. Soc.*, **9** (1992) 271–283.
7. Thomas, H. A. J. & Stevens, R., Aluminium titanate—a literature review, Part 1: Microcracking phenomena. *Br. Ceram. Trans. J.*, **88** (1989) 144–151.
8. Thomas, H. A. J. & Stevens, R., Aluminium titanate —a literature review, Part 2: Engineering properties and thermal stability. *Br. Ceram. Trans. J.*, **88** (1989) 184–190.
9. Thomas, H. A. J. & Stevens, R., Aluminium titanate —a literature review, Part 3: Preparation of powders. *Br. Ceram. Trans. J.*, **88** (1989) 229–233.
10. Moreira, M. C., Segadães, A. M., Salvini, V., Mariano, W. A. & Morelli, M. R., Relações de compatibilidade no sistema Al_2O_3–TiO_2–MnO e a sua relevância na sinterização da alumina baixas temperaturas. *Cerâmica (São Paulo)*, **34**[227] (1988) 184–188.

Journal of the European Ceramic Society **16** (1996) 1099–1106

PII: S0955-2219(96)00031-6
0955-2219/96/$15.00

Influence of the Oxygen Pressure on the Chemical State of Yttrium in Polycrystalline α-Alumina. Relation with Microstructure and Mechanical Toughness

M. K. Loudjani & C. Haut

Laboratoire de Métallurgie Structurale, CNRS URA 1107, bât.413, Université Paris XI, 91405 Orsay, France

(Received 15 November 1995; revised version received 16 January1996; accepted 23 January 1996)

Abstract

The influence of yttrium on the microstructure and toughness of α-alumina is studied as a function of oxygen partial pressure and chemical state of the doping element. For doping amounts higher than 0·03 mol% of Y_2O_3, $Y_3Al_5O_{12}$ garnet precipitates and the alumina grain size is then limited by such a precipitation along grain boundaries. For doping amounts lower than or equal to 0·03 mol% of Y_2O_3, yttrium ions are in solid solution as defect complexes of the type $(2Y'_{Al} + mV_O^{\cdot\cdot} + nO_i'')^{2(m-n)\cdot}$ and segregates along grain boundaries. The stability of the defect complexes is promoted by low oxygen pressures and the grain size is limited by the yttrium segregation along grain boundaries. At high oxygen pressures, the yttrium solubility decreases and an enrichment in yttrium is observed at the sample surface. Simultaneously, an abnormal alumina grain growth appears. The alumina toughness, estimated by indentation, is improved by the presence of defect complexes at low oxygen pressures while the $Y_3Al_5O_{12}$ garnet precipitates increase the alumina brittleness.

Nous avons étudié le rôle de l'yttrium sur la microstructure et sur la ténacité de l'alumine-α en relation avec la pression partielle d'oxygène et l'état chimique du dopant. Pour des teneurs en dopant plus grandes que 0,03% mol. Y_2O_3, l'yttrium précipite sous forme $Y_2Al_5O_{12}$, la taille de grains est alors limitée par la précipitation de cette phase aux joints de grains. Pour des teneurs ≤ 0,03% mol. Y_2O_3 l'yttrium est en solution solide et ségrège aux joints de grains. Dans cet état l'yttrium forme des défauts complexes du type $(2Y'_{Al} + mV_O^{\cdot\cdot} + nO_i'')^{2(m-n)\cdot}$ dont la stabilité est favorisée par les faibles pressions partielles d'oxygène. Dans ce cas, la taille de grains et leur grossissement anormal sont limités par la ségrégation de l'yttrium aux joints de grains. Les fortes pressions d'oxygène au contraire diminuent la solubilité de l'yttrium ce qui induit alors, après recuit un énrichissement de la surface des echantillons en yttrium provenant du coeur du matériau et un grossissement anormal des grains d'alumine. La ténacité de l'alumine a été évaluée par indentation: La ténacité de l'alumine est légèrement améliorée en présence de complexes de défauts introduits aux basses pressions d'oxygène alors que la phase durcissante $Y_3Al_5O_{12}$ rend le matériau plus fragile.

1 Introduction

Alumina is one of the most stoichiometric oxides and both its transport properties and its microstructure are strongly dependent on the amount of impurities present.

In the case of an intrinsic ceramic, the thermodynamic factors responsible for the creation of point defects during its elaboration are the temperature and the oxygen pressure. At high oxygen partial pressure, the promoted point defects consists of aluminium vacancies ($[V_{Al}'''] \propto (pO_2)^{3/16}$) and oxygen interstitials ($[O_i''] \propto (pO_2)^{1/6}$) whereas, at low oxygen pressure, the promoted point defects are the oxygen vacancies ($[V_O^{\cdot\cdot}] \propto (pO_2)^{-1/6}$) and the aluminium interstitials ($[Al_i^{\cdot\cdot\cdot}] \propto (pO_2)^{-3/16}$).

In the case of an extrinsic alumina doped by yttrium, studies by EXAFS of the local disorder around yttrium atoms and by electron diffraction[1–3] indicate that for yttrium contents greater than 300 ppm mol Y_2O_3, most of the yttrium is precipitated as yttrogarnet phase $Y_3Al_5O_{12}$, while for yttrium contents less than or equal to 300 ppm mol Y_2O_3, yttrium atoms are in solid solution in the polycrystalline alumina samples. This is shown schematically in Figs 1(a) and (b) where it appears that the Fourier

transformed spectra of 1 or 0·1 mol% Y_2O_3-doped Al_2O_3 are close to that of $Y_3Al_5O_{12}$ [Fig. 1(a)] while the spectrum related to 300 ppm mol Y_2O_3-doped Al_2O_3 is close to that of Al_2O_3 [Fig. 1(b)], indicating that yttrium ions (Y^{3+}) in solid solution are localized on cationic sites. The number of first neighbouring atoms around yttrium on aluminium sites ($N_1 \approx 3$, see Table 1) is lower than that around aluminium ions in alumina ($N_1 \approx 6$) or that in standard compounds such as Y_2O_3 and $Y_3Al_5O_{12}$, for which the coordination is equal to 6 or 8, respectively. Due to their great size, yttrium ions in solid solution induce oxygen lattice distortions:[1-3] around each yttrium ion 'm' oxygen vacancies ($V_O^{\cdot\cdot}$) are created

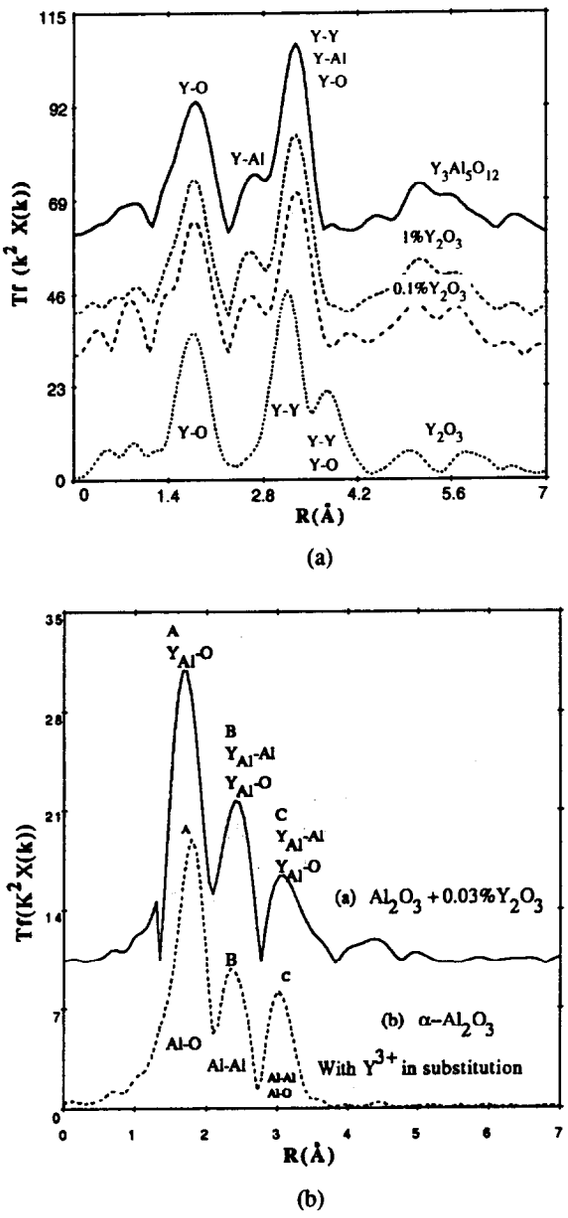

Fig. 1. (a) Fourier transform spectra (uncorrected for phase shift) of standards: $Y_3Al_5O_{12}$, Y_2O_3 and highly doped α-aluminas (1 mol% of Y_2O_3). (b) Fourier transform spectrum calculated for α-Al_2O_3 with dissolved yttrium ions located on aluminium sites (taking into account the size effect of yttrium ions with the creation of oxygen vacancies in the first shell of oxygen neighbouring species) and experimental spectrum for the 0·03 mol% Y_2O_3-doped α-alumina.

Table 1. Values of the parameters R_j(Å) and N_j for undoped alumina, and determined from the A and B peaks for the 0·03 mol% Y_2O_3 polycrystalline doped alumina [Fig. 1(b)]. R_j(Å) is the distance between neighbouring atoms and N_j is the number of neighbouring atoms

Sample	*Shell*	$\overline{R_j(Å)}$	$\overline{N_j}$
Al_2O_3	Y_{Al}–O	1·912	6
	Y_{Al}–Al	2·755	4
	Y_{Al}–Al	3·403	9
	Y_{Al}–O	3·405	9
0·03 mol% Y_2O_3	<Y–O>1	2·325 ± 0·08	2·7 ± 0·5
	<Y–Al>2	2·741 ± 0·08	2·6 ± 1
	<Y–O>3	2·845 ± 0.08	1·7 ± 1

with $m \approx 2{\cdot}7$, and 'n' oxygen interstitials appear in a second intermediate shell with $n \approx 1{\cdot}7$. This corresponds to the creation of defect complexes which can be written as:

$$3O_O + 2Y_{Al}^{x} \Leftrightarrow (2Y_{Al}^{x} + mV_O^{\cdot\cdot} + nO_i'')^{2(m-n)\cdot} + \frac{3-n}{2} O_2 + 2(m-n)e' \text{ with } m > n \quad (1)$$

with $m > n$. Thus, the concentration of the defect complex $(2Y_{Al}^{x} + mV_O^{\cdot\cdot} + nO_i'')^{2(m-n)\cdot}$ depends on the oxygen pressure.

Observations and analyses by transmission electron microscopy have suggested that most of the yttrium is segregated along grain boundaries.[1,3] Segregation phenomena and the amount and nature of the point defects in a ceramic such as alumina are very important for most of its properties, particularly for transport and mechanical properties or for the protective character of alumina scales developed on former alumina alloys. Thus it is important to relate the microscopic defects (point defects, segregation, etc.) to the macroscopic properties of alumina. In the first part of this work, the effect of yttrium doping on the microstructure of α-alumina will be presented, and the influence of oxygen pressure on the amount and nature of the point defects and on segregation phenomena will be analysed. In the second part, the evolution of alumina toughness as a function of the microstructure and the chemical state of yttrium will be presented and discussed.

2 Experimental Procedure

2.1 Materials and heat treatments

Several α-aluminas, either without or with yttrium doping corresponding to 1, 0·1 and 0·03 mol% Y_2O_3,[3,4] were prepared by powder sintering carried out under secondary vacuum in a graphitic crucible ($pO_2 \approx 10^{-13}$ atm).[5] The microstructural observations were made on five types of sample: as-sintered samples ($pO_2 \approx 10^{-13}$ atm); and samples heat-treated

at either 1400 or 1650°C for times varying between 15 min to 75 h, then air-quenched.

The heat treatments were performed either in air in an alumina crucible or at low oxygen pressure via CO gas ($pO_2 \approx 10^{-16}$ atm at 1650°C). In the case of heat treatments in a reducing atmosphere, in order to avoid carbon contamination the samples were placed first in a alumina crucible which, in turn, was placed in a closed graphitic crucible.

2.2 Microstructural observations and image analyses

The sample microstructure was observed by scanning electron microscopy (SEM) with backscattered electrons on a digitalized Stereoscan Leica 260 SEM equipped with an energy-dispersive X-ray analysis (EDAX) system. Image treatment was conducted via OPTILAB software from Graftek. It is first necessary to reproduce the sample surface microstructure obtained from backscattered electrons on tracing paper. Such plots are then transformed via an optical camera into binary images which are then transferred to the computer to be analysed.

Complementary data were obtained by chemical analyses performed on thin foils by transmission electron microscopy (TEM) equipped with scanning tunnelling electron microscopy (STEM) device and an EXDS system. Such a technique was used especially for the α-alumina doped with 0·03 mol% Y_2O_3.

2.3 Toughness measurements

In order to characterize the ceramic toughness and the effect of yttrium doping, indentation tests were performed in macrohardness mode with a load of 1 kg and in microhardness mode with a load of 200 g, using a Vickers indentor. This technique, first proposed by Evans and Charles,[6] allows a quick determination of the toughness of small samples of ceramic materials.[6–9] In the conditions used, the imprints have an average size of about 30 μm with the macrohardness mode and 15 μm with the microhardness mode. The relations enabling the Vickers hardness H_v and the toughness K to be calculated are:

$$H_v = 1{\cdot}8544 \frac{Pg}{(2a)^2}$$

and

$$K = 0{\cdot}014 \left(\frac{E}{H_v}\right)^{1/2} \frac{Pg}{c^{3/2}}$$

where P is the applied load, g is the acceleration due to gravity, $2a$ is the imprint diameter, E is the Young's modulus of the material and $2c$ is the radial crack length. Measurement of the crack length ($2c$) and the imprint size ($2a$) was performed by optical and scanning electron microscopies.

3 Results and Discussion

3.1 Morphology of samples heat-treated in air at 1400 or 1650°C

Grain size distribution plots were established on a population of about 1300 grains at 1400 and 1650°C. As an example, Fig. 3 shows the grain size distribution as a function of the amount of yttrium dopant (0, 0·03 and 1 mol% of Y_2O_3) and duration of the heat treatment (1, 24 and 72 h) at 1400°C, in air. Simultaneously, observations of the sample surface by SEM (Fig. 4) indicate that, whatever the temperature and duration of the heat treatment in air, the grain size of highly doped alumina samples (1 mol% of Y_2O_3) is smaller than that of other alumina samples (undoped or 0·03 mol% of Y_2O_3). In the highly doped samples, the grain size and the distribution of the precipitated second phase ($Y_3Al_5O_{12}$) are homogeneous on all the sample, whatever the heat treatment temperature [Fig. 4(a)]. In contrast, for the weakly doped samples [particularly for 0·03 mol% of Y_2O_3, Fig. 4(b)], there is heterogeneous grain size distribution with an abnormal grain growth. Such an analysis indicates that the amount of yttrium necessary to avoid the abnormal grain growth during heat treatments in air at high temperature is around 1 mol% Y_2O_3.

The results of a kinetic study on the surface segregation of yttrium associated with precipitation of the yttrogarnet phase $Y_3Al_5O_{12}$ at 1400 and 1650°C are collected in Fig. 5 for the density of precipitates according to their surfaces and in Fig. 6 for the microstructure in the case of α-alumina doped with 0·03 mol% Y_2O_3 as an example. Whatever the temperature and the yttrium content, the amount of $Y_3Al_5O_{12}$ phase at the alumina surface increases with time. This indicates that a dynamic segregation occurring during cooling can be excluded and that the precipitation of yttrogarnet results from an equilibrium segregation. The relative proportion of the $Y_3Al_5O_{12}$ phase localized along grain boundaries

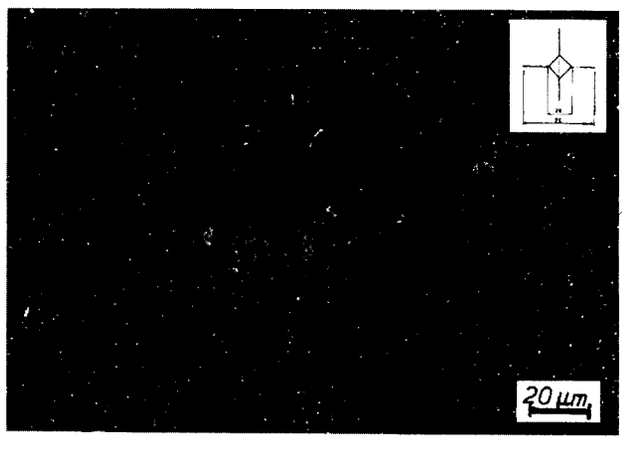

Fig. 2. Micrograph and scheme of Vickers indentation on doped α-Al_2O_3 (1 mol% Y_2O_3), showing the radial crack extension.

and in the bulk of the grains (Fig. 5) varies with time, and the ratio $[Y_3Al_5O_{12}]_{gb}/[Y_3Al_5O_{12}]_{bulk}$ decreases with heat treatment duration from about 8 after 1 h to about 2 after 72 h of treatment. For a treatment at 1650°C and for the same duration (72 h), the amount of $Y_3Al_5O_{12}$ precipitates along grain boundaries is

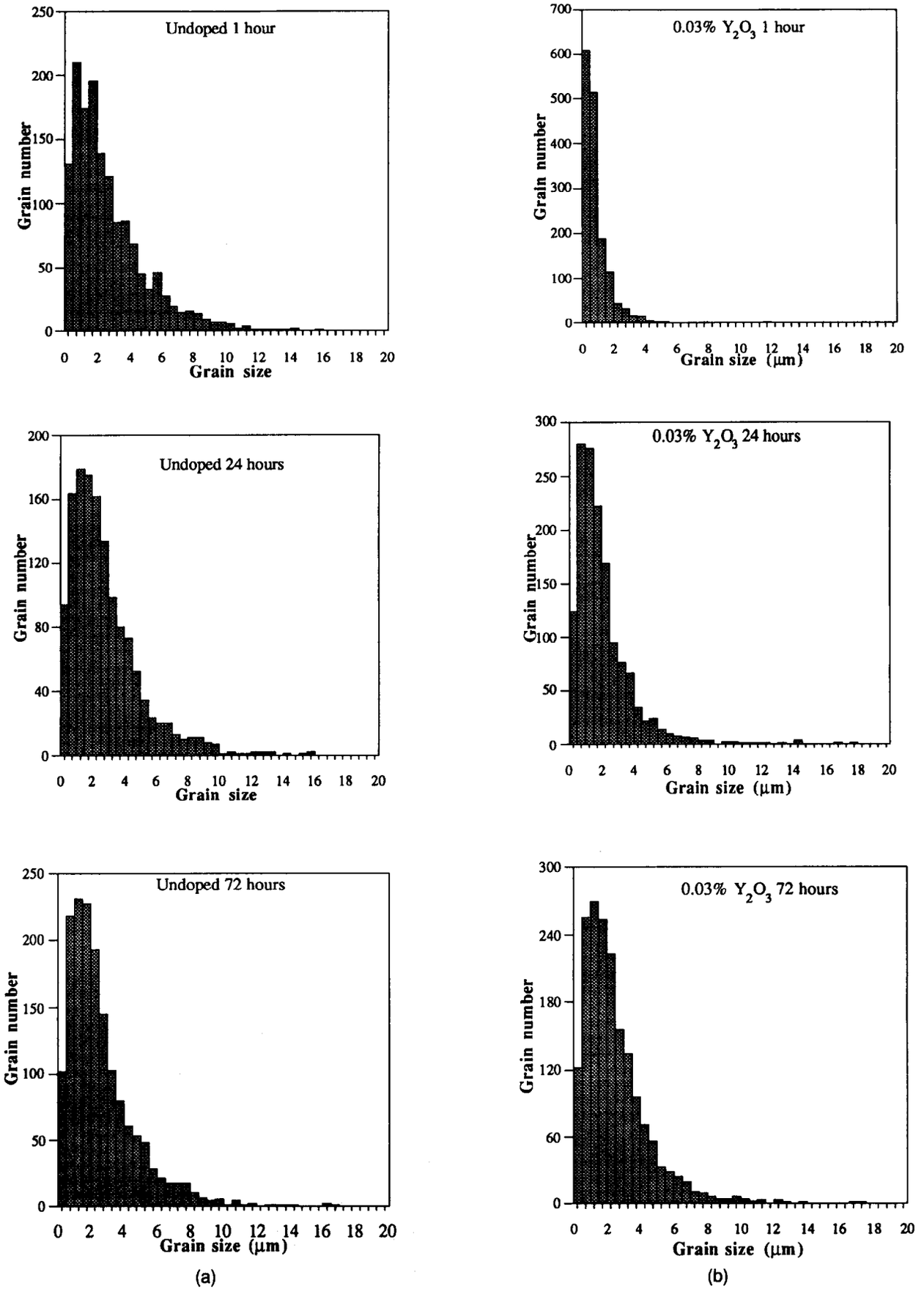

Fig. 3. Distribution of the grain size of undoped alumina (a) 300 ppm yttrium-doped alumina (b) and 1 mol% Y_2O_3-doped alumina (c) samples as a function of the heat treatment duration at 1400°C in air.

three times greater than the amount of yttrogarnet precipitates in the bulk of the grains due to the grain size variation with temperature.

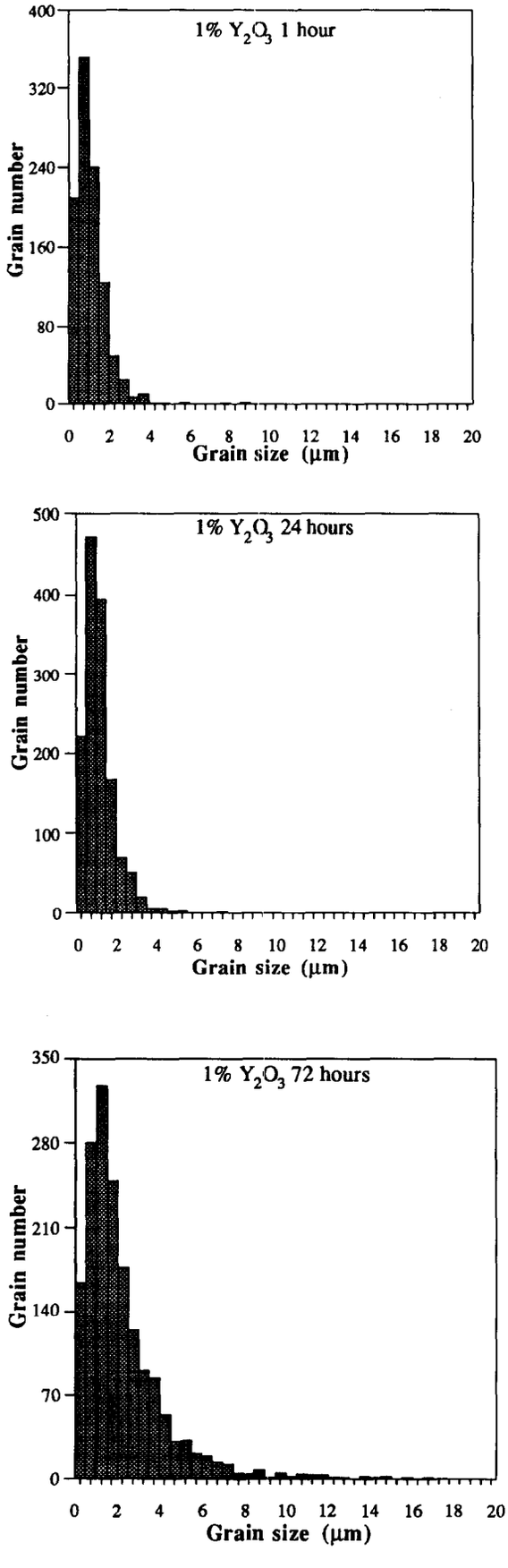

(c)

Fig 3. Continued

3.2 Influence of oxygen partial pressure on the microstructure of α-alumina doped with 0.03 mol% Y_2O_3

Chemical analyses of thin foils by TEM were performed on alumina samples doped with 0·03 mol% Y_2O_3. On as-sintered samples (i.e. elaborated at a low oxygen pressure, $pO_2 \approx 10^{-13}$ atm, see section 2.1), the analyses show an important increase of the yttrium concentration towards grain boundaries (Fig. 6). The amount of yttrium along grain boundaries C_{gb} is greater than the amount of yttrium in the bulk C_b, and the concentration ratio $C_{gb}/C_b \approx 50$. However, on samples heat-treated in air at 1650°C, no yttrium segregation or precipitation is observed along grain boundaries.

SEM observations of weakly doped samples (0·03 mol% Y_2O_3) heat-treated in a reducing atmosphere of CO can be compared with the microstructures obtained in air (compare Figs 4(b) and 7). The micrographs indicate that the morphology of the grain boundaries and the grain size are different, depending on the oxygen partial pressure during heat treatment. For the samples heat-treated in air [Fig. 4(b)] a bimodal distribution of the grain size is

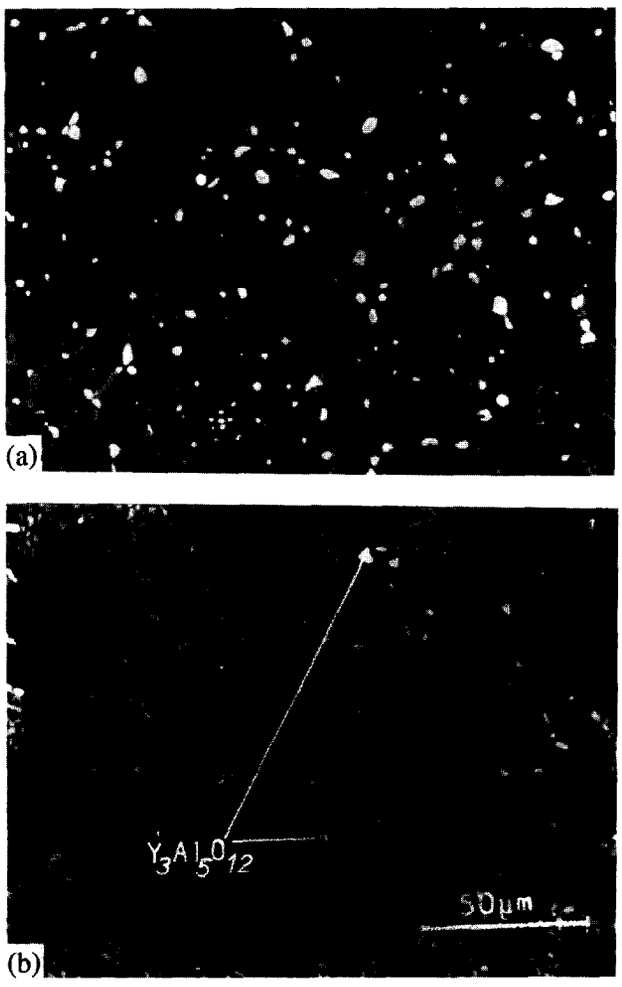

Fig. 4. Influence of yttrium on the microstructure of samples heat-treated for 24 h at 1650°C in air. White particles are $Y_3Al_5O_{12}$ (arrow), average size = 1·8–2·6 μm. (a) 1 mol% of Y_2O_3-doped sample; (b) 0.03 mol% Y_2O_3-doped sample.

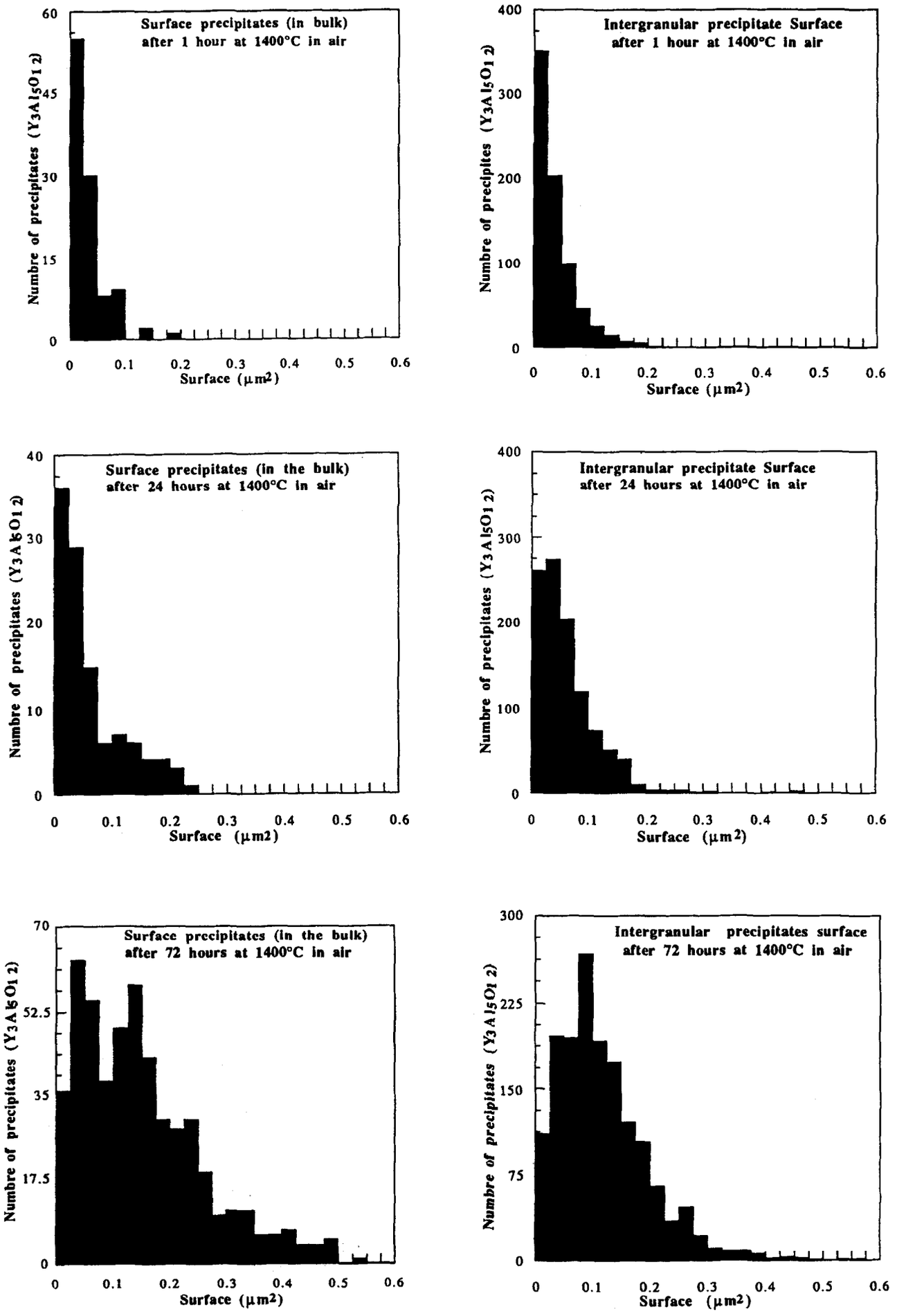

Fig. 5. Density of the yttrogarnet precipitates according to their surface versus the duration of the heat treatment in air at 1400°C. (a) Precipitates localized along grain boundaries; (b) precipitates localized in the bulk of the grains.

observed: some of the grains have a small size (1–5 μm) while others can reach 140 μm (abnormal growth). Simultaneously, the amount of $Y_3Al_5O_{12}$ precipitates at the sample surface increases with heat treatment duration (cf. Fig. 6). In contrast, for samples heat-treated in CO (Fig. 7) the number of garnet precipitates at the sample surface is negligible and the grain size distribution is homogeneous: most of the grains have a size between 4 and 15 μm. These observations indicate that the yttrium solubility in the bulk of the α-alumina samples is greater at low oxygen pressure than at high pO_2 The yttrium segregation along grain boundaries (cf. Fig. 6) hinders both the segregation at the surface and the abnormal grain growth which are observed after heat treatment in air. This means that the yttrium draining from the sample bulk towards the sample surface during heat treatment in air is due to the driving force related to the concentration gradient of point defects such as oxygen vacancies or interstitials ($V_O^{\cdot\cdot}$, O_i'') from the bulk to the surface:[10–13]

$$F_C \propto kT\frac{\Delta C}{C}$$

The diffusion of these defects is the origin of the yttrium segregation associated with the precipitation of $Y_3Al_5O_{12}$ at the sample surface.

3.3 Toughness

The variation of the toughness of the samples as a function of the yttrium content is reported in Fig. 8 for as-sintered samples [Fig. 8(a)] and for samples heat-treated for 24 h at 1400°C in air [Fig. 8(b)]. The average values of toughness obtained in this work are of the same order of magnitude as those given by Mckinney *et al.*[9] for polycrystalline commercial alumina but somewhat higher than those determined on single crystals by Evans and Charles.[6] In our case, it can be observed that heat treatments

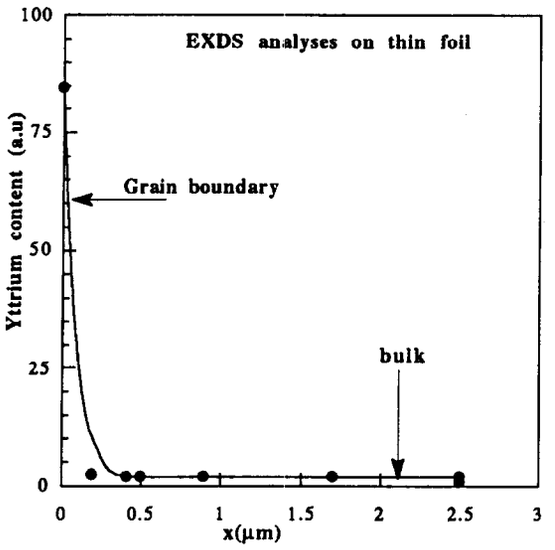

Fig. 6. STEM analyses on thin foils of as-sintered α-alumina doped with 0·03 mol% of Y_2O_3, showing the evolution of the $L\alpha_Y$ X-ray emission from a grain boundary to the bulk.

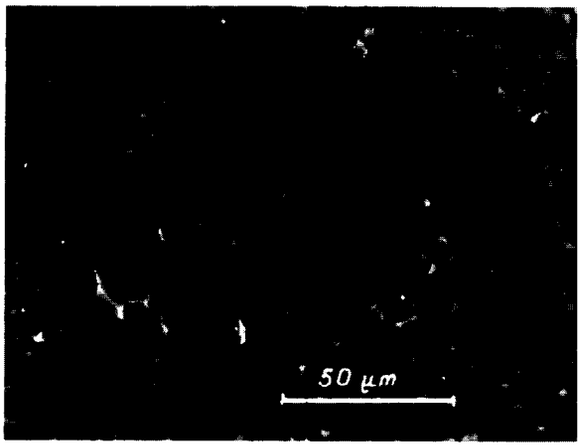

Fig. 7. Microstructure of 0·03 mol% Y_2O_3-doped alumina heat-treated in a CO atmosphere (in carbon graphite crucible) at 1650°C for 24 h.

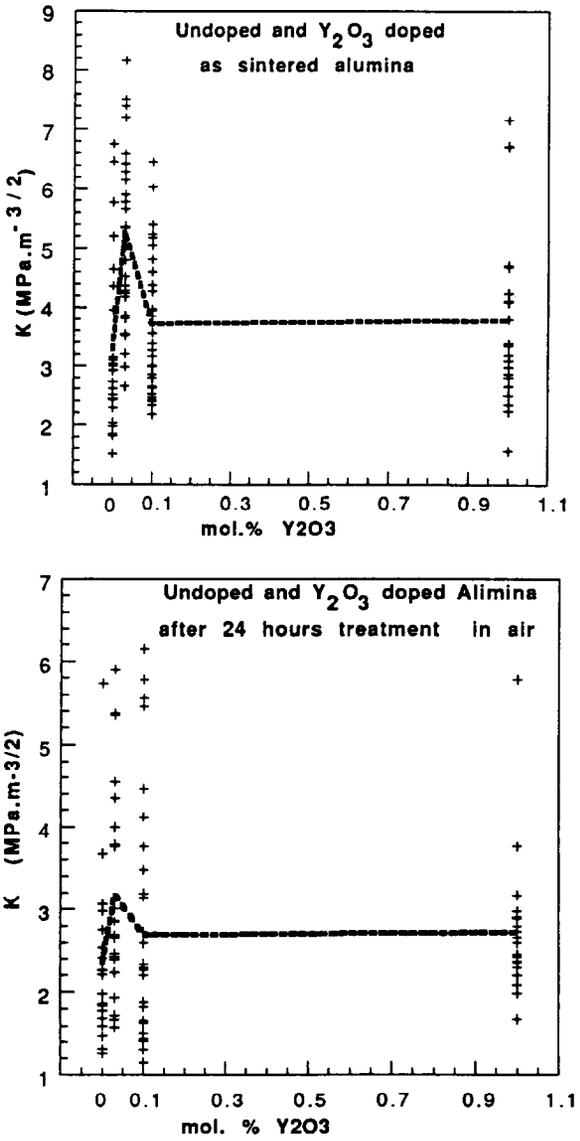

Fig. 8. Variations of toughness as a function of yttrium doping amount. (a) As-sintered samples (treatment in a reducing atmosphere); (b) samples heat-treated in air for 24 h at 1400°C. (+) Experimental points, line represents average value.

in air lead to slightly smaller average toughness values than when the alumina samples are heat-treated in CO atmosphere. Moreover, independent of the atmosphere (air or CO), the toughness variations go through a maximum value for the weakly doped samples (0·03 mol% of Y_2O_3). Thus the toughness seems to be more dependent on the stoichiometry and the microchemistry of the samples (point defects, yttrium grain boundary segregation) than on the alumina macrostructure (grain size, heterogeneous distribution of the garnet precipitates). Indeed, in the case of the as-sintered alumina samples doped with 300 ppm Y_2O_3, yttrium ions in solid solution in the bulk or segregated along grain boundaries (see Fig. 6) lead to the generation of defect complexes according to eqn (1). This type of defect seems to improve the mechanical properties of alumina. After a heat treatment in air, the amount of $Y_3Al_5O_{12}$ precipitates at the sample surface increases significantly and simultaneously a decrease of the toughness is observed whatever the material may be.

4 Conclusion

A study of the microstructure and toughness of polycrystalline α-aluminas doped with various amounts of yttrium and heat-treated either in reducing atmosphere or in air leads to the following results.

(1) In alumina, the amount of yttrium necessary to avoid grain growth of the garnet phase is about 1 mol% of Y_2O_3.
(2) The yttrium solubility increases when the oxygen pressure decreases.
(3) At low oxygen pressure, the abnormal grain growth is less important than at high oxygen pressure. This is related to the yttrium segregation along grain boundaries which is promoted at low pO_2. This phenomenon corresponds to an equilibrium segregation.
(4) The mechanical properties of α-alumina are improved when yttrium is either in solid solution or segregated along grain boundaries. Precipitation of the $Y_3Al_5O_{12}$ phase decreases the alumina toughness, whereas, in contrast, the toughness is improved by the presence of structural defects introduced during the elaboration (point defects, grain boundary segregation).

Acknowledgements

The authors are indebted to A. M. Huntz and P. Carry, Institut de Science des Matériaux, Orsay, for fruitful discussions, to P. Carry for providing sintered aluminas and to S. Parisot for her help with the experimental work.

References

1. Loudjani, M. K., Huntz, A. M. & Cortès, R., Influence of yttrium on microstructure and point defect in α-Al_2O_3. Relation with oxidation. *J. Mater. Sci.*, **28** (1993) 6466–6473.
2. Loudjani, M. K. & Cortès, R., X-ray absorption study of the local structure and the chemical state of yttrium in polycrystalline α-alumina. *J. Eur. Ceram. Soc.*, **13** (1994) 77.
3. Loudjani, M. K., Thèse de Docteur d'Etat, Université Paris XI, Orsay, France, 1992.
4. Loudjani, M. K., Lesage, B. & Huntz, A. M., Influence du dopage et du mode d'élaboration sur la microstructure de l'alumine-α polycristalline — relation avec les propriétés de transport. *Industrie Céramique*, **801** (1986) 53.
5. Sato, E. & Carry, C., Sintering and yttrium grain boundary segregation in sub-micron size alumina. *J. de Phys. IV, Colloque C7*, **3** (1993) 1335.
6. Evans, A. G. & Charles E. A., Fracture toughness determinations by indentation. *J. Am. Ceram. Soc.*, **59**[7] (1976) 371.
7. Lawn, B. R., Evans, A. G. & Marshall D. B., Elastic plastic indentation damage in ceramics. The median radial cracks system. *J. Am. Ceram. Soc.*, **63**[9] (1980) 574.
8. Cook, R. F. & Pharr, G. M., Direct observation and analysis of indentation cracking in glasses and ceramics. *J. Am. Ceram. Soc.*, **73**[4] (1990) 787.
9. Mckinney, K. R., Chaskelis, H. H. & Freiman, S. W., Prediction of flaw sizes from acoustics emission measurement in ceramics. *J. Am. Ceram. Soc.*, **59**[7] (1976) 369.
10. Mackrodt, W. C., The calculated equilibruim segregation of Fe^{3+}, Y^{3+}, and La^{3+} at the low index surfaces of α-Al_2O_3. *Adv. Ceram.*, **23** (1987) 247.
11. Mackrodt, W. C. & Tasker, P. W., Segregation isotherms at the surfaces of oxides. *J. Am. Ceram. Soc.*, **72**[9] (1989) 1576.
12. Petot-Ervas, G. & Petot, C., Point defects and mass transport under a thermodynamic potential gradient, *J. Phys. Chem. Solids*, **51** (1990) 901.
13. Monceau, D., Petot-Ervas, G. & Petot, C., Kinetic demixing profile calculation in oxide solid solutions under chemical potential gradient. *Solid State Ionics*, **45**, (1990), 231.

Journal of the European Ceramic Society **16** (1996) 1107–1114

PII: S0955-2219(96)00038-6
0955-2219/96/$15.00

Indentation Fracture Toughness and Surface Flaw Analysis of Sintered Alumina/SiC Nanocomposites

C. C. Anya & S. G. Roberts*

University of Oxford, Department of Materials, Parks Road, Oxford OX1 3PH, UK

(Received 25 October 1995; revised version received 16 January 1996; accepted 23 January 1996)

Abstract

The fracture toughness (K_{Ic}) of pressureless-sintered monolithic α-alumina and its composites with 5, 10 and 15 vol% SiC nano-sized particles was investigated using Vickers indentation and a new Hertzian (ball) indentation technique. Both methods showed that the fracture toughness of the composites is better than that of alumina, although the results from the Vickers indentations were complicated by a change in crack geometry from median/radial (alumina) to Palmqvist (composites) An analysis of the number and size of surface flaws using the Hertzian test indicates that, for the same polishing treatment, the composites have a better surface finish. © 1996 Elsevier Science Limited.

Introduction

Small additions of nano-sized SiC particles to alumina (to produce 'nanocomposites') enhance its bend strength, compared with 'pure' alumina of the same grain size.[1,2] The mechanisms behind this enhancement of the mechanical properties remain unclear. Possible mechanisms could be:

(1) an increase in fracture toughness;
(2) a reduction in the number and size of processing-induced flaws; and
(3) an improved response to grinding and polishing, resulting in a reduction in the number and size of polishing-induced flaws.

While increases in strength as high as 186%[1] and 36%[2] have been reported for unannealed 5 vol% SiC–alumina composite (≥99.5% theoretical density), only modest increases in toughness have been reported. For instance, using the Vickers indentation technique, Zhao *et al.*[2] reported a maximum increase in K_{Ic} of 24% for this 5 vol% SiC–alumina 'nanocomposite'. (A similar sample, sintered to 98·2% of its theoretical density, showed a 7% reduction in K_{Ic}.[2])

* To whom correspondence should be addressed.

Use of Vickers indentation methods to determine fracture toughness can be problematic. Ponton and Rawlings[3] list 15 formulae for deriving K_{Ic} from measurements of surface crack lengths (c, measured as half the total crack span) around indentations made with a load P, in a material with Young's modulus E and hardness H, assuming that the crack geometry is of the 'median/radial' type. These are generally of the forms:

$$K_{Ic} = \alpha (E/H)^n (P/c^{3/2}) \quad (1)$$

or

$$K_{Ic} = \beta (P/c^{3/2}) \quad (2)$$

with varying pre-factors α and β depending on the assumptions that have been made about the indentation stress field, and n equal or close to 0·5. Given the very complex nature of deformation beneath a sharp indenter, especially in brittle materials, it is not easy to justify the choice of one variant of these formulae over the others, although versions where the hardness and elastic modulus of the material are included [eqn (1)] are probably preferable. Thus this method should be regarded with suspicion if *absolute* values for the fracture toughness are derived. Even if the Vickers indentation method is used simply for comparative studies of materials, the possibility that the crack geometry could change from one material to another should be considered. In eqns (1) and (2) the cracks are generally assumed to be 'half-penny' shaped (Fig. 1) — and this is not always, or even often, the case.[4] A further possibility is that the geometry of the crack may change more radically to the 'Palmqvist' type (Fig. 1), typically found in tougher ceramics such as WC–Co. Again, several formulae[3] have been produced relating K_{Ic} to crack length (l, the surface crack length on one side of the indentation), load P, and the indentation's semi-diagonal length a. They are generally of the form:

$$K_{Ic} = \gamma (E/H)^\delta P/(al^{1/2}) \quad (3)$$

In previous studies of the indentation fracture toughness of nanocomposites,[5] it has generally been assumed the indentation cracks are of the median/

radial type. In this study, we examine this assumption more closely by performing experiments to establish the actual crack shapes.

An alternative method for determining the fracture toughness of brittle materials has recently been established,[6] based on Hertzian indentation. Here a spherical indenter is used, so that the stress field under the indenter is well defined (unlike the case for the sharp indenter used in Vickers tests), and values of K_{Ic} in good agreement with values determined by four-point bend tests are obtained. The method makes use of a full analysis of the Hertzian contact field, in which it was found that even for a badly abraded surface, where a dense population of flaws of all sizes exists, there is always a minimum load needed to cause formation of the characteristic Hertzian 'ring crack'. This minimum load depends only on K_{Ic}, E and ν (Poisson's ratio) of the test material, and on the size of indenting ball used.

The Hertzian test can also be used to determine the size of the surface flaw which, in a given test, results in the formation of a ring crack. Analysis of many such tests (~20 or more) on a sample enables the density (number per unit surface area) of such flaws to be determined.[7]

This study investigates the fracture toughness of pressureless-sintered Al_2O_3–SiC composites by both Vickers and Hertzian indentation methods, and also uses the Hertzian tests to investigate the surface flaw sizes and densities in these materials.

Materials and Experimental Methods

The powders used were α-Al_2O_3 (AES 11c, Sumitomo) and α-SiC (UF-45, Lonza) with average particle sizes of 400 and 200 nm, respectively. Monolithic alumina and three composites with 5, 10 and 15 vol% SiC in an alumina matrix were fabricated. Powders were mixed by attrition milling, and then cold-isostatically pressed to 175 MPa. Materials were then pressureless-sintered at 1560°C for 2 h (alumina) and at 1775°C for 4 h (composites). The materials produced were found to be of ≥99·7% of their theoretical densities. The grain sizes of all materials were 3·5 ± 1·5 μm, though the alumina showed a bimodal grain structure. Full details of the preparation routes will be reported elsewhere.

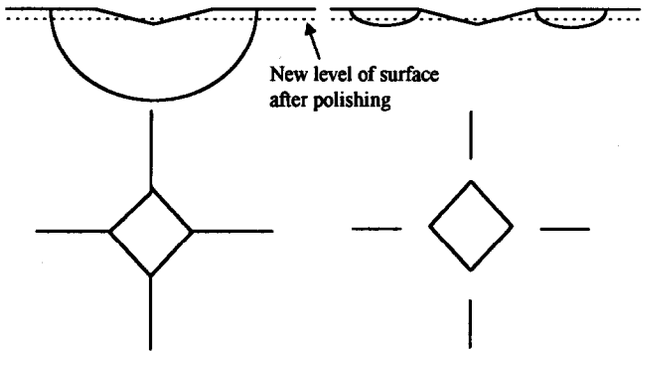

Fig. 1. Schematic representation of median/radial (left) and Palmqvist (right) crack systems. Upper diagrams show cross-sections of the crack systems below the surface, and lower diagrams plan views after polishing to the level shown. The crack trace becomes detached from the indentation for the Palmqvist system.

The Young's modulus E of the materials and their Poisson's ratios were determined by use of a 'Grindosonic' instrument (MK4i). Results are given in Table 1.

Samples of 6 mm thickness were cut from all four types of material using a diamond saw. They were all simultaneously ground and polished to a 3 μm finish. Vickers indentations were carried out at loads of 49, 98, 196 and 294 N. For each load at least five indentations were made, and the average indentation size and crack length parameters were used in analysis. To reduce any possible effects of environmentally assisted cracking, the measurements were always made within 2 h of indentation. Some indented samples were then polished to remove ~5 μm from the surface, to identify the crack geometry as either median/radial or Palmqvist. Analysis of fracture toughness based on these results is discussed later.

The Hertzian indentations were made with a 5 mm diameter alumina ball using a modified 'ET500' testing machine (Engineering Systems, Nottingham, UK). The loads at which ring cracks were formed were detected by acoustic emission. The loads were recorded, and the sizes of the matching ring cracks were measured by optical microscopy using Normarski differential interference contrast to enhance visibility of the ring cracks. Tests were performed on alumina, alumina–5% SiC and alumina–15% SiC composites. The test surfaces were finished with either 3 or 14 μm diamond paste. The 3 μm finish was used to compare the surface finishes produced by a 'good' polish on the various materials, while the 14 μm finish, with larger surface cracks, was used to determine K_{Ic}. Whereas the ring-cracks on the 3 μm polished composite could be observed without any further treatment, the cracks in the 14 μm ground samples required etching with KOH at 400°C, followed by light polishing with 3 μm diamond paste, to render the cracks visible. Ring cracks in monolithic alumina were made more visible by etching in KOH.

Results and Discussion

Vickers indentation

Crack paths

Table 1 gives a summary of the Vickers indentation results. Analysis of the results to give K_{Ic} requires knowledge of the crack type around the indentations.

One method[4] of doing this would be to fit the data of crack length to load: one would expect $c \propto P^{2/3}$ for median/radial cracks [eqns (1) and (2)] or $l \propto P^{1/2}$ for Palmqvist cracks [eqn (3)]. However, the data in Table 1 do not fit either relationship well; no conclusion can be drawn from these data about the active crack types.

Figure 2 shows the results of polishing away the surface of indented samples. The crack system in monolithic alumina is median/radial (cracks are continuous under the indentations), while that of all the composites is of Palmqvist type (cracks are separate wings on either side of the indentations). The continuity of the crack system across the indentation in

Table 1. Vickers indentation results

	Load (N)	*Diagonal* (μm)	*Crack length* (μm)	H *(conv.)* (GPa)	H *(Hamer)* (GPa)	K_{Ic} *(median)* ($\alpha = 0.016$) (MPa $m^{1/2}$)	K_{Ic} *(median)* ($\alpha = 0.022$) (MPa $m^{1/2}$)	K_{Ic} *(Palmqvist)* (MPa $m^{1/2}$)
Alumina	49·1	72·8 ± 0·5	106 ± 10	17·16 ± 0·24	18·51 ± 0·26	**2·14 ± 0·23**	3·06 ± 0·33	4·09 ± 0·28
	98·1	103 ± 2·0	167 ± 8	17·15 ± 0·69	18·49 ± 0·74	**2·25 ± 0·17**	3·22 ± 0·24	4·61 ± 0·30
E = 397·4 ± 3·0 GPa	196·2	150 ± 1·0	249 ± 11	16·17 ± 0·22	17·44 ± 0·23	**2·57 ± 0·15**	3·67 ± 0·22	5·31 ± 0·20
ν = 0·249	294·3	181 ± 1·4	299 ± 13	16·66 ± 0·26	17·97 ± 0·28	**2·88 ± 0·17**	4·11 ± 0·24	5·95 ± 0·24
5% SiC	49·1	69·6 ± 0·7	98 ± 12	18·78 ± 0·38	20·25 ± 041	2·28 ± 0·31	3·25 ± 0·44	**4·31 ± 0·39**
	98·1	99·2 ± 0·3	170 ± 6	18·49 ± 0·11	19·94 ± 0·12	2·16 ± 0·10	3·08 ± 0·15	**4·62 ± 0·13**
E = 399·5 ± 4·0 GPa	196·2	142·2 ± 0·4	260 ± 18	17·99 ± 0·10	19·41 ± 0·11	2·36 ± 0·20	3·38 ± 0·28	**5·26 ± 0·24**
ν = 0·254	294·3	176 ± 0·3	309 ± 30	17·62 ± 0·06	19·00 ± 0·06	2·73 ± 0·30	3·90 ± 0·43	**5·90 ± 0·35**
10% SiC	49·1	69·3 ± 1·00	90 ± 7	18·94 ± 0·56	20·43 ± 0·60	2·52 ± 0·24	3·60 ± 0·34	**4·53 ± 0·32**
	98·1	97 ± 0·5	140 ± 7	19·33 ± 0·20	20·85 ± 0·22	2·68 ± 0·16	3·83 ± 0·23	**5·15 ± 0·19**
E = 407·2 ± 2·0 GPa	196·2	135 ± 1·0	245 ± 15	19·96 ± 0·30	21·53 ± 0·32	2·47 ± 0·19	3·53 ± 0·27	**5·52 ± 0·27**
ν = 0·250	294·3	168 ± 0·5	338 ± 20	19·34 ± 0·12	20·85 ± 0·12	2·40 ± 0·17	3·43 ± 0·25	**5·74 ± 0·35**
15% SiC	49·1	65·8 ± 0·4	83 ± 5	21·01 ± 0·26	22·66 ± 0·28	2·67 ± 0·19	3·82 ± 0·27	**4·78 ± 0·22**
	98·1	95·5 ± 0	124 ± 14	19·95 ± 0·00	21·51 ± 0·00	3·04 ± 0·35	4·34 ± 0·50	**5·50 ± 0·36**
E = 409·5 ± 4·0 GPa	196·2	134 ± 2·0	235 ± 18	20·26 ± 0·62	21·85 ± 0·67	2·59 ± 0·26	3·70 ± 0·37	**5·66 ± 0·42**
ν = 0·237	294·30	163 ± 1·0	308 ± 40	20·54 ± 0·25	22·15 ± 0·27	2·63 ± 0·30	3·76 ± 0·55	**6·06 ± 0·54**

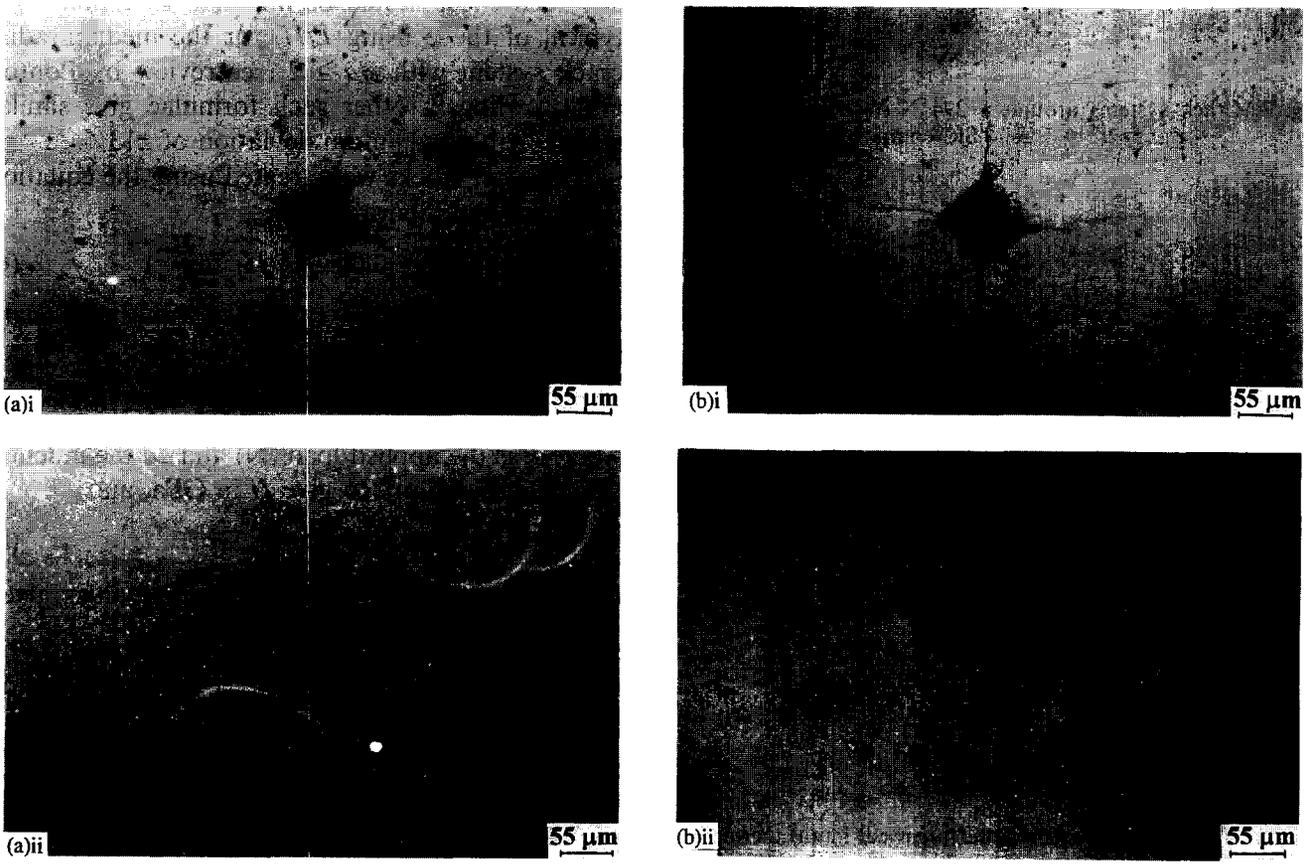

Fig. 2. Crack systems of materials around 98 N Vickers indentations: (a) as indented — (i) alumina, (ii) 5 vol% SiC composite; (b) polished after indentation — (i) alumina, (ii) 5 vol% SiC composite. The 10% and 15% composites are similar to the 5 vol% SiC composite.

the monolithic alumina has a tendency to encourage grain fall-out in these indentations. It has been suggested[8,9] that Palmqvist cracks at lower loads could evolve into median types at higher loads. This was not the case in this study. Figure 3 shows surfaces polished after indentation with 294 N load for alumina [median/radial type cracking, Fig. 3(a)] and 5 vol% SiC composite [Palmqvist type, Fig. 3(b)].

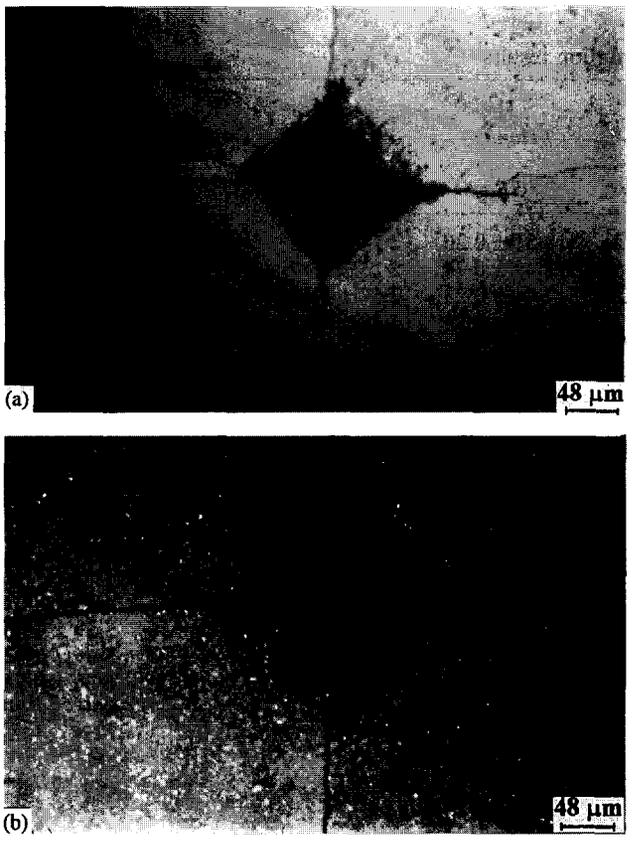

Fig. 3. Crack systems around a 294 N Vickers indent: (a) alumina; (b) 5 vol% SiC composite.

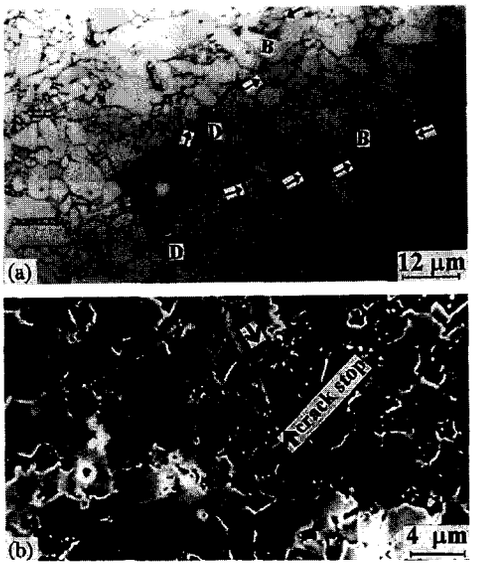

Fig. 4. Micrographs of crack paths (arrowed) in: (a) thermally etched Al_2O_3 (optical image); (b) chemically etched 5% SiC composite (scanning electron image). Note the intergranular nature of the path in alumina [with bridge (B) and deflection (D) positions marked] and the transgranular path in the composite.

The crack paths are predominantly intergranular for alumina [Fig. 4(a)] with bridges (for example, B) and deflections (D), whereas in the composites [Fig. 4(b)] cracks are principally transgranular. This possibly indicates a strengthening of the grain boundaries relative to those in monolithic alumina. This difference in crack paths has been observed by other workers.[10]

Determination of K_{Ic} *values*

Table 1 shows K_{Ic} values determined for the materials tested. The formula used for median/radial cracks was the equation proposed by Anstis *et al.*[11]

$$K_{Ic} = 0{\cdot}016(E/H)^{1/2}(P/c^{3/2}) \quad (4)$$

The table also shows K_{Ic} determined in this manner but with a deformation field geometry constant of 0·022:

$$K_{Ic} = 0{\cdot}022(E/H)^{1/2}(P/c^{3/2}) \quad (5)$$

Equation (5) was used so as to compare our results directly with those obtained for sintered 5 vol% SiC nano-composite by Zhao *et al.*[2] They used eqn (5) in order 'to compensate for the effects of environmentally assisted crack growth' (although they did not show that this had occurred). However, since we measured crack lengths soon after indentation, any such effect should be minimal. Equation (4) is typical of those using E/H, for the median/radial crack system with $c/a \geq 2$ (see review by Ponton and Rawlings[3]); other such formulae give similar results with a maximum deviation of ±13%.

Palmqvist cracks were treated using the equation proposed by Niihara *et al.*:[12]

$$K_{Ic} = 0{\cdot}0089(E/H)^{2/5}(al^{1/2}) \quad (6)$$

Hardness values were calculated with the standard equation:

$$H = 1854{\cdot}4P/(2a)^2 \quad (7)$$

where P is the applied load (N) and $2a$ the indentation diagonal (μm), to give H in GPa, and

$$H = 1000P/2a^2 \quad (8)$$

for direct comparison with hardness values given using this equation by Zhao *et al.*[2]

Vickers indentation K_{Ic} *results*

Table 1 shows that SiC additions appear to improve the toughness of alumina with the greatest change being between monolithic alumina and alumina–15% SiC. However, these differences depend on using the equations appropriate to the crack geometries seen (values given in bold in the table); the differences disappear if the same equation is used for all

materials. Given the uncertainties in the numerical pre-factors in equations such as (4)–(6), due to the poorly defined indentation stress fields, the results from this type of test must thus be regarded with extreme caution.

For a given material, the calculated fracture toughness increases with increasing load and thus crack size, as shown in Fig. 5(a). Such increases may be due to a number of effects, e.g. crack bridging and friction in the crack wake, or effects of residual stresses. If the effect is due solely to an internal stress field (as will arise from the thermal expansion mismatch of the SiC particles in the Al_2O_3 matrix), one might, by analogy with effects seen in transformation-toughened zirconia,[13] expect the toughness to increase linearly with the square root of the crack size. That is not, however, the case for our materials [see Fig. 5(b)]; any direct effects of residual stresses on K_{Ic} appear to be less important than other possible '*R*-curve' mechanisms.

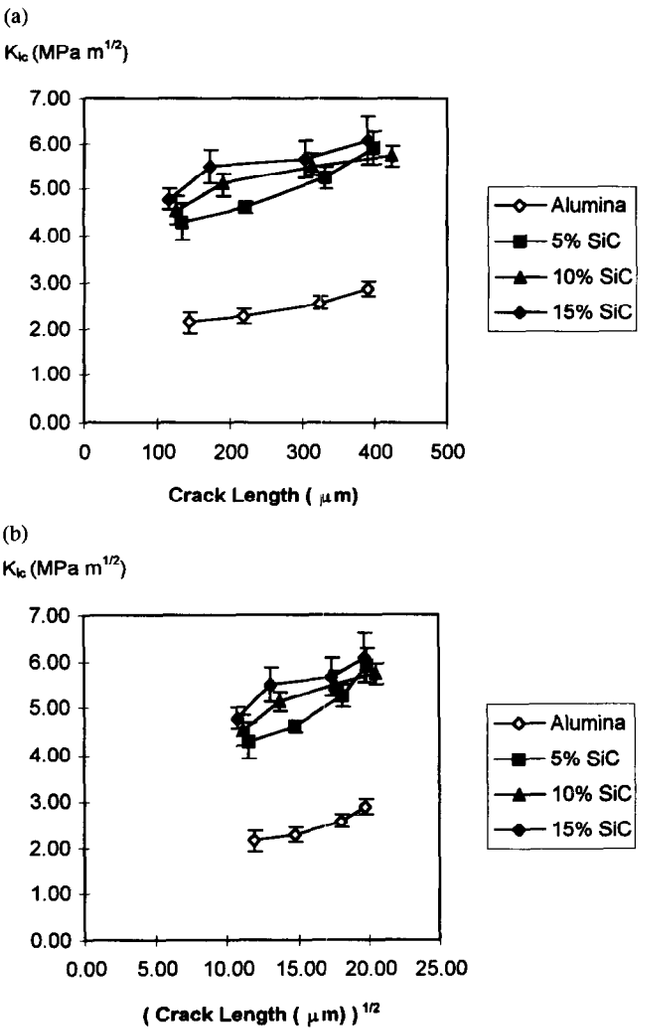

Fig. 5. Vickers indentation toughness K_{Ic} as a function of: (a) crack length; (b) square root of crack length.

Since the Vickers indentation methods for determining K_{Ic} in these materials gave ambivalent results, highly dependent on the formulae used, another method for determining K_{Ic} was used. This method is based on Hertzian indentation.

Hertzian indentation

Fracture toughness

Recent analyses of the stress intensity acting on cracks in the Hertzian stress field (that due to the elastic contact between a sphere and a flat surface, or between two spheres) have led to a new technique for determining the fracture toughness of brittle materials.[6] The near-surface radial stresses of the Hertzian field are tensile only very close to the surface, and rapidly become compressive with depth. The stresses also decay rapidly away from the contact area. Detailed analysis shows that there is a *minimum* load at which a surface flaw can propagate into the characteristic Hertzian 'ring/cone' crack, even if the surface is densely populated with flaws of all sizes and orientations. This minimum load depends only on the elastic moduli of the ball and surface and the fracture toughness of the surface (for cases where the ball and surface have the same elastic moduli; if they are dissimilar, then frictional tractions also must be taken into account). The method has been shown to give accurate values for K_{Ic}, compared with four-point bend measurements, for alumina and glass.[6]

Tests are performed by indenting a moderately abraded surface (to give a high density of surface flaws, so that one corresponding to the minimum load for fracture is likely to be found near a given indentation). The fracture toughness K_{Ic} may be calculated with the formula[6]

$$K_{Ic} = [(E^* P_{Fmin})/CR]^{1/2} \quad (9)$$

$$E^* = E/2(1 - \nu^2) \quad (9a)$$

where P_{Fmin} is the minimum fracture load in all tests, C is a constant depending only on the Poisson's

Table 2. Fracture toughness measured by Hertzian indentation

	Surface finish			
	3 μm diamond		*14 μm diamond*	
Material	$P_{Fmin}(N)$	$K_{Ic}(MPa\ m^{1/2})$	$P_{Fmin}(N)$	$K_{Ic}(MPa\ m^{1/2})$
Al_2O_3	330 ± 9	2·9 ± 0·1	335 ± 9	2·9 ± 0·1
Al_2O_3–5% SiC	465 ± 5	3·6 ± 0·1	511 ± 14	3·7 ± 0·1
Al_2O_3–15% SiC	520 ± 15	4·0 ± 0·1	590 ± 30	4·3 ± 0·1

ratio ν of the material being tested, E is its Young's modulus and R is the radius of the spherical indenter (polycrystalline Al_2O_3).

Values of K_{Ic} obtained are shown in Table 2. The values obtained with the two different surface finishes are reasonably consistent. The results are also consistent with the trends in the values obtained from the Vickers indentation tests, if the differences in crack geometry between the alumina and the composite samples are taken into account. We are thus confident that the fracture toughness of the composites is genuinely higher than that of pure alumina of the same grain size.

Flaw statistics

Figure 6 shows the cumulative probability of ring-crack formation with increasing load in a Hertzian test for the alumina and a 5% SiC composite. The fracture loads for the composite are ~80% higher than those for alumina. Since the fracture toughness values of the materials vary only by ~40%, this indicates that the surface flaws from which fracture originates are smaller in the composite material, although all materials received the same nominal surface finish. By measuring the ring-crack size for each test, it is possible to calculate the depth of the original surface flaw from which the ring crack originated.[7]

Figure 7 shows the results of such analysis on samples finished with 14 μm diamond [Fig. 7(a)] and 3 μm diamond [Fig. 7(b)], as histograms of the fraction of surface flaws found in a given size range. The majority of the surface flaws for the composites finished with 14 μm diamond are in the 3·5–5·5 μm size range, while for the alumina, flaws of all sizes up to 13 μm deep were found. It was not possible to measure ring-crack sizes on 3 μm finished alumina samples, but the nanocomposites finished to this level of polish showed a tighter distribution of flaws than those finished with 14 μm diamond.

Further analysis of the results gives the area density of surface flaws in a given size range, using a development by Warren *et al.*[7] of Wilshaw's 'searched area' method.[14] The new analysis takes into account the variation with depth of the Hertzian

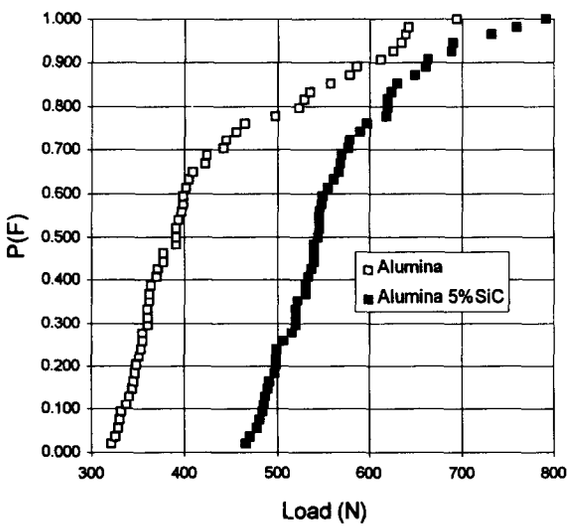

Fig. 6. Cumulative probability of failure $P(F)$ versus Hertzian indentation fracture loads for the monolithic alumina and the 5% SiC composite, both finished with 3 μm diamond paste.

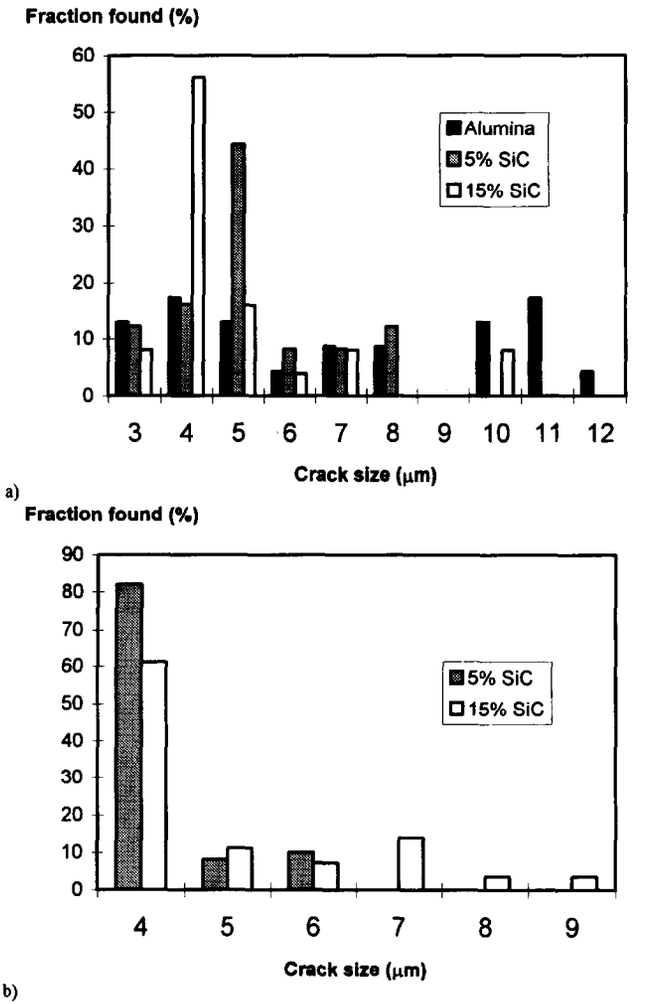

Fig. 7. Flaw statistics on samples finished with (a) 14 μm diamond and (b) 3 μm diamond, as histograms of the fraction of surface flaws in a 1 μm size range centred about the value shown.

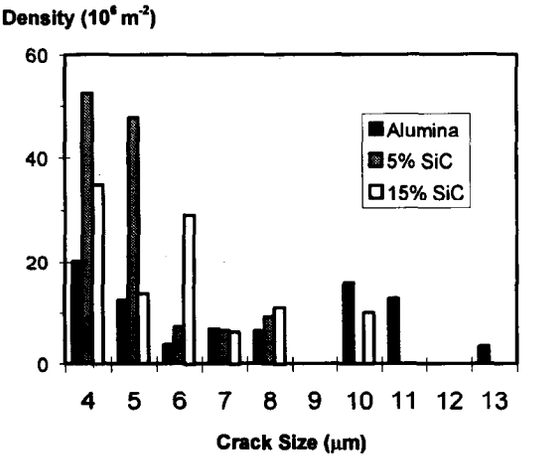

Fig. 8. Flaw statistics on samples finished with 14 μm diamond, as area density of surface flaws in a 1 μm size range centred about the crack depth shown.

stress field and all possible orientations of surface flaws. Results for the 14 μm polished specimens are shown in Fig. 8. As expected from Fig. 6, the composites have a much higher density of small surface flaws compared with the alumina, which has a significant density of large flaws.

Typical ring cracks are shown in Fig. 9(a) for alumina and Figs 9(b) and (c) for the 5 vol% SiC composite. It can be seen that the rings are not as well formed in alumina as in the composite. Note also the large number of grain pull-outs in the alumina surface compared with the composite; this may be either a result of, or a cause of, the large flaws found on the alumina surfaces.

A common method of analysing data similar to those in Fig. 6 is to perform a 'Weibull analysis', assuming that the probability of failure $P(F)$ varies with stress σ, and area (volume) tested A, as:

$$1 - P(F) = \exp\left[-\frac{A}{A_0}\left(\frac{\sigma}{\sigma_0}\right)^m\right] \qquad (10)$$

where σ_0 is a normalizing stress and A_0 is a normalizing load. For simple cases (e.g. bend tests, tensile tests), the stress and stress intensity on a flaw rises linearly with applied load (L) in the test. In this case, plotting $\ln\{\ln[1/(1-P(F))]\}$ against $\ln(L)$ yields a straight line with gradient m. Figure 10 shows such plots for the data of Fig. 6. It is immediately apparent that a straight line does not result. This is because of the complexity of the stress field around a Hertzian indenter, which has two effects on the assumptions of the Weibull analysis:

(1) the stress intensity on a given flaw does not rise linearly with applied load, especially for larger flaws; and
(2) the area 'searched' for a flaw of a given size is not the whole specimen, but depends in a complex way on the loads applied in the whole series of tests.

Warren[15] has analysed a simplified case of the effects of Hertzian indentation on a surface with a flaw distribution where the flaw density $\rho(c)$ for a given flaw size, c, is given by:

$$\rho(c) = A\, c^{-r} \qquad (11)$$

where r is a constant. In this case, for small flaws (i.e. those that are totally contained within the tensile surface stress), a relationship exists between the slope on a 'Hertzian Weibull' plot (such as Fig. 10), m_H and the normal Weibull modulus, m:

$$m = 3m_H - 2 = 2(r - 1) \qquad (12)$$

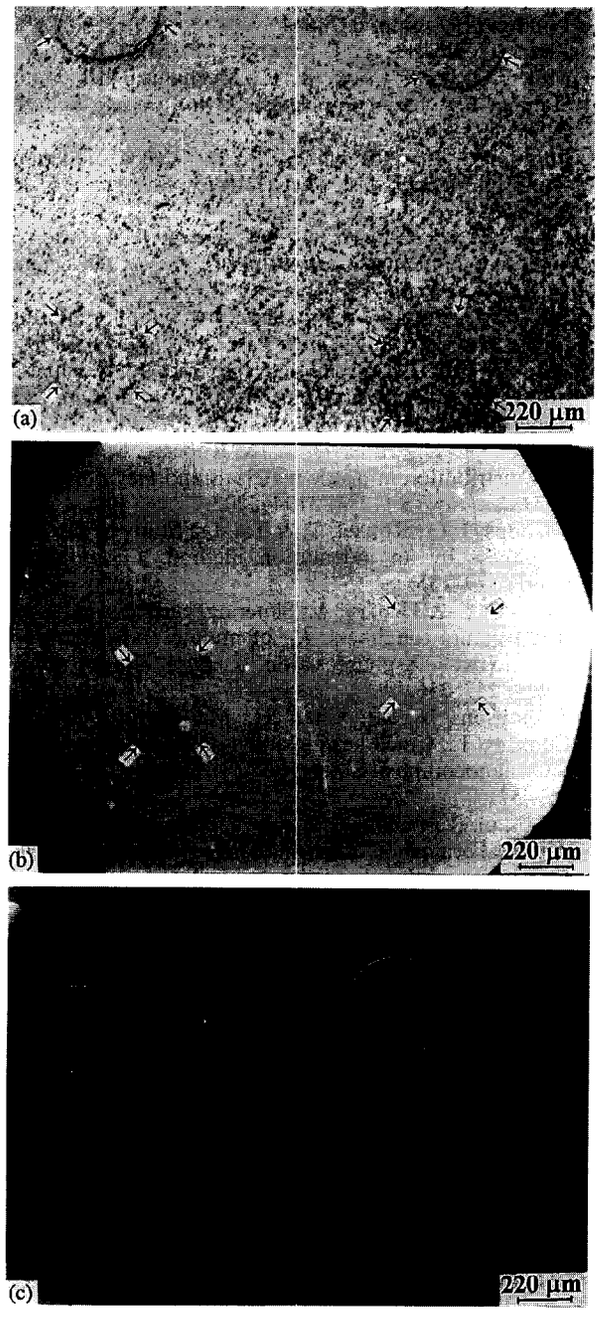

Fig. 9. Ring cracks from Hertzian indentations: (a) alumina, ground to 14 μm finish; (b) 5 vol% SiC composite, ground to 14 μm finish; (c) 5 vol% SiC composite, ground to 3 μm finish. The rings, or segments, are arrowed for clarity.

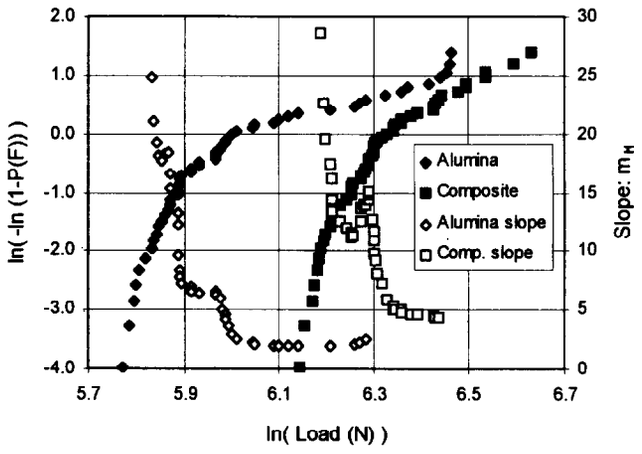

Fig. 10. 'Weibull plot' of data from Fig. 6. Note the non-linearity of the plots, especially in the low fracture load (i.e. large flaw) regime. The local slopes, m_H, of the lines are calculated as 'floating' linear regressions of 20 points centred around the load shown.

The 'small flaw' region on Fig. 10 corresponds to the highest fracture loads, where indeed the gradient is very nearly constant. Values of m derived from Fig. 10 are: alumina, $m \approx 4$ (i.e. $m_H \approx 2$); alumina 5% SiC, $m \approx 10$ (i.e. $m_H \approx 4$). However, our data only give information about the 'small flaw' end of the complete flaw distribution; flaws in this size range are not those likely to cause failure in bending or tension. The Weibull moduli thus derived may not, therefore, apply directly to the relative tensile reliability of these materials.

Conclusions

The results given in detail above may be summarized as follows.

(1) Indentation of sintered monolithic alumina produces a median/radial crack geometry, while indentation of its composites with up to 15 vol% SiC particles produces Palmqvist cracks.

(2) Calculation of Vickers indentation fracture toughness using formulae appropriate to the crack types gives K_{Ic} values of ~2·0–3·0 MPa $m^{1/2}$ for the alumina and ~4·5–6·0 MPa $m^{1/2}$ for the composites.

(3) The Vickers indentation K_{Ic} of all the materials tested increases with crack length (higher loads) — a behaviour similar to that of materials with an 'R-curve' characteristic.

(4) Hertzian indentation gives K_{Ic} values of 2·9 MPa $m^{1/2}$ for the alumina and ~3·5–4·0 MPa $m^{1/2}$ for the composites. The Hertzian method deals with the extension of cracks in the 1 to 10 μm range, so the differences between these results and those from the Vickers indentations may be a reflection of the different crack sizes operative in the two techniques.

(5) Identical polishing treatments produce different surface finishes on the alumina and the composites. The composites have flaw distributions centred around a smaller flaw size, and with a tighter distribution, compared with the alumina. Larger flaws in alumina seem to be associated with grain pull-out, which is almost totally suppressed in the composites.

Future papers will report on the strength and wear resistance of these materials.

Acknowledgements

This project was funded by the EPSRC (Grant No. GR/J/77542). We thank Cookson plc for use of the Isopress and furnace facilities. We thank Dr R. W. Davidge and Dr B. Derby for discussion of the results. We are grateful to Dr P. D. Warren for discussions of the Hertzian indentation methods, and for provision of computer programs to process the data.

References

1. Niihara, K. & Nakahira, A., Particulate strengthened oxide nanocomposites. In *Advanced Structural Inorganic Composites*, ed. Vincenzini. Elsevier Science Publishers, London (1990), pp. 637–664.
2. Zhao, J., Stearns, L. C., Harmer, P. M., Chan, H. M., Miller, G. A. & Cook, R. F., Mechanical behaviour of alumina–SiC 'nanocomposites'. *J. Am. Ceram. Soc.*, **76**[2] (1993) 503–510.
3. Ponton, C. B. & Rawlings, R. D., Vickers indentation fracture toughness test: Part 1. *Mater. Sci. Tech.*, **5** (1989) 865–872.
4. Cook, R. F. & Pharr, G. M., Direct observation and analysis of indentation cracking in glasses and ceramics. *J. Am. Ceram. Soc.*, **73**[4] (1990) 787–817.
5. Sakai, M. & Bradt, R. C., Fracture toughness testing of brittle materials. *Int. Mater. Rev.*, **38**[2] (1993) 53–78.
6. Warren, P. D., Determining the fracture toughness of brittle materials by Hertzian indentation. *J. Eur. Ceram. Soc.*, **15**[3] (1995) 201–207.
7. Warren, P. D., Hills, D. A. & Roberts, S. G., Surface flaw distribution in brittle materials and Hertzian fracture. *J. Mater. Res.*, **9** (1994) 3194–3202.
8. Glandus, J. C., Rouxel, T. & Tai, Q., Study of the Y-TZP toughness by an indentation method. *Ceram. Int.*, **17** (1991) 129–135.
9. Anya, C. C. & Hendry, A., Sintering, hardness and indentation fracture toughness, K_{Ic} of mullite and its composite with 15 wt% X-phase sialon. *J. Euro. Ceram. Soc.*, **13** (1994) 247–256.
10. Thompson, A. M., Chan H. M., Harmer, M. P. & Cook, R. F., Crack healing and stress relaxation in Al_2O_3–SiC 'nanocomposites'. *J. Am. Ceram. Soc.*, **78**[3] (1995) 567–571.
11. Anstis, G. R., Chantikul, P., Lawn, B. R. & Marshall, D. B., A critical evaluation of indentation techniques for measuring fracture toughness by direct crack measurements. *J. Am. Ceram. Soc.*, **64**[9] (1981) 533–538.
12. Niihara, K., Morena, R. & Hasselman, D. P. H., Evaluation of K_{Ic} of brittle solids by the indentation method with low crack-to-indent-ratios. *J. Mater. Sci. Lett.*, **1** (1982) 13–16.
13. Ikuma, Y. & Virkar, A. V., Crack-size dependence of fracture toughness in transformation-toughened ceramics. *J. Mater. Sci.*, **19** (1984) 2233–2238.
14. Wilshaw, T. R., The Hertzian fracture test. *J. Phys. D: Appl. Phys.*, **4** (1971) 1567–1581.
15. Warren, P. D., Private communication.

Journal of the European Ceramic Society **16** (1996) 1115–1120

PII: S0955-2219(96)00025-8
0955-2219/96/$15.00

Polymer-Derived Ceramic Coatings on C/C–SiC Composites

J. Bill & D. Heimann

Max-Planck-Institut für Metallforschung, Institut für Werkstoffwissenschaft, Pulvermetallurgisches Laboratorium, and Institut für Nichtmetallische Anorganische Materialien, Universität Stuttgart, Heisenbergstr. 5, D-70569, Stuttgart, Germany

(Received 20 December 1994; revised version received 3 January 1996; accepted 8 January 1996).

Abstract

A protective coating has been developed to enhance the oxidation stability of C fibre reinforced SiC (C/C–SiC). The coating was prepared by pyrolysis of a polysilazane layer, which was obtained by dip-coating. Silicon powder was added to the polysilazane solution to prevent shrinkage during pyrolysis. The ceramic coating was characterized regarding layer thickness, adhesion, and oxidation protection for C-fibres. Under the prevailing conditions the thickness of the ceramic layer was determined to be up to 5 μm after one coating–pyrolysis cycle and could be increased by further coating. Additionally, the thickness could be varied by changing the viscosity of the polymer solution as well as the withdrawal speed. The highest values measured for the adhesion of the ceramic coating on the substrate were 14 MPa. The lifetime of the composite material at high temperatures in air could be increased by up to 120% with the coating, compared with the uncoated samples. © 1996 Elsevier Science Limited.

1 Introduction

Carbon-fibre reinforced composites are one of the most promising materials with which to realize lightweight structures at high temperatures, and find application in areas such as the aircraft and space industry as well as in automotive and energy technologies.[1]

The crucial drawback for C fibres is their low stability in an oxygen-containing atmosphere at elevated temperatures. While the C fibres inside a carbon-fibre reinforced SiC (C/C–SiC) composite are protected by the surrounding SiC matrix,[2] the top fibres are unprotected at the surface due to additional machining. These fibres can be oxidized easily and so carry the oxidation through the entire component. Thus it is necessary to develop an effective ceramic coating that prevents oxidation of the C fibres. Among other methods, such ceramic oxidation protective films can be made by chemical vapour deposition (CVD), sputter and spray processes.[3]

In this research work polymer pyrolysis, which is a suitable method for the manufacture of ceramic bodies, fibres, powders and thin layers,[4–6] has been used for the development of protective coatings. Metal organic polymers, and especially organosilicon polymers, are used as starting materials. Pyrolysis at temperatures around 1000°C leads to silicon-based amorphous ceramics. By raising the temperature up to 1400–1600°C, transformation into the corresponding crystalline modifications occurs.[7] Two points in favour for polymer pyrolysis are the low reaction temperatures (around 1000°C) as well as the ability to control the purity of the products easily.

2 Experimental

2.1 Dip-coating

C/C–SiC composite samples were coated by means of dip-coating (Fig. 1). This process, well known from the sol–gel technique to produce oxide ceramic layers, allows simple, rapid and economical coating.[8,9] The substrate is dipped into the precursor solution and withdrawn after a few minutes with a certain velocity, v.

The thickness of the adherent polymer layer can easily be varied in a wide range by changing the velocity v as well as the viscosity η of the solution and the concentration c of the polymer.[10] After coating the adherent polymer layer is pyrolyzed in an inert atmosphere forming an amorphous ceramic coating.

2.2 Materials

Commercially available polysilazane NCP 200 (Nichimen Corp., Japan), with a number-average molecular weight (M_n) of 1100–1300 g mol^{-1},[11] was used as starting material. Pyrolysis up to 1100°C in nitrogen or argon leads to an amorphous ceramic

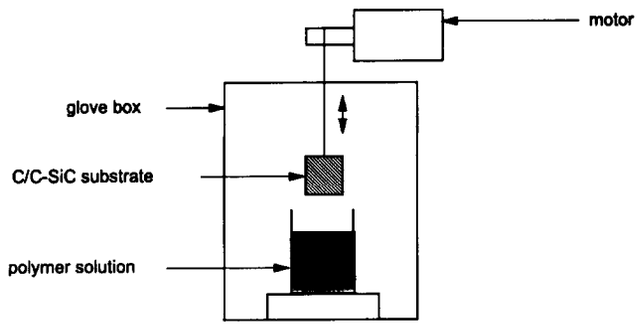

Fig. 1. Dip-coating facility.

with the composition $SiC_{0.7}N$ determined by chemical analysis. During the transformation of the polymer into Si/C/N ceramic several gaseous reaction products, such as hydrogen, ammonia and methane, are released. This is shown schematically in Fig. 2. The appropriate heating programme is illustrated in Fig. 3.

Solutions were prepared by dissolving NCP 200 in distilled toluene (Aldrich) which was dried over sodium. Silicon powder (Elcem) with $d_{90} < 3$ μm was added to the polymer solution and dispersed by ultrasonic mixing and intensive stirring. During the coating process no sedimentation could be observed.

Two-dimensional (0°/90°; C fibres: T300, Toray, Japan) C/C–SiC (20 × 10 × 3 mm^3) with a carbon content of 57–60 wt%, a silicon carbide content of 33–37 wt% and a free silicon content of 3–6 wt% was used as substrate. The material (ρ = 1·95 g cm^{-3}) was produced by infiltration of a C/C preform with fused silicon.[12] The substrates were ground using a 65 μm diamond emery paper, cleaned in toluene and finally heated in vacuum (10^{-2} mbar) up to 900°C for 5 h.

2.3 Layer thickness

The thickness of the ceramic coatings produced as described above was measured by optical microscopy and scanning electron microscopy (SEM) on the specimen cross-sections, as well as by profilometry (alpha step).[13]

2.4 Adhesion

Adhesion of the ceramic layer on the C/C–SiC substrate was determined by the direct pull method.[14] According to this method, a stamp, which first was sand-blasted and then cleaned in toluene, was pasted on the degreased ceramic layer by means of a mixed adhesive or a cyanoacrylate cement. After hardening of the adhesive, the stamp was pulled off by a force F perpendicular to the substrate surface. The withdrawal installation was fixed on a cardanic mount to prevent shearing strain, which would falsify the result. The velocity of withdrawal was 5 mm min^{-1}. The force F necessary to remove the ceramic layer from the substrate was measured, so that the adhesion σ of the coating on the substrate could be cal-culated using the equation $\sigma = F/A$ with A = 34 mm^2.

Due to the small quantity of cement used, the high viscosity and the rapid hardening of the cement, penetration through the ceramic layer to the substrate could be excluded, as was additionally shown by light micro-scopic inspection of the cross-section of the samples.

2.5 Oxidation behaviour

Oxidation behaviour of the coated C/C–SiC material was investigated thermogravimetrically by measuring the weight-change during heat treatment in air using a Netzsch STA 409 TGA.

3 Results and Discussion

The ability to produce ceramic layers on composite materials by polymer pyrolysis has already been

$$[RSiHNH]_m\,[RSiN]_n \xrightarrow[Ar;N2]{1100°C} Si_xC_yN_z + CH_4 + NH_3 + H_2$$

(polysilazane) (amorphous ceramic) (gas)

R = CH_3, C_2H_5, C_2H_3

Fig. 2. Schematic description of the decomposition of a polysilazane (e.g. NCP 200).

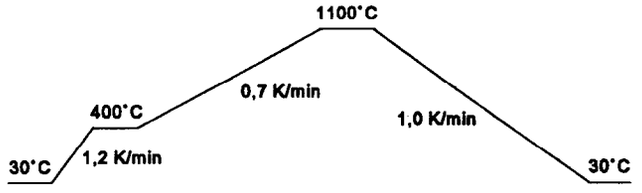

Fig. 3. Heating programme for pyrolysis of the pre-ceramic coating.

reported,[15] yet it was impossible to produce thick (several μm), crack-free and large-area ceramic coatings in one coating–pyrolysis cycle by this method. Also, in our investigations, the use of highly concentrated polymer solutions always led to the formation of cracks. Figure 4 shows a typical result. This layer was prepared by dipping the C/C–SiC substrate into a 67 wt% solution of NCP 200 in toluene, followed by pyrolysis. The velocity v was 2·7 cm min^{-1}.

One reason for the formation of cracks is the volume shrinkage that occurs during pyrolysis. The polymer, with a density of about 1·1 g cm^{-3}, is transformed into an amorphous ceramic with a much higher density of approximately 2·4 g cm^{-3}. In the case of manufacturing ceramic bodies the total volume shrinkage was up to 60%. At the same time, due to the release of volatile reaction products, an open porosity of up to 12% occurred.[16] In the case of ceramic bodies a certain amount of filler can be added to the starting polymer to reduce shrinkage as well as porosity.[17]

Another reason for the formation of cracks is the exceeding of a certain critical layer thickness, h_c. In layers thicker than h_c, the stress energy due to the different thermal expansion coefficients of the substrate and the layer is released by the formation of cracks during the cooling phase.[18]

In our investigations, however, we produced (several μm) thick, almost crack-free, well-adherent ceramic layers on the C/C–SiC composites by adding a certain amount of silicon powder to the polymer solution.[19,20] Silicon is assumed to be a passive filler in the pyrolysis schedule. In an oxygen-containing atmosphere silicon reacts at high temperatures forming silicon dioxide, which may close pores and increase the protective ability of the ceramic coating. The filler content has to be chosen in such a way that the shrinkage of the coating is minimized but the viscosity of the dispersion is usable.

The use of a 60 wt% solution of NCP 200 in toluene with a filler content of 45 vol% (related to the polymer weight) and a withdrawal speed of 2·7 cm min^{-1} leads to an approximately 5 μm thick, almost crack-free ceramic layer after one coating–pyrolysis cycle. This is shown in Figs 5 and 6.

In Fig. 7 the dependence of the layer thickness h on the withdrawal velocity v is illustrated. For this investigation a 37·5 wt% polysilazane solution in toluene with a filler content of 42 vol% (viscosity: 12 mPa s measured at 23°C with a rotary viscosimeter, Haake RV 12, D = 2000 s^{-1}) was used. At lower velocities (<14 cm min^{-1}) the layer thickness does not increase much on raising the withdrawal speed, whereas at higher velocities (>14 cm min^{-1}) a considerable increase occurs. However, the higher the velocity, the higher the number of cracks in the obtained ceramic layer.

The adherence of the ceramic layer on the C/C–SiC material depends on the pre-treatment of the substrate as well as on the pyrolysis conditions. In general, the adhesion of the ceramic coating was determined to be in the range of 6 MPa with highest values up to 14 MPa. The adhesion of the ceramic layers could be increased by 30% by

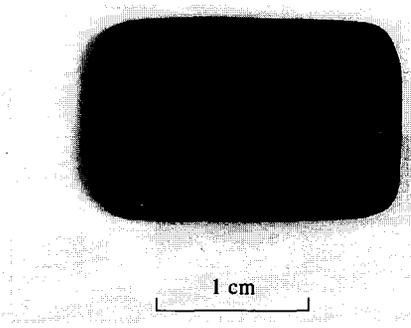

Fig. 5. Non-cracked ceramic layer on C/C–SiC substrate; prepared by dip-coating with a 60 wt% solution of NCP 200 in toluene, 45 vol% silicon powder, pyrolysis up to 1100°C; withdrawal speed = 2·7 cm min^{-1}.

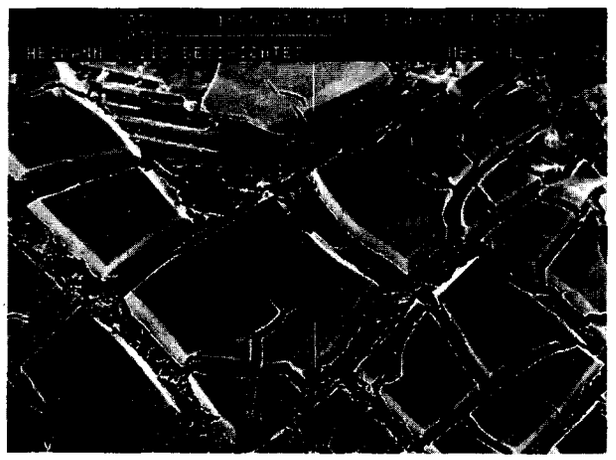

Fig. 4. Ceramic layer on C/C–SiC substrate; prepared by dip-coating with a 67 wt% solution of NCP 200 in toluene and followed by pyrolysis up to 1100°C; withdrawal speed = 2·7 cm min^{-1}.

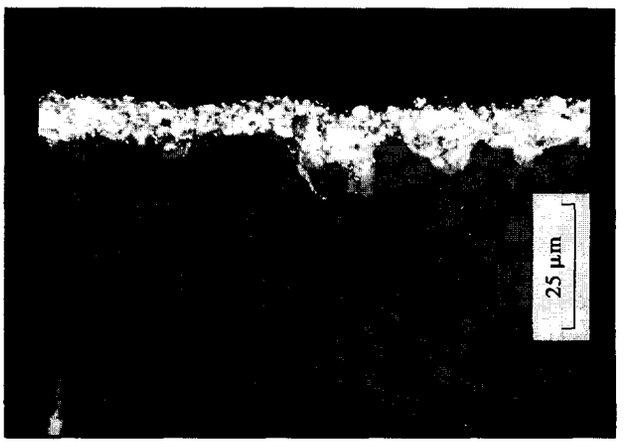

Fig. 6. Cross-section of the coated C/C–SiC specimen, prepared by dip-coating with a 60 wt% solution of NCP 200 in toluene, 45 vol% silicon powder; pyrolysis up to 1100°C; withdrawal speed = 2·7 cm min^{-1}.

additional annealing of the samples in nitrogen atmosphere at 1350°C. This may due to nitridation of the silicon filler and must be investigated in future work. It should be mentioned that, in most cases, the layer was not pulled off but the substrate was broken (Fig. 8). Thus the real value of σ must be higher than the measured one.

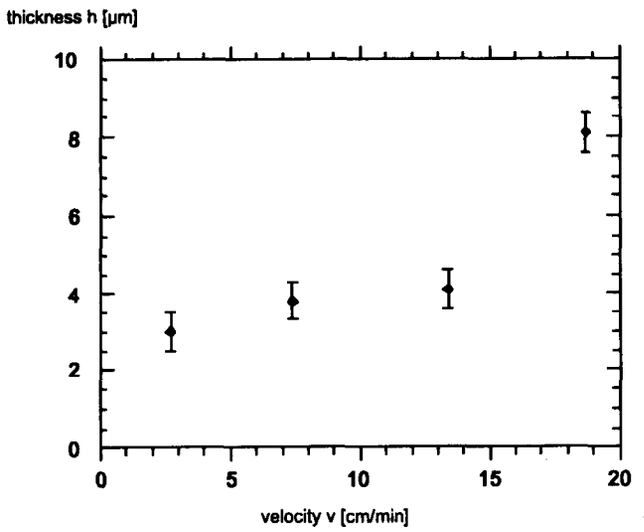

Fig. 7. Thickness h of the ceramic layer vs. withdrawal velocity v. The ceramic layers were manufactured by dip-coating with a 37·5 wt% polysilazane solution in toluene, 42 vol% silicon powder and subsequent pyrolysis up to 1100°C.

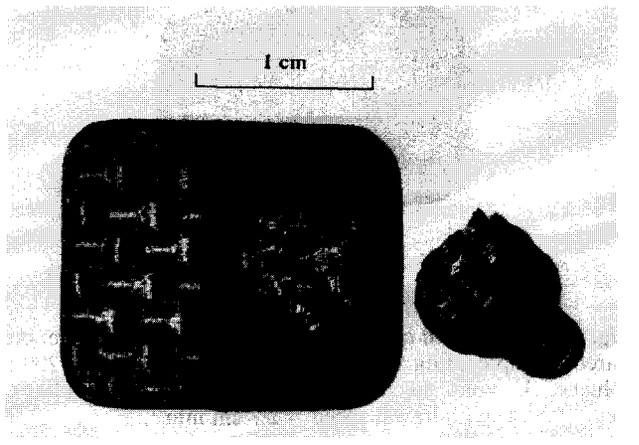

Fig. 8. Coated C/C–SiC sample after direct-pull test. The ceramic layer was obtained by dip-coating with a 60 wt% solution of NCP 200 in toluene, 45 vol% silicon powder; pyrolysis up to 1100°C; withdrawal speed = 2·7 cm min^{-1}. Parts of the substrate were pulled off.

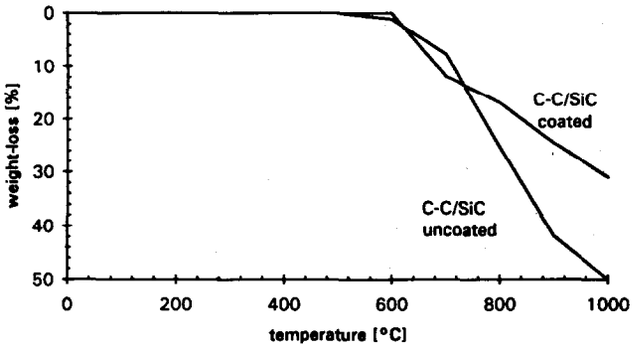

Fig. 9. Thermogravimetric investigation in air at 1000°C.

The oxidation behaviour of the coating and the ability to protect the C/C–SiC substrate against oxidation was investigated using thermogravimetric analysis. Figure 9 shows the weight loss of an uncoated (reference) and a coated C/C–SiC sample during a heat treatment in air at atmospheric pressure up to 1000°C. Both samples were heated up at 1 K min^{-1} and then cooled down at 8 K min^{-1}. After the test the reference sample showed a weight loss of more than 50%, whereas the sample coated with an only 10 μm thick ceramic layer (using a 60 wt% solution of NCP 200 in toluene containing 45 vol% of Si filler; v = 2·7 cm min^{-1}), lost about 30% of its original weight.

The reference sample starts to oxidize at about 500°C. The beginning of oxidation of the coated sample is shifted to approximately 600°C. Up to 750°C the oxidation rate of the coated sample is at least as high as that of the reference, while at higher temperatures the oxidation rate of the coated sample decreases. One reason for this might be a reduction of the porosity of the ceramic coating by the formation of silicon dioxide, leading to a lower diffusion rate of oxygen through the pores.

Cross-sections of both samples are shown in Figs 10 and 11. In the case of the uncoated specimen (Fig. 10) all the C fibres were burned out, while in the case of the coated sample (Fig. 11) carbon fibres are still present.

Thermogravimetrical investigations in flowing air (30 cc min^{-1}) were carried out at 1160 and 1260°C. In Fig. 12 (1160°C) and Fig. 13 (1260°C) the weight loss vs. time is shown; only the part until no further weight loss was observed, i.e. until weight stabilization occurred, is illustrated. The values of weight loss measured (55–61 wt%) are in the same range as the C fibre content in the composite (57–60 wt%). In all cases no fibres could be observed after the test by SEM investigation. In other words, all the carbon

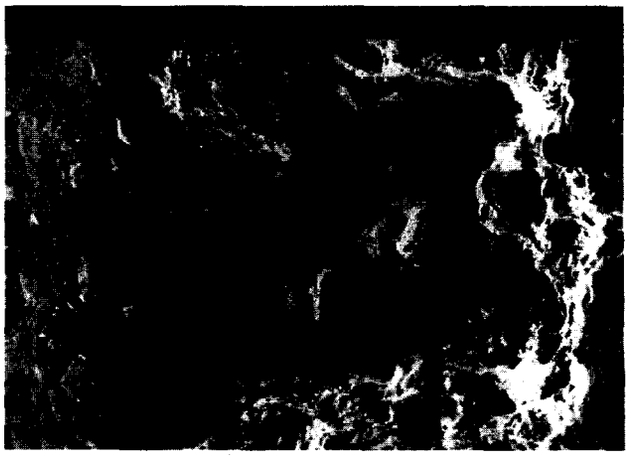

Fig. 10. Uncoated C/C–SiC sample after oxidation test in air.

Fig. 11. Coated C/C–SiC sample after oxidation test in air.

fibres were burned off. The time until weight stabilization is observed was extended by 120% at 1160°C and by 36% at 1260°C by a coating with a thickness of approximately 20 μm obtained after four coating– pyrolysis cycles.

The reasons for the weight loss in the case of coated samples are the porosity of the layer as well as some microcracks that may occur during the cooling phase of the pyrolysis step, due to the difference between the thermal expansion coefficients α of the substrate ($0{\cdot}6$–$0{\cdot}8 \times 10^{-6}$ K^{-1} between 20 and 1000°C in fibres plain) and the coating ($3{\cdot}4 \times 10^{-6}$ K^{-1} between 20 and 1100°C).

Further investigations with other filler materials such as SiC and Si_3N_4 (passive filler) or Ti (active filler), which react with the gaseous species evolved during pyrolysis, will be carried out to examine their influence on the porosity of the ceramic coating as well as on the crack formation. Moreover, new tailor-made polymers leading to a higher ceramic yield and a ceramic residue with a value of α close to that of the substrate ($0{\cdot}6$–$0{\cdot}8 \times 10^{-6}$ K^{-1}) will be used, to minimize crack formation. The synthesis of such a suitable polymer, which leads to a ceramic material in the system Si/B/C/N with $\alpha \approx 1 \times 10^{-6}$ K^{-1} (100–1000°C), has already been reported.[21]

4 Summary

An almost crack-free, oxidation-protective ceramic coating on C/C–SiC substrates was produced by dip-coating, using a 60 wt% solution of NCP 200 in toluene with a filler content of 45 vol% Si powder, followed by pyrolysis of the adherent polymer/filler layer in a nitrogen atmosphere at 1100°C. The thickness of the ceramic layer was up to 5 μm after one coating– pyrolysis cycle. For the adhesion of the coating on the substrate, values up to 14 MPa were measured using the direct-pull method. Oxidation tests showed that the durability of coated samples in air at 1160°C and 1260°C was much higher than that of uncoated samples.

Acknowledgments

This work was supported by the DFG and is the summary of a report[19] written within the scope of SFB 259 'Hochtemperaturprobleme rückkehrfähiger Raumtransportsysteme'. The authors would like to thank Professor Dr F. Aldinger, Universität Stuttgart, Institut für Nichtmetallische Anorganische Materialien, for helpful conversation and support; Professor Kochendörfer and co-workers at

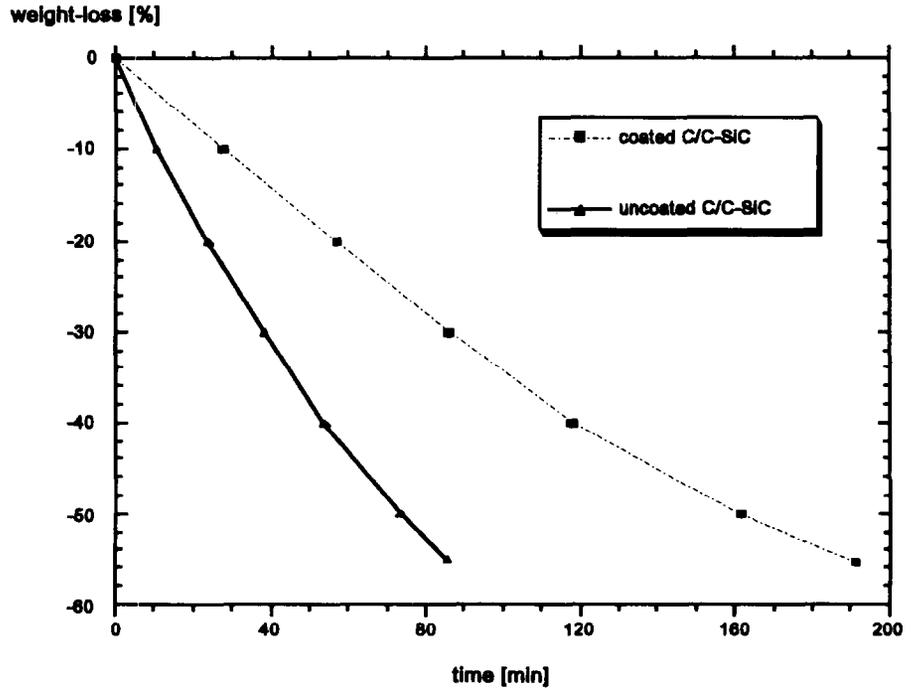

Fig. 12. Thermogravimetric investigation in flowing air at 1160°C.

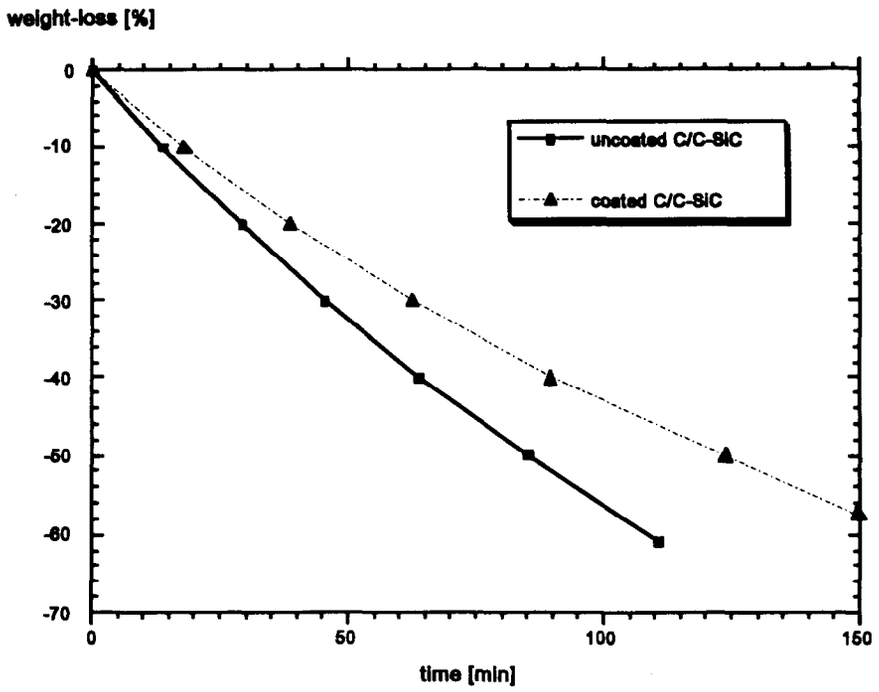

Fig. 13. Thermogravimetric investigation in flowing air at 1260°C.

DLR, Institut für Bauweisen- und Konstruktionsforschung, Stuttgart, for supply of the C/C–SiC composite materials; and Professor Dulog, Dr Rösler, Mr Klinke and co-workers of the Institut für Pigmente und Lacke e.V., Stuttgart, for performing the direct-pull measurements.

References

1. Hüttinger, K. J. & Greil, P., Keramische Verbundwerkstoffe für Höchsttemperaturanwendungen. *DKG 69*, **2** (1989) 395–400.
2. Schanz, P. & Krenkel, W., Description of the mechanical and thermal behavior of liquid siliconized C/C. Presented at *6th European Conf. on Composite Materials ECCM*, Bordeaux, September 1993.
3. Oberflächen- und Dünnschicht-Technologie Teil I, ed. R. A. Haefer. Springer-Verlag, 1987.
4. Wynne, K. J. & Rice, R. W., Ceramics via polymer pyrolysis. *Ann. Rev Mater.*, **14** (1984) 297–334.
5. Lipowitz, J., Polymer-derived ceramic fibres. *Ceram. Bull.*, **70**[12] (1991) 188–193.
6. Mucalo, M. R., Milestone, N. B., Vickridge, I. C. & Swain, M. V., Preparation of ceramic coatings from pre-ceramic precursors. *J. Mater. Sci.*, **29** (1994) 4487–4499.
7. Riedel, R., Passing, G., Schönfelder, H. & Brook, R. J., Synthesis of dense silicon-based ceramics at low temperatures. *Nature*, **355** (1992).
8. Sakka, S. & Yoko, T., Sol–gel derived coating films and applications. *Structure and Bonding*, **77** (1992) 89–117.
9. Dislich, H. & Hussmann, E., Amorphous and crystalline dip-coating obtained from organometallic solutions: procedures, chemical process and products. *Thin Solid Films*, 77 (1981) 129–139.
10. Landau, L. & Levich, B., Dragging of a liquid by a moving plate. *Acta Physicochim. U.R.S.S.*, **XVII**, [1–2] (1942) 42–54.
11. Nichimen Corporation, NCP 200 Data sheet, 13-1 Kyobashi 1-chome, Tokyo 104, Japan.
12. Krenkel, W. & Gern, F., Microstructure and characteristics of CMC manufactured via the liquid phase route. Presented at *9th Int. Conf. on Composite Materials*, Madrid, Spain, 12–16 July 1993.
13. Vogel, K., Messung der Schichtdicke von Lackierungen und ähnlichen Beschichtungen, Prüftechnik bei Lackherstellung und Lackverarbeitung. *Fachbuchreihe 'Lackiertechnik' der Zeitschrift 'Industrie Lackierbetrieb', Vol. 2,* Curt R. Vincentz Verlag, Hannover, 1992, pp. 7–12.
14. Sickfield, J. & Raabe, H. J., Beurteilung der Haftfestigkeit durch Abreißversuch nach DIN ISO 4624. *Farbe + Lack*, **87**[8] (1981) 653–655.
15. Coblenz, W. S., Wiseman, G. H., Davis, P. B. & Rice, R. W., Formation of ceramic composites and coatings utilizing polymer pyrolysis. *Mater. Sci. Res.*, (1984) 271–285.
16. Schönfelder, H., Siliciumcarbidnitridkeramik aus Polysilazan. PhD thesis, University Stuttgart, 1992.
17. Seibold, M. & Greil, P., Thermodynamics and microstructural development of ceramic composite formation by active fillercontrolled pyrolysis (AFCOP). *J. Eur. Ceram. Soc.*, **11** (1993) 105–113.
18. Hutchinson, J. W. & Suo, Z., *Adv. Appl. Mech.*, **28** (1991) 126–149.
19. Bill, J., Aldinger, F. & Heimann, D., Oberflächenschutz von Si-infiltriertem SiC. DFG-Zwischenbericht für den Sonderforschungsbereich 259, 'Hochtemperaturprobleme rückkehrfähiger Raumtransportsysteme', March 1994.
20. Heimann, D., Bill, J. & Aldinger, F., Herstellung oxidationsbeständiger, keramischer Schutzschichten durch Polymer-Pyrolyse. Presented at the General Meeting of the Deutsche Gesellschaft für Materialkunde, Göttingen, Germany, 24–27 May 1994.
21. Bill, J., Kienzle, A., Sasaki M., Riedel, R. & Aldinger, F., Novel routes for the synthesis of materials in the quaternary system Si–B–C–N and their characterisation. *Proc. World Ceramic Congress,* Florence, Italy, 20 June–4 July 1994 (in press).

Journal of the European Ceramic Society **16** (1996) 1121–1126

PII: S0955-2219(96)00026-X
0955-2219/96/$15.00

Low-Temperature Oxidation of Silicon Nitride by Water in Supercritical Condition

Edoardo Proverbio[a] & Fabio Carassiti[b]

[a]University of Rome 'La Sapienza', Department ICMMPM, via Eudossiana 18, 00184 Roma, Italy
[b]Third University of Rome, Department of Mechanics and Automation, via Segre 60, 00146 Roma, Italy

(Received 28 April 1995; revised version received 10 January 1996; accepted 12 January 1996)

Abstract

Oxidation tests carried out in supercritical water (400–500°C) revealed a noticeable corrosion attack on the silicon nitride surface in spite of the low temperatures. Increasing water pressure generally caused an increase in the oxidation phenomena. Oxidation scale evolution depended strictly on the silicon nitride sintering process, sintering aids, porosity and impurities, which influenced oxidation kinetics and surface morphology. In such test conditions the solubility of silica in water seemed to have a great influence on the stability of the oxidation scale, mainly in reaction-bonded silicon nitride samples. © 1996 Elsevier Science Limited.

1 Introduction

The most promising properties of silicon nitride, from the viewpoint of extensive applications such as thermal barriers and antiwear coatings, are hardness and chemical stability, these resulting from strong covalent bonds. Silicon nitride may also find applications in high-temperature environments as combustion engines, burners and high-temperature gas heat exchangers, while other applications include low-temperature high-water-pressure environments such as steam generators, nuclear reactors or chemical plants.

However, like all non-oxide ceramics (SiC, B_4C, AlN, BN), silicon nitride is inherently unstable in an oxidizing atmosphere, and water too can act as an oxidizing agent either at low or high temperature.[1] The influence of water vapour at high temperatures (1000–1500°C) on the oxidation of Si_3N_4 was described about 20 years ago,[2,3] but it is only recently that more accurate investigations have been carried out. Singhal[3] reported that the activation energy for oxidation of silicon nitride is 488 ± 30 kJ mol^{-1} in wet oxygen and 375 ± 25 kJ mol^{-1} in dry oxygen. Such an influence could result from the diffusion and dissolution of OH^- ions through the surface oxide film. More recently, Opila[4] reported some results on the oxidation kinetics of chemically vapour deposited SiC in wet oxygen. The oxidation rates of SiC in oxygen containing 10% water vapour were only very slightly enhanced over the rates found in dry oxygen, the obtained activation energies were 41 and 142 kJ mol^{-1}, respectively. The influence of water on corrosion kinetics was strongly enhanced by the presence of alkali impurities. Oxidation tests carried out in a high-purity Al_2O_3 tube (80–200 ppm Na_2O), instead of a quartz tube, led to an activation energy of 249 kJ mol^{-1} in oxygen containing 10% water vapour. According to Opila the water vapour plays a role in the transport of sodium and aluminium from the reaction tube to the sample surface, since contamination did not occur when experiments were performed with the Al_2O_3 reaction tube in dry oxygen. The impurities, as well as water[3,5,6], increase the crystallization rate of silica and enhance the transformation of crystobalite to tridymite.[7] Thus, the impurity effects should not be isolated from the oxidation rate enhancement due to water vapour. Devitrification and phase transformation promote the formation of cracks and fissures, thus exposing new, free Si_3N_4 for oxidation. Roughening of the surface by bubbles and pits was also observed[5] on the oxidized silicon nitride surface.

Since the oxidation resistance of Si_3N_4 depends on the formation of protective SiO_2, it should be supposed the material can suffer from corrosive phenomena under high water pressure even at low temperatures. It was reported[8–10] that the solubility of silica in water is strongly dependent on pressure and temperature, amorphous silica being about an order of magnitude more soluble than crystalline silica.

Yoshimura and co-workers[11–14] have studied the oxidation mechanisms of Si_3N_4 and SiC under hydrothermal conditions from 10 to 100 MPa, at temperature as low as 200 or 600°C: oxidation yielded amorphous silica scales (a hydrosilica sol was proposed instead by Hirayama *et al.*[15]) and

NH_3, and CH_4, CO, CO_2 and H_2, respectively. Under 10 MPa, Si_3N_4 yielded $N_2 + H_2$ instead of NH_3. In a wear test condition at 300°C and 8·53 MPa water pressure, C_2H_6 gas was also detected in the SiC/H_2O system.[16] In the same system the formation of carbon layers was observed and investigated.[13,14,17] The oxidation kinetics of silicon nitride follow the parabolic law, but at high temperature (>800°C) it seems that the oxidation rate was unaffected by water vapour pressure above 1·5 MPa, as reported by Sato *et al.*[18]

Sintered Si_3N_4 with and without sintering aids has been studied at 300°C and 8·6 MPa by Yoshio and Oda.[19] Corrosion damage of doped Si_3N_4 was characterized by pit formation with the development of different shapes, depending on the sintering aids used. The pit size and population, and the formation of pit agglomerate, depended on the duration of exposure to the aggressive environment. On the other hand, the corrosion behaviour of Si_3N_4 without additives was characterized by intergranular attack due to selective dissolution of the SiO_2 phase at grain boundaries.[20] As the grain boundaries dissolve, the Si_3N_4 grains are undermined and fall into the solution, hence accelerating corrosion.

In the present study, a series of oxidation tests was carried out in the range 14–40 MPa in the water supercritical region (temperature >400°C) on different types of silicon nitride in order to evaluate the influence of sintering process and environment aggressiveness on the corrosion resistance of silicon nitride.

2 Experimental Procedure

Two kinds of oxidation tests were performed: a short-time exposure at different water pressures and different temperatures to determine the influence of such parameters on corrosion phenomena, and a time-dependent exposure at fixed pressure and temperature to provide a rough evaluation of the oxidation kinetics.

2.1 Materials

Hot-pressed (HPSN; Cercom Coors Inc., USA), sintered reaction-bonded (SRBSN; Nitrasil S, AED Ltd, UK) and reaction-bonded (RBSN; Nitrasil R, AED Ltd, UK) commercially available silicon nitride samples were used in these experiments. Before testing samples were characterized chemically and physically. Grain size was revealed by microscope observation after chemical etch (5 min in molten KOH). Open porosity was measured by means of an intrusion mercury porosimeter. Results are summarized in Table 1.

Crystalline phase and elementary composition were determined by means of X-ray diffraction, using Cu K_α radiation filtered by a LiF monochromator and an EDS electron microprobe, respectively. Results are reported in Table 2.

For the first test sequence, one of the larger surfaces of the sample to be tested (4 × 10 × 4 mm) was ground to 1 μm finish with diamond paste. For the second test sequence, some coupons (10 × 10 × 1 mm) were obtained by cutting the as-received sample with a diamond saw. Surfaces were then ground with a 16 μm diamond wheel.

2.2 Oxidation

Oxidation tests were carried out in a closed Nimonic 105 autoclave heated by means of a heater strip. After being cleaned ultrasonically in acetone, the samples were placed in a platinum crucible with the polished surface upwards. A second platinum crucible, containing the calculated amount of distilled water to reach the scheduled pressure, was then placed above the previous one. Eight different oxidation tests were performed in total, as summarized in Table 3.

For the time-dependent oxidation test, a minimum of four coupons was used for each type of silicon nitride; after being carefully weighed with a precision balance, these specimens were placed in different platinum crucibles. Tests were performed for 5, 40 and 100 h at 400°C and 36 MPa. After cooling down the autoclave, samples were dried and re-weighed.

2.3 Characterization of oxidized samples

Oxidized samples were characterized by means of three different techniques. Morphological characterization was performed by scanning electron microscopy (SEM). Information on the composition of the oxidation scale was obtained by Fourier transform infra-red spectroscopy (FTIR), which provided information on the amorphous phase in the outer oxidation layer, and also by X-ray diffraction (XRD). FTIR analysis was carried out on bulk samples using a single-beam diffuse reflectance

Table 1. Microstructural parameters of samples

Sample	*Density (g cm^{-3})*	*Avrg. grain length (μm)*	*Avrg. grain diameter (μm)*	*Open porosity (% vol)*	*Avrg. pore diameter (μm)*
HPSN	3·31	6	1	0·07	6·1
SRBSN	3·22	10	2·5	0·16	2·0
RBSN	2·60	–	–	21·96	0·1

Table 2. Sample composition as determined from X-ray diffraction patterns and EDS microanalysis

Sample	*Main phase*	*Main secondary phase*	*Sintering aids and impurities content (wt% as oxide)*			
			Y_2O_3	Al_2O_3	Fe_2O_3	CaO
HPSN	β-Si_3N_4	$Y_5N(SiO_4)_3$	9·7	1·8	0·3	–
SRBSN	β-Si_3N_4	–	1·5	3·2	–	–
RBSN	α-Si_3N_4 (60%)	β-Si_3N_4 (40%)	–	0·6	0·2	0·2

Table 3. Temperature and pressure for each oxidation test (duration = 24 h in each case)

Test	*Temperature (°C)*	*Pressure (MPa)*
A	400	12
B	400	22
C	400	30
D	400	40
IA	500	14
IB	500	20
IC	500	30
ID	500	40

configuration in the spectral range from 1400 to 200 cm^{-1} with a resolution of 2 cm^{-1}. A silvered mirror was used for background measurement.

3 Results

The first oxidation test sequence was carried out to evaluate the influence of temperature and pressure on the oxidation process, keeping the soaking time constant, to try to elucidate the different behaviour of the samples. In fact, by comparing the results obtained at the same operating condition, it was possible to evaluate differences in oxidation behaviour as a function of the silicon nitride formation technology.

With the second oxidation test it was possible to obtain a rough estimate of the kinetics of the oxidation process itself. However, results are only indicative because the weight changes during the process were influenced by many mechanisms, sometimes being in contrast with each other. Some of them led to a weight loss, others to a weight gain.

3.1 RBSN oxidation

Reaction-bonded silicon nitride is composed almost exclusively of a mixture of α-Si_3N_4 and β-Si_3N_4 with some impurities. So the oxidation process is conditioned by the direct reaction of silicon nitride with the external environment and by porosity. After the low-pressure test (14 MPa at 400 and 500°C) the morphology of the sample surface remained almost unchanged. However, the FTIR spectra showed a slight increase of the intensity of the peak corresponding to the Si–O stretching vibrational mode (1105 cm^{-1}), and a decrease of the Si–N stretching vibrational mode (Si–Nbs) due to the β-Si_3N_4 molecule (959 cm^{-1}) was noticed. In the diffraction patterns a broad peak positioned around the SiO_2 reflection (amorphous silica) was found; a sharp peak of low intensity due to the trydimite reflection was also detected.

In the test carried out at 20 MPa, the RBSN behaviour was little influenced by temperature. However, the amount of silicon nitride β-phase on the surface was reduced, as evidenced by FTIR analysis. Such an observation confirms that the β-phase is preferentially oxidized with respect to the α-phase, similar results have been reported by Contet *et al.*[11] for silicon nitride powder after hydrothermal oxidation. In the supercritical region oxidation is more marked (Fig. 1). The surface silica content increases and the presence of calcium silicate (probably rankiite) becomes evident (round particles in Fig. 2).

The time-dependent test (Fig. 3) showed that RBSN exhibited a weight increase at intermediate times (40 h), whereas after long exposure (100 h) the sample underwent a dramatic weight reduction. The strong initial weight gain may be explained by initial internal oxidation of the pores, which follows parabolic kinetics. The SiO_2 film grew on the pore walls, eventually closing the pores. After this the oxidation rate decreased, the weight increment being due only to external oxide growth.[21] The subsequent weight loss could be due to dissolution of the silica in the supercritical water, following linear kinetics.

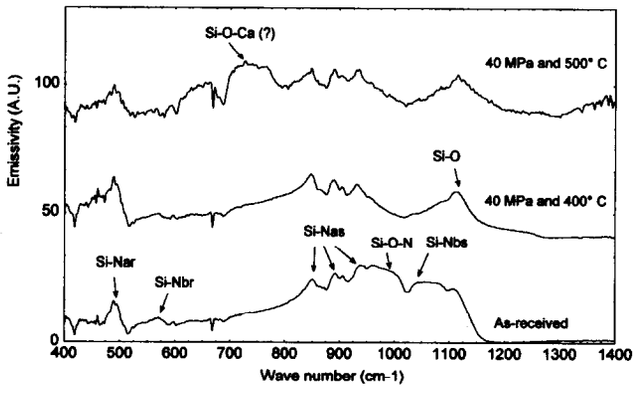

Fig. 1. FTIR spectra of RBSN samples after oxidation tests. Si–Nbs, beta-silicon nitride stretching vibrational mode, Si–Nbr, beta-silicon nitride rocking vibrational mode; Si–Nas, alpha-silicon nitride stretching vibrational mode; Si–Nar, alpha-silicon nitride rocking vibrational mode.

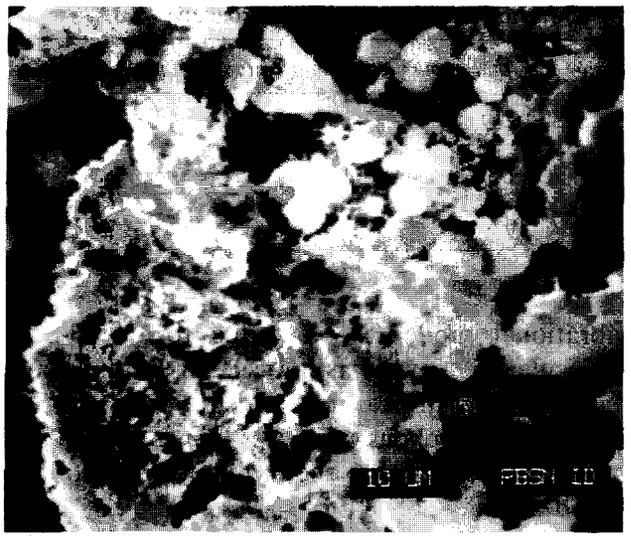

Fig. 2. SEM micrograph of RBSN sample after oxidation tests at 500°C and 40 MPa water pressure.

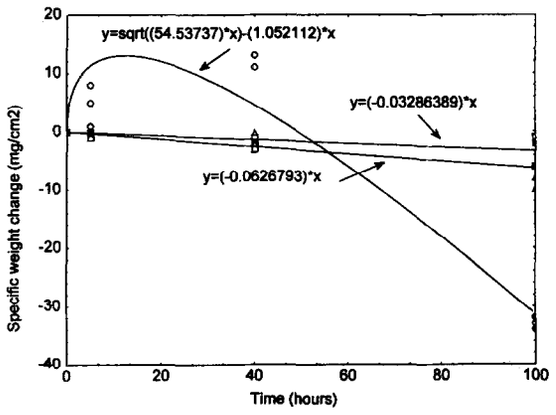

Fig. 3. Weight change vs. time for RBSN (○), HPSN (□) and SRBSN (△) samples after exposure at 400°C and 36 MPa water pressure.

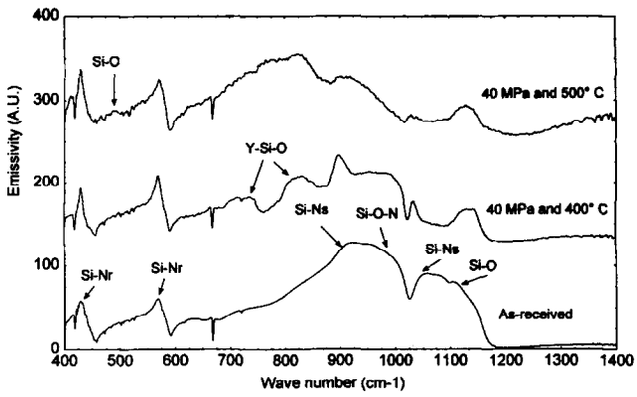

Fig. 4. FTIR spectra of HPSN samples after oxidation tests. Si–Ns, beta-silicon nitride stretching vibrational mode; Si–Nr, beta silicon nitride rocking vibrational mode.

Fig. 5. SEM micrograph of HPSN sample after oxidation tests at 400°C and 30 MPa water pressure.

3.2 HPSN oxidation

The oxidation resistance of hot-pressed silicon nitrides is conditioned strictly by the presence of sintering aids. In the low-temperature low-pressure test, the surface was practically unaffected by oxidation phenomena. On increasing the temperature, a noticeable amount of silica associated with a reduction of the stretching vibrational mode peak of silicon nitride was observed in FTIR spectra (Fig. 4). At higher pressure, but in the subcritical region, the surface was damaged markedly. Surface roughening was due to intense silica formation (strongly marked at 500°C) and was coupled with a reduction of the Si–O–N reflection in the FTIR spectra (960 cm^{-1}).

At 30 MPa and 400°C there was a noticeable increase in the content of yttrium silicon oxynitries ($Y_2ON_4Si_{12}O_{48}$ crystal and vitreous phase) as clearly shown in Fig. 5. Greater differences than in the subcritical region were revealed in the corresponding high-temperature test. In fact, at 500°C the above glassy phase disappeared as also confirmed by X-ray diffraction analysis. Such phenomena could be explained by detachment of the incoherent glassy phase itself due to its excessive growth. At the maximum pressure reached such a situation was more evident.

As far as the oxidation kinetics are concerned, the time-dependent test revealed a continuous, but limited, weight loss (Fig. 3).

3.3 SRBSN oxidation

The oxidation mechanism of sintered reaction-bonded silicon nitride was similar to that observed for HPSN. At low temperature the formation of a superficial glassy phase was observed. At 40 MPa this layer became incoherent and detached easily, exposing a silica-rich substrate (Fig. 6). Very interesting results were observed for tests conducted at 500°C: the nucleation and progressive growth of $Y_2Si_2O_5$ yttrium silicate crystals (Fig. 7). The growth of such crystals was strongly influenced by the water pressure, being maximized at 40 MPa. FTIR analysis revealed the almost complete disappearance

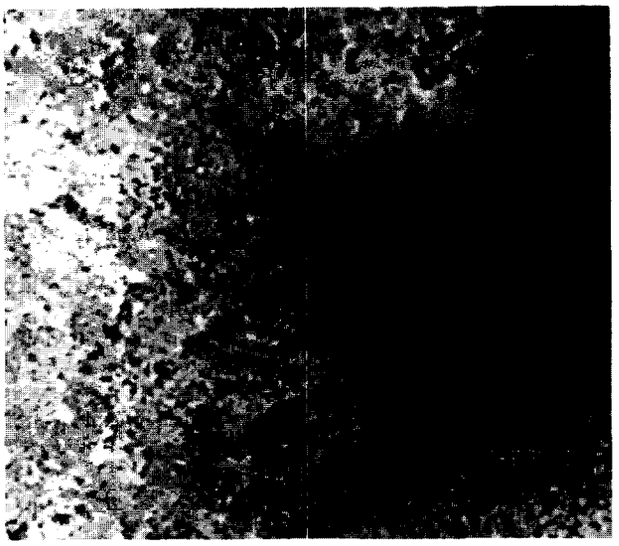

Fig. 6. SEM micrograph of SRBSN sample after oxidation tests at 400°C and 40 MPa water pressure.

Fig. 7. SEM micrograph of SRBSN sample after oxidation tests at 500°C and 40 MPa water pressure. The arrows indicate yttrium silicate crystals.

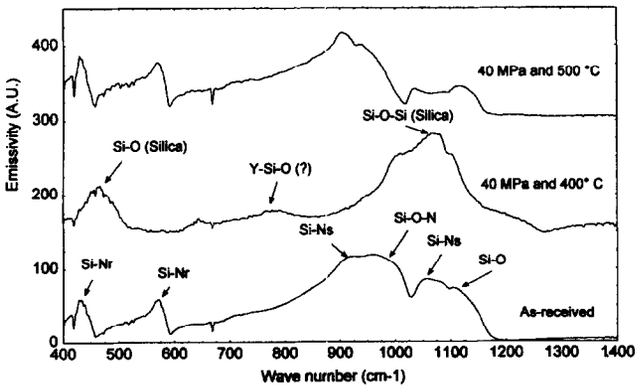

Fig. 8. FTIR spectra of SRBSN samples after oxidation tests. Si–Ns, beta-silicon nitride stretching vibrational mode; Si–Nr, beta-silicon nitride rocking vibrational mode.

of Si–O–N and Si–O–Si (silica) peaks (Fig. 8). The oxidation kinetics also showed a behaviour similar to that observed for HPSN with a weight loss increasing with time, but in this case a little more marked.

4 Discussion

Different considerations have to be made in the case of silicon nitride samples containing sintering aids and those comprising almost pure reaction-bonded silicon nitride. In the former case the growth of a silica glassy phase rich in metal ions is predominant. This is followed by debonding of such layers, exposing the underlying silica-rich scale, and thus increasing the environment aggressiveness. In the case of HPSN and SRBSN the oxidation reactions lead to a weight decrease with time. The loss of material in gas form (N_2, H_2 or NH_3), due to dissolution in supercritical water, and due to mechanical debonding of the incoherent scale, is predominant. Assuming linear kinetics for the weight loss, an apparent linear rate constant of 0·033 and 0·063 mg cm^{-2} h^{-1} was calculated for HPSN and SRBSN, respectively (Table 4).

A situation which should be discussed separately is the oxidation process at 500°C of SRBSN. In this case the nucleation and growth of yttrium silicate crystals over the oxidation scale were observed. Such phenomena could be related to the hydrothermal growth of crystals.[22] The different amount of sintering aids (and probably of minor contaminants), leading to a different composition, solubility and viscosity of the glassy phase, may explain the lack of a similar process for HPSN samples. However, further tests are required for a fuller explanation.

In the case of RBSN, internal oxidation due to its high open porosity characterizes the first oxidation stage with a noticeable weight gain.[21] The solubility of silica in supercritical water, following linear kinetics, could be the main factor influencing the weight loss observed after 100 h exposure at 400°C and 36 MPa. Such an assertion is supported also by visual observations: after cooling down the autoclave, there was a white deposit (silica powder) all over the platinum crucible and autoclave walls. Coupling the two processes, the

Table 4. Parabolic rate constant k_p (mg^2 cm^{-4} h^{-1}) and linear rate constant k_l (mg cm^{-2} h^{-1}) calculated from experimental data

Sample type	k_p	k_l
HPSN	–	0·033
RBSN	54·53	1·052
SRBSN	–	0·063
Silica glass[10]	–	0·176

effective weight changes of RBSN should follow the relationship

$$\frac{dw}{dt} = \frac{k_p}{t} - k_l$$

where w is the specific weight change (mg cm^{-2}), k_p the parabolic rate constant (mg^2 cm^{-4} h^{-1}) and k_l the linear rate constant (mg cm^{-2} h^{-1}). Fitting the experimental data (Fig. 3) by using the quasi-Newton estimation method and a least-squares loss function with the parametric function

$$w = \sqrt{k_p t} - k_l t$$

yielded an apparent parabolic oxidation rate constant (k_p) of 54·53 mg^2 cm^{-4} h^{-1} and an apparent linear weight loss rate constant k_l of 1·05 mg cm^{-2} h^{-1}. This last value is about six times higher than that reported by Ito and Tomozawa,[10] 0·176 mg cm^{-2} h^{-1}, for silica glass (a density of 2·2 g cm^{-3} was assumed here) in distilled water at 285°C under 100 MPa pressure. For comparison, the corresponding values of the constants for HPSN and SRBSN are reported in Table 4.

At high water pressure, independent of the temperature, the oxidation scale is characterized by enrichment in ion impurities, mainly calcium, which lead to the formation of incoherent oxidation product. The selective oxidation of the β-silicon nitride phase was evidenced by FTIR spectra. This preferential oxidation could however be an artefact, since if the β-phase origin is a film over the α-grains,[11] its consumption will undoubtedly be faster and predominant over the α-phase. Such assumptions have yet to be demonstrated.

5 Conclusions

(1) In spite of the low temperature, high-pressure water oxidation tests significantly alter the surface of sintered silicon nitride. Increasing both pressure and temperature causes the oxidation attack to be stronger and stronger.

(2) In such situations sintering aids and impurities also have a detrimental effect on oxidation behaviour, promoting the formation of incoherent glassy phase over the surface in analogy with the high-temperature (1000°C) oxidation mechanism.

(3) The high open porosity has a strong influence on the oxidation kinetics of RBSN. A noticeable weight gain was observed after 40 h exposure at 400°C and 36 MPa.

(4) The solubility of silica in supercritical water seems to have a great influence on the stability of the oxidation scale, mainly on the RBSN sample surface.

References

1. Gogotsi, Y. G. & Yoshimura, M., Water effect on corrosion behaviour of structural ceramics. *MRS Bull.*, **19**[10] (1994) 39–54.
2. Horton, R. M., Oxidation kinetics of powdered silicon nitride. *J. Am. Ceram. Soc.*, **52**[3] (1969) 121–124.
3. Singhal, S. C., Effect of water vapor on the oxidation of hot pressed silicon nitride and silicon carbide. *J. Am. Ceram. Soc.*, **59**[1–2] (1976) 81–82.
4. Opila, E. J., Oxidation kinetics of chemically vapor-deposited silicon carbide in wet oxygen. *J. Am. Ceram. Soc.*, **77**[3] (1994) 730–736.
5. Maeda, M., Nakamura, K. & Ohkubo, T., Oxidation of silicon nitride in a wet atmosphere. *J. Mater. Sci. Lett.*, **24** (1989) 2120–2126.
6. Proverbio, E., Rossi, D. & Cigna, R., Influence of water vapour on high-temperature oxidation of Al_2O_3–MgO doped hot-pressed silicon nitride. *J. Eur. Ceram. Soc.*, **9** (1992) 453–458.
7. Opila, E. J., Influence of alumina reaction tube impurities on the oxidation of chemically vapor-deposited silicon carbide. *J. Am. Ceram. Soc.*, **78**[4] (1995) 1107–1110.
8. Kennedy, G., A portion of the system silica–water. *Econ. Geol.*, **45**[7] (1950) 629–653.
9. Iler, R. K., *The Chemistry of Silica*. John Wiley & Sons, Inc., New York, 1979.
10. Ito, S. & Tomozawa, M., Stress corrosion of silica glass. *J. Am. Ceram. Soc.*, **64** (1981) C-60.
11. Contet, C., Kase, J. I., Noma, T. & Yoshimura, M., Hydrothermal oxidation of Si_3N_4 powder. *J. Mater. Sci. Lett.*, **6** (1987) 963–964.
12. Yoshimura, M., Kase, J. I., Hayakawa, M. & Somiya S., Oxidation mechanism of nitride and carbide powders by high-temperature, high-pressure water. *Ceram. Trans.*, **10** (1990) 337–354.
13. Gogotsi, Y. G. & Yoshimura, M., Low-temperature oxidation, hydrothermal corrosion, and their effects on properties of SiC (Tyranno) fibers. *J. Am. Ceram. Soc.*, **78**[6] (1995) 1439–1450.
14. Gogotsi, Y. G. & Yoshimura, M., Degradation of SiC (Tyranno) fibers in high-temperature, high-pressure water. *J. Mater. Sci. Lett.*, **14** (1995) 755–759.
15. Hirayama, H., Kawakubo, T., Goto, A. & Kaneko, T., Corrosion behaviour of silicon carbide. *J. Am. Ceram. Soc.*, **72**[11] (1989) 2049–2053.
16. Kitaoka, S., Tsuji, T., Katoh, T., Yamaguchi, Y. & Kashiwagi, K., Tribological characteristics of SiC ceramics in high-temperature and high-pressure water. *J. Am. Ceram. Soc.*, **77**[7] (1994) 1851–1856.
17. Gogotsi, Y. G., Kofstad, P., Yoshimura, M. & Nickel, K., Formation of sp^3-bonded carbon upon hydrothermal treatment of SiC. *Diamond Relat. Mater.*, (in press).
18. Sato, T., Haryu, K., Endo, T. & Shimada M., High temperature oxidation of silicon nitride-based ceramics by water vapour. *J. Mater. Sci.*, **22** (1987) 2635–2640.
19. Yoshio, T. & Oda, K., Aqueous corrosion and pit formation of Si_3N_4 under hydrothermal conditions. *Ceram. Trans.*, **10** (1990) 367–385.
20. Oda, K., Yoshio, T., Miyamoto, Y. & Koizumi, M., Hydrothermal corrosion of pure, hot isostatically pressed silicon nitride. *J. Am. Ceram. Soc.*, **76**[5] (1993) 1365–1368.
21. Thümmler, P. F., Oxidation mechanism of porous silicon nitride. *J. Mater. Sci. Lett.*, **19** (1984) 1283–1295.
22. Somiya, S., Yoshimura, M., Suzuki, & M. L. Yamaguchi, T., Mullite powder from hydrothermal processing. *Ceram. Trans.*, **6** (1990) 287–310.

Journal of the European Ceramic Society **16** (1996) 1127–1132

PII: S0955-2219(96)00032-5
0955-2219/96/$15.00

Changes in Surface Characteristics of Silicon Nitride Prepared for Extrusion

R. M. Torres Sanchez,[a] A. B. Garcia[b] & A. M. Cesio[a]

[a]CETMIC, Cno Centenario y 508, CC.49 (CP 1897) M. B. Gonnet, Buenos Aires, Argentina
[b]Instituto Nacional del Carbón, CSIC, La Corredoria s/n Apdo. 73, 33080-Oviedo, Spain

(Received 24 July 1995; revised version received 18 January 1996; accepted 23 January 1996)

Abstract

The preparation step for extrusion (with binders) of Si_3N_4 powder, as well as the extrusion process itself, modify the original properties of the powder so that its recovery and subsequent rework are not possible.

X-ray photoelectron spectroscopy (XPS), X-ray diffraction, infra-red spectroscopy, potentiometric titrations and zeta potential determinations have been used to identify the surface modifications in Si_3N_4 due to addition of binders, and to examine powders after elimination of the binders by extraction with organic solvents and heat treatment.

The original Si_3N_4 with binders showed a shift in zeta potential and point of zero charge (PZC) to lower pH, indicating the adsorption of organic compounds on the Si_3N_4 surface at this step. The appearance of one O_{ls} peak at 532·3 eV in the XPS spectrum showed the presence of Si_2N_2O. After extraction with organic solvents the PZC value was close to that of the Si_3N_4 + binders (pH = 3·2), indicating incomplete removal of organics; this was confirmed by XPS determination (C_{ls} intensity data) and chemical analysis. The presence of Si_2N_2O was not modified as shown by XPS and the value of the isoelectric point. Heat treatment removes the organics completely but produces an oxidation of Si_3N_4 to SiO_2 as evidenced by a shift in the binding energy of the O_{ls} photopeak to 534·0 eV.
© 1996 Elsevier Science Limited.

La mélange du Si_3N_4 en poudre avec des liants organiques et son postérieur processus d'extrusion, produit des modifications dans les propriétés originelles du Si_3N_4 qui ne permettent pas sa récupération et subsequent réutilisation. L'identification des modifications superficielles du Si_3N_4 avec des liants et après élimination des liants par extraction par solvents organiques et traitement thermique, ont été suivis par ESCA, DRX IR, titrages potenciomètriques et potentiel zèta.

Le Si_3N_4 avec liants a montré une diminution de la valeur du potentiel zèta et du point de zero charge (PZC), par rapport au Si_3N_4, ce qui indique l'existence d'adsorptions organiques superficielles. Le spectre ESCA, avec une pic à 532·4 eV (O_{ls}) démontre la présence du Si_2N_2O. Après l'extraction par solvents organiques, la valeur du PZC, près du Si_3N_4 + binders (pH = 3.2), marque la disparition partiel des liants organiques, aussi bien que les donnés d'intensité du C_{ls} et des analises chimiqués. L'ESCA et la valeur de IEP ont montré aussi la présence du Si_2N_2O. Le traitement thermique élimine completement les liants organiques mais produit l'oxidation du Si_3N_4 à SiO_2 comme montré l'apparition d'un pic a 534·0 eV du O_{ls}.

Introduction

The processing of silicon nitride powders to produce ceramics and the characteristics of the ceramics have been widely studied and reported.[1] Properties such as high fracture strength and decomposition point, and good wear, oxidation and thermal shock resistances make silicon nitride ceramics attractive for application in high-temperature machine parts.

The main forming process is injection (or extrusion) moulding; binders are mixed with Si_3N_4 powder and the forming process is similar to those used for plastics. Different and at times complex shapes, which are required by machine parts, can be achieved using this method. However, the binders (15–25%) must be removed before sintering. When a hot isostatic press (1000–3000 kg cm^{-2}, 500–2000°C) is employed, the application of binders is not necessary. In this case, the powder is formed and sintered in one step, but this is a high-cost process and complexity of the part shape is a limiting factor. In consequence, extrusion and the subsequent sintering process are used extensively.

Obviously, after the sintering temperature has been applied to the brown body and a material with high fracture strength obtained, recovery and subsequent rework of the powder is not possible. Therefore, the silicon nitride will be wasted if the shape or other

properties of the final product do not satisfy the requirements.

Although recovery of the powder with its original properties from the brown body might be feasible, it has not been achieved to date.[2] Binders can be adsorbed with no subsequent elimination, modifying the surface properties of the silicon nitride powder and hindering its recovery not only after extrusion but also after thermal treatment for 1 week at 500°C. Thick, immobile, adsorbed layers of silane coupling agents have been reported[3] to be responsible for the creation of defects during binder removal. Consequently, study of the surface properties of Si_3N_4 powder, as well as those of brown bodies, is very important for exploring the possibility of powder recovery before sintering.

It is well known that surface composition influences the colloidal dispersion behaviour of silicon nitride powders in aqueous suspensions. This has a strong influence on the physical properties of the final sintered product.[4–8] Measurements of the surface charge by means of titration techniques have been used to characterize as-received and treated silicon nitride powders. Minor differences in powder surface compositions lead to changes in the point of zero charge (PZC) as determined by surface titration. In this way, depending on the source of the material, the PZC of silicon nitride powder has been found in the pH range 3–9.[5] X-ray photoelectron spectroscopy (XPS) is a surface-sensitive technique that has been used to analyse the surface layer composition of several commercial silicon nitride powders.[9] Even when these powders are just exposed to ambient conditions, different proportions of silica and silicon oxynitride compounds have been identified. Consequently, these alterations in surface layer composition and structure would influence the behaviour of binders during steps in the formation of green and brown bodies.

This research is aimed at gaining an understanding of the transformations undergone by silicon nitride powder as a consequence of (1) the addition of binders and (2) their later elimination, by heat treatment or organic solvent extraction. Changes in surface composition have been studied by XPS and measurement of the surface charge by potentiometric titration and microelectrophoresis, whereas X-ray diffraction (XRD) and infra-red (IR) spectroscopy were used to monitor changes in the bulk sample.

Experimental

Materials

A commercial α-Si_3N_4 (95%) powder from Ube (SN-E10), with a particle size (80%) <0·8 μm and specific surface area of 9–13 $m^2\ g^{-1}$ (manufacturer's specifications), was selected for this research. The brown bodies, prepared from this powder, were kindly supplied by the Industrial Research Institute Aichi Prefectural Government. The binders utilized were polypropylene, polystyrene, propyl methacrylate, stearic acid and dioctylphtalate, in a ratio of binders/Si_3N_4 close to 20%.

Binder elimination methods

Binder elimination from brown bodies was carried out by heat treatment. The sample was milled by hand and heated at 500°C for 1 week. Heat treatment is the usual method employed in the industrial processing of silicon nitride powders. In the second method, not used in manufacturing processes, the binders were eliminated by extraction with organic solvents. In these experiments, the sample was treated with concentrated nitric acid followed by slow drying at 100°C, washed with water until neutral pH and washed again with ethanol. After this first treatment was completed, the residue was consecutively Soxhlet extracted and solvent washed with toluene (3 h), chloroform (4 h) and ethanol (1 h), heated in the presence of H_2O_2 to dryness and finally washed several times with distilled water.

Characterization techniques

X-ray diffractograms were obtained on a Philips PW 1140 diffractometer using CuK_α radiation and an Ni filter. The working conditions were 40 kV and 20 mA. Samples were analysed by means of the powder mounting technique.

Infra-red spectra of samples were obtained on KBr pellets (1% sample/KBr) using a Perkin–Elmer 577 spectrometer. The spectra were recorded on absorbance.

XPS analyses were performed in an ESCA Shimadzu 750 spectrometer with an Escapac 750 system. An Mg anode (1253 eV) operating at 30 mA and 8 mV was used as excitation source in a residual vacuum of 10^{-5} Pa. An energy correction was made to account for sample charging based on the C_{1s}, peak at 285 eV. The XPS spectra were normalized, the area of the peaks integrated and the full width at half-maximum (FWHM) measured.

Potentiometric titration experiments were carried out by first dispersing 5 g of sample in 90 ml of 0·1 or 0·001 M KCl supporting electrolyte. These dispersions were then titrated in nitrogen atmosphere with 0·1 M HCl or KOH solutions by adding a fixed volume of titrant every 15 min.[10] For each experiment, the relative adsorption of proton or hydroxyl ions by the solid, reported as $\mu C\ g^{-1}$, was plotted as a function of the dispersion pH. The common intersection point in the potentiometric curves obtained at different electrolyte concentrations was

considered as the point of zero charge (PZC) of the sample. Samples were washed with water and ultracentrifuged before potentiometric titration was carried out.

Electrokinetic potentials of samples were determined using a Laser Zee Meter 501. The electrophoretic mobilities were converted into zeta potentials according to the Smoluchowski equation. For each determination, 0·05–0·1 g of sample was dispersed in 100 ml of 0·01 M KCl solution and the slurry stirred magnetically for at least 18–24 h before the measurements were carried out. To generate zeta potential versus pH curves and from them the isoelectric point (IEP), the pH of the slurry was adjusted using dilute HCl and KOH solutions followed by magnetic stirring to equilibrium.

Results and Discussion

Bulk characterization

Comparison of the XRD pattern of original silicon nitride (Si_3N_4) with those corresponding to samples obtained after binder addition (Si_3N_4 + binders) and subsequent removal by organic extraction (Si_3N_4 + binders/organic) or heat treatment (Si_3N_4 + binders/500°C), shown in Fig. 1, does not reveal any differences in number or in position of the peaks between the samples. These results indicate that the introduction and later elimination of the binders, by both organic extraction and heat treatment, do not lead to modifications of the crystalline species of the silicon nitride powder.

The IR spectra of the samples are illustrated in Fig. 2. The spectrum of Si_3N_4 + binders (spectrum b) shows bands at 1380, 1460, 2850, 2930 and 2970 cm^{-1} and at 1730 cm^{-1} which correspond to aliphatic C–H bonds and carbonyl (C=O) groups, respectively, of the organic compounds used as binders. These bands disappear after the sample has been treated to eliminate the binders (spectra c and d) and the spectra are similar to that obtained from original silicon nitride powder (spectrum a). The addition of binders followed by their removal does not introduce changes in the structure of the silicon nitride powder detectable by IR. However, a residual carbon content of 0·75% has been determined chemically in the Si_3N_4 + binders/organic sample No carbon was found in the Si_3N_4 + binders/500°C sample. The organic carbon concentration of the Si_3N_4 + binders sample was 18·2%.

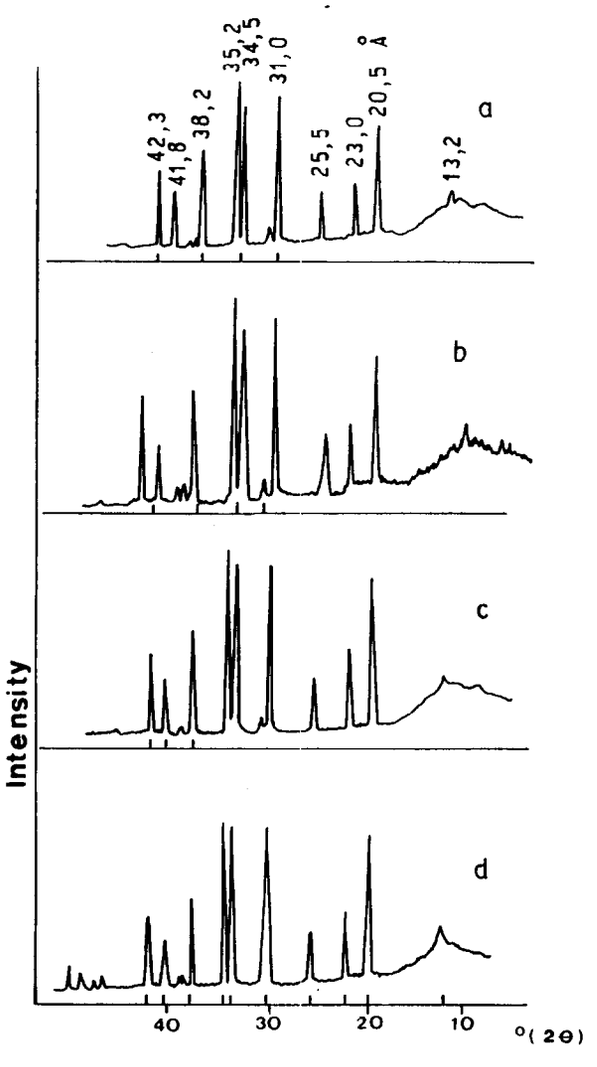

Fig. 1. XRD patterns of samples: (a) Si_3N_4, (b) Si_3N_4 + binders, (c) Si_3N_4 + binders/organic and (d) Si_3N_4 + binders/500°C.

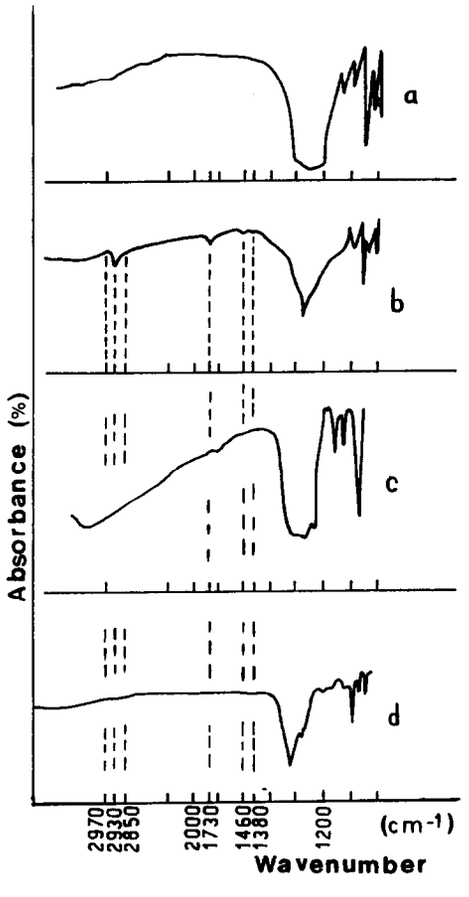

Fig. 2. IR spectra of samples: (a) Si_3N_4, (b) Si_3N_4 + binders, (c) Si_3N_4binders/organic and (d) Si_3N_4 = binders/500°C.

Table 1. Area (a.u.) and FWHM (eV) measured for C_{ls}, N_{ls}, O_{ls} and Si_{2p} peaks in the XPS spectra of samples

	Si_3N_4 + binders	*Si_3N_4 + binders/organic*	*Si_2N_4 + binders/500°C*
Peak area			
C_{ls}	70113	31436	24023
N_{ls}	3411	7102	29630
O_{ls}	23085	25487	61106
Si_{2p}	4320	4638	18576
FWHM			
C_{ls}	2·2	2·1	3·0
N_{ls}	1·8	1·9	2·0
O_{ls}	2·7	2·9	2·5
Si_{2p}	2·3	2·2	2·4

Surface characterization

Table 1 shows values of the area and FWHM for peaks in the XPS spectra of Si_3N_4 + binders, Si_3N_4 + binders/organic and Si_3N_4 + binders/500°C. The N_{ls} and Si_{2p} peaks were symmetrical and could not be deconvoluted, their FWHM values being similar to those obtained by Bergstrom and Pugh[7] for three silicon nitride powders of different origin (N_{ls} = 2·1 ± 0·07 eV and Si_{2p}= 2·4 ± 0·04 eV). As expected, the removal of organic compounds led to a decrease in the C_{ls} peak area. In the case of the Si_3N_4 + binders/organic sample, the area decrease was less sharp. This result agrees with the residual carbon content that was chemically determined in this sample as mentioned above. Unlike carbon, oxygen content at the surface increases upon elimination of binders, this being especially remarkable for the Si_3N_4 + binders/500°C sample Thus compared with those of Si_3N_4 + binders and Si_3N_4 + binders/organic, the area of the O_{ls}, peak for Si_3N_4 + binders/500°C is more than doubled. These results suggest the oxidation of the sample surface during binder elimination mainly by heat treatment. The increase of N_{ls} and Si_{2p} areas could be due to organic screen elimination.

The measured binding energies (BE) of N_{ls}, O_{ls} and Si_{2p} electron levels from XPS spectra of Si_3N_4 + binders, Si_3N_4 + binders/organic and Si_3N_4 + binders/500°C are given in Table 2, together (for comparison) with binding energies for Si_3N_4, SiO_2 and Si_2N_2O previously reported by other authors.[7–9,11,12] The addition of binders to silicon nitride powder does not modify the binding energies of the N_{ls} and Si_{2p} electron levels. However, a signal appears at 532·5eV which can be ascribed to O_{ls} from Si_2N_2O. The peaks corresponding to N_{ls} and Si_{2p} are shifted to higher energies after the removal of binders. In addition, for Si_3N_4 + binders/500°C, the energy increase of the Si_{2p} level is higher and approaches that of SiO_2. The energies of Si_{2p} and O_{ls} for the Si_3N_4 + binders/organic sample are comparable to those of Si_2N_2O. When the Si–N bond is converted to Si–O by surface oxidation, the charge on Si atoms will increase. Consequently, the binding energy of Si_{2p} will be higher. The Pauling charge on Si atoms for samples have been estimated based on a linear relationship established by Brown and Pantano[6,11] between average charge on Si atoms and binding energy of Si_{2p} level for several silicon compounds. Average charges on Si atoms of 1·67, 1·89 and 2·30 eV for Si_3N_4 + binders, Si_3N_4 + binders/organic and Si_3N_4 + binders/500°C, respectively, have been obtained. Values of 1·56, 1·81 and 2·34 eV were previously determined on Si atoms for Si_3N_4, Si_2N_2O and SiO_2. These results suggest that the outer surfaces of the brown bodies studied are on the whole silica-like when heat treatment is applied, whereas the predominant compound in the solvent extracted samples seems to be oxynitride-like.

The titration curves of silicon nitride, silicon nitride with binders and those samples obtained after binder removal are illustrated in Fig. 3. The PZC of silicon nitride occurs at pH 6·2 [Fig. 3(a)]. This result is in agreement with that previously reported for this powder.[5] The presence of binders shifts the PZC value of silicon nitride to pH 2·8 [Figure 3(b)] and the subsequent extraction with organic solvents to pH 3·2 [Fig. 3(c)]. This result shows the presence of acidic groups after addition of binders. The PZC for Si_3N_4 + binders/500°C at pH = 5·5 [Fig. 3(d)] is close to that of the original silicon nitride powder [Fig. 3(a)]. It seems that removal of binders by heat treatment partly restores the original titrated surface groups of silicon nitride powder, but the charge density does not attain the original Si_3N_4 value (e.g. at pH 7 for Si_3N_4 the charge density was

Table 2. Binding energies (BE in eV) of N_{ls}, O_{ls} and Si_{2p} in the XPS spectra of samples and those of silica, silicon nitride and silicon oxynitride[7–9,11,12]

Sample	*N_{ls}*	*O_{ls}*	*Si_{2p}*
Si_3N_4	397·3–397·7	–	101·4–101·7
Si_3N_4 + binders	397·9	532·5	101·7
Si_3N_4 + binders/organic	398·2	532·6	102·1
Si_3N_4 + binders/500°C	399·0	534·0	103·0
Si_2N_2O	397·7–397·9	532·6	101·9–103·1
SiO_2	–	533·6	103·6

10×10^6 $\mu C\ g^{-1}$ and for Si_3N_4 + binders/500°C was $0{\cdot}5 \times 10^6$ $\mu C\ g^{-1}$). The oxidation of Si_3N_4 to Si_2N_2O or SiO_2, detected by XPS results, is not evidenced by titration curves.

An isoelectric point (IEP) at pH range 6–7 has been reported for the silicon nitride powder employed in this work.[4,12] As shown in Table 3, the addition of binders to silicon nitride to form the brown body shifts the IEP value to lower pHs. Si_3N_4 + binders shows an IEP at pH = 2·1. In addition, the removal of binders does not lead to the recovery of the original IEP at pH range 6–7. The IEP has been reported to provide an estimate of the acidity of the solid surface, which increases as the IEP is shifted to lower pHs. Based on this, the addition of binders to silicon nitride powder clearly increases its acidity. These results suggest that the surface of silicon nitride was oxidized during the first step of processing, in agreement with XPS results, as a consequence of binder addition. Therefore, their subsequent elimination will result in changes in surface composition but the oxidized surface groups will remain or even increase in concentration, depending on the binder removal method used. The IEP differences between solvent extracted (IEP at pH 2·2) and heat-treated (IEP at pH 3·3) samples may be due to the remaining organic compounds adsorbed on the surface of the former. The difference between the IEP and PZC values (pH = 5·5 and 3·3, respectively) for the Si_3N_4 +binders/500°C sample indicates the surface adsorption of a compound of lower PZC such as SiO_2 (PZC of SiO_2 pH = 2 to 2.5[14]).

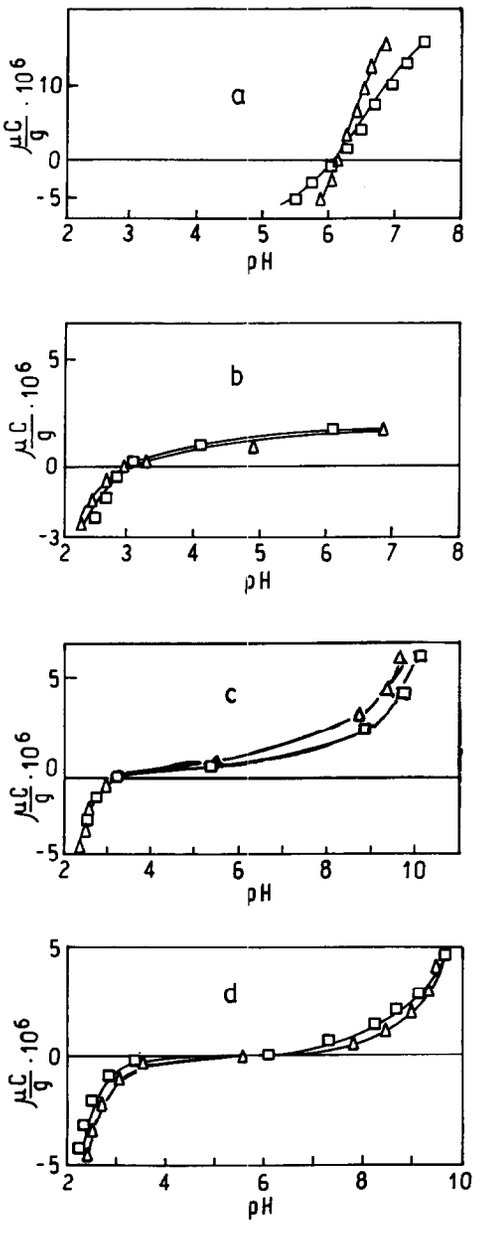

Fig. 3. Titration curves of samples: (a) Si_3N_4, (b) Si_3N_4 + binders, (c) Si_3N_4 + binders/organic and (d) Si_3N_4 + binders /500°C. In KCl supporting electrolyte: (□) 10^{-1} and (△) 10^{-3} M.

Table 3. IEPs of samples from zeta potential versus pH curves and that of silicon nitride[5,13]

Samples	pH_{IEP}
Si_3N_4	6–7
Si_3N_4 + binders	2·1
Si_3N_4 + binders/organic	2·2
Si_3N_4 + binders/500°C	3·3

The surface oxygen content has been found to have a clear influence on the pH of the IEP of silicon nitride powders. In fact, a linear relationship between the surface oxygen content and the pH of the IEP was established for these compounds.[9] For example, by applying this equation the to the IEP value of the Si_3N_4 + binders/500°C sample, a surface oxygen content of 0·10 g/cm^{-2} was estimated, whereas the oxygen content of the original silicon nitride powder was 0·04 g/cm^{-2}. This surface oxygen increase of more than twice in Si_3N_4 + binders/500°C is assigned to SiO_2 in agreement with XPS results, and corroborates the difference observed between IEP and PZC values.

Conclusion

The addition of binders to Si_3N_4 powders, for extrusion, leads to surface changes which hinder its recovery from the brown body step and after extraction by organic solvents or heat treatments.

Binder addition results in adsorption of organic compounds on the Si_3N_4 surface, evidenced by an abrupt decrease in the pH values of IEP and PZC from 6·2 and 6–7 to 2·1 and 2·8, respectively. A surface oxidation to Si_2N_2O was revealed by the appearance of an O_{1s}, photopeak, in the XPS spectra, at 532·3 eV.

Binder extraction by treatment with organic solvents produces an intense but not total elimination of organic adsorption as shown by the decrease of C_{1s}

peak area from 70 113 to 31 436 (a.u.) and by chemical analysis. The similar IEP and PZC values obtained for samples Si_3N_4 + binders and Si_3N_4 + binders/organic indicate that surface modifications remain unaltered.

Heat treatment eliminates the surface organic adsorption and produces Si_3N_4 oxidation to SiO_2, as revealed by the more than two-fold increase in the O_{1s} photopeak area and the difference between IEP and PZC values.

Acknowledgements

The authors would like to thank Dra. L. Cornaglia of the Departamento de Fisico-Quimica, Facultad de Ingenieria, Universidad del Litoral, for assistance in XPS.

References

1. Meethan, G. W., High temperature materials — a general review. *J. Mater. Sci.*, **26** (1991) 853–860.
2. Seno, A., Personal communication, Industrial Research Institute Aichi Prefectural Govenment.
3. Edirisinghe, M. J., The use of silane coupling agents in ceramic injection moulding: effect on polymer removal. *J. Mater. Sci. Lett.*, **9** (1990) 1039–1041.
4. Withman, P. K. & Fede, D. L., Colloidal characterization of ultrafine silicon carbide and silicon nitride powders. *Adv. Ceram. Mater.*, **1**[4] (1986) 366–370.
5. Whitman, P. K. & Fede, D. L., Comparison of the surface charge behavior of commercial silicon nitride and silicon carbide. *J. Am. Ceram. Soc.*, **71**[12] (1988) 1086–1093.
6. Brown, R. K. & Pantano, C., Compositionally dependent Si_{2p} binding energy shifts in silicon oxynitride thin films. *J. Am. Ceram. Soc.*, **69**[4] (1986) 314–316.
7. Bergstrom, L. & Pugh, R. J., Interfacial characterization of silicon nitride powders. *J. Am. Ceram. Soc.*, **72**[1] (1989) 103–109.
8. Rahaman, M. N., Boiteux, Y. & De Jonghe, L. C., Surface characterization of silicon nitride and silicon carbide powders. *Am. Ceram. Soc. Bull.*, **65**[8] (1986) 1171–1176.
9. Greil, P., Nitzsche, R., Friedich, H. & Hermel, W., Evaluation of oxygen content on silicon nitride powders surface from measurement of the isoelectric point. *J. Eur. Ceram. Soc.*, **7** (1991) 353–359.
10. Block, L. & De Bruyn, P. L., The ionic double layer at ZnO/solution interface. I The experimental point of zero charge. *J. Coll. Interf. Sci.*, **32** (1970) 518–521.
11. Brown, R. K. & Pantano, C., Thermochem. nitridation of microporous silica films in ammonia. *J. Am. Ceram. Soc.*, **70**[1] (1987) 9–14.
12. Torres Sanchez, R. M., Etude de la relation entre le fer externe et la kaolinite. Thesis, Univ. Cath. de Louvain, Belgium, 1983.
13. Greil, P., Colloidal procesing of silicon nitride ceramics review. In *Proc. 3rd Int. Ceramic Materials and Components for Engines*, ed. V. Tennery. Am. Ceram. Soc., Westerville, OH, 1989, pp. 319–329.
14. Iller R. K., in *The Chemistry of Silica*, Wiley Interscience Publishers, 1972, p. 660.

Journal of the European Ceramic Society 16 (1996) 1133–1139

PII: S0955-2219(96)00030-1
0955-2219/96/$15.00

Plasma-Sprayed Ceramic Coatings for SiAlON Ceramics

B. S. B. Karunaratne & M. H. Lewis

Centre for Advanced Materials, University of Warwick, Coventry CV4 7AL, UK

(Received 10 October 1995; revised version received 8 January 1996; accepted 12 January 1996)

Abstract

Plasma-sprayed coatings of yttria-stabilized ZrO_2 and $Al_2O_3.TiO_2$ used as a protective barrier on β-Si_3N_4-based sialon ceramics were investigated. The coatings showed better cohesion with the pre-oxidized surfaces due to the reaction between the SiO_2-rich oxidation layer and the coating materials. Formation of low thermal expansion zircon and aluminium titanate on the pre-oxidized ceramic was studied using scanning electron microscopy and X-ray diffraction. Preliminary experiments on oxidation and molten metal immersion, showed that the coatings provide significant protection against oxidation and molten metal attack. © 1996 Elsevier Science Limited.

1 Introduction

Si_3N_4-based sialon ceramics are possible candidate materials for a number of advanced heat engine applications, molten metal containment, wear-resistant applications, etc. However, oxidation, hot salt corrosion and molten metal attack are some of the major limitations for high-temperature applications of these ceramics. These effects are more pronounced in pressureless-sintered sialon ceramics due to the presence of intergranular glass phases.[1] The problem of oxidation, above 1200°C, of pressureless-sintered sialon ceramics has been partially solved by stabilizing the metallic ions by the crystallization of the residual intergranular glass phase.[2] However, this improves oxidation resistance only up to 1300°C. Above this temperature, the crystalline intergranular phase becomes a liquid silicate due to its reaction with oxidation products on the surface (mainly SiO_2) and the problem of oxidation becomes severe.

Protective coatings are widely used to improve the corrosion, oxidation and wear resistance of high-temperature components.[3–5] The main objective of this work was to explore the feasibility of using plasma-spraying to produce a protective diffusion or corrosion barrier on sialon ceramics. Plasma-spraying has several advantages over other surface coating techniques such as chemical vapour deposition (CVD). Spraying of plasma coatings is simple, relatively inexpensive and can be carried out in a short time in a controlled manner. However, plasma-spraying at ambient pressure in moderately oxidizing conditions restricts the sprayed powders to the oxides. In addition, the availability of powders having suitable particle size for plasma-spraying imposes further restrictions. The major problem associated with ceramic oxide coatings is the mismatch in thermal expansion coefficient, α, with the substrate ceramics (α for oxides is typically 6–10 $\times$ 10^{-6} K^{-1} and α for sialon ceramics 3 $\times$ 10^{-6} K^{-1}). However, the use of intermediate layers of mid-range thermal expansion may alleviate the problem of layer cracking or spalling on thermal cycling. The intermediate layers may be formed by pre-oxidation of the substrate ceramic or prior deposition of silicate films of selected composition. These silicate films are reactive with the plasma-sprayed coating and are expected to provide good cohesion. In this work, zirconia (ZrO_2) and aluminium titanate (Al_2TiO_5) were chosen for plasma-spraying on the sialon ceramics.

It is known that pure ZrO_2 undergoes a volume expansion when it transforms from the tetragonal phase to the monoclinic phase[6,7] during cooling below 1200°C. This could lead to extensive micro-cracking and hence reduction in the protective properties of the coating. However, the addition of about 15 mol% Y_2O_3 results in the formation of a stabilized cubic phase which does not transform[7] into the monoclinic phase. ZrO_2 in all its polymorphic forms has a high thermal expansion coefficient (α) compared with sialon. However, its reaction product with SiO_2, believed to be zircon, has a value of α (4 $\times$ 10^{-6} K^{-1}) comparable to that of sialon ceramics (3 $\times$ 10^{-6} K^{-1}).

Al_2TiO_5 has a very low thermal expansion coefficient and should help alleviate the problem

of spalling during thermal cycling. The low thermal expansion property is due to the expansion anisotropy of individual orthorhombic Al_2TiO_5 crystals[8] giving rise to a stable microcracked structure[9,10] in the polycrystalline state. However, due to the non-availability of a suitable pre-reacted aluminium titanate powder, a powder mixture of Al_2O_3 and TiO_2 was sprayed on the sialon ceramics. A reaction between Al_2O_3 and TiO_2 to form Al_2TiO_5 could be expected during plasma-spraying, due to the very high temperature of the plasma.

2 Materials and Spraying Conditions

2.1 Substrate ceramic

Pressureless-sintered, diphasic sialon samples of dimensions 3 mm × 3 mm × 50 mm were used as the substrate ceramic. The two phases of this material are β' (Al-substituted β-Si_3N_4) and an Y/Al-rich silicate matrix (YAG).[2] One side of the substrate ceramic was exposed to the plasma in various surface conditions:

(i) diamond cut and lapped to 1 μm grit;
(ii) similar surface finish to (i) and pre-oxidized at 1220°C to form a SiO_2-rich layer;
(iii) diamond cut and lapped to ~30 μm grit; and
(iv) similar surface finish to (iii) and pre-oxidized at 1220°C.

2.2 Spraying powders

A 13 wt% yttria-stabilized ZrO_2 (YSZ) powder (Plasmatex 1081), of particle size in the range 20–75 μm, was sprayed via a H_2/argon plasma at a distance of 110 mm from the ceramic substrate. Different layer thicknesses of YSZ were sprayed on ceramic substrates having pre-oxidized layers of thicknesses in the range of 5–30 μm. The thickness of the plasma layer was preselected to match the oxide layer in order to obtain complete growth of a low thermal expansion zircon ($ZrSiO_4$) film during post-spraying heat treatment.

A powder mixture of 60 wt% Al_2O_3 and 40 wt% TiO_2 (Plasmatex 1021), of particle size in the range 5–25 μm, was sprayed under similar conditions. However, to form a complete aluminium titanate (Al_2TiO_5) coating, it is necessary to use an equimolar (56·1 wt% Al_2O_3 and 43·9 wt.% TiO_2) mixture of powders in plasma-spraying. The phase diagram of Al_2O_3/TiO_2 shows that the powder mixture (Plasmatex 1021) is very slightly away from the eutectic composition. Hence the coating should have a diphasic structure (Al_2O_3 and Al_2TiO_5).

3 Microstructural Analysis

3.1. As-sprayed coatings

There was limited adhesion of both YSZ and $Al_2O_3.TiO_2$ films on the polished surfaces of the substrate. The adhesion of coatings was improved with pre-oxidation of the substrate surface. This is due to the reaction between the SiO_2 layer and the coating materials. In addition, the presence of the SiO_2 layer is necessary in ZrO_2 coatings to produce the low thermal expansion reaction product, zircon. In the case of aluminium titanate, it has been reported that addition of SiO_2 up to 20% does not influence the thermal expansion coeffcient of Al_2TiO_5.[11,12] This is probably due to the substitution of some Si atoms for Ti atoms without changing the expansion anisotropy of individual orthorhombic Al_2TiO_5 crystals. Addition of a small quantity of Si to Al_2TiO_5 to form a solid solution is also advantageous in controlling the thermal decomposition below 1300°C of Al_2TiO_5 into Al_2O_3 and TiO_2.[13,14] However, some investigators,[15] have observed that the Al_2TiO_5 samples containing SiO_2 underwent decomposition at 1370°C under reducing conditions.

The coatings were extensively craze-cracked (Fig. 1), especially in the thinner areas, due to the rapid cooling of droplets after striking the cold substrate. Heating the substrate ceramic during plasma-spraying may prevent craze-cracking by reducing microstresses.[16] It is also clear that the molten or semi-molten particles from the plasma gun have flattened and spread on the substrate in the diameter range 30–60 μm, after striking it (Fig. 2). The YSZ coatings were 15–60 μm thick and the $Al_2O_3.TiO_2$ coatings were 50–100 μm thick. The laminated appearance of the cross-section of $Al_2O_3.TiO_2$ coatings [Fig. 2(b)] is a result of the lateral spreading of molten particles. Energy dispersive X-ray analysis (EDAX) revealed that the light areas were TiO_2 and the dark areas were Al_2O_3. The small amount of ZrO_2 occasionally detected was probably due to contamination of the spraying equipment. There was no indication of reaction between Al_2O_3 and TiO_2 during plasma-spraying.

The X-ray diffraction (XRD) studies of YSZ coatings confirmed that ZrO_2 was in cubic stabilized form. The XRD studies of $Al_2O_3.TiO_2$ coatings revealed that α-Al_2O_3 in the initial plasma powder mixture of Al_2O_3 and TiO_2 has been transformed to a metastable, face-centred cubic γ-phase. This transformation has been reported earlier[17] in Al_2O_3 plasma coatings on metal substrates. The formation of the metastable γ-phase is due to the rapid cooling of molten particles, thus limiting the subsequent diffusion of oxygen

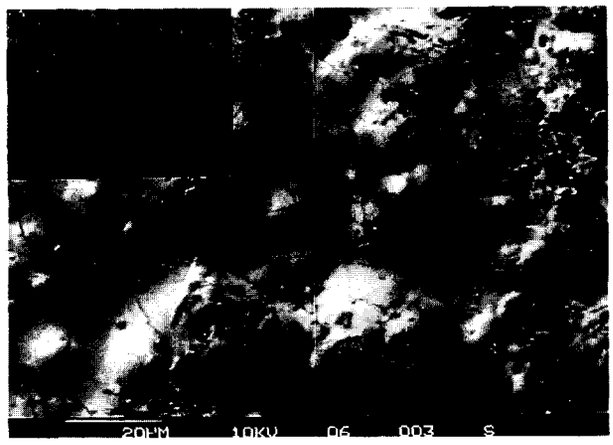

Fig. 1. SEM micrograph showing craze-cracking in as-sprayed coatings (ZrO_2) due to rapid cooling of droplets after striking the cold substrate. The insert shows an extensively craze-cracked thinner area.

Fig. 2. Backscattered SEM micrographs showing the spreading and flattening of molten droplets ($Al_2O_3.TiO_2$) on the substrate after striking it. (a) View of the coating surface and (b) laminated structure of a cross-section of the coating. The dark and the light contrast represent Al_2O_3 and TiO_2 droplets, respectively.

and aluminium atoms necessary for the formation of the stable α-phase.

Although the outer surface of the coatings was mainly crystalline, in the interface region of the as-sprayed coatings some amorphous material is likely to be present, due to the relatively rapid cooling expected to occur in this region during plasma-spraying. The volume shrinkage experienced during crystallization of the interface region can give rise to buckling of the coating. It has been proposed[18] that buckling is prerequisite to spalling of coatings.

3.2 Heat-treated coatings

Since there was no reaction between ZrO_2 and SiO_2 or Al_2O_3 and TiO_2 during plasma-spraying as expected, various post-spraying heat treatments were conducted between 1200 and 1400°C to promote reaction. Heat treatments below 1300°C in air resulted in partially reacted zones in both coatings (Figs 3 and 4). Lengthy heat treatments (1220°C for 600 h), however, showed a little improvement in achieving a complete reaction layer. The partially reacted zone in $Al_2O_3.TiO_2$ coatings was identified by XRD as orthorhombic aluminium titanate (Al_2TiO_5). Coatings of both materials had poor adhesion to the substrate ceramic and were also found to be brittle after heat treatments. However, many coatings spalled from the substrate during heat treatments as a result of thermal expansion mismatch between the substrate and the high thermal expansion unreacted initial powders.

In order to accelerate the reaction to form low thermal expansion products on the substrate, heat treatments were conducted at a higher temperature range (1350–1400°C). However, severe oxidation reactions of the substrate ceramic at this temperature range inhibited the growth of low thermal expansion products and hence heat treatments were carried out in an argon atmosphere and in vacuum (10^{-5} torr). These higher temperature treatments resulted in the formation of larger regions of $ZrSiO_4$ and Al_2TiO_5. However, as expected, a small amount of Al_2O_3 was present in the reacted products of Al_2TiO_5 coatings. This is due to the presence of excess Al_2O_3 (8·9%) in the starting plasma powder. The XRD studies also showed that the γ-Al_2O_3 present in the as-sprayed coatings of $Al_2O_3.TiO_2$ was transformed to α-phase via θ-Al_2O_3. It is worth noting that an equimolar $Al_2O_3.TiO_2$ pellet sintered at 1450°C did not show the Al_2O_3 peaks in XRD.

Heat treatments in non-oxidizing environments reduced coating spalling due to the formation of low thermal expansion products. The coatings of $Al_2O_3.TiO_2$ exhibited a volume expansion on formation to Al_2TiO_5. This gave rise to a curling effect of the coatings. This was clearly evident in long and thicker coatings (Fig. 5). The formation of Al_2TiO_5 is accompanied by an 11% increase in molar volume.[19] This volume expansion may be partly responsible for the spalling of the coatings. The curling effect was reduced by coating thinner layers on the substrates. However, very thin coatings were porous and detrimental to protective properties. A denser thin coating may be obtained by optimizing the spraying parameters such as powder particle size, power level and spraying distance. Since there was no reaction between Al_2O_3 and TiO_2 during plasma-spraying, it would be worth exploring the possibility of plasma-spraying of pre-alloyed aluminium titanate powder. This will avoid the unnecessary post-spraying heat treatments and hence the curling effect.

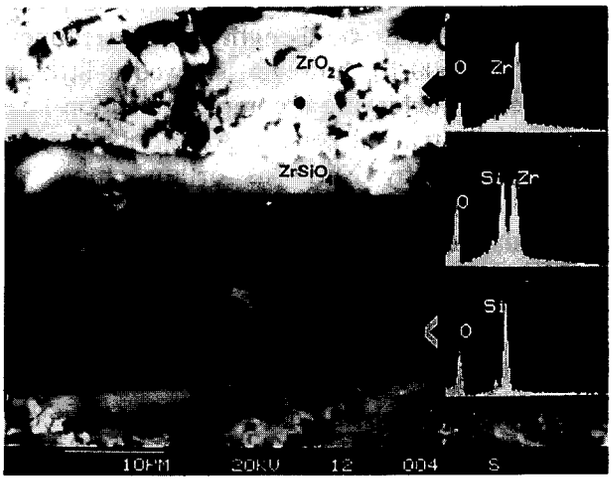

Fig. 3. Backscattered SEM micrograph and EDAX spectra (inserts) of a heat-treated (1300°C) ZrO_2 coating showing a partially formed $ZrSiO_4$ layer between SiO_2 and ZrO_2.

Fig. 4. Backscattered SEM micrograph of a heat-treated (1300°C) $Al_2O_3.TiO_2$ coating showing partial formation of Al_2TiO_5.

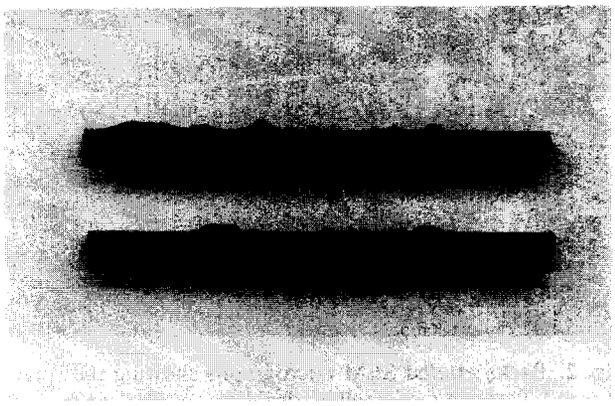

Fig. 5. Photograph showing the curling effect of the $Al_2O_3.TiO_2$ coatings due to volume expansion during the formation of Al_2TiO_5.

4 Preliminary Study of Oxidation Resistance and Protection of Heat-treated Coatings from Molten Metal Attack

The samples were ultrasonically cleaned in methanol prior to the oxidation and molten metal immersion experiments. The extent of oxidation and the effect of molten metal attack was studied on the transversely cut cross-sections in a scanning electron microscope (SEM). The conventional ceramic polishing techniques were employed to prepare the SEM specimens. However, a very good surface finish could not be achieved particularly in the molten metal immersion samples because of the differences in hardness between the metal and the ceramic.

4.1 Oxidation

Oxidation experiments were conducted in static air, in an open alumina tube furnace at 1200 to 1400°C for 50 h. The test samples were kept in an alumina boat supported by pure platinum mesh to avoid contact with the alumina boat. The SEM study showed that the exposed surfaces of the samples had undergone extensive oxidation at 1400°C (Fig. 6) compared with the coated surfaces. The oxidation reaction in sialon ceramic forms an yttrium-rich aluminosilicate with evolution of N_2 gas (visible in Fig. 6). The mechanism of oxidation of sialon ceramics has been discussed elsewhere.[1] It is clearly evident from the micrographs that both $ZrSiO_4$ and Al_2TiO_5 coatings provide sufficient protection against oxidation by preventing oxygen diffusion into the substrate ceramic. Furthermore, EDAX analysis of the coatings showed no evidence of the diffusion of metal atoms from the substrate ceramic to the coatings during oxidation. However, it can also be seen in the micrographs that the coatings have lifted off slightly from the substrate surface. The lack of oxidation on the substrate ceramic surface where the coating has lifted, suggests that this probably has occurred during cooling or preparation (cutting or polishing) of cross-sections for the SEM observation.

4.2 Molten metal attack

Ferrous metals are more reactive with sialon ceramics[20–22] and therefore low melting cast iron was chosen to study the effect of molten metals on plasma coatings. Cast iron (carbon equivalent 4·3 and liquidus 1150°C) was heated in an alumina crucible above its melting temperature (1300°C) and the ceramic samples with one side plasma-coated were gradually dipped into the crucible. The crucible was kept in a box furnace in static air and the sample was introduced into the cru-

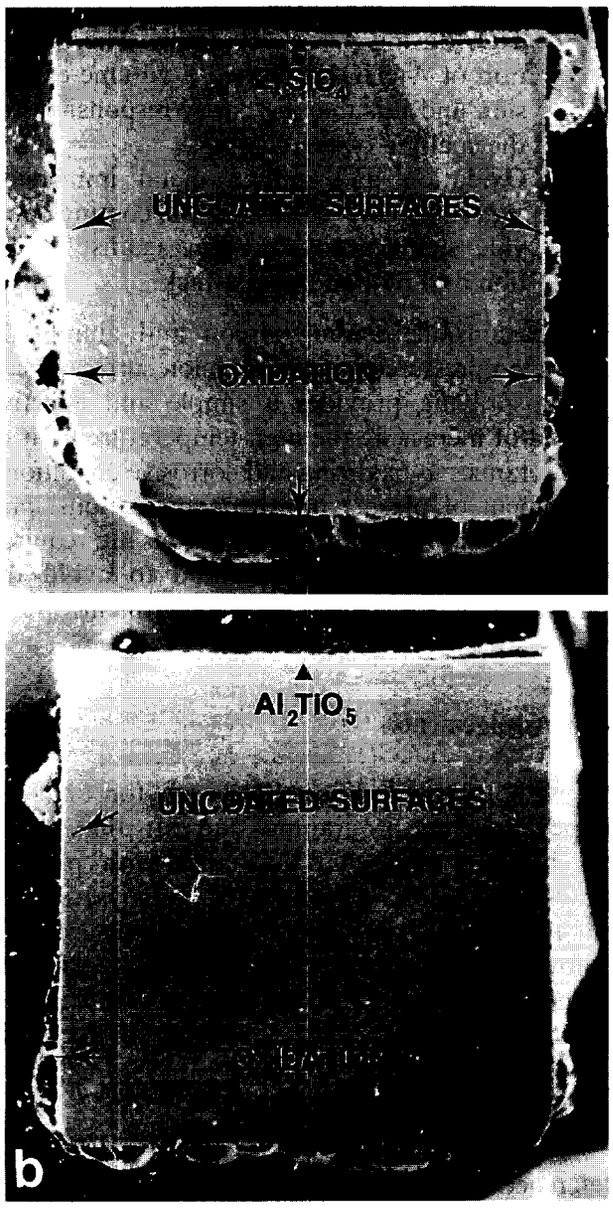

Fig. 6. Backscattered SEM micrographs showing oxidation resistance of (a) the $ZrSiO_4$ coating and (b) the Al_2TiO_5 coating compared with the uncoated surfaces.

cible from the top by means of a support alumina rod. The immersed samples were withdrawn from the molten cast iron after leaving them in the melt for different time durations.

It was observed (Fig. 7) that a vigorous reaction of molten cast iron with the uncoated surfaces occurred, with a strong pitting corrosion after leaving the samples in the metal for about 1 h. It was also observed that the molten cast iron attack was significantly aggravated with increasing temperature of the melt as well as the duration of the immersion. In contrast, both the coatings showed excellent protection against molten cast iron (Fig. 8). Although the molten metal had wetted the $ZrSiO_4$ coatings and penetrated surface irregularities, there was no evidence of either iron diffusion into the plasma layer or metal ions from the plasma layer diffusing into the cast iron melt.

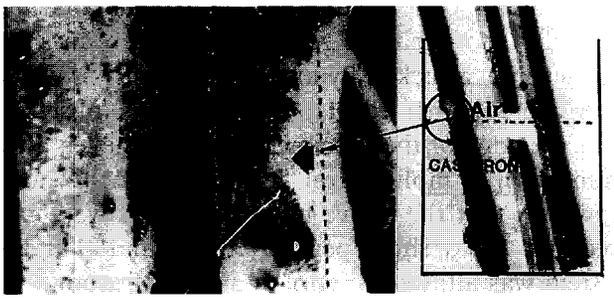

Fig. 7. Photographs showing attack of molten cast iron on an uncoated sialon sample. A strong pitting corrosion is evident at the air–metal interface of the uncoated sample.

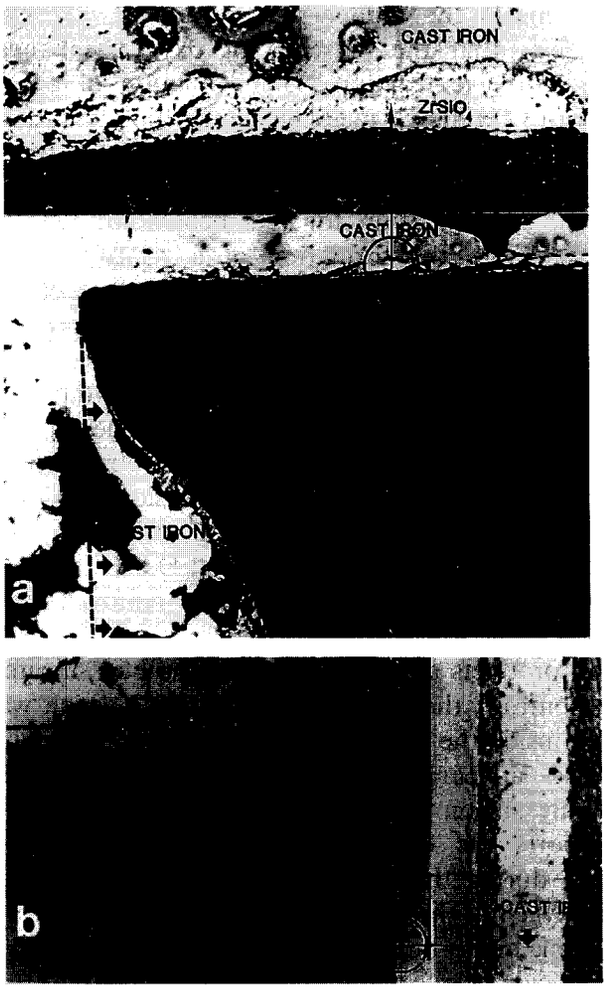

Fig. 8. Backscattered SEM micrographs showing the excellent protection of the coatings against attack by molten cast iron. (a) Sample coated with $ZrSiO_4$ and (b) sample coated with Al_2TiO_5.

In the case of the Al_2TiO_5 coating, a very thin reaction zone limited to a few micrometres was just detected by determining the iron concentration using EDAX analysis. However, the backscattering contrast was poor due to a relatively small difference of the atomic numbers of Ti and Fe.

There is limited information available regarding the resistance of sialon to molten metal attack. Results from the tests carried out by Lumby *et al.*[21] indicate that sialon has a very high resistance

to molten metal attack. Tests by Yeomans and Page,[20,22] show that, in general, sialon ceramics are not severely attacked by any of the metals in which they were immersed. However, it was observed that the edge of the specimens looked uneven after immersion in molten iron. It is important to note, however, that the above immersion tests were carried out for a short period (150 s) and that the system was allowed to cool in a flow of argon.

The pitting corrosion of uncoated samples was mainly observed in the air–molten cast iron interface region. There was very little corrosive reaction observed in the part of the sample which was well inside the molten cast iron (Fig. 7). This suggests that the presence of oxygen enhances the corrosive reaction. The formation of a low liquidus (~1200°C) metal silicate in the presence of oxygen in the interface region, which could allow more molten metal to react with the ceramic, is a possible explanation for this behaviour. On the other hand, the formation of a relatively high liquidus metal silicide film on the surface of the lower part of the sample could act as a protective layer for further reaction.

EDAX analysis showed no evidence of the presence of iron in the remaining part of the ceramic after the corrosive reaction. Similar observations have been reported earlier in immersion tests with molten iron[20] and in machining tests with cast iron.[23] However, SEM and EDAX analysis showed that the reaction products removed from the ceramic were distributed in the melt. The reaction products seem to be iron-rich metal silicates. In contrast, the section of the ceramic which was well inside the molten cast iron showed no multiphase appearance and analysis showed that mainly silicon and some iron were present. This supports the formation of a silicide protective layer during the reaction. However, the presence of oxygen in the pre-oxidized layer of the substrate ceramic made it difficult to conclude whether silicate or silicide was formed in the interface region.

5 Summary and Conclusions

(i) Plasma-sprayed coatings were found to be crystalline.

(ii) The coatings showed better cohesion with the pre-oxidized surface due to the reaction between SiO_2 and coating materials. The presence of the SiO_2 layer is necessary in ZrO_2 coatings to produce the low thermal expansion reaction product, zircon.

(iii) Thin layer coatings showed better cohesion than thicker layer coatings on thermal cycling.

(iv) There was no reaction between Al_2O_3 and TiO_2 during plasma-spraying. The formation of Al_2TiO_5 exhibited a volume expansion and this may be partly responsible for the spalling of the coatings.

(v) Oxidation and molten metal immersion experiments revealed that the coatings provide significant protection against oxidation and molten metal attack.

In conclusion, coating zircon and aluminium titanate on pressureless-sintered sialon surfaces using plasma-spraying provides a simple and effective method of increasing the high-temperature limit of these ceramics in oxidizing and corrosive conditions. Refinement of plasma powder compositions, prealloying and varied spraying conditions are required to optimize coating structure and to avoid the complexity of post-spraying heat treatment.

Acknowledgements

We wish to thank Lucas Research for financial support for this programme and Mr Jim Taylor and Ms Fee Wellhofer assistance with plasma-spraying. B.S.B.K. is grateful to the Royal Society and the Nuffield Foundation for the award of a Fellowship during the period of this research. Thanks are also due to Mr G. Smith, Mr S. York, Mr S. Carpenter and Mr K. Briggs for technical assistance.

References

1. Lewis, M. H. & Barnard, P., Oxidation mechanisms in Si–Al–O–N ceramics. *J. Mater. Sci.*, **15** (1980) 443–448.
2. Lewis, M. H., Bhatti, A. R., Lumby, R. J. & North, B., Crystallization of Mg-containing phases in β'–Si–Al–O–N ceramics. *J. Mater. Sci.*, **15** (1980) 438–442.
3. Goward, G. W., Protective coatings—purpose, role and design. *Mater. Sci. Technol.*, **2** (1986) 194–200.
4. Schmittthomas, K. G. & Dietl, U., Thermal barrier coatings with improved oxidation resistance. *Surf. Coat. Technol.*, **68** (1994) 113–115.
5. Nicoll, A. R., Gruner, H., Wuest, G. & Keller, S., Future developments in plasma spray coating. *Mater. Sci. Tech.*, **2** (1986) 214–219.
6. Garvie, R. C., Hannink, R. H. & Pascoe, R. T., Ceramic steel. *Nature*, **258**, (1975) 703–704.
7. Scott, M. G., Phase relationships in the zirconia–yttria system. *J. Mat. Sci.*, **10** (1975) 1527–1535.
8. Bayer, G., Thermal expansion characteristics and stability of pseudobrookite-type compounds, Me_3O_5. *J. Less Common Met.*, **24** (1971) 129–138.
9. Cleveland, J. J. & Bradt, R. C., Grain size/microcracking relations for pseudobrookite oxides. *J. Am. Ceram. Soc.*, **61** (1978) 478–481.
10. Thomas, H. A. J. & Stevens, R., Aluminum titanate — a literature review. 1. Microcracking phenomena. *Br. Ceram. Trans. J.*, **88** (1989) 144–151.

11. Silich, L. M., Bobkova, N. M. & Dyatlova, E. M., Thermostable ceramic materials based on crystal phases with a low thermal linear expansion coefficient. *Interceram*, **34** (1985) 19–20.
12. Kajiwara, M., Sintering and properties of stabilized aluminum titanate. *Br. Ceram. Trans. J.*, **86** (1987) 77–80.
13. Ishitsuka, M., Sato, T., Endo, T. & Shimada, M., Synthesis and thermal stability of aluminum titanate solid solutions. *J. Am. Ceram. Soc.*, **70** (1987) 69–71.
14. Thomas, H. A. J. & Stevens, R., Aluminum titanate — a literature review. 2. Engineering properties. *Br. Ceram. Trans. J.*, **88** (1989) 2521–2525.
15. Djambazov, S., Lepkova, D. & Ivanov, I., A study of the stabilization of aluminium titanate. *J. Mater. Sci.*, **29** (1994) 438–442.
16. Levit, M., Grimberg, I. & Weiss, B. Z., Residual micro- and macrostresses in the plasma-sprayed zirconia-based TBCs. *Mater. Lett.*, **19** (1994) 48–52.
17. Berndt, C., Electron microscopic studies of plasma-sprayed coatings. *Mat. Sci. Res. (Advances in Materials Characterization II)*, **19** (1985) 265–278.
18. Evans, A. G., Engineering property requirements for high-performance ceramics. *Mater. Sci. Eng.*, **71** (1985) 3–21.
19. Freudenberg, B. & Mocellin, A., Aluminum titanate formation by solid-state reaction of fine Al_2O_3 and TiO_2 powders. *J. Am. Ceram. Soc.*, **70** (1987) 33–38.
20. Yeomans, J. A. & Page, T. F., The chemical stability of ceramic cutting tool materials exposed to liquid metals. *Wear*, (1989) 163–175.
21. Lumby, R. J., North, B. & Taylor, A. J., Properties of sintered sialons and some applications in metal handling and cutting. In *Ceramics for High Performance Applications II*, eds J. J. Burke, E. N. Lenon & R. N. Katz. Brook Hill Publishing Company, MA, 1978, pp. 893–906.
22. Yeomans, J. A. & Page, T. F., Studies of ceramic–liquid metal reaction interfaces. *J. Mater. Sci.*, **25** (1990) 2312–2320.
23. Bhattacharyya, S. K., Jawaid, A., Lewis, M. H. & Wallbank, J., Wear mechanisms of Sialon ceramic tools when machining Ni-based materials. *Met. Technol.*, **10** (1983) 481–489.

Journal of the European Ceramic Society **16** (1996) 1141–1144

PII: S0955-2219(96)00016-7
0955-2219/96/$15.00

NiAl Diffusion Coatings on Inconel 738 using a Pre-Heated $AlCl_3$ + H_2 Gas Mixture

T. Araki[a] & S. Motojima[b]*

[a]Business Development Div., Iwatani Int. Co. Ltd, 3-4-8 Hommachi, Chuo-ku, Osaka 541, Japan
[b]Department of Applied Chemistry, Faculty of Engineering, Gifu University, Gifu 501-11, Japan

(Received 30 June 1995; revised version received 19 December 1995; accepted 3 January 1996)

Abstract

Aluminized diffusion coatings were obtained on an Inconel 738 specimen at 800–1000°C using a pre-heated $AlCl_3$ + H_2 gas mixture with a 0·3 s holding time. It was found that the pre-heating treatment was very effective for a high deposition rate of the aluminide coatings. The thickness of the aluminide coatings was 1·5–4·7 times higher than that without pre-heating. © 1996 Published by Elsevier Science Limited.

1 Introduction

Aero-engine blades are exposed to extremely severe environmental conditions such as high temperatures of 950–1100°C, severe oxidation, carburization and corrosive atmospheres. Under marine and industrial service conditions, the blades encounter even more corrosive and/or erosive atmospheres but the operating temperature range is relatively low, 700–850°C. Accordingly, various surface coatings are applied to these components to withstand such severe conditions and thereby extend component lifetime.

There are two main coating processes: diffusion coatings and overlay coatings. In the production of diffusion coatings, metal layers of Al, Cr, Ni, Si, etc. are deposited on the substrate followed by thermal diffusion to form corrosion-resistant diffusion coatings. Aluminized diffusion layers are frequently used for hot corrosion protection of gas turbine blades. Among the various diffusion coatings, the pack coating process is the most widely used technique for aluminide coatings.[1–4] However, there is some difficulty in uniform feeding of the pack powder into the narrow passages (<0·5 mm diameter) that are used for cooling air and then subsequently removing the powder. The metal–organic chemical vapour deposition (CVD) process has been used for aluminium or aluminide coatings.[5,6] However, the aluminium or aluminide coatings obtained by this process are generally not adherent to a substrate and the growth rate is very low. Furthermore, the coating operation is not easy because the alkyl aluminium source is very unstable to moisture and oxygen, and is flammable in air.

The conventional thermal CVD process using $AlCl_3$ or $AlBr_3$ as the aluminium source has frequently been used for aluminide coatings. Aluminide coatings using the direct hydrogen reduction of $AlCl_3$ or $AlBr_3$ need a temperature above 1000°C, or about 1200°C if thick coating layers are needed. Accordingly, AlCl, which has a high reactivity and is obtained using the reaction of $AlCl_3$ with molten aluminium at 900–1000°C, is generally used.[7–9] However, this process has the disadvantage of some difficulty in the handling of the molten aluminium. Thus, the development of other, more effective processes is needed for obtaining aluminized coatings.

In this work, we have obtained aluminide diffusion coatings on an Inconel 738 specimen at 800–1000°C using an $AlCl_3$ + H_2 gas mixture which was pre-heated at 800–1000°C for about 0·3 s using a graphite pre-heating chamber. The effect of reaction conditions on the formation of the aluminized layers was examined.

2 Experimental Procedure

The $AlCl_3$ gas was prepared *in situ* by the chlorination of aluminium metal by HCl gas at 330°C. The gas mixture of $AlCl_3$ + H_2 was then introduced into the pre-heating chamber prior to introduction into the reaction zone. The reaction chamber (Inconel 601, 350 mm internal diameter × 1·430 m long) was heated from the outside. Bare and Ni and Cr electro-plated Inconel 738 discs (25 mm diameter × 5 mm thick) were used as specimens for the coatings. The pre-heating chamber, which was made of graphite and had a 600 mm path length and 3280 cm^3 of total

*To whom correspondence should be addressed.

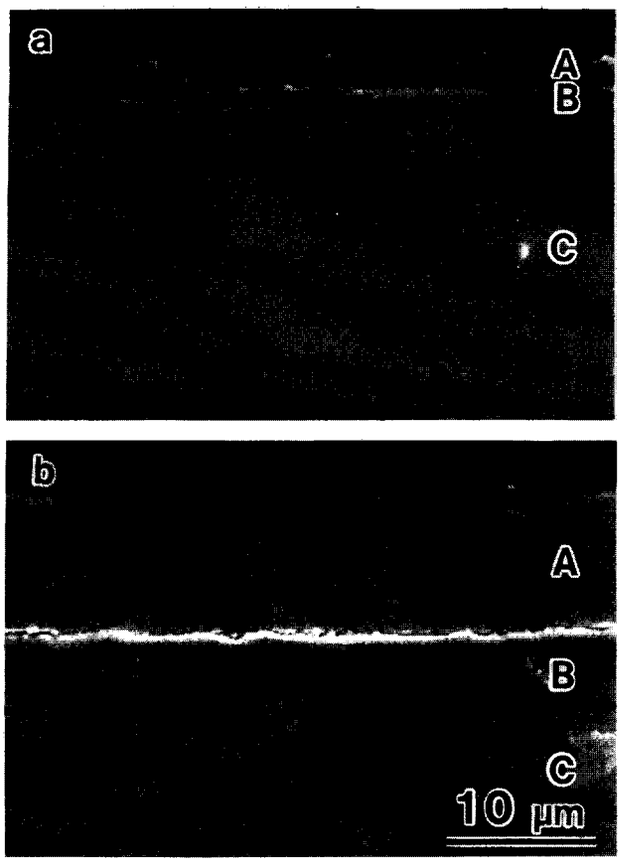

Fig. 1. Polished cross-section of aluminized Inconel 738; reaction temperature = 850°C, reaction pressure = 4×10^4 Pa. (a) Without pre-heating, (b) with pre-heating. (A) Outer NiAl layer, (B) inner diffusion layer, (C) specimen layer.

path volume, was set in the lower part of the reaction chamber. The experiment was also carried out without using the pre-heating chamber for reference.

3 Results and Discussion

The aluminized coatings were composed of two layers: an outer and an inner layer as shown in Fig. 1, subsequently analysed as NiAl and a more complex NiAl/Inconel interdiffusion zone, respectively. The total thicknesses of the coatings deposited with and without pre-heating were 14·2 and 3.0 μm, respectively. That is, the total thickness of the aluminized layer with pre-heating is 4·7 times larger than that without pre-heating. The effect of reaction temperature on the total thickness of the aluminized coatings obtained with and without pre-heating after a 4 h reaction time is shown in Fig. 2, in which the pre-heating temperature and time were fixed at 950–1000°C and 0·3 s, respectively. It was observed that the total thickness with pre-heating was 1·5–4·7 times larger than that without pre-heating. That is, the pre-heating treatment of the gas mixture of $AlCl_3$ + H_2 is very effective for obtaining thicker aluminized coatings. This effect was particularly marked at temperatures of 850°C and below. This effect may be caused by the effective formation of

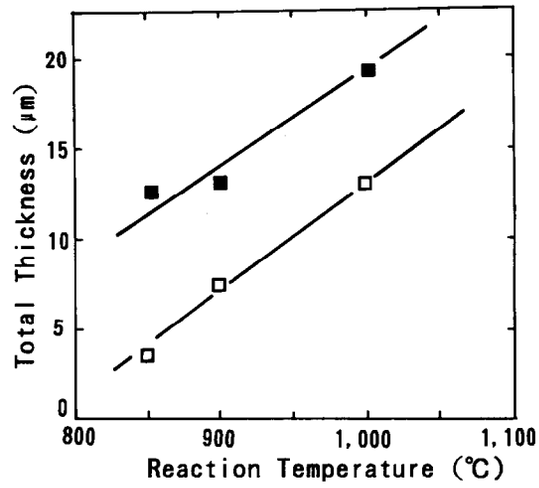

Fig. 2. Effect of reaction temperature on the total thickness of the aluminized layers; pre-heating temperature = 950–1000°C, reaction time = 4 h. (■) With pre-heating, (□) without pre-heating.

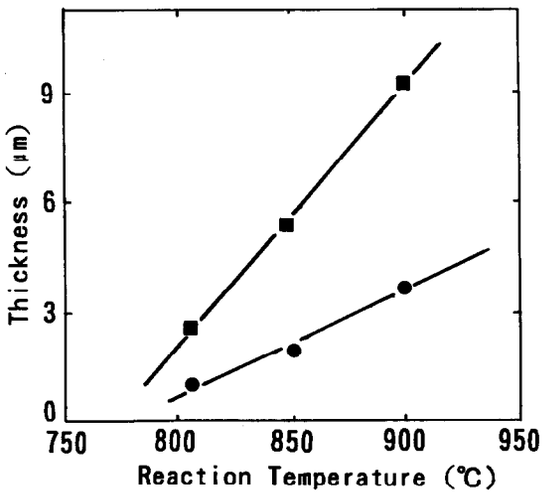

Fig. 3. Effect of reaction temperature on the layer thickness; pre-heating temperature = 950°C, reaction time = 4 h. (■) Outer NiAl layer, (●) inner diffusion layer.

reactive AlCl gas species due to the pre-heating, while the holding time of the gas mixture of $AlCl_3$ + H_2 in the pre-heating chamber is very short, 0·3 s. The effects of reaction conditions with pre-heating on the formation of the aluminized coatings were then examined.

The effect of reaction temperature on the thickness of the A and B layers in Fig. 1(b) is shown in Fig. 3, in which the pre-heating temperature was fixed at 950°C. Both outer and inner layer thicknesses increased linearly with increasing reaction temperature, and the thickness of the outer NiAl layer was about 1·6 times that of the inner diffusion layer.

The effect of $AlCl_3$ gas flow rate on the layer thickness obtained at the reaction temperature of 850°C is shown in Fig. 4. The thickness of the respective layers increased parabolically with increasing $AlCl_3$ gas flow rate. This result suggests that the rate-determining step is the hydrogen reduction of $AlCl_3$ to $AlCl_{3-x}$ and finally to Al

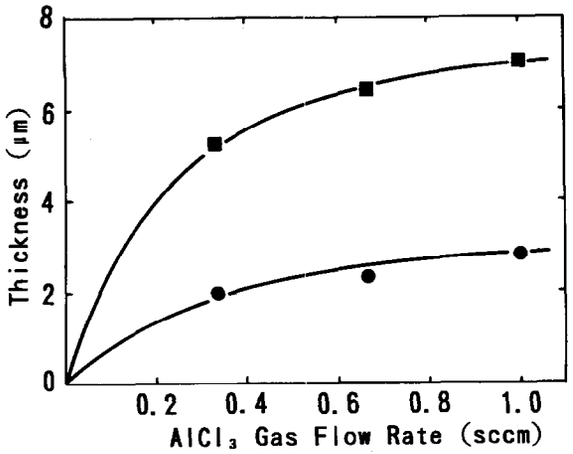

Fig. 4. Effect of $AlCl_3$ gas flow rate on the layer thickness; reaction temperature = 850°C, pre-heating temperature = 950°C. (■) Outer NiAl layer, (●) inner diffusion layer.

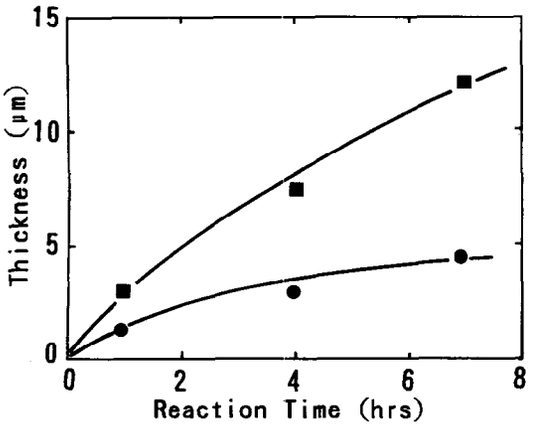

Fig. 5. Effect of reaction time on the layer thickness; reaction temperature = 850°C, pre-heating temperature = 950°C. (■) Outer NiAl layer, (●) inner diffusion layer.

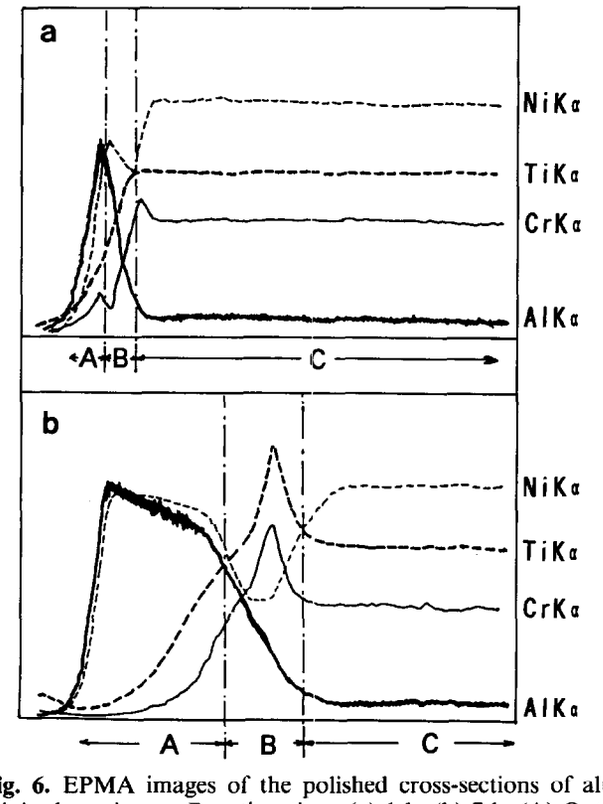

Fig. 6. EPMA images of the polished cross-sections of aluminized specimens. Reaction time: (a) 1 h, (b) 7 h. (A) Outer NiAl layer, (B) inner diffusion layer, (C) specimen layer. Full counts (cps) of the peaks: Ni K_α = 20000, Ti K_α = 2000, Cr K_α = 20000, Al K_α = 50000.

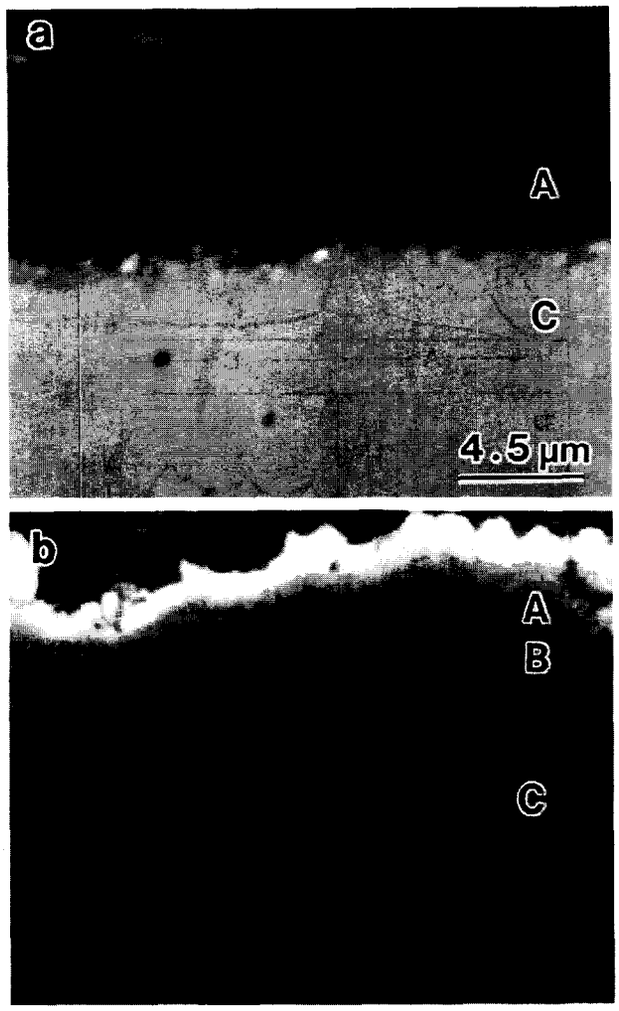

Fig. 7. Polished cross-sections of aluminized Inconel 738 electroplated with Ni and Cr; thickness of electroplated Ni or Cr = about 4 μm, reaction temperature = 350°C, pre-heating temperature = 950°C, reaction time = 4 h. (a) With Ni plating, (b) with Cr plating. (A) NiAl layer, (B) diffusion layer, (C) specimen layer.

metal, and/or the diffusion of Al species through the gas boundary layers present on the specimen surface. The effect of reaction time on the layer thickness is shown in Fig. 5, in which reaction temperature was fixed at 850°C. It was observed that the thickness of the respective layers increased parabolically with increasing reaction time, and a total thickness of about 12 μm was obtained after a 7 h reaction time.

Figure 6 shows the profiles of electron probe microanalysis (EPMA) of the polished cross-section of the aluminized specimen. Enrichment of Cr in the boundaries of the outer/inner aluminized layers and inner/substrate layers was observed during the initial aluminizing stage after 1 h in Fig. 6(a). Figure 6(b) shows that, with increasing reaction time to 7 h, Ti and Cr were significantly enriched in the thickened inner diffusion layer. Figures 6(a) and 6(b) confirm the formation of NiAl in the outer layer.

The polished cross-sections of specimens electroplated with ~4 μm thick Ni and Cr films, and

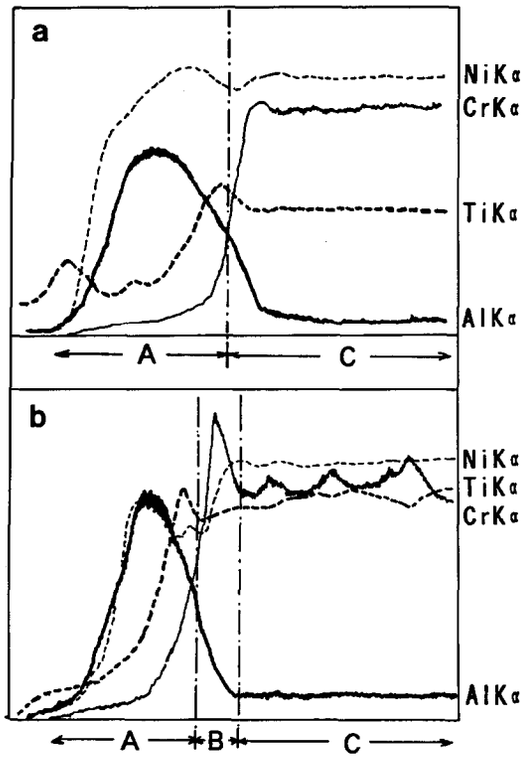

Fig. 8. EPMA images of the cross-sections shown in Fig. 7. (a) With Ni plating, (b) with Cr plating. (A) NiAl layer, (B) diffusion layer, (C) specimen layer. Refer to Fig. 6 for full counts (cps) of peaks.

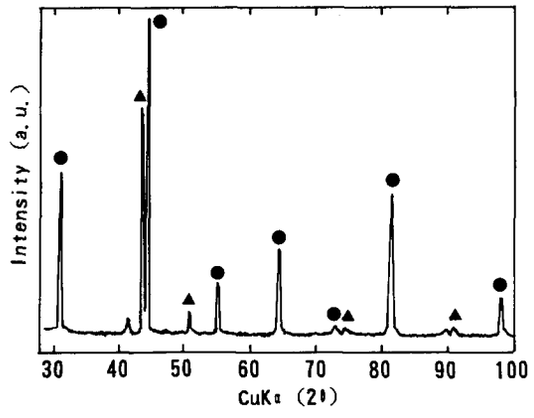

Fig. 9. XRD profiles of the surface of aluminized specimen with pre-heating. (●) NiAl, (▲) Ni_3Al.

then aluminized with pre-heating at 850°C for 4 h, are shown in Fig. 7. With the Ni plating in Fig.7(a), a single 5·6 μm thick aluminized layer only was obtained, because of preferential aluminizing of the electroplated Ni layers. On the other hand, with the Cr plating in Fig. 7(b), double layers with 6·5 μm total thickness were obtained. Figure 8 shows the corresponding EPMA traces of the cross-sections shown in Fig. 7. For the Ni plating in Fig. 8(a), Ti was enriched in the outer NiAl layer adjacent to the boundary, and similar Ti enrichment for the Cr plating is shown in Fig. 8(b). In both cases, Cr was not present in the outer NiAl layer, but was enriched in the inner diffusion layers.

Figure 9 shows the X-ray diffraction (XRD) profile of the surface of the aluminized layer for the Ni-plated specimen. It was observed that sharp peaks of Ni_3Al as well as NiAl were observed. The formation of the Ni_3Al phase is considered to be caused by the Ni-plating layers. On the other hand, a single NiAl phase only was observed for the Cr-plated specimen. Greater Ni enrichment in the outer layer for the Ni-plated specimen than for the non- or Cr-plated specimen may be caused by the formation of the Ni_3Al phase.

In conclusion, we have successfully obtained aluminide coatings on an Inconel 738 disc specimen at the relatively low temperature of 800–900°C using $AlCl_3 + H_2$ gas mixtures which were pre-heated at 950–1000°C for about 0·3 s in a graphite pre-heating chamber. This pre-heating process is very useful from the standpoint of being a simple, flexible and productive process.

References

1. Nicholls, J. R. & Stephenson, D. J., in *Metals and Materials*, 1991, pp. 156–163.
2. Papp, R. A., Wang, D. & Weisert T., in *High Temperature Coating*, (1987), pp. 131–141.
3. Cocking, J. L., Richards, P. G., Johnson, G. R., *Surface Coatings Technol.*, **36** (1988) 37–47.
4. Harper, M. A., Miller, D. M. & Rapp, R. A., *Oxid. Met.*, **42** (1994) 311–320.
5. Carisson, J. O., Gorbatkin, S., Lubben, D. & Greene, J. E., *J. Vac. Sci. Technol.*, **B9** (1991) 2759–2770.
6. Cabrera, A. L., Zehner, J. E. & Armor, J. N., *Oxid. Met.*, **36** (1991) 265–280.
7. Singheiser, L., Wahl, G. & Thiele, W., *Thin Solid Films*, **107** (1983) 443–454.
8. Brennfleck, K., Fitzer, E. & Kehr, D., *Proc. 7th Int. Conf. CVD*, The Electrochemical Soc., Princeton, NJ, 1979, pp. 578–582.
9. Kojima, Y. & Yamaguchi, S., *Hyomen-Gijutsu*, **43** (1992) 839–843.

Journal of the European Ceramic Society **16** (1996) 1145–1148

PII: S0955-2219(96)00034-9
0955-2219/96/$15.00

Preparation and Microstructure of TiB_2–TiC–SiC Platelet-Reinforced Ceramics by Reactive Hot-Pressing

G. J. Zhang, X. M. Yue & Z. Z. Jin

China Building Materials Academy, Beijing 100024, People's Republic of China

(Received 19 December 1995; revised version received 16 January 1996; accepted 23 January 1996)

Abstract

Using TiH_2, Si and B_4C as raw materials, a platelet-reinforced ceramic composite of TiB_2–TiC–SiC was prepared by reactive hot-pressing. The product has three phases: TiB_2 (in plate-like shape), TiC and β-SiC. The microstructural characteristics of the composite were observed by scanning electron microscopy and the phase chemistry was analysed by energy-dispersive X-ray analysis. The mechanical properties of the composite were also determined. © 1996 Elsevier Science Limited.

1 Introduction

In the ternary system of TiB_2–TiC–SiC, the binary composites of TiB_2–TiC, SiC–TiB_2 and SiC–TiC have better mechanical properties than the corresponding monolithic ceramics. Furthermore, de Mestral and Thevenot reported that the mechanical properties of TiB_2–TiC–SiC ternary composites are better than those of the above three binary composites.[1]

Ceramic composites prepared by reaction techniques exhibit several advantages when compared with conventionally processed ceramics.[2] The main advantages are low-cost raw materials, simple processing and the ability to produce special microstructures and mechanical properties in the resulting materials. In the ternary system of TiB_2–TiC–SiC, SiC–TiB_2 composites were prepared by *in situ* synthesis of TiB_2 in a SiC matrix from the reaction of TiN and B or TiO_2, B_4C and C[3,4] or TiC and B[5] or TiH_2, Si and B_4C.[6] Ti(C, N)–SiC composites were prepared by the reaction of TiC and Si_3N_4 when TiN was added.[7] TiB_2–SiC composites were prepared by the reaction of TiH_2, Si and B_4C.[8] Recently, TiB_2-TiC composites were fabricated by liquid infiltration of titanium into a B_4C preform at 1600–1800°C in an Ar atmosphere[9] and titanium–boron–carbon composites with plate-like Ti_3B_4 phase by transient plastic phase processing (TPPP) using Ti and B_4C as starting materials.[10]

In consideration of the low oxidation resistance of TiB_2–TiC composites, SiC was thought to be an effective additive. Therefore, a series of TiB_2–TiC–SiC ternary composites was prepared by reaction synthesis, which was reported in a previous paper.[11] This present paper presents the preparation process and the microstructure of the composite ceramics produced by reactive hot-pressing according to the following reaction:

$$TiH_2 \rightarrow Ti + H_2\uparrow$$

$$4Ti + 0{\cdot}5Si + 1{\cdot}5B_4C \rightarrow 3TiB_2 + TiC + 0{\cdot}5SiC \quad (1)$$

The volume contents of the phase composition according to the above reaction are 71·52% TiB_2, 18.79% TiC and 9·68% SiC.

2 Experimental Procedure

The starting powders were TiH_2 (purity 99·5%, particle size <45 μm), Si (purity > 99%, particle size <45 μm) and B_4C (purity 99%, particle size 5–8 μm). The stoichiometric powders were mixed in alcohol with WC–Co balls for 4 h in a nylon pot and then dried. The composite was fabricated by reactive hot-pressing in a graphite die with BN coating at 2000°C under 30 MPa for 60 min in an Ar atmosphere. Figure 1 shows the temperature and pressure as a function of time in the process of reactive hot pressing. As shown in the plot, there is a 15 min stage at the temperature of 1500°C in order to give enough time for chemical reaction, then the pressure was gradually applied. Otherwise, if the pressure was applied too early and too fast, some metal melt would flow out of the die.

The product was electrical-discharge machined to specimens and then ground and polished. Phase composition was determined by X-ray diffraction (XRD). The water displacement method was used to

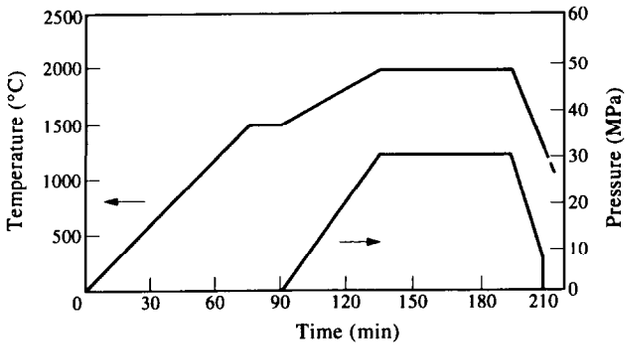

Fig. 1. Reactive hot-press control showing the temperature and pressure as function of time.

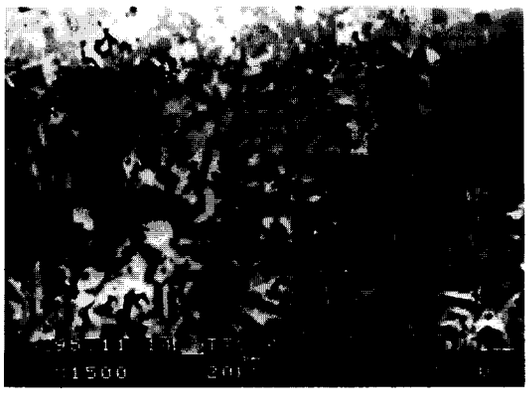

Fig. 2. SEM photograph of the composite. The grey phase is TiB_2, white phase TiC and dark phase β-SiC.

test the density. Fracture toughness was determined using the single-edge notched beam (SENB) method (three-point bending, just broken from the notch);[12] the specimen size was 2 × 4 × 20 mm, the notch width was <0·2 mm and the notch depth was about 1·6 mm, and the crosshead speed was 0·5 mm min^{-1}. Fracture strength was tested using the three-point bending method; the specimen size was 3 × 4 × 36 mm and the crosshead speed was 0·5 mm min^{-1}. The microstructure of the composite was examined by scanning electron microscopy (SEM). Energy-dispersive X-ray analysis (EDAX) associated with SEM was used to determine phase chemistry.

3 Results and Discussion

According to the XRD patterns shown in a previous paper,[11] there are only TiB_2, TiC and β-SiC in the composite, indicating that the high-temperature reaction was in accordance with reaction (1). Actually, reaction (1) is a sum of the two following reactions:

$$3Ti + B_4C \rightarrow 2TiB_2 + TiC \quad (2)$$

$$Ti + 0{\cdot}5Si + 0{\cdot}5B_4C \rightarrow TiB_2 + 0{\cdot}5SiC \quad (3)$$

The above two reactions were almost finished at 1350°C after 30 min in an Ar atmosphere,[8,13] and TiB_2 and TiC or TiB_2 and β-SiC were formed.

The properties of the composite are listed in Table 1, in which each value is an average of five or six measurements. Table 1 shows that a dense body can be obtained by reactive hot-pressing under the present sintering condition, and the mechanical properties of the composite are satisfactory.

Figure 2 is an SEM photograph of the polished surface of the composite, in which the grey phase is TiB_2, the white phase is TiC and the black phase is β-SiC. It can be seen from the picture that TiB_2 phase is generally plate-like in shape, and the phases are not uniformly distributed. This kind of microstructure can be attributed to the coarse particle size of the starting powders and the dispersion process of the starting powders. Therefore, the microstructure of the composite can be improved by the use of finer starting powders and a more effective dispersion process.

Figure 3 presents the EDAX spectra of TiB_2, TiC, β-SiC and the whole area in Fig. 2. No Si was detected in the TiB_2 phase indicating that there is no reaction between TiB_2 and SiC. However, Si and Ti were detected in TiC and SiC, respectively, revealing that there is a reaction between the TiC and SiC and solid solutions formed. These results are consistent with the investigation of de Mestral and Thevenot.[1]

It can also be seen from Fig. 2 that the TiB_2 platelets grew very well in TiC-rich regions, as shown in Fig. 4(a), and grew relatively imperfectly in SiC-rich regions, as shown in Fig. 4(b). According to results reported for the TiB_2/SiC system prepared by reaction (3), the SiC phase was converted from the previously formed TiC phase and the TiB_2 phase was quasi-spherical in shape.[8] Therefore, it is suggested that the formation of TiB_2 platelets is closely related to the existence of the TiC phase, and the existence of the SiC phase prohibited the growth of TiB_2 platelets. Details of this phenomenon will be reported after further investigation.

In TiB_2-rich regions, the growth of TiB_2 platelets was prohibited and, if the agglomeration

Table 1. Properties of TiB_2–TiC–SiC platelet composite

Relative density (% of theoretical)	*Fracture strength (MPa)*	*Fracture toughness (MPa $m^{1/2}$)*	*Phase composition*
99·8	680·5 ± 69·3	6·90 ± 0·18	TiB_2, TiC, β-SiC

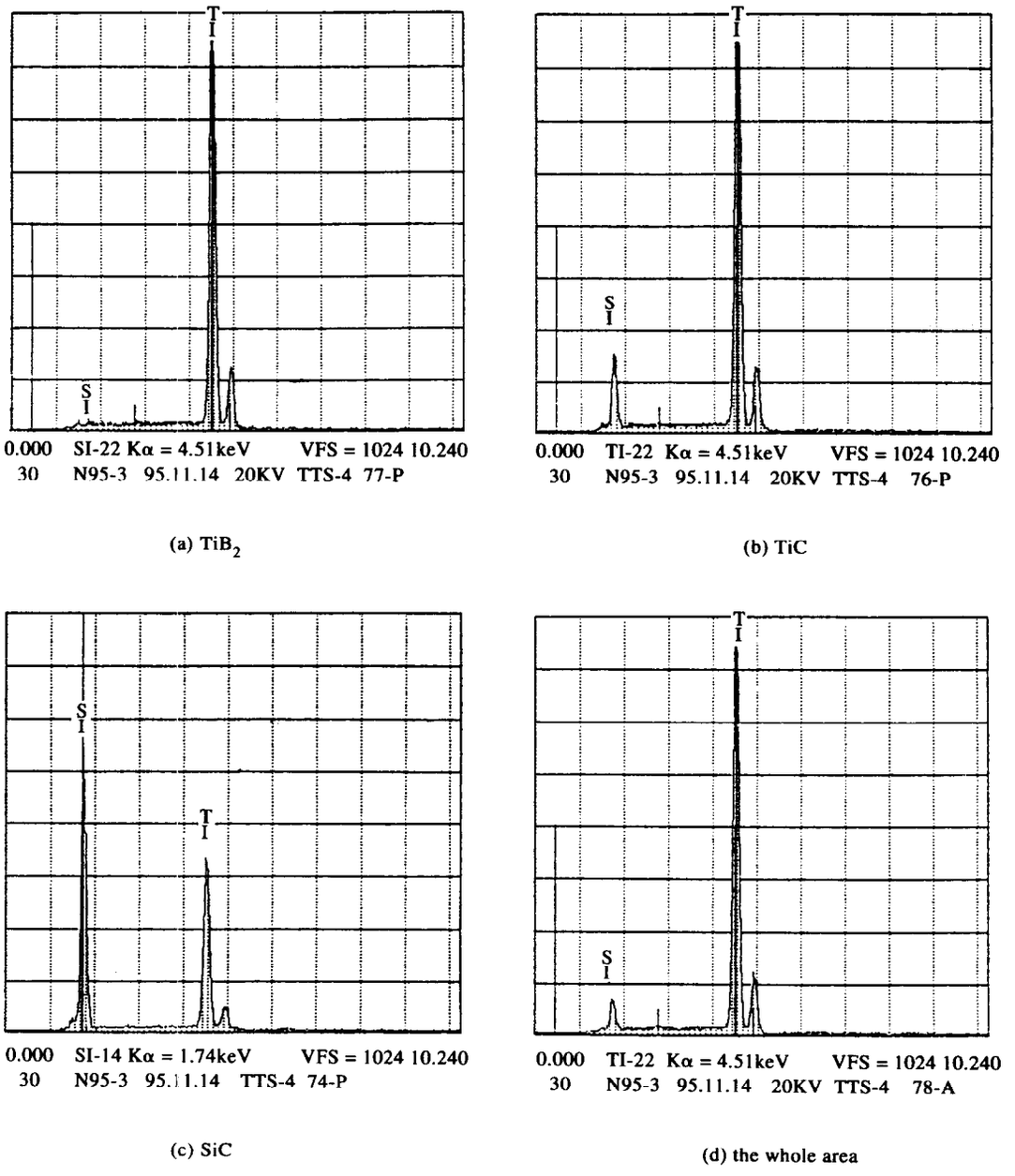

Fig. 3. EDAX spectra of (a) TiB_2, (b) TiC, (c) SiC and (d) the whole area in Fig. 2.

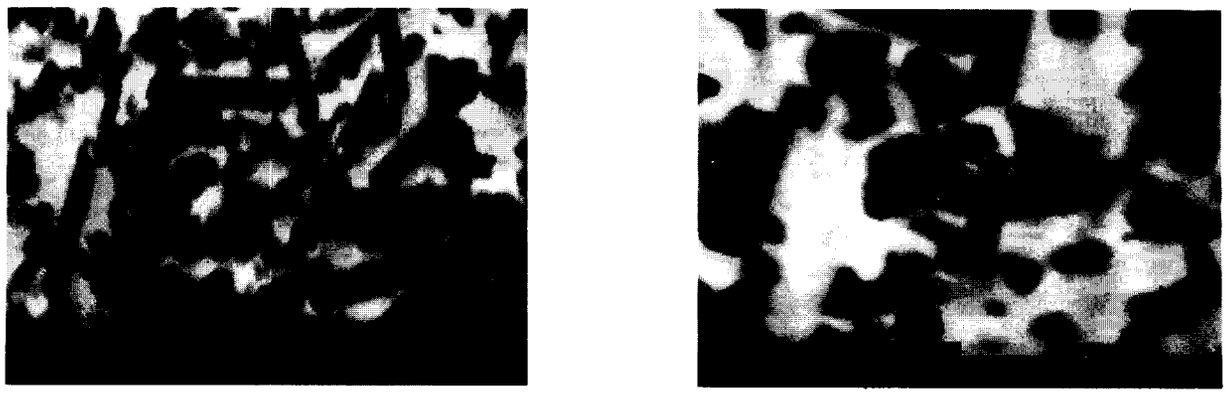

Fig. 4. The shape of the TiB_2 phase in different regions: (a) TiC-rich region; (b) SiC-rich region.

region of TiB_2 was large enough, quasi-spherical TiB_2 particles were formed, as shown in Fig. 5. This means that good distribution of each phase in the composite and/ or reducing the TiB_2 content will help the growth of TiB_2 platelets, and better mechanical properties of the composite may be obtained.

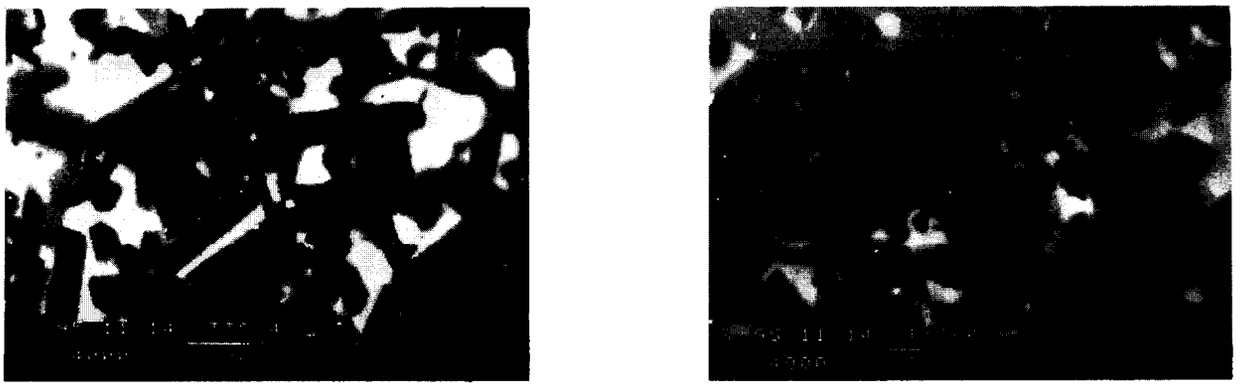

(a) (b)

Fig. 5. Effect of TiB_2 agglomeration on the shape of the TiB_2 phase: (a) in TiB_2-rich region; (b) in a large agglomeration region of TiB_2.

4 Conclusions

A platelet-reinforced ceramic composite of TiB_2–TiC–SiC was prepared by reactive hot-pressing using TiH_2, Si and B_4C as starting materials. The growth of TiB_2 platelets was different in different regions of the composite. The platelets grew very well in the TiC-rich regions and imperfectly in the SiC-rich regions, with agglomeration of TiB_2 prohibiting the growth of TiB_2 platelets. Additionally, the EDAX results show that there is no reaction between TiB_2 and SiC while there is reaction between TiC and SiC, forming solid solutions. The mechanical properties of the composite are satisfactory.

Acknowledgement

This work was supported by the National Natural Science Foundation of China (NSFC), Grant No. 59502008.

References

1. de Mestral, F. & Thevenot, F., Ceramic composites: TiB_2–TiC–SiC, Part I. Properties and microstructures in the ternary system. *J. Mater. Sci.*, **26** (1991) 5547–5560.
2. Claussen, N., Janssen, R. & Holz, D., Reaction bonding of aluminum oxide (RBAO). *J. Ceram. Soc. Jpn*, **103** (1995) 749–758.
3. Tani, T. & Wada, S., SiC matrix composites reinforced with internally synthesized TiB_2. *J. Mater. Sci.*, **25** (1990) 157–160.
4. Tani, T. & Wada, S., Pressureless-sintered and HIPed SiC–TiB_2 composites from SiC–TiO_2–B_4C–C powder compacts. *J. Mater. Sci.*, **26** (1991) 3491–3496.
5. Ohya, Y., Hoffmann, M. J. & Petzow, G., Sintering of in-situ synthesized SiC–TiB_2 composites with improved fracture toughness. *J. Am. Ceram. Soc.*, **75** (1992) 2479–2483.
6. Zhang, G. J., Yue, X. M., Jin, Z. Z. & Dai, J. Y., In-situ synthesized TiB_2 toughened SiC. *J. Eur. Ceram. Soc.*, **16** (1996) 409–412.
7. Kamiya, A. & Nakano, K., Reaction synthesis of SiC-reinforced Ti(C,N) composites from TiC and Si_3N_4. *J. Mater. Sci. Lett.*, **12** (1993) 430–432.
8. Zhang, G. J., Jin, Z. Z. & Yue, X. M., Reaction synthesis of TiB_2–SiC composites from TiH_2–Si–B_4C. *Mater. Lett.*, **25** (1995) 99–100.
9. Lee, S. K., Kim, D. H. & Kim, C. H., Fabrication of TiB_2/TiC composites by the directional reaction of titanium with boron carbide. *J. Mater. Sci.*, **29** (1994) 4125–4130.
10. Barsoum, M. W. & Houng, B., Transient plastic phase processing of titanium–boron–carbon composites. *J. Am. Ceram Soc.*, **76** (1993) 1445–1451.
11. Zhang, G. J., Jin, Z. Z. & Yue, X. M., TiB_2–Ti(C,N)–SiC composites prepared by reactive hot pressing. *J. Mater. Sci. Lett.*, **15** (1996) 26–28.
12. Zhang, Q. C., *Mechanical Properties of Ceramic Materials*, Science Publisher, Beijing, China, 1987, pp. 376–377.
13. Zhang, G. J., In-situ reaction synthesis of TiB_2–Ti(C,N)–SiC composites. PhD thesis, China Building Materials Academy, Beijing, China, 1995.

Journal of the European Ceramic Society **16** (1996) 1149–1156

PII:S0955-2219(96)00052-0
0955-2219/96/$15.00

Protonic Conduction in $Sr_{1-y}(Zr_{1-x}Dy_x)O_{3-\delta}$ Ceramics

B. Gharbage,[a] F. M. B. Marques[b,*] & J. R. Frade[b]

[a]Instituto Politécnico de Viana do Castelo, ESTG, Ap. 51, 4900 Viana do Castelo, Portugal
[b]Departamento de Engenharia Cerâmica e do Vidro, Universidade de Aveiro, 3810 Aveiro, Portugal

(Received 30 November 1995; revised version received 12 February 1996; accepted 20 February 1996)

Abstract

Ceramic materials derived from strontium zirconate were prepared by high-temperature solid-state reaction starting from oxides and carbonates. Distorted ABO_3-type perovskite structures, indexed to the orthorhombic system, were obtained for A-site substoichiometric and/or B-site Dy-doped materials. The conductivity of $Sr(Zr_{1-x}Dy_x)O_{3-\delta}$ is slightly lower than found for Y-doped strontium zirconate with identical trivalent dopant content, and increases with water vapour pressure, as expected for proton-conducting materials. For Dy-free perovskites with slight A-site substoichiometry ($Sr_{1-y}ZrO_{3-\delta}$, with $y \leq 0{\cdot}02$), the conductivity drops a few orders of magnitude and is nearly independent of water vapour pressure. The corresponding B-site doped materials [$Sr_{1-y}(Zr_{1-x}Dy_x)O_{3-\delta}$] have the highest conductivities, again dependent on water vapour pressure. This indicates that B-site doping is essential to obtain significant proton conductivity. The behaviour of these materials can be understood based on a classical defect chemistry type of approach, if one assumes that electron hole mobilities at low temperature ($\approx 300°C$) are smaller than for protons. This trend is reversed at higher temperatures ($>500°C$). For highly substoichiometric perovskites ($y \geq 0{\cdot}05$), even when B-site doped, the conductivity is minimal and independent of water vapour pressure. A blocking intergrain phase is believed to control the electrical transport properties of these materials. Copyright © 1996 Elsevier Science Ltd

1 Introduction

Protonic conduction has been found in several ABO_3 perovskite materials derived from strontium or barium cerates and zirconates, with B-site doping by Y, Yb, Nd, etc.[1–8] The basis for interpreting the behaviour of these materials was formulated by the pioneering work of Iwahara and co-authors,[1,2] who explained the observed dependence of electrical conductivity on water vapour pressure (P_w) by the formation of mobile protonic defects. Proton conductivity increases with P_w in cerates and zirconates,[2,5–7] even at relatively low temperatures when grain boundaries might play a significant role on the behaviour of polycrystalline ceramics. Nevertheless, results obtained with single crystals of Y-doped $SrZrO_3$ showed that bulk conductivity is also higher in wet than in dry atmospheres, and this demonstrates that protonic conduction is clearly a bulk property.[6]

Most cerate and zirconate materials have been studied at temperatures higher than about 600°C. However, lower temperature applications might also be feasible. For example, Iwahara *et al.*[8] used $BaCe_{0.9}Nd_{0.1}O_{3-\delta}$ as efficient H_2 sensors for temperatures down to about 200°C. Results reported by Liu and Nowick[5] showed that Nd-doped $BaCeO_3$ materials might also be used for water vapour sensors at temperatures of about 450°C. This suggests that further attention should be paid to the low-temperature behaviour of these materials.

Dy instead of Y is an obvious option for B-site doping, considering the similarities between the corresponding cations. In the case of $BaZrO_3$, it has been found that maximum conductivities are observed for Y or Dy B-site doped materials.[9] The information available on Dy-doped $CaZrO_3$ is that the sinterability is poor, but no reference has been found on the role of this dopant in $SrZrO_3$.[9] Also, A-site substoichiometry is expected to cause changes in transport properties as found for $LaMnO_3$-based materials,[10] and might also explain the improved electrical conductivity and sinterability of $SrZrTi_xO_{3+\delta}$ relative to $SrZrO_3$.[11] Metal vacancies can be compensated by different positive defects depending on working conditions. Improved densification might also be expected for A-site

*To whom correspondence should be addressed.

substoichiometric perovskites, when metal vacancies are relevant for the sintering process as found in many circumstances. The purpose of this work was thus to investigate the low-temperature behaviour of some $SrZrO_3$-based materials, using substoichiometry in the perovskite A-site position to test both the effectiveness of metal vacancies in originating protonic defects for charge compensation, and the role of this parameter on the sinterability of Dy-doped ceramics.

2 Experimental Procedure

Dy-doped strontium zirconate specimens of generic formula $Sr_{1-y}(Zr_{1-x}Dy_x)O_{3-\delta}$, with $y \leq 0{\cdot}10$ and $x \leq 0{\cdot}10$, were synthesized by solid-state reaction of oxides and carbonates. The compositions being studied include A-site stoichiometric and B-site doped materials of generic formula $[Sr(Zr_{1-x}Dy_x)O_{3-\delta}]$, A-site substoichiometric and B-site undoped zirconates $[Sr_{1-y}ZrO_{3-\delta}]$ and both A-site deficient and B-site doped materials $[Sr_{1-y}(Zr_{1-x}Dy_x)O_{3-\delta}]$. ZrO_2, Dy_2O_3 and $SrCO_3$ were mixed in a ball mill, calcined at 1350°C, pressed isostatically and sintered at 1650–1700°C for 2 h. Each material was characterized by scanning electron microscopy (SEM) and X-ray diffraction (XRD).

The electrical behaviour was investigated by impedance spectroscopy on discs with about 15 mm diameter and 2 mm thickness, using an HP4284A FRA in the 20–10^6 Hz frequency range. Measurements were undertaken at temperatures in the range 290–840°C, with partial pressures of water vapour in the range 3×10^2 to 8×10^3 Pa, using air or N_2 as carrier gas. The water vapour dosage in the gas phase was obtained by saturation of the carrier gas at different temperatures, or using a desiccant (sulfuric acid). Measurements were recorded after reaching steady state, which required less than 1 h.

3 Results and Discussion

3.1 Structure and microstructure

X-Ray diffractograms showed distorted perovskite structures, which were indexed to the orthorhombic system. Strontium deficiency and increasing Dy content caused a decrease in unit cell parameters. Furthermore, the diffractograms of samples with strontium deficiency >5% showed an extra peak attributed to cubic zirconia. The intensity of this peak increased with rising substoichiometry. In addition, SEM micrographs combined with energy-dispersive spectroscopy (EDS) showed

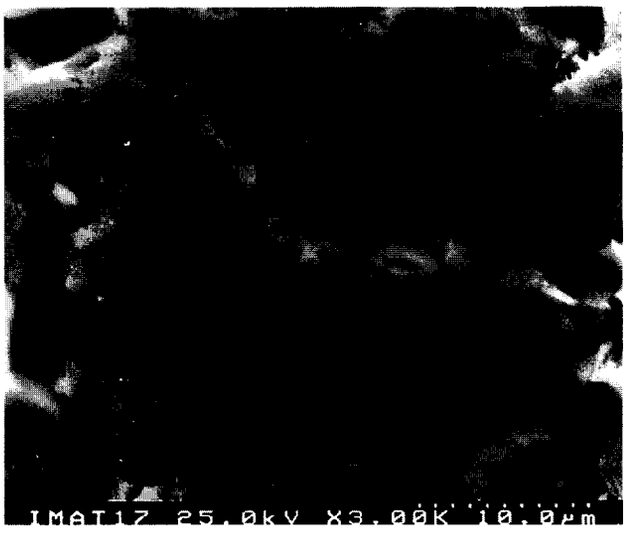

(a)

(b)

Fig. 1. Microstructure of a Sr deficient composition: (a) fracture surface showing vestiges of a liquid phase in between grains; (b) after polishing and thermal etching, showing the presence of a second phase mostly concentrated in triple contact points between grains.

a Zr- and Dy-rich amorphous phase located at grain boundaries [Fig. 1(a)]. During thermal etching it is believed that this phase concentrates mostly in triple contact points between grains [Fig. 1(b)]. Density measurements and SEM observations of this and the remaining compositions revealed significant porosity and poor microstructures in most specimens. The densities of A-site substoichiometric materials were about 90% of theoretical density, and the densities of corresponding A-site stoichiometric materials were slightly lower (between 80 and 90%). This means that, in general, substoichiometry indeed gave rise to improved densities.

3.2 Conductivity dependence on water vapour pressure, in air

Figure 2 shows typical impedance diagrams for $Sr(Zr_{0{\cdot}9}Dy_{0{\cdot}1})O_{3-\delta}$ at 400°C, in wet air with different

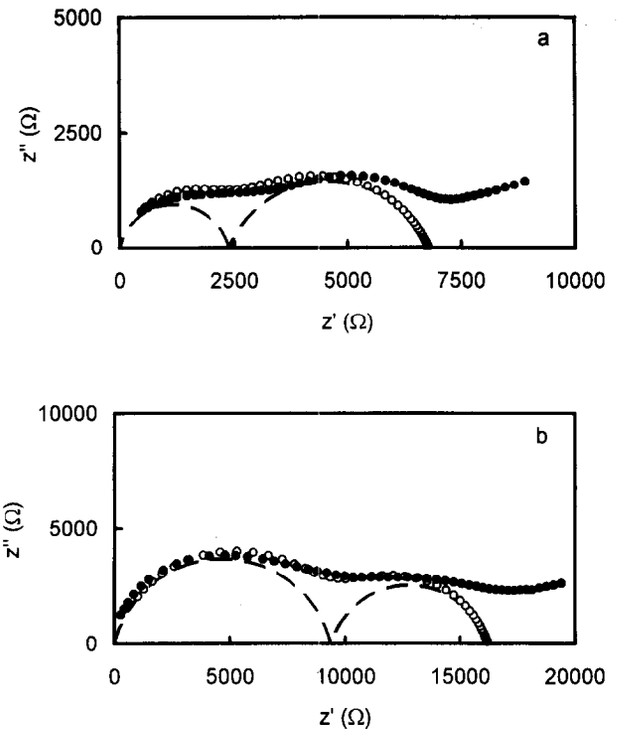

Fig. 2. Impedance diagrams for $Sr(Zr_{0.9}Dy_{0.1})O_{3-\delta}$ at 400°C, in wet air with different water contents: (a) P_w=7·3 × 10^3 Pa; (b) P_w=3 × 10^2 Pa. Solid lines correspond to estimated bulk and grain boundary contributions while the resulting total impedance is shown as open symbols.

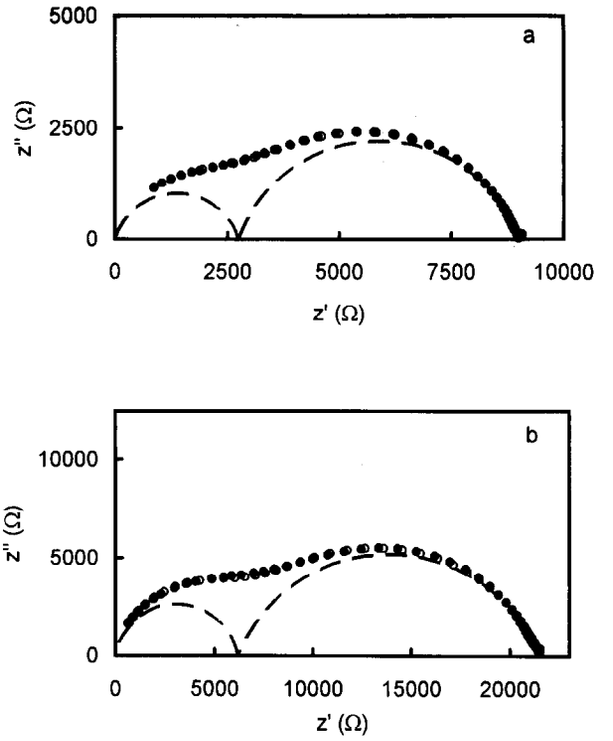

Fig. 3. Impedance diagrams for $Sr_{0.98}(Zr_{0.9}Dy_{0.1})O_{3-\delta}$ at 290°C, in wet air with different water contents: (a) P_w=7·3 × 10^3 Pa; (b) P_w=3 × 10^2 Pa. Solid lines correspond to estimated bulk and grain boundary contributions while the resulting total impedance is shown as open symbols.

water contents (P_w = 7·3 × 10^3 and 3 × 10^2 Pa). Arcs tend to be depressed but this might be related to poor densification of these materials, rather than to the intrinsic electrical behaviour of this composition. In fact, several samples of different microstructures are often needed to assess the effects of porosity and densification on impedance spectra.[12] However, this was not the objective of the present work, and the following discussion will be based on the experimental finding that the spectra can be solved simply into two arcs. The high-frequency arc goes through the origin and will be assigned to the bulk behaviour, while the second arc in the medium frequency range will be attributed to blocking effects due to grain boundaries. These bulk and grain boundary arcs are sensitive to humidity, which demonstrates the existence of protonic conductivity. In addition, the interfacial impedance at low frequencies is also dependent on water vapour pressure, which suggests that the main charge carriers are ionic, at least at low temperature.

Figure 3 shows the diagrams for $Sr_{0.98}(Zr_{0.9}Dy_{0.1})O_{3-\delta}$ at 290°C, in wet air with different water contents. Again, the bulk and grain boundary arcs are sensitive to humidity, which demonstrates the existence of a protonic conductivity contribution. This composition has the highest conductivity, and was thus selected for the remaining part of this study.

Figure 4 shows that the impedance spectrum obtained for $Sr_{0.98}ZrO_{3-\delta}$ at 600°C, in wet air (P_w = 2 × 10^3 Pa), reduces to a single arc; this can probably be attributed to the resistive grain boundary. In fact, expanding the high-frequency data reveals a small contribution, which remained unnoticed on using a much larger scale required for representing the grain boundary contribution. Total impedance is nearly independent of humidity, which indicates that protonic conductivity is negligible. In addition, comparison of data shown in Figs 2–4, and consideration of the differences in temperature, also show that the overall impedance of $Sr_{0.98}ZrO_{3-\delta}$ is much higher than for the remaining compositions with small or no A-site substoichiometry, and B-site doped [$Sr_{1-y}(Zr,Dy)O_{3-\delta}$, $y \leq 0.02$].

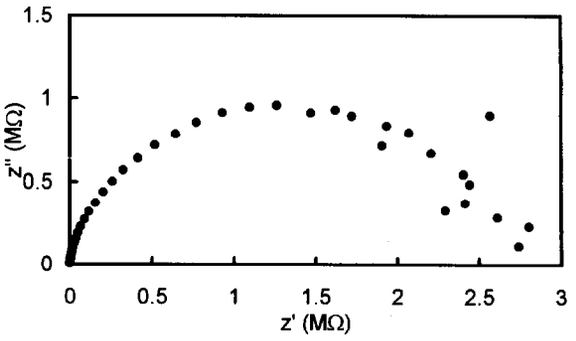

Fig. 4. Impedance diagram for $Sr_{0.98}ZrO_{3-\delta}$ at 600°C, in wet air (P_w=2 × 10^3 Pa). No significant difference was found on changing the water vapour pressure.

3.3 Dependence of conductivity on composition and temperature

The role of composition in the electrical behaviour can be further demonstrated by the temperature dependence of conductivity shown in Fig. 5 for several samples in wet air. $Sr_{0.95}(Zr_{0.95}Dy_{0.05})O_{3-\delta}$ (curve d) is highly resistive when compared with the other compositions. The liquid phase located at grain boundaries of this highly substoichiometric composition might be responsible for the resistive effect (see again Fig. 1). An intermediate level of conductivity is observed for the Dy-free composition (curve c). The activation energies found for these highly resistive compositions were about 1·8 and 1·5 eV, respectively. These high activation energies also indicate that protonic conductivity is not dominant in these materials.

A third level of conductivity is observed for Dy-doped materials with relatively small or no substoichiometry in the A-site (curves a and b). The conductivities of these compositions are somewhat smaller than for Y-doped $SrZrO_3$, and the activation energies (0·7–0·8 eV) are slightly higher than those reported for other proton-conducting perovskite materials.[13,14] However, this does not exclude protonic conduction because the overall behaviour is probably strongly influenced by grain boundary effects. For example, the temperature dependence of bulk and grain boundary conductivities of $Sr_{0.98}(Zr_{0.90}Dy_{0.10})O_{3-\delta}$ corresponds to activation energies of 0·54 and 0·78 eV, respectively. Note that the value for the activation energy of bulk conductivity is in close agreement with values reported for Y-doped $SrZrO_3$ single crystals.[14]

A slight enhancement in conductivity can be seen for materials with a small A-site deficiency and 10% Dy (Fig. 5, curves a and b). Improved conductivity for A-site substoichiometric compositions might correspond only to improved densification of these samples. Data corresponding to curves a and c suggest that B-site doping is essential in determining protonic conductivity. Negative defects originated by A-site substoichiometry might also originate protonic defects for charge compensation, but this idea finds no support in the present experimental observations.

3.4 Effect of P_w and P_{O_2} on the conductivity of $Sr_{0.98}(Zr_{0.9}Dy_{0.1})O_{3-\delta}$

Figures 2 and 3 have already shown that water vapour pressure affects the electrical conductivity of different samples. A more detailed study was carried out for the composition with the highest conductivity. The effect of water vapour pressure on the conductivity of $Sr_{0.98}(Zr_{0.9}Dy_{0.1})O_{3-\delta}$ when air and nitrogen are used as carrier gases is shown in Fig. 6.

The nitrogen used in these experiments has a small oxygen content, corresponding to an oxygen partial pressure (P_{O_2}) of the order of 1–10 Pa, which is three to four orders of magnitude smaller than in air (21 kPa).

A dependence of conductivity on $P_W^{1/2}$ is observed in air, at low temperatures (290°C), and for P_w lower than about 2×10^3 Pa. Impedance spectra used to separate the bulk from grain boundary contributions have demonstrated that bulk and grain boundary conductivities both increase approximately with $P_W^{1/2}$, at least within a limited range of working conditions. This conductivity dependence on water vapour pressure is in general agreement with the predicted behaviour for these protonic conductors and has already been reported for other protonic conductors.[2] The negligible dependence of conductivity on water

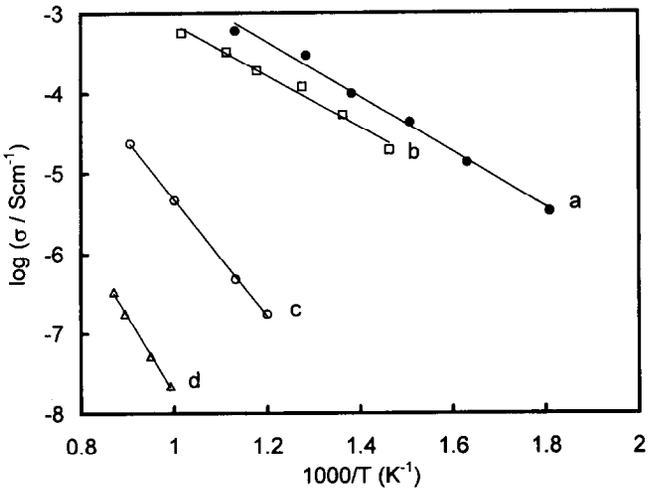

Fig. 5. Arrhenius plot of total conductivity for several samples in wet air (P_w ranging from 3×10^3 to 4×10^4 Pa): (a) $Sr_{0.98}(Zr_{0.9}Dy_{0.1})O_{3-\delta}$; (b) $Sr(Zr_{0.9}DY_{0.1})O_{3-\delta}$; (c) $Sr_{0.98}ZrO_{3-\delta}$; (d) $Sr_{0.95}(Zr_{0.95}Dy_{0.05})O_{3-\delta}$.

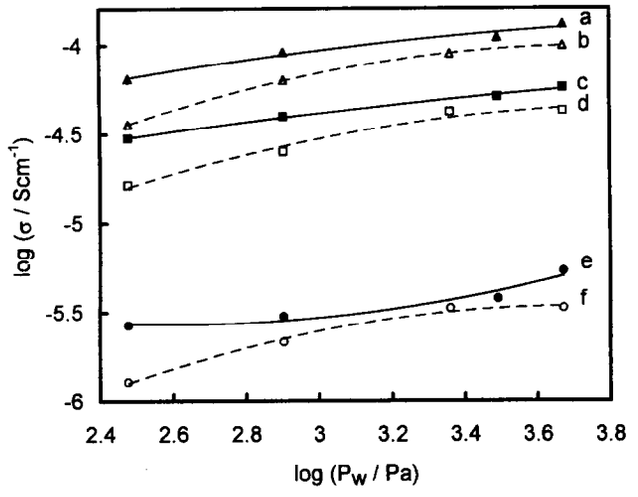

Fig. 6. Effect of P_w on conductivity of $Sr_{0.98}(Zr_{0.9}Dy_{0.1})O_{3-\delta}$ when N_2 (solid lines) or air (dashed lines) is used as carrier gas. Curves (a), (b) 450°C; (c), (d) 400°C; (e), (f) 290°C.

vapour pressure above certain values can be understood as a saturation effect, which ideally should correspond to full charge compensation of the dopant by protons.[5]

From curves shown in Fig. 6 a few more general observations can be made: (1) at constant temperature the conductivity is higher when nitrogen is used as a carrier gas than in air with identical moisture content; (2) the difference in conductivity in air and nitrogen is higher the lower the water vapour partial pressure; and (3) conductivity always increases with increasing water vapour pressure. These data were found to be reproducible in different runs. The differences shown in Fig. 6 cannot be attributed to electron hole conductivity which should be small in all cases at temperatures much lower than 600°C.[7] Also, hole conductivity is usually expected to increase with increasing oxygen partial pressure, and this is contradicted by experimental evidence. In fact, data previously published show that, at relatively high temperature, the electrical conductivity in dry atmospheres (oxygen, air and nitrogen) tends to increase with P_{O_2}.[1] This trend has also been observed in the present experiments at temperatures of the order of 800°C. A justification for this behaviour is attempted in the next section.

3.5 Defect chemistry of $SrZrO_3$-based protonic conductors

Using Kroger–Vink notation, the following equation suggested by Iwahara and co-workers[1,2] can be used to describe the formation of protonic defects in oxides:

$$H_2O\ (g) + 2h^{\cdot} = 2H_i^{\cdot} + 1/2\ O_2\ (g) \qquad (1)$$

To discuss in further detail the relations between composition, conductivity and working conditions (temperature, P_w and P_{O_2}), it is desirable to assume some type of dominant intrinsic ionic defects. In a previous paper we have shown that dominant Schottky-type defects can provide a good basis for interpretation of the transport properties of these materials.[15] This was also assumed in the present work when attempting to prepare A-site deficient perovskites. The dominant negative defects might be strontium vacancies (V_{Sr}'') or Dy ions in the B-site (Dy_{Zr}'), and their concentrations depend on the A-site substoichiometry and B-site dopant levels. The relevant positive defects involved in charge transport should be in this case oxygen vacancies ($V_O^{\cdot\cdot}$), electron holes ($h^{\cdot}$) and protons ($H_i^{\cdot}$). In addition, interaction between ionic and electronic defects can be obtained from usual defect formation reactions:

$$O_O = 1/2\ O_2\ (g) + V_O^{\cdot\cdot} + 2e' \qquad (2)$$

$$0 = V_{Sr}'' + V_{Zr}'''' + 3V_O^{\cdot\cdot} \qquad (3)$$

$$e_v = e' + h^{\cdot} \qquad (4)$$

Equations (2) and (4) can be combined to describe directly the interaction between instrinsic positive defects, which gives:

$$O_O + 2h^{\cdot} = 1/2\ O_2\ (g) + V_O^{\cdot\cdot} \qquad (2a)$$

Reactions (2)–(4) describe the formation of oxygen vacancies, Schottky defects and electronic defects, respectively, and the corresponding equilibrium constants can be written in the usual manner.

For a given composition one may compute $[V_{Sr}'']$ and $[Dy_{Zr}']$, but finding suitable relations between defect concentrations and water vapour or oxygen partial pressures still requires additional relations. The first one is derived from the unit A:B site ratio in the perovskite, including cation vacancies and Dy for Zr substitution:

$$[Sr_{Sr}] + [V_{Sr}''] = [Zr_{Zr}] + [Dy_{Zr}'] + [V_{Zr}''''] \qquad (5)$$

A relation between P_w and P_{O_2} might also be needed in reducing conditions. In fact, reducing conditions are usually achieved with H_2-containing gas mixtures, on assuming equilibrium between H_2, O_2 and H_2O. Similarly, water vapour might be reduced to H_2 by electrochemical pumping, and combination with a mass balance of hydrogen yields P_w as a function of P_{O_2}. All defect concentrations can thus be related to P_{O_2}.[13] Nevertheless, the H_2:H_2O ratio becomes negligible in relatively oxidizing conditions, and in this case P_w and P_{O_2} can be adjusted independently. This condition holds for the experimental conditions selected for this work.

The third relation required to evaluate the effects of water vapour and oxygen partial pressures on the concentration of charge carriers is obtained on assuming electroneutrality for the combined contributions of all charged defects. However, a simple procedure for obtaining solutions is usually based on selecting pairs of one negative defect and one positive defect, each pair being dominant within a certain range of working conditions. A set of consecutive simplified electroneutrality conditions are thus obtained on changing P_{O_2} or P_w; this is certainly valid when the material's behaviour can be studied within large ranges of working conditions and dominant defects can be clearly identified. However, this is not possible when the range of values of P_{O_2} or P_w is relatively small, as for the present work, and it has been considered useful to work with a more general electroneutrality condition, based on one single negative defect and three positive defects. The rationale for this will become obvious from the following discussion.

The work being reported now has involved mostly perovskites with a slight deficit at the A-site and a relatively high dopant concentration at the B-site. For this reason it can be assumed that Dy'_{Zr} dominates over the remaining negative defects. Also, it has been shown that proton conduction is not expected when substoichiometry dominates the formation of negative-charged defects in these materials, which means that A-site substoichiometry must be much smaller than the trivalent dopant content for significant protonic conductivity to be retained. This is a further reason to concentrate our attention on negative defects originated by B-site doping. On the other hand, the dominant positive defects ($h^{\cdot}$, $V_o^{\cdot\cdot}$ or $H_i^{\cdot}$) might change depending on working conditions, and a partly simplified electroneutrality condition can be written as:

$$[Dy'_{Zr}] = p + 2[V_o^{\cdot\cdot}] + [H_i^{\cdot}] \qquad (6)$$

This is the same as neglecting the role of A-site vacancies, including those formed by Schottky disorder [reaction (3)].

The method for obtaining solutions for the defect diagram can now be based on using the equilibrium constant K_1 of reaction (1) to express p as a function of P_w, P_{O_2} and $[H_i^{\cdot}]$, and then using this result and equilibrium constants K_2 and K_4 of reactions (2) and (4) to express $[V_o^{\cdot\cdot}]$. Substitution of both expressions in eqn (6) thus yields

$$[H_i^{\cdot}] = [-\beta + (\beta^2 - 4\,\alpha\gamma)^{1/2}]/2\alpha \qquad (8)$$

with $\alpha = (1 + P_{O_2}^{1/4}/(K_1P_w)^{1/2})$, $\beta = (2K_2/K_4^2K_1P_w)$ and $\gamma = -[Dy'_{Zr}]$. Note that it has been assumed here that P_{O_2} and P_w can be adjusted independently, as expected for oxidizing conditions. For a specific set of values for equilibrium constants K_i, and partial pressures P_{O_2} and P_w, one computes the value of proton concentration, and the remaining defect concentrations can be easily calculated from that value.

This method can be used to predict defect diagrams for variable P_w while keeping P_{O_2} constant, or vice-versa. For example, Fig. 7 was obtained following this approach. Solid lines are for air P_{O_2} = 21 kPa), and the dashed lines are for a typical condition expected for commercial N_2 ($P_{O_2} \approx 10$ Pa). The values for the K_i were adjusted to ensure that working conditions identical to those used in this work would be consistent with the experimental trends already reported, namely that a dominant protonic conductor would have increasing conductivity on increasing the water vapour partial pressure at constant P_{O_2}, and higher conductivity in N_2 than in air, at constant P_w. The partial defect diagrams shown in these figures indeed indicate that such behaviour is possible if protons

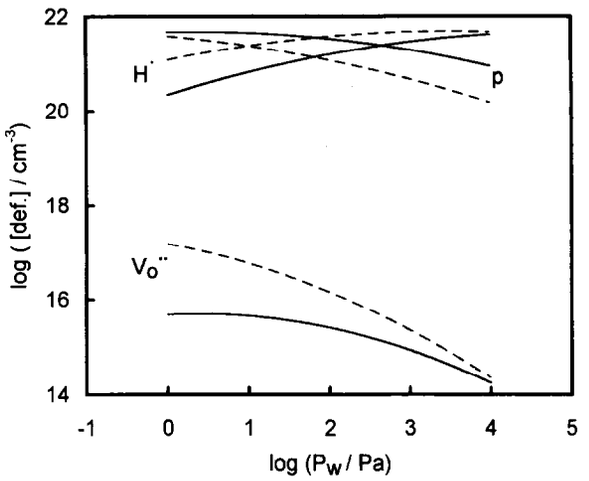

Fig. 7. Suggested defect diagram for Dy-doped $SrZrO_3$-based ceramics, at constant oxygen partial pressure and variable water vapour pressure. Solid lines: P_{O_2} = 21 kPa; dashed lines: P_{O_2} = 10 Pa.

and electron holes are the dominant positive defects, but only if the mobility of protons is higher than hole mobility in this range of temperatures. If this assumption is true, Fig. 8 also suggests that differences in conductivity between experiments performed in air and nitrogen must decrease with increasing water vapour pressure. In fact, this agrees with the experimental trend found at relatively low temperatures (see Fig. 6). While the trends of defect concentrations are commonly accepted in most of the work previously reported on this type of proton-conducting material, the suggested relationship between defect mobilities is not obvious and requires further discussion.

3.6 Final remarks

A comprehensive explanation of experimental data now being reported would require proton

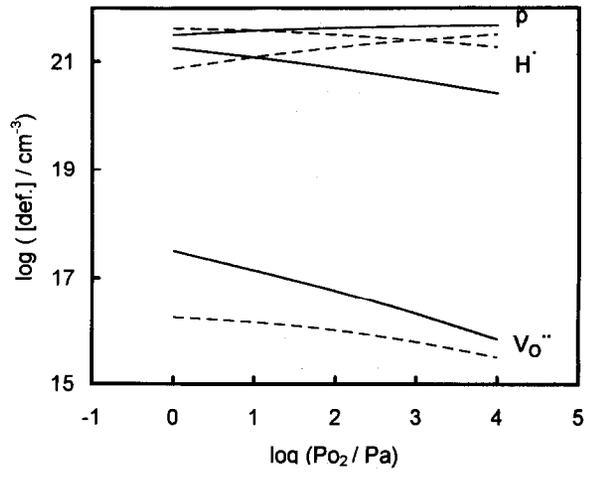

Fig. 8. Suggested defect diagram for Dy-doped $SrZrO_3$-based ceramics, at constant water vapour pressure and variable oxygen partial pressure. Solid lines: P_w = 1 Pa; dashed lines: P_w = 100 Pa.

and hole concentrations of the same order of magnitude, and dominant proton conductivity. This can only be achieved with an electron hole mobility lower than proton mobility in the temperature range 300–500°C. Measurements on proton concentration and mobility have already been reported in the literature and indicate that the concentration of protons is usually insufficient to balance the negative charges originated by B-site doping.[5] This means that most of the simplified electroneutrality conditions indeed include either a contribution by oxygen vacancies, a contribution by electron holes, or both. Expected mobilities of protons can also be found in the literature,[4,16] with activation energies in the range 0·5–0·6 eV, and extrapolation to lower temperatures yields values of about 9×10^{-8} and 5×10^{-7} cm^2 V^{-1} s^{-1} for the mobility of protons in $SrCe_{0.95}Yb_{0.05}O_{3-\delta}$ at 300 and 500°C. The mobility of oxygen vacancies is expected to be quite low at temperatures lower than 500°C, and this excludes a significant oxygen-ion conductivity contribution at such low temperatures, even if the oxide vacancy concentration is significant. Finally, electron hole conduction is likely to occur, especially at relatively high temperatures. Most authors have found significant electron hole conductivity contribution at temperatures higher than about 600°C, and in air, but this should disappear at lower temperatures as a result of decreasing defect concentration and/or defect mobility.

To our knowledge electron hole mobilities have not been reported for these perovskite-type materials. Nevertheless, data reported for other materials might be useful to predict the order of magnitude for electron hole mobilities in $SrZrO_3$-based materials. In fact, this material can be viewed as an ordered structure in the system SrO–ZrO_2, and one might thus estimate the order of magnitude of electron hole mobilities from data reported for zirconia-based electrolyte materials.[17] Extrapolation from high temperatures with an activation energy of about 1·4 eV yields electron hole mobilities of about 1.7×10^{-10} and 1.9×10^{-7} cm^2 V^{-1} s^{-1} at 300 and 500°C. These values are lower than the above-mentioned predictions for proton mobilities, which shows that the possibility of predominant protonic conduction with major electron hole concentrations should not be ruled out at low temperature. This trend can be reversed at high temperatures because the activation energies for the mobility of protons are probably much lower than for the mobility of electron holes. Note also that, from reported data,[17,18] the relative magnitude of mobilities of electronic and ionic defects in YSZ is expected to be reversed with change in temperature.

The overall role of substoichiometry and Schottky-type disorder on the defect chemistry and electrical transport properties has so far been ignored in this discussion, for the sake of simplicity. However, an additional comment should be added for cases when the Dy^{3+} content is similar to or lower than the A-site substoichiometry. Dy^{3+} is a large cation which might replace both Sr^{2+} in A-site and Zr^{4+} in B-site positions in these perovskites. This means that writing formulae for these perovskites suggesting that all Dy is in the B-site position might be inaccurate. Indeed, if Dy^{3+} cations share both sites in the lattice, this would originate both positive and negative defects ($Dy_{Sr}^{\cdot}$ and Dy_{Zr}'), and a decrease in the overall concentration of effective charge carriers ($h^{\cdot}$, $H_i^{\cdot}$ or $V_O^{\cdot\cdot}$). However, this would have no major impact on the previous discussion which was based on the case when the content of Dy^{3+} is much higher than the A-site substoichiometry.

At last, a final comment on the possible existence of B-site substoichiometry. No attempt has been made to prepare such compositions. However, if the structure might accept a significant concentration of B-site vacancies, the overall result would still fit in the model behaviour previously described. The dominant negative defects, whether dopant cations or vacancies in the B-site, would have to be compensated by the same positive defects, and their relevance would depend on working conditions.

4 Conclusions

The low-temperature behaviour of a number of $SrZrO_3$-based ceramics without or with slight A-site substoichiometry, and B-site doping by Dy, is strongly influenced by resistive grain boundaries. This is clearly the result of the processing route, namely poor sinterability, which in general can be improved with a slight deficit in the perovskite A-site position. Nevertheless, A-site substoichiometry has been found to be useless in determining protonic conduction, while B-site doping has been found to be a fundamental requirement for significant proton conductivity. Water vapour affects both bulk and grain boundary conductivities, and the relevant dependence suggests that $Sr_{0.98}(Z_{0.9}Dy_{0.1})O_{3-\delta}$ is a mixed proton and electron hole conductor. The relative importance of both conductivity components depends on temperature, water vapour and oxygen partial pressures. The role of oxygen partial pressure in the total conductivity can only be understood on assuming that electron holes at low temperature have mobilities lower than protons.

Acknowledgement

This work was sponsored by JNICT, Portugal, contract STRD/CTM/664/92.

References

1. Iwahara, H., Esaka, T., Uchida, H. & Maeda, N., *Solid State Ionics*, **3/4** (1981) 359.
2. Uchida, H., Maeda, N. & Iwahara, H., *Solid State Ionics*, **11** (1983) 103.
3. Uchida, H., Yoshikawa, H. & Iwahara, H., *Solid State Ionics*, **34** (1989) 103.
4. Uchida, H., Yoshikawa, H. & Iwahara, H., *Solid State Ionics*, **35** (1989) 229.
5. Liu, J. F. & Nowick, A. S., *Solid State Ionics*, **50** (1992) 131.
6. Huang, H. H., Ishigame, M. & Shin, S., *Solid State Ionics*, **47** (1991) 251.
7. Yajima, T., Suzuki, H., Yogo, T. & Iwahara, H., *Solid State Ionics*, **51** (1992) 101.
8. Iwahara, H., Uchida, H., Ogoki, K. & Nagato, H., *J. Electrochem. Soc.*, **138** (1991) 296.
9. Iwahara, H., Yajima, T., Hibino, T., Ozaki, K. & Suzuki, H., *Solid State Ionics*, **61** (1993) 65.
10. Takeda, Y., Nakai, S., Kojima, T., Kanno, R., Imanishi, N., Shen, G. Q., Yamamoto, O., Mori, M., Asakawa, C. & Abe, T., *Mater. Res. Bull.*, **26** (1991) 153.
11. Zboroska, M., Grylicki, M. & Zborowski, J., *Ceramurgia Int.*, **6** (1980) 99.
12. Kleitz, M., Pescher, C. & Dessemond, L., in *Science and Technology of Zirconia V*, eds S. P. S. Badwal, M. J. Bannister & R. H. J. Hannink. Technomic Publishing Co., Inc., Basel, 1993, p. 593.
13. Shin, S., Huang, H. H., Ishigame, M. & Iwahara, H., *Solid State Ionics*, **40/41** (1990) 910.
14. Huang, H. H., Ishigame, M. & Shin, S., *Solid State Ionics*, 7 (1991) 255.
15. Labrincha, J. A., Frade, J. R. & Marques, F. M. B., *Solid State Ionics*, **61** (1993) 71.
16. Iwahara, H., in *Proton Conductors — Solids, Membranes and Gels — Materials and Devices*, ed. P. Colomban. Cambridge University Press, Cambridge, 1992, p. 122.
17. Weppner, W., *Z. Naturforsch.*, **A31** (1976) 1336.
18. Kleitz, M., Fernandez, E., Fouletier, J. & Fabry, P., *Advances in Ceramics, Vol. 3*, ed. A. H. Heuer & L. W. Hobbs. American Ceramic Society, Columbus, OH, 1981, p. 349.

Journal of the European Ceramic Society **16** (1996) 1157–1161

PII:S0955-2219(96)00040-4
0955-2219/96/$15.00 + .00

Characterization of Grain Boundary Phase of a Lead-Based Relaxor by Raman Scattering Spectroscopy

Hideyuki Kanai,[a] Yohachi Yamashita,[a] Masato Kakihana[b] & Masahiro Yoshimura[b]

[a]Research and Development Center, Toshiba Corporation, 1 Toshiba-cho, Saiwai-ku, Kawasaki 210, Japan
[b]Materials and Structures Laboratory, Tokyo Institute of Technology, 4259 Nagatudacho, Midori-ku, Yokohama 227, Japan

(Received 8 January 1996; revised version received 22 January 1996; accepted 30 January 1996)

Abstract

The grain boundary phase of a lead-based relaxor was identified by Raman scattering spectroscopy using standard specimens including PbO, PbO_2, and Pb_3O_4, as well as standard specimens synthesized from the compositions of the grain boundary phase analyzed by a scanning transmission electron microscope. It was revealed that the grain boundary phase contains the PbO phase along with the main perovskite phase in addition to the pyrochlore phase. This result agrees well with the results of X-ray photoelectron spectroscopy studies and strongly supports a previously described degradation mechanism for insulation resistance under humid loading conditions: dissolution of PbO in the grain boundary phase into water is the trigger phenomenon leading to degradation. Copyright © 1996 Elsevier Science Ltd

1 Introduction

Lead-based dielectrics called relaxors are solid solutions of perovskite compounds such as $Pb(Mg_{1/3}Nb_{2/3})O_3$, $Pb(Zn_{1/3}Nb_{2/3})O_3$, and $Pb(Fe_{1/2}Nb_{1/2})O_3$. Yonezawa[1] developed the dielectric ceramics $Pb(Fe_{2/3}W_{1/3})O_3$–$Pb(Fe_{1/2}Nb_{1/2})O_3$ and first used them as a dielectric in MLCs (Multilayer Ceramic Capacitors). Since then, many dielectric compounds for use in MLCs have been reported.[2–4] The interest in relaxors results from their great potential, since they are high dielectric constant materials with sintering temperatures below 1100°C. Such low sintering temperatures allow the use of inexpensive internal electrodes, such as Ag/Pd mixtures or alloy, in the MLC production process.

A previous report by the authors[9] revealed that the reliability of a relaxor under humid loading conditions is a function of the nonstoichiometry of A/B, which is the molar ratio of all the elements at A-sites in the ABO_3 perovskite structure to those at B-sites.[5,6] When A/B is equal to or greater than 1·00, a 2–3 nm-thick secondary phase exists at grain boundaries. Assuming that this secondary phase is soluble in water, the grain boundaries can then dissolve into water. The result is a silver metal path formed by the migration of silver through the partially water-filled grain boundaries from the anode side to the cathode side. Ultimately, the resistance of the dielectric material falls. It has generally been accepted that there exists a continuous or semi-continuous amorphous grain boundary phase (approximately 5–10 nm thick) comprising primarily PbO.[7,8] However, it had not been confirmed that the grain boundary phase is PbO. Therefore, the authors made a successful attempt to identify the lead-based grain boundary phase using X-ray photoelectron spectroscopy (XPS); the grain boundary phase was found to consist mainly of PbO and PbO_2. In this paper, identification of the grain boundary phase is attempted using Raman Scattering Spectroscopy (RSS) as a means of confirming the results of the XPS study. The final objective of successive attempts to identify the grain boundary phase of a lead-based relaxor is to explain why the grain boundary phase is the determinant of reliability.

2 Experimental Procedure

The composition of the relaxor dielectric ceramic used in this experiment was $[(Pb_{0.875}Ba_{0.125})]_A[(Mg_{1/3}Nb_{2/3})_{0.5}(Zn_{1/3}Nb_{2/3})_{0.3}Ti_{0.2}]_BO_3$, where the total molar number of elements occupying the A- and B-sites in the perovskite structure are denoted by A and B, respectively. The temperature coefficient of dielectric constant (K) for this relaxor satisfies the Y5U designation of the Electronic Industries Associations (EIA) standard.[10] In order to ensure

the presence of intergranular fractures — and thus the formation of a grain boundary phase — specimens with A/B = 0·95, 1·00, and 1·05 were prepared. Specimens without a grain boundary phase (A/B = 0·95) exhibiting a transgranular fracture were also produced for comparison.

The raw materials used throughout this experiment were reagent-grade oxides and carbonates. The constituents were weighed, mixed by ball-milling with pure water for 24 hours, and then calcined in a closed alumina crucible at 800°C for two hours. After ball-milling the calcined powder with pure water and drying it, 7 wt% of an aqueous solution of 5 wt% polyvinyl alcohol was added. The result was granulated and pressed into disk pellets 10 mm in diameter and 1·5 mm in height at 100 MPa. After binder burnout at 600°C for 10 minutes, the pellets were fired for two hours in a closed magnesia crucible, at 1050°C for A/B = 1·05, and at 1100°C for A/B = 0·95 and 1·00 to obtain dense specimens. An optimum firing temperature was selected to obtain maximum density.

The valence of lead in the grain boundary phases was determined by Raman scattering spectroscopy (Jobin Yvon - Atagobussan T64000, Longjumeau, France). Spectra activated by an argon ion laser (514·5 nm) were measured between 100 and 1200 cm^{-1}. The beam diameter was 1 μm. The fired specimens were cracked open to obtain the 1–2 nm-thick grain boundary phase on the fractured surfaces of A/B = 1·00 and 1·05. Because specimens with A/B = 0·95 break right through the grains, the Raman spectra reflect the internal state of the grains. After being cracked open, specimens were transferred to the specimen holder of a Raman spectroscope, and spectra from the grain boundary phase were measured. Standard specimens used for identification of Raman spectra were PbO (99·99%, High Purity Chemicals Lab., Ltd), PbO_2 (99·9%, High Purity Chemicals Lab., Ltd), and Pb_3O_4 (99·99%, High Purity Chemicals Lab., Ltd). In addition, the composition of two locations in the grain boundaries of specimens with A/B = 1·05 was analyzed by a scanning transmission electron microscope (STEM) (Table 1). Specimens with these compositions (GB#1 and GB#2) were synthesized in the same manner as described above. GB#1 and GB#2 were sintered at 1000°C, 1050°C, and 1100°C for two hours for identification of Raman spectra from the grain boundary phase.

Table 1. Composition of the grain boundary phase, analyzed by STEM, in specimen with A/B = 1·05 fired at 1050°C for 2 h

	Grain boundary phase		
Component	*GB#1*	*GB#2*	*Inside of grains*
PbO	70·4	66·5	61·7
BaO	4·02	4·91	5·08
Nb_2O_3	16·6	19·4	21·73
ZnO	2·16	2·15	2·29
MgO	2·33	2·23	3·10
TiO_2	4·44	4·88	6·06

3 Results and Discussion

3.1 Identification of the grain boundary phase by RSS

Figure 1 shows Raman spectra from the fractured surfaces of specimens with A/B = 0·95, 1·00, and 1·05. Spectra for each specimen consist of six peaks and they are very similar to each other, with the following features: a small peak at 130 cm^{-1} for the specimen with A/B = 0·95, but a broad peak at 139·8 cm^{-1} for specimens with A/B = 1·00 and 1·05 containing the grain boundary phase; the peak at 268·2 cm^{-1} for A/B = 1·00 and 1·05 is shifted toward low wave number, as compared with that for the specimen with A/B = 0·95. Since there is little difference in spectra from the grain boundary phase and within the grain, we speculate that either the grain boundary phase is similar to the perovskite phase inside the grain or signals from the 1–2 nm-thick grain boundary phase on the grain surfaces were diluted by signals from within the grain due to the Ar laser penetrating further than a few hundred nanometers.

Because STEM analysis has clarified that lead is the main component of the grain boundary phase,[6,11] we investigated whether lead mono-oxide exists in the grain boundary phase by comparison with Raman spectra of standard specimens of PbO, PbO_2, and Pb_3O_4. As shown in Fig. 2, the spectrum of PbO at 140·7 cm^{-1} corresponds to the broad spectrum at 139·8 cm^{-1} for A/B = 1·00 and 1·05, even though the peaks present at smaller wave numbers for PbO_2 and Pb_3O_4 do not correspond. In addition, the peak at 268·2 cm^{-1} for A/B

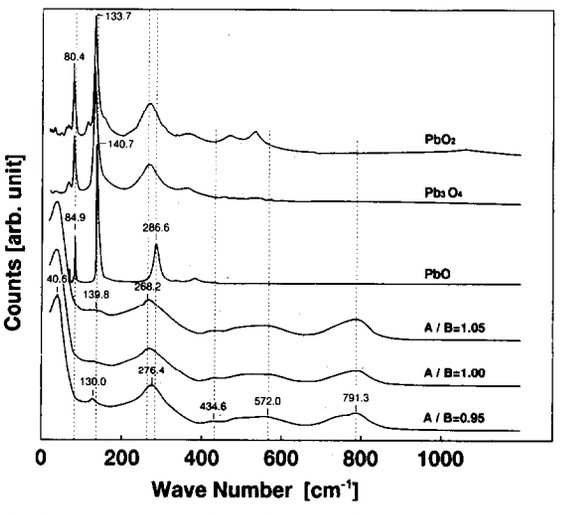

Fig. 1. Raman spectra from fractured surfaces of specimens with (A/B = 1·00 and 1·05) and without (A/B = 0·95) the grain boundary phase as well as reference specimens.

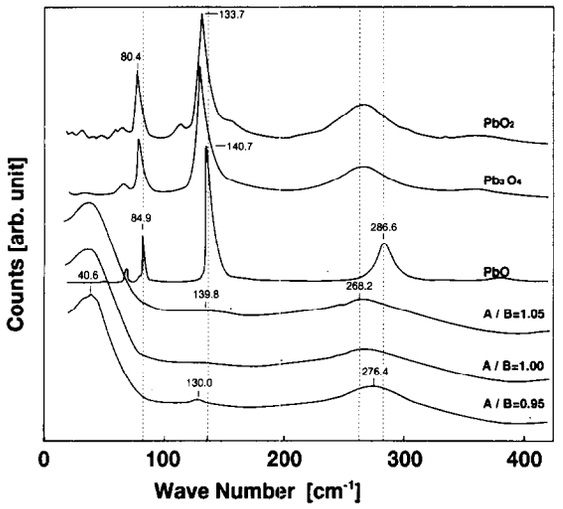

Fig. 2. Detailed view of the low wave number portion of Fig. 1 with an enlarged scale on the horizontal axis.

= 1·05 is broad on the high wave number side, compared to the peak at 276·4 cm^{-1}. Since there is a peak at 286·6 cm^{-1} in the spectrum of the standard specimen of PbO, the spectra for A/B = 1·05 should be convoluted by the interaction of the spectra for the unknown phase and the PbO phase. Moreover, the reason for the slightly broadened peak at 84·9 cm^{-1} for A/B = 1·00 and 1·05 with the grain boundary phase is probably interaction with the spectrum for PbO. Therefore, PbO is not the main constituent of the grain boundary phase, even though the grain boundary phase consists of PbO and an unknown other phase.

In order to identify the grain boundary phase in more detail, grain boundary phases GB#1 and GB#2 were synthesized using the compositions determined by STEM analysis of the grain boundary in the fired specimen with A/B = 1·05. As shown in Fig.3, X-ray diffraction peaks due to the PbO phase, the perovskite phase, and the pyrochlore phase were present in GB#1 and GB#2 fired at 1050°C for two hours. These peaks did not correspond to those for PbO_2 and Pb_3O_4. Since GB#1

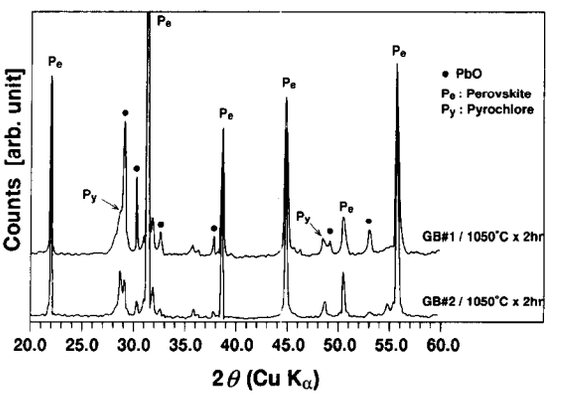

Fig. 3. Powder X-ray diffraction patterns of GB#1 and GB#2 fired at 1050°C for 2 h: GB#1 and GB#2 mainly comprise the perovskite phase in addition to the PbO phase and the pyrochlore phase.

and GB#2 have the compositions given below, the PbO phase and the perovskite phase are expected to be formed in the sintered material.

GB#1:

80 mol%$(Pb_{0.89}Ba_{0.11})[(Mg_{1/3}Nb_{2/3})_{0.44}(Zn_{1/3}Nb_{2/3})_{0.33}Ti_{0.23}]O_3$ + 16 mol% PbO + 4 mol% MgO

or

80 mol%$(Pb_{0.89}Ba_{0.11})[(Mg_{1/3}Nb_{2/3})_{0.71}(Zn_{1/3}Nb_{2/3})_{0.06}Ti_{0.23}]O_3$ + 16 mol% PbO + 4 mol% ZnO

GB#2:

91 mol%$(Pb_{0.89}Ba_{0.11})[(Mg_{1/3}Nb_{2/3})_{0.5}(Zn_{1/3}Nb_{2/3})_{0.28}Ti_{0.22}]O_3$ + 8 mol% PbO + 1 mol% MgO

or

91 mol%$(Pb_{0.89}Ba_{0.11})[(Mg_{1/3}Nb_{2/3})_{0.59}(Zn_{1/3}Nb_{2/3})_{0.19}Ti_{0.22}]O_3$ + 8 mol% PbO + 1 mol% MgO

Raman spectra for GB#1 and GB#2 were measured, as shown in Figs 4 and 5. These spectra are very similar to those for A/B = 1·00 and 1·05 with the grain boundary phase. Three sharp peaks appear at 84·9, 140·7, and 286·6, and these correspond to the peaks for PbO. In addition, since GB#1 and

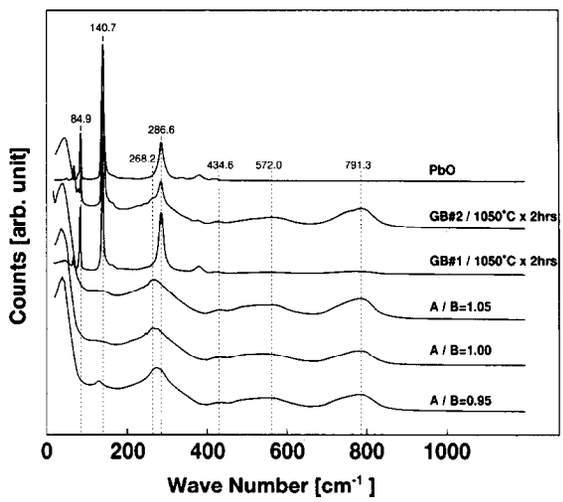

Fig. 4. Raman spectra from fractured surfaces of specimens (GB#1 and GB#2) fired at 1050°C for 2 h.

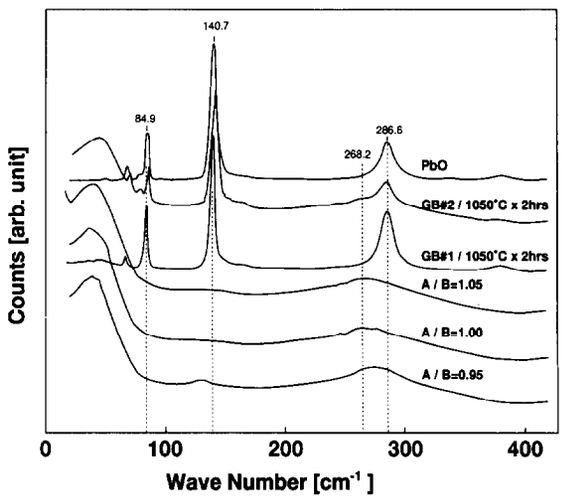

Fig. 5. Detailed view of the low wave number portion of Fig. 4 with an enlarged scale on the horizontal axis.

GB#2 comprise the PbO phase, the perovskite phase, and the pyrochlore phase according to the X-ray diffraction analysis, the remaining broad peaks reflect the perovskite phase and the pyrochlore phase. In Figs 4 and 5, spectra indicating the perovskite phase and the pyrochlore phase in GB#1 and GB#2 correspond to broad spectra for A/B = 1·00 and 1·05 with the grain boundary phase. This confirms that the unknown phases in the grain boundary are the perovskite phase and the pyrochlore phase.

The peak at 268·2 cm^{-1} for A/B = 1·00 and 1·05 with the grain boundary phase is present at slightly lower wave number than that for A/B = 0·95 without the grain boundary phase. In A/B = 0·95, oxygen vacancies may be created to compensate for defects at the A-site in the perovskite, causing binding length shortening. As a result, the wave number increases. In specimens with A/B less than 1.00, the deficiency at the A-site is compensated for the formation of the pyrochlore phase. This result indicates the existence of defects at the A-site in the perovskite structure as well as the formation of the pyrochlore. One reason for peaks for the perovskite phase being broader than those for the PbO phase is that the perovskite phase consists of multiple components, resulting in the existence of multi-vibrational modes. This is in addition to the mixing of the pyrochlore phase into the perovskite phase.

We conclude that the grain boundary phase comprises the PbO phase, the perovskite phase, and the pyrochlore phase. This conclusion strongly supports the degradation mechanism previously presented by the authors.[6] According to this mechanism, the grain boundary phase first dissolves into water and then the grain boundaries fill with water. This leads to Ag migration from the Ag electrode. Thus, PbO peaks in GB#1 would be lower for GB#1 held in water. Change in PbO peaks fractured surfaces of GB#1 fired at 1050°C was investigated by RSS after keeping the fractured specimens in hot water at 85°C for various times. As shown in Fig. 6, the main peak at 140·7 cm^{-1} for PbO started to decrease after 20 hours, and then the peak completely disappeared after 50 hours. A small peak can still be seen after 140 hours, maybe due to distribution of thickness of the grain boundary phase. Thus, it is confirmed that PbO in the grain boundary phase can dissolve in water, suggesting justification of our degradation mechanism for insulation resistance.

3.2 Electrical properties of the grain boundary phase

Figure 7 shows the temperature dependence of the dielectric constant of GB#1. The maximum dielectric constant is 5000 for 1000°C firing and 6500

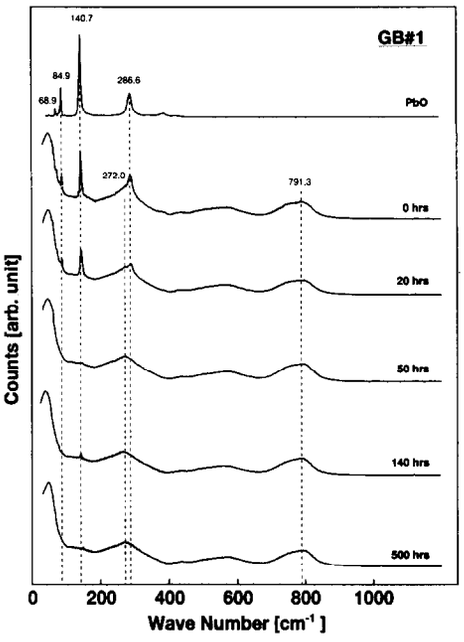

Fig. 6. Raman spectra from fractured surfaces of GB#1 treated in hot water at 85°C for various times.

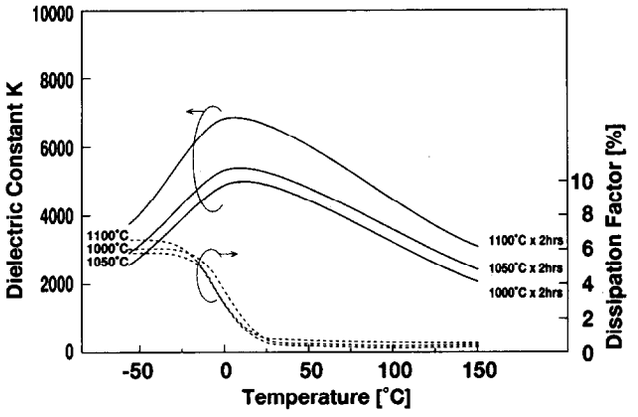

Fig. 7. Dielectric constant and dissipation factor of GB#1 at 1 kHz as a function of temperature.

for 1100°C firing. A previous study reports that there is a PbO-rich grain boundary phase with a dielectric constant of 26.[11] If a grain boundary phase with the low dielectric constant of 26 is present, the decrease in dielectric constant of the bulk specimen would be given as follows, according to the series model:[12] (2 nm-diameter grain with dielectric constant of 12 500)-(2 nm-thick grain boundary phase)-(2 nm diameter grain with dielectric constant of 12 500)

$$C/C_0 = k_2 d_1/(K_2 d_1 + K_1 d_2)$$

where K_1 is the dielectric constant (12 500) of the grain, d_1 is the grain diameter (2 μm), K_2 is the dielectric constant (26) of the grain boundary phase, and d_2 is the thickness (2 nm) of the grain boundary phase. This equation tells us that the dielectric constant decreases by 33% if the dielectric constant of the grain boundary phase is 26, and 0·4% for 6000.

Table 2. Electrical properties of GB#1

	Firing temperature (°C)					
	1,000		*1,050*		*1,100*	
	25°C	*125°C*	*25°C*	*125°C*	*25°C*	*125°C*
C[nF]	7·634	3·961	7·867	4·348	9·033	5·034
DF[%]	0·86	0·27	0·68	0·33	0·85	0·50
IR[Ω]	$0{\cdot}42 \times 10^5$	$0{\cdot}42 \times 10^5$	$0{\cdot}28 \times 10^5$	$0{\cdot}27 \times 10^5$	$0{\cdot}27 \times 10^5$	$0{\cdot}27 \times 10^5$
CR[ΩF]	320	170	190	120	360	210

In a previous study,[12] we reported that the dielectric constant when A/B ≥ 1·01 did not greatly decrease in spite of the existence of the grain boundary phase. This is how we conclude that the main component of the grain boundary phase is not PbO nor the pyrochlore phase with a low dielectric constant, but rather the perovskite phase. This conclusion supports the results of grain boundary phase identification by Raman scattering spectroscopy. Table 2 shows the product of capacitance and resistance (CR) after 1 min at 25°C and 125°C. Independent of firing temperatures CR values at 25°C were 200–400 [ΩF] and at 125°C were 100–200 [ΩF]. These values are considerably lower than those for bulk specimens;[5] that is, they are much less than 10 000 [ΩF] at 25°C and 125°C. If the grain boundary phase is continuously present, the total resistance of bulk specimens should suffer from the effect of the low-resistance grain boundary phase. However, this was not the case. Since the CR value is greater than 10 000 [ΩF] both at 25°C and 125°C,[5] this result suggests that the grain boundary phase is not present continuously in the grain boundaries.

4 Conclusions

It has been clarified that the grain boundary phase of a relaxor dielectric ceramic contains the PbO phase along with the main perovskite phase in addition to the pyrochlore phase. This conclusion strongly supports our degradation model for insulation resistance under humid loading conditions;[6] the insulation resistance degradation in relaxor dielectric ceramics with A/B ≥ 1.00 under humid loading conditions is attributed to dissolution of PbO in the grain boundary phase into water. In addition, the reason for the dielectric constant of specimens with A/B ≥ 1.00 and the grain boundary phase not falling decrease greatly was also elucidated.

Acknowledgement

We would like to thank Mr M. Osada of Tokyo Institute of Technology for carrying out Raman scattering spectrum measurements.

References

1. Yonezawa, M. *et al.*, Properties of $Pb(Fe_{2/3}W_{1/3})O_3$-$Pb(Fe_{1/2}Nb_{1/2})O_3$ Ceramics. *Proc. 1st meeting on ferroelectrics and their application* (1977) 297–302.
2. Maher, G. H., Improved dielectrics for multilayer ceramic capacitors. *Proc. Electro Components Conf.*, **27** (1977) 391–9.
3. Furukawa, K. *et al.*, Dielectric properties of $Pb(Mg_{1/3}Nb_{2/3})O_3$-$PbTiO_3$ ceramics for capacitor materials. *Proc. Japan-US Study Seminar on Dielectrics and Piezoelectric Ceramics* (1982) p. T–4.
4. Kato J. *et al.*, "Dielectric properties of $Pb(Mg_{1/3}Nb_{2/3})O_3$-$Pb(Ni_{1/2}W_{1/2})O_3$ ceramics. *Jpn J. Appl. Phys.*, **24** (1985) suppl. 24-3, p. 90.
5. Kanai, H., Furukawa, O., Nakamura, S. & Yamashita, Y., Effect of stoichiometry on the dielectric properties and the life performance of $(Pb_{0.875}Ba_{0.125})[(Mg_{1/3}Nb_{2/3})_{0.5}(Zn_{1/3}Nb_{2/3})_{0.3}Ti_{0.2}]O_3$ relaxor dielectric ceramics: Part I, Dielectric properties. *J. Am. Ceram. Soc.*, **76** (1993) 454–8.
6. Kanai, H., Furukawa, O., Nakamura, S. & Yamashita, Y., Effect of stoichiometry on the dielectric properties and the life performance of $(Pb_{0.875}Ba_{0.125})[(Mg_{1/3}Nb_{2/3})_{0.5}(Zn_{1/3}Nb_{2/3})_{0.3}Ti_{0.2}]O_3$ relaxor dielectric ceramics: Part II, Life performance. *J. Am. Ceram. Soc.*, **76** (1993) 459–64.
7. Goo, E. & Thomas, G., Microstructure of lead-magnesium niobate ceramics. *J. Am. Ceram. Soc.*, **69** (1986) C-188–C-190.
8. Gorton, A. J. & Chen J., Microstructure and properties of PMN ceramics — influence of powder purity. *Proc. Sixth IEEE Intl Symp. Appl. Ferroelectrics* (1986) 150–3.
9. Kanai, H., Yoshiki, M., Hayashi, M. & Yamashita, Y., Grain boundary phase identification of relaxor dielectric ceramics by XPS. *J. Am. Ceram. Soc.*, 77 (1994) 2229–31.
10. Furukawa, O., Harata, M., Yamashita, Y., Inagaki, K. & Mukaeda, S., A lead perovskite Y5U dielectric for multilayer ceramic capacitor. *J. Appl. Phys. Suppl.*, **26** (1987) 34–7.
11. Hui-Chieh Wang & Schulze, W. A. The role of excess magnesium oxide or lead oxide in determining the microstructure and properties of lead magnesium niobate. *J. Am. Ceram. Soc.*, **73** (1990) 825–32.
12. Payne, D. A. & Cross, L. E., *Proc. Sixth International Materials Symposium, Ceramic Microstructure '76*, ed. R. M. Fulrath & J. A. Pask (1976) 584–97.

Journal of the European Ceramic Society **16** (1996) 1163–1169

PII:S0955-2219(96)00046-5
0955-2219/96/$15.00

Low-Temperature Sintering of 0·99 SnO_2–0·01 CuO: Influence of Copper Surface Diffusion

J. P. Bonnet,* N. Dolet & J. M. Heintz

I.C.M.C.B., Université Bordeaux I, Château Brivazac, Av. Dr Schweitzer, 33608 Pessac Cedex, France

(Received 31 May 1995; revised version received 1 February 1996; accepted 8 February 1996)

Abstract

The influence of CuO on the surface reactivity and on the shrinkage behaviour of a SnO_2 powder has been studied at low temperature ($T \leq 900°C$). Surface diffusion of copper ions, effective at a temperature as low as 400°C, results in an homogeneous distribution of copper cations on the grain surfaces. The powder's ability to fix water and oxygen-derived species is then modified. Simultaneously to the formation of oxygen vacancies in the outer part of the grains, a densification phenomenon is observed at 850°C. The corresponding shrinkage kinetics can be fitted using the model proposed by Scherer to describe viscous flow sintering of a low-density array of particles. A relation between the atomic defects present near the surface of the grains and the viscous flow-like behaviour is suspected. Copyright © 1996 Elsevier Science Ltd

1 Introduction

Pure SnO_2 is known to be very difficult to densify by natural sintering, i.e heat treatment gives rise to an increase of the size of both pores and grains.[1,2] However, addition of a small amount of CuO (1 molar %) favours densification. High-density ceramics (i.e. 98% of the theoretical density) can be obtained after sintering at 1150°C. We have shown, in a previous work, that the fast shrinkage observed at this temperature is related to the presence of a copper oxide-rich liquid phase.[3]

In addition, we have observed that the presence of CuO also promotes the densification of SnO_2 at temperatures (850 and 900°C) lower than that of the liquid phase formation (≈ 940°C).[4] At such low temperatures, grain surface diffusion can be the predominant matter transfer process. Therefore, the purpose of this work is to identify the contribution of the interface to the phenomena involved in the slow densification observed when $T < 940°C$.

*Present address: ENSCI, 47 Av. Albert Thomas, 87065 Limoges Cedex, France.

2 Experimental Procedure

2.1 Preparation of the green compacts

SnO_2 (Aldrich 99·9%) and CuO (Prolabo Normapur 99%) were used as starting powders. Their specific surface areas were 7·3 and 14·8 $m^2.g^{-1}$, respectively. In order to get 0·99 SnO_2–0.01 CuO molar mixture, appropriate quantities of the powders were mixed in an agate ball mill in pure ethanol. After calcination for 3 h in air at 400°C, the powder mixture was uniaxially pressed to form cylindrical samples (6 mm diameter). The density of the green samples was $3·6 \pm 0·1$ g cm^{-3}.

2.2 Determination of the shrinkage kinetics

The isothermal shrinkage rate was determined at 850 and 900°C in air, using a Netzch dilatometer. The furnace was heated at the desired temperature and then the green sample, set on the measuring device, was introduced in 5 min into the isothermal zone. The shrinkage evolution was recorded during 80 min.

2.3 Study of water and oxygen sorption phenomena

SnO_2 is known as a material that chemisorbs oxygen and water easily.[5,6] These phenomena are also dependent on the grain surface composition. Therefore, study of the exchange between gas phase and SnO_2-based materials, using thermogravimetric analysis, can give information on an eventual evolution of the grain surface composition during heat treatment. Further insights in the sintering mechanisms of 0·99 SnO_2–0·01 CuO mixture can then be deduced since the composition of the surface of the grains is one of the parameters that control the sinterability of a ceramic powder at low temperature.

Thermogravimetric measurements were performed using a Setaram MTB 10-8 equipment. The equipment accuracy was 10 μg with an initial sample weight of about 700 mg. The behaviour of four samples was investigated: (i) a pure SnO_2 powder calcined at 400°C for 3 h, (ii) a 0·99 SnO_2–0·01 CuO powder calcined at 400°C for 3 h,

Table 1. Definitions of the main terms used in section 3

m_O	Initial mass of a sample
m_{H_2O}	Mass attributed to water desorbed during heating
m_{O_2}	Mass attributed to oxygen adsorbed during cooling
n	Number of cationic positions on the grain surface per gram of material
n_{Sn}	Number of Sn on the grain surface per gram of material [$n_{Sn}/n = 1$ for "pure" SnO_2]
n_{H_2O}	Number of H_2O molecules desorbed per gram of material
n_{Cu}	Number of Cu lying in substitutional position on the grain surface per gram of material [$n_{Cu}/n = 1 - n_{H_2O}/n$]
n_{V_O}	Number of oxygen vacancies on the grain surface per gram of material [corresponding to O_2 molecules adsorbed during cooling]
n_V	Number of surface oxygen vacancies per gram due to Cu distribution [$n_V/n = n_{V_O}/n - (n_{V_O}/n)$ pure $SnO_2 = n_{V_O}/n - 0{\cdot}18$]

(iii) a 0·99 SnO_2–0·01 CuO calcined powder sintered at 850°C for 20 min, (iv) a 0·99 SnO_2–0·01 CuO calcined powder sintered at 850°C for 60 min. Each specimen was prepared as a cylindrical pellet and presented almost the same initial density (≈ 3·6 g cm^{-3}). The samples were heated in flowing air at 200°C h^{-1} up to 800°C or 850°C, then held for 15 min in a dried oxygen flow, before cooling down to 20°C at 200°C h^{-1} in the same atmosphere. The recorded weight changes were corrected for buoyancy force changes. The BET specific surface areas were determined using N_2 gas as adsorbate at 77 K with a Micromeritics 2100 E apparatus. From TGA and BET measurements, numbers of species present on the surface of the grains have been calculated. Definitions of the terms used are given in Table 1.

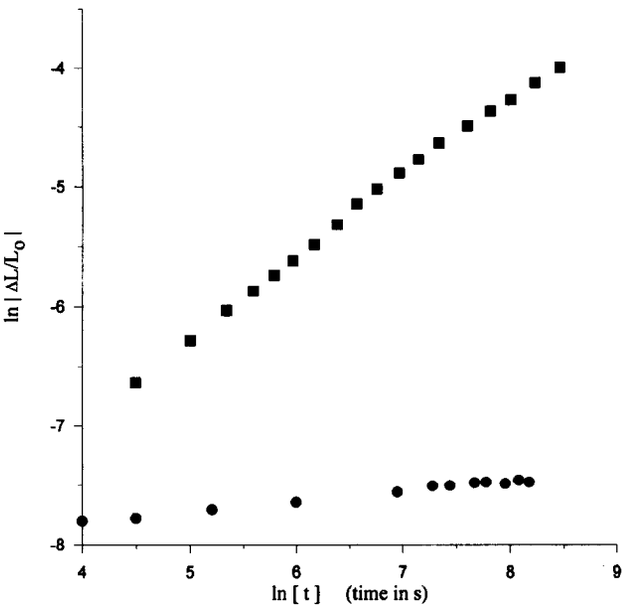

Fig. 1. Isothermal shrinkage at 850°C in air of (●) 'pure' SnO_2 and (■) 0·99 SnO_2–0·01 CuO materials.

3 Results and Discussion

3.1 Isothermal shrinkage kinetics

At 850 and 900°C, the evolution of the isothermal shrinkage, $|\Delta L/L_0|$, of 0·99 SnO_2–0·01 CuO samples versus sintering time, t, can be described by the relation:

$$|\Delta L/L_0| = A \cdot t^p \qquad (1)$$

with $p = 0{\cdot}66 \pm 0{\cdot}02$. That value of p does not correspond to any of the known liquid-phase sintering mechanisms, i.e. $p \leq 0{\cdot}3$.[9] Furthermore, the fast initial densification step usually observed for this material during the liquid phase formation when $T_S \geq 940$°C is not observed. Those results lead us to consider that in this range of temperature (850–900°C) sintering does not involve a liquid phase. However, the influence of copper oxide on the densification rate is already marked for very short sintering time as it can be seen in Fig. 1 where the shrinkage kinetics at 850°C of 'pure' SnO_2 and of 0·99 SnO_2–0·01 CuO are compared. Such a behaviour suggests that the distribution of copper ions in SnO_2-based material occurs either during the calcination treatment at 400°C or very rapidly during the heating up to 850°C.

3.2 Copper ion distribution after calcination at 400°C

The thermogravimetric study of water and oxygen sorption phenomena has been performed on green compacts of SnO_2 and 0·99 SnO_2–0·01 CuO powders previously calcined at 400°C in air for 3 h. The relative weight losses, $(m\text{-}m_O)/m_O$, related to desorption during heating up to 400°C in air, are reported in Fig. 2, where m_O and m are the weight of the sample measured in air at 20°C and at a temperature T, respectively. Considering the low amount of CuO in the mixture powder (≈0·5 wt%), the difference between the two curves in Fig. 2 when $100 \leq T \leq 300$°C is too large to be attributed to sorption phenomena on CuO grains. Relative density (0·52) and specific surface area (7·3 m^2 g^{-1}) of the two samples being identical, only a modification of the SnO_2 grain surface composition can explain the difference in desorption behaviour. As a consequence, it can be considered that diffusion of copper ions on the surface of the SnO_2 grains occurred during the previous calcination treatment at 400°C.

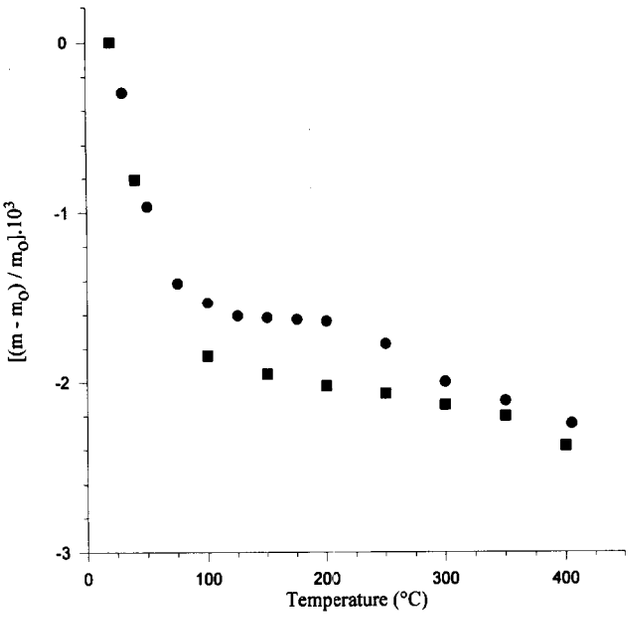

Fig. 2. Relative weight losses observed during the heating in air of calcined powders: (●) 'pure' SnO_2, (■) 0·99 SnO_2–0·01 CuO.

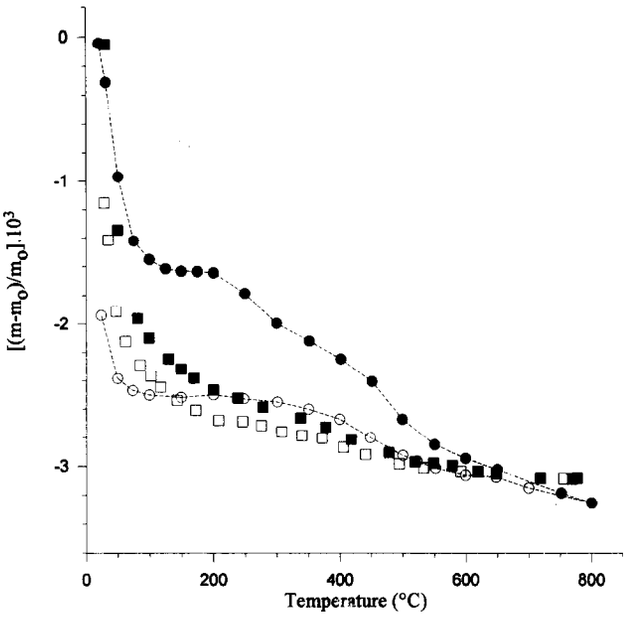

Fig. 3. Relative weight variations observed during heating in ambient air and cooling in dry oxygen of: calcined SnO_2 (● heating, ○ cooling) and 0·99 SnO_2–0·01 CuO calcined mixture sintered at 850°C for 20 min. (■ heating, □ cooling).

3.3 Evolution of grain surface composition during sintering at 850°C

3.3.1 Copper concentration

Many studies have been performed to determine the location of water and oxygen-derived species on rutile-type crystal surfaces.[7,8] Based on their conclusions, the following assumptions can be proposed in order to relate sorption phenomena to SnO_2 grain surface composition: (i) sorption of water-derived species (H_2O, OH^-, ...) is related to Sn cations[7] whereas Cu cations are not directly involved in this phenomenon,[9] (ii) O_2 molecules are chemisorbed at low temperature (T < 200°C) by oxygen vacancies,[7,9] (iii) on the grain surface, Cu cations are located in Sn position.[8]

The relative weight evolution versus temperature of a calcined SnO_2 powder and of a 0·99 SnO_2–0·01 CuO calcined mixture sintered for 20 min in air at 850°C is presented in Fig. 3. Experiments performed in dry atmosphere have shown that after a first heating up to 800°C, the weight changes observed during further heat treatments are reversible and are not dependent on the difference of oxygen partial pressure existing between dry air and dry oxygen. Therefore, the difference observed in the TGA curves between the heating in ambient air and the cooling in oxygen must be due to water species departure. Results reported in Fig. 4 (curves (3) and (4)) show for a 0·99 SnO_2–0·01 CuO sample that the longer the sintering time at 850°C, the weaker the water loss during the heating up to 850°C.

Assumption (i) relative to the role of Sn cations in water adsorption phenomena leads to association of the observed behaviour to a decrease of the tin cation number per gram of material (n_{Sn}) on the grain surface when CuO is present in the sample. BET measurements revealed that specific surface area was not significantly modified by sintering at 850°C or by thermogravimetric heat treatment; specific surface area variations were always lower than 5%. This effect appears strongly enhanced during sintering at 850°C (curves (3) and (4) in Fig. 4). As the specific surface area remains almost constant, the corresponding decrease of the n_{Sn}/n ratio must be related to the progressive substitution of tin by copper on the surface of the grains.

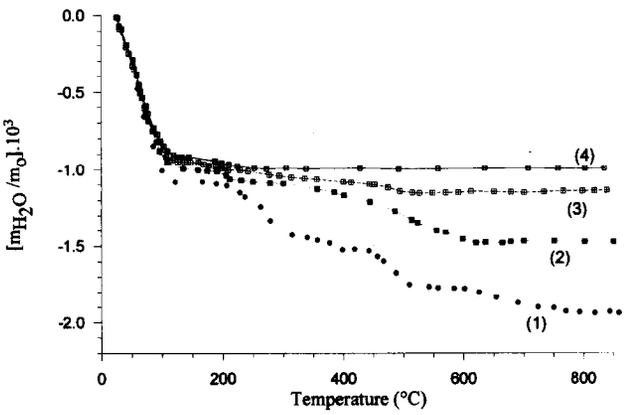

Fig. 4. Relative weight losses due to water loss during heating in air of: (1) calcined SnO_2, (2) calcined 0·99 SnO_2–0·01 CuO, (3) calcined 0·99 SnO_2–0·01 CuO sintered for 20 min at 850°C, (4) calcined 0·99 SnO_2–0·01 CuO sintered for 1 h at 850°C.

According to Jones and Hockey[7] the surface of a rutile-type structure is composed of 60% of (110) planes, 20% of (101) planes and 20% of (100) planes.

Table 2. Relative weight losses (m_{H_2O}/m_O) due to water loss during heating up to 800°C and corresponding numbers of H_2O and Cu per normal cationic position on the grain surface

	SnO_2	0·99 SnO_2–0·01 CuO		
	3 h 400°C	3 h 400°C	3 h 400°C 20 min 850°C	3 h 400°C 1 h 850°C
m_{H_2O}/m_O	$1·9 \times 10^{-3}$	$1·5 \times 10^{-3}$	$1·1 \times 10^{-3}$	$1·0 \times 10^{-3}$
n_{H_2O}/n	1·02	0·79	0·61	0·54
n_{Cu}/n	0	0·23	0·41	0·48

Assuming a similar partition in SnO_2 and taking into account the equivalent area of a tin cation on each type of plane, the value of n calculated from $S_{BET} = 7·3$ m^2 g^{-1} should be $6·2 \times 10^{19}$ atom g^{-1}. The relative water weight loss, m_{H_2O}/m_O, and the relative number of H_2O molecules desorbed per gram of material, n_{H_2O}/n, are reported in Table 2 for each type of sample. The n_{H_2O}/n value is close to 1 for 'pure' SnO_2. This result leads us to assume that, at room temperature, one H_2O species is bound to one Sn cation. In the absence of interaction between Cu and H_2O (assumption (i)) the difference $(1 - n_{H_2O}/n)$ should be representative of the relative amount, n_{Cu}/n, of copper lying in substitutional position on the grain surface. The corresponding values reported in Table 2 agree with a progressive spreading of copper on the surface of the SnO_2-based grains during heat treatment.

3.3.2 Oxygen vacancy concentration

The increase of weight observed during cooling in oxygen from 200°C to 20°C must be related to oxygen adsorption on grain surfaces. The corresponding ratios m_{O_2}/m_O are given in Table 3. When CuO is present in the initial mixture, m_{O_2}/m_O increases with the temperature and the time of the pre-treatment. Assuming that one O_2 molecule is adsorbed by one oxygen vacancy,[7,9] the number of oxygen vacancies per cationic site on the grain surface, n_{V_O}/n, can be determined. The corresponding values reported in Table 3 lead to the consideration that the distribution of copper ions on the surface is associated to the formation of oxygen vacancies. Although copper ions migrate on tin oxide grains during isothermal heat treatment of 0·99 SnO_2–0·01 CuO at 850°C, no weight change is observed (Fig. 5). Therefore, a simple reaction can be proposed to summarise the whole process:

$$CuO \xrightarrow{SnO_2} Cu''_{Sn} + V_O^{\cdot\cdot} + O_O \qquad (2)$$

Since $n_{V_O}/n = 0·18$ for pure SnO_2 grains, some oxygen vacancies already exist without any CuO addition. The difference n_{V_O}/n–0·18 = n_V/n can be considered as characteristic of the relative amount of surface oxygen vacancies due to copper distribution (Table 3). The n_V/n_{Cu} ratios, reported in Table 3, are almost independent of pre-treatment conditions. The value, $n_V/n_{Cu} = 0·65$, seems to be characteristic of the grain surface of 0·99 SnO_2–0·01 CuO material. It differs significantly from the one imposed by reaction (2), i.e., $n_V/n_{Cu} = 1$. In the absence of weight change during heat treatment at 850°C (Fig. 5), this discrepancy indicates that about 35% of the oxygen vacancies formed during distribution of copper on the grain surface are unable to chemisorb oxygen. Two possibilities can be proposed to explain that effect: location of oxygen vacancies inside the grains or formation of clusters on the grain surface involving copper ions and oxygen vacancies. In the latter case, all vacancies would be located on the grain surface and would not contribute to the shrinkage.

3.4 Modelling of the low-temperature sintering

The p exponent characteristic of the shrinkage kinetics at 850 or 900°C is 0·66 ± 0·02. This value does not correspond to any known model involving

Table 3. Relative weight variations due to oxygen adsorption during cooling from 200 to 20°C and surface defects relative concentrations

	SnO_2	0·99 SnO_2–0·01 CuO		
	3 h 400°C	3 h 400°C	3 h 400°C 20 min 850°C	3 h 400°C 1 h 850°C
$(m_{O_2}/m_O)_{200-20°C}$	$0·6 \times 10^{-3}$	$1·1 \times 10^{-3}$	$1·5 \times 10^{-3}$	$1·6 \times 10^{-3}$
n_{V_O}/n	0·18	0·33	0·45	0·49
n_{Cu}/n	0	0·23	0·41	0·48
n_V/n	—	0·15	0·27	0·31
n_V/n_{Cu}	—	0·65	0·66	0·64

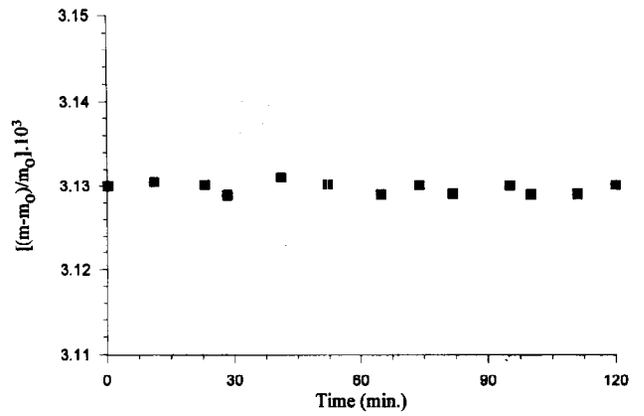

Fig. 5. Relative weight variation during sintering at 850°C in air of a calcined 0·99 SnO_2–0.01 CuO mixture. The sample was heated up to 850°C in 5 min.

solid-state sintering. Furthermore, Frenkel proposed that, under the influence of surface tension, crystalline bodies can display a viscous flow similar to that of amorphous bodies.[10] The possible presence of a large number of vacancies inside the grains would support such a behaviour quite well. As a consequence, shrinkage evolution of our ceramics can be compared with that associated with a viscous flow mechanism. Using Scherer's approach,[11] the sintering rate of a model structure is determined based on the assumption that the energy dissipated in the viscous flow is equal to the energy gained by the decrease in surface area during sintering. That ideal geometry (Fig. 6a) corresponds to a porous microstructure[11,12] constituted of cylinders arranged in a cubic array (length of side: 1). The cylinder radius, α, is expected to represent the average particle radius. This description is in agreement with the microstructure observed in a 0·99 SnO_2–0·01 CuO calcined sample sintered for 16 min at 900°C (Fig. 6b).

Scherer has expressed the theoretical variation of the relative density, ρ/ρ_{th}, as a function of the reduced time, $x_t = K)(t-t_O)$. ρ is the apparent density at t and ρ_{th} is the theoretical density. t_O is the fictitious time at which $\alpha/1 = 0$. The value of K is given by:

$$K = \gamma \,.\, (\rho_{th}/\rho_O)^{1/3} / (\eta \,.\, l_O) \qquad (3)$$

where γ is the specific surface excess of free energy, ρ_O the initial apparent density, η the 'viscosity' and l_O the initial value of l. The plot of ρ/ρ_{th} versus x_t is given in Fig. 7.

Assuming an isotropic shrinkage, ρ/ρ_{th} can be calculated for each value of t using the isothermal dilatometric experiments (ρ_{th} = 6·95 g cm^{-3}). Those experimental data can be fitted to the theoretical curve (Fig. 7) to deduce the reduced time abscissas, x_t. Since K and t_O are not time-dependent for a given sintering temperature, a linear relationship

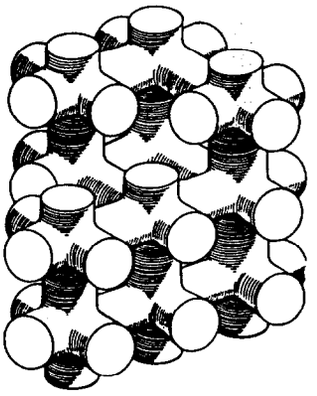

(a)

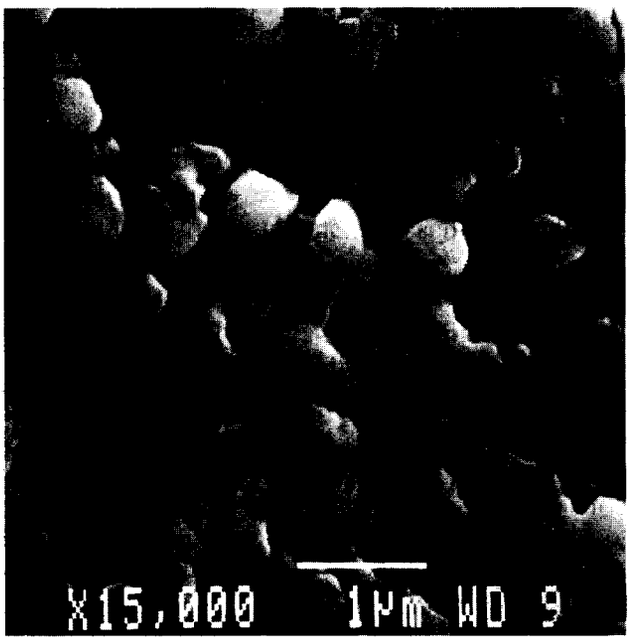

(b)

Fig. 6. (a) Idealized microstructure geometry used in the Scherer's model (from Ref 11). (b) microstructure of a 0·99 SnO_2–0·01 CuO ceramic sintered for 16 min at 900°C.

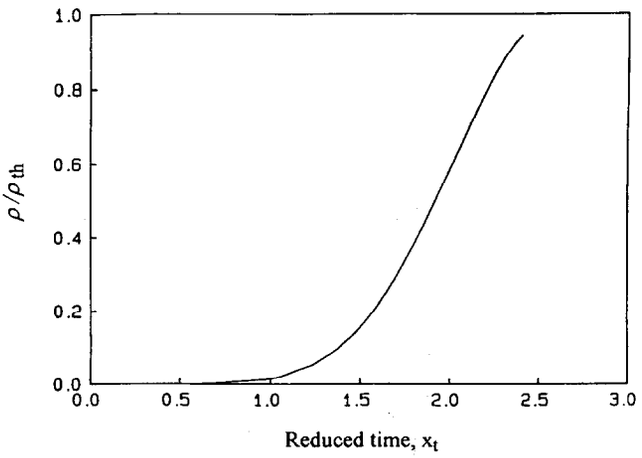

Fig. 7. Theoretical evolution of ρ/ρ_{th} versus reduced time corresponding to a viscous-flow sintering using the microstructure geometry described in Fig. 6(a).

is expected between the reduced and the sintering times if the Scherer's model is applicable. The plot of the experimental sintering times, t, versus x_t is given for T_S = 850, 900 and 940°C in Fig. 8. The straight lines obtained for 850 and 900°C suggest that the shrinkage behaviour of a 0·99 SnO_2–0·01 CuO calcined mixture is similar to the one observed at these temperatures during a viscous-flow sintering. The K values determined from the slopes (K^{-1}) of the straight lines are $1{\cdot}1 \times 10^{-5}$ and $3{\cdot}4 \times 10^{-5}$ s^{-1} at 850 and 900°C, respectively. The evolution of K with T_S is in agreement with the expected variation of the viscosity with the temperature (eqn (3)). The non-linear behaviour observed at T_S = 940°C, the temperature at which the sintering is controlled by a liquid phase,[4] confirms the specific nature of the low-temperature ($T_S \leq 900$°C) shrinkage mechanism for 0·99 SnO_2–0·01 CuO powders.

In fact, it is not necessary for the whole material to be viscous to observe a viscous-flow type shrinkage. It has been shown recently that a packing of hard particles coated by a 'soft' phase can sinter at a rate comparable to that of particles without a rigid core, i.e. following a viscous-flow mechanism, provided the thickness of the viscous layer is sufficient.[13,14] In the case of spherical particles, Jagota[13] showed that a normalised coating thickness t/R = 0·2 (R is the radius of the hard core of the grain) is sufficient to reach full density at almost the same rate as the viscous material. Moreover, when the relative density of the material remains low, its sintering kinetics is the same as that of the coating for a value of t/R as low as 0·1. Considering that the relative density of the 0·99 SnO_2–0·01 CuO ceramics described in this paper was lower than 56%, a thick disordered layer near the surface of the grains, possibly due to the formation of oxygen vacancies inside the grain during the copper distribution, could play the role of that viscous layer. Its thickness was estimated, applying Jagota's approach to our shrinkage and using the size of the grains deduced from specific area measurements (r = 0·06 μm). A value of the order of a nanometre, which seems rather likely.

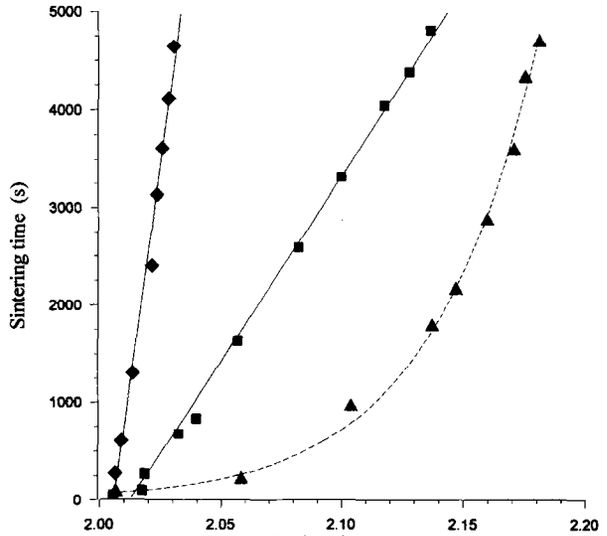

Fig. 8. Evolution of the sintering time of 0·99 SnO_2–0·01 CuO calcined samples versus reduced time obtained from Fig. 7. Sintering temperatures were: ◆ 850°C, ■ 900°C and ▲ 940°C.

4 Conclusion

A small addition (1 molar %) of copper oxide results in a large change in the shrinkage behaviour at low sintering temperature, 800 or 850°C, compared to 'pure' SnO_2. In this range of temperature, occurrence of a liquid phase appears doubtful. Study of the influence of temperature on the weight evolution of various 0·99 SnO_2–0·01 CuO heat-treated powders has allowed us to follow the distribution of copper ions and free oxygen vacancies on the grain surface. First, distribution of copper ions occurs through surface diffusion at temperatures as low as 400°C. Second, at higher temperatures (850–900°C) a part of oxygen vacancies are not able to chemisorb O_2 molecules. Simultaneously, densification is observed and its kinetics can be fitted by the model proposed by Scherer to describe viscous-flow sintering. The possible location of oxygen vacancies which are not free on the surface of the grains, within a thick layer, could then be related to that unusual shrinkage behaviour. That layer (≈ nm) would play the role of a viscous coating of the SnO_2 grains.

References

1. Kimura, T., Inada, S. & Yamaguchi, T., Microstructure development in SnO_2 with and without additives. *J. Mater. Sci.*, **24** (1989) 220–6.
2. Torvela, D. L. & Leppavuori, S., Microstructure and conductivity of short duration sintered tin oxide ceramics. *Int. J. High Tech. Cer.*, **3** (1987) 309–19.
3. Dolet, N., Heintz, J. M., Onillon, M. & Bonnet, J. P., Densification of 0·99 SnO_2–0·01 CuO mixture: evidence for liquid phase sintering. *J. Eur. Ceram. Soc.*, **9** (1992) 19–25.
4. Dolet, N., Heintz, J. M., Rabardel, L., Onillon, M. & Bonnet, J. P., Sintering mechanisms of 0·99 SnO_2–0.01 CuO mixtures. *J. Mater. Sci.*, **30** (1995) 365–8.
5. Mukode, S. & Futata, H., A semiconductive humidity sensor. *Sensor and Actuators*, **16** (1989) 1–11.
6. McAleer, J. F., Maigna, A., Moseley P. T. & Williams, D. E., Tin dioxide gas sensor. *J. Chem. Soc. Faraday Trans.*, **85** (1989) 783–99.
7. Jones, P. & Hockey, J. A., Infra-red studies of rutile surfaces. *Trans. Faraday Soc.*, **67** (1971) 2679–85.
8. Varela, J. A., Whittemore, O. J. & Ball, M. J., Sintering evolution during the sintering of SnO_2 and SnO_2-2% mole CuO. In *Sintering 85*, ed. G. C. Kuczynski *et al.* Plenum Press, Washington, 1987, pp. 256–69.

9. Dolet, N., Etudes des paramètres régissant le frittage et les propriétés électriques des céramiques denses à base de SnO_2. Thesis no. 742, University Bordeaux I, 1992.
10. Frenkel, J., Viscous flow on crystalline bodies under the action of surface tension. *J. Phys.*, **9** (1945) 385–91.
11. Scherer, G. W., Sintering of low density glasses: I, theory. *J. Am. Ceram. Soc.*, **60** (1977) 236–9.
12. Scherer, G. W., Cell models for viscous sintering. *J. Am. Ceram. Soc.*, **74** (1991) 1523–31.
13. Jagota, A., Simulation of the viscous sintering of coated particles. *J. Am. Ceram. Soc.*, **77** (1994) 2237–9.
14. Boccaccini, A. R., Sintering of glass matrix composites containing Al_2O_3 platelets inclusions. *J. Mater. Sci.*, **29** (1994) 4273–8.

Journal of the European Ceramic Society **16** (1996) 1171–1178

PII:S0955-2219(96)00048-9
0955-2219/96/$15.00

Sinterability of Spinel ($MgAl_2O_4$)-Zirconia Composite Powder Prepared by Double Nozzle Ultrasonic Spray Pyrolysis

Takayuki Suzuki, Kiyoshi Itatani,* Mamoru Aizawa, F. Scott Howell & Akira Kishioka

Department of Chemistry, Faculty of Science and Engineering, Sophia University, 7-1 Kioi-cho Chiyoda-ku, Tokyo 102, Japan

(Received 8 November 1995: revised version received 4 February 1996; accepted 20 February 1996)

Abstract

Two kinds of spinel ($MgAl_2O_4$)-zirconia (ZrO_2) composite powders were prepared by double nozzle ultrasonic spray pyrolysis; the aqueous solutions in the $Mg(NO_3)_2$-$Al(NO_3)_3$ and $ZrOCl_2$-YCl_3 systems were spray-pyrolysed in a hot zone of an electric furnace heated at 900°C, using two ultrasonic vibrators. The compositions of the composite powders were as follows: (1) Sample No. 1: $MgAl_2O_4$ 93·36 mol% and yttria-stabilized tetragonal ZrO_2 polycrystals (Y-TZP) 6·64 mol% and (2) Sample No. 2: $MgAl_2O_4$ 75·51 mol% and Y-TZP 24·49 mol%. While $MgAl_2O_4$ and Y-TZP were present in both powders, MgO was additionally detected from Sample No. 2; such MgO disappeared when it was heated up to 1100°C or higher. The composite powders contained spherical particles with diameters of below 2 μm and, in part, acicular particles with long axis lengths of 1 to 2 μm. The wet-milled powder of Sample No. 1 showed an excellent sinterability; when the composite powder compact was fired at 1700°C for 10 h, the relative density attained 97·6%. Copyright © 1996 Elsevier Science Ltd

1 Introduction

Since spinel ($MgAl_2O_4$) ceramic has a high melting point (2105°C) and excellent resistance to acid and alkali, a large amount of $MgAl_2O_4$ ceramics is now used as a refractory for furnace walls and firebricks.[1–3] Attention has also been directed toward the application of $MgAl_2O_4$ ceramics to humidity sensors.[4–6] Except for these practical and potential uses, the application of $MgAl_2O_4$ to other fields has been restricted, chiefly due to the insufficient mechanical strength at room and high temperatures.[7] In order to improve the mechanical strength of $MgAl_2O_4$ ceramics, many researchers investigated the fabrication of (i) dense ceramics and/or (ii) composites with other materials.[8] Dense $MgAl_2O_4$ ceramics may be fabricated using powders with primary particle sizes of ≤ 200 nm prepared by various advanced techniques: coprecipitation,[9] vapour-phase oxidation,[10] spray pyrolysis,[11] freeze drying[12] and sol-gel techniques.[13] The composites of $MgAl_2O_4$ with ZrO_2 are expected to enhance the mechanical strength, because Fujita *et al.*[8] demonstrated that the maximum fracture toughness (K_{IC}) is 6·3 MPa $m^{1/2}$ and the bending strength of ZrO_2-dispersed MgO-Al_2O_3 ceramics attains 400 MPa. Nevertheless, no information on ZrO_2-dispersed stoichiometric $MgAl_2O_4$ ceramics has been available.

The authors prepared various calcium phosphate powders by spray pyrolysis;[14–16] this technique has the advantages of preparing the powders with (i) submicrometer-sized primary particles, (ii) narrow particle size distribution and (iii) homogeneous composition.[17] Nevertheless, conventional spray pyrolysis is not always suitable for the preparation of composite powders containing two or more compounds, partly because it is difficult to prepare a solution containing such multicomponent ions without precipitation, and partly because the difference in solubility among metal salts in the starting solution often causes compositional inhomogeneity in the spray-pyrolysed powder.[17] In order to prepare ZrO_2-dispersed stoichiometric $MgAl_2O_4$ without a mixing operation, we assembled a novel spray pyrolysis apparatus using two ultrasonic vibrators. By using this apparatus, we examined (i) the preparation conditions of ZrO_2-dispersed stoichiometric $MgAl_2O_4$ powders and (ii) the sinterabilities of the resulting composite powders.

*To whom correspondence should be addressed.

2 Experimental Procedure

2.1 Preparation of composite powders

Figure 1 shows the schematic diagram of the reaction apparatus. This apparatus was composed of (I) a spraying zone, (II) a heating zone and (III) a powder collecting zone. Each zone will be explained below.

(I) Spraying zone

The preparation conditions of the starting solutions are shown in Table 1. The starting solutions for $MgAl_2O_4$ and Y-TZP were prepared as follows: (i) the desired concentrations of $Mg(NO_3)_2 \cdot 6H_2O$ and $Al(NO_3)_3 \cdot 9H_2O$ were dissolved in deionized water to form the solutions for preparing $MgAl_2O_4$; (ii) the desired concentrations of $ZrOCl_2 \cdot 8H_2O$ and $YCl_3 \cdot 6H_2O$ with Y/(Zr+Y) = 0·03 were dissolved in deionized water to form the solutions for preparing Y-TZP. The droplets were formed using ultrasonic vibrators (a).

(II) Heating zone

The droplets were introduced into the mullite tube (e), heated by an electric furnace (d) using a carrier gas: Ar gas (b) for preparing $MgAl_2O_4$ and O_2 gas (c) for preparing ZrO_2. The spray pyrolysis was carried out at 900°C. The temperature was recorded using thermocouples (f).

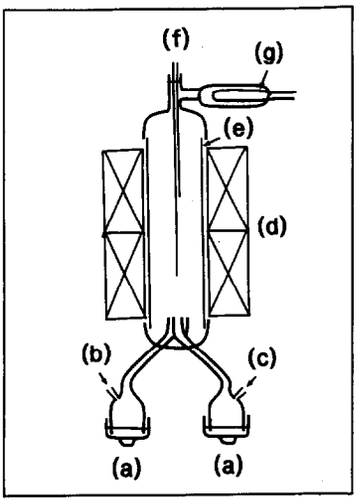

Fig. 1. Schematic diagram of the reaction apparatus. (a) Ultrasonic vibrator, (b) Ar carrier gas, (c) O_2 carrier gas, (d) Electric furnaces (length: 600 mm), (e) Mullite tube (diameter: 60 mm), (f) Thermocouple (Pt-Pt· 13% Rh), (g) Test-tube type filter.

(III) Powder collecting zone

The resulting powder was collected by a test-tube type filter (g); the gas formed by the spray pyrolysis was inhaled by an aspirator.

2.2 Calculation of the mean diameter of droplets

The mean diameter of the droplets ($\bar{d}$) was determined by the following equation:[18]

$$\bar{d} = 0{\cdot}34\left(\frac{8\pi\sigma}{\rho f^2}\right)^{\frac{1}{3}} \quad (1)$$

where σ is the surface tension of the solution, ρ is the density of the solution, and f is the frequency (= 2·4 MHz) of the ultrasonic vibrator.

2.3 Sintering of composite powders

A part of the resulting powder was wet-milled using a zirconia mortar and pestle in the presence of acetone. The as-prepared and wet-milled powders were uniaxially pressed at 120 MPa in steel dies to form cylindrical compacts with diameters of 10 mm and thickness of ~2 mm; then the compacts were cold-isostatically pressed at 150 MPa. The compacts were heated in an electric furnace (heating elements: $MoSi_2$) at a temperature between 1400°C and 1700°C for 10 h in air. The heating rate from room temperature up to the desired temperatures was 10°C min^{-1}. The bulk densities of the green and sintered compacts were calculated on the basis of the weights and dimensions. The relative density was calculated by dividing the bulk density by the true density measured picnometrically.

2.4 Evaluations of resulting powders and sintered compacts

The crystalline phases of the resulting powders and sintered compacts were examined using an X-ray diffractometer (XRD; 40 kV, 25 mA; Model RAD-IIA, Rigaku, Tokyo) with Ni-filtered CuKα radiation and a Fourier-transform infrared spectrophotometer (FT- IR; Model 8600PC, Shimadzu, Kyoto). The quantitative analyses of the powders were conducted using an X-ray fluorescence apparatus (XRF; Model SXF1200, Shimadzu, Kyoto).

The specific surface areas of the powders were measured by a Brunauer-Emmett-Teller (BET) technique, using nitrogen (N_2) as an adsorption gas. The true densities of the powders were mea-

Table 1 Preparation conditions of starting solutions

Sample No.	Spray I			Spray II		
	$Mg(NO_3)_2$ mol dm^{-3}	$Al(NO_3)_3$ mol dm^{-3}	Ar flow rate dm^3 min^{-1}	$ZrOCl_2$ mol dm^{-3}	YCl_3 mol dm^{-3}	O_2 flow rate dm^3 min^{-1}
1	$2{\cdot}0 \times 10^{-1}$	$4{\cdot}0 \times 10^{-1}$	820	$9{\cdot}7 \times 10^{-2}$	$3{\cdot}0 \times 10^{-3}$	400
2	$2{\cdot}0 \times 10^{-1}$	$4{\cdot}0 \times 10^{-1}$	820	$9{\cdot}7 \times 10^{-2}$	$3{\cdot}0 \times 10^{-3}$	800

sured picnometrically at 25°C. The agglomerate strengths were examined from the data on the relationship between relative densities of the compacts and compressed pressures.

The particle shapes of the powders were observed using a transmission electron microscope (TEM; Model H-9000, Hitachi, Tokyo), while the microstructures of the sintered compacts were observed using a scanning electron microscope (SEM; Model S-430, Hitachi, Tokyo). The dispersion states of elements in the sintered compacts were examined using an energy-dispersive X-ray analyser (EDX; Model EMAX-1500, Horiba, Kyoto). The crystal system of ZrO_2 in the sintered compacts was examined using a Raman spectroscope (Ar laser tuned to 514·5 nm).

3 Results and Discussion

3.1 Preparation of $MgAl_2O_4$-ZrO_2 composite powders

3.1.1 Crystalline phases of the resulting powders

Figure 2 shows the XRD patterns of the resulting powders. While $MgAl_2O_4$[19] and t-ZrO_2 (yttria-stabilized ZrO_2 polycrystals: Y-TZP)[20] were present in both powders, MgO[21] was additionally detected from Sample No. 2. The X-ray intensities of Y-TZP in Sample No. 2 were higher than those in Sample No. 1.

The compositions of the powders heat-treated at 1400°C were examined using XRF. The composition of Sample No. 1 was: $MgAl_2O_4$, 93·36 mol% and Y-TZP, 6·64 mol%, whereas that of Sample No. 2 was: $MgAl_2O_4$, 75·51 mol% and Y-TZP, 24·49 mol%. Hereafter, Samples No. 1 and 2 are designated as MZ(6·64) and MZ(24·49), respectively. The numbers in parentheses indicate the Y-TZP content.

As shown above, the Y-TZP content in MZ(24·49) powder is higher than that in MZ(6·64) powder, when the flow rate of O_2 gas for preparing Y-TZP is enhanced from 150 to 800 cm^3 min^{-1}. It should be noted that the Y-TZP content is controlled by changing the flow rate of O_2 gas. Regardless of the $MgAl_2O_4$ contents being higher than Y-TZP contents in MZ(6·64) and MZ(24·49) powders, however, X-ray intensities of $MgAl_2O_4$ are lower than those of Y-TZP. Since MgO was detected from MZ(24·49), this phenomenon is explained by assuming that the crystal growth of $MgAl_2O_4$ is inhibited by the sluggish reaction between MgO and Al_2O_3.

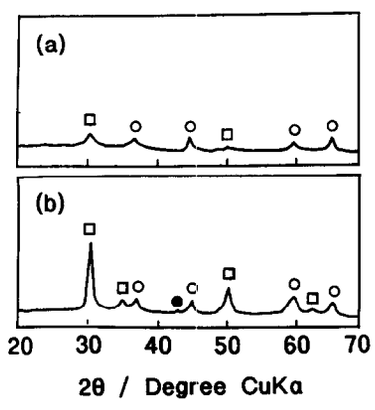

Fig. 2. XRD patterns of the resulting powders. (a) Sample No. 1, (b) Sample No. 2; ○: $MgAl_2O_4$, □: t-ZrO_2, ●: MgO.

The residence time of the droplets in the present furnace is estimated to be only ~40 s; thus it is probable that the spray-pyrolysed powders contain unreacted materials and adsorbed water. FT-IR analysis was conducted to elucidate whether these materials were included in the powders or not. Results are shown in Fig. 3. In MZ(6·64) and MZ(24·49) powders, the broad absorption bands appeared in the range of 2700 to 3650 cm^{-1}, whereas the absorption peaks appeared in the range of 1300 to 1700 cm^{-1}. The absorption peaks in the range of 1300 to 1700 cm^{-1} may be assigned to the NO_3^- and the band in the range of 2700 to 3650 cm^{-1} to the H_2O stretching vibration.[22]

The powder appears to be formed via the following spray-pyrolysis routes: (i) the evaporation of solvent (water), (ii) the pyrolysis of the precipitated metal salts, and (iii) the solid-state reactions of the metal salts/metal oxide. Since four kinds of starting materials are employed in the present experiment, the spray pyrolysis process seems to be quite complex; but it probably includes the pyrolysis of each starting material.

$$Mg(NO_3)_2{\cdot}6H_2O \xrightarrow{95°C} \text{melt} \xrightarrow{250°C}$$
$$2MgO{\cdot}Mg(NO_3)_2{\cdot}5H_2O \xrightarrow{430°C} MgO \quad (2)[23]$$

$$Al(NO_3)_3{\cdot}9H_2O \xrightarrow{73°C} \text{melt} \xrightarrow{140°C}$$
$$4Al_2O_3{\cdot}3N_2O_5{\cdot}14H_2O \xrightarrow{200°C} Al_2O_3 \quad (3)[24]$$

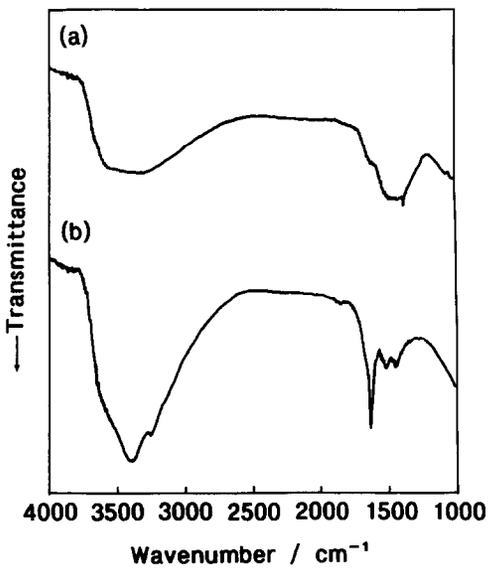

Fig. 3. FT-IR spectra of the resulting powders. (a) MZ(6.64) powder and (b) MZ(24.49) powder.

The reaction of MgO with Al_2O_3 may participate in the formation of $MgAl_2O_4$, because MgO was detected from MZ(24.49) powder.

$$MgO + Al_2O_3 \rightarrow MgAl_2O_4 \quad (4)$$

The FT-IR results indicate that NO_3^- and H_2O are present in MZ(6·64) and MZ(24·49) powders; these materials which are released by the pyrolysis of magnesium and aluminium salts are adsorbed on the resulting powders.

On the other hand, the thermal decompositions of zirconium and yttrium salts ($ZrOCl_2 \cdot 8H_2O$ and $YCl_3 \cdot 6H_2O$) may occur via the following routes:

$$ZrOCl_2 \cdot 8H_2O \xrightarrow{150°C} ZrOCl_2 \cdot 2H_2O \xrightarrow{210°C} ZrOCl_2 \xrightarrow{410°C} ZrO_2 \quad (5)[25]$$

$$YCl_3 \cdot 6H_2O \xrightarrow{\sim 240°C} YCl_3 \xrightarrow{715°C} YOCl \xrightarrow{1000°C} Y_2O_3 \quad (6)[26]$$

The resulting Y_2O_3 must be solid-dissolved into ZrO_2, because Y-TZP was detected by XRD.

3.1.2 Powder properties

Figure 4 shows the TEM micrographs and particle size distributions of the resulting powders. The solid spherical particles, hollow spherical particles, fragments of spherical particles and needle-like particles were present in MZ(6.64) powder (Fig. 4(a)). Most of the diameters of the spherical particles ranged from 0·1 to 1·4 μm (Fig. 4(a')). Although the long-axis lengths of the acicular particles are not plotted in the figure, they ranged from 1 to 2 μm. The particle shapes of MZ(24·49) powder (Fig. 4(b)) were similar to those of MZ(6·64) powder; however, the particle-size distribution width of MZ(24·49) powder (Fig. 4 (b')) was wider than that of MZ(6·64) powder.

Although the mean diameters of the droplets for preparing $MgAl_2O_4$ and Y-TZP are found from calculation to be 2·3 μm, the actual mean particle diameters are 0·47 and 0·60 μm, respectively; moreover, some spherical particles had diameters as large as ~1·5 μm. The spherical particles with diameters of ~0·5 μm are completely filled or 'solid'; however, the particles with diameters of ~1·5 μm appear to be 'hollow', because the insides of these large particles are translucent (see Fig. 4(b)). Such large particles may form when the coalesced droplets are spray-pyrolysed; the fragments are formed by the explosion of some spherical droplets/particles during the spray pyrolysis. It is noted that needle-like particles are present in the powder, although their formation route is unclear.

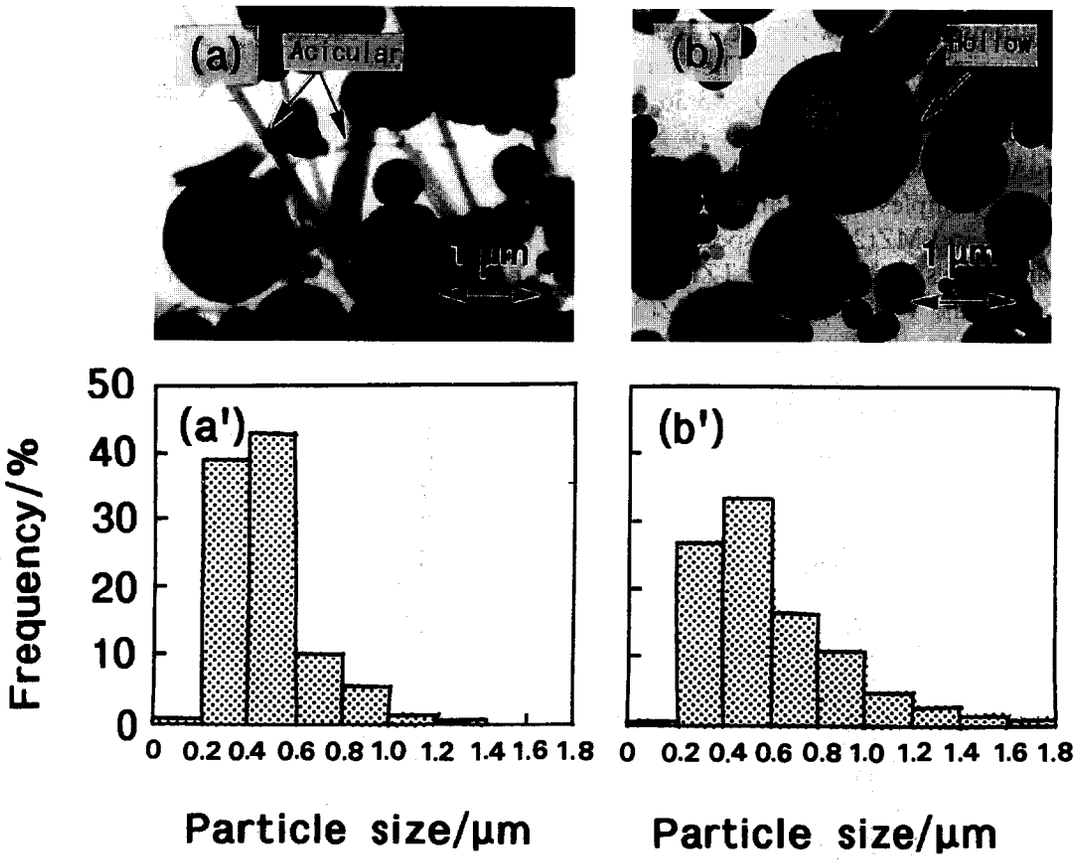

Fig. 4. TEM micrographs and secondary particle size distributions of the resulting powders. (a), (a'): TEM micrograph and secondary particle size distribution of MZ(6·64) powder; (b), (b'): TEM micrograph and secondary particle size distribution of MZ(24·49) powder.

The true densities of MZ(6·64) and MZ(24·49) powders were 3·68 and 4·36 g cm^{-3}, respectively. The density of MZ(24·49) powder is higher than that of MZ(6·64), reflecting the fact that the Y-TZP content is higher in the former than the latter. These densities are almost in accord with the theoretical densities calculated from their compositions.

The specific surface areas of MZ(6·64) and MZ(24·49) powders were 26·9 $m^2 g^{-1}$ and 14·9 $m^2 g^{-1}$, respectively. Since the Y-TZP content in MZ(24·49) powder is higher than that in MZ(6·64), the specific surface area appears to be reduced with Y-TZP content. This phenomenon is ascribed to more appreciable crystal growth of ZrO_2 than that of $MgAl_2O_4$ (see Fig. 2).

The sintering may be restricted when 'hard' agglomerates are present in the powder.[27] Thus the agglomerate strengths of the resulting powders were examined by plotting the relative densities against the compaction pressures. Results are shown in Fig. 5. The plots of the relative densities of MZ(6·64) powder compact against compaction pressures were expressed as two straight lines with the inflection point at ~90 MPa. The inflection point in the case of the wet-milled powder appeared at ~60 MPa; moreover, the relative densities of the wet-milled powder compacts were higher than those of the as-prepared powder compacts. The plots of the relative densities of MZ(24·49) powder compact against the compaction pressures were also expressed as two straight lines with one inflection point at ~110 MPa. The inflection point of the wet-milled powder compacts appeared at ~50 MPa; the relative densities of these compacts were higher than those without the milling operation.

The inflection point indicates the pressure at which the 'hard' agglomerates start to fracture; the fragments are rearranged into closer packing with higher compaction pressure.[28] When the relative densities of spray-pyrolysed ZrO_2 powder compacts were plotted against compaction pressures, one inflection point appeared at ~80 MPa. Similar results have been obtained by Haberko.[29] The pressures (~90 MPa) of the inflection points in the case of as-prepared powder compacts are almost in accord with those (~80 MPa) in the case of pure ZrO_2 powders, which suggests that most of the 'hard' agglomerates can be regarded as Y-TZP. These 'hard' agglomerates may be easily fractured into several pieces, because the inflection points in the case of wet-milled powder compacts appear at lower pressure than those in the case of as-prepared powder compacts.

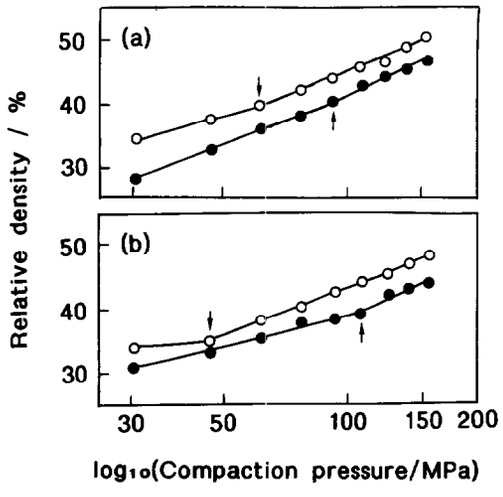

Fig. 5. Relationship between relative density of the compact and compaction pressure. (a) MZ(6·64), (b) MZ(24·49); ●: as-prepared powder compact, ○: wet-milled powder compact. Arrow marks indicate the inflection points.

3.1.3 Phase changes during heating of the resulting powders

The MZ(24·49) powder contains MgO, together with $MgAl_2O_4$ and Y-TZP. Thus it is important to determine whether or not MgO disappears during the heating of the resulting powder. First, DTA-TG measurements of the resulting powders were performed from room temperature up to 1400°C. Results are shown in Fig. 6. The DTA curve of MZ(6·64) (Fig. 6(a)) showed that the endothermic and exothermic effects started to appear at ~310°C and above 1270°C, respectively. Corresponding to these effects, the weight losses occurred stepwise in the ranges of 100–200°C, 200–400°C, 400–750°C and over 750°C. The DTA curve of MZ(24·49) (Fig.6 (b)) showed that the endothermic effects appeared at 66°C, 105°C, 160°C and 380°C. The weight losses occurred stepwise in the ranges of 50–150°C, 150–450°C and over 450°C.

The phase changes during heating of MZ(6·64) and MZ(24·49) powders were checked by X-ray

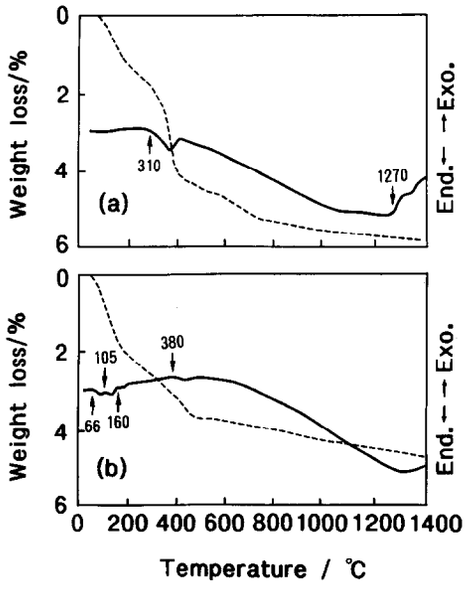

Fig. 6. DTA-TG curves of (a) MZ(6·64) powder and (b) MZ(24·49) powder. Heating rate: 10°C min^{-1}.

diffractometry. Results are shown in Fig. 7. In the case of MZ(6·64) powder, MgO was present in the temperature range of 300°C to 1100°C; the crystallinity of $MgAl_2O_4$ was enhanced above 1100°C. In the case of MZ(24·49) powder, the crystallinity of $MgAl_2O_4$ increased but that of ZrO_2 decreased slightly with temperature above 1000°C; MgO was present in the temperature range of 400°C to 1000°C.

The stepwise weight losses below 200°C indicate the releases of chemically and physically adsorbed water and of NO_3^- ions. On the other hand, the endothermic effects which start at 310°C in the case of MZ(6·64) powder and at 380°C in the case of MZ(24·49) powder are attributed to the formation of MgO. The crystallinity of $MgAl_2O_4$ increases with decreasing crystallinity of MgO at and above 1000~1100°C, which indicates that MgO reacts with Al_2O_3 to form $MgAl_2O_4$.

3.2 Sintering of $MgAl_2O_4$–Y-TZP powders

3.2.1 Effect of milling operation on sintering of the composite powders

Since the 'hard' agglomerates are included chiefly in the Y-TZP powder, the effects of milling operation on sintering of the powders are discussed in this section. Figure 8 shows the changes in relative density of the sintered compact with firing temperature from 1400°C to 1700°C. The relative density of MZ(6·64) compact was enhanced by the wet-milling operation; the maximum relative density attained 97.6% at 1700°C. Although the results for MZ(24·49) compact were similar to those for MZ(6·64) compact, the former relative densities were lower than the latter ones; moreover, the relative density of MZ(24·49) compact was reduced above 1600°C.

The above results reveal that the wet-milling operation is effective for enhancing the relative densities of the sintered compacts. This phenomenon may be ascribed to the decrease in the number of 'hard' agglomerates,[27] due to the milling operation (see Fig. 5). The effect of the milling operation on sintering of MZ(6·64) powder appears more appreciable than on that of MZ(24·49) powder, because the agglomerate strengths of MZ(6·64) powder seem to be lower than those of MZ(24·49) powder. Since the collapse of the hard agglomerates becomes difficult with Y-TZP content, the remaining 'hard' agglomerates in MZ(24·49) powder make their homogeneous packing difficult, thus retarding the densification. Moreover, the mass transfer of $MgAl_2O_4$ may be inhibited by Y-TZP. Details will be explained in the next section.

3.2.2 Microstructural evaluation of sintered compacts

Since the dense composite compact with the relative density of 97·6% could be fabricated at the firing temperature of 1700°C, the microstructure of this sintered MZ(6·64) compact was examined using SEM, XRD and Raman spectroscopy. Results are shown in Fig. 9. The SEM micrograph (Fig. 9(a)) showed that the large polyhedral grains with sizes of ~20 μm were packed closely: the small spherical grains with diameters of ~3 μm were present not only on grain boundaries but also inside the large grains. The XRD pattern (Fig. 9(b)) revealed that $MgAl_2O_4$ and t-ZrO_2 were detected from the sintered body. The Raman spectrum (Fig. 9(c)) showed that the crystal system of the ZrO_2 was assigned to be tetragonal.[30] These results indicate that ZrO_2 is stabilized by Y_2O_3 and that no reaction is observed between $MgAl_2O_4$ and Y-TZP.

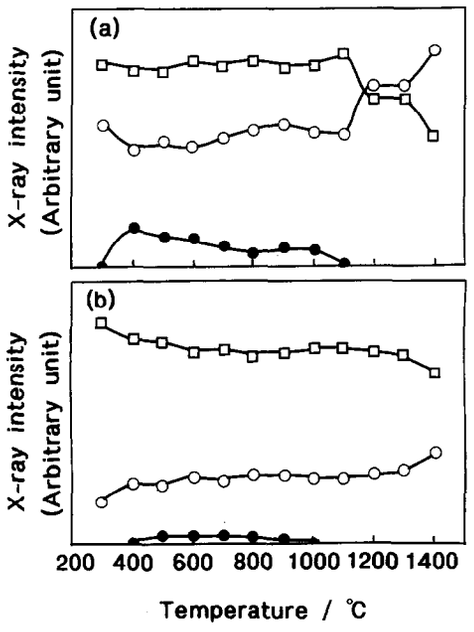

Fig. 7. Phase changes during the heating of (a) MZ(6·64) and (b) MZ(24·49); ○: $MgAl_2O_4$; (2θ = 36·8°), □: t-ZrO_2; (2θ = 29·8°), ●: MgO; (2θ = 42·9°).

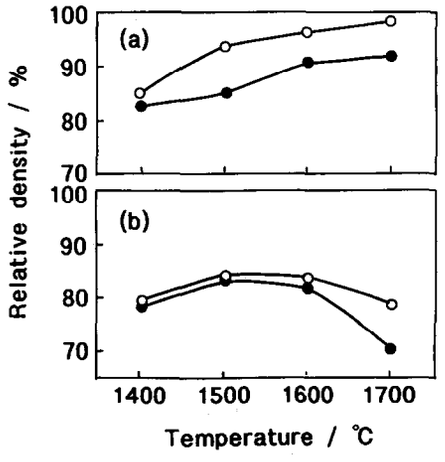

Fig. 8. Changes in the relative density of (a) MZ(6·64) compact and (b) MZ(24·49) compact with firing temperature. ●-●: as prepared powder compact, ○-○: wet-milled powder compact.

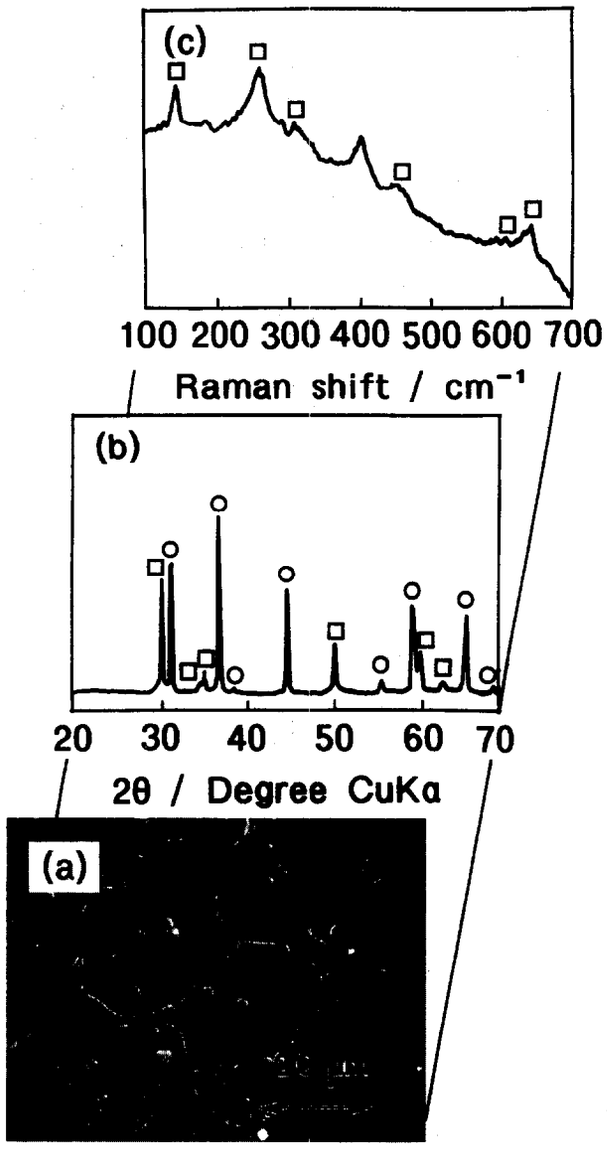

Fig. 9. (a) SEM micrograph, (b) XRD pattern and (c) Raman spectrum of the MZ(6.64) compact fired at 1700°C for 10 h. ○: $MgAl_2O_4$, □: t-ZrO_2, ●: MgO.

To check the crystalline phases of the large and small grains in the sintered body, EDX analysis was performed. Results are shown in Fig. 10. The elements Mg and Al were detected in the large polyhedral grains, whereas Zr and Y were detected in the small spherical grains. Thus the large polyhedral grains and small spherical grains correspond to $MgAl_2O_4$ and Y-TZP, respectively.

As shown above, Y-TZP grains are present not only on boundaries but also inside the $MgAl_2O_4$ grains. Since the mass transfer of $MgAl_2O_4$ is retarded by these Y-TZP grains present on grain boundaries, it cannot be promoted until Y-TZP grains are entrapped in the $MgAl_2O_4$ grains.

It is concluded from the present results that the double-nozzle ultrasonic spray pyrolysis technique is useful for preparing the composite powder without a mixing operation. By this technique, we can now examine the conditions for preparing many kinds of composite powders.

4 Conclusions

Spinel ($MgAl_2O_4$)-zirconia (ZrO_2) composite powders were prepared by the double nozzle ultrasonic spray pyrolysis technique. The results obtained are summarized as follows:

(1) The compositions of the composite powders were as follows: (1) Sample No. 1: $MgAl_2O_4$ 93·36 mol% and yttria-stabilized ZrO_2 polycrystals 6·64 mol% and (2) Sample No. 2: $MgAl_2O_4$ 75·51 mol% and Y-TZP 24·49 mol%. The powder compositions could be controlled by changing the flow rate of the carrier gas.

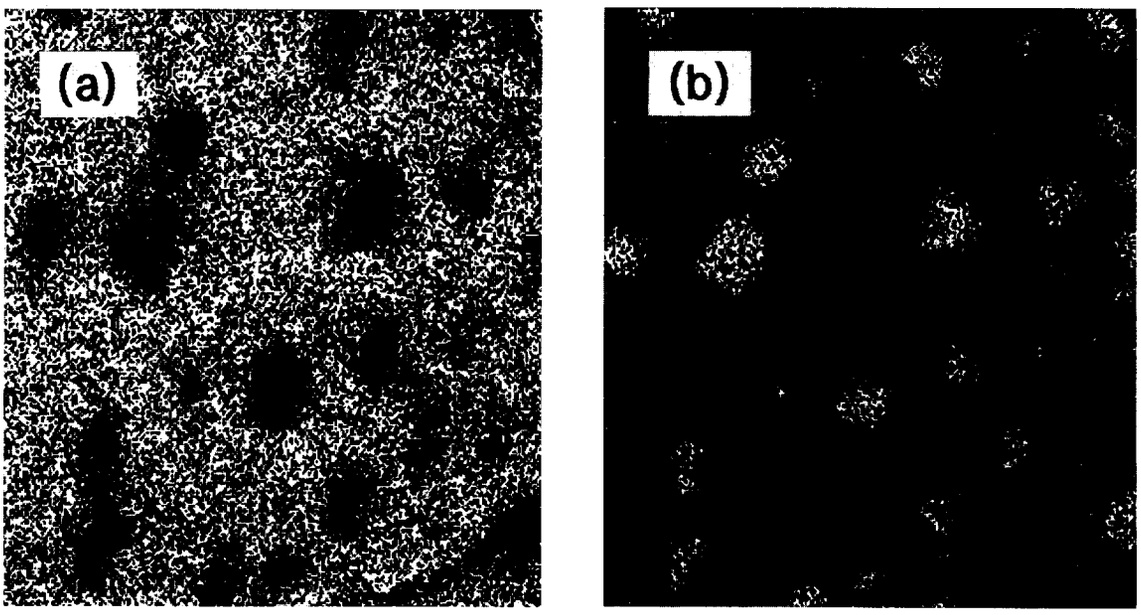

Fig. 10. EDX analysis of MZ(6.64) compact fired at 1700°C for 10 h. (a) MgKα and AlKα spectra, (b) ZrLα and YLα spectra.

(2) While $MgAl_2O_4$ and Y-TZP were present in both powders, MgO was additionally detected from Sample No. 2; such MgO disappeared when the powders were heated at and above 1100°C. The powders contained spherical particles with diameters of 2 μm.
(3) The wet-milled composite powder of Sample No. 1 showed excellent sinterability. When this powder compact was fired at 1700°C for 10 h, the relative density of the sintered compact attained 97·6%. The microstructural observation revealed that ZrO_2 grains were present not only on boundaries but also inside the $MgAl_2O_4$ grains.

Acknowledgements

The authors wish to express their thanks to Professor Dr T. Sekine and Ms T. Tanokura of Sophia University for Raman spectroscopic measurements and to Professor Dr Y. Toda and Dr Ka. Hashimoto of Chiba Institute of Technology for taking the TEM micrographs.

References

1. Alper, A. M., McNally, R. N., Ribbe, P. H. & Doman, R. C., The system MgO-$MgAl_2O_4$. *J. Am. Ceram. Soc.*, **45** (1962) 263–8.
2. Cooper, S. C. & Hodson, P. T. A., Magnesia-magnesium aluminate spinel as a refractory. *Br. Ceram. Trans. J.*, **81** (1982) 121–8.
3. Maschio, R. D., Fabbri, B. & Fiori, C., Industrial applications of refractories containing magnesium aluminate spinel. *Ind. Ceram.*, **8** (1988) 121–6.
4. Seiyama, T., Yamazoe, N. & Arai, H., Ceramic humidity sensors. *Sensors and Actuators*, **4** (1983) 85–96.
5. Shimizu, Y., Arai, H. & Seiyama, T., Theoretical studies on the impedance-humidity characteristics of ceramic humidity sensors. *Sensors and Actuators*, **7** (1985) 11–22.
6. Gusmano, G., Montesperelli, G., Traversa, E. & Mattogno, G., Microstructure and electrical properties of $MgAl_2O_4$ thin films for humidity sensing. *J. Am. Ceram. Soc.*, **76** (1993) 743–50.
7. Baudin, C., Martinez, R. & Pena, P., High-temperature mechanical behavior of stoichiometric magnesium spinel. *J. Am. Ceram. Soc.*, **78** (1995) 1857–62.
8. Fujita, M., Yoshimatsu, H., Osaka, A. & Miura, Y., Preparation and properties of ZrO_2-dispersed MgO-Al_2O_3 ceramic. *J. Ceram. Soc. Jpn*, **103** (1995) 81–4.
9. Bratton, R. L., Characterization and sintering of reactive $MgAl_2O_4$ spinel. *Am. Ceram. Soc. Bull.*, **48** (1969) 759–62.
10. Itatani, K., Sakai, H., Howell, F. S., Kishioka, A. & Kinoshita, M., Sinterability of spinel ($MgAl_2O_4$) powder prepared by vapour-phase oxidation technique. *Br. Ceram. Trans. J.*, **88** (1989) 13–16.
11. Kanzaki, S., Nishida, T., Otsuka, N., Saito, K., Nakagawa, Z. & Hamano, K., Sintering of spray pyrolysed Mg-Al spinel powder. *Yogyo-Kyokai-Shi*, **91** (1983) 24–30.
12. Nakagawa, Z., Hamano, K., Sakaguchi, M. & Kanzaki, S., Characterization and sinterability of Mg-Al spinel powders prepared with a thermal decomposition of a freeze-dried sulfate. *Yogyo-Kyokai-Shi*, **90** (1982) 312–19.
13. Lepkova, D., Batarjav, A., Samunevz, B., Ivanova, Y. & Georgieva, L., Preparation and properties of ceramics from magnesium spinel by sol-gel technology. *J. Mater. Sci.*, **26** (1991) 4861–4.
14. Itatani, K., Nishioka, T., Seike, S., Howell, F. S., Kishioka, A. & Kinoshita, M., Sinterability of β-calcium orthophosphate powder prepared by spray-pyrolysis. *J. Am. Ceram. Soc.*, **77** (1994) 801–5.
15. Itatani, K., Takahashi, O., Kishioka, A. & Kinoshita, M., Properties of hydroxyapatite prepared by spray-pyrolysis technique. *Gypsum & Lime*, No. 213 (1988) 19–27.
16. Aizawa, M., Itatani, K., Kishioka, A. & Kinoshita, M., Properties of calcium metaphosphate and calcium diphosphate powders prepared by spray-pyrolysis technique. *Gypsum & Lime*, No. 237 (1992) 22–30.
17. Messing, G. L., Zhang, S. C. & Jayanthi, G. C., Ceramic powder synthesis by spray pyrolysis. *J. Am. Ceram. Soc.*, **76** (1993) 2707–26.
18. Lang, R. J., Ultrasonic atomization of liquids. *J. Acoust. Soc. Am.*, **34** (1962) 6–8.
19. Powder Diffraction File Card No.21-1152, JCPDS International Center for Diffraction Data, Newtown Square, PA (1971).
20. Powder Diffraction File Card No. 24-1164, JCPDS International Center for Diffraction Data, Newtown Square, PA (1973).
21. Powder Diffraction File Card No. 4-0829, JCPDS International Center for Diffraction Data, Newtown Square, PA (1949).
22. Arai, Y. & Yasue, T., *Gypsum & Lime*, No. 187 (1983) 357–66.
23. Hamano, K., Nakagawa, Z. & Watanabe, H., Effects of magnesium compound additives on sintering of magnesia. In *Sintering—Theory and Practice*, ed. D. Kolar, S. Pejovni & M. M. Ristić. Elsevier Scientific Publishing Co., Amsterdam, 1981, pp. 159–64.
24. *Kagaku Daijiten*, Vol. **4**, Compiled by the Committee of Kagaku Daijiten, Kyoritsu Shuppan, Tokyo, Japan, 1979, p. 772.
25. *Kagaku Daijiten*, Vol. **2**, Compiled by the Committee of Kagaku Daijiten, Kyoritsu Shuppan, Tokyo, Japan, 1979, p. 39.
26. *Gmelin Handbook of Inorganic Chemistry*, ed. H. Bergmann. Springer Verlag, Berlin, 1982, pp. 43–4.
27. Itatani, K., Kishioka, A. & Kinoshita, M., Synthesis of starting powders for ceramics by spray-pyrolysis technique. *Gypsum & Lime*, No. 241 (1992) 25–34.
28. Matsumoto, R. L. K., Generation of powder compaction response diagrams. *J. Am. Ceram. Soc.*, **69** (1995) C-246–C-247.
29. Haberko, K., Characteristics and sintering behaviour of zirconia ultrafine powders. *Ceramurgia International*, **5** (1979) 148–54.
30. Phillippi, C. M. & Mazdiyasni, K. S., Infrared and Raman spectra of zirconia polymorphs. *J. Am. Ceram. Soc.*, **54** (1971) 254–8.

Journal of the European Ceramic Society **16** (1996) 1179–1188

PII:S0955-2219(96)00050-7
0955-2219/96/$15.00

Reactions and Phase Transformation in SiO_2–ZrO_2 Sol–Gel Coated Alumina Powder

Stefan Ebener* & Wolfgang Winter†

Institute of Mineralogy, Technical University of Darmstadt, Schnittspahnstraße 9, D-64287 Darmstadt, Germany

(Received 20 December 1994; revised version received 18 January 1996; accepted 20 February 1996)

Abstract

TEOS and zirconium-n-propoxide have been hydrolysed in a two-step process in the presence of Al_2O_3 powder in order to coat the alumina grains with two layers of SiO_2 and ZrO_2. The reactions and phase transformations during sintering of the coated powders to a mullite–zirconia composite were investigated by means of differential thermal analyses, X-ray diffraction, transmission electron microscopy and scanning electron microscopy. The sequence of coating influences the crystallization temperature of tetragonal zirconia from the amorphous ZrO_2 layer. In the Al_2O_3 powder that was coated first with ZrO_2 the temperature of the tetragonal zirconia crystallization is 65 K lower than in the powder coated first with SiO_2. Mullite is not formed through the direct reaction of Al_2O_3 cores and the amorphous SiO_2 layer, but only through the reaction of Al_2O_3 with the metastable precursor phases cristobalite and zircon ($ZrSiO_4$). A second generation of tetragonal zirconia crystals is formed during the decomposition of zircon, simultaneously increasing the tetragonal to monoclinic ZrO_2 ratio. Copyright © 1996 Elsevier Science Ltd

Deux couches, une d'oxyde de zirconium et l'autre d'oxyde de silicium, ont été appliquées sur les grains d'une poudre fine d'alumine en hydrolysant successivement, du TEOS et du n-propoxide de zirconium. Les réactions et transformations des phases lors du frittage des grains enrobés afin d'obtenir un composite mullite–zircone ont été étudiées par DTA, XRD, TEM et MEB. L'ordre dans lequel les couches sont déposées influence la température de cristallization de la phase tétragonale de l'oxyde de zirconium à partir de la couche amorphe de ZrO_2. Lorsque la poudre de Al_2O_3 est d'abord recouverte d'une couche de ZrO_2, la température de cristallization de l'oxyde de zirconium tétragonal est plus basse (de 65K) que si la poudre est enduite en premier d'une couche de SiO_2. Dans les deux cas, la mullite n'est jamais formée par réacction dirècte entre l'alumine et la couche amorphe de SiO_2, mais seulement par réaction de Al_2O_3 avec des phases intermédiaires métastables, cristobalite et zircon ($ZrSiO_4$). De l'oxyde de zirconium tétragonal se forme également par la réaction secondaire de décomposition du zircon, augmentant ainsi la proportion entre les phases tétragonale et monoclinique de ZrO_2.

In einem zweistufigen Prozeß wurden durch Hydrolyse von TEOS und Zirkon-n-Propoxid zwei Schichten, bestehend aus ZrO_2 und SiO_2, auf die Körner eines Al_2O_3-Pulvers abgeschieden. Die Reaktionen und Phasenumwandlungen während der Sinterung der beschichteten Pulver zu einer Mullit–Zirkonoxid Dispersionskeramik wurden mittels DTA, XRD, TEM und REM untersucht. Die Reihenfolge der Beschichtungen beeinflußt die Kristallisationstemperatur von tetragonalem Zirkonoxid in der amorphen ZrO_2-Schicht. So zeigt das Al_2O_3 Pulver, bei dem zuerst die ZrO_2-Schicht abgeschieden wurde, eine um 65 K niedriger einsetzende Kristallisation von tetragonalem ZrO_2 als das Pulver, das zuerst mit einer SiO_2-Schicht beschichtet wurde. Mullit wird nicht durch eine direkte Reaktion der Al_2O_3-Kerne mit der amorphen SiO_2-Schicht gebildet, sondern entsteht durch Reaktion des Al_2O_3 mit den metastabilen Vorläuferphasen Cristobalit und Zirkon ($ZrSiO_4$). Eine zweite Generation von tetragonalen ZrO_2 Kristalliten wird durch den Zerfall des Zirkons gebildet, wodurch sich gleichzeitig das Verhältnis von tetragonalem zu monoklinem ZrO_2 erhöht.

1 Introduction

The properties of advanced ceramics such as homogeneity, density and microstructure are strongly

*Present address: ITC-WGT/TM, Forschungszentrum Karlsruhe, Postfach 3640, D-76021 Karlsruhe, Germany.
†Present address: Laboratoire de Science des Matériaux Vitreux, Université Montpellier II, F-34095 Montpellier, France.

dependent on the characteristics of the starting powders. Some powder characteristics such as sintering behaviour or reactivity depend mainly on the properties of the surface. Other powder surface-related properties that are of interest for diverse applications such as pigments, magnetic tapes, phamaceuticals, catalysts and dispersion-strengthened alloys include surface charge, as well as magnetic, optical and adsorptive characteristics. Hence, in recent years several new powder synthesis techniques have been developed, one of them being the hydrolysis and condensation of metal alkoxides or salts via the sol–gel technique. Work has been done to control the powder surface properties by coating particles via the sol–gel technique with a thin layer of different chemical composition. An extensive review of the coating technique is given by Sparks[1] and Garg and Matijevic.[2]

Major areas for the use of coated powders are the improvement of sinterability and the homogeneous incorporation of additives. For example, the difficulties in sintering electroceramic materials such as ferrites, PMZN relaxor dielectrics, doped SnO_2 or $BaTiO_3$ can be overcome by coating the powders with a layer consisting of amorphous SiO_2 together with Li_2O or B_2O_3.[3–5] The densification of such powders proceeds via a liquid-phase sintering mechanism which allows the sintering temperatures and the total amount of incorporated second phases to be lowered compared with the conventional mixing method. The coating technique also helped in the homogeneous incorporation of dopants, counterdopants and additives into PTCR $BaTiO_3$ thermistors. Numerous studies exist in the literature concerning the kinetics of viscous sintering of glass powders with rigid inclusions and coated inclusion particles.[6–10]

Another important field for the application of coated powders is the formation of particulate- or whisker-reinforced materials. Homogeneous composites with sufficient densities can be obtained by sintering Si_3N_4 powder coated with Al_2O_3 and/or Y_2O_3, or by sintering SiC whiskers coated with Al_2O_3.[11–15] Zirconia-toughened alumina, mullite, spinel and cordierite ceramics were also formed from coated starting powders.[16–19] In the case of cordierite composites, the ZrO_2 coating also yields an evident improvement of the powder sinterability.

Sacks *et al.*[20,21] developed a process for the fabrication of mullite ceramics and mullite–zirconia/alumina or mullite–SiC composites referred to as transient viscous sintering (TVS). This method starts from alumina, ZrO_2 and SiC particles that have been coated with an amorphous SiO_2 layer. These particles could be sintered to almost full density at about 1300°C via viscous flow of the amorphous coating and then converted to mullite through the reaction of SiO_2 and the Al_2O_3 cores at 1500–1600°C. A combination of sintering and reaction between inner cores and outer coatings was also used to fabricate aluminium titanate ceramics from TiO_2-coated alumina particles.[22]

In our study alumina particles were coated with a double layer consisting of SiO_2 and ZrO_2. Sintering of these powders at 1500–1550°C yields dense mullite–zirconia composites.[23] This paper reports the phase formation and the reactions during heating between the alumina cores and the two coatings. Furthermore, the effects of the sequence of the SiO_2 and ZrO_2 coatings on these reactions were investigated.

2 Experimental Procedure

The coatings of silica and zirconia on alumina particles were achieved by controlled hydrolysis of tetraethylorthosilicate (TEOS) and zirconium-n-propoxide (Alpha Products) in an alcoholic dispersion of fine-grained alumina powder. For the synthesis, a fraction of Al_2O_3 powder, with a grain size not exceeding 1 μm and an average grain size of 0.35 μm, was used, which had been separated by centrifuge from a commercial α-alumina powder (Martoxid CS400/M). The hydrolysis of the two metal organic components was carried out separately in a two-step process, where anhydrous 2-propanol was used as reaction medium for the hydrolysis of zirconium-n-propoxide and ethanol for the hydrolysis of TEOS. The molar ratio of Al_2O_3 to TEOS was 3:2, while zirconium-n-propoxide was added corresponding to 20 wt% of zirconia in the final product. For each sample 6 g of alumina powder was used, yielding about 10 g of coated powder. The total volume of alcohol in each hydrolysis step added up to 500 cm.[3]

For the coating process, the alumina powder or single-coated powder was dispersed ultrasonically in the required alcohol and the precursor was then added while intensively stirring. The suspension was heated under reflux to a temperature of 50°C for 2 h. TEOS was hydrolysed by adding a mixture of ammoniated water in ethanol (R_{NH_3} = 2, R_{H_2O} = 4), whereas for the hydrolysis of zirconium-n-propoxide a mixture of distilled water in 2-propanol was used (R_{H_2O} = 15). Two powders have been synthesized which differ in the sequence of the alkoxide addition: in powder ZT zirconium-n-propoxide was hydrolysed first and TEOS hydrolysed in a second step; in powder TZ the sequence was reversed. After each hydrolysis step

the powders were separated from the reaction medium with a centrifuge, washed with ammoniated water and dried at 100°C.

The coated powders were characterized using transmission electron microscopy (TEM) equipped with a device for energy-dispersive X-ray analysis (EDX) (Philips CM12, 120 kV). The powder samples for the TEM studies were dispersed ultrasonically in ethanol and applied on Formvar-coated Cu nets. The grain size distribution of the powders was measured by means of X-ray sedimentation methods (Sedigraph 5000D). The powders were studied also by means of differential thermal analysis (DTA) (Netzsch 404EP, heating rate 7·5 K min^{-1}).

For further studies, pellets of 5 mm in diameter and 5 mm in height were formed by uniaxial pressing. These samples were isothermally annealed for 4 to 12 h at temperatures ranging from 900 to 1550°C. Crystallization and reactions between phases as a function of temperature were monitored by X-ray powder diffraction (XRD) methods. The microstructures were studied by means of scanning electron microscopy (SEM) (Philips SEM505).

3 Results

Figures 1 and 2 show the result of the coating process on the alumina powder. The individual SiO_2 and ZrO_2 coatings are difficult to distinguish because they superimpose each other with the exception of the very rim. On Fig. 2 the inner ZrO_2 coating and the outer SiO_2, coating are marked with arrows. In both cases, samples ZT and TZ, concentration profiles of Al_2O_3, ZrO_2 and SiO_2 were measured by means of EDX in the nanoprobe mode. Due to superposition of the coatings with Al_2O_3 the EDX data have merely a

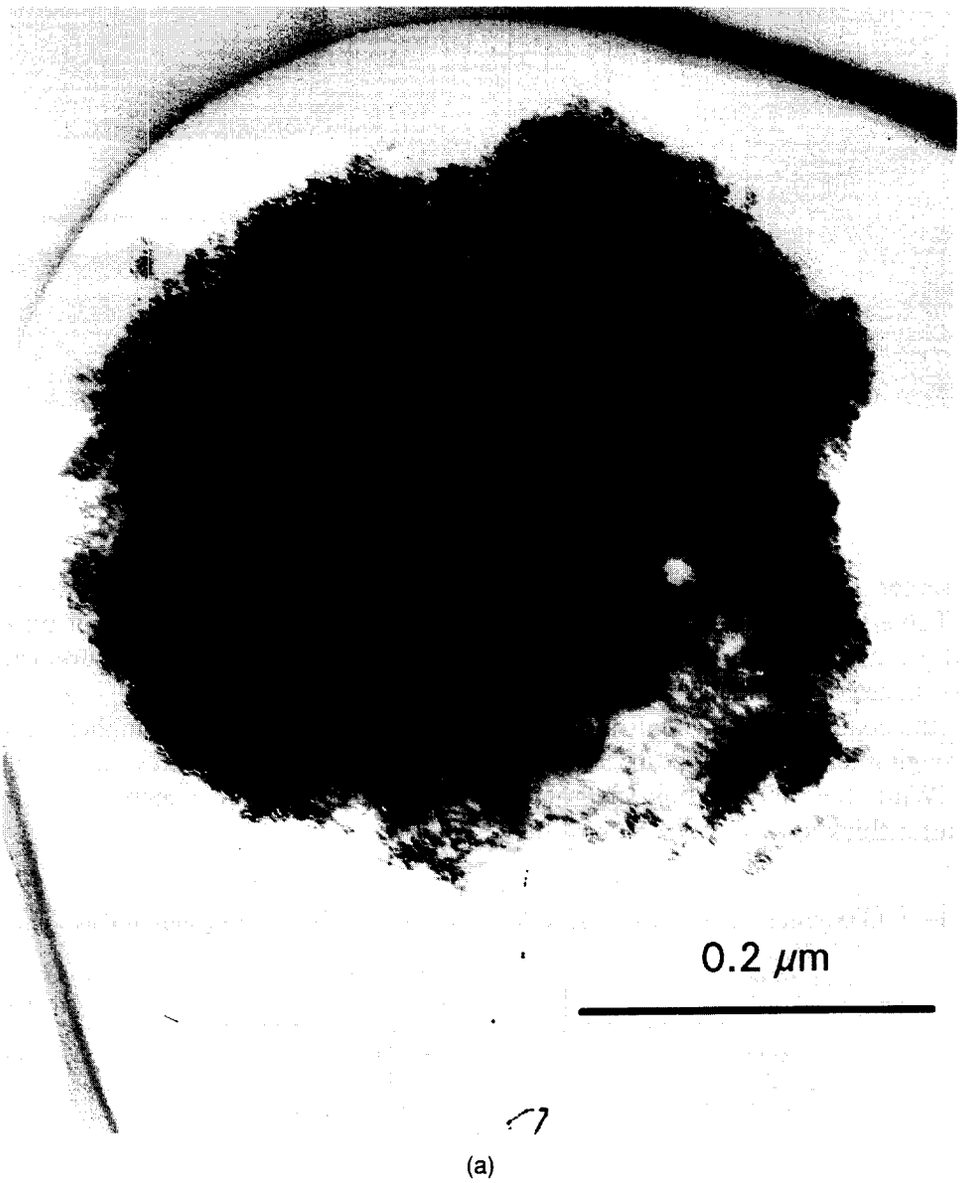

(a)

Fig. 1. TEM micrographs of powder TZ after coating with SiO_2 and ZrO_2: (a) bright-field and (b) dark-field image with 10-1 of Al_2O_3.

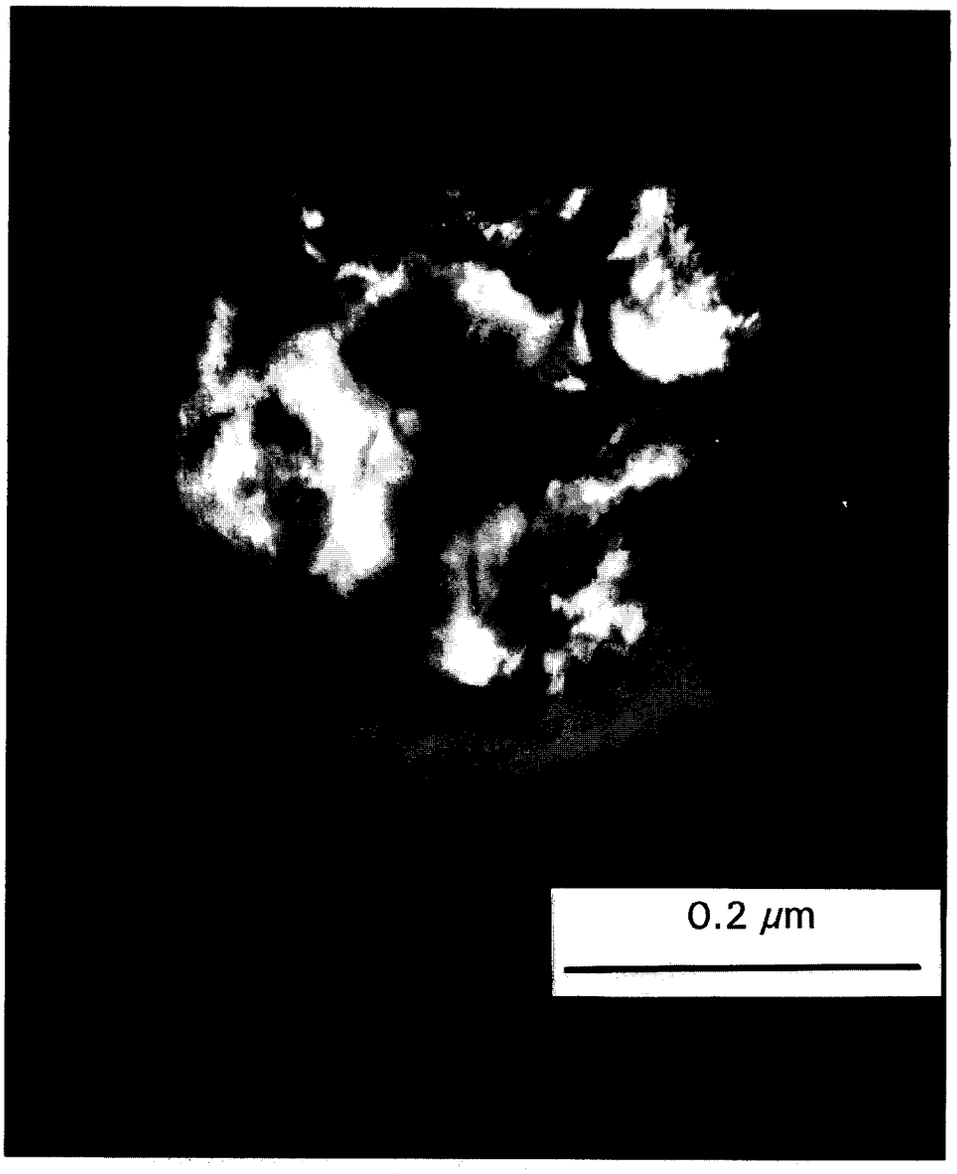

(b)

Fig. 1.–*Contd.*

qualitative character. However, comparing the EDX results in Table 1 of the measurements taken from the coated grains shown in Figs 1 and 2, as well as from their mixed layers, the expected respective sequence of the coatings can be confirmed.

Diffraction imaging showed that both coatings are amorphous. While the SiO_2 coating is smooth and compact with a thickness of about 50 nm, the ZrO_2 coating has a coarser and more fluffy structure resulting in a thickness of up to 100 nm. The Sedigraph grain size measurements gave mean particle sizes of 2·5 and 2·7 μm for TZ and ZT, respectively, which are higher than the expected ones. This is mainly due to an agglomeration of the coated powder, which was also observed with TEM.

Table 1. EDX results as measured in TEM in the nanoprobe mode of the grains in Figs 1 and 2

Sample	*Oxide*	*EDX measurement over the whole grain*	*EDX measurement in the middle of the coating*
TZ	Al_2O_3	45·0	6·3
	SiO_2	24·8	35·1
	ZrO_2	30·2	58·6
ZT	Al_2O_3	48·4	15·0
	SiO_2	27·1	45·2
	ZrO_2	24·5	39·8

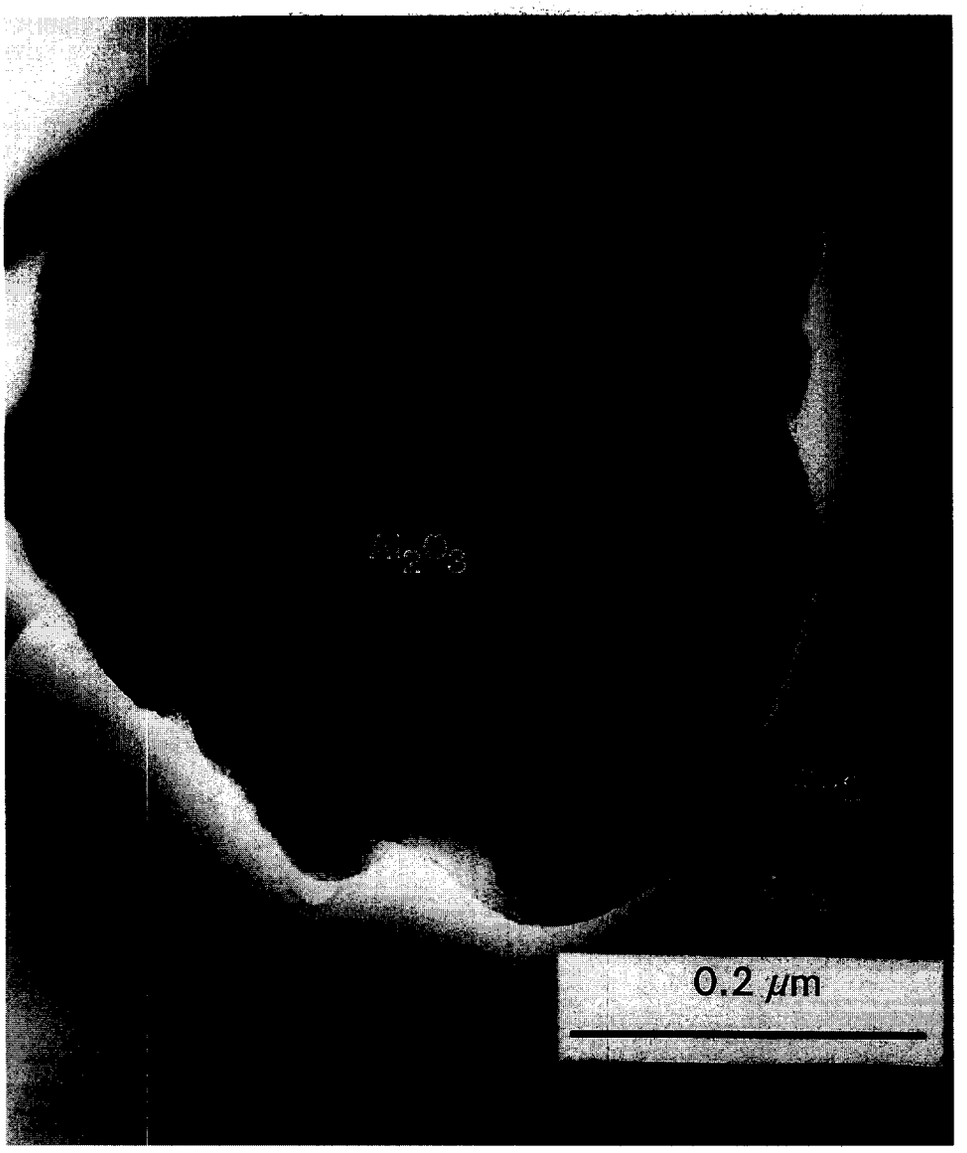

(a)

Fig. 2. TEM micrographs of powder ZT after coating with ZrO_2 and SiO_2. The layers of ZrO_2 and SiO_2 are marked at the very rim of the particle. (a) Bright-field and (b) dark-field image with 10-1 of Al_2O_3.

The thermochemical behaviour of the coated powders on continuous heating was studied by DTA up to 1000°C (Fig. 3). The broad endothermic peak at low temperatures is due to elimination of adsorbed H_2O, alcohols and other organic compounds. An exothermic peak evolves at 840 and 905°C for ZT and TZ, respectively. X-ray diffraction (Fig. 4) of samples heated up to 840 and 905°C with the same heating schedule as applied for the DTA runs showed that this exothermic peak results from the crystallization of tetragonal zirconia in the ZrO_2 coatings. In the 905°C samples the diffraction peaks of zirconia are broader in the case of powder TZ compared with powder ZT, indicating a lower grain size of tetragonal zirconia in the former. This can also be observed by TEM: Fig. 5 shows the dark-field image of a small agglomerate of coated particles of sample TZ heated up to 905°C imaged with the 10-1 reflection of Al_2O_3. The ZrO_2 coating consists of tiny zirconia crystallites which give no discrete reflections in the diffraction pattern but only diffraction rings. In contrast, in powder ZT the zirconia diffraction rings are not homogeneous but can be partly resolved into several weak and some strong reflections (2 2 0 and 1 1 3). Imaging with the 2 2 0 reflection of tetragonal zirconia in the dark-field mode reveals some zirconia crystallites that have a size of about 5–20 nm (Fig. 6).

Isothermal heating of the powders at 1200–1550°C for 4 h results in further crystallization of tetragonal zirconia and partial transformation into the monoclinic form. The development of the ratio of tetragonal to monoclinic zirconia was calculated from the X-ray intensities of the (1 1 1) diffraction peaks according to Evans *et al.*[24] and is represented in Fig. 7. With increasing temperature the tetragonal zirconia content decreases to 53–64% of the total zirconia

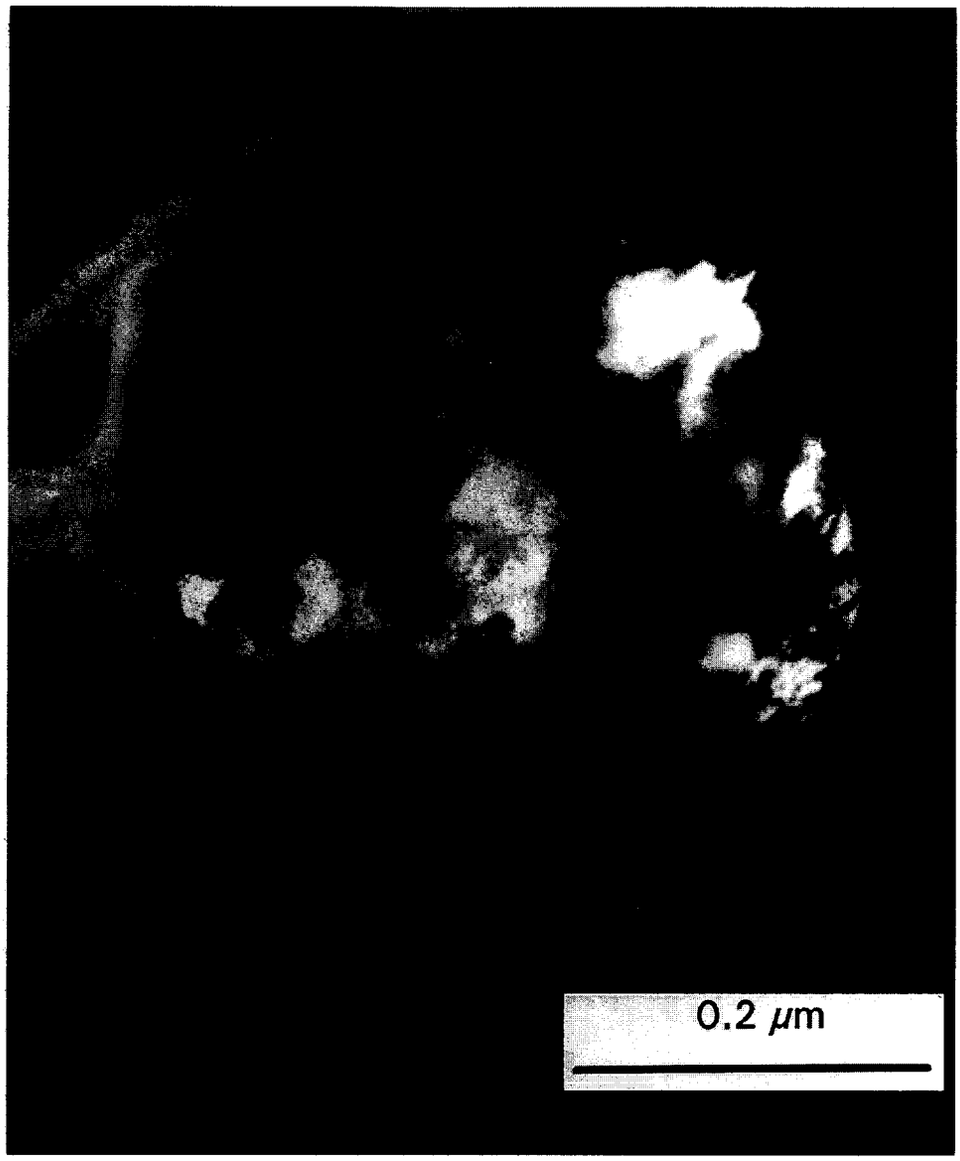

(b)

Fig. 2.–*Contd.*

content at 1300°C. At 1400°C, a sharp increase up to 70–77% tetragonal zirconia was observed which is transformed again at higher temperatures.

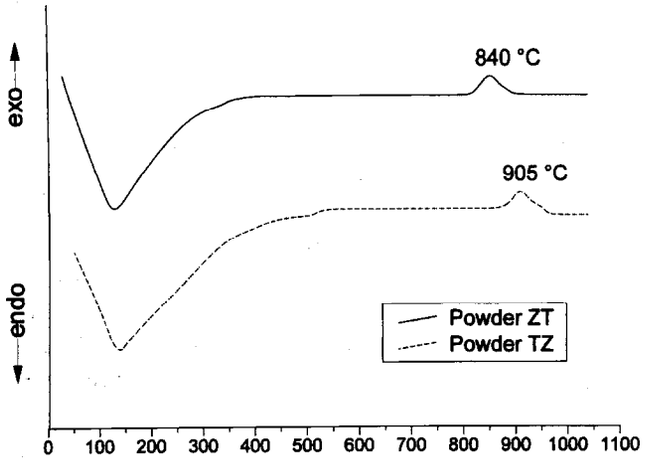

Fig. 3. DTA of the coated powders between 25 and 1040°C, rate of heating 10°C min.$^{-1}$

At 1300°C the SiO_2 layer reacts with ZrO_2 to give zircon ($ZrSiO_4$) and cristobalite. At 1400°C the latter has reacted completely with Al_2O_3 to give the first mullite. On prolonged heating at 1400–1550°C zircon reacts with Al_2O_3 to mullite and ZrO_2. Heating the powders at 1550°C for 12 h results in an enhanced growth of ZrO_2 grains. The zircon decomposition and mullite formation is completed and the sample consists only of mullite and tetragonal as well as monoclinic zirconia (Fig. 8). The size of the ZrO_2 crystals seems to be bimodal with one fraction between 1 and 1·5 μm and the other <0·5 μm.

4 Discussion

The present investigation shows that it is possible to coat Al_2O_3 particles with a double layer of SiO_2

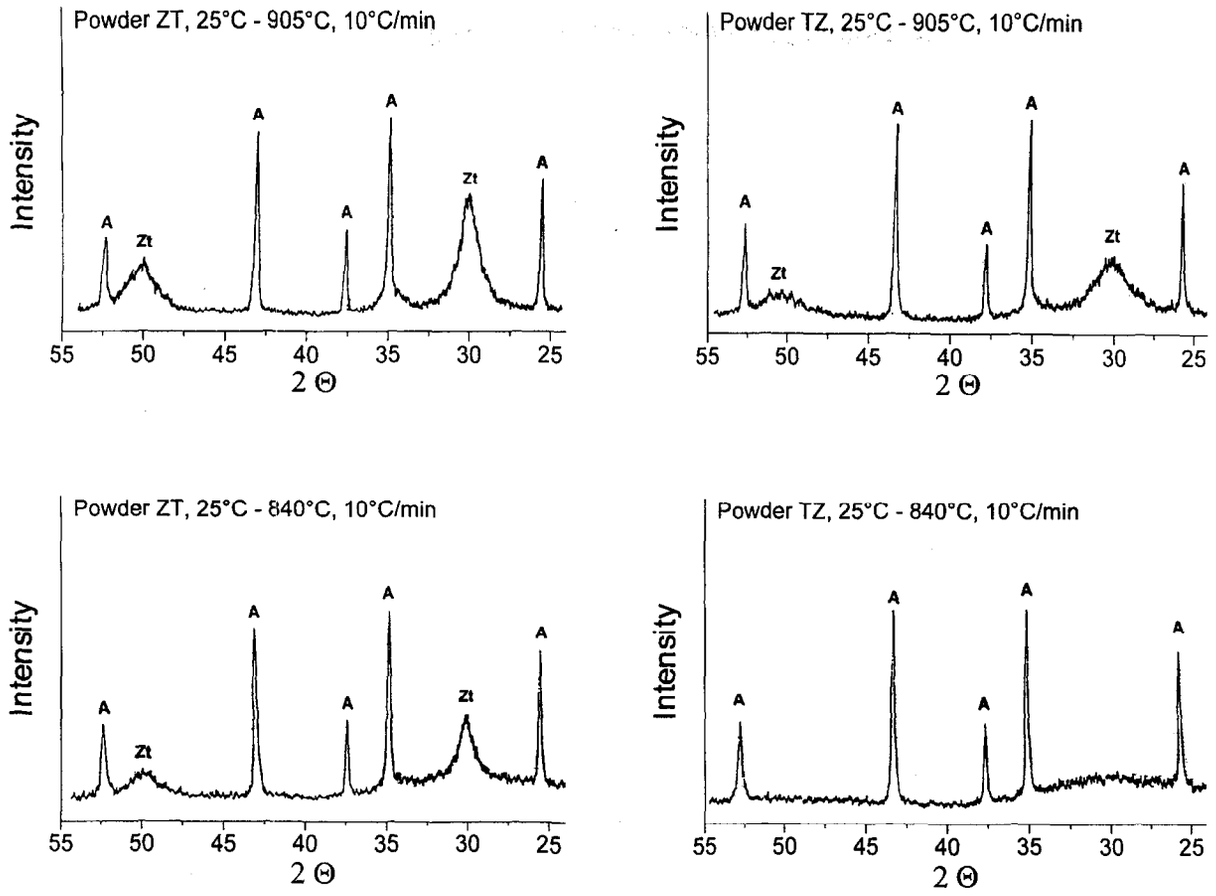

Fig. 4. X-ray diffraction of samples TZ and ZT heated to 840 and 905°C with a heating rate of 10°C $min.^{-1}$ **A** indicates the peaks of alumina and **Zt** those of tetragonal ZrO_2.

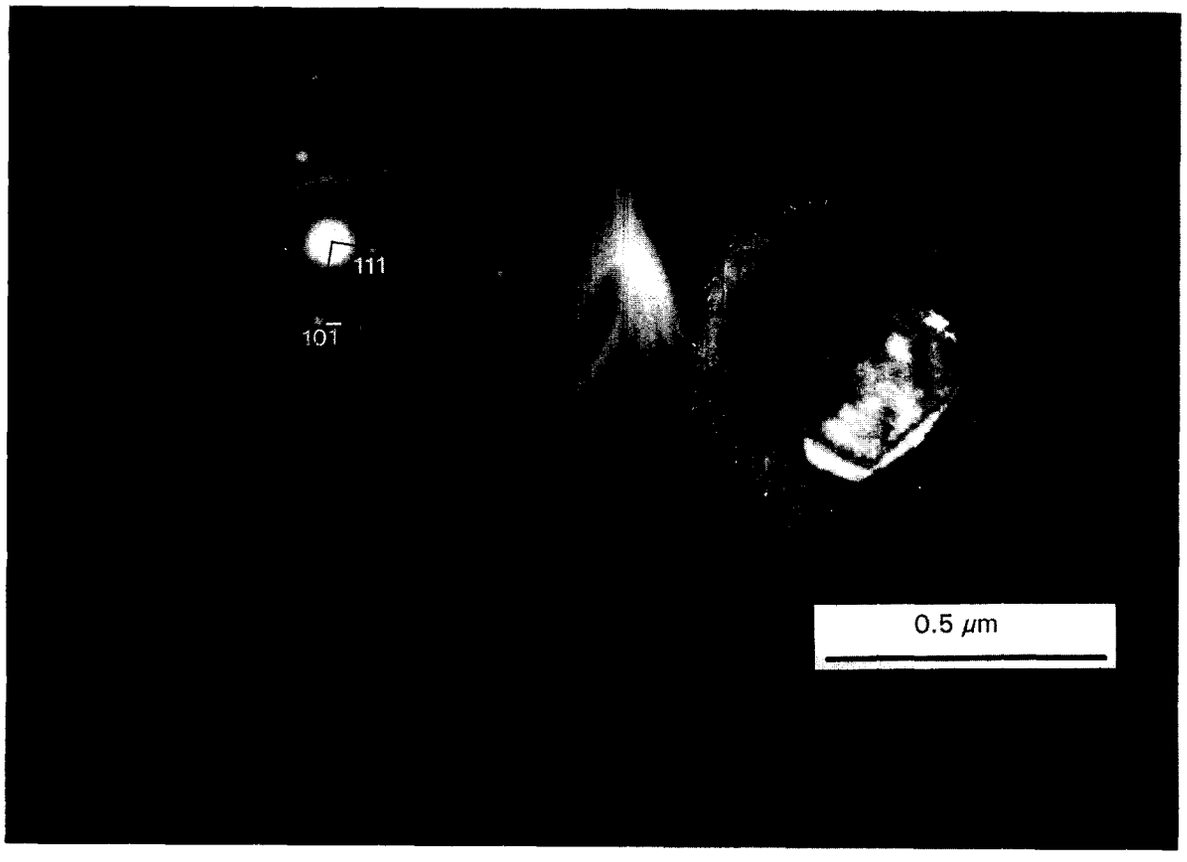

Fig. 5. TEM micrograph of sample TZ continuously heated up to 905°C: (a) Diffraction pattern showing 1 1 1 and 1 0 -1 of Al_2O_3 and diffraction rings of tetragonal ZrO_2; (b) dark-field image with 1 0 -1 of Al_2O_3.

Fig. 6. TEM micrograph of sample ZT continuously heated up to 905°C: (a) diffraction pattern showing 1 1 1 and 1 0-1 of Al_2O_3 and diffraction rings with some discrete reflections (*z*) of tetragonal ZrO_2; (b) dark-field image with 1 0-1 of Al_2O_3; (c) dark-field image with 2 2 0 of ZrO_2.

and ZrO_2 in a two-step process. The results of DTA measurements indicate the crystallization of tetragonal zirconia at 840 and 905°C, which is in accordance with the results obtained by Palladino *et al.*,[25] Nogami *et al.*[26] and Ruin *et al.*,[19] who found crystallization temperatures between 800 and 930°C for ZrO_2–SiO_2 gels and ZrO_2-coated alumina powders. The sequence of the SiO_2 and ZrO_2 coatings itself seems to have no great influence on the crystallization and phase reactions except that the crystallization temperature of sample ZT, where ZrO_2 is the inner coating, is about 65 K lower than that of sample TZ. Obviously, the surface of the crystalline Al_2O_3 core represents a better nucleation site than the surface of the amorphous silicon layer in the case of sample TZ. This is undoubtedly due to a lowering of the heterogeneous nucleation enthalpy by the periodical crystal structure of the alumina surface. Ruin *et al.*,[19] who investigated the coating of Al_2O_3 with

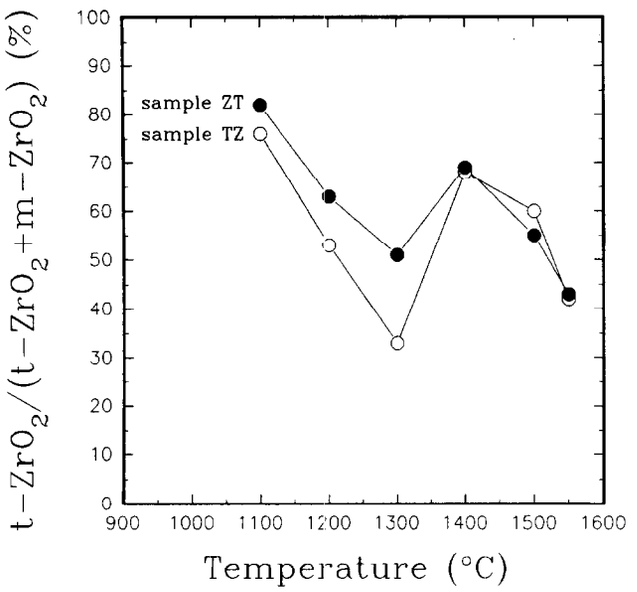

Fig. 7. Development of the tetragonal zirconia content as calculated from X-ray intensities of (1 1 1) diffraction peaks of tetragonal and monoclinic zirconia.

ZrO_2, reported an orientation relationship between the tetragonal ZrO_2 crystals and the Al_2O_3 core. In several cases [1 1 0] of ZrO_2 was parallel to [1 1 -2 0] of Al_2O_3. This observation is supported by the similar *d*-values (2.574 and 2.379 Å for tetragonal ZrO_2 and Al_2O_3, respectively) which differ only by 7·5%. Thus, the larger grain size of tetragonal zirconia in sample ZT heated up to 905°C compared with sample TZ is also due to the earlier crystallization and the favourable effect of the Al_2O_3 surface on crystal growth.

Mullite is not formed through the reaction of the SiO_2 layer with the Al_2O_3 core, not even in sample TZ where SiO_2 and Al_2O_3 are in direct contact. In both samples cristobalite and, in a larger temperature range, zircon appear as precursor phases. Metastable zircon forms above 1200°C but becomes unstable at longer heating times. A remarkable point related to the mullite and zircon formation is the increase of the tetragonal ZrO_2 content at 1400°C. This increase coincides with the beginning of decomposition of zircon, observed from X-ray diffraction. Zircon decomposes into SiO_2 which reacts with Al_2O_3 to form mullite, and ZrO_2 which crystallizes seemingly as tetragonal zirconia. The stability of tetragonal ZrO_2 against transformation into the stable monoclinic polymorph is a function of grain size. ZrO_2 particles in a reaction-sintered mullite matrix smaller than about 1.2 μm keep their tetragonal structure down to room temperature.[27] Thus, the ZrO_2 crystals that form from the decomposition products of zircon at 1400°C must be of a relatively small grain size, since a simultaneous increase of the tetragonal zirconia content was observed. Hence, the ZrO_2 crystals observed in samples heated above 1400°C comprise two generations: the first one crystallizes directly from the amorphous ZrO_2 layer and has grown to a size of 1–1·5 μm at 1550°C; the second generation originates from the decomposition of zircon above 1400°C and is of a smaller grain size. This bimodal grain size distribution can be observed by SEM (Fig. 8). In order to maximize the amount of tetragonal zirconia it seems therefore advantageous to favour the metastable formation of zircon and to suppress the direct ZrO_2 crystallization.

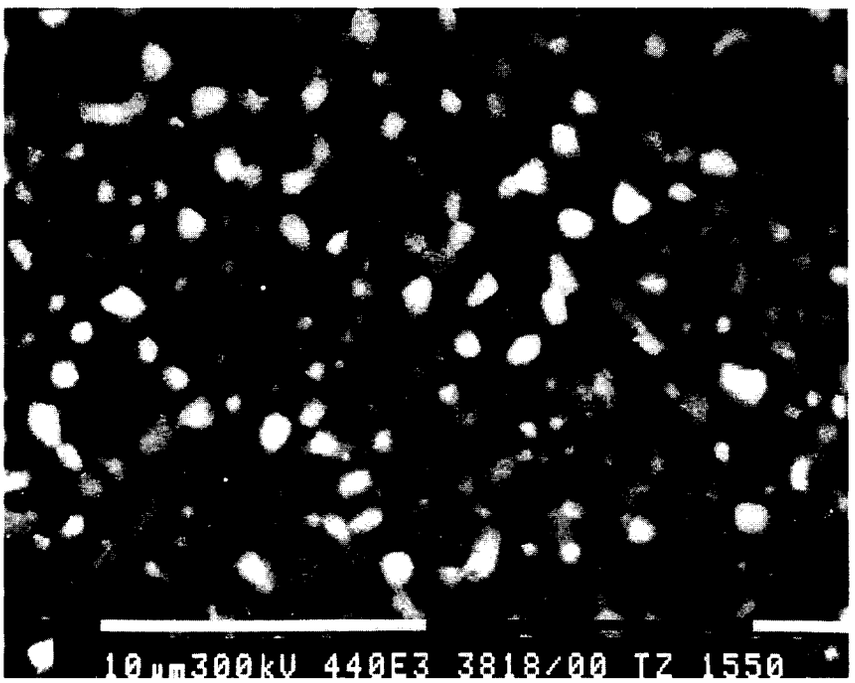

Fig. 8. SEM micrograph of sample TZ sintered at 1550°C for 12 h.

References

1. Sparks, R. E., Microencapsulation. In *Encyclopedia of Chemical Technology, Vol. 15*, eds M. Grayson & D. Eckroth. Wiley, New York, 1981, p. 470.
2. Garg, A. & Matijevic, E., Preparation and properties of uniformly coated inorganic colloidal particles. 2. Chromium hydrous oxide on hematite. *Langmuir*, **4** (1988) 38–44.
3. Selmi, F. A. & Amarakoon, V. R. W., Sol–gel coating of powders for processing electronic ceramics. *J. Am. Ceram. Soc.*, **71**[11] (1988) 934–7.
4. Brooks, K. G. & Amarakoon, V. R. W., Sol–gel coating of lithium zinc ferrite powders. *J Am. Ceram. Soc.*, **74**[4] (1991) 851–3.
5. Fagan, J. G. & Amarakoon, V. R. W., Reliability and reproducibility of ceramic sensors: Part II, PTC thermistors. *Am. Ceram. Soc. Bull.*, **72**[2] (1993) 69–76.
6. Scherer, G. W., Sintering with rigid inclusions. *J. Am. Ceram. Soc.*, **70**[10] (1987) 719–25.
7. Rahaman, M. N. & De Jonghe, L. C., Effect of rigid inclusions on the sintering of glass powder compacts. *J. Am. Ceram. Soc.*, **70**[12] (1987) C348–51.
8. Bordia, R. K. & Scherer, G. W., On constrained sintering — III. Rigid inclusions. *Acta Metall.*, **36**[9] (1988) 2411–16.
9. Scherer, G. W., Viscous sintering of particle-filled composites. *Am. Ceram. Soc. Bull.*, **70**[6] (1991) 1059–63.
10. Hu, C.-L. & Rahaman, M. N., Factors controlling the sintering of ceramic particulate composites: II. Coated inclusion particles. *J. Am. Ceram. Soc.*, **75**[8] (1992) 2066–70.
11. Kim, J. S., Schubert, H. & Petzow, G., Sintering of Si_3N_4 with Y_2O_3 and Al_2O_3 added by coprecipitation. *J. Eur. Ceram. Soc.*, **5** (1989) 311–19.
12. Garg, A. K. & De Jonghe, L. C., Microencapsulation of silicon nitride particles with yttria and yttria–alumina precursors. *J. Mater. Res.*, **5**[1] (1990) 136–42.
13. Kapolnek, D. & De Jonghe, L. C., Particulate composites from coated powders. *J. Eur. Ceram. Soc.*, **7** (1991) 345–51.
14. Wang, C. M. & Riley, F. L., Alumina coating of silicon nitride powder. *J. Eur. Ceram. Soc.*, **10** (1992) 83–93.
15. Kulig, M., Oroschin, W. & Greil, P., Sol–gel coating of silicon nitride with Mg–Al oxide sintering aid. *J. Eur. Ceram. Soc.*, **5** (1989) 209–17.
16. Fegley, B., White, P. & Bowen, H. K., Preparation of zirconia–alumina powders by zirconium alkoxide hydrolysis. *J. Am. Ceram. Soc.*, **68**[2] (1985) C60–2.
17. Guinebretiere, R., Ruin, P., Lecomte, A. & Dauger, A., Fabrication and sintering of zirconia sol–gel coated cordierite powder. In *Ceramic Powder Science III Vol. 12*, eds G. L. Messing, S. I. Hirano & H. Hausner. American Ceramic Society, Westerville, OH, 1990, pp. 929–36.
18. Guinebretiere, R., Dauger, A. & Lecomte, A., Preparation and densification of zirconia toughened cordierite. In *Eurogel '91*, eds S. Vilminot, R. Nass & H. Schmidt. North-Holland, Amsterdam, 1992, pp. 391–8.
19. Ruin, P., Melin, G., Guinebretiere, R., Lecomte, A. & Dauger, A., Coating of oxide powders with alkoxide derived zirconia. *J. Sol–Gel Sci. Technnol.*, **2** (1994) 539–44.
20. Sacks, M. D., Bozkurt, N. & Scheiffele, G. W., Fabrication of mullite and mullite-matrix composites by transient viscous sintering of composite powders. *J. Am. Ceram. Soc.*, **74**[10] (1991) 2428–37.
21. Sacks, M. D., Scheiffele, G. W., Bozkurt, N. & Raghunathan, R., Fabrication of ceramics and composites by viscous and transient viscous sintering of composite particles. In *Ceramic Powder Science IV Vol. 22*, eds G. L. Messing, S. H. Hirano & H. Hausner, American Ceramic Society, Westerville, OH, 1991, pp. 437–55.
22. Okamura, H., Barringer, E. A. & Bowen, H. K., Preparation and sintering of monosized Al_2O_3–TiO_2 composite powder. *J. Am. Ceram. Soc.*, **69**[2] (1986) C22–4.
23. Ebener, S., Synthesis of a mullite–ZrO_2 ceramic from sol–gel coated powder. Master thesis, Technical University of Darmstadt, 1994.
24. Evans, P. A., Stevens, R. & Binner, J. G. P., Quantitative X-ray diffraction analysis of polymorphic mixes of pure zirconia. *Br. Ceram. Trans. J.*, **83**[2] (1984) 39–43.
25. Palladino, M., Pirini, F., Chiurlo, P., Cogliati, G. & Costa, L., Sol–gel formation of silica–zirconia glasses. *J. Non-Cryst. Solids*, **147&147** (1992) 335–9.
26. Nogami, M. & Tomozawa, M., Zirconia-transformation-toughened glass-ceramics prepared by the sol–gel process from metal alkoxides. *J. Am. Ceram. Soc.*, **69**[2] (1986) 99–106.
27. Leriche, A., Mechanical properties and microstructures of mullite–zirconia composites. In *Ceramic Trans. Vol. 6: Mullite and Mullite-Matrix Composites*, eds S. Somiya, R. F. Davis & J. A. Pask. American Ceramic Society, Westerville, OH, 1991, pp. 541–51.

Journal of the European Ceramic Society **16** (1996) 1189–1200

PII:S0955-2219(96)00044-1
0955-2219/96/$15.00

The Influence of Shaping Method on the Grain Size Dependence of Strength in Dense Submicrometre Alumina

Andreas Krell & Paul Blank

Fraunhofer-Institut für keramische Technologien und Sinterwerkstoffe (IKTS), D-01277 Dresden, Germany

(Received 15 August 1995; revised version received 29 January 1996; accepted 8 February 1996)

Abstract

The grain size dependence of the strength of pressureless sintered aluminas is investigated with specimens fabricated by uniaxial pressing, cold isostatic pressing, pressure filtration, gel casting, and combinations thereof. The strength depends on the flaw population, and the observed grain size effect is different with different shaping approaches: with reduced grain sizes the diversity of measured strength averages broadens including increasingly high values for some of the shaping procedures only. Submicrometre grain sizes are, however, not an indispensable prerequisite for a high strength: grain sizes of 1–2 μm are sufficient to achieve 800–900 MPa by pressureless sintering, but present microstructures with grain sizes <1 μm do not indicate a further increase of the strength. Under certain technological conditions, the highest strengths can be associated with a surprisingly small standard deviation. The measured data are discussed considering recent micromechanical investigations of the same materials. Copyright © 1996 Elsevier Science Ltd

1 Introduction

Sintered alumina with its unique combination of high hardness, corrosion resistance, thermodynamic stability and economic advantages is a material that has acquired a wide acceptance in industry. It is used for hip implants, sliding and sealing elements, thread guides, cutting tools, grinding grits and other applications. The typical bending strength of pure and high-quality sintered alumina is about 400–500 MPa after pressureless sintering and in the range of 500–600 MPa in a hot-pressed state.

Riedel *et al.* were among the first who described a pressureless sintered alumina with an improved bending strength of 680 MPa at a grain size of 0·9 μm.[1] Remarkable further progress was achieved during the last years in both processing and properties, but often the best properties result from approaches that are expensive and limit the size and geometrical diversity of the sintered bodies. For example, expensive hot isostatic pressing (HIP) of pure corundum powders gives a strength of about 800 MPa for microstructures with grain sizes between 0·8 and 2 μm;[2,3] after pressureless sintering the strength was about 700 MPa in these experiments.[2] An even higher strength of 908 MPa at a grain size of 1·5 μm was observed when hot-pressing was combined with subsequent hot isostatic pressing.[4] A reported strength of 1300 MPa in a hot isostatically pressed alumina microstructure with 0·8 μm grain size is not clear in all details (in this report, samples with 4–5 μm grain size were measured to give a strength of about 700 MPa which is surprisingly high for such coarse-grained microstructures).[5] It was also observed that even pressureless sintering may produce samples with an average strength of 797 MPa, but a corundum powder with an extremely high sintering activity provided by a very high specific surface of 35 m^2/g was required, and the strength dropped to less than 500 MPa when powders with a surface of 8–22 m^2/g were used.[6] Such a result does not stimulate efforts in pressureless sintering, since processing of powders with high specific surfaces >20 m^2/g is very difficult when macroscopic ceramic bodies with a low frequency of flaws have to be produced under industrial conditions.

On the other hand, until now the properties achieved by novel processing routes that produce complex shapes in combination with pressureless sintering do not compete with the advanced properties given by other approaches. For example, shaping of alumina green compacts by enzyme-catalyzed reactions was performed using an alumina powder with a grain size of 0·5 μm and a specific surface area of 10 m^2/g.[7] As a consequence of difficult dispersion, no strength data that differed significantly from traditional pressureless sintered alumina (i.e. >500 MPa) were reported. Gelcasting, which implies the immediate solidification of a cast

slurry by polymerization of a monomer used as organic binder, seems to be even more difficult: comparing this process for two alumina powders with average particle sizes of 0·5 and 1·5 μm, respectively, the problem of a sufficient degree of dispersion was solved for the coarser one only, and the resulting strength after pressureless sintering was less than 300 MPa.[8]

It is generally assumed that high-purity powders are essential for a high strength (which requires both a sufficiently high fracture toughness K_{Ic} and a small size of the critical flaw at instability). Any subcritical crack growth (usually preceding unstable fracture and increasing the size of the flaw produced on manufacturing) will reduce the strength.[9] Subcritical fracture preferentially follows the grain boundaries because they represent a strong disorder compared with the crystal lattice of the grains, and because subcritical crack growth rates are higher under the condition of disorder (e.g. in amorphous materials, as an extreme).[10] Therefore, impurities that form amorphous grain boundary phases are assumed to prevent a high strength of polycrystalline non-transforming microstructures with equiaxed grains.

Further, it is suggested that a small grain size favours a high strength. The wish physically to understand the influence of the grain size D on the strength $\sigma(D)$ has led to some preference for an Orowan–Petch plot[11,12]

$$\sigma(D) = \sigma_{D\to\infty} + k \cdot D^{-1/2} \qquad (1)$$

where the intercept $\sigma_{D\to\infty}$ has been attributed to microplasticity or residual stress effects, and the analogy with Griffith's theory[13] gives a proportionality of the factor k with the square root of Young's modulus and the work of fracture (k has the dimension of a stress intensity). Often hundreds of data points obtained from different sources have been fitted by such plots without any regard for different processing which must have provided different flaw populations in all these specimens. This neglect of processing is the less convincing since already one of the first analyses[11] reported that different processing of alumina powders (hot pressing and sinter forging) yields plots with different $\sigma_{D\to\infty}$ and k parameters — the very same finding of a grain size effect that depends on processing as will be derived in the present work. There are, however, two more fundamental reasons why an Orowan–Petch plot seems inappropriate: (i) There is no physical basis to describe such different influences as the resistance against microplastic deformation and elastic residual stresses by a single parameter $\sigma_{D\to\infty}$. (ii) At $\sigma_{D\to\infty} = 0$, eqn (1) has to be compared with Griffith's relationship which correlates the strength with the energy of fracture and with a flaw size. Hence, the grain size in eqn (1) needs an interpretation as a defect or at least as a stress concentrator. This may be true when very coarse microstructures are investigated, but it is an improbable assumption for the grain size range between 0·4 and 4 μm discussed here, and even in the intermediate grain size range the experimental evidence of a generally valid $\sigma(D)$ versus $D^{-1/2}$ relationship is poor. For example, a recent treatment that stresses eqn (1) again uses the hypothesis of a proportionality between the grain size and the size of 'pre-existing defects'. To explain that proportionality, the authors associate a flaw size which is 7·5 times the grain diameter with cleavage processes.[14] However, without microscopic evidence for the collective cleavage of many neighbouring grains (which is not a commonly observed phenomenon in fine-grained alumina ceramics) such a hypothesis does not offer a strong argument against the generally accepted idea of technologically caused defects as the fracture origin in most ceramics. In the range between 1·7 and 11 μm, another recent work[15] claims the observation of a linear relationship of strength versus inverse square root of grain size and resumes the idea of peripherically cracked spherical pores with a crack length proportional to the grain size to explain this behaviour. In fact, a least squares fit of their measured data in a double logarithmic plot gives a power of the grain size of –0·29 which is rather different from an inverse square root, and careful fractographic investigations did not present any evidence of the assumed proportionality between a peripherical crack length and the grain size.

It is beyond the scope of the present work to present an alternative theoretical explanation. However, a number of microstructural processes are known with more indirect possible influences of the grain size on strength. For example, small grain sizes promote the visco-elastic relaxation of residual stresses during cooling the sintered microstructures,[16,17] an effect that may reduce grain boundary microflaws[18] and results in an increased resistance against subcritical crack growth. This increase of strength by reduced subcritical crack growth rates due to an increased micromechanical stability of the grain boundaries was demonstrated experimentally by comparing Al_2O_3, ZrO_2(3 mol-% Y_2O_3), Al_2O_3/TiC, and ZrO_2(3 mol-% Y_2O_3)/TiC.[19] However, the actual importance of such an influence in different grain size regions is not clear, and there is no reason to expect that a reduced grain size automatically increases the strength: several investigations indicate that the importance of grain sizes for a high strength can only be discussed in close relationship with the influence of flaws. For example, recent experiments with sintered aluminas representing a broad grain size range of

1–60 μm suggested that under the condition of a fixed technology a grain size effect proportional to the inverse square root of the grain size exists only when the grain size is larger than the typical size of the flaws which initiate failure.[20] Similarly, early systematic measurements with different sintering procedures revealed a trend of different grain size influences depending on the approach of fabrication,[11] i.e. depending on the different flaw populations. Therefore, it is evident that a low frequency of small flaws cannot be achieved by simply sintering a highly pure, extremely fine-grained powder at low temperatures (avoiding grain growth and producing a microstructure with submicrometre grain size). This feature is illustrated by a comparison of two investigations which used an identical alumina powder† and similar shaping procedures (cold isostatic pressing) but nevertheless showed quite different hardness values of about 19 and 22 GPa at similar grain sizes of 0·85 and 0·65 μm, respectively.[21,22] Also, the bending strength was lower than 400 MPa in the first report. Obviously, the potential advantages of very fine-grained powders with respect to lower sintering temperatures are opposed by additional difficulties in shaping when a high homogeneity and a low frequency of defects in the green (unsintered) body are required. This difficulty is not restricted to individual technologies, and there is no approach that generally might avoid this problem. For example, reduced powder grain sizes between 2·5 and 0·05 μm were observed to be accompanied by increasing agglomeration and reduced green densities even under the condition of careful pressure filtration with a preceding ultrasonic treatment of the aqueous slurry at low pH $\approx$2–4 (where the electrochemical surface potential of alumina and repulsive forces are high).[23] On solid state sintering, these agglomerates have a twofold detrimental effect: locally different shrinkage rates in more and in less dense subregions increase the size of flaws (between agglomerates), and the elimination of associated porosity (with a large size of these defect-like pores) requires an increase of the sintering temperature and promotes grain growth.[24]

The present work was intended to investigate the influences of the grain size on the strength of pressureless sintered alumina ceramics for a range of different processing approaches. All of the investigated technologies had been optimized first to minimize the probability of accidental results where the strength would be determined by different control of processing, and only the final results of these optimizations are given here. It is, of course, obvious that any 'optimization' is temporary, and further improvements are probable. It was another objective to compare possible grain size effects with recent micromechanical studies on these and similar materials.

2 Materials and Methods

Powder technology with aqueous slurries was used to produce pressureless sintered alumina bodies with relative densities in a narrow range of 99·2 ± 0·4%; the densities were measured following Archimedes' principle and related to a theoretical density of 3·9865 g/cm^3. Most batches were prepared with a high-purity alumina powder Taimicron TM-DAR‡. In a first step, it was dispersed in distilled water with an organic dispersant and, for batches that were freeze dried, with a binder solution of polyvinyl alcohol and glycerin. With few exceptions given below, all specimens were sintered in air for two hours. Different powder processing resulted in green bodies with different packing homogeneity, requiring different sintering temperatures to achieve the desired density which was then associated with different grain sizes (grain sizes were determined by linear interception: average grain size D = 1·56 × average linear intercept). Hence, the characteristic differences of the approaches will be described here, but it is not intended to discuss details of the technology and of the microstructural development in the present paper.

With Taimicron-DAR, uniaxial pressing required a high sintering temperature (1450°C) to achieve a relative density of about 99%. Bars were formed at a pressure of 200 MPa with a freeze-dried slurry that had been homogenized in an attrition mill for one hour at 1000 rev/min. The relative green density obtained was 57·3%. The high sintering temperature produced an average grain size of 1·25 μm. These specimens were compared with the strength results of coarser microstructures (grain size 2·8 μm) fabricated previously by the same shaping procedure but using A16# as the raw powder, doped with 0·14 wt% MgO (introduced as a solution of $MgCl_2 \cdot 6H_2O$), and sintered at 1590°C for 2·5 hours in air.

Uniaxial pressing of plates (60 × 60 × 7 mm^3) at 50 MPa followed by cold isostatic pressing (CIP) at 700 MPa increased the green density with Taimicron-DAR to 60% and reduced the required sintering temperature by 50 K (to 1400°C). After

†Taimei CHBS Chemicals, Tokyo, Japan, average grain size 0·2 μm, specific surface (BET) 14 m^2/g, >99·99% Al_2O_3.

‡Taimei CHBS Chemicals, Tokyo, Japan, average grain size 0·2 μm (about 75 wt% smaller than 0·4 μm), specific surface (BET) 14 m^2/g, >99·99% Al_2O_3.

#Alcoa, Bauxite, AR, USA, average grain size 0·6 μm (about 75 wt% smaller than 0·8 μm), specific surface (BET) 9·5 m^2/g, >99·9% Al_2O_3.

sintering, bars were cut from the cold isostatically pressed bodies. Compared with uniaxial pressing, CIP samples exhibited a significantly reduced grain size of 0·65 μm; almost equal microstructures and strength data were obtained with reduced pressures of 30 MPa (uniaxial) combined with 350 MPa (CIP). With MgO doping (0·1 wt% added as an $Mg(NO_3)_2$ solution), application of ultrasonically assisted dispersion, and a vacuum de-gassing of the slurry it was possibly to produce green bodies that sintered to a density of 99·0% at 1275°C, but both the microstructure and the strength remained approximately constant. Again, comparative experiments were performed with a coarser microstructure (4·5 μm) fabricated by cold isostatic pressing of A16 powder and sintered at 1620°C for one hour.

Pressure filtration of binder-free slurries on a 0·1 μm membrane at a pressure of 20 bar was preceded by an ultrasonically assisted dispersion of the 0.2 μm powder. Slow drying was required to get samples with a low flaw density. The green density was 66%. Sintering at 1300°C yielded a relative density of 99.0% and an average grain size of 0·59 μm.

Further progress towards smaller grain sizes was achieved by cold isostatic pressing of the green bodies after pressure filtration: after sintering at 1300–1350°C the grain size was 0·4 μm. Differences in details of the processing approach caused a different packing homogeneity of the green bodies and required different sintering temperatures between 1300 and 1400°C. In this way, microstructures with grain sizes up to 4 μm were produced. No significant influence of MgO doping was observed with respect to microstructures or properties.

Aqueous gel casting was performed with a monomer combination of acrylamide (AM) and *N,N'*-methylene-bis-acrylamide (MBAM) described by Young *et al.*[8] Tested monomer concentrations (sum of AM and MBAM related to alumina) were 3·8 and 7·4 wt%, the weight ratio of AM : MBAM was 24 : 1. Before polymerization, the powder in the slurry was carefully dispersed for 0·5 and 2 hours, respectively. Ammonium persulfate was added as initiator. After casting, the molds were immediately placed into a drying chamber under slight vacuum (200 mbar). The chamber was then filled with nitrogen to avoid oxidation, and the temperature was raised to 60°C for one hour. No catalyst was added to accelerate the polymerization. The molds were kept under nitrogen for 8–10 hours after polymerization was finished. The subsequent drying procedure was the same as applied following pressure filtration. One of the gelcast batches was additionally cold isostatically pressed (called batch 2 below).

Casting and pressure filtration are approaches that may give rise to some cooperative alignment of powder particles and to mutual orientation effects which can be assumed to contribute to reduced residual microstresses and to the strength. No detailed X-ray studies were performed to exclude such effects, but a careful scanning and transmission electron microscopy of the raw materials did not reveal any morphological features that might make the powders liable to alignment. Also, X-ray investigations to measure residual microstresses[17] did not give indications of a preferential orientation in the sintered microstructures.

With the large body of fractographic investigations published during the past 20 years it is obvious that such studies can distinguish typical types of flaws that act as an origin of fracture (e.g. defects in the volume of hot-pressed Si_3N_4 but mostly surface and corner flaws in both pressureless sintered and in hot-pressed Al_2O_3 associated with stress corrosion in the latter material in the presence of (humid) air[25]). However, on the rough fracture surfaces it is often very difficult to identify the individual (one?) flaw that initiated failure, and subcritical crack growth frequently obscures the borders (the size) of the flaws. Also, little is known about a statistical analysis of the frequency of flaws per volume unit by fractographic means in ceramics (contrary to some efforts in glasses). Since the question addressed here is focused on the parameters of typically observed strength distributions and does not concern the flaw characteristics of an individual specimen with a given (measured) strength and toughness, the search for flaws on fracture surfaces would promise less insight than the investigation of the volume of the samples, e.g. by investigating the elastic response (which did not reveal significant differences) or by analysing carefully polished cross-sections. A frequency of flaws (FF) was determined by counting all defects $\geq$0·3 μm (different kinds of pores, crack-like flaws). Additionally, a dimensionless flaw 'density' ρ_{fl} that considers both the frequency and the size distribution of defects as observed on polished and thermally etched cross sections was measured using a definition introduced previously for the characterization of microcracks in zirconia-toughened alumina:[26]

$$\rho_{fl} = \frac{\sum l_i^2}{A} \tag{2}$$

where l_i are the apparent maximum lengths of flaws seen on a polished cross-section, and A is the analysed area. In previous studies, this definition provided the best correlation between the microcrack density and the mechanical behaviour compared with other treatments of a given size distribution of microcracks.[27] Probably, this advantage has to

be attributed to the strong impact of larger flaws caused by the square in eqn (2). It is suggested here that this measure might also describe a statistical correlation of flaws observed in the volume of sintered alumina specimens with their strength.

All specimens were ground in the direction of their axes on four sides (to a cross-section of 3×4 mm^2) and chamfered with a resin-bonded diamond wheel of 40–50 μm grain size at a feed rate of 0·01 mm per cut. The strength was measured in three-point-bending with a 24 mm span and with a cross-head velocity of 0·5 mm/min; the load-bearing pins of the jig were free to rotate around and to slide along their axes to minimize frictional effects. Vickers indentations at a load of 98·1 N (10 kgf) were used to measure the indentation toughness K_{Ic} (formula (4) derived by Anstis *et al.*[28] was applied with a parameter $\S_V^R = 0{\cdot}023$ that results from their fitting plot for the Al_2O_3 ceramics investigated there). To test the reliability of the resulting K_{Ic}, some of the batches were chosen for comparative strength-in-bending[29] measurements. No significant difference was observed between the results of the two methods. In each single experiment the average was determined from 5–8 specimens; the typical standard deviations of σ_f and K_{Ic} were ±7–10% with some exceptions that will be discussed separately.

The Young's modulus was derived from the measured resonance frequency. However, all results were quite similar and in the range between about 370 and 390 GPa. No conclusions about the flaw populations could be drawn from the small differences observed.

Careful experiments to study subcritical crack growth kinetics with short cracks (stable fracture of bending bars) revealed significant differences when different materials were compared,[19] but it was not possible to resolve the different kinetics in sintered aluminas of different quality. Another shortcoming is the expense in performing tests with the stable fracture of macroscopic bars which actually makes statistically substantiated results impossible. Therefore, here it was attempted to get a qualitative measure of subcritical crack propagation by comparing the time-dependent growth of indentation cracks in air. Generally, this kind of experiment depends on the driving force that arises from the residual stress at the indentation and does not relax significantly on unloading. However, the value of such investigations is limited when in air most of the subcritical growth occurs immediately after unloading before the first measurement can start. To avoid this problem, the crack length was measured three times: at t_0 immediately after indentation, at t_1 six weeks later, and at t_2 six months after indentation. With a crack length 2c, the observed scatter in the subcritical growth increment $\Delta(2c) = 2c(t_2)-2c(t_1)$ was much less than for the time interval t_1-t_0. Hence, only the results for the growth between t_1 and t_2 are reported here.

With an indentation load of 98·1 N, the typical crack lengths were in the range of 100–200 μm which is 'short' compared with the crack length in precracked bending bars but large compared with typical flaw sizes in high-strength ceramics. In spite of the probable absence of R-curve effects in the fine-grained microstructures investigated here the degree of a possible equivalence in the behaviour of the indentation cracks compared with the growth of shorter flaws is unknown, and any interpretation should be done with care.

Individual samples from batches that represent the whole range of shaping procedures and grain sizes were chosen for this investigation; the number of analysed indentation cracks was about 10–20 in each test. The average crack growth rates were 3×10^{-12} m/s–13×10^{-12} m/s in the first period $t < t_1$ and dropped to $0{\cdot}3 \times 10^{-12}$ m/s–$2{\cdot}3 \times 10^{-12}$ m/s when for $t_1 < t < t_2$ the crack tip proceeded to more distant regions with lower residual stress.

3 Results

Figure 1 compares the influence of different shaping approaches and of the associated green densities on the temperature effect in densification on sintering (2 h, air). Whereas there is no significant effect of the observed green densities, a great shift to lower isothermal sintering temperatures is achieved by the choice of a proper shaping procedure.

The strength results are given in Fig. 2; straight lines represent least square fits calculated for the different shaping approaches. Figure 2 also provides an immediate comparison of the grain size effects

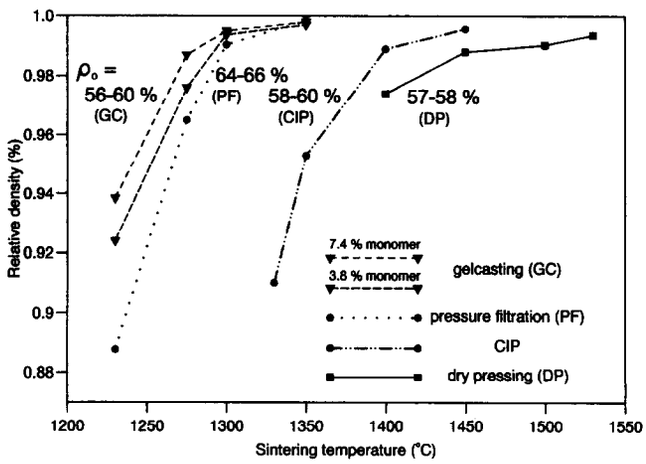

Fig. 1. Influence of shaping approaches and of the associated green densities on the temperature effect in densification on isothermal sintering (2 h, air). All experiments performed using the same corundum powder TM-DAR.

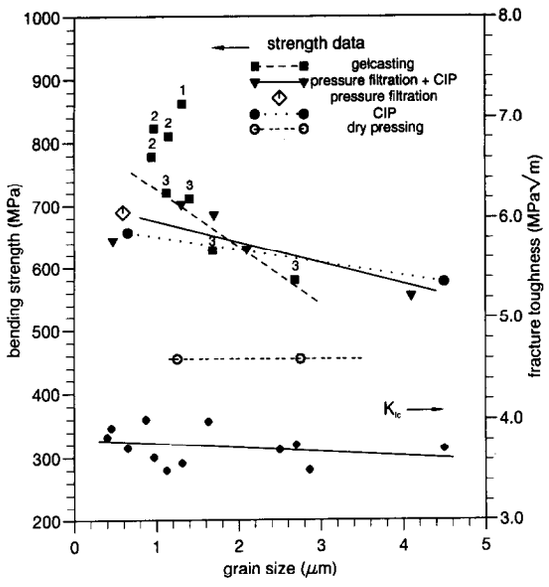

Fig. 2. Grain size and technology effects in the strength and toughness of pressureless sintered alumina. Each data point represents the averages of grain size and strength measured for a group of specimens sintered at the same temperature. The numbers that distinguish different gel casting routes refer to Table 1, different data points for one casting route refer to microstructures sintered at different temperatures.

(the slopes) in strength and toughness. For this end, the axes of strength and toughness are defined such that equal percentages of variations in both properties give approximately equal slopes. It is important to emphasise that each data point in Fig. 2 is an average value of a group of fractured specimens: due to the high number of tested individual specimens, the reliability of the given grain size effects is high even when the slopes are very small. For example, the confidence that the slopes for toughness or for the strength of samples prepared by pressure filtration (+ CIP) are different to zero is higher than 99·9%! Different shaping procedures by gelcasting were tested and are distinguished in Fig. 2 by numbers; results of larger grain size variations are given for batch 3 only, and the least squares fit includes only the data for this batch.

In agreement with recently published results for the special case of isostatically shaped and hot isostatically sintered (pressure 100 MPa) high-purity alumina materials,[14] Fig. 2 shows a grain size effect in the strength which for most of the investigated technological approaches cannot be explained by the almost constant toughness. Obviously, the general trend of increasing strength at reduced grain size is quite different depending on the applied shaping technology. No submicrometre grain size is required to produce pressureless sintered alumina bodies with a high strength of 800–900 MPa. As shown by the example of gelcasting in the grain size range of 1–1·3 μm, relatively small variation of the dispersion procedure within the narrow limits of one technological framework can provide a substantial increase of the strength at almost constant grain size. Table 1 compares microstructures produced by three different gelcasting procedures for the special case of sintering conditions that resulted in similar grain sizes of about 1·15 ± 0·15 μm. The duration of slurry dispersion and differences in the monomer concentration did not affect the sintering temperatures (1275–1300°C) and the grain sizes (1–1·3 μm), but the strength was increased significantly by the improved dispersion. Table 1 suggests that probably both the average strength and the strength distribution are strongly affected by such technological changes. The small standard deviation given in Table 1 for batch 2 at an average grain size of about 1 μm would represent a Weibull modulus of 40–50, but the numbers of specimens in the present investigations are too small to draw final conclusions about the statistics of the observed strength behaviour.

With the strong impact of powder processing demonstrated by Fig. 2, a closer inspection of flaw populations becomes necessary. Figures 3–6 show typical, thermally etched microstructures. Probably, the crack-like flaws in dry-pressed and in cold isostatically pressed samples are relicts from hard granules (Fig. 3a, Fig. 4a). Hence, no such defects exist in the microstructures produced by the wet shaping techniques (pressure filtration (Fig. 5), gel casting (Fig. 6)). Counting all defects >0·3 μm, the frequency of flaws is given in Table 2. In a conventionally dry-pressed microstructure with a strength of 400 MPa this flaw frequency is about two orders of magnitude higher than in the gelcast batch 1 with a strength >800 MPa or in batch 2 with its extremely small standard deviation (Table 1). A similar correlation is obtained with the microflaw density ρ_{fl} that additionally incorporates the size distribution of the flaws: it drops to about 1% when a dry-pressed batch is compared with high-strength gelcast bodies (Table 2).

Table 1. Strength data of gelcast aluminas after pressureless sintering

Batch number	*Monomer content (wt%)*	*Duration of slurry dispersion (min)*	*Grain size (μm)*	*Average strength (MPa)*	*Standard deviation (MPa)*
1	3·8	130	1·31	862	±102
2	7·4 (+CIP)	130	0·97	822	±19
3	3·8	40	1·12	720	±47

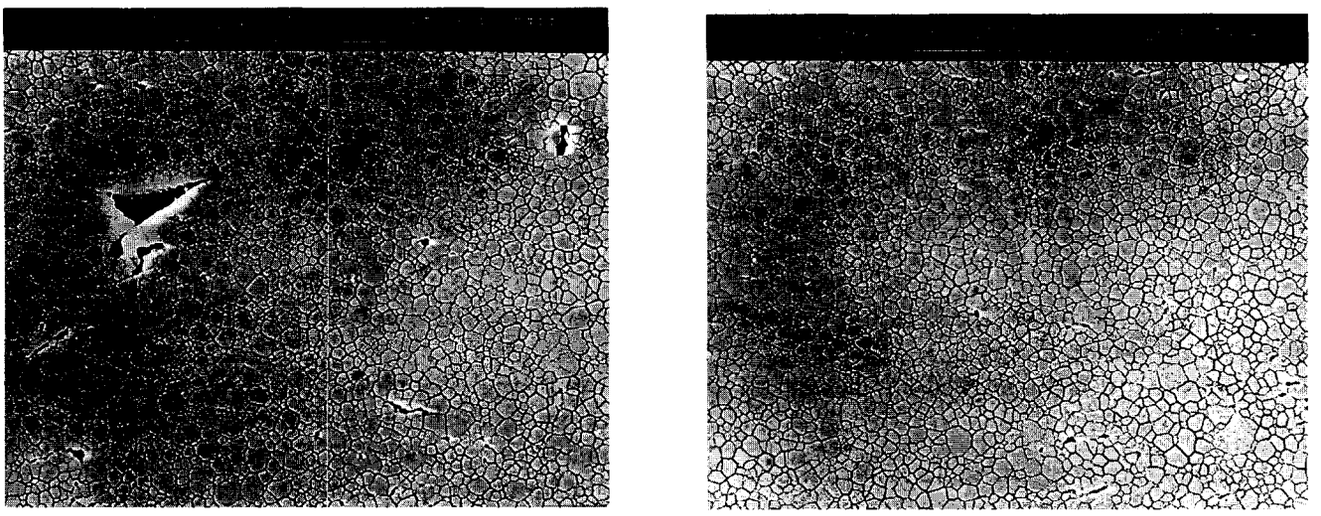

Fig. 3. Heterogeneous flaw distribution in a dry-pressed microstructure sintered at 1450°C. Average grain size 1·25 μm, average strength of this batch 400 ± 60 MPa. (a) Large pores and crack-like flaws, (b) subregion with small flaws only.

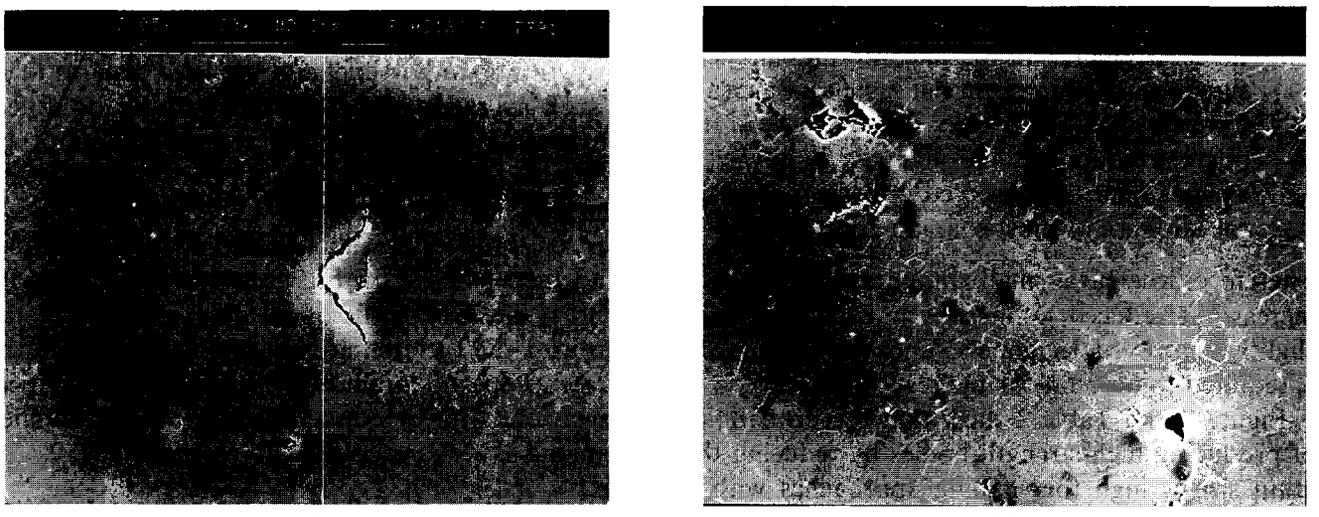

Fig. 4. Smaller defects in alumina bodies fabricated by cold isostatic pressing and sintering at 1400°C. Average grain size 0·65 μm, average strength of this batch 635 ± 32 MPa. (a) Crack-like flaw, (b) pores ≤ grain size.

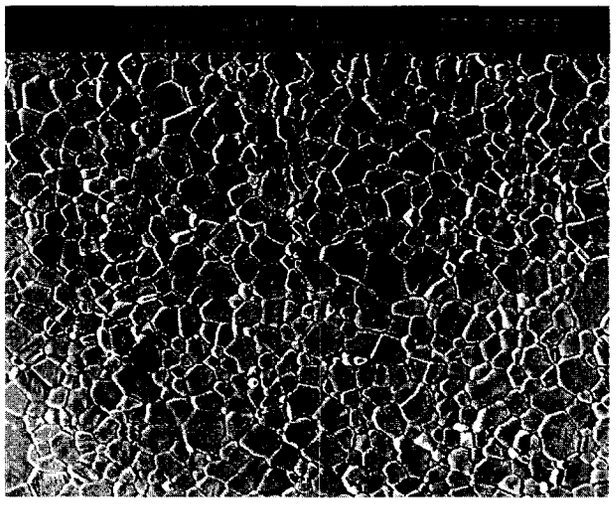

Fig. 5. Homogeneous microstructure: pressure filtration and sintered at 1300°C. Average grain size 0·59 μm, average strength of this batch 689 ± 63 MPa.

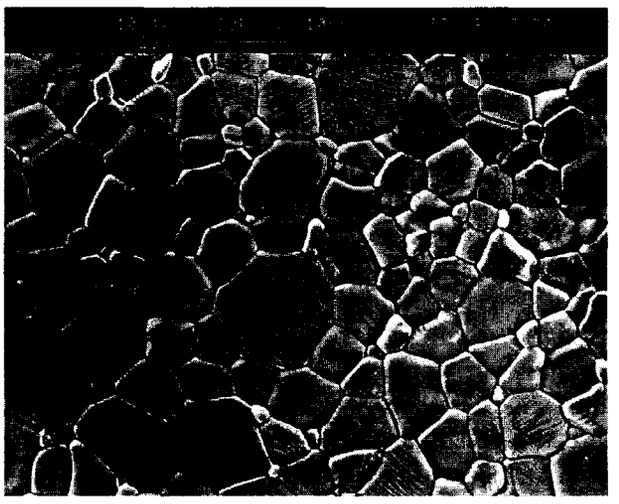

Fig. 6. Gelcast batch 1 (cp. Table 1) sintered at 1300°C. Average grain size 1·31 μm, average strength of this batch 862 ± 102 MPa.

Table 2. Frequency of flaws ≥0·3 μm (FF) and microflaw density ρ_{fl} defined by equation (2)

Shaping approach	*Bending strength (MPa)*	*Grain size (μm)*	*Frequency of flaws FF (10^9 m^{-2})*	*Flaw density ρ_{fl} (10^3)*
Gel casting 1	862 ± 102	1·31	0·7	1
Gel casting 2 (+CIP)	822 ± 19	0·97	0·2	4
Dry pressing	400 ± 60	1·25	50	96

Figure 2 also addresses the question whether the observed variations in strength can be attributed to grain size or technological influences on the fracture toughness:

- Unlike the strength, there is no influence of different processing routes on the toughness, and all data can be described by one least squares' fit.
- Whereas the influence of the grain size on K_{Ic} is so small that none of the measured averages is significantly distinguished from another when individual averages of data sets are compared, the least squares' fit that incorporates all measurements shows a slight but significant increase towards smaller grain sizes. The influence of the microstructure on the toughness is, however, smaller than the observed grain size effect in the strength of most shaping approaches.

Therefore, whereas a small amount of the strength increase at reduced grain sizes is explained by a slightly improved toughness, another mechanism is required to account for the rest.

Figure 2 and Table 2 show that the probability of producing high-strength bodies by reducing the grain size is high for shaping approaches with a potential to give low flaw densities. As suggested in the introduction, reduced subcritical crack growth might explain this observation. However, if some of the strength increase is caused by the toughness, the subcritical effect does not need to be very strong, and stable indentation crack growth had to be assessed for a long time to get measurable results. The lower part of Fig. 7 shows the measured subcritical growth of indentation cracks (testing load 98·9 N) for the time interval t_1 = six weeks → t_2 = six months. As expected, the least squares approximation in Fig. 7 correlates growing subcritical crack elongation with decreasing strength and vice versa. The upper part of Fig. 7 gives the average strength–grain size relationship of those eight batches that were selected for the subcritical measurements. To compare with the following Fig. 8, here the full line is a least squares plot resulting from a linear regression analysis of these eight data points in Fig. 7. To make the comparison with Fig. 2 easier, the broken and the dotted lines in Fig. 7a are the same least squares fits for gelcasting and for cold isostatic pressing as already given in Fig. 2.

With Fig. 8, a plot of the subcritical crack elongation versus the grain size was derived to compare whether the (shaping-influenced!) increase of the strength with reduced grain size in Fig. 2 (and Fig. 7) was really associated with a grain-size effect in subcritical crack propagation. However, whereas more than 150 samples were required to derive the grain size–strength result in Fig. 2, the subcritical tests had to be restricted to a much smaller number. Hence, a proper analysis of possible influences of the shaping procedures on the subcritical crack growth was impossible, and the least squares fit in Fig. 8 averages over samples produced by different approaches. Therefore, the slope cannot be compared with any of the slopes in Fig. 2 but with the slope of the full line in Fig. 7a which characterizes these eight subcritically analysed samples and their batches. In Fig. 8 the measurements 5/6 (CIP), the average fit of all data points, and the group 1–3/7 (gelcasting) indicate an increase of the larger slope for grain-size effect in the subcritical behaviour with the same *technologically* determined ranking as seen in the strength results of Fig. 2.

4 Discussion

The technological background of the different strength–grain size relationships in Fig. 2 and of the different flaw populations demonstrated by Figs 3–6 and Table 2 is, of course, the role of the applied shaping approaches. The data on green densities and sintering in Fig. 1 clearly show that it is really the microstructural homogeneity of the 'green' samples and not simply the green density that dominates the performance: there are differences in the green densities, but just the limiting examples — gel casting and dry pressing — exhibit quite similar green densities which cannot explain the very different densification on sintering. With the identical powder used for all experiments in Fig. 1, the one explanation is a greatly improved homogeneity in the sequence dry pressing, cold isostatic pressing, pressure filtration and gelcasting. With this understanding of the microstructural homogeneity — i.e. the absence of flaws —

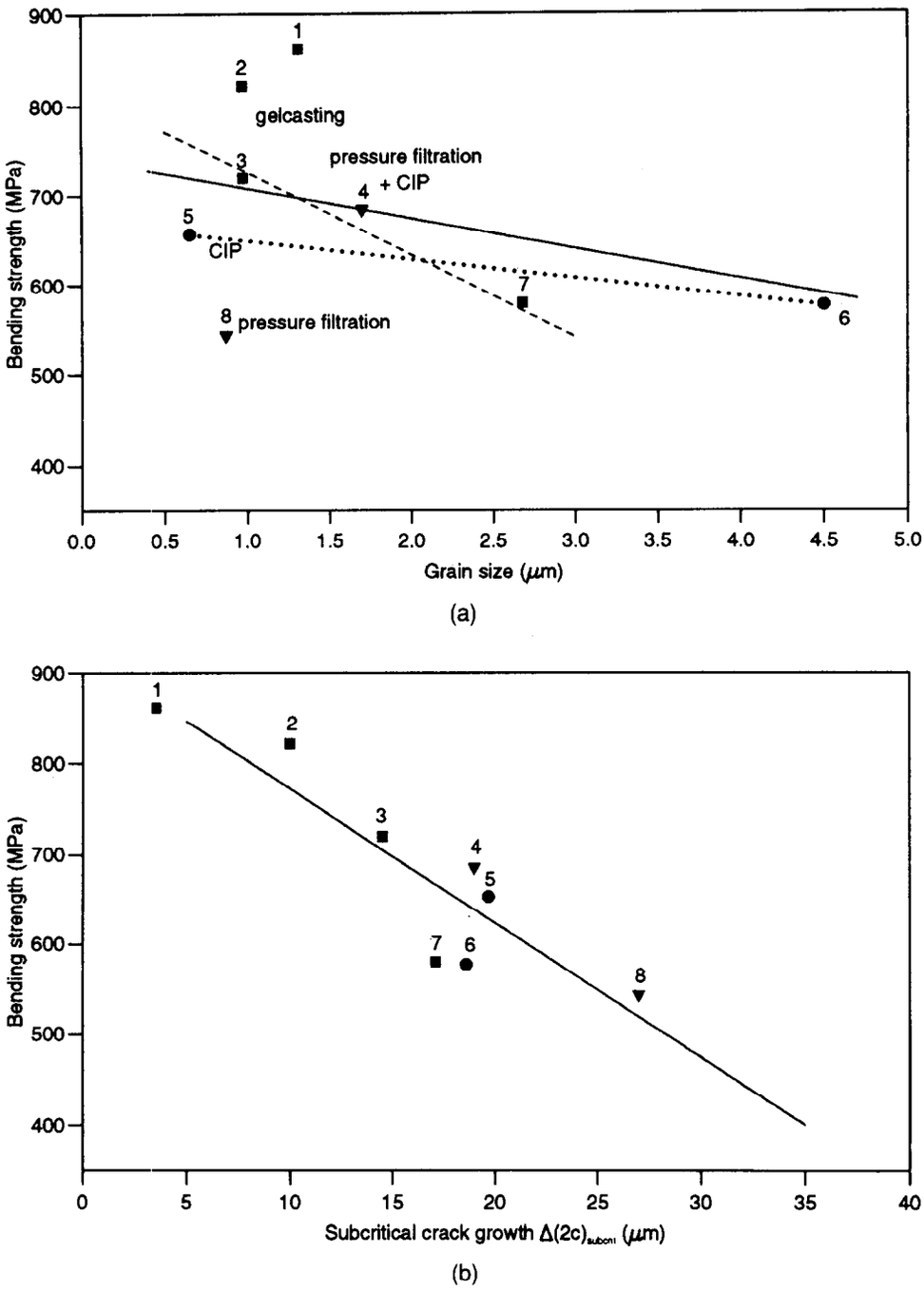

Fig. 7. Strength–grain size relationship (a) and subcritical growth of radial indentation cracks (b) of sintered batches selected from Fig. 2. Straight lines are least squares fits. Strength ranking numbers associate specimens in (b) to batches in graph (a), numbers 1–3 are consistent with Table 1 and Fig. 2.

in the green bodies as the reason of the extremely low sintering temperature of the gelcast samples, it is not surprising to find a low frequency of flaws also in the sintered microstructures (Table 2) and an extremely high strength associated with a very small standard deviation (Table 1, batch 2: high monomer content, + CIP).

The observed trend of an increasing strength at reduced grain size is consistent with other investigations which, on the other hand, also confirm that under constant technological conditions the grain-size effect is small in the grain-size range less than 5 μm.[20] The strongest influence observed in the present experiments (gelcast batch 3) is of the same order as, for example, described for Al_2O_3/Ti(C,N) composites with grain sizes between 0·5 and 2 μm.[30] Actually, the grain-size effect documented in Fig. 2 is small for most of the batches, and the most important conclusion is that within the range investigated, reducing the grain size in the absence of other processing changes does not constitute a useful means of developing high-strength sintered alumina products. For example, a previous report[21] used the same raw material, and an essentially equal shaping procedure (CIP), and arrived at a similar submicrometre grain size

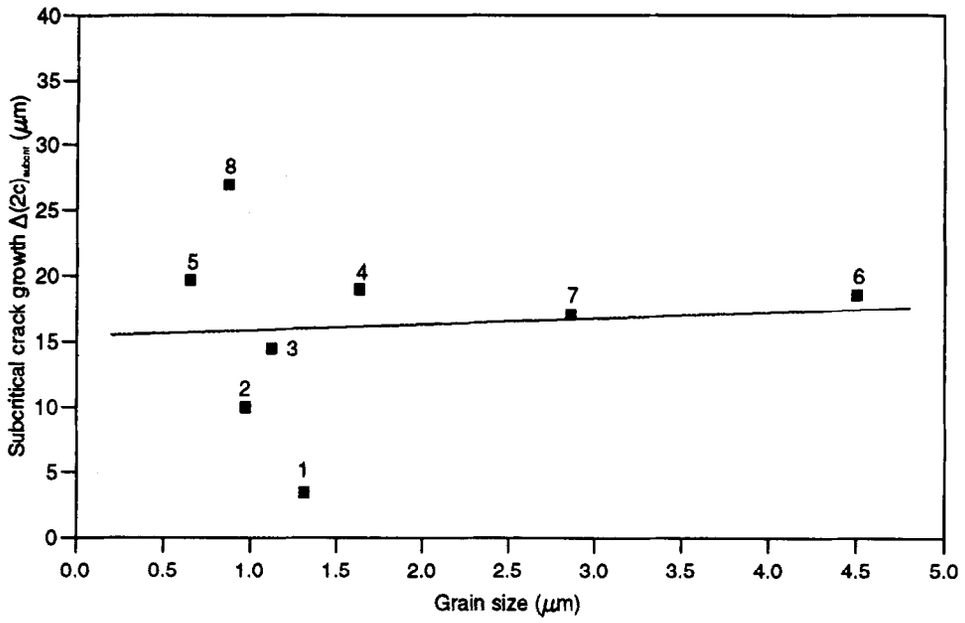

Fig. 8. Subcritical growth of radial indentation cracks versus grain size for the time interval between six weeks and six months after indentation. The straight line is a least squares fit. Strength ranking numbers are identical with Fig. 7.

of 0·8 μm — but the maximum strength was only 380 MPa compared with 660 MPa at 0·65 μm in the present work. The one way to understand these differences is to analyse the flaw structures. Figure 2 and Figs 3–6 together with the observed correlation of flaw densities and strengths (Table 2) demonstrate that the most powerful tool is to develop shaping and sintering procedures that avoid larger defects.

Reduced grain sizes are essential for a high hardness,[22] but they only assist efforts to increase strength or toughness (Fig. 2). Additional mechanisms other than the stress concentration at flaws and the effect of the fracture toughness are probably contributing to the observed high strength of advanced pressureless sintered aluminas and may introduce the observed effects of grain sizes. In analogy with the explanation of the improved wear resistance of sintered fine-grained alumina which is caused by reduced grain pull out,[31] it is suggested that a small grain size and the associated reduced residual stress level may correlate with more perfect grain boundaries and with reduced subcritical growth of the flaws. In fact, reduced subcritical crack growth has been observed to give smaller flaw sizes at instability associated with an increased strength in sintered alumina,[25] zirconia,[19] and in TiC-reinforced oxide ceramics.[10,19] The present results in Fig. 7 strongly support the idea of reduced flaw sizes by decreased subcritical crack growth. Certainly, together with the 6% increase in K_{Ic} for the grain-size range investigated here (Fig. 2) the moderate grain-size effect in the subcritical crack growth data in Fig. 8 (+12%) is too small to explain the 29% strength increase of the investigated batches (Fig. 7). However, with the strong evidence of a shaping influence on the grain-size effect in strength from Fig. 2, the selection of samples from only eight different batches for the subcritical studies imposes significant limitations as to the significance of the fit in Fig. 8, and the real effect may be stronger as indicated by the fit. For example, the gelcast samples 1–3 and 7 suggest a strongly reduced subcritical crack growth at decreasing grain size — a behaviour which compares well with the strong grain-size effect in the strength of only the gelcast batches in Fig. 2 and which may correlate with the fact that with the apparent absence of larger flaws in gelcast microstructures (Fig. 6) defects able to initiate fracture need subcritical growth for their formation. Further, the grain-size influence on subcritical crack growth may depend on the crack propagation rate and may be different at other crack growth velocities than the about 10^{-12} m/s assessed here. On the other hand, the limited significance of the data in Fig. 8 should not be used for extended speculations, and additional subcritical measurements with an expenditure of samples comparable with the strength analyses in Fig. 2 are obviously required to confirm the observed trend of a grain-size effect in the slow growth of flaws.

It is not clear whether this potential ability to increase the strength by reducing the grain size into the region of 1–2 μm will hold in the submicrometre range as well. In the present investigations, none of the tested technological approaches resulted in a significantly improved strength when the grain size was reduced from about 1–1·5 μm to less than 1 μm, and a similar trend was

observed in hot isostatically pressed alumina where a grain-size reduction from 1·1 to 0·8 μm caused a slight drop of the average strength from about 825 to 775 MPa.[14]

New shaping approaches do not only result in an average strength that is twice the level known for conventional alumina or for previous gelcasting results. The measured low frequency of flaws in the high-strength gelcast batch 2 with its small standard deviation of about ±2% indicates that a very high reliability can be achieved in spite of an only moderate toughness if appropriate technologies are developed, but more data with larger series of samples are required to draw valid conclusions about the statistical mechanical behaviour. Nevertheless, the great progress from previously published strength data for gelcast alumina to the present results demonstrates the high potential of this shaping approach.

5 Conclusions

High-purity alumina exhibits an increasing potential for higher strengths at decreasing grain sizes. In advanced high-strength materials, the grain-size effect of the strength is stronger than the slight increase of the toughness. Surprisingly, maximum strength averages were obtained with grain sizes of 1–1·5 μm; contrary to hardness[22] and wear resistance,[31] there was no indication of a further strength improvement in the submicrometre range.

It depends on the flaw population whether this *potential* for a high strength can be exploited or not: the actual significance of the grain-size effect on strength depends on the applied processing, shaping, and sintering approaches. There is a correlation of increasing strength and reduced subcritical crack growth in finer-grained alumina microstructures, but with grain sizes between 0·4 and 4 μm the contribution of defect-avoiding technologies to the achieved increase in strength generally seems to be more important than the pure grain-size effect. With a fixed technology, a decrease of the grain size from the range of 2–5 μm to 0·4–1·5 μm never increased the strength by more than about 150 MPa. On the other hand, technological improvements increased the strength of pressureless sintered bars to more than 800 MPa which is about 400 MPa above the conventional level of high-quality aluminas. With sufficient dispersion, wet-shaping techniques are most promising to reduce the flaw density independent of the different applied approaches (pressure filtration, gel casting).

A reduced flaw density is assumed to be the most effective tool to improve the reliability of pressureless sintered alumina bodies. The results indicate a chance for both a high average strength of more than 800 MPa and a very small standard deviation that represents a Weibull modulus of about 40–50. Such strength properties together with the high hardness,[22] wear resistance[31] and thermodynamic (i.e. oxidative and corrosive) stability will make these advanced alumina ceramics attractive for both well-known and new fields of applications.

Acknowledgments

The investigations have been supported in part by the Deutsche Forschungsgemeinschaft under contract Kr 1398/1-1.

References

1. Riedel, G., Bürger, W., Chylek, S. & Vrbacky, I., Feinkristalline, niedrigsinternde Korundkeramik (Fine crystalline corundum ceramics sintered at low temperature, in German). *Silicates Ind.*, **54** (1/2) (1989) 29–35.
2. Mizuta, H., Oda, K., Shibasaki, Y., Maeda, M., Machida, M. & Oshima, K., Preparation of high-strength and translucent alumina by hot-pressing. *J. Am. Ceram. Soc.*, **75** (1992) 469–73.
3. Hayashi, K., Kobayashi, O., Toyoda, S. & Morinaga, K., Transmission optical properties of polycrystalline alumina with submicron grains. *Mater. Trans.*, **32** (1991) 1024–9.
4. Staehler, J. M., Predebon, W. W. & Pletka, B. J., High strength alumina and process for producing same. Patent Application US-5 352 643, Int. Class. C04B35/10, published 4 Oct 1994.
5. Takahashi, T., Katsumura, Y. & Suzuki, H., Cutting performance of white ceramic tools having high strength (in Japanese). *J. Japan. Soc. Powder & Powder Metall.*, **41** (1994) 33–7.
6. Rajendran, S., Production of ultrafine alpha alumina powders and fabrication of fine grained strong ceramics. *J. Mater. Sci.*, **29** (1994) 5664–72.
7. Graule, T. J., Baader, F. H. & Gauckler, L. J., Shaping of ceramic green compacts direct from suspensions by enzyme-catalyzed reactions. *cfi/Ber. Dt. Keram. Ges.*, **71** (1994) 317–23.
8. Young, A. C., Omatete, O. O., Janney, M. A. & Menchenhofer, P. A., Gelcasting of alumina. *J. Am. Ceram. Soc.*, **74** (1991) 612–16.
9. Krell, A. & Pompe, W., The influence of subcritical crack growth on the strength of ceramics. *Mater. Sci. Eng.*, **89** (1987) 161–8.
10. Krell, A. & Seidel, J., Hochfeste Keramiken auf Al_2O_3-Basis durch kontrollierte Korngrenzenstrukturen (High-strength ceramics on the basis of Al_2O_3 by controlled grain boundary structures, in German). *Fortschrittsber. der Dt. Keram. Ges.*, **9** (1994) 138–57.
11. Rice, R. W., Strength/grain-size effects in ceramics. *Proc. Brit. Ceram. Soc.*, **20** (1972) 275–97.
12. Carniglia, S.C., Reexamination of experimental strength-vs-grain-size data for ceramics. *J. Am. Ceram. Soc.*, **55** (1972) 243–7.
13. Griffith, A. A., The phenomena of rupture and flow in solids. *Philos. Trans. Roy. Soc. (London)*, **221A** (1920–21) 163–98.
14. Miyahara, N., Yamaishi, K., Mutoh, Y., Uematsu, K. & Inoue, M., Effect of grain size on the strength and

fracture toughness in alumina. *JSME International Journal*, **A37** (1994) 231–7.
15. Seidel, S., Claussen, N. & Rödel, J., Reliability of alumina ceramics: Effect of grain size. *J. Europ. Ceram. Soc.*, **15** (1995) 395–404.
16. Blendell, J. E. & Coble, R. L., Measurement of stress due to thermal expansion anisotropy in Al_2O_3. *J. Am. Ceram. Soc.*, **65** (1982) 174–8.
17. Krell, A., Teresiak, A. & Schläfer, D., Grain size dependent residual microstresses in submicron Al_2O_3 and ZrO_2. *J. Europ. Ceram. Soc.*, **16** (1996) 803–11.
18. Krell, A. & Pompe, W., Grain boundary microdamage due to visco-elastic relaxation of residual stresses in alumina ceramics. *Phys. Stat. Sol. (A)*, **111** (1989) 109–17.
19. Krell, A., Grain boundary relevant micromechanical investigations and microstructural observations in ZrO_2 ceramics. In *Proc. 3rd Conf. of the Europ. Ceram. Soc., Vol. 3*, ed. P. Duran & J. F. Fernandez. Faenza Editrice Iberica, San Vicente, 1993, pp. 489–94.
20. Koyama, T., Nishiyama, A. & Niihara, K., Effect of grain morphology and grain size on the mechanical properties of Al_2O_3 ceramics. *J. Mater Sci.*, **29** (1994) 3949–54.
21. ZumGahr, K.-H., Telle, R., Zimmerlin, B. & Park, S.-H., Einfluß der Korngröße auf mechanische Eigenschaften und den ungeschmierten reversierenden Gleitverschleiß von Al_2O_3-Keramik (Influence of grain size on mechanical properties and the unlubricated fretting wear of Al_2O_3 ceramics, in German). *Materialwiss. und Werkstofftechnik*, **23** (1992) 329–38.
22. Krell, A., Grain size dependence of hardness in dense submicron alumina. *J. Am. Ceram. Soc.*, **78** (1995) 1118–20.
23. Nienburg, N., Stein, P. & Harbach, F., Nasse Formgebung von feinkörnigen homogenen α-Al_2O_3-Keramiken (Wet shaping of fine-grained homogeneous α-Al_2O_3 ceramics, in German). *cfi/Ber. Dt. Keram. Ges.*, **66** (1989) 189–97.
24. Lange, F. F., Sinterability of agglomerated powders. *J. Am. Ceram. Soc.*, **67** (1984) 83–9.
25. Kim, B.-N. & Kishi, T., Fractography of Al_2O_3 ceramics strengthened by precoarsening treatments. *J. Ceram. Soc. Japan (Int. Edn.)*, **102** (1994) 1155–9.
26. Krell, A., Blank, P. & Weiss, T., Influence of microcracking and homogeneity on the mechanical behaviour of (Al_2O_3 + ZrO_2) ceramics. *J. Mater. Sci.*, **22** (1987) 3304–8.
27. Krell, A. & Schulze, D., Quantitative Untersuchungen von Mikrorißstrukturen in gesintertem Aluminiumoxid (Quantitative assessment of microcrack structures in sintered alumina, in German). *Silikattechnik*, **36**(12) (1985) 294–6.
28. Anstis, G. R., Chantikul, P., Lawn, B. R. & Marshall, D. B., A critical evaluation of indentation techniques for measuring fracture toughness: I, Direct crack measurements. *J. Am. Ceram. Soc.*, **64** (1981) 533–8.
29. Chantikul, P., Anstis, G. R., Lawn, B. R. & Marshall, D. B., A critical evaluation of indentation techniques for measuring fracture toughness: II, Strength method. *J. Am. Ceram. Soc.*, **64** (1981) 539–43.
30. Koyama, T., Uchida, S. & Nishiyama, A., Effect of microstructure on mechanical properties and cutting performance of Al_2O_3-Ti(C,N) ceramics. *J. Ceram. Soc. Japan (Int. Edn)*, **100** (1992) 520–4.
31. Krell, A. & Klaffke, D., Effects of grain size and humidity on fretting wear in fine-grained alumina, Al_2O_3/TiC, and zirconia. *J. Am. Ceram. Soc.*, **79** (1996) 1139–46.

Journal of the European Ceramic Society **16** (1996) 1201–1207

PII:S0955-2219(96)00055-6
0955-2219/96/$15.00

Discrimination of Multiaxiality Criteria Using Brittle Fracture Loci

A. Brückner-Foit,[a] T. Fett,[b] K.-S. Schirmer[a] & D. Munz[a]

[a]Karlsruhe University, Institute for Reliability and Failure Analysis, PO Box 36 40, D-76021 Karlsruhe, Germany
[b]Research Centre, Karlsruhe, IMF II, PO Box 36 40, D-76021 Karlsruhe, Germany

(Received 19 December 1995; revised version received 26 February 1996; accepted 28 February 1996)

Abstract

The statistical distribution of brittle fracture loci was measured in the Brazilian disc test. A logical circuit was used to identify the fracture event in addition to fractographic examination. The empirical distribution of brittle fracture loci is compared with the predictions of the multiaxial Weibull theory. The results indicate that a shear-insensitive criterion is more suitable than a shear-sensitive criterion to describe the fracture behaviour of natural flaws in ceramic materials. Copyright © 1996 Elsevier Science Ltd

1 Introduction

The failure behaviour of ceramics under multiaxial loading can be described by the Weibull theory, which is developed in Refs 1–4. In this theory, the failure behaviour of natural flaws such as pores, inclusions and grain boundary wedges, is analysed by a fracture mechanics model. The natural flaws are replaced by planar cracks of ideal shapes, and the loading of each crack is quantified in terms of the corresponding stress intensity factors. In general, a randomly oriented crack in a multiaxial stress field is subjected to mixed-mode loading, and an appropriate multiaxiality criterion has to be chosen (see Ref. 5 for a summarizing description of available criteria).

Keeping in mind that the planar cracks in the Weibull theory are in reality natural flaws of various shapes and differing in physical nature, it cannot be concluded without a substantial amount of experimental evidence that there is a universal multiaxiality criterion.[6] Rather, the multiaxiality criterion seems to be specific to a given material and has to be determined by suitable experimental procedures.

Ceramic components are designed to meet a given level of reliability. Within the framework of the Weibull theory, the calculated value of reliability depends on the Weibull parameters and on the multiaxiality criterion. While there is a standard procedure for estimating the Weibull parameters (e.g. Ref. 7), no commonly accepted method exists for determining the failure behaviour of ceramics under multiaxial loading. It can be shown[5] that the variation of the calculated reliability value with the multiaxiality criterion is almost negligible compared with the accuracy of the experimental results if failure is triggered from regions in which a stress state with positive principal stresses prevails. However, great differences may occur if there are positive and negative principal stresses in critical regions, e.g. if a uniaxial tensile operational stress is superimposed on compressive residual stresses. Hence, the multiaxiality criterion can be determined by comparing two different test series — the first performed with specimens in which a tensile stress state prevails, and the second performed with specimens in which the stress tensor is composed of positive and negative principal stresses. Examples are given in Refs 8 and 9.

The problem with all these test series is that specimens having different shapes that were made using different finishing and possibly manufacturing procedures have to be compared with each other. This may lead to incompatible results,[8] even though the Weibull theory is still valid. Hence, a test procedure relying on only one type of specimen seems to be necessary.

This paper deals with the theoretical and experimental evaluation of the local risk of rupture,[10,11] which can be used to discriminate between multiaxiality criteria. The following section contains the definition of the local risk of rupture and the corresponding cumulative distribution function. This quantity can be determined if the location of the critical flaw is measured on the fracture surface of a failed specimen. The corresponding experimental procedure is described in the next section. The experimental results including the Weibull analysis are then presented, while theory and experiment are compared in the final section.

Theory

Most of the information presented in this section has already been given in previous publications[5,11] and is repeated here for the sake of completeness. First, the basic ideas of the Weibull theory will be summarized. The probability that the size of a given flaw will exceed the critical flaw size a_c is expressed by:

$$Q_1 = \int_V f_x(x) \int_\Omega f_\Omega(\Omega) \int_{a_c(x,\Omega)}^{\infty} f_a(a)\, \mathrm{d}a\, \mathrm{d}\Omega\, \mathrm{d}x \quad (1)$$

where V denotes the volume of the component considered, Ω the surface of a unit radius sphere, x the coordinate vector, and $f_x(x)$, $f_\Omega(\Omega)$, $f_a(a)$ are the probability density functions of the corresponding random variables.

The critical flaw size can be determined using fracture mechanics, if the natural flaws can be approximated by planar cracks. Within the framework of this model, a multiaxial stress state gives rise to mixed-mode loading of a crack, and the critical crack size is a function of the mode I to mode III stress intensity factors K_I, K_{II}, K_{III}:

$$a_c = a_c(K_I, K_{II}, K_{III}) \quad (2)$$

with

$$K_I = \sigma_n \sqrt{a Y_I}$$
$$K_{II} = \tau \sqrt{a Y_{II}} \quad (3)$$
$$K_{III} = \tau \sqrt{a Y_{III}}$$

where Y_I, Y_{II} and Y_{III} are correction factors. The stress σ_n normal to the crack plane is given by the following relation:

$$\sigma_n = (\sigma_1 \cos^2\phi + \sigma_2 \sin^2\phi) \sin^2\theta + \sigma_3 \cos^2\theta \quad (4)$$

where σ_1, σ_2, σ_3 are the principal stresses and ϕ, θ are the polar angles determining the orientation of the crack plane relative to the principal axes. The shear stress τ in the crack plane is given by:

$$\tau = \sqrt{\tau_{r\phi}^2 + \tau_{r\theta}^2} \quad (5)$$

with

$$\tau_{r\phi} = (\sigma_2 - \sigma_1) \sin\phi \cos\phi \sin\theta \quad (6)$$

and

$$\tau_{r\theta} = (\sigma_1 \cos^2\phi + \sigma_2 \sin^2\phi - \sigma_3) \sin\theta \cos\theta \quad (7)$$

An equivalent mode I stress intensity factor K_{Ieq} can be introduced with

$$K_{Ieq} = \sigma_{eq} \sqrt{a Y_I} \quad (8)$$

where the equivalent stress σ_{eq} depends on σ_n, τ and on Y_I, Y_{II} and Y_{III}. The critical crack size is given by:

$$a_c = \left(\frac{K_{Ic}}{\sigma_{eq} Y_I} \right)^2 \quad (9)$$

where K_{Ic} denotes the fracture toughness. A variety of multiaxiality criteria are given in the literature leading to different expressions for σ_{eq}. A summary is contained in Ref. 5.

An example of one of these criteria for penny-shaped cracks is[12]

$$\sigma_{eq} = \left[\sigma_n^4 + 6 \left(\frac{2}{2-\nu} \right)^2 \sigma_n^2 \tau^2 + \left(\frac{2}{2-\nu} \right)^4 \tau^4 \right]^{1/4} \quad (10)$$

which is derived on the assumption that the crack extends on the plane where the energy release rate is maximum. The shear insensitive criterion:

$$\sigma_{eq} = \sigma_n \quad (11)$$

is applicable if the natural flaws extend solely because of mode I loading.

In the Weibull theory the following expression is used for the integral over the crack size in eqn (1):[7]

$$\int_{a_c(x,\Omega)}^{\infty} f_a(a)\mathrm{d}a = \left(\frac{\sigma_{eq}(x,\Omega)}{\tau_0} \right)^m \quad (12)$$

where eqn (9) was used for the critical crack size. The parameters m and τ_0 in eqn (12) depend on the toughness of the matrix material and on the statistical properties of the flaw size distribution.

If all locations of flaws and all orientations occur with equal probability, the material is homogeneous and isotropic, and $f_x(x)$ and $f_\Omega(\Omega)$ can be replaced by uniform distributions:

$$Q_1 = \frac{1}{V} \int_V \frac{1}{4\pi} \int_\Omega \left(\frac{\sigma_{eq}}{\tau_0} \right)^m \mathrm{d}\Omega \mathrm{d}x \quad (13)$$

The number n of cracks in the volume V is also a random variable and can be described by a Poisson distribution. The probability of having exactly n cracks in V is given by:

$$p_n = \frac{M^n \mathrm{e}^{-M}}{n!} \quad (14)$$

where M is the average number of cracks in V. The following relation is obtained for the failure probability P_f, from eqns (13), (14)[5] and by summing up all possible numbers of cracks:

$$P_f = 1 - \exp(-M\, Q_1) \quad (15)$$

These basic ideas of the Weibull theory will now be used to define the local risk of rupture.

The probability that a flaw is located in a subvolume V_s and propagates unstably is equal to

$$Q_1(V_s) = \frac{1}{V} \int_{V_s} \frac{1}{4\pi} \int_\Omega \left(\frac{\sigma_{eq}}{\tau_0} \right)^m \mathrm{d}\Omega \mathrm{d}x \quad (16)$$

The survival probability of a flaw located in V_s or $V - V_s$ is given by:

$$R_1(V) = 1 - Q_1(V) \tag{17}$$

If n flaws are present in V, none of them propagates unstably with the probability

$$R_n(V) = (1 - Q_1(V))^n \tag{18}$$

Hence fracture is triggered by one flaw in V_s and all other $n - 1$ flaws remain stable with the probability

$$S_n(V_s) = n\, Q_1(V_s)\,(1 - Q_1(V))^{n-1} \tag{19}$$

Combining eqn (19) with the probability p_n, eqn (14), to have n flaws in V and summation over n yields the probability that there is exactly one unstable flaw contained in the subvolume V_s and an arbitrary number of non-propagating flaws in V:

$$S(V_s) = \sum_{n=0}^{\infty} p_n\, S_n(V_s) \tag{20}$$

i.e.

$$S(V_s) = M\, Q_1(V_s) \exp(-M\, Q_1(V)) \tag{21}$$

The normalized quantity

$$P_0(V_s) = \frac{S(V_s)}{S(V)} \tag{22}$$

is the quotient of the fracture risks associated with the volumes V_s and V, respectively, and can be written as:

$$P_0(V_s) = \frac{Q_I(V_s)}{Q_I(V)} \tag{23}$$

$P_0(V_s)$ is independent of the applied load level.

For a very small subvolume, $V_s = \mathrm{d}x$, the integral over V_s can be replaced by the integrand times $\mathrm{d}x$, and the probability is obtained that failure is caused by a flaw at point x in the interval $[x, x + \mathrm{d}x]$:

$$p_0(x)\,\mathrm{d}x = \frac{\int_\Omega (\sigma_{eq})^m\,\mathrm{d}\Omega}{\int_V \int_\Omega (\sigma_{eq})^m\,\mathrm{d}\Omega \mathrm{d}x} \tag{24}$$

The quantity p_0 corresponds to the marginal probability density function of the location of the fracture origins obtained by Matsuo and Kitakami[10] using the competing risk theory, and P_0 in eqn (23) is the corresponding probability distribution function if V_s is defined as an interval in three-dimensional space. p_0 also corresponds to the local risk of fracture.

The cumulative probability distribution function of the fracture loci:

$$P_0(X \le x_0,\ Y \le y_0,\ Z \le z_0)$$

$$= \frac{\int_0^{x_0} \int_0^{y_0} \int_0^{z_0} \int_\Omega \sigma_{eq}^m(\Omega, x, y, z)\,\mathrm{d}\Omega\,\mathrm{d}z\mathrm{d}y\mathrm{d}x}{\int \int_V \int \int_\Omega \sigma_{eq}^m(\Omega, x, y, z)\,\mathrm{d}\Omega\,\mathrm{d}z\mathrm{d}y\mathrm{d}x} \tag{25}$$

can be determined for any specimen or component, if the location (x_0, y_0, z_0) of the fatal flaw is measured.

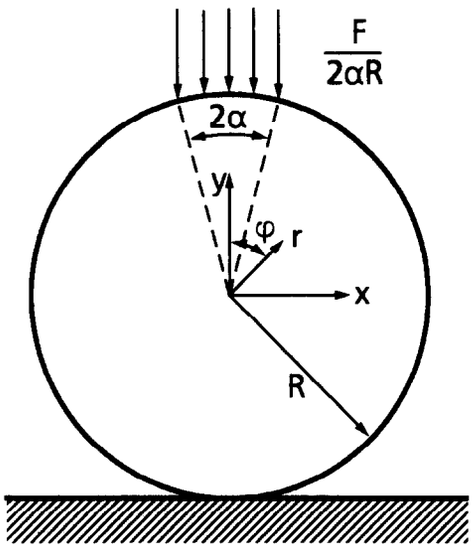

Fig. 1. Brazilian disc test.

Experiments

In the Brazilian disc test a circular disc is subjected to diametral compression (Fig. 1). A biaxial stress state is induced which contains both tensile and compressive components (see next section). The test was applied successfully to rock materials and low-strength ceramics.[13,14] Preliminary tests with high-strength ceramics[15] showed that fracture of the majority of specimens was triggered by flaws on the perimeter in the vicinity of the load pins where a zone of global damage develops due to high compressive loads. An additional failure mode (splitting of a specimen parallel to the disc surface) could be attributed to high tensile stresses on the perimeter normal to the disc surface that are induced by friction between the load pins and the disc.[16] These unwanted failure modes can be almost completely eliminated by a special design of the specimen grips (Fig. 2). A compressive force perpendicular to the disc surface is imposed by the screws in the vicinity of the load pins.

The location of the fracture origins was measured in two different ways. First, a careful fractographic examination was carried out in which both the fracture pattern (see Fig. 3) and the fracture surfaces were studied. In a second method of evaluation, a series of parallel conducting strips of silver was deposited on the disc surfaces. They were used as logical electrical switches which are in the 'on' state in the case of the intact disc and change to the 'off' state upon passage of the crack tip. A logical circuit analyses the time sequence of rupture and allows the location of the failure origin to be determined.

A mounted specimen is shown in Fig. 4. The fracture origin is assumed to be located in the vicinity of the first ruptured strip. Those specimens for which no fracture locus could be identified

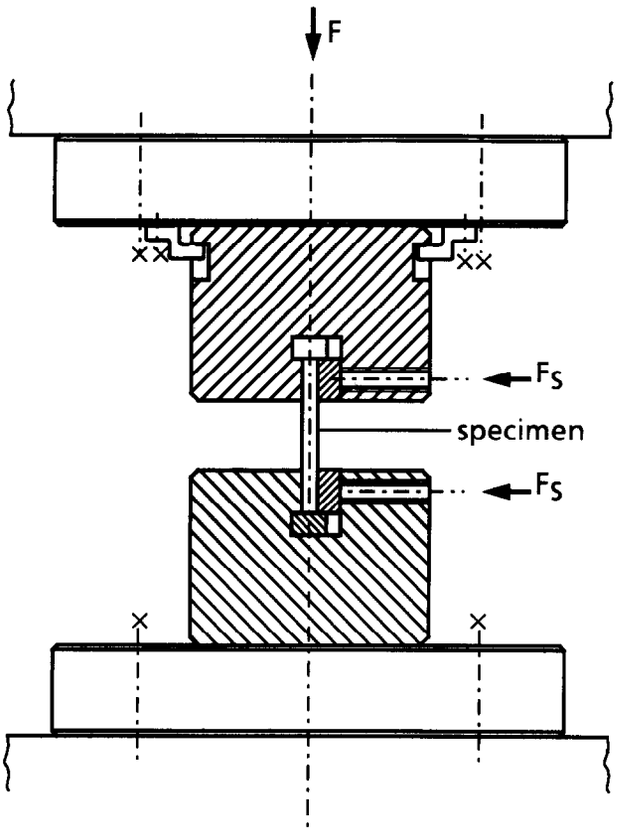

Fig. 2. Schematic representation of the test rig for the Brazilian disc test.

outside the specimen grips were eliminated from the test series, because failure may have been triggered from the damage zone in the vicinity of the load pins.

Three different materials were tested, a low-strength ceramic (stoneware trade name: Keraion), and two high-strength silicon nitride materials. The material parameters are summarized in Table 1. The radius of the discs was R = 22·5 mm in all cases. The thickness t of the stoneware disks was 7·4 mm, whereas t = 4·0 mm was used for the silicon nitrides. The loading rate was comparatively small (7 MPa s^{-1} for the stoneware material, 3 MPa s^{-1} for the silicon nitrides) in order to avoid complete specimen destruction after fracture. The load was transferred to the disc via comparatively soft steel plates, which deformed plastically under the high compressive loads.

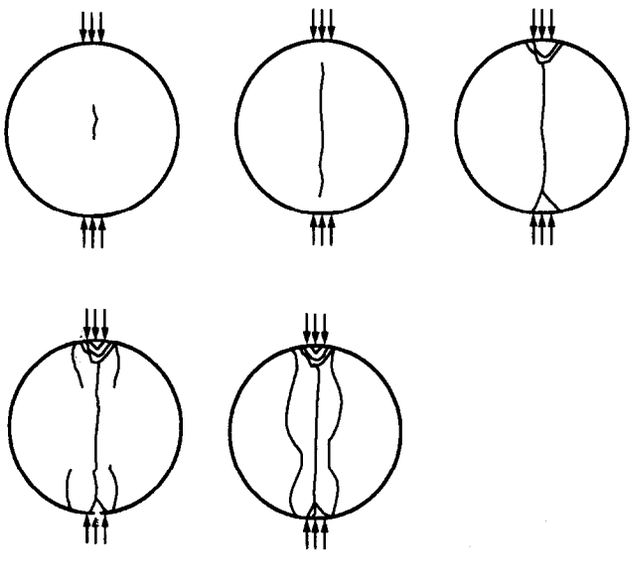

Fig. 3. Development of a typical fracture pattern starting from a central crack.

Results

The Weibull exponent m is required for the prediction of the distribution of fracture loci [see eqn (24)]. Therefore, a statistical analysis was performed of the fracture stresses. First, the test results were plotted on Weibull paper. Then, the parameters of the corresponding Weibull distributions were calculated using the maximum likelihood method.[17] A bias correction factor was introduced for the parameter m.[17] The results of the Weibull analysis are summarized in Table 2. The Weibull parameter b in Table 2 is defined as:

$$b = \tau_0 \left[\frac{M}{V} \int_V \frac{1}{4\pi} \int_\Omega \left(\frac{\sigma_{eq}}{\sigma^*} \right)^m d\Omega dx \right]^{-1/m} \quad (26)$$

with the reference stress σ^*, from which the failure probability can be written in terms of a Weibull distribution:

$$P_f = 1 - \exp\left[-\left(\frac{\sigma^*}{b} \right)^m \right] \quad (27)$$

The fractographic examination yielded results which are only reliable for the silicon nitrides. The fracture loci were very hard to identify on the fracture surface for the stoneware material, and the analysis had to be based on the rupture of the silver strips. Hence, only the y-coordinate of the fracture loci (see Fig. 1) was available.

The observed values y_i were ranked in ascending order and the empirical probability

$$P_i(y_i) = \frac{i}{N} \quad (28)$$

was attributed to the ith value, where N is the sample size. The resulting step functions are shown in Figs 5–7.

Discussion

The stress field of the Brazilian disc is given by:[18]

$$\sigma_{rr} = -\frac{F}{\pi t R} \quad (29)$$

$$\times \left\{ 1 + \sum_{n=1}^{\infty} \left[1 - \left(1 - \frac{1}{n} \right) \frac{r^2}{R^2} \right] \left(\frac{r}{R} \right)^{2n-2} \frac{\sin 2n\alpha}{\alpha} \cos 2n\phi \right\}$$

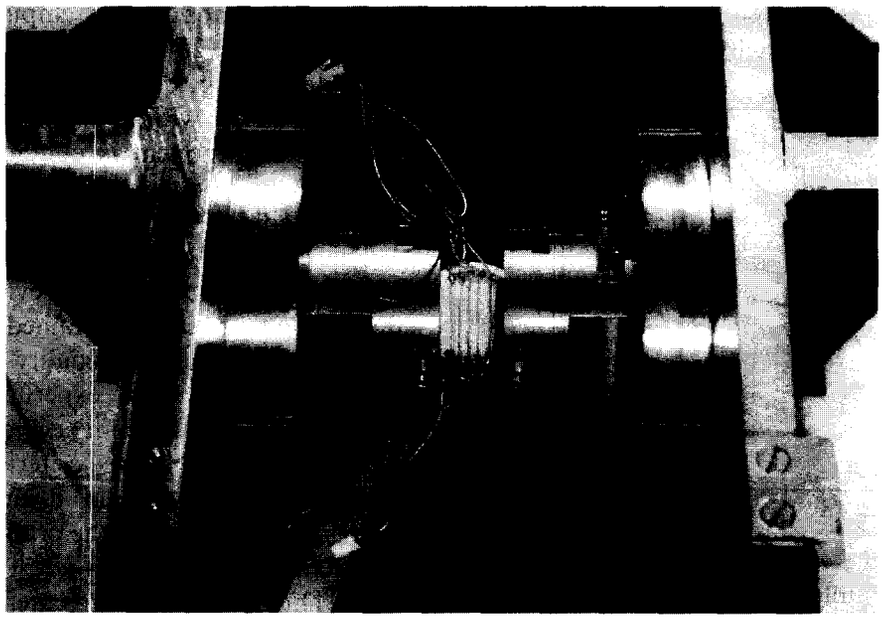

Fig. 4. Fixture with specimen mounted.

$$\sigma_{\phi\phi} = -\frac{F}{\pi\, t\, R} \times \left\{1 - \sum_{n=1}^{\infty}\left[1 - \left(1 + \frac{1}{n}\right)\frac{r^2}{R^2}\right]\left(\frac{r}{R}\right)^{2n-2}\frac{\sin 2n\alpha}{\alpha}\cos 2n\phi\right\} \quad (30)$$

$$\sigma_{r\phi} = -\frac{F}{\pi\, t\, R} \times \left\{\sum_{n=1}^{\infty}\left[1 - \left(1 + \frac{1}{n}\right)\frac{r^2}{R^2}\right]\left(\frac{r}{R}\right)^{2n-2}\frac{\sin 2n\alpha}{\alpha}\cos 2n\phi\right\} \quad (31)$$

where r, ϕ are the polar coordinates defined in Fig. 1. The loading angle α defines the area on the perimeter over which the load is uniformly distributed. The stress fields perpendicular to the loading axis ($y = 0$) and along the loading axis ($x = 0$) are shown in Figs 8 and 9, respectively.

This stress field is inserted in the appropriate multiaxiality criterion, eqns (10) and (11), respectively, in order to determine σ_{eq} which, in turn, is inserted in the marginal probability distribution of fracture loci:

$$P_0\,(Y \le y_0) = \frac{2\int_0^{\pi}\int_0^{r_0}\int_0^{t}\int_{\Omega}\sigma_{eq}^{m}\,d\Omega\,dz r dr d\phi}{2\int_0^{\pi}\int_0^{R}\int_0^{t}\int_{\Omega}\sigma_{eq}^{m}\,d\Omega\,dz r dr d\phi} \quad (32)$$

where $y_0 = r_0 \sin\phi$ and r and ϕ are the polar coordinates defined in Fig. 1; R denotes the radius of the disc, and t its thickness.

Table 1. Material parameters

Material	*Manufacturer*	*Poisson's ratio*	*Young's modulus (GPa)*	*Fracture toughness* ($MPa\sqrt{m}$)
Keraion (stone-ware)	Keramische Betriebe Buchtal	0·25	52	0·9
HIPSN	ABB	0·24	300	4·3
HIPSN	ESK	0·24	300	4·9

Table 2. Results of Weibull analysis

Material	*Sample size*	*Weibull exponent,* m	*Weibull parameter,* b *(MPa)*
Stoneware	20	35·6 [26·4, 48·4]	37·5 [37·1, 37·9]
HIPSN (ABB)	14	10·5 17·3. 15·2]	553 [529, 579]
HIPSN (ESK)	21	6·0 [4·5, 8·2]	672 [630, 718]

Equation (32) implies that fracture is triggered from a flaw at $0 \leq y \leq y_0$ with the probability P_0.

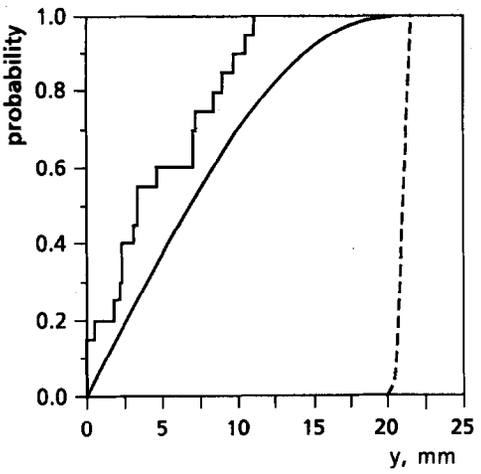

Fig. 5. Cumulative distribution function of brittle fracture loci, stoneware material: ———, prediction using the shear-insensitive criterion, eqn (11); – – – –, prediction using the shear-sensitive criterion, eqn (10).

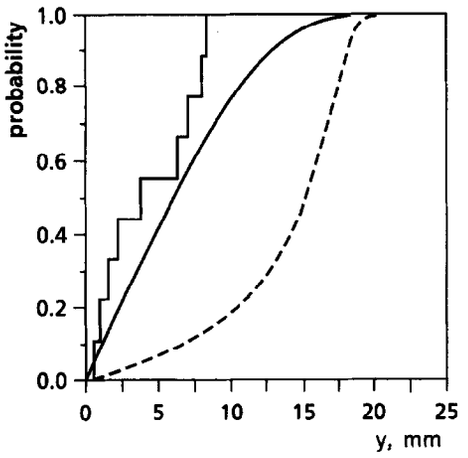

Fig. 6. Cumulative distribution function of brittle fracture loci, HIPSN (ABB material); ———, prediction using the shear-insensitive criterion, eqn (11); – – – –, prediction using the shear-sensitive criterion, eqn (10).

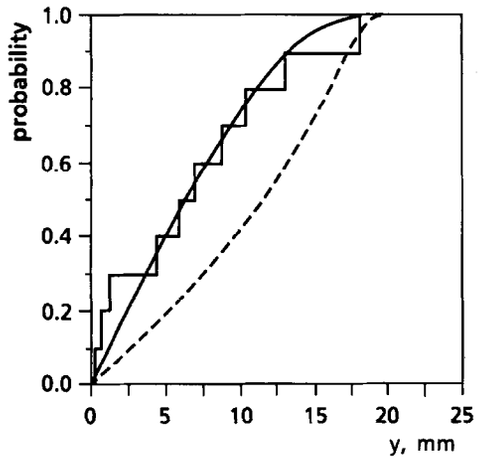

Fig. 7. Cumulative distribution function of brittle fracture loci, HIPSN (ESK material): ———, prediction using the shear-insensitive criterion, eqn (11); – – – –, prediction using the shear-sensitive criterion, eqn (10).

This corresponds to the empirical probability p_i defined in eqn (28). The integrals in eqn (32) were evaluated using the multiaxiality criteria [eqns (10) and (11)], with the bias-corrected values of the Weibull exponent m contained in Table 2. In Figs 5–7 the results are compared with the experimental findings.

The empirical distribution of the fracture loci of the stoneware material deviates strongly from the theoretical curve obtained with eqn (32) if a shear-sensitive multiaxiality criterion is used. The theoretical and experimental distribution functions are only compatible with each other if the shear-insensitive criterion is applied. In this case, the maximum distance between both curves does not exceed the critical distance defined in a Kolmogorov–Smirnov test at 95% confidence level. This result is in agreement with the findings in Ref. 9 where the distributions of fracture stress obtained in different test series including the Brazilian disc test were compared with each other.

Similar results are obtained for the silicon-nitride materials. The difference between the shear-sensitive and the shear-insensitive criteria is less pronounced than for the Keraion material due to lower values of the Weibull exponent m. Nevertheless, the shear-sensitive criterion is ruled out by comparison of the theory with the experiment,

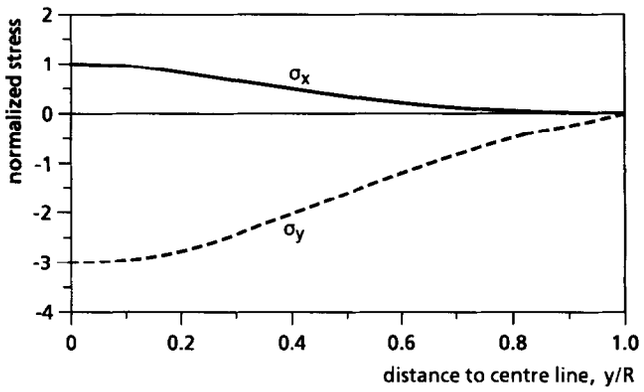

Fig. 8. Stress distribution in the disc perpendicular to the load axis.

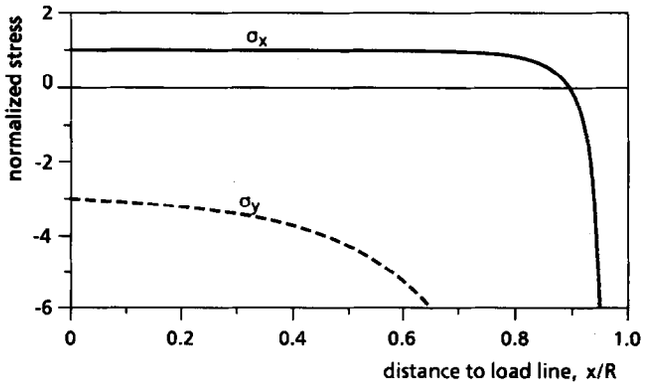

Fig. 9. Stress distribution in the disc along the load axis.

whereas the shear-insensitive criterion yields a distribution function which is compatible with the empirical distribution in terms of a Kolmogorov–Smirnov test. A similar result was obtained by comparing the Weibull distributions obtained with various test series.[9]

The agreement between theory and experiment appears to be slightly better for the silicon nitride materials than for the stoneware material, although in all cases the discrepancies between predicted and measured distributions are within the range of statistical uncertainty. However, this tendency may be attributed to the fact that for the silicon nitride materials the empirical distributions are based on fractographic evidence, whereas the results for the stoneware rely completely on the indications of the logical circuit. This may reduce the accuracy of the experimental values for the brittle fracture loci.

Conclusions

The cumulative distribution function of the fracture loci can be derived using the local risk of rupture. As the distribution function depends on the multiaxiality criterion in a way similar to the failure probability of the multiaxial Weibull theory, this quantity can be used to discriminate between various criteria. The advantage of this procedure is that only specimens of a specific type have to be compared with each other, and the well-known problems concerning different manufacturing routines and surface-finishing procedures are avoided, which may greatly influence the results obtained with test series performed with different kinds of specimens. The cumulative distribution function of fracture loci was measured using low- and high-strength ceramics. The test method selected was the Brazilian disc test, because the complicated stress state prevailing in the specimens leads to great differences in the predictions obtained with different multiaxiality criteria. The comparison between theory and experiment indicates that the failure behaviour of natural flaws in the materials tested should be described by a shear-insensitive criterion. This means that if a planar crack is assigned to each natural flaw, this crack fails through pure mode I fracture.

References

1. Batdorf, S. B. & Crose, J. G., A statistical theory for the fracture of brittle structures subjected to nonuniform polyaxial stress. *J. Appl. Mech.*, **41** (1974) 267–72.
2. Batdorf, S. B. & Heinisch, H. L., Weakest link theory reformulated for arbitrary fracture criterion. *J. Am. Ceram. Soc.*, **61** (1978) 355–8.
3. Evans, A. G., A general approach for the statistical analysis of multiaxial fracture. *J. Am. Ceram. Soc.*, **61** (1978) 302–8.
4. Matsuo, Y., A probabilistic analysis of the brittle fracture loci under bi-axial stress state. *Bull. JSME*, **24** (1981) 290–4.
5. Thiemeier, T., Brückner-Foit, A. & Kölker, H., Influence of the fracture criterion on the failure probability of ceramic components. *J. Am. Ceram Soc.*, **74** (1991) 48–52.
6. Lamon, J., Statistical approaches to failure for ceramic reliability assessment. *J. Am. Ceram. Soc.*, **71** (1988) 106–12.
7. DIN 51110, Parts 1–3, Prüfung von keramischen Hochleistungswerkstoffen, 1990.
8. Brückner-Foit, A., Berweiler, W., Hollstein, T., Mann, A., Munz, D. & Schirmer, K.-S., Mechanical characterization of engineering ceramics. Final Report, IEA Annex II, Subtask 5, University of Karlsruhe, September 1993.
9. Brückner-Foit, A., Fett, T., Munz, D. & Schirmer, K.-S., Discrimination of multiaxiality criteria with the Brazilian disk test. *J. Eur. Ceram. Soc.*, in press.
10. Matsuo, Y. & Kitakami, K., On the statistical theory of fracture location combined with competing risk theory. In *Fracture Mechanics of Ceramics, Vol. 7*, eds R. C. Bradt *et al.* Plenum Press, New York, 1986, pp. 223–35.
11. Brückner-Foit, A., Heger, A. & Munz, D., Effect of proof testing on the failure probability of multiaxially loaded ceramic components. In *Life Prediction Methodologies and Data for Ceramic Materials, ASTM STP 1201*, eds C. R. Brinkmann & S. F. Duffy. American Society for Testing and Materials, Philadelphia, 1994.
12. Hellen, T. K. & Blackburn, W. S., The calculation of stress intensity factors for combined tensile and shear loading. *Int. J. Fract.*, **11** (1975) 605–17.
13. Jaeger, J. C. & Hoskins, E. R., Rock failure under the confined Brazilian test. *J. Geophys. Res.*, **71** (1966) 2651–5.
14. Marion, R. H. & Johnstone, J. K., A parametric study of the diametral compression test for ceramics. *Am. Ceram. Soc. Bull.*, **56** (1977) 998–1002.
15. Bernauer, G., Untersuchung zu Anwendbarkeit des Spaltzugversuchs zur Ermittlung der Zugfestigkeit. Master Thesis, University of Freiburg, 1991.
16. Schäfer, R., Soltész, U. & Bernauer, G., 3-D-Finite-Elemente-Analyse zur Lokalisierung des Bruchursprungs im Spaltzugversuch, *IWM-Report W 3/95*, Fraunhofer-Institute for Mechanics of Materials, Freiburg, 1995.
17. Thoman, D. R., Bain, L. J. & Antle, C. E., Inferences of the parameters of the Weibull distribution. *Techometrics*, **11** (1969) 445–60.
18. Hondros, G., The evaluation of Poisson's ratio and the modulus of materials of a low tensile resistance by the Brazilian disk test with particular reference to concrete. *Australian J. Appl. Sci.*, **10** (1959) 243–68.

Journal of the European Ceramic Society **16** (1996) 1209–1212

PII:S0955-2219(96)00047-7
0955-2219/96/$15.00

The Median Crack Driven by a Point Force

D. A. Hills, D. N. Dai & P. D. Warren*

Department of Engineering Science, Oxford University, Parks Road, Oxford OX1 3PJ, UK

(Received 13 December 1995; revised version received 16 February 1996; accepted 20 February 1996)

Abstract

The shape of a median crack, driven by a point force, is deduced. It is shown that if it is assumed that self-arrest occurs when the crack tip stress intensity factor falls below the fracture toughness, a near-circular crack may be expected to develop. A universal calibration for the crack tip stress intensity factor is given. Copyright © 1996 Elsevier Science Ltd

Introduction

When a sharp indenter is pressed into a brittle material, median cracks are observed to develop on planes normal to the free surface and aligned with the vertices. This test provides the possibility of determining the fracture toughness of a brittle material and other useful surface information. It is experimentally observed that median cracks form during the loading phase of indentation, but often extend during the unloading phase,[1,2] clearly propelled by residual stresses left by plasticity arising at the tip of the indenter. Recently, both Giannakopoulos *et al.*[3] and Murakami and Matsuda[4] have produced very thorough solutions to the problem of indentation of an elastic–plastic solid by a Vickers pyramid. Each used the finite element method, the former incorporating special elements to allow for the singular stress state arising along the vertices, to produce an accurate, versatile solution. Neither, however, solved the unloading phase, so that the residual stress state remaining upon removal of the indenter has not been found. This is one of the two obstacles remaining before a physical interpretation of the results of the test can be used quantitatively. The second is that a precise calibration for the crack tip stress intensity factor arising around the crack front is needed. In this paper we intend to address the second problem, and, in the absence of a solution for the residual stress state, we shall use an idealized contact pressure distribution. We shall therefore revert to an idealization of the contact load as a point force, as employed in an earlier analysis[5] and by Murakami and Sakae.[6]

*Present address: Department of Materials Science, Leeds University, Leeds LS2 9JT, UK.

Crack Shape

We will idealize the material being indented as a linear elastic material, and the contact pressure, in reality distributed over a small finite area, approximately square in shape, by a point force. By St. Venant's principle we expect this idealization to be satisfactory beneath the surface, but to be rather poor in the immediate neighbourhood of the contact patch. A corollary of using a point force to represent the contact pressure is that the effects of surface friction may not be included, and we will also assume that only a single crack grows in the median plane. A further consequence of using the point force as the source of contact loading is that the surface layers are put into a state of compression, i.e. $\sigma_{\theta\theta} < 0$ above a conical region, making an angle of approximately 38° with the surface, as depicted in Fig. 1. This highlights the influence of residual stresses in propelling cracks in real materials showing some plastic behaviour.

In our earlier analysis of the problem[5] we noted the form of contours of the stress component $\sigma_{\theta\theta}$ induced by a point force, using Boussinesq's solution,[7] where the coordinate set of Fig. 1 is employed. From this, we idealized the median crack as a circular arc with two tangential straight lines, as shown in Fig. 1. Crack tip stress intensity factors arising around the crack front were then found using the eigenstrain procedure. The problem was subsequently reanalysed by Murakami and Sakae[6] who used an alternative idealized crack shape in the form of a semicircle, but permitted crack closure adjacent to the surface. Thus, one boundary of the open part of the crack was prescribed, but the other, the line of closure, became an unknown of the problem.

In this paper, we wish to adopt an alternative algorithm for determining the shape of the crack:

as the contact load is increased the stresses in the vicinity of the contact patch increase until at a particular flaw the critical stress intensity factor will be reached and the crack will extend. As it does so, the increase in size of the crack will *increase* the crack tip stress intensity, but at the same time the crack front is growing into a region of *decreasing* stress. Eventually, the stress intensity factor falls below the fracture toughness value again. At this point, because of the basic principle of reversibility of the crack extension criterion in linear elastic fracture mechanics,[8] self-arrest will occur. Thus, the final shape of the crack is one where the crack tip stress intensity factor around the crack front is constant, and equal to the material's fracture toughness. This argument assumes that quasi-static extension of the crack occurs, and that crack growth occurs under elastic conditions.

Formulation

The eigenstrain method was used in the analysis. A full introduction to this procedure is given in Ref. 9, but a brief résumé of the principles will be included here. It is a three-dimensional technique, well suited to the analysis of cracks present in steep stress gradients, but a drawback is that only relatively simple remote boundaries may usually be included, such as an infinite space, half-space or a layer. In the present problem we will employ the half-space, and first find the solution for a point force, exerted at an arbitrary point within the solid. From this, the solution for a point

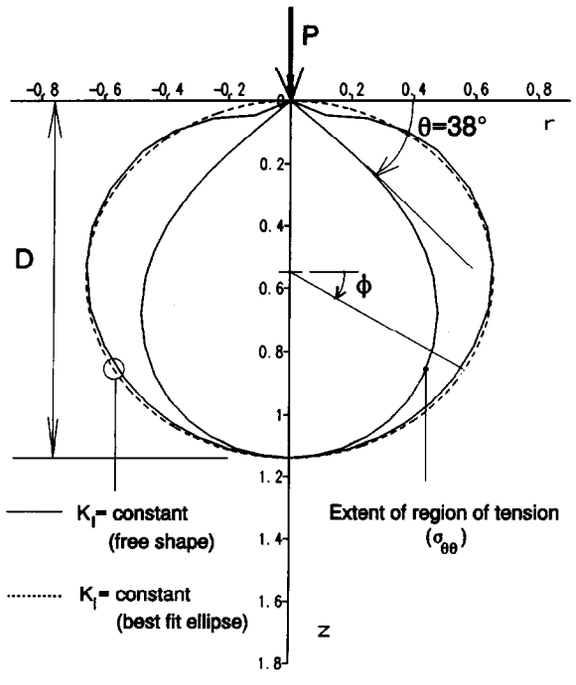

Fig. 1. Geometry of the problem, region where $\sigma_{\theta\theta}$ is positive, and possible crack front shapes.

displacement discontinuity may be found, and this, in turn, is used to build up the stress field associated with an eigenstrain element. The eigenstrain element may be viewed in different ways, but one physical interpretation is to think of its boundary as forming a Somigliana dislocation loop, where the Burgers vector may vary from point to point around the edge. Indeed the idea of a 'shape function', from finite element theory, is used to prescribe the form of the variation of the strength of the dislocation throughout the element, which may normally be either piecewise constant or piecewise linear. An influence function is defined, which relates the strength of the Burgers vector at any general node to the magnitude of the stress state induced at a general point. Hence, a matrix is established giving the resultant stress within each eigenstrain element in terms of the strength of all the elements used to model the crack. That stress resultant is set equal and opposite to the tractions induced by the far field loading *in the crack's absence*, so that the crack faces are thereby rendered stress-free. The following additional points about the method may be noted.

(1) As both the formulation for an individual element and the nominal stress state in the crack's absence are both solved in closed form for the body as a whole, all of the remote boundary conditions (such as the free surface of the half-space remaining traction-free) are automatically satisfied.
(2) In addition to the basic shape function described, crack front elements have a further form of variation of the internal Burgers vector variation imposed on them; this is to ensure that the displacement and stress field follow the required asymptotic forms along the crack front, which accelerates convergence of the solution.
(3) Because the far-field conditions are satisfied exactly, and only the crack itself needs to be modelled, the solution converges very much more quickly than a corresponding classical finite element solution, and requires far fewer degrees of freedom, for the attainment of a given level of accuracy.

These attributes mean that the technique is ideal for the problem we are addressing here, where the overall geometry is quite simple, but the stresses arising on the plane of the crack, in its absence, vary rapidly with position. Piecewise linear triangular elements were employed,[10] and the asymptotic behaviour required at the crack front was incorporated into adjacent elements only. A uniform (as opposed to graded) mesh was employed, as it has been found that this produces

the best convergence.[4] An example of a mesh for the $\sigma_{\theta\theta}$ = constant case is shown in Fig. 2.

Two forms of the possible crack shape were analysed. First, the assumed shape of the crack was that of an ellipse, with the ellipticity left as a free variable, which was adjusted so as to minimize the variation of K_I from point to point around the free edge. Surprisingly, this gives a very good approximation to the constant K requirement, and the variation is very much less than when the crack front was made to follow the contour delineating a constant tension.

To improve the shape of the crack further, the geometric restriction that it be elliptical was removed, and free meshing was employed. The crack was then 'grown', by incrementing the crack size at each point around the crack front, in proportion to the local stress intensity factor found, i.e.

$$\delta c = AK_I^n$$

where A, n are arbitrary constants, the former dimensional, chosen so that the actual increase in crack size is only a small percentage of the current value. This process was carried out several times, until it became clear that the crack was developing in a self-similar manner, i.e. without change in shape, and the stress intensity factor found was uniform around the edge, at all points save the point of application of the load itself, which is singular. It should be noted that, as the contact loading is idealized by a point force, there is no intrinsic length scale in the problem, so that when once a steady state has been reached, the shape of the crack may be expected to remain geometrically similar, i.e. it will develop in a self-similar way. This is, of course, a consequence of the idealized contact loading; had a finite contact patch been employed this would not be true. Another feature of the geometry of the model is that no mode II or III crack tip stress intensity factor can arise, because of the symmetry of the configuration.

Results

The optimal ellipticity found for the constrained crack shape was D/a = 0·85, where D is the depth of the crack and a is the breadth parallel with the surface, as shown in Fig. 1 by a broken curve. The variation of normalized stress intensity factor occurring around the front is shown in Fig. 3. It may be seen that, excluding a very small zone immediately beneath the point of application of the load, where the state of stress is singular, the stress intensity factor varies by up to 25%.

After permitting incremental growth of the model crack, the shape also shown in Fig. 1 was found. The variation of stress intensity factor around the front is shown in Fig. 3; if we again avoid the point of loading, the variation in crack tip stress intensity factor is now less than 8%. Also included in the figure, for completeness, is the original variation of crack tip stress intensity around the crack front associated with a crack shape delineating a constant value of $\sigma_{\theta\theta}$, such as the $\sigma_{\theta\theta}$ = 0 curve shown in Fig. 1. It should be noted that there is no intrinsic length dimension in the problem, save that of the depth of crack, D, itself. Thus the normalized stress intensity factor found, $K_I/P\sqrt{\pi D} \approx 0{\cdot}04$, is a universal value, and this means that a knowledge of the final depth of

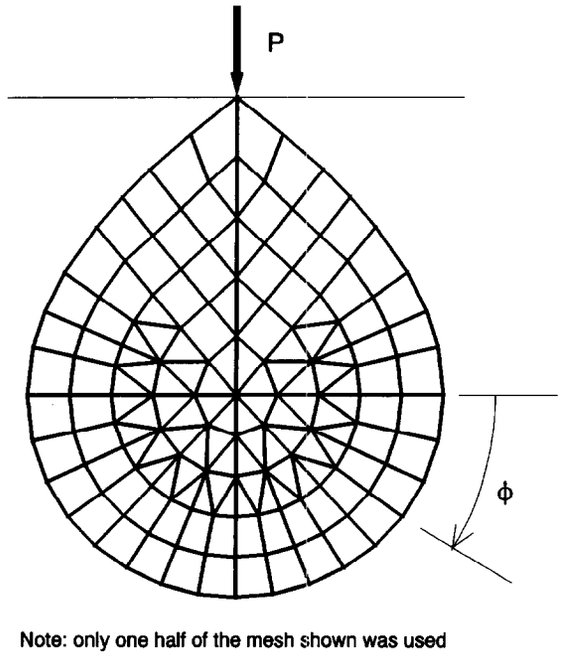

Fig. 2. Example mesh used in one part of the eigenstrain analysis.

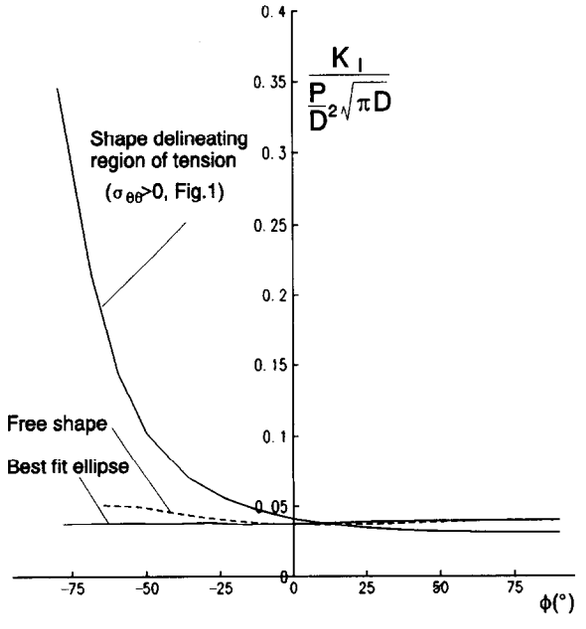

Fig. 3. Variation of crack tip stress intensity factor around crack front for the three possible crack shapes shown in Fig. 1.

the crack, together with the applied load present, is sufficient to determine the fracture toughness, with the assumptions stated at the outset. In practice, as has been stated, removal of the load may well give rise to further crack growth, propelled by residual stresses, but it is felt that the result just presented has merit in its own right, as it provides a rigorous calibration to the idealized problem posed. If an indentation test is stopped without removing the load, and the crack depth measured, the calibration is accurate, save for the area in the immediate vicinity of the contact, where the finite contact pressure distribution and plastic zone have been ignored.

The next step in providing a rigorous solution to the problem posed will be a re-evaluation of the crack shape for the case when the contact pressure distribution is modelled precisely, and the material is given an elastic–plastic stress–strain law. We feel that the bulk of the crack extension will occur upon removal of the indenter, so that propulsion is provided by the residual stress field. For 'nearly brittle' material such as ceramics and glasses these residual stresses will be quite high, as there will be a considerable re-distribution of the load compared with the elastic solution, but at the same time crack-front plasticity will be quite limited, so that the eigenstrain procedure may again be used to advantage in inferring both the crack front shape and the resultant stress intensity factor.

References

1. Cook, R. F. & Pharr, G. M., Direct observation and analysis of indentation cracking in glasses and ceramics. *J. Am. Ceram. Soc.*, **73** (1990) 787–817.
2. Lawn, B. R. & Wilshaw, T. R., Indentation fracture: principles and applications. *J. Mater. Sci.*, **10** (1975) 1049–81.
3. Giannakopoulos, A. E., Larsson, P.-L. & Vestergaard, R., Analysis of Vickers indentation. *Int. J. Solids Struct.*, **31**[19] (1994) 2679–708.
4. Murakami, Y. & Matsuda, K., Analysis of Vickers hardness by the finite element method. *J. Appl. Mech.*, **61** (1994) 822–8.
5. Li Yingzhi & Hills, D. A., The analysis of three dimensional cracks developed by sharp indentation. *J. Mech. Phys. Solids*, **38** (1990) 255–72.
6. Murakami, Y. & Sakae, C., Analysis of stress intensity factors for three dimensional cruciform cracks. *Int. J. Fract.*, **66** (1994) 339–55.
7. Timoshenko, S. P. & Goodier, J. N., *Theory of Elasticity*, 3rd Edn. McGraw-Hill, New York, 1970, pp. 398–402.
8. Kanninen, M. F. & Popelar, C. H., *Advanced Fracture Mechanics*. Oxford University Press, New York, 1985, pp. 158–64.
9. Hills, D. A., Kelly, P. A., Dai, D. N. & Korsunsky, A. M., *Solution of Crack Problems; The Distributed Dislocation Technique*. Kluwer, Dordrecht, 1996.
10. Dai, D. N., Hills, D. A. & Nowell, D., Formulation and implementation of eigenstrain method employing higher order elements. *Int. J. Solids Struct.*, **33**[3] (1996) 331–42.

Journal of the European Ceramic Society **16** (1996) 1213–1220

PII:S0955-2219(96)00051-9
0955-2219/96/$15.00

SiC Platelet-Reinforced Al_2O_3 Composites by Free Sintering of Coated Inclusions

X. Yang & M. N. Rahaman*

University of Missouri-Rolla, Department of Ceramic Engineering, Rolla, MO 65401, USA

(Received 19 December 1995; revised version received 8 February 1996; accepted 20 February 1996)

Abstract

SiC platelets were coated with a fine-grained Al_2O_3 precursor powder by controlled heterogeneous precipitation from solution. After calcination, the coated platelets were compacted and sintered at a constant heating rate of 5°C min^{-1} in a helium atmosphere. The parameters that control the coating process and the sintering behaviour of the coated powders were investigated. For given reactant and platelet concentrations, pH and temperature, the presence of a small amount of poly(vinylpyrrolidone) (PVP) produced a more homogeneous coating which, in turn, produced an improvement in the sinterability of the coated platelets. Composites formed from the coated platelets, with an initial matrix density of 40–45% of the theoretical and containing ≈20 vol% platelets, reached nearly full density after sintering at 1800°C for 30 min. By comparison, similar composites formed by mechanical mixing of the SiC platelets and freely precipitated Al_2O_3 powder reached a density of only ≈70% of the theoretical under identical sintering conditions. The strength and fracture toughness of the sintered composites formed from the coated platelets were measured in three-point loading at room temperature. For the composite containing 20 vol% platelets, the strength and fracture toughness values were 240 MPa and 5.4 MPa $m^{1/2}$, respectively. They are comparable to the highest values reported for similar composites produced by hot-pressing of mechanically mixed systems. Copyright © 1996 Elsevier Science Ltd

1 Introduction

Polycrystalline ceramic matrix composites formed by conventional methods are difficult to sinter to the high densities normally required for structural applications, without the application of an external pressure or the use of a large amount of liquid phase. The factors responsible for the reduced sinterability have been considered in detail elsewhere.[1,2] It is now generally accepted that network formation between the reinforcing particles (the inclusions) and inhomogeneous packing of the matrix phase (particularly in the regions surrounding the inclusions) are the key factors that restrict the sintering of polycrystalline ceramic matrix composites. Transient stresses due to the mismatch in shrinkage rates between the matrix and the inclusions may also play a limited role in reducing the densification.[3,4]

For densification by a solid-state mechanism, De Jonghe and co-workers[5,6] and Rahaman and co-workers[7,8] have demonstrated that the sintering impediments due to network formation and packing can be significantly alleviated by the use of an alternative processing route based on the preparation of coated particles. The preparation of coated particles was pioneered by Matijevic and co-workers.[9–11] The method was also used later by Garg and De Jonghe[12] for the preparation of Si_3N_4 coated with yttria and yttria–alumina precursors. For particulate composites, the reinforcement phase is coated with the required thickness of the matrix phase by controlled heterogeneous precipitation in a suspension of particles or whiskers. The coated powders are then collected, compacted by normal ceramic powder forming methods (e.g. pressing in a die or isostatic pressing) and densified by conventional, pressureless sintering (referred to as free sintering). Composites reinforced with up to ≈40 vol% particles or 20–30 vol% whiskers have been sintered to almost full density under conditions fairly similar to those used for the unreinforced materials. From the point of view of ease of fabrication, the route based on the use of coated particles may therefore have considerable benefits. Sacks *et al.*[13] employed an alternative method based on the use of coated powders. They prepared amorphous coatings on core particles in order to take advantage of the easier densification

*To whom correspondence should be addressed.

of the coating by viscous flow. After densification, the amorphous phase can be crystallized or reacted with the core particles to produce a crystalline product.

Compared with nearly equiaxial inclusions, the use of whisker reinforcement can provide improvement in the mechanical properties of the ceramic matrix.[14–16] However, various questions have arisen concerning the health hazards posed by the use of whiskers. Platelets may provide an effective reinforcing phase for improvement of the strength and fracture toughness of ceramics.[17,18] At the same time, they are not associated with any known health hazards.

The work described in the present paper forms an extension of the earlier work of Rahaman and co-workers to the fabrication of platelet-reinforced composites from coated inclusions. The factors that control the coating of SiC platelets with an alumina precursor powder and the sinterability of composites formed from the coated platelets were investigated. The strength and fracture toughness of the fabricated composites were measured at room temperature and compared with the values reported for similar composites produced by hot-pressing.

2 Experimental Procedure

2.1 Preparation of coated powders and mechanically mixed powders

Following the procedure described by Hu and Rahaman[8] for the coating of SiC whiskers with an alumina precursor powder, the key parameters of the process were varied to produce a uniform coating without significant precipitation of free powder. The parameters included the concentration of the reactants in solution, the concentration of SiC platelets in the suspension, the temperature and the pH. The following procedure was initially found to produce coated platelets. A coating solution consisting of 0.18 mol l^{-1} $Al(NO_3)_3$, 0.05 mol l^{-1} $Al_2(SO_4)_3$ and 32 g l^{-1} urea was prepared. (All of the chemicals were reagent grade, obtained from Aldrich Chemical Co., Milwaukee, WI.) SiC platelets (-400 mesh, Type T; Third Millenium Technology Co., Knoxville, TN), at a concentration of 3.2 g l^{-1} were added to the solution. The platelets had a diameter of 0.5 to 3 μm and an aspect ratio of ≈ 10. The suspension was heated, under vigorous stirring, for 48 h at 83 ± 2°C. During the process, the pH of the suspension was monitored. This procedure produced coated platelets. However, the coating contained cracks and, in many cases, parts of the cracked coating fell off, leaving uncoated surfaces on the platelets. The addition of poly(vinylpyrrolidone) (PVP, molecular weight ~30 000; Aldrich Chemical Co., Milwaukee, WI) at a concentration of 0.7 g l^{-1} prior to heating the suspension to the coating temperature, produced a relatively smooth coating that did not show any evidence of cracking.

After the coating process, the suspension was cooled quickly. The coated platelets were collected, washed with distilled water and dried for 8 h at 100°C. The dried material was then placed in a high-purity Al_2O_3 crucible and heated in helium for 15 min at 1250°C to decompose the alumina precursor powder.

After calcination, the coated powder was doped with MgO (Mg:Al atomic ratio = 250 ppm) for grain growth control during sintering. In the process, the required amount of $Mg(NO_3)_2.6H_2O$ (purity 99.99%; Aesar/Johnson Matthey, Ward Hill, MA) was added to a suspension of the coated powder in ethanol. The mixture was stirred until it was dry and then calcined in air for 2 h at 1000°C to incorporate the Mg into solid solution.

For a comparison of the sintering kinetics, mechanically mixed systems were also prepared. In this case, free alumina precursor powder was precipitated from the solution under the same conditions described earlier for the coating process. The precipitated powder was mixed with the required amount of SiC platelets, while dispersed in ethanol, for 2 h in a ball mill using zirconia balls as the milling media. After drying, the mixture was calcined and doped using the same procedure described earlier for the coated powder.

2.2 Sintering of the composites

The coated platelets and the mechanically mixed systems were compacted by pressing lightly in a uniaxial die (under a pressure of ≈ 40 MPa), followed by cold-isostatic pressing (≈ 250 MPa) to form pellets (6 mm in diameter by 5 mm) for sintering. Plates (48 by 28 by 6 mm) for mechanical testing experiments were prepared by compacting the powders in a rectangular die followed by cold-isostatic pressing under the pressures outlined above for the preparation of the pellets. The matrix density of the compacted samples formed from both the coated platelets and the mechanically mixed systems was 40–45% of the theoretical density of α-Al_2O_3.

Sintering was performed in a high-purity helium atmosphere (flow rate 50 cm^3 min^{-1}) in a graphite element furnace (model 1000; Thermal Technology, Inc., Santa Rosa, CA) at a constant heating rate of 5°C min^{-1} to ≈ 1800°C. In the experiments, the powder compacts were placed in a high-purity graphite crucible and surrounded by loose powder of the same composition in order to minimize

weight loss during sintering. The densities of the fired samples were determined from their mass and dimensions. The values were checked by Archimedes' method.

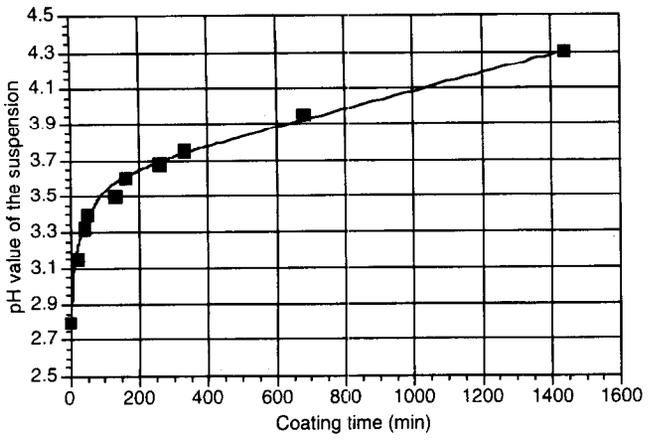

Fig. 1. The pH of the suspension during the coating process at 83 ± 2°C.

2.3 Measurement of mechanical properties

The flexural strength and fracture toughness of the sintered materials were determined by three-point bending of beams (3 by 4 by 30 mm) at a crosshead speed of 0.5 mm min^{-1}. The test samples were cut from the fired plates and then polished with SiC papers to 600-grit. The edges were bevelled during the polishing step. Fracture toughness values were determined using a single-edge notched beam (SENB) technique. The beams were notched at the centre using a diamond wheel (0.6 mm thick) to produce a notch depth (a) to the beam width (w) ratio of 0.4–0.5. At least five specimens were tested for each reported value.

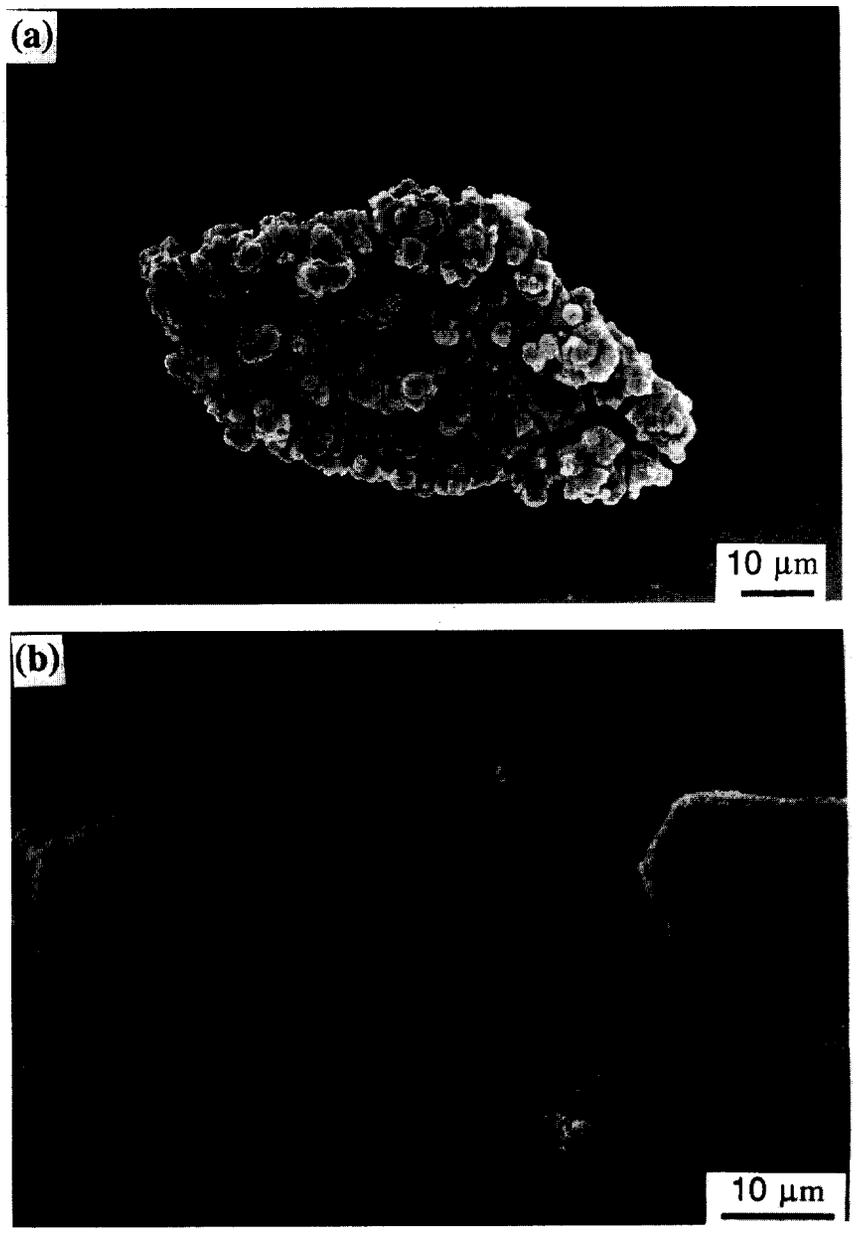

Fig. 2. SEM micrographs of the coated platelets prepared by chemical precipitation: (a) without PVP and (b) with PVP.

2.4 Structural and microstructural characterization

X-ray diffraction (XRD) was used to analyse the coatings after drying as well as after the calcination step. The structure of the coating on the SiC platelets was observed by scanning electron microscopy (SEM). The microstructure of the sintered samples was observed by SEM and by optical microscopy of fractured surfaces and polished surfaces.

3 Results and Discussion

Figure 1 shows the data for the pH of the suspension as a function of time at the coating temperature of 83 ± 2°C. At this temperature, the urea decomposed slowly, leading to an increase in the hydroxyl ion concentration. The pH value of the solution increased until the conditions for precipitation of aluminium hydroxide were reached.

The production of coated particles depends on the ability to achieve heterogeneous nucleation and growth from the solution, in contrast to the case of free powder which is produced by homogeneous nucleation and growth. For the preparation of coated platelets, a general requirement is to achieve a balance between the total available surface area of the platelets in suspension and the rate of precipitation. The total surface area is determined by the specific surface area and the concentration of the platelets, while the rate of precipitation depends on the concentration of the reactants (urea and aluminium salts) and the temperature of the solution. Successful coating of the platelets in suspension therefore requires some trial and error for achieving the proper concentration of platelets and reactants under a set of fixed reaction conditions.

The initial experiments employed the same conditions as those used earlier by Hu and Rahaman[8] for the coating of SiC whiskers with an alumina precursor powder. These conditions produced a mixture of coated platelets and free powder. However, a significant increase in the concentration of the platelets produced coated platelets primarily. Figure 2(a) shows an SEM micrograph of the product from the conditions of increased platelet concentration. The coating suffers from extensive cracking which can be alleviated by the addition of PVP to the solution prior to the coating process [Fig. 2(b)]. The presence of the PVP also leads to a change in the structure of the alumina precursor coating.

The volume fraction of the platelets in the composites is controlled by the total amount of aluminium ion in the solution. By completing the precipitation reaction, almost all the aluminium ions can be precipitated at pH values greater than ≈4.3. For the coated platelets shown in Fig. 2, the volume fraction of the platelets (based on the fully dense composite) is ≈20%. The error in the platelet volume fraction determined by this method is estimated at ±1%.

The quality of the coating on the platelets influences the sintering characteristics. For the highly cracked coating prepared without the addition of PVP [Fig. 2(a)], the composites reached a density of ≈92% of the theoretical after sintering for 30 min at 1800°C. In comparison, the composites formed from the coated powders prepared with the addition of PVP [Fig. 2(b)] reached a density of 98% of the theoretical under identical sintering

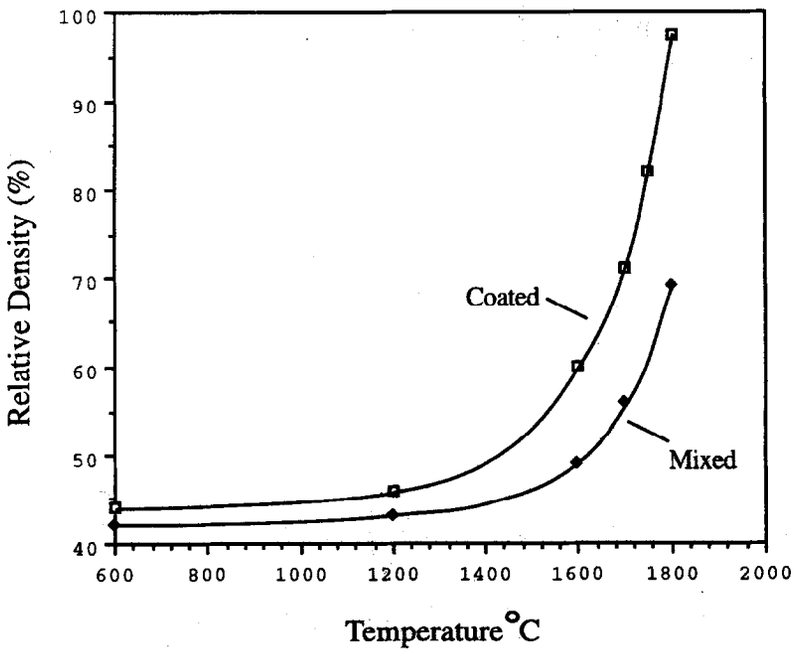

Fig. 3. Relative density versus temperature for composites formed from (a) the coated powder and (b) the mechanically mixed powder, during constant heating rate sintering of 5°C min^{-1} to 1800°C.

conditions. The results indicate that the more uniform coating produced with the addition of PVP leads to a higher sintered density.

The sinterability of the composites formed from the coated powders was compared with that for similar composites formed from mechanically mixed systems. Figure 3 shows the sintered densities of composites at various temperatures. The volume fraction of the platelets in the composites was ≈20 vol%. The sintered density of the composite formed from the mixed powders is significantly lower than that for the composite formed from the coated powders.

Scanning electron micrographs of the fractured surfaces of the sintered composites formed from the coated powder and from the mixed powder are shown in Fig. 4. The micrograph of the composite formed from the coated powder [Fig. 4(a)] reveals a dense microstructure in which all the platelets are separated from one another by the matrix phase. However, for the composite formed from the mixed powder [Fig. 4(b)], a highly porous microstructure is observed. Furthermore, most of the porosity is concentrated immediately around the platelets. Several platelets appear to be interconnected, with a large amount of porosity associated with this type of structure. Both microstructures reveal an average grain size of the matrix equal to 5–10 μm.

Figure 5 is an optical micrograph of the polished surface of the composite formed from the coated powder after sintering for 30 min at 1800°C. A fairly uniform distribution of the platelets (light phase) in a highly dense matrix (dark phase) is observed. There is almost no evidence for clustering of platelets, as is normally observed for hot-pressed composites formed from mechanically mixed systems.

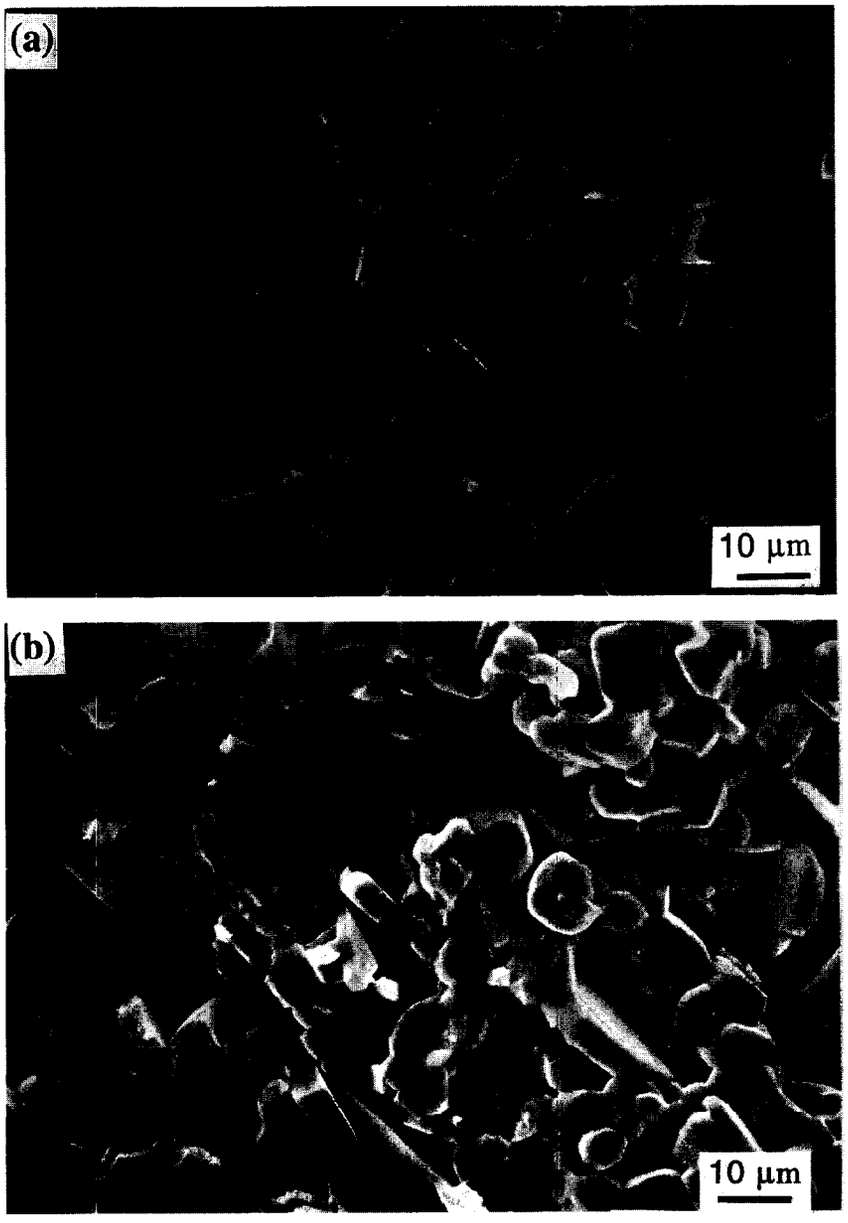

Fig. 4. The microstructures of the fractured surfaces of the composites formed from (a) the coated powder and (b) the mechanically mixed powder after sintering.

The data for the flexural strength and fracture toughness of the sintered composites produced from the coated platelets are shown in Table 1. The strength is ≈240 MPa while the fracture toughness is ≈5.4 MPa $m^{1/2}$. For comparison, the data for unreinforced Al_2O_3, produced from the

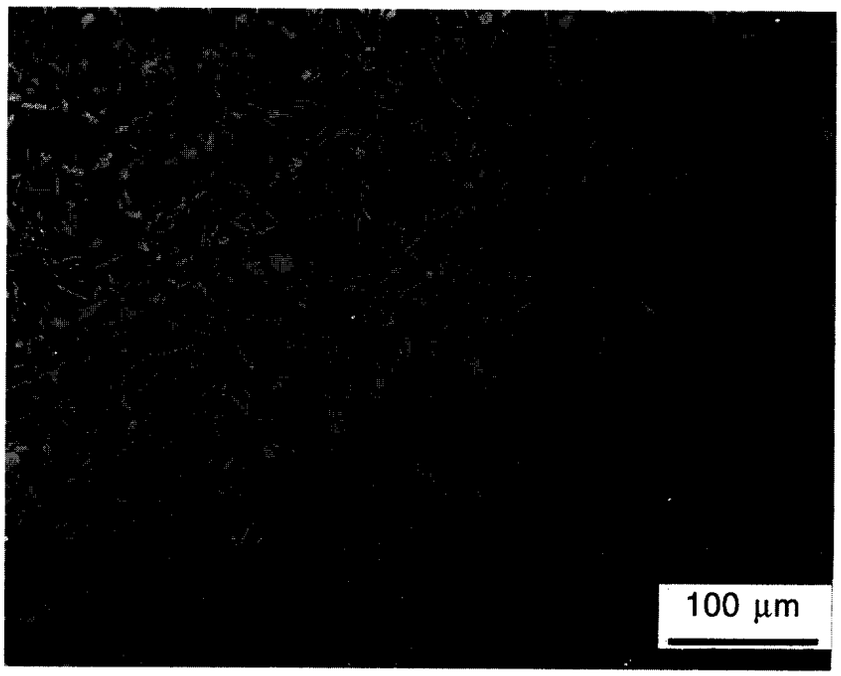

Fig. 5. Optical micrograph of the polished surface of the sintered composite formed from the coated powder, showing a fairly uniform distribution of the platelets (light phase) in a highly dense matrix (dark phase).

Table 1. Flexural strength and fracture toughness values for unreinforced Al_2O_3 and Al_2O_3/20 vol% SiC platelet-reinforced composites produced in the present work. Values reported in the literature for similar composites are also shown

Composition	*Fabrication route*	*Flexural strength (MPa)*	*Fracture toughness (MPa $m^{1/2}$)*
Al_2O_3 (present work)	Sintering	262 ± 20	3.8 ± 0.4
Al_2O_3/20 vol% SiC (present work)	Sintering	240 ± 14	5.4 ± 0.2
Al_2O_3/20 vol% SiC (Refs 19,20)	Hot-pressing	120–280	4.5–5.4

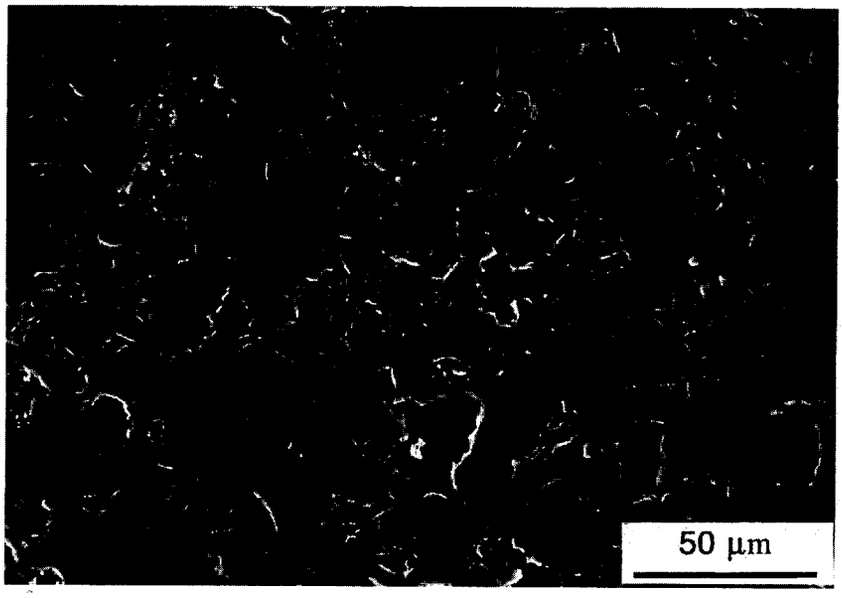

Fig. 6. SEM micrograph of a machined surface of the composites (20 vol% SiC platelet) used in the flexural strength tests.

precipitated alumina precursor powder are also included. The calcination, doping and sintering steps for the unreinforced Al_2O_3 were similar to those for the composites formed from the coated platelets. In addition, the grain size of the fabricated Al_2O_3 material was approximately the same as that of the matrix phase of the composite. Within the limits of experimental error, the strength values are approximately the same but the fracture toughness of the composite is ≈ 1.5 times higher than that of the unreinforced Al_2O_3. Table 1 also shows the range of data reported in the literature[19,20] for similar composites produced by hot-pressing of mechanically mixed systems. For the data reported in the literature, while the average grain size of the Al_2O_3 matrix is not known, the SiC platelets were similar to those used in the present work. Furthermore, the methods used to measure the flexural strength and fracture toughness were similar to those employed in the present work. Qualitatively, the data show that the strength and fracture toughness of the composites produced in the present work by the free sintering of coated platelets are approximately the same or even better than the values reported for the hot-pressed composites. At least two factors can have an influence on the strength of the composites: (i) the interfacial bonding between the platelets and the matrix and (ii) the surface finish of the specimens used in the mechanical tests. No detailed work was performed for the characterization of the interface. However, the surface finish of the specimens was observed. As shown in Fig. 6, the surface of the specimens contains defects which are as large as the platelets. The defects were produced during grinding and polishing of the surfaces prior to mechanical testing. Such defects can significantly reduce the strength. An optimized surface finish may therefore be expected to lead to an improvement of the measured strength value.

4 Conclusions

Conditions were determined for the coating of SiC platelets with a uniform, crack-free layer of an alumina precursor powder by heterogeneous precipitation from solution. The thickness of the precursor layer was controlled to achieve a platelet volume fraction of 20% based on the theoretically dense composite. After calcination to convert the precursor layer to Al_2O_3, the coated platelets were compacted and freely sintered to produce highly dense composites. Under identical sintering conditions, similar composites formed from mechanically mixed systems were highly porous. The flexural strength and fracture toughness of the sintered composites formed from the coated platelets are comparable to the highest values reported for similar composites produced by hot pressing of mechanically mixed systems. The present work provides further demonstration of the effectiveness of the fabrication route based on the use of coated inclusions for the production of ceramic matrix composites by free sintering.

References

1. Fan, C.-L. & Rahaman, M. N., Factors controlling the sintering of ceramic particulate composites: I, conventional processing. *J. Am. Ceram. Soc.*, **75**[8] (1992) 2056–65.
2. Hu, C.-L. & Rahaman, M. N., Factors controlling the sintering of ceramic particulate composites: II, coated inclusion particles. *J. Am. Ceram. Soc.*, **75**[8] (1992) 2066–70.
3. Sudre, O. & Lange, F. F., Effect of inclusions on densification: I, microstructural development in an Al_2O_3 matrix containing a high volume fraction of ZrO_2 inclusions. *J. Am. Ceram. Soc.*, **75**[3] (1992) 519–24.
4. Sudre, O., Bao, G., Fan, B., Lange, F. F. & Evans, A. G., Effect of inclusions on densification: II, numerical model. *J. Am. Ceram. Soc.*, **75**[3] (1992) 525–31.
5. Mitchell, T. D. Jr. & De Jonghe, L. C., Processing and properties of particulate composites from coated powders. *J. Am. Ceram. Soc.*, **78**[1] (1995) 199–204.
6. Kapolnek, D. & De Jonghe, L. C., Particulate composites from coated powders. *J. Eur. Ceram. Soc.*, **7**[6] (1991) 345–51.
7. Hu, C.-L. & Rahaman, M. N., Dense ZrO_2/Al_2O_3 composites by free sintering of coated powders. *J. Am. Ceram. Soc.*, **77**[3] (1994) 815–19.
8. Hu, C.-L. & Rahaman, M. N., SiC whisker reinforced Al_2O_3 composites by free sintering of coated powders. *J. Am. Ceram. Soc.*, **76**[10] (1993) 2549–54.
9. Gherardi, P. & Matijevic, E., Interactions of precipitated hematite with preformed colloidal titania dispersions. *J. Colloid Interface Sci.*, **109**[1] (1986) 57–68.
10. Kratohvil, S. & Matijevic, E., Preparation and properties of coated, uniform inorganic colloidal particles: I, aluminum hydrous oxide on hematite, chromia, and titania. *Adv. Ceram. Mater.*, **2**[4] (1987) 798–803.
11. Garg, A. K. & Matijevic, E., Preparation and properties of uniformly coated inorganic colloidal particles, II: chromium hydrous oxide on hematite. *Langmuir*, **4** (1988) 38–44.
12. Garg, A. K. & De Jonghe, L. C., Microencapsulation of silicon nitride particles with yttria and yttria–alumina precursors. *J. Mater. Res.*, **5**[1] (1990) 136–42.
13. Sacks, M. D., Bozkurt, N. & Scheiffele, G. W., Fabrication of mullite and mullite matrix composites by transient viscous sintering of composite powders. *J. Am. Ceram. Soc.*, **74**[10] (1991) 2428–37.
14. Faber, K. T. & Evans, A. G., Crack deflection processes — I. theory. *Acta Metall.*, **31**[4] (1983) 565–76.
15. Becher, P. F., Hsueh, C.-H., Angelini, P. & Tiegs, T. N., Toughening behavior in whisker-reinforced ceramic matrix composites. *J. Am. Ceram. Soc.*, **71**[12] (1988) 1050–61.
16. Bengisu, M. & Inal, O. T., Whisker toughening of ceramics: toughening mechanism, fabrication, and composite properties. *Ann. Rev. Mater. Sci.*, **24** (1994) 83–124.
17. Brandt, G. & Thelin, A., Ceramic cutting tool with improved toughness behavior. *European Patent Application 0 295 228 A2.*

18. Heussner, K.-H. & Claussen, N., Yttria- and ceria-stabilized tetragonal zirconia polycrystals (Y-TZP, Ce-TZP) reinforced with Al_2O_3 platelets. *J. Eur. Ceram. Soc.*, **5** (1989) 193–200.
19. Sakai, H., Matsuhiro, K. & Furuse, Y., Mechanical properties of SiC platelet reinforced ceramic composites. *Mater. Res. Soc. Symp. Proc.*, **271** (1992) 765–71.
20. Fisher, W. F., Haber, R. A. & Anderson, R. M., Mechanical properties of alumina matrix composites reinforced with silicon carbide platelets and particles. *Mater. Res. Soc. Symp. Proc.*, **271** (1992) 773–9.

Journal of the European Ceramic Society **16** (1996) 1221–1230

PII:S0955-2219(96)00042-8
0955-2219/96/$15.00

Low-Temperature Sintering of Silicon Carbide with Li_2O–Al_2O_3–SiO_2 Melts as Sintering Aids

Y. Pan & J. L. Baptista

Departamento de Engenharia Cerâmica e do Vidro, Universidade de Aveiro, 3800 Aveiro, Portugal

(Received 13 December 1995; revised version received 5 January 1996; accepted 8 February 1996)

Abstract

With reference to sintering of SiC with Li_2O–Al_2O_3–SiO_2 (LAS) melts, equilibrium partial pressures of SiO, CO and Al_2O resulting from reactions of SiC and LAS have been thermodynamically estimated by taking carbon activity and temperature into account. Experimental work involving various LAS compositions and different powder beds showed that SiC/40 v% LAS (65·2 wt% SiO_2, 15·0 wt% Al_2O_3, 19·8 wt% Li_2O or 55·0 wt% SiO_2, 22·5 wt% Al_2O_3, 22·5 wt% Li_2O) can be densified in carbon rich powder bed to above 95%. The sintering temperature (100°C above m.p. of LAS) of these were the lowest of all. Thermodynamic estimations were used to explain the results. XRD, optical microscopy and SEM studies also supported the explanation. Copyright © 1996 Elsevier Science Ltd

1 Introduction

The difficulties with the sintering of silicon carbide ceramics have been attributed to the covalent nature of its chemical bond, particularly to the low surface energy and the low self diffusion coefficient resulting from the covalent bond. Successful sintering of silicon carbide has been reported and liquid-phase promotion or additives to improve diffusivity and surface energy were usually needed for the sintering. The most promising additives for liquid-phase sintering are metallic or oxide forms of aluminium,[1,2] mixtures of alumina and yttria,[3] and carbon and boron.[4] Aluminium or alumina, and alumina and yttria form a liquid phase during sintering of SiC. Carbon and boron were believed to improve the diffusivity of the components of SiC. Most of these sinterings had to be done on hot press and at high temperature (≥ 1900°C), which has, to some extent, limited the application of these technologies.

The Li_2O–Al_2O_3–SiO_2 (LAS) system has been successfully used as a binder of silicon carbide fibre and the composite made in this way had bending strength and fracture toughness as high as 1380 MPa and 17 MPa m^{-2}, respectively.[5] LAS has also been used as part of the matrix of a 55 wt% SiC–45 wt% (LAS/MAS/TiO_2) composite. The glass matrix was molten at the processing temperature playing a role of sintering aid of SiC.[6] Since liquid-phase-forming temperatures in the LAS system are relatively low, low-temperature liquid-phase sintering of silicon carbide with LAS melts as sintering aids could be a feasible method to widen the application of silicon carbide ceramics, for example, in cases where high-temperature strength is not important. Moreover, most LAS glasses can be crystallised through proper heat treatment, and therefore, the final parts could have satisfactory properties for some applications.

Reported in this paper is an exploration of liquid-phase sintering of SiC with LAS melts with eight different compositions. The first problem encountered was not the problem of the liquid-phase sintering on its own, but the problem caused by reactions of silicon carbide and LAS components. Systematic thermodynamic analysis of the reactions of silicon carbide with SiO_2, Li_2O and Al_2O_3 in LAS melts has been done and is here reported.

2 Chemical Equilibrium of SiC and LAS Melts

Chemical equilibrium of SiC and LAS melts involves the reactions of SiC with the SiO_2, the Li_2O and the Al_2O_3 in LAS glass. These reactions usually produce evaporating phases, such as SiO, Al_2O and CO, and solid phases, such as Li_2C_2 and Al_4C_3. Understanding and controlling these reactions is of great importance in liquid-phase sintering of SiC/LAS. Thermodynamic analyses of this system may start with the following reaction

$$SiC(s) + 2\ SiO_2(l) = 3\ SiO(g) + CO(g) \quad (1)$$

At certain equilibrium temperature T and certain activity of SiO_2, A_{SiO_2} in LAS melts, the equilibrium

partial pressures of SiO and CO, P_{SiO} and P_{CO} are related by

$$3 \ln P_{SiO} + \ln P_{CO} = f_1(T) + 2 \ln A_{SiO_2} \quad (2)$$

where $f_1(T) = \Delta_1 G^0/(-RT)$, $\Delta_1 G^0$ is the standard free energy change of reaction (1), R is the gas constant and T the absolute temperature.

The ranges of variation of P_{SiO} and P_{CO} are confined by possible reactions taking place as the carbon activity A_C and the silicon activity A_{Si} in silicon carbide are unity, respectively. For $A_C = 1$, a reaction taking place is:

$$C(s) + SiO_2(l) = CO(g) + SiO(g) \quad (3)$$

and

$$\ln P_{SiO} + \ln P_{CO} = f_3(T) + \ln A_{SiO_2} \quad (4)$$

For $A_{Si} = 1$, another reaction taking place is:

$$Si(l) + SiO_2(l) = 2\ SiO(g) \quad (5)$$

and

$$2\ln P_{SiO} = f_5(T) + \ln A_{SiO_2} \quad (6)$$

In Fig. 1, in which P_{CO} and P_{SiO} are related by eqn (2) at different temperatures, the upper limits of P_{SiO} and P_{CO}, A, are determined by eqn (2) and eqn (4), and the lower limits, A', are determined by eqn (2) and eqn (6). Between the two limits, P_{SiO} and P_{CO} are determined by taking A_C or A_{Si} in eqn (3) and (5) into consideration. A_C and A_{Si} are not independent of one another, since the following equations will always be held at any temperature:

$$SiC(s) = Si(l) + C(s) \quad (7)$$

and

$$\ln A_{Si} + \ln A_C = f_7(T) \quad (8)$$

P_{SiO} as well as P_{CO} is thus a function of T and A_C.

Another possible reaction taking place in the system SiC–LAS is the reaction of SiC with Li_2O, which may be expressed as follows:

$$3\ SiC(s) + 2\,Li_2O(s,l) + CO(g) = 3\ Li_2C_2(s) + 3\ SiO(g) \quad (9)$$

and

$$3 \ln P_{SiO} - \ln P_{CO} = f_9(T) + 2 \ln A_{Li_2O} \quad (10)$$

where A_{Li_2O} is the activity of Li_2O in LAS. Equation (10) is also shown in Fig. 1. The varying ranges of P_{SiO} and P_{CO} are also determined by the A_C in SiC. At $A_C = 1$, the upper limits of P_{SiO} and P_{CO}, B, in Fig. 1 are determined by eqn (10) and the following equations:

$$3\ C(s) + Li_2O(s,l) = Li_2C_2(s) + CO(g) \quad (11)$$

and

$$\ln P_{CO} = f_{11}(T) + \ln A_{Li_2O} \quad (12)$$

The lower limits B' are located by eqn (10) and the following:

$$2\ SiC(s) + Li_2O(s,l) = Li_2C_2(s) + SiO(g) + Si \quad (13)$$

and

$$\ln P_{SiO} = f_{13}(T) + \ln A_{Li_2O} \quad (14)$$

AA' has a negative slope of 3 and BB' has a positive slope of 3, which are determined by eqns (1) and (9) in double logarithm scale (Fig. 1).

$f_i(T) = \Delta_i G^0/(-RT)$ for each equation can be estimated by using thermodynamic data in JANAF Thermodynamical Tables.[7] As activities of SiO_2 and Li_2O are not considered, A-A' as well as B-B' at temperatures from 827°C (1100 K) to 1727°C (2000 K) have been estimated and the A-A' and B-B' in Fig. 1 are the results of these calculations.

In Fig. 1, it can be seen that, at 827°C (1100 K) and 927°C (1200 K), B-B' are on the left side of A-A', which means that the reaction between SiC and SiO_2 takes place, but the one between SiC and Li_2O will not, or that the interface between SiC and SiO_2 is not stable but the interface between SiC and Li_2O is. Above 1427°C (1700 K), B-B' are on the right side of A-A', which means that the interface between SiC and SiO_2 is stable and the interface between SiC and Li_2O is not. At 1027°C, 1127°C, 1227°C, 1327°C and 1427°C (1300, 1400,

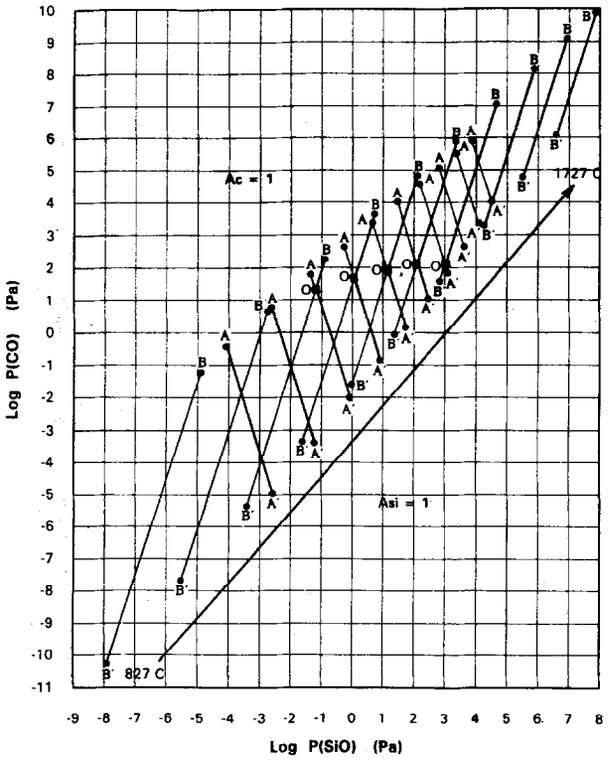

Fig. 1. Relationship between equilibrium partial pressures of CO and SiO in the reaction of SiC with LAS at different temperatures: AA' for reaction (1), BB' for reaction (9), O crossed points by AA' and BB' at temperatures 1027, 1127, 1227, 1327 and 1427°C. Bold lines refer to the predominant reactions at each temperature.

1500, 1600 and 1700 K, respectively), *A-A'* and *B-B'* cross. The crossed points correspond to the following equilibrium

$$4\ SiC(s) + 2\ SiO_2(s.l) + 2\ Li_2O(s.l) = 6\ SiO + 2\ Li_2C_2 \quad (15)$$

in which A_C is fixed for each temperature (degree of freedom is reduced by one), and the P_{SiO} and P_{CO} at the crossed points, O, calculated accordingly.

Since Al_2O_3 is also an important component in LAS melts, the following equilibrium may also be established:

$$Al_2O_3(s) + SiC(s) = Al_2O(g) + SiO(g) + CO(g) \quad (16)$$

and

$$\ln P_{Al_2O} + \ln P_{SiO} + \ln P_{CO} = f_{16}(T) \quad (17)$$

Therefore, P_{Al_2O} is also a function of T and A_C. Oxygen partial pressure can be also estimated, but it is very low ($\leq 10^{-19}$ Pa according to calculation) so that it is neglected hereafter.

P_{SiO}, P_{CO} and P_{Al_2O} as functions of T and A_C are plotted in Figs 2a, 2b and 2c, respectively. In these figures, A_C is varying from unity to $A_C = A_C(T)$ at which $A_{Si} = 1$ and T = 827, 927, ...1727°C. P_{SiO}, P_{CO} and P_{Al_2O} shown in Fig. 2 are those produced by thermodynamically most possible reactions. This means that, for T = 827°C and 927°C, they are produced by reaction (1), for T = 1527°C and above, they are produced by reaction (9), for T = 1027, 1127, 1227, 1327 and 1437°C, they are, in the carbon-rich side, produced by reaction (9) and in the silicon-rich side, produced by reaction (1). The inflections on these curves are corresponding to the alternatives chosen for the reactions. The partial pressures at these inflections are the same as the cross points O in Fig. 1.

The total pressure of evaporating phases, $P = P_{SiO} + P_{CO} + P_{Al_2O}$ is also plotted against A_C at different temperatures in Fig. 3. Besides the inflection resulting from P_{SiO} versus A_C, P_{CO} versus A_C and P_{Al_2O} versus A_C in Fig. 2, it can be also seen that the total pressures are above 10^5 Pa at temperatures above 1277°C as $A_C = 1$ or at temperatures above 1527°C as $A_{Si} = 1$. At each temperature, P is decreased with reducing A_C, but below 1527°C the minimum total pressure is not at $A_{Si} = 1$ and is somewhere in between but close to $A_{Si} = 1$. They may be picked up and are listed in Table 1.

In LAS melts the activities of SiO_2, Li_2O and Al_2O_3 are reduced. The reduced activities will affect the partial pressures of evaporating phases. But these effects are not taken into account because many factors affecting them are unknown. Thermodynamic and kinetics of reactions of SiC and Al_2O_3 and SiC and SiO_2 have been studied by Misra[8] and Jacobson *et al.*[9] but the sight angles were different from that of this paper. Some results can be translated to one another.

High total partial pressure is produced by consuming SiC and LAS melts, which, besides decomposing SiC, is harmful to the sintering process. Bloating bubbles filled with these high-pressure evaporating gases hinder shrinkage and leave large volume fractions of voids. Successful sintering has to be conducted in such conditions that the total partial pressure is as low as possible. According to Misra[8] and Jacobson, *et al.*,[9] the total pressure has to be lower than ambient in order to keep SiC stable.

3 Experimental

The starting materials used in this work are: α-SiC powder, produced by H. C. Starck, Germany, the BET specific surface of which is 5600 m^2/kg and the carbon content of which is 28·8 wt%, lower than that of stoichiometric silicon carbide (29·2 wt%); lithium carbonate produced by M&B, England; silica precipitated and acid washed produced by BDH, England; and aluminium oxide also produced by BDH, England.

LAS glasses were prepared by making and firing the mixtures with various compositions shown in Table 2 in platinum crucibles. The amount of lithium carbonate in the mixture is 5 wt% higher than the designed composition so that the loss of lithium oxide during melting may be compensated. The firing temperature of each glass was about 200°C above the liquidus of the corresponding composition in the LAS phase diagram[10] and the dwell time at this temperature was more than one hour. The LAS melts were quenched into cold water to become transparent glasses, which were subsequently broken and milled by attrition milling into powders of sub-micron size. Some larger pieces of transparent glasses were chosen for the measurement of the 'theoretical' density of these glasses. Part of each glass was crystallised through heat treatment and the phases identified by XRD were all in agreement with the LAS phase diagram[10] being listed in Table 2. Eight different LAS systems listed in Table 2 were used as candidates of sintering aids of SiC ceramics.

Since this paper is focused on the effects of evaporating phases produced by the reaction of SiC and LAS melts on the sintering behaviour of SiC/LAS, the experimental work mainly covered the following:

α-SiC powder and each of the LAS glass powders listed in Table 2 were mixed and ball milled for 8 h in deionised water using an agate container and agate balls. The pH value of the suspension was adjusted in advance to 11 according to the suggestion of Almeida *et al.*[12] The good suspensions

obtained were dried and powders were screened through 200 mesh. Samples with different LAS glasses were made exactly in the same way. The relative amount of LAS in all samples was the same, i.e. 40 v% which guaranteed enough liquid phase for rearrangement of silicon carbide particles during liquid-phase sintering. The samples were all first uniaxially pressed under 150 MPa and then cold isostatic pressed under 300 MPa into pellets of 10 mm diameter and 4–6 mm thickness. Sample number was the same number of the glass list in Table 2, for example, Sample 3 means SiC/40 v% glass 3. The

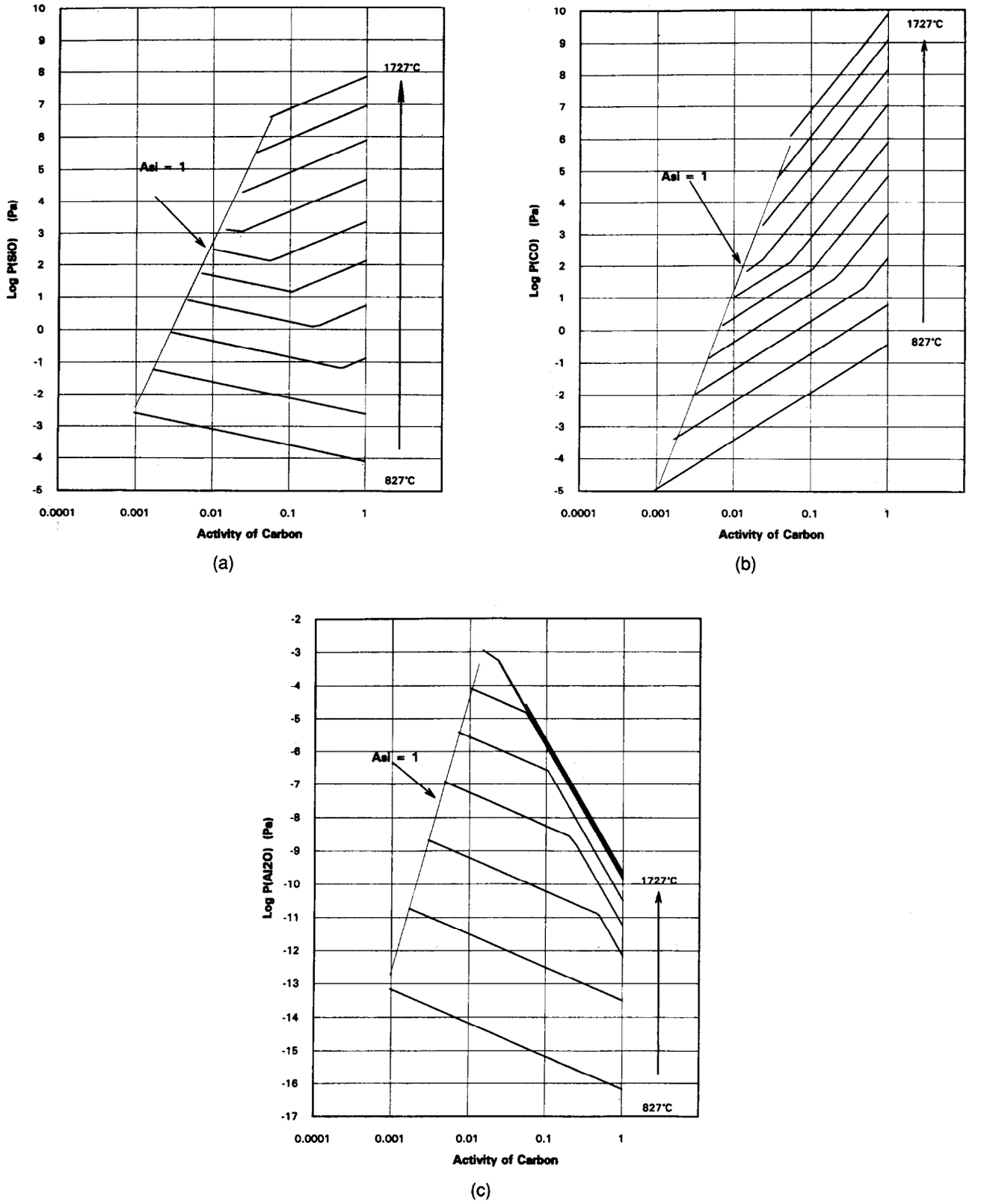

Fig. 2. (a) Carbon activity dependence of equilibrium partial pressure of SiO produced by predominant reactions at different temperatures. (b) Carbon activity dependence of equilibrium partial pressure of Al_2O produced by predominant reactions at different temperatures. (c) Carbon activity dependence of Al_2O produced by predominant reactions at different temperatures.

heating rate was 50°C/min, the sintering temperature was the temperature 100°C above the melting point (liquidus) of the glass in the sample and the dwell time was always 0·5 h. In cooling, the power supply to the sintering furnace was turned off and cooling water kept running. Three kinds of powder bed were chosen: PD1 was the same powder as the samples in which reaction of SiC with different components is assumed approximately stoichiometric, PD2 was an equimolar mixture of carbon black and each sample powder, in which carbon activity is unity, PD3 was an equimolar mixture of pure silicon and each sample powder, in which silicon activity is unity. Sintering processes were conducted in a furnace (Thermal Technology Inc., USA) with graphite heating element. Samples and powder beds were put in a closed alumina crucible so that they were isolated from the carbon atmosphere of the furnace. Inert gas (argon) was always used and the sintering process was always in a well-closed chamber, which means that argon was flowing through the furnace until 600°C and the furnace then tightly closed until the sintering was over, during which argon was over-pressured by 75 kPa. Weight, density and dimension of samples before and after sintering were carefully measured. XRD, SEM and optical microscopy were used for characterisations. Relative density and weight loss shown in this paper are the average of 12 samples of the same sort of composition in three runs in the same conditions.

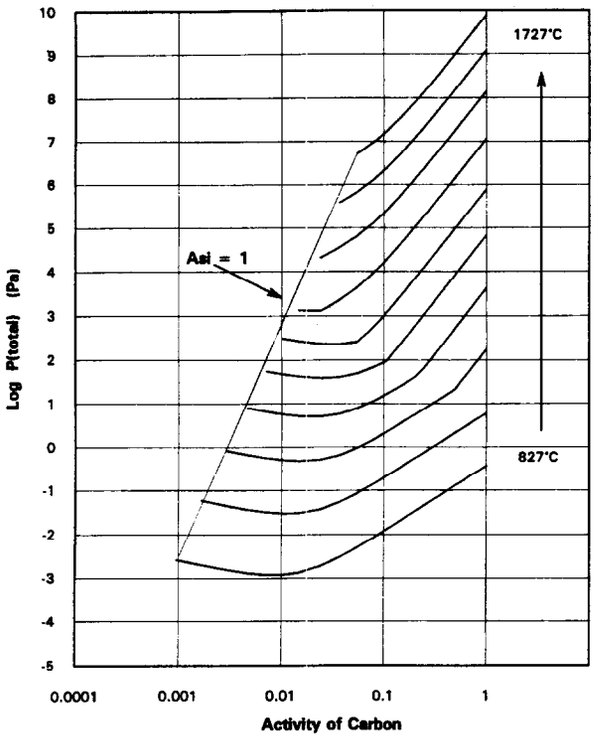

Fig. 3. Carbon activity dependence of total equilibrium partial pressure of evaporating phases produced by predominant reactions at different temperatures.

4 Results and Discussion

After several runs of closed-chamber sintering, some fine powder deposits on the furnace wall could

Table 1. Total partial pressure of evaporating phases in the equilibrium of SiC with LAS

Temp. (°C)	$P \times 10^5$ *Pa* as $A_C = 1$	$P_{min} \times 10^5$ *Pa*	A_C at P_{min}	$P \times 10^5$ *Pa* as $A_{Si} = 1$	A_C *as* $A_{Si} = 1$
827	3·70E-06	1·19E-08	0·010328	2·64E-08	0.000956
927	5·99E-05	3·02E-07	0·010328	5·99E-07	0·001665
1027	0·00176	4·74E-06	0·014716	8·33E-06	0·002919
1127	0·042209	5·03E-05	0·023875	7·93E-05	0·004723
1227	0·676196	0·000382	0·023875	0·000554	0·007168
1327	7·799071	0·00229	0·036792	0·003073	0·010328
1427	114·1237	0·012685	0·023875	0·013293	0·014716
1527	1409·583	—	—	0·205525	0·023875
1627	12054·54	—	—	3·819429	0·036792
1727	77309·13	—	—	51·075	0·054274

Table 2. LAS glasses used as SiC sintering aids in this paper

No	*Composition (wt%)* SiO_2	Al_2O_3	Li_2O	*Point in LAS phase diagram*[10]	*Liquidus* (°C)	*Melt at* (°C)	*Density* (g/cm^3)
1	65·2	15·0	19·8	Eutectic of LS&(LA4S)	1027	1227	2·33
2	55·0	22·5	22·5	Triple point at 1050°C	1050	1257	2·23
3	64·8	21·5	13·7	Hyper-eutectic of LS*&LA4S	1250	1427	2·40
4	65·2	25·0	9·8	Hyper-eutectic of LS*&LA4S	1327	1527	2·46
5	47·6	40·5	11·9	$Li_2OAl_2O_32SiO_2$(LA2S)	1400	1607	2·50
6	64·5	27·4	8·1	$Li_2OAl_2O_34SiO_2$ (LA4S)	1425	1627	2·48
7	40·0	50·0	10·0	(LA2S + LA* + L5A* + Al_2O_3)[11]	1577	1777	2·80
8	10·0	77·8	12·2	Eutectic of $LiAl_2O_4$&Al_2O_3	1650	1877	2·81

Note: *LS = Li_2OSiO_2, LA = Li_2O Al_2O_3, L5A = $Li_2O5Al_2O_3$.

always be found and XRD analyses of these powders often gave Si, SiC and SiO_2, which are believed to be the products of low-temperature condensations of evaporating phases produced at high temperature by the reactions of SiC and LAS. This kind of reaction and the effects of these reactions on the sintering behaviour of SiC/LAS are the focal point of this paper.

Wettability of LAS glasses listed in Table 2 to SiC used in this study was proved by simply melting LAS on the top of SiC pellets. It has been found that all these glasses spread on the surface of SiC pellets and infiltrated into the pellets at the temperatures 100°C higher than the melting point, i.e. the sintering temperatures. The driving force of liquid-phase sintering is the capillary pressure between solid particles exerted by the liquid phase, which is dependent on the wettability of the liquid on the solid.[13] The resistance of liquid-phase sintering is from the viscosity of the liquid phase.[13] Since the sintering temperature was always 100°C higher than the LAS melting point, viscosity of these glasses should not be very different. Sintering time was kept to 30 min, which has been thought long enough for the completion of rearrangement of solid particles in LAS melts. It may be reasonably assumed that the controlling factor of the liquid-phase sintering of SiC in LAS is only the reactions of SiC with the components in LAS. These reactions consumed the materials within the samples and the evaporating phases produced permeated and filled voids inside the samples, strongly hindering centre-to-centre approaching and rearrangement of SiC particles in liquid phase. High partial pressure of the evaporating phases is apparently harmful to sintering.

Figures 4, 5 and 6 show the results (relative density and weight loss) of closed-chamber sintering of SiC with different LAS in PD1, PD2 and PD3, respectively. The numbers in these figures are the sample numbers. From these figures, it can be seen that, when the sintering temperature was

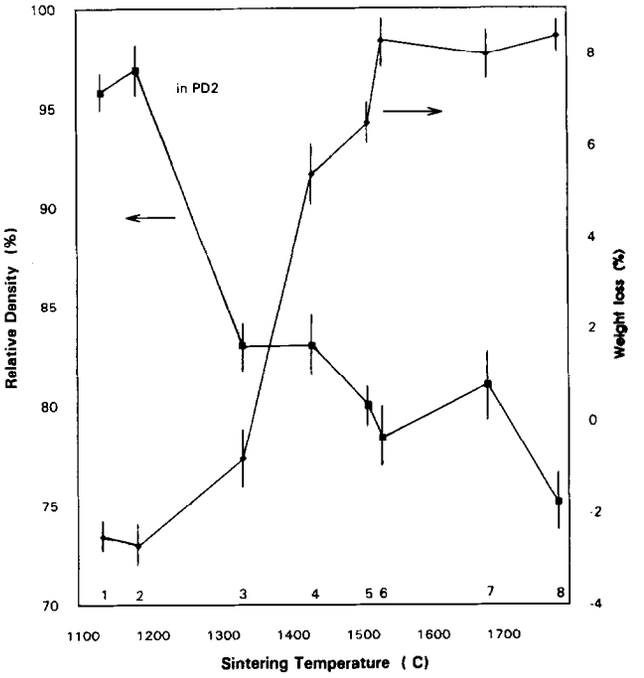

Fig. 5. Relative densities and weight losses of the samples in PD2 (carbon-rich). The numbers are sample number related to the sintering temperatures, 100°C higher than the liquidus (melting point) of LAS composition inside the samples.

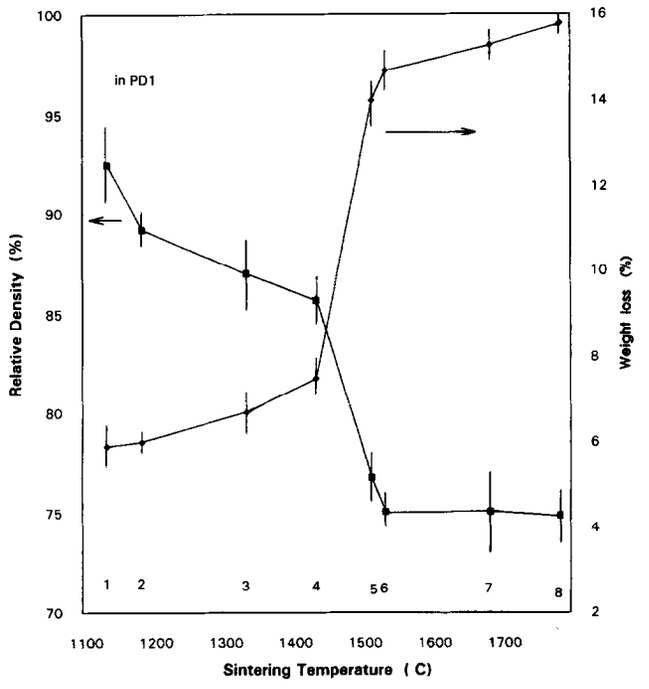

Fig. 4. Relative densities and weight losses of the samples in PD1 (stoichiometric). The numbers are sample number related to the sintering temperatures, 100°C higher than the liquidus (melting point) of LAS composition inside the samples.

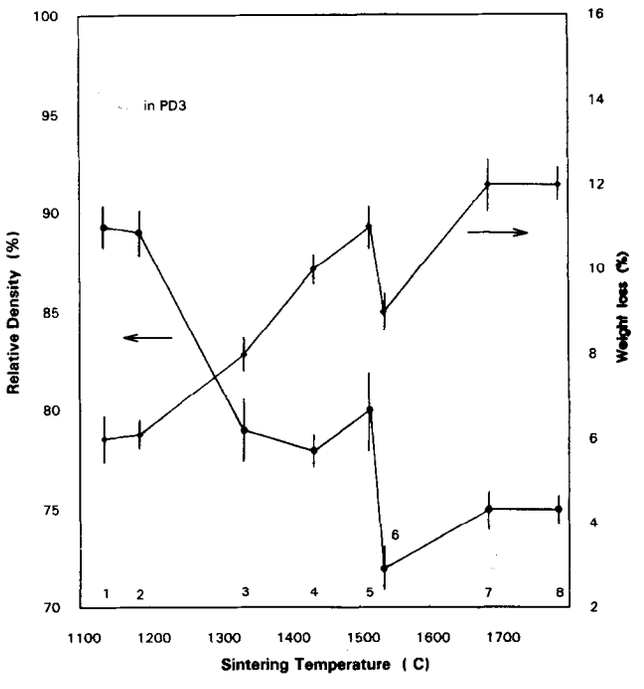

Fig. 6. Relative densities and weight losses of the samples in Pd3 (silicon-rich). The numbers are sample number related to the sintering temperatures, 100°C higher than the liquidus (melting point) of LAS inside the samples.

increased from sample 1 to 8, the relative density decreased. For samples sintered in PD1, the fastest relative density decrease appeared at temperatures from 1427°C (sample 4) to 1507°C (sample 5) (Fig. 4), and for samples sintered in PD2, density drop occurred from 1177°C (sample 2) to 1327°C (sample 3) (Fig. 5). This could be explained by the following:

In Fig. 4, since PD1 has the same composition of embedded samples, the reactions taking place in PD1 and inside samples should be thermodynamically the same. Higher relative density obtained at lower sintering temperature may be attributed to the lower partial pressures of evaporating phases resulting from these reactions taking place at these lower temperatures. It is suggested in Fig. 1 that, at any temperature from 1027 to 1427°C, *AA'* and *BB'* are crossed and a three-component reaction, reaction (15) may be dominant, particularly during the sintering at 1427°C (sample 4 in PD1). The total equilibrium partial pressure of evaporating phases produced by reaction (15) at 1427°C is relatively low (O in Fig. 1 and inflection points in Fig. 3) since the raw SiC powder used in this study was carbon-poor (28·8 wt% of carbon instead of 29·2 wt% for stoichiometric SiC). But at the temperatures above 1427°C, *BB'* is on the far right side of *AA'*, and reaction (9) is dominant. The total partial pressure of the evaporating phases is thus orders of magnitude higher than at temperatures of 1427°C and below (Fig. 3). The big jump of total equilibrium partial pressure from 1427 to 1507°C may be responsible for the fastest relative density decrease occurring in the same temperature range. The sudden increase in weight loss in Fig. 4 from 7·5% to 14% in the same range also supports this explanation. The sintered samples were X-rayed and Li_2C_2 was not found in sample 4 (PD1, 1427°C) and samples sintered below 1427°C, but was detected in sample 6 (PD1, 1527°C) (see A and C in Fig. 7). Li_2C_2 is the product of either reaction (9) or reaction (15). For low partial pressure (low temperature) samples, Li_2C_2 may be too small to be found. The Li_2C_2 detected in sample 6 (PD1 1527°C) was most likely produced by reaction (9) because only this reaction is predominant and gives higher pressure gas phases as well as a large amount of Li_2C_2.

In Fig. 5, sample 1 (PD2 1127°C) and sample 2 (PD2 1177°C) gave the highest relative densities and a negative weight loss (weight gain). A quick density decrease was found from sample 2 (PD2 1177°C) to sample 3 (PD2 1327°C) and the weight loss started to be positive after sample 2. As has been said, PD2 is carbon-rich, and therefore the highest total partial pressure of evaporating phases is expected (Figs 1 and 3). However, total equilibrium partial pressures of evaporating phases through reactions inside the samples are much lower because A_c inside the samples was reduced (SiC powder used was carbon-poor, 28·8% instead 29·2% for stoichiometric SiC; see also Fig. 3). Therefore, the reactions in PD2 prevailed over the possible reactions inside samples 1 and 2. Moreover, P_{SiO} and P_{CO} by PD2 (A_c = 1) at 1127°C and 1157°C may even make reaction (1) inside the samples proceed from right to left. No in-situ evaporating phases could be generated and no mass consumption could occur, and thus no sintering resistance existed. The weight gain found in these samples may also partially be caused by these. As sintering temperature was increased (from sample 3 PD2, 1327°C onwards), since the total partial pressures are above 0·1 MPa (Fig. 3), evaporating gases from PD2 may diffuse into the sample and tiny amount of carbon may be formed inside the samples through the reversible reaction (3), making A_c inside the samples change from less stoichoimetric towards 1 and initiating the reactions with high A_c between SiC and the LAS inside the samples. Partial pressure of evaporating gases higher than 0·1 MPa due to high carbon activity, may start to be created and high amount of mass consumption may occur, thus giving much lower relative density and positive weight loss (Fig. 5). This situation may be defined as an equilibrium between powder bed and sample.

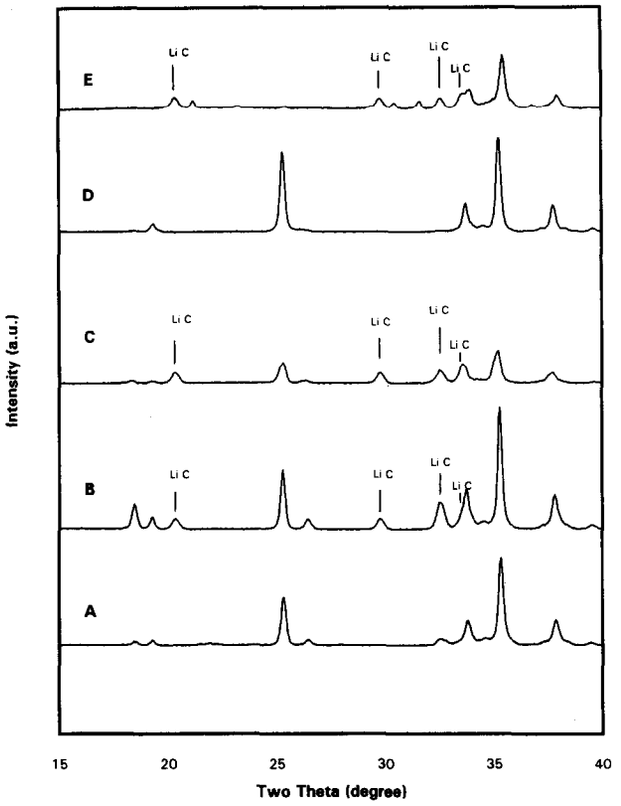

Fig. 7. X-ray diffraction results of sintered samples:

A:	Sample 4	PD1	1427°C	LiC not found
B:	Sample 3	PD2	1327°C	LiC found
C:	Sample 6	PD1	1527°C	LiC found
D:	Sample 1	PD2	1127°C	LiC not found
E:	Sample 7	PD3	1677°C	LiC found.

The establishment of this equilibrium certainly needs higher temperature and higher gas pressure. Sample 1 (PD2 1127°C) and sample 3 (PD2 1327°C) were also examined with XRD. Li_2C_2 was detected in sample 3 (see Fig. 7B), but not seen in sample 1 (see Fig. 7D). Li_2C_2 was also found in higher-temperature samples in PD2. This supports the presumption that gas-generating reactions really took place inside the sample 3 (PD2 1327°C) and other higher-temperature samples, but may not exist in low-temperature samples (e.g. sample 1 PD2 1127°C).

Weight gain found in samples 1 and 2 (PD2) could also possibly result from the condensation inside the samples of the evaporating phases generated by PD2 — mass transport from carbon-rich powder bed to sample during cooling. This condensation may also exist in other samples, and the weight loss in these samples was probably the net result of the condensation and gaseous phase evaporating (materials consuming). Samples 1 and 2 (PD2) in Fig. 5, which were 95·8% and 96·2% dense, respectively, were polished and photographs taken from optical microscopy are shown in Figs 8 A and B, respectively. They were also examined under SEM using back-scattering, shown in Fig. 9. They were basically close porosity. SiC particles were regularly arranged in the glass matrix (bright particles are SiC and dark background is glass). X-ray results (Fig. 7) show that the glass phase was crystallised even without post-sintering heat treatment.

Sample 7 (PD2 1677°C) was also examined under SEM (Fig. 10), β-SiC whiskers were found inside a hole of this sample. SiC whiskers are usually formed through gas reaction which has been discussed by many researchers, typically referred to Miller.[14] The appearance of SiC whiskers provides more evidence that evaporating phases were generated during sintering and the evaporating phases could be condensed to become secondary carbide, e.g. SiC whiskers. SEM observation was also done on sample 4 (PD2 1427°C); small particle agglomerates between SiC grains shown in Fig. 11 could

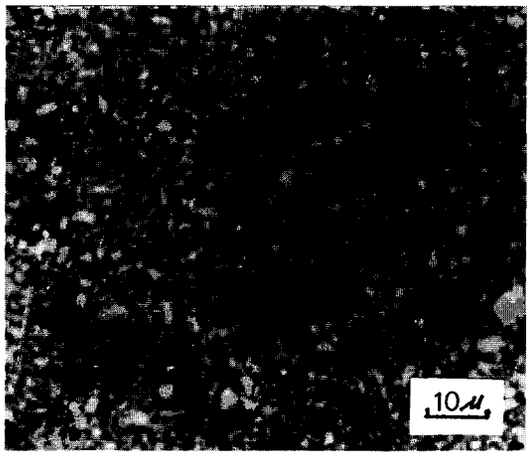

A

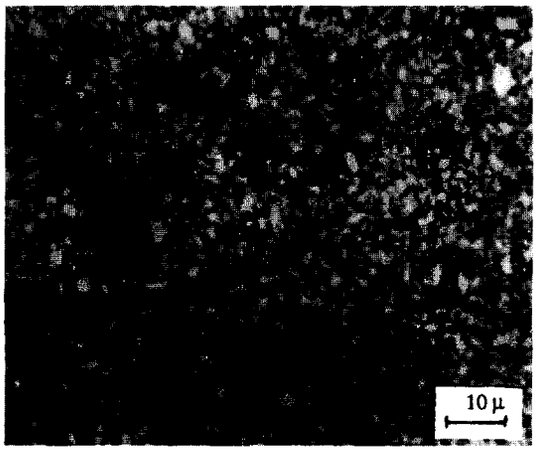

B

Fig. 8. Optical micrographs of polished samples
A: Sample 1 PD2 1127°C
B: Sample 2 PD2 1177°C.

A

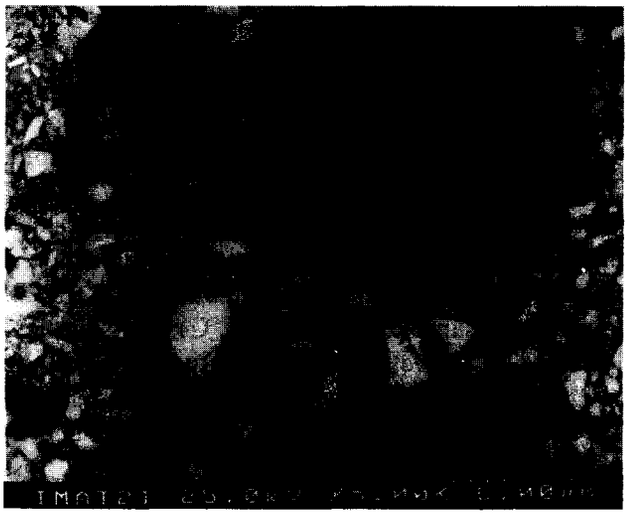

B

Fig. 9. SEM back-scattering micrographs of polished samples
A: Sample 1 PD2 1127°C
B: Sample 2 PD2 1177°C.

Fig. 10. SEM secondary electron micrographs of sample 7 sintered in PD2 at 1677°C. (SiC whiskers were found in a hole).

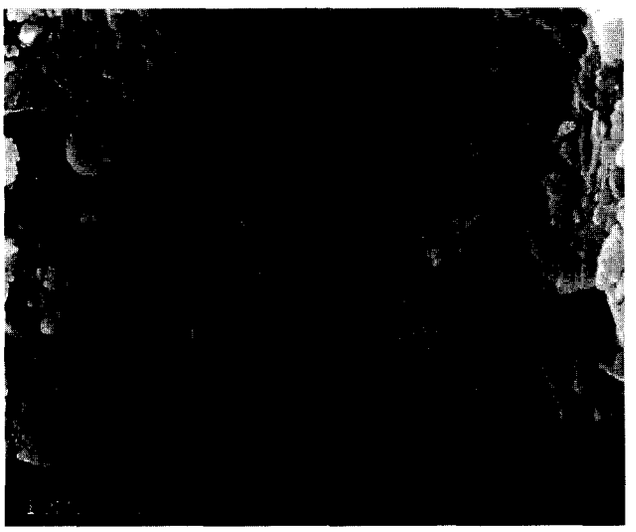

Fig. 11. SEM secondary electron micrographs of sample 4 sintered in PD2 at 1427°C. (Carbide agglomerates were found between SiC particles).

also be a newly formed secondary carbide by the reversible reactions inside the sample.

Samples sintered in PD3 were never well densified and weight losses were relatively large as shown in Fig. 6. Since PD3 was Si-rich ($A_{Si} = 1$), A_C in PD3 was the least. The total equilibrium partial pressure inside PD3 should be always lower than that inside the samples, where A_C is slightly less than stoichiometric (Fig. 3). Materials inside samples may be transferred to powder bed (PD3) by an expansion of the gases inside the samples. Even for samples 1 and 2 sintered in PD3, the sintering temperatures were relatively low, and the relative densities were lower than those sintered in PD1 and PD2. At higher sintering temperatures, above 1507°C, e.g. samples 5–8, the predominant reaction both inside the samples and inside PD3 is reaction (9) instead of reaction (1). The gas pressure by reaction (9) is higher than that by reaction (1) in the whole range of A_C (Fig. 1). Even though the equilibrium between PD3 and the samples may also be established and the A_C inside the samples may be also reduced to approach the minimum ($A_{Si} = 1$), and the total partial pressure inside the samples may be lower than that before the equilibrium, the absolute pressure is high, about $0{\cdot}21 \times 10^5$ Pa, $3{\cdot}82 \times 10^5$ Pa and $51{\cdot}08 \times 10^5$ Pa for samples 6 (1527°C), 7 (1677°C) and 8 (1777°C), respectively according to Table 1. Silicon-rich powder beds (PD3) may never favour the sintering. XRD for sample 7 (PD3 1677°C) also gave Li_2C_2 (Fig. 7E) which indicated that reaction (9) may be predominant at 1677°C. Weight loss in Fig. 6 was not significantly larger than for other cases even though relative density was lower.

It becomes necessary to recall that the calculation results in Section 2 are all for equilibrium states; equilibrium between SiC and LAS (in either powder bed or in sample), and the equilibrium partial pressures of evaporating phases are, according to the calculations, very high, e.g. 77309.13×10^5 Pa for $A_C = 1$ at 1727°C (Fig. 3 and Table 1). It seems, therefore, that kinetic factors have to be considered in most cases. Jacobson *et al.*[9] studied the kinetics of the reaction of SiC with SiO_2 and showed that the reaction from commencement to equilibrium may need 2–3 h or longer. The sintering time of this study was only 30 min, which probably means that the results reported here were far away from equilibrium. Explanation of these results on the basis of thermodynamic calculations may be only referred to as the tendency of these reactions. Kinetic considerations are beyond the scope of this paper, but it is suggested that kinetic resistance could be used to avoid these reactions which are harmful to sintering. Lowering the temperature of sintering via adjusting compositions in LAS melts not only lowered equilibrium partial pressures but also offered a high kinetic resistance.

Another equilibrium discussed above is the equilibrium between powder bed and sample. A_C inside samples was initially almost the same (28·8 wt% of carbon in SiC, slightly less than stoichiometric). During the equilibration between powder bed and sample, the A_C inside the samples and the A_C in powder beds will approach each other. This equilibrium may also have kinetic resistance. In the sintering of samples 1 (PD2 1127°C) and 2 (PD2 1177°C), the kinetic resistance may be too high to increase A_C inside the samples to reach the equilibrium so that the reactions inside the samples were effectively inhibited and successful sintering was realised. During sintering at higher temperatures, the kinetic resistance towards equilibrium will be reduced and carbon-rich powder beds will not help with the densification of the samples.

5 Conclusions

1 Thermodynamics has predicted that SiC reacts with the components in LAS melts. The equilibrium partial pressures of SiO, CO and Al_2O have been calculated by varying carbon activity and equilibrium temperature.

2 SiC/40 v% LAS (65·2 wt% SiO_2, 15·0 wt% Al_2O_3, 19·8 wt% Li_2O or 55·0 wt% SiO_2, 22·5 wt% Al_2O_3, 22·5 wt% Li_2O) has been successfully sintered at low sintering temperatures (1127°C and 1177°C, respectively) by using a powder bed with unity carbon activity. High carbon activity in powder bed and low sintering temperature inhibited the reactions producing evaporating phases inside the samples.

3 SiC/40 v% LAS (other compositions) had to be sintered at higher temperatures and the sintering was less successful. This could be attributed to the reactions of SiC with the components of LAS. Thermodynamic explanation, XRD and SEM observations all suggested that these reactions were responsible for the unsuccessful sintering.

4 The reactions of SiC with LAS could be controlled by changing carbon activity both in the powder bed and in the samples and by lowering sintering temperature. Advantages in kinetic resistance should always be taken for good sintering.

Acknowledgement

The authors acknowledge Zhejiang University for permitting Dr Yi Pan a leave of absence for working in The Department of Ceramics and Glass Engineering, University of Aveiro, Portugal.

References

1. Alliegro, R. A., Coffin, L. B. & Tinklepaugh, J. R., Pressure sintered silicon carbide. *J. Am. Ceram. Soc.*, **39** (1956) 386–9.
2. Lange, F. F., Hot-pressing behaviour of silicon carbide powder with additions of aluminium oxide. *J. Mater. Sci.*, **10** (1975) 314–20.
3. Omori, M. & Takei, H., Preparation of pressureless sintered SiC-Y_2O_3-Al_2O_3. *J. Mater. Sci.*, **23** (1988) 3744–9.
4. Bocker, W. & Hausner, H., The influence of boron and carbon additions on the microstructure of sintered alpha silicon carbide. *Powder Metall. Int.*, **10** (1978) 87–90.
5. Liu Zhien, Sun Yihui, Du Xijiang & Cheng Jijian, Preparation and crystallisation of ultrafine Li_2O–Al_2O_3–SiO_2 powders. *J. Mater. Sci.*, **30** (1995) 390–4.
6. Panek, Z., Liquid phase sintering of chemically unstable silicon carbide-lithium magnesium aluminosilicate-titania composites, *J. Mater. Sci.*, **29** (1994) 5383–9.
7. Chase, M. W., Jr, Davies, C. A., Downey, J. R., Frurip D. J., McDonald, R. A. & Syverud, A. N. *JANAF Thermodynamic Tables* (3rd edn). American Chemical Society and American Institute of Physics for the National Bureau of Standards, New York, 1985.
8. Misra, A. K., Thermochemical analysis of the silicon carbide-alumina reaction with reference to liquid phase sintering of silicon carbide, *J. Am. Ceram. Soc.*, **74** (1991) 345–51.
9. Jacobson, N. S., Lee, K. N. & Fox, D. S., Reaction of silicon carbide (IV) oxide at elevated temperatures, *J. Am. Ceram. Soc.*, **75** (1992) 1603–11.
10. Levin, E. M., Robins, C. R. & McMurdie, H. F., *Phase Diagram for Ceramists. 1969 supplement*. America Ceramic Society, 1969.
11. Sacramento, J. M. G., Si_3N_4/SiC Composites Processed with Liquid Phases in LAS System. PhD Dissertation, University of Aveiro, 1993.
12. Almeida, J. C. M., Sacramento, J. M. G., Correia, R. N., Fonseca, A. T. & Baptista, J. L., Dispersion and packing of mixtures of Si_3N_4 powders with SiC whiskers. In *Fabrication Technology British Ceramic Proceedings* ed. R. W. Davidge & D. P.Thompson, 1989, pp. 179–86.
13. Kingery, W. D., Bowen H. K. & Uhlmann, D. R., *Introduction to Ceramics*. John Wiley & Sons, New York, 1975, pp. 491–501.
14. Miller, P. D., Lee, J. G. & Cutler, I. B., The reaction of silica with carbon and silicon carbide. *J. Am. Ceram. Soc.*, **62** (1979) 147–9.

Journal of the European Ceramic Society **16** (1996) 1231–1236

PII:S0955-2219(96)00056-8
0955-2219/96/$15.00

Vitreous Joining Process of SiC_f/SiC Composites

Patrick Lemoine, Monica Ferraris,* Milena Salvo & Margherita Appendino Montorsi

Materials Science and Chemical Engineering Department, Polytechnic of Torino, c.so Duca degli Abruzzi 24, I-10129 Torino, Italy

(Received 20 November 1995; revised version received 22 February 1996; accepted 28 February 1996)

Abstract

The reactive joining of an SiC_f/SiC composite with a zinc borate glass was studied at various temperatures, in order to optimize the joining process and to fully understand the reactivity between glass and composite. A temperature-dependent gas-producing redox reaction between ZnO and SiC was found to give gradual disappearance of the bubbles and crystallites always present in the range from 700 to 1200°C, and to yield a highly amorphous, bubble-free joint. This study permitted us to prepare single lap shear test specimens with minimal void content in the joint, i.e. a fully reacted and amorphous joint. The shear strength value obtained for these joints was higher than 15 MPa at room temperature.

Introduction

SiC-fibre reinforced SiC composites (SiC_f/SiC) have good thermomechanical properties and chemical inertness, making them attractive structural materials for high-temperature applications.[1] However, the non-weldability and poor workability of these materials hinder the fabrication of large or complex structural parts. Assembling techniques such as mechanical fastening have limitations because of the inherent brittleness of the fibrous composite surface and the stress concentration around rivet and bolt holes. There is, therefore, a strong need for simple adhesive joining techniques, able to give thermomechanically reliable structures.

Joining of monolithic SiC has been demonstrated using various techniques including diffusion bonding,[2] brazing with alloys[3] and the utilization of a polymeric precursor.[4] These studies give useful information on chemical reactivities but the composite and monolithic SiC have different microstructural and microchemical surface properties and, hence, the joining techniques developed for monolithic SiC are not directly transferable to SiC_f/SiC composites. Yet there is only a limited amount of literature available on this subject. Rabin[5] joined SiC_f/SiC composites by hot-pressing and combustion of Ti–C–Ni joining agents, while Coon[6] studied the joining of SiC_f/SiC composites using various lithium aluminosilicate glasses.

Indeed, vitreous joining offers some distinct advantages. First, the mechanical and structural properties of the joint can be tailored by controlling the glass composition (i.e. wettability with the composite, interfacial strength and reactivity, glass infiltration into the composite porosity). Moreover, the strength of the joint can be improved by ceramisation of the glass. Finally, vitreous joining is usually performed at a temperature where the glass is already softened or even melted and, therefore, it does not require application of an external pressure. This last point may be interesting for applications involving components of large dimensions or difficult access.

In a previous paper[7] we reported on the reactivity of SiC_f/SiC composites with a zinc borate glass, chosen as joining agent. We found that the glass developed a redox reaction among SiC fibres, free carbon present in the composite and the ZnO present in the glass. In the present work we have attempted to investigate which reactions occur between ZBM glass and SiC_f/SiC composites for a wide range of temperature, and then to use the results of this study to prepare joints of maximized shear strength.

Experimental

The molar composition of the glass chosen as joining material is: 50·46% ZnO, 29·48% B_2O_3, 9·12% MgO, 4·53% SiO_2, 4·04% Al_2O_3 and 2·37% Na_2O.[7,8] Powders of the different oxides were mixed together in a platinum crucible and heated for 30 min at 1200°C. The melt was poured and cooled to room temperature. The resulting transparent glass was ground down for X-ray

*To whom correspondence should be addressed.

diffraction analysis (XRD; Philips PW1710), differential scanning calorimetry (DSC; Perkin–Elmer 7) and differential thermal analysis (DTA; Netzsch 4045). A heating microscope (Leitz GmbH; AII) permitted observation of the softening and melting of the glass. Cube samples of dimensions 3 × 3 × 3 mm^3 were formed with pressed glass powder, or by hard-grit paper polishing and shaping of a bulk glass sample. The cubes were positioned on a Pt-coated Al_2O_3 plate in the microscope's furnace and heated to 1200°C (10°C min^{-1}).

The SiC_f/SiC composite utilized in this study was a unidirectional reinforced material (from Dornier GmbH and German Aerospace) prepared by the liquid infiltration pyrolysis technique.

The reactions between the ZBM glass and the SiC_f/SiC composite were studied in the heating microscope on sandwiches made from two polished composites and a thin, pressed pellet of glass powder (0·3 to 0·6 mm thickness). One sandwich was heated from room temperature to 1200°C under argon flow at about 20°C min^{-1} and some photographs were taken while heating, as shown in Fig. 1 (the composite/glass interfaces were graphically superimposed).

To determine the best joining temperature, other sandwiches were heated to the chosen temperature (700, 800, 880, 900, 930 and 1200°C) and isothermally treated for 45 min. The samples were then analysed using scanning electron microscopy and energy-dispersive spectroscopy (SEM-EDS; Philips 525M SEM and Philips 9100 EDAX); the results for the polished and cross-sectioned sandwiches (Fig. 2) are shown in Table 1. Finally, mechanical testing of the most promising joints was performed on single lap shear specimens of the ASTM 2733 type, with a SINTEC D/10 material testing machine.

Results and Discussion

The characteristic temperatures of the ZBM glass were found by DSC, DTA and heating microscopy: the glass transition (T_g) is at 536 ± 3°C; the first and second crystallizations (T_{x1} and T_{x2}) are at 676 ± 10 and 779 ± 5°C, respectively; the softening point is at 650 ± 10°C; and the melting temperature onset is at 880 ± 10°C.[7]

In order to investigate the reactivity between glass and composites, one sandwich was heated on the heating microscope from room temperature to 1200°C: Figures 1(a)–(i) show contrast photographs taken in the microscope during heating. First, softening of the glass pellet can be seen at 650°C [Fig. 1(b)]. Then, from 650 to 1200°C [Figs 1(b)–(i)], the vitreous joint expands, reacts and shows the formation of some bubbles. This bubbling is strong enough to displace the upper composite [Figs 1(g) and (h)] and seems to be at its maximum around 1100–1200°C. Above this temperature range the bubbles progressively disappeared and the joint regained its homogeneous and bubble-free appearance, with a good wetting angle with the composite (θ = 35°) [Fig. 1(i)].

Zinc oxide has a well-known reactivity towards carbon to give metallic zinc and carbon monoxide [see below, reaction (1)]: the same reaction could be foreseen between zinc oxide and silicon carbide to give metallic zinc, carbon monoxide and silicon monoxide [reaction (2)]. Since free carbon is always present in the SiC_f/SiC composites in variable percentages depending on the preparation process, reaction (1) is the most probable at the glass/composite interface. At 906°C Zn is a gas and there are at least two gaseous species present above this temperature: gaseous zinc and carbon monoxide (effectively, some metallic Zn was always found at the cold bottom of the oven after the joining process). The observed swelling and displacement of the upper composite in Figs 1(g) and (h) are likely to be due to these gaseous products.

$$ZnO(s) + C(s) \rightarrow Zn(g) + CO(g) \quad (1)$$

$$2ZnO(s) + SiC(s) \rightarrow 2Zn(g) + SiO(g) + CO(g) \quad (2)$$

By observing Fig. 1, one could say that a heating treatment of about 45–50 min from room temperature up to 1200°C (20°C min^{-1}) can apparently give joints without bubbles, but no information is given about the kinetics of the process: i.e. it is not known how long it takes for the gaseous species to complete their reactions at a given temperature. For example, Fig. 1(d) taken at 950°C shows an evident increase of the joining material volume, but it is not clear whether this is due to the formation of bubbles and/or to a crystallization with volume increase; also, it cannot be predicted how long this reaction takes to end.

For these reasons, other sandwiches were heated from room temperature to a temperature in the range 700–1200°C and isothermally heated for 45 min at that temperature. (Longer heating times would probably be detrimental for the mechanical properties of the composites.) Furthermore, we tried to obtain sandwiches joined at the crystallization temperatures of the glass, with the aim of preparing a glass-ceramic joint that would be thermally and mechanically more stable than a vitreous one.

SEM micrographs of the cross-sections of sandwiches prepared at different temperatures are shown in Figs 2 (a)–(f). The first joined structure [Fig. 2(a)], obtained at 700°C (above the softening

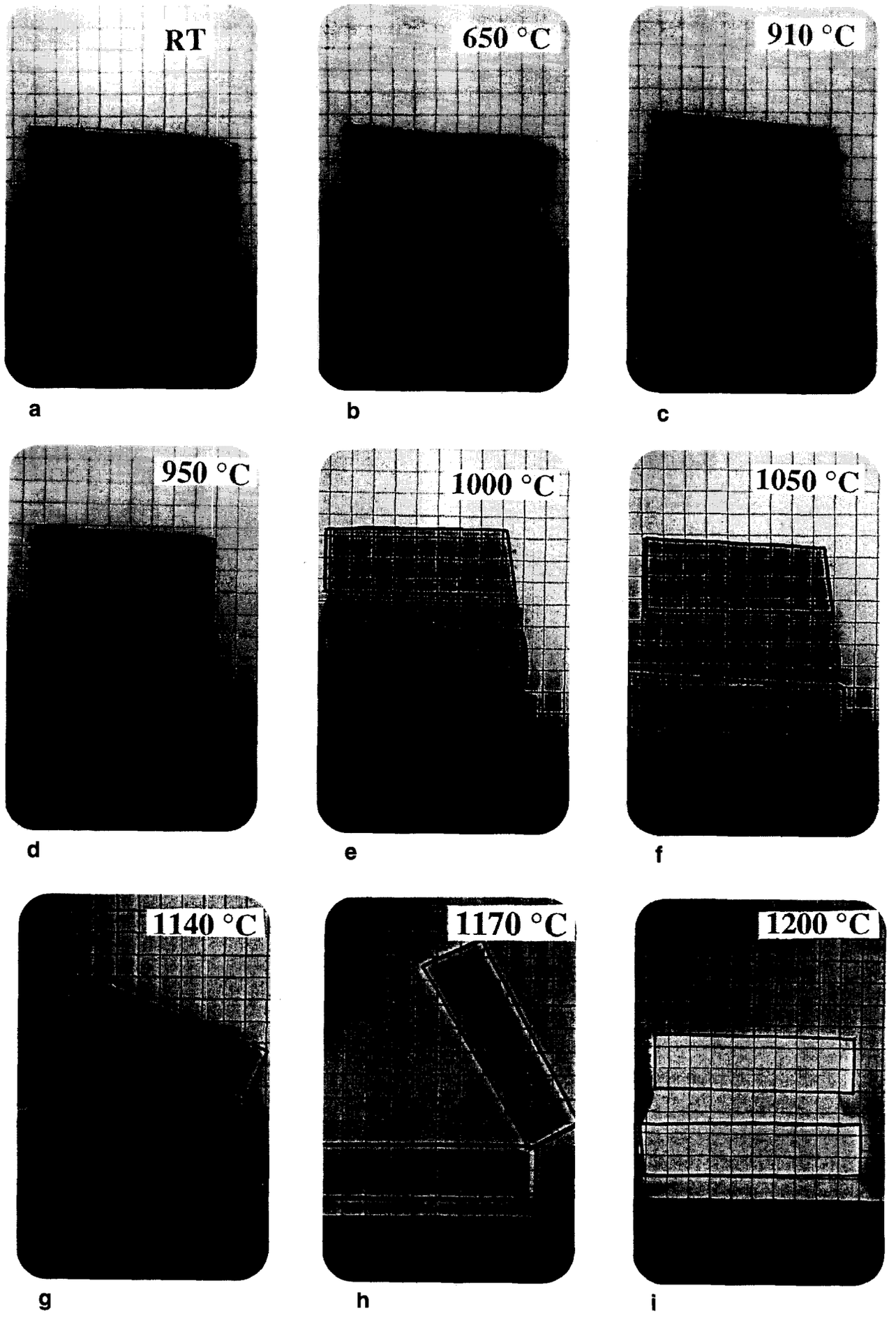

Fig. 1. Contrast photographs of an SiC_f/SiC/ZBM/SiC_f/SiC sandwich (magnification: 3×) taken in the heating microscope during heating. The temperatures at which the photographs were taken are indicated. The composite/glass interfaces have been graphically superimposed.

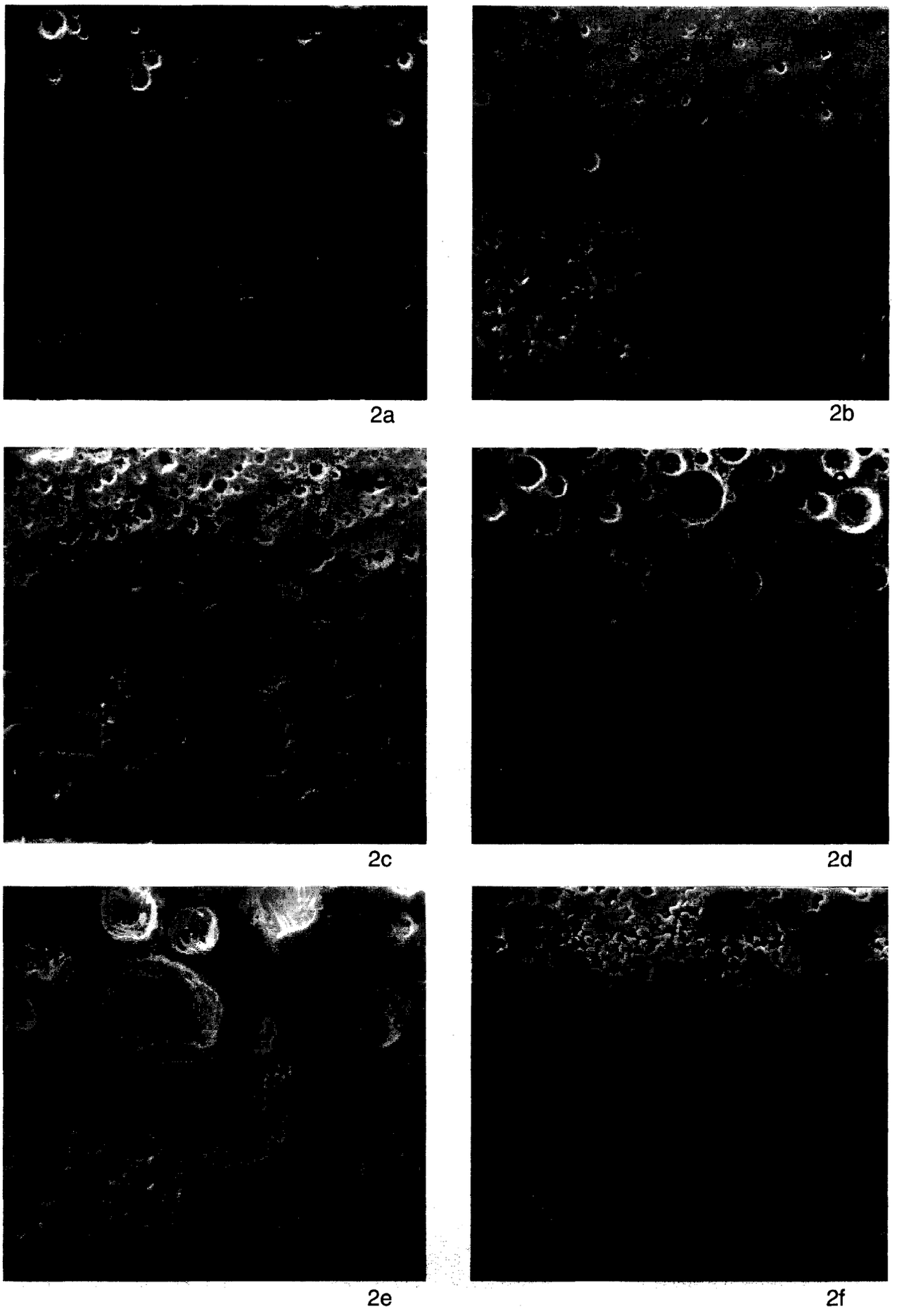

Fig. 2. SEM micrographs of cross-sectioned $SiC_f/SiC/ZBM/SiC_f/SiC$ sandwiches heat-treated for 45 min at different temperatures, as indicated on the micrographs.

Table 1. Effect of heat treatment on morphology and structure of the joints. The first column indicates the temperature at which the sandwiches were heated for 45 min and in which micrograph the sandwich is shown (in parentheses); Na, Mg, Al, Si and Zn reported are wt% measured by EDS (the values obtained for bulk ZBM are included for comparison)

Temperature (°C)	*Composition (wt%)*					*Pores*	*Morphology*
	Na	*Mg*	*Al*	*Si*	*Zn*		
ZBM bulk	7·16	0·59	3·12	2·41	86·7	—	amorphous
700 (2a)	5·94	0·56	3·88	3·73	85·88	yes	crystalline
800 (2b)	9·16	0·52	2·49	3·77	84·03	yes	crystalline
880 (2c)	5·82	—	5·52	4·5	84·14	yes	crystalline
900 (2d)	6·29	—	3·63	6·07	83·99	yes	crystalline
1200 (2f)	—	—	1·29	97·84	0·87	no	amorphous

point and T_{x1}, but below T_{x2}), presents a joined layer that is slightly bubbled and partially crystallized [$Zn_3(BO_3)_2$, as detected by XRD and EDS]. The interface between glass and composite is partially discontinuous. The samples shown in Figs 2(b) and (c), obtained by heating at temperatures above T_{x2} (800 and 880°C, respectively), gave bubbled and crystallized joints with partially discontinuous interfaces; when the joining temperature was above the melting temperature [Figs 2(d) and (e)] the interface between glass and composite was improved with respect to that produced at lower temperature [Figs 2(a)–(c)] but the amount of gaseous product becomes predominant, as already observed by heating microscopy [see Figs 1(d) and (e)]. Clearly the glass matrix is reacting with the composite and drastically changing its composition, with the production of gaseous species.

One can also note that the joint shown in Fig. 2(e) does not show any crystalline phase or porosity, in contrast to the samples of Figs 2(b)–(d). As the crystalline phase has been found to be $Zn_3(BO_3)_2$, its disappearance could be explained by zinc removal from the ZBM glass matrix, as discussed above [reaction (1)] and shown in Table 1. The reaction between the ZBM glass and the SiC_f/SiC composite appears to be complete after 45 min at a temperature of about 1200°C, leaving a continuous, bubble-free and amorphous joint region [Figs 1(i) and 2(f)].

The Zn content (wt%), measured by EDS analysis in the joint region of the above-described sandwiches, gives information about the onset and completion temperature for the reaction between glass and composite (Table 1: only the Zn percentages are reliable and significant, as the others are too low for the detection limits of this instrument). As can be seen, the Zn content decreases from the starting concentration to a few wt% when the temperature increases towards 1200°C. The vitreous and bubble-free joint obtained at 1200°C *no longer contains zinc oxide*: the reactive joining process gave rise to a glass of different composition with respect to the starting ZBM one.

To understand the influence of ZnO in these reactions, we performed identical joining experiments with a borate glass containing all oxides present in the ZBM glass except ZnO. The new glass composition was adjusted to keep the relative molar percentages of the other oxides identical to those of the ZBM glass: i.e. 59·5% B_2O_3, 18·4% MgO, 9·1% SiO_2, 8·2% Al_2O_3 and 4·8% Na_2O. Its preparation and characterization were identical to those of the ZBM glass. This glass (called BMA) had T_g = 565 ± 3°C (30°C higher than that of the ZBM), one crystallization peak at 810 ± 10°C and T_m = 1050 ± 10°C. First attempts at obtaining bubble-free sandwiches with the BMA glass failed: a sandwich $SiC_f/SiC/BMA/SiC_f/SiC$ heat-treated for 45 min at 880°C is shown in Fig. 3 as a typical example. Here again the glass wetted and reacted with the composite, but the joint contains many bubbles. We can therefore conclude that ZnO is not the only reacting oxide in ZBM glass; some new glass compositions will be tested to understand this feature.

In the case of ZBM joints, the data showed that all reactions producing gases are completed after

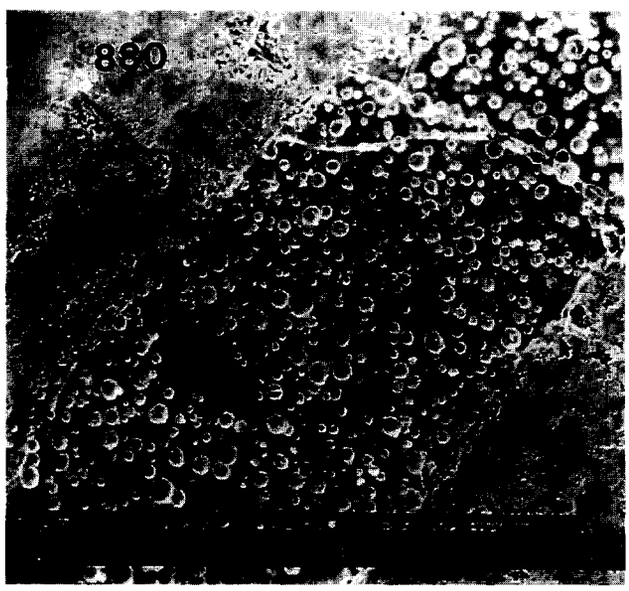

Fig. 3. SEM micrographs of cross-sectioned $SiC_f/SiC/BMA/SiC_f/SiC$ sandwich heat-treated for 45 mins at 880°C.

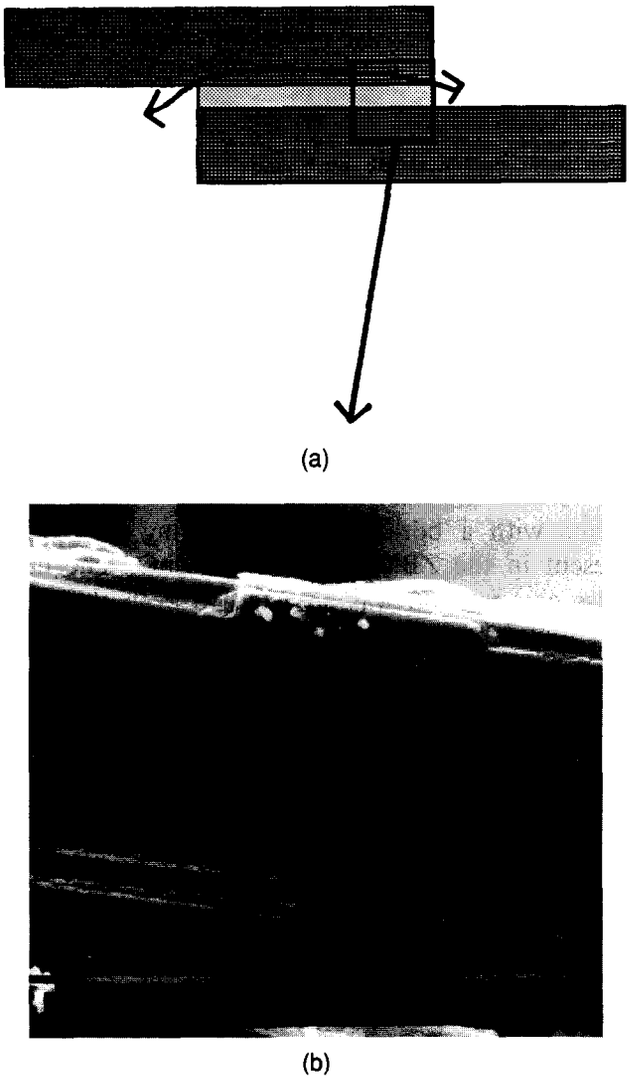

(a)

(b)

Fig. 4. (a)View of lap joint and fracture mode after shear tests and (b) cross-sectioned view of the fractured region indicated in Fig. 4(a), for a joined $SiC_f/SiC/BM/SiC_f/SiC$ structure prepared at 1200°C for 45 min.

45 min at 1200°C. Therefore, it being impossible to obtain bubble-free joints at lower temperatures even by changing the glass composition, we followed the route of a reactive joining, by heating the $SiC_f/SiC/ZBM/SiC_f/SiC$ sandwiches for 45 min at 1200°C. We prepared completely reacted and continuous joined structures and tested them in single lap shear experiments.

Failure always occurred in the composite by peeling stress with minimal bending of the adherends, for an average shear stress of 15 MPa on the joint. A cross-sectioned view of the fracture region shows that the specimen broke in the composite region nearest the joint [Figs 4(a) and (b)], the composite probably having been weakened by the heat treatment and/or because of the interfacial strength of the glassy joint. We can therefore state that the joint shear strength τ is superior to 15 MPa. This result compares well to the shear strength value found for a partially reacted joined structure (1000°C, 45 min: $\tau = 2{\cdot}6$ MPa in Ref. 7). The authors' belief is that the better surface coverage obtained for the 1200°C heat treatment is responsible for this significant improvement of the joint strength.

This lower limit of 15 MPa for the joint shear strength is an encouraging result for a vitreous, oxidation-resistant joint.

Conclusions

We have studied the temperature dependence of the reactions between a zinc-borate joining glass and an SiC_f/SiC composite. The results show that all gas-producing reactions are complete after 45 min at 1200°C; the composition of the joining glass changes during the process and the new glass wets the composite well, giving a continuous and stable interface. This study permitted the preparation of oxidation-resistant joints having acceptable shear strength.

Acknowledgements

The authors are indebted to Dr Schiller (JRC-Ispra, Va, Italy) for kind donation of the composites, to A. Favero and Ing. C. Baeli for assistance in performing the mechanical tests, and to ASP (To, Italy), HCM Programme (EC) and Fiat Research Centre (CRF, To, Italy) for supporting this research.

References

1. Lamicq, P. J., Bernhart, G. A., Dauchier, M. M. & Mace, J. G., *J. Am. Ceram. Soc.*, **65**[2] (1986) 336–8.
2. Moore, T. J., *J. Am. Ceram. Soc.*, **68**[6] (1985) C151.
3. McDermid, J. R. & Drew, R. A. L., *J. Am. Ceram. Soc.*, **74**[8] (1991) 1855.
4. Yajima, S., Okamura, K., Shishido, T., Hasegawa, Y. & Matsuzawa, T., *Am. Ceram. Soc. Bull.*, **60**[2] (1981) 253.
5. Rabin, B. H., *Mater. Sci. Eng.*, **A130** (1990) L1.
6. Coon, D. N., Vitreous joining of SiC fiber reinforced SiC composites. *NTIS DE90-012951*, Composite Materials Research Group, Dept of Mechanical Eng., University of Wyoming, 1989.
7. Lemoine, P. Salvo, M., Ferraris, M., Montorsi, M. & Scholz, H., *J. Am. Ceram. Soc.*, **78**[6] (1995) 1691.
8. Donald, I. W., *J. Mater. Sci.*, **28** (1993) 2841.

Journal of the European Ceramic Society **16** (1996) 1237–1244

PII:S0955-2219(96)00041-6
0955-2219/96/$15.00

Densification and Crystallisation Behaviour of Barium Magnesium Aluminosilicate Glass Powder Compacts

K. Lambrinou,[a] O. van der Biest,[a] A. R. Boccaccini*[b] & D. M. R. Taplin*[c]

[a]Department of Metallurgy and Materials Engineering, Katholieke Universiteit Leuven, B-3001 Heverlee, Belgium
[b]School of Metallurgy and Materials, University of Birmingham, Birmingham B15 2TT, UK
[c]University of North London, London N7 8DB, UK

(Received 15 November 1995; revised version received 25 January 1996; accepted 30 January 1996)

Abstract

The densification and crystallisation of barium magnesium aluminosilicate (BMAS) glass powder has been investigated. The aim of the study was to draw conclusions of value for the optimisation of the processing parameters for BMAS matrix ceramic composites. Pressureless sintering and hot-pressing techniques were investigated. The pressureless densification behaviour of cold-uniaxially pressed compacts was determined at isothermal and constant heating rate conditions using a high temperature microscope. The samples could be densified isothermally to full density at 930°C prior to the onset of crystallisation. For compacts sintered at constant heating rates between 800 and 1100°C, it was found that the simultaneous occurrence of crystallisation and densification strongly depends on the heating rate. Using hot-pressing (pressure = 20 MPa) results in full densification in the amorphous state after 1 hour at 925°C. X-ray diffraction analysis was used to characterise the crystallinity of pressureless sintered and hot-pressed samples that were fabricated at temperatures between 850° and 1300°C. The crystallisation behaviour did not change, in qualitative terms, with the pressure applied during hot-pressing. Combination of the densification and crystallisation results demonstrated that the BMAS glass can be densified completely at relatively low temperatures (930°C) in the glassy state. The material can be subsequently crystallised at higher temperatures (between 1100 and 1300°C) yielding a high-temperature-resistant microstructure consisting of Ba-osumilite, celsian and cordierite. Copyright © 1996 Elsevier Science Ltd

*Also with: Department of Environmental Sciences, University of Plymouth PL4 8AA, UK

1 Introduction

Densification prior to crystallisation (the glass-ceramic route) is particularly important for forming high-density composites. Many experimental studies have demonstrated that glass (amorphous) matrices are easier to densify around the rigid inclusions used as reinforcement phase (such as particulates, chopped fibres, whiskers, platelets and continuous fibre tows or mats) compared with polycrystalline matrices.[1–5] At an equivalent inclusion content, glass matrices have been shown to exhibit a much higher sinterability compared to crystalline matrices,[2] and therefore the beneficial sintering characteristics of glass can be conveniently exploited. After the densification step, however, it is necessary to control the nucleation and growth of the crystalline phase to obtain the required crystalline microstructure for structural or high-temperature applications. If the onset of crystallisation occurs before the glass has reached full density, further densification will be impeded by crystallisation due to the increase in viscosity caused by the crystalline phase.[1,6–8] In this context, an understanding of the interaction between densification and crystallisation of a given glass during sintering is essential for optimisation of the processing parameters which lead to the objective of obtaining a fully dense material before the onset of crystallisation occurs. Renewed interest has arisen, therefore, in studies of the sintering and crystallisation behaviour of glasses with compositions suitable for post-sintering crystallisation, which are candidate matrices for composites for high-temperature applications. While for dispersion-reinforced composites a pressureless sintering route may be applied to obtain dense products,[1–5,9] the use of continuous reinforcement, such as long

fibres or fibre mats, requires hot-pressing to achieve complete densification.[10] Thus, the interaction of densification and crystallisation in glass-ceramics must be investigated for both techniques, i.e. pressureless sintering and hot-pressing, for a complete assessment of the material as a candidate composite matrix.

The present study involves a comprehensive investigation of the densification and crystallisation behaviour of a barium magnesium aluminosilicate (BMAS) glass. The investigations were directed to gain useful information on the material's behaviour, allowing for the optimisation of processing parameters, rather than to perform a detailed study of the physics and kinetics of the processes involved. A similar BMAS material has been investigated in commercially available glass-ceramic matrix composites reinforced with SiC (Tyranno) fibres.[11,12] These are thought to be useful for structural applications at high temperature (up to ~1100°C).[11,12] Another group has studied extensively the mechanical behaviour of SiC (Nicalon) fibres-reinforced composites with similar BMAS glass-ceramic matrices.[13,14] Little is known, however, about the matrix densification and crystallisation behaviour during the processing of these materials.

2 Experimental Procedure

A commercial BMAS glass powder (provided by AEA Technology, Harwell) was used in this work. The theoretical density of the glass used is 2·74 g/cm^3, as determined in a previous work.[15] Quantitative Electron Micro Probe Analysis (EMPA) and X-ray diffraction (XRD) analysis were conducted on the as-received material to determine its exact composition and crystallinity. The as-received glass cullet was milled in a planetary mill and classified to obtain two mean particle sizes, 10·5 and 6·9 μm with narrow size distributions, as measured by laser diffraction analysis (Coulter L5130). Scanning electron microscopy (SEM) was used to investigate the glass powder morphology. Milled powder was used for Differential Scanning Calorimetry (DSC) measurements at heating rates of 10°C/min. In a previous study the surface energy and the viscosity of the glass (at 930°C) were determined to be γ = 0·440 N/m and $\eta = 8{\cdot}1 \times 10^7$ Pa s respectively.[16]

The experimental technique chosen for studying the pressureless densification behaviour is high-temperature microscopy, because it provides a number of advantages over dilatometry, as reviewed recently.[17] The most relevant advantage, in relation to the sintering of glass compacts, is the possibility of measuring both axial and radial shrinkages without exertion of external loads that could significantly affect viscous flow behaviour. Thus, 'true' pressureless sintering experiments can be conducted.[17] A complete description of the technique has been given elsewhere:[4,15,17] only relevant details will be presented here. Cylindrical compacts (5 mm in diameter by 5 mm) were used, which were formed by uniaxial compression of the 10-μm powder in a die without using a binder. Green densities of 0·51 ± 0·02 of the theoretical were obtained using pressures of 250 MPa. For the isothermal experiments the furnace of the heating microscope was first heated to the sintering temperature (which after trial and error experiments was determined to be T = 930°C) and subsequently the compacts were inserted quickly, in order to provide isothermal conditions for the whole stage of sintering. For the constant heating rate experiments the specimens were first heated to 800°C in about 1 hour with no glass sintering (shrinkage) observed up to this temperature. Then the samples were heated at a constant heating rate to a final temperature of 1100°C. Two heating rates, 15°C/min and 1°C/min, were used and two speciments were used for each heating rate and the results averaged. For both sets of experiments photographs of the samples were taken to record the lengths and diameters of the samples at predetermined intervals during the sintering process. In this way the axial and radial shrinkages could be calculated as explained elsewhere.[15] The mass and dimensions of the pressed and sintered compacts were measured and the geometrical densities determined. The final density of the sintered pellets was also measured using Archimedes' principle. The density as a function of time and temperature during sintering was determined from the green density and the measured axial and radial shrinkages, as shown below. Polished cross-sections of the sintered cylinders were prepared and the microstructures were observed by SEM. The crystalline composition of selected sintered samples was investigated by XRD analysis of polished surfaces.

The densification and crystallisation of the BMAS glass were also studied under hot-pressing conditions, since this is the technique relevant for manufacturing continuous-fibre-reinforced composites. The powder milled to an average particle size of 6·9 μm was used for these experiments. This is the optimum particle size for fabricating composites via a slurry infiltration technique, as determined elsewhere.[18] Hot-pressing of 30-mm diameter specimens was performed, using a KCE model facility, in vacuum at different temperatures, pressures and holding times. Three pressures (5·7, 12 and 20 MPa) were used. On the basis of the constant-heating-

rate and pressureless sintering experiments, a very quick heating rate was chosen to avoid crystallisation occurring prior to complete densification. The heating rates in all experiments were fixed at 100°C/min. A typical hot-pressing cycle involved heating up at 100°C/min to the holding temperature, which was varied between 850 and 1000°C, followed by a dwell time, which was varied between 2·5 and 60 min and then cooling down in the hot-press. In all cases the pressure started to be applied at 850°C and was maintained until the beginning of cooling. In another set of experiments, involving temperatures ≥1000°C, the sample was heated up to 900°C, maintained at this temperature for 15 min, subsequently heated up to a higher temperature, which was varied between 1000 and 1300°C, for given holding times, and finally cooled down. Here again the pressure started to be applied at 850°C and was maintained until the beginning of cooling. Post-fabrication pressureless heat treatment of samples that had been fabricated by hot-pressing at 950°C for 60 min with 12 MPa applied pressure was also carried out. As-hot-pressed and heat-treated samples were characterised by XRD analysis of polished surfaces. Selected samples were polished and prepared for SEM observation.

3 Results and Discussion

3.1 Material characterisation

The XRD pattern of the as-received glass powder is shown in Fig. 1, indicating that the material is amorphous in the range of detectability of XRD. The chemical composition of the as-received material, as determined by EMPA analysis is shown in Table 1. Figure 2 shows a SEM micrograph of the glass powder after milling to a mean particle size of 10 μm. The nonspherical shape of the particles, an important variable affecting the sintering behaviour of this glass as shown elsewhere,[16] is evident. The DSC curve, shown in Fig. 3, indicates that the softening point of the glass is 850°C, its crystallisation takes place between 1080 and 1140°C with the peak crystallisation temperature at ≈1120°C, while the melting point lies at ≈1400°C. These results supplied a preliminary guideline according to which the further densification and crystallisation experiments were designed.

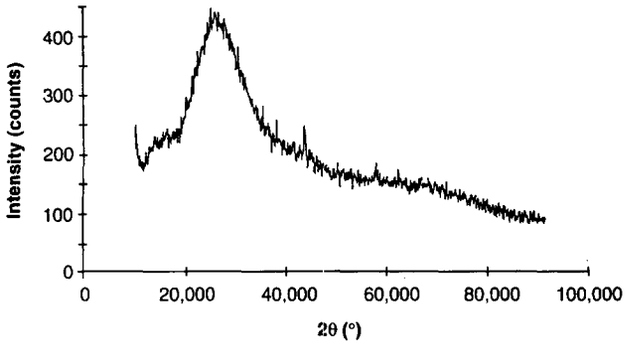

Fig. 1. XRD pattern of the as-received BMAS glass powder, showing its amorphous character.

Table 1. Chemical composition of as-received BMAS glass

Oxide	*Content (wt%)*
BaO	13·9 ± 0·5
Al_2O_3	27·7 ± 0·5
SiO_2	52·0 ± 1·0
MgO	6·4 ± 0·2

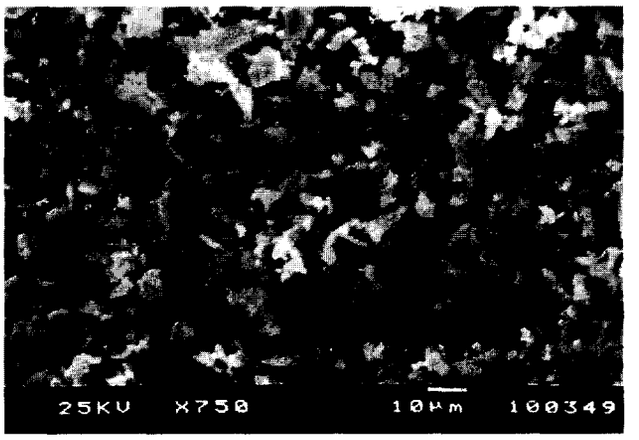

Fig. 2. Scanning electron micrograph of the BMAS glass powder investigated after milling to a mean particle size of 10 μm.

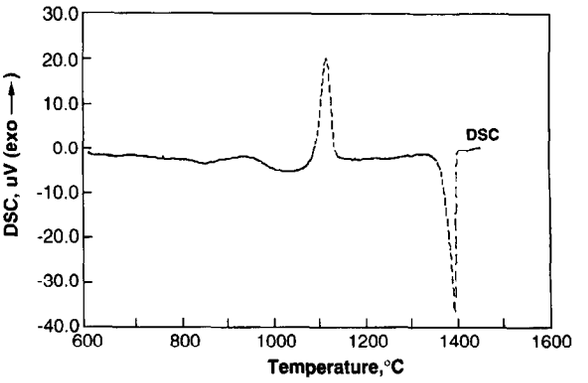

Fig. 3. DSC curve of BMAS powder milled to a mean particle size of 5·8 μm showing the exothermal crystallisation peak between 1080 and 1140°C.

3.2 Pressureless densification behaviour

Comprehensive studies of the sintering behaviour of BMAS powder compacts have been conducted recently[15,16] including a comparison of experimental values with theoretical models for viscous sintering, the consideration of shrinkage anisotropy effects and the assessment of densification and creep rates. Therefore, only a summary of the relevant results pertinent for the purposes of this paper will be presented in the following sections.

3.2.1 Sintered density

From the experimental data for the axial and radial shrinkages during sintering supplied by the heating microscopy measurements, the density (ρ) at any time (for the isothermal sintering experiments) or temperature (for the constant-heating-rate experiments) can be found using the following equation.[4,17]

$$\rho = \frac{\rho_0}{(1 - \Delta R/R_0)^2 (1 - \Delta H/H_0)} \quad (1)$$

where $\Delta R = R_0 - R$, $\Delta H = H_0 - H$ and ρ_0 represents the green density. R_0 and H_0 are the initial radius and length, respectively, and R and H are the instantaneous radius and length, respectively, of the sample.

Figures 4(a) and (b) show the densification curves for samples sintered isothermally at 930°C and at two different constant heating rates, 15 and 1°C/min, respectively. The density values were calculated using eqn (1), the data for radial and axial shrinkage, and the green densities. The data shown are averages of two runs under the same conditions

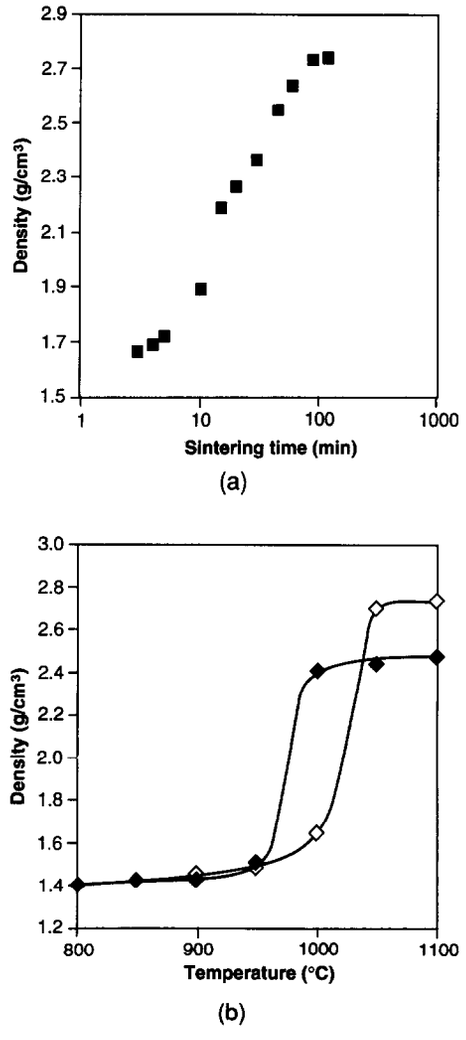

Fig. 4. Densification behaviour of BMAS glass powder compacts pressureless sintered: (a) isothermally at 930°C and (b) under constant heating rate conditions of (◇) 15°C/min and (◆) 1°C/min.

and have a maximum relative error of 4%. The final densities calculated from eqn (1) were in good agreement with the values determined using Archimedes' principle. Interesting conclusions about the pressureless densification behaviour of BMAS glass powder compacts can be drawn from Fig. 4. It is shown, for example, that a fully densified body (ρ = 2·74 g/cm^3) can be obtained after two hours of isothermal sintering at 930°C, a result which supports the technological approach of producing dense glass-ceramics in the BMAS system via a simple pressureless powder technological route. That the densification of BMAS powder at this temperature takes place via a viscous flow mechanism was confirmed in a previous study[16] by comparing the experimental results with the prediction of a theoretical model for viscous flow sintering.[19]

Figure 4(b) demonstrates qualitatively the influence of heating rates on the interaction between densification and crystallisation. It is observed that for both heating rates the densification curves reach a plateau. However, the reason for this is different for each heating rate. For the faster heating rate (15°C/min), the plateau is reached because the sample is nearly fully densified at ≈1050°C with a relative density ≈98% of the theoretical. For the lower heating rate (1°C/min) there must be another reason for the abrupt change in the slope of the densification curve at a lower temperature (1000°C), since the density is only ≈89% of the theoretical. This behaviour can be attributed to the onset of crystallisation at this temperature, as shown in a separate study,[20] in which the shear strains for both heating rates were calculated. The curve for the lower heating rate showed a typical sigmoidal behaviour with the shear strain first increasing with temperature as the viscosity of the glass decreases. An abrupt change in slope occurred near 1000°C, however, indicating that the material became suddenly more viscous, i.e. it began to crystallise. This can be directly related to the change of slope in the densification curve at approximately the same temperature, as shown in Fig. 4(b). These results are also in qualitative agreement with the DSC measurements (Fig. 3), that showed the onset of crystallisation at ≈1080°C. This temperature is slightly higher than that indicated by the densification curve of the 1°C/min sample (Fig. 4(b)), which is probably because the DSC measurements were carried out at a higher heating rate (10°C/min). Thus increasing heating rate delays the onset of crystallisation, as found by others.[6,7] Observation of the microstructure by SEM and the results of XRD analysis confirm that, for the compacts heated at the lower heating rate, crystallisation took place before completion of the densification process, as shown next.

3.2.2 Microstructural observation

Figures 5 and 6 show SEM micrographs of samples sintered isothermally for two hours at 930°C and at 1°C/min up to 1100°C, respectively. The material sintered at 930°C remained amorphous, at least in the detectability limit of XRD, and it is fully dense with only some isolated pores visible. On the contrary, using a low heating rate (1°C/min) has resulted in the early (partial) crystallisation of the material and the lack of complete densification. The XRD pattern of this sample is shown in Fig. 7. Celsian, Ba-osumilite and cordierite are the main crystalline phases found. This result is comparable with the crystallisation of the hot-pressed samples, as shown in the next section.

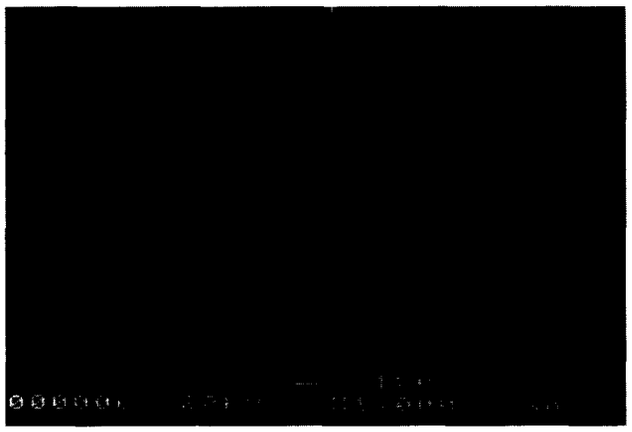

Fig. 5. Scanning electron micrograph of a polished section of a compact pressureless sintered for two hours at 930°C. Complete densification has been achieved without crystallisation.

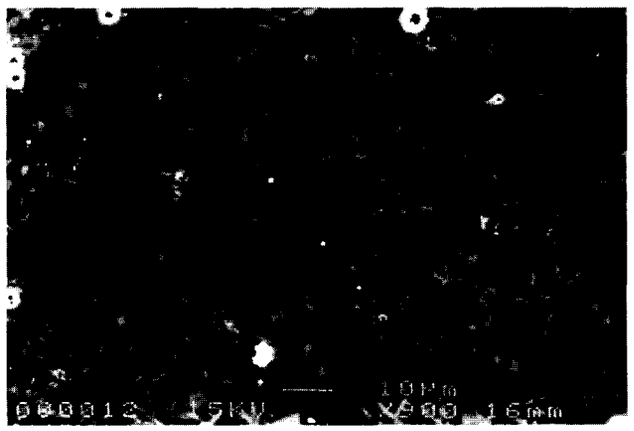

Fig. 6. Scanning electron micrograph of a polished section of a compact pressureless sintered at 1°C/min to 1100°C. Partial crystallisation and residual porosity are evident.

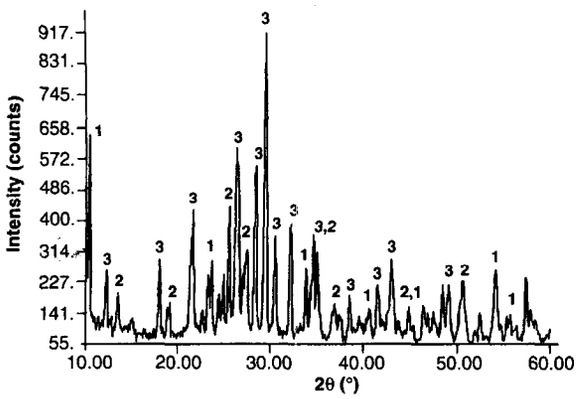

Fig. 7. XRD pattern of the polished surface of a sample sintered under the conditions given in Fig. 6 showing the appearence of: 1 = cordierite, 2 = celsian, 3 = Ba-osumilite.

3.3 Hot-pressing technique

3.3.1 Densification behaviour

The results of the density measurements of the as-hot-pressed samples indicated that complete densification could not be achieved for the lowest pressure employed (5·7 MPa) and holding times shorter than 1 hour, even for temperatures up to 1000°C. Compared with the pressureless sintering experiments described above, this result shows the importance of a sufficient holding time for achieving a fully dense sample, as well as the optimisation of the heating rates. Although the extremely high heating rates employed in the hot-pressing experiments are effective in suppressing the onset of crystallisation, they may negatively affect the viscous flow behaviour of the glass, leading to the development of closed cavities, which could not be completely eliminated by mass transport via viscous flow due to the short dwell times employed (<60 min). Complete densification could be achieved, on the other hand, for samples pressed at higher pressures. Pressing for 60 min at 950°C using a pressure of 12 MPa and at 925°C using 20 MPa resulted in complete densification. Thus, as expected, when compared with the pressureless sintering experiments, application of external pressure during sintering has reduced the densification time significantly but has not modified the sintering temperature.

The relative influence of temperature and pressure on densification can be further assessed by considering the experiments at higher temperatures using the low pressure of 5·7 MPa. As mentioned above the hot-pressing experiments for which the holding temperatures were above 1000°C comprised an initial step in which the sample was held for 15 min at 900°C. Microstructural examination done on samples pressed at 5·7 MPa proved that 15 min 'soaking' time at 900°C was insufficient to densify the glass completely. This is demonstrated by Figs 8(a) and 8(b), SEM micrographs of samples hot-pressed at 1070°C for 30 min and at 1300°C for 60 min, respectively, in which considerable homogeneously distributed spherical porosity is presented. This result is a further demonstration that once crystallisation has begun the material can no longer be fully densified, even using temperatures as high as 1300°C for 60 min, Fig. 8(b), and a residual porosity remains.

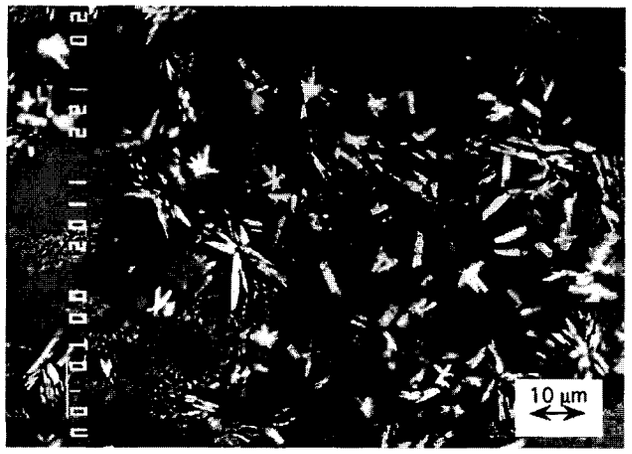

(a)

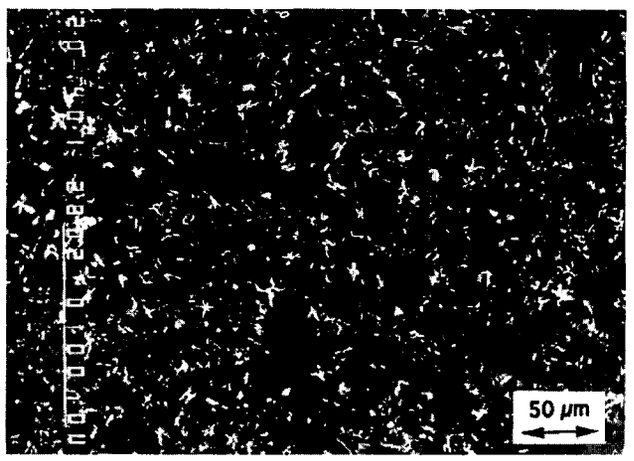

(b)

Fig. 8. Scanning electron micrographs of polished sections of samples hot-pressed using 5·7 MPa for (a) 30 min at 1070°C and (b) 60 min at 1300°C. The samples were partially crystallised before densification was completed.

3.3.2 Crystallisation behaviour

Crystallised glass-ceramics produced by hot-pressing of amorphous BMAS glass under pressures of 5·7, 12 and 20 MPa contained without exception Ba-osumilite ($BaMg_2Al_3(Si_9Al_3O_{30})$-hexagonal) as the major phase, and celcian ($BaAl_2Si_2O_8$-monoclinic) and cordierite ($Mg_2Al_4Si_5O_{18}$-orthorombic) as the minor phases. These phases have been found to be the main components in commercial BMAS glass-ceramic composite products,[11–14] being responsible for the high-temperature capability (≈ 1100°C) of these composites. Considering the results for all hot-pressed samples it is found that the material always becomes crystalline if it is pressed at 1025°C for 20 min or more. A typical XRD diagram is shown in Fig. 9. When compared with the results for the pressureless sintered material sintered at a low heating rate (1°C/min) (Fig. 7), the results for the hot-pressed samples indicate that the application of external pressure during densification has no major effect, at least

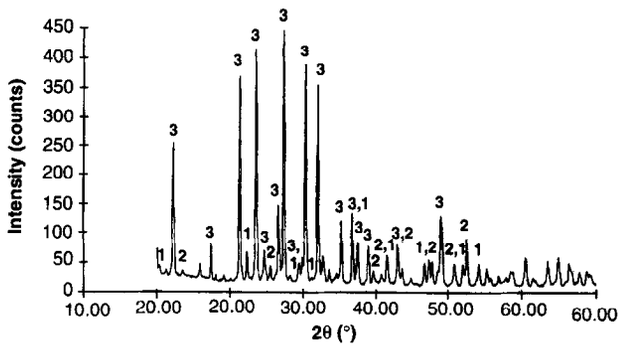

Fig. 9. Typical XRD pattern for hot-pressed samples fabricated at any pressure, showing crystallisation: 1 = cordierite, 2 = celsian, 3 = Ba-osumilite.

qualitatively, on the crystalline structure developed in BMAS glass-ceramics. A more detailed quantitative investigation of the crystallisation behaviour during hot-pressing, including crystal nucleation and growth processes and their dependence on pressure, time and temperature, is the focus of on-going studies.[18] On reference to Fig. 8(a) it can be seen that the microstructure of the crystalline samples contains white dendritic crystals spread inside the bulk glassy material and some 'eutectic-like' formations. EPMA measurements on the different phases showed that the composition of the dendrites is close to the stoichiometric composition of Ba-osumilite, while the composition of the 'eutectic-like' formations varies between the compositions of Ba-osumilite and celsian. The similarity between the microstructures of the partially densified hot-pressed samples, Figs 8(a) and 8(b), and the pressureless sintered sample that was sintered at the low heating rate of 1°C/min (Fig. 6) should also be noted.

The crystallisation behaviour was also investigated by long-duration (12 h) heat-treatment of hot-pressed dense samples after they had been cooled down to room temperature. A SEM micrograph of a sample hot-pressed for 60 min at 950°C and 12 MPa is shown in Fig. 10. Although this material was amorphous under XRD analysis, the presence of a few isolated crystals with dendritic shape is evident in the micrograph. The further micrographs, Figs 11(a)–(c), are SEM micrographs showing the microstructure of dense hot-pressed samples after heat treatment for 12 h at 1070, 1120 and 1300°C, respectively. Again Ba-osumilite was the main phase found, although celsian and cordierite were also present, as revealed by EPMA. In Fig. 11(a) the different crystalline phases are indicated. The big dark grey areas correspond to Ba-osumilite crystals, while celsian and cordierite appear as forming a network (celsian being the bright phase and cordierite the black one). The crystals are surrounded by an amor-

phous 'matrix' which appears of a homogeneous grey colour. With increasing heat-treatment temperature clearly the crystallinity of the samples also increases, with fewer islands of amorphous matrix phase. The number of the big Ba-osumulite crystals decreases with higher heat-treatment temperatures, while the interconnectivity of the celsian/cordierite network increases, Figs 11(b) and (c). Long-term heat-treatment at 1300°C, therefore, seems to be sufficient for complete 'ceraming' of the material. A more detailed study of the crystallisation kinetics, however, is beyond the scope of this work, being the subject of ongoing studies.[18]

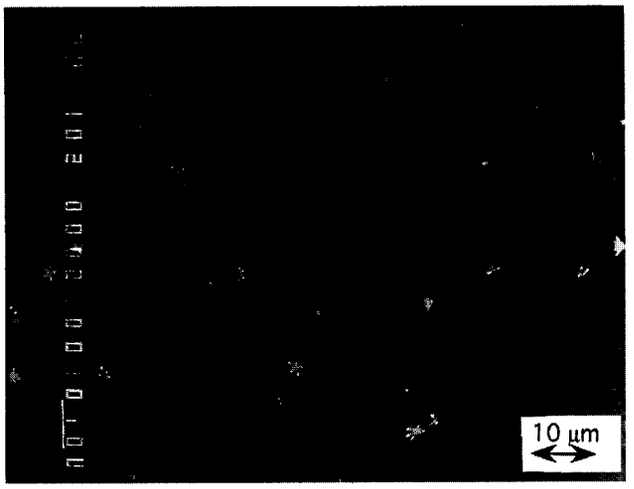

Fig. 10. Scanning electron micrographs of the polished section of a compact hot-pressed at 950°C for 60 min using 12 MPa. Complete densification has been achieved and a few dendritic crystals are distributed in the glassy matrix.

From the results of the XRD analyses, a Transformation–Temperature–Time (TTT) diagram, can be drawn. It approximately indicates the temperature/time 'window' for fabricating glass-ceramics from the amorphous BMAS powder by viscous flow densification in the glassy state, without crystallisation occurring. Such a diagram is shown in Fig. 12, where also the results of the pressureless sintering route have been included. Thus, the data represented in the TTT diagram can be conveniently used for designing the manufacturing route, via pressureless sintering or hot-pressing, of monolithic BMAS glass-ceramics and BMAS glass-ceramic matrix composites.

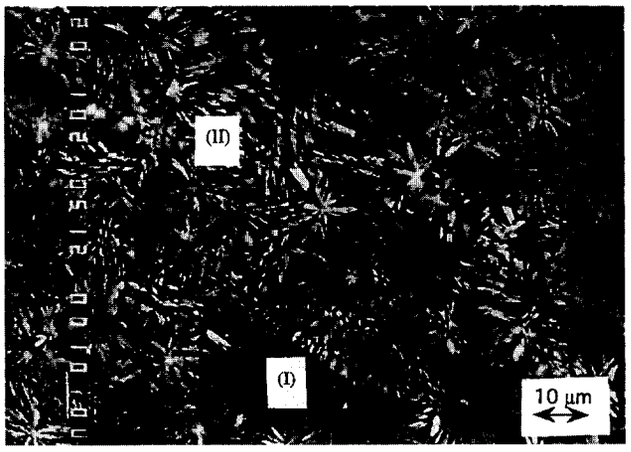

(a)

(b)

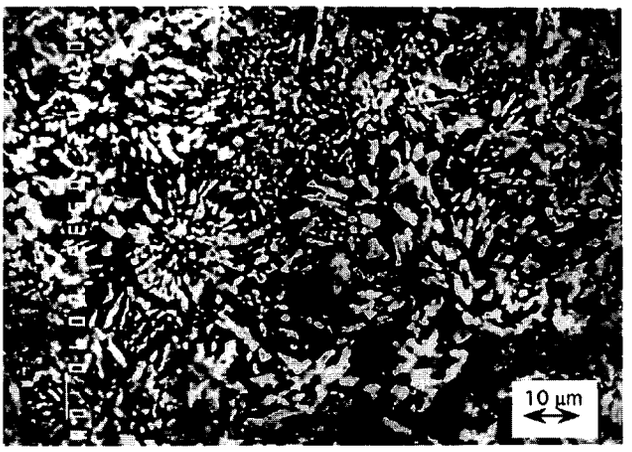

(c)

Fig. 11. Scanning electron micrographs of polished sections of samples hot-pressed under the conditions given in Fig. 10 and subsequently heat-treated for 12 h at: (a) 1070°C, (b) 1120°C and (c) 1300°C. (I) Ba-osumilite, (II) celsian/cordierite network. Crystallisation increases with heat-treatment temperature.

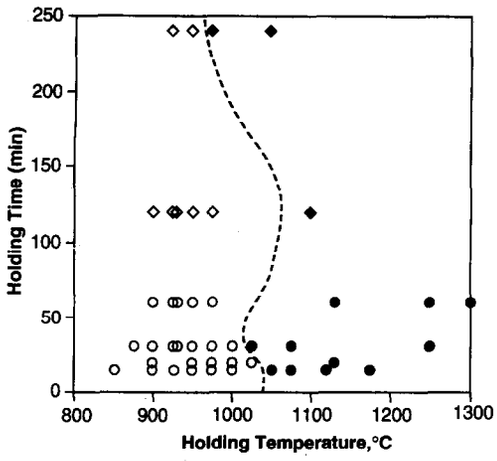

Fig. 12. TTT diagram constructed from the results of the XRD analyses for hot-pressing and pressureless sintering conditions: (◇) amorphous state, pressureless sintering, (○) amorphous state, hot-pressing, (◆) crystalline state, pressureless sintering, (●) crystalline state, hot-pressing.

4 Conclusions

A non-spherical BMAS glass powder with a composition suitable for producing glass-ceramics after a post-sintering heat-treatment was investigated in terms of densification and crystallisation behaviour. By appropriate selection of processing parameters, in pressureless sintering and hot-pressing techniques, complete densification can be achieved by viscous flow before the onset of crystallisation at relatively low temperatures (930°C). By subsequent heat-treatment at higher temperatures the desired refractory crystalline microstructure containing Ba-osumilite, celsian and cordierite is developed. These results are useful for designing the fabrication route for preparing BMAS glass-ceramics and fibre-reinforced BMAS glass-ceramic matrix composites.

Acknowledgements

The authors acknowledge the financial support of the European Commission with the provision of Brite-Euram contracts BE 4610, BRE2-CT93-3004 and BRE2 CT94 3064.

References

1. Jeng, D. Y. & Rahman, M. N., Effect of rigid inclusions on the sintering of mullite synthesized by sol-gel processing. *J. Mat. Sci.*, **28** (1993) 4421–6.
2. Bordia, R. K. & Raj, R., Analysis of sintering of a composite with a glass or ceramic matrix. *J. Am. Ceram. Soc.*, **69** (1986) C-55–C-57.
3. Boccaccini, A. R., Sintering of glass powder compacts containing rigid inclusions. *Sci. Sint.*, **23** (1991) 151–8.
4. Boccaccini, A. R., Sintering of glass matrix composites containing Al_2O_3 platelet inclusions. *J. Mat. Sci.*, **29** (1994) 4273–8.
5. Rahaman, M. N. & De Jongue, L. C., Effect of rigid inclusions on the sintering of glass powder compacts. *J. Am. Ceram. Soc.*, **70** (1987) C-348–C-355.
6. Panda, P. C. & Raj, R., Sintering and crystallisation of glass at constant heating rates, *J. Am. Ceram. Soc.*, **72** (1989) 1564–6.
7. Rudolph, T., Weisskopf, K., Pannhorst, W. & Petzow, G., Microstructural development of a P_2O_5-modified cordierite glass-ceramic during sintering. Part 2. *Glastech. Ber.*, **64** (1991) 305–9.
8. Du, Y.-J., Holland, D. & Pittson, R., Sintering and crystallisation behaviour of BaO-Al_2O_3-SiO_2 and BaO-ZnO-Al_2O_3-SiO_2 xerogel powders, *Phys. Chem. Glasses*, **34** (1993) 104–8.
9. Dutton, R. E. & Rahaman, M. N., Sintering, creep and electrical conductivity of model glass-matrix composites, *J. Am. Ceram. Soc.*, **75** (1992) 2146–54.
10. Prewo, K. M., Brennan, J. J. & Layden, G. K., Fibre reinforced glasses and glass-ceramics for high performance applications, *Ceram. Bull.* **65** (1986) 305–22.
11. *Fibre Reinforced Ceramics. Product Information.* AEA Technology Harwell, UK, 1992.
12. West, G., Boccaccini, A. R. & Taplin, D. M. R., Creep and creep-fatigue behaviour of continuous fibre reinforced glass-ceramic matrix composites. *Matwiss. u. Werkstofftech.*, **26** (1995) 368–73.
13. Brennan, J. J., Interfaces in BN coated fiber reinforced glass-ceramic matrix composites, *Scr. Metall. Mat.*, **31** (1994) 959–64.
14. Sun, E. Y., Nutt, S. R. & Brennan, J. J., Interfacial microstructure and chemistry of SiC/BN dual-coated Nicalon-fiber-reinforced glass-ceramic matrix composites, *J. Am. Ceram. Soc.*, **77** (1994) 132–9.
15. Boccaccini, A. R., Taplin, D. M. R., Trusty, P. A. & Ponton, C. B., Creep and densification during anisotropic sintering of glass powders, *J. Mat. Sci.*, **30** (1995) 5652–6.
16. Boccaccini, A. R., Trusty, P. A. & Taplin, D. M. R., Anisotropic shrinkage of barium magnesium aluminosilicate glass powder compacts during sintering, *Mat. Letters*, **24** (1995) 199–205.
17. Boccaccini, A. R. & Bossert, J., Using the Leitz heating microscope to study the sintering behaviour of powder compacts. *Mitt. f. Wiss. u. Tech.*, **10** (1994) 274–82.
18. Lambrinou, K., PhD Thesis, KUL-Leuven, in preparation (1995).
19. Exner, H. E. & Giess, E. A., A stereology-based equation for isotropic shrinkage during sintering by viscous flow. In *Proceedings of the VII World Round Table Conference on Sintering*, Herceg-Novi, Yugoslavia, Plenum Press, NY, 1990, pp. 73–83.
20. Boccaccini, A. R., Stumpfe, W., Taplin, D. M. R. & Ponton, C. B., Densification and crystallisation of glass powder compacts during constant heating rate sintering, *Mat. Sci. Eng. A*, (1996) accepted.

Journal of the European Ceramic Society 16 (1996) 1245–1251

PII:S0955-2219(96)00054-4
0955-2219/96/$15.00

Influence of ZrO_2 Addition on Melting Kinetics of a YSiAlO Glass-Ceramic

P. Vomacka[a] & D. S. Wilkinson[b]

[a]Department of Engineering Materials, Luleå University of Technology, S-951 87 Luleå, Sweden
[b]Department of Materials Science and Engineering, McMaster University, Hamilton, Ontario L8S 4L7, Canada

(Received 8 January 1996; revised version received 21 February 1996; accepted 28 February 1996)

Abstract

A ZrO_2-free YSiAlO glass of composition 27Y: 42Si:31Al in equivalent % and one with the addition of 6 wt% ZrO_2 were prepared in a nitrogen atmosphere at 1700°C. These glasses were treated in a nitrogen atmosphere at a controlled rate, during which the glass partially crystallizes to form a glass-ceramic. Under continued heating melting occurs. This behaviour was monitored by differential thermal analysis, scanning electron microscopy and X-ray diffraction. The original dendritic appearance of the crystallized microstructures changed to a blocky one in the early stages of the melting process. The ZrO_2 addition was found to increase the kinetics of the phase transformations occurring during the melting. Copyright © 1996 Elsevier Science Ltd

1 Introduction

Yttria–alumina–silica glasses have motivated numerous investigations over the past 20 years due to their potential for forming glass-ceramic materials and also due to the use of Y_2O_3 and Al_2O_3 as sintering additives in the production of structural ceramics such as silicon nitride (Si_3N_4).[1–4] A review of the crystallization studies on Y_2O_3–Al_2O_3–SiO_2 glasses was reported previously.[5] Oxide and oxynitride glasses in this system are generally considered as self-nucleating,[6] which has been confirmed in recent studies using ZrO_2 as a nucleating agent.[7,8] However, there are indications that the addition of zirconia influences the devitrification reactions in these glasses and in (Y_2O_3 + Al_2O_3)-fluxed sintered Si_3N_4.[9,10] In a previous study on yttria–alumina–silica glasses with zirconia additions,[11] two endothermic reactions were observed by differential thermal analysis (DTA) at temperatures exceeding 1400°C. Since the thermogravimetric measurements showed no mass changes these two endotherms were interpreted as representing melting reactions, assuming a formation of two immiscible liquids by a monotectic reaction.

The aim of the present work is to investigate the influence of ZrO_2 addition to a YSiAlO glass on the melting of YSiAlO glass-ceramics.

2 Experimental Procedure

A ZrO_2-free YSiAlO glass of composition 27Y: 42Si:31Al (eq. %), and one with the addition of 6 wt% unstabilized ZrO_2,[7] were prepared from mixtures of high purity yttria, alumina and silica (Rhone Poulenc, Alcoa Chemicals and Johnson Matthey, respectively) in the appropriate proportions. The equivalent% method representation of composition has been reported elsewhere.[12] The powders were mixed in polyethylene containers on a Siemens roller mill for 10 h using propanol, dried and sieved. Batches of approximately 100 g each were then mechanically compacted into molybdenum crucibles, melted under 0·17 MPa nitrogen pressure at 1700°C for 2·5 h, and furnace cooled. The cooling rate from the firing temperature to 1400°C was 20°C min^{-1}, from 1400 to 950°C, 15°C min^{-1} and from 950 to 500°C, 10°C min^{-1}. This rate was dictated by the natural cooling of the furnace (cold wall vacuum / pressure furnace with a graphite heater) after it had been switched off. Chemical analysis on as-received glasses was performed using X-ray fluorescence (Philips PW 3510, Rh tube), to verify the final composition of the glasses.

DTA (Netzsch STA instrument) was performed on 0·2 g powdered glass samples (particle size of approximately 50–90 μm) mechanically compacted into Al_2O_3 crucibles. The measurements were carried out in a nitrogen atmosphere using an Al_2O_3 powder reference standard and a heating rate of 5°C min^{-1}. The DTA runs were interrupted abruptly at the temperatures indicated in Table 1

Table 1. Compositions of the studied glasses, experimental conditions and phases identified by X-ray diffraction after cooling to room temperature (v.s., very strong; s., strong; m., medium; w., weak; v.w., very weak)

Sample designation	*Compositions (as-batched)*								*Max. temp. of DTA scan (°C)*	*Phases*
	eq %				*wt %*					
	Y	*Si*	*Al*	*O*	Y_2O_3	Al_2O_3	SiO_2	ZrO_2		
A	27	42	31	100	46·9	24·3	28·8	0	1370	β-$Y_2Si_2O_7$ (s.) mullite (v.w.) YAG (v.w.)
									1420	β-$Y_2Si_2O_7$ (s.) mullite (v.w.) YAG (v.w.)
									1430	β-$Y_2Si_2O_7$ (s.) YAG (m.) γ-$Y_2Si_2O_7$ (v.w.)
A + 6 wt% ZrO_2					44·1	22·8	27·1	6	1370	β-$Y_2Si_2O_7$ (s) mullite (v.w.) YAG (v.w.) Al_2O_3 (v.w.) ZrO_2 (v.w.)
									1400	β-$Y_2Si_2O_7$ (s.) mullite (v.w.) YAG (v.w.) Al_2O_3 (v.w.) ZrO_2 (v.w.)
									1420	β-$Y_2Si_2O_7$ (m.) YAG (s.) Al_2O_3 (s.) ZrO_2 (v.w.)

by switching the DTA furnace off and allowing the specimens to cool in the furnace. The cooling rate of the DTA furnace was approximately 20°C min^{-1} between the maximum temperature and 1000°C. The cooling rate was assumed to be high enough to avoid significant additional crystallization on cooling. Samples obtained in the DTA furnace were cut and polished with a dispersion of 1 μm diamond in kerosene as a final step. X-ray diffraction (Siemens diffractometer, CuK_α radiation) was performed on the specimens to identify crystalline phases after the heat treatments. Scanning electron microscopy (SEM) investigations were carried out using a Philips 515 scanning electron microscope with attached energy dispersive X-ray detector (EDX).

3 Results and Discussion

3.1 Glass preparation

Both compositions formed homogeneous glasses on melting without any traces of crystalline phases in the X-ray diffraction patterns. However, SEM examination of the as-received glasses revealed a very small amount of ZrO_2 precipitates in the microstructure of the ZrO_2-containing glass. These precipitates are believed to have either survived the melting or precipitated from the parent glass on cooling from the melting temperature. The latter is possible due to the limited solubility of ZrO_2 in the yttrium aluminosilicate liquid. The results of the chemical analysis of as-received glasses by X-ray fluorescence are summarized in Table 2. These results indicate a compositional shift, compared with the as-batched compositions, into the $Y_2Si_2O_7$–Al_2O_3–$Y_3Al_5O_{12}$ (YAG) compatibility triangle with the eutectic temperature of 1505°C,[3] caused probably by losses of some of the constituents (Al and Si) during melting of the glass.

3.2 Differential thermal analysis

Figure 1 shows typical DTA traces of the ZrO_2-free and ZrO_2-containing glasses at a temperature interval of 800–1550°C. An exothermic peak was detected at 1100 and at 1093°C for the ZrO_2-free

Table 2. Chemical analysis of as-received glasses

Sample	Y_2O_3	Al_2O_3	SiO_2	ZrO_2	*Std deviation (wt%)*
	(wt%)[a]				
A	56·5	18·8	24·7	0	0·2
A + 6 wt% ZrO_2	52·2	17·6	22·8	7·4	0·2

[a]Detectability limit 0·01%.

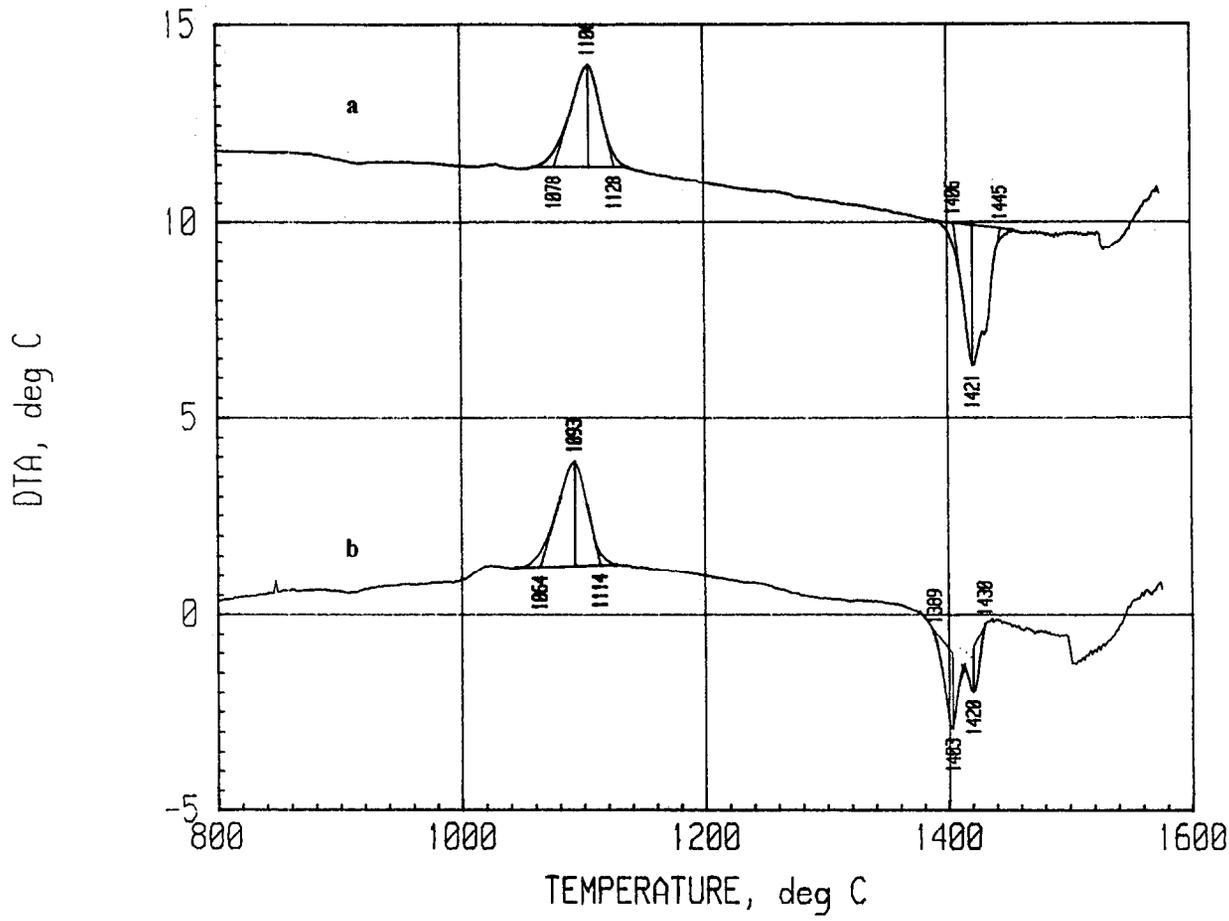

Fig. 1. DTA traces of the as-received glasses A (a) and A + 6 wt% ZrO_2 (b).

and the ZrO_2-containing glass, respectively, indicating crystallization of the glasses to form glass-ceramics. Three endothermic peaks can be distinguished on the curve of the ZrO_2-containing glass while the second endotherm appears only as a weak endothermic shoulder on the ZrO_2-free curve. Three DTA scans were carried out for each composition. The first one was interrupted for both compositions at 1370°C before the onset of the endothermic reactions. The second and third scans were interrupted at temperatures corresponding to the peak temperatures of the first and second endothermic reactions (at 1420 and 1430°C for the ZrO_2-free composition, and at 1400 and 1420°C for the ZrO_2-containing composition, respectively) as indicated in Table 1 and Fig. 1.

3.3 Phase identification and microstructure

The crystalline phases identified by X-ray diffraction analysis, following heat treatment in the DTA rig, are listed in Table 1 for both compositions and all the maximum temperatures. The phases detected are in general agreement with those expected from the equilibrium ternary phase diagram,[3] namely $Y_2Si_2O_7$, Al_2O_3 and YAG. However, some small amount of non-equilibrium mullite was also detected for both compositions. A cubic yttria-stabilized zirconia was observed additionally in the X-ray diffraction patterns of the A + 6 wt% ZrO_2 glass-ceramics.

Since the starting material was a glass powder with a significant specific surface area and due to a non-isothermal heat treatment, it is assumed that nucleation of the crystallization occurs predominantly at the surfaces. Figure 2 shows the microstructure of the glass-ceramics after the DTA scans were interrupted at 1370°C. The microstructures consist mainly of dendrites of the β-$Y_2Si_2O_7$ phase. β-$Y_2Si_2O_7$ side branches are seen to develop from the larger β-$Y_2Si_2O_7$ dendrites. A small amount of glassy phase remains in the microstructures. The A + 6 wt% ZrO_2 composition also contains small precipitates of the yttria-stabilized zirconia phase.

When the DTA scans were interrupted at temperatures corresponding to the first endothermic peak (at 1420 and 1400°C for A and A + 6 wt% ZrO_2, respectively), the dendritic morphologies of both microstructures have given way to a blocky morphology with a grain size of approximately 3–10 μm (Fig. 3). The X-ray diffraction patterns showed the same phases as for the heat treatment to 1370°C (see Table 1). The amount of glassy phase however increased slightly. (This could not

(a)

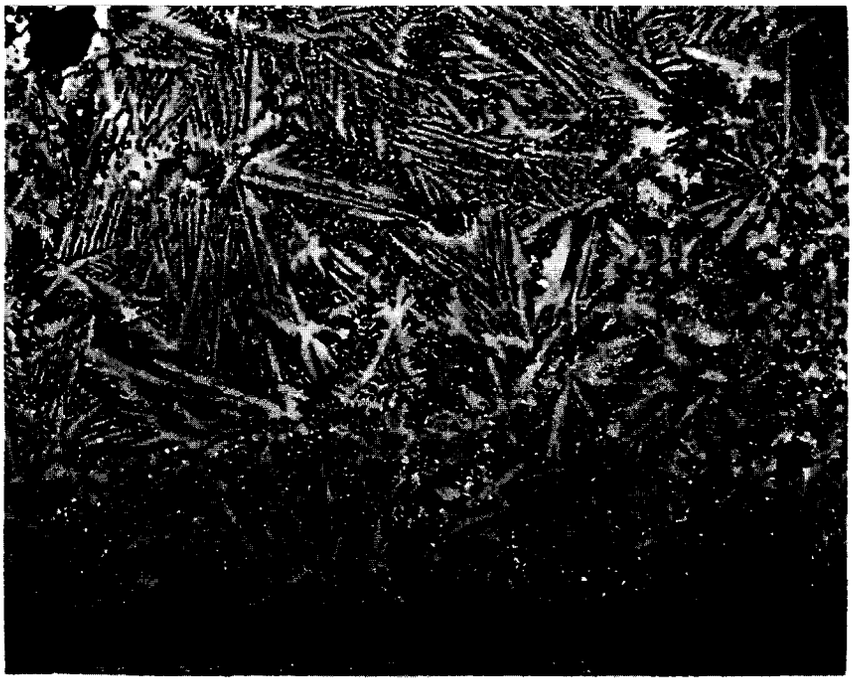

(b)

Fig. 2. Micrographs of the glass-ceramics A (a) and A + 6 wt % ZrO_2 (b) at 1370°C-backscatter image of β-$Y_2Si_2O_7$ dendrites in a glassy matrix. Small bright crystals in (b) are the yttria-stabilized zirconia.

be detected by X-ray diffraction but was measured by careful analysis of the microstructure using SEM and the point counting method.) Thus, the appearance of the first endotherm is attributed to the partial dissolution of a very small amount of the β-$Y_2Si_2O_7$, and other non-equilibrium phases present. The crystallization of both glasses involves large compositional changes when the crystalline phases crystallize out from the parent glass. Therefore diffusion of ions over large distances is required in order to achieve the equilibrium phase content. The viscosity of the retained glass in the microstructure controls the diffusion rates. At the end of crystallization, the retained glass in the glass-ceramics A and A + 6 wt% ZrO_2 is rich in SiO_2 and Al_2O_3 because of the crystallization of the β-$Y_2Si_2O_7$. This involves the rejection of Si, O, Al (and Zr for the A + 6 wt% ZrO_2 composition) ahead at the glass/crystal interphase.[13] The viscosity of the retained glass at the temperature approaching the onset of the endothermic reaction is low enough to cause the change of the morph-

(a)

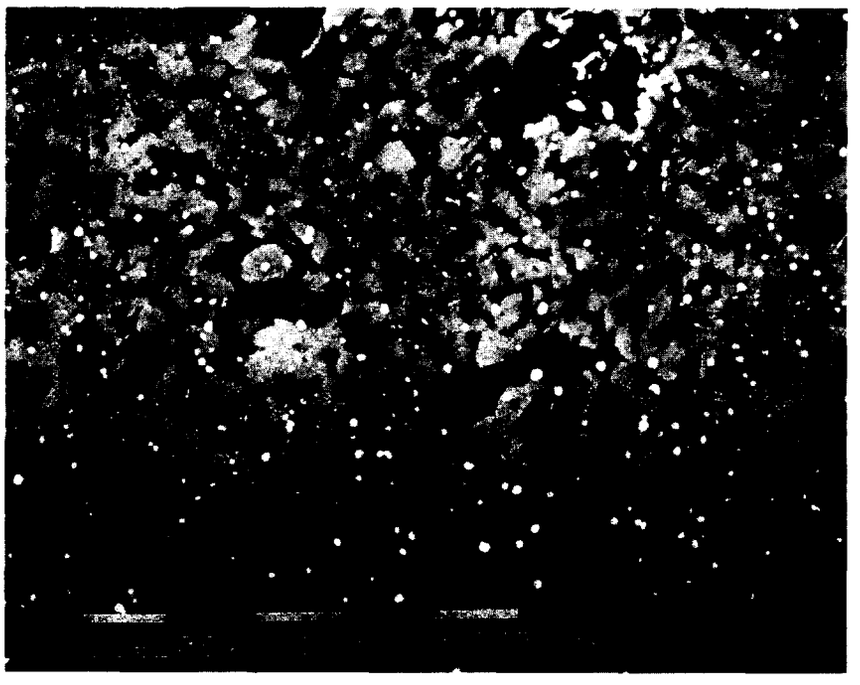

(b)

Fig. 3. Micrographs of the glass-ceramics A (a) and A + 6 wt% ZrO_2 (b) at the temperature of the first endothermic peak-backscatter image.

ology. The thermodynamic driving force for this change is lowering of the surface energy as the dendritic crystals with high specific surface area are continuously transformed into a microstructure with a lower specific area. The onset temperature of the first endothermic reaction is lowered by approximately 20°C for the A + 6 wt% ZrO_2 composition compared with the A composition. This can be attributed to the influence of the Zr^{4+} cation which acts as a glass-network modifier and decreases the viscosity of the retained glass at this high temperature. The heat of reaction (proportional to the area bounded by the endothermic peak and the DTA base line) of the first endothermic reaction is lower for the A + 6 wt% ZrO_2 glass, probably due to an additional exothermic crystal growth of the yttria-stabilized zirconia crystals in the microstructure.

The phase assemblage observed at the second endothermic peak temperature (1430 and 1420°C for A and A + 6wt% ZrO_2, respectively) indicates a partial dissolution of the β-$Y_2Si_2O_7$ phase and

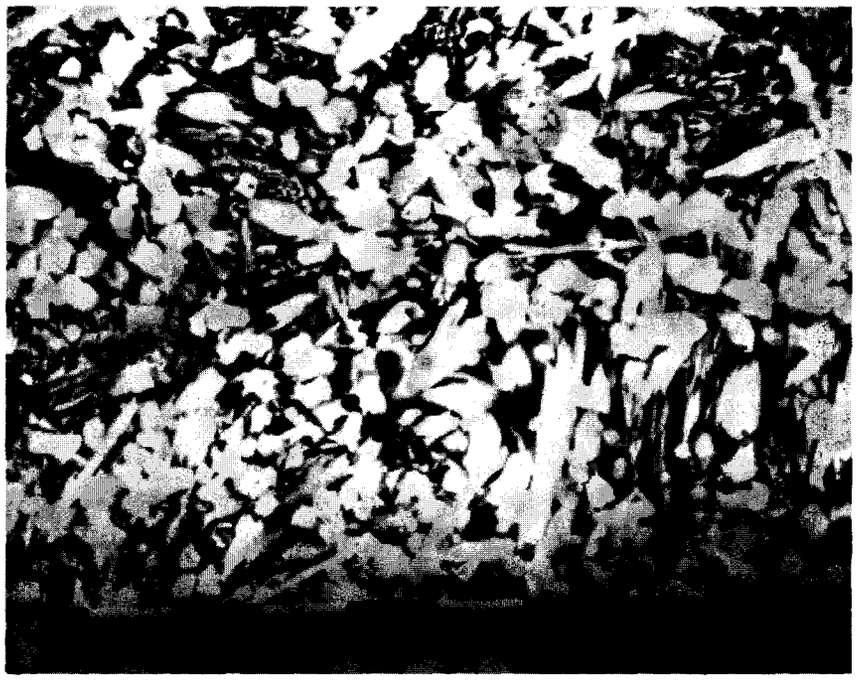

(a)

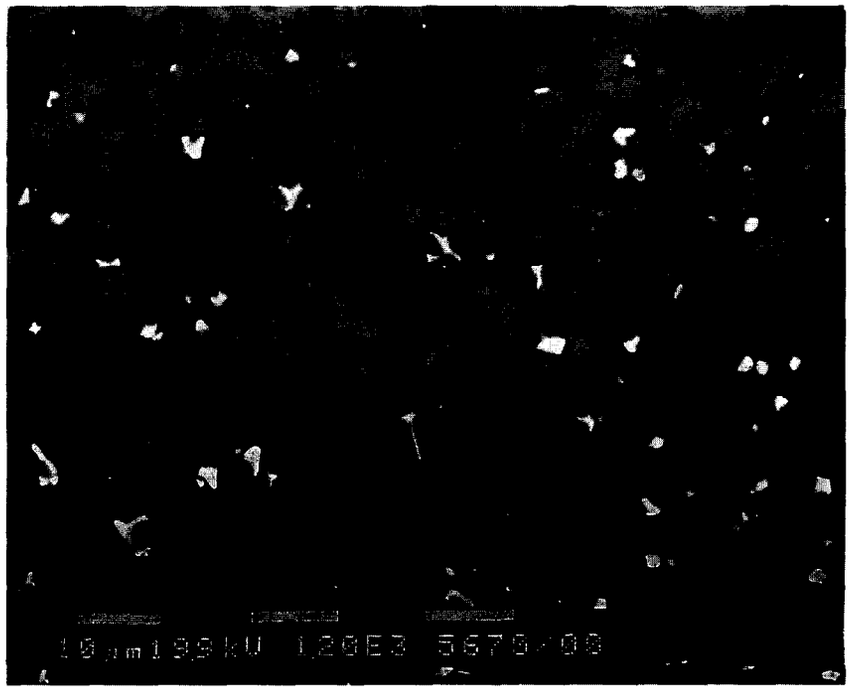

(b)

Fig. 4. Micrographs of the glass-ceramics A (a) and A + 6 wt% ZrO_2 (b) at the temperature of the second endothermic peak-backscatter image of a mixture of β-$Y_2Si_2O_7$, YAG and yttria-stabilized zirconia crystals.

crystallization of the YAG phase. Micrographs of the samples at the temperatures of the second endothermic reaction are shown in Fig. 4. The intensity of the YAG peaks in the X-ray pattern of the A + 6 wt% ZrO_2 composition was much higher than in the A composition. EDX analysis confirmed a much higher content of the YAG phase in the A + 6 wt% ZrO_2 microstructure. Although no noticeable Al_2O_3 crystallization was detected by X-ray diffraction of the A composition, a small amount could be observed when examined by EDX. γ-$Y_2Si_2O_7$ could be detected in small amounts for the A sample due to the high temperature. (The equilibrium transformation temperature of β-$Y_2Si_2O_7$ to γ-$Y_2Si_2O_7$ is 1445°C in the binary Y_2O_3–SiO_2 system.[14]) An increase of the Al_2O_3 amount and the glassy phase content was noticed for the A + 6 wt% ZrO_2 composition. The significant YAG and Al_2O_3 crystallization as well as the crystal growth of the yttria-stabilized zirconia, which are probably exothermic reactions, lower the overall endothermic heat of reaction of

the A + 6 wt% ZrO_2 composition. The effect of zirconia on lowering the viscosity of the retained glassy phase (or more accurately liquid phase) is more obvious at this high temperature of the second endothermic reaction. The kinetic rates of the phase transformations occurring during melting are increased due to the presence of a larger amount of the liquid phase. Consequently, Al_2O_3 and a larger amount of the YAG phase can precipitate out from the liquid phase in the A + 6 wt% ZrO_2 composition.

A third endothermic peak could be seen on the DTA charts at 1530 and 1500°C for A and A + 6 wt% ZrO_2, respectively. Due to cracking of the Al_2O_3 crucibles at higher temperatures than 1500°C, samples of both compositions were prepared at 1500±20°C in a conventional furnace of the same type as used for the glass preparation. The same atmosphere and heating rate were applied as in the DTA furnace. For the A composition the YAG phase was the major phase detected, accompanied by γ–$Y_2Si_2O_7$ and a smaller amount of β–$Y_2Si_2O_7$. The A + 6 wt% ZrO_2 composition formed a homogeneous glass with some ZrO_2 crystals precipitated in the microstructure. This observation and the DTA results imply that the last crystalline phases dissolve into the liquid at 1530 and 1500°C for the A and the A + 6 wt% ZrO_2, respectively.

3.4 Zirconia in an oxynitride glass-ceramic

The same DTA scans as described above were performed on oxynitride and ZrO_2-containing oxynitride glasses with the same Y:Si:Al ratio with 10 eq% of nitrogen incorporated into the glass structure by adding an appropriate amount of silicon nitride powder (Kema Nord Industrikemi) to the oxide mixtures prior to firing at 1700°C. The same tendency of lowering the onset temperature of the endothermic reaction could be observed for the composition containing 6 wt% of zirconia.

4 Conclusions

The influence of ZrO_2 addition on the melting behaviour of a YSiAlO glass-ceramic has been assessed. ZrO_2 lowers the viscosity of the retained glassy phase in the glass-ceramic and consequently increases the kinetics of the phase transformations occurring during melting. The onset temperature of the endothermic reaction representing melting is lowered by approximately 20°C. The overall heat of reaction of the endothermic reaction is also lowered. The same influence of ZrO_2 addition was observed in the oxynitride glass-ceramic with the same Y:Si:Al cation ratio and 10 eq% of nitrogen.

References

1. Hyatt, M. J. & Day, D. E., Glass properties in yttria–alumina–silica system. *J. Am. Ceram. Soc.*, **70**[10] (1987) C-283–7.
2. Leng-Ward, G. & Lewis, M. H., Crystallisation in Y–Si–Al–O–N glasses. *Mater. Sci. Eng.*, **71** (1985) 101–11.
3. O'Meara, C., Dunlop, G. L. & Pompe, R., Phase relationship in the system Y_2O_3–Al_2O_3–SiO_2. In *Proc. World Congress on High Tech. Ceramics* (6th CIMTEC), Milan, Italy, ed. P. Vicenzini. Elsevier Science Publishers, Amsterdam, 1986, pp. 265–70.
4. Lewis, M. H., Crystallization of grain boundary phases in silicon nitride and sialon ceramics. *Key Eng. Mater.*, **89–91** (1994) 333–8.
5. Arita, I. H., Wilkinson, D. S. & Purdy, G. R., Crystallisation of yttria–alumina–silica glasses. *J. Am. Ceram. Soc.*, **75**[12] (1992) 3315–20.
6. Hampshire, S., Oxynitride glasses and glass ceramics. *Mater. Res. Soc. Symp. Proc.*, **287** (1993) 93–103.
7. Vomacka, P., Babushkin, O. & Warren, R., Zirconia as a nucleating agent in an yttria–alumina–silica glass. *J. Eur. Ceram. Soc.*, **15** (1995) 1111–17.
8. Vomacka, P., Ramesh, R. & Hampshire, S., Influence of zirconia addition on the crystallization kinetics of a YSiAlON glass. *J. Eur. Ceram. Soc.*, in press.
9. Braue, W., Wotting, G. & Ziegler, G., Devitrification effect of grain boundary phases on high-temperature strength of sintered Si_3N_4 materials. In *Proc. 2nd Int. Symp. On Ceramics and Components for Engines*, Lubeck-Travemunde, 14–17 April 1986.
10. Thomas, G., Ahn, C. & Weiss, J., Characterization and crystallisation of Y–Si–Al–O–N glass. *J. Am. Ceram. Soc.*, **65**(11), (1982) C-185–8.
11. Vomacka, P. & Babushkin, O., Yttria–alumina–silica glass with addition of zirconia. *J. Eur. Ceram. Soc.*, **15** (1995) 921–8.
12. Hampshire, S., Nestor, E., Flynn, Besson, J. L., Goursat, P. & Thompson, D., Yttrium oxynitride glasses: properties and potential for crystallization to glass-ceramics. *J. Eur. Ceram. Soc.*, **14** (1994) 261–73.
13. Dinger, T. R., Rai, R. S. & Thomas, G., Crystallization behaviour of a glass in the Y_2O_3–SiO_2–AlN system. *J. Am. Ceram. Soc.*, **71**[4] (1988) 236–44.
14. Kumar, S. & Drummond, C. H. III, Crystallization of various compositions in the Y_2O_3–SiO_2 system. *J. Mater. Res.*, **7**[4] (1992).

Journal of the European Ceramic Society 16 (1996) 1253–1262

PII:S0955-2219(96)00049-0
0955-2219/96/$15.00

Influence of Zirconia Addition on the Crystallization Kinetics of a Y–Si–Al–O–N Glass

P. Vomacka,[a] R. Ramesh[b] & S. Hampshire[b]

[a] Department of Engineering Materials, Luleå University of Technology, S-951 87 Luleå, Sweden
[b] Materials Research Centre, University of Limerick, Limerick, Ireland

(Received 13 December 1995; revised version received 14 February 1996; accepted 20 February 1996)

Abstract

The crystallization behaviour of YSiAlON glasses with and without ZrO_2 additives, prepared by melting at 1700°C, were studied by means of differential scanning calorimetry, scanning microscopy and X-ray powder diffraction analysis. The optimum nucleation temperatures were determined to be T_g + 65°C and T_g + 50°C for the ZrO_2-free and the ZrO_2-containing glass, respectively. The crystallization of the glasses was found to be dominated by the surface mechanism of nucleation and growth. The added zirconia acted as a growth modifier rather than a nucleating agent. Copyright © 1996 Elsevier Science Ltd

1 Introduction

Silicon nitride based ceramics contain oxynitride glass phases at the grain boundaries that control the high-temperature properties and subsequent behaviour. The desire to understand the nature of these grain boundary phases has resulted in a number of investigations on oxynitride glass formation and properties.[1–5] Much of the earlier interest centred largely on the influence of nitrogen, which in silicate glasses increases their viscosity, glass transition temperature and hardness.[3–5] Further, the improvement obtained in the thermomechanical properties of Si_3N_4 ceramics following crystallization of the grain boundary oxynitride glass[6,7] has prompted more detailed work on the microstructure and crystallization behaviour of bulk materials similar to the glass phases present at the grain boundaries of these ceramics. Such studies have been largely carried out in the YSiAlON system[8–10] since Y_2O_3 and Al_2O_3 have proven to be effective additives for Si_3N_4 ceramics.

Control of nucleation is extremely important in the formation of glass-ceramics. The crystalline phases formed on heat treatment and the extent of their formation will determine the properties of the particular material. The phases formed depend on both the composition of the parent glass and the heat treatment process. Some glasses require the addition of a nucleating agent to promote crystallization. The YSiAlON glasses, in general, appear to be self-nucleating.[9–11] However, Thomas *et al.*[12] observed improved crystallization behaviour for an oxynitride glass containing a small addition of ZrO_2. Furthermore, Braue *et al.*[13] found a significant improvement of high-temperature strength of (Y_2O_3 + Al_2O_3) fluxed sintered Si_3N_4 partially doped with small amount of ZrO_2. In contrast, the work of Cheng and Thompson[14] and Shaw *et al.*[15] on zirconia additions to nitrogen ceramics show no appreciable improvements in mechanical properties and this has been attributed to the difficulty of retaining transformable ZrO_2 in this system.

In previous studies[16,17] on yttria–alumina–silica glasses with addition of zirconia as a nucleating agent, zirconia was considered to act as a growth modifier rather than a catalyst nucleating agent. The solubility limit of zirconia in a YSiAlO melt at 1700°C was found to be 6 wt%. In the present work, the influence of ZrO_2 addition on the crystallization kinetics of an oxynitride glass prepared at 1700°C is studied. The crystallization mechanisms, the optimum nucleation temperatures and the activation energies for the crystallization process in ZrO_2-free and ZrO_2-containing compositions are compared by means of differential scanning calorimetry (DSC), scanning electron microscopy (SEM) and X-ray powder diffraction analysis. The Y:Si:Al ratio (in equivalent %) chosen for the oxynitride glass in the present investigation is the same as in the previously studied oxide glass.[16] Nitrogen (10 equivalent %) is incorporated into the oxide composition to form the oxynitride glass.

2 Experimental

2.1 Glass preparation

A YSiAlON glass of composition (in equivalent %) 27Y:42Si:31Al:90O:10N without ZrO_2 and one

with the addition of 6 wt% monoclinic ZrO_2 (Sigma Chemical) was prepared from mixtures of silicon nitride (KemaNord Industrikemi), high-purity yttria, alumina and silica (Rhone Poulenc, Alcoa Chemicals, Johnson Matthey) in the appropriate proportions. The equivalent % method of representation of composition has been reported previously.[18] The powders were mixed in polyethylene containers on a Siemens roller mill for 10 h using propanol as mixing medium. The alcohol was then evaporated and the powder mixtures were sieved. Batches of approximately 100 g each were then mechanically compacted into molybdenum crucibles and melted under 0.17 MPa nitrogen at 1700°C for 2·5 h, after which the melt was rapidly cooled down to 880°C and then annealed at this temperature for 1 h prior to slow furnace cooling.

2.2 Glass characterization

To study quality and homogeneity, observations on melting and final appearance were made. X-ray analysis was carried out using a Philips X-ray powder diffractometer (Cu K_α radiation) in order to detect any crystalline phases present in the glasses. SEM analysis was carried out using a Jeol 840 scanning electron microscope to assess homogeneity. The densities were measured by Archimedes' principle using water as the working fluid. Microhardness was obtained using a Vickers indentor with a load of 300 g applied for 15 s. A Stanton-Redcroft differential scanning calorimeter was used to determine glass transition (T_g) and crystallization (T_c) temperatures. Similar characterization techniques were employed for the glass-ceramics obtained after two-stage heat treatments in the tube furnace.

2.3 Heat treatments using DSC for optimum nucleation temperature determination

Differential scanning calorimetry was performed on the glasses to determine the optimum nucleation temperature using the method outlined by Marotta *et al.*[19] The relationship between the number of nuclei N_n and the time t_n of nucleation heat treatment is given by:

$$N_n = It_n^b \quad (1)$$

where I is the kinetic rate constant of nucleation and b is a parameter related to the nucleation mechanism. If the samples are held for the same time t_n at each temperature T_n of the heat treatment, then the following equation applies:

$$\ln I = (E_c/R)(1/T_p - 1/T_{p'}) + \text{constant} \quad (2)$$

where E_c is the activation energy for crystallization, R is the gas constant, T_p and $T_{p'}$ are the crystallization exotherm temperatures obtained after and without a nucleation hold, respectively. The factor $(1/T_p - 1/T_{p'})$ has been shown to be a function of T_n, the nucleation hold temperature, and a plot between them gives a bell-shaped curve, the maximum of which is the temperature at which optimum nucleation occurs.[19]

Small quantities of powdered glass samples of particle size 53 to 90 μm were held in boron nitride lined platinum crucibles and alumina was used as a reference material. These were then heated at 20°C min^{-1} in a flowing nitrogen atmosphere to temperatures ranging between T_g (glass transition temperature) and T_g + 100°C for 1 h, after which heating was continued at 10°C min^{-1} until the crystallization peak (T_{c2}) was observed. The reason for choosing the T_{c2} peak will become apparent later. From the DSC traces the peak temperatures of crystallization corresponding to the different nucleation hold temperatures were recorded. Prior to these experiments, an initial DSC run was carried out without a nucleation hold and this was used as a reference for determining the shift in crystallization peaks resulting from the nucleation treatment in the other runs. The isothermal heat treatment that resulted in the greatest depression in crystallization temperature is taken as the optimum nucleation temperature.

The activation energy for the crystallization process was determined using the method of Matusita and Sakka[20] on the basis that the crystallization of glass is advanced by a nucleation and growth mechanism. The method involves DSC runs performed at several heating rates and subsequent analysis of variation of peak temperature with heating rate. Five different heating rates (5, 8, 10, 15 and 20°C min^{-1}) were employed, maintaining the same particle size (53 to 90 μm). The relationship between heating rate and exothermic peak temperature is given by:

$$\ln(\alpha^n/T_p^2) = -m\,E_c/RT_{p'} + \text{constant} \quad (3)$$

where α is the heating rate, $T_{p'}$ the maximum crystallization exothermic peak temperature, E_c the activation energy for crystallization, R is the gas constant and n and m are numerical constants which depend on the crystallization mechanism ($n = m = 1$ for surface-dominated nucleation and $n = m = 3$ for bulk crystallization from a constant number of nuclei[21]). In order to determine the mechanism of crystallization, i.e. whether crystallization proceeds by bulk or surface nucleation, additional DSC runs were carried out under identical conditions on three samples of varying particle sizes for both glass compositions. Considering the nucleation process as surface-dominated, as

will be seen below, the values of $\ln(\alpha/T_p^2)$ were determined and plotted against $1/T_p$. The resulting slope was used to calculate the activation energy (E_c).

2.4 Heat treatments in tube furnace

A two-stage heat treatment was carried out in a nitrogen atmosphere using a tube furnace. Coupons (10 mm × 10 mm × 2 mm) cut from these glasses were placed in a bed of boron nitride in an alumina crucible in a tube furnace and heat-treated at the optimum nucleation temperature (determined using DSC) for 10 h, followed by a treatment at the crystal growth temperature for 30 min. Crystal phases of the heat-treated specimens were analysed by X-ray diffraction, and both surface and sectioned morphologies observed using scanning electron microscopy on diamond-polished sections without etching.

3 Results

3.1 Glass characterization

Table 1 shows the X-ray analysis and observations on melting for both ZrO_2-free and ZrO_2-containing glass compositions. As can be seen, both compositions gave fully amorphous material. However, a slight difference was observed with regard to their appearance. The ZrO_2-free composition produced a faint yellow transparent glass while the ZrO_2-containing composition gave a yellowish grey transparent glass. Further, SEM analysis indicated glasses to be homogeneous. Some of the physical properties obtained on the as-melted compositions are summarized in Table 2. The minimum point in the endothermic drift of the DSC curves (Fig. 1) corresponding to the end of the transition range is reported as the glass transition temperature (T_g) in Table 2, while T_{c1} and T_{c2}

Table 1. Characterization of as-melted glass compositions

Composition (eq%)	*X-ray analysis*	*Observations on melting*
27Y:42Si:31Al:90O:10N	Amorphous	faint yellow transparent glass
27Y:42Si:31Al:90O:10N + 6 wt% ZrO_2	Amorphous	yellowish grey transparent glass

Table 2. Physical properties of as-melted glass compositions

Composition (eq%)	T_g *(°C)*	T_{c1} *(°C)*	T_{c2} *(°C)*	*Density (g cm^{-3})*	*Hardness (GPa)*
27Y:42Si:31Al:90O:10N	952	1 106	1 238	3·60	10·21 ± 0·35
27Y:42Si:31Al:90O:10N + 6 wt% ZrO_2	945	1 116	1 245	3·65	10·46 ± 0·4

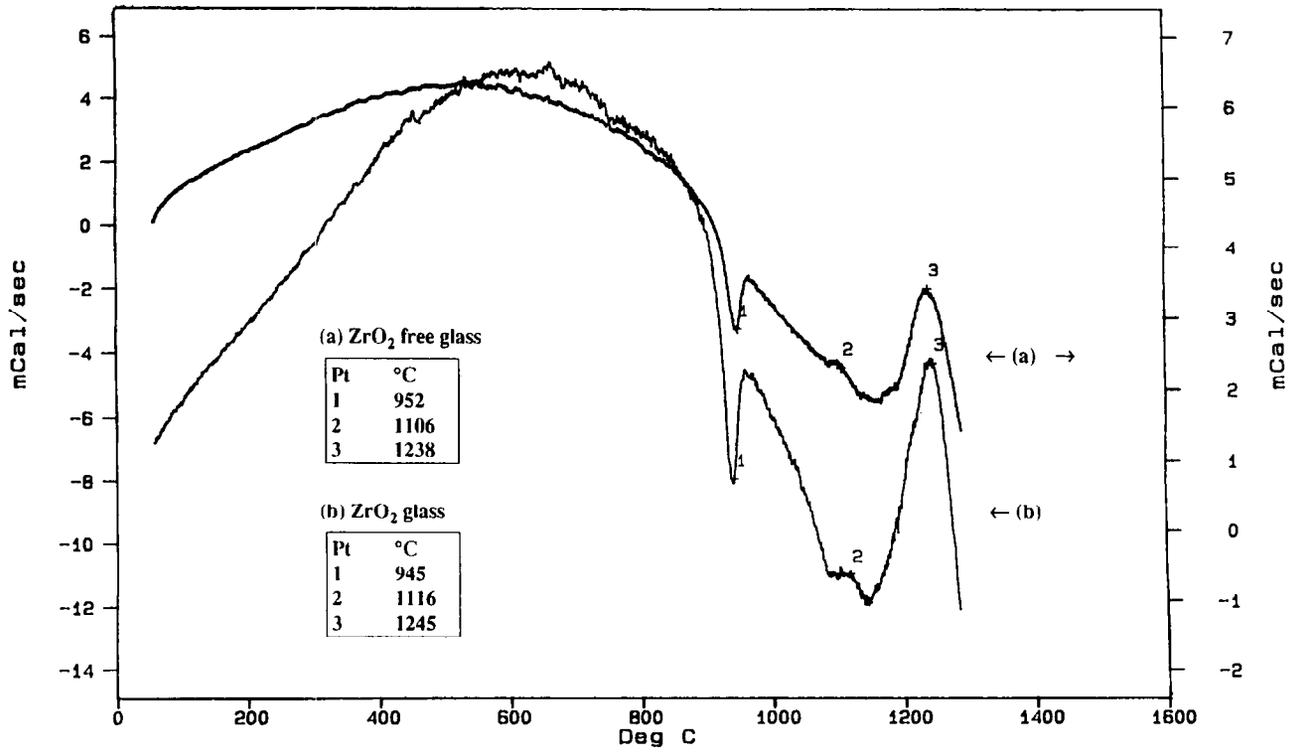

Fig. 1. Non-isothermal DSC traces for YSiAlON glasses (a) without ZrO_2 and (b) with ZrO_2.

are the first and second crystallization exotherm temperatures, respectively, obtained from the maxima of the exothermic peaks. From these results it can be seen that zirconia addition slightly shifts the T_g to lower temperatures and crystallization peaks (T_{c1} and T_{c2}) to higher temperatures. Further, from the DSC curves shown in Fig. 1 it can be seen that, for both glass compositions, exothermic peaks corresponding to T_{c1} are rather weak while those corresponding to T_{c2} are sharp and distinct. Because of this, the shift in the T_{c2} peak was monitored below to determine the optimum nucleation temperature and the activation energy for crystal growth. With regard to other properties, the density and the hardness values were slightly higher for the ZrO_2-containing glass composition.

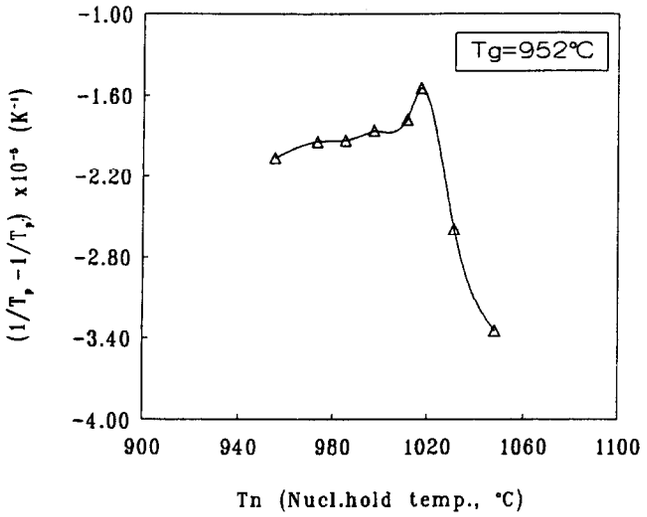

Fig. 2. Nucleation rate–temperature curve for ZrO_2-free YSiAlON glass.

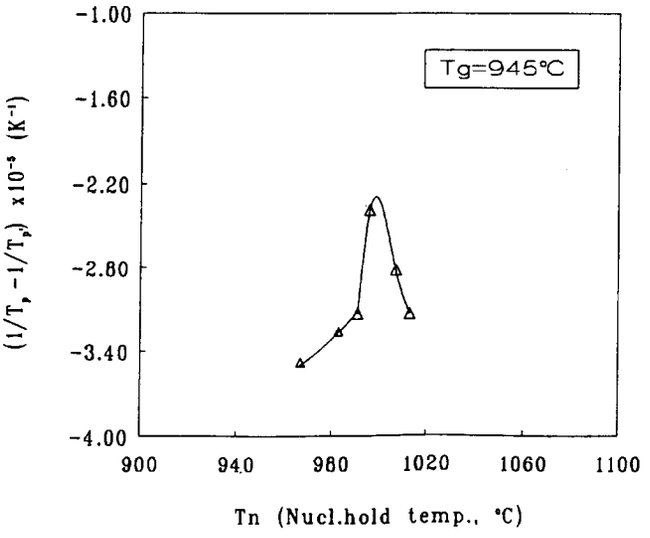

Fig. 3. Nucleation rate-temperature curve for ZrO_2-containing YSiAlON glass.

3.2 Heat treatments using DSC for optimum nucleation temperature determination

The $(1/T_p - 1/T_{p'})$ versus nucleation hold temperature (T_n) plots obtained from the peak shifts measured on the DSC traces are shown in Figs 2 and 3 for ZrO_2-free and ZrO_2-containing YSiAlON glass compositions, respectively. Table 3 summarizes the results of these plots. As can be seen, for the glass without ZrO_2 the maximum nucleation occurs at 1017°C, corresponding to T_g + 65°C, while for the ZrO_2-containing glass it occurs at 995°C, which corresponds to T_g + 50°C. Another observation is that the slope of the left side of the curve for the ZrO_2 glass is steeper compared with that for the ZrO_2-free glass, which indicates that maximum nucleation occurs closer to the glass transition temperature for the ZrO_2-containing glass.

In order to determine the activation energy for crystallization, the mechanism of crystallization, i.e. whether crystallization proceeds by bulk or surface nucleation, should be taken into account. For this purpose, additional non-isothermal DSC runs with a heating rate of 15°C min^{-1} were carried out on three samples of varying particle sizes. The exothermic peak temperatures (T_{c2}) obtained from DSC traces of these experiments are shown in Table 4. It can be seen that as the particle size increases the crystallization peaks are shifted to higher temperatures for the same heating rate (15°C min^{-1}) for both compositions. This variation in exothermic peak temperature with varying particle sizes is indicative of a surface nucleation mechanism.

Figures 4 and 5 respectively show the activation energy plots obtained using the Matusita method for the ZrO_2-free and ZrO_2-containing glass compositions. The activation energy for crystallization was calculated from the slope of these straight lines according to eqn (3) taking $n = m = 1$ for surface-dominated nucleation. The values thus obtained are 365 kJ mol^{-1} for the ZrO_2-free glass and 280 kJ mol^{-1} for the ZrO_2-containing glass. Without emphasizing the actual magnitudes of these values too much, it is pertinent to note that the addition of ZrO_2 lowers the activation energy for crystallization.

Table 3. Optimum nucleation temperatures obtained using DSC technique

Composition (eq%)	T_g(°C)	*Opt. nucleation temperature*
27Y:42Si:31Al:90O:10N	952	T_g + 65°C
27Y:42Si:31Al:90O:10N + 6 wt% ZrO_2	945	T_g + 50°C

Table 4. Crystallization temperatures (T_{c2} in °C) obtained for both glass compositions of varying particle size

Composition (eq%)	*Particle size*		
	<53 μm	*53–90 μm*	*>150 μm*
27Y:42Si:31Al:90O:10N	1198	1238	1257
27Y:42Si:31Al:90O:10N + 6 wt% ZrO_2	1202	1245	1266

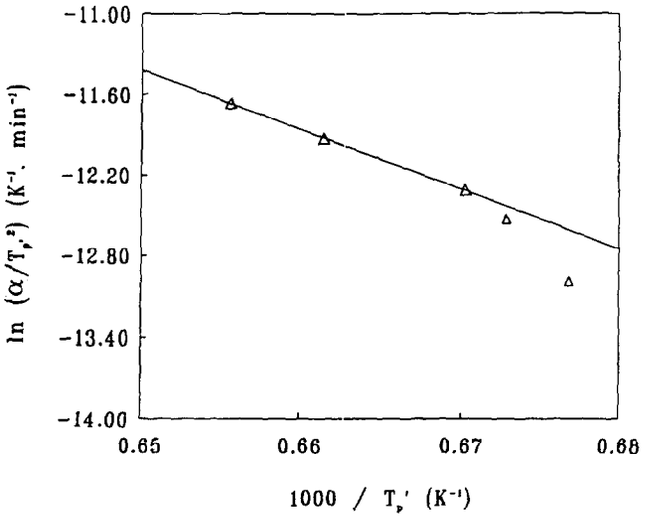

Fig. 4. Activation energy plot for the crystallization process occurring in ZrO_2-free YSiAlON glass.

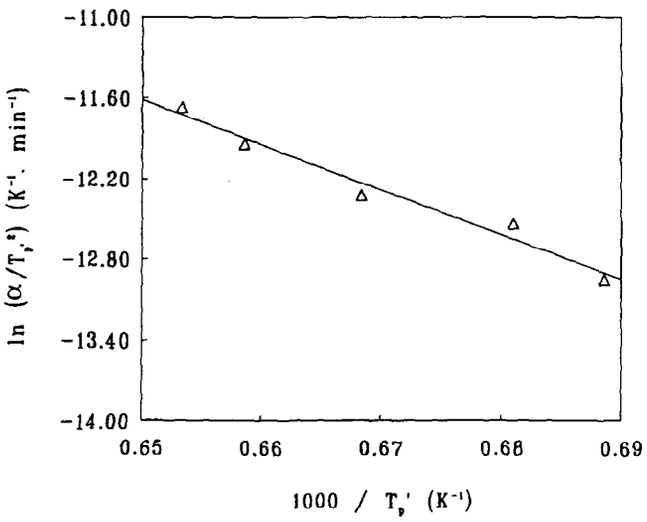

Fig. 5. Activation energy plot for the crystallization process occurring in ZrO_2-containing YSiAlON glass.

3.3 Tube furnace experiments

Both glasses were subjected to two-stage heat treatments employing a tube furnace at temperatures corresponding to optimum nucleation and crystal growth. Thus the schedule for the heat treatment of the ZrO_2-free composition involved a nucleation treatment at T_g + 65°C (1017°C) for 10 h followed by a crystallization treatment at 1230°C for 30 min. For the ZrO_2-containing glass, a nucleation treatment for 10 h was given at a temperature corresponding to T_g + 50°C (995°C), followed by a crystallization treatment at 1220°C. The chosen crystal growth temperatures correspond to the exotherm temperatures observed in DSC (Figs 6 and 7) during the nucleation hold at the respective temperatures.

Phase assemblages of the heat-treated glass samples identified by X-ray diffraction (Table 5) include yttrium disilicate ($Y_2Si_2O_7$) and $Y_4Al_2O_9$ (YAM) as the major crystalline phases and also traces of mullite ($Al_6Si_2O_{13}$). For the ZrO_2-containing glass, yttrium disilicate exists in both β and γ polymorphs while only the β form was observed for the ZrO_2-free glass. In addition, for the ZrO_2-containing glass, cubic yttria-stabilized ZrO_2 ($Y_{0.15}Zr_{0.85}O_{1.93}$) was noted.

The surface and sectioned morphologies of the glass-ceramic microstructures obtained following two-stage heat treatments at temperatures corresponding to optimum nucleation and crystal growth are shown in Figs 8 and 9 for ZrO_2-free and ZrO_2-containing glass, respectively. The morphologies of both glass-ceramics are dendritic in nature with crystals being relatively coarser for ZrO_2-containing glass-ceramic. The small bright crystals seen in the surface micrograph of ZrO_2-containing glass-ceramic are yttria-stabilized ZrO_2 crystallizing out from the parent glass as XRD analysis would indicate. Further, for both glass-ceramics, examination of the sectioned morphologies [Figs 8(b) and 9(b)] reveal much lower volume fraction crystallization compared with the surface layers. This indicates the predominance of surface nucleation for these glass-ceramics and is in good agreement with the DSC results mentioned above (Table 4).

The results of the additional characterization carried out on heat-treated specimens of both compositions are summarized in Table 6. Devitrification of both glasses produced dark grey coloured glass-ceramics and these were opaque in nature. Comparing Tables 2 and 6 it can be seen that there is a slight decrease in density and an increase in hardness after crystallization in both glass compositions. The ZrO_2-containing glass and glass-ceramic are marginally harder than the ZrO_2-free composition.

4 Discussion

The glass transition temperature of the as-prepared oxynitride glasses determined in this study

are higher than the values obtained on the corresponding oxide glasses.[16,17] This increase is attributed to the incorporation of nitrogen into the glass structure leading to a more rigid glass network, as reported elsewhere.[4,5]

Though small, there exists a difference in the physical properties of YSiAlON glasses with and without ZrO_2 additives (Table 2). It is interesting to note that zirconia addition shifts T_g to a slightly lower temperature and it is assumed that the addition of ZrO_2 causes a decrease in viscosity of the glass. Crystallization temperatures (T_{c1} and T_{c2}) move to higher values and, from a thermodynamic point of view, this is feasible since an additional component would lead to an increase in the entropy of the system, thereby hindering crystal-

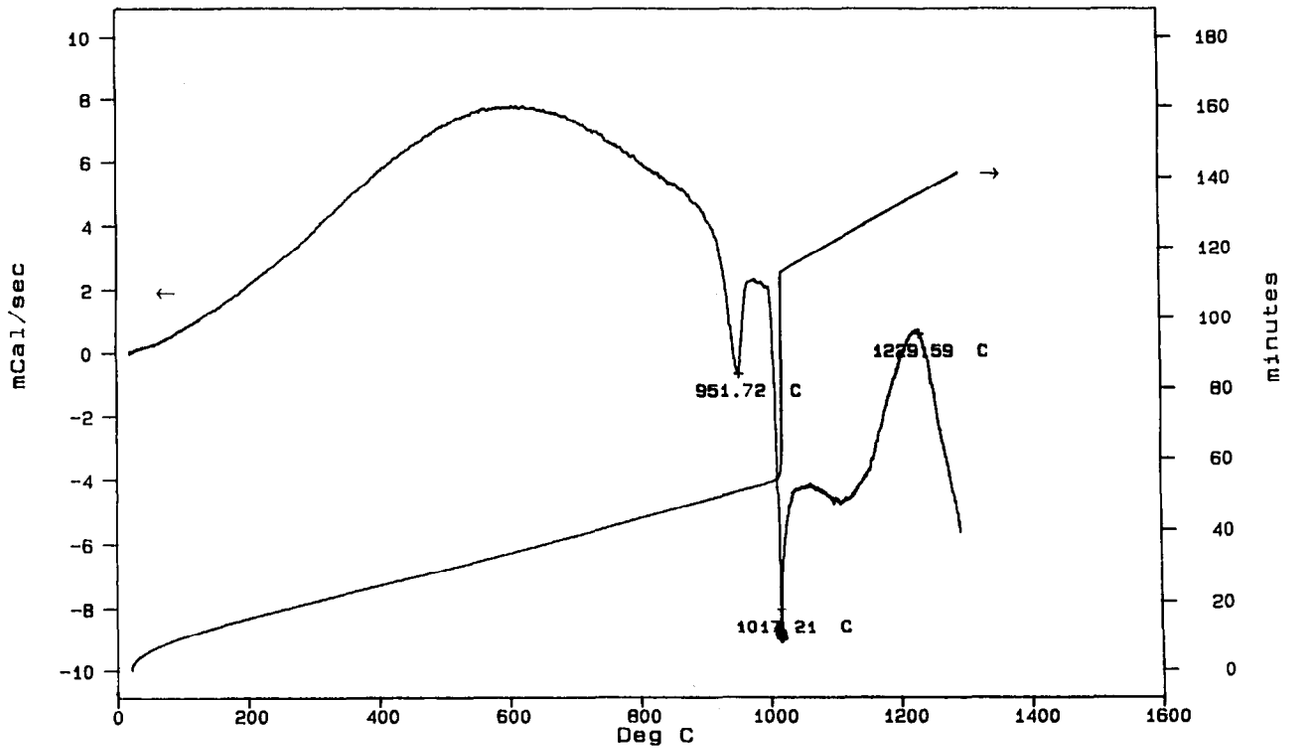

Fig. 6. DSC trace of ZrO_2-free glass obtained following the isothermal test carried out at T_g + 65°C.

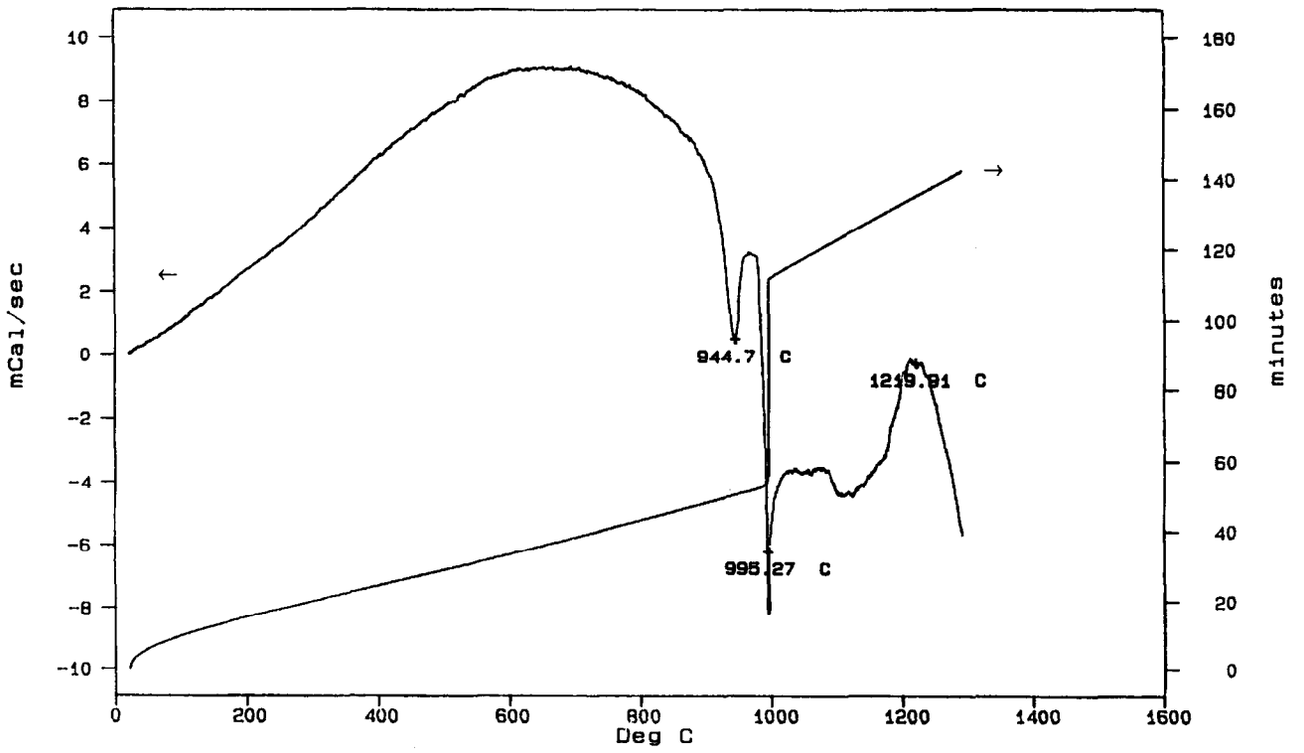

Fig. 7. DSC trace of ZrO_2-containing glass obtained following the isothermal test carried out at T_g + 50°C.

lization. The increase in density and hardness observed for the ZrO_2-containing glass can perhaps be attributed to higher nitrogen retention during melting than for the glass without the additive. This argument is based on the fact that nitrogen has a higher affinity towards zirconia and that nitrogen itself can be incorporated into the zirconia structure.[14,15,22]

The optimum nucleation temperatures for the ZrO_2-free and ZrO_2-containing glasses, derived from the DSC data in Figs 2 and 3, are 1017°C (T_g + 65°C) and 995°C (T_g + 50°C), respectively. These temperatures correspond to the maximum in the ($1/T_p$ - $1/T_{p'}$) versus T_n curve. Thus it is evident that the optimum nucleation temperature is lowered by the addition of ZrO_2, with the highest nucleation rate closer to the glass transition temperature for the ZrO_2-containing glass. However, for both glasses the crystallization process seems to depend on the specific surface area of the glass samples used in the DSC experiments (Table 4). For samples of high specific surface area (<53 μm), the crystals grow from a large number of surface nuclei and consequently lower T_{c2} values

Table 5. Crystalline phases observed after two-stage heat treatment for both glass compositions

Composition (eq%)	*Phase assemblage*
27Y:42Si:31Al:90O:10N	β–$Y_2Si_2O_7$, $Y_4Al_2O_9$, $Al_6Si_2O_{13}$[a]
27Y:42Si:31Al:90O:10N + 6 wt% ZrO_2	γ–$Y_2Si_2O_7$, β–$Y_2Si_2O_7$, $Y_4Al_2O_9$, $Y_{0.15}Zr_{0.85}O_{1.93}$, $Al_6Si_2O_{13}$[a]

[a] Trace amounts.

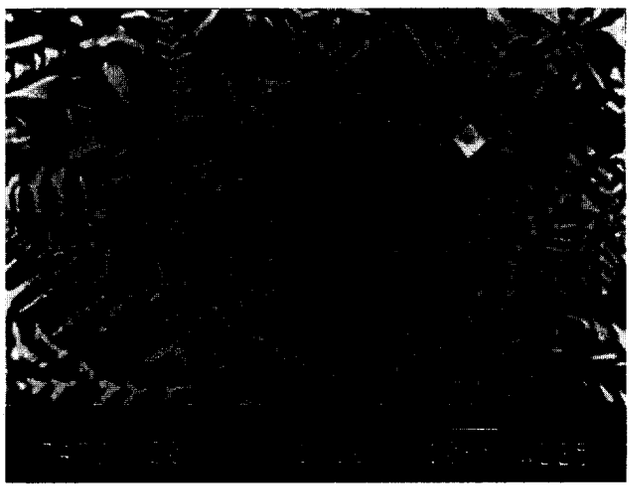

(a)

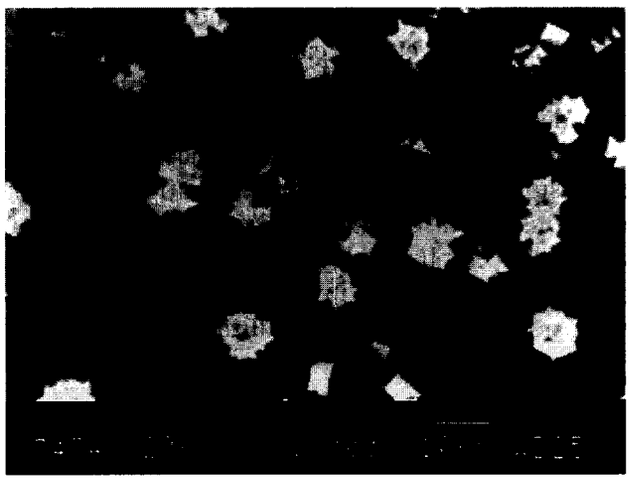

(b)

Fig. 8. Micrographs of ZrO_2-free YSiAlON glass obtained following two-stage heat treatments (1017°C for 10 h, 1230°C for 30 min): (a) surface morphology and (b) sectioned morphology.

(a)

(b)

Fig. 9. Micrographs of ZrO_2-containing YSiAlON glass obtained following two-stage heat treatments (995°C for 10 h, 1220°C for 30 min): (a) surface morphology and (b) sectioned morphology.

were observed. As the particle size increases, due to the lower specific surface area of the sample, the number of surface nuclei decreases and if surface nucleation is dominant, then, given the constant heating rate used in the DSC experiments, the T_{c2} peak should be shifted to higher temperatures. This was indeed the case observed for both glass compositions. The difference observed in the shape of the $(1/T_p - 1/T_{p'})$ versus T_n curves (Figs 2 and 3) can then be said to simply imply that a significant nucleation occurs over a much narrower temperature interval for the ZrO_2-containing glass compared with the ZrO_2-free glass. However, from the SEM analysis, some bulk nucleation had occurred to a limited extent, possibly associated with the presence of Fe/Si impurity particles in the glass or with the precipitated ZrO_2 crystals.

The surface morphologies of both glass-ceramics after the two-stage heat treatment in the tube furnace are of dendritic appearance (Figs 8 and 9). However, the crystals are relatively coarser for the ZrO_2-containing glass-ceramic. This implies that the crystal growth on the surface proceeds from a smaller amount of nuclei for the ZrO_2-containing glass than for the ZrO_2-free glass. The sectioned morphology of the ZrO_2-free glass-ceramic [Fig. 8(b)] consists mainly of spherulites of the $Y_2Si_2O_7$ phase, which indicates a rapid growth of the $Y_2Si_2O_7$ crystals during the crystal growth treatment. Similar spherulitic appearance of $Y_2Si_2O_7$ phase was observed in the previous study[16] on the crystallization behaviour of the pure oxide compositions in the ZrO_2-free glass. The sectioned morphology of the ZrO_2-containing glass-ceramic is somewhat different [Fig. 9(b)] and consists of mainly yttria-stabilized ZrO_2 and fine platelet-like $Y_2Si_2O_7$ crystals. It is rather interesting to note that $Y_2Si_2O_7$ crystals appear to be embedded in the region where zirconia is crystallizing out from the parent glass. This seems to suggest that ZrO_2 may provide heterogeneous nucleation sites for additional crystallization to take place. However, sectioned morphologies reveal much lower volume fraction crystallization compared with the surface layer and, in fact, this is similar to that observed for the ZrO_2-free glass, suggesting that ZrO_2 crystals do not act as heterogeneous nucleation sites.

To determine the activation energy for crystallization, the mechanism of crystallization must be known in order to apply eqn (3) correctly, i.e. to substitute correct values for the constants m and n. Based on the non-isothermal DSC runs (T_{c2} variation with particle size) and the sectioned morphologies obtained on the tube furnace heat-treated samples, it was assumed that surface crystallization is the dominant mechanism for both glass-ceramics and therefore values of $n = m = 1$ were considered appropriate. For the ZrO_2-free glass only three experimental values, corresponding to the heating rates of 20, 15 and 10°C min^{-1}, were used to determine the slope of the plot of $\ln(\alpha/T_{p'}^2)$ versus $1/T_{p'}$ in Fig. 4 and subsequently to estimate the activation energy of crystallization. This is because at the low heating region there appears to be a significant contribution of bulk crystallization as evident from the deviation from a linear plot. For the ZrO_2-containing glass, all the experimental data were taken into account for estimating the activation energy since no significant deviation from the straight line at the region of low heating rate was observed (Fig. 5), implying no appreciable contribution of bulk crystallization (mainly of yttria-stabilized zirconia) to the overall crystallization. The activation energy for crystallization process thus determined indicated a lower value (280 kJ mol^{-1}) for the ZrO_2-containing glass than for the ZrO_2-free glass (365 kJ mol^{-1}). It has to be stressed that the activation energies so obtained using variable heating rate methods are 'apparent' activation energies and may be the compound result of a number of simultaneous events, e.g. crystallization of more than one phase.[21] Nevertheless, these data are useful as aids in determining overall trends in crystallization behaviour.

The properties of the heat-treated glass-ceramics indicate a slight decrease in density and an increase in hardness after crystallization in both glass compositions (Tables 2 and 6). While the hardness improvement can be attributed to the devitrification process, the synergistic observation of a decrease in density and an increase in hardness seems to suggest the occurrence of a volume expansion as a result of crystallization. Zirconia additions increase the hardness only marginally. It should be emphasized that the objective of the present study was to investigate the influence of ZrO_2 addition on the crystallization process and

Table 6. Physical characterization of glass-ceramics

Composition (eq%)	*Appearance*	*Density ($g\ cm^{-3}$)*	*Hardness (GPa)*
27Y:42Si:31Al:90O:10N	dark grey opaque material	3·45	12·46 ± 0·6
27Y:42Si:31Al:90O:10N + 6 wt% ZrO_2	dark brown opaque material	3·48	12·68 ± 0·55

not to establish the optimum morphology in terms of maximum volume fraction crystallization from the parent glass. Therefore no attempts were made to optimize the crystal growth temperature and the duration of either the nucleation or the crystal growth treatments with respect to the maximum volume fraction crystallized as reported by Ramesh *et al.*[11] in an earlier study. Consequently, the hardness values of the glass-ceramics reported in Table 6 may not perhaps be the highest values possible.

With regard to the role of zirconia during the devitrification process, the following points should be noted. The XRD results reported in Table 5 reveal the crystalline phase assemblage in the ZrO_2-containing glass-ceramic to be more complex than in the ZrO_2-free glass-ceramic, with more different phases crystallizing from the parent glass. Cubic zirconia is stabilized by Y_2O_3 as revealed by the presence of $Y_{0.15}Zr_{0.85}O_{1.93}$ phase and this is completely crystallized easily from the parent glass accounting for the overall lower activation energy for crystallization.

Since there are no nitrogen-containing crystalline phases, the residual glass after devitrification would be enriched with nitrogen. The viscosity of the residual glass would be higher for the ZrO_2-containing glass-ceramic due to crystallization of more non-nitrogen containing crystalline phases. As nitrogen is known to stabilize these glasses, a residual glass richer in nitrogen would inhibit further crystal growth. Under these conditions it can be stated that ZrO_2 acts as a growth modifier during the crystal growth process. The intensity of the T_{c2} peak for the ZrO_2-containing glass after isothermal test becomes even lower compared with that for the ZrO_2-free glass (Figs 1, 6 and 7). This is again an indication of the lower crystallization rate of the ZrO_2-containing glass. Although the sectioned morphology of the ZrO_2-containing glass-ceramic shows the yttrium disilicate crystals to be embedded on zirconia, the fact that there are no obvious improvements in the volume fraction crystallization compared with the ZrO_2-free glass-ceramic suggests that the role of ZrO_2 in oxynitride glasses is not one of an effective nucleating agent. Lack of predominance of bulk nucleation seen during non-isothermal DSC runs for the ZrO_2 glass provides additional support to the above argument. Further, since the exact role of the Zr^{4+} cation in this silicate glass network is not known and no phase separation was observed, the lower activation energy obtained for the ZrO_2-containing glass can perhaps be attributed to the differences in the activation energies for crystallization of different crystal species in the ZrO_2-free and ZrO_2-containing glasses or to any structural reorganization that might have occurred by the stabilization of the zirconia structure. Since ZrO_2 addition to the oxynitride glass lowers the contribution of bulk crystallization to the overall crystallization, it appears that the essential role of zirconia in oxynitride glasses is one of a growth modifier rather than a nucleating agent.

5 Conclusions

Differential scanning calorimetry was used to determine the optimum nucleation temperature of ZrO_2-free and ZrO_2-containing oxynitride glasses. The results indicate that the optimum nucleation temperatures for the glasses with and without ZrO_2 are T_g + 50°C and T_g + 65°C, respectively. The activation energies for crystallization in the glasses calculated from the slope of the ln (α/T_p^2) versus $1/T_p$ plot indicated a lower value for the ZrO_2-containing glass due to the easier crystallization of a yttria-stabilized cubic zirconia phase. The influence of sample specific surface on the devitrification mechanisms has been estimated. Surface nucleation was found to be the dominant nucleation mechanism for both glass-ceramics. The essential role of zirconia in oxynitride glasses has been shown to be one of growth modifier rather than that of nucleating agent.

References

1. Jack, K. H., Sialon glasses. In *Nitrogen Ceramics*, ed. F.L. Riley. Noordhoof, The Hague, 1977, p. 257.
2. Shillito, K. R., Willis, R. R. & Bennett, R. B., Silicon metal oxynitride glasses. *J. Am. Ceram. Soc.*, **61**[11–12] (1978) 537.
3. Loehman, R. E., Preparation and properties of yttrium–silicon–aluminium oxynitride glasses. *J. Am. Ceram. Soc.*, **62**[9–10] (1979) 491.
4. Drew, R. A. L., Hampshire, S. & Jack, K. H., Nitrogen glasses. In *Special Ceramics 7*, eds P. Popper & D. E. Taylor. *Proc. Brit. Ceram. Soc.*, **31** (1981) 119.
5. Hampshire, S., Drew, R. A. L. & Jack, K. H., Viscosities, glass transition temperatures and microhardness of Y–Si– Al–O–N glasses. *J. Am. Ceram. Soc.*, **67** (1984) C46.
6. Ahn, C. C. & Thomas, G., Microstructure and grain boundary chemistry of hot pressed silicon nitride with yttria and alumina. *J. Am. Ceram. Soc.*, **66** (1983) 14.
7. Lewis, M. H., Mason, H. & Szweda, A., Syalon ceramic for application at high temperature and stress. In *Non-Oxide Technical and Engineering Ceramics*, ed. S. Hampshire. Elsevier-Applied Science Publishers, London, 1986, p. 175.
8. Leng-Ward, G. & Lewis, M. H., Crystallization in Y–Si–Al–O–N glasses. *Mater. Sci. Eng.*, **71** (1985) 101.
9. Dinger, T. R., Rai, R. S. & Thomas, G., Crystallization behaviour of a glass in the Y_2O_3–SiO_2–AlN system. *J. Am. Ceram. Soc.*, **71**[4] (1988) 236.
10. Hampshire, S., Oxynitride glasses and glass-ceramics. *Mater. Res. Soc. Symp. Proc.*, **287** (1993) 93.

11. Ramesh, R., Nestor, E., Pomeroy, M. J. & Hampshire, S., Optimisation of heat treatments for oxynitride glass-ceramics. *Key Eng. Mater.*, **99–100** (1995) 211.
12. Thomas, G., Ahn, C. & Weiss, J., Characterisation and crystallization of Y–Si–Al–O–N glass. *J. Am. Ceram. Soc.*, **65**[11] (1982) C-185.
13. Braue, W., Wotting, G. & Zeigler, G., Devitrification effect of grain boundary phases on high temperature strength of sintered Si_3N_4 materials. In *Ceramic Materials and Components for Engines*, eds W. Bunk & H. Hausner. Verlag Deutsche Keramische Gesellschaft, Bad Honnef, 1986, p. 503.
14. Cheng, Y. & Thompson, D. P., Nitrogen containing tetragonal zirconia. *J. Am. Ceram. Soc.*, **74** (1991) 1135.
15. Shaw, B. A., Cheng, Y. & Thompson, D. P., Nitrogen stabilization of tetragonal zirconias. *Brit. Ceram. Proc.*, **50** (1993) 143.
16. Vomacka, P., Babushkin, O. & Warren, R., Zirconia as a nucleating agent in an yttria–alumina–silica glass. *J. Eur. Ceram. Soc.*, **15** (1995) 1111–17.
17. Vomacka, P. & Babushkin, O., Yttria–alumina–silica glass with addition of zirconia. *J. Eur. Ceram. Soc.*, **15** (1995) 921.
18. Hampshire, S., Drew, R. A. L. & Jack, K. H., Oxynitride glasses. *Phys. Chem. Glasses*, **26** (1985) 182.
19. Marotta, A., Buri, A., Branda, F. & Saiello, S., Nucleation and crystallization of $Li_2O.2SiO_2$ glass—a DTA study. In *Advances in Ceramics*, eds J. H. Simmons, D. R. Uhlmann & B. H. Beall. American Ceramics Society, OH, 1982, p. 146.
20. Matusita, K. & Sakka, S., Kinetic study on crystallisation of glass by differential thermal analysis—criterion on application of Kissinger plot. *J. Non-Cryst. Solids*, **38&39** (1980) 741.
21. Donald, I. W., Metcalfe, B. L. & Morris, A. E. P., Influence of transition metal oxide additions on the crystallization kinetics, microstructures and thermal expansion characteristics of lithium zinc silicate glass. *J. Mater. Sci.*, **27** (1992) 2979.
22. Ekstrom, T., Falk, L. K. L. & Knutson-Wedel, E. M., Si_3N_4–ZrO_2 composites with small Al_2O_3 and Y_2O_3 additions prepared by HIP. *J. Mater. Sci.*, **26** (1991) 4331.

Journal of the European Ceramic Society 16 (1996) 1263–1269

PII:S0955-2219(96)00027-1
0955-2219/96/$15.00

Crystallization of $Y_3Al_5O_{12}$ from an Oxynitride Glass Monitored by High-Temperature X-Ray Diffractometry

P. Vomacka & O. Babushkin

Department of Engineering Materials, Luleå University of Technology, S-951 87 Luleå, Sweden

(Received 24 October 1995; revised version received 10 January 1996; accepted 12 January 1996)

Abstract

It is well established that the glassy phase in a β-SiAlON material, with addition of Y_2O_3, can be crystallized to yttrium aluminium garnet ($Y_3Al_5O_{12}$–YAG) by a post-sintering heat treatment. The crystallization of the YAG phase from an oxynitride glass with composition 46·1 wt% Y_2O_3, 26·3 wt% Al_2O_3, 21·6 wt% SiO_2 and 6 wt% Si_3N_4 was studied by means of high-temperature X-ray diffractometry. The kinetics of the crystallization were monitored in terms of the (420)) YAG peak area versus isothermal soaking time at 1150°C during different heat treatments. The crystallization of the YAG phase was found to proceed as a surface crystallization. The results are relevant to developing improved crystallization treatments for glasses with potential for crystallization to YAG-based glass-ceramics and for heat treatments of YAG/β-SiAlON materials. Copyright © 1996 Elsevier Science Ltd

1 Introduction

β-SiAlONs ($Si_{6-z}Al_zO_zN_{8-z}$) are of interest for applications as ceramic components for high-temperature engineering systems because of properties such as high-temperature strength, high hardness, and high oxidation and corrosion resistance. They are usually prepared by dissolution of Al_2O_3 and AlN in α-Si_3N_4 in the presence of an intergranular liquid phase.[1–6] The consequent presence of intergranular glass in sialon ceramics has a strong influence on their mechanical properties and oxidation behaviour. It has been shown that the glassy phase in a β-SiAlON material, with addition of Y_2O_3, can be crystallized to yttrium aluminium garnet ($Y_3Al_5O_{12}$–YAG) by a post-sintering heat treatment at temperatures between 1200 and 1400°C or by slow cooling from the sintering temperature.[7–11] To achieve a perfect β + YAG two-phase structure, it is necessary that as the matrix transforms to YAG, the excess components diffuse into the β phase or precipitate as β of modified composition. Crystallization is promoted by increased polytypoid content (usually 21R which is a structural and compositional variant of the AlN-wurzite structure). Ceramics with high 21R levels crystallize partially during normal process cooling; those with low levels either do not crystallize during a normal (e.g. 5 h) treatment at 1400°C while for longer times additional phases such as yttrium disilicate form. This general trend may be simply interpreted via the ternary oxide liquidus surface and the influence of 21R on liquid composition; i.e. low 21R ceramics have matrix compositions within the eutectic trough in which the liquid is stable above 1300°C and with increased 21R compositions move towards the YAG phase field with increased liquidus temperature.[3,4]

Bonell *et al.*[12] studied YAG crystallization during annealing of a β-SiAlON/YAG ceramic at 1250°C and 1350°C for 40 h. At complete crystallization a very fine film (of the order of 1 to 2 nm) of amorphous phase was found to exist at two-grain junctions and assumed to be a stable configuration. Hohnke and Tien[2] studied YAG crystallization during annealing of β-SiAlON/YAG ceramic at 1200, 1300 and 1400°C for 50 h and found a catalytic effect of Pt added as a nucleating agent. Small amounts of glass retained in grain boundaries and triple points were identified in the microstructure. Bentsen *et al.*[13] investigated the effect of annealing of a β-SiAlON/YAG ceramic on the thermal diffusivity of the material and found a significant increase after an annealing treatment at 1350°C for 20 h.

The aim of the present work was to study the crystallization of the YAG phase from an oxynitride glass by means of high-temperature X-ray diffractometry (HT-XRD). An oxynitride glass composition, prepared in a nitrogen atmosphere

at 1700°C, was subjected to different heat treatments in a high-temperature X-ray diffraction unit. The YAG crystallization from the parent glass was monitored by high-temperature X-ray diffraction during the heat treatment.

2 Experimental

2.1 Glass preparation

Glass with composition 46·1 wt% Y_2O_3, 26·3 wt% Al_2O_3, 21·6 wt% SiO_2 and 6 wt% Si_3N_4[14] was prepared from high-purity Y_2O_3, Al_2O_3, SiO_2 and Si_3N_4 powders (Rhone Poulenc, Alcoa Chemicals, Johnson Matthey Alfa Products and KemaNord Industrikemi). The powders were weighed in a precision balance, and mixed in polyethylene containers on a Siemens roller mill for 10 h using propanol as mixing medium. The alcohol was then evaporated and the powder mixtures were sieved. A batch of approximately 100 g was then compacted into a molybdenum crucible and fired in a nitrogen atmosphere (pressure of 0·17 MPa) at 1700°C for 2·5 h. The heating rate up to the firing temperature was 5°C min^{-1}, the cooling rate from the firing temperature to 1400°C was 20°C min^{-1}, from 1400 to 950°C, 15°C min^{-1}; and from 950 to 500°C min^{-1}. The cooling rate was the natural cooling rate of the furnace (cold wall vacuum/pressure furnace with a graphite heater) after it had been switched off. A mass change of less than 1 wt% was observed.

2.2 Glass and glass-ceramics characterization

The glass transition temperature (T_g) and the temperature of crystallization (T_c) were measured by differential thermal analysis (DTA) on a powdered as-quenched glass sample in a nitrogen atmosphere. An Al_2O_3 powder reference standard and heating rate of 10°C min^{-1} were used.

As a complement to HT-XRD, microhardness and infra-red spectroscopy were also used to study the possible structural changes in the glass during heat treatment. These measurements were carried out on samples heat-treated as follows: 2 g pieces of glass were placed in an Si_3N_4 powder bed in molybdenum boats and heat-treated at temperatures between 900 and 1000°C for 6 h in a static atmosphere of 0·13 MPa N_2 in the cold wall vacuum/pressure furnace with a graphite heater mentioned above. All the samples were weighed on a precision balance before and after the heat treatments to check for mass changes; none were observed. Vickers hardness measurements were performed with a commercial hardness tester (Matsuzawa Seiki Mxt α). A load of 300 g was applied for 15 s on the sample whose surface had been polished with 3 μm spray diamond. At least 10 indentations were made on each sample, the hardness being calculated on the basis of the average length of the indentation diagonals. The infra-red (IR) spectra were measured using a Perkin–Elmer 1760 X Fourier transform spectrometer equipped with a triglycine sulfate (TGS) detector. The measurements were carried out on discs pressed from powdered samples mixed with KBr.

Scanning electron microscopy (SEM) was carried out using a CamScan S4-80DV electron microscope. Room-temperature powder X-ray diffraction was performed on all samples heat-treated as bulk material in the cold wall furnace.

2.3 High-temperature X-ray unit

The high-temperature unit used in this investigation is based on an Anton-PAAR HTK-10 high-temperature chamber. This standard equipment was re-engineered to increase the maximum working temperature to more than 2300 K in an inert atmosphere or in vacuum. The platinum strip which is used as heater in the standard HTK-10 equipment is replaced by a graphite furnace. The basic unit in this system is a Philips powder diffractometer with a vertical goniometer PW 1050/25, graphite monochromater PW 1752/00, proportional counter for reflected beam PW 1711/10 and PW 1730/10 generator. The X-ray diffraction is controlled by a PW 1710 diffractometer control system. The raw data are collected, processed and analysed with PC-APD (PW-1877) software supplied by Philips.

The graphite furnace was coated with silicon nitride by first applying a layer of Si powder to the graphite and then nitriding at temperatures between 1150 and 1450°C. The coating had a thickness of approximately 0·75 mm, a relative density of 0·65 and a pore size of 0·2 μm. It showed good mechanical strength and thermal shock resistance. The voltage required to achieve a given temperature and the resistance of the furnace at that voltage were not significantly affected by the coating. The graphite furnace design and the high-temperature X-ray unit have been described in previous studies by Babushkin *et al.*[15] and Ashkin *et al.*[16]

2.4 Experimental set-up with the HT-XRD unit

Small amounts of as-quenched glass were powdered and the powder was freely compacted to form 8 × 10 × 1·5 mm plate samples. These were put into the coated graphite furnace and subjected to one of two possible heat treatments: (i) a single-stage heat treatment at 1150°C, (ii) a two-stage

heat treatment with various temperatures in a first pre-treatment stage (T_g - 90°C, T_g - 60°C, T_g - 30°C, T_g and T_g + 20°C) for 1 h followed by a second stage at the higher temperature, 1150°C. The first pre-treatment stage was used to cause a partial sintering of the powdered glass sample and consequently to decrease its specific surface area with increasing temperature of the first stage. The heating rate of both heat treatments was 450°C h^{-1}, with the exception of the temperature interval between T_g and 1000°C for which it was 200°C h^{-1} and during which internal nucleation in the glass was expected to occur. The temperature of the sample was measured with a Pt–13% Rh/Pt thermocouple. The heat treatments were conducted in a static atmosphere of 0·13 MPa N_2 (<5 ppm O_2).

During the heat treatment two separate X-ray scans were performed: one over a 2θ range of 31·5 to 35° at a rate of 0·05° s^{-1} in approximately 20 min intervals and a second between 20 and 40° at a rate of 0·05 s^{-1} in 60 min intervals. After the soaking temperature had been reached the scans were performed more frequently (Fig. 5). The first was used to follow the crystallization of the YAG phase [(420) peak at 2θ = 33·5°], the second to check for possible additional phases developing during the heat treatment, mainly δ- and γ-yttrium disilicates.[14] The X-ray generator settings were 50 kV and 30 mA with a Cu-target tube. All the performed high-temperature X-ray runs were repeated twice to ensure reliability of the results. A Marguardt non-linear least-squares algorithm was used to calculate the (420) YAG peak areas in order to obtain a quantitative measure of the amount of crystallized YAG phase. To confirm the nature of phases obtained during the heat treatments in the HT-XRD unit, an additional scan over a 2θ range of 10 to 80° at a rate of 0·02° s^{-1} was performed on the cooled specimens by a room-temperature XRD unit (Philips X-ray diffractometer, Cu K_α radiation).

3 Results and Discussion

3.1 DTA Measurements

Figure 1 shows the DTA chart with an endothermic peak at 943°C corresponding to the glass transition temperature (T_g) and two exothermic peaks at 1075 and 1145°C respectively, corresponding to crystallization processes in the glass. In a previous study[14] it was concluded that different crystal species crystallize from the parent glass at these two different temperatures. The first maximum corresponds to the crystallization of an intermediate phase accompanied by the crystallization of $Y_2Si_2O_7$ and the second one to the crystallization of the YAG phase.

3.2 Microhardness measurements

Figure 2 shows the results of Vickers microhardness measurements performed on bulk glasses heat-treated at 900, 925, 950, 980 and 1000°C for 6 h. These samples were transparent after the heat treatment, amorphous (as indicated by X-ray) and appeared to be homogeneous glasses without any traces of crystalline material when examined by SEM. A change of colour from yellow to light green was observed. However, a weak surface crystallization could be observed on samples heat-treated at 980 and 1000°C. For comparison, two additional microhardness measurements performed on samples heat-treated at 1050 and 1100°C for only 2 h are included in Fig. 2. The microstructures of these two samples contained crystalline material as could be evidenced by SEM observations.

The microhardness of as-quenched glass (without any subsequent heat treatment) was found to be 10·0 ± 0·39 GPa. A decrease of microhardness of samples heat-treated at 980–1000°C can be seen in Fig. 2. This temperature range corresponds approximately to the annealing temperature range

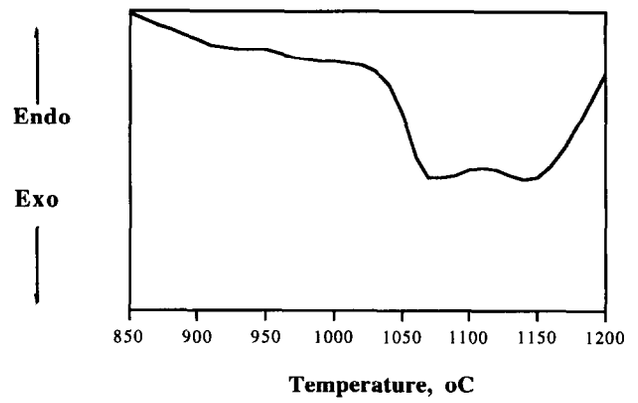

Fig. 1. DTA curve of the glass at a heating rate of 10°C min^{-1}.

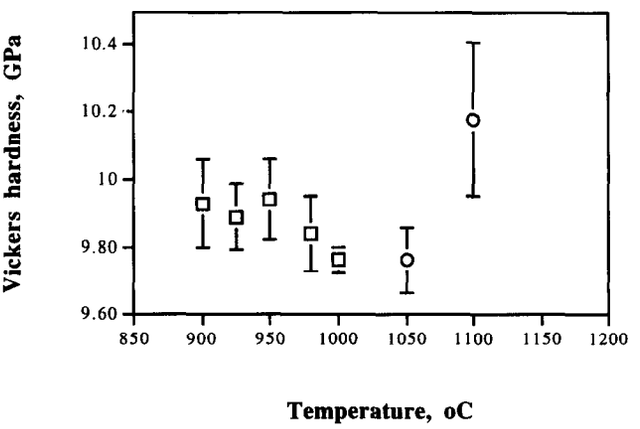

Fig. 2. Hardness of the glass heat-treated for 6 h (□) and 2 h (○).

for this type of glass.[17] Therefore it is believed that the decrease is due to the relaxation processes.[18] The increase of microhardness of the sample heat-treated at 1100°C can be attributed to the increased volume fraction of crystallized material in the parent glass revealed by the X-ray diffraction and SEM observations.

3.3 Infra-red spectroscopy

Figure 3 shows the IR spectra of 4 mg powdered specimens previously heat-treated as bulk glasses at 900, 950 and 1000°C for 6 h. The IR spectra of all three samples were similar with a broad absorption band located around 850–1100 cm^{-1}. The broad absorption is a result of integrated absorption from Si–O and Si–N bond vibrations.[19,20] Figure 3 also indicates a small increase of absorption of the glass heat-treated at 950°C and a large increase of absorption of the glass heat-treated at 1000°C compared with that heat-treated at 900°C. Therefore it can be concluded that some structural changes in the network of the glass took place during the heat treatments at 900–1000°C.

In order to explore the nature of these changes, IR spectra were collected on 1 mg powdered specimens prepared from the same samples as before, as well as on samples heat-treated at 1050 and 1150°C for 2 h and on YAG powder sintered at 1600°C in air. The IRDM deconvolution software included in the Perkin–Elmer equipment was applied to the collected data and after this modification revealed some additional absorption peaks. Thus the evolution of absorption bands related to the YAG phase (790, 730, 695, 565, 515 and 470 cm^{-1}) can be seen in Fig. 4. Since the microstructure of the sample heat-treated at 1150°C contained a large amount of crystalline YAG phase (as evidenced by X-ray powder diffraction), the absorption bands may be related to the developed YAG crystals. This spectrum is very similar to that of the sintered YAG phase. The amount of YAG crystals in the microstructure heat-treated at 1050°C was much less (amorphous when X-rayed) than in that heat-treated at 1150°C. Therefore the IR spectrum of the 1050°C specimen shows less intensity of the characteristic absorption bands attributed to the YAG phase. The microstructure of the sample heat-treated at 1000°C was amorphous with only some surface crystals as observed by SEM. Therefore the weak absorption bands at 790, 730, 695 and 515 cm-l can be attributed mainly to nuclei formed in the glass with the YAG-like structure. The IR spectra of glasses heat-treated at 900 and 950°C did not show any additional peaks after computer treatment, and therefore it was concluded that no nucleation or crystal growth occurred in the glass during the heat treatments at these low temperatures within 6 h.

3.4 Heat-treatments in the HT-XRD unit

Figure 5 shows the crystallization of the YAG phase from the parent as-quenched glass in terms of (420) YAG peak area (hereafter termed intensity) versus isothermal soaking time at 1150°C

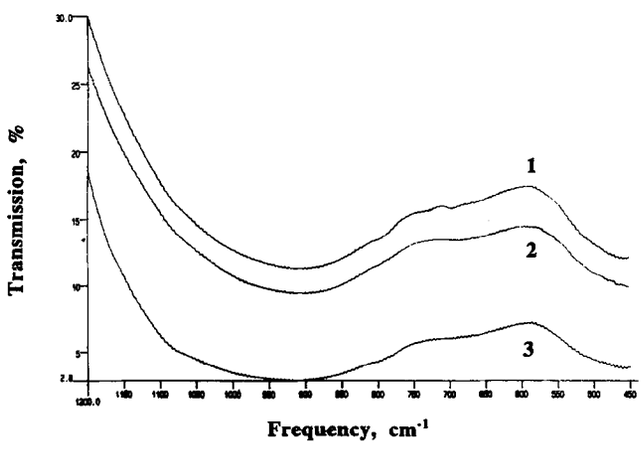

Fig. 3. IR spectra of the glass heat-treated at 900°C (1), 950°C (2) and 1000°C (3).

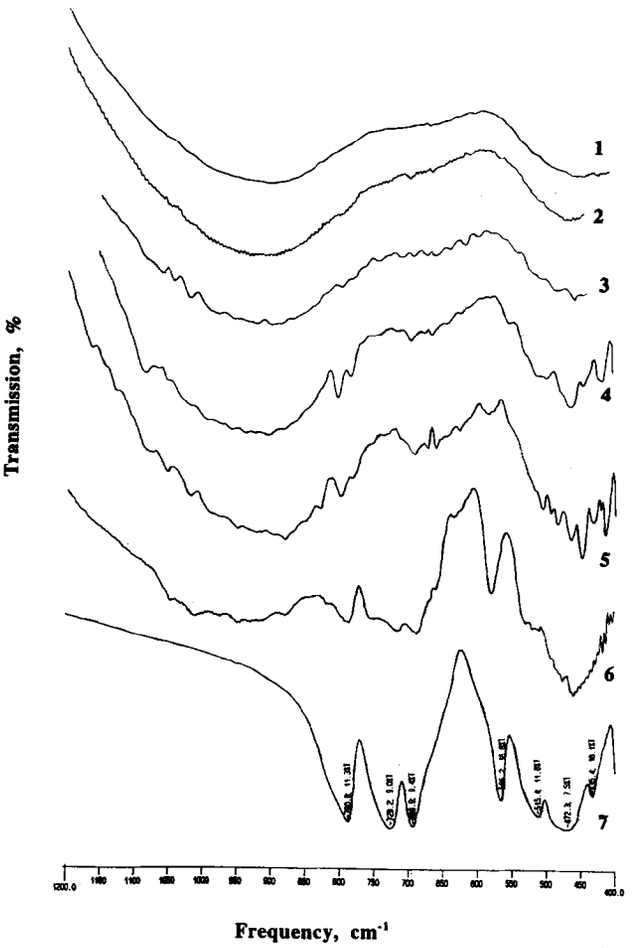

Fig. 4. Deconvoluted IR spectra of the glass as-quenched (1), and heat-treated at 900°C (2), 950°C (3), 1000°C (4), 1050°C (5) and 1150°C (6), and the IR spectrum of the YAG sintered at 1600°C (7).

during different heat treatments in the HT-XRD unit described in the Experimental Section. All the X-ray diffraction patterns collected during heating to the soaking temperature were free of any peaks from crystalline phases. Two groups of data, one low-intensity group (I) and one high-intensity group (II) can be distinguished. Group I included those two-stage heat treatment samples with the first stage treatment at T_g – 30°C and at T_g Group II included the single-stage heat treatment sample and the two-stage heat treatment samples with the first stage treatment at T_g – 90°C and T_g – 60°C. Thus, the crystallization process appears to be influenced by the temperature of the first pre-treatment stage. The intensity of the (420) YAG peak is reduced (group I) when the temperature of the first stage treatment is high enough to cause a partial sintering of the powdered glass within 1 h. This suggests that the crystallization of the YAG phase is influenced by changes of the specific surface area of the powdered glass due to the partial sintering in the first stage heat treatment. According to the IR measurements (Fig. 4) these temperatures are still too low for nucleation in the glass to proceed effectively and consequently the nucleation would occur mainly during heating to the second stage temperature. The influence of the specific surface area indicates that surface nucleation and growth are the dominant mechanisms of crystallization of the YAG phase in the investigated powdered glass. Figure 6 shows a SEM backscattered image of a polished surface of a sample with crystals growing from retained pore surfaces.

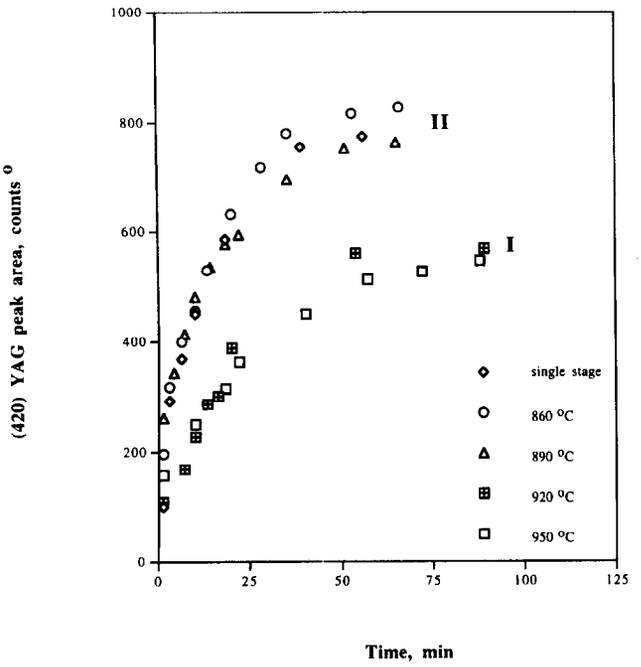

Fig. 5. Kinetics of the YAG crystallization in the glass at 1150°C during a single-stage heat treatment and following an initial pre-treatment at the indicated lower temperatures.

When the temperature of the first stage was increased to T_g + 20°C (≈970°C) and the same procedures were applied, some crystalline peaks started to develop in the X-ray pattern at the end of the initial first stage treatment, i.e. after approximately 40 min at this temperature. This behaviour implies that the nucleation rate in the glass had increased significantly at this temperature and subsequently the developed surface nuclei continued to grow to crystals which could be detected by the X-ray unit (Fig. 7).

The temperature of the first stage treatment also influenced the development of other phases in the microstructure in addition to the YAG phase. Two additional low-intensity peaks appeared in the X-ray patterns of samples heat-treated with the first stage at temperatures close to the T_g (i.e. T_g – 30°C, T_g and T_g + 20°C). These peaks at 2θ = 32·7° and 2θ = 31° correspond to the unidentified intermediate 'silicate' phase observed in previous studies[14,19,21] and to the δ-$Y_2Si_2O_7$ phase, respectively. Inspection of the X-ray patterns indicated that the intermediate phase crystallized from the glass at low temperatures (already around 970°C) and when the temperature was raised it started to transform probably to $Y_2Si_2O_7$ (Fig. 7). Additional peaks were not observed in the X-ray patterns of samples heat-treated with the first stage temperature at T_g – 90°C and at T_g – 60°C or in single-stage treatments. However, SEM observations revealed the presence of $Y_2Si_2O_7$ crystals in the microstructure of these samples (Fig. 8). These observations indicate that the crystallization of the $Y_2Si_2O_7$ phase was enhanced when the specific surface area of the powdered sample and the crystallization of the YAG phase decreased, and consequently that bulk nucleation and crystal growth were the dominant mechanisms of crystallization of the $Y_2Si_2O_7$ phase from the investigated

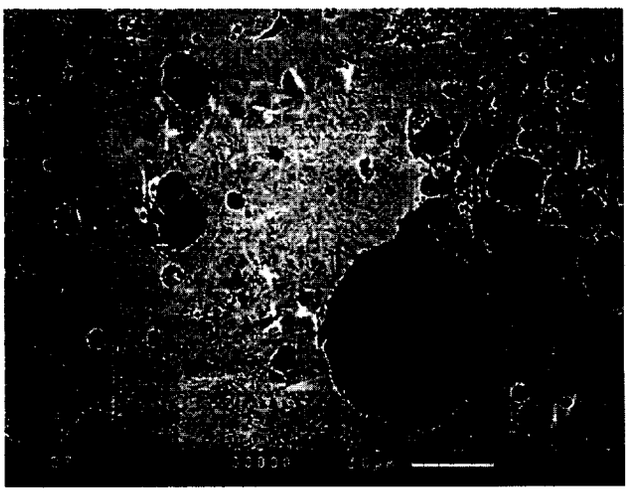

Fig. 6. YAG crystals growing from pore surfaces in the glass during a two-stage treatment with the first stage at T_g – 90°C for 1 h (backscatter image 500x).

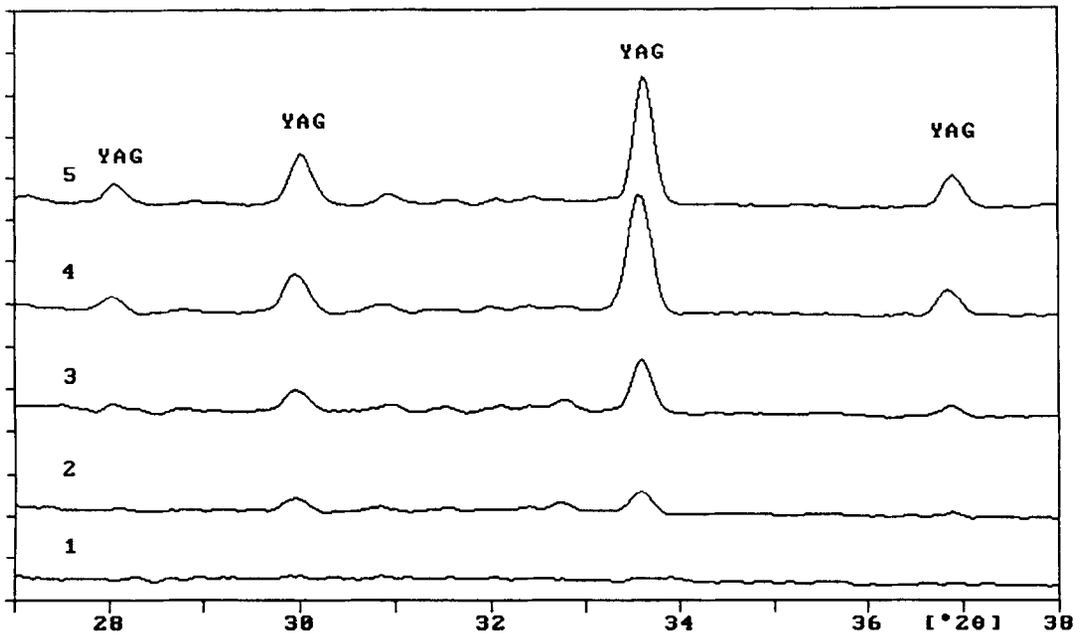

Fig. 7. X-ray patterns of the glass during a two-stage treatment with the first stage at T_g + 20°C (970°C) for 1 h; after 5 min at 970°C (2), after 5 min at 1150°C (3), after 60 min at 1150°C (4) and after 80 min at 1150°C (5).

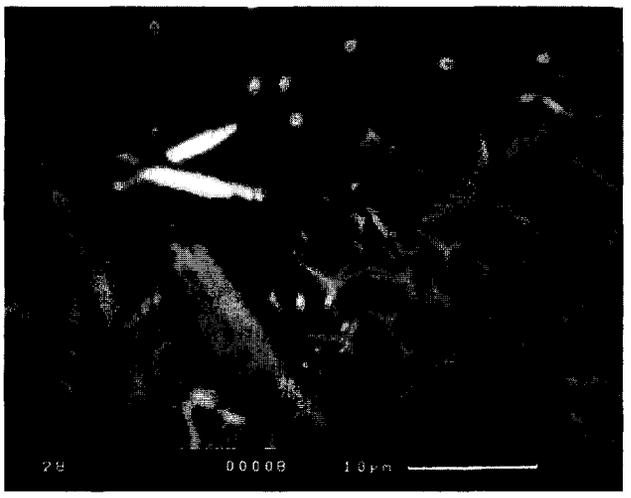

Fig. 8. $Y_2Si_2O_7$ crystals (bright crystals) developed in the microstructure of the glass during a two-stage treatment with the first stage at T_g–60°C for 1 h (backscatter image 2500x).

glass. Since the crystallization of the $Y_2Si_2O_7$ phase proceeded by a bulk process in competition with the surface crystallization of the YAG phase and since the amounts of $Y_2Si_2O_7$ phase crystallizing were small, no kinetic measurements of the $Y_2Si_2O_7$ crystallization were attempted. No oxynitride phase was detected in the microstructure of the glass-ceramics during the heat treatments and therefore it is assumed that the retained glassy phase was enriched by nitrogen.

The suggestion that the main mechanism of crystallization of the $Y_2Si_2O_7$ phase is a bulk process is consistent with results obtained by Ramesh *et al.*[22] using DTA measurements to characterize the crystallization process in a powdered oxynitride glass in the Y–Si–Al–O–N system. In that study the bulk nucleation and growth of the $Y_2Si_2O_7$ phase was identified as the main mechanism responsible for devitrification of the glass. Lewis *et al.*,[10] studying the crystallization of the glassy phase in a YAG/β-SiAlON material, observed that the number of nuclei was restricted and that there was a preference for nucleation of the YAG phase on free surfaces such as microcavities rather than at β-SiAlON/glass interfaces. This was attributed to a compositional influence in addition to the direct effect of surface energy; thus species may be lostto the vapour phase or may surface-segregate, reducing the local viscosity or increasing the driving force for nucleation. Regions of phase separation were also recognized as possible nucleation sites for crystallization of the YAG phase.

4 Conclusions

The crystallization of an oxynitride glass was investigated using high-temperature X-ray diffractometry, IR spectroscopy and microhardness measurements. The crystallization processes were found to begin around 1000°C. The crystallization of the powdered glass at 1150°C was followed in HT-XRD and shown to occur predominantly by YAG formation. The nucleation of the YAG occurred preferentially at free surfaces. A small amount of crystallization occurred by the formation of $Y_2Si_2O_7$ nucleating in the bulk. The results are relevant to developing improved crystallization treatments for glasses with potential for crystallization to YAG-based glass-ceramics and for heat treatment of YAG/β-SiAlON materials.

References

1. Einarsrud, M. A. & Mitomo, M., Mechanism of grain growth of β-sialon. *J. Am. Ceram. Soc.*, **76**[6] (1993) 1624–6.
2. Hohnke, H. & Tien, T. Y., Solid–liquid reactions in part of the system Si, Al, Y/N, O. *Progress in Nitrogen Ceramics Proc.*, ed. F. L. Riley. Martinus Nijhoff, The Hague, 1983, pp. 101–10.
3. Lewis, M. H. & Lumby, R. J., Nitrogen ceramics: liquid phase sintering. *Powder Metall.*, **26**[2] (1983) 73–81.
4. Lewis, M. H., Sialons and silicon nitrides; microstructural design and performance. *Mater. Res. Soc. Symp. Proc.*, **287** (1983) 159–72.
5. Esktröm, T. & Nygren, M., SiAlON ceramics. *J. Am. Ceram. Soc.*, **75**[2] (1992) 259–76.
6. Hampshire, S., Engineering properties of nitrides. *Engineered Materials Handbook. Vol. 4: Ceramics and Glasses.* ASM International, Materials Park, OH, 1992.
7. Thompson, D. P., Alternative grain-boundary phases for heat-treated Si_3N_4 and β-sialon ceramics. *Br. Ceram. Proc.*, **45** (1989) 1–13.
8. Lewis, M. H., Crystallisation of grain boundary phases in silicon nitride and sialon ceramics. *Key Eng. Mater.*, **89–91** (1994) 333–8.
9. Falk, L. K. L. & Dunlop, G. L., Crystallization of the glassy phase in an Si_3N_4 material by post-sintering heat treatments. *J. Mater. Sci.*, **22** (1987) 4369–76.
10. Lewis, M. H., Bhatti, A. R., Lumby, R. J. & North, B., The microstructure of sintered Si–Al–O–N ceramics. *J. Mat. Sci.*, **15** (1980) 103–13.
11. Leng-Ward, G. & Lewis, M. H., Crystallization in Y–Si–Al–O–glasses. *Mater. Sci. Eng.*, **71** (1985) 101–11.
12. Bonell, D. A., Tien, T. Y. & Ruhle, M., Controlled crystallization of the amorphous phase in silicon nitride ceramics. *J. Am. Ceram. Soc.*, **70**[7] (1987) 460–5.
13. Bentsen, L. D., Hasselman, D. P. H. & Tien, T. Y., Effect of crystallization of the grain boundary phase on the thermal diffusivity of a sialon ceramic. *J. Am. Ceram. Soc.*, (May 1984) C-85–6.
14. Vomacka, P., Crystallization of yttrium oxynitride glasses to $Y_3Al_5O_{12}$-based glass ceramics. *J. Eur. Ceram. Soc.*, submitted.
15. Babushkin, O., Harrysson, R., Lindbäck, T. & Tegman, R., A high-temperature graphite furnace for X-ray powder diffraction. *Meas. Sci. Technol.*, **4** (1993) 816–19.
16. Ashkin, A., Ashkin, D. & Babushkin, O., Investigation of α-sialon formation by high-temperature X-ray diffraction. *Key Eng. Mater.*, **89–91** (1994) 373–7.
17. Hampshire, S., Nestor, E., Flynn, R., Besson, J.-L, Rouxel, T., Lemercier, H., Goursat P., Sebai, M., Thompson, D. P. & Liddell, K., Yttrium oxynitride glasses: properties and potential for crystallization to glass-ceramics. *J. Eur. Ceram. Soc.*, **14** (1994) 261–73.
18. Zarzycki, J., *Glasses and the Vitreous State.* Cambridge University Press, Cambridge, 1991, pp. 11–36.
19. Vomacka P. & Babushkin, O., Yttria–alumina–silica glasses with addition of zirconia. *J. Eur. Ceram. Soc.*, **15** (1995) 921–8.
20. Ding Yuquan, Ding Zishang & Jiang Zhonghua, Formation and properties of Y–Al–Si–O–N system in the grain boundaries of Si_3N_4 ceramics. *J. Non-Cryst. Sol.*, **112** (1989) 408–12.
21. Vomacka, P., Babushkin, O. & Warren, R., Zirconia as a nucleating agent in an yttria-alumina-silica-glass. *J. Eur. Ceram. Soc.*, **15** (1995) 1111–17.
22. Ramesh, R., Nestor, E., Pomeroy, M. J. & Hampshire, S., Optimization of heat treatments for oxynitride glass ceramics. In Proc. *10th Irish Materials Forum*, Coleraine, N. Ireland, 1994, in press.

Journal of the European Ceramic Society **16** (1996) 1271–1275

PII:S0955-2219(96)00045-3
0955-2219/96/$15.00

The Effect of Process Atmosphere on the Intergranular Phase in Silicon Nitride Ceramics

O. J. Pullum & M. H. Lewis

Centre for Advanced Materials, Department of Physics, University of Warwick, Coventry CV4 7AL, UK

(Received 20 November 1995; revised version received 30 January 1996; accepted 6 February 1996)

Abstract

The influence of the process atmosphere in the gas pressure sintering of silicon nitride has been investigated, particularly with regard to formation of the intergranular phase. The intergranular phases identified after different gas pressure sintering cycles were compared with that present in a material fabricated by the hot isostatic pressing of an identical powder composition, allowing comparison of the two processing methods. The results suggested infiltration of the nitrogen processing gas into the sintering body, which adversely affected the intergranular phase formation in a composition that had been tailored for optimal mechanical behaviour. The duration of exposure to the processing gas and the post-sintering cooling cycle were identified as being critical factors in the intergranular phase crystallisation. Copyright © 1996 Elsevier Science Ltd

Introduction

The potential for improving the mechanical properties of silicon nitride ceramics arises from greater microstructural control, mainly achieved by finely tailoring the initial powder composition and optimising the fabrication conditions. As is well known, limitations to the possible high-temperature applications of these ceramics are mainly imposed by the properties of the residual intergranular phase formed after the reaction of sintering additives with the silicon nitride grains. The chemical composition of this phase is critically important to the overall oxidation resistance while the viscosity of the liquid phase, formed above the eutectic temperature, influences the microstructural development during sintering and also determines the interfacial characteristics that affect creep behaviour. A considerable amount of research has been carried out specifically related to the composition of the intergranular phase, with sintering additives being selected for the optimum combination of their ease of sintering and the compatibility of the residual phase with Si_3N_4 and its oxidation product, SiO_2. A well-known intergranular phase associated with improvements in high-temperature mechanical properties is $Y_2Si_2O_7$, which has been formed in hot isostatically pressed (HIPed) Si_3N_4 ceramics using a correctly balanced mixture of Y_2O_3 and SiO_2 sintering additives.[1]

The powder composition used for this investigation is one that has been well researched in HIPed ceramics and is associated with an absence of creep cavitation.[1] In the research presented here, the ceramics have been fabricated using gas pressure sintering (GPS), a less expensive form of fabrication, to enable the particular influence of the GPS processing method to be evaluated.

The GPS process allows unusually high temperatures to be reached during sintering while suppressing the thermal decomposition of Si_3N_4 via the application of external N_2 pressure. The high sintering temperatures encourage the β-Si_3N_4 grains to grow abnormally and this leads to enhanced fracture toughness from mechanisms of crack bridging and pull-out and to improved reliability of the final ceramic. The ceramic powders are not generally encapsulated during the processing, in contrast to the HIPing procedure where encapsulation typically results in some surface oxidation to Si_2N_2O due to the interaction of the ceramic powders with the glass encapsulant. This means that the ceramic phase formation is much more susceptible to the atmospheric effects of the processing environment. For example, Neidhardt *et al.*[2] found an oxygen/nitrogen gradient to exist in GPS-fabricated ceramics as a result of the reduction potential of the graphite sintering crucible in the nitrogen atmosphere.

Possible atmospheric effects of the nitrogen processing atmosphere on the intergranular ceramic phases were of particular interest in this investigation.

Experimental Procedures

The Si_3N_4 powder used was UBE SN-E10, with the initial oxygen content found to be 1·6 wt%. The composition prepared was 7·5 wt% Y_2O_3, 2·5 wt% SiO_2 and 90 wt% Si_3N_4. These powders were ball-milled together for 72 hours in propanol, then dried and cold isostatically pressed into billets at 90 MPa. Two-stage GPS was carried out at T & N, Rugby, at 1800–1900°C and 10–100 bar. Additionally, some fully densified material of the same composition, already fabricated by HIPing at 1775°C and 150 MPa, was processed further by GPS for comparison of the resulting intergranular phases and microstructure. After sintering, the phases present in the ceramics were evaluated using Cu K_α X-ray diffraction and the densities were determined according to Archimedes' principle. Annealing was carried out in argon, at 1200°C for 24 hours, to promote crystallisation of the glassy phases. For more detailed investigation by transmission electron microscopy (TEM), slices of the resultant ceramics were diamond-ground to a thickness of 30 μm, polished to a finish of $^1/_4$ μm and finally thinned to electron transparency by argon ion beam bombardment.

Ceramic Characterisation

The major phase identified in all the GPS-fabricated ceramics was β-Si_3N_4, indicating a complete phase transformation of the initial α-Si_3N_4 powder. However, it should be noted that the occurrence of this phase transformation during GPS is not necessarily accompanied by full ceramic densification.[3]

(i) Intergranular phase

The HIPed material contained α-$Y_2Si_2O_7$ as the intergranular phase prior to the additional GPS processing and was assumed to be fully dense. At the high sintering temperatures during GPS, the α-$Y_2Si_2O_7$ phase reverted to the liquid state and after GPS was recrystallised during post-GPS annealing at 1200°C, forming a mixture of β-$Y_2Si_2O_7$, α-$Y_2Si_2O_7$ and the 'y-yttrium silicate' phase,[4] with no evidence of the higher temperature γ-$Y_2Si_2O_7$ and δ-$Y_2Si_2O_7$ polymorphs. Figure 1 shows a comparison between the XRD spectra for the initial HIPed material and that from the same material after the additional GPS processing and annealing in air for 70 hours at 1200°C. After similar annealing treatments, the same intergranular phases were identified in the ceramics fabricated by GPS.

As was also found in the previous research on the HIPed Si_3N_4, carried out at Warwick and reviewed in Ref. 5, the post-sintering crystallisation of the residual intergranular phase was extremely sensitive to the cooling rate, with mainly glassy phase formation occurring at 'natural' cooling rates of 20–30°C/min. Therefore, the ceramics were annealed to promote crystallisation of the glassy phases. The results of this earlier research had shown that the β-$Y_2Si_2O_7$ polymorph tends to crystallise in the range 1500–1400°C at the slowest cooling rates inside the HIP furnace (4°C/min), with subsequent nucleation of the α-$Y_2Si_2O_7$ polymorph at temperatures below this. As the crystallisation proceeds, the likelihood of 'y-phase' formation is believed to increase as the liquid volume is reduced, which enhances the effect of impurities in stabilising this phase.[4] Liddell and Thompson[4] have discussed the various explanations for the 'y-phase' occurrence, attributing its formation either to localised, high concentrations of impurity ions in the intergranular glass, which give rise to crystallisation of a phase with formula $RY_5Si_6O_{21}$ where R represents the impurity cation or to the oxidation of the Y-Si-O-N intergranular glass.

It is well known that the simultaneous presence of both the α- and β-$Y_2Si_2O_7$ polymorphs is detrimental to the mechanical properties since tensile stresses are introduced by the different atomic volumes of the polymorphs causing isolated β-$Y_2Si_2O_7$ regions to be held in compression. From the earlier research,[5] the crystallisation of β-$Y_2Si_2O_7$ seemed to occur readily during the annealing (1200°C) of residual glassy phases, except in those cases where the α-$Y_2Si_2O_7$ phase had already crystallised and then remained stable. Once formed, the β-$Y_2Si_2O_7$ polymorph showed no tendency to transform into the α-$Y_2Si_2O_7$ phase and a mixture of β-$Y_2Si_2O_7$ and the 'y-yttrium silicate' has even been observed to remain after 500 hours at 1400°C. Hence, to tailor the intergranular phase for the optimal mechanical properties, it is apparent that formation of the most desirable α-$Y_2Si_2O_7$ polymorph and avoidance of β-$Y_2Si_2O_7$ are critically controlled by the post-sintering cooling cycle.

Further GPS runs were carried out to examine the frequency of the yttrium disilicate intergranular phase formation with some variations in the GPS thermal cycle. Some typical results following annealing from the different GPS runs are given in Table 1. The intergranular phases identified after the shorter sintering cycles were comparable with those formed after HIPing this composition and the GPS environment appears to have had little

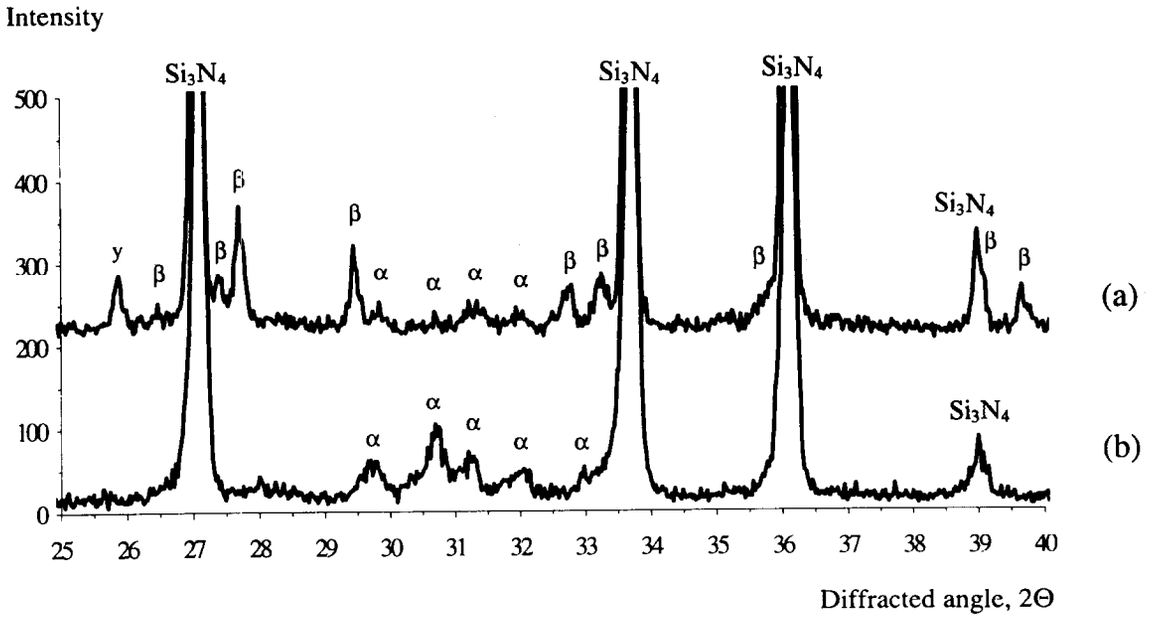

Fig. 1. XRD comparison of intergranular phases present in (a) HIPed material after additional GPS processing and annealing and (b) after HIPing only. Peaks marked 'α', 'β' and 'y' refer to α-$Y_2Si_2O_7$, β-$Y_2Si_2O_7$ and 'y'-$Y_2Si_2O_7$, respectively.

Table 1. Intergranular phase variation with different GPS cycles

	Temperature (stage 1) (°C)	*Pressure (stage 1) (bar)*	*Dwell time (stage 1) (h)*	*Temperature (stage 2) (°C)*	*Pressure (stage 2) (bar)*	*Dwell time (stage 2) (h)*	*Post-annealing intergranular phases*
1	1800	10	1	1900	70	1	α and β-$Y_2Si_2O_7$ and y-phase (trace)
2	1800	10	1	1900	100	1	α and β-$Y_2Si_2O_7$
3	1800	10	2	1900	70	1·5	β-$Y_2Si_2O_7$, y-phase, and apatite (trace)
4	1725	2	2	1900	100	2·5	Apatite and melilite
5	—	—	—	1900	65	6	Apatite and melilite
6	1880	10–20	4	1950	100	4	Melilite only

effect on the intergranular phase formation in these instances. However, from Table 1, it is apparent that the nitrogen content of the sintering liquid increased during longer exposures to the N_2 processing atmosphere, resulting in the formation of apatite ($Y_5N[SiO_4]_3$) and the more nitrogen-rich melilite ($Y_2Si_3N_4O_3$) phase, both of which are known to cause severe degradation in Si_3N_4 ceramics during oxidation. The nitrogen dissolution into the sintering liquid is believed to arise from gaseous infiltration of the processing gas, aided by the relatively high liquid phase content, and hence good interconnectivity between the Si_3N_4 grains and also from the partial decomposition of Si_3N_4 at internal pore surfaces. Kang and Greil[6] have investigated the influence of the gas pressure on densification during liquid phase sintering, finding that the difference between the internal pore pressure and exterior surface decreased with increasing applied gas pressure. Hence, the contribution of the internal Si_3N_4 decomposition to the nitrogen dissolution would be expected to become less significant with higher gas processing pressure and unlikely to occur during HIPing. Although one advantage of the GPS process over HIPing is that no encapsulation is required, an encapsulant might provide a protective barrier to prevent the formation of more nitrogen-rich phases in this composition during the longer 'stage 2' dwell times required to promote high temperature grain growth.

(ii) Constitutional variations

After prolonged GPS processing the HIPed material developed a mottled appearance, associated with a marked increase in porosity. Figure 2 is taken from a polished cross-section of the HIPed material after the additional GPS (there was no further heat treatment). This shows some evidence of gaseous evolution and as silicon and oxygen were the only elements identified by EDX analysis in this region, the oxygen being detected from the residual intergranular phase, it is believed that some thermal decomposition of the Si_3N_4 had

taken place. This may result from a reducing atmosphere existing inside the graphite sintering crucible,[2] or may indicate that the applied nitrogen pressure was insufficient to suppress decomposition within the pores.[6]

In all the GPS-fabricated ceramics, some difference between the surface region and the bulk was visible as optically diffuse bands extending 50–100 μm from the outer surfaces. Figure 3, taken from a specimen fabricated in run 6 (see Table 1), illustrates the difference between the corresponding XRD spectra from the surface and the bulk regions and in which there is an apparent absence of any secondary phase in the bulk material. The reduction of any detectable crystalline intergranular phase in the bulk material was linked to a decrease in density from the surface to the bulk region, since the smaller quantities of the intergranular phase present in the central, porous regions were less easy to detect by XRD. An additional factor which may have inhibited the densification is the dissolution of nitrogen into the sintering liquid, which is believed to increase the liquid phase viscosity.[7]

The microstructure formed in this composition after GPS is shown in Fig. 4, taken from the same specimen as for Fig 3. The intergranular network is the phase of darker contrast surrounding the Si_3N_4 grains. The grain size variation seen in Fig. 4 is typical of GPS-fabricated Si_3N_4 and, unlike the more uniform, fine-grained microstructure observed in HIPed ceramics, contains some anisotropic grains of several μm in diameter, which may contribute towards an enhanced fracture toughness. Although the intergranular phase could not be detected by XRD from the central regions, TEM revealed pockets of the intergranular network, together with extensive porosity (not shown here). The intergranular phase in these regions was identified by electron diffraction as being the same nitrogen-rich phase as that present in the surface regions, suggesting that the nitrogen/oxygen ratio remained constant from the surface to the bulk. As the relatively high sintering liquid content in this composition provides a continuous network between the Si_3N_4 grains, this has enabled the uniform dissolution of the processing gas into this network.

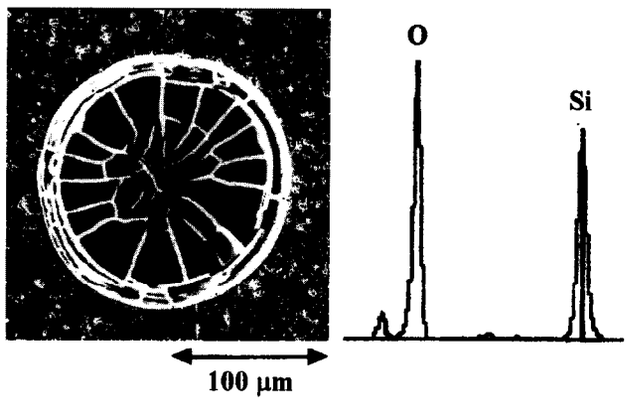

Fig. 2. Secondary electron microscope image showing evidence for a burst gas bubble, with EDX analysis from the central region.

Conclusions

The intergranular phases formed in the Si_3N_4 ceramics fabricated with this high-additive composition were found to vary according to the length of exposure to the N_2 processing gas, which evenly

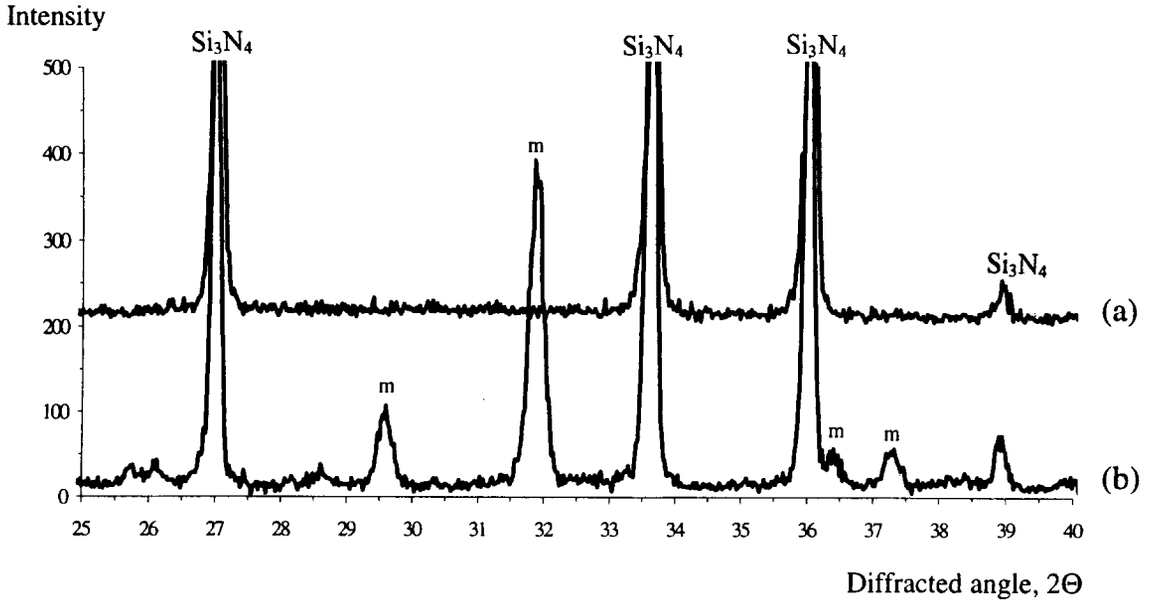

Fig. 3. Comparison of the XRD spectra from two different regions of a ceramic fabricated from GPS run no. 6: (a) a few hundred μm into the bulk and (b) the outer surface. The peaks marked 'm' identify the melilite phase present in this ceramic.

Fig. 4. TEM microstructure of a GPS-fabricated ceramic from run no. 6 (see Table 1), with electron diffraction pattern identifying the melilite intergranular phase.

infiltrated the sintering liquid. A substantial variation in the oxygen/nitrogen ratio was detected in the intergranular phase found in ceramics fabricated according to different GPS cycles, although no phase variation was identified within individual ceramic specimens. It was found that the formation of nitrogen-rich phases could be avoided only for the shorter GPS cycles, which were of insufficient duration to promote more pronounced grain growth than is typically observed in GPS-processed Si_3N_4.

The GPS process allows more rapid cooling than HIPing and the control of the post-sintering cooling cycle was found to have a significant influence on the intergranular phase formation. This was particularly important since the annealing treatments to promote crystallisation from a rapidly-cooled glass often resulted in an undesirable combination of the $Y_2Si_2O_7$ polymorphs.

Acknowledgements

The authors would like to thank Mr J. Woodthorpe, T & N Technology Ltd, Rugby for his assistance in carrying out the GPS experiments and the EPSRC for financial support of this research.

References

1. Tuersley, I. P., Leng-Ward, G. & Lewis, M. H., High-temperature Si_3N_4-based ceramics. *Proc. 3rd Int. Symp. on Ceramic Materials & Components for Engines*, ed. V. J. Tennery. Am. Ceram. Soc., 1988, pp. 786–95.
2. Neidhardt, U., Schubert, H., Bischoff, E. & Petzow, G., Gas pressure sintering of Si_3N_4 in $N_2/CO/CO_2$ atmosphere, *Proc. Silicon Nitride '93, Key Engineering Materials*, 89-91, ed. M. J. Hoffmann, P. F. Becher & G. Petzow. Trans. Tech. Pub., 1993, pp. 187–92.
3. Mitomo, M., Yang., N., Kishi, Y. & Bando, Y., Influence of powder characteristics on gas pressure sintering of Si_3N_4. *J. Mater. Sci.*, **23** (1988) 3413–19.
4. Liddell, K. & Thompson, D. P., X-ray diffraction data for yttrium silicates. *Br. Ceram. Trans. J.*, **85** (1986) 17–22.
5. Lewis, M. H., Sialons and silicon nitride: Microstructural design and performance. *Proc. Mat. Res. Soc. Symp.* 287. Mat. Res. Soc. 1993, pp. 159–72.
6. Kang, S-J. L. & Greil, P., Elimination of large pores during gas pressure sintering of β'-sialon. *J. Am. Ceram. Soc.*, **72** (1989) 1166–9.
7. Hampshire, S., Drew R. A. L. & Jack K. H., Viscosities, glass transition temperatures and microhardness of Y-Si-Al-O-N glasses. *Comm. Am. Ceram. Soc.*, **67**(3) (1984) C46–C47.

Journal of the European Ceramic Society **16** (1996) 1277–1282

PII:S0955-2219(96)00053-2
0955-2219/96/$15.00

Subsolidus Phase Relationships in the System Dy_2O_3–Si_3N_4–AlN–Al_2O_3

W. Y. Sun,[a] D. S. Yan,[a] L. Gao,[a] H. Mandal[b] & D. P. Thompson[b]

[a] The State Key Lab on High Performance Ceramics and Superfine Microstructure, Shanghai Institute of Ceramics, Academia Sinica, Shanghai, People's Republic of China
[b] Wolfson Laboratory, Materials Division, Department of Mechanical, Materials & Manufacturing Engineering, University of Newcastle upon Tyne, UK

(Received 20 November 1995; revised version received 20 February 1996; accepted 28 February 1996)

Abstract

Subsolidus phase relationships in the system Dy–Si–Al–O–N have been determined. Forty-two compatibility tetrahedra were established in the region Dy_2O_3–Si_3N_4–AlN–Al_2O_3. Within this region, DyAG($Dy_3Al_5O_{12}$) and M'-phase ($Dy_2Si_{3-x}Al_xO_{3+x}N_{4-x}$) are the only two important compounds which have tie lines joined to β-sialon and AlN polytypoid phases. α-Sialon coexists with both M' phase and DyAG (only with oxygen-rich α'). Copyright © 1996 Elsevier Science Ltd

1 Introduction

The importance of using rare earth oxides for the densification of silicon nitride ceramics has been recognised in recent years. Not only are they very effective along with alumina for densification, either singly or in combination with yttria, but they can also be accommodated in the α-Si_3N_4 lattice forming α-sialon (α-Si_3N_4 solid solution with the composition $Ln_xSi_{12-(m+n)}Al_{m+n}O_nN_{16-n}$, also called α'), thus providing an opportunity for decreasing the transient liquid phase content after sintering and hence reducing the amount of residual grain boundary glass. Therefore, phase relationships in Ln–Si–Al–O–N systems are of particular interest.

It is known that elements in the lanthanide (Ln) series are similar to yttrium in compound formation and phase relationships. Previous work on Ln–Si–O–N subsystems,[1] indicates that the phase relationships are nearly the same as in the Y–Si–O–N system, but in Ln–Al–O–N systems[2] the phase relationships vary with the atomic number of the rare earth element. The phase relationships in systems with high Z-value of the rare earth element are similar to those in Y–Al–O–N.[3] In the systems Ln–Al–O–N (where Ln = Ce → Sm) two N-containing compounds exist — Ln_2AlO_3N and $Ln_2Al_{12}O_{18}N_2$ (magneto-plumbite, MP compound) — and no garnet phase occurs; instead, the aluminate with 1 : 1 becomes stable.[2] The Ln_2AlO_3N and MP compounds do not occur in those systems containing rare earth oxides with cations smaller than that of Gd.[2,4] Therefore, in the five-component systems with low Z-value rare earth elements, the phase relationships become a little bit different from those in Y–Si–Al–O–N.[5–7] In the oxygen-rich region where two five-component phases[8,9] — U-phase ($Ln_3Si_{3-x}Al_{3+x}O_{12+x}N_{2-x}$) and W-phase ($Ln_4Si_9Al_5O_{30}N$) — exist, the former is stable for rare earth cations between La and Dy and the latter stable only in La, Ce and Nd systems. Recent work on Ln-melilite[10,11] indicates that the formation of melilite solid solution ($Ln_2Si_{3-x}Al_xO_{3+x}N_{4-x}$) occurs easily for melilite containing light rare earth elements and that the top solubility limit of Al and O decreases with increasing Z-value (x = 1 for Nd and x = 0·6 for Er). In recent years, work has focused on the Sm(or Nd)–Si–Al–O–N system.[12,13] The results indicate Nd has the same behaviour as Sm: below the subsolidus temperatures Nd(Sm)AlO_3 coexists with β-sialon (β-Si_3N_4 solid solution, $Si_{6-z}Al_zO_zN_{8-z}$, β') and all AlN polytypoids and α-sialon can only be compatible with melilite solid solution. Dysprosium is one of the central elements in the rare earth series; in this region, phase relationships in Ln–Si–Al–O–N systems are changing from those observed for the low-Z elements (La, Nd, Sm) to those observed for the high-Z elements (Er, Yb... and Y). Studies on the Dy–Si–Al–O–N system will therefore give an indication of whether these changes occur simultaneously or whether there is overlap in this region between the different phase relationships observed for the high-Z and low-Z

regimes. To elucidate the variation of phase relationships in the Ln–Si–Al–O–N system with rare earth element and to study the Dy–Si–Al–O–N system itself, the aim of the current work is to determine the subsolidus phase relationships in the region defined by the four end-members Si_3N_4, AlN, Al_2O_3 and Dy_2O_3 (Fig. 1). This region includes the phases α-sialon, β-sialon and AlN polytypoids, and covers the range of compositions used for the design and processing of commercial multi-phase sialon ceramics.

2 Experimental Procedure

The present paper is the result of two work programmes carried out separately at Shanghai Institute of Ceramics and the University of Newcastle upon Tyne. The symbol * is used to represent the experiments carried out at Newcastle. The starting powders used were α-Si_3N_4 (Starck H1 and Starck LC10*), AlN (supplied by Zhuzhou Institute of Hard Metal Alloys, containing 1·2% oxygen and Starck Grade B*), Al_2O_3 (99·99%, produced by decomposing ammonium alum and Alcoa A17*), Dy_2O_3 (99·9%, Yaolung Chemical Works, China and 99·9%, Aldrich Chemical Co. Ltd*). The oxygen contents of the nitride powders were taken into account in calculating compositions. The starting powders were weighed out and ground in absolute alcohol or isopropanol* using an agate pestle and mortar. The mixed powders were dried, pressed into pellets 10 mm in diameter and then isostatically pressed under a pressure of 200 MPa. The specimens prepared at Shanghai were fired in a graphite-resistant furnace with a rather slow cooling rate (~ 50°C min^{-1}), whilst those at Newcastle were fired in graphite-resistant furnace which could be cooled down to room temperature very quickly (~ 100°C min^{-1}). A nitrogen atmosphere was used in all cases. The specimens with compositions near liquid-phase region were heat-treated after firing. All specimens were examined by X-ray diffractometry or using a Hägg–Guinier focusing camera. Only specimens showing less than 3% weight loss after firing were used for data analysis.

3 Results and Discussion

Twenty-three compositions in the region bounded by Si_3N_4, AlN, Al_2O_3 and Dy_2O_3 were studied to establish compatibility relationships. The binary tie lines established were based on the results listed in Table 1. Based on the much more extensive knowledge of phase relationships in the Y–Si–Al–O–N and Sm(Nd)–Si–Al–O–N systems and other information in the literature listed above, 42 compatibility tetrahedra were established in this region (Table 2). In the present work α-sialon is considered as a point composition and its detailed solid solution range has not been determined.

As indicated in this table, DyAG($Dy_3Al_5O_{12}$) is a stable phase and is compatible with all the AlN polytypoid phases, β-sialon (from β_{10} to β_{60}) and α-sialon (oxygen-rich), forming 12 AlN-polytypoids-containing compatibility tetrahedra (Fig. 2) and one α'-β'-containing compatibility tetrahedron, α'-β_{10}–DyAG–12H (Fig. 3). M' was also found to have tie lines with β-sialon from

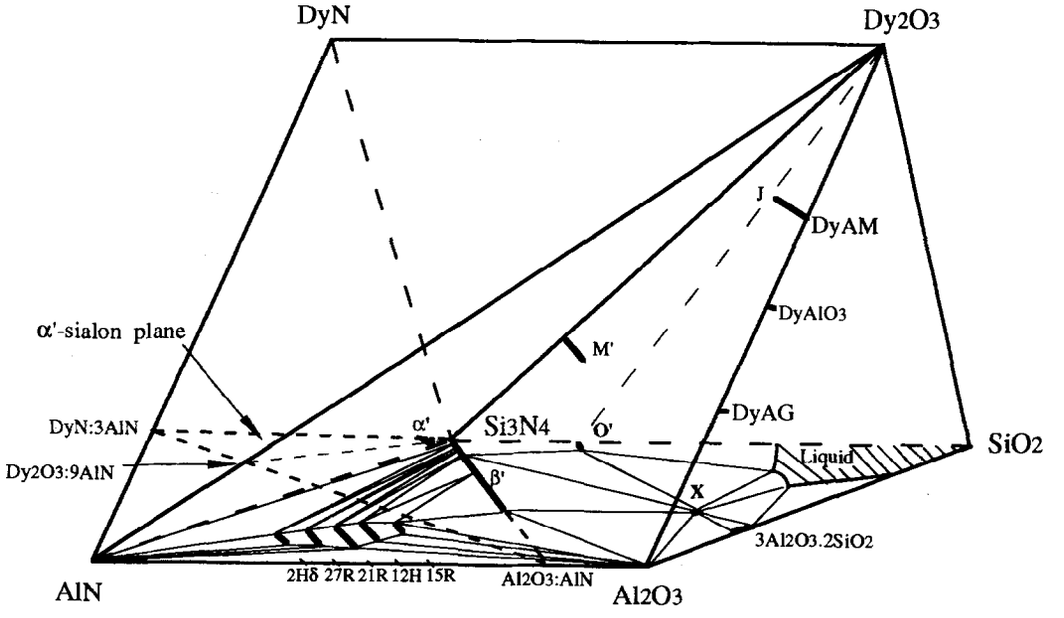

Fig. 1. Representation of Dy-SiAlON system showing phases occurring in the region bounded by Si_3N_4, Dy_2O_3, Al_2O_3 and AlN, and Si–Al–O–N behaviour diagram at 1700°C (α-sialon plane = the plane with α-sialon composition $Dy_xSi_{12-(m+n)}Al_{m+n}O_nN_{16-n}$).

Table 1. Compositions studied in the system Si_3N_4-AlN–Al_2O_3–Dy_2O_3

No.	Composition (wt%)				Firing (°C–h)	Phases present[a]	Heat treatment (°C–h)	Phases present[a]
	Si_3N_4	AlN	Al_2O_3	Dy_2O_3				
1*	80·52	2·74	2·92	13·83	1750–1	β(s); M' (w)	1350–24 1550–5^	β (s); M' (m); DyAG (w) β (s); M' (m)
2	77·70	5·14	2·55	14·62	1800–1	β (s); M' (w)	1350–24	β (s); M' (m); DyAG (w)
3*	73·43	6·09	5·86	14·61	1750–1	β' (s) ; α' (m)	1550–24 1550–5^	β' (s); α' (mw); DyAG (m); M' (w) β' (s); α' (w); M' (m)
4	70·00	0·00	6·44	23·56	1800–1	β (s); M' (s)	1350–24 1550–5^	β (ms); M' (m); DyAG (w) β (ms); M' (m)
5	69·39	5·53	11·26	13·81	1750–1	β' (s); α' (m); 21R (m)	1350–24	β_{10} (s); DyAG (s)
6	63·75	6·82	15·16	13·74	1800–1	α' (m); β' (m); 21R (s)	1350–24	β_{10} (s); DyAG (s)
7	53·22	9·85	23·13	13·80	1700–1	β' (s); 15R (vw)	1350–24	β_{20} (s); DyAG (s)
8	49·88	9·24	21·18	19·70	1750–1	β' (s); 15R (vw)	1350–24	β_{20} (s); DyAG (s)
9	49·69	10·88	11·71	27·72	1750–1	α' (m); β' (w); K(m)	1350–24 1550–5	DyAG (s); α' (m); β' (w); K (w?) DyAG (s); α' (m); β' (w); K (w?)
10*	38·43	31·97	11·03	18·58	1800–1	α'(m); 21R (m)	1350–24 1550–5	α' (m); 21R (m) α' (m); 21R (m); M'(m)
11*	35·38	29·34	17·49	17·79	1800–1	12H (ms); α' (m); β' (w)	1350–24 1550–5	12H (m); α' (m); DyAG (m); β' (w) 12H (m); α' (m); DyAG (m); β' (w)
12	16·05	1·29	1·87	80·78	1700–1	M' (x = 0·3) (s); J' (x = 1) (ms)		
13	13·30	1·29	4·87	80·56	1700–1	M' (x = 0·75) (s); J' (x = 1·4) (w)		
14	11·28	37·05	13·85	37·80	1700–1	M' (s); DyAG (s); 21R (m)		
15	11·14	—	—	88·86	1700–1	J (s)		
16	7·80	—	3·61	88·59	1700–1	J' x = 0·6) (s)		
17	7·64	32·40	23·13	36·83	1700–1	DyAG (s); 21R (w)		
18	6·28	0·77	19·60	73·35	1600–1	DyAG (s); M' (ms); DyAP (w); (J' (w)		
19	6·28	0·77	12·85	80·10	1650–1	J' (x = 1·4) (m); DyAP (m); M' (w)		
20	5·57	—	6·01	88·42	1700–1	J' (x = 1) (s)		
21	3·34	—	8·42	88·24	1700–1	J' (x = 1·4) (s)		
22	1·67	30·00	1·80	66·53	1550–1	Dy_2O_3(s); J' (x = 0·6) (s) AlN (m)		
23	0·84	40·00	9·14	50·02	1600–1	DyAP; (s); J' (x=1) (m) AlN (m)		

[a] α = α – Si_3N_4; α' = α-sialon ($Ln_xSi_{12-(m+n)}Al_{m+n}O_nN_{16-n}$); β = β-Si_3N_4; β', β_{10}, β_{20}... = β-sialon (β_{10}, β_{20} ≈ β' with z = 0·8, 1·5, $Si_{6-z}Al_zO_zN_{8-z}$); DyAp = $LnAlO_3$; M' = $Dy_2Si_{3-x}Al_xO_{3+x}N_{4-x}$ (x = 0 → 0·75); J' = $Dy_4Si_{2-x}Al_xO_{7+x}N_{2-x}$ (x = 0 → 2); K = $Dy_2Si_2O_4N_2$; s = strong; m = medium; mw = medium weak; ms = medium strong; vw = very weak.

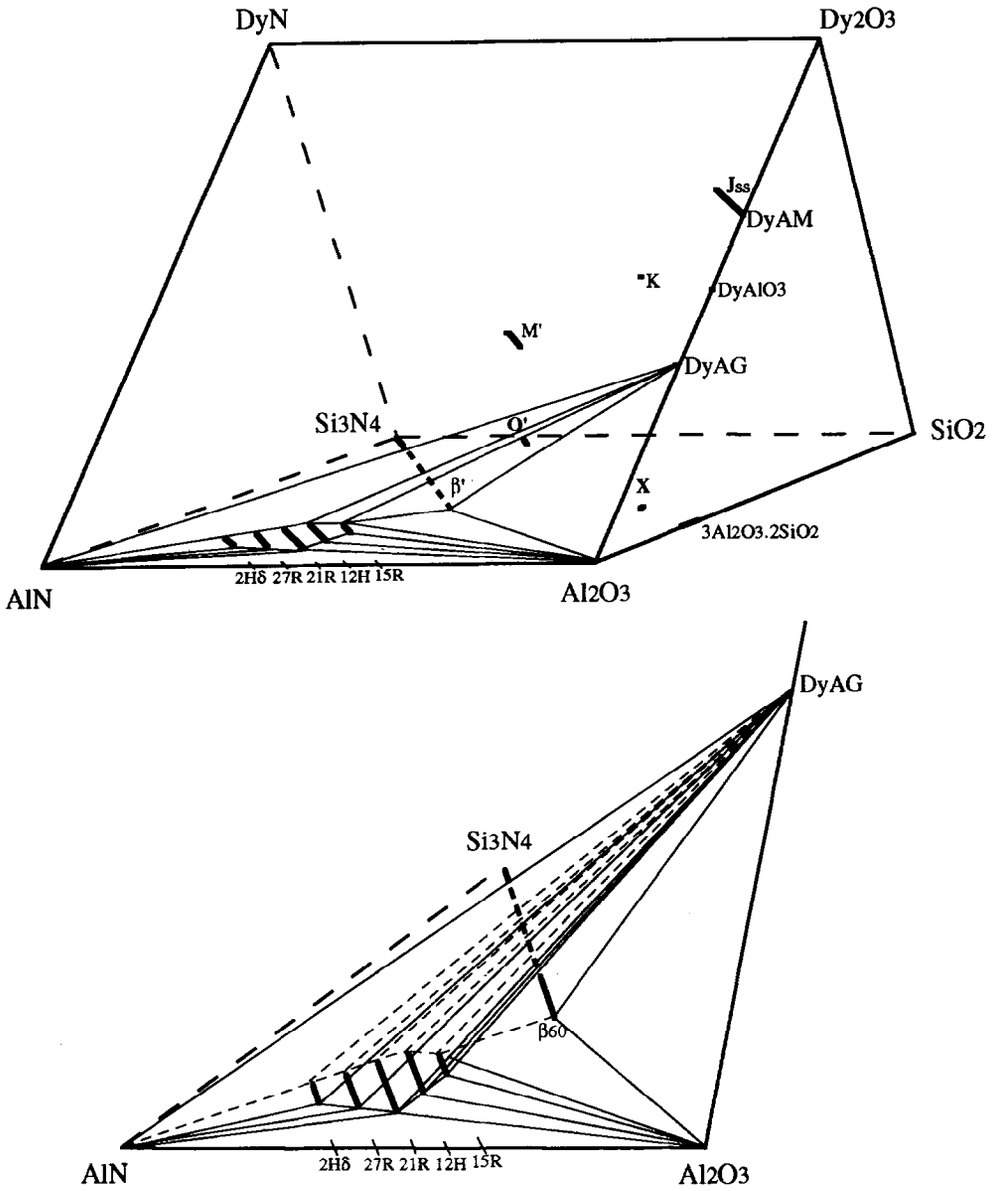

Fig. 2. DyAG($Dy_3Al_5O_{12}$) is compatible with Al_2O_3, all polytypoid phases and AlN forming 12 compatibility tetrahedra: DyAG–β_{60}–15R–Al_2O_3,DyAG–15R–Al_2O_3, DyAG–15R–12H, DyAG–12H–21R, DyAG–21R–27R, DyAG–27R–$2H^{\delta}$, DyAG–$2H^{\delta}$–AlN, DyAG–$2H^{\delta}$–AlN–27R, DyAG–27R–AlN–21R,DyAG–21R–AlN–Al_2O_3, DyAG–21R–Al_2O_3–12H and DyAG–12H–Al_2O_3–15R.

$\beta_0(\beta$–$Si_3N_4)$ to β_{10} and α', forming two α'–β'-containing compatibility tetrahedra: α'–β_0–β_{10}–M' (Fig. 4) and α'–β_{10}–M'–DyAG. $Dy_4Si_2O_7N_2$ (J-phase) also forms a continuous solid solution with $Dy_4Al_2O_9$ in a way similar to $Y_4Si_2O_7O_2$. In the Y–Si–Al–O–N system, the variation of unit cell dimensions (monoclinic) of J'-phase (solid solution of J-phase) with composition is not linear and the compositions near the centre of the range have simple X-ray patterns which index on a tetragonal unit cell related to the monoclinic cell.[5] A similar variation of unit cell dimensions also occurs for Dy-J'-phase. The X-ray patterns of the compositions near $x = 1{\cdot}4$ ($Dy_4Si_{2-x}Al_xO_{7+x}N_{2-x}$) can index on both tetragonal and monoclinic unit cells. The variation of the unit cell dimensions of Dy-J' phase will be further determined and published elsewhere. The compound $DyAlO_3$ was found to be compatible only with M' (melilite solid solution) and Si-rich terminals of AlN polytypoids (from AlN to 21R). The tie line between β' and $LnAlO_3$ that occurs in the Nd(Sm)–Si–Al–O–N systems does not exist in the Dy–Si–Al–O–N system.

In the region studied, DyAG, $DyAlO_3$, M'-phase and J'-phase were the main Dy-containing stable phases observed. In the Si_3N_4-rich compositions, DyAG phase could only be observed in the specimens after post-sintering heat treatment at a temperature around 1350°C and M'-phase was also observed to increase in post-sintering heat treatment around 1550°C. With the crystallization of DyAG and M'-phase during heat-treatment, the α-sialon, which was not expected to occur in these compositions, transformed into β'-sialon. Therefore, in establishing subsolidus phase relationships, judgement of the correct equilibrium

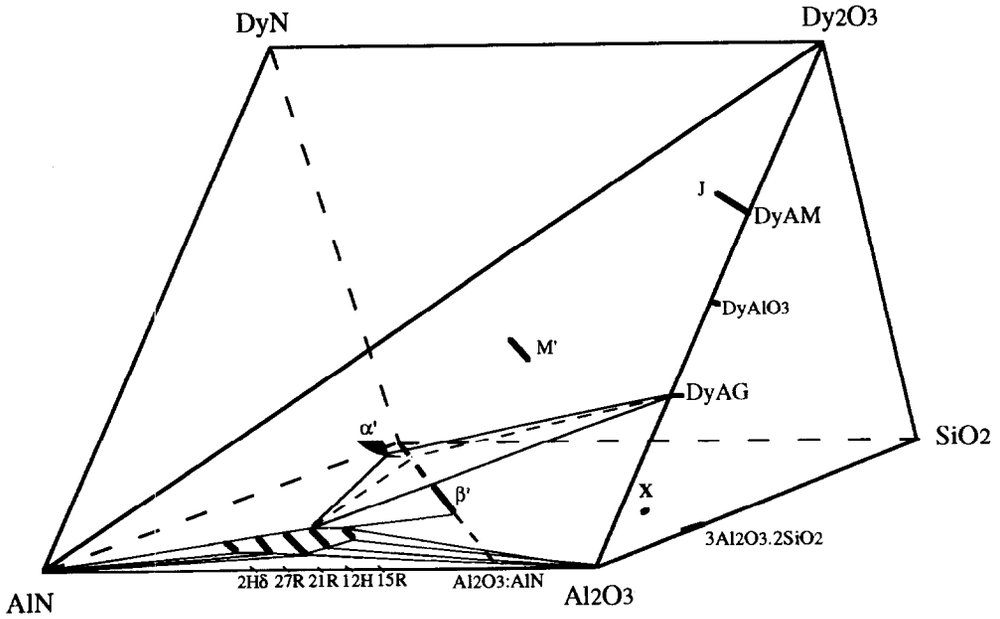

Fig. 3. DyAG($Dy_3Al_5O_{12}$) is compatible with β-sialon (β_{10}–β_{60}) and α-sialon (oxygen-rich) forming α'–β_{10}–12H–DyAG compatibility tetrahedron.

phases under subsolidus temperature conditions can sometimes be a difficult problem. Using phase assemblages observed at the same temperature for all conditions studied might lead to mistaken results, since different compositions may need different temperatures to fully crystallize the liquid phase. In the present work, all starting compositions were designed to fall on supposed tie lines or into supposed compatibility triangles. For example, compositions Nos 2 and 3 were on the lines between M' ($Ln_2Si_2AlO_4N_3$) and β-sialon (β_5 and β_{10}) and Nos 1, 5, 6 and 7 were designed on the composition lines between DyAG and β-sialon (β_0, β_{10} and β_{15} and β_{30}, respectively). If the expected phases were obtained after heat-treatment under a particular set of conditions, then equilibrium was believed to have been achieved. Based on this philosophy, compositions marked with the symbol ^ in Table 1, i.e. compositions Nos 1, 3, and 4, were believed to have achieved equilibrium and were used to establish the subsolidus phase relationships. In the compositions 3,5 and 6, the expected phases are β' with DyAG (Nos 5 and 6) or M'-phase (No. 3). These phase assemblages could only be achieved in post-sintering heat-treatment. The occurrence of α-sialon as a transitional phase can be attributed to the kinetic priority in the formation of Dy–α-sialon over the formation of DyAG and M'-phase at high temperatures. In heat treatment the DyAG and M'-phase is crystallized out at the exhaustion of Dy content in the liquid phase, thus making α-sialon transform

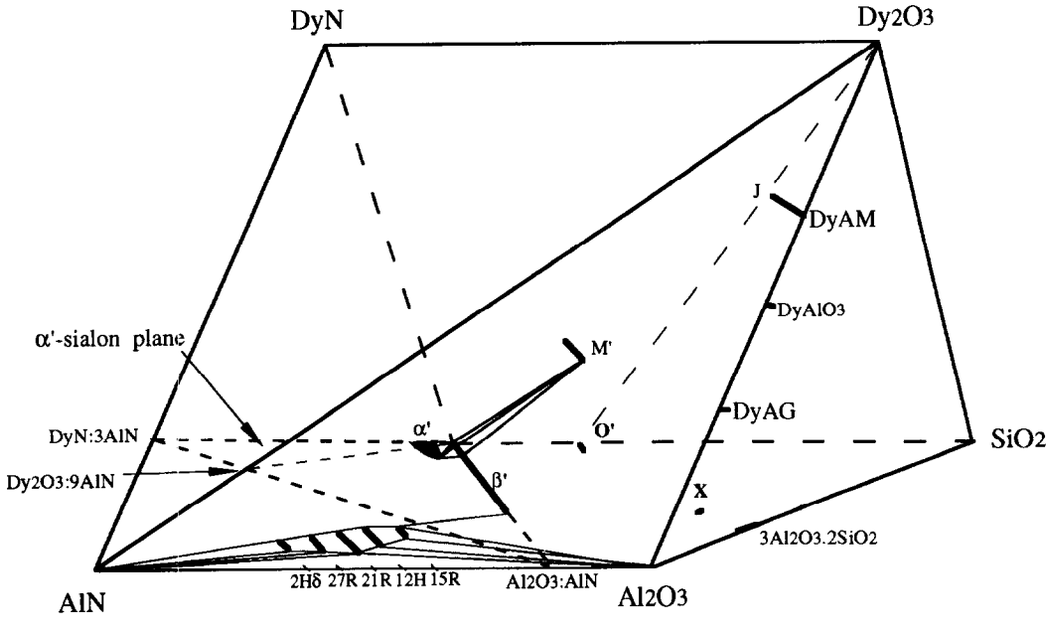

Fig. 4. M' (melilite solid solution) is compatible with β-sialon (β_0–β_{10}) and α-sialon forming α'–β'–M' compatibility tetrahedron.

Table 2. Subsolidus compatibility tetrahedra in the systems Si_3N_4–AlN–Al_2O_6–Dy_2O_3

Al_2O_3–β_{60}–15R–DyAG	Al_2O_3–15R–15R'–DyAG
Al_2O_3–15R'–12H'–DyAG	Al_2O_3–12H'–21R'–DyAG
Al_2O_3–21R'–AlN–DyAG	15R–15R'–12H–12H'–DyAG
12H–12H'–21R–21R'–DyAG	21R–21R'–27R–27R'–DyAG
27R–27R'–$2H^{\delta}$–$2H^{\delta*}$–DyAG	$2H^{\delta}$–$2H^{\delta*}$–AlN–DyAG
21R'–27R'–AlN–DyAG	27R'–$2H^{\delta*}$–AlN–DyAG
β_{60}–β_{25}–15R–DyAG	β_{25}–15R–12H–DyAG
β_{25}–β_{10}–12H–DyAG	β_{10}–12H–21R–α'
21R–β_{10}–β_8–α'	β_8–21R–27R–α'
27R–β_8–β_5–α'	β_5–27R–$2H^{\delta}$–α'
$2H^{\delta}$–β_5–β_2–α'	β_2–$2H^{\delta}$–AlN–α'
AlN–β_2–β_0–α'	β_0–β_{10}–α'–M'
β_{10}–12H–α'–DyAG	12H–21R–α'–DyAG
21R–27R–α'–M'	27R–$2H^{\delta}$–α'–M'
$2H^{\delta}$–AlN–α'–M'	AlN–$2H^{\delta}$–M'–DyAP
$2H^{\delta}$–27R–M'–DyAP	27R–21R–M'–DyAP
AlN–$2H^{\delta}$–YAP–DyAG	$2H^{\delta}$–27R–DyAP–DyAG
27R–21R–YAP–DyAG	21R–M'–DyAG–DyAP
21R–α'–M'–DyAG	α'–β_{10}–DyAG–M'
J' (middle)–DyAM–DyAP–AlN	Dy_2O_3–J' (whole)–AlN
J–J' (middle)–M–M'–AlN	J' (middle)–M'–DyAP–AlN

DyAM = $Dy_4Al_2O_9$; DyAP=$DyAlO_3$; DyAG = $Dy_3Al_5O_{12}$; 15R, 12H, 21R, 27R, $2H^{\delta}$ are Si-rich terminals of AlN polytypoids; 15R', 12H', 21R', 27R', $2H^{\delta*}$ are Al-rich terminals of AlN polytypoids, for others see Table 1.

into β-sialon to achieve the subsolidus phase equilibrium. Our current work on $\alpha' \rightleftharpoons \beta'$ phase transformation in the Ln–Si–Al–O–N systems during heat-treatment shows that, besides the liquid phase which assists the transformation,[14] there still exist other effects, especially for Ln-α-sialons with low Z-values. Of the 42 compatibility tetrahedra established in the present work, the following five—which involve α–β-sialon and AlN polytypoids (which could be used as reinforcement phase for α', β' or α'–β' because of its fibre-like morphology) and the promising grain boundary phases DyAG and M'—are the most useful for the design of multiphase sialon ceramics. They are α-sialon–β_0–β_{10}–M'; α-sialon–β_{10}–M'–DyAG; α-sialon–β_{10}–DyAG–12H; α-sialon–12H–21R–DyAG; and β_{10}–β_{25}–12H–DyAG.

4 Conclusions

Subsolidus phase relationships in the system Dy_2O_3–Si_3N_4–AlN–Al_2O_3 have been determined. Forty-two compatibility tetrahedra have been established in this region. DyAG coexists with β-sialon, approximately from β_{10} (z = 0·8) to β_{60} (z = 4), α' (oxygen-rich composition) and all AlN polytypoids. The coexistence of M' with β-sialon is restricted to the range β_0–β_{10}. α-Sialon is also compatible with M'. The compatibility tetrahedra α-sialon–β_0–β_{10}–M', α-sialon–β_{10}–M'–DyAG, α-sialon–β_{10}–DyAG-12H, α-sialon–12H–21R–DyAG and β_{10}–β_{25}–12H–DyAG are the most useful for the design and processing of multiphase sialon ceramic materials.

Acknowledgements

This work was supported by NNSF (National Natural Science Foundation, China, contract number 59482001) and the Royal Society, UK.

References

1. Mitomo, M., Izumi, F., Horiuchi, S. & Matsui, Y., Phase relationships in the system Si_3N_4–SiO_2–La_2O_3. *J. Mater. Sci.*, **17** (1982) 2359–66.
2. Sun, W. Y., Yen, T. S. & Tien, T. Y., Subsolidus phase relationships in the system Re–Al–O–N (where Re = rare earth elements). *J. Solid State Chem.*, **95** (1991) 424–9.
3. Sun, W. Y., Huang, Z. K., Tien, T. Y. & Yen, T. S., Phase Relationships in the System Y–Al–O–N. *Mater. Lett.*, **11** (1991) 67–9.
4. Huang Z. K., Tien, T. Y. & Yen, T. S., Subsolidus phase relationships in Si_3N_4–AlN–rare-earth oxide systems. *J. Am. Ceram. Soc.*, **69** (1986) C-241–2.
5. Thompson, D. P., Phase relationships in Y–Si–Al–O–N ceramics. In *Proc. Int. Symp. Tailoring Multiphase and Composite Ceramics*, ed. R. E. Tressler *et al. Mater. Res. Soc. Symp. Proc.* (1986) 93–102.
6. Sun, W. Y., Huang, Z. K. & Chen, J. X., Subsolidus phase relationships in the system Y_2O_3–Al_2O_3:AlN–Si_3N_4. *Trans. Brit. Ceram. Soc.*, **82** (1983) 173–5.
7. Sun, W. Y., Tien, T. Y. & Yen, T. S. (Yan, D. S.), Subsolidus phase relationships in part of the system Si,Al,Y/N,O: the system Si_3N_4–AlN–YN–Al_2O_3–Y_2O_3. *J. Am. Ceram. Soc.* **74** (1991) 2753–8.
8. Mandal, H., Thompson, D. P. & Ekström, T., Heat-treatment of Ln–Si–Al–O–N glasses. In *Proc. 7th Irish Mater. Forum Conf. IMF7*, eds M. Buggy & S. Hampshire. Trans. Tech Publications, Switzerland, 1992, pp. 187–203.
9. Thompson, D. P., New grain-boundary phases for nitrogen ceramics. *Mater. Res. Soc. Symp. Proc.* **287** (1993) 79–92.
10. Cheng, Y.-B. & Thompson, D. P., Aluminium-containing nitrogen melilite phases. *J. Am. Ceram. Soc.*, **77** (1994) 43–8.
11. Wang, P. L., Yu, H. Y., Sun, W. Y., Nygren, M. & Ekstrom, T., Study on the solid solubility of Al in the melilite systems $R_2Si_{3-x}Al_xO_{3+x}N_{4-x}$. *J. Eur. Ceram. Soc.*, **15** (1995), 689–96.
12. Sun, W. Y., Yan, D. S., Gao, L., Mandal, H., Liddell, K. & Thompson, D. P., Subsolidus phase relationships in the systems Ln_2O_3–Si_3N_4–AlN–Al_2O_3(Ln=Nd,Sm). *J. Eur. Ceram. Soc.*, **15** (1995) 349–55.
13. Tu, H. Y., Sun, W. Y., Wang, P. L. & Yan, D. S., Glass forming region in the Sm–Si–Al–O–N system. *J. Mater. Sci. Lett.*, **14** (1995) 1118–22.
14. Sun, W. Y., Wang, P. L. & Yan, D. S., The $\alpha' \rightarrow \beta'$ phase transformation in sialon ceramics by heat treatment. *Mater. Lett.*, **26** (1996) 9–16.

Journal of the European Ceramic Society 16 (1996) 1283 1291

PII: S0955-2219(96)00058-1
0955-2219/96/$15.00

Degradation of Dispersant During Milling

T. Chartier, S. Souchard, J. F. Baumard & H. Vesteghem

LMCTS-URA CNRS 320, ENSCI, 47 avenue A.Thomas, 87065 Limoges, France

(Received 24 October 1995, revised version received 20 February 1996; accepted 28 February 1996)

Abstract

Deterioration of the ammonium salt of poly(methacrylic acid) ($PMAA\text{-}NH_3$), used as a dispersant during wet ball-milling of an alumina, has been investigated. Rheological behaviour, sedimentation tests, adsorption isotherms, pH and isoelectric point measurements, and infra-red analysis have allowed us to conclude that degradation of the dispersant takes place in two stages: (i) decrease of the charge by dehydration and (ii) complete neutralization of the dispersant by the formation of monodentate COOX groups, which can lead to desorption of the polymer from the alumina surface. This second phenomenon involves a strong increase of viscosity. A low viscosity can be recovered by a subsequent addition of $PMAA\text{-}NH_3$ at the end of milling.

1 Introduction

Ceramic processing includes many operations to transform raw materials into ultimate products. Milling, and more particularly wet ball-milling, is often used to break aggregates and to reduce the average particle size, as well as to add and mix some organic additives such as binders and plasticizers.

In order to achieve high solid contents, suspensions must contain an amount of water and organic additives that is as low as possible. Nevertheless, the slurry viscosity should be kept low enough during milling to confer efficiency to the milling media. It has been observed that viscosity increases a lot during ball-milling, thus reducing the efficiency and leading to rheological properties that are not fully compatible with the following stage of the process.[1,2]

Many factors can affect the state of dispersion during milling: (i) change in the specific surface area of the powder, (ii) change of the nature of surfaces of particles, (iii) change in pH of the solution and (iv) degradation of the dispersant.

The tumbling media in a rotating mill produce a grinding action by impacting and shearing the particles on their surfaces.[3] Polymer chains of dispersants are adsorbed on particle surfaces and are also present in water surrounding the particles. Impacts between particles and media can affect the polymer structure and possibly lead to desorption from the particle surfaces.

The aim of this study was to follow the efficiency of a common polyelectrolyte, an ammonium salt of poly(methacrylic acid), used for this purpose. Sedimentation tests, viscosity, pH and isoelectric point (IEP) measurements, adsorption isotherms and infra-red observations (FTIR) were used to follow the evolution of the dispersion state of alumina slurries during milling.

2 Experimental

2.1 Powder and dispersant

The ceramic powder used in this study was a calcined α-alumina formed from the Bayer process (P122, Aluminium Péchiney, France). This powder consists of ~35 μm mean diameter aggregates containing ~3 μm mean diameter elementary particles (Fig. 1). The specific surface area of the starting powder was 0·7 $m^2\ g^{-1}$. The major impurities, located mainly, on the surface of particles, are SiO_2, CaO, Fe_2O_3 and Na_2O with respective concentrations of 1050, 600, 300 and 150 ppm.

Polyelectrolytes are generally used as dispersants for ceramic powders. Polyelectrolytes are macromolecules delivering a large number of ionic charges in solution, with small inorganic counterions. The dispersant used here was an ammonium salt of poly(methacrylic acid) ($PMAA\text{-}NH_3$), which, as received, contains 25 wt% active species and 75 wt% water (Darvan C, R. T. Vanderbilt Company, Inc., USA). This polyelectrolyte has been used extensively to deagglomerate and disperse alumina powders in aqueous media.[4,5] Depending on the charge, and then on the

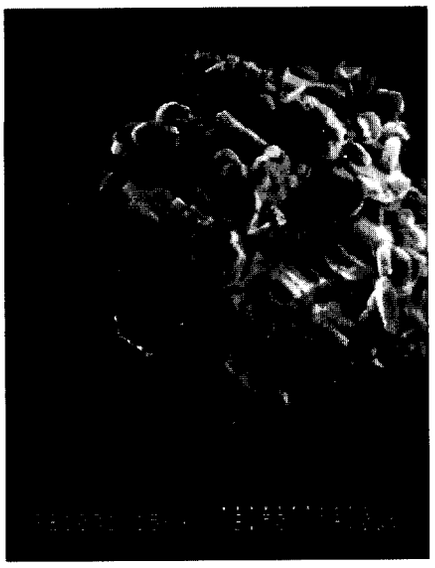

(a)

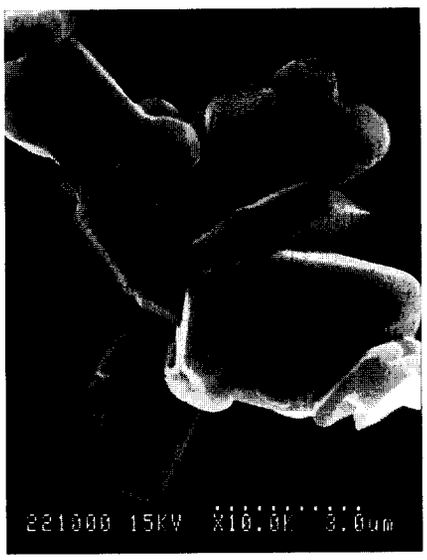

(b)

Fig. 1. Aggregate of P122 alumina (a) containing 3 μm mean diameter elementary particles as shown on a smaller aggregate (b).

repulsion between the segments of the chains, these polymeric dispersants may adsorb in trains on the powder surface, in extended tails in the solution or in loops.[1,6] Thus stabilization of suspensions, using PMAA-NH_3 as dispersant, is due to an electrostatic repulsion combined with steric interactions, the global effect being called electrosteric stabilization. Figure 2 shows that the functional groups of PMAA-NH_3 are carboxylic acid groups, COO-, which can be protonated when the pH decreases.

2.2 Slurry preparation

The concentration of alumina in the slurries was 10 vol% (30·7 wt%) and the concentration of PMAA-NH_3 was 0·6 wt% with respect to alumina.

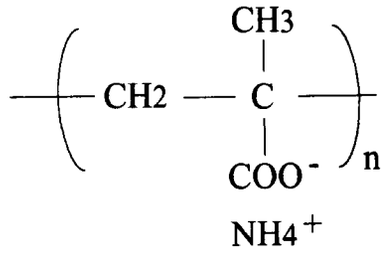

Fig. 2. Chemical structure of PMAA-NH_3.

The water used was deionized. Ball-milling was performed using a load factor (mass of alumina balls/mass of powder) equal to 8. Slurries were prepared by milling for several durations, i.e. 2, 8, 15, 18, 21 and 24 h.

2.3 Characterization

2.3.1 Grain size distribution and specific surface area

After each milling time, grain size distribution (SediGraph 5100, Micromeritics, USA) and specific surface area (DeSorb/FlowSorb II 2300A, Micromeritics, USA) were measured.

2.3.2 Agglomeration of particles

The amount of dispersant adsorbed on the particle surfaces, the configuration of the adsorbed molecules and the electric surface charge on the particles, developed by the polymeric chains, govern the agglomeration state and the stability of the dispersion. Ball milling may alter all these parameters by damaging (scission), desorbing or decreasing the charge of the polymeric dispersant. The efficiency of the PMAA-NH_3 during ball-milling was evaluated in terms of the agglomeration state of particles in the suspensions by sedimentation tests and viscosity measurements.

2.3.2.1 Sedimentation tests. Sedimentation tests were performed in order to follow the evolution of the particle agglomeration in the slurry. The average porosity of a sediment bed has been shown to be mainly a function of the size and shape of particles and of the state of agglomeration.[7–9] Thus the specific sediment volume and the average volume fraction of solid allowed us to determine the state of particle agglomeration in a suspension.

A part of each slurry (15 ml) was poured in a closed test tube. After agitation, the end of which determines the reference time, the mixture was allowed to settle until the sediment reached, a constant volume. The upward movement of the sediment/suspension interface, as well as the downward movement of the suspension/clear liquid interface, were reported on sedimentation curves.

A classification of suspensions may be made on the basis of the settling behaviour as proposed by Scott[10] and Hasset.[11]

In an infinite medium, a large number of identical particles settles down more rapidly than a single one, because the surrounding liquid is dragged down by the movement of falling particles. On the other hand, when the suspension settles in a tube, the liquid flow is disturbed because of friction effects at the wall, and the particles settle down more slowly.[12] Their velocity decreases as the powder concentration increases.

Figure 3, from Tiller and Khatib,[8] shows a typical settling curve for a non-flocculated suspension with a uniform concentration. The settling rate and build-up of the sediment are constant, until the particle velocity decreases when they reach the bottom of the tube, due to an upward flow of liquid passing up through the suspension. When all particles come to contact, compression point C is reached. Then, compression of the sediment occurs as liquid flows out of the sedimentation zone, until the structure stabilizes and the sediment reaches its ultimate volume.

For a flocculated suspension, particles are already in contact and settle very rapidly. The sediment was formed at the beginning of the test, and the sedimentation curve began at compression point C (Fig. 3).

2.3.2.2 Viscosity measurements. The evolution of the efficiency of the PMAA-NH_3 during ball-milling was also evaluated by viscosity measurements. A low viscosity, at a high powder loading, is representative of a good dispersion of non-agglomerated particles. Flow curves were obtained with a controlled stress rheometer (Carri-Med CLS 100, UK).

2.3.3 IEP determination

The isoelectric points of as-received alumina and alumina ball-milled for 24 h were measured using an acoustophorometer (ESA 8000, Matec Applied Sciences, Hopkinton, MA, USA).

2.3.4 Adsorption isotherms

In order to determine the influence of milling on the adsorption of dispersant, adsorption isotherms were plotted for (i) the as-received alumina and (ii) the alumina wet ball-milled without addition of dispersant and dried. The milling conditions were adjusted to obtain similar characteristics (grain size distribution and specific surface area) as for a 24 h wet ball-milling in the presence of 0·6 wt% of PMAA-NH_3. Slurries were centrifuged after 24 h of equilibrium. The resulting supernatants were dried at 110°C. The drying temperature was chosen according to a thermogravimetric analysis, in order to remove water and to avoid the thermal degradation of the PMAA-NH_3. Then, the residual amounts of dispersant were weighed, and therefore the adsorbed amounts were determined.

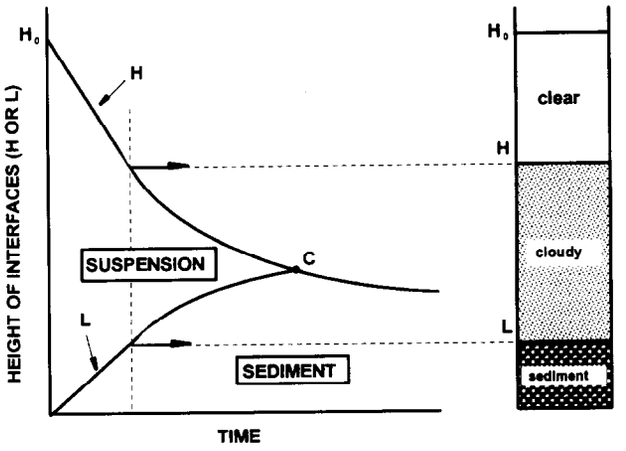

Fig. 3. Typical settling curve for a non-flocculated suspension with uniform concentration, from Tiller and Khatib.[8]

2.3.5 Infra-red study

Infra-red spectroscopy has commonly been used to investigate the adsorption of polymers. For instance, Joppien and Hamman[13] studied the adsorption of polyester resin on silica, alumina, titania and iron oxide powders, and gave spectroscopic evidence of loop formation by the polymers. Fontana and Thomas[14] reported the adsorption of poly(alkyl methacrylate) on silica surfaces. They noted that the C=O stretching mode at ~1710 cm^{-1} shifted to lower wavenumber (22–30 cm^{-1}) when the polymer was adsorbed on the silica surface by hydrogen bonding. These studies were mainly performed on high surface-area powders, using transmission spectroscopy.

In this work, transmission spectroscopy was used to detect eventual desorption of PMAA-NH_3 from the alumina surface and/or changes of the PMAA-NH_3 structure due to degradation by ball-milling. The slurries, prepared for each milling time, were centrifuged. Both the centrifuged alumina and the supernatant were dried at 110°C in order to analyse the alumina with the species adsorbed on its surface, as well as organic species dissolved in the supernatant, respectively. In the infra-red analysis we neglect the PMAA-NH_3 present in the water contained in the sediment, which can deposit on the surface of alumina during drying. The KBr pellet method was used for spectral analysis, using thoroughly mixed and pressed pellets containing 1 mg of the investigated sample in 100 mg of KBr.

Spectra of dried alumina and of supernatant were collected after each milling time; they were also obtained for a water solution of PMAA-NH_3 and for the dried, as-received, alumina to get spectral references.

Table 1. Evolution of particle size and specific surface area

Milling time (h)	*Average particle size (μm)*	*Surface area ($m^2 g^{-1}$)*
0	35·00	0·7
2	4·53	0·8
8	3·18	2·1
13·5	2·61	2·7
15	2·58	3·2
18	2·42	3·3
21	2·20	4·3
24	1·19	4·9

3. Results and Discussion

3.1 Evolution of particle size and specific surface area

Average particle size decreases and surface area increases with milling time (Table 1). Whereas the observed viscosity became high for milling times longer than 18 h, the particle size continues to decrease. Figure 4 shows that the particle size decreases rapidly at the beginning of the milling (from 35 to 4·5 μm after 2 h), with no significant evolution of the specific surface area. During the first stage of the milling, brittle aggregates are broken down [Fig. 5(a)]. For longer times of treatment, the particle size continues to decrease slowly (from 4·5 to 1·2 μm after 22 h) with a rather linear increase of the specific surface area, suggesting that deaggregated particles are now milled during this second stage [Fig. 5(b)].

3.2 Rheological study

The rheological behaviour of the slurry obtained after ball-milling for 24 h is represented by curve 1 in Fig. 6. A subsequent addition of 0·6 wt% PMAA-NH_3 to this slurry resulted in a marked decrease of the viscosity (Fig. 6, curve 2). This suggests that the initial amount of dispersant (0·6 wt%) used for ball-milling was too low to prevent the agglomeration of alumina particles with a sevenfold increase in surface area (from 0·7 to 4·9 $m^2 g^{-1}$ or conversely that the efficiency of the dispersant decreased during milling.

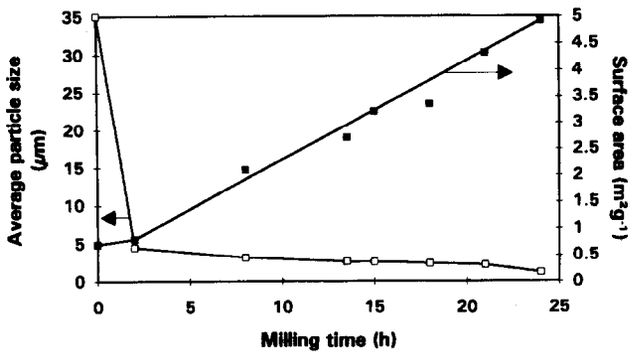

Fig. 4. Evolution of particle size and surface area during ball-milling.

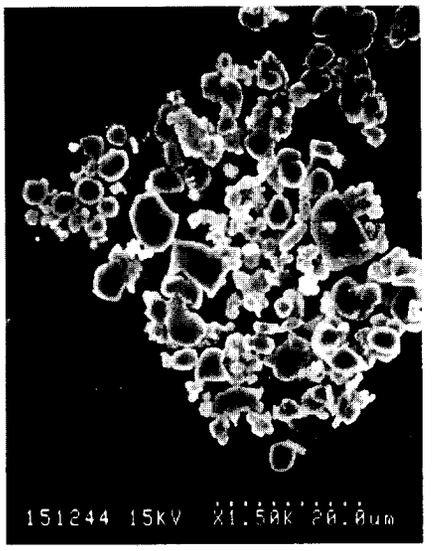

(a)

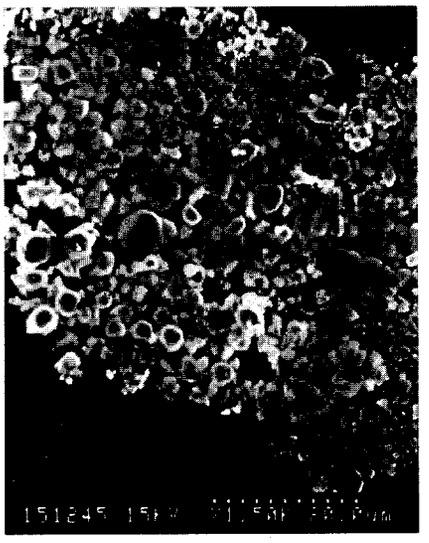

(b)

Fig. 5. Alumina particles after ball-milling for 2 h (a) and 24 h (b)

In order to elucidate this point, the alumina slurry containing 0·6 wt% PMAA-NH_3 was ball-milled for 24 h and the suspension was then centrifuged. The clear supernatant was removed and the solid phase calcined at 600°C for 1 h to eliminate organic species contained in the sediment. The powder obtained was redispersed under the same conditions as previously with 0·6 wt% dispersant (Fig. 6, curve 3). Curves 2 and 3 being quite similar, one can safely conclude that an amount of 0·6 wt% of fresh PMAA-NH_3 is large enough to provide good dispersion of the alumina powder when the specific surface area reaches 4·9 $m^2 g^{-1}$.

3.3 Sedimentation tests

During sedimentation tests, two behaviours were observed depending on the milling time. After

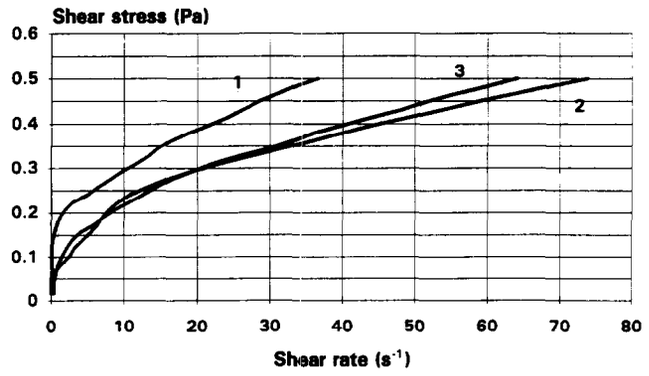

Fig. 6. Influence of PMAA-NH_3 degradation on the rheological properties of alumina suspensions: (1) ball-milled for 24 hours with 0·6 wt% PMAA-NH_3; (2) same as (1), but 0·6 wt% PMAA-NH_3 was added just before the end of ball-milling, and (3) same as (1), the powder was then centrifuged, dried and pyrolysed before redispersion with 0·6 wt% PMAA-NH_3.

milling times shorter than 15 h, three zones were observed in the tubes during the test, corresponding to a sediment bed, a cloudy liquid zone and a clear liquid zone. Slurries behave as non-flocculated suspensions. The sediment volume increased with time (Fig. 7). No compression of sediments was observed. For milling times longer than 15 h, only two zones were observed, i.e. a clear liquid zone and a sediment bed. The sediments formed rapidly and their volume decreased with time, an observation which is typical of flocculated slurries (Fig. 8).

The heights of the final equilibrium sediments obtained after various milling time, are shown in Fig. 9. The equilibrium height of sediment (H_{eq}) was the smallest after 13·5 h of milling. After 15 h H_{eq} is slightly higher, but particles in suspension always form a cloudy zone. For milling times longer than 18 h, H_{eq} increases continuously with milling time. Equilibrium height of sediment is reached more rapidly for slurries milled for long times, i.e. 90 min for a 18 h milling and 300 min for a 13·5 h milling. After 13·5 h of milling, particles reagglomerated and the stability of the slurries decreased.

Sedimentation tests confirm that the dispersant lost its efficiency during ball-milling.

Figure 10 shows the difference between the equilibrium sediment volumes of the slurries milled for 24 h with and without a subsequent addition of 0·6 wt% PMAA-NH_3 at the end of milling. The addition of PMAA-NH_3 allowed an

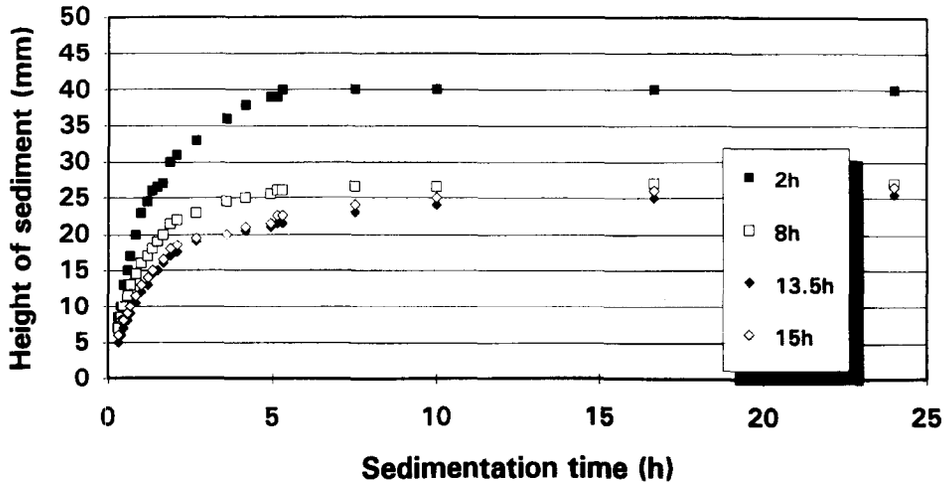

Fig. 7. Settling of alumina suspensions ball-milled for 2, 8, 13·5 and 15 h.

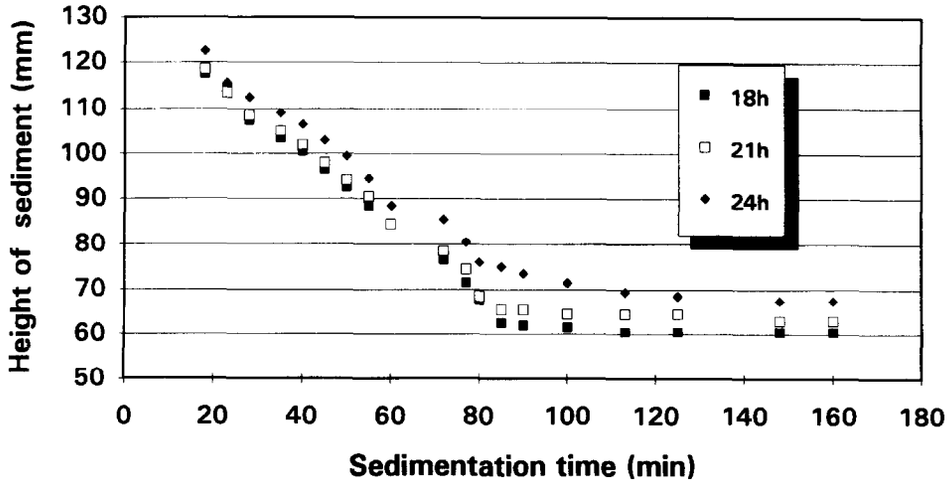

Fig. 8. Settling of alumina suspensions ball-milled for 18, 21 and 24 h.

important decrease of the sediment volume, while changing drastically the settling behaviour. Thus, additional PMAA-NH_3 redispersed the agglomerated particles.

Many factors can decrease the efficiency of the dispersant and then deteriorate the state of the dispersion during milling: (i) change in the specific surface area of the powder, then modification of the amount of adsorbed dispersant, (ii) change of the nature of surfaces of particles, then modification of the zeta potentiel and adsorption of the dispersant onto these particles, (iii) change in pH, then the degree of dissociation of PMAA-NH_3 and the charge on the particles and (iv) degradation of the dispersant.

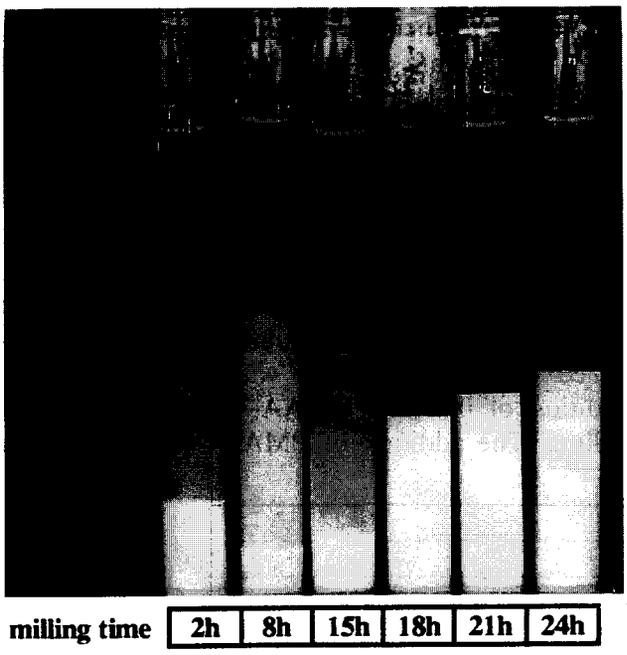

Fig. 9. Influence of milling time on the equilibrium height of the alumina sediment.

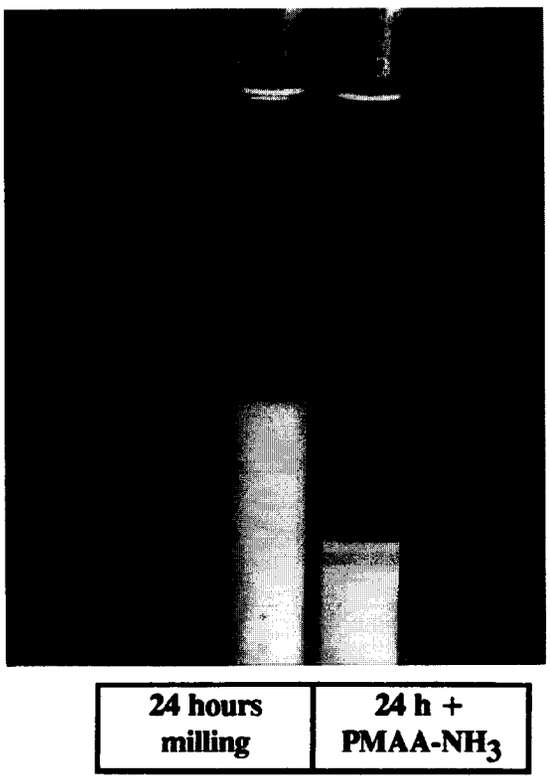

Fig. 10. Influence of an addition of PMAA-NH_3 on the equilibrium height of the alumina sediment.

The rheological measurements suggested that the initial amount of dispersant (0·6 wt%) used for ball-milling was sufficient to provide a good dispersion of the alumina powder when the specific surface area increased up to 4·9 $m^2 g^{-1}$.

The IEP value of the P122 alumina increased from 7·8 for the as-received powder to 8·8 after a 24 h of wet milling. On the other hand, the pH of the slurry varied from 8·5 for the as-received powder to 9·6 after a 24 h of wet milling (Fig. 11). Perrin[15] reported an amorphization of the surface of particles of a similar alumina during dry ball-milling, associated with a decrease of the number of acidic sites, then with an increase of the IEP. The same behaviour was reported in the case of wet ball-milling of an alumina powder.[16] The evolution of the pH during milling may be attributed to the passage in solution of cations (Ca^{2+}, Mg^{2+}, Na^+) contained as impurities in the as-received alumina powder. These impurities are mainly located on the surface of alumina particles. For pH values higher than the IEP of alumina, divalent ions adsorbed onto the negative surface of alumina particles increased the affinity of the negatively charged PMAA-NH_3 with alumina.[16]

The milling modified both the nature of the alumina surface and the adsorption/desorption of cations. These parameters may greatly affect the adsorption of the dispersant. Figure 12 shows adsorption isotherms of PMAA-NH_3 on as-received alumina and alumina previously ball-milled without addition of dispersant and dried. The adsorption of PMAA-NH_3 onto ball-milled alumina was three times less than for unmilled powder.

During milling, the basic pH of the solution was maintained higher than the IEP, so the surface of the alumina particles remained weakly

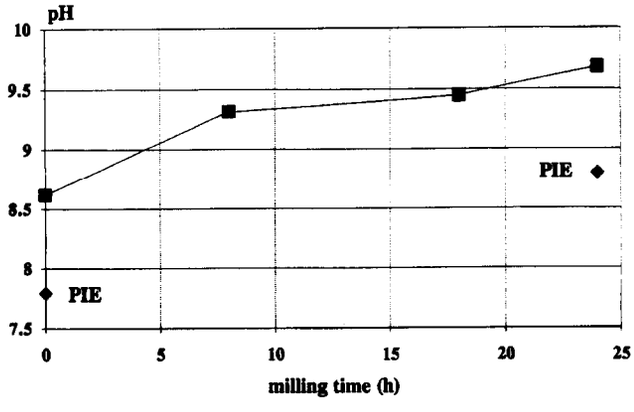

Fig. 11. Variation of pH and the IEP of alumina during wet ball-milling.

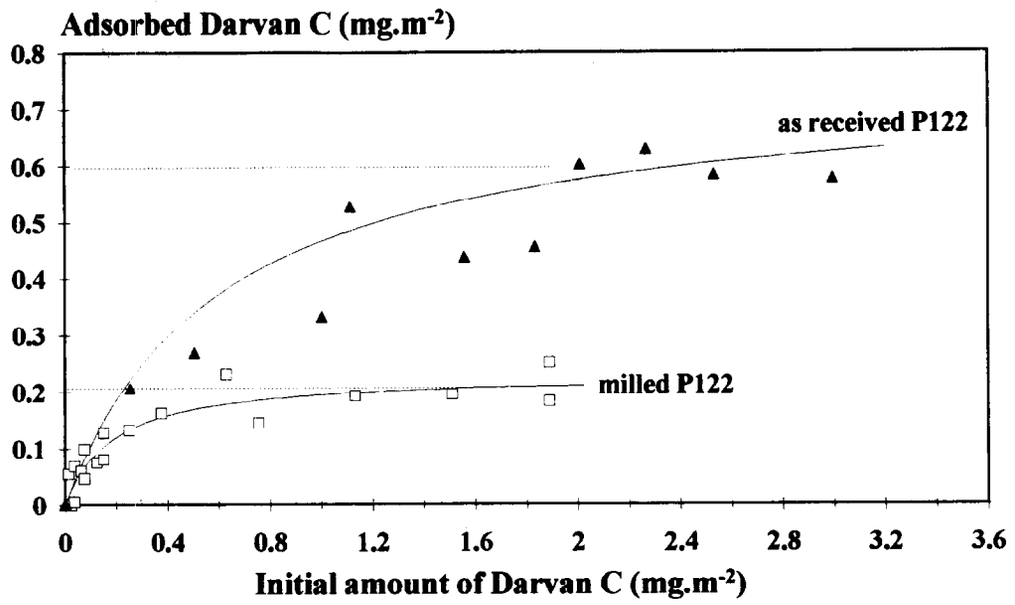

Fig. 12. Adsorption isotherms of PMAA-NH_3 on as-received alumina and alumina previously ball-milled without addition of dispersant and dried. The milling conditions were adjusted to obtain similar characteristics (particle size distribution and specific surface area) as for a 24 h wet ball-milling in the presence of 0·6 wt% of PMAA-NH_3.

negative and the PMAA-NH_3 entirely dissociated.[4] This suggests that variations of the IEP and pH did not significantly influence the adsorption of the dispersant.

The deterioration of the state of dispersion cannot be attributed to the lower adsorption of the PMAA-NH_3 onto the ball-milled alumina particles (i.e. to a lower charge of particles) because a viscosity as low as 25 mPa s was achieved for a 70 wt% suspension of milled particles (24 h) with an addition of 0·6 wt% (i.e. 1·2 mg m^{-2}) PMAA-NH_3, corresponding to the beginning of saturation of the surface (Fig. 12).

To summarize, the evolution of the specific surface area, the modification of the surface of particles and the change in pH seem to be not sufficient to explain the decrease of the efficiency of the dispersant during wet ball-milling of alumina. Thus, the degradation of the dispersant during milling remains the most probable factor which can affect the state of dispersion.

3.4 Infra-red analysis

Figure 13 shows IR spectra of dried pure PMAA-NH_3 and of the dried supernatant after milling times of 8, 18 and 24 h.

The bands at 1534 and 1415 cm^{-1} in Darvan C can be assigned to antisymmetrical and symmetrical vibrations of $-COO^-$ groups while the band at 1444 cm^{-1} can be assigned to the NH_4^+ deformation mode.

After 8 h of milling, a change of the dispersant was observed with the appearance of bands at 3525, 3450, 1688 and 1621 cm^{-1}. These bands may be attributed to amide functions ($-CO-NH_2$). According to this assumption, one explanation

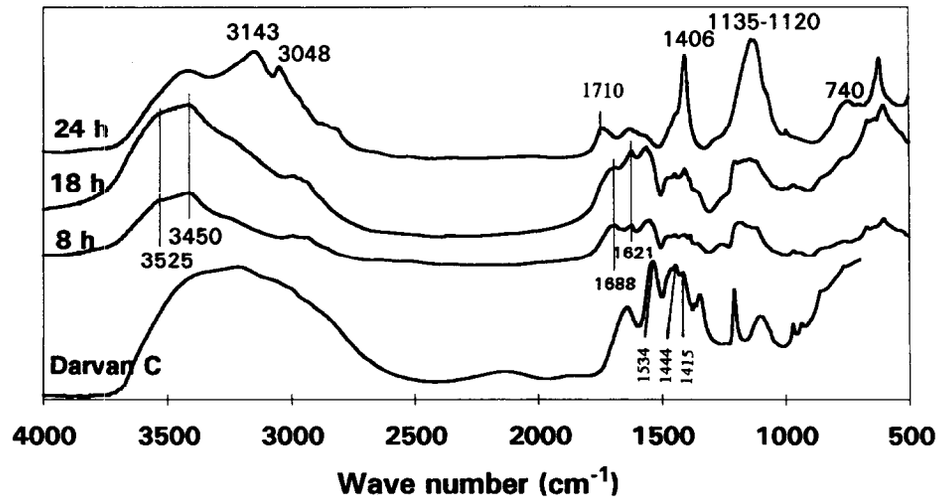

Fig. 13. Infra-red spectra of dried pure PMAA-NH_3 and of dried supernatant after milling times of 8, 18 and 24 h.

could be dehydration of the PMAA-NH_3 adsorbed on the alumina surface according to the global reaction:[17]

$$R\text{–}COO^-, NH_4^+ \rightarrow R\text{–}CO\text{–}NH_2 + H_2O$$

Bands near 1550 and 1400 cm^{-1} illustrate the presence of $-COO^-$ groups and indicate that dehydration is not complete. The $-COO^-$ groups can bind to the Al^{3+} on the surface of fine alumina particles remaining in suspension, in spite of centrifugation. Bands near 600 cm^{-1} illustrate the presence of alumina in the supernatant. The degradation of the dispersant observed with sedimentation tests between 13·5 and 18 h seems to result from a decrease of the polymer charge due to dehydration. Thus the increase of sediment volume after 13·5 h of milling, relative to some reagglomeration, can be attributed to a reduced electrostatic repulsion.

After 18 hours of milling, the IR spectrum is drastically different. Bands which appear at 3143, 3048, 1406, 1135, 1120 and 740 cm^{-1} are difficult to attribute. The appearance of the 1710 cm^{-1} band, which is characteristic of the C=O stretching vibration of monodentate COOX group,[18] is coincident with the disappearance of the $-COO^-$ groups. PMAA-NH_3 seems to be fully degraded, which can possibly in turn affect adsorption of the polymer onto the alumina surface.

The decrease of the efficiency of the PMAA-NH_3 dispersant, during milling, involved two stages. The first, at the beginning of milling, may be attributed to reduced electrostatic repulsion due to decrease of the charge by dehydration. The second stage, after longer milling times, may be due to complete neutralization of the dispersant by the formation of COOX groups. In addition, the results obtained suggest that the dispersant has been irreversibly altered during milling.

4 Conclusion

Results of this study showed that the ammonium salt of poly(methacrylic acid), generally used as dispersant of alumina, was degraded during wet ball-milling. Degradation takes place in two stages:

(1) the decrease of the charge by dehydration induced a small agglomeration of alumina particles, but the rheological behaviour of the slurry was not affected; and
(2) the complete neutralization of the dispersant by the formation of monodentate COOX groups, which can lead to a desorption of the polymer from the alumina surface, involved a significant agglomeration.

The deterioration of the dispersant certainly depends on experimental conditions: size and velocity of the mill, size of the media relative to size of the feed material, loading of the mill, relative volumes of media and feed material, and viscosity of the slurry. Our results were obtained for slurries containing a low concentration of alumina (30 wt%). Industrial slurries contain up to 70–80 wt% of powder, for a capacity up to several tons. In this case, deterioration of dispersant involves a strong increase in viscosity and media could be hindered in their rotating movement. Then, milling could be less efficient as expected, and would require additional time, and energy, to produce the desired distribution of particle size.

A simple solution should be to add a determined amount of dispersant during milling, or just before the end, to balance its deterioration.

Acknowledgements

This study has been led with financial support of Aluminium Péchiney, 13541 Gardanne, France.

References

1. Sacks, M. D., Kadikar, C. S., Scheiffele, G. W., Shenoy, A. V., Dow, J. H. & Sheu, R. S., Dispersion and rheology in ceramic processing. In *Advances in Ceramics, Vol. 21, Ceramic Powder Science*, eds G. L. Messing, K. S. Mazdiyasni, J. W. McCauley & R. A. Haber. The American Ceramic Society, Columbus, OH, 1987, pp. 495–513.
2. Konsztowicz, K. J., Maksym, G., Maksym, H. W., King, H. W., Caley, W. F. & Vargha-Butler, E., The role of surface tension in formation of donut-shaped granules during spray-drying. In *Ceramic Transactions, Vol. 26, Forming Science and Technology for Ceramics*, ed. M. J. Cima. The American Ceramic Society, Columbus, OH, 1987, pp. 46–53.
3. Reed, J. S. *Introduction to the Principles of Ceramic Processing*. J. Wiley & Sons, New York, 1988.
4. Cesarano III, J. & Aksay, I. A., Stability of aqueous α-alumina suspensions with poly(methacrylic acid) polyelectrolyte. *J Am. Ceram. Soc.*, **71**[4] (1988) 250–5.
5. Cesarano III, J. & Aksay, I. A., Processing of highly concentrated aqueous α-alumina suspensions stabilized with polyelectrolytes. *J. Am. Ceram. Soc.*, **71**[12] (1988) 1062–7.
6. Shashidhar, N., Varner, J. R. & Condrate Sr., R. A., Adsorption of polyacrylates on Powders. In *Ceramic Transactions, Vol. 12, Ceramic Powder Science III*, ed. G. L. Messing. The American Ceramic Society, Columbus, OH, 1990, pp. 443–50.
7. Deliso, E. M., Srinivasa Rao, A. & Cannon, W. R., Electrokinetic behavior of Al_2O_3 and ZrO_2 powders in dilute and concentrated aqueous dispersions. In *Advances in Ceramics, Vol. 21, Ceramic Powder Science*, eds G. L. Messing, K. S. Mazdiyasni, J. W. McCauley & R. A. Haber. The American Ceramic Society, Columbus, OH, 1987, pp. 525–35.
8. Tiller, F. M. & Khatib, Z., The theory of sediment volumes of compressible, particulate structures. *J. Colloid Interf. Sci.*, **100**[1] (1984) 55–67.

9. Le Bars, N., Relation entre la structure des couches adsorbées, l'état de dispersion et les propriétés rhéologiques dans les suspensions concentrées des poudres céramiques. *Ph.D. Thesis*, University of Orléans, France, 1992.
10. Scott, K. J., Theory of thickening: factors affecting settling rate of solids in flocculated pulps. *Trans Inst. Min. Metall.*, **77** (1968) C85–97.
11. Hasset, N. J., Mechanism of thickening and thickener design. *Trans. Inst. Min. Metall.*, **75** (1965) 627–56.
12. Blanc, R. & Guyon, E., La physique de la sédimentation. *La Recherche*, **234**[22] (1991) 866–73.
13. Joppien, G. R & Hamann, K., The structure of adsorbed polymers at pigment/solution interfaces and their influence on the dispersion stability of pigments in paints. *J Oil Col. Chem. Assoc.*, **6**[10] (1977) 412–23.
14. Fontana, B. J. & Thomas, J. R., The configuration of adsorbed alkyl methacrylate polymers by infrared and sedimentation studies. *J. Phys. Chem.*, **65**[3] (1961) 480–7.
15. Perrin, J. M., Propriétés de surface d'alumines: influence des impuretés minérales, du broyage et des traitements thermiques. Relation avec l'adsorption de polymères. *Ph.D. Thesis*, University of Haute-Alsace, France, 1991.
16. Dupont, L., Analyses théorique et expérimentale des interactions ioniques dans l'adsorption de poly(acide acrylique) sur plusieurs alumines. Application aux propriétés rhéologiques de suspensions concentrées de ces alumines. *Ph.D. Thesis*, University of Franche-Comté, France, 1993.
17. Hart, H. & Conia, J. M., *Introduction à la Chimie Organique*. Inter Editions, Paris, 1987.
18. Bellamy, L. J., *The Infra-Red Spectra of Complex Molecules*. Chapman and Hall, London, 1975.

Journal of the European Ceramic Society **16** (1996) 1293–1298

PII: S0955-2219(96)00061-1
0955-2219/96/$15.00

Kinetic Aspects of the Formation of Lead Zirconium Titanate

O. Babushkin,[a] T. Lindbäck,[a]* J.-C. Luc[b] & J.-Y. M. Leblais[b]

[a] Division of Engineering Materials, Luleå University of Technology, S-971 87 Luleå, Sweden
[b] Quartz et Silice Research Institute, B.P. 95, F-77792 Nemours, France

(Received 30 November 1995; revised version received 1 March 1996; accepted 14 March 1996)

Abstract

The kinetics of the second calcination step in the formation of PZT solid solution (with perovskite ABO_3 lattice) has been investigated by using two different particle sizes of the B-site precursor (1·91 and 5·08 μm), the finer size being obtained by prolonged milling. In-situ *analysis performed by high-temperature X-ray diffractometry in a non-isothermal mode (20-800°C) revealed a reduction of the calcination temperature by 100°C with a decrease in particle size of the precursor. In order to clarify the mechanism of the solid-state reaction to PZT, isothermal heat treatment of the mixtures was performed in the temperature range 540–700°C. The activation energies for the fine and the coarse powders were estimated as 150 and 210 kJ mol^{-1} respectively, and the reaction was found to follow the Jander model for diffusion-controlled solid-state reaction kinetics.* © *1996 Elsevier Science Limited*

1 Introduction

The basic electrical and mechanical properties of PZT ceramics are strongly influenced by the chemical composition of the raw materials and the subsequent calcination and sintering processing. As far as the calcination stage is concerned, it can have a large influence on the piezoelectric properties since it can affect the homogeneity of the final solid solution. In the calcination to PZT, studies of solid-state reaction sequences have shown the dependence of the formation mechanism of PZT on powder characteristics (particle size, impurities, morphology of the precursors, etc.). When the calcination is performed in one step, i.e. starting from the three individual oxides, the problem of PbO vaporization limits the calcination temperature and as a consequence prolongs the calcination. It has been shown that increased homogeneity, which enhances the final properties of the PZT solid solution, can be achieved by carrying out the calcination in two steps.[1–3] In the first step the B-site oxides are prereacted to form a B-site zirconium titanate precursor according to the following reaction.

$$0{\cdot}52ZrO_2(s) + 0{\cdot}48\ TiO_2(s) \rightarrow Zr_{0{\cdot}52}Ti_{0{\cdot}48}O_2\ (ss)\ (1)$$

The formation of the precursor without PbO suppresses intermediate phases when forming the perovskite phase in the second stage as given in the following expression

$$Zr_{0{\cdot}52}Ti_{0{\cdot}48}O_2(ss) + PbO(s) \rightarrow PbZr_{0{\cdot}52}Ti_{0{\cdot}48}O_3(ss)(2)$$

The present investigation, made using high-temperature X-ray diffractometry, was performed in order to clarify the influence of particle size of the B-site precursor on the kinetics of the second reaction.

2 Experimental

Two $PbO/Zr_{0{\cdot}52}Ti_{0{\cdot}48}O_2$ powder mixtures were prepared having two different particle sizes of the $Zr_{0{\cdot}52}Ti_{0{\cdot}48}O_2$ precursor. Both powders were attrition-milled. One of them, termed the 'fine' powder, had an average particle size of 1·91 μm and the other 'coarse' powder had a particle size of 5·08 μm. The commercial PbO had a purity of 99·6% (orthorombic crystal structure plus several wt% of tetragonal form). The powders were carefully mixed and isostatically pressed to pellets at 100 MPa with a maximum thickness of 1·0–1·5 mm.

X-ray diffractograms were obtained using a Philips PW-1710 automatic diffractometer with a step and a continuous scanning device. The basic unit in this system is a Philips powder diffractometer with a vertical goniometer PW 1050/25, graphite mono-chromator PW 1752/00, proportional counter for reflected beam PW 1711/10 and a PW

*To whom correspondence should be addressed.

1730/25 generator. Diffraction patterns were measured in a 2θ range of 20–40° using Cu K_α radiation of 50 kV and 30 mA. The at-temperature investigations were performed in an Anton Paar high-temperature attachment re-engineered by the authors.[4] The temperature of the sample was measured with a Pt–13% Rh/Pt thermocouple placed close to the sample. The measurements of the developing lead zirconate titanate phase were made in two different modes. The first set of measurements was made during heating to 800°C with a nominally constant heating rate of 10°C min^{-1} and 3 min scans in the above-mentioned 2θ range starting from 500°C with a scan at every 50°C. The second set was made during isothermal heat treatments in the temperature range 450–800°C with a maximum soaking time of 120 min.

The quantitative estimation of phase content was derived from an equation which relates the intensity of the diffraction peaks to the phase abundance[5]

$$I_{ij} = \frac{K_j C_{ij}}{\rho_j \mu_{li}} = \frac{\beta_j C_{ij}}{\sum_{j=1}^{n} \mu_j C_{ij}} \qquad (3)$$

where

K_j is a constant.
C_{ij} is the weight fraction of the jth phase in the ith sample.
I_{ij} is the intensity of a diffraction peak of phase j.
μ_{li} is the mass absorption coefficient of the sample.
μ_j is the mass absorption coefficient of phase j.
ρ_j is the density of phase j.
$\beta_j = K_j/\rho_j$) is the calibration constant, defined by the crystal structure, the composition of the analysed phase and the instrumental conditions.
n is the number of phases in the sample.
i is the sample number.
j is the phase number.

It is evident that the determination of C_{ij} from eqn (3) requires a knowledge of β_j and μ_{li}. Fortunately, the equation is simplified especially if it is assumed that chemical composition of the investigated sample remains unchanged during heat treatment and by ignoring texturing effects (because of *in-situ* mode data collection). Then, assuming that the mass absorption coefficient of the sample is constant, eqn (3) becomes

$$C_{ij} = B_j I_{ij} \qquad (\text{where } B_j = 1/\beta_j) \qquad (4)$$

Then the conversion of PbO to PZT can be written as

$$C_{PZT} = \frac{S_{PZT}}{S_{PZT} + S_{PbO}} \qquad (5)$$

where C_{PZT} is the fraction of newly formed PZT phase, S_{PZT} is the integrated intensity of the cubic PZT (1 1 0) peak and S_{PbO} is the integrated intensity of the PbO (1 1 1) peak.

Precise quantitative phase analysis requires accurate measurement of the integrated intensities of the diffracted lines. Count integration techniques work very well, when the lines are isolated and on simple backgrounds. However, when one or more lines overlap the line of interest, or if a complex background is present, profile fitting techniques are required in order to eliminate interferences. In order to fit the main peaks of PbO (1 1 1) and PZT (1 1 0) a profile model based on asymmetric Lorentzians for fitting the instrument- and wavelength-related components of the powder diffraction profile, together with a Marguardt non-linear least-squares algorithm, were used.[6]

3 Results and Discussion

3.1 Dynamic heat treatment

The phase composition of the initial mixtures contained two polyforms of PbO, namely massicot as the main phase and a small amount of litharge formed during preparation. In many commercial powders the metastable massicot is stabilized by the addition of small amounts of impurities (dopants), preventing its transformation to stable litharge at room temperature but allowing transformation to litharge when a mechanical force is applied. The other main phase was $Zr_{0.52}Ti_{0.48}O_2$, the main diffraction peaks of which were strongly overlapped by PbO. *In-situ* analysis made in the non-isothermal mode (temperature range 20–800°C) revealed dissolution of the main phases and corresponding formation of the PZT phase with cubic symmetry (Fig. 1). Special attention was paid to scanning in the temperature range 400–600°C, where the formation of a pyrochlore phase was expected. Diffractograms of samples in that temperature interval did not reveal the main peak of the pyrochlore phase located at $29° < 2\theta < 30°$ (Fig. 1). From this it was concluded that the formation of the PZT phase in this investigation can be considered as a uniform process without formation of intermediate phases.

The quantitative analysis showed that during the non-isothermal treatment the rate of formation of PZT was dependent on the particle size of the $Zr_{0.52}Ti_{0.48}O_2$ powders (Fig. 2). In both cases the curves are characterized by a sigmoidal shape, the main stages of the process being: the start of the reaction between 400 and 500°C, a constant rate stage between 500 and 700°C and a decreasing reaction rate at temperatures over 700°C. Figure 2

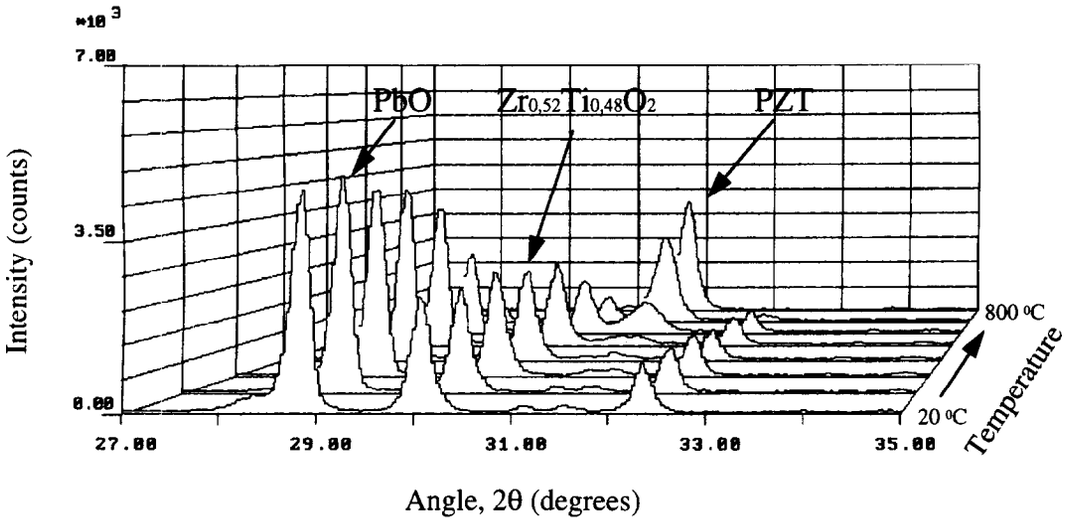

Fig. 1. Phase composition for the coarse $Zr_{0.52}Ti_{0.748}O_2$–PbO powder during heating.

clearly shows that the reaction to PZT is not autocatalytic and that the maximum rate of PZT formation for the two powders differs by approximately 100°C. A similar particle size effect on the calcination temperature was observed by Shrout[1] and Fukai *et al.*[7] The latter also showed that PZT was produced at a lower temperature than 600°C without formation of intermediate phases.

3.2 Isothermal heat treatment

Heat treatment of the powders was performed in an isothermal mode in the temperature range 540–700°C, in order to obtain more information about the solid-state reactions taking place during the PZT formation [Figs 3(a) and (b)]. As can be seen from the figures, the isothermal runs showed the absence of a measurable incubation time for the reaction. For the fine powder, the temperature of reaction is around 100°C lower than for the coarse. As a further quantitative assessment of the powder mixtures, the reactivity of the powders was estimated from the value of the apparent activation energies of reaction.

The overall rate of change of a microscopic transformation that proceeds via a large number of atomic processes is given by[8]

$$\text{rate} = v \exp(\Delta S/k) \exp(-\Delta H/kT) \qquad (6)$$

where v is a complex function that depends on the vibration frequency of the atoms, ΔS the activation entropy, k the Boltzmann constant, T the absolute temperature and ΔH the activation enthalpy. In condensed systems the activation enthalpy and the activation energy (ΔE_a) are nearly the same. Therefore, on the molarity scale, the rate of transformation may be expressed as an exponential function of an empirical activation energy which is characteristic of the transformation process

$$\frac{d\alpha}{dt} = f(\alpha) \cdot A e^{-\Delta E_a/RT} \qquad (7)$$

where α is the fraction converted, $f(\alpha)$ is a function of α and A is a constant. Integration of eqn (6) gives

$$\int_0^{t_{\alpha_f}} dt = \int_0^{\alpha_f} [Af(\alpha)]^{-1} e^{\Delta E_a/RT} d\alpha \qquad (8)$$

or

$$\ln t_{\alpha_f} = \ln\left\{ \int_0^{\alpha_f} [Af(\alpha)]^{-1} d\alpha \right\} + \frac{1}{R} \cdot \frac{E_a}{T} \qquad (9)$$

where t_{α_f} is the time required to obtain a certain fraction converted, α_f.

In this case the activation energy can be estimated in a straightforward manner, without assuming a specific kinetic model. It follows from eqn (9) that the activation energy is found by plotting the logarithm of time versus $1/T$ for a given constant fraction converted (α_f). Plots of ln t versus $1/T$ shown in Fig. 4 are reasonably straight parallel

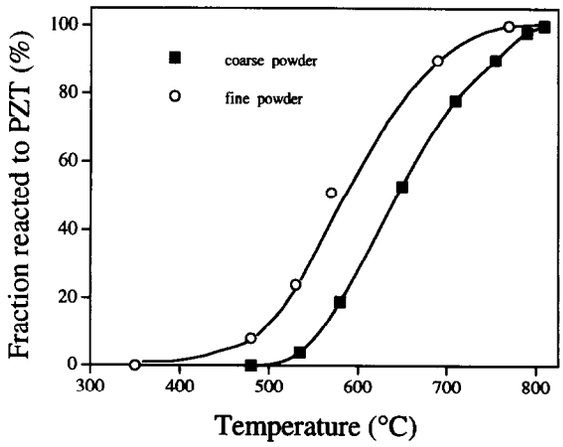

Fig. 2. Fraction of PZT formed versus temperature.

lines, indicating that the PZT formation reactions are characterized by a uniform mechanism. The calculated values of activation energy for the fine and the coarse powders are 150 and 210 kJ mol^{-1} respectively. In the literature,[9-12] quoted values for the activation energy vary from 100 to 500 kJ mol^{-1}. It is obvious that the physical meaning of the activation energy obtained from solid-state reactions in powder systems cannot be directly related to concepts used for describing kinetic processes in, for example, gas systems. In solid-state reactions the numbers of reacting species and reaction steps are more uncertain. Generally, these depend on the type of atomic interaction, the extent and geometry of the contact regions in the particle system, the type of crystal lattice and its degree of perfection. An example is provided by investigations performed on the reaction between PbO and ZrO_2.[10] The growth of the product layer between bulk PbO and ZrO_2 samples could be described by parabolic kinetics and the activation energy of the reaction was approximately 500 kJ mol.$^{-1}$ In contrast, in studies of mixed powders with different thermal prehistories, morphology and chemical activity, the phase transformations were shown to follow the Jander and the Kolmogorov–Erofeev models having activation energies of 188 and 100 kJ mol^{-1}, respectively.[11,12] The values for the activation energies obtained in this investigation are consistent with the literature data and indicate that the activation energy for solid-state reactions mainly reflects the reactivity of the powders used in the investigation.

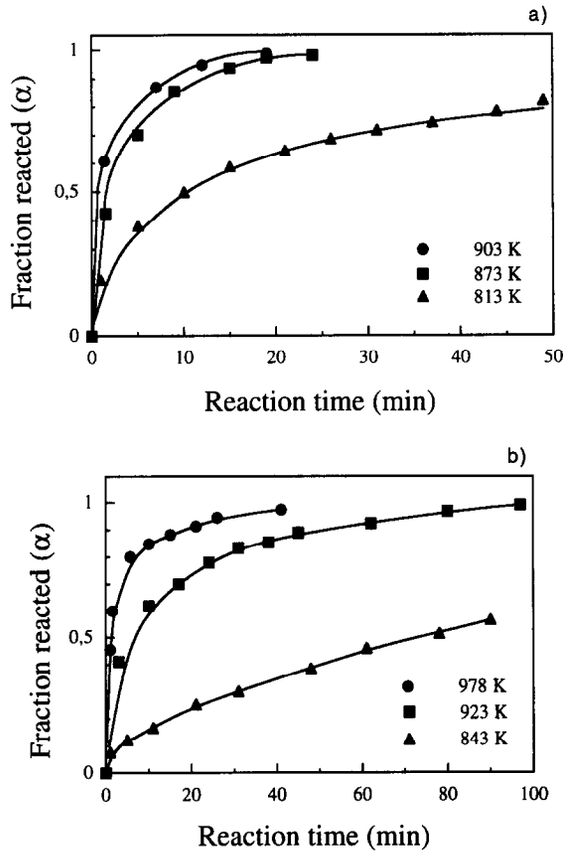

Fig. 3. Fraction of PZT formed versus time at different temperatures: (a) fine and (b) coarse powder.

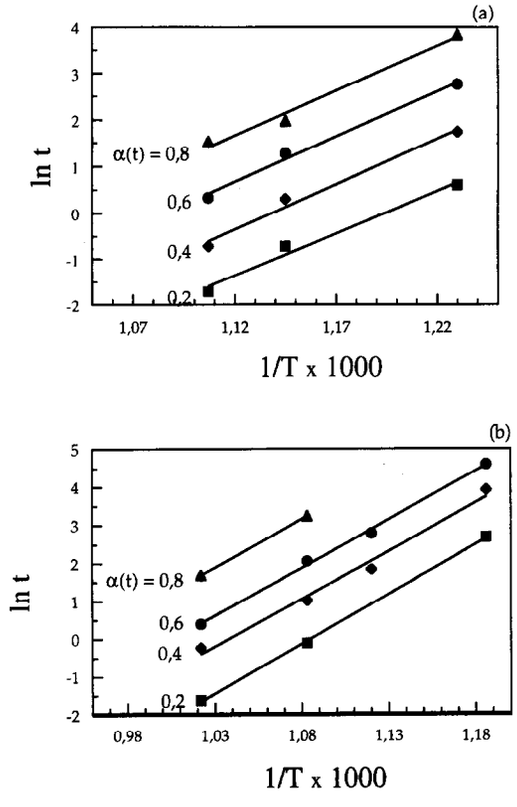

Fig. 4. The logarithm of time as a function of reciprocal temperature for various extents of the reaction, where (a) and (b) are the fine and the coarse powders, respectively.

3.3 Evaluation of the kinetic model

Investigations performed on PbO–TiO_2 and PbO–ZrO_2 systems have revealed that the formation of the binary compounds proceeds via reactions with material transport as the rate-controlling process.[7,10,11] It was also shown that, for powder compacts, the formation of $PbTiO_3$ and $PbZrO_3$ followed the Jander model for diffusion-controlled solid-state reaction kinetics.[11] In diffusion couples it was observed that the lead diffuses faster than the zirconium and titanium; thus few Ti^{4+} and Zr^{4+} ions were found in the PbO plate, while large numbers of Pb^{2+} ions were found in both the TiO_2 and ZrO_2 plates.[10] Attempts have been made to apply rate equations to powder mixtures with a distribution of sizes. It was found that the Valency–Carter diffusion model was applicable in all temperature intervals, when describing a particle size distribution of precursors reacting to $PbTiO_3$ and $PbZrO_3$.[9,13]

The above observations suggest that the formation of the ternary $Pb(Zr,Ti)O_3$ compound would occur predominantly by solid-state diffusion of Pb^{2+} and O^{2-} ions. Three diffusion-controlled models are chosen here to help identify the nature

of the diffusion mechanism: (i) the Jander model which is based on the solution for diffusion in a plane interface, without any change in volume or motion of the interface; (ii) the Ginstling and Brounshtein equation for a diffusion-controlled reaction starting on the exterior of a spherical particle[14] and (iii) the Valesi and Carter equation for spherical particles, taking into account the difference in volume of the reaction product and the initial material.[14 16] When the experimental data were fitted to these equations, the best fit was obtained with the Jander equation

$$r_A^2[1 - (1 - \alpha_t)^{1/3}]^2 = 2k\,t \qquad (10)$$

where α_t is the relative amount of A transformed into reaction product, r_A is the radius of the original spherical particles of A and k is the parabolic rate constant. The derivation of the equation is based on the premise that equal-sized spheres of reactant A are embedded in a quasi-continuous medium of reactant B. The closeness of fit is demonstrated in Figs 5 and 6 for the fine powder mixture. On the basis of this it is proposed that, when the fine powders are heated, either rapid surface diffusion or a high vapour pressure of PbO provides a uniform supply of Pb^{2+} and O^{2-} ions over the entire surface of the $Zr_{0.52}Ti_{0.48}O_2$ particles. Since the vapour pressure of PbO is rather low, varying from 1.5×10^{-9} atm at 500°C to 5×10^{-7} atm at 700°C,[17, 18] the second alternative seems less probable. Thus the extent of contact regions, together with the activation energy for bulk diffusion of Pb^{2+} and O^{2-} ions, will play a dominant role in the formation rate of the PZT solid solution.

In the derivation of the Jander equation, a parabolic growth law has been assumed. This is only valid for a diffusion-controlled one-dimensional reaction process, and not for a process with spherical geometry. Therefore it may appear somewhat surprising that the Jander equation gives the best fit to the experimental data. However, after milling, the $Zr_{0.52}Ti_{0.48}O_2$ particles consist of finely divided, far from spherical, nanometre-sized crystallites with a high defect density.

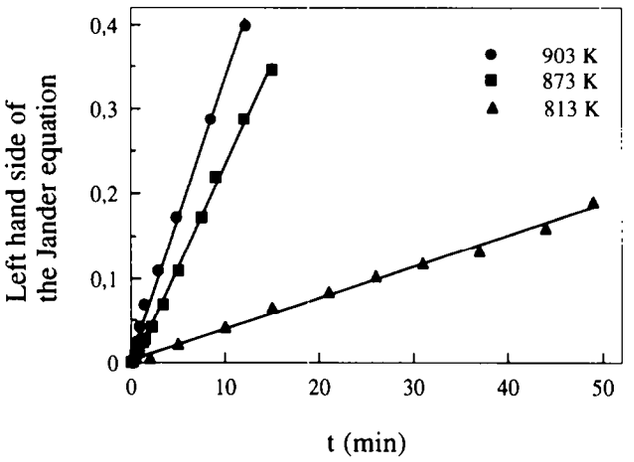

Fig. 5. Fitting of the Jander equation to experimental date of the reaction $Zr_{0.52}Ti_{0.48}O_2 + PbO \rightarrow Pb(Zr_{0.52}Ti_{0.48})O_3$ in the fine powder mixture.

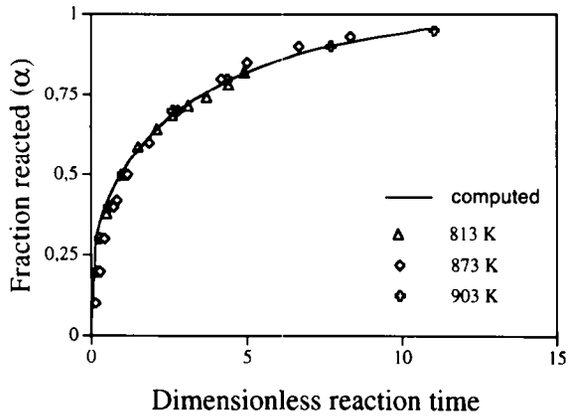

Fig. 6. Amount of PZT formed (α), for the fine powder mixture, as a function of reduced time, $t/t_{0.5}$. The full line is computed on the basis of the Jander model.

4 Conclusion

The second calcination stage in the formation of PZT solid solution was investigated by means of high-temperature X-ray diffractometry. The constant heating rate experiment of the powder mixtures of PbO and $Zr_{0.52}Ti_{0.48}O_2$ showed a direct formation of PZT solid solution without any intermediate X-ray-crystalline phases. By reducing the particle size of the B-site precursor from 5·08 to 1·91 μm, the calcination temperature was reduced by 100°C. The measured activation energy of the reaction was 150 kJ mol^{-1} for the mixture containing the fine precursor activated by prolonged milling and 210 kJ mol^{-1} for the mixture containing the coarse precursor. The reaction was found to follow the Jander model for diffusion-controlled solid-state reaction kinetics.

Acknowledgements

The authors thank Professor Richard Warren for stimulating discussions and for suggesting improvements to the manuscript. Financial support from the Swedish National Board for Industrial and Technical Development is gratefully acknowledged.

References

1. Shrout, T. R., Conventionally prepared submicron electroceramic powders by reactive calcination. *Proceedings of the International Conference Chemistry of Electronic*

Ceramic Materials, National Institute of Standards and Technology Special Publication 804, 1990, pp. 105–10.
2. Swartz, S. L. & Shrout, T. R., Fabrication of perovskite lead magnesium niobate. *Mater. Res. Bull.*, **17** (1982) 1245–50.
3. Yamamoto, T., Optimum preparation methods for piezoelectric ceramics and their evaluation. *Ceram. Bull.*, **71**[6] (1992) 978–85.
4. Babushkin, O., Harrysson, R., Lindbäck, T. & Tegman, R., A high-temperature graphite furnace for X-ray powder diffraction,. *Meas. Sci. Technol.*, **4** (1993) 816-19.
5. Klug, H. P. & Alexander, L. E., *X-Ray Diffraction Procedure for Polycrystalline and Amorphous Materials*. Wiley, New York, 1974.
6. Schreiner, W. N. & Jenkins, R., Profile fitting for quantitative analysis. *Adv. X-Ray Anal.*, **26** (1983) 141–48.
7. Fukai, K., Ueda, N., Hidaka, K., Aoki, M., Abe, K. & Igarashi, H., Easy sinterable $Pb(Zr_{0.53}Ti_{0.47})$ ceramic powder from $Zr_{0.53}Ti_{0.47}O_2$ solid solution. *Ceramic Powder Science III*, San Diego, USA, 1990, pp. 741–8.
8. Cahn, R. W. & Haasen, P., *Physical Metallurgy*. North-Holland Physics Publishing, 1983.
9. Sasaki, H., Introduction of particle-size distribution into kinetics of solid state reaction. *J. Am. Ceram. Soc.*, **47**[10] (1964) 512–16.
10. Prisedskii, V. V., Klevtsova, L. G. & Klimov, V. V., Mechanism and kinetics of reactive diffusion during the formation of lead titanate and lead zirconate. *Izv. Akad. Nauk. SSSR, Nerg. Mater.*, **10** (1974) 2166–72.
11. Mangel, A. & Doskocil, J., *Ber. Deut. Keram. Gesells.*, **51** (1975) 329.
12. Tretyakov, Y. D., *Solid State Reactions*. Chemistry Publishing, Moscow, 1978.
13. Kapur, P. C., Kinetics of solid state reactions of particulate ensembles with site distribution. *J. Am. Ceram. Soc.*, **56**[2] (1973) 79-81.
14. Ginstling, A. M. & Bronstein, B. I., Concerning the diffusion kinetics of reactions in spherical particles. *J. Appl. Chem. USSR*, **23**[12] (1950) 1249–59.
15. Schmalzried, H., *Solid State Reactions*. Verlag Chemie Gmbh, Weinheim, 1981.
16. Carter, R. E., Kinetic model for solid-state reactions. *J. Chem. Phys.*, **6**[34] (1961) 210–5.
17. Northrop, D. A., Vaporisation of lead zirconate-lead titanate materials. *J. Am. Ceram. Soc.* **17**[9] (1967) 441–5.
18. Chandratreya, S. S., Fulrath, R. M. & Pask, J. A., Reaction mechanisms in the formation of PZT solid solutions. *J. Am. Ceram. Soc.*, **64**[7] (1981) 422–5.

Journal of the European Ceramic Society **16** (1996) 1299–1308

PII: S0955-2219(96)00062-3
0955-2219/96/$15.00

Structural Evolution in Gel-Derived Mullite Precursors

K. J. D. MacKenzie,[a] R. H. Meinhold,[a] J. E. Patterson,[a] H. Schneider,[b] M. Schmücker[b] & D. Voll[b]

[a]New Zealand Institute for Industrial Research and Development, PO Box 31-310, Lower Hutt, New Zealand
[b]Institute for Materials Research, German Aerospace Research Establishment, 51140 Köln, Germany

(Received 19 December 1995; revised version received 27 February 1996; accepted 14 March 1996)

Abstract

The evolution of mullite from organo-metal gel precursors above 700°C is found to be strongly influenced in both gel pieces and powdered samples by the thermal pretreatment at lower temperatures. Under the present conditions, the optimum preheating temperature was found to be 350°C, at which temperature an anomalously high concentration was found of an Al species with a characteristic ^{27}Al magic-angle spinning NMR resonance at about 30 ppm. Such Al sites are often described as pentacoordinated, but an alternative assignment is considered. The optimum temperature for the formation of this Al site is also optimal for the catalytic formation of aromatic molecules from the residual organic fragments and/or solvent present. Mass spectrometry shows that under the present reaction conditions, these aromatics are thermally stable up to at least 900°C in air, and the prolonged presence of their decomposition products (CO and water) could facilitate the transformation of the gel to crystalline mullite. The ^{29}Si NMR spectra indicate at least three different Si environments, including one which may arise from the formation of silicon oxycarbide glasses in these gels. © *1996 Elsevier Science Limited*

1 Introduction

Because of its increasing importance as a high-technology ceramic, considerable interest is being shown in the production by sol–gel synthesis routes of high-purity mullite with reproducible particulate characteristics. Since the mechanism by which mullite evolves when these gel precursors are heated depends strongly on the homogeneity of the gels, considerable effort has been put into understanding how the degree of mixing of the silica and alumina components is influenced by the various possible different starting reagents and reaction conditions, as reviewed in two recent papers.[1,2] Taylor and Holland[1] have suggested that in very homogeneous gels, the Al is largely incorporated into the tetrahedral silica network, and mullite is the major phase appearing after recrystallization at about 980°C. By contrast, less homogeneous gels contain extensive Al- and Si-rich regions, the former being characterized by octahedral Al; this type of gel transforms to an Al-rich spinel, which forms mullite only on further heating.[1] These conclusions are largely supported by the observations of Selvaraj *et al.*[2] on gels produced using different hydrolysis conditions.

Schneider *et al.*[3] have investigated mullite precursors derived from tetraethoxysilane (TEOS) or $SiCl_4$ and aluminium sec-butoxide by both slow and rapid hydrolysis, which they designate type I and type III precursors, respectively. They observed, as did previous authors,[1,2] resonances in the ^{27}Al magic-angle spinning (MAS) nuclear magnetic resonance (NMR) spectra at about 30 ppm, variously attributed to 5-coordinated Al[1,2,4,5] or very strongly distorted tetrahedra.[6] In other structures containing well-defined 5-coordinate Al, the isotropic chemical shift is 35–36 ppm.[7] The Al in this coordination state, which has been suggested by Taylor and Holland to occur in the interfacial material between the silica-rich and alumina-rich domains,[1] appears to be implicated in the reaction which occurs at 980°C, since the 30 ppm resonance disappears abruptly at about this temperature.[1–3] Schneider *et al.*[3] reported that type I precursors are extremely homogeneous, containing a random assortment of 4-, '5'- and 6-coordinate Al which, although X-ray amorphous below about 900°C, crystallize above this temperature to mullite. Type III precursors differ, in forming an Al-rich spinel above 900°C.

During preliminary experiments in which thermally induced changes in type I mullite precursors were monitored by MAS NMR, it was observed that the reaction route to mullite (i.e. whether directly or via the spinel phase) was strongly influenced by the lower temperature pre-calcination conditions.

The aim of the present work was to investigate in greater detail the effect of thermal pretreatments at various temperatures on the structural evolution in type I precursors, using thermal analysis, X-ray diffraction and ^{27}Al and ^{29}Si MAS NMR.

2 Experimental

The type I precursors were synthesized to mullite stoichiometry (72 wt% Al_2O_3, 28 wt% SiO_2) by diluting TEOS and Al sec-butylate with isopropyl alcohol, mixing and slowly hydrolysing in a humidity chamber at 40% relative humidity for 14 days. The subsequent heating experiments were carried out on two types of sample, viz. gel pieces resulting directly from the synthesis and powders prepared by grinding the gel pieces. After drying at 150°C, one portion of the precursor phase was heated directly to various temperatures up to 650°C and held at temperature for 15 h before cooling. Another sub-set of these preheated samples was further heat-treated at 700°C for 15 h. All the heated samples were ground if necessary, and examined by X-ray powder diffraction (Siemens D500 computer-controlled powder diffractometer with Cu K_α radiation), and by ^{27}Al and ^{29}Si MAS NMR. The solid-state MAS NMR spectra were obtained at 11·7 T using a Varian Unity 500 spectrometer and 5 mm Doty probe spun at up to 12 kHz. The ^{27}Al spectra were acquired at 130·3 MHz with a 15° pulse of 1 μs and a recycle time of 0·1 or 1s. The spectra were referenced to $Al(H_2O)_6^{3+}$. The 11·7 T ^{29}Si spectra were acquired at 99·3 MHz using a 90° pulse of 6 μs and recycle times up to 3000 s (but typically 100 s). The spectra were referenced to tetramethylsilane (TMS). ^{29}Si cross-polarization (CP) spectra were also obtained at 4·7 T for some of the samples using a 5 μs contact time and a 3 s delay between the pulses. Thermal analyses were carried out using a Netzsch DSC 404 at a heating rate of 10°C min^{-1} in air. Evolved gas analyses (EGA) were carried out by packing the sample into a silica capillary tube through which was passed a stream of air (3 cm^3 min^{-1}) while heating in a micro furnace at a linear heating rate of 20°C min^{-1} up to 900°C. The effluent gas was analyzed using a Dycor MA100M quadrupole mass spectrometer fitted with a Varian 301/s triode ion pump and a 60 μm silicone rubber membrane inlet.

3 Results and Discussion

The most obvious difference in all the samples was their colour, which ranged for the powder samples from pure white for the 150°C-dried sample, through ochre at 250°C to grey at 350–450°C and black at 550–650°C. The gel piece samples displayed very weak colour effects in samples preheated at 250–450°C only, the other preheated materials being transparent. After reheating at 700°C, all the powder samples appeared black, indicating the presence of either carbon or unoxidized organic residues, or structural defects which can also cause dark coloration. The reheated gel pieces were all transparent.

3.1 Differential thermal analysis (DTA)

The thermal analysis curve of mullite precursor type I dried at 150°C is as expected for a gel precursor, showing a large, low-temperature endotherm centred at about 150–250°C, caused by the removal of residual water and solvent. Other broad and weak endotherms at 550–700°C are probably related to the further removal of solvent and residual organics. A sharp exotherm at about 980°C, typical of monophase type I mullite precursors, is associated with the formation of Al_2O_3-rich mullite.

3.2 X-ray diffractometry (XRD)

X-ray powder diffraction showed both the preheated powder and gel piece samples to be amorphous, with two broad humps in the diffraction baseline centred at about 3·5 and 1·4 Å. The XRD patterns of the reheated samples are shown in Fig. 1, and indicate a complex temperature-dependent phase development. The reheated powder sample preheated at 250°C [Fig. 1(E)] contains a cubic spinel phase with a cell parameter similar to that of γ-Al_2O_3. The reheated powder samples preheated at 350°C and 450°C [Figs 1(D) and (C)] show evidence of crystalline mullite, whereas the reheated powder samples preheated at 550°C and 650°C [Figs 1(B) and (A)] are still amorphous. Reheated gel piece samples preheated at 200°C show weak Al-spinel reflections [Fig 1(K)] which become progressively weaker in samples preheated at 250°C and 350°C [Figs 1(J) and (I)], but become markedly stronger in the sample preheated at 450°C [Fig 1(H)]. Preheating the gel pieces at 550°C produces a lower Al-spinel content in the reheated sample, which also contains evidence of another transition alumina, θ-Al_2O_3 [Fig. 1(G)], typical of an Al-rich system which has progressed further in its high-temperature transformations. The reheated gel piece sample preheated at 650°C is amorphous [Fig. 1(F)]. These

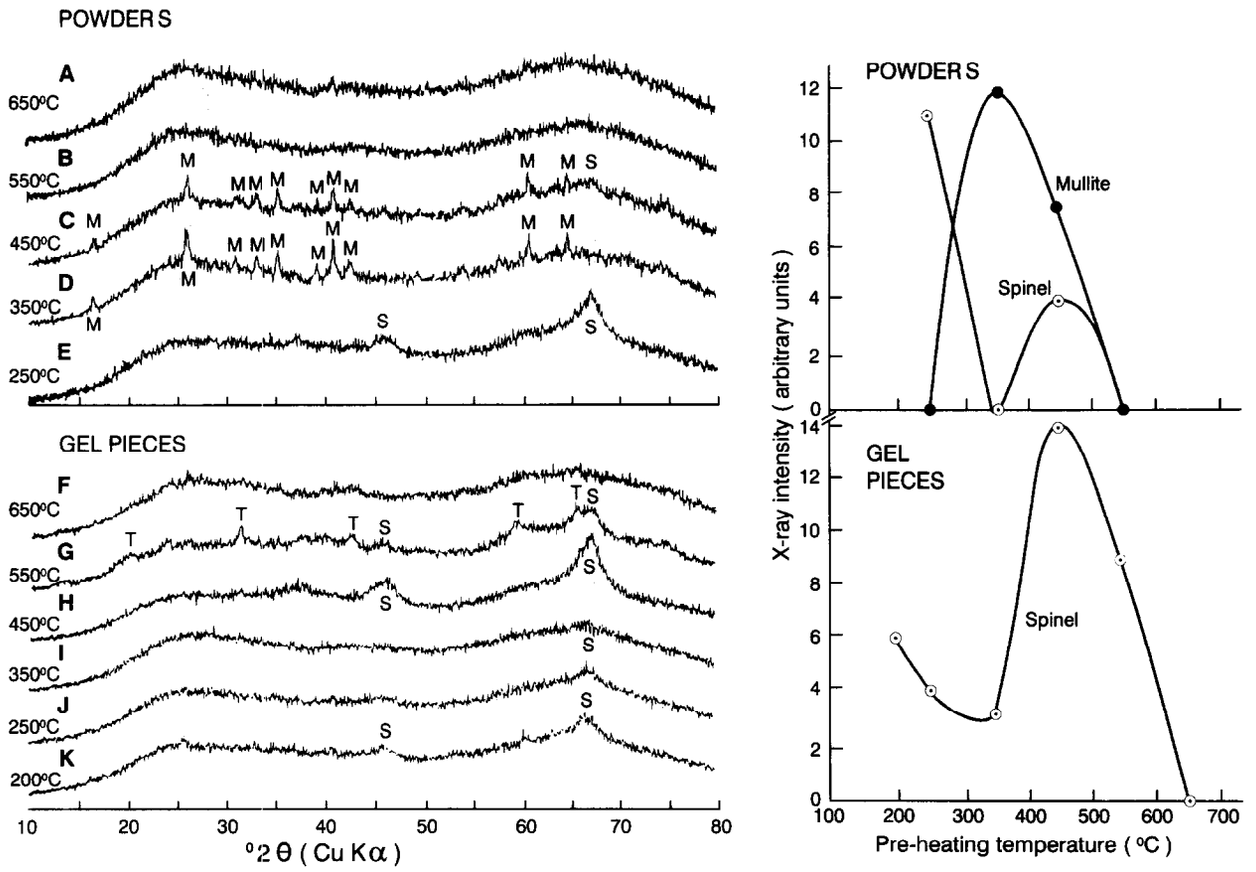

Fig. 1. XRD traces of mullite precursors preheated for 15 h at the marked temperatures, then reheated at 700°C for 15 h. (A)–(E) powdered samples, (F)–(K) gel piece samples. Right-hand diagram: semi-schematic representation of the variation in the XRD intensity of mullite and Al-spinel in reheated powder and gel samples, as a function of preheating temperature. Key: M = mullite, S = Al-spinel, T = θ-Al_2O_3.

changes in the mullite and spinel content are shown semi-schematically as a function of preheating temperature in Fig. 1, constructed from measurements of the 440 spinel peak areas and the 210 mullite peak heights.

3.3 MAS NMR

A selection of typical ^{27}Al MAS NMR spectra of powdered samples, both preheated and reheated to 700°C, is shown in Fig. 2, with the corresponding spectra for the gel piece samples shown in Fig. 3. All the ^{27}Al MAS NMR spectra contain three resolvable resonances at about 0, 30 and 55 ppm. The resonances near 0 and 55 ppm indicate 6-fold and 4-fold coordinated Al respectively, whereas the 30 ppm signal has been attributed to 5-coordinated Al.[1] Each of the spectra was fitted to three Gaussian peaks, from which the relative intensities were obtained by integration. The relative areas of the 0, 30 and 55 ppm spectral components are plotted in Fig. 4 as a function of the preheating temperature for the powder and gel piece samples, both preheated only [Fig. 4(A)] and reheated at 700°C after pre-heating [Fig. 4(B)].

Figure 4 indicates that in all the samples there is a general trend with increasing temperature towards greater concentrations of 30 ppm Al, at the expense of 4- and 6-coordinated Al. The samples preheated at 350–450°C are rather anomalous, showing a discontinuity in the amount of 30 ppm

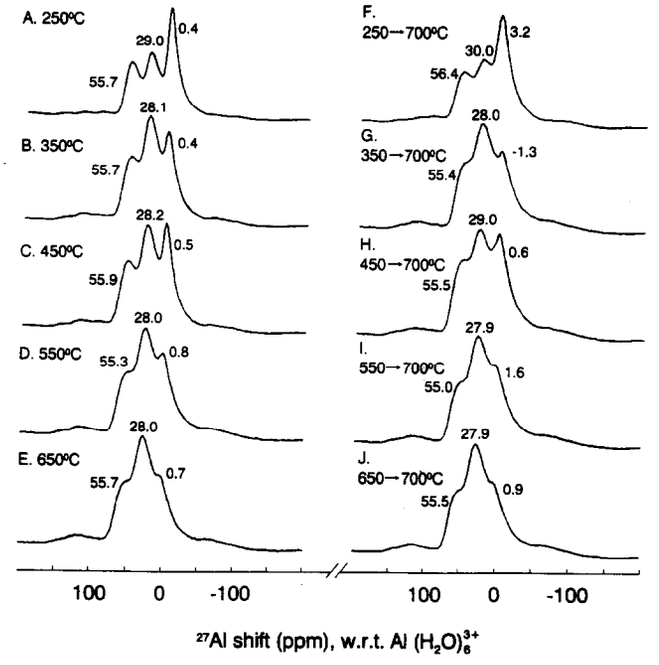

Fig. 2. 11·7 T ^{27}Al MAS NMR spectra of powdered mullite precursor gel: (A)–(E) preheated for 15 h at the indicated temperatures; (F)–(J) preheated for 15 h at the indicated temperatures, then reheated for 15 h at 700°C.

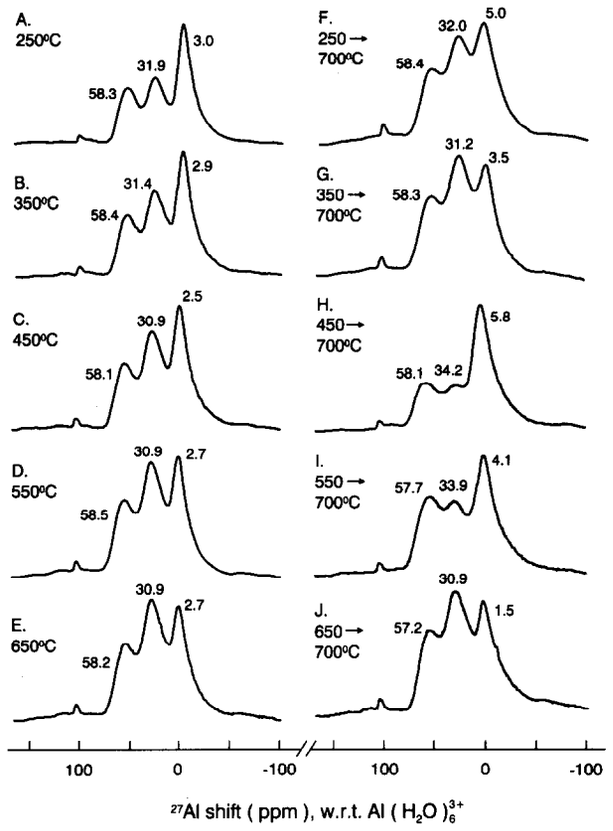

Fig. 3. 11·7 T ^{27}Al MAS NMR spectra of gel piece mullite precursors: (A)–(E) preheated for 15 h at the indicated temperatures; (F)–(J) preheated for 15 h at the indicated temperatures, then reheated for 15 h at 700°C.

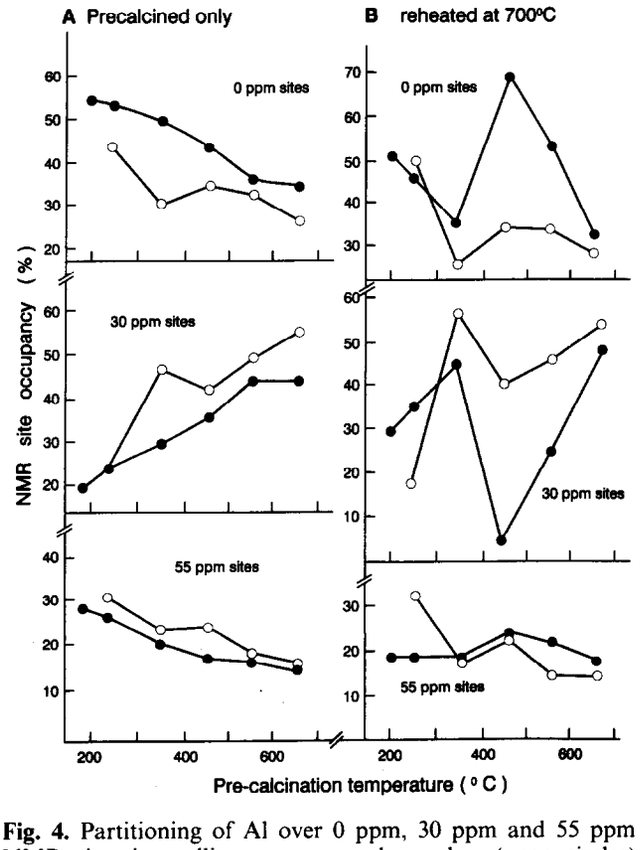

Fig. 4. Partitioning of Al over 0 ppm, 30 ppm and 55 ppm NMR sites in mullite precursor gel powders (open circles) and gel pieces (filled circles) as a function of preheating temperature. (A) Samples preheated for 15 h; (B) samples preheated for 15 h then reheated for 15 h at 700°C.

Al at these temperatures, especially in the powdered samples. A similar but even stronger effect is observed in both the powder and gel piece samples reheated at 700°C; both the powders and gel piece samples display a similar evolution of polyhedra, with reciprocal dependences between the 30 ppm Al and 6-fold coordinated Al. The high proportion of Al(6) and low proportion of 30 ppm Al in the reheated gel piece samples preheated at 450°C and 550°C [Fig. 4(B)] is typical of materials containing Al-spinel, and is consistent with the XRD results for these samples (Fig. 1). By contrast, the higher proportions of 30 ppm Al and decreased Al(6) observed in both powders and gels preheated at 350°C is more typical of a mullite-forming system, and has frequently been described in alumina-rich gels and glasses in the alumina–silica system,[1–3] the evolution of 30 ppm Al reaching a maximum in both gels and glasses just prior to mullite crystallization. Taylor and Holland[1] have related the Al coordination in aluminosilicate gels to their homogeneity, suggesting that Al(4) sites exist in regions of high homogeneity, and reflect efficient incorporation of Al into the tetrahedral silicate network. By contrast, less homogeneous regions, containing discrete alumina-rich and silica-rich domains, are suggested to be characterized by Al(6) sites. Taylor and Holland assign the 30 ppm Al sites to pentacoordinated Al in the interfacial regions between the homogeneous and inhomogeneous domains.[1] On this basis, the present starting material dried at 150°C would be fairly inhomogeneous, but as the sample is progressively preheated to higher temperatures, the number of interfacial 30 ppm Al sites increases, reflecting a progressive improvement in homogeneity with a decrease in the size of the domains and their improved distribution throughout the sample volume. Thus, the crystallization product of the most highly homogeneous systems is predicted to be mullite, as is found to be the case for the sample preheated at 350°C. However, although the NMR and XRD are self-consistent, they do not explain how the degree of homogeneity — which seems to be determined by thermal treatments at relatively low temperatures — is preserved throughout subsequent high-temperature reactions.

An alternative interpretation of the origin of the 30 ppm Al NMR resonance has recently been suggested.[8] This suggestion, which is supported by spectroscopic data and analysis of X-ray pair correlation functions for mullite gel precursors, is that the 30 ppm Al resonance does not arise from pentacoordinated Al but from distorted tetrahedral environments associated with Al triclusters sharing one common oxygen. Such Al sites occur

in crystalline mullite, in which they lead to a ^{27}Al resonance at about 43 ppm.[9] In non-crystalline mullite precursors, the elongated bond lengths between the tricluster common oxygens and their adjacent aluminiums are more readily accommodated, permitting increased distortion from tetrahedral symmetry and an associated increase in electric field gradients (EFGs), reflected in an increased upfield chemical shift towards 30 ppm.[8] Since these triclusters are an essential element of the mullite structure, it is suggested that their increased concentration in the gel precursors, reflected by the strength of the 30 ppm Al signal, will lead to increased mullite formation on reheating by the principle of structural continuity.

However, the question remains as to why the concentration of 30 ppm Al sites, whether arising from pentahedral interfacial sites or distorted tetrahedral triclusters, should be so increased by thermal pretreatment at 350°C. The processes involved in the formation of both phase-separated microdomains and oxygen-deficient Al triclusters involve breaking and re-forming of bonds, the kinetics of which seems likely to be influenced by the presence of hydroxyls and organic functional groups. Both types of species are present in the gel precursors, and it will be shown below that the nature and thermal stability of the latter vary with thermal pretreatment.

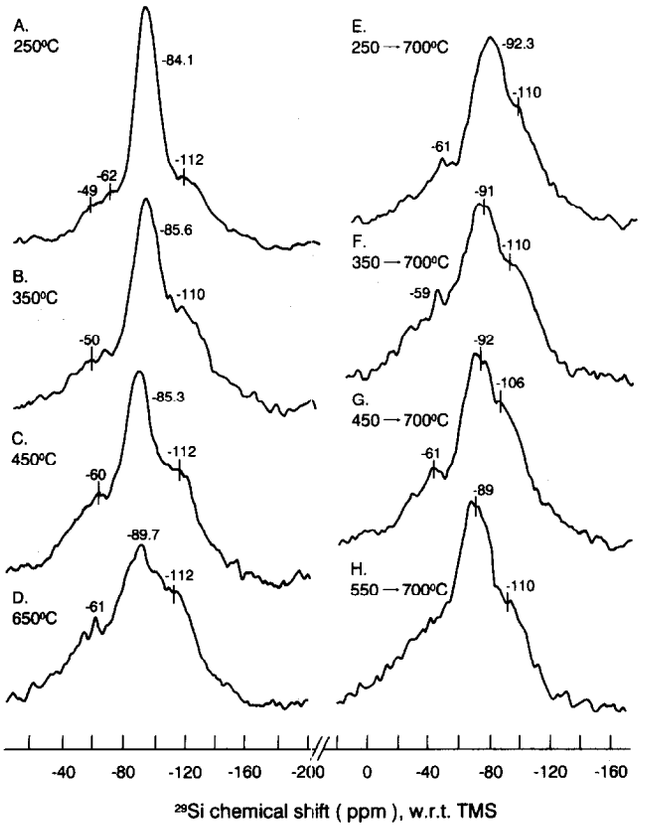

Fig. 5. Typical 11·7 T ^{29}Si MAS NMR spectra of powdered mullite precursor gel: (A)–(D) preheated for 15 h at the indicated temperatures; (E)–(H) preheated for 15 h at the indicated temperatures, then reheated for 15 h at 700°C.

Figures 5 and 6 show a selection of typical ^{29}Si MAS NMR spectra for powdered and gel piece samples, respectively, both after preheating and reheating at 700°C. All the ^{29}Si NMR spectra of the powder samples contain a main region of intensity at about –88 ppm, with two broad but distinguishable shoulders at about –55 and –113 ppm; the gel piece sample spectra (Fig. 6) are more symmetrical. All the powder sample spectra can be fitted by three peaks (Fig. 7), with positions that are essentially independent of the heating conditions.

The peak of maximum intensity shifts slightly from about –85 ppm in the powder and gel piece samples preheated at 250°C, to about –91 ppm in the gel piece sample preheated at 650°C. This spectral region is associated with aluminosilicates such as mullite.[6] The small but significant upfield trend observed in the position of this peak with increasing preheating temperature may reflect an increase in the number of –Si–O–Si– bonds with respect to –Si–O–Al– bonds, caused by the gradual disappearance of unbridged –Si–O–H or –Si–O–R (R = organic residual) structural units.

The broad shoulder at about –110 to –117 ppm, particularly noticeable in the spectra of the powder samples (Fig. 5), indicates the presence of varying amounts of uncombined X-ray amorphous SiO_2 in these samples, which has been cited as evidence for gel inhomogeneity.[2] The formation of –Si–O–Si– domains in the powder precursor

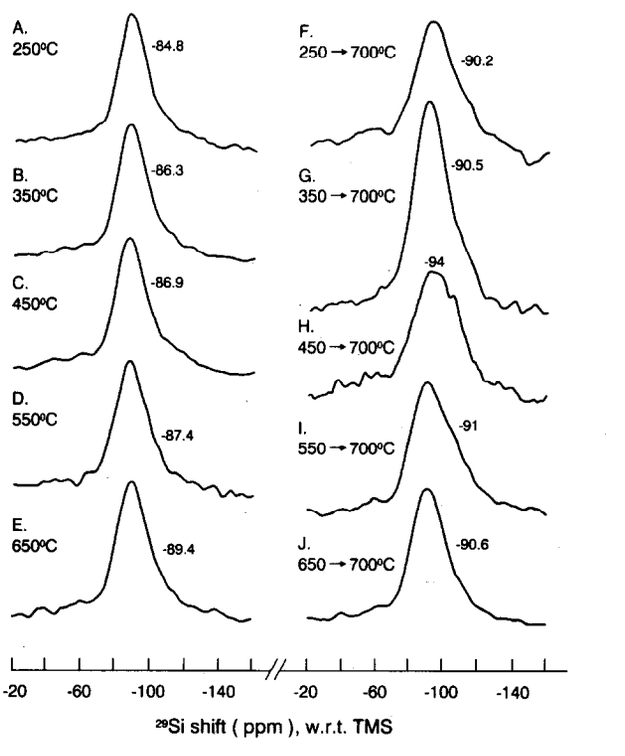

Fig 6. Typical 11·7 T ^{29}Si MAS NMR spectra of mullite precursor gel pieces: (A)–(E) preheated for 15 h at the indicated temperatures; (F)–(J) preheated for 15 h at the indicated temperatures, then reheated for 15 h at 700°C.

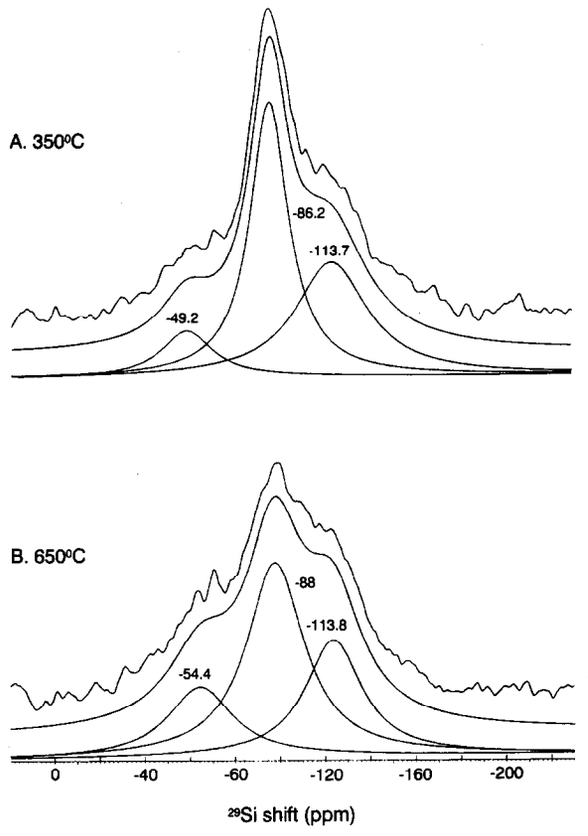

Fig. 7. Typical fits of three Gaussian peaks to ^{29}MAS NMR spectra of mullite precursor gel preheated as indicated.

may be due to weak phase separation which is necessary for the formation of alumina-rich mullite plus silica above about 980°C. This phase separation must be much weaker than in type III mullite precursors,[3] which at about 980°C form Al-spinel plus non-crystalline silica. Phase separation into alumina-rich and silica-rich phases prior to recrystallization is less evident in the gel piece samples, possibly due to slower diffusion processes in the gel pieces by comparison with the higher surface area powder samples.

The origin of the lower-field ^{29}Si intensity present in all these spectra at about –55 ppm is more difficult to explain, since this shift is low for Si–O resonances. The olivine minerals $(Mg,Fe)_2SiO_4$, with ^{29}Si chemical shifts of about –62 ppm,[10] represent one of the few entities resonating in this region, but the absence of divalent cations in the present system militates against this explanation for the observed spectra. Another possibility, consistent with the dark colours of the present gels and the persistence of organic residues up to at least 700°C (see below), is the presence of stable amorphous oxycarbide ('black glass'). The $SiCO_3$ unit, one of the species present in gel-derived silicon oxycarbide, has a broad ^{29}Si resonance centred at about –67 ppm, with another unit, SiC_2O_2, giving rise to a peak at about –30 to –40 ppm.[11] These oxycarbide glasses also contain a major SiO_4 resonance at about –110 ppm,[11] consistent with the present spectra. Although such entities may well occur in the samples reheated at 700°C, they are unlikely to be present in the samples which had been only preheated at lower temperatures. In these, the origin of the lower-field NMR resonances is more likely to be precursor organosilicon species such as:

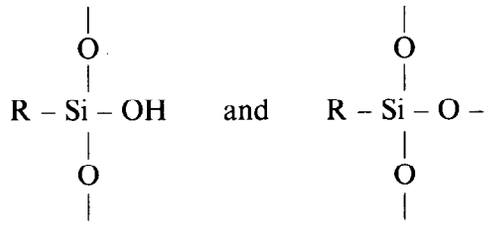

which have been reported[12] as having ^{29}Si resonances at about –56 and –66 ppm, respectively.

To investigate the relationship of protons to the Si atoms, and their possible retention during the thermal treatments, ^{29}Si cross-polarized (CP) spectra were obtained for several samples. The Si atoms detected in this way are those in proximity to protons, and produced spectra which were similar to those run at the same field strength without cross-polarization, suggesting that the protons are distributed throughout the sample and not localized at one particular type of Si site. Although the sample weights within the coil volume were somewhat variable, making the analysis only semi-quantitative, the CP intensity was approximately constant up to 450°C, decreasing as expected to about 39% of its original value after heating at 650°C, with a further decrease to about 31% after reheating at 700°C. These results indicate that thermal treatment removes the silanol protons more or less uniformly, but since some of these remain in the structure up to recrystallization temperatures, their presence could influence mullite formation. However, the CP results give no indication that abnormal proton activity might be implicated in the enhanced transformation to mullite of the sample preheated at 350°C.

3.4 Evolution of organic species during heating

Mass spectra were continuously recorded of the effluent gas streams from the preheated and reheated gel samples as they were heated in flowing air up to 900°C. A selection of three-dimensional mass spectra plotted as a function of heating temperatures is shown in Fig. 8 for the samples which had been preheated to various temperatures as marked.

The spectra of samples preheated at 150 and 250°C [Figs 8(A) and (B)] are characterized by the evolution of a series of fragments of mass 56–58, which begin to appear at about 600°C, reaching their maximum concentration in the gas stream at

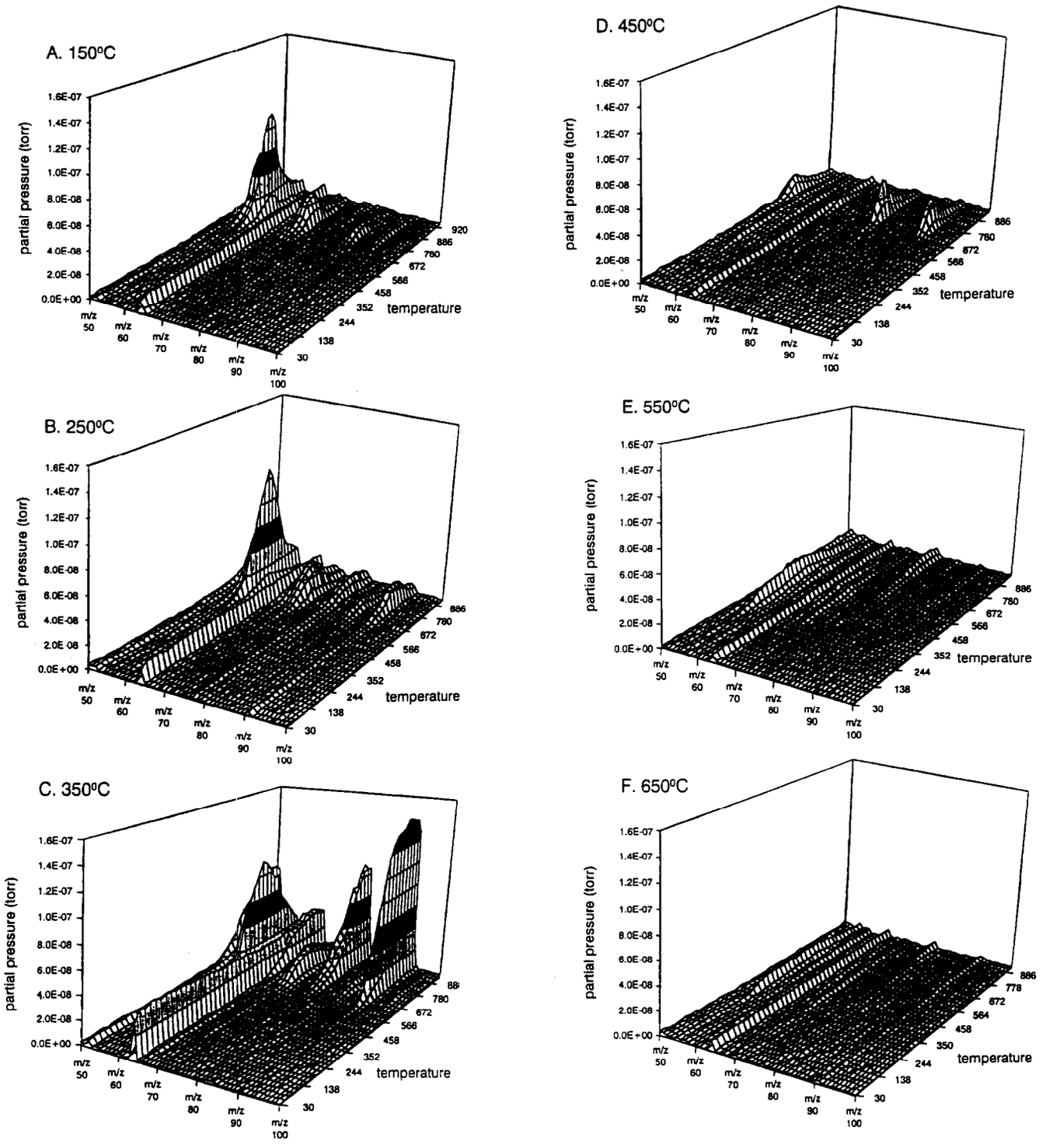

Fig. 8. Mass spectra of gases evolved during heating of mullite precursor gels in air at 20°C min^{-1}. Prior to this experiment, the gels were preheated for 15 h at the indicated temperatures.

about 800°C and disappearing by about 900°C [Fig. 9(A)]. A maximum in the mass signal for CO_2 at 800°C suggests that these species are rather resistant to oxidation up to this temperature, after which their disappearance is related to their oxidation. The unambiguous identification of these organic species is complicated by the possible presence of a mixture of compounds, but the complete mass spectra including the lower-intensity cracking fragments are consistent with organic species such as hexane, heptane or their cyclic forms, or cyclohexanone. These compounds apparently originate from the organic by-products of gel formation, perhaps with residual traces of solvent, but their considerable thermal stability, which extends into the temperature region of gel crystallization, is unexpected.

Even less expected is the mass spectrum from the sample preheated at 350°C [Fig. 8(C)] which shows, in addition to the group of masses at

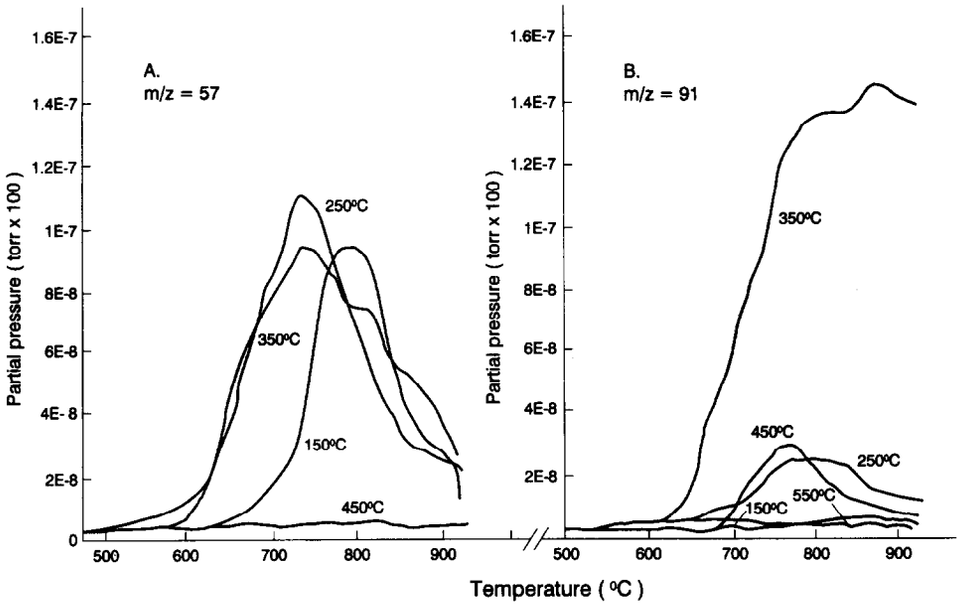

Fig. 9. Temperature dependence of the thermal evolution of two representative organic species from mullite precursor gels preheated for 15 h at the temperatures indicated on each curve: (A) species of mass 57, (B) species of mass 91.

56–58, significant concentrations of masses 76–79, 90–93 and 103–106. These species are even more thermally stable, beginning to be evolved at about 700°C and continuing to increase in concentration up to 900°C [Fig. 9(B)]. Based on their cracking patterns, these species represent mixtures of aromatic-containing benzene and ethyl- and methyl-substituted benzenes. Their formation in the sample preheated at 350°C for a long period (15 h) appears to be related both to the catalytic activity known to be associated with alumina gels containing high proportions of $Al^{[5]}$ (the so-called 'high-5' gels[13] and the preheating temperature, which is sufficient to promote the catalytic reactions of the residual organic species but not sufficiently high to cause oxidation. The effect of the preheating temperature is clearly shown in Fig. 10, in which are plotted the maximum ion signals for masses 57 and 91 as a function of the preheating temperature. Figure 10 shows a marked increased in the aromatic masses in the sample heated in 350°C, whereas at > 350°C the amounts of all organics rapidly decrease, having apparently been carbonized, consistent with the increasingly darker colours of these samples. Mass spectra resembling Figs 8(E) and (F) were obtained from all the preheated samples which had been subsequently reheated at 700°C for 15 h; the reheating conditions were apparently sufficient to remove most of the organic species formed during the preheating stage.

These results suggest that catalytic reactions of the residual organic species are optimized at 350°C with respect to the formation of aromatic compounds that have a high degree of stability towards further heating in air. It was suggested earlier in this paper that the presence of residual organic species could facilitate the formation of the 30 ppm Al sites which may be related to the incipient mullite structure; these Al sites may also be implicated in the catalytic rearrangement of the organic residues during prolonged preheating at lower temperatures. The question remains, however, as to whether these relatively stable organic compounds might also influence the gel crystallization at higher temperatures. One possibility is

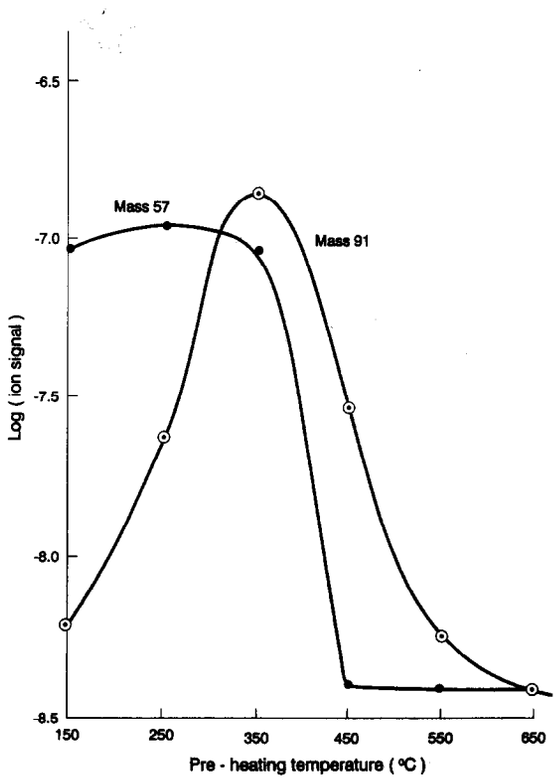

Fig. 10. Maximum concentration of species of mass 57 and 91 evolved from mullite precursor gels as a function of the gel preheating temperature.

that the presence of the thermal degradation products carbon and CO may influence the formation of mullite by providing a locally reducing atmosphere in intimate association with the incipient mullite grains. Although such an atmosphere effect has not previously been demonstrated for gel-derived mullites, it has been shown that the formation of mullite from kaolinite is assisted by reducing atmospheres in the presence of carbon.[14] Another interesting question arising from these results is whether the aromatic species formed at 350°C might somehow modify the catalytic sites in the gel by remaining tightly bound even at temperatures at which crystallization begins, and thereby influence the course of the high-temperature transformations. Further work is required to clarify these matters.

4 Conclusions

(1) The thermal evolution of mullite from organically derived gel precursors, in the form of both pieces and powders, is markedly influenced by thermal pretreatment at low temperatures (<450°C).

(2) Prolonged thermal pretreatment at the optimum temperature (OPT) (250–350°C in the present samples) produces an anomalously high concentration of Al species appearing in the ^{27}Al NMR spectra at ≈30 ppm. This situation is perpetuated when the preheated samples are reheated at higher temperatures, leading to the predominance of the 30 ppm Al signal immediately prior to mullite recrystallization.

(3) The 30 ppm Al signal is often attributed to pentacoordinated Al, which may be located in the mullite precursor gels at the interface between Si-rich and Al-rich microdomains. Alternatively, this Al signal could arise from the distorted tetrahedral Al environment in the region of an O-deficient tricluster which constitutes a distinctive element of the mullite structure on recrystallization. The enhanced formation of the 30 ppm Al sites during prolonged thermal treatment at the OPT may be related to the presence of residual hydroxyl groups or organic residues, which facilitate the atomic movements necessary for the formation of either microdomains or tricluster structures.

(4) The gels contain Si in at least three environments: (i) in an aluminosilicate, characterized by a ^{29}Si chemical shift of about −86 ppm, (ii) in uncombined silica (chemical shift of about −112 ppm) and (iii) in an environment which may be associated with residual carbon from the organic precursor (chemical shift of about −55 ppm). After heat treatment, the position of the aluminosilicate resonance moves upfield slightly, reflecting an increase in the number of Si–O–Si bonds resulting from phase separation or from the condensation of Si–OH or Si–OR groups.

(5) Thermal analysis and ^{29}Si cross-polarization experiments indicate the persistence of residual protons in the gels even above the OPT. These protons are not localized on any particular Si site, but may be implicated in the anomalous behaviour of the gels preheated at the OPT, by facilitating the atomic movements necessary for both phase separation and the formation of tricluster structures.

(6) The gels retain up to high temperatures residual organic species from the reactants and possibly traces of solvent. Below the OPT these are predominantly straight-chain or cyclic hydrocarbons, but prolonged heating at the OPT results in their conversion to aromatic species, possibly resulting from the enhanced catalytic properties of the high concentration of 'pentacoordinated' Al in these samples. Prolonged preheating above the OPT destroys the aromatic species, probably by oxidation; once formed, however, these species are thermally stable under dynamic heating conditions to at least 900°C. Their presence in the system at high temperatures could influence the structural evolution of the gel by providing a locally reducing and/or humid atmosphere which facilitates such transformations. Thus, the previously unreported influence of prolonged thermal preconditioning on the structural evolution of the gels under the present conditions appears to be related to the presence of organic residues, which may play an essential role in the formation of catalytically active Al sites characterized by the 30 ppm NMR resonance. These sites could influence subsequent mullite formation both because they form an essential element of the mullite structure, and by their catalytic conversion of the residual organic species to entities whose thermal stability at the recrystallization temperature allows them to participate in these transformations.

References

1. Taylor, A. & Holland, D., The chemical synthesis and recrystallisation sequence of mullite. *J. Non-Cryst. Solids*, **152** (1993) 1–7.

2. Selvaraj, U., Komarneni, S. & Roy, R. J., Structural differences in mullite xerogels from different precursors characterized by ^{27}Al and ^{29}Si MAS NMR. *Solid State Chem.*, **106** (1993) 73–82.
3. Schneider, H., Voll, D., Saruhan, B., Sanz, J., Schrader, G., Rüscher, C. & Mosset, A., Synthesis and structural characterization of non-crystalline mullite precursors. *J. Non-Cryst. Solids*, **178** (1994) 262–71.
4. Yoldas, B. E., Thermochemically induced photoluminescence in sol–gel-derived oxide networks. *J. Non-Cryst. Solids*, **147–8** (1992) 652–56.
5. Okada, K. & Otsuka, N., Characterization of the spinel phase from SiO_2–Al_2O_3 xerogells and the formation process of mullite. *J. Am. Ceram. Soc.*, **69** (1968) 652.
6. Schneider, H., Merwin, L. & Sebald, A., Mullite formation from non-crystalline precursors. *J. Mater. Sci.*, **27** (1992) 805–12.
7. Massiot, D., Kahn-Harari, A., Michel, D., Muller, D. & Taullele, F., Aluminium-27 MAS NMR of $Al_2Ge_2O_7$ and $LaAlGe_2O_7$: two pentacoordinated aluminium environments. *Magn. Reson. Chem.*, **28** (1990) 582.
8. Schmucker, M., Schneider, H., MacKenzie, K. J. D. & Meinhold, R. H., Al polyhedron in non-crystalline Al-rich gels and glasses of the system Al_2O_3–SiO_2. *Proc. PACRIM 2, 2nd Internat. Meeting Pacific Rim. Ceramic Societies*, Cairns, Australia 1996.
9. Merwin, L., Sebald, A., Roger, H. & Schneider, H., ^{29}Si and ^{27}Al MAS NMR spectroscopy of mullite. *Phys. Chem. Mineral.*, **18** (1991) 47–52.
10. Sherriff, B. L., Grundy, H. D. & Hartman, J. S., The relationship between ^{29}Si MAS NMR chemical shift and silicate mineral structure. *Eur. J. Mineral.*, **3** (1991) 751–68.
11. Soraru, G. D., D'Andrea, D., Campostrini, R., Babonneau, F. & Mariotto, G., Structural characterization and high-temperature behaviour of silicon oxycarbide glasses prepared from sol–gel precursors containing Si–H bonds. *J. Am. Ceram. Soc.*, **78** (1995) 379–87.
12. Zhang, H. & Pantano, C.G., Synthesis and characterization of silicon oxycarbide glasses. *J. Am. Ceram. Soc.*, **73** (1990) 958–63.
13. Wood, T. E., Siedle, A. R., Hill, J. R., Skarjune, R. P. & Goodbrake, C. J., Hydrolysis of aluminium — are all gels created equal? *Mater. Res. Symp. Proc.*, **180** (1990) 97–116.
14. MacKenzie, K. J. D., Meinhold, R. H., Brown, I. W. M. & White, G. V., The effect of reaction atmosphere on the early stage carbothermal reduction of kaolinite: an XRD, ^{29}Si and ^{27}Al MAS NMR study. *J. Mater. Sci.*, **29** (1994) 5631–40.

Journal of the European Ceramic Society **16** (1996) 1309–1318

PII: S0955-2219(96)00059-3
0955-2219/96/$15.00

Synthesis and Characterization of Y_2O_3–ZrO_2 and Y_2O_3–CeO_2–ZrO_2 Precursor Powders

T. Settu & R. Gobinathan

Ceramic Technology Division, Department of Chemical Engineering, Alagappa College of Technology, Anna University, Madras-600 025, India

(Received 24 April 1995; revised version received 6 March 1996; accepted 14 March 1996)

Abstract

Thixotropic gels of the precursor powders of the titled compounds have been prepared by the addition of oxalic acid to the mixed solutions of metal salts at room temperature (≈27°C). The clear sols of yttrium–zirconyl oxalate (YZO) and yttrium–cerium–zirconyl oxalate (YCZO) gelled within a few hours and were oven-dried at 40°C. The various stages of gelation behaviour of the sols are explained on the basis of DLVO theory. By repeptizing the dried gel powders with water, concentrated sols were prepared. The gelation time as a function of chloride ion concentration is discussed for both sols. The nature of the temperature dependence of the dried gel powders was studied by means of thermogravimetric analysis and differential thermal analysis. Powder X-ray diffraction was used to study the crystallization behaviour of the dried amorphous gel powders. It is found that these powders crystallize in tetragonal phase when calcined at 850°C for 1 h. Estimation of surface area and infra-red characterization have also been carried out for the prepared powders. © 1996 Elsevier Science Limited

1 Introduction

With the increasing development of ceramic materials, there has been enormous interest in their preparation. The preparation technique depends on the applications of a particular material, such as the mixed oxide method for refractory applications and chemical routes for structural and functional applications. The development of zirconia-based ceramic materials is of prime interest because of their superior properties such as toughness, oxidation, corrosion and erosion resistance and tolerance to severe environments, which enables numerous industrial applications. The pioneering work of Garvie *et al.*[1] and Gupta and co-workers[2,3] stimulated considerable attention on this area.

Although various liquid precursor routes are available for the preparation of fine ceramic materials, the sol–gel method is a promising processing technique because of its inherent advantages such as controlled particle size, shape and distribution, desired composition, relatively low-temperature sinterability, etc., and because of its recent advancement for industrial applications.[4–6]

Many reports on the preparation of fine particles of yttria-stabilized zirconia are available, several of which involved precipitation/sol–gel methods.[7–13] Most of them yielded sinteractive powders of fine size. The spray pyrolysis method has been used by Xiaming *et al.*[14] for the preparation of ZrO_2–Y_2O_3 powders.

Even though yttria-stabilized tetragonal zirconia has good mechanical properties, it suffers severely from low-temperature degradation[15–20] which leads to deleterious properties, and therefore the material turns out to be a failure. On the other hand, yttria–ceria-stabilized tetragonal zirconia has not shown low-temperature degradation.[20,21]

Many reports are available on the preparation of yttria–ceria-stabilized zirconia (YCZ) and its characterization.[19–22] Duh *et al.*[20] and Leach and Khan[22] have reported the mechanical behaviour, tolerance of the material in a hostile environment and the good phase stability of the YCZ system. The phase stability and mechanical behaviour of the stabilized zirconia are clearly explained by Hirano.[23]

The present work reports on the preparation of yttria- and yttria–ceria-stabilized zirconia by oxalate gelation using metal salts of chloride and nitrate, and oxalic acid solutions. The characterization of the prepared powders [by X-ray powder diffraction (XRD), thermogravimetric analysis (TGA), differential thermal analysis (DTA), surface area measurement and infra-red spectroscopy (IR)] and the preparation of concentrated sols are also discussed.

2 Experimental Procedure

The parent materials for the preparation of the titled powders were the water-soluble salts of metal nitrates and chlorides such as zirconyl chloride octahydrate (LR grade, CDH Chemicals), cerium nitrate hexahydrate (AR grade, CDH Chemicals), yttrium nitrate hexahydrate (AR grade, CDH Chemicals) and oxalic acid dihydrate (SD Fine Chemicals). Triple distilled water was used throughout the experiments. All the solutions were used as-prepared after filtration.

2.1 Preparation of gels

2.1.1 Yttrium–zirconyl oxalate (YZO) gel

Aqueous solutions (1 M) of zirconyl chloride and yttrium nitrate were prepared by dissolving the respective salts in water, and the solutions then thoroughly mixed together (corresponding to 5 mol% of Y_2O_3 in the final oxide powder). A desired amount of oxalic acid solution (1 M) was slowly added to the mixed cation solution with continuous stirring. White gelatinous precipitates were formed immediately, and gave a thick gel. The formed thick gel was vigorously stirred/shaken, yielding a clear sol. This sol was allowed to form a clear thixotropic gel at room temperature (≈27°C) by physical gelation. The addition of a stoichiometric ratio of oxalic acid led to the formation of a turbid aggregated sol. The physical and thixotropic gel obtained from the clear sol was oven-dried at 40°C. The dried gel powder has repeptizable character when mixed with water.

2.1.2 Yttrium–cerium–zirconyl oxalate (YCZO) gel

Solutions (1 M) of zirconyl chloride, cerium nitrate and yttrium nitrate were prepared by dissolving the salts in water. Cerium nitrate solution was first mixed well with zirconyl chloride solution and then the yttrium nitrate solution was thoroughly mixed with the combined solutions (corresponding to 4 mol% of Y_2O_3 and 7 mol% of CeO_2 in the final oxide powder). An appropriate quantity of oxalic acid solution (1 M) was mixed with the combined cation solution, slowly and with continuous stirring, at room temperature (≈27°C). During the formation of sol and gel, the observed characteristics of the YCZO system were the same as those of the YZO system. The prepared gels were oven-dried at 40°C and crushed in a mortar and pestle. The powders thus obtained were used to study the gelation time as a function of chloride ion concentration for repeptized sol. They were also calcined at different temperatures, 460, 600 and 850°C for 1 h, to study the crystallization behaviour and to estimate the surface area. Thermal behaviour and IR studies of the dried gel powders were also carried out.

The following flow chart shows the experimental procedure for the preparation of these powders.

Oxalic acid solution
↓
*Solutions of yttrium nitrate and zirconyl chloride
↓
White flocculation
↓
Clear sol
↓
Physical gelation
↓
Dried at 40°C
↓
Powder
↓
Characterization

*For the preparation of YCZO gel, cerium nitrate solution was mixed with the yttrium nitrate and zirconyl chloride solutions.

3 Results and Discussion

3.1 Formation of gels

Immediately after the oxalic acid solution is mixed with the combined solutions of yttrium nitrate and zirconyl chloride at room temperature (27°C), white flocculates are formed due to the localized concentration of the ions and the flocculates disappear spontaneously. If the addition of oxalic acid is continued, the rate of disappearance of the flocculates decreases and finally a white thick gel is obtained. After vigorous stirring/shaking of the gel, a clear sol is formed. Possible reasons for the variation of the rate of disappearance of the flocculates may be the higher ionic concentration of the solution and an uneven distribution of the ions. Vigorous stirring/shaking favours the even distribution of the ions and the adsorption of protons on the colloidal particles, thereby creating an electrical double layer. As time increases the clarity of the sol decreases slightly, which may be due to clustering of the colloidal particles. It has also been noticed that the atmospheric conditions have a marked effect on the formation of the transparent sol, gel and gelation time. For example, if the humidity of the atmosphere is greater than 95%, the formed sol and gel are highly transparent at room temperature and the time taken for

gelation is more; if the humidity is less than 90%, the formed sol is of aggregative nature and the gel is opaque. This may be due to the difference in the reaction rates for the formation of the sol and gel. However, a systematic study needs to be carried out to understand the effect of atmospheric conditions on sol and gel formation.

The YCZO gel was prepared by slow addition of oxalic acid to the combined cations solution with continuous stirring. The characteristics observed for this gel during preparation are similar to those of the YZO gel. The addition of a stoichiometric ratio of oxalic acid to the mixed cations solution leads to the formation of an unclear sol which then turns out to be a white opaque gel, whereas a transparent sol and gel are observed when the addition of oxalic acid is sufficient to form the zirconyl oxalate gel alone, i.e. the molar ratio of $(ZrO)^{2+}$ to $(C_2O_4)^{2-}$ is equal to 1 M for both YZO and YCZO gels. However, the time taken for the formation of the clear YCZO sol is less than that taken to form the YZO sol. Moreover, the transparency is higher for the YCZO than for the YZO system.

The cerium and yttrium ions are mixed in the form of their respective nitrate salts. The nature of the dopants in the zirconyl oxalate gel structure is not clearly understood. As Tohge *et al.*[24] suggested for glasses, here also we can think of the dopants as being uniformly distributed on the pore surface of the zirconyl gel structure; during calcination the dopant ions are substituted for zirconium ions in the crystal structure which favours the formation of the stabilized zirconia.

Although many forces are active in the solutions,[25] a possible qualitative explanation for the disappearance of the white flocculates at the beginning stage, the formation of the white thick gel at the middle stage and the clear sol at the final stage can be given by means of DLVO theory based on Refs 25 and 26. Conveniently, the existence of these three stages may be classified as follows: (1) the initial stage where the formed white flocculates disappear immediately after the oxalic acid is added to the mixed salt solutions; (2) the intermediate stage where the continued addition of oxalic acid to the combined solution of salts gives white flocculates which, instead of disappearing, lead to the formation of a white thick gel; and (3) the final stage where the observed white thick gel is slowly transformed to a clear transparent sol by continuously stirring/shaking.

It may be considered that the hydrochloric acid formed according to the following equation, which is for the preparation of pure zirconyl oxalate gel,[27] is one of the reasons for the coagulation and formation of the thick gel:

$$ZrOCl_2 + H_2C_2O_4 \rightarrow ZrOC_2O_4 + 2HCl \quad (1)$$

According to the DLVO theory, a potential energy barrier exists between two colloidal particles. Depending on the magnitude of the barrier, particles may be either coagulated or dispersed. The total potential energy of the interaction between two particles can be described by:

$$V_t = \frac{-\chi r}{12H} + 2\pi\epsilon r\psi_0^2 \exp(-\kappa H) \quad (2)$$

where H = inter-particle separation, ϵ = dielectric permitivity of the liquid medium, ψ_0 = surface potential and κ = Debye–Huckel parameter, given by

$$\kappa = ez\sqrt{\frac{n}{KT\epsilon}}$$

with K = Boltzmann constant, T = temperature, e = charge of an electron, z = number of charges on a particle and n = number of particles per unit volume.

From eqn (2), the energy barrier, V_b, can be derived as:

$$V_b = \frac{-\chi\kappa r}{12} + 2\pi\epsilon r\psi_0^2 \quad (3)$$

where r = particle diameter and χ = Hamaker constant. From eqn (3) it is clear that the energy

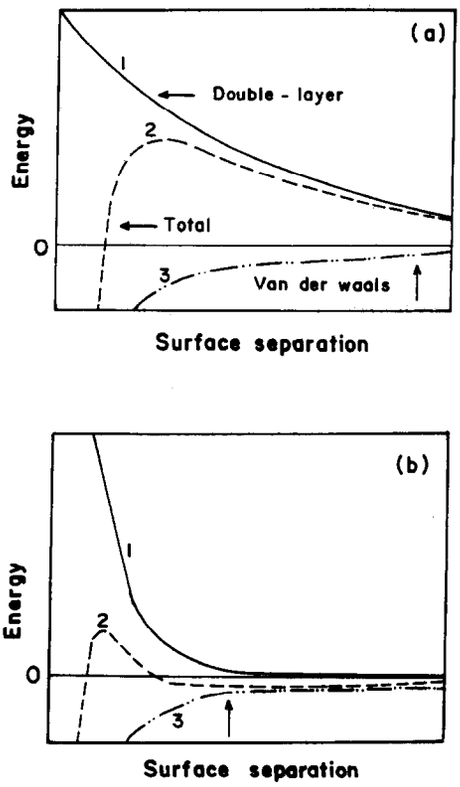

Fig. 1. Schematic plots of the energy of interaction between two surfaces across a polar liquid. Electrical double-layer repulsion gives a positive contribution which decreases exponentially as surface separation increases (line 1); van der Waals' attraction gives a negative term which is an inverse power-law function of separation (line 3). The net energy (line 2) is given by the sum of these two.[25]

barrier decreases when the dielectric constant of the medium decreases. When the oxalic acid is added to the mixed aqueous solutions of zirconyl chloride and yttrium or cerium nitrate, the dielectric constant of the total system may be decreased due to the formation of hydrochloric acid, so that the formed white flocculates disappear immediately. This may be due to the thickness of the electrical double layer, which is explained on the basis of Fig. 1.

As shown in Fig. 1(a), at low electrolytic concentration the double-layer term dominates at large separations, giving a maximum in the energy. The height of this energy barrier depends on the surface charge density and the electrolyte concentration. On the basis of the reaction it is clear that 2 moles of hydrochloric acid are formed for the addition of 1 mole of oxalic acid with zirconyl chloride. Considering the entire solution system, at the beginning stage, the addition of a small amount of oxalic acid to zirconyl chloride gives only a small amount of hydrochloric acid. This may result in a very small decrease in the dielectric constant and hence the formed flocculates disappear.

As the addition of oxalic acid to zirconyl chloride solution continues, more hydrochloric acid is formed which causes a further decrease in the dielectric constant of the system. Although the like ionic repulsion is more, the particles collide with sufficient kinetic energy which is greater than the repulsion and hence they can stick together to give thick colloidal gel. Similar observations have been reported by Li and Messing[28] in the preparation of spherical zirconia particles.

It can be seen from Fig. 1(b) that, at higher concentrations, the double-layer term may decay so rapidly that the van der Waals' attraction is still significant at a separation beyond the range of the repulsion, and the particles can reside in a secondary minimum [arrow in Fig. 1(b)]. This gives a much weaker attraction, which could easily be overcome by shear. According to this, if the formed gel is continuously stirred/shaken, the thick-white gel will slowly disappear and give a clear sol.

3.2 Crystallization behaviour

To study the crystalline nature of the prepared dried gel powders and calcined powders, X-ray diffraction analysis has been carried out. Figures 2 and 3 show the XRD patterns for the dried and calcined powders of YZO and YCZO gels, respectively, calcined at different temperatures for 1 h. Both powders, dried at 40°C, are amorphous. At 460°C, the powders start to crystallize in tetragonal phase. For calcination temperatures of 600°C and above, retention of the tetragonal phase has been observed for both systems. The increased crystallite size is reflected in Figs 2 and 3 as the decrease in the width of the spectral lines.

To identify whether the formed phase is tetragonal or cubic, higher-angle XRD patterns (insert in Figs 2 and 3) have been recorded for both powders calcined at 850°C for 1 h. From the insert in the figures, it is observed that both tetragonal and cubic phases are present. These are identified from the reflections $(0\,0\,4)_t$, $(0\,0\,4)_c$ and $(4\,0\,0)_t$.

3.3 Thermal analysis

TGA and DTA studies were carried out to analyse the weight loss and phase transition behaviour of the dried YZO and YCZO gels (for all curves, heating rate = 10°C min^{-1} and atmosphere = air). Figure 4 shows the TGA curve for the dried YZO gel powder in the temperature range 30 to 800°C. It can be observed that there are three major weight losses of 17·91, 12·22 and 19·74%. The first weight loss corresponds to the removal of water

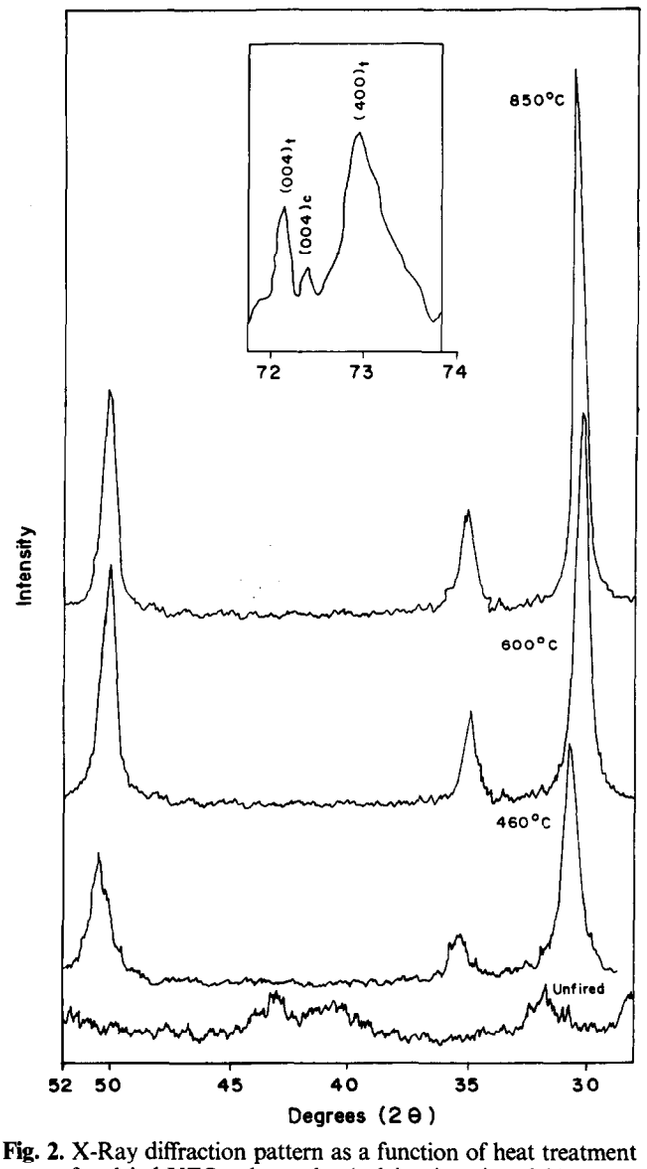

Fig. 2. X-Ray diffraction pattern as a function of heat treatment for dried YZO gel powder (calcination time 1 h).

and the next one is due to the decomposition of the nitrate. The last weight loss may be due to the decomposition of oxalate with the simultaneous formation of amorphous and tetragonal zirconia powder. Two more weight losses of 1·48 and 2·80% have also been observed. These losses may be due to the liberation of adsorbed/occluded chlorides in the dried gel powder.

Figure 5 shows the DTA curve of the dried YZO gel powder, in which two endothermic and an exothermic peaks are observed. The endothermic peak around 170°C is due to the removal of adsorbed water as observed in the TGA curve. A small endothermic peak around 250°C is observed which may be due to the removal of structural hydroxyl groups, and is not resolved even in the DTG curve. The existence and removal of the hydroxyl group has been confirmed by IR spectra for the samples collected at their peak temperatures, 170 and 250°C, respectively. The decomposition of nitrate has not been well resolved in the DTA curve. The shoulder around 285°C in the second broad endothermic peak may be due to the decomposition of nitrates, which is clearly identified in the TGA curve. The endothermic peak around 345°C may be attributed to the decomposition of oxalate as observed in the TGA curve. The oxalate decomposition step starts before complete decomposition of the nitrate. The exothermic peak around 467°C is due to the crystallization of amorphous oxide powder in tetragonal phase.

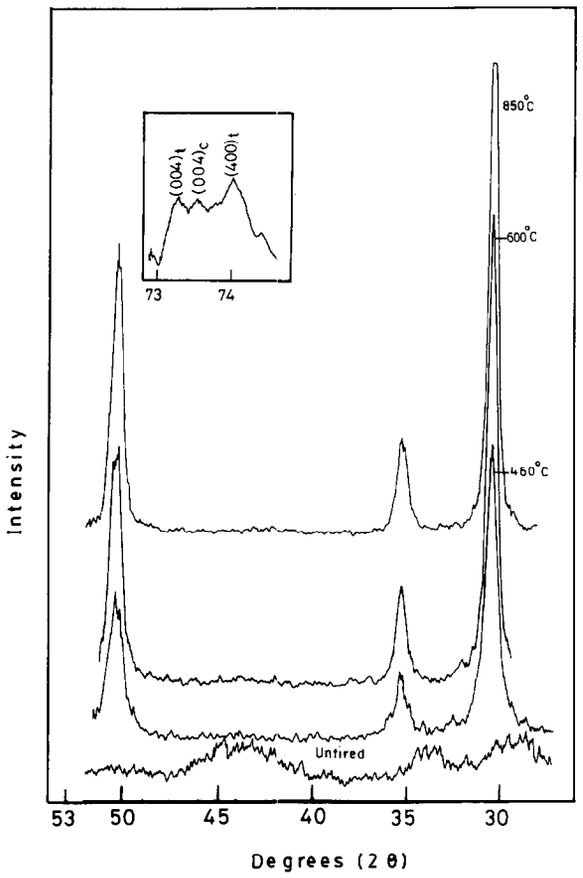

Fig. 3. X-ray diffraction pattern as a function of heat treatment for dried YCZO gel powder (calcination time 1 h).

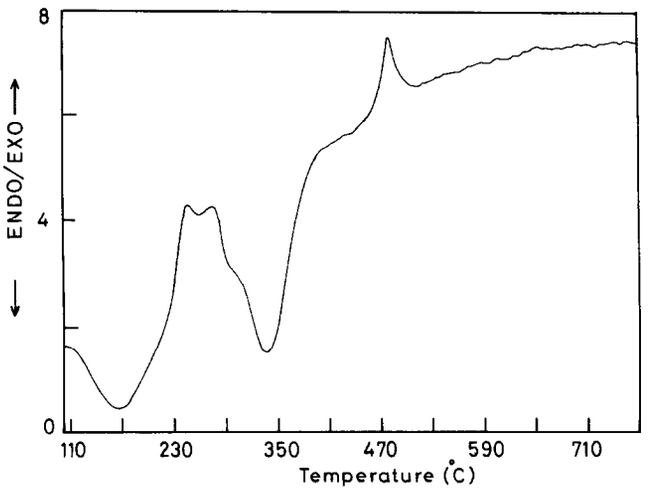

Fig. 5. DTA curve for the YZO gel powder dried at 40°C.

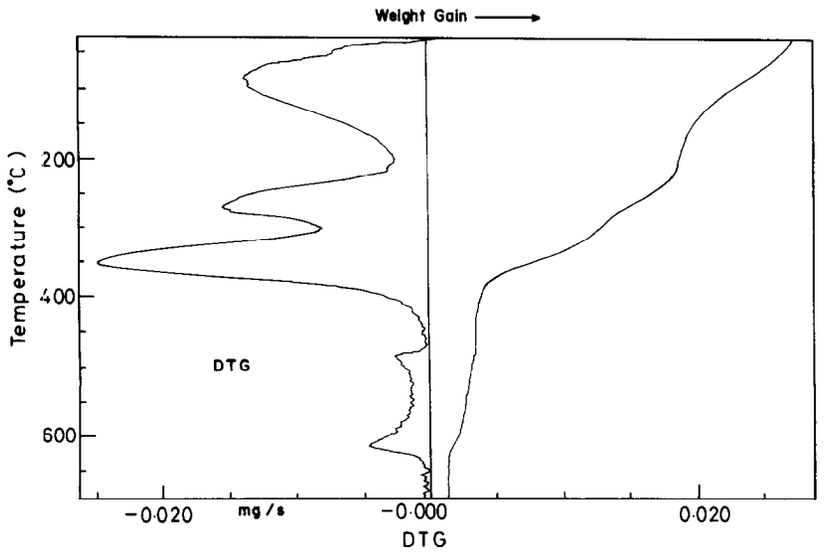

Fig. 4. TGA curve for the YZO gel powder dried at 40°C.

This is confirmed by the X-ray diffractogram (Fig. 2) for the sample that has been isothermally heat-treated at 460°C for 1 h. The liberation of chlorides has not been observed in the DTA curve, which may be due to the smooth release of the same.

From the TGA curve (Fig. 6) of the dried YCZO gel powders, it is clear that there are three major weight losses of 18·83, 17·64 and 12·9%. The first is due to the removal of adsorbed water and the second corresponds to the decomposition of nitrate. The third weight loss may be due to the decomposition of oxalate.

Although nitrate and oxalate decompositions seem to be single step, the oxalate step is actually a double decomposition. The first partial oxalate decomposition overlaps with the nitrate decomposition. This is not resolved by the TGA or the DTG curves. The second oxalate decomposition step occurred in the temperature range 289 to 462°C.

There are two more small weight losses observed in the temperature range 470 to 640°C. These may be attributed to the smooth release of adsorbed/occluded chloride and residual carbon dioxide, respectively.

It can be seen from Fig. 7, the DTA curve for the dried YCZO gel powder, that there are one endothermic and three exothermic peaks corresponding to

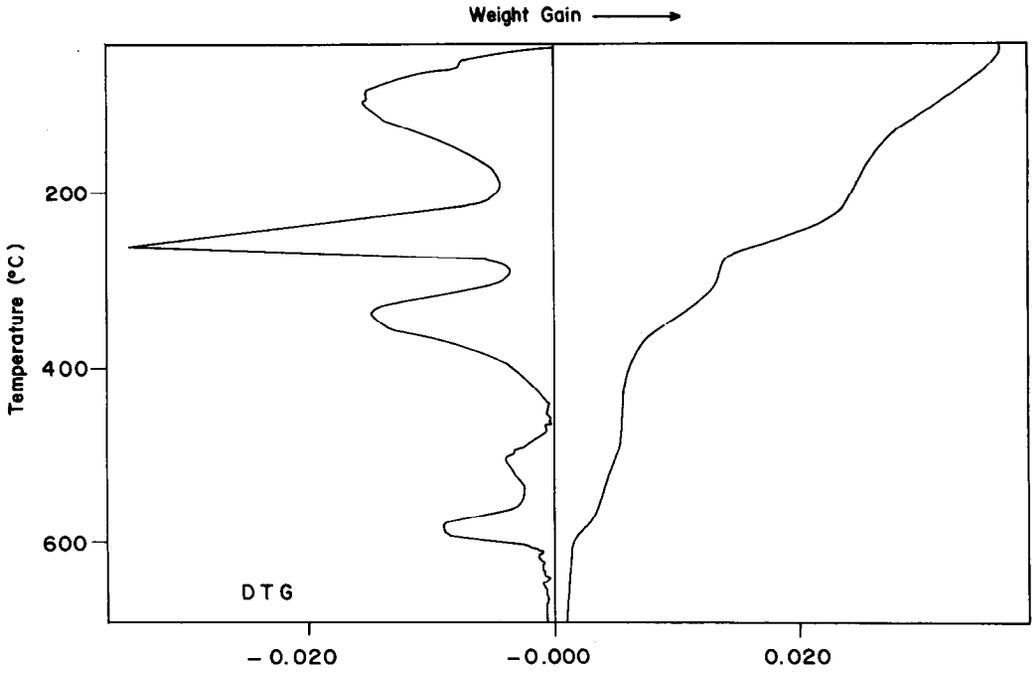

Fig. 6. TGA curve for the YCZO gel powder dried at 40°C.

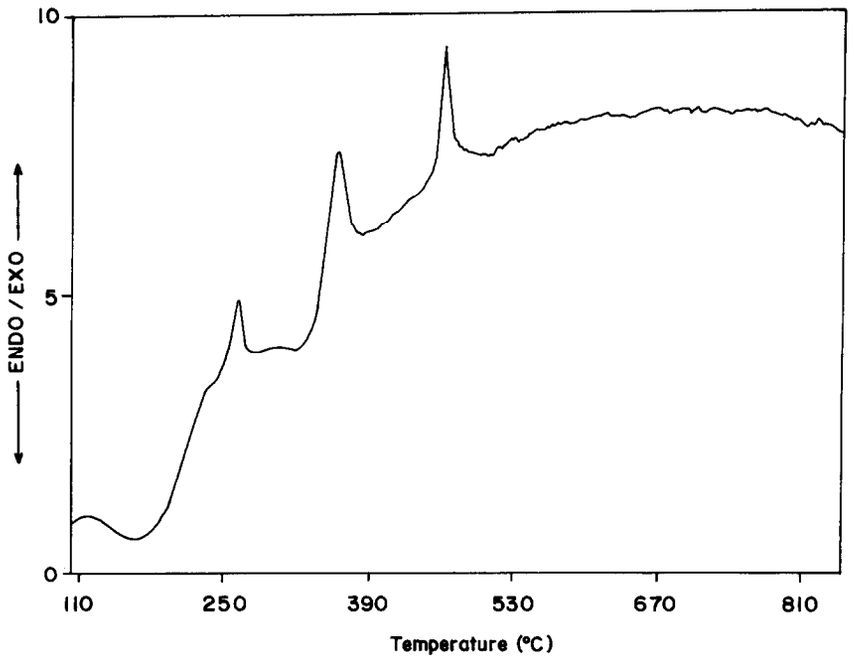

Fig. 7. DTA curve for the YCZO gel powder dried at 40°C.

temperatures around 170, 270, 340 and 470°C, respectively. The endothermic peak around 170°C is due to the removal of physisorbed water, as observed in the TGA curve. As observed in the TGA curve, the burning and release of nitrate occurred at around 270°C. The peak around 340°C may be attributed to the decomposition of oxalate, which has also been observed in the TGA curve. It can be seen that the decomposition of oxalate is not resolved by the DTA curve also. The exothermic peak around 470°C is due to the crystallization of amorphous YCZO powder in tetragonal phase with the simultaneous release of chlorides. The formation of tetragonal phase has clearly been confirmed by the X-ray diffraction patterns (Fig. 3) for the sample which was isothermally heat-treated at 460°C for 1 h. The liberation of chloride and carbon dioxide has not been observed explicitly in the DTA curve.

It is quite interesting to note that all the decomposition steps, for the dried YCZO gel powder, are exothermic in nature (except for water removal) whereas endothermic peaks have been observed for the dried YZO gel powder. The observed difference in the decomposition nature of these compounds lies in the presence of cerium ions. In our previous work.[29] we reported the exothermic decomposition of ceria–zirconia amorphous precursor powders. Accordingly, during the decomposition step, Ce^{3+} ions oxidize to Ce^{4+} ions. By considering the ionic radius, the possibility of substitution of the Ce^{3+} ions into the ZrO_2 crystal structure is highly remote at low temperatures and hence the only chance is the formation of Ce^{4+} ions due to the oxidation of Ce^{3+} ions. These Ce^{4+} ions substitute for Zr^{4+} ions in the ZrO_2 crystal structure and favour the formation of tetragonal solid solution. However, in reducing atmospheres at temperatures above 1200°C, the formation of $Ce_2Zr_2O_7$ has also been reported.[30] But the X-ray diffraction patterns (Fig. 3) do not show the existence of Ce_2O_3 reflections. This shows, conclusively, that the observed exothermic peaks are due to the exothermic oxidation of dried YCZO gel powder.

3.4 Preparation of concentrated sol

The preparation method of sol 1 (for both YZO and YCZO) has been clearly discussed in an earlier section. The gel that was formed by the gelation of sol 1 was oven-dried at 40°C. The gel powder obtained from the dried gel was slowly added to water with continuous stirring. The powder slowly dissolved in water giving a more clear sol, namely sol 2, than sol 1. The quantity of water taken for the preparation of sol 2 is the same as that for sol 1. This process was repeated a number of times. As given in eqn (1), the hydrochloric acid formed during the reaction of the reactants plays an important role for the repeptization of the dried gel powder and the formation of a more clear gel by sol 2. Along with the chloride ions the nitrate ions are also responsible for the repeptization of the dried gel powder. The adsorption of the positive charges on the surfaces of the particles may be the reason for the repeptization of the dried gel powder. The different stages of the gelation and cycling processes are given in the following chart.

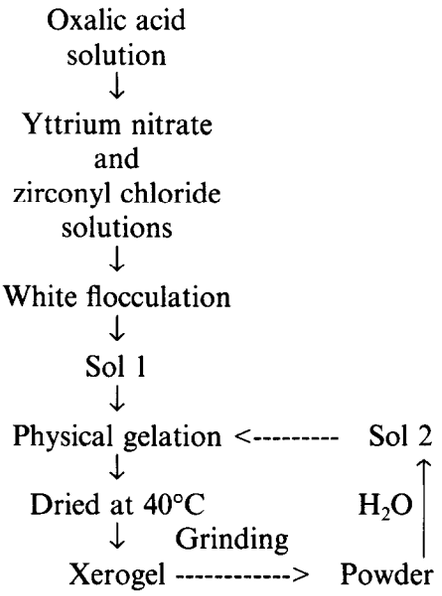

The gelation time as a function of chloride ion concentration for sol 1 and sol 2 is shown

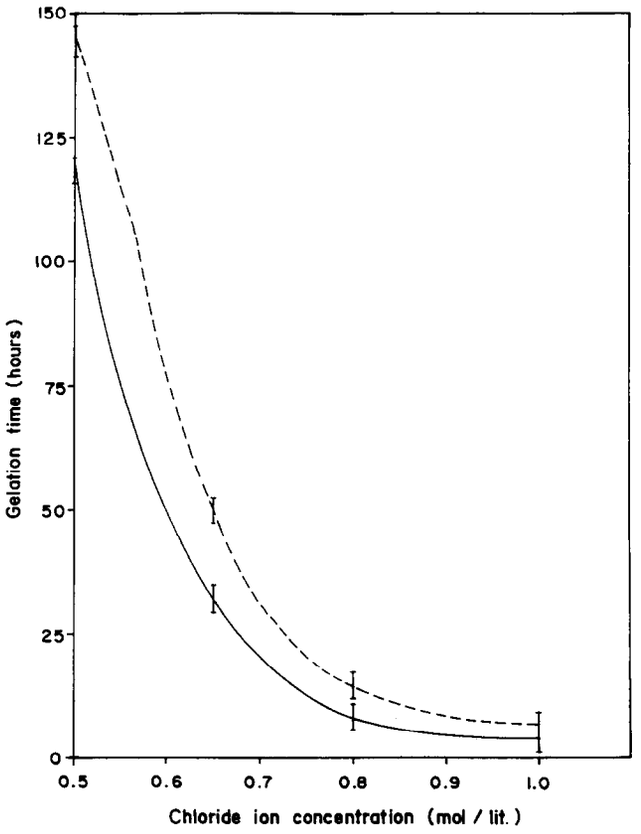

Fig. 8. Gelation time as a function of concentration of chloride ion for sol 1 —, YZO system; – – –, YCZO system.

in Figs 8 and 9, respectively. It is found that, for sol 1, the gelation time has exponential character with the concentration of the chloride ion whereas for sol 2 the character is linear. As the concentration of the oxide powder (chloride ion) increases, the gelation time decreases. The concentration of the chloride ions in sol 2 has been estimated using Volhard's volumetric method. The gelation time has been calculated as the time taken from the formation of the clear sol to the gelation point. The approximate gelation point was that time at which the semi-rigid mass did not come out of the beaker while tilting it.

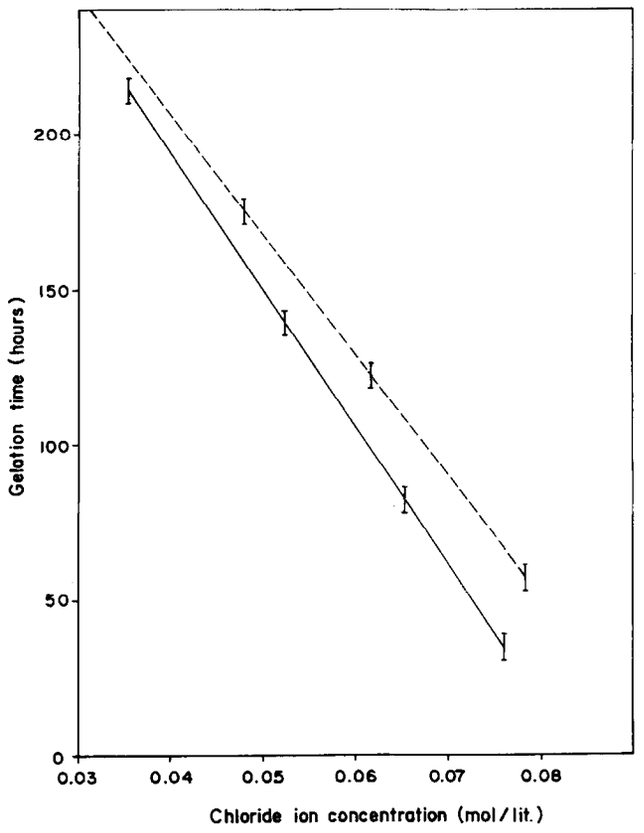

Fig. 9. Gelation time as a function of concentration of chloride ion for sol 2 —, YZO system; – – –, YCZO system.

It is possible to increase the concentration of the oxide powder in the sol using the dried gel powders. Sol 1 of YZO and YCZO contains 5·81 wt% and 6·17 wt% of their respective oxide powders. For the same wt% of the respective powders, the gelation time for the repeptized sol 2 is higher than that of sol 1. This may be due to removal of the excess of hydrochloric acid that was formed during reaction of the reactants. It has been observed that the wt% of the oxide powder can be increased up to 10 wt% for the YCZO powder in sol 2, whereas the wt% of YZO in sol 2 cannot be increased because of its highly viscous nature. There is a difference in gelation times observed for sol 2 of YZO and YCZO. This may be due to the observed difference in the viscous nature of their respective repeptized sols.

Viscosimetric studies were carried out to study the viscous nature of the sols. Immediately after the formation of clear sol 1, the observed viscosity is almost the same as that of water. The viscosity is approximately 16000 mPa s after 15 min for sol 1 of YZO, whereas for sol 1 of YCZO the same value of viscosity is observed after 40 min. However, as observed for sol 1, the rate of increase of viscosity is more for sol 2 of YZO than for sol 2 of the YCZO system.

The large difference observed in gelation time for sols 1 and 2 arises from the total concentration of ions. In the repeptized sol, due to removal

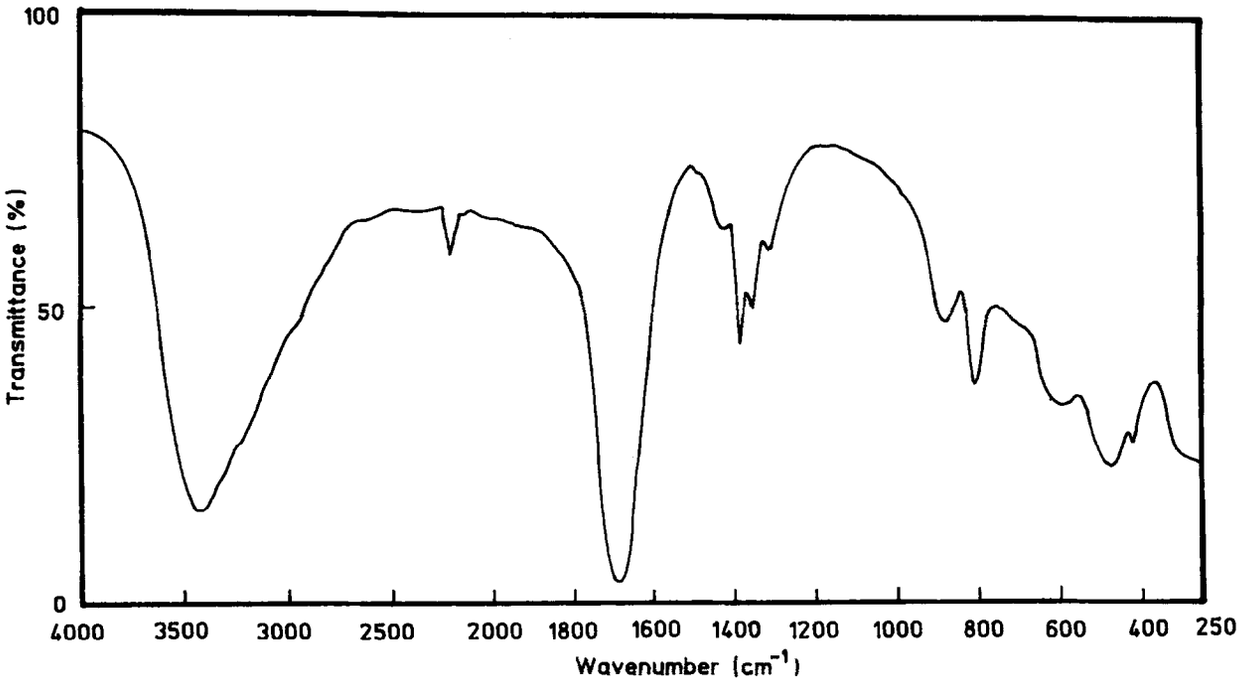

Fig. 10. IR spectrum for the YZO gel powder dried at 40°C.

of the excess hydrochloric acid during drying, the total concentration of ions in sol 2 is reduced and hence the thickness of the electrical double layer is increased.

3.5 IR characterization

Figures 10 and 11 show the IR spectra for the YZO and YCZO powders dried at 40°C. It has been reported that the oxalate ion has a quadridentate structure with the zirconium ion.[27] It seems that the addition of yttrium and cerium ions as their nitrates does not affect the structure of the zirconyl oxalate. Compared with our earlier results,[29] the appearance of the peak at 1390 cm^{-1} is due to the presence of nitrates in the dried oxalate gel powder. On calcination of the dried gel powders, the removal of water and decomposition of nitrate and oxalate are observed, as indicated from the TGA and DTA results. As mentioned before in the DTA results of the dried YZO gel powder, the small peak around 250°C is due to the removal of the hydroxyl group as confirmed from the IR spectrum taken for the sample collected at this peak temperature. Table 1 shows the vibrational frequencies of the dried powders of the YZO and YCZO gels.

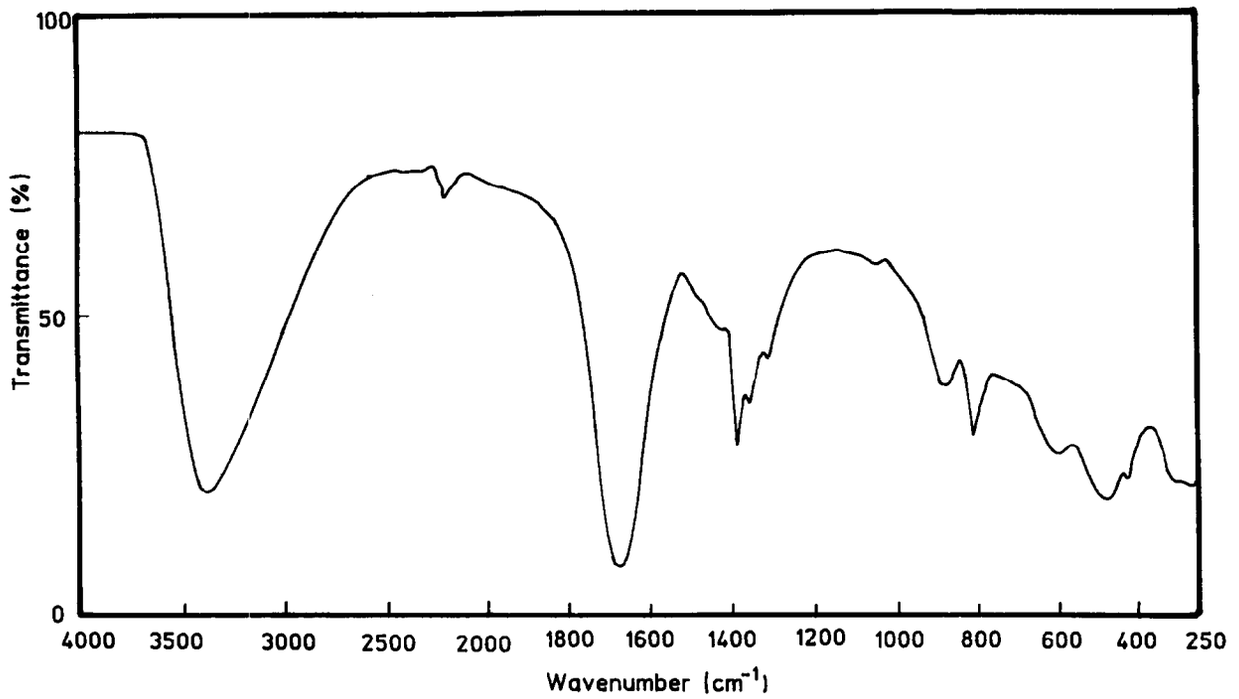

Fig. 11. IR spectrum for the YCZO gel powder dried at 40°C.

Table 1. Assignment of IR bands

Vibrational frequency (cm^{-1})			*Group*
CZO[a] (Ref. 29)	*YZO*	*YCZO*	
1680	1670	1670	ν_{as} (C=O)
1425	1420	1420	ν_s (C–O) + ν (C–C)
1390	1380	1835	$(NO_3)^-$
1355	1350	1355	ν_s (C–O) + δ (O–C=O)
900	880	885	ν_s (C–O) + δ (O–C=O)
815	805	805	ν(Zr–O) + δ (O–C=O)
480	470	475	(Zr–O–Zr)

[a] CZO is the cerium–zirconyl oxalate dried gel powder.

Table 2. Variation of surface area as a function of temperature, measured by BET technique

	YZO			*YCZO*		
Firing temperature (°C)	460	600	850	460	600	850
Specific area ($m^2 g^{-1}$)	34	23	5	35	27	6
Average crystallite size (nm)	24	32	112	23	27	114

3.6 Surface area measurement

Specific surface area has been estimated for the YZO and YCZO powders using the BET technique with nitrogen. The dried gel powders were calcined at different temperatures such as 460, 600 and 850°C for 1 h. Assuming the prepared calcined powder particles to be spherical in shape, the average crystallite sizes of the powders have been calculated. From Table 2 it is found that the surface area of the calcined powders decreases as the calcination temperature increases, due to the increase of the crystallite size.

4 Conclusion

Transparent, physical and thixotropic YZO and YCZO gels have been prepared by oxalate

gelation. A possible explanation has been presented for the various stages of gel formation by means of DLVO theory. Because of the repeptizable character, it is possible to prepare concentrated sols. DTA studies show the YZO and YCZO dried amorphous gel powders are crystallized in the tetragonal phase around 470°C. This has been confirmed by powder X-ray diffraction studies. These amorphous dried gel powders may be useful for the preparation of the fine tetragonal zirconia polycrystalline powders.

Acknowledgements

The authors acknowledge the interest shown by Professor F. D. Gnanam, Alagappa College of Technology, Anna University, Professor T. Nagarajan, Head, and thank Dr V. Sridharan, Department of Nuclear Physics, University of Madras, for the thermal analysis experiments. One of the authors (T. S.) thanks the Council of Scientific and Industrial Research, Government of India for providing a fellowship to carry out this work.

References

1. Garvie, R. C., Hannink, R. H. & Pascoe, R. T., Ceramic steel? *Nature*, **258** (1975) 703–5.
2. Gupta, T. K., Bechtold, R. C., Kuznicki, C. L. H. & Rossing, B. R., Stabilization of tetragonal phase in polycrystalline zirconia. *J. Mater. Sci.*, **12** (1977) 2421–6.
3. Gupta T. K., Lange F. F. & Bechtold, T. H., Effect of stress-induced phase transformation on the properties of polycrystalline zirconia containing metastable tetragonal phase. *J. Mater. Sci.*, **13** (1978) 1464–70.
4. Wenzel, J., Trends in sol–gel processing: toward 2004. *J. Non-Cryst. Solids*, **73** (1985) 693–9.
5. Dislich, H., Sol–gel: science, processes and product. *J. Non-Cryst. Solids*, **80** (1986) 115–21.
6. Wilson, G. & Heathcote, R., Role of sol–gel powders in thermal-spray process. *Bull. Am. Ceram. Soc.*, **69** (1990) 1137–9.
7. Mazdiyasni, K. S., Lynch, C. T. & Smith II, J. S., Cubic phase stabilization of translucent yttria–zirconia at very low temperature. *J. Am. Ceram. Soc.*, **50** (1967) 532–7.
8. Uchiyama, K., Ogihara, T., Ikemoto, T., Mizutani, N. & Kato, M., Preparation of monodispersed Y-doped ZrO_2 powders. *J. Mater. Sci.*, **22** (1987) 4343–7.
9. Aiken, B., Hsu, W. P. & Matijevic, E., Preparation and properties of uniform mixed and coated colloidal particles. *J.Mater. Sci.*, **25** (1990) 1886–94.
10. Groot Zevert, W. F. M., Winnubst, A. J. A., Theunissen, G. S. A. M. & Burggraaf, A. J., Powder preparation and compaction behaviour of fine-grained yttria doped tetragonal zirconia polycrystals (Y-TZP). *J. Mater. Sci.*, **25** (1990) 3449–55.
11. Wen, T. L., Hebert, V., Vilminot, S. & Bernier, J. C., Preparation of nanosized yttria-stabilized zirconia powders and their characterization. *J. Mater. Sci.*, **26** (1991) 3787–91.
12. Bourell, D. L., Parimal & Kaysser, W., Sol–gel synthesis of nanophase yttria-stabilized tetragonal zirconia and densification behavior below 1600 K. *J. Am. Ceram. Soc.*, **76** (1993) 705–11.
13. Samdi, A., Durand, B., Daoudi, A., Chassagneux, F., Deloume, J. P., Taha, M., Paletlo, J. & Fantozzi, G., Influence of formation pH and grinding of precursors on compaction and sintering behaviours of 3 mol% Y_2O_3–ZrO_2. *J. Eur. Ceram. Soc.*, **114** (1994) 131–41.
14. Xiaming, D., Qingfeng, L. & Yuying, T., Study of phase formation in spray pyrolysis of ZrO_2 and ZrO_2–Y_2O_3 powders. *J. Am. Ceram. Soc.*, **76** (1993) 760–2.
15. Kobayashi K., Kuwajima, H. & Masaki, T., Phase change and mechanical properties of ZrO_2–Y_2O_3 solid electrolyte after aging. *Solid State Ionics*, **3–4** (1981) 489–93.
16. Sato, T. & Shimada, M. Crystalline phase change in yttria partially stabilized zirconia by low temperature annealing. *J. Am. Ceram. Soc.*, **67** (1984) C212–3.
17. Sato, T. & Shimada, M., Transformation of yttria doped tetragonal ZrO_2 crystals by annealing in water. *J. Am. Ceram. Soc.*, **68** (1985) 356–9.
18. Sato T., Ohtaki, S. & Shimada, M., Transformation of yttria partially stabilized zirconia by low temperature annealing in air. *J. Mater. Sci.*, **20** (1985) 1466–70.
19. Hernandez, T. M., Jurado, R. J., Duran, P. & Fierro, J. L. G., Subeutectoid degradation of yttria-stabilized tetragonal zirconia polycrystal and ceria-doped yttria-stabilized tetragonal zirconia polycrystal ceramics. *J. Am. Ceram. Soc.*, **74** (1991) 1254–8.
20. Duh, J. G., Dai, H. T. & Chiou, S. B., Sintering, microstructure, hardness, and fracture toughness behaviour of Y_2O_3–CeO_2–ZrO_2. *J. Am. Ceram. Soc.*, **71** (1988) 813–19.
21. Tsukuma, K. & Shimada, M., Strength, fracture toughness and Vickers hardness of CeO_2-stabilized tetragonal ZrO_2 polycrystals (Ce-TZP). *J. Mater. Sci.*, **20** (1985) 1178–84.
22. Leach, C. & Khan, N., Stability of zirconia–ceria–yttria ceramics in hostile environments. *J. Mater. Sci.*, **26** (1991) 2026–30.
23. Hirano, M., Inhibition of low temperature degradation of tetragonal zirconia ceramics — a review. *Br. Ceram. Trans. J.*, **91** (1992) 147–50.
24. Tohge, N., Moore, G. S. & Mackenzie, J. D., Structural developments during the gel to glass transition. *J. Non-Cryst. Solids*, **63** (1984) 65–103.
25. Horn, R. G., Surface forces and their action in ceramic materials. *J. Am. Ceram. Soc.*, **73** (1990) 1117–35.
26. Pottel, R., in *Water — A Comprehensive Treatise*, Vol. 3, ed. Felix Franks. 1982.
27. Etienne, J., Larbot A., Guizard, C., Cot, L. & Alary, J. A., Preparation and characterization of zirconyl oxalate gel. *J. Non-Cryst. Solids*, **125** (1990) 224–9.
28. Li, M. & Messing, L., Preparation of spherical zirconia particles by controlled coagulation in zirconia sols. In *Ceramic Transactions Vol. 12, Ceramic Powder Science III*, eds L. Messsing & H. Hausner. *Am. Ceram. Soc.*, Westerville, OH, 1990.
29. Settu, T. & Gobinathan, R., Preparation and thermal evolution of sol–gel derived zirconia and ceria–zirconia precursors. *Bull. Chem. Soc. Jpn*, **67** (1994) 1999–2005.
30. Zhu, H. Y., Hirata, T. & Muramatsu, Y., Phase separation in 12 mol% ceria-doped zirconia induced by heat treatment in H_2 and Ar. *J. Am. Ceram. Soc.*, **75** (1992) 2843–8.

Journal of the European Ceramic Society **16** (1996) 1319–1327

PII: S0955-2219(96)00063-5
0955-2219/96/$15.00

Colloidal Processing of a Mullite Matrix Material Suitable for Infiltrating Woven Fibre Preforms Using Electrophoretic Deposition

A. R. Boccaccini,[a] P. A. Trusty,[b] D. M. R. Taplin[c] & C. B. Ponton[d]

[a]School of Metallurgy and Materials, The University of Birmingham, Birmingham B15 2TT, UK
and Department of Environmental Sciences, University of Plymouth, Plymouth PL4 8AA, UK
[b]IRC in Materials for High Performance Applications, The University of Birmingham, Birmingham B15 2TT, UK
[c]Research Office, University of North London, London N7 8DB, UK
[d]School of Metallurgy and Materials and IRC in Materials for High Performance Applications, The University of Birmingham, Birmingham B15 2TT, UK

(Received 13 December 1995; revised version received 29 February 1996; accepted 14 March 1996)

Abstract

Commercially available alumina and silica precursors for the preparation of mullite ceramic via colloidal processing and viscous transient sintering have been identified, including fumed nanosize powders and colloidal suspensions. These materials were chosen due to the fact that they can be used in the form of a sol, as mullite matrix precursors, to infiltrate woven fibre preforms using electrophoretic deposition. The sintered density of the mullite matrices sintered for 2 h, at the upper temperature for fabricating SiC-fibre reinforced composites (1300°C) is only ≈90% of theoretical. However, by exploiting a viscous flow densification mechanism, it is envisaged that hot-pressing can be used to produce fully dense mullite matrix composites at the required temperatures. Additionally, using a simple pressureless sintering route, almost fully dense (98% of theoretical density) monolithic mullite has been obtained from the pre-mullite powders. A very homogeneous and fine microstructure was achieved by sintering for 5 h at a temperature of ≈1450°C.

1 Introduction

Mullite ($3A1_2O_3.2SiO_2$) has a number of desirable properties for high-temperature structural applications, such as excellent high-temperature strength and creep resistance, very good chemical and thermal stability, a low thermal expansion coefficient and high thermal shock resistance.[1] Thus, mullite is an ideal material for use as matrix in the development of ceramic matrix composites (CMCs) for engineering and structural applications at elevated temperatures. Although considerable progress has been made over the last 10 years in the synthesis and processing of monolithic mullite,[2–4] particulate-, whisker- and platelet-reinforced mullite[1,5–8] and even *in-situ* reinforced mullite matrix composites,[9] there has been much less research work on the fabrication of continuous-fibre reinforced mullite matrix composite.[10–13]

A novel approach for manufacturing SiC woven-fibre reinforced mullite has been developed recently.[14,15] It is based on the colloidal processing of mixed $A1_2O_3$ and SiO_2 sols and the infiltration of the fibre mats using a patented electrophoretic deposition (EPD) process.[16] The particular grade of SiC fibre used (Nicalon C607) possesses a carbon coating which enables the fibres to conduct electricity, and, hence, be used as an electrode in an EPD cell. There are a number of requirements, however, that the alumina and silica starting materials must fulfil in order to be useful for composite manufacture using this approach.[14] These are:

(1) Particle size in the nanometre range — for full infiltration of tightly woven fibre mats, the size of the alumina and silica particles must be in the nanometre range (<100 nm).
(2) Stability of the mixed sol — in order for both species to infiltrate the fibre mat, 'composite' heterocoagulated particles must be formed in the sol, i.e. maximum mutual attraction of silica and alumina particles must be achieved. The sol, however, must remain stable, i.e. dispersed, to allow particle mobility in the EPD cell.
(3) Mullite formation and densification at relatively low temperatures — the starting

materials should enable full densification of the mullite composition matrix at relatively low temperatures (T <1300°C), and eventually, enable the use of hot-pressing to complete the densification process.

While starting materials (for mullite production) that fulfil requirements (1) and (2)[14, 15] have been identified, further work is needed to assess whether or not these mullite precursors are capable of forming dense mullite at low temperatures.

The third condition mentioned above suggests the employment of the mullite preparation technique known as transient viscous sintering (TVS).[17] In this approach, the mullite composition matrix material remains amorphous (or weakly crystalline) up to temperatures of 1200°C to allow densification by viscous flow, and then subsequently crystallizes rapidly to yield mullite at temperatures below ≈1300°C. Densification by viscous flow has the additional advantage of allowing the use of hot-pressing, with little or no damage being caused to the fibres during pressing.

TVS has been used in the past by several authors[17–21] using different starting materials. Sacks *et al.*,[17] for example, obtained composite particles which consisted of an inner core of α-alumina and an outer coating of amorphous silica. Powder compacts prepared with these particles were sintered at relatively low temperatures (≈1300°C). The α-alumina particles used, however, had an average diameter of ≈0·2 μm, and would therefore be too large to infiltrate woven fibres using EPD.[14] The same can be said of the system studied by Shyu and Chen,[18] who used alumina particles of ≈0·1 μm. In further studies, Wang *et al.*[19,20] and Miao *et al.*[21] have used sol–gel processing for obtaining mullite ceramics via the TVS mechanism. They were successful in preparing 'composite' particles (i.e. silica-coated alumina particles) on the nanometre scale using controlled heterocoagulation of mixed sols. Owing to the low reactivity of the starting alumina and silica materials employed, however, very high temperatures (≈1550 to 1700°C) were required to complete the mullitization process. In addition, cristobalite formed at lower temperatures, which retarded the densification process. In a further paper, the same authors[22] studied the effect of green density on the densification and mullitization of powder compacts made from the 'composite' particles mentioned. They found that both the crystallization temperature of the amorphous silica layer coated on the surface of alumina powder particles and the subsequent mullitization temperature during TVS decreased with increasing green density. For relatively high green densities (70% of the theoretical), mullitization was completed at 1600°C giving 95–96% of theoretical density in the sintered compacts.[22] Thus, according to the previous results, both the nature of the alumina/silica precursors employed and the processing conditions, including the compact green density, influence the observed TVS behaviour.

In this paper we report on the TVS preparation of mullite ceramics from starting materials which are also suitable for the EPD impregnation of fibre mats and, thus, are potentially useful as matrices in CMCs. However, no deliberate effort was made to prepare the 'ideal' composite particles described above, i.e. silica-coated alumina particles. It was envisaged that the nature and particle size of the precursors selected would allow their mixing as alumina/silica clusters on a scale of approximately 5 to 50 nm which, according to the literature,[23–25] leads to substantial densification and mullitization in the temperature range between 1200 and 1300°C, as desired. This material should be able to serve as a matrix for the SiC-fibre reinforced composites under investigation,[14,26] in which the densification and mullitization stages must be completed at temperatures between ≈1250 and ≈1300°C due to the limited temperature window available for processing without damaging the fibre as explained earlier. Furthermore, the simple pressureless densification route which has been developed in the present work for the preparation of monolithic mullite may be used for fibre-reinforced composites, with the understanding, however, that hot-pressing may be necessary for full densification.

2 Experimental Procedure

2.1 Starting materials

Different commercially available silica and alumina precursors, in the form of sols or fumed nanosize powders, were used in the preliminary studies to find the optimal starting materials for the complete impregnation of fibre mats using EPD.[27] NaOH–stabilized silica sols were not selected since they are prone to crystallization and cristobalite formation at relatively low temperatures, which prevents full densification of the mullite matrix.[20] In addition, the easy availability, low cost and environmental safety of the materials have also been taken into consideration during their selection. On this basis, organometallic compounds were not considered. Thus, only commercial boehmite and ammonia-stabilized silica sols, and high-purity, fumed alumina and silica nanosize powders remain as suitable precursors. These include:

(1) Fumed amorphous silica (Aerosil OX50, Degussa Ltd, UK) — a spherical particle shape highly dispersed powder with a broad particle size distribution (10 to 100 nm) and average particle size of 40 nm. The pH range in water for achieving a stable sol using this silica was 3·8 to 4·8.
(2) Fumed amorphous silica (Aerosil 200, Degussa Ltd, UK) — a spherical particle shape, highly dispersed powder with a narrow particle size distribution and average particle size of 12 nm. The pH range in water for obtaining a stable sol of this silica was 3·6 to 4·3.
(3) Ammonia-stabilized silica sol (Nyacol 2040 NH4, Akzo-PQ, The Netherlands), containing 40 wt% solid. The pH of the as-received sol was 9 and the average particle size 20 nm.
(4) Boehmite (γ-AlOOH) sol (Remal A20, Remet Corp., USA), containing 20 wt% solid. The boehmite particles had a mean particle size of 50 nm and a fibrillar morphology. The pH of the as-received sol was 4.
(5) Fumed δ-alumina (Aluminium Oxide C, Degussa Ltd, UK) — a highly dispersed quasi-spherical particle shape alumina powder with average particle size of 13 nm. The pH in water ranged from 4·5 to 5·5.

The mixed silica/alumina sols tested are listed in Table 1, together with the pH at which they are stable.

2.2 Processing and characterization

The precursors were mixed in a proportion such that the resulting ceramic after firing would be stoichiometric mullite i.e. 72 wt% alumina – 28 wt% silica. For the preparation of sols I and II the fumed silica nanosize powders were added slowly to the boehmite sol which was stirred continually to avoid powder agglomerates forming in the mixture. Sol I was prepared successfully in this way, with a stable sol being obtained at pH ≈ 4·4. Thus, the pH of the original boehmite sol was changed only a little on the addition of the single-component fumed silica. However, when the two-component fumed silica was added to the boehmite to prepare sol II, the resultant mixture gelled immediately. This is due to the strong electrostatic attraction between the silica and alumina (boehmite) particles occurring at this pH, as discussed later. To prepare sol III, the fumed δ-alumina particles were added slowly to the silica sol whilst stirring continuously. The pH was adjusted to a value of ≈9 by adding dilute NH_3(aq) dropwise. Sol IV was prepared by adding the alumina and silica fumed nanosize particles to an aqueous solution of pH ≈ 4·8, which was stirred magnetically for 5 h; note that the δ-alumina particles were added first. Transmission electron microscopy (TEM) was employed using a JEOL 4000 FX-TEM to investigate the spatial distribution and clustering arrangements of the alumina (boehmite) and silica particles in the colloidal suspensions.

After magnetic stirring for 5 h, sols I, III and IV and the gel from sol II were all dried slowly at ≈80°C in a muffle furnace overnight. The dried gels were ground subsequently using an Al_2O_3 mortar and pestle and then sieved to obtain a powder with a nominal particle size <63 μm. The resulting powders were then used for the sintering and crystallization experiments. Green compacts (12 mm diameter; ≈7 mm high) were pressed uniaxially using two different compaction pressures (i.e. 170 and 450 MPa). The geometrical density of the green compacts was determined. These compacts were sintered for 2 h at temperatures between 900 and 1450°C in order to assess both the densification behaviour and the crystalline phase development (heating rate: 20°C min^{-1}). Powdered sintered samples were investigated by X-ray diffraction (XRD) analysis using Cu K_α radiation. Microstructural characterization was performed solely on samples of sol I. These samples were prepared by compacting the powder at 450 MPa and firing the resultant compacts at 1200°C for 2 h, followed by 5 h at 1450°C. Selected samples were prepared for reflected light optical microscopy and for scanning electron microscopy (SEM) using a JEOL 6300 SEM and a Hitachi S4000 FEG SEM. Polished samples were etched thermally to reveal the grain structure. SEM was also used to examine the fracture surfaces of fired samples. Differential

Table 1. Silica/alumina mixed colloidal suspensions investigated

Sol	*Alumina precursor*	*Silica precursor*	*Comments*
I	Remal A20	Aerosil OX 50	stable sol at pH ≈4·4
II	Remal A20	Aerosil OX 50 and Aerosil 200 in 1:1 proportion by mass	no stable sol was obtained (gelation occurred)
III	Aluminium oxide C	Nyacol 2040 NH4	stable sol at pH ≈9
IV	Aluminium oxide C	Aerosil OX50 and Aerosil 200 in 1:1 proportion by mass	stable sol at pH ≈4·8

thermal analysis (DTA) was performed on a 10 mg powdered sample of sol I, at a heating rate of 20°C min^{-1} using a Labtherm Scientific STA-780 DTA/TGA apparatus.

3 Results

Table 2 presents a summary of the X-ray diffraction analysis results for the fired samples that were compacted at a pressure of 450 MPa. Only a qualitative study of the crystallization development was conducted and so the crystalline phases are listed only in order of decreasing predominance at each temperature. The samples compacted at 170 MPa showed the same evolution of crystalline phases.

The crystallization behaviour of the samples made from sols I and II is very similar. Up to 1200°C, no mullite formation was detected. The samples from sol II did, however, show the presence of δ-alumina at 1200°C. The presence of δ-alumina in sol I at this temperature should not be ruled out. However, its content must be under the detectability limit of XRD. For sols I and II, mullite was the sole crystalline phase detected at 1300°C and above. In contrast, sol III showed the presence of cristobalite in addition to mullite at 1300°C with mullite already being formed at 1200°C in sol IV, δ-alumina and cristobalite are present at 1200°C and δ-alumina is still present at 1300°C, in addition to mullite. The XRD diffraction patterns of powder compacts made from sol I and sintered at 1200 and 1250°C for 2 h are shown in Fig. 1, indicating that between these two temperatures the mullitization reaction has taken place. The seeming presence of a halo at $2\theta = 20°$ in Fig. 1(b) could possibly indicate the presence of a trace amount of amorphous silica at 1250°C. This halo disappeared at 1300°C, however.

Figures 2(a) and 2(b) present the variation in the sintered density of the compacts as a function of the sintering temperature for the two powder compaction pressures of 170 and 450 MPa, respectively. As expected, the density increases

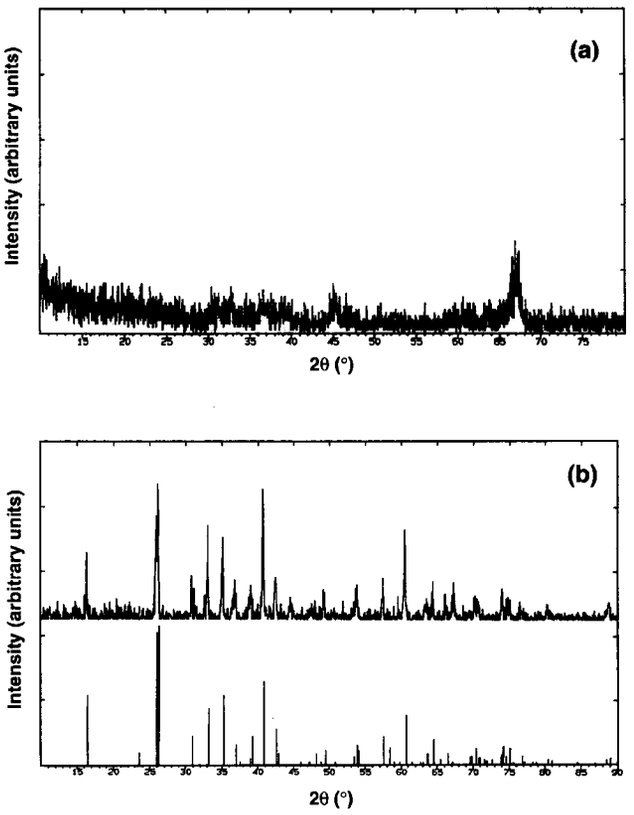

Fig. 1. XRD patterns for powder compacts made from sol I and sintered for 2 h at (a) 1200°C and (b) 1250°C, showing that mullitization has taken place within this temperature interval. (The diffraction pattern corresponding to pure mullite is also shown for comparison).

with increasing temperature. It can be seen also that using a higher powder compaction pressure has a positive effect on increasing the final sintered density, as may be expected so long as the compaction pressure is not excessive. A very high compaction pressure may lead to a decrease in the crystallization temperature of the amorphous silica, jeopardising its viscous flow behaviour, and hence, the densification of the compacts at the transient sintering temperature.[20,22]

Since sol I showed the best behaviour, in terms of both densification and crystalline phase development (according to the criteria stated in the Introduction), further in-depth study was restricted to this system.

Table 2. Crystalline phases present in the fired samples (as detected by XRD)

Sol	*Temperature (°C)*				
	900	*1100*	*1200*	*1300*	*1450*
I	—	—	—	mullite	mullite
II	—	—	δ-alumina	mullite	mullite
III	δ-alumina	δ-alumina	mullite δ-alumina cristobalite	mullite cristobalite	mullite
IV	δ-alumina	δ-alumina	δ-alumina cristobalite	mullite δ-alumina	mullite

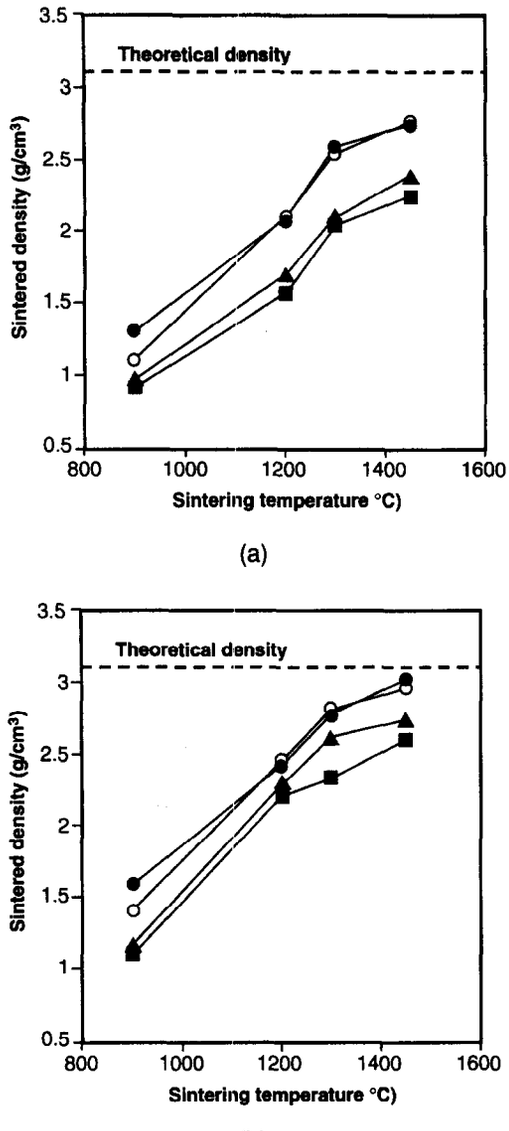

Fig. 2. Density of mullite compacts as a function of sintering temperature for two different uniaxial powder compaction pressures: (a) 170 MPa and (b) 450 MPa. Sols I, (●) II, (○) III (▲) and IV. (■).

A TEM photomicrograph of sol I is presented in Fig. 3. It shows clearly the spherical shape of the silica particles and the fibrillar nature of the boehmite sol used. The result of the DTA experiment for sol I is shown in Fig. 4. The broad exotherm between ≈200 and 500°C including the peak at ≈300°C is attributed to the removal of hydroxyl (OH) groups. The curve also exhibited an exothermic peak at ≈1360°C, which is attributed to the formation of mullite. Figure 5 shows the polished surface of a sample fired at 1200°C for 2 h, followed by 5 h at 1450°C. A polished and then thermally etched surface of the same sample is shown in Fig. 6. These micrographs show that the material is almost fully dense, with only some small isolated pores being observed occasionally. In addition, the matrix is composed of very fine equiaxed grains (grain size <≈ 1 μm). An SEM micrograph of the fracture surface of a

Fig. 3. TEM micrograph of sol I at pH ≈4·4 showing the intimate mixture on a nanometre scale of spherical silica and fibrillar boehmite particles.

sample fired at 1200°C for 2 h, followed by 5 h at 1450°C, is shown in Fig. 7; it reveals the homogeneity of the crystalline structure.

4 Discussion

On the basis of the XRD results in Table 1, sol I shows the behaviour desired for the preparation of mullite via transient viscous sintering. The material remains amorphous up to temperatures of 1200°C, allowing densification by viscous flow

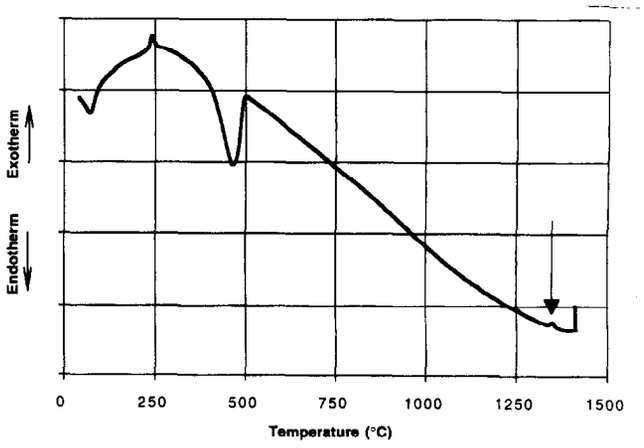

Fig. 4. DTA curve for the pre-mullite powder derived from sol I for a 20°C min^{-1} heating rate. The arrow indicates mullite formation at ≈1360°C (exothermic peak).

to take place. The mullitization process is complete at 1300°C, with no other crystalline phases being detectable using XRD. The DTA results for this material are in agreement with the XRD data. The DTA curve showed an exothermic peak at

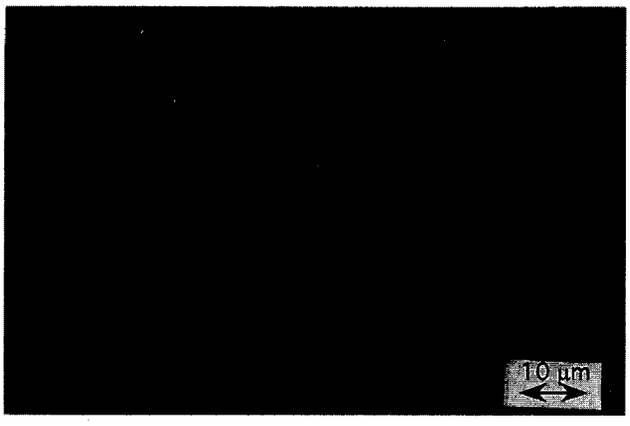

Fig. 5. Optical micrograph of a polished section of a mullite sample sintered at 1200°C for 2 h, followed by 5 h at 1450°C, showing that almost full densification was achieved.

Fig. 6. SEM micrograph of a polished and thermally etched section of a mullite sample sintered at 1200°C for 2 h, followed by 5 h at 1450°C, showing the very fine and homogeneous microstructure.

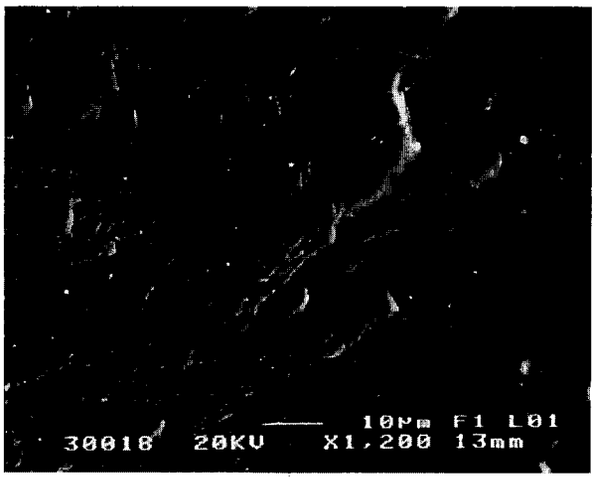

Fig. 7. SEM micrograph of the fracture surface of a mullite sample sintered at 1200°C for 2 h, followed by 5 h at 1450°C, showing the homogeneous microstructure.

≈1360°C, which is attributed to the solid-state reaction for mullite formation. The XRD data, however, showed that mullite had formed after 2 h at 1250°C. The discrepancy in these mullite formation temperatures is explained by the isothermal versus the non-isothermal (i.e. constant heating rate) conditions of the sintering and DTA experiments, respectively.

These results are in broad agreement with previous studies on the colloidal processing of mullite.[21–25] Mullite formation in alumina/silica mixtures occurs within different temperature regimes, depending on both the nature of the alumina and silica precursors and the scale of mixing achieved. As stated in the literature, when using colloidal processing, the alumina and silica precursors are present as discrete entities and any chemical reactions between them are of minimal magnitude during gelation. Only at temperatures in excess of ≈1250°C is mullite produced from a mixture of transition (pre-α) aluminas, such as δ- or θ-alumina (which are weakly crystalline), and amorphous silica.[23,24] At the pH at which sols I and II were prepared (i.e. pH ≈ 4·4), there is a strong electrostatic attraction between the negatively charged silica and the positively charged boehmite particles, as shown with reference to their zeta potential versus pH curves.[23] Thus, electrostatic attraction is expected to lead to heterocoagulation and the maximum pairing of unlike particles. This behaviour would normally be expected for both sol I and II. The reason why sol II gelled at the same pH is due to the greater number of much smaller silica particles present, since it was a 1:1 mixture of 40 nm and 12 nm average size particles, whereas sol I comprised only 40 nm average size particles. Small particles coagulate more rapidly than large particles because their double layer potential, which is responsible for interparticle repulsion, is much lower than for larger particles suspended in the same medium and, hence, flocculation and gelation can occur more readily.[28] The TEM micrograph of sol I (Fig. 3) confirms that the silica and boehmite particles are mixed intimately on a nanometre scale. It is important to note also that the DTA results for sol I do not indicate the formation of an Al–Si spinel phase at ≈960°C, which has been observed by other authors to be the transitional phase that forms prior to mullite.[4,29–31] Although a TEM characterization of all sols was not conducted, it is reasonable to assume that, due to the nature (primary particle size) of the precursors employed, the scale of alumina/silica mixing is similar for all sols investigated, being in the nanometre range. The shape of the silica- and alumina-bearing precursor particle is, however, different: spherical for the silica

precursors, fibrillar for the boehmite sol (employed in sols I and II) and spherical for the fumed δ-alumina (employed in sols III and IV). This difference in particle morphology could have led to different particle packings during gelation of the sols and consequently to the different crystallization and densification behaviour of sols I and II in comparison with sols III and IV. Moreover, the chemistry of the starting materials in terms of the impurity content and surface reactivity could probably account for such different behaviour also. While sol I and sol II, which show similar crystallization behaviour, were made by starting materials with identical chemical composition, the behaviour of sols III and IV, made from other precursor combinations, was different. Sol III, for example, showed cristobalite formation at a temperature of 1200°C. which may be a consequence of using an ammonia-stabilized silica sol. This cristobalite formation has been reported very frequently in the literature when similar silica sols were used.[21–23,32] In sols I and II cristobalite formation, which has been shown in the literature to retard viscous densification,[20,22] was suppressed by using high-purity fumed silicas. The crystallization of sol IV, producing cristobalite despite the same fumed silica having been used, may be a consequence of the poor chemical homogeneity of the starting sol, which was prepared using three fumed powders. This is in contrast to sols I and II which were prepared using two nanosized powders and one colloidal solution. Poor mixing of sol IV has probably resulted in the formation of more AA and BB type clusters than the desired AB cluster. As a consequence the silica phase has been able to transform partially to cristobalite prior to mullitization. The same degree of non-mixing to form AB type clusters probably occurred in sol III. This sol was stable at a pH about 9, at which both the silica and alumina particles are negatively charged, thus resulting in reduced heterocoagulation and hence number of AB type clusters.

The best results in terms of final sintered density for the conditions investigated here were achieved for sols I and II. The lower densification achieved with sols III and IV may be attributed to their different crystallization behaviour, as discussed above, which showed the presence of cristobalite prior to mullite formation, thus hindering the viscous flow sintering mechanism of the amorphous silica, as frequently found in the literature.[18–20] The presence of very fine silica particles ($d_{av} \approx 12$ nm) with a very narrow particle size distribution (i.e. Aerosil 200) in sol II did not affect the densification behaviour significantly in comparison with sol I, in which larger silica particles ($d_{av} \approx 40$ nm) with a broader particle size distribution were used (i.e. Aerosil OX 50). At 1200°C, according to Table 2, the material is XRD amorphous (sol I) or only weakly crystalline due to the presence of δ-Al_2O_3 (sol II), and so densification can take place via viscous flow. This indicates that the preparation of 'composite' particles by coating alumina particles with a layer of silica particles is not strictly necessary for achieving near-full densification by transient viscous sintering of the pre-mullite powder compacts prepared from the commercial precursors used in the present work. At 1300°C, the samples achieved a density of 2·84 g cm^{-3} (i.e. ≈90% of theoretical taking the theoretical density of mullite as 3·16 g cm^{-3}).[5] These densities can be improved, however, if hot-pressing is employed. It is envisaged, moreover, that when using hot-pressing for manufacturing composites, the mullite matrices derived from sols I and II may be densified fully at even lower temperatures. However, the effect of pressure on the densification and mullitization kinetics and their interaction, needs to be addressed and is the focus of current studies.

The study of the pressureless densification of compacts made from sol I powders has shown that an almost fully dense, monolithic mullite material can be obtained by sintering the green compacts at 1200°C for 2 h, followed by 5 h at 1450°C. This result is relevant for the preparation of monolithic mullite ceramics via conventional uniaxial pressing and pressureless sintering. Other authors have used much higher temperatures (up to 1700°C) to obtain dense mullite.[21,33–36] The possibility of densification by viscous flow may also be of importance for the development of dispersion-reinforced mullite ceramic composites, since an amorphous matrix sinters more easily around a dispersed reinforcement phase compared with a polycrystalline matrix.[37] In addition, the specimens sintered at 1450°C have a very fine equiaxed grain morphology, with a mean grain size of 0·8 μm. Since no elongated grains were formed, it can be concluded that there was no liquid phase formation during sintering after the viscous flow densification occurred.[38] Both the high degree of microstructural homogeneity and the fine grain size achieved suggest that the material may have interesting properties for load-bearing applications or for applications where infra-red transparency is required.[35]

5 Conclusions

Suitable commercially available alumina and silica precursors have been identified for the preparation of mullite ceramics via colloidal processing and

viscous transient sintering. These precursor materials also fulfil the requirements specified for the sol-based mullite matrix material to be used for infiltrating SiC woven fibre preforms using electrophoretic deposition. Owing to the lack of high-temperature thermal stability of the SiC fibres under investigation,[12,13] the processing temperature for manufacturing these composites is limited to ≈1300°C. At this temperature, the sintered density of the mullite matrices investigated in the present work is only ≈90% of theoretical. However, upon exploiting a viscous flow densification mechanism, it is envisaged that hot-pressing will produce fully dense mullite matrix composites at these relatively low temperatures. This is the subject of on-going studies. The simple pressureless sintering route developed using pre-mullite powders derived from sol I has demonstrated the production of dense (≈ 98% of theoretical density) monolithic mullite samples with a very fine, homogeneous microstructure at a sintering temperature of ≈1450°C.

Acknowledgements

Professors J. F. Knott and M. H. Loretto are acknowledged gratefully for the provision of laboratory facilities in the School of Metallurgy and Materials and the IRC in Materials for High Performance Applications, respectively, at The University of Birmingham. Helpful discussions with Dr E. G. Butler are also appreciated. We also thank Degussa Ltd, UK for the Aerosil material. A.R.B. acknowledges the financial support of the European Commission via contract BRE2.CT94. 3064.

References

1. *Mullite and Mullite Matrix Composites*, Ceramic Transactions. Vol. 6, eds S. Somiya, R. F. Davis & J. A. Pask. The American Ceramic Society. Inc., Westerville, OH, 1990.
2. Sacks, M. D. & Lee, H.-W., A review of powder preparation methods and densification procedures for fabricating high density mullite. *Ceram. Trans.*, **6** (1990) 167–207.
3. Aksay, I. A., Dabbs, D. M. & Sarikaya, M., Mullite for structural, electronic and optical applications. *J. Am. Ceram. Soc.*, **74** (1991) 2343–58.
4. Schneider, H., Merwin, L. & Sebald, A., Mullite formation from non-crystalline precursors. *J. Mater. Sci.*, **27** (1992) 805–12.
5. Jeng, D. & Rahaman, M. N., Effect of rigid inclusions on the sintering of mullite synthesized by sol–gel processing. *J. Mater. Sci.*, **28** (1993) 4421–6.
6. Zhou, Y., Vleugels, J., Laoui, T. & Van der Biest, O., Toughening of sol–gel derived mullite matrix by Al_2O_3 platelets. *J. Mater. Sci. Lett.*, **13** (1994) 1089–91.
7. Wu, M. & Messing, G. L., Fabrication of oriented SiC-whisker-reinforced mullite matrix composites by tape casting. *J. Am. Ceram. Soc.*, **77** (1994) 2586–692.
8. Wei, G. C. & Becher, P. F., Development of SiC-whisker-reinforced ceramic. *Am. Ceram. Soc. Bull.*, **64** (1985) 298–304.
9. Ho, C. T., In situ reacted TiB_2 reinforced mullite. *J. Mater. Sci.*, **30** (1995) 1338–42.
10. Mouchon, E. & Colomban, Ph., Oxide ceramic matrix/oxide fibre woven fabric composites exhibiting dissipative fracture behaviour. *Composites*, **26** (1995) 175–82.
11. Singh, R. N. & Gaddipati, A. R., Mechanical properties of a uniaxially reinforced mullite-silicon carbide composite. *J. Am. Ceram. Soc.*, **71** (1988) C-100–03.
12. Wu, J., Chen, M., Jones, F. R. & James, P. F., Mullite and alumina–silica matrices for composites by modified sol–gel processing. *J. Non-Cryst. Solids*, **162** (1993) 197–200.
13. Ha, J.-S. & Chawla, K. K. Mechanical behaviour of mullite composite reinforced with mullite fibres. *Mater. Sci. Eng.*, **A203** (1995) 171–6.
14. Boccaccini, A. R., Taplin, D. M. R., Butler, E. G., Marquis, P. M. & Ponton, C. B., Manufacturing of ceramic matrix composites via electrophoretic deposition. In *Proc. 4th EUROMAT Conference*, Venice/Padua, Italy, 25–28 September 1995, pp. 325–30.
15. Boccaccini, A. R. & Ponton, C. B., Processing ceramic-matrix composite using electrophoretic deposition. *J. Met.*, **47**[10] (1995) 34–7.
16. Illston, T. J., *et al.*, UK Patent 9124822.9, 1991.
17. Sacks, M. D., Bozurt, N. & Scheiffele, G. W., Fabrication of mullite and mullite-matrix composites by transient viscous sintering of composite powders. *J. Am. Ceram. Soc.*, **74** (1991) 2428–37.
18. Shyu, J.-J. & Chen, Y.-C., Zirconia–mullite ceramics made from composite particles coated with amorphous phase: I Effect of zirconia addition. *J. Mater. Res.*, **10** (1995) 63–70.
19. Wang, J., Piramoon, M. R., Ponton. C. B. & Marquis, P. M., Sol–gel processing of monolithic and composite mullite ceramics. In *Nanoceramics*, ed. R. Freer. Br. Ceram. Proc. No. 51, 117–33.
20. Wang, J., Piramoon, M. R., Ponton, C. B. & Marquis, P. M., Fabrication and microstructure–property relationships in the transiently/reaction sintered mullite composites. *Proc. Euromat 91*, eds T. W. Clyne & P. J. Withers. The Institute of Materials, Vol. 2, (1991), pp. 287–99.
21. Miao, X., Ponton, C. B. & Marquis, P. M., Production of mullite nanoceramics through controlled heterocoagulation of sols. In *Nanoceramics*, ed. R. Freer. Br. Ceram. Proc. No. 51, 1993, pp. 157–64.
22. Wang, J. G., Ponton, C. B. & Marquis, P. M., Effects of green density on crystallization and mullitization in the transiently sintered mullite. *J. Am. Ceram. Soc.*, **75** (1992) 3457–61.
23. Huling, J. C. & Messing, G. L., Surface chemistry effects on homogeneity and crystallisation of colloidal mullite sol–gels. *Ceram. Trans.*, **6** (1990) 220–8.
24. Komarneni, S. & Roy, R., Mullite derived from diphasic nanocomposite gels. *Ceram. Trans.*, **6** (1990) 209–19.
25. Huling, J. C. & Messing, G. L., Hybrid gels for homoepitactic nucleation of mullite. *J. Am. Ceram. Soc.*, **72** (1989) 1725–9.
26. Trusty, P. A., Boccaccini, A. R., Butler, E. G. & Ponton, C. B., Novel techniques for manufacturing woven fibre reinforced ceramic matrix composites. *Mater. Manuf. Processes*, **6** (1995) 1215–26.
27. Boccaccini, A. R., Engineered fibre strengthened ceramic composites: structural integrity and performance in energy conversion and processing systems. Quarterly Report), submitted to DG XII-Brussels, April 1995.
28. Clasen, R., Electrophoretic deposition of compacts of nano-sized particles. In *Science, Technology and Applications of Colloidal Suspensions, Ceram. Trans.* Vol. **54**. The American Ceramic Society, Westerville, OH, 1995, pp. 169–84.
29. Hsi, C.-S., Lu, H.-Y. & Yen, F.-S., Thermal behaviour of alumina–silica xerogels during calcination. *J. Am. Ceram. Soc.*, **72** (1989) 2208–10.

30. Okada, K. & Otsuka, N., Characterisation of the spinel phase from SiO_2–Al_2O_3 xerogels and the formation process of mullite. *J. Am. Ceram. Soc.*, **69** (1986) 652–6.
31. Okada, K. & Otsuka, N., Formation process of mullite. *Ceram. Trans.*, **6** (1990) 375–387.
32. Lee, J. S. & Yu, S. C., Mullite formation kinetics of coprecipitated Al_2O_3–SiO_2 gels. *Mater. Res. Bull.*, **27** (1992) 405–16.
33. Kanka, B. & Schneider, H., Sintering mechanisms and microstructural development of coprecipitated mullite. *J. Mater. Sci.*, **29** (1994) 1239–49.
34. Ismail, M. G., Nakai, Z. & Somiya, S., Microstructure and mechanical properties of mullite prepared by the sol–gel method. *J. Am. Ceram. Soc.*, **70** (1987) C-7–C-8.
35. Mroz, T. & Laughner, J. W., Microstructures of mullite sintered from seeded sol–gels. *J. Am. Ceram. Soc.*, **72** (1989) 508–9.
36. Hilz, G. & Ziegler, G., Reaction-sintered and reaction-hot-pressed mullite prepared from mixtures of commercial Al_2O_3- and SiO_2-powders. In *Fourth Euro Ceramics*, Vol. 4. ed. A. Bellosi. 1995, pp. 479–86.
37. Bordia, R. K. & Raj R., Analysis of sintering of a composite with a glass or ceramic matrix. *J. Am. Ceram. Soc.*, **69** (1986) C55–C57.
38. Kara, F. & Little, J. A., Sintering of pre-mullite powder obtained by chemical processing. *J. Mater. Sci.*, **28** (1993) 1323–6.

Journal of the European Ceramic Society **16** (1996) 1329–1335

PII: S0955-2219(96)00065-9
0955-2219/96/$15.00

Preparation of SiC Particles Coated with Alumina Hydrate: Effect of Reaction Condition on Particle Coalescence

H. Nakamura,[a] M. Yoshinaga,[b] S. Nagashima[b] & A. Kato[b]*

[a]Inorganic Materials Department, Kyushu National Industrial Research Institute, AIST, Shuku-machi, Tosu-shi 841, Japan
[b]Department of Chemical Science and Technology, Faculty of Engineering, Kyushu University, Fukuoka 812, Japan

(Received August 1993; revised version received 8 February 1996; accepted 28 March 1996)

Abstract

Alumina-hydrate-coated SiC particles were prepared via a homogeneous precipitation method using urea, and the conditions for uniform coating and less coalescence of the particles were investigated. Coalescence of coated particles could be said to occur by collision and agglomeration followed by deposition of alumina hydrate on the agglomerated particles. Coalescence of coated particles was suppressed by use of low reaction temperature, low concentration of aluminium sulfate, high concentration of urea, intensive stirring, and a flow reactor.
© 1996 Elsevier Science Limited

1 Introduction

Recently, composite particles in which a core particle is coated by another phase have attracted attention from various viewpoints. The main objectives of applying the coating are the improvement of chemical stability and/or surface character[1–5] and uniform addition or mixing of a second phase.[6–10] Such composite particles were also useful to improve sinterability.[11]

In the preparation of composite particles, uniform coating and suppression of particle coalescence are essential. To achieve these, fine control of the deposition rate of the second phase is necessary. Thus, many researchers have used alkoxide as a starting material for composite particles, because of the ease of control of its precipitation rate, to prevent the formation of coagulated particles. On the other hand, inorganic salts can also be used as a starting material,[12–18] mostly via the homogeneous precipitation method which is also characterized by easy control of precipitation rate.

In the preparation of composite particles from inorganic precursors with the homogeneous precipitation method, it is not easy to prevent the coalescence of particles. A number of efforts have been made to prevent the coalescence. Matijevic and co-workers prevented coalescence of particles by using dilute dispersions and/or adding surfactants.[13,14] De Jonghe and co-workers also used surfactants.[16,17] However, it is still rather difficult to prevent the coalescence, especially when coating layers are thick and dispersions are concentrated. In the present study, we prepared alumina-hydrate-coated SiC particles and investigated the effects of reaction conditions on the coalescence of composite particles. The reaction conditions investigated were reaction temperature, aluminium sulfate and urea concentrations, stirring rate, and reactor type.

2 Experimental Procedure

A batch or a flow reactor was used as a reactor (Fig. 1). SiC particles (Ibigawa Electric Industry Co., Ltd; median diameter = 0·6 μm as shown in Fig. 2) were dispersed in distilled water and then aluminium sulfate (reagent grade, Wako Pure Chemical) was dissolved in it, and followed by supersonic agitation for 15 min. The dispersion was heated to a given temperature. During heating, the dispersion was stirred (batch reactor) or was made to flow (flow reactor). Then, urea (reagent grade, Wako Pure Chemical) was added to start the reaction. The amount of reacting solution was 100 ml for the batch reactor and 250 ml for the flow reactor. During the reaction, the suspension was stirred with a wing-type stirrer (batch reactor) or circulated (flow reactor). The pH

*To whom correspondence should be addressed.

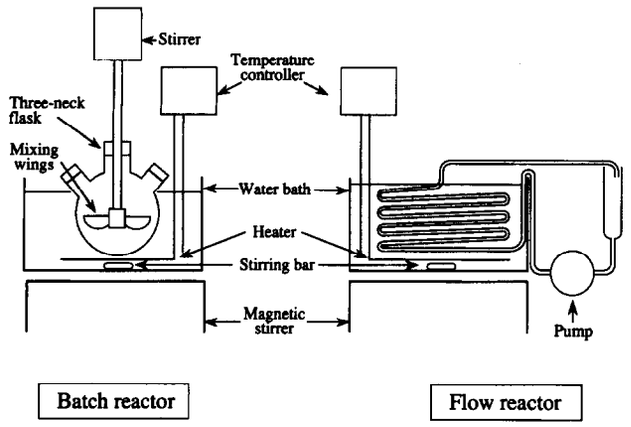

Fig. 1. Schematic illustrations of reactors.

of the dispersion was measured and the reaction was stopped at pH = 7·0, where the deposition of alumina hydrate was complete. The precipitate was filtered and washed with distilled water and finally with ethanol. The precipitate was dried *in vacuo* at 70°C. The alumina hydrate deposited was amorphous.

To evaluate the degree of coalescence of coated particles, the particle size distributions of the powders were measured. A small amount (1–2 mg) of the as-coated powder was dispersed in 5 ml of ethanol using ultrasonic agitation, and one drop of the dispersion was dropped on a glass plate for observation under a scanning electron microscope (SEM). The particle size distributions were measured from the SEM photographs. In this measurement, particles which were hardly discriminated from aggregates were omitted. The as-coated powder was also characterized using an X-ray microanalyser (XMA). Zeta-potential measurements were performed on a few samples using the electrophoresis method.

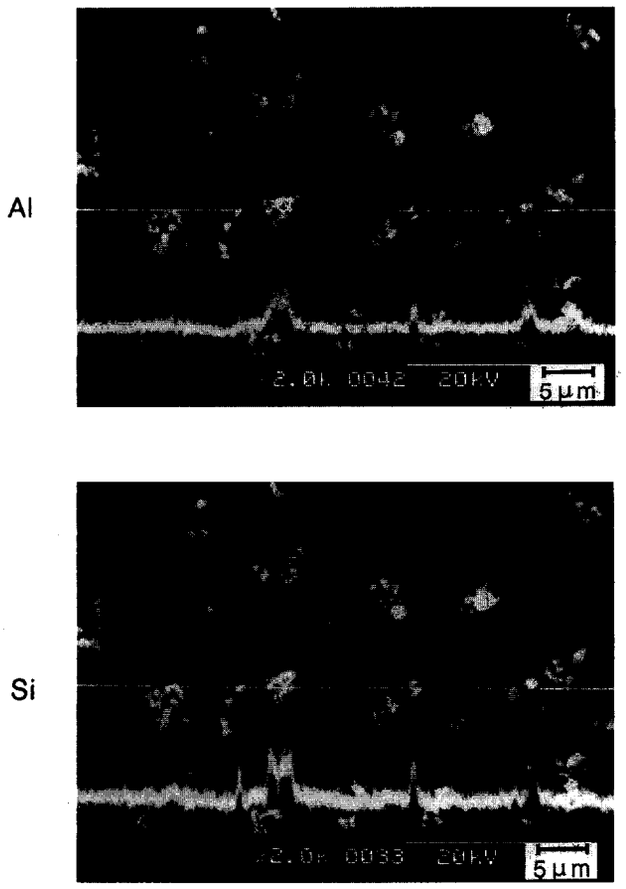

Fig. 3. Distribution of Al and Si elements. $[Al_2(SO_4)_3]$ = 0·075 mol l^{-1}, [SiC] = 9·0 g l^{-1}, [urea] = 10·8 mol l^{-1}, reaction temperature = 70°C, stirring rate = 3000 rev min^{-1}, batch reactor.

3 Results

Figure 3 shows the distributions of silicon and aluminium elements in the alumina-hydrate-coated SiC particles. Good coincidence in the distributions of both elements indicates that SiC

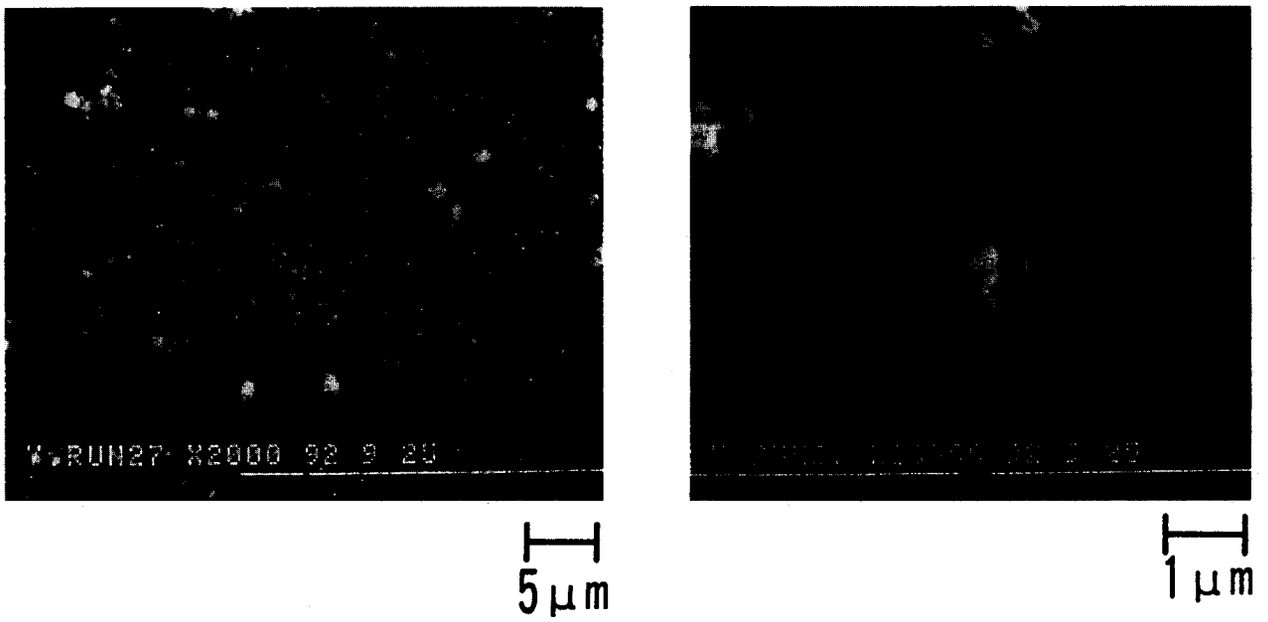

Fig. 2. SiC particles.

particles are coated uniformly with alumina hydrate and that there is little formation of separately precipitated alumina hydrate particles. Another important parameter, the degree of particle coalescence, was evaluated from the size distribution of coated particles.

3.1 Effects of reaction temperature and urea concentration on coalescence of composite particles

The deposition rate of the alumina hydrate is considered to affect the coalescence of coated particles. The deposition rate is governed by the hydrolysis rate of urea. The hydrolysis rate of urea depends on reaction temperature and concentration of urea according to the following formula.[18]

$$r = 6{\cdot}5 \times 10^{15}[\text{urea}]\exp(-1{\cdot}3 \times 10^5/RT) \quad [\text{mol l}^{-1}\ \text{min}^{-1}]$$

where [urea] is the concentration of urea (mol l^{-1}), R is the gas constant (8·31 J (mol^{-1} K^{-1})) and T is absolute temperature. The effect of deposition rate of alumina hydrate on the coalescence of composite particles was investigated by using batch reactor under different reaction temperatures and urea concentrations. Other reaction conditions were: aluminium sulfate concentration ($[Al_2(SO_4)_3]$) = 0·075 mol l^{-1}, dispersion amount of SiC particles ([SiC]) = 9·0 g l^{-1}, stirring rate = 170 rev min^{-1}. The ideal diameter of a coalescence-free composite particle for this [SiC]/[Al_2O_3] ratio was calculated to be 1·0 μm. Figure 4 shows the effect of reaction temperature under [urea] = 10·8 mol l^{-1}. The degree of coalescence decreases slightly with decrease in reaction temperature (i.e. decrease in hydrolysis rate of urea). Figure 5 shows the effect of urea concentration on the coalescence of particles. The coalescence of composite particles tends to be suppressed by increasing urea concentration.

3.2 Effect of stirring rate on coalescence of composite particles

Stirring rate was found to have a remarkable effect on the coalescence of composite particles during coating as shown in Fig. 6. The ideal diameter of a coalescence-free composite particle at the [SiC]/[Al_2O_3] ratio used is calculated as 1·0 μm. Figure 6 shows that the coalescence of composite particles is suppressed significantly under a high stirring rate above a few thousand rev min^{-1}. Particle size distributions were also measured by a laser diffraction light scattering method (MICROTRAC model 7995-30, Leeds & Northrup Instruments). A result is illustrated in Fig. 7 for the effect of stirring rate. Both Figs 6 and 7 show that SEM and the light scattering method give close results, although the size distribution curves by the latter method are shifted slightly to the finer side.

3.3 Effect of aluminium sulfate concentration on coalescence of composite particles

The concentration of aluminium sulfate also affects the coalescence of composite particles; the results are summarized in Table 1. With decreasing aluminium sulfate concentration, i.e. with decreasing thickness of alumina hydrate coating, the observed diameters of composite particles

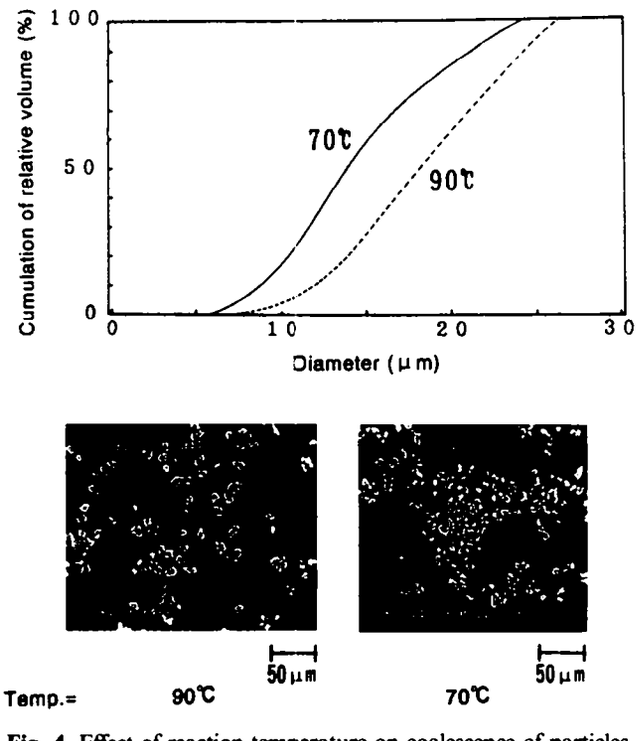

Fig. 4. Effect of reaction temperature on coalescence of particles. $[Al_2(SO_4)_3]$ = 0·075 mol l^{-1}, [SiC] = 9·0 g l^{-1}, [urea] = 10·8 mol l^{-1}, stirring rate = 170 rev min^{-1}, batch reactor.

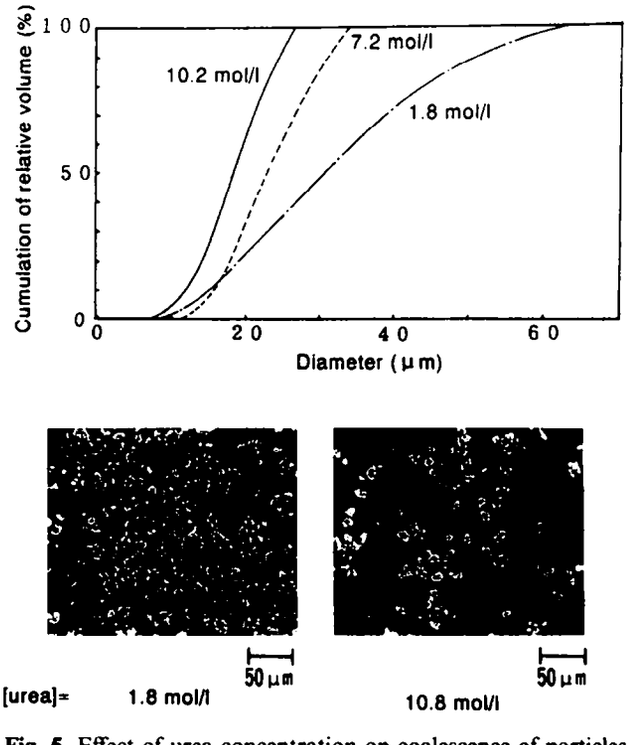

Fig. 5. Effect of urea concentration on coalescence of particles. $[Al_2(SO_4)_3]$ = 0.075 mol l^{-1}, [SiC] = 9.0 g l^{-1}, reaction temperature = 90°C, stirring rate = 170 rev min^{-1}, batch reactor.

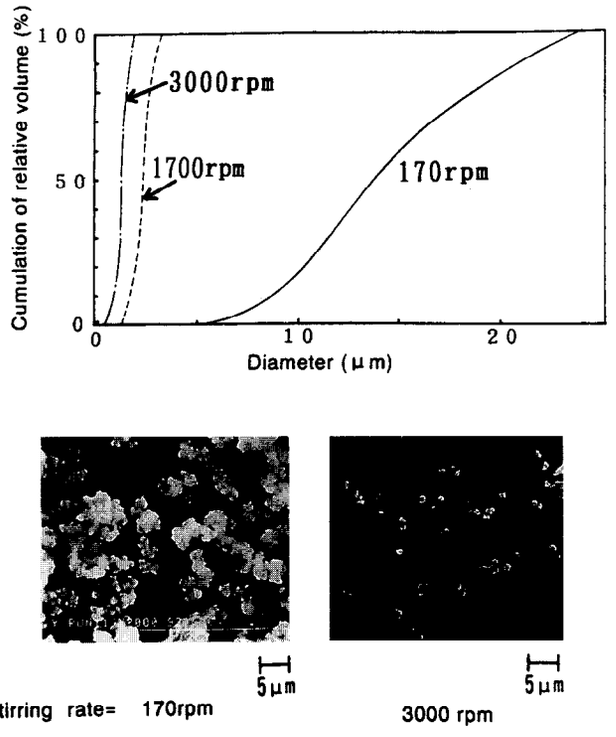

Fig. 6. Effect of stirring rate on coalescence of particles (measured from SEM photographs). $[Al_2(SO_4)_3]$ = 0·075 mol l^{-1}, [SiC] = 0·9 g l^{-1}, [urea] = 10·8 mol l^{-1}, reaction temperature = 70°C, batch reactor.

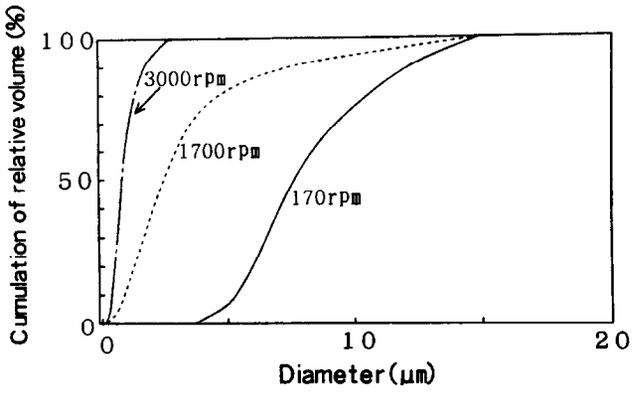

Fig. 7. Effect of stirring rate on coalescence of particles (measured by laser diffraction light scattering method). The samples measured are shown in Fig. 6.

become close to the value calculated on the assumption of no coalescence. Typical examples of composite particles are shown in Fig. 8.

3.4 Effect of reactor type on coalescence of composite particles

The results described above were obtained using the batch reactor. Composite particles were also prepared using the flow reactor shown in Fig. 1. In the flow reactor method, the reacting solution containing suspended SiC particles was circulated at a flow rate which resulted in almost laminar flow (Reynold's number was 2×10^3). As shown in Fig. 9, the flow reactor gave less coagulated particles comparable to the particles obtained at

Table 1. Ideal and median diameters of composite particles[a]

No.	*$[Al_2(SO_4)_3]$ (mol l^{-1})*	*Ideal diameter[b] (μm)*	*Median diameter (μm)*	*Median diameter/ ideal diameter*
1	0·0047	0·65	0·6	0·9
2	0·0063	0·66	1·1	1·6
3	0·0094	0·69	1·3	1·9
4	0·019	0·76	1·8	2·3
5	0·038	0·87	2·3	2·6
6	0·075	1·04	3·2	3·1

[a]Reaction conditions: [SiC] = 9·0 g l^{-1}, [urea] = 10·8 mol l^{-1}, reaction temperature = 70°C, stirring rate = 1700 rev min^{-1}, batch reactor.
[b]Ideal diameter was calculated on the assumptions: original SiC diameter = 0·6 μm, uniform coating of alumina hydrate on SiC particles, and no coalescence of composite particles.

1700 rev min^{-1} stirring rate using the batch reactor. Although further investigations are required to determine the optimum reaction condition, one can say that use of a flow reactor may aid in the preparation of coalescence-free composite particles.

4 Discussion

Coalescence of composite particles would occur by collision of coated particles followed by deposition of alumina hydrate on the agglomerates in a similar manner as in the formation of alumina-hydrate-coated SiC whiskers.[18] The coalescence process is shown schematically in Fig. 10. The coalescence may depend on the probability of formation of agglomerates and the deposition rate of alumina hydrate. The probability of formation of agglomerates is thought to be affected by the collision frequency of particles and the probability of cohesion. The deposition rate of alumina hydrate depends on the hydrolysis rate of urea.

As described above, coalescence of composite particles was suppressed by (1) intensive stirring, (2) use of a flow reactor, (3) low reaction temperature, (4) high concentration of urea, and (5) low concentration of aluminium sulfate. These conclusions are the same as those drawn on the formation of alumina-hydrate-coated SiC whiskers.[18] It was also observed in the formation of YSZ-coated SiC particles that intensive stirring suppressed particle coalescence.[19]

Intensive stirring is considered to suppress the coalescence of composite particles by breaking agglomerated composite particles before further deposition of alumina hydrate, which strengthens the agglomerated structure to form the coagulated particles. Williams *et al.* also reported that the degree of particle aggregation in dispersion

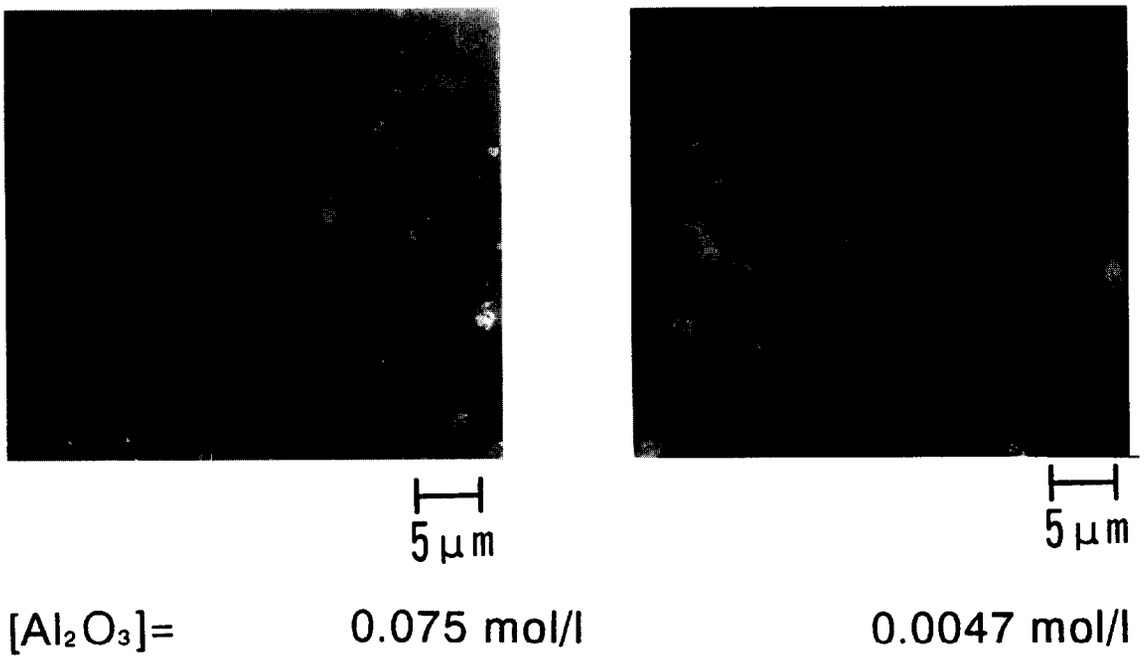

Fig. 8. Typical example of the effect of thickness of coating layer on coalescence of particles. [SiC] = 9·0 g l^{-1}, [urea] = 10·8 mol l^{-1}, reaction temperature = 70°C, stirring rate = 1700 rev min^{-1}, batch reactor.

decreased with increasing stirring rate.[20] Use of a flow reactor under a laminar flow condition my suppress the coalescence by decreasing the collision frequency of dispersion particles. Suppression of the formation of coalesced particles by decrease in reaction temperature may be mainly due to the decrease in the deposition rate of alumina hydrate, thereby increasing the chance of breakage of agglomerated particles.

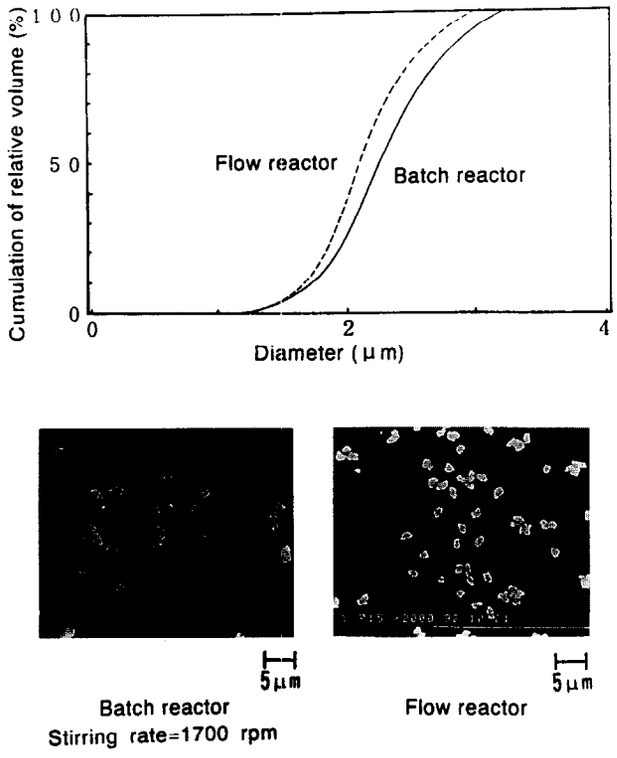

Fig. 9. Effect of reactor type on coalescence of particles. $[Al_2(SO_4)_3]$ = 0·075 mol l^{-1}, [SiC] = 9·0 g l^{-1} [urea] = 10·8 mol l^{-1}, reaction temperature = 70°C.

The effect of urea concentration is complex. From the viewpoint of deposition rate of alumina hydrate alone, the increase in urea concentration should enhance the coalescence as described above. However, this observation was not the case. Thus, there are some strong functions of urea other than the increase in hydrolysis rate itself. Vincent *et al.* reported that the surface charge of AgI increased in the presence of absorbed neutral substances.[21] Thus, zeta-potentials of the as-coated powders were measured at 25°C under different urea concentrations (1.8 or 10·2 mol l^{-1}) in the presence of aluminium sulphate (0·075 mol l^{-1}). The zeta-potentials were +2 mV for 1·8 mol l^{-1} urea concentration and +8 mV for 10·2 mol l^{-1} urea concentration. Both values are in the range of zeta-potential where colloids are commonly accepted as unstable. In addition to the change of zeta-potential, the following functions of urea may be considered. One can suppose (1) a steric effect — urea molecules are adsorbed on the alumina hydrate coating and decrease the probability of cohesion between coated particles; (2) the formation of a complex with Al^{3+}-carrying species in solution which modifies the deposition rate of alumina hydrate; (3) the increase in viscosity of the solution decreases the collision frequency of particles and/or increases the shear force to redisperse aggregated particles. In the hydrolysis of $TiOSO_4$, the presence of urea also has a remarkable effect on the formation of discrete spherical titania particles even under conditions of negligible hydrolysis of urea.[22]

For the decrease of particle coalescence under low concentration of aluminium sulfate, there

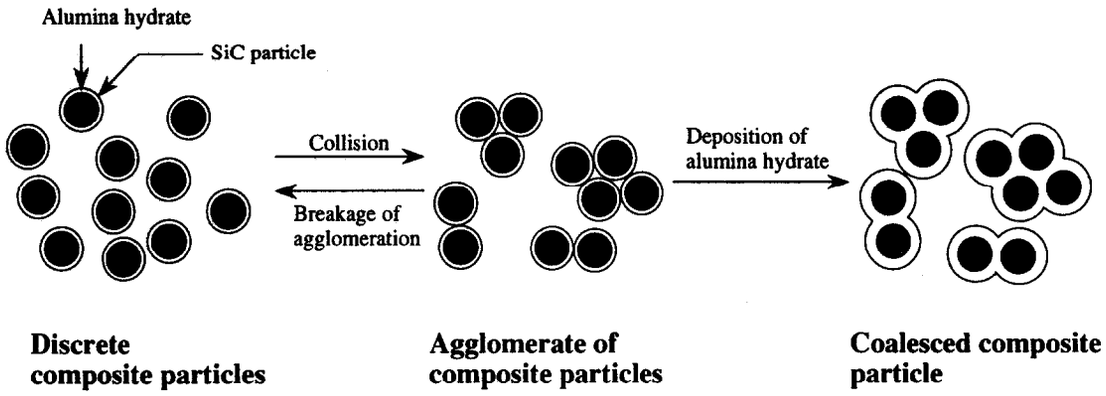

Fig. 10. Schematic representation of coalescence process of particles.

are many reasons to be taken into account. With thinning of the coating layer, (A) the collision frequency of composite particles will decrease following a decrease in collision cross-section, and (B) the cohesion probability at collision will decrease following a decrease in neck cross-section formed with cohesion of two particles (Fig. 11). Both multivalent Al^{3+} and SO_4^{2-} ions have a high flocculation power. That is, (C) a decrease in the concentration of aluminium sulfate gives a low ionic strength of the reacting solution which may increase the thickness of the electric double layer, resulting in a decrease in the collision frequency of composite particles. (D) Decrease in coating duration at low aluminium sulfate concentrations may decrease the chance for coalescence. In order to reveal the dominant factor, concentrations of the raw materials (i.e. [SiC] and $[Al_2(SO_4)_3]$) were changed under fixed $[SiC]/[Al_2(SO_4)_3]$ ratio. Other conditions were equal to those in Table 1. The ratio of observed to ideal particle diameters is shown in Table 2. Under a fixed $[SiC]/[Al_2(SO_4)_3]$ ratio, a higher concentration of raw materials results in a higher ionic strength of the reacting solution, longer reaction time, and thus more frequent collisions. In Table 2, in spite of the large difference in concentration of raw materials [four times for no. 7/no. 4, nine times for no. 8/no. 3; average particle distance varies inversely with the cube root of the number of particles (i.e. concentration)], the ratios of both diameters are equal or very close. These results show that the increase in collision frequency (A) resulting from the increased concentration of SiC particles does not affect the particle coalescence under the conditions examined and that the change of the concentration of aluminium sulfate (C and D) does not affect the particle coalescence under the same ratio of $[SiC]/[Al_2(SO_4)_3]$. Consequently, it can be said that (B), the decrease of cohesion probability, is the main reason for the decrease of coalescence under low concentration of aluminium sulfate.

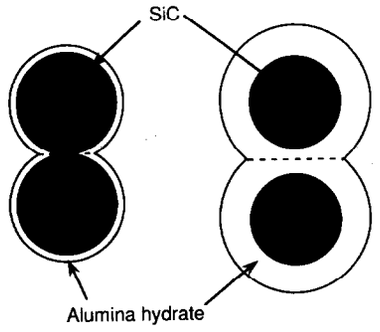

Fig. 11. Effect of coating layer thickness on cohesion area.

5 Conclusions

Alumina-hydrate-coated SiC particles were prepared by homogeneous precipitation using urea. It

Table 2. Effect of raw material concentration on particle coalescence

No.	*[SiC] (g l^{-1})*	*$[Al_2(SO_4)_3]$ (mol l^{-1})*	*$[SiC]/[Al_2(SO_4)_3]$ (g mol^{-1})*	*Ideal diameter[a] (μm)*	*Median diameter (μm)*	*Median diameter/ ideal diameter*
4	9·0	0·019	470	0·76	1·8	2·3
7	36	0·075			1·8	2·3
3	9·0	0·0094	950	0·69	1·3	1·9
8	72	0·075			1·5	2·2

[a]Ideal diameter was calculated on the assumptions: original SiC diameter = 0·6 μm, uniform coating of alumina hydrate on SiC particles, and no coalescence of composite particles.

can be said that coalescence of coated particles occurred by collision and agglomeration followed by deposition of alumina hydrate on the agglomerated coated particles. Coalescence of coated particles was suppressed under the conditions of intensive stirring, thin coating layer, low reaction temperature, high urea concentration and a use of flow reactor.

References

1. Yoshimatsu, H., Osaka, A., Miura, Y. & Kawasaki, H., *J. Ceram. Soc. Jpn*, **99** (1991) 594–599.
2. Higashi, Y., Nogami, K. & Ohshima, N., *J. Ceram. Soc. Jpn*, **100** (1992) 646–651.
3. Sando, M., Towata, A. & Tsuge, A., *Ceramics Transactions Vol. 22*, eds S. Hirano, G. L. Messing & H. Hausner. American Ceramics Society, Inc., Westerville, OH, 1991.
4. Liden, E., Bergstrom, L., Persson, M. & Carlsson, R., *J. Eur. Ceramic Soc.*, **7** (1991) 361–368.
5. Ohmori, M. & Matijevic, E., *J. Colloid Interface Sci.*, **150** (1992) 594–598.
6. Hirano, S., Hayashi, S. & Kato, C., *Funtai Oyobi Funmatsu Yakin*, **37** (1990) 371–375.
7. Okumura, H., Barringer, E. A. & Bowen H. K., *J. Mater. Sci.*, **24** (1989) 1867–1880.
8. Fegley Jr, B., Barringer, E. A. & Bowen, H. K., *J. Am. Ceram. Soc.*, **67** (1984) C113–116.
9. Fegley Jr, B., White, P. & Bowen H. K., *J. Am. Ceram. Soc.*, **68** (1985) C60–62.
10. Takahashi, Y. & Chisaki, J., *J. Ceram. Soc. Jpn*, **96** (1988) 240–246.
11. Hu, C.-L. & Rahman, M. N., *J. Am. Ceram. Soc.*, **75** (1992) 2066-2070.
12. Kratohvil, S. & Matijevic, E., *Adv. Ceram. Mater.*, **2** (1987) 798–803.
13. Garg, A. K. & Matijevic, E., *J. Colloid Interface Sci.*, **126** (1988) 645–649.
14. Kawahashi, N. & Matijevic, E., *J. Colloid Interface Sci.*, **138** (1990) 534–543.
15. Kim, B.-K. & Yasui, I., *J. Mater. Sci.*, **23** (1988) 637–642.
16. Kapolnek, D. & De Jonghe, L. C., *J. Eur. Ceram. Soc.*, **7** (1991) 345–351.
17. Garg, A. K. & De Jonghe, L. C., *J. Mater. Res.*, **5** (1990) 136–142.
18. Nakamura, H. & Kato, A., *J. Ceram. Soc. Jpn*, **101** (1993) 773–778.
19. Nagashima, S., Yoshida, T., Nakamura, H. & Kato, A., *J. Jpn Soc. Powder & Powder Metall.*, **40** (1993) 987–992.
20. Williams, R. A., Peng, S. J. & Naylor, A., *Powder Technol.*, **73** (1992) 75–83.
21. Vincent, B., Bijsterbosh, B. H. & Lyklema, J., *J. Colloid Interface Sci.*, **37** (1971) 171–178.
22. Kato, A., Takeshita, Y. & Katatae, Y., *Mater. Res. Soc. Symp. Proc.*, **155** (1989) 13–22.

Journal of the European Ceramic Society 16 (1996) 1337–1343

PII: S0955-2219(96)00066-0
0955-2219/96/$15.00

Microstructure and Flexure Creep Behaviour of SiC-Particle Reinforced Al_2O_3 Matrix Composites

Zhen-Yan Deng, Yu-Feng Zhang, Jian-Lin Shi & Jing-Kun Guo

The State Key Laboratory of High Performance Ceramics and Superfine Microstructure, Shanghai Institute of Ceramics, Chinese Academy of Sciences, Shanghai 200050, People's Republic of China

(Received 26 January 1996; revised version received 22 March 1996; accepted 28 March 1996)

Abstract

The flexure creep behaviour of monolithic Al_2O_3 and 10 vol% SiC-particle reinforced Al_2O_3 matrix composites was investigated in air atmosphere at 1160 to 1400°C and under a stress of 40 to 125 MPa. Two kinds of SiC particles with different particle sizes and oxygen contents were used in the composites, one having an average size of 0·6 μm with 1·7 vol% SiO_2 impurities and the other of average size 2·7 μm with 3·4 vol% SiO_2 impurities. Compared with the creep behaviour of monolithic Al_2O_3 the strain rate of the composites with 0·6 μm SiC particles did not decrease; however, the composites with 2·7 μm SiC particles exhibited excellent creep resistance. Microstructure analysis showed that the Al_2O_3 grains in the composites with 0·6 μm SiC particles were mainly equiaxed with most of the SiC particles lying at the grain boundaries or triple-grain junctions, whereas the grain features of the composites with 2·7 μm SiC particles were irregular and elongated and most of the SiC particles were entrapped into Al_2O_3 matrix grains. It was revealed that the entrapment of 2·7 μm SiC particles into Al_2O_3 matrix grains was related to the high SiO_2 impurity content on SiC particle surfaces, and the change of grain morphology and the good high-temperature oxidation resistance were responsible for the creep resistance increase of the composites with 2·7 μm SiC particles. © 1996 Elsevier Science Limited

1 Introduction

Over the past few years, the high-temperature creep and creep fracture behaviour of monolithic Al_2O_3 have been studied extensively,[1–5] owing to the increasing emphasis on the development of structural ceramics for high-temperature applications. Although Al_2O_3 itself is not suitable as a high-temperature structural material, it is a potential matrix material for some structural composites with high-temperature capability because of the good microstructured stability of Al_2O_3 at high temperature. For example SiC whiskers have been successfully incorporated into Al_2O_3 by many researchers[6–8] and the high-temperature creep resistance of Al_2O_3 was apparently improved. However, SiC whiskers are expensive for practical applications and pose health hazards during material processing. These shortcomings would be overcome if the SiC whiskers could be replaced by cheap SiC particles.

Recently, Niihara[9] has successfully developed Al_2O_3/SiC nanocomposites which were formed by dispersion of nanometre-size SiC particles into Al_2O_3 matrix grains and at grain boundaries. He found that addition of as little as 5 vol% 0·3 μm SiC particles could increase the strength of hot-pressed alumina from 350 MPa to over 1 GPa and the fracture toughness from 3·25 to 4·7 MPa $m^{1/2}$, this high strength being maintained up to 1200°C. Ohji *et al.*[10] subsequently conducted tensile creep tests for Al_2O_3/17 vol% SiC nanocomposites and monolithic Al_2O_3 at 1200 to 1300°C and under a stress of 50 to 150 MPa. They revealed that the minimum creep rate of the nanocomposites was about three orders of magnitude lower and the creep life was 10 times longer than those of the monolithic Al_2O_3. The purpose of this paper is to study the effects of different SiC particles on the morphology and creep properties of SiC-particle reinforced Al_2O_2 matrix composites.

2 Experimental

Highly pure α-Al_2O_3 was obtained by calcining γ-Al_2O_3, with a mean particle size of 1 μm. SiC particles with two different sizes, 0·6 and 2·7 μm, were used in this study; these are represented by S and L in the figures hereafter. The main impurity in the SiC particles was SiO_2: 1·7 and 3·4 vol% SiO_2 in the 0·6 and 2·7 μm SiC particles, respectively. In the composites, 10 vol% SiC particles and 0·5 vol% MgO

were added. The monolithic Al_2O_3 and composites were obtained by hot-pressing under 20 MPa in a flowing Ar atmosphere at 1700°C for 30 min.

The dense monolithic Al_2O_3 and composite tiles were ground and sectioned into 2 × 4 × 40 mm^3 test bars with the edges chamfered for creep experiments. Density measurements performed on the specimens showed that the density of monolithic Al_2O_3 was over 99·9% of theoretical density, and those of the composites with 0·6 μm SiC particles (ASS) and with 2·7 μm SiC particles (ASL) were 99·6 and 99·5% of theoretical density, respectively. The flexure creep tests were conducted in air atmosphere at 1160 to 1400°C under the stress of 40 to 125 MPa. The specimens were loaded in a four-point flexure fixture with inner and outer span lengths of 10 and 30 mm, respectively. The applied stress and resultant strain were calculated using the method described by Cannon *et al.*[1] in the small strain situation. The microstructures of as-received and creep specimens were analysed by scanning electron microscopy (SEM) and transmission electron microscopy (TEM), the samples of creep specimens for TEM observation being cut from the tensile side of the specimen.

3 Creep Results

The creep curves of monolithic Al_2O_3 and composites at 1260°C and 75 MPa are shown in Fig. 1. Apart from the ASS specimen which fractured in the creep test, monolithic Al_2O_3 and ASL specimens were crept to reach minimum strain rate. Compared with the monolithic Al_2O_3, the strain rate of ASS does not decrease, but ASL exhibits excellent creep resistance.

Figure 2 shows stress dependences of steady-state or minimum creep rates for the monolithic Al_2O_3 and composites at T = 1260°C. Apparent linear fitting indicates that the stress exponent of

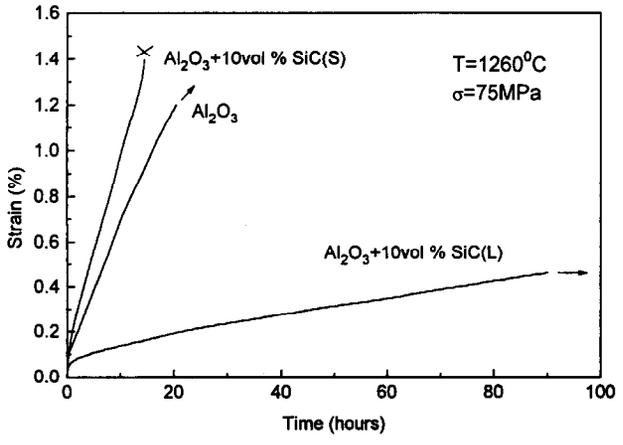

Fig. 1. Flexure creep curves of monolithic Al_2O_3 and composites at 1260°C and 75 MPa, where the ASS specimen fractured in the creep test.

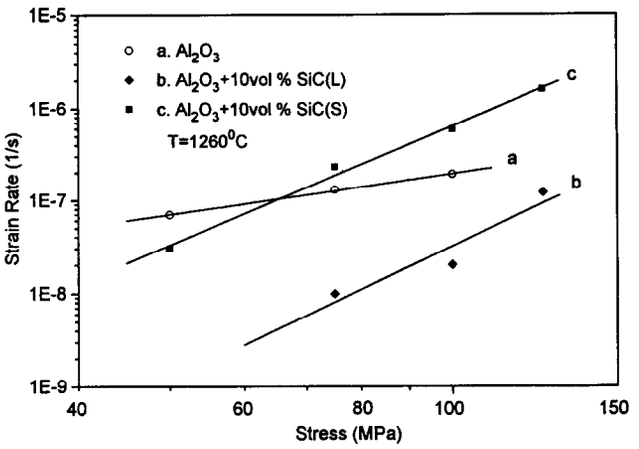

Fig. 2. Stress dependences of steady-state or minimum creep rate for the monolithic Al_2O_3, and composites at 1260°C. The stress exponent for strain rate is 1·45 for monolithic Al_2O_3, 4·27 and 4·75 for ASS and ASL, respectively.

monolithic Al_2O_3 is 1·45, which agrees reasonably well with the results reported by Cannon *et al.*[1] and is smaller than the stress exponent of 2·9 reported for polycrystalline Al_2O_3 prepared by nanometre-sized Al_2O_3 powders.[10] The stress exponents of ASS and ASL are 4·27 and 4·75, respectively, which approach the stress exponents of SiC-whisker reinforced Al_2O_3 matrix composites[11,12] and are larger than the stress exponent of 2·2 for Al_2O_3/SiC nanocomposites.[10] Crudely, the strain rate of ASL is about one order of magnitude lower than those of monolithic Al_2O_3 and ASS. Because the stress exponent of ASS is higher than that of monolithic Al_2O_3, the strain rate of the former is lower than that of the latter at the low stress region and higher than that of the latter at the high stress region. Activation energies of monolithic Al_2O_3 and composites for steady-state or minimum strain rate were obtained from Arrhenius plots by apparent linear regression analysis, as shown in Fig. 3. The activation energy of monolithic Al_2O_3 at 75 MPa is 531 kJ mol^{-1}, which is consistent

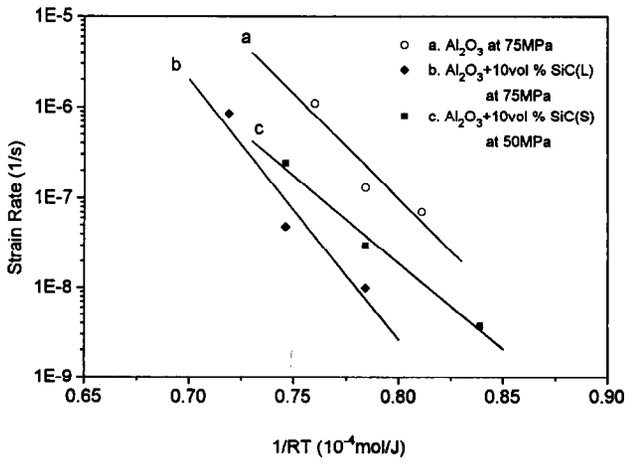

Fig. 3. Arrhenius plots at 75 MPa for monolithic Al_2O_3 and ASL, and at 50 MPa for ASS.

with the results previously reported[1,6] for polycrystalline Al_2O_3. The activation energy of ASS at 50 MPa is 444 kJ mol^{-1}, which is smaller than that of monolithic Al_2O_3. Because the activation energy decreases with the increase in the applied load,[1] the activation energy of ASS at 75 MPa should be smaller than 444 kJ mol^{-1}. On the other hand, the activation energy of ASL at 75 MPa is 666 kJ mol^{-1}, which is larger than that of monolithic Al_2O_3.

4 Discussion

4.1 Al_2O_3 grain morphology

Figure 4 shows the grain morphology of the as-received monolithic Al_2O_3 and composites. In Fig. 4(A) it can be seen that the monolithic Al_2O_3 has a uniform grain-size distribution and equiaxed grain morphology, with an average grain size of about 5 μm. The TEM micrograph of ASS [Fig. 4(B)] indicates that most of the SiC particles are on the grain boundaries or triple-grain junctions (grey particles). In general, the Al_2O_3 matrix grains in ASS have regular equiaxed morphology and the average grain size is smaller than that of monolithic Al_2O_3 due to grain growth suppression by the SiC particles.[13] Occasionally elongated Al_2O_3 grains can also be seen which, as estimated under TEM observation, account for about 10% of the total Al_2O_3 matrix grains, as shown in Fig. 4(B) (indicated by arrow). The features of ASL are significantly different from those of ASS. Figure 4(C) shows that most of the Al_2O_3 matrix grains in ASL are elongated and the grain boundaries are very irregular, their grain sizes being even larger than those of monolithic Al_2O_3. One unexpected observation is that most of the SiC particles in ASL are entrapped into the Al_2O_3 matrix grains, as shown in Fig. 4(D) (grey particles).

4.2 Effects of SiO_2 impurities in hot-pressing process

According to the growth dynamics of ceramic materials,[14] small SiC particles are easy to entrap

Fig. 4. Grain morphology of as-received specimens: (A) SEM micrograph of the fracture surfaces of monolithic Al_2O_3; (B) TEM micrograph of ASS; (C) and (D) TEM micrographs of ASL.

into the Al_2O_3 matrix grains because the force exerted by an inclusion on a grain boundary is proportional to its radius, and the large SiC particles on the grain boundary hinder grain-boundary breakaway and decrease the propensity for second-phase entrapment.[14] So why are the 2·7 μm SiC particles entrapped into Al_2O_3 matrix grains while the 0·6 μm SiC particles are not? The answer may be related to the impurities included in the starting SiC particles, because the SiC particles used in this study have small amounts of SiO_2 impurities. The SiO_2 impurities and MgO additive could form the MgO–Al_2O_3–SiO_2 system liquid phase with the Al_2O_3 matrix during the hot-pressing process.[15] This liquid phase facilitates the dissolution and reprecipitation process of Al and O ions and accelerates Al_2O_3 matrix grain growth. The effects of liquid phase on the grain growth in Al_2O_3 have been studied in detail by Kaysser *et al.*[16] who showed that the liquid phase on the grain boundaries leads to growth anisotropy of Al_2O_3 matrix grains, and an elongated Al_2O_3 grain morphology forms in the Al_2O_3-containing glassy phase. Because the SiO_2 content in 2·7 μm SiC particles (3·4 vol%) is twice that in 0·6 μm SiC particles (1·7 vol%) and the total surface area of the 0·6 μm SiC particles is 4·5 times larger than that of 2·7 μm SiC particles when their volume is the same, the SiO_2 content per unit area on 2·7 μm SiC particle surfaces is about one order of magnitude higher than that on 0·6 μm SiC particle surfaces. The large amount of SiO_2 on 2·7 μm SiC particle surfaces would form a large amount of MgO–Al_2O_3–SiO_2 liquid phase during the hot-pressing process, which could accelerate Al_2O_3 grain growth and grain boundary movement near SiC particles. This is the reason why most of the 2·7 μm SiC particles are entrapped into the Al_2O_3 matrix grains and the 0·6 μm SiC particles are on the grain boundaries. In addition, the elongated grain morphology and irregular grain boundaries in ASL are also related to the liquid phase capping SiC particles in the hot-pressing process. Although the small amount of SiO_2 on 0·6 μm particle surfaces cannot entrap most of the SiC particles into Al_2O_3 matrix grains, small amounts of elongated Al_2O_3 grains (10%) are also seen in their morphology.

4.3 Creep deformation mechanisms and oxidation effects

Grain-boundary diffusion is the most predominant deformation mechanism of polycrystalline Al_2O_3 at temperatures below 1400°C.[7] The stress exponent, 1·45, of monolithic Al_2O_3 shows that grain-boundary sliding without a glassy phase, some accommodated by diffusion and some unaccommodated, is the principal creep mechanism.[1,17] This has been substantiated by TEM observation of the crept monolithic Al_2O_3 sample on the tensile side, as shown in Fig. 5(A), which indicates that large extensive voids exist at triple-grain junctions and grain boundaries on the tensile side of crept monolithic Al_2O_3 specimens formed by unaccommodated grain-boundary sliding. The creep mechanisms in multiphase ceramics cannot be reliably inferred from measured values of activation energies or stress exponents.[7] In our observations, small amounts of cavities have been observed in triple-grain junctions in the two kinds of crept composite specimens, and there is no evidence of dislocation glide in the matrix. We conclude that grain-boundary sliding, some accommodated by diffusion and some unaccommodated, is also the principal creep mechanisms in the composites.[7]

Ohji *et al.*[10] reported that the improvement of creep resistance for Al_2O_3/SiC nanocomposite was due to the pinning effect of the intergranular SiC particles, because the intergranular SiC particles rotated and plunged into the Al_2O_3 grains during the grain-boundary sliding when creep occurred. In our ASS composites, although most of the SiC particles are on the grain boundaries, no apparent improvement of creep resistance is observed. This behaviour can be attributed to the serious oxidation of SiC near particles on the grain boundaries during creep in air, as shown in Fig. 5(B), where most SiC particles near Al_2O_3 grain interfaces have been oxidized (indicated by arrow). The by-product of oxidation reaction is SiO_2, which forms a glassy phase with MgO additive and Al_2O_3 matrix on the grain boundaries. The presence of a viscous amorphous film along interfaces undoubtedly facilitates grain-boundary and interface sliding, decreases the interface bond strength, and decreases the creep resistance of the composites. A layer of glassy phase at the grain boundaries and interfaces would also facilitate Al_2O_3 dissolution–reprecipitation reactions. The MgO–Al_2O_2–SiO_2 glass film along boundaries would permit Al_2O_3 to dissolve and reprecipitate, thus allowing grains to change their shape to accommodate deformation under applied stress, so only a small amount of small cavities existed at triple-grain junctions of crept ASS specimens. Raj and Ashby[18] calculated the sliding rate with diffusional accommodation when secondary particles were present on the grain boundaries and showed that creep was not slowed if the diffusivity of the particle–matrix interface was equivalent to that of the matrix–matrix interface. Although the diffusion ability in the pure SiC–Al_2O_3 interface is significantly lower than that in the Al_2O_3–Al_2O_3 interface[13] as exemplified by the Al_2O_3/SiC nanocomposite,[10] the

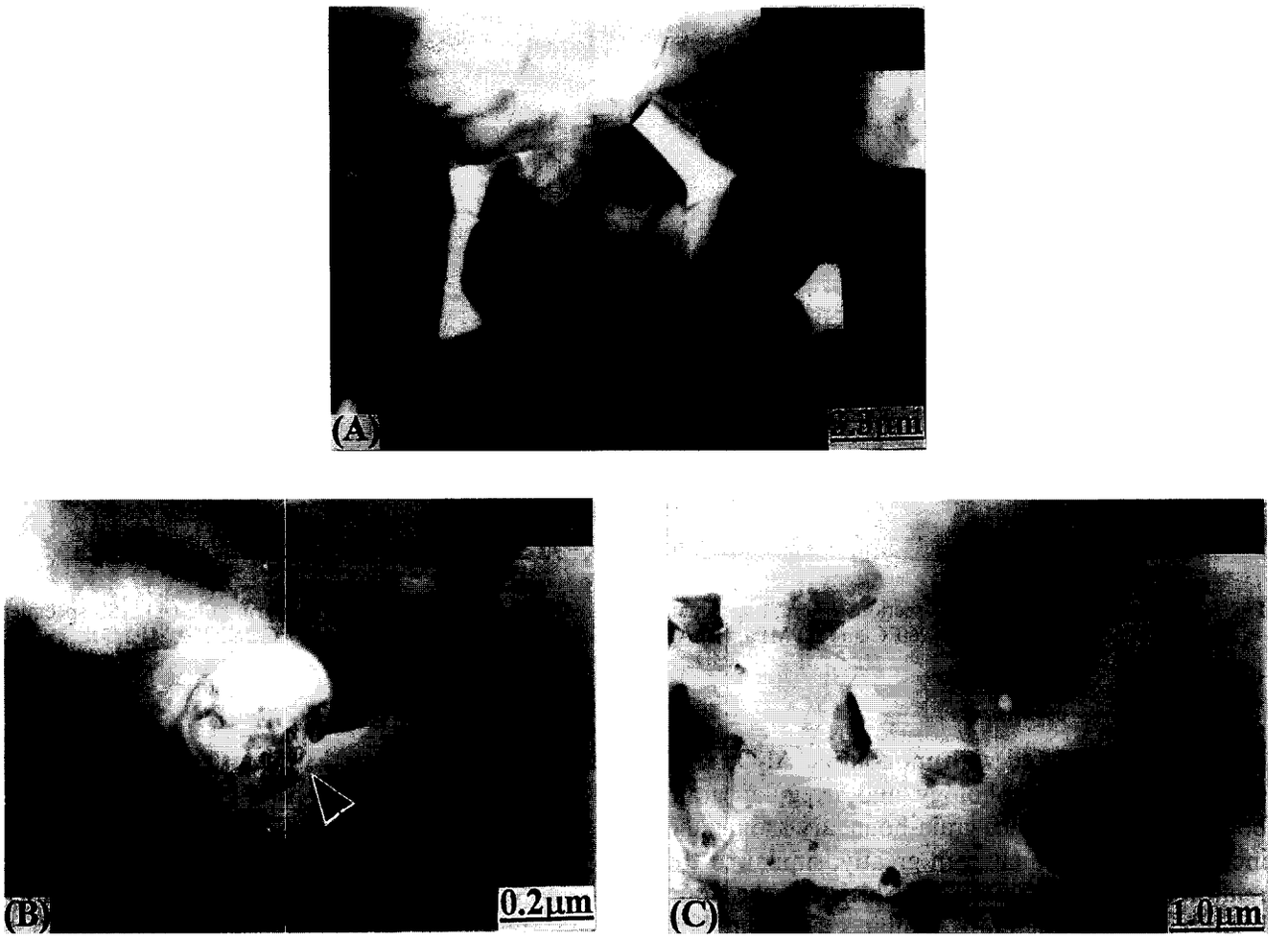

Fig. 5. TEM micrographs of samples taken from the tensile side of crept specimens: (A) monolithic Al_2O_3 crept for 73 h at T = 1260°C and 50 MPa with creep strain of 2·27%; (B) ASS specimen crept for 71 h at T = 1260°C and 50 MPa with creep strain of 1·23%; (C) ASL specimen crept for 88 h at T = 1260°C and 100 MPa with creep strain of 0·53%.

glass phase formed by oxidation reaction along SiC–Al_2O_3 interfaces in our ASS makes the diffusivity of SiC–Al_2O_3 interfaces larger than that of pure Al_2O_3–Al_2O_3 interfaces. These are the reasons why the creep resistance of ASS is not improved compared with that of monolithic Al_2O_3.

The situation in ASL is different from that in ASS, owing to the fact that most of its SiC particles are entrapped into Al_2O_3 matrix. The oxidation reactions for SiC particles inside the Al_2O_3 matrix are not as serious as those for SiC particles on the grain boundaries, because oxygen lattice diffusion in alumina is one order of magnitude lower than that of oxygen grain boundary diffusion.[15] Figure 5(C) shows that the SiC particles inside the Al_2O_3 matrix in ASL have no apparent oxidation after being crept for 88 h at T = 1260°C and 100 MPa. The large difference of oxidation behaviour between the two kinds of composites can also be seen from the surface oxidation layer of crept specimens. Figure 6 shows cross-sections of the crept composite specimens prepared by mechanical fracture and grinding, and indicates that the crept ASS specimen surface has been seriously oxidized, accompanied by carbon monoxide-induced bubbles on its surface layer.[19] The thickness of the surface oxidation layer is about 100 μm, as shown in Fig. 6(A), when the specimen was crept for 71 h in air at T = 1260°C and 50 MPa. The ASL specimen exhibits excellent high-temperature oxidation resistance, as shown in Fig. 6(B), where there is no apparent oxidation layer on the specimen surface after creep testing for 88 h in air at T = 1260°C and 100 MPa. Because of the good oxidation resistance at high temperature, the amount of glass phase on grain boundaries of ASL is much lower. Although 3·4 vol% SiO_2 existed on the starting 2·7 μm SiC particle surfaces, these SiO_2 impurities may be not on the Al_2O_3 grain boundaries due to the SiC particles being entrapped into Al_2O_3 matrix grains.

The lack of glass phase on the Al_2O_3 grain boundaries would enhance the creep resistance of ASL, compared with ASS. The elongated grain morphology and irregular grain boundaries are the main causes for the improved creep resistance

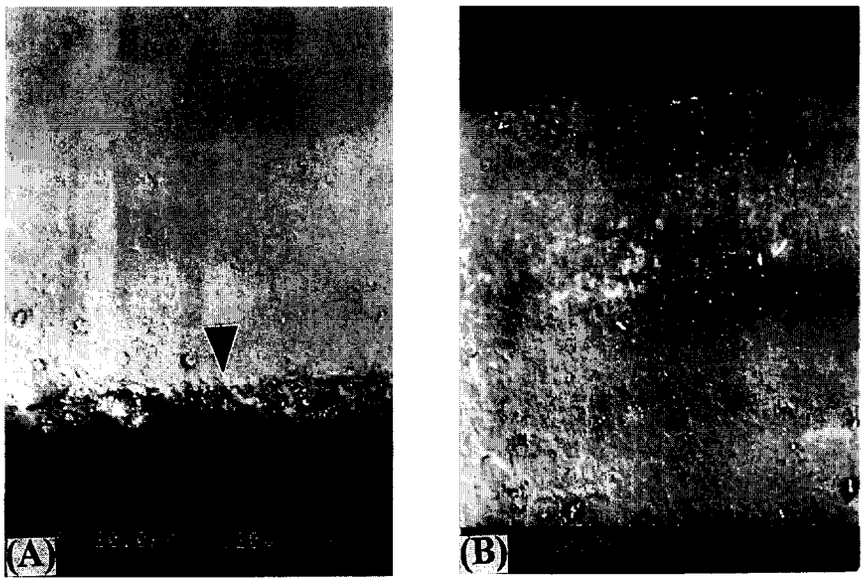

Fig. 6. SEM micrographs of cross-sections of crept specimens prepared by mechanical fracture and grinding: (A) ASS specimen crept for 71 h at $T = 1260°C$ and 50 MPa; (B) ASL specimen crept for 88 h at $T = 1260°C$ and 100 MPa.

of ASL, as compared with monolithic Al_2O_3. The elongated grain morphology and irregular grain boundaries could reduce grain-boundary sliding and increase the diffusional path greatly, similar to the reinforcing effect of whiskers which pin the grain boundaries and therefore inhibit grain-boundary sliding.[6,8] In addition, the small amount of SiC particles on grain boundaries in ASL may also inhibit grain-boundary sliding by pinning grain boundaries[10] and improve the creep resistance of ASL, due to the larger size of SiC particles in ASL. On the other hand, the grain size is a factor affecting creep strain rate,[6,17] but it could account for only a small amount of the difference between monolithic Al_2O_3 and composites.

The different creep behaviours of monolithic Al_2O_3 and composites also reflect the difference in their activation energies. Because of the glass phase along grain boundaries formed by the oxidation reaction in ASS, grain-boundary diffusion becomes easy and the activation energy (444 kJ mol^{-1}) of ASS is smaller than that (531 kJ mol^{-1}) of monolithic Al_2O_3. The high activation energy (666 kJ mol^{-1}) of ASL could be attributable to diffusion being more difficult along the elongated and irregular grain boundaries in ASL than along the equiaxed grain boundaries in monolithic Al_2O_3.

5 Conclusions

We have investigated the flexure creep behaviour of monolithic Al_2O_3 and composites with two kinds of different SiC particles, in air atmosphere at 1160 to 1400°C and under stresses from 40 to 125 MPa. The following results were obtained.

(1) The ASL composites (with 10 vol% 2·7 μm SiC particles) exhibited excellent creep resistance due to their elongated grain morphology, irregular grain boundaries and good oxidation resistance. The creep resistance of ASS (with 10 vol% 0·6 μm SiC particles) was not as good as that of ASL, because of the serious oxidation of the SiC particles on grain boundaries in ASS during creep tests.

(2) Most of the 2·7 μm SiC particles were found to be entrapped into Al_2O_3 matrix grains. This is believed to result from the fact that a high content of SiO_2 impurities existed on 2·7 μm SiC particle surfaces: the SiO_2 formed liquid phase which accelerated the Al_2O_3 grain growth and grain-boundary movement near SiC particles in the hot-pressing process.

(3) Oxidation of the SiC particles on grain boundaries formed thin glass films along grain boundaries in ASS during creep tests, and reduced the activation energy of ASS. The elongated grain morphology and irregular grain boundaries in ASL increased the activation energy of ASL.

Acknowledgement

This work was supported by the Shanghai Postdoctoral Foundation and the Young Scientist Foundation of the Chinese Academy of Sciences.

References

1. Cannon, R. M., Rhodes, W. H. & Heuer, A. H., Plastic deformation of fine-grained alumina (Al_2O_3): I, Interface-controlled diffusional creep. *J. Am. Ceram. Soc.*, **63** (1980) 46–53.
2. Heuer, A. H., Tighe, N. J. & Cannon, R. M., Plastic deformation of fine-grained alumina (Al_2O_3): II, Basal slip and nonaccommodated grain-boundary sliding. *J. Am. Ceram. Soc.*, **63** (1980) 53–58.
3. Robertson, A. G., Wilkinson, D. S. & Càceres, C. H., Creep and creep fracture in hot-pressed alumina. *J. Am. Ceram. Soc.*, **74** (1991) 915–921.
4. Wilkinson, D. S., Càceres, C. H. & Robertson, A. G., Damage and fracture mechanisms during high-temperature creep in hot-pressed alumina. *J. Am. Ceram. Soc.*, **74** (1991) 922–933.
5. Murphy, D., Jakus, K., Ritter, J. E. & Hill, B. C., High-temperature behavior of indent and creep-nucleated cracks in vitreous-bonded alumina. *J. Am. Ceram. Soc.*, **78** (199) 1914–1920.
6. Arellano-López, A. R., Cumbrera, F. L., Domínguez-Rodríguez, A., Goretta, K. C. & Routbort, J. L., Compressive creep of SiC-whisker-reinforced Al_2O_3. *J. Am. Ceram. Soc.*, **73** (1990) 1297–1300.
7. Lipetzky, P., Nutt, S. R., Koester, D. A. & Davis, R. F., Atmospheric effects on compressive creep of SiC-whisker-reinforced alumina. *J. Am. Ceram. Soc.*, **74** (1991) 1240–1247.
8. Arellano-López, A. R., Domínguez-Rodríguez, A., Goretta, K. C. & Routbort, J. L., Plastic deformation mechanisms in SiC-whisker-reinforced alumina. *J. Am. Ceram. Soc.*, **76** (1993) 1425–1432.
9. Niihara, K., New design concept of structural ceramics—ceramic nanocomposites. *J. Ceram. Soc. Jpn*, **99** (1991) 974.
10. Ohji, T., Nakahira, A., Hirano, T. & Niihara, K., Tensile creep behavior of alumina/silicon carbide nanocomposite. *J. Am. Ceram. Soc.*, **77** (1994) 3259–3262.
11. Nutt, S. R., Lipetzky, P. & Becher, P. F., Creep deformation of alumina–SiC composites. *Mater. Sci. Eng.*, **A126** (1990) 165–172.
12. Tuffe, S., Dubois, J., Jorand, Y., Fantozzi, G. & Barbier, G., Processing and fracture behaviour of hot pressed silicon carbide whisker reinforced alumina. *Ceram. Int.*, **20** (1994) 425–432.
13. Stearns, L. C., Zhao, J. H. & Harmer, M. P., Processing and microstructure development in Al_2O_3–SiC 'nanocomposites'. *J. Eur. Ceram. Soc.*, **10** (1992) 473–477.
14. Piciacchio, A., Lee, S. H. & Messing, G. L., Processing and microstructure development in alumina–silicon carbide intragranular particulate composites. *J. Am. Ceram. Soc.*, **77** (1994) 2157–2164.
15. Kingery, W. D., *Introduction to Ceramics*, 2nd edition. Wiley, New York, 1976, p. 307 and 240.
16. Kaysser, W. A., Sprissler, M., Handwerker, C. A. & Blendell, J. E., Effect of a liquid phase on the morphology of grain growth in alumina. *J. Am. Ceram. Soc.*, **70** (1987) 339–343.
17. Cannon, W. R. & Langdon, T. G., Review creep of ceramics: Part 1 Mechanical characteristics. *J. Mater. Sci.*, **18** (1983) 1–50.
18. Raj, R. & Ashby, M. F., Grain boundary sliding and diffusional creep. *Metall. Trans.*, **2** (1971) 1113–1127.
19. Chiu, C. C., Influence of surface oxidation on thermal shock resistance and flexural strength of SiC/Al_2O_3 composites. *J. Mater. Sci.*, **29** (1994) 2078–2082.

Journal of the European Ceramic Society **16** (1996) 1345–1349

PII: S0955-2219(96)00079-9
0955-2219/96/$15.00

Controlling the Flaw Size and Mechanical Properties of ZTM/SiC_p Composites

Ruisong Guo, Zhengfu He, Zhengfang Yang, Qiming Yuan & Yuru Chen

Department of Materials Science and Engineering, Tianjin University, Tianjin 300072, People's Republic of China

(Received 19 December 1995; revised version received 23 March 1996; accepted 2 April 1996)

Abstract

Ultrafine mullite and zirconia powders were prepared by sol–gel and precipitation processes, then mixed homogeneously with μm-sized silicon carbide particles (SiC_p) to obtain composite powder. A dense green body with homogeneous microstructure was prepared by the pressure filtration technique. After being dried carefully, the green body was hot-pressed under different conditions to optimize its microstructure. The effect of different hot-pressing conditions on the mechanical properties was investigated and the hot-forging effect was also taken into account. It was found that the strength of the composite was greatly increased, from about 600 MPa reported to 810 MPa at room temperature and 830 MPa at 1000°C, under the conditions of moderately low hot-pressing temperature and long holding time, while the fracture toughness of the composite remained almost unchanged. From this it was shown that the control of strength-limiting processing defects was effective. Because of the homogeneous microstructure improved during forming and optimized during sintering and a combination of various strengthening mechanisms, it was possible to enhance the strength of the composite significantly. © 1996 Elsevier Science Limited

1 Introduction

Zirconia-toughened mullite (ZTM) based composites have great importance in advanced structural oxide ceramics. During the past decade investigations of fibre- or whisker-reinforced composites have been widely conducted[1–12] and the mechanical properties of the composites have also been significantly improved.[4,6,10,12] Due to the complicated preparation technique, high cost and health hazards associated with the use of whisker reinforcements, however, it appears that ZTM reinforcement by particles is more acceptable. Unfortunately, only a few reports on particle-reinforced mullite system have been published so far. Although the mechanical properties of particle-reinforced materials have not yet reached the level of fibre- or whisker-reinforced ones, strength at the level of 600 MPa and fracture toughness of 6–7 MPa $m^{1/2}$, SiC-particle reinforced ZTM has attracted much attention owing to its significant potential in mechanical properties.

Mullite ceramics obtained by the sol–gel process are a good candidate material for high-temperature applications. It has been reported that highly pure, ultrafine mullite powder can be prepared by the sol–gel process, then formed carefully to avoid flaws and sintered at a moderate temperature to prevent abnormal grain growth of mullite and to improve microstructure. According to $\sigma_f = K_{IC}/Yc^{1/2}$, although fracture toughness was not very satisfactory, a high strength was still obtained because the flaw size c decreased. In our previous work we prepared ZTM/SiC_p composites with the same composition as those in this paper and by the same processing route except for hot-pressing directly from composite powders. Although K_{IC} was very close to or even a little higher than that published, the strength never reached the level of 600 MPa, which clearly showed the flaw size in the body was considerably large. Therefore, the main reinforcement strategy of the present study was to focus on the strength-limiting flaws originating from processing defects, in collaboration with triggering of other strengthening mechanisms and improvement of microstructure of the composites.

2 Experimental Procedure

The starting materials were tetraethyl orthosilicate (TEOS), aluminium chloride, $ZrOCl_2 \cdot 8H_2O$, and μm-sized SiC particles. First, ultrafine mullite (ratio of Al_2O_3 to SiO_2 = 68 to 32) was prepared by the sol–gel process for investigations of the green body characteristics. The precursor powder was calcined at 1300°C, then shaped via different

methods. The powder was granulated, followed by pressing and/or cold-isostatic pressing. Stable, well-dispersed slurry was produced for pressure filtration (PF) forming by ball-milling for 8 h, keeping constant pH value (pH = 9) and adding a small amount of surfactant, polyacrylic acid (PAA). Density, pore size distribution, morphology and sinterability of the green body were determined.

Secondly, ultrafine mullite (same composition as above) and zirconia powders were prepared by sol–gel and precipitation processes, respectively. After being calcined at 1000°C, mullite powder was mixed homogeneously with commercial SiC_p and $Zr(OH)_4$ slurry, precipitated from $ZrOCl_2 \cdot 8H_2O$ by adjusting the pH value to 8·5, by a coating–coprecipitation method. This composite powder was calcined again at low temperature (600°C). The average grain size of mullite and zirconia was about 15 nm by transmission electron microscopy (TEM) observation. SiC powder was milled before mixing and its average grain size was about 1–3 μm. The composition of the composite powder was 40% mullite / 25% ZrO_2 / 35% SiC (by volume). The green disc body was obtained by PF of composite slurry which was prepared by the same way as mentioned above. After being dried carefully, the green body, whose diameter was a few millimetres smaller than that of graphite die, was hot-press(HP)ed under different conditions in an Ar atmosphere. The HPing pressure was 36 MPa.

The HPed bodies were ground and cut into bars with cross-section of 2·5 × 5 mm, then polished. The strength was measured by three-point bending with spans of 20 and 30 mm for room-temperature strength and high-temperature strength, respectively. The fracture toughness was determined by the single-edge notched beam method at room temperature. Every strength value reported was the average of at least five samples and every fracture toughness value was obtained from at least three bars. The microstructural morphology of the sample surface and fractured surface was observed by scanning electron microscopy (SEM) and TEM.

3 Results and Discussion

3.1 Characteristics of green body and control of flaw size

Studies of the dry- and wet-forming techniques and the compact characteristics of highly pure, ultrafine mullite obtained by the sol–gel process, which had been calcined at 1300°C and had an average grain size of 50 nm, have been performed previously by the present authors.[7] It can be seen from Table 1 that the green compact density by the PF route is 8% higher than that by dry-forming. The PF compact reached 46% theoretical density (TD), but it was only 38% TD for the dry-forming one. Microstructural observation revealed that the PF compact was much more homogeneous than the dry-forming one. The fracture surface of the PF compact was homogeneous, fine and smooth. There were no large agglomerates left in the body, as these had been crushed by ball-milling. Static- and stereo-stabilizing mechanisms had operated very well while preparing the slurry. Therefore the particles were well dispersed and stable in the suspension. Moreover, the pore size distribution of the green body was much narrower by PF than by dry-forming. Its main peak located at about 100–120 Å, which corresponds exactly to the size of the tetrahedron pore formed by four primary particles (diameter 50 nm) according to the close-packing principle. No pores larger than 600 Å existed. After sintering at 1590°C for 4 h in air, the density difference between the two bodies was considerably large. The PF compact density was 19% higher than the other, reaching 95% TD, which could undoubtedly be attributed to microstructural improvement and the elimination of large pores from the green body. It is very difficult to eliminate the flaws related to dry-forming during sintering. So it is clear from the above that the compact, whose density was not high enough, could also be well sintered provided it was homogeneous enough and the pores in the body were fine and well distributed.

Based on the results and discussion above, the PF route was employed as a primary strategy to realize elimination of processing defects and therefore improvement of microstructure. Then the body was sintered by the HPing route under different conditions as a second measure to finely adjust and optimize the microstructure. In the meanwhile, the hot-forging effect was taken into account to achieve flaw-free materials. Comparison of the surface morphology of two kinds of samples, i.e. those HPed from a disc body by PF and those obtained directly from composite powder at the same conditions, showed that the former was homogeneous and dense. No large agglomerates remained. Its room-temperature strength reached 720 MPa, although no large K_{IC} difference existed between both materials, which resulted obviously

Table 1. Density of green body formed by different routes and sintered body

Forming method	*Green body*		*Sintered body*	
	ρ(g cm^{-3})	ρ/ρ_{th} (%)	ρ(g cm^{-3})	ρ/ρ_{th} (%)
Dry-forming	1·21–1·24	37·7–38·6	2·29–2·44	71·3–76·0
PF	1·47	45·9	3·06	95·3

Sintered at 1590°C for 4 h in air; ρ_{th} = 3·21 g cm^{-3}.

from the effective control of processing defects and the improvement of microstructure.

3.2 Effect of different HPing conditions on composite mechanical properties

Four different HPing conditions (nos 1–4) were chosen to investigate the mechanical properties of the composites. Condition no. 5 was used as a comparison with nos 2 and 4. The mechanical properties of the composites are summarized in Table 2. It can be seen that there is no great difference in fracture toughness among the samples. The strength of sample 1 was the lowest, which can be attributed to low HPing temperature although it had the longest holding time. When the composite was sintered at such a low temperature, its microstructure (grain growth and grain bonding, etc.) had not been optimized. Increasing the HPing temperature to 1575°C increased the strength to the maximum value of 730 MPa because of improvement of the microstructure. But the strength of sample 4 (HPed at 1600°C) decreased and its K_{IC} value was also the lowest, which was related to its short holding time. As the holding time at 1600°C increased (Sample 5), strength and K_{IC} were enhanced. In addition, the strength of samples 2 and 5, tested at 1000°C, decreased only slightly and was still over 650 MPa. It is well known that the zirconia transformation toughening mechanism almost fails at this temperature. It was considered, in that case, that apart from SiC particle reinforcement, effective control of flaws was also an important factor for enhancing the strength of the composite. Strength at 1200°C decreased significantly, which was related to impurities introduced into the composite by the SiC powder.

To control the flaw size and to hinder grain growth, it was inadvisable to choose a high HPing temperature. The mechanical properties of the composites HPed at 1550°C for different holding times are shown in Fig. 1. The room-temperature strength exceeded 600 MPa for all the samples and the K_{IC} values were similar. As holding time increased to 80 min, the strength also increased to maximum 810 MPa, and the strength at 1000°C reached 836 MPa. This revealed that the major source for strength improvement was microstructural factors. It is proposed that the processing defects are limited to minimum extent after being sintered at appropriate conditions if the green body is homogeneous and no large pores remained in it. Meanwhile, the microstructural factors, e.g. ZrO_2 transformation strengthening and toughening mechanism, are also optimized. Under a comparable condition, the transformable ZrO_2 content of this composite was highest. As the holding time was increased continuously, the strength of the composite decreased but it was still above 720 MPa,

Table 2. Mechanical properties of composites HPed under different conditions

No.	*HPing conditions*		*Strength (MPa)*			K_{IC} *(MPa m$^{1/2}$)*
	Temperature (°C)	*Time (min)*	*RT*	*1000°C*	*1200°C*	
1	1525	80	599			5·9
2	1550	60	686	653	490	5·5
3	1575	40	730			5·7
4	1600	25	689			5·2
5	1600	60	720	657	485	6·0

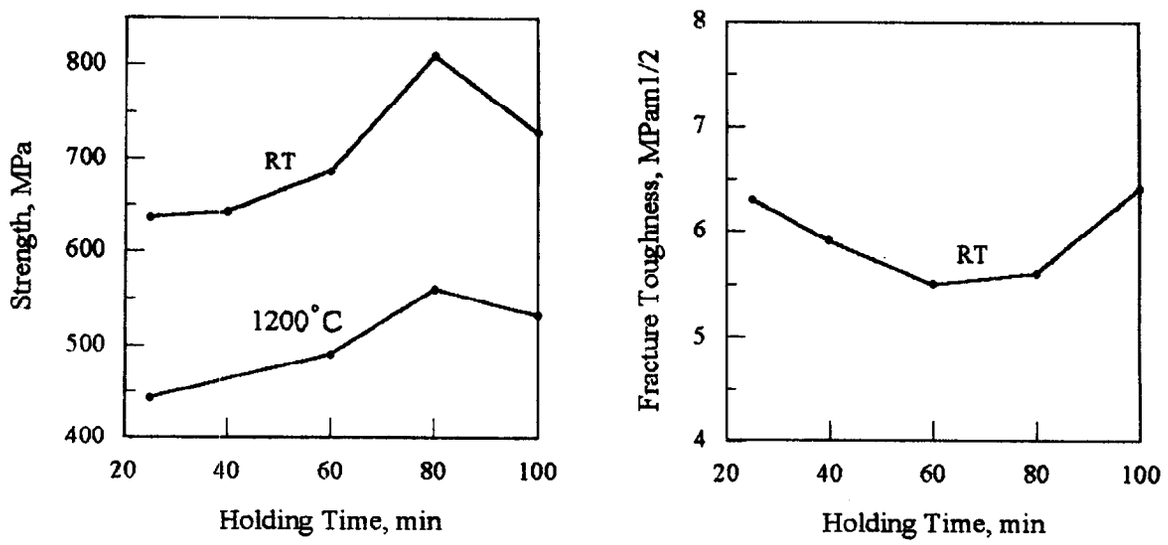

Fig. 1. Mechanical properties versus holding time (HPing temperature 1550°C).

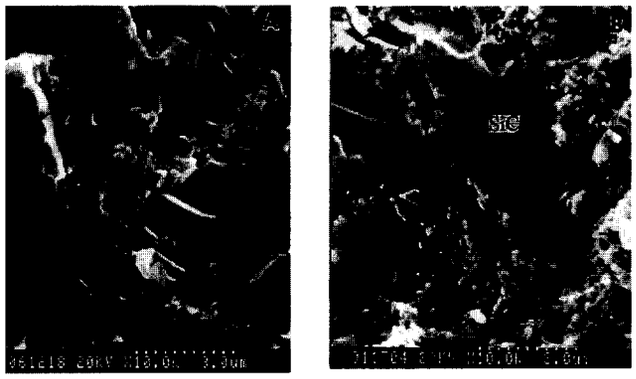

Fig. 2. SEM micrographs of fracture surface of ZTM/SiC_p composites HPed from a disc body by PF.

which is higher than that for a holding time of 60 min. The strength at 1200°C followed the same trend except for a downwards shift in value by about 200 MPa. It was consequently revealed that if the material was hot-pressed at moderately low temperature and for moderately long holding time, improved microstructure and excellent properties could be achieved.

3.3 Hot-forging

It has been reported that hot-forging is a good way to obtain flaw-free material. In this paper this strategy was also taken into account. The diameter of the green disc was a few millimetres smaller than that of the graphite die. During HPing, the disc not only suffered a vertical pressure resulting in decreasing thickness, but also was squeezed to expand in diameter to the size of the graphite die. Agglomerates were broken down and grain sliding and rearrangement occurred. Obviously it is very advantageous for pores to be eliminated before complete densification, giving rise to a flaw-free material.

3.4 Microstructure observation and strengthening mechanism

The mechanical properties of the ZTM/SiC_p composites produced in this work have been much improved compared with our previous results, the strength reaching 810 MPa at room temperature and 836 MPa at 1000°C. It is strongly suggested that elimination of processing defects and optimization of microstructure are of vital importance for strengthening the composite. Microstructural investigations of the fracture surface revealed features that correlated with the strength data. It can be seen from Fig. 2 that the fracture surface of the composite HPed from a PF disc body was very rough. Holes are visible in the fracture surface caused by particle pull-out and transgranular fracture across SiC particles has occurred, which all contributed greatly to improving strength. In addition, stress-induced transformation toughening of ZrO_2 and microstress fields around ZrO_2 particles produced by ZrO_2 transformation, ZrO_2 and SiC particle reinforcement[3] all contribute to strengthening of the composite. When a propagating crack in a fine matrix encountered a μm-sized SiC particle embedded in the matrix, it would be impeded severely by the particle, causing crack deflection, crack bridging and consequently significant enhancement of the fracture energy. Figure 3(a) shows the deflection of a crack by SiC and ZrO_2 particles. Figure 3(b) shows the main crack bridged by a t-ZrO_2 particle and demonstrates that a microstress field existed at boundaries between ZrO_2 and mullite. It also reveals that the main crack stopped by cutting and transformation of t-ZrO_2 during propagation [Fig. 3(c)]. The crack could propagate across SiC_p [Fig. 2(b)] when the energy needed for crack deflection was too high.

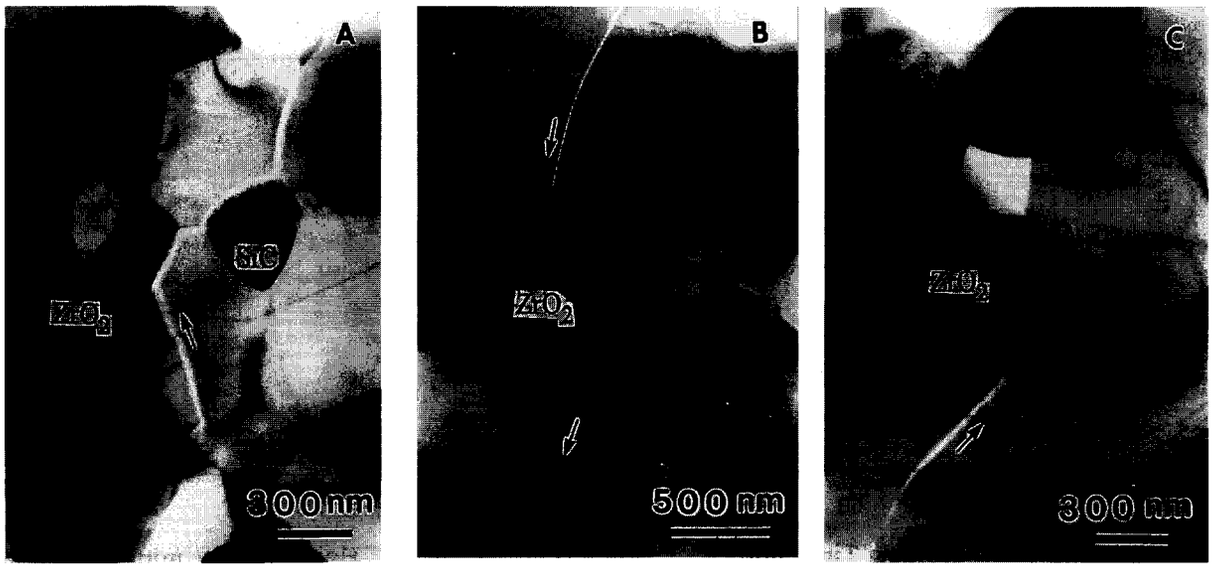

Fig. 3. TEM micrographs of ZTM/SiC_p composites showing crack deflection, bridging and stopping.

Fig. 4. Dislocations in mullite.

Dislocations were often found to exist in mullite grains. Figure 4(a) shows dislocations pinned by second phase particles. These pinned dislocations would need more energy to remove them because the resistance of dislocation sliding was increased. Extremely high dislocation density was observed in mullite after high-temperature strength determination, which explains the much improved high-temperature strength. Dislocations climbed at high temperature and twined with each other forming a network, which greatly decreased the mobility of dislocations. These dislocations would strongly hinder the propagation of cracks, and therefore improve the strength of the composite.

4 Summary

Strength-limiting flaws originating from processing defects could be effectively eliminated and the microstructural homogeneity of ZTM/SiC$_p$ composite could be greatly improved by the pressure filtration route. This material could further be optimized under HPing conditions of moderately low temperature and long holding time. As a result of various strengthening mechanisms, the strength of the composite at room temperature and at 1000°C increased significantly while the fracture toughness remained almost unchanged.

References

1. Yang, Z F., Xu, H. Y., Tan, J. Q., *et al.*, Mechanical properties of mullite-based composites. *J. Chinese Ceram. Soc.*, **17**[5] (1989) 467–471.
2. Xu, M. X., Cui, F., Jin, Z. G., *et al.*, Study on preparation of ultra-fine mullite powder. *J. Chinese Ceram. Soc.*, **19**[1] (1991) 80–85.
3. Liu, Q., Chen, Y. R., Yuan, Q. M., *et al.*, Mechanism of strengthening and toughening by zirconia in mullite–zirconia composite. *J. Chinese Ceram. Soc.*, **20**[4] (1992) 353–359.
4. Becher, P. F. & Tiegs, T. N., Toughening behavior involving multiple mechanisms: whisker reinforcement and zirconia toughening. *J. Am. Ceram. Soc.*, **70**[9] (1987) 651–654.
5. Huang, X. X., Hong, J. S. & Guo, J. K., SiC particle and Y-TZP reinforced mullite matrix composites. In *Proc. 4th Int. Symp. on Ceramic Materials and Components for Engines*, eds R. Carlsson, T. Johansson & L. Kahlman. Elsevier Applied Science, New York, 1992, pp. 795–799.
6. Nakano, K., *et al.*, in *Extended Abstracts of Annual Meeting*, The Ceramic Society of Japan, Tokyo, 1989, p. 311 (2E36).
7. Guo, R. S., Yang, Z. F., Yuan, Q. M., *et al.*, Preparation of ultrafine mullite powder and characteristics of its compact. *J. Chinese Ceram. Soc.*, **22**[3] (1994) 299–303.
8. Somiya, S. & Hirata, Y., Mullite powder technology and applications in Japan. *Am. Ceram. Soc. Bull.*, **70**[10] (1991) 1624–1632.
9. Okada, K., Otsuka, N. & Somiya, S., Review of mullite synthesis routes in Japan. *Am. Ceram. Soc. Bull.*, **70**[10] (1991) 1663–1640.
10. Zhou, G., The optimization study of preparing process of mullite-based composites. Master thesis, Tianjin University, China, 1991.
11. Guo, R. S., He, Z. F., Yang, Z. F., *et al.*, Controlling of flaw size and strength of ZTM/SiC$_p$ composites. *J. Chinese Ceram. Soc.*, **23**[1] (1995) 92–96.
12. Schneider, H., Okada, K. & Pask, J., *Mullite and Mullite Ceramics*. John Wiley & Sons, Chichester, 1994.

Journal of the European Ceramic Society **16** (1996) 1351–1363

PII: S0955-2219(96)00068-4
0955-2219/96/$15.00

Growth Stage Kinetics in the Synthesis of Al_2O_3/Al Composites by Directed Oxidation of Al–Mg and Al–Mg–Si Alloys

H. Venugopalan & T. DebRoy*

Department of Materials Science and Engineering, Pennsylvania State University, University Park, PA 16802, USA

(Received 20 August 1995; revised version received 18 March 1996; accepted 28 March 1996)

Abstract

Although synthesis of ceramic matrix composites by the directed oxidation process offers significant advantages over traditional composite processing routes, the scientific basis for the process is not fully understood. This paper is addressed to understanding the mechanism of composite growth from Al–Mg and Al–Mg–Si alloys theoretically and experimentally. Analysis of the oxidation kinetics of Al–Mg and Al–Mg–Si alloys for various oxygen pressures, temperatures and durations of oxidation, obtained in this study and reported in the literature, demonstrates that the growth kinetics can be tailored by the control of alloy composition. For the Al–Mg alloys, transport of oxygen through a thin alloy layer near the surface controls the growth rate. When Si is added to the alloy, the oxidation mechanism is completely changed. The rate of oxidation of Al–Mg–Si alloys depends on the transport of electronic species through a thin MgO layer at the top surface of the composite. Apart from contributing to a more complete understanding of the growth stage, the mechanism of composite growth will serve as a basis for improving growth rates.

Introduction

In the directed melt oxidation (DIMOX) process, a molten aluminium alloy is oxidized to produce ceramic/metal composites.[1] Figure 1 illustrates schematically the formation of composite materials in this process. Under appropriate conditions of alloy composition, temperature and oxygen pressure, a rapid reaction of the molten alloy with the oxidant to form α-alumina occurs and the reaction product grows outwards from the original metal surface. The reaction is fed by transport of liquid metal through the reaction product.[1] The resulting material is an Al_2O_3/Al composite with an interconnected network of unoxidized metal.[2] Reinforced composites with the desired structural properties can be obtained by growing the 'composite' matrix into preforms consisting of reinforcing particulates, whiskers or fibres of Al_2O_3, SiC, etc.[3–5] Composites made by directed oxidation can be tailored to have good toughness, thermal shock resistance, wear resistance, high stiffness, and high temperature stability. They are being used or evaluated for use in turbine engine components, armour applications, heat exchangers and furnace components.[6] Several ceramic composite systems based on the directed metal oxidation technology have been developed, as listed in Table 1.[3]

It is now recognised that the presence of volatile elements like Mg or Zn is crucial for directed oxidation of aluminium alloys to take place.[1,7] Dopants like Mg or Zn are believed to hinder the formation of a protective alumina film on the alloy surface and thus allow continued oxidation of the alloy. Additional elements such as Si are usually added to improve alloy/preform compatibility. These dopants can be either applied to the surface of the aluminium exposed to the oxidant or, if soluble, alloyed with the parent metal. Three distinct stages can be observed in the oxidation of Al–Mg alloys at a given temperature[8] (Fig. 2). When Al–Mg alloys are heated in argon to a given temperature and then exposed to an oxygen atmosphere, an initial stage of rapid weight gain occurs.[8] During this period, MgO forms by oxidation of Mg vapour and subsequently falls back on to the melt surface.[9] Formation of a dense, thin layer of $MgAl_2O_4$ beneath the MgO halts the initial stage of oxidation and corresponds to the start of incubation.[8] During incubation, metal

*To whom correspondence should be addressed.

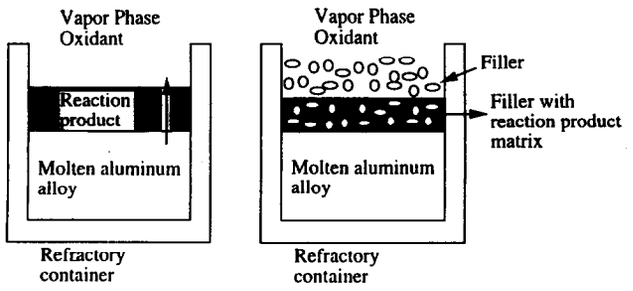

Fig. 1. Schematic description of formation of ceramic matrix composites by the directed oxidation process.

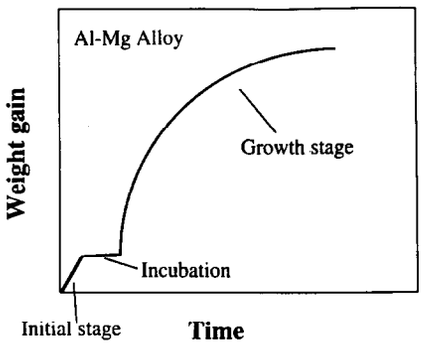

Fig. 2. Schematic plot of weight gain as a function of time for directed oxidation of Al–Mg alloys.

channels are observed to form in the spinel. The arrival of these metal channels at the top of the spinel is believed to correspond to the end of incubation and the start of the growth stage.[10] Composite formation in the growth stage starts when the near-surface aluminum alloy becomes depleted in Mg and reaches a concentration where Al_2O_3 formation becomes more favourable than $MgAl_2O_4$.[10] During growth, bulk oxidation of Al to Al_2O_3 occurs epitaxially on the spinel.[11]

Several models have been proposed to explain the kinetics of oxidation of Al to Al_2O_3 in the growth stage.[8,12] It has been suggested that during the growth stage of directed oxidation of Al–Mg alloys, a continuous MgO film exists at the top of the alumina matrix with a thin aluminium alloy film separating the two layers[11,13] (Fig. 3). The presence of this continuous MgO film restricts the formation of a protective alumina layer on the surface. At the MgO/Al-alloy film interface, MgO dissociates and oxygen dissolves in the Al-alloy film. The magnesium ions formed by dissociation of MgO diffuse through the MgO layer to the MgO/air interface where they are oxidized to regenerate MgO. During the outward transport of magnesium ions through MgO, electrical neutrality is maintained by the simultaneous transport of electronic defects.[12] The oxygen dissolved in the alloy film is transported, from the MgO/alloy film interface, to the alloy film/Al_2O_3 interface where composite growth takes place epitaxially. The supply of aluminium to the alloy film/Al_2O_3 interface is thought to be sustained by the wicking of metal

Table 1. Example of Lanxide®[a] ceramic matrix systems[3]

Parent metal	*Reaction product*
Al	Oxide, nitride, boride, titanate
Si	Nitride, boride, carbide
Ti	Nitride, boride, carbide
Zr	Nitride, boride, carbide
Hf	Boride, carbide
Sn	Oxide
La	Boride

[a]Lanxide® is a registered trademark of Lanxide Corporation, DE, USA.

through channels in the alumina. One or more of the above-mentioned reaction steps could be the rate-controlling mechanism in the growth stage.

Nagelberg *et al.*[12] conducted directed oxidation studies of Al–Mg alloys to which Si was added. According to Nagelberg *et al.*,[12] the rate of oxidation of Al–Mg–Si alloys in the growth stage is controlled by the electronic conductivity of the continuous, external, MgO layer. To investigate the role of electronic transport in the oxidation kinetics in the growth stage, DebRoy *et al.*[14] carried out directed oxidation experiments of an Al–Mg alloy (Al–5056 alloy) in which platinum wires were positioned inside the alloy so that the wires would extend through the composite matrix and the top MgO layer to facilitate electronic transport. They[14] observed that the rate of oxidation in the growth stage was independent of the presence or absence of Pt wires, indicating that the transport of electronic species does not control the oxidation kinetics of Al–Mg alloys that do not contain silicon. Thus, in the absence of silicon, electronic transport through the MgO layer is no longer the rate-controlling mechanism in the growth stage of Al–Mg alloys. In view of the crucial difference in the oxidation mechanism of Al–Mg alloys with or without the presence of Si, the role of silicon in the mechanism of composite growth from Al–Mg alloys needs to be investigated in detail.

In this paper, we examine the directed oxidation of Al–Mg and Al–Mg–Si alloys experimentally and theoretically. The oxidation kinetics are studied by thermogravimetry. The weight gain in the growth stage is monitored as a function of oxygen pressure, time and temperature. By analysing the experimental results reported in this paper and the available independent results in the literature, the role of silicon in the rate of composite growth is investigated. We show that the oxygen transport in the near-surface alloy layer controls the rate of alumina formation in the growth stage of directed oxidation of binary Al–Mg alloys. Analysis of the influence of silicon on the various steps in the growth

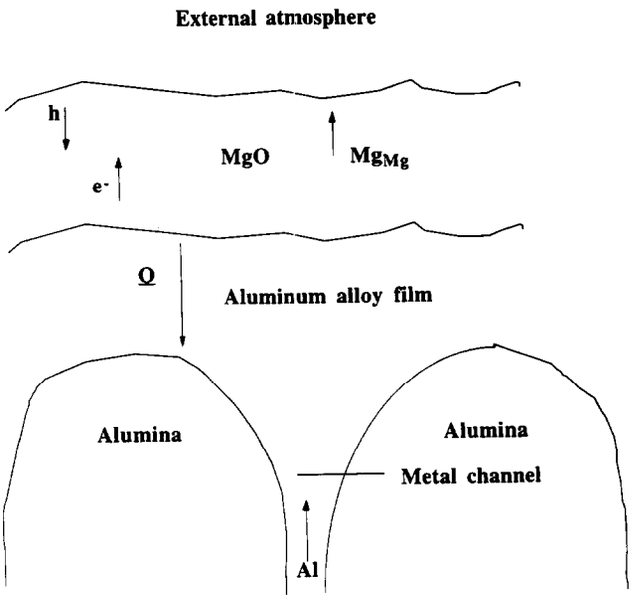

Fig. 3. Schematic diagram of the composite structure. Mg_{Mg} denotes a magnesium ion on the cationic site in MgO, and h denotes a hole.

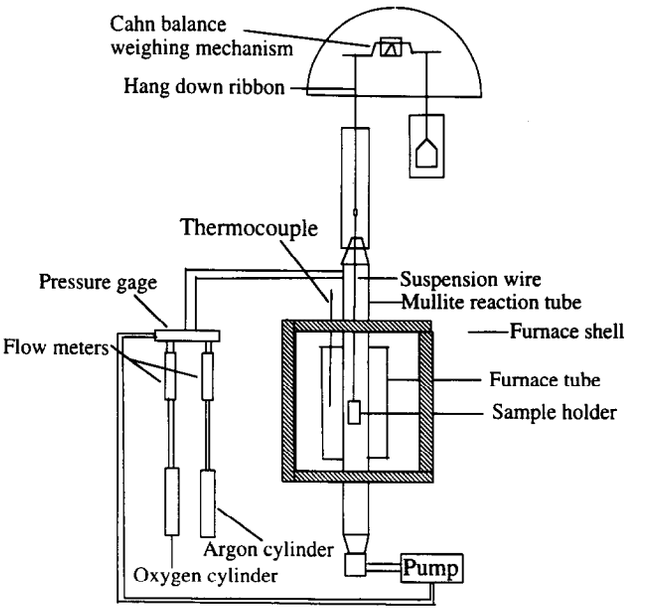

Fig. 4. Schematic diagram of the thermogravimetric set-up.

stage indicates that silicon additions increase the rate of oxygen transport through the alloy layer and decrease the rate of electronic transport through the MgO layer. As a result, electronic transport through the outer MgO layer controls the rate of oxidation of Al–Mg–Si alloys.

Experimental Procedure

The thermogravimetric set-up, used for studying reaction kinetics in the directed oxidation of Al–Mg alloys, consisted of a Cahn model 1000 automatic recording electric balance, a high-temperature silicon carbide tube furnace, and a gas flow and pressure control system. A schematic diagram of the experimental set-up is shown in Fig. 4. The balance had a sensitivity of 0·5 μg and the measurement accuracy was 0·1% of the range. The quartz reaction tube was of 48 mm internal diameter and had a 25 mm equi-temperature zone at the centre of the furnace. The furnace was equipped with an electronic temperature controller which regulated the temperature to ± 5 K.

A cylindrical sample, 14 mm in diameter and 8 mm in length, of an Al 5056 alloy (5 wt% Mg, 0·10 wt% Cu, 0·40 wt% Fe, 0·10 wt% Zn, 0·10 wt% Mn and balance Al) was placed in an alumina crucible, 14·2 mm in diameter and 27 mm in length. SiO_2 powder (99·9%, –325 mesh) was added to the surface of some samples as Si source. A previous investigation[15] of the kinetics of reaction between SiO_2 and molten aluminium revealed that SiO_2 is completely reduced by the aluminium melt during initial heating to the test temperature (>1350 K), which takes about an hour. Thus, SiO_2 additions of 205 mg effectively result in a composition of 3·3 mol% Si in the alloy. The crucible, containing the alloy, was suspended by a platinum wire from the balance and positioned within the equi-temperature zone of the furnace. Prior to conducting each experiment, the reaction tube was evacuated and purged with argon. The samples were then heated to the test temperature at a heating rate of 0·33 K s^{-1} in a pure argon atmosphere. When the target temperature was reached, a mixture of ultrahigh purity oxygen and argon was introduced at predetermined flow rates with the help of mass flow controllers, to obtain a target gas composition. Oxidation experiments were conducted at various partial pressures of oxygen, and reactor temperatures. Experiments were done at a constant total pressure of 93·3 kPa. Experiments were repeated to check the reproducibility of the weight gain data. The total gas flow rate was kept constant at 8333 mm^3 s^{-1} STP (298 K and 101·3 kPa). A typical scatter of 1–5% was observed in the weight gain measured during oxidation. The weight of the sample was continuously recorded using a computer data acquisition system. Subsequently, the recorded data were differentiated numerically to obtain the weight gain rate. The zero of the time axis is when oxygen of the desired partial pressure is introduced in the reactor. It takes about 75 s for the gas to reach the crucible. No correction of the zero of the time axis was made since the total oxidation time is of the order of about 60 ks. The internal cross-sectional area of the crucible, 154 mm^2, was used for the calculation of reaction rates.

In the directed oxidation of binary Al–Mg alloys, the oxidation product, Al_2O_3, often grew along the crucible walls in the growth stage. The behaviour

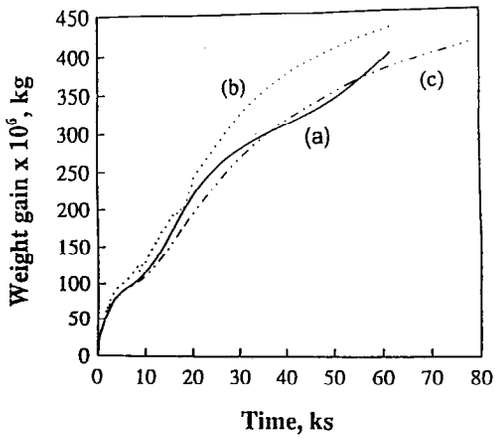

(A)

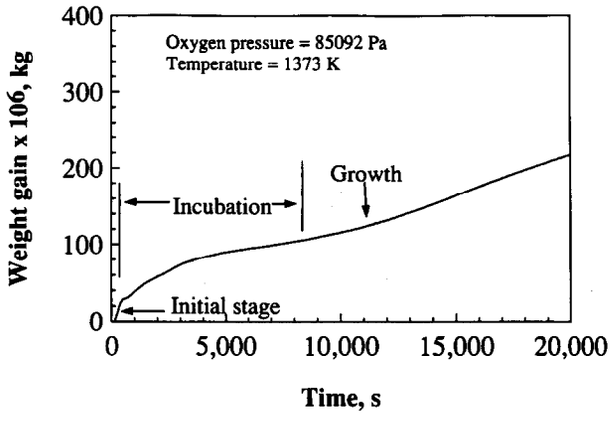

(B)

Fig. 5. (A) Weight gain versus time for the Al–Mg alloy at different oxygen pressures in the growth stage: (a) 85 092 Pa, (b) 21 273 Pa and (c) 42 546 Pa. The oxygen pressure was initially maintained at 85 092 Pa and subsequently changed in the growth stage. The total pressure, temperature and the total gas flow rate were maintained constant at 93 303 Pa, 1373 K and 8333 mm^3 s^{-1} STP, respectively. (B) Weight gain versus time for the Al–Mg alloy, at 1373 K and oxygen pressure of 85 092 Pa, at short oxidation times.

is similar to the preferential growth of alumina on the crucible wall observed by Xiao and Derby[16] and Manor *et al.*[17] The creeping is not surprising since the MgO which forms in the gas phase coats the crucible walls.[9] MgO is unstable in the presence of the Al–5 wt% Mg alloy at the temperatures involved in directed oxidation.[18–20] Therefore, there is a net driving force for the reaction between Al and MgO. The reaction causes Al to wet MgO,[21] creep along the walls and react with oxygen in the external atmosphere to form alumina. The metal creeping leads to a change in the melt cross-sectional area exposed to the oxygen atmosphere with time and complicates study of reaction kinetics. Investigation of initial stage kinetics[9] reveals that higher the oxygen pressure, the lower the total amount of MgO formed in the initial stage. Hence to minimize creeping in the directed oxidation of binary Al–Mg alloys, the oxygen pressure in the

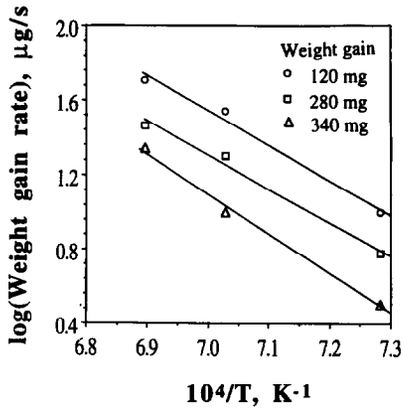

Fig. 6. Weight gain rate versus temperature for Al–Mg alloy for an oxygen pressure of 85 092 Pa, for different weight gains. The computed activation energies were 357·9, 345·9 and 407·8 kJ mol^{-1} for 120, 280 and 350 mg weight gains, respectively. The total pressure and the total gas flow rate were maintained constant at 93 303 Pa and 8333 mm^3 s^{-1} STP, respectively.

initial stage and in the incubation period was kept at a high value of 85·1 kPa and the oxygen pressure was subsequently changed in the growth stage. The end of incubation was identified from the weight gain data (in the course of the experiment) as the time at which there is an increase in the weight gain rate.

Results and Discussion

A typical weight gain versus time curve observed in the directed oxidation of Al–Mg alloys is shown in Fig. 2. The process starts with a rapid but limited oxidation event upon introduction of oxygen in the furnace. The initial oxidation, corresponding to the formation of MgO, ends abruptly with the formation of an $MgAl_2O_4$ film on the alloy surface. This event is followed by an incubation period where the weight gain is small. The onset of bulk growth is marked by a substantial increase in the oxidation rate. The kinetics and mechanism of the growth stage of composite synthesis from Al–Mg alloys, with or without silicon, are discussed in the following sections.

Mechanism of oxidation of Al–Mg alloys in the growth stage

Figure 5(A) is a plot of weight gain versus time for Al–Mg alloys for oxygen pressure of 85·1 kPa in the initial and incubation stages and varying oxygen pressures in the growth stage. It is observed that the oxidation rate in the growth stage decreases with time and, within experimental uncertainty, remains practically independent of oxygen pressure. Figure 5(B) is a plot of weight gain versus time at short oxidation times. Three different stages in the oxidation plot can be distinguished. Weight gain,

as a function of time, was also measured at various temperatures (1373–1450 K) for an oxygen pressure of 85·1 kPa. The weight gain rates in the growth stage, for different weight gains, were measured from the slopes and are plotted in Fig. 6. (Note that, for parabolic kinetics, weight gain rate measured at a constant weight gain would be proportional to the rate constant. The temperature dependence of the rate constant gives the activation energy.) Several important questions arise from the perusal of the rate data. Why does the weight gain rate decrease with time? Why is the weight gain rate practically independent of oxygen pressure? What is the rate-controlling mechanism in the growth stage of directed oxidation of Al–Mg alloys?

As shown in Fig. 3, the composite structure near the growth surface[11–13] consists of a continuous Al_2O_3-doped MgO layer on top of the alumina matrix with a thin aluminium alloy film separating the two layers. At the MgO/Al-alloy film interface, MgO dissociates, and the oxygen dissolves in the alloy film and is transported to the Al_2O_3/Al-alloy film interface where composite growth takes place epitaxially. The magnesium ions formed by the dissociation of MgO diffuse through the MgO layer to the MgO/air interface where they are oxidized to regenerate MgO. This ionic transport is accompanied by electronic conduction (holes or electrons) to maintain charge neutrality and is taken to be the rate-limiting process in the regeneration of MgO.[12] The supply of liquid aluminium to the alloy film/alumina interface is sustained by wicking of metal through channels in the alumina. Thus, the three possible rate-controlling steps in the growth of Al_2O_3/Al composites from Al–Mg alloys are: (i) electronic transport through the external MgO layer, (ii) transport of liquid metal by capillarity through the interconnected metal channels in the alumina, and (iii) dissociation of MgO and the subsequent transport of oxygen from the MgO/alloy film interface to the Al_2O_3/alloy film interface.

The existence of long columns of composite containing Al_2O_3 grains of similar orientation[11,13] disqualifies any process involving repeated nucleation of grains. This indicates that the growth process is continuous. Indeed, it can be observed from the composite macrostructure (Fig. 7) that the growth surface on the whole is macroscopically smooth. Hence, a one-dimensional model can be used to theoretically estimate the rates of the various transport processes involved in Al_2O_3 growth. The experimental results in Figs 5 and 6 are analysed below in detail to determine which of the above-mentioned steps are consistent with the observed growth rate and its dependence on time, oxygen pressure and temperature.

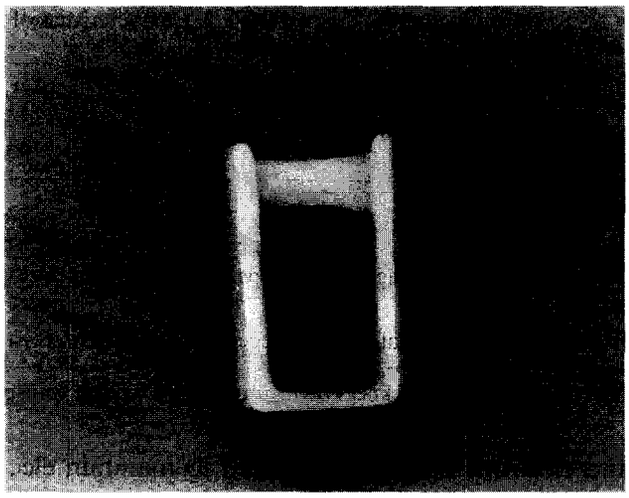

Fig. 7. Macrograph of composite (top region of crucible) grown from Al– 5 wt% Mg alloy (bottom region of crucible).

Electronic transport through MgO

Since MgO is unstable for the alloy compositions typically used in directed oxidation,[18–20] MgO dissociates at the alloy film/MgO interface to give up oxygen which is subsequently transported to the Al_2O_3/alloy film interface. The MgO could be regenerated either by the outward diffusion of magnesium ions to the external surface or by the inward diffusion of oxygen ions from the MgO/air interface to the MgO/alloy film interface (Fig. 3). According to Nagelberg *et al.*,[12] transport through the MgO layer is controlled by grain boundary diffusion of magnesium ions. This ionic transport is accompanied by electronic conduction (holes or electrons) to maintain charge neutrality and is taken to be the rate-limiting process. Near the external surface, in the Al_2O_3-doped MgO, holes are the dominant electronic defect and their concentration is proportional to $P_{O_2}^{1/4}$, where P_{O_2} is the partial pressure of oxygen in the reaction chamber.[12] This behaviour follows from the following defect reactions for the dissolution of alumina and oxygen in MgO:

$$Al_2O_3 \rightarrow 2Al_{Mg}^{\bullet} + V_{Mg}'' + 3O_O \qquad (1)$$

$$\frac{1}{2}\,O_2 \rightarrow O_O + V_{Mg}'' + 2h \qquad (2)$$

where V_{Mg}'' denotes a magnesium ion vacancy, $Al_{Mg}^{\bullet}$ represents the dissolved aluminium concentration in MgO and h indicates a hole. Similarly, for the low oxygen pressures near the alloy film, the concentration of electrons in MgO would be high.

$$\frac{1}{2}\,O_2 + 2e \rightarrow O_O + V_{Mg}'' \qquad (3)$$

Thus, the outward transport of magnesium ions in the MgO towards the external surface is accompanied by the transport of holes near the external surface

Table 2. Characteristics of various events in the growth stage

Event	*Oxygen pressure dependence of growth rate*	*Time dependence of growth rate*	*Activation energy (kJ mol^{-1})*	*Weight gain rate (mg cm^{-2} h^{-1}) at 1373 K*
Magnesium ion flux	$P_{O_2}^{1/4}$	Independent of time	310	17.44
Liquid metal transport	Independent of oxygen pressure	Decreases with time	6.1	6415
Oxygen transport through alloy film	Independent of oxygen pressure	Decreases with time	243.6	53.17[a]
Experimental growth rate	Independent of oxygen pressure	Decreases with time	361	12.75

[a]For an alloy layer thickness of 12 μm, rate of oxygen transport is 13.39 mg cm^{-2} h^{-1}.

and electrons near the alloy film to maintain electrical neutrality. From reaction (2), the hole concentration, p, is given as:

$$p = \left[\frac{K}{V''_{Mg}}\right]^{1/2} P_{O_2}^{1/4} \quad (4)$$

where K is the equilibrium constant of reaction (2).

From charge neutrality, we have:

$$V''_{Mg} = \frac{1}{2} Al^{\bullet}_{Mg} \quad (5)$$

The flux of magnesium ions and the corresponding flux of oxygen is proportional to the hole concentration, p.[12] Following the procedure of Nagelberg *et al.*,[12] the oxygen flux, J, in g cm^{-2} s^{-1}, at 1373 K, is given as:

$$J \propto \left[\frac{K}{V''_{Mg}}\right]^{1/2} P_{O_2}^{1/4} = 3{\cdot}15 \times 10^6 P_{O_2}^{1/4} \exp\left(\frac{-310 \times 10^3}{RT}\right) \quad (6)$$

where P_{O_2} is the partial pressure of oxygen in atmospheres, R is the gas constant in J mol^{-1} K^{-1}, and T is the temperature in K. The activation energy for the process is 310 kJ mol^{-1} which corresponds to the mobility of holes in MgO (Table 2).

Oxygen pressure and time dependences of magnesium ion transport. It is seen from eqn (6) that if magnesium ion flux through MgO were rate-limiting, the oxygen flux (growth rate) would exhibit a $P_{O_2}^{1/4}$ dependence. Thus eqn (6) predicts that, for a change in oxygen pressure from 21·3 to 85·1 kPa, the weight gain rate would increase by 41·4%. However, a 6·5% decrease in the weight gain rate is observed in the average experimental growth rate (Fig. 5) when the oxygen pressure is changed from 21·3 to 85·1 kPa. Equation (6) also predicts that the oxygen flux should be independent of time. Experimentally, however, the weight gain rate (growth rate) decreases with time. Thus, this mechanism cannot explain either the manner in which the rate varies with time or the observed effect of oxygen pressure on the growth rate. Therefore, this event is ruled out as a rate-limiting step.

Liquid metal transport

Rate expression. The reaction of Al with oxygen to form Al_2O_3 requires the continued supply of aluminium to the Al-alloy film/Al_2O_3 interface. This is believed to occur via convective flow of metal by wicking (capillary action) through the thickening Al_2O_3 reaction product via the interconnected metal channels. If liquid metal transport through metal channels is rate-controlling, the total metal flow through the channels would determine the composite growth rate. Furthermore, the growth rate will show the same dependence on time and P_{O_2} as capillary flow. Therefore, the time and P_{O_2} dependences of metal flow rate and the corresponding oxygen weight gain rate need to be analysed. As shown in Appendix A, the weight gain rate per unit area, J, is given by:

$$J = \frac{48}{54} \frac{f\rho_{Al} R \gamma_{LV} \cos\theta}{4\mu x} = \frac{48}{54} \frac{f\rho_{Al}}{4} \left[\frac{2R\gamma_{LV}\cos\theta}{\mu t}\right]^{1/2} \quad (7)$$

where f is the total metal channel area per unit area of the composite, ρ_{Al} the density of molten aluminium alloy, R is the radius of the channel, γ_{LV} is the surface tension of the molten alloy, θ is the contact angle between the molten alloy and alumina, μ is the viscosity of the molten alloy, x is the thickness of the composite, and t is the time of oxidation.

Oxygen pressure and time dependences of rate of liquid metal transport. It is seen from eqn (7) that if liquid metal transport is rate-controlling, the growth rate would be independent of oxygen pressure and decrease with time. The experimentally observed oxygen pressure and time dependences of rate (Fig. 5) are qualitatively consistent with that predicted by eqn (7) for liquid metal transport. If the predicted growth rate is also in good agreement with the experimentally observed growth rate for the Al–5 wt% Mg alloy, transport of liquid metal can then be considered as the rate-controlling step in the growth of Al_2O_3/Al composites.

Table 3. Data used for the calculation of rate of liquid metal transport

Property	*Symbol*	*Value*	*Ref.*
Total metal channel area per unit area of the composite	f	10^{-5}	2
Density of aluminium (kg m^{-3})	ρ_{Al}	2300	22
Channel radius (m)	R	3×10^{-6}	11
Viscosity of molten aluminium (N s m^{-2})	μ	$6{\cdot}21 \times 10^{-4}$	23
Vapour pressure of magnesium (N m^{-2})	P_c	5019	18–20
Gravitational pressure (N m^{-2})	P_g	2955[a]	This study
Capillary pressure (N m^{-2})	P_v	$6{\cdot}3 \times 10^5$	Appendix A

[a]For a composite thickness of 0·00131 m. This corresponds to a weight gain of 3×10^{-4} kg.

Comparison of the rate of liquid metal transport with the experimental growth rate. The experimental results (Fig. 5) indicate that the weight gain rate decreases with time and is independent of the oxygen pressure. These trends are consistent with a situation where the transport of liquid metal controls the oxidation rate [eqn (7)]. However, the calculated weight gain rate needs to be compared with the experimentally observed value to confirm that the transport of liquid metal through the oxide matrix controls the oxidation rate. The value of $\gamma_{LV}\cos\theta$ in eqn (7) is deduced, as shown in Appendix A. The data used in the calculation of rate based on eqn (7) are shown in Table 3. For a weight gain of 300 mg, which corresponds to a composite thickness of 0·13 cm, the weight gain rate is predicted to be 6415 mg cm^{-2} h^{-1} based on eqn (7), while the experimentally observed weight gain rate is found from Fig. 7 to be 10·8 mg cm^{-2} h^{-1}. It is seen that the experimentally observed weight gain rate is about two orders of magnitude lower than the lowest estimate of the predicted weight gain rate (Table 2). Furthermore, the theoretical activation energy for the liquid metal transport corresponds to the temperature sensitivity of viscosity of the liquid aluminium alloy [eqn (7)] and is about 6·1 kJ mol^{-1},[23] while the experimentally observed value is 361 kJ mol^{-1}. Thus, liquid metal transport through the metal channels does not control the rate of oxidation of Al to Al_2O_3 in the growth stage.

Oxygen transport through alloy film

Flux of oxygen. The flux of dissolved oxygen from the MgO/Al-alloy interface to the Al_2O_3/Al-alloy interface can be estimated using Fick's law as:

$$J = \frac{16D_O(X_O^I - X_O^{II})}{LV_m} \quad (8)$$

where J denotes the flux of oxygen, D_O is the diffusion coefficient of oxygen in molten aluminium, X_O^I is the mole fraction of dissolved oxygen in the alloy film at the MgO/alloy film interface, X_O^{II} is the mole fraction of dissolved oxygen in the alloy film at the Al_2O_3/alloy film interface, L is the thickness of the alloy film, and V_m is the molar volume of the alloy. The value of X_O^I can be estimated from the MgO/Al-alloy equilibrium:

$$MgO = \underline{Mg} + \underline{O}\ (1\ mol\%) \quad (9)$$

where $\underline{Mg}$ and $\underline{O}$ denote magnesium and oxygen dissolved in the alloy film respectively. From reaction (9) we get:

$$X_O^I = \frac{\exp(-\Delta G_m^\circ/RT)}{100\gamma_{Mg}X_{Mg}} \quad (10)$$

where ΔG_m° is the standard free energy change of reaction (9), X_{Mg} is the mole fraction of magnesium in the aluminium alloy, and γ_{Mg} is the activity coefficient for magnesium in liquid aluminium. A similar expression can be derived for X_O^{II} from the Al_2O_3/Al-alloy equilibrium:

$$Al_2O_3 = 2\ \underline{Al} + 3\ \underline{O}\ (1\ mol\%) \quad (11)$$

$$X_O^{II} = \frac{\exp(-\Delta G_A^\circ/3RT)}{100\ [\gamma_{Al}(1 - X_{Mg})]^{\frac{2}{3}}} \quad (12)$$

where ΔG_A° is the standard free energy change of reaction (11) and γ_{Al} is the activity coefficient of aluminium in the alloy. It can be seen from eqns (10) and (12) that an increase in the Mg concentration leads to a decrease in the dissolved oxygen concentration at the MgO/alloy interface and an increase in the dissolved oxygen concentration at the Al_2O_3/alloy interface. As a result, the rate of oxygen transport across the alloy film decreases [eqns (8), (10) and (12)]. Thus, with increasing Mg concentration in the alloy film, oxygen transport across the alloy film becomes an important transport step in the growth stage of directed oxidation of Al–Mg alloys.

Oxygen pressure and time dependences of oxygen flux. The Al–Mg alloy in the composite channels attains equilibrium with $Al_2O_3/MgAl_2O_4$.[12,16,24] Based on the available thermodynamic data,[18–20] this equilibrium alloy composition is 0·19 mol% Mg at 1373 K. The Ag–Mg alloy wicks through the metal channels, reacts with the dissolved oxygen and forms fresh alumina epitaxially on the existing alumina. The solubility limit for Mg in Al_2O_3 is 0·012 mol% at 2073 K[25] and the solubility decreases rapidly with decreasing temperature. As the

Table 4. Data used in the calculation of oxygen transport through the near-surface alloy layer

Property	*Symbol*	*Value*	*Ref.*
Diffusivity of oxygen in molten aluminium[a] ($m^2 s^{-1}$)	D_O	1.3×10^{-8}	23
Thickness of alloy layer (m)	L	3×10^{-6}	13
Oxygen concentration in the alloy film at the MgO/film interface[b] (mole fraction)	X_O^I	2.5×10^{-5}	18–20, 27
Oxygen concentration in the alloy film at the Al_2O_3/film interface[b] (mole fraction)	X_O^{II}	1.1×10^{-6}	18–20, 27

[a]Tracer diffusivity of oxygen in molten aluminium is approximated by the diffusivity of aluminium in molten aluminium.
[b]Oxygen concentrations calculated at 1373 K for Mg concentration of 0·19 mol% in the alloy film.

aluminium in the alloy gets oxidized to alumina, the concentration of magnesium in the alloy film tends to increase to values higher than 0·19 mol% Mg. The build-up of magnesium concentration in the alloy film continues with time unless magnesium back-diffusion down the metal channels into the bulk alloy occurs at appreciable rates. Since liquid metal transport through the channels to the reaction interface is fairly rapid, the solute enrichment is likely to continue. It can be seen from eqns (10) and (12) that when the magnesium concentration in the alloy increases, the equilibrium oxygen concentration at the MgO/alloy interface decreases. At the same time, the dissolved oxygen concentration at the Al_2O_3/alloy interface increases. Thus, the increase of magnesium concentration in the alloy film leads to a lower oxygen concentration gradient across the film. As a result, the rate of oxygen transport in the near-surface alloy layer decreases with time. Furthermore, it is observed from eqn (8) that the rate is independent of oxygen pressure. These trends are consistent with the experimentally observed dependence of growth rate on time and oxygen pressure.

As the growth stage progresses, continued Mg enrichment in the near-surface alloy film can lead to the precipitation of $MgAl_2O_4$ spinel, between the MgO and the underlying metal, as observed by several investigators.[8,11,26] $MgAl_2O_4$ forms beneath the MgO rather than on top of Al_2O_3 owing to nucleation considerations.[26] The spinel subsequently demixes due to the presence of the oxygen gradient across the alloy film, exposing the film to MgO. A fresh nucleation of Al_2O_3 occurs on the existing alumina layer.[11,26] This is consistent with the proposed mechanism for the growth stage. The oxygen required for alumina formation is supplied by dissociation of MgO. The observed continuing decrease in the growth rate with time[8] is consistent with our proposed model.

Oxygen flux through the near-surface alloy layer and the growth rate. The data used in eqn (8) for calculation of the maximum rate of oxygen transport are presented in Table 4. Note that the oxygen transport rate would be maximum at the start of the growth stage when the Mg concentration in the alloy film corresponds to about 0·19 mol%, i.e. the Mg concentration in the alloy corresponding to the $MgAl_2O_4/Al_2O_3$ equilibrium at 1373 K. The maximum rate of oxygen transport at 1373 K is estimated to be 53·17 mg cm^{-2} h^{-1}. This value is within an order of magnitude of the experimentally observed maximum growth rate of 12·75 mg cm^{-2} h^{-1}. The estimated rate of oxygen transport would be exactly equal to the experimental growth rate for a metal layer thickness of about 12 μm. This value of thickness of the metal layer is higher than the values of 1 to 3 μm reported by Antolin *et al.*[13] However, this value is probably not unreasonable in view of the uncertainties involved in the calculation, and the possibility that the metal layer thickness during the reaction may be higher than that observed after cooling to room temperature. The experimentally determined rate values are consistent with the possibility that oxygen transport through the metal layer is the rate-limiting step in the composite growth stage.

Activation energy of oxygen flux across alloy film. Since the oxygen concentration at the MgO/alloy film interface is much higher than the dissolved oxygen concentration at the Al_2O_3/metal interface (Table 4), eqn (8) can be approximated as:

$$J = \frac{16 D_O X_O^I}{L V_m} \tag{13}$$

Using eqn (10) in (13) we get:

$$J = \frac{16 D_O \exp(\Delta H_m^\circ / RT) \exp(\Delta S_m^\circ / R)}{100 \gamma_{Mg} X_{Mg} L V_m} \tag{14}$$

where ΔH_m° is the standard enthalpy change for reaction (9) and ΔS_m° is the standard entropy change for reaction (9). The activation energy for oxygen diffusion in liquid aluminium is small (6·1 kJ mol^{-1}).[23] Therefore, the variation of D_O is insignificant over the temperature range of 1373–1450 K examined in this study. The activation energy for oxygen flux is deduced from eqn (14) as ΔH_m°, and is equal to 243·6 kJ mol^{-1}.[18–20,27] Thus, the observed activation energy and weight gain rate in the growth stage are in fair agreement with those predicted for oxygen transport through the near-surface alloy layer. Considerations of the liquid

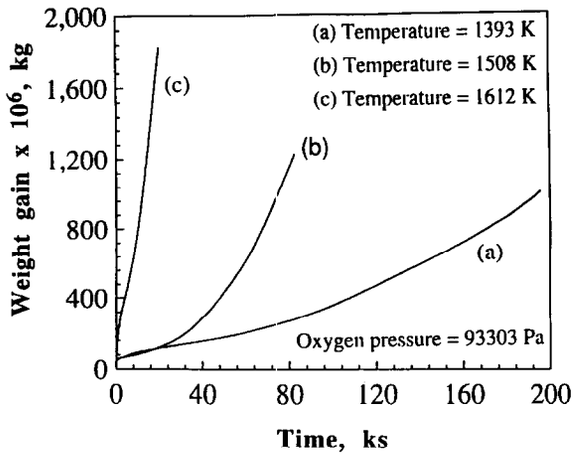

Fig. 8. Weight gain versus time for Al–Mg–Si alloy at different temperatures: (a) 1393 K, (b) 1508 K and (c) 1612 K. The total pressure, oxygen pressure and the total gas flow rate were maintained constant at 93 303 Pa, 93 303 Pa and 8333 $mm^3\ s^{-1}$ STP, respectively.

metal transport through channels in the composite or magnesium ion transport through the MgO layer cannot explain the observed oxidation behaviour. The predictions of the oxygen transport model are consistent with the observations of Vlach *et al.*[8] and Xiao and Derby,[16] who reported parabolic oxidation kinetics in the growth stage and an activation energy of around 270 kJ mol^{-1}. Thus, the transport of oxygen through the near-surface alloy layer is the rate-controlling event in the growth stage of directed oxidation of Al–Mg alloys in the temperature range 1373 to 1450 K.

The proposed model for growth stage kinetics of Al–Mg alloys can be used to predict the effect of additional alloying elements on the growth rate. It is known that Ni additions to Al–Mg alloys refine the composite microstructure.[5] The effect of Ni additions on the composite growth rate can be predicted with the help of the oxygen transport model. There is a strong interaction between Ni

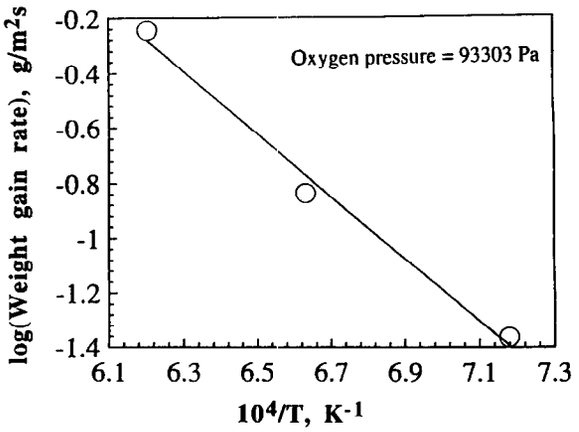

Fig. 9. Weight gain rate versus temperature for Al–Mg–Si alloy for an oxygen pressure of 93 303 Pa. The total pressure and the total gas flow rate were maintained constant at 93 303 Pa and 8333 $mm^3\ s^{-1}$ STP, respectively.

Table 5. Growth rate of Al–Mg–Si alloy as a function of oxygen pressure at 1612 K

Oxygen pressure (kPa)	*Growth rate (g $m^{-2}\ s^{-1}$)*
93·3	0·567
46·6	0·522
23·3	0·439

and Al as indicated by the highly negative heat of formation of Ni–Al intermetallics.[20] Therefore, Ni additions to the Al–Mg alloy would be expected to reduce the activity coefficient of Al in the melt. On the other hand, Ni does not form highly stable intermetallics with Mg.[20] As a result, Ni would not be expected to influence the Mg activity coefficient in the Al melt. Therefore, it can be seen from eqns (8), (10) and (12) that Ni additions to an Al–Mg alloy would reduce the growth rate. Thus, in addition to refining the composite microstructure,[5] Ni additions would reduce the composite growth rate.

Mechanism of oxidation of Al–Mg–Si alloys in the growth stage

Figure 8 is a plot of weight gain versus time at various temperatures (1393–1612 K) for an oxygen pressure of 93·3 kPa. The weight gain versus time data in the growth stage in Fig. 8, at a given temperature, could be fitted to a straight line. The average weight gain rates in the growth stage were plotted as a function of temperature in Fig. 9 and the activation energy is found to be 218 kJ mol^{-1}. Weight gain rates were also measured at different oxygen pressures at a temperature of 1612 K (Table 5). The experimental results indicate that the oxidation rate in the growth stage is independent of time and varies as $P_{O_2}^{1/4}$. These trends are consistent with a situation where electronic transport through MgO controls the oxidation rate. This is consistent with the observation of Nagelberg *et al.*[12] that electronic transport controlled the growth rate of Al–Mg–Si alloys. Several important questions arise from the analysis of the data. How does silicon addition to Al–Mg alloy shift the oxidation mechanism from oxygen transport through the near-surface alloy layer to electronic transport through MgO?

Influence of silicon on the oxygen transport through the alloy layer

Formation of Mg–Si clusters in binary Mg–Si liquid solutions[28] indicates that silicon additions to Al–Mg alloys could affect the activity of magnesium. The change in the activity of magnesium in the near-surface alloy layer, observed in directed oxidation, would affect the solubility of oxygen at

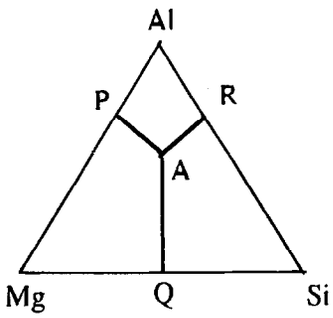

Fig. 10. Schematic description of estimation of Al–Mg–Si thermodynamics from the limiting binaries using the shortest distance composition path. Al–Mg–Si thermodynamics at composition A estimated from the thermodynamics of Al–Mg at composition P, of Mg–Si at composition Q and of Al–Si at composition R, respectively. Compositions P, Q and R were obtained by drawing perpendiculars from A to the three limiting binaries.

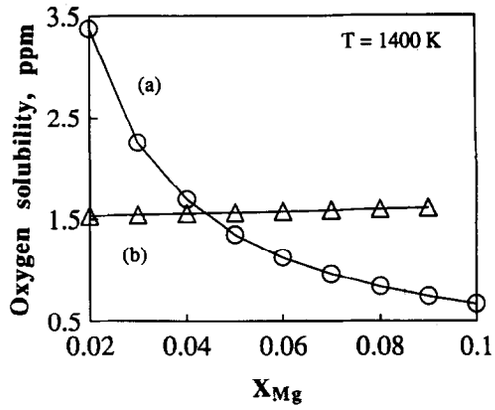

Fig. 11. Calculated equilibrium solubility in the Al–Mg alloy film at (a) the MgO/alloy film interface and (b) the Al_2O_3/alloy film interface, for varying magnesium contents.

the MgO/Al-alloy interface [eqn (10)]. Silicon could also affect the Al activity in the alloy layer. Thus silicon additions are expected to alter the oxygen solubility gradient across the alloy film and, thereby, affect the rate of oxygen transport [eqn (8)]. The effect of silicon additions on the activities of Mg and Al in the near-surface alloy layer can be estimated from Al–Mg–Si ternary liquid solution thermodynamics. Though thermodynamic data on Al–Mg–Si liquid solutions are not available, they can be estimated as shown in Appendix B. The thermodynamics of Al–Mg–Si for the composition A is deduced from the thermodynamics of Al–Mg at composition P, Mg–Si at composition Q and Al–Si at composition R (Fig. 10) by the equation:

$$RT\ln\gamma_{Mg} = \frac{X_{Al}^{A}(X_{Al}^{A} + X_{Si}^{A})\Delta\bar{G}_{Mg/Al\text{-}Mg}^{XS}}{(1 - X_{Mg}^{P})^2} + \frac{X_{Si}^{A}(X_{Al}^{A} + X_{Si}^{A})\Delta\bar{G}_{Mg/Mg\text{-}Si}^{XS}}{(1 - X_{Mg}^{Q})^2} - \frac{X_{Al}^{A}X_{Si}^{A}\Delta G_{m/Al\text{-}Si}^{XS}}{X_{Al}^{R}X_{Si}^{R}} \quad (15)$$

where γ_{Mg} denotes the activity coefficient of Mg in the Al–Mg–Si ternary at the composition A, $\Delta\bar{G}_{Mg/Al\text{-}Mg}^{XS}$ denotes the excess partial molar free energy of mixing of Mg in the Al–Mg binary at the composition P, $\Delta\bar{G}_{Mg/Mg\text{-}Si}^{XS}$ denotes the excess partial molar free energy of mixing of Mg in the Mg–Si binary at composition Q, and $\Delta G_{m/Al\text{-}Si}^{XS}$ denotes the excess free energy of mixing of Al–Si binary at composition R. The symbols X_{Al}^{A}, X_{Mg}^{A} and X_{Si}^{A} denote the molar compositions of Al, Mg and Si, respectively, at point A in the Al–Mg–Si ternary diagram. X_{Al}^{P} and X_{Mg}^{P} denote the mole fractions of Al and Mg respectively at composition P, X_{Mg}^{Q} and X_{Si}^{Q} denote the mole fractions of Mg and Si respectively at composition Q, and X_{Al}^{R} and X_{Si}^{R} denote the mole fractions of Al and Si respectively at composition R. Similarly, the activity coefficient of Al in the Al–Mg–Si ternary can be deduced as shown in Appendix B.

Figures 11 and 12 show the effect of Si on the oxygen solubility gradient across the alloy film for Al–Mg and Al–Mg–Si alloys, respectively. It can be observed that the presence of silicon in the melt reduces the oxygen solubility gradient in the alloy film from the MgO/Al-alloy interface to the Al_2O_3/Al-alloy interface. For the Al-Mg alloy used in this study, SiO_2 additions result in a silicon content in the alloy of 3·3 mol.%. Thermodynamic calculations indicate that silicon addition of 3·3 mol% reduces the activity of Mg in the alloy channels by a factor of 0·67 at a temperature of 1393 K. However, silicon additions do not affect the activity of Al in Al–Mg–Si significantly. Equation (14) indicates that the rate of oxygen transport is inversely proportional to the activity of Mg in the near-surface alloy layer. Thus, for the alloy used in this study, silicon additions accelerate the rate of oxygen transport by a factor of 1·5 at 1393 K. As a result of the enhanced oxygen transport, this step becomes less important in the oxidation of Al–Mg–Si alloys than in that of Al–Mg alloys.

Influence of silicon on electronic transport through MgO

Since silicon is present in the melt, a small proportion would be incorporated into the MgO which is present on top of the near-surface alloy melt. The dissolution of silicon in MgO would increase the concentration of magnesium ion vacancies according to the equation:

$$V_{Mg}'' = \frac{1}{2}Al_{Mg}^{\bullet} + Si_{Mg}^{\bullet\bullet} \quad (16)$$

where $Si_{Mg}^{\bullet\bullet}$ represents the dissolved silicon concentration in MgO. It is seen from eqn (16) that silicon

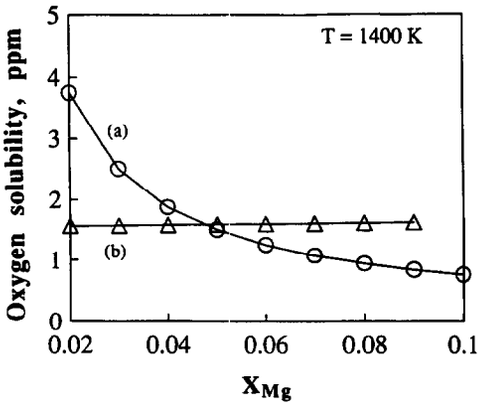

Fig. 12. Calculated equilibrium solubility in the Al–Mg–3·28 wt% Si alloy film at (a) the MgO/alloy film interface and (b) the Al_2O_3/alloy film interface, for varying magnesium contents.

additions increase V''_{Mg}. Since the hole concentration, p, is inversely proportional to V''_{Mg} [eqn (4)], silicon additions would thus decrease p. It is known that the rate of electronic transport in MgO is proportional to the hole concentration, p [eqn (6)].[12] As a result, silicon additions to Al–Mg alloys decrease the rate of electronic transport through MgO.

Thus, it is seen that silicon additions to Al–Mg alloys increase the rate of oxygen transport through the alloy film and decrease the rate of electronic transport through MgO, respectively. As a result of the reduced rate of electronic transport through MgO, this step becomes more important in the oxidation of Al–Mg–Si alloys than in that of Al–Mg alloys. The experimental results on the oxygen pressure and time dependences of the growth rate of Al–Mg–Si alloys are consistent with the characteristics of an oxidation reaction controlled by electronic transport through MgO, i.e. growth rate independent of time and proportional to $P_{O_2}^{1/4}$. Thus, the addition of 3.3 mol% Si to Al–5.5 mol% Mg shifts the oxidation mechanism from oxygen transport through the near-surface alloy layer to electronic transport through MgO.

Summary and Conclusions

The oxidation rates in the growth stage of directed oxidation of Al–Mg and Al–Mg–Si alloys have been investigated. The weight gain rate in the growth stage of Ag–Mg alloys decreased with time and was independent of oxygen pressure. The activation energy for the growth process was found to be 361 kJ mol^{-1}. The oxygen pressure, time and temperature dependences of the growth rate of Al–Mg alloys are consistent with the characteristics of an oxidation reaction controlled by oxygen transport through the near-surface alloy layer.

The weight gain rate in the growth stage of Al–Mg–Si alloys was independent of time and proportional to $P_{O_2}^{1/4}$. Analysis of the influence of silicon on the various steps in the growth stage indicates that silicon additions increase the rate of oxygen transport through the alloy layer and decrease the rate of electronic transport through the MgO layer. As a result, electronic transport through the outer MgO layer controls the growth stage mechanism in the directed oxidation of Al–Mg–Si alloys, which is consistent with the experimental results. Thus, silicon additions to Al–Mg alloys alter the oxidation mechanism from oxygen transport through the near-surface alloy layer to electronic transport through the MgO layer.

Acknowledgments

The authors wish to thank Dr K. Tankala for useful discussions and Professor R. Roy for his interest in the work. This work was supported by the National Science Foundation, Division of Materials Research under Grant No. DMR-9118075.

References

1. Newkirk, M. S., Urquhart, A. W., Zwicker, H. R. & Breval, E., Formation of Lanxide™ ceramic composite materials. *J. Mater. Res.*, **1**[1] (1986) 81–89.
2. Venugopalan, H., Tankala, K. & DebRoy, T., Electrical conductivity of alumina/aluminum composites synthesized by directed metal oxidation. *J. Am. Ceram. Soc.*, **77**[11] (1994) 3045–3047.
3. Newkirk, M. S., Lesher, H. D., White, D. R., Kennedy, C. R., Urquhart, A. W. & Claar, T. D., Ceramic matrix composites: matrix formation by the directed oxidation of molten metals. *Ceram. Eng. Sci. Proc.*, **8**[7–8] (1987) 879.
4. Andersson, C. A., Barron-Antolin, P., Schiroky, G. H. & Fareed, A. S., Properties of fiber-reinforced Lanxide™ alumina matrix composites. *Whisker and Fiber Toughened Ceramics*, ASM International, Materials Park, OH, 1988, pp. 209–215.
5. Nagelberg, A. S., Fareed, A. S. & Landini, D. J., Production of ceramic matrix composites for elevated temperature applications using the DIMOX™ directed metal oxidation process. *Processing and Fabrication of Advanced Materials*, The Minerals, Metals and Materials Society, Warrendale, PA, 1992, pp. 127–142.
6. Urguhart, A. W., Novel reinforced ceramics and metals: a review of Lanxide's technologies. *Mater. Sci. Eng.*, **A144** (1991) 75–82.
7. Nagelberg, A. S., Growth kinetics of Al_2O_3/metal composites from a complex aluminum alloy. *Solid State Ionics*, **32/33**, (1989) 783–788.
8. Vlach, K. C., Salas, O., Ni, H., Jayaram, V., Levi, C. G. & Mehrabian, R., A thermogravimetric study of the oxidative growth of Al_2O_3/Al composites. *J. Mater. Res.*, **6**[9] (1991) 1982–1995.
9. Venugopalan, H., Tankala, K. & DebRoy, T., Probing the initial stage of synthesis of Al_2O_3/Al composites by directed oxidation of Al–Mg alloys. *Metall. Trans. B*, **27B** (1996) 43–50.

10. Salas, O., Jayaram, V., Vlach, K. C., Levi, C. G. & Mehrabian, R., Early stages of composite formation by oxidation of liquid aluminum alloys. *J. Am. Ceram. Soc.*, **78**[3] (1995) 609–622.
11. Salas, O., Ni, H., Jayaram, V., Vlach, K. C., Levi, C. G. & Mehrabian, R., Nucleation and growth of Al_2O_3/metal composites by oxidation of aluminum alloys. *J. Mater. Res.*, **6**[9] (1991) 1964–1981.
12. Nagelberg, A. S., Antolin, S. & Urquhart, A. W., Formation of Al_2O_3/metal composites by the directed oxidation of molten aluminium–magnesium–silicon alloys: Part II, Growth kinetics. *J. Am. Ceram. Soc.*, **75**[2] (1992) 455–462.
13. Antolin, S., Nagelberg, A. S. & Creber, D. K., Formation of Al_2O_3/metal composites by the directed oxidation of molten aluminum–magnesium–silicon alloys: Part I, Microstructural development. *J. Am. Ceram. Soc.*, **75**[2] (1992) 447–454.
14. DebRoy, T., Bandhopadhyay, A. & Roy. R., Oxide matrix composite by directional oxidation of a commercial aluminum–magnesium alloy. *J. Am. Ceram. Soc.*, **77**[5] (1994) 1296–1300.
15. Standage, A. E. & Gani, M. S., Reaction between vitreous silica and molten aluminum. *J. Am. Ceram. Soc.*, **50**[2] (1967) 101–105.
16. Xiao, P. & Derby, B., Alumina/aluminum composites formed by the directed oxidation of aluminum using sodium hydroxide as a surface dopant. *J. Am. Ceram. Soc.*, **77**[7] (1994) 1771–1776.
17. Manor, E., Ni, H., Levi, C. G. & Mehrabian, R., Microstructure evolution of SiC/Al_2O_3/Al-alloy composites produced by melt oxidation. *J. Am. Ceram. Soc.*, **76**[7] (1993) 1777–1787.
18. Tiwari, B. L., Thermodynamic properties of liquid Al–Mg alloys measured by the emf method. *Metall. Trans. A*, **18A** (1987) 1645–1651.
19. Chase Jr, M. W., Davies, C. A., Bowary Jr, J. R., Fromp, D. J., McDonald, R. A. & Syverud, A. N., *JANAF Thermochemical Tables*, 3rd edn. American Chemical Society, Washington, DC, 1986.
20. Kubaschewski, O., Alcock, C. B. & Spencer, P. J., *Materials Thermochemistry*. Pergamon Press, 1993.
21. Aksay, I., Hoge, C. E. & Pask, J. A., Wetting under chemical equilibrium and non-equilibrium conditions. *J. Phys. Chem.*, **78**[12] (1974) 1778–1783.
22. Brandes, E. A. & Brook, G. B. (eds), *General Physical Properties: Smithells Metals Reference Handbook*, 7th edn. Butterworth-Heinemann, London, UK, 1992, pp. 14–10.
23. Levin, F. S., Polytherms of the viscosity and self-diffusion of molten aluminum. *Izv. Akad. Nauk SSSR, Met.*, **5** (1971) 72–78.
24. Sindel, M., Travitsky, N. A & Claussen, N., Influence of magnesium–aluminum spinel on the directed oxidation of molten aluminum alloys. *J. Am. Ceram. Soc.*, **73**[9] (1990) 2615–2618.
25. Ando, K. & Momoda, M., Solubility of MgO in single crystal Al_2O_3. *J. Ceram. Soc. Jpn, Int. Edn*, **95** (1987) 343–347.
26. Salas, O., Jayaram, V., Vlack, K. C., Levi, C. G. & Mehrabian, R., Banded microstructures in Al_2O_3/Al composites produced by oxidation of molten Al–Mg alloys. In *Processing and Fabrication of Advanced Materials for High Temperature Applications*, eds V. A. Ravi & T. S. Srivatsan. TMS, Warrendale, PA, 1992.
27. Otsuka, S. & Kozuka, Z., Thermodynamic study of oxygen in liquid elements of Group Ib to VIb. *Trans. J. Inst. Met.*, **22**[8] (1981) 558–566.
28. Nayeb-Hashemi, A. A. & Clark, J. B., The magnesium–silicon system. *Bull. Alloy. Phase. Diag.*, **5**[6] (1984) 584–592.
29. Young, T., *Trans. Roy. Soc.*, **95** (1805) 65.
30. Nikolopoulos, P., Surface, grain-boundary and interfacial energies in Al_2O_3 and Al_2O_3–Sn, and Al_2O_3–Co systems. *J. Mater. Sci.*, **20** (1985) 3993–4000.
31. Jacob, K. T. & Fitzner, K., The estimation of the thermodynamic properties of ternary alloys from binary data using the shortest distance composition path. *Thermochim. Acta*, **18** (1977) 197–206.
32. Murray, J. L. & McAlister, A. J., The aluminum–silicon system. *Bull. Alloy. Phase. Diag.*, **5**[1] (1984) 74–84.

Appendix A: Determination of Rate Expression for Liquid Metal Transport

The volumetric flow rate of the liquid alloy through existing capillaries in the composite is given by the Poiseuille equation:

$$\frac{dV}{dt} = \frac{\pi R^4 \Delta P}{8\mu x} \tag{A1}$$

where R is the capillary radius, ΔP is the pressure difference driving the flow, μ is the viscosity of the liquid alloy, and x is the depth of penetration of the liquid at time t. The pressure difference, ΔP, can be represented as:

$$\Delta P = P_c - P_v - P_g \tag{A2}$$

where P_c is the capillary pressure, P_v is the vapour pressure of magnesium in the channel, and P_g is the gravitational pressure due to the weight of the liquid in the channel. The capillary pressure, P_c, driving the flow is given by the expression:

$$P_c = \frac{2\gamma_{LV} \cos\theta}{R} \tag{A3}$$

where γ_{LV} is the surface tension of the liquid aluminium alloy and θ is the contact angle between the liquid Al-alloy and alumina. Exact values of the contact angle, θ, and the surface tension, γ_{LV}, are not available. However, they can be estimated as shown below.

From Young's equation,[29] we have

$$\gamma_{LV} \cos\theta = \gamma_{SV} - \gamma_{SL} \tag{A4}$$

where γ_{SV} is the surface energy of alumina and γ_{SL} is the interfacial energy between the molten aluminium alloy and the solid Al_2O_3. Since the metal channels are present in the grain boundaries of alumina,[1] the metal is considered to have spread along the grain boundaries. The condition for metal spreading is given by the following equation:

$$\gamma_{SL} \leq \frac{\gamma_{SS}}{2} \tag{A5}$$

where γ_{SS} is the grain boundary energy in alumina. A lower estimate for $\gamma_{LV} \cos\theta$ is, therefore, given as:

$$\gamma_{LV} \cos\theta = \gamma_{SV} - \frac{\gamma_{SS}}{2} \tag{A6}$$

From eqn (A4) it can be seen that the higher estimate for $\gamma_{LV} \cos\theta$ can be determined by setting γ_{SL} as

zero. The values of γ_{SV} and γ_{SS} can be estimated from the data of Nikolopoulos.[30] The lower and the higher estimates for $\gamma_{LV}\cos\theta$ at 1373 K are 0·9455 and 1·4826 J m^{-2}, respectively.

For the lower estimate of $\gamma_{LV}\cos\theta$, P_c is 9·884 $\times$ 10^5 N m^{-2} at 1373 K. From Table 3, it is seen that P_g and P_v are much smaller than P_c and are therefore neglected in the determination of ΔP. Therefore, the mass flow rate of Al, (dM/dt) in mol s^{-1}, through a single metal channel is given as:

$$\frac{dM}{dt} = \rho_{Al}\frac{dV}{dt} = \frac{\rho_{Al}\pi R^3\gamma_{LV}\cos\theta}{4\mu x} \tag{A7}$$

If f is the ratio of the total metal channel area to the area of the composite, the total mass flow rate of Al per unit area of the composite is ($f/\pi R^2$) (dM/dt). Formation of alumina requires 48 g of oxygen for every 54 g of aluminum. Hence the oxygen weight gain rate per unit area, J, is given as:

$$J = \frac{48}{54} f\frac{dM/dt}{\pi R^2} = \frac{48}{54}\frac{f\rho_{Al}R\gamma_{LV}\cos\theta}{4\mu x} \tag{A8}$$

Equation (A1) can be rewritten as:

$$\pi R^2\frac{dx}{dt} = \frac{\pi R^4\Delta P}{8\mu x} = \frac{\pi R^3\gamma\cos\theta}{4\mu x} \tag{A9}$$

Integrating eqn (A9) we get an expression for the depth of liquid penetration, x, as a function of time, t:

$$x = \left[\frac{Rt\gamma_{LV}\cos\theta}{2\mu}\right]^{1/2} \tag{A10}$$

Using the above expression for x in eqn (A8) we get a relation between the flux, J, and the time of oxidation, t:

$$J = \frac{48}{54} f\frac{\rho_{Al}}{4}\left[\frac{2R\gamma_{LV}\cos\theta}{\mu t}\right]^{1/2} \tag{A11}$$

Appendix B: Determination of Al–Mg–Si Liquid Solution Thermodynamics

The thermodynamics of Al–Mg–Si liquid solutions can be estimated from the three limiting binaries (Al–Mg, Mg–Si and Al–Si) using the shortest distance composition path.[31] The thermodynamics of three limiting binaries (Al–Mg, Mg–Si and Al–Si) is well understood.[18,28,32] The primary advantage of this technique, over other empirical techniques used for thermodynamic estimation, is that the binary values incorporated into eqn (15) correspond to the binary compositions closest to the ternary point A (Fig. 10). The excess free energies of mixing for the Al–Mg, Al–Si and Mg–Si binaries can be deduced from experimental data reported in the literature.[18,28,32] For a given ternary composition A (Fig. 10), X^P_{Al}, X^P_{Mg}, X^Q_{Mg}, X^Q_{Si}, X^R_{Al} and X^R_{Si} can be determined as shown below. These, along with the thermodynamic data of the binaries, can then be incorporated into eqn (15) to determine the activity coefficient of Mg in the Al–Mg–Si ternary.

$$\begin{aligned}
X^P_{Mg} &= X^A_{Mg} + \frac{X^A_{Si}}{2}\\
X^P_{Al} &= X^A_{Al} + \frac{X^A_{Si}}{2}\\
X^Q_{Mg} &= X^A_{Mg} + \frac{X^A_{Al}}{2}\\
X^Q_{Si} &= X^A_{Si} + \frac{X^A_{Al}}{2}\\
X^R_{Al} &= X^A_{Al} + \frac{X^A_{Mg}}{2}\\
X^R_{Si} &= X^A_{Si} + \frac{X^A_{Mg}}{2}
\end{aligned} \tag{B1}$$

The activity coefficient of Al in the Al–Mg–Si ternary can be similarly estimated from the limiting binaries using the following equation:[31]

$$\begin{aligned}
RT\ln\gamma_{Al} = {} & \frac{X^A_{Si}(X^A_{Mg} + X^A_{Si})\Delta\bar{G}^{XS}_{Al/Al\text{–}Si}}{(1 - X^R_{Al})^2}\\
& + \frac{X^A_{Mg}(X^A_{Mg} + X^A_{Si})\Delta\bar{G}^{XS}_{Al/Al\text{–}Mg}}{(1 - X^P_{Al})^2}\\
& - \frac{X^A_{Mg}X^A_{Si}\Delta G^{XS}_{m/\,Mg\text{–}Si}}{X^Q_{Mg}X^Q_{Si}}
\end{aligned} \tag{B2}$$

where γ_{Al} denotes the activity coefficient of Al in the Al–Mg–Si ternary at the composition A, $\Delta\bar{G}^{XS}_{Al/Al\text{–}Mg}$ denotes the excess partial molar free energy of mixing of Al in the Al–Mg binary at the composition P, $\Delta\bar{G}^{XS}_{Al/Al\text{–}Si}$ denotes the excess partial molar free energy of mixing of Al in the Al–Si binary at composition R, and $\Delta G^{XS}_{m/\,Mg\text{–}Si}$ denotes the excess free energy of mixing of Mg–Si binary at composition Q.

Journal of the European Ceramic Society **16** (1996) 1365–1375

PII: S0955-2219(96)00057-X
0955-2219/96/$15.00

Controlled Wet Erosive Wear of Polycrystalline Alumina

A. Franco & S. G. Roberts*

Department of Materials, University of Oxford, Oxford OX1 3PH, UK

(Received 10 January 1996; revised version received 14 February 1996; accepted 28 February 1996)

Abstract

Controlled wet erosive wear tests were performed on polycrystalline alumina specimens of mean grain size G = *1·2, 3·8 and 14·1 μm and on sapphire specimens. The tests were performed by using an apparatus consisting of a jet body that rotates immersed in the slurry medium (SiC grits). Impacts are normal to the target surface. The construction and calibration of the apparatus are described. The impacting velocity used was 2·7 m* s^{-1}. *The weight loss of polycrystalline alumina and sapphire specimens increased linearly with impacting time. The wear rate of polycrystalline alumina specimens increased with grain size. Wear rates of 1·83, 8·36 and 11·3 nm* s^{-1} *correspond to* G = *1·2, 3·8 and 14·1 μm, respectively. For sapphire specimens the wear rate was 9·56 nm* s^{-1}. *Worn surfaces of both polycrystalline alumina and sapphire specimens were analysed by scanning electron microscopy.* © *1996 Elsevier Science Limited*

1 Introduction

It is well known that the wear resistance of polycrystalline alumina materials has a strong dependence on grain size. For example, in wear due to sliding,[1–5] grinding,[5,6] sawing,[7] dry erosion[8] and wet erosion,[9] the wear rate increases with the grain size.

In the study of wet erosive wear of a series of polycrystalline alumina specimens reported by Miranda-Martinez *et al.*,[9] the tests were conducted using an apparatus where the specimens were discs clamped between blocks of polyurethane in a central shaft that rotates immersed in a pot filled with slurry. Approximately 50% of the disc area was exposed to impacts. The most worn area was the lower part (bottom) of the exposed area. Using this tester, it is quite difficult to control some important parameters, such as impact velocity, impact angle and the number of impacting particles per unit of time.

Several other types of wear tester have been used to study the mechanisms and rates of erosion produced by single and multiple particle impacts, carried by either wet or dry media, on brittle materials.[10–20] None of these machines is suitable for the study of the early stages or basic mechanisms of surface damage, because even for a very short test time the amount of material removed is large and the control of impacting angle is quite difficult.

Here we report the design and use of a new slurry wear tester. Controlled particle impacts are produced normal to the test surface. The velocity of impacting particles was determined by comparing the crater depths produced by particle impacts and hardness indentation. Normal particle impact tests were performed on polycrystalline alumina and sapphire specimens using SiC grits in water as the eroding medium. In order to observe the evolution and mechanisms of surface damage in the early stages of wear on a polished surface, tests were performed for 1 and 15 min. To measure the weight loss and wear rate, tests were of 660 min duration.

2 Wear Machine — Construction and Calibration

2.1 Description

The rotating jet slurry wear tester is shown schematically in Fig. 1. It consists basically of three parts: (1) an electric motor, (2) a jet body–sample holder and (3) a slurry pot. The motor operates at nominal rotating speeds ranging from 10 to 200 rev min^{-1}. The jet body–sample holder is mounted on one end of a 275 mm stainless steel arm attached to a stainless steel shaft connected to the motor. At the other end of the arm a stainless steel paddle is attached to mix the slurry. Both the jet body and the paddle rotate in a groove delimited by the pot's inner wall and a fibreglass cylinder in

*To whom correspondence should be addressed.

the centre of the pot. The groove width is 65 mm and the jet body rotates 20 mm from the bottom of the pot in the groove. A buffer system is mounted 3 mm above the rotating arm in order to prevent the slurry from rotating with the jet body. The buffer system consists of eight stainless steel blades. The pot is placed on a table and attached to a mechanical jack to control its position in

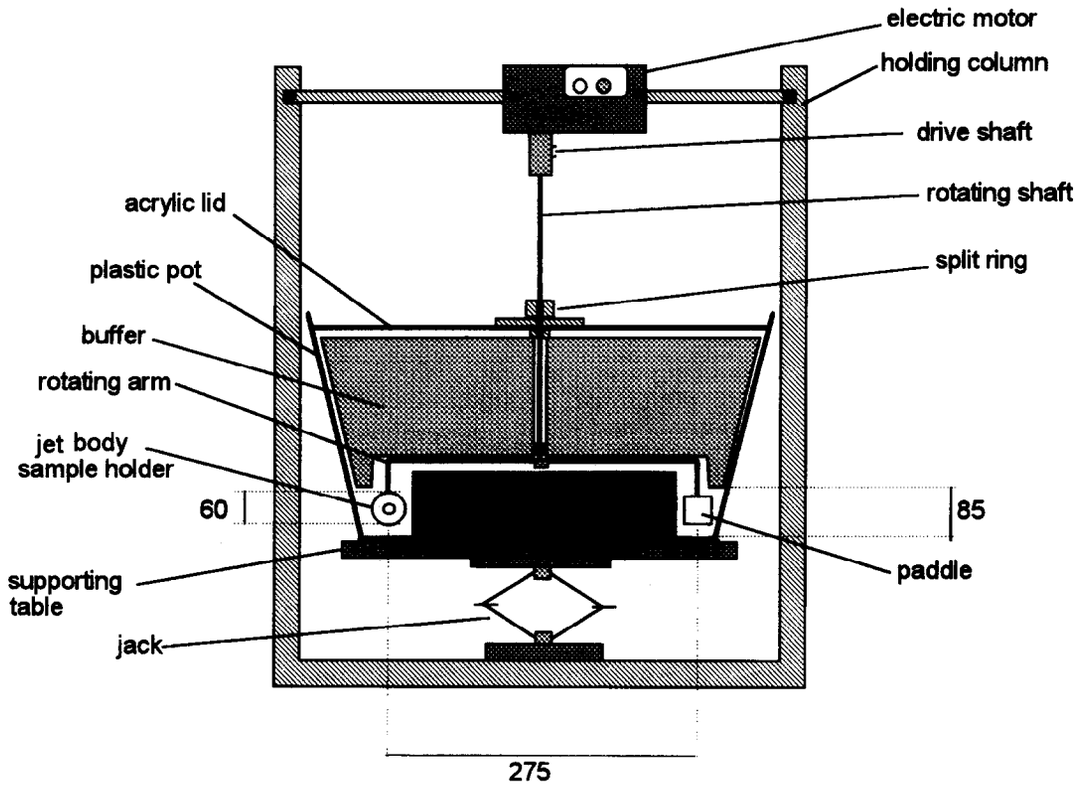

Fig. 1. Schematic diagram of the wear test machine. The machine consists of three parts: a motor, rotating jet body and slurry pot. Dimensions are in mm.

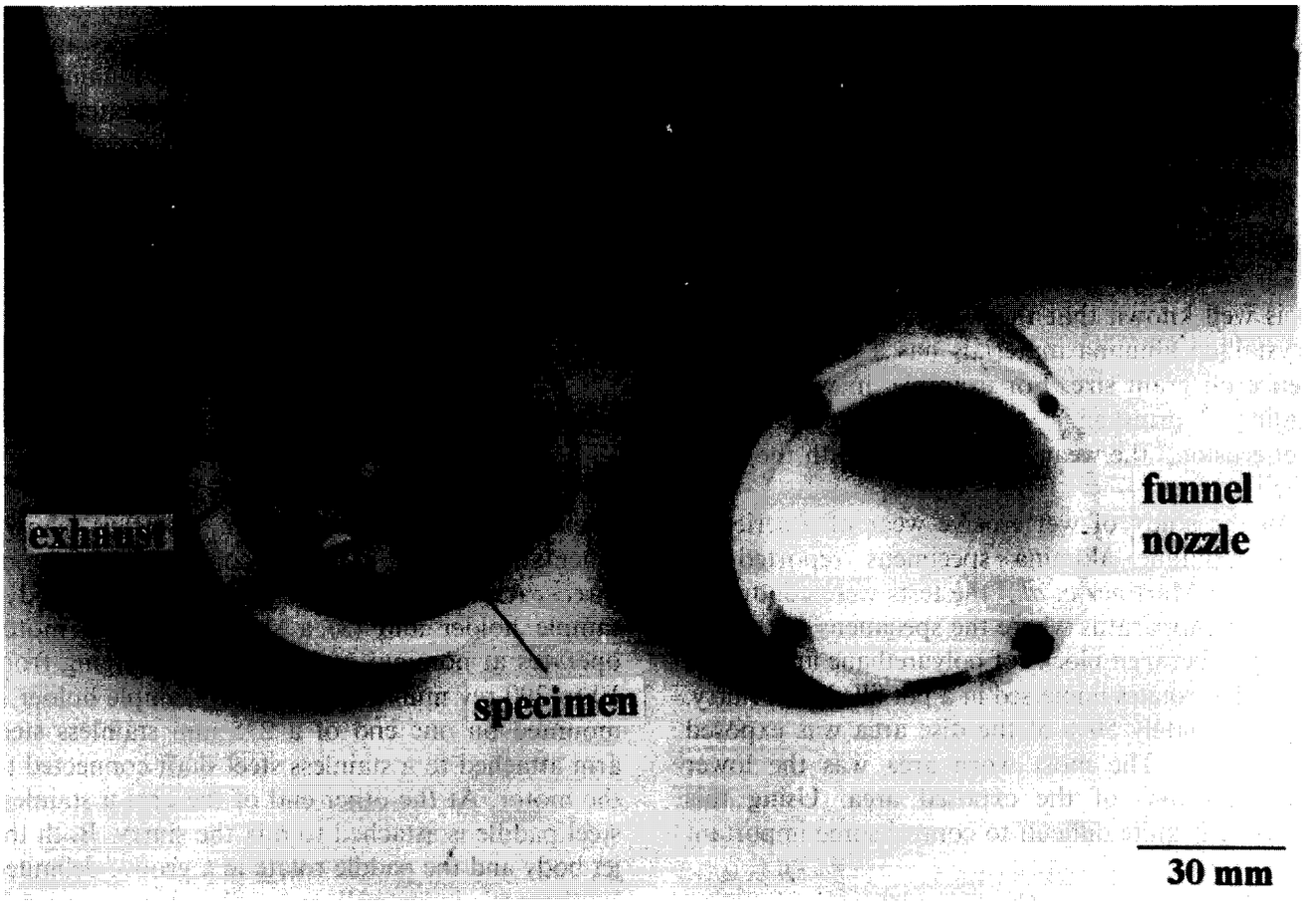

Fig. 2. The jet body–sample holder, showing the sample holder, slurry exhaust and funnel–nozzle system.

relation to the rotating arm. The jack also is used to lower and lift the pot during specimen and slurry changes.

The jet body–sample holder is made of nylon and consists of a funnel–nozzle and a lid as shown in Fig. 2. The diameters of funnel mouth and nozzle are 50 and 5 mm, respectively. The ratio of 10 between the funnel mouth and nozzle is responsible for accelerating the slurry when the jet body rotates. The sample holder is a nylon disc (40 mm diameter) placed in the bottom of the lid.

2.2 Calibration

2.2.1 Theoretical consideration—impact velocity

When a jet body rotates at a frequency f in a fluid, its linear velocity v_f can be calculated by

$$v_f = 2\pi r_a f \tag{1}$$

where r_a is the rotating arm length. If the jet body is a funnel–nozzle system, the velocity at which the fluid flows into the funnel is the same as the velocity v_f of the jet body. Hence, the velocity of the fluid at the nozzle v_n is given by

$$v_n = 2\pi\left(\frac{r_f}{r_n}\right)^2 r_a v \tag{2}$$

where r_f and r_n are the radii of the funnel and nozzle cross-section areas, respectively.

If a spherical particle strikes a metal surface, at low speed, producing plastic deformation, the crater size and maximum penetration should be a function solely of the normal kinetic energy during the impact. According to Hutchings,[21] approximately 90% of the particle's kinetic energy, during normal impacts on soft metals, is dissipated in plastic deformation (~80% heat and ~10% stored energy) and 10% is used in rebound velocity. The dissipated energy due to plastic deformation is given by

$$K_{imp} = \frac{1}{2}m(v_{imp}^2 - v_r^2) = \frac{1}{2}mv_{imp}^2(1 - e^2) \tag{3}$$

where m is the mass of particle, v_{imp} is the normal impact velocity, e is the coefficient of restitution (v_r/v_{imp}) and v_r is the normal rebound velocity. The fraction of the kinetic energy at impacts that is dissipated in plastic deformation is given by $(1 - e^2)$, and e varies with impact velocity as shown by Kosel *et al.*[22] On the other hand, if the same sphere is slowly loaded onto the same soft surface, the work done by the load to produce plastic deformation (plastic work) during indentation (of depth h_{max}) is given by

$$W = \int_0^{h_{max}} P\mathrm{d}h = Ph_{max} \tag{4}$$

where P is the indentation load and h_{max} is the maximum penetration of the spherical indenter (indentation depth).

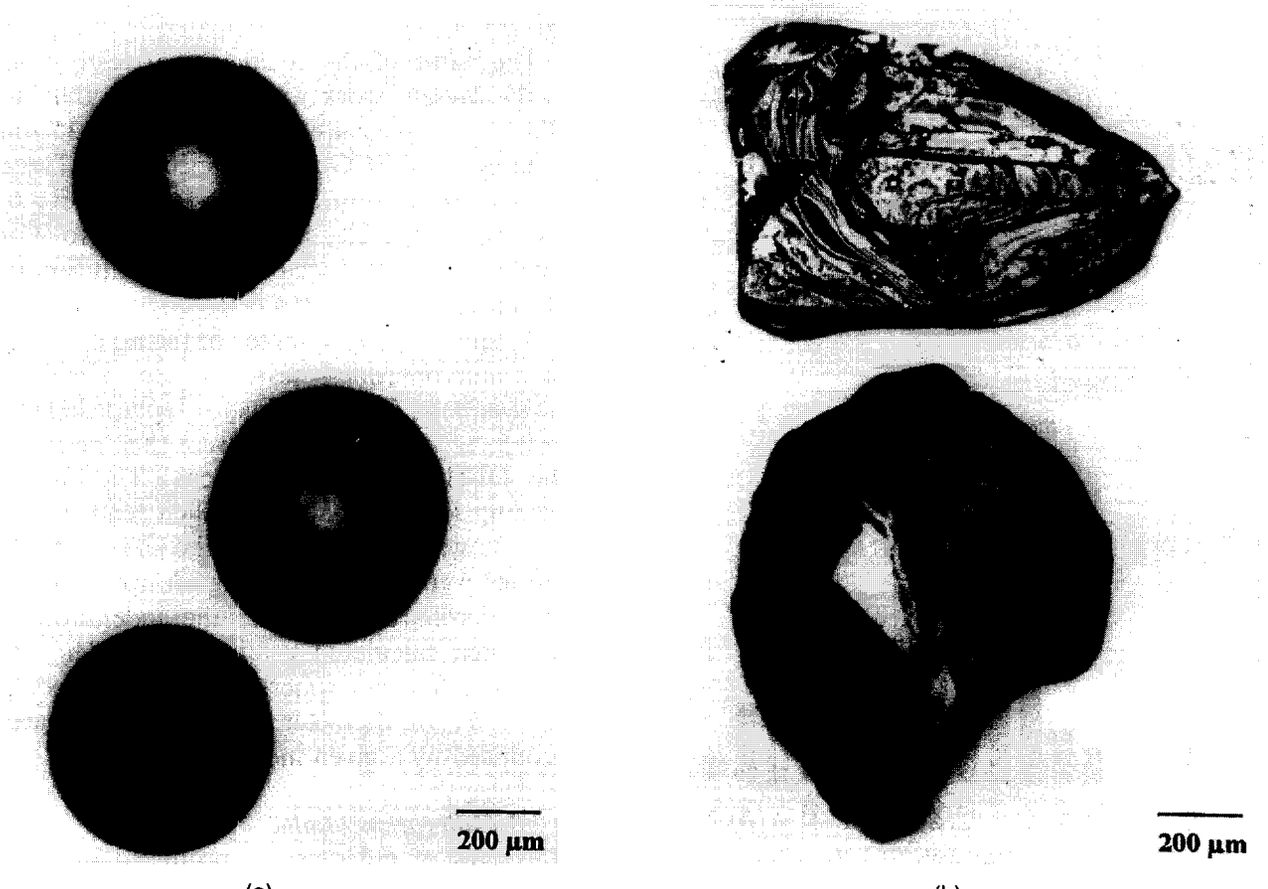

(a) (b)

Fig. 3. Optical micrographs of (a) ballotini (lead glass beads) and (b) SiC grits.

Assuming that the response of soft materials to plastic deformation is independent of strain rate[21–24] so that the depths of the craters produced by single particle impacts and slow load indentation are the same, the velocity of single particle impacts can be calculated by combining eqns (3) and (4).

$$v_{imp} = \left[\frac{2Ph_{max}}{m(1-e^2)}\right]^{1/2} \quad (5)$$

where P is the applied load to produce an indentation of the same size as the single particle impact crater of depth h_{max}.

The depth, h_{max} can be calculated by Pythagoras' theorem:

$$h_{max} = R - (R^2 - r^2)^{1/2} \quad (6)$$

where R is the radius of the spherical indenter and r is the radius of the crater produced either by single particle impact or slow load indentation.

2.2.2 Measurement method — impacting velocity

The velocity of normal particle impacts in this apparatus was calculated by measuring the crater depth produced by single particle impacts onto soft metal and using the energy balance model.

Lead glass beads (ballotini), provided by Jencons Scientific Limited, Leighton Buzzard, UK [Fig. 3(a)], were used as impacting particles and OFHC copper as the target material. The rotating speed f of the jet body immersed in the slurry was measured using a tachometer. Table 1 shows the values of v_f and v_n for each rotating speed f.

Table 1. Jet body rotating speed (f), and velocity of the fluid at the funnel entrance (v_f) and at the nozzle exit (v_n)

Jet body rotating speed f (*rev min* $^{-1}$)	v_f (*m s* $^{-1}$) [*eqn (1)*]	v_n (*m s* $^{-1}$) [*eqn (2)*]
60	0·63	13·29
80	0·84	17·73
100	1·04	22·16
120	1·26	26·59
140	1·47	31·02
160	1·67	35·45
180	1·88	39·88
200	2·10	44·32

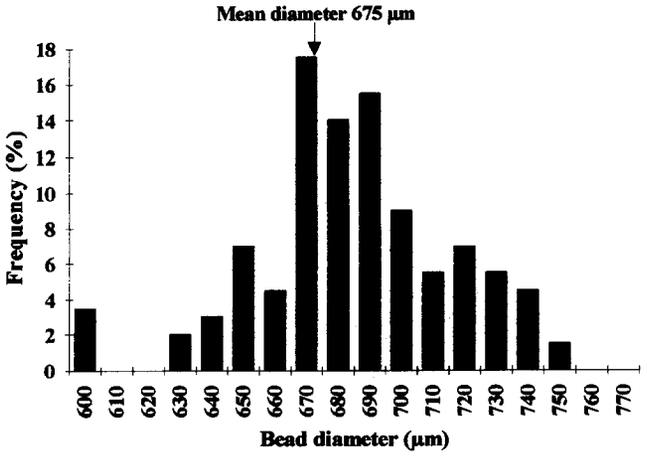

Fig. 4. Size distribution of 200 ballotini. The mean diameter is 675 μm.

A histogram of the diameter of 200 ballotini, measured using a micrometer, is shown in Fig. 4. The average diameter is 675 μm. The average weight of a ballotino was determined (by weighing 600 beads) as $5{\cdot}625 \times 10^{-4}$ g. OFHC copper bars of 2 × 3 × 3 mm were cut, annealed at 300°C for 1 h, mechanically ground with 1 μm alumina slurry and polished on 14, 6 and 1 μm diamond-paste impregnated cloths. To obtain strain-free and highly reflecting surfaces, the specimens were electropolished for 15 min, at 1·8 V DC, using a copper cathode, in a solution of 700 ml of orthophosphoric acid and 300 ml of distilled water.

The copper bars were mounted in the jet body system. The specimen surface was positioned at 3 mm from the end of the nozzle, facing normal to its centre. The slurry consisted of 1 kg of ballotini dispersed in 8 litres of water. Each test was performed for a time of 15 s, chosen so as to make it possible to measure crater diameters by giving a sufficient number of craters produced by single particle impacts without a large number of craters overlapping. Two rotating jet body speeds (140 and 180 rev min^{-1}) were tested. For each speed, 30 isolated craters were measured and the corresponding crater depths were calculated by using eqn (6).

The value of the coefficient of restitution used in the present work was the same as that used by Clark[25] and measured by Kosel[26] for 635 μm steel spheres on OFHC copper specimens. The coefficient of restitution decreases from 0·43 to 0·30 as the impact velocity increases from 5 to 27 m s^{-1}. The value for the coefficient of restitution used in all our calculations was 0·36.

A ballotino was mounted in the tip of an indenter of a microhardness tester (model MHT-1, Matsuzawa Seiki Co. Ltd, Tokyo, Japan). Indentations of 0·5, 1, 2, 3, 5 and 10 N were then performed on the OFHC copper specimens. The indentation holding time was 5 s. For each load a set of 20 indents was performed and the sizes of the indentations were measured using an optical system on the microhardness tester; the indentation depth was then calculated using eqn (6). The test was repeated for two spherical steel indenters of 500 and 1000 μm diameter to compare the crater sizes produced by a given indentation load.

2.2.3 Calibration results

The sizes of indentations produced by slow load indentation on OFHC specimens are shown in Fig. 5. In this plot there are three curves which

correspond to the indentation depth produced by spherical indenters of mean diameters 500, 675 and 1000 μm. The depth increases linearly with the applied load and, for a given load, the indentation depth decreases as the indenter diameter increases.

A best-fit polynomial regression of first order for the indentation depth versus load curve produced by the 675 μm ballotino indenter is given by the following equation

$$h_{imp} = (0{\cdot}10756 + 0{\cdot}62157\,P) \times 10^{-6} \quad (7)$$

where P is the applied load to produce plastic deformation of depth h_{imp}. Inserting the above equation into eqn (5), the particle impact velocity (v_{imp}) can be determined by measuring the depth of craters produced by impacts h_{imp} as

$$v_{imp} = \left[\frac{2}{m(1-e^2)}\left(\frac{h_{imp} - 0{\cdot}10756 \times 10^{-6}}{0{\cdot}62158 \times 10^{-6}}\right)h_{imp}\right]^{1/2} \quad (8)$$

Figure 6 shows the distribution of crater depths produced by single ballotino impacts. In Fig. 6 (a) (140 rev min^{-1}), crater depths range from 0·11 to 0·45 μm; in Fig. 6(b) (180 rev min^{-1}), crater depths range from 0·78 to 1·61 μm. This scatter in crater depth can be attributed to:

(1) The ballotini used as impacting particles showed a scatter in size, as shown in Fig. 3; and
(2) fluid turbulence causes particles to collide with each other and with the nozzle wall, which decelerates them and changes their trajectory before striking the target. Some researchers[27,28] attributed some deceleration to the formation of a thin layer of water between the particles and the target during impacts.

Impact velocities were calculated using the most frequent crater depths (Fig. 6), the average mass of the impacting particle, (5·625 $\times$ 10^{-4} g) and the coefficient of restitution (0·36) in eqn (8); the results are shown in Table 2. For a rotating speed of 140 rev min^{-1} the impact velocities range from 0·28 to 0·52 m s^{-1}. For a jet body rotating speed of 180 rev min^{-1} the impact velocities range from 1·78 to 2·96 m s^{-1}.

Figure 7(a) shows a micrograph of indentations produced by slow loads (5 s holding time) of 0·5, 1, 2, 3, 5 and 10 N, using a ballotino indenter, while Fig. 7(b) shows a micrograph of craters produced by single ballotino impacts onto an OFHC copper specimen at 180 rev min^{-1}. Typical impact crater dimensions of 0·815 and 1·26 μm diameter correspond in size to indentations made with 1 and 2 N loads, respectively.

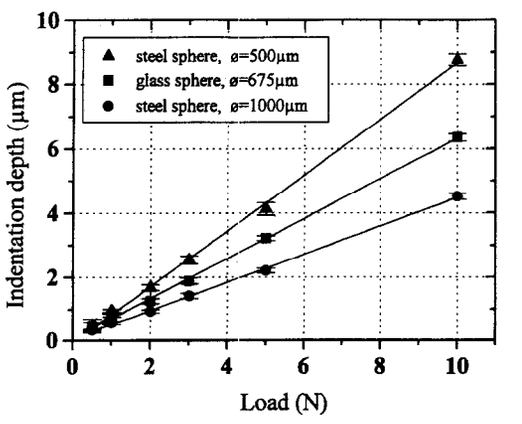

Fig. 5. Slow load indentation into OFHC copper. The indentation depth increases linearly with the indenter diameter for loads ranging from 0·5 to 10 N. For a given load, the smaller the indenter, the deeper the crater produced.

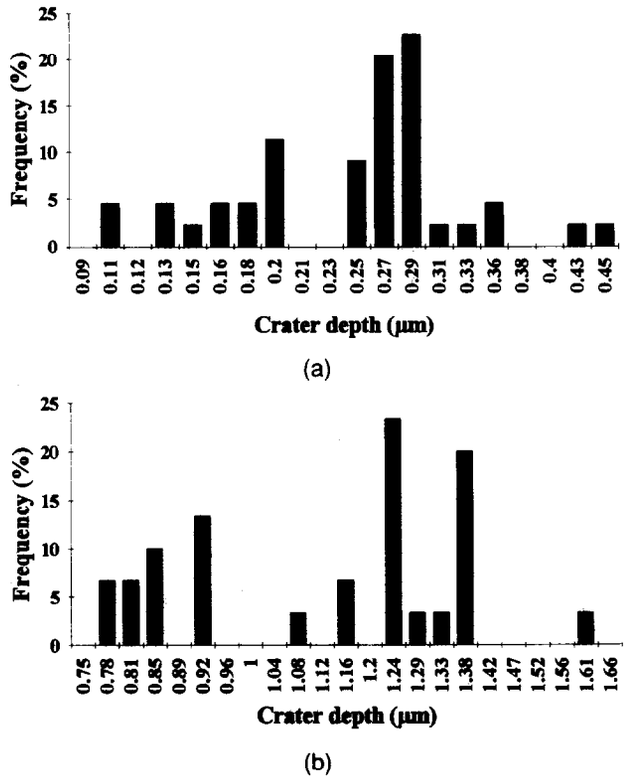

Fig. 6. Crater size distribution produced by single ballotino impact at normal incidence onto OFHC copper specimens. Jet body rotating speeds (a) 140 and (b) 180 rev min^{-1}.

Table 2. Impact velocities calculated using eqn (8) corresponding to the most frequently observed crater depths produced by rotating speeds of 140 and 180 rev min^{-1}

Rotating speed, f (rev min^{-1})	*Crater depth h_{imp} (μm) [eqn (6)]*	*Crater depth frequency %*	*Impact velocity v_{imp} (m s^{-1}) [eqn (8)]*
140	0·20	11·36	0·28
	0·25	9·09	0·42
	0·27	20·45	0·47
	0·29	22·72	0·52
180	0·85	10·00	1·78
	0·92	13·33	1·95
	1·16	6·66	2·47
	1·24	23·33	2·66
	1·38	20·00	2·96

3 Wet Erosive Wear Tests on Polycrystalline Alumina and Sapphire Specimens

3.1 Sample fabrication

Polycrystalline alumina materials were fabricated using high purity, (99·9%) α-Al_2O_3 powder (Sumitomo AKP-50, Japan) of mean particle size ~180 nm. Alumina specimens of mean grain size G = 1·2 μm (referred to later as F) were produced by hot-pressing the powder in a 25 mm diameter graphite die at 20 MPa and 1300°C for 30 min. Specimens of grain size 3·8 and 14·1 μm (referred to later as M and C, respectively) were produced by pressureless-sintering, in air, of powder discs 37 mm diameter that had been uniaxially pressed at 50 MPa in a stainless steel die then cold-isostatically pressed at 300 MPa. The sintering conditions and characteristics of the hot-pressed alumina specimens are shown in Table 3.

3.2 Wet erosive wear tests

The specimens were cut into bars of dimensions 9 × 4 × 4 mm, mechanically ground with 14 μm SiC slurry, polished on cloths impregnated with 6 μm polycrystalline diamond and finished with a 'Syton' polish. The tests were done in a slurry medium of 1·5 kg of SiC grits with a mean size of ~780 μm and a mean mass of 9·10 × 10^{-4} g, dispersed in 8 litres of water. SiC grits (specified as 24 C6) were provided by Washington Mills, Electro Mineral Ltd, Manchester, UK. [Fig. 3(b)]. The jet body rotating speed was 180 rev min^{-1}. Assuming that the 780 μm diameter SiC grit particles travel at the same velocity as 675 μm ballotini under the same fluid flow conditions, the impact velocity is most likely to be 2·7 ± 0·4 m s^{-1} (Table 2).

Tests were performed for different periods, 1 and 15 min, to observe the mechanisms and evolution of surface damage, and for 660 min to measure the weight loss of each specimen. The wear rate, R, was calculated as:

Table 3. Sintering and hot-pressing conditions and characteristics of polycrystalline alumina specimens

Material	*Sintering condition*		*Bulk density* ($g\ cm^{-3}$)	*Mean grain size* (μm)
	Temp. (°C)	*Holding time* (h)		
M	1450	3	3·938	3·8 ± 0·8
C	1600	3	3·947	14·1 ± 1·5
Material	*Hot-pressing condition*		*Bulk density* ($g\ cm^{-3}$)	*Mean grain size* (μm)
	Temp. (°C)	*Pressure* (*MPa*)		
F	1300	20	3·89	1·2 ± 0·5

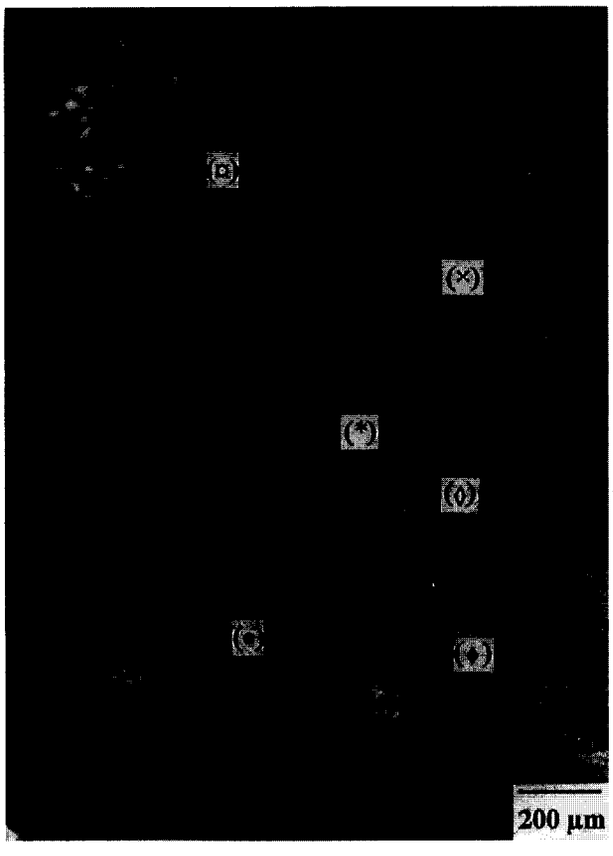

(a)

(b)

Fig. 7 Optical micrographs (Nomarski interference contrast). (a) Craters produced by slow indentation at loads of (×) 0·5 N, (*) 1 N, (◇) 2 N, (◆) 3 N, (●) 5 N and (○) 10 N and (b) craters produced by normal particle impacts at 180 rev min^{-1}.

$$R = -\frac{\Delta w}{A_{imp}\rho\Delta t} \quad (9)$$

where $\Delta w = w - w_0$. w_0 is the specimen weight before testing (t_0) and w is the specimen weight after testing for a time t. A_{imp} is the impacting area (worn area) and ρ is the specimen density.

4 Wet Erosive Wear Results of Polycrystalline Alumina and Sapphire Specimens

Figure 8 shows worn surfaces of polycrystalline alumina, mean grain size G = 1·2, 3·8 and 14·1 μm, and sapphire specimens, due to normal particle impacts at ~2·7 m s^{-1}(180 rev min^{-1}) for 660 min. The frontal view of the worn area for each specimen is shown in Fig. 8(a). For the same worn area the greatest amount of material removed is for the coarse-grained specimen, and this decreases as the grain size of the specimens becomes finer. This is more evident in the lateral views of the worn area as shown in Fig. 8(b). Notice that for all specimens the area exposed to impacts is the same although the damage depth varies.

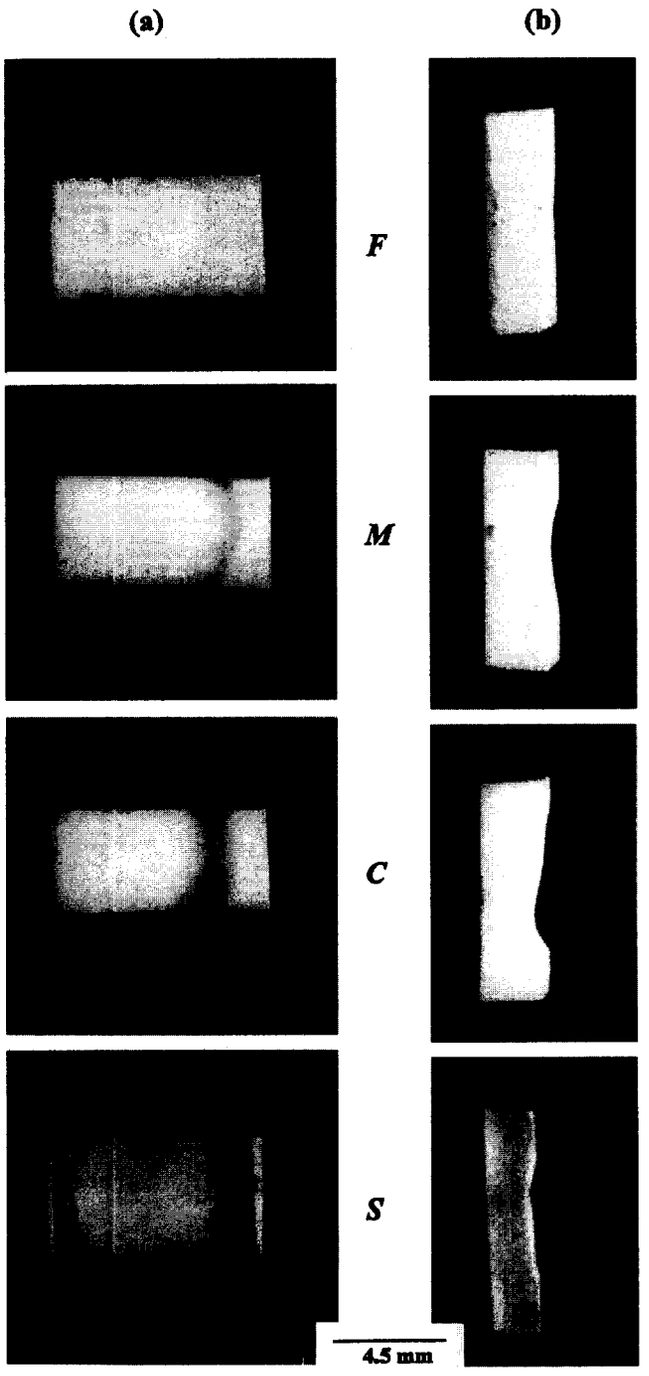

Fig. 8. (a) Frontal and (b) lateral views of the eroded surfaces of polycrystalline alumina [grain sizes 1·2 (F), 3·8 (M) and 14·1 μm (C)] and sapphire (S) specimens. Erosion rate increases with grain size.

Scanning electron micrographs of worn surfaces of polycrystalline alumina, G = 1·2, 3·8 and 14·1 μm, and sapphire specimens due to tests run for 1, 15 and 660 min at 2·7 m s^{-1} impact speed (180 rev min^{-1}) are shown in Figs 9, 10 and 11, respectively. In tests run for a short period of time (Fig. 9), single particle impacts produce clusters of damage which may be isolated or linked to each other. Also, there is some plastic deformation similar to that produced by Vickers hardness indentation. At this early stage of damage it is already clear that the wear of the polycrystalline alumina specimens is grain-size-dependent. The damage evolution is clear for tests run for a longer period of time (Fig. 10), where loss of whole grains and transgranular fracture are already evident. At a later stage (Fig. 11) the damage is much more severe and grain loss and transgranular fracture are predominant. Notice that for the finest grain size specimen (G = 1·2 μm) plastic deformation or polishing is always present.

The weight loss versus impacting time for each specimen is plotted in Fig. 12. The weight loss increases linearly with time. The weight loss of polycrystalline alumina specimens increases with the grain size.

Figure 13(a) shows the wear rate for polycrystalline alumina and sapphire specimens calculated using eqn (9). The worn area was measured directly on the specimens and was the same for all specimens, 3·32 × 10^{-5} m^2. The density for polycrystalline specimens was taken as in Table 3, and for the single crystal specimen as 3·98 g cm^{-3}. The coarse-grained specimen, C, exhibited a wear rate about one order of magnitude higher than that of the finest grain size specimen, F. For the sapphire specimen, S, the wear rate was intermediate between those of the medium grain (M) and coarse grain (C) specimens.

The wear rates due to normal particle impacts presented here are apparently about 10 times lower than the results presented by Miranda-Martinez *et al.*[9], Table 4, for specimens of the same grain size and sintered under the same conditions. However, the two experimental methods used vary in the following respects.

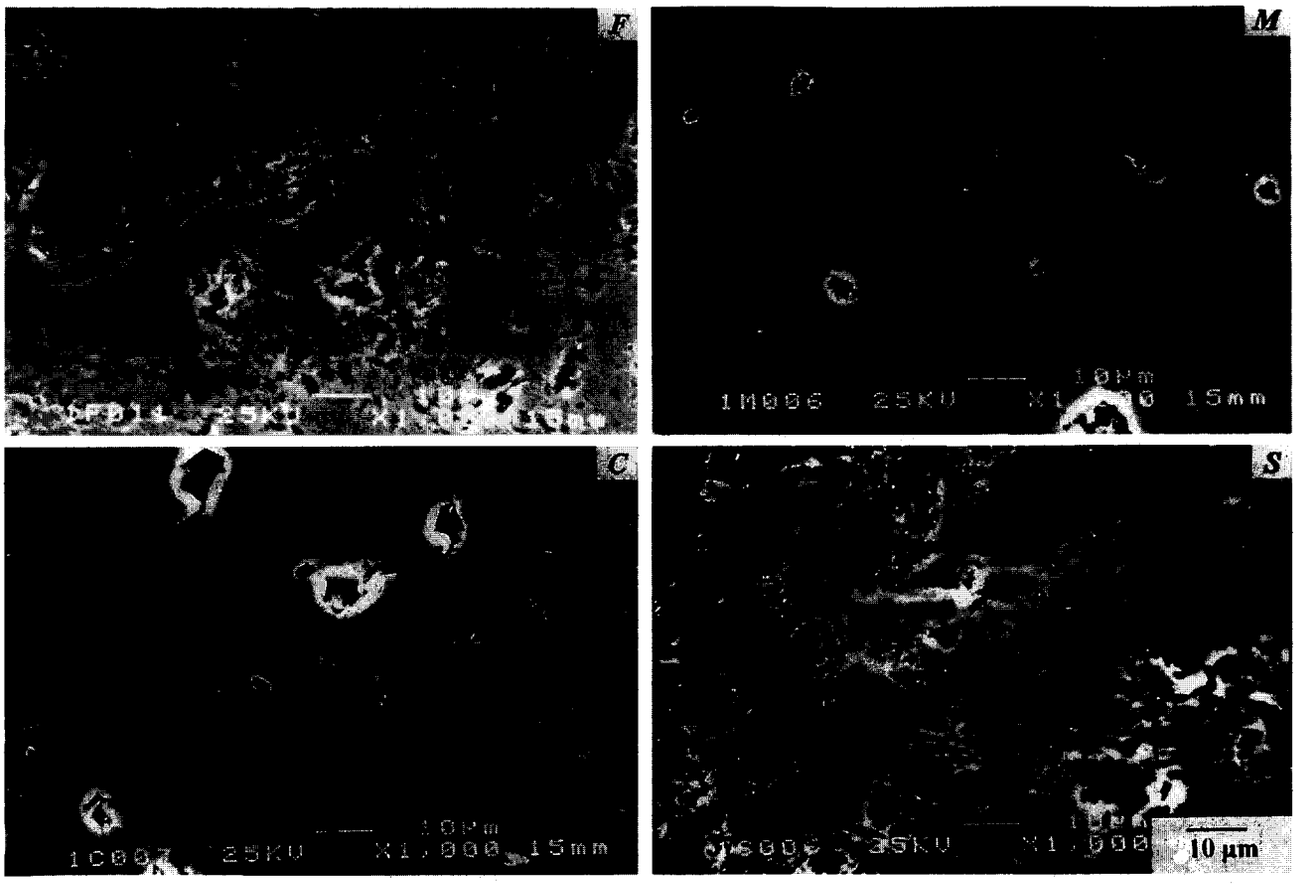

Fig. 9. Scanning electron micrographs of eroded surfaces of polycrystalline alumina [grain sizes 1·2 (F), 3·8 (M) and 14·1 μm (C)] and sapphire (S) specimens. Test time: 1 min.

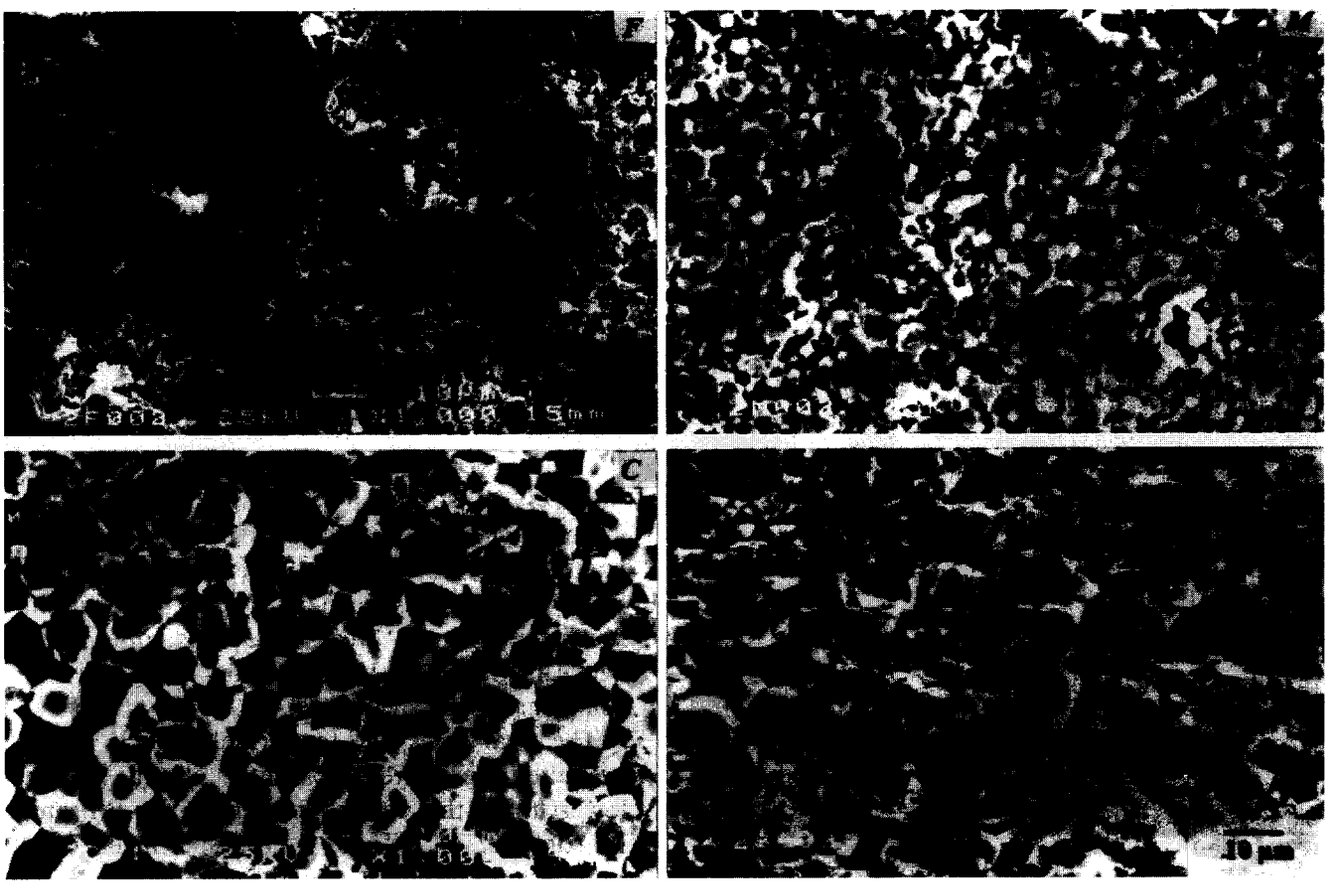

Fig. 10. Scanning electron micrographs of eroded surfaces of polycrystalline alumina [grain sizes 1·2 (F), 3·8 (M) and 14·1 μm (C)] and sapphire (S) specimens. Test time: 15 min.

(1) The particle flux — in our experiments this is $8{\cdot}6 \times 10^7$ particles m^{-2} s^{-1}; for Ref. 9 we estimate (using data from Riley[20]) a flux of $1{\cdot}92 \times 10^9$ particles m^{-2} s^{-1}. In Fig. 13(b) and Table 4, results are shown normalized to the same flux, as erosion rate per impacting particle. The erosion rates from Ref. 9 are then approximately four times lower per particle than in our results.
(2) The velocity of impact — this is ~2·7 m s^{-1} in our experiments, ~1·9 m s^{-1} in those of Ref. 9. Lower impact velocities would be expected to give lower erosion rates.
(3) The angle of incidence of the particles — in our experiments this is always 90°; in those of Ref. 9 the angle is not controlled and probably ranges from 0 to 90°. For ceramic materials, the erosion rate decreases markedly as the impact angle decreases from 90°.

Both the last two factors will tend to give lower erosion rates per impacting particle for the results of Miranda-Martinez *et al.*[9] as observed.

5 Conclusions

A new apparatus to study the erosive wear mechanism of brittle materials due to normal particle impacts has been designed and constructed. The apparatus consists of a jet body (funnel–nozzle) which rotates immersed in a slurry medium in a pot.

The velocity of particle impacts was determined by a model [eqn (8)] based on the balance between the kinetic energy of a spherical particle and the work of slow load indentation of a spherical indenter to produce the same plastic deformation in soft materials. The model enables us to calculate the normal impact velocity solely as a function of the crater depth produced by impacts.

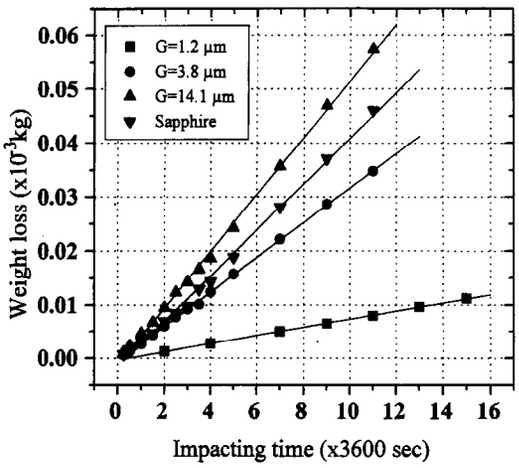

Fig. 12. Weight loss versus impacting time. The weight loss increases linearly with test duration, and depends strongly on grain size.

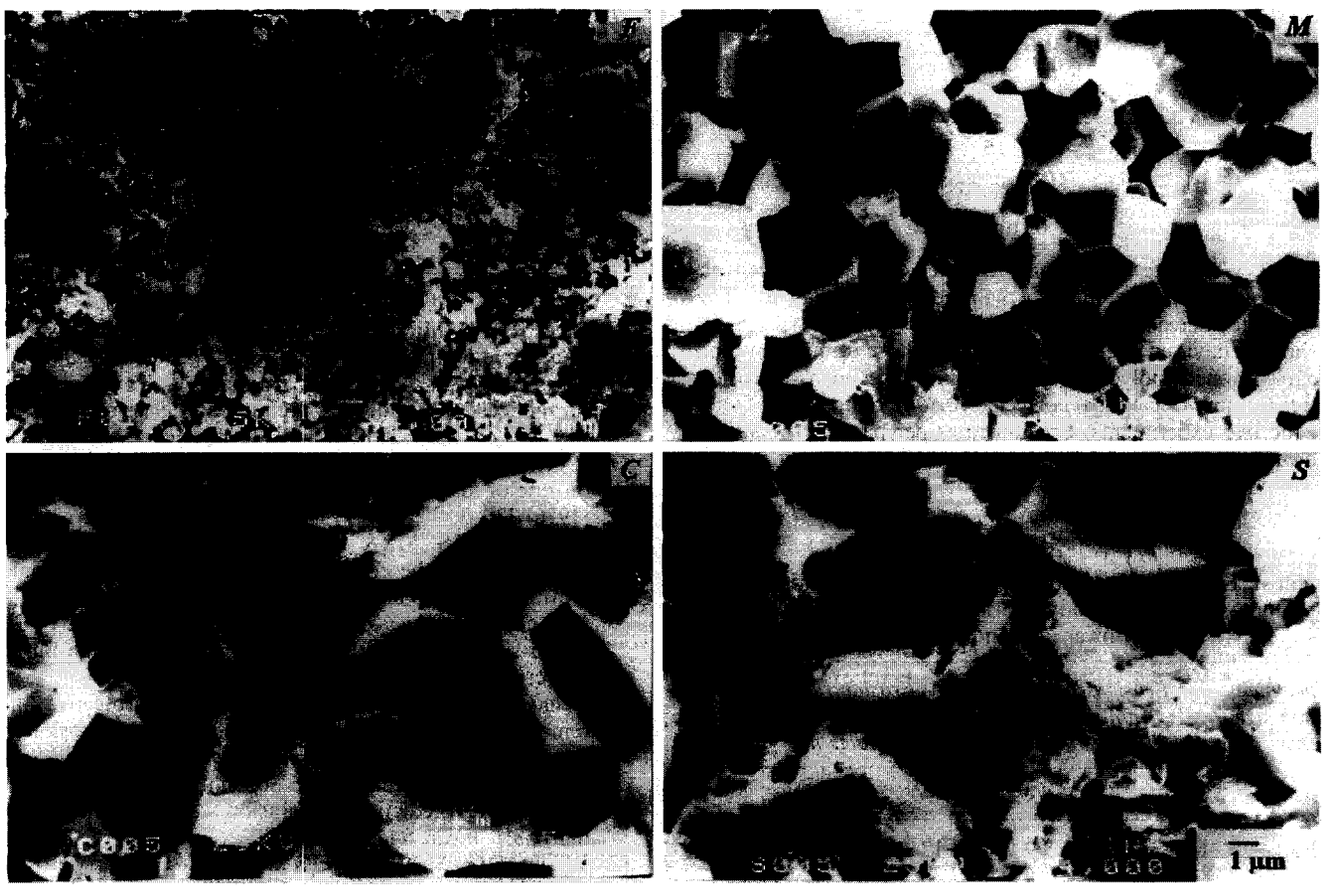

Fig. 11. Scanning electron micrographs of eroded surfaces of polycrystalline alumina [grain sizes 1·2 (F), 3·8 (M) and 14·1 μm (C)] and sapphire (S) specimens. Test time: 660 min.

Worn surfaces of polycrystalline alumina specimens produced by normal particle impacts at ~2·7 m s^{-1} for test times of 1, 15 and 660 min were studied. The wear mechanism at the early stage of damage is similar to that at a later stage where severe damage has taken place.

Weight loss of polycrystalline alumina and sapphire specimens due to normal particle impacts of SiC grits in water increased linearly with impacting time.

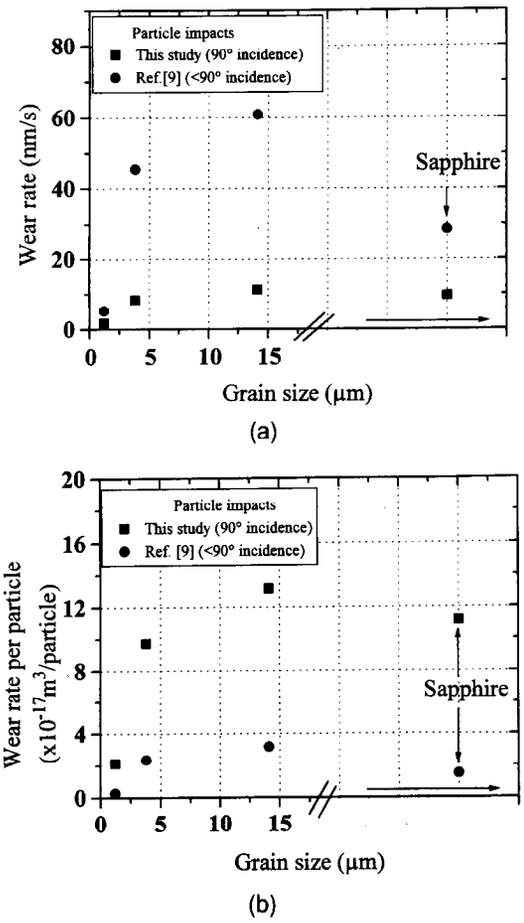

Fig. 13. Wear rate versus grain size for normal incidence (this study) and from the study of Miranda-Martinez *et al.*[9] The wear rate increases with grain size and sapphire specimens exhibit behaviour intermediate between those of medium- and coarse-grained polycrystalline alumina specimens. Erosion rates (a) uncorrected, (b) corrected for different particle fluxes in the two experiments. Erosion rates per particle (b) due to normal impacts are higher than those due to lower impact angles.[9]

Table 4. Erosion rate of polycrystalline alumina and sapphire specimens, from this study (normal impacts, 90°) and from Ref. 9 (lower incidence angles. <90°)

Specimen grain size (*μm*)	*Erosion rate* (*nm* s^{-1}) *Impacts at*		*Erosion rate* (10^{-17} m^3 *per particle*) *Impacts at*	
	90°	*<90°*	*90°*	*<90°*
1·2	1·83 ± 0·7	5·9	2·12 ± 0·08	0·27
3·8	8·36 ± 0·8	45·6	9·72 ± 0·09	2·37
14·1	11·30 ± 0·6	61·0	13·14 ± 0·06	3·18
Sapphire	9·56 ± 0·6	28·6	11·20 ± 0·08	1·48

The measured wear rate of polycrystalline alumina specimens is grain-size-dependent, being about one order of magnitude greater for Al_2O_3 of 14·1 μm grain size than for 1·2 μm grain size. For sapphire, the wear rate is between those of the medium and coarse grain size polycrystalline alumina specimens.

The erosion rates per impacting particle from our study are about four to 10 times higher than those of Miranda-Martinez *et al.*,[9] which we attribute to the effects of impacting angle[30] and particle velocity on erosion rate.

Acknowledgements

A. Franco thanks CAPES (Brazilian Government) for financial support. This work was also supported by the EPSRC under Grant No. J86513. We thank F. L. Riley, R. W. Davidge and P. Twigg for assistance with specimen preparation, provision of data in advance of publication, and for many useful discussions. Many thanks to J. Short for assistance with the construction of the machine, and to A. McKnight for photographic assistance.

References

1. Wu, C. Cm., Rice, R. W., Johnson, D. & Platt B. A., Grain size dependence of wear in ceramics. *Ceram. Eng. Sci. Proc.*, **6** [7–8] (1985) 995–1011.
2. Cho, S.-J., Hockey, B. J., Lawn, B. R. & Bennison, S. J., Grain-size and R-curve effects in the abrasive wear of alumina. *J. Am. Ceram. Soc.*, **72** (1989) 1249–52.
3. Deckman, D. E., Jahanmir, S. & Hsu, S. M., Wear mechanisms of α-alumina lubricated with a paraffin oil. *Wear*, **149** (1991) 155–68.
4. Liu, H. & Fine, M. E., Modelling of grain-size dependent microfracture-controlled sliding wear in polycrystalline alumina. *J. Am. Ceram. Soc.*, **76** (1993) 2393–6.
5. Rice, R. W., Micromechanics of microstructural aspects of ceramic wear. *Ceram. Eng. Sci. Proc.*, **6** (1985) 940–58.
6. Marshall, D. B., Lawn, B. R. & Cook, R. F., Microstructural effects on grinding of alumina and glass ceramics. *J. Am. Ceram. Soc.*, **70** (1987) C-139–40.
7. Rice, R. W. & Speronello, B. K., Effect of microstructure on rate of machining of ceramics. *J. Am. Ceram. Soc.*, **59** (1976) 330–3.
8. Wiederhorn, S. M. & Hockey, B. J., Effect of material parameters on the erosion resistance of brittle materials. *J. Mater. Sci.*, **18** (1983) 766–89.
9. Miranda-Martinez, M., Davidge, R. W. & Riley, F. L., Grain size effects on the wet erosive wear of high-purity polycrystalline alumina. *Wear*, **172** (1994) 41–8.
10. Zahavi, J. & Wagner, H. J., The role of protective film removal and growth on the rate of erosion-corrosion in metals. *Proc. 5th Int. Conf. on Erosion by Liquid and Solid Impact*, Cambridge, UK, 3–6 September 1979, Paper 50.
11. Elkholy, A., Prediction of abrasion wear for slurry pump materials. *Wear*, **84** (1983) 39–49.
12. Wright, I. G., Shetty, D. K. & Clauer, A. H., Slurry erosion of WC–Co cermets and its relationship to materials properties. *Proc. 6th Int. Conf. on Erosion by Liquid and Solid Impact*, Cambridge, UK, 5–8 September 1983, Paper 63.

13. Sagüés, A. A., Spencer, D. K., Sethi, V. K. & Sargent G. A., Slurry erosion and abrasion of metal-ceramic coatings. In *Slurry Erosion, Uses, Applications, and Test Methods* eds J. E. Miller & F. E. Schmidt, Jr. ASTM STP 946, American Society for Testing and Materials, Philadelphia, PA, 1987, pp. 19–44.
14. Matsumura, M., Oka, Y. & Yamawaki, M., Slurry erosion–corrosion of commercially pure iron in fountain-jet testing facility—mechanism of erosion. *Proc. 7th Int. Conf. on Erosion by Liquid and Solid Impact*, Cambridge, UK, 7–10 September 1987, Paper 40.
15. Zu, J. B., Hutchings, I. M. & Burstein, G. T., Design of a slurry erosion test rig. *Wear*, **140** (1990) 331–44.
16. Lee, Y. H. & Clark, H. McI., The relative erosion of coal–oil, coal–water, and petroleum coke–oil slurries. In *Slurry Erosion, Uses, Applications and Test Methods*, eds J. E. Miller & F. E. Schmidt, Jr. ASTM STP 946, American Society for Testing and Materials, Philadelphia, PA, 1987, pp. 44–61.
17. Tsai, W., Humphrey, J. A. C., Cornet, I. & Levy, A. V., Experimental measurement of accelerated erosion in a slurry pot tester. *Wear*, **68** (1981) 289–303.
18. de Bree, S. E. M., Rosenbrand, W. F. & de Gee, A. W. J., On the erosion resistance in water–sand mixtures of steels for application in slurry pipelines. *Proc. 8th Int. Conf. on the Hydraulic Transport of Solid in Pipes*, Johannesburg, 25–27 August 1982. BRHA Fluid Eng., Cranfield, Bedfordshire, 1982, Paper C3.
19. Schumacher, W. J., Ball mill and hub test methods for slurry erosion evaluation of materials. In *Slurry Erosion, Uses, Applications and Test Methods*, eds J. E. Miller & F. E. Schmidt, Jr. ASTM STP 946, American Society for Testing and Materials, Philadelphia, PA, 1987, pp. 5–18.
20. Clark, H. McI., On the impact rate and impact energy of particles in slurry pot erosion tester. *Wear*, **147** (1991) 165–83.
21. Hutchings, I. M., A model for erosion of metals by spherical particles at normal incidence. *Wear*, **70** (1981) 269–81.
22. Kosel, T. H., Anand, K., Sundararaman, V., Sriram, T. S., Kotteyil, M. & Nailos, P. J., Rebound of erodent particles from metal surfaces. In *Corrosion–Erosion–Wear of Materials at Elevated Temperatures*, ed. A. V. Levy. NACE, 1991, pp. 8–1–8–28.
23. Tabor, D., *The Hardness of Metals*. Clarendon Press, Oxford, 1951.
24. Hutchings, I. M., Strain rate effects in microparticle impact. *J. Phys. D*, **10** (1977) L179–84.
25. Clark, H. McI., A comparison of particle impact in gas–solid and liquid–solid erosion. In *ELSI VIII, Proc. 8th Int. Conf. on Erosion by Liquid and Solid Impact*, eds I. M. Hutchings & J. A. Little. Cambridge, UK, 4–8 September 1994, pp. 465–72.
26. Kosel, T. H., Private communication, University of Notre Dame, 1992.
27. Tabor, D., Collisions through liquid layers. *Engineering*, **167** (1949) 145–7.
28. Wong, K. K. & Clark, H. McI., A model of particle velocities and trajectories in a slurry pot erosion test. *Wear*, **160** (1993) 95–104.
29. Riley, F. L., Private communication, University of Leeds, 1995.
30. Finnie, I., Erosion of surfaces by solid particles. *Wear*, **3** (1960) 87–103.

Journal of the European Ceramic Society **16** (1996) 1377–1383

PII: S0955-2219(96)00060-X
0955-2219/96/$15.00

Estimating Tensile Creep Rate of Ceramics from Flexure Data

Dong-Joo Lee

Department of Mechanical Engineering, Yeungnam University, Gyungsan, Gyungbuk, Korea

(Received 18 April 1994; revised version received 4 March 1996; accepted 14 March 1996)

Abstract

A new model of ceramic creep in four-point bending is proposed to determine the creep rate that corresponds to tensile creep at an elevated temperature. Based on the assumption that ceramics creep only in tension and there is no creep in compression, the tensile creep rate which is invariant with time in the secondary mode is calculated in a simple way. Since the initially applied maximum tensile stress does not correspond to the stress at the secondary creep range, the creep-induced stress at the time of measurement is calculated based on beam deflection. Then, the calculated tensile creep rates from four-point bending data are compared with observed tensile creep rates for both an alumina ceramic at 1000°C and a silicon nitride ceramic at 1200°C. This study shows the usefulness of flexural creep tests not only to verify the accuracy of tensile creep tests, but also to obtain the tensile creep data in a less expensive and easier way. © 1996 Elsevier Science Limited

Introduction

A knowledge of the creep behaviour of ceramic materials is of importance in computing their lifetime at high temperatures. For brittle ceramic materials, the power-law creep parameters are commonly deduced from load–point displacement data generated by four-point bend experiments under the assumption that tensile and compressive behaviours obey the same constitutive law. However, because of the microcracking and cavitation that occur preferentially under tension, it is now well recognized[1,2] that this premise may not always be valid. Also, bend data reflect a combination of tensile and compressive responses, so individual effects of creep deformation and damage evolution cannot be distinguished readily. The real stress/strain in a flexural creep test cannot be calculated properly unless an evaluation of the creep parameters describing compressive and tensile creep is considered. Therefore, flexural creep measurements for ceramic materials are easy to perform, but difficult to analyse.

For reasons of simplicity and economy, however, ceramic tensile responses are evaluated by bend tests.[3,4] There are also rigorous efforts to estimate the uniaxial creep behaviour.[1,5] But the flexural creep tests have been analysed by the method of Hollenberg *et al.*,[6] who assumed that the neutral axis is the midplane of the flexure specimen. This approach was widely used to interpret and calculate the ceramic creep versus stress as if compressive and tensile creep behaved symmetrically in ceramic materials.[3,7]

Chuang[5] analysed flexural creep for materials whose compressive and tensile creep behaviours are not symmetrical. Using the power-law function of stress to present the strain rate in secondary creep, he presented the two governing equations to derive the location of the neutral axis of a beam under bending as related to the curvature rate. That axis does not pass through the centroid of the beam's cross-section. To solve complicated functions, he adopted an approximation method of double integration to estimate the variation of the neutral axis curvature. As pointed out by Krause,[8] Chuang's analysis is awkward to execute and its accuracy is limited to the size of the incremental step in the curvature rate generated in his approximation. Also, experimental implementation to measure accurately the curvature is extremely difficult. Therefore, many researchers[9,10] measured the creep behaviour of ceramic materials using the method of Hollenberg *et al.*[6] until recently, even though such calculations involve error if the materials behave differently in compressive and tensile creep. Indeed, Ferber *et al.*[9] found that the compressive and tensile creep properties are not symmetrical by measuring directly the compressive and tensile properties of the same material. However, they proceeded to predict values of flexural strain and flexural creep rate using the relation

that the midplane of the specimen is the neutral axis of strain. Frett *et al.*[11] also investigated the creep behaviour of a ceramic in four-point bend tests and showed the relations between the local creep state in transient and stationary creep ranges and the global deformation. They also concluded that stationary creep under compressive stresses must be negligible.

The objectives of this study are to offer a simple analytical model to estimate the tensile creep rate from four-point bending data. By introducing certain hypotheses on the creep and subsequent mathematical modelling of the situation, the experimental creep data of Ferber *et al.*[9] are recalculated and then the measured tensile creep rate is compared with the calculated tensile creep rate. Various aspects of these results are discussed. This study not only shows the usefulness of flexural creep tests to verify the accuracy of tensile creep tests, but also provides a simple way to calculate tensile creep rate during the secondary mode of creep in flexure without using the compressive and tensile properties of the same material.

A Simplified Model of Tensile Creep During Four-Point Bending

As is evident from an analysis of relevant literature,[3,8] most ceramic materials creep in tension much more easily than in compression. The presence of such creep micromechanisms as growth of pores or grain boundary sliding accounts for the difference. Recently, Frett *et al.*[11] concluded that stationary creep under compressive stresses must be negligible by measuring the expansion of the specimen after the creep test. By assuming the absence of creep in compression, this can be implemented into a model considering the limiting case and, in order to obtain a simple closed-form solution, two major assumptions are made:

(1) the material creeps only in tension and there is no creep in compression; and
(2) stress is distributed across the extended part of the cross-section as shown in Fig. 1.

Then, according to existing experimental data, the strain rate ($\dot{\varepsilon}_t$) dependence on the tensile stress (σ_t) can be approximated by a power law in the steady state as

$$\dot{\varepsilon}_t = \alpha \sigma_t^{\beta} \tag{1}$$

where α and β are the material constants and β is always >1. The creep in a flexed beam is more intensive in the volumes of material closer to the tensile surface of the beam where the stresses are higher, as shown in Fig. 1. The redistribution of stresses takes place during the initial period of creep, with a tendency to level the stress across the portion of the cross-section in tension. A rather complex computer simulation of the process of stress redistribution (Fig. 2) is published in the literature.[12] It is clear that eventually this redistribution can be approximated by a simpler one as shown in Fig. 1.

The model relationships are obtained on the basis of the following considerations. First, the central section of the beam is in pure bending; therefore, the cross-sections which were plane before deformation remain plane after deformation

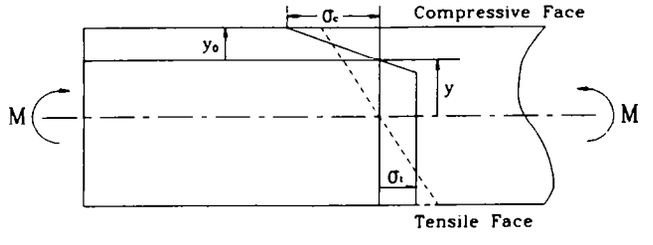

Fig. 1. Stress distribution due to bending.

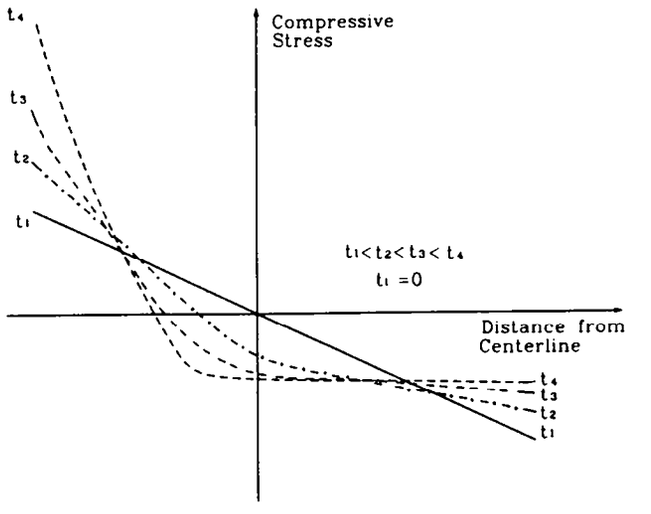

Fig. 2. Bending-stress redistribution at increasing times: t_1, t_2, t_3 and t_4 (Ref. 12).

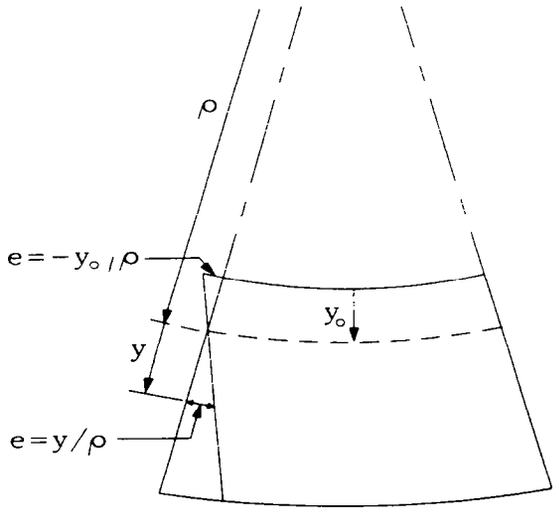

Fig. 3. Segment of a bent beam.

including creep. These sections rotate against the neutral plane, the position of which is defined by an ordinate y_0 from the outer compressed surface of the beam. A beam has a rectangular cross-section. The total beam height is h and its width is b (Fig. 3). The ordinate y_0 which before creep initiation is $y_0 = h/2$ becomes $y_0 < h/2$ and shifts monotonically towards the outer compression surface as the volumes in tension proceed to creep. A layer of the beam at distance y from the neutral layer (Fig. 3) experiences the total strain as

$$e = y/\rho \tag{2}$$

where ρ is the radius of the beam curvature. From the assumption on the absence of creep in compression and eqn (2) follows an expression for the maximum stress in compression

$$\sigma_c = Ey_0/\rho \tag{3}$$

Two equations for the balance of external forces and internal stresses in cross-section F are

$$\int_F \sigma dF = 0 \tag{4a}$$

$$\int_F y\sigma dF = M \tag{4b}$$

These can be used to establish a relationship between σ_t, the uniformly distributed tensile stress; y_0, the position of the neutral plane; M, the applied moment; and ρ, the radius of curvature. One additional assumption, when writing out the integrals in eqns (4a) and (4b), simplifies the expressions while introducing negligible imprecision for the case of well developed creep. Namely, one assumes that the tensile stress, σ_t, is distributed uniformly across the whole area in tension and not as shown in Fig. 1. The difference in calculation of integrals (4a) and (4b) is small if a well developed state of creep is considered and the area where σ_t changes is small. Then, expression (4a) can be written as

$$\sigma_t (h - y_0)b = \sigma_c y_0 b/2 \tag{5}$$

Similarly, for expression (4b) as

$$\sigma_t(h - y_0)^2 b/2 + \sigma_c y_0^2 b/3 = M \tag{6}$$

By substituting eqn (2) for eqns (5) and (6), one obtains

$$\sigma_t(h - y_0) = Ey_0^2/2\rho \tag{7}$$

and

$$\sigma_t(h - y_0)^2/2 + Ey_0^3/3\rho = M/b \tag{8}$$

Expressing σ_t from eqn (7) as

$$\sigma_t = \frac{Ey_0^2}{2(h - y_0)\rho} \tag{9}$$

and substituting for eqn (8), one obtains a cubic algebraic equation with respect to an unknown y_0 as follows

$$y_0^3 + 2h\, y_0 = 12M\rho/bE \tag{10}$$

The radius of curvature, ρ, can be found as a function of the measured displacement, Δ (see Fig. 4), as

$$\rho = L\, L_1/2\Delta \tag{11}$$

where L and L_1 are the lengths of outer and inner spans, respectively. If one assumes that the areas outside the inner span do not creep, eqns (10) and (11) allow one to find y_0 as a function of M, Δ, E and the specimen geometry. Then, σ_t is found from eqn (9). The corresponding strain rate can be found by using an expression for the maximum tensile strain

$$e_{max} = (h - y_0)/\rho \tag{12}$$

Since e_{max} consists of two components, elastic and creep,

$$e_{max} = e^e_{max} + e^c_{max} \tag{13}$$

Since the elastic one is $e^e_{max} = \sigma_t/E$ and the creep component is e_c, one then can write it as

$$\sigma_t/E + e_c = (h - y_0)/\rho \tag{14}$$

By differentiation of eqn (14) with respect to time, one can find

$$\dot{\sigma}_t/E + \dot{e}_c = -\dot{y}_0/\rho - (h - y_0)\,\dot{\rho}/\rho^2 \tag{15a}$$

from which

$$\dot{e}_c = -\dot{\sigma}_t/E - \dot{y}_0/\rho - (h - y_0)\,\dot{\rho}/\rho^2 \tag{15b}$$

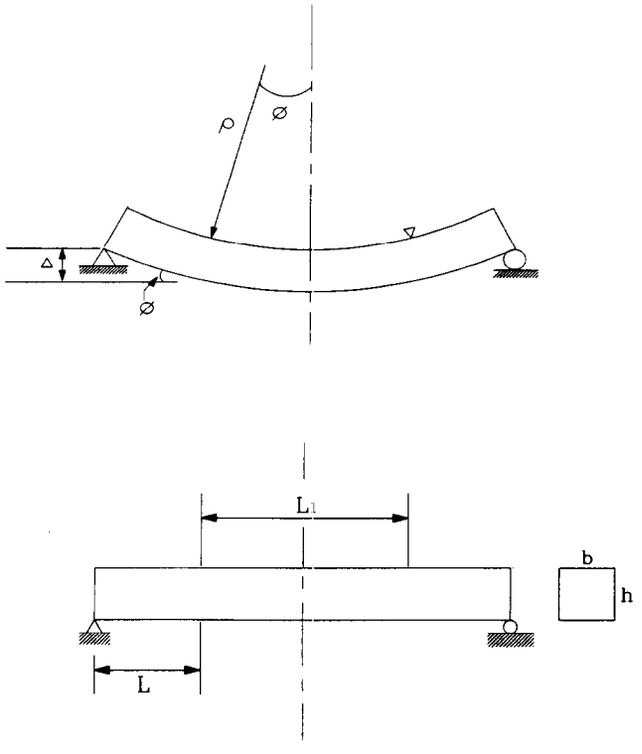

Fig. 4. Specimen geometry and deformed beam in bending.

For calculation of $\dot{\epsilon}_c$, the derivatives ρ, y_0 and σ_t in eqn (15b) can be expressed in terms of displacement rate, $\dot{\Delta}$. From eqn (11)

$$\dot{\rho} = -L\,L_1\dot{\Delta}/2\Delta^2 \tag{16}$$

By solving eqns (10) and (11), a relationship between y_0 and Δ can be established. The calculated function $y_0 = y_0(\Delta)$ is graphically presented in Fig. 5 in ln y_0 versus ln Δ coordinates for the cases of different values of modulus. The ln y_0 versus ln Δ function turned out to be linear in the range of well developed creep, i.e. ln $y_0 = k$ ln Δ + ln c where slope $k = -0{\cdot}9$ for $E = 400$ GPa, $k = -0{\cdot}88$ for $E = 300$ GPa and $k = -0{\cdot}77$ for $E = 210$ GPa. Then, the derivative y_0 can be analytically expressed through Δ as

$$\dot{y}_0 = y_0 k\dot{\Delta}/\Delta \tag{17}$$

From eqn (9), one obtains

$$\dot{\sigma}_t = -\frac{y_0^2 E}{2\Delta\rho(h-y_0)}\left[\frac{L\,L_1\dot{\Delta}}{2\Delta\rho} + \frac{(2h-y_0)k\dot{\Delta}}{(h-y_0)}\right] \tag{18}$$

By substituting eqns (16), (17) and (18) for eqn (15), one obtains the following expression for $\dot{\epsilon}_c$ in terms of $\dot{\Delta}$, y and ρ:

$$\dot{\epsilon}_c = \frac{\dot{\Delta}}{LL_1}\left[(h-y_0) - 2ky_0 - \frac{y_0^2}{(h-y_0)}\left(1+\frac{(2h-y_0)k}{(h-y_0)}\right)\right] \tag{19}$$

Discussion

In order to compare the measured tensile creep rate with the calculated tensile creep rate from four-point bending data, the model described in the previous section is applied. Ferber *et al.*[9] measured the creep rate of commercially available Al_2O_3 (AD94, Coors Ceramics, Golden, CO) at 1000°C and Si_3N_4 (SN220M Kyocera American Inc., Des Plains, IL) at 1200°C using tension, compression and flexure specimens. They found a pronounced difference in the creep deformation behaviours measured in tension and compression for both ceramics. They also found a general agreement between the flexural creep data and the predicted data from existing creep deformation models. In their paper they also used Chuang's method[5] to predict the stress dependence of the neutral axis location and specimen midspan displacement rate from the tension and compression data. But, they improperly calculated flexural creep strains directly from load–displacement rate data by assuming that the midplane of the specimen was the neutral axis of strain. Therefore, their comparison of flexural creep strain rates from the respective compression and tension tests was questionable.

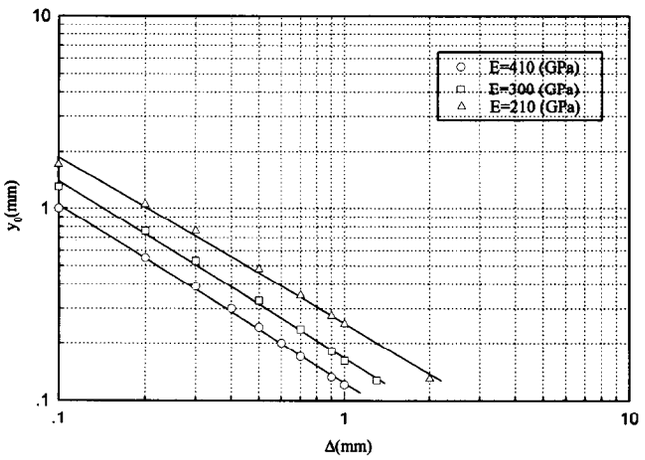

Fig. 5. Position of neutral axis as a function of modulus.

In this study, it is clear from the assumption on stress distribution (see Fig. 1) that the model should be applied only when the creep deformation reaches an advanced stage of creep. To calculate the tensile creep rate from experimental creep data under flexural loading, the measured flexural creep rate and the deflection rate should be recalculated from the data of Ferber *et al.*[9] Also, the displacement at the loading point is needed from their displacement at the centre of the sample relative to the inner load points. Then the calculated tensile creep rate according to the model described in the previous section can be compared with the experimentally measured tensile creep rate of Ferber *et al.*[9]

From the measured flexural creep rate ($\dot{\epsilon}_{max}$), the deflection rate, $\dot{\Delta}_r$, at the centre of the beam relative to the two inner load points can be calculated from a simple relation as

$$\dot{\epsilon}_{max} = 4\,h\,\dot{\Delta}_r/L_1^2 \tag{20}$$

Then, the deflection rate at the loading point is obtained from eqn (11) as

$$\dot{\epsilon}_{max} = h/2\dot{\rho} = h\dot{\Delta}/LL_1 \tag{21}$$

From the two relations and $L_1 = 2L$, one can obtain $\dot{\Delta} = 2\dot{\Delta}_r$ and similarly $\Delta = 2\Delta_r$. From the curve of creep strain for AD94 alumina measured in flexure (Fig. 4(c) in Ref. 9), the deflection at 40 h as steady-state creep in the secondary mode is calculated from the above relations. The predicted values of neutral axis position are obtained from Fig. 5 with the measured displacement. In this study, modulus values of 350 and 300 GPa are used for AD94 alumina and SN220M silicon nitride, respectively. The top half of Table 1 summarizes the experimentally obtained creep strain, displacement rate, beam deflection after 40 h of creep and values of neutral axis location associated with flexure loading. Using the above data and eqn (19), the tensile creep rate for AD94 is calculated. The lower half of Table 1 shows the same

values for SN220M after 80 h of creep. Flexural creep data of higher stress, where the material typically failed in the range of transient creep, are not used in this calculation for both materials.

In order to compare the measured tensile creep rate, invariant with time in the secondary mode of creep, with the calculated tensile creep rate from the flexural creep test, the corresponding tensile stress at the time of measurement should first be calculated. Since there is considerable stress relaxation during the creep test especially after a large deflection, it is not adequate to compare the tensile creep rate with an initial maximum applied stress. Therefore, the creep-induced stresses at the time of measurement are needed to compare with the experimental data under tensile loading. The corresponding tensile stress can be calculated from simple elastic beam theory, but considering the change of neutral axis. Since the equilibrium of the forces acting on the cross-section can be expressed by strain (ϵ) as $dF = b dy$ and $\epsilon = y/\rho$, the equilibrium equations can be written from eqn (4a) as

$$\int_{-\epsilon_c}^{\epsilon_t} f(\epsilon) d\epsilon = 0 \tag{22}$$

and from eqn (4b) as

$$\int_{-\epsilon_c}^{\epsilon_t} f(\epsilon)\epsilon d\epsilon = M(\epsilon/y)^2/b \tag{23}$$

By differentiating with respect to the curvature using Leibnitz's rule, one can obtain the outer maximum tensile stress

$$\sigma_t = \frac{\dot{M}(\epsilon + \epsilon_c) + 2M(\dot{\epsilon}_t + \dot{\epsilon}_c)}{h^2\dot{\epsilon}_t} \tag{24}$$

For a small deflection of the beam under a static bending test, the change of moment is assumed to be zero. Then one can rearrange eqn (24), since $\epsilon_t = (h - y_0)/\rho$ and $\epsilon_c = y_0/\rho$, from eqns (16) and (17) as

$$\sigma_t = \frac{FL}{h[(h - y_0) - ky_0]} = \frac{2M}{bh[(h - y_0) - ky_0]} \tag{25}$$

Assuming that the initial strain prior to creep deformation is linear elastic, the initial stress (σ_i) that exists on the tension side is defined by

$$\sigma_i = 6M/bh^2 \tag{26}$$

After obtaining the applied moment from the initially applied stresses and using the data in Table 1, the creep-induced stresses (σ_t) at the time of measurement are obtained and shown in Table 2. Then the tensile creep rate is calculated using eqn (19) in the previous section. Figures 6 and 7 show the predicted stress dependence of tensile creep rates for AD94 alumina and SN220M silicon nitride, respectively, compared with experimental data. Even though the calculated tensile creep rates are not exactly as the measured data, the figures show reasonable fit for both ceramics. Considering the original strain analysis is done from a simple elastic relation for small deflection, the values of displacement and displacement rate may be different. The

Table 2. Applied moment, calculated creep-induced stress and predicted stress values by Ferber *et al.*[9] associated with flexure loading

	σ (*MPa*)	M (*N mm*)	σ_t (*MPa*)	σ_f (*MPa*)
AD94 Alumina	80	480	26·9	39·0
	60	360	22·8	31·5
	50	300	17·4	27·5
SN220M Silicon Nitride	80	480	33·42	40·6
	60	360	25·3	32·2
	50	300	20·6	27·0

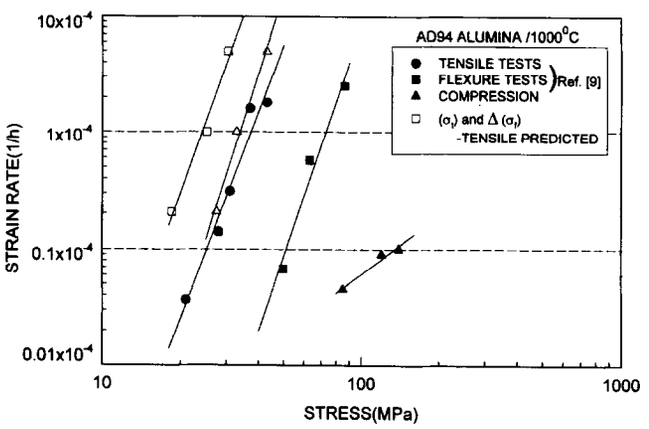

Fig. 6. Stress dependence of creep rate for AD94 alumina at 1000°C.

Table 1. Elastic stress, measured creep strain, displacement rate at measuring point and loading point, predicted neutral position and steady state creep rate associated with flexure loading.

	σ (*MPa*)	$\dot{\epsilon}$ ($^{-1}$) ($\times 10^{-4}$)	$\dot{\Delta}_r$ (*mm h*$^{-1}$)	$\dot{\Delta}$ (*mm*)	y_0 (*mm*)	Δ (*mm*)	$\dot{\epsilon}_c^{-1}$ ($\times 10^{-4}$)
AD94 Alumina	80	2·50	0·0094	0·0188	0·35	0·3	5·02
	60	0·57	0·0020	0·0040	0·4	0·29	1·07
	50	0·069	$2·0 \times 10^{-4}$	$4·0 \times 10^{-4}$	1·5	0·07	0·22
SN220M Silicon Nitride	99	3·50	0·0106	0·0212	0·38	0·5	5·62
	77	1·6	0·00555	0·0111	0·37	0·45	3·06
	60	1·0	0·00347	0·0069	0·52	0·3	2·00

modulus values used in the calculation might not be the same as those of the tested materials, even though changes can be small. Also, it is difficult to measure accurately the creep rate of ceramic materials at high temperature. These can be the sources of a small discrepancy as shown in Figs 6 and 7.

The creep-induced stress along the tensile surface of the flexure samples was calculated by Ferber *et al.*[9] using estimated values of the material constants α and β for both compression and tension, the location of the neutral axis and the predicted flexural creep strain rate as given in their eqns (5a) and (5b). Table 2 shows a comparison between the creep-induced stresses (σ_f) obtained by Ferber *et al.*[9] and σ_t from eqn (25). The stress drop associated with the effect of the creep-induced stress relaxation is large, as shown in Table 2, the values obtained by eqn (25) being a little more severe than the values obtained by Ferber *et al.*[9] However, the values of tensile creep rate obtained from σ_f show the better fit than the creep data obtained from σ_t by eqn (25) when compared with experimental tensile data, as shown in Figs 6 and 7. But their analysis involved not only using the questionable predicted values, but also experimental data of tension and compression, and time-consuming calculation. Therefore, the use of their predicted values should be reconsidered. However, one needs more experimental data of creep — tensile and flexural — on the same materials to verify the relations between σ_t and σ_f. Ferber *et al.*[9] tried to verify this stress relaxation by measuring the short-term strength of samples before and after creep testing at high temperature. The systematic tests of this kind can be useful to verify it. However, the creep-induced tensile stress calculated using eqn (25) is simple and does not involve the use of estimated and experimental values under compression and tension. Frett *et al.*[11] also tried to obtain the creep-induced tensile stress as a function of time after loading, but there is a strange hump around 10 h of loading and so their results are not compared with data of this work. In a previous paper,[13] the creep rates of six ceramics were measured in four-point bending at 1100°C and the tensile creep rate was calculated. Using those data and the tensile creep rate of these ceramics, the creep-induced stress will be discussed elsewhere in detail.

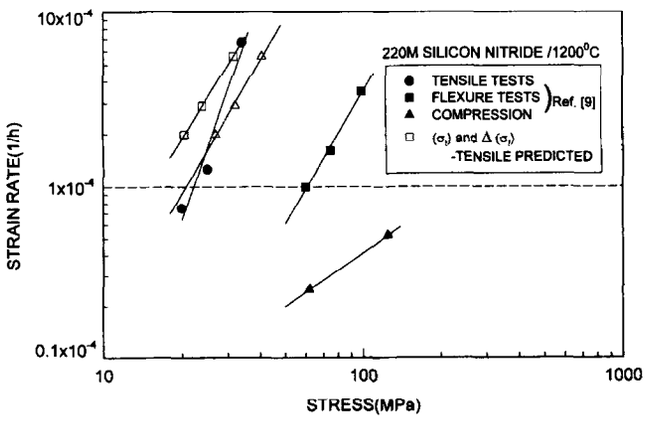

Fig. 7. Stress dependence of creep rate for SN 220M silicon nitride at 1200°C.

Recently, Krause[8] recalculated experimental data of Ref. 9 to compare the observed and theoretical values of the normalized curvature rate versus bending moment, and concluded that stresses and strains during secondary creep tests in flexure cannot be properly calculated unless an evaluation of the compressive and tensile creep properties is appropriately considered. Flexural creep tests, however, can be used to verify the accuracy of tensile creep tests on a material. This analysis shows the way to determine the tensile creep behaviour of a material using the flexural creep test in a simple way. Since ceramics do creep in compression, a new model considering the influence of compressive creep, even though it will be extremely small, will be developed.

For more accurate and easier testing of ceramic creep in four-point bending as mentioned by Hollenberg *et al.*,[6] it is believed that use of the three probes required in measuring Δ_r deflections at three points is more complex and prone to experimental difficulties than the two-probe scheme used in this work. If there is a limitation of any kind and one needs tensile creep data, then as an alternative way that is less expensive and easier to perform, a simple procedure of four-point loading using eqn (19) and load-point deflection (Δ) should be used.

Conclusion

A novel method of flexural creep analysis has been developed to calculate the tensile creep rate in a simple way. The calculated tensile creep data are compared with experimental tensile creep data on the same ceramic materials. Based on a few assumptions about flexure creep, only the displacement rate, invariant with time in the secondary mode of creep, and beam deflection in four-point bending are needed to calculate the tensile creep rate. After obtaining the creep-induced tensile stress that corresponds to the applied tensile stress in the steady state of secondary creep, the tensile creep rate is compared with experimental creep data. These data show a reasonably good agreement for Al_2O_3 and Si_3N_4 ceramics. Therefore, the flexural creep test can be used not only to obtain the tensile creep rate but

also to verify the accuracy of the tensile creep test data. Flexural creep tests are much less expensive and easier to conduct for ceramic materials than tensile creep tests.

References

1. Rosenfield, A. R., Shetty, D. K. & Duckworth, W. H., Estimating tensile creep data from flexure data. *J. Am. Ceram. Soc.*, **69**[5] (1986) C108–9.
2. Carroll, D. F., Chuang, T. J. & Weiderhorn, S. M., A comparison of creep rupture behavior in tension and bending. *Ceram. Eng. Sci. Proc.* **9**[7–8] (1988) 635–42.
3. Chuang, T. J. & Weiderhorn, S. M., Damage-enhanced creep in a siliconized silicon carbide: mechanics of deformation. *J. Am. Ceram. Soc.*, 7[7] (1988) 595–601.
4. Talty, P. K. & Dirks, R. A., Determination of tensile and compression creep behavior of ceramic materials from bend tests. *J. Mater Sci.*, **13** (1978) 580–6.
5. Chuang, T. J., Estimation of power-law creep parameters from bend test data. *J. Mater. Sci.*, **21** (1986) 165–75.
6. Hollenberg, G. W., Terwilliger, G. R. & Gordon, R. S., Calculation of stresses and strains in four-point bending creep tests. *J. Am. Ceram. Soc.*, **54** (1971) 196–9.
7. Lin, H. T. & Becher, P. F., Creep behavior of a SiC-whisker reinforced alumina. *J. Am. Ceram. Soc.*, **73** (1990) 1378–81.
8. Krause, R. F. Jr, Observed and theoretical creep rate for an alumina ceramic and a silicon nitride ceramic in flexure. *J. Am. Ceram. Soc.*, **75**[5] (1992) 1307–10.
9. Ferber, M. K., Jenkins, M. G. & Tennery, V. J., Comparison of tension, compression and flexure creep for alumina and silicon nitride ceramic. *Ceram. Eng. Sci. Proc.*, **11**[7–8] (1990) 1028–45.
10. Jou, Z. C. & Virkar, A. V., High temperature creep and cavitation of polycrystalline aluminum nitride. *J. Am. Ceram. Soc.*, **73**[5] (1990) 1928–35.
11. Frett, T., Keller, K. & Munz, D., An analysis of the creep of hot pressed silicon nitride in bending. *J. Mater. Sci.*, **23** (1988) 467–74.
12. Dryden, J. R. & Watt, F., Re-distribution of stresses during creep-bending of grain boundary sliding materials. In *Proceedings of Surfaces and Interfaces in Ceramic and Ceramic–Metal Systems. Mater. Sci., Res.*, **19** (1981) 105–13.
13. Lee, D. J. & Palley, I., Tensile creep in ceramics using four-point bending test. *KSME J.*, **8**[3] (1994) 325–31.

Journal of the European Ceramic Society **16** (1996) 1385–1387

0955-2219/96/$15.00

Contributor Index

Journal of the European Ceramic Society **16** (1996) 1389–1398

0955-2219/96/$15.00

Contents of Volume 16

Number 1

Number 2

Number 3

Number 4

Number 6

Short Reports

Number 7

Number 10

Number 11

Number 12

JOURNAL OF THE EUROPEAN CERAMIC SOCIETY

The *Journal of the European Ceramic Society* publishes the results of original research relating to the structure, properties and processing of ceramic materials. Papers of either an experimental or theoretical character will be welcomed on a fully international basis. Papers may cover any of the branches of ceramic science and technology and may relate to any of the so called categories, structural, functional and traditional ceramics. The central objective will be to sustain a high standard of research quality by means of appropriate reviewing procedures.

SUBSCRIPTIONS

1996—One volume, 12 issues per volume (Volume 16). Annual Institutional Subscription Rates 1996: £625.00/US$994.00. **Members of the European Ceramic Society can subscribe to the journal at the special rate of £110.00/US$175.00.** Subscription prices exclude VAT. Non-VAT registered customers in the European Community will be charged the appropriate VAT in addition to the price listed. Prices include postage and insurance and are subject to change without notice. All journals are distributed worldwide by air-speeded delivery at no extra cost to the subscriber. US Mailing Agent: USA Postmaster: Second Class postage paid at Newark, New Jersey and additional entry points. The *Journal of the European Ceramic Society* (ISSN 0955-2219) is published monthly, January to December in one volume, by Elsevier Science Ltd, The Boulevard, Langford Lane, Kidlington, Oxford OX5 1GB, UK. The annual subscription in the USA is $994. The *Journal of the European Ceramic Society* is distributed by Virgin Mailing and Distribution, 10 Camptown Road, Irvington, New Jersey 07111-1105. POSTMASTER: Please send address corrections to *Journal of the European Ceramic Society*, c/o Elsevier Science Inc., 660 White Plains Road, Tarrytown, NY 10591-5153.

Subscription orders should be addressed to:

THE OXFORD FULFILMENT CENTRE
PO Box 800, Kidlington, Oxford, OX5 1DX, England

In the United States and Canada: For further information contact:

Elsevier Science Inc., 660 White Plains Road,
Tarrytown, NY 10591-5153, USA